MULTIAXIAL FATIGUE

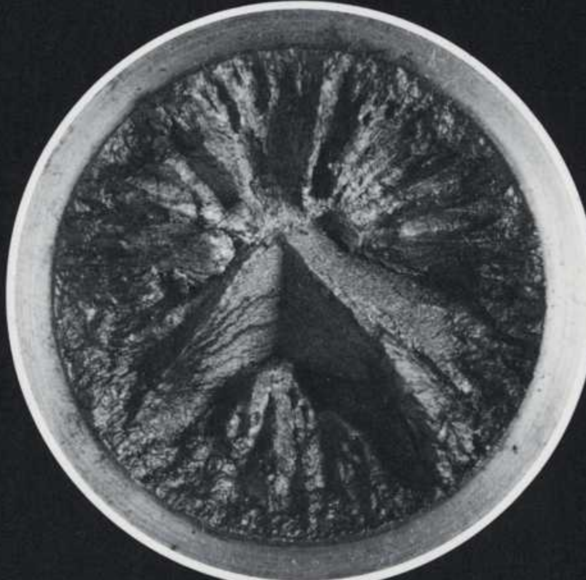

Miller / Brown
editors

ASTM STP 853

MULTIAXIAL FATIGUE

A symposium
sponsored by ASTM
Committees E-9 on Fatigue
and E-24 on Fracture Testing
San Francisco, CA, 15–17 Dec. 1982

ASTM SPECIAL TECHNICAL PUBLICATION 853
K. J. Miller and M. W. Brown, University of
Sheffield, editors

ASTM Publication Code Number (PCN)
04-853000-30

1916 Race Street, Philadelphia, PA 19103

Library of Congress Cataloging-in Publication Data

Multiaxial fatigue.

(ASTM special technical publication; 853)
"ASTM publication code number (PCN) 04-853000-30."

Includes bibliographies and index.
1. Materials—Fatigue—Congresses. I. Miller, K. J. (Keith John) II. Brown, M. W. (Michael W.), 1947- . III. American Society for Testing and Materials. Committee E-9 on Fatigue. IV. ASTM Committee E-24 on Fracture Testing. V. Series.
TZ418.38.M85 1985 620.1'126 85-7376
ISBN 0-8031-0444-8

Copyright © by AMERICAN SOCIETY FOR TESTING AND MATERIALS 1985
Library of Congress Catalog Card Number: 85-7376

NOTE

The Society is not responsible, as a body,
for the statements and opinions
advanced in this publication.

Printed in Ann Arbor, MI
August 1985

Foreword

This publication, *Multiaxial Fatigue,* contains papers presented at the symposium on Biaxial/Multiaxial Fatigue which was held in San Francisco, California, 15–17 December 1982. The symposium was sponsored by ASTM Committees E-9 on Fatigue and E-24 on Fracture Testing in cooperation with the American Society of Mechanical Engineers, the American Society for Metals, and the Society of Automotive Engineers. K. J. Miller, University of Sheffield, J. R. Ellis, Oak Ridge National Laboratory, and M. W. Brown, University of Sheffield, presided as symposium chairmen. K. J. Miller and M. W. Brown are editors of this publication.

Related ASTM Publications

Methods and Models for Predicting Fatigue Crack Growth Under Random Loading, STP 748 (1981), 04-748000-30

Fatigue Crack Growth Measurement and Data Analysis, STP 738 (1981), 04-738000-30

Effect of Load Variables on Fatigue Crack Initiation and Propagation, STP 714 (1980), 04-714000-30

Part-Through Crack Fatigue Life Prediction, STP 687 (1979), 04-687000-30

Fatigue Crack Growth Under Spectrum Loads, STP 595 (1976), 04-595000-30

A Note of Appreciation to Reviewers

The quality of the papers that appear in this publication reflects not only the obvious efforts of the authors but also the unheralded, though essential, work of the reviewers. On behalf of ASTM we acknowledge with appreciation their dedication to high professional standards and their sacrifice of time and effort.

ASTM Committee on Publications

ASTM Editorial Staff

Helen M. Hoersch
Janet R. Schroeder
Kathleen A. Greene
Bill Benzing

Contents

FORMATION AND GROWTH OF SHORT CRACKS

Introduction

Multiaxial fatigue is a subject of concern to both engineers and research scientists. In the eventuality of failure, fatigue lifetime is determined in the majority of cases by the applied multiaxial stress-strain state, whether generated by multiple loading or the component geometry itself. Thus multiaxial stresses should be taken into consideration by the designer, and it is important to note that material data generated in laboratories under constrained situations (for example, uniaxial loading or Mode I crack growth specimens) cannot be used in practice without recourse to some multiaxial criterion. The introduction of stresses on two or three axes in fatigue experiments, therefore, can provide valuable insight concerning both the micromechanisms of fatigue crack formation and growth and also the uses and limitation of multiaxial correlation factors.

The multiaxial behavior of metals has been studied throughout the twentieth century, and the engineers concern with the fatigue limit in the design of safe structures has led to a number of useful criteria which were developed prior to 1960, based on, for example, the pioneering work of Gough and Sines. Two more recent developments associated with the finite life of structures are fracture mechanics and life prediction techniques for high-strain fatigue, both of which have required the development of additional criteria. In these cases a knowledge of the extent of plastic deformation is important since inelastic strains are used not only in low cycle fatigue analyses but also in advanced elastic-plastic fracture mechanics. However, a number of problems remain to be solved, since fatigue cracks are invariably associated with notches or surface defects, and frequently experience aggressive environments.

This volume presents a number of papers which were read at the International Symposium on Biaxial/Multiaxial Fatigue, sponsored by the American Society for Testing and Materials in collaboration with the American Society of Mechanical Engineers, the American Society for Metals and the Society of Automotive Engineers. The need for a conference was recognized in 1979 after preliminary discussions in Sheffield between the editors and European friends, but, because much new work in multiaxial fatigue had been funded by the Nuclear Regulatory Commission in Washington, it was thought proper to approach ASTM to see if they would sponsor the event in the USA. First contacts were made at the Bal Harbour meeting in Florida in 1980 via such people as Jane Wheeler and Don Mowbray. The three day meeting, held in San Francisco in December 1982, led to many stimulating discussions among the delegates from several

www.astm.org

countries, many of whom are actively involved in different aspects of the multiaxial problem. It was apparent that a variety of approaches are now being developed, and this book summarizes the current state of the art in each area of concern.

The 38 papers have been divided into eight groups, of which the first two present the various tools available to the materials scientist, that is, laboratory testing followed by the characterization of cyclic deformation response and the stress analysis of cracks. The importance of fatigue crack development, in terms of both the propagation rate and the plane and direction of growth, is highlighted by papers on mixed mode cracking and short cracks in metals. The group of papers on composite materials illustrates other mechanisms of damage accumulation. Life prediction techniques have been broadly based on crack development concepts, and new methods are compared with the older criteria and current design codes, showing that the new methods have much potential. Two areas requiring more attention are nonproportional stressing and elevated temperature aspects such as creep fatigue. Apart from these topics many other problems remain, but this volume shows that significant progress has been achieved towards predicting finite fatigue life behavior, and it should provide a useful aid in interpreting failures and understanding the mechanics of fatigue.

The success of the symposium and the production of this book would not have been possible without the hard work and support of the ASTM staff. We would also like to thank our able cochairman, J. R. Ellis, and the invaluable assistance of B. N. Leis in editorial matters subsequent to the symposium. Both have given much time and generous advice. The detailed work of the reviewers has greatly strengthened many papers presented here, and we appreciate the assistance of session chairman, the international group of experts who supported the symposium, ASTM committees E-9, and E-24 who sponsored the conference, and the staff of the Mechanical Engineering Department of the University of Sheffield.

K. J. Miller
M. W. Brown
Department of Mechanical Engineering, University of Sheffield, Sheffield, U.K. symposium chairmen and editors.

General Discussion

Henry O. Fuchs[1]

On the Definition of Planes of Maximum Shear Strain

REFERENCE: Fuchs, H. O., **"On the Definition of Planes of Maximum Shear Strain,"** *Multiaxial Fatigue, ASTM STP 853,* K. J. Miller and M. W. Brown, Eds., American Society for Testing and Materials, Philadelphia, 1985, pp. 5–8.

ABSTRACT: The concept of planes of strain is contrary to accepted definitions. "Planes of maximum shear strain" are defined as planes normal to the lines of maximum shear strain. They are the same as planes of maximum shear stress. The latter designation is unambiguous, simple, and in accord with accepted definitions. It is proposed that the designation "planes of maximum shear stress" be used unless it can be shown that planes of maximum shear strain are different from the former and more important as fatigue variables.

KEY WORDS: planes, shear strains, multiaxial fatigue, definitions

Several papers in this symposium refer to planes of maximum shear strain. This concept deserves careful examination.

Strictly speaking strains are not related to planes but to directions, while stresses are related to the planes on which the forces are acting. Stresses are defined as forces per unit area, for example, newtons per square metre (N/m^2). For a given state of stress the direction of the area determines the stress and its components. Stresses can not be seen nor measured directly.

Strains are defined as relative changes in length of line segments (normal strains) or as changes in angle between two initially perpendicular lines (shear strains). They can be measured by strain gages, or seen by the change in shape and size of small circles or squares marked on surfaces.

Figure 1 shows strains on the surface of a twisted circular bar. This surface is free of stress, but the amount of shear strain visible or measureable on it is greater than on any other plane in the bar. However, this is not the plane of maximum shear strain to which the papers in this symposium refer.

The maximum shearing stresses in the bar of Fig. 1 occur on transverse and on axial planes through a point on the surface. These are also the "planes of maximum shear strain" to which many authors in this volume refer. To define them in terms of strain we might say that they are two planes, each perpendicular

[1] Professor, Mechanical Engineering Department, Stanford University, Stanford, CA 94305.

Copyright© 1985 by ASTM International www.astm.org

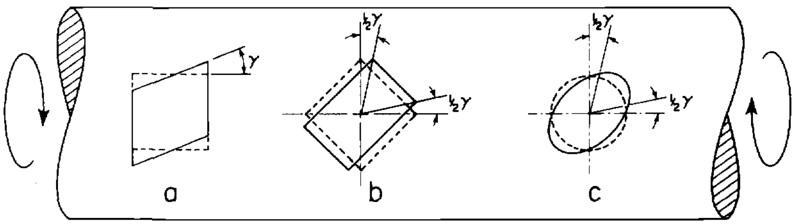

(*a*) Deformation of a square.
(*b*) Deformation of another square.
(*c*) Deformation of a circle.

FIG. 1—*View of shear strains on a twisted shaft. (Solid lines show final position, dashed lines show original position.)*

to one of the initial directions of the lines which between them show the maximum shear strain. They will be called *P*-planes in this note.

Note that sigma and epsilon are clearly positive or negative. Gamma is an absolute value because the previously right angle between two lines becomes acute in two quadrants but obtuse in the two other quadrants when the strain gamma is applied. An arbitrary sign convention can of course be defined when desired, but its definition must be explicit as it is not implied in the physical events. Similarly an arbitrary sign convention is used to define the algebraic value of tau.

The use of strains rather than stresses as fatigue criteria has obvious advantages when the deformations are largely plastic, as in low-cycle fatigue; this need not prevent identification of critical planes by reference to stresses, and identification of crack growth direction by reference to stress direction. Combined stress-strain criteria can be useful.

The writer urges careful definition of the concepts used in discussion of

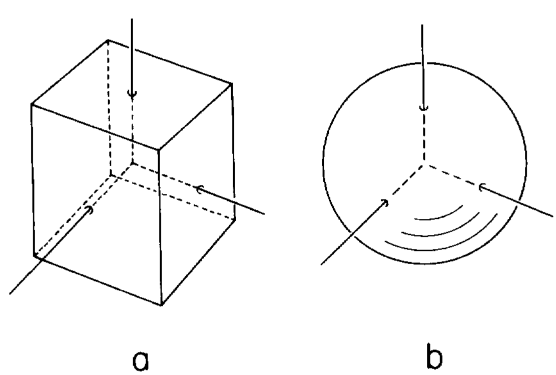

(*a*) According to Tresca
(*b*) According to von Mises

FIG. 2—*Yield criteria in shear stress space.*

multiaxial fatigue. He suggests that planes of stress and directions of maximum shear stress are much easier to define than planes and directions of maximum shear strain. He proposes that planes and directions of shear stress be used rather than "planes of maximum shear strain" at least until there is evidence that P-planes can be different from and more critical than planes of maximum shear stress.

In all cases which the writer was able to imagine the P-planes are also planes of maximum shear stress. To call them planes of maximum shear stress would have two advantages: It would avoid ambiguity and it would permit easy consideration of the direction of shear stress which is important for the direction of growth of cracks. The direction of shear strain on the P-planes would need a special new definition.

In connection with the directions of shear strains it is interesting to recall the now obsolete definition which von Mises used when he proposed the yield criterion known by his name.[2] He used a shear stress space in which the principal shear stresses are the coordinates. In such a space the Tresca yield criterion is a cube, the von Mises criterion is a sphere, as in Fig. 2. A similar method might be required to define directions of shear strain.

In some theories of multiaxial fatigue Mohr's circles of strain are used. They are similar to Mohr's circles of stress, but the meaning of directions in them is quite different: In the stress circle a radius at angle X from a principal stress direction defines a plane at angle $(X/2)$ from the plane of principal stress. In

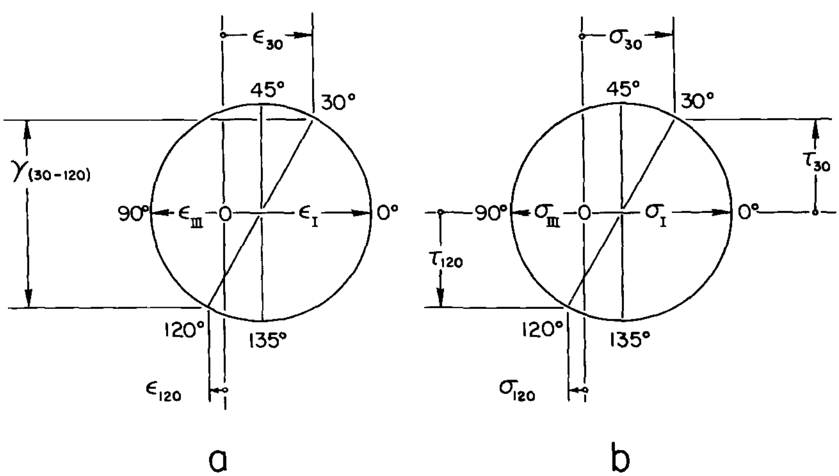

(*a*) For strains.
(*b*) For stresses.

FIG. 3—*Mohr's circles.*

[2]von Mises, R., *Nachrichten der Gesellschaft der Wissenschaften,* Gottingen, Mathematisch-Physikalische Klasse, 1913, p. 582.

the strain circle one must consider diameters, not radii. A diameter at angle Y from a direction of principal normal strain defines two lines in the plane of two principal normal strains, one at angle $(Y/2)$ from the reference direction, the other at $(Y/2 + 90°)$. The shear strain between those two lines is proportional to the vertical distance between the end points of that diameter, as shown in Fig. 3.

Multiaxial Fatigue Testing

Michael S. Found,[1] Upul S. Fernando.[1] and Keith J. Miller[1]

Requirements of a New Multiaxial Fatigue Testing Facility

REFERENCE: Found, M. S., Fernando, U. S., and Miller, K. J., "**Requirements of a New Multiaxial Fatigue Testing Facility,**" *Multiaxial Fatigue, ASTM STP 853,* K. J. Miller and M. W. Brown, Eds., American Society for Testing and Materials, Philadelphia, 1985, pp. 11–23.

Abstract: A new multiaxial fatigue testing facility is described. It can strain a thin-walled tubular specimen in three independently controlled loading modes by the use of torsion, axial load, and internal and external pressure. Any stress state having a principal stress ratio between equibiaxial ($\lambda = +1$) and torsion ($\lambda = -1$) with any orientation of the maximum principal stress and the specimen axis can be chosen, with a maximum principal stress of 700 MN/m^2. The significance of specimen geometry is examined in relation to multiaxial fatigue testing and the design of a suitable specimen is discussed. Test data for a 1Cr-Mo-V steel are presented to show the variation in multiaxial fatigue results for similar stress states obtained using different test systems and specimen geometries. The possibility of undertaking wider investigation of the effects of anisotrophy and cumulative damage is discussed.

KEY WORDS: biaxial stresses, triaxial stresses, fatigue strength, high pressure, specimen geometry, crack propagation, orientation, anisotropy, accumulative damage

Fatigue failures are still perhaps the commonest mode of failure among engineering components and structures despite the generation of a wealth of test data on the subject over many decades of research. However most of these data have been obtained from laboratory experiments involving uniaxial loading conditions which are seldom present in practical engineering situations. For example, components and structures found in power and chemical plants, such as pressure vessels and piping systems, aircraft structures, turbine blades, and drive shafts are subjected to multiaxial stress conditions during cyclic loading. Many components are exposed to varying degrees of multiaxial strain especially at notches or geometric discontinuities. In order to apply these limited fatigue data to more complex stress conditions attempts have been made to correlate multiaxial fatigue loading to an equivalent uniaxial fatigue loading condition as suggested in some design codes [*1*,*2*].

It is now generally recognized that fatigue is concerned with the initiation and

[1]Lecturer, research assistant, and professor, respectively, Department of Mechanical Engineering, University of Sheffield, Sheffield, U.K.

Copyright© 1985 by ASTM International www.astm.org

growth of a crack to a critical size. Multiaxial fatigue is concerned with the effect of biaxial and triaxial stresses or strains on the orientation and growth rate of cracks on the lifetime of a component. For example, under torsional loading cracks propagate along the surface, while in the reversed bending of flat plates crack growth is through the thickness, and therefore normally more dangerous. In both these cases the equivalent stress or strain may be similar, but the number of cycles to cause failure will be quite different. Brown and Miller [*3*] have shown that under multiaxial loading conditions fatigue endurance is governed by the maximum shear strain and the tensile strain normal to the plane of maximum shear. Furthermore, the orientation of the surface to this plane is important since this defines either Type A or Type B cracks, which may propagate in both Stage I and Stage II phases of crack growth. The principal strain values do not fully describe the fracture process under multiaxial fatigue since it is possible for similar strain conditions to give different fatigue lives. A similar approach has been used by Lohr and Ellison [*4*] to analyze cracks growing away from the surface under in-phase loading conditions. They have shown that fatigue crack growth rate is controlled by the maximum shear strain on planes driving the crack through the thickness and that the direct strain acting normal to the plane of maximum shear exerts a secondary modifying influence.

Analysis of the results of available published data indicates that there is a need for a multiaxial fatigue testing facility that will (*a*) permit the coverage of all 3-D stress-strain states from pure torsion through the uniaxial state and plane strain to the equibiaxial strain state, and (*b*) apply these 3-D stress-strain states at any desired angle to the specimen axis. This paper briefly reviews existing multiaxial fatigue systems and outlines the design requirements for a new testing facility presently being installed in the Department of Mechanical Engineering at the University of Sheffield.

Multiaxial Fatigue Systems

With the development of servohydraulic testing machines and associated closed-loop control systems it is now possible to perform fatigue tests under complex stress-strain conditions by various means. It is intended here to mention briefly some of these loading methods, a more comprehensive description being given by Refs *5–7*. The test methods may be divided into two distinct categories; one in which a single load system is used with specimens of variable geometry to obtain different biaxial stress states and the other in which the biaxial stresses are obtained by applying two or more loads to a specimen of fixed geometry. Examples of the first category are cantilever bending, anticlastic bending, and bulge tests of flat plate specimens, pressurized tubes, and rotating disks. The second category includes tension-torsion, tension-pressure, and tension-torsion-pressure of tubular specimens, uniaxial tests plus hydrostatic pressure and cruciform specimen loading [*5–7*].

The first grouping, with the exception of the rotating disk experiment, requires relatively simple test facilities together with suitable loading fixtures. Features of these methods are the ease of control of test parameters and of the measurement of load and deflection. However the major disadvantage is the problem of interpretation of the results. In addition to difficulties in determining the stress-strain distribution and the effect of stress gradients in each specimen geometry the use of a different geometry itself may influence the fatigue life due to variations in crack initiation and propagation behavior. Therefore, these test methods are only suitable for evaluating similar stress-strain conditions.

For the second grouping more expensive servohydraulic test systems are usually necessary since accurate control and load and strain measurements are required. With the exception of the tension-torsion test and the cruciform specimen, all these methods involve direct fluid pressure on the specimen which creates additional problems. Fatigue endurance will be reduced due to the hydrowedge effect, and there may be also an environmental influence on crack initiation and propagation due to the fluid. However these effects may be minimized by the use of a suitable protective sleeve. For the complex geometry of the cruciform specimen, stress and strain measurement is difficult, and it is usually necessary to determine the stress-strain distribution in the test section by elastic-plastic finite element analysis.

In order to compare the influence of both stress-strain state and the orientation of the principal strains on fatigue behavior it is necessary to perform all tests over the complete range of biaxial stress states under similar conditions. This highlights the need for a single test facility which will permit any stress-strain state with respect to any principal stress orientation to be obtained on the same specimen geometry [*8*]. A number of important requirements have been identified [*9*] for an ideal multiaxial fatigue testing facility, and these are summarized next.

1. Coverage of the complete range of biaxial/multiaxial stress states using a single specimen geometry.
2. Control of the orientation of the principal stresses independent of the biaxial stress states and provision of a complete range of biaxial stress states with respect to any principal orientation.
3. Uniform stress-strain distribution over the gage length with minimum strain concentration at the end of the gage section.
4. Stable specimen response for all stress states with a means of accurately determining stresses and strains in the gage area.
5. Continuous controlling, monitoring, and recording of stresses and strains in each principal direction.
6. Flexibility in defining and controlling the fatigue load cycle with provision for the following functions:
    (*a*) Choice of control mode; load, strain, or displacement.
    (*b*) Independent control over each principal load to permit in-phase or out-of-phase loading.

(*c*) Independent adjustments for mean value and amplitude of stress and strain in each principal direction.
(*d*) Selection of cycle waveform and frequency.
(*e*) Block programming facilities.

7. Elevated temperature facility.
8. Observation of the specimen during test.

Two possible methods of obtaining most of these requirements were considered; namely, a modified cruciform specimen and a tubular specimen subjected to torsion, axial load, and internal/external pressure. Using an hexagonal shaped specimen with six loading arms it is possible to apply three independent axial loads to obtain the desired stress state. With this specimen it is difficult to perform an accurate stress-strain analysis, and control of the loads in the individual arms is complex due to the constraints of the other arms. However such a test method permits observation of the specimen during testing and is suitable for elevated temperature work.

The thin-walled tubular specimen is a simpler geometry enabling accurate stress-strain analysis even in the plastic range. The torsion and axial loads can be applied without mutual interaction, and the axial stress component due to pressurization can be monitored and easily corrected. However it is not possible to observe the specimen during testing, precise measurement of strain in the gage length can be difficult, and the maximum temperature is limited by the properties of the pressurizing medium. Fatigue of thin-walled tubes is highly influenced by their machining history, especially grinding. However, it is thought that by careful polishing of the gage length and honing of the bore this problem could be minimized. Consideration of these facts indicated that a thin-walled tubular specimen would best meet our requirements.

Multiaxial Fatigue Machine

The new multiaxial fatigue testing machine is capable of straining a thin-walled tubular specimen in three independently controlled loading modes, namely, torsion, axial load, and internal and external pressure. By applying axial load and internal/external pressure any biaxial stress-strain state with fixed principal directions can be produced. The orientation of the principal stresses is rotated by superimposing a torsional load; hence, cracks may be generated on any required plane. The loading systems are continuously and independently controlled so that fully reversed predetermined biaxial stresses may be applied in any direction on the specimen. The use of pulsating external pressure as well as internal pressure permits a greater combination of mean and alternating hoop stress to be explored, and the effect of mean stress on fatigue can be controlled. Therefore, any stress state having a principal stress ratio λ between equibiaxial ($\lambda = +1$) and pure shear ($\lambda = -1$) with any orientation α of the maximum principal stress to the specimen axis can be chosen (Fig. 1), with a maximum

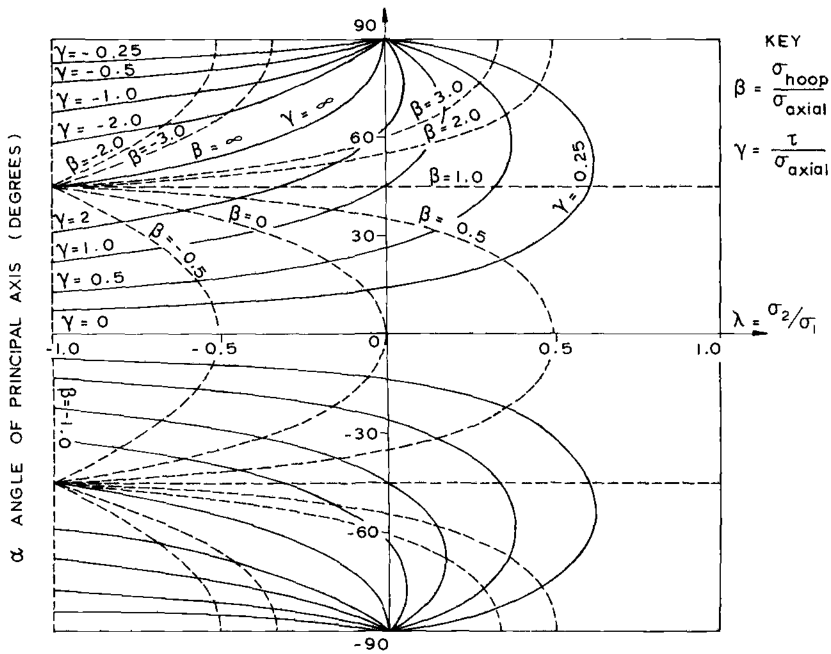

FIG. 1—*Contours of various stress states that can be induced in a single specimen by the fatigue machine.*

principal stress value of up to 700 MN/m^2. For a limited range of stress states it is possible to achieve a maximum principal stress of up to 1000 MN/m^2.

The rig comprises of a loading frame, pressure vessel, hydraulic power pack, and electronic controls. The loading frame is a Schenck four column tension-torsion fatigue testing machine which provides axial and torsional loads of up to ±400 kN and ±1 kNm, respectively. The specimen is held between two identical chucks using two specimen holders. The upper chuck is connected to the upper crosshead of the load frame via the upper sealing rod and the tension-torsion load cell. The lower chuck is attached via the lower sealing rod to the tension-torsion actuator which is fixed to the base of the loading frame as shown in Fig. 2*a*. The specimen and attached components are enclosed in a pressure vessel (Fig. 2*b*) which is fixed to the lower crosshead and has the freedom to move vertically along the specimen axis permitting specimen assembly to take place on the machine. The pressure vessel end closures can be readily disconnected, thus allowing the vessel to move down without affecting the dynamic seals on the upper and lower sealing rods, and hence avoiding any possible damage that could cause oil leakage.

The loading frame and load carrying components are much stiffer than the specimen. Therefore, the alignment of the upper sealing rod (that is, the load cell) to the lower sealing rod (that is, the actuator) is maintained even when the

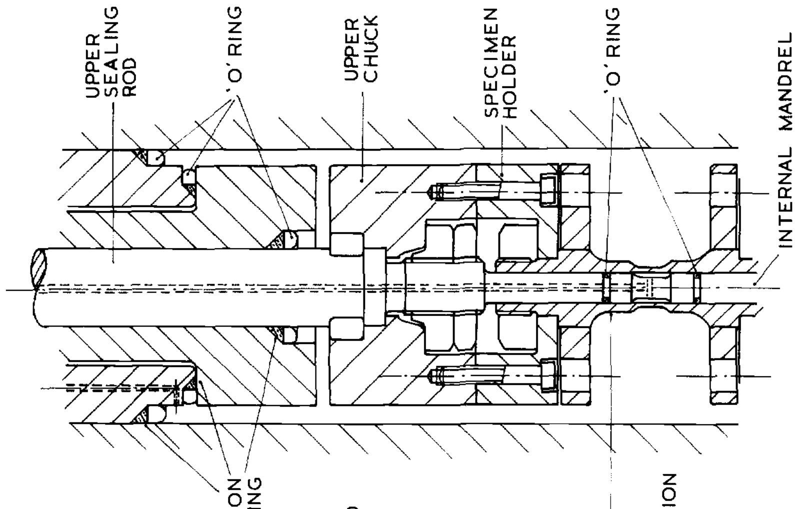

FIG. 2b—*Specimen gripping and sealing arrangement.*

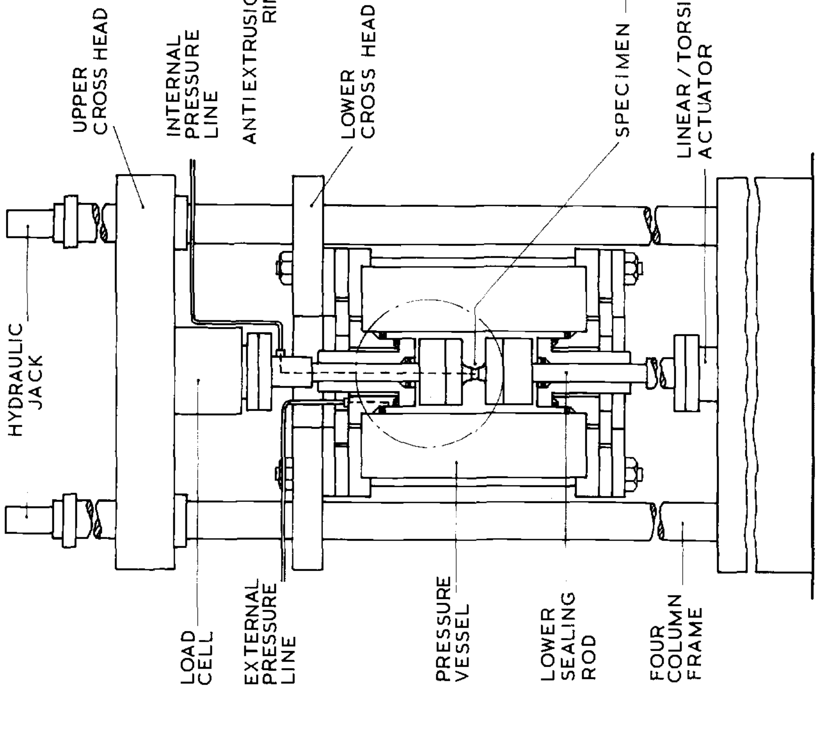

FIG. 2a—*Loading system for multiaxial fatigue testing machine.*

specimen is not in the machine. The alignment of the specimen to the loading axis is achieved by locating it on an internal mandrel which is permanently attached to the upper sealing rod. The mandrel when engaged in the lower sealing rod acts as an additional safeguard to avoid introduction of misalignment of the specimen during assembly or testing. The specimen holder consists of two parts. The specimen is held in one part using a large nut which also transmits the axial load. The second part, which is locked to the first part using a Morrison grip [*10*] and transmits pure torque to the specimen without introducing any significant bending loads to the gage area.

The hydraulic circuit diagram for the test rig is shown in Fig. 3. Two intensifiers are employed to supply internal and external pressure to the system. The external pressure and internal/external pressure difference are controlled independently from zero to 1700 bar by two servovalves located on the low pressure side of the intensifiers. Thus, the hoop stress or pressure difference across the specimen can be accurately controlled by a given command signal. Internal pressure is supplied to the specimen through the upper sealing rod and mandrel and sealed at the bore of the specimen. The oil for the external pressure is fed directly to the pressure vessel. Hence, there is no making or breaking of high pressure pipes during assembly of the specimen. An automatic make up system is used so that any oil leakage can be replaced by injecting new oil into the system via a second pair of intensifiers while cycling continues. Preliminary tests carried out to check the efficiency of the dynamic seals on the sealing rods indicated a very small leakage so that make up requirements should be relatively low. These pressure systems are connected to the low pressure supply which provide the bulk amount of oil at the start of a test. A single hydraulic power pack capable of delivering oil at 80 L/min supplies the low pressure oil to the intensifiers and to the tension-torsion hydraulic circuits.

The control system incorporates load, strain, and position control modes. Each mode may be controlled independently for any waveform selected on the signal generator with different mean level, phase, hold time, and cycle time. The axial load on the specimen may comprise of two components, one due to the load applied via the actuator and the other due to the end load exerted by the external pressure. In order to be able to control the load on the specimen under these conditions a special feedback loop is incorporated so that the pressure load is interfaced with the axial load.

Load measurements are obtained from the tension-torsion load cell and internal and external pressures are measured using ultrahigh pressure transducers. Strain measurements are made on the gage length using two tranducers per mode, one measuring the displacement relative to the other fixed one, to counter any possible pressure effects. Chart recorders and x-y plotters are used to record load and strain ranges as well as hysteresis loops.

A set of safety trips able to detect overloads, failure of the oil supply or cooling water supply, and controlled emergency shut down circuit permit the machine

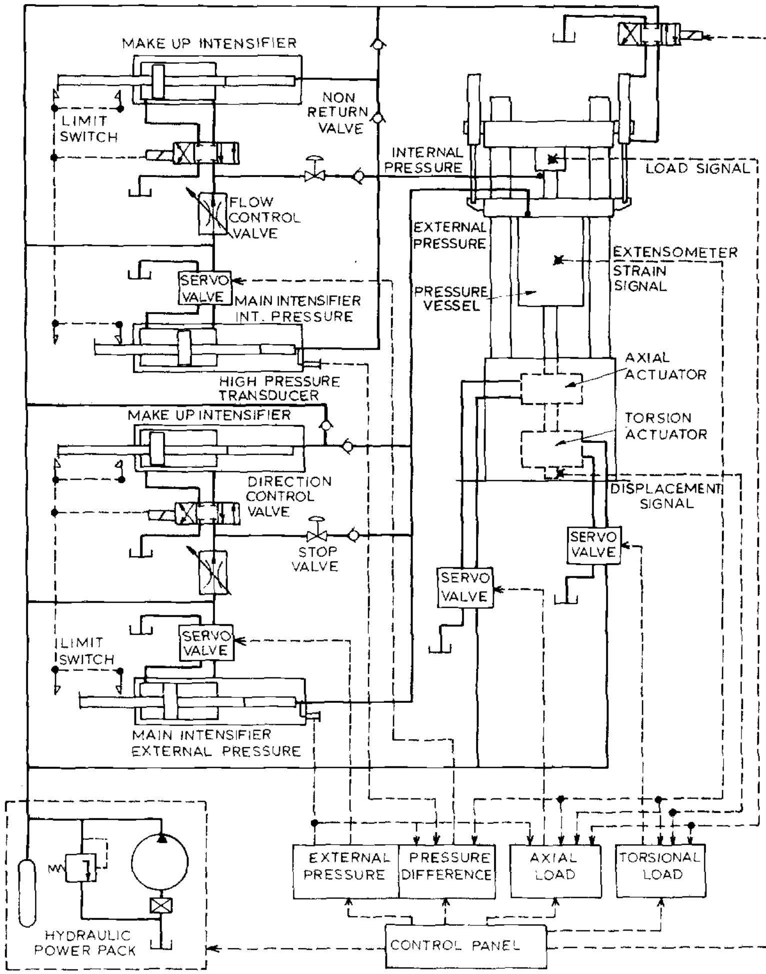

FIG. 3—*Schematic diagram of hydraulic circuits.*

to run unattended for long-term tests. Safety screens are placed round the rig, in case of high pressure leakages, and are interlocked with the machine controls.

Specimen Geometry

Some of the requirements for specimen selection have been discussed earlier when a thin-walled tubular specimen was chosen for the test system. One of the major advantages of using a tubular specimen for high-strain multiaxial fatigue studies is that it enables a fairly uniform stress-strain distribution to be obtained which can be determined accurately even in the plastic range [*11*]. Furthermore, due to its simple geometry it is possible to manufacture the specimen to close

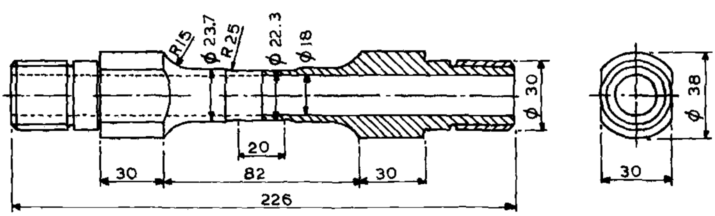

FIG. 4*a*—*Multiaxial fatigue specimen.*

tolerances at a reasonable cost. Final selection of the specimen dimensions are a compromise between the conflicting requirements of crack formation, stress distribution, and stability.

The fatigue specimen designed for the test rig is shown in Fig. 4*a*. It has a 20 mm parallel gage section, a 22.3 mm outer diameter, and a 18 mm bore. The ends of the gage length contain a 25 mm radius which gives the best possible stress-strain distribution over the gage area.

Of the loading modes available axial load produces the most variable stress-strain distribution. The axial strain distribution in the gage section due to axial tension obtained by elastic-plastic finite element analysis is shown in Fig. 4*b*.

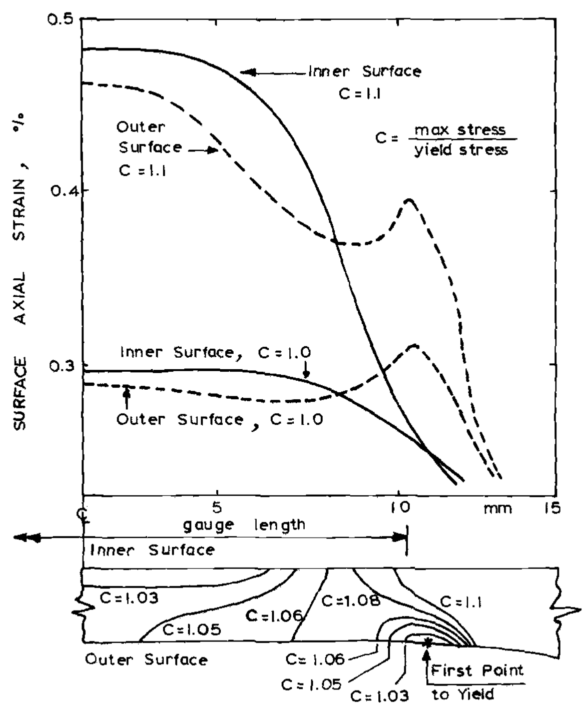

FIG. 4*b*—*Axial strain profiles due to axial tension.*

The analysis was performed for different specimen dimensions, and the results indicate that the influence of specimen shoulders, even with large fillet radii to reduce the stress concentration, produces significant strain variations over the gage length. An increase in load produces more plastic strain at the center of the gage area, and, at high strains, fatigue cracks are expected to initiate at the bore in the region of maximum strain. At low strain levels the stress concentration at the fillets is more effective, and cracks are likely to initiate at both fillets and the center of the gage area. Propagation of the cracks at the fillets will be localized and be inhibited by the high-strain gradient at these regions, and fatigue failure is more likely to occur at the center of the gage area. When subjected to torsion or pressure the strain distribution is not significantly modified with increasing load. For torsional loading cracks are expected to initiate at the outer surface while under pressure cracks should initiate at the bore.

The ratio of internal to external diameters of the gage area is important, since an increase in the ratio leads to a thicker wall section which in turn increases the resistance to buckling under compression. Furthermore, the thicker walls minimizes errors caused by possible eccentricity of the specimen and allows more material for propagation of Stage II Type B cracks. It is reported [*12*] that during high-strain torsional cyclic loading tubular specimens accumulate plastic strain in the axial direction. This effect is more pronounced in thin-walled specimens and thus favors the use of a thicker tube for the specimens. The major disadvantage of using a thicker tube is that it requires very high pressures to obtain substantial hoop strains which causes practical difficulties in designing the rig and increases the hazards of testing. For the specimen just described the diameter ratio is about 0.8 for which thickness effects on fatigue life are not too significant and the specimen is sufficiently stiff to obtain fatigue lives of the order of 500 cycles without causing instability in compression.

Discussion

In recent years many multiaxial fatigue tests have been conducted on a variety of materials using different test systems and specimen geometries, and often the results are difficult to interpret and compare. However, some results obtained for 1Cr-Mo-V steel have been well documented and have been recently analyzed by Brown [*13*]. He compared the results obtained from tension-torsion [*14*], tension-pressure [*15*], and plate bending [*16*] tests at room temperature performed on the same material. Brown replotted the results at two lives on the Γ-plane as shown in Fig. 5. The tension-torsion data correspond to Type A cracks and the tension-pressure and plate bending results to Type B cracks with the uniaxial test separating the two types. Figure 5 shows that the Type B cracks (*dashed line*) are more damaging than the Type A cracks (*solid line*) leading to lower fatigue strengths. The plate bending (*dotted line*) appears to extend the Type B fatigue life probably because the cracks propagating into the specimen meet a reducing stress gradient compared with a more uniform stress in the

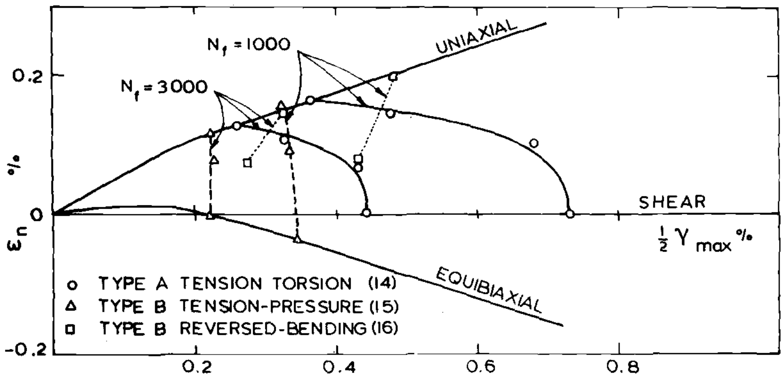

FIG. 5—*Comparison of results for different test systems for 1Cr-Mo-V steel plotted on the Γ-plane* [13].

tension-torsion test (*solid line*). The uniaxial test data also highlight differences between tension-pressure and tension-torsion tests. The former, which may be influenced by an oil environment, employed a thin-walled tube while the latter used a thick-walled tube and gave a higher strength.

From the foregoing it can be readily seen that trying to understand multiaxial fatigue behavior under similar stress states using different test systems and specimen geometries is fraught with difficulties. With the multiaxial fatigue testing facility previously described it will be possible to examine the response of a single specimen geometry to a given stress state in several different ways. For example, examination of the vertical line drawn through the stress ratio $\lambda = 0$ in Fig. 1 indicates that many combinations of β and γ will give the desired stress ratio; for example, $\beta = 0$ $\gamma = 0$, $\beta = 1$ $\gamma = \pm 1$, and $\gamma = 0$ $\beta = \pm\infty$. For stress ratios $-1 \leq \lambda \leq 0$ cracks will propagate along the surface (Type A) of the specimen and for stress ratios $0 \leq \lambda \leq +1$ away from the surface (Type B). The fatigue machine thus permits the possibility of initiating a crack on one plane and propagating it along another plane. Therefore, it is possible to study the hydrowedge effect due to oil pressure on the growth of short cracks by separating out the initiation and propagation stages in the tension-torsion regime. For example, this can be examined at stress ratio $\lambda = -1$ by applying pure torsion ($\beta = 0$ $\gamma = \pm\infty$), pressure and axial load ($\beta = -1$ $\gamma = 0$), and other value for γ with $\beta = -1$. For different values of λ different pressures are required.

Most if not all engineering materials are nonisotropic in their behavior. Anisotropy may be introduced during manufacture by rolling, forging, or extrusion or during cyclic deformation which produces a specifically orientated metallographic texture. Thus the fracture resistance for a particular loading mode may be increased by texturing a material in a preferred direction. A crack may still propagate on the same plane and in the same direction but at a different rate if the orientation of the specimen relative to the texture is changed or if the cyclic deformation response changes. The fatigue machine will enable tests to be performed on anisotropic materials for any selected stress state aligned with any given direction in the material. In order to separate out deformation and fracture response from the influence of specimen geometry and loading mode further tests can be performed on specimens taken from a block of material at other orientations followed by testing at the identical stress state and material orientation previously selected.

Engineering components that do not contain inherent defects and operate at stress levels near to the fatigue limit, spend most of their life in the initiation and short growth regimes. Therefore, the understanding of the accumulation of damage in the initiation phase is of great importance. The well known Palgrem-Miner rule $\left(\sum \frac{n}{N} = 1\right)$ for the summation of damage assumes that damage accumulates in a linear manner independent of the sequence of loading and is based on the results of uniaxial tests. With the fatigue machine it will be possible to perform cumulative damage fatigue tests in order to explore damage summation under multiaxial stress-strain conditions which will be more applicable for use in design codes. It will be also possible to undertake cumulative damage studies for situations in which defects can be orientated in any desired plane relative to the 3-D stress field.

Conclusions

The design and preliminary development of a new multiaxial fatigue testing facility has been described for studying low-cycle high-strain fatigue. It is capable of straining a thin-walled tubular specimen in three independently controlled loading modes. It will permit the coverage of all 3-D stress-strain states from pure torsion through the uniaxial state and plane strain to the equibiaxial strain state and apply the 3-D stress-strain state at any desired angle to the specimen axis. The design of a suitable specimen geometry has been outlined.

Acknowledgments

The authors wish to acknowledge the funding of this project by the Science and Engineering Research Council. U. S. Fernando wishes to acknowledge the financial support given by UNESCO and The Royal Commission for the Exhibition of 1851.

The authors wish to thank Dr. M. W. Brown for his encouragement and advice and Mr. M. R. Goldthorpe for the use of his elastic-plastic finite-element program.

References

[1] ASME Boiler and Pressure Vessel Code Section VIII Division 2, ASME, New York, 1980, Appendix 5, pp. 475–483.

[2] BS 5500, Specification for Unfired Fusion Welded Pressure Vessels, BSI, London, 1982, Appendix C, pp. C1–C7.
[3] Brown, M. W. and Miller, K. J., *Proceedings*, Institution of Mechanical Engineers, Vol. 187, 1973, pp. 745–755.
[4] Lohr, R. D. and Ellison, E. G., *Journal of Fatigue of Engineering Materials and Structures*, Vol. 3, No. 1, 1980, pp. 1–17.
[5] Evans, W. J., "Deformation and Failure under Multiaxial Stress—A Survey of Laboratory Techniques and Experimental Data," Note No. NT833, National Gas Turbine Establishment, Hants, U.K., 1972.
[6] Andrews, J. M. H. and Ellison, E. G., *Journal of Strain Analysis*, Vol. 8, No. 3, 1973, pp. 168–175.
[7] Brown, M. W., *Proceedings*, Conference on Measurement of High Temperature Mechanical Properties of Materials, Chapter 12, National Physical Laboratory, U.K., 1981.
[8] Hsu, T. C., *Proceedings*, Institution of Mechanical Engineers, Vol. 180, 1965, pp. 269–278.
[9] Fernando, U. S., "A New Machine for Multiaxial Fatigue Testing," M. Eng. thesis, University of Sheffield, U.K., 1982.
[10] Morrison, J. L. M., *Proceedings*, Institution of Mechanical Engineers, Vol. 142, 1939, p. 203.
[11] Brown, M. W., *Journal of Strain Analysis*, Vol. 13, No. 1, 1978, pp. 23–28.
[12] Miller, K. J. and Chandler, D. C., *Proceedings*, Institution of Mechanical Engineers, Vol. 184, Part 1, 1969–1970, pp. 433–448.
[13] Brown, M. W. in *Fatigue at High Temperatures*, R. P. Skelton, Ed., Applied Science, London, 1983, Chapter 3.
[14] Brown, M. W. and Miller, K. J., *Journal of Fatigue of Engineering Materials and Structures*, Vol. 1, No. 2, 1979, pp. 217–229.
[15] Lohr, R. D. and Ellison, E. G., *Journal of Fatigue of Engineering Materials and Structures*, Vol. 3, No. 1, 1980, pp. 19–37.
[16] Adams, W. R., "Uniaxial and Biaxial Low Cycle Fatigue Behaviour under Isothermal and Temperature Cycling Conditions," Ph.D. thesis, University of Nottingham, U.K., 1972.

Stephen D. Downing[1] and Dale R. Galliart[1]

A Fatigue Test System for a Notched Shaft in Combined Bending and Torsion

REFERENCE: Downing, S. D. and Galliart, D. R., "**A Fatigue Test System for a Notched Shaft in Combined Bending and Torsion,**" *Multiaxial Fatigue, ASTM STP 853*, K. J. Miller and M. W. Brown, Eds., American Society for Testing and Materials, Philadelphia, 1985, pp. 24–32.

ABSTRACT: This paper describes the design of a two-channel test system that can generate combinations of torque and bending on a round notched specimen. The test frame consists of a specially designed set of hardware for the size and shape of the SAE Fatigue Design and Evaluation Committee's round specimen. The two RAM computer-controlled hydraulic closed loop system provides independent control for each RAM. Load cells and stroke transducers are mounted in-line to provide signals for control and data processing. In addition to a description of the hardware, this paper defines the software that is used to control the system and perform data analysis on five channels of data. The data consist of the two channels of load and three channels of strain from a rectangular rosette. An ultrasonic surface wave technique is used to detect a crack of defined size and automatically halt the test.

KEY WORDS: biaxial fatigue, test system, notched shaft, computer controlled, ultrasonic, bending, torsion, rosette strain gage

The test system described in this paper is the result of an effort in support of the Society of Automotive Engineers Fatigue Design and Evaluation Committee. This committee set out to extend its fatigue life activities by initiating a biaxial fatigue test program. Because the participants represent the ground vehicle industry, a notched shaft under combined bending and torsional loading was chosen as a typical component. To satisfy the needs of this program, a test system that could perform the following tasks was developed:

1. The system should be capable of providing any combination of in-phase and out-of-phase bending and torsional loads. Preliminary calculations determined that the system should be capable of 7000 Nm of bending and torsion for the selected specimen and material. Specimen dimensions are given in Fig. 1. The selected material was normalized 1045 steel (430 MPa yield strength, 620 MPa ultimate strength, and 55% reduction in area).

[1]Senior research engineer and manager of Metals Research, respectively, The Technical Center, Deere and Company, Moline, IL 61265

Copyright© 1985 by ASTM International www.astm.org

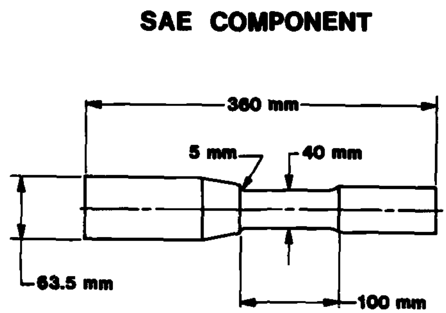

FIG. 1—*SAE notched shaft specimen.*

2. The system should be capable of duplicating variable amplitude measured field loads or ''simulated'' field loads.
3. The system should record sufficient data during the test cycle for analysis of fatigue life prediction theories. These were resolved to be life to crack initiation (which is defined in a later section), life to final fracture, the applied loads, and the surface strain tensor at the expected crack initiation site.
4. A load controlled test system would appropriately simulate the loading of this specimen.

The simple loading scheme illustrated by Fig. 2 was considered appropriate for these requirements. Two linear actuators controlled by a single computer is an effective method of generating any combination of bending and torque with known phase relationships.

Mechanical Hardware

The load frame configuration was designed to meet the following criteria:

1. Sufficient fatigue strength for the specimen size and material.
2. Accommodate two hydraulic actuators (44 KN maximum load and 150 mm stroke) with in-line load cells.
3. Convenient access to the specimen by the operator.

The final load frame design was a welded steel frame outlined in Fig. 3. The bending and torsional moment arms are 155 and 203 mm, respectively.

The specimen gripping system is shown in Fig. 4. The large end of the specimen is simply clamped between two machined steel blocks. The small end is gripped by a heat-treated wedge collet. In preliminary tests, no collet slippage occurred until approximately 3000 Nm of torque was applied. Subsequent to the development of this collet, a commercially available version with greater gripping capacity was found. The attachment at the load cell was by monoball studs. Likewise, the lower end of the ram was attached to the base plate by monoball

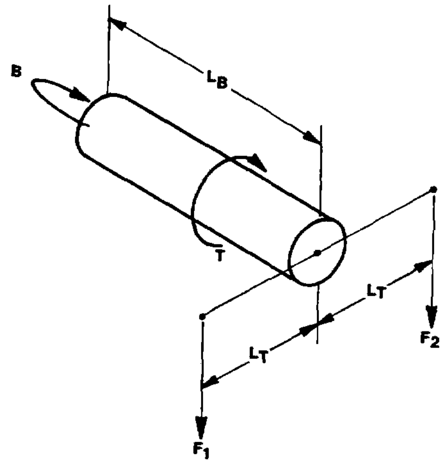

FIG. 2—*Two-axis loading scheme.*

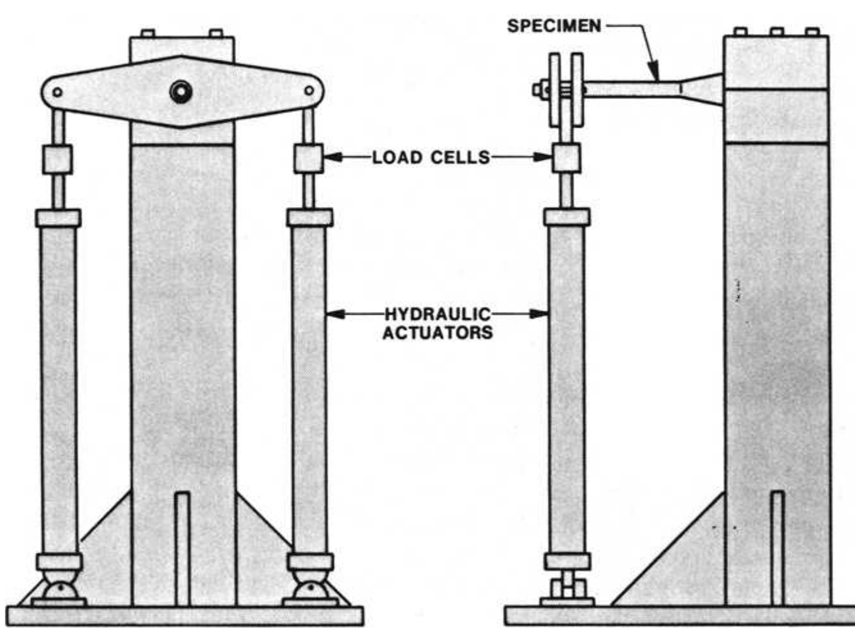

FIG. 3—*Bending-torsion load frame.*

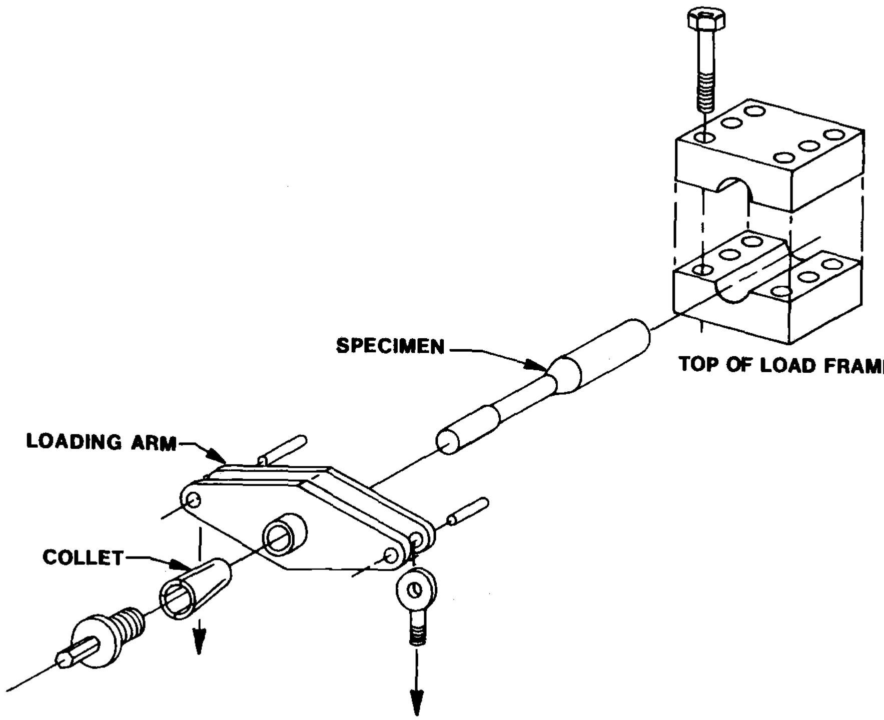

FIG. 4—*Specimen gripping system.*

fixtures to allow for movement in two directions. A photograph of the specimen mounted in the load frame is shown in Fig. 5.

Instrumentation

The instrumentation system is comprised mainly of standard equipment available to most of the test participants. Figure 6 shows a block diagram of the instrumentation system components which are outlined below.

Servohydraulic Control

Each hydraulic actuator is load controlled by separate servohydraulic test consoles. These units condition the command and transducer signals and provide closed-loop control of the servovalves so that the desired forces are applied to the hydraulic actuators.

Computer and Interfaces

A 16 bit minicomputer with 28 k words of random access memory and dual floppy disk drives communicates with hydraulic equipment through a hardware

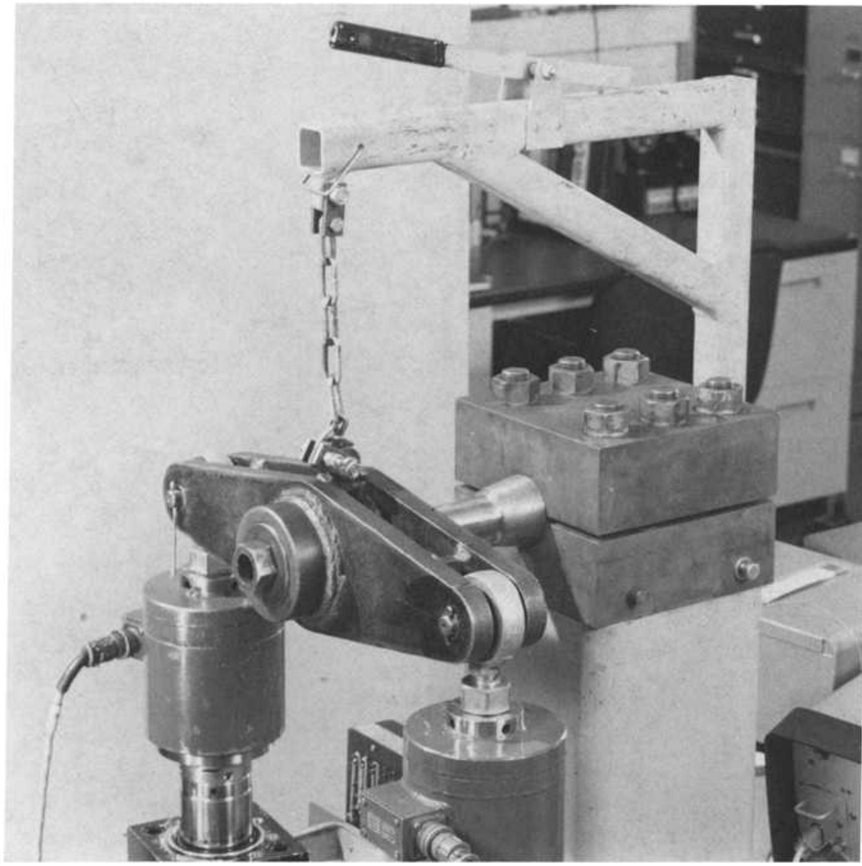

FIG. 5—*Specimen mounted in load frame.*

interface. This interface is equipped with two 12 bit D/A converters and eight 12 bit A/D converters. Peripherals include a graphics display terminal, a digital plotter, and a hardcopy unit.

Crack Detection

In order to detect small cracks with minimum operator intervention, an ultrasonic surface wave transducer was used. This transducer transmits an ultrasonic sound wave along the surface of the specimen and receives reflected waves from certain reference points as well as crack interfaces. The path of the surface wave is illustrated in the upper portion of Fig. 7. The bottom half shows a representative output from the oscillograph of the ultrasonic instrument. Three blips corresponding to reflected waves from Points A, B, and C are seen. At Point A, the transmitted wave from the transducer strikes the specimen. Point C is a discon-

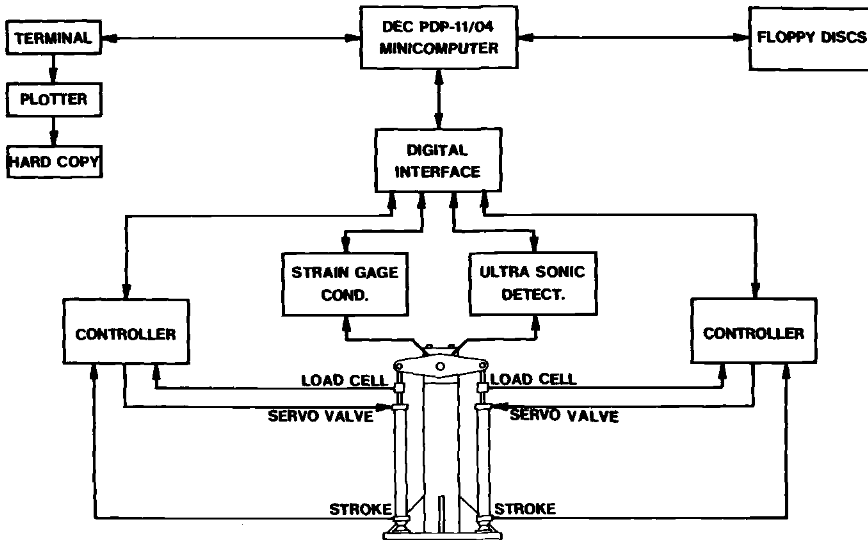

FIG. 6—*Block diagram of instrumentation system.*

tinuity at the top of the specimen radius. An initiated crack would cause an intermediate blip at Point B. The ultrasonic instrument is capable of turning on an alarm if the height of this blip exceeds a presettable limit.

The procedure for calibrating the ultrasonic instrumentation is given as follows:

1. Adjust the gain and attenuation of the ultrasonic unit so that the alarm circuit is activated by a machined 0.7 mm notch on a special calibration specimen. This depth was chosen as the approximate size of crack in the small, round, smooth polished specimens which are used to obtain material properties.

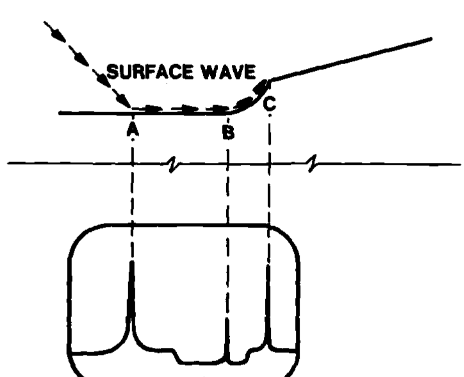

FIG. 7—*Path of ultrasonic surface wave.*

2. Transfer the transducer from the calibration specimen to the test specimen.
3. The fatigue computer program checks the voltage of the alarm circuit which is normally zero volts. When activated, the output is a zero-to-four volt square wave.
4. Upon detection of this alarm signal, the program will print the number of current test cycles and stop the test for visual inspection.

Software

The following discussion is limited to the software for conducting constant amplitude fatigue tests under combined bending and torsion and for analyzing the rosette strain gage data resulting from these tests. Care was taken to develop a simple scheme for inputing test parameters and an effective disk filing system so that data may be completely analyzed after the test is over.

Software for running the test must be able to do the following:

1. Output proper command signals to the servoamplifiers.
2. Record loads and strains at various times during the tests and store on disk.
3. Monitor certain variables as conditions for test shutdown.

The scheme chosen for inputing bending and torsion control parameters is described next. End levels are input for five points in a test cycle for both bending and torque. The signal to be output through the D/A converters to the individual servoamplifiers is calculated from these end levels. Output waveforms may be configured as either ramps or haversines, and the number of individual steps making up these waveforms (up to 100/cycle) is input by the test operator.

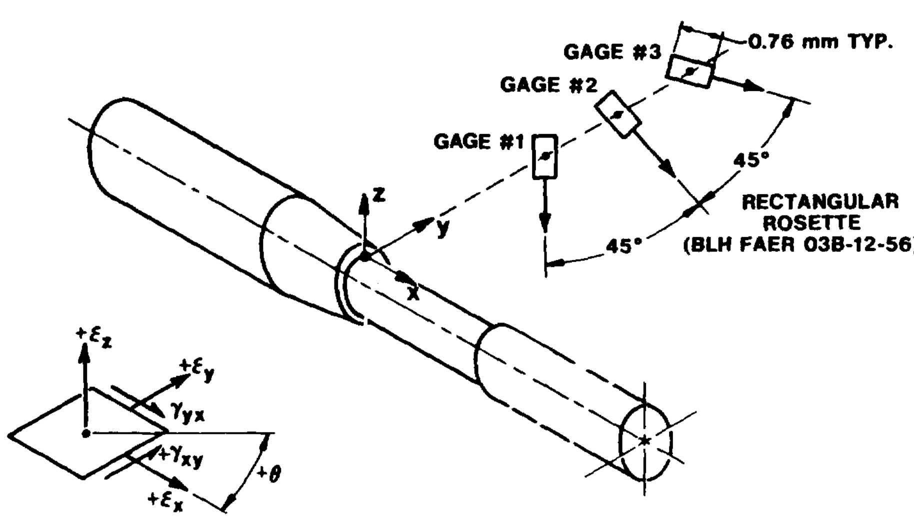

FIG. 8—*Rosette strain gage orientation.*

During the first part of the fatigue test, a rosette strain gage (Fig. 8) is monitored, and the following scheme for data acquisition is used:

1. The first 100 peaks and valleys of normal and shear strains are detected and stored to help characterize early material hardening or softening or both.
2. A two-cycle burst of load and strain data is collected and stored on a disk at specified cycle counts (1, 501, 1001, 5001, 10 001, etc.). The number of simultaneous data scans/cycle (up to 100) is set by the test operator at startup.

After the strains have stabilized (or the gage failed), the strain gage is removed and the ultrasonic crack detector is installed. The program now monitors the alarm circuitry of the ultrasonic instrument and performs a test shutdown when a crack is detected. At this point, the crack detector is removed, and the test is run to specimen fracture. The stroke transducers are continously monitored for large changes in specimen compliance, thus alerting the test operator to the eventuality of fracture. Whenever a test shutdown occurs (either manually or by failure criteria), the number of accumulated cycles is output and automatically copied.

Another computer program was written to fully analyze the load and strain data previously stored on a disk by the test program. Most of the program options are involved with characterizing the strain tensor at the root of the specimen notch.

Test Procedure

The following shows the typical sequence of events needed to run constant amplitude biaxial fatigue tests with this system.

1. Gage specimen.
2. Install specimen in load frame.
3. Run single cycle test.
4. Run fatigue test to strain stability.
5. Remove gage and install crack detector.
6. Run test to crack initiation.
7. Remove crack detector.
8. Take replica and restart test.
9. Run test to final fracture.
10. Analyze strain data.

Discussion

The described system meets the defined objectives for performing constant amplitude load controlled fatigue tests in combined bending and torsion. The simple, two actuator scheme for applying loads, although theoretically incapable of pure torque, provides an economical means for generating combined bending and torsion. Practically speaking, the deflections observed in testing to date are small enough so that any unwanted bending during torsion loading is insignificant.

The only disappointment of the system as configured is its relatively slow speed (maximum of 3 Hz). It is felt that a lowering of computer overhead and a general tightening of the mechanical system will help overcome this shortcoming.

Acknowledgments

The authors are indebted to Gilbert Curless whose tireless efforts and innovative ideas aided the development of this system. MTS Systems Corporation made the preliminary design of the load frame. Financial support was provided jointly by Deere & Company and the National Science Foundation.

Charles C. Lawrence[1]

Multiaxial Fatigue Testing Machine for Polymers

REFERENCE: Lawrence, C. C., "**Multiaxial Fatigue Testing Machine for Polymers,**" *Multiaxial Fatigue, ASTM STP 853*, K. J. Miller and M. W. Brown, Eds., American Society for Testing and Materials, Philadelphia, 1985, pp. 33–46.

ABSTRACT: Plastics are now increasingly used as engineering materials; consequently, there is a need to establish the propensity of the material to fail under fatigue loading. However, in general terms, conventional methods for establishing the fatigue life of a plastic component cannot be used, and alternative ways have to be found. Multiaxial and "in service" load simulation is suggested as a method of tackling this problem. The possibilities of this alternative technique are outlined, and, because of the peculiar and stringent demands on the design of the loading apparatus, this is discussed in detail. The evolution of this apparatus has led to the development of techniques that have solved many of the difficulties found in the application of a multiaxial load and, in addition, offer marked improvements in the field of testing plastics in general.

KEY WORDS: plastics, viscoelastic behavior, fatigue data, fatigue loading, triaxial fatigue apparatus, torsion, tension, compression, internal pressurization, environmental fluid, servocontrol, instrumentation

Fatigue and corrosion have been the two most intractable problems confronting engineers, since fatigue and corrosion are insipient in nature and invariably proceed from faults in the product that are inherent or inadvertent. Both are usually difficult to observe or quantify before the damage is irreparable. There is clearly a need to obtain more information about the fatigue behavior of plastics. The most common method hitherto has been to subject a perfect specimen (or an otherwise perfect specimen with controlled damage) to very precise loading conditions, and from the resulting data the mean behavior of the material is established. While the data from metals show considerable scatter, the results are consistent enough to allow design computation. The position with respect to plastics is far less defined. All the limiting factors found in the testing of metals are present, but, in the fatigue testing of plastics, there are in addition a gamut of more serious problems, of which the most serious follow:

1. Internal heating with high frequency/strain loading due to the viscoelastic behavior of the material and its low thermal conductivity. Associated with this

[1]Reader, Department of Manufacturing Studies and Mechanical Engineering, North East London Polytechnic, Dagenham, Essex, U.K.

Copyright© 1985 by ASTM International www.astm.org

characteristic is the relatively small temperature band over which the material properties can be exploited usefully in engineering components. This band is usually only modestly above or below room temperature.

2. Large variations in the formulations of commercial plastics occur within the basic specification. This is an important factor because of the disproportionate effects of small concentrations of low molecular weight constituents.
3. Plastics can be very sensitive to strain rate (method of loading).
4. They exhibit remarkable creep recovery, a factor that may be exploited in an actual component, but masked in a fatigue test.
5. The residual stresses resulting from basic production and machining processes can be greater than the applied stress and are difficult, if not impossible, to relieve without serious loss of specimen/component geometry or material (structural) change [*1*].

It is against this background that fatigue studies on engineering type plastics must be undertaken. Clearly, the generation of a data bank for the designer is not possible because of these restrictions, and consequently a whole order of certainty is removed. The design then becomes intuitive based on creep, tensile, and similar data. The design process may be supplemented by the adoption of one of the following three strategies:

1. Full scale testing of a component under actual working or test rig conditions.
2. Overdesigning the component and overdesigning the remedy of any subsequent faults that might appear in service, although this strategy can result in an actual worsening of the problem.
3. Simulation of the fatigue load by modeling the worst stress conditions and applying this loading pattern to the gage length of a specimen.

This third option has the limitation that it serves to highlight an inappropriate choice of design or material by premature failure rather than validifying actual component life. There are other systems of evaluating plastics which employ the same philosophy (especially minimum "standards specifications"); however, this third approach is the only one of the three methods that does not commit the manufacture to heavy financial involvement and does give a rapid indication of the suitability of any design. It is the establishment of this technique and other desirable features that are incidental that has stimulated the work reported here, but such are the demands of the technique that it has resulted in a machine concept that has had to meet practically all the requirements of conventional machines in one piece of apparatus.

Test Requirements

Most engineering components are subject to complex stresses that are fluctuating, not necessarily cyclicly or uniformly. Often these stresses are superimposed on a mean stress. Provided that the maximum stress is below the yield point, then creep processes are not of major importance when testing metals under these conditions, but in plastics creep processes occur at low loads which can result in stress whitening and even failure eventually. In the loading cycle of an actual component the creep processes may not proceed because there is time for creep recovery, but creep may prevent a sustained test program. In practice the component is designed so that any loads that are sustained (for example those that are supportive, "bolt-up" or assembly type) are kept so low that the creep is insignificant over the lifetime of the component. Other types of in-built stresses are those due to molding, glueing or machining. In general the machining process is the most harmful together with some adhesives, since the removal of material not only leaves stresses in the surface, but there is residual damage that is particularly prone to crack initiation. In the surface of a good quality molding on the other hand there are compressive stresses in an otherwise continuous surface layer. However, moldings can have their own short comings, such as severe shrinkage, material orientation, or modification.

It is clear from what has been already stated that in any specimen based fatigue simulation test, the match of test materials to that of the component is going to be extremely difficult, especially when compared with, say, rotating bend test in metals. A detailed consideration of these problems is outside the scope of this paper [2].

There is one aspect of a fatigue simulation approach, however, that can be closely approximated; that is the "worst" loading pattern within the component. There are a number of ways of estimating/quantifying these stresses such as strain gaging, photoelastic methods, extensometry, and coating techniques. Strain gaging is the best method by far since it gives a direct reading.

The question that arises is if there are so many imponderables, is the method worth pursuing? The answer lies in the lack of alternatives that are currently available.

There are many unknowns undoubtedly, but, significantly, the preparation of specimens can be as rigorous as that adopted for any other test. The loading pattern can be also made extremely representative, and provided there is no degradation of properties, there is the possibility of enhancement to shorten the test program.

Thus the requirement is a machine that will induce in the gage length of a specimen a loading pattern equivalent to the stress/strain seen in the component. Therefore, this implies the need for a biaxial and possibly a triaxial stress. As a minimum requirement the machine must be capable of subjecting a specimen to compression, tension, and torsion. If an internal pressure can be supplied to a hollow specimen this will give a triaxial component. Internal pressurization is the classical way that workers have induced a triaxial state. However, this gives a strict ratio of stresses depending on the geometry of the specimen. This dependency can be modified as will be shown in the section on internal pressurization. The working arrangement should allow derivatives of normal testing machines such as three-point bending. The load regime may be either stress or strain dependent, static or dynamic, in phase or out of phase with all modes independently applicable. Ideally this should be done on a specimen geometry that is common with nondamaging gaging and minimum chucking interference. The test should enable an environmental control facility. This paper describes the basic design philosophy of a family of machines developed to undertake this work within the specification just outlined.

Design Considerations

The normal tension testing machine such as the Instron, Schenk, and Avery can provide the push-pull requirement, but has not got the frame stiffness or head development for torsion. Neither do such machines have an axially supplied pressure source; they have to be contrived to extend the test beyond the tensile mode. If a machine is to provide a variable triaxial loading system, then the design requirement is for two surfaces that can move towards and away from each other (tensile) and which can rotate relative to each other both clockwise and anticlockwise (torsion), together with a supply of high-pressure fluid that is acceptable environmentally (internal pressure).

Internal pressure is not the only way of applying triaxial stress, but is by far the simplest that has so far been developed. The machine described can be considered "totally stiff" with respect to the specimen, that is, any untoward deflection and displacement of these surfaces resulting from the applied load are trivial compared with that of the specimen. Again this is comparable with conventional tension test machines. Justification for this totally stiff approach is given by Lawrence [*3*].

It is an established principle that axiality can be only maintained if the working section is contained within a ladder framed structure [*4*]. This means that the moving parts must be housed in a system of bearings that are not only spaced widely but are also over designed by conventional loading criteria in order to maintain stiffness and minimal run out. In this respect the main bearing assembly has to carry out a similar function to the headstock of a good quality lathe but able to withstand a greater axial load (tensile/compressive). Torsion has to be possible in both directions and the changeover free from backlash, that is, be virtually undetectable at the specimen. The torsional load has to be resisted without distortion of the frame (racking). In practice this means that the ladder frame required for the axial load has to be braced externally against the torsional load, if it is to be consistent with the totally stiff concept.

If the design principle of flexibility between and within modes is to be maintained, then the internal pressure system must be continuously controllable, with the pressurizing fluid isolated from the primary pressure source (since hydraulic oil is incompatible with most plastics when under stress). The safety precautions in this mode are particularly important and have a marked effect on the design. There are also more elaborate loading procedures for this mode that can affect the chucking techniques for the other two modes.

Operationally the loading systems must be independent and under individual control within themselves, but at the same time these systems must be capable of control centrally. If this objective is to be realized, then the individual modes must be capable of maintaining their program irrespective of the demands on the other modes.

Implicit in this is that any demands must be kept within the design response capability of the various modes. If the test is to be controlled in the strain mode, it is only possible if the feedback is derived from the specimen itself. This strain feedback requirement necessitates a very sophisticated gaging system. Such a gaging system can be difficult to achieve when testing plastics because of the high strains and low hardness of the surface.

Ideally the machine should be able to take the most appropriate gaging available which may be supportive or suspended extensometry including that which is commercially available or that designed specifically. There should also be sufficient space around the specimen for an environmental control facility.

Present Facility

These basic design requirements have been incorporated in a family of machines developed to carry out tests on a variety of materials, sizes, and loads. The machine is the most recent, and it is used to illustrate how these design principles are achieved in practice. It is a laboratory machine developed to test plastic specimens in the range most commonly used for tension tests on this class of materials (see Fig. 1.) The basic loading capacity is plus and minus 30 kN axial force (tensile), clock and anticlockwise, 1.4 kNm (torsion), and two ranges of internal pressure 0 to 25 MN/m^2 and 0 to 125 MN/m^2. Each stress mode can be operated from static to dynamic, with a typical loading pattern of 2% strain at 2 Hz (sinusoidal) which would be held within $\pm 1\%$. This example of load and frequency is given since it is an appropriate choice for many plastics, but the machine is not limited to this set of conditions, provided there are no step change in the loading pattern, that is, they are basically sine wave or saw tooth in profile, although not necessarily cyclic, and all systems are within $\pm 1\%$. However, the intended range of frequency does affect the response and the machine performs best when the controllers are adjusted to a particular set of test conditions. Much of the literature concerned with the dynamic testing of plastics refers to "square wave" applications, because it simplifies some of the associated mathematical modeling.

However, a square wave input is not feasible, but this constraint has not deterred workers from attempting such a test and the subsequent analysis. If a square wave mode of operation is considered essential the control system used in this machine can be adjusted to a damping ratio of approximately 0.6. This results in an overshoot of between 2 to 8% with a return to steady state within three quarters of a cycle of the natural frequency of the particular test setup, for example, one twentieth of the loading cycle given as an example earlier (2 Hz). "Critically damped" for the same loading conditions (2 Hz) results in a "time constant" of approximately 0.05 s. Square wave inputs are clearly the most

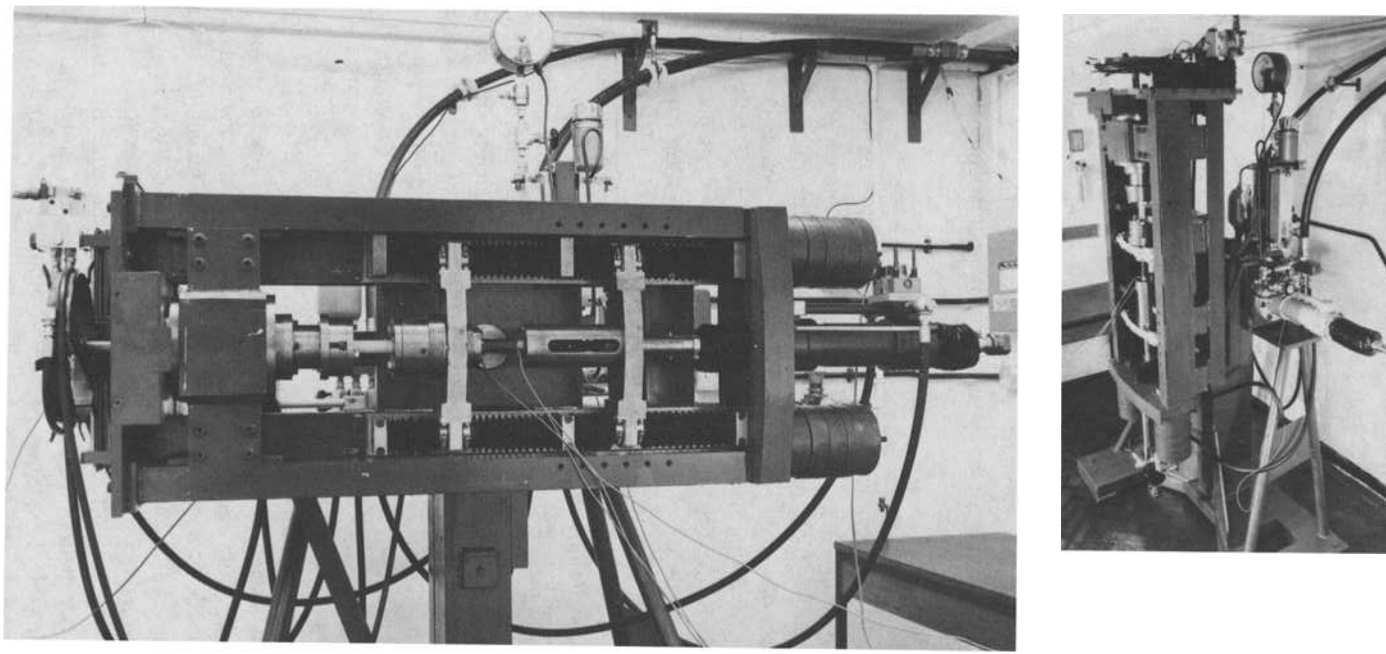

FIG. 1—*View of the triaxial fatigue machine shown in the horizontal position.* (Right) *shows machine in vertical position, conventional working.*

extreme with respect to error in the control of the machine plus specimen, but equally important is the behavior of plastics under these conditions. The behavior of the material is very complex with only small changes in test conditions such as frequency, dwell times, temperature, off-set loads, etc., making whole order differences in performance. The inevitable error in the control system further adds to the overall complexity and extreme care must be exercised if the data derived are to be used in simplified mathematical models.

Test Equipment

Basic Structure

The requirements outlined previously are very demanding and require machine concepts that are comparatively unusual. Only those parts that are unique to the method will be described, and the rest of the engineering is assumed to be at least as good as that seen on conventional machines. Multiaxial machines are affected exceptionally by interaction between modes, and, therefore, stresses caused by misalignment of the machine must be avoided. The design is influenced by the machining and assembly requirements. Figure 2 shows an exploded view of the machine and the use of bracketed lower case letters in the text refers to this figure.

The main frame (*a*) was constructed as a box with sides made from 150 by 75 mm channel closed with 12.5-mm-thick plate. The bearing (torsion) head (*b*) and end plate (*c*) were made from solid plate.

The tensile/compression axis was designed to be along the centerline of this rectangular frame for stability but would have been weak inherently in torsion. A subframe (*d*) was constructed using as ribs 100 by 50 mm box section and 75 mm equal angle section as longitudinal stiffeners (*e*). This behaved in a skeletal way like a large piece of pipe halved along its diameter. Laying along the diaametral edge of the quasi half pipe were welded two steel plates (*f*) that were wide enough to bolt to the side members of the frame and to act as a platform for the bearing mounts. These two plates were subsequently ground flat after the frame was stress relieved as were the sides of the frame. The machining of the subframe was facilitated by using the longitudinal stiffeners (*f*) as the machining base. These stiffeners coupled with a central plate provided the base for the central pivot mounting (*g*). The structure was therefore like a ribbed boat with angle sections either side of the keel. This elaborate framework and machining were necessary to ensure that the machine could be aligned accurately and provide a solid base for the linear bearing carrying the crossheads (*h*), a datum for the main bearing (*b*) and a datum for frame mounted extensometry. The frame is massively overdesigned by conventional standards. The justification for this approach is given elsewhere [*3*], but, as a consequence when maximum loads were applied, there was no discernable deflection (as indicated by appropriately placed dial gages). The moving section was constrained by linear bearings that were matched to the tracks that were bolted to

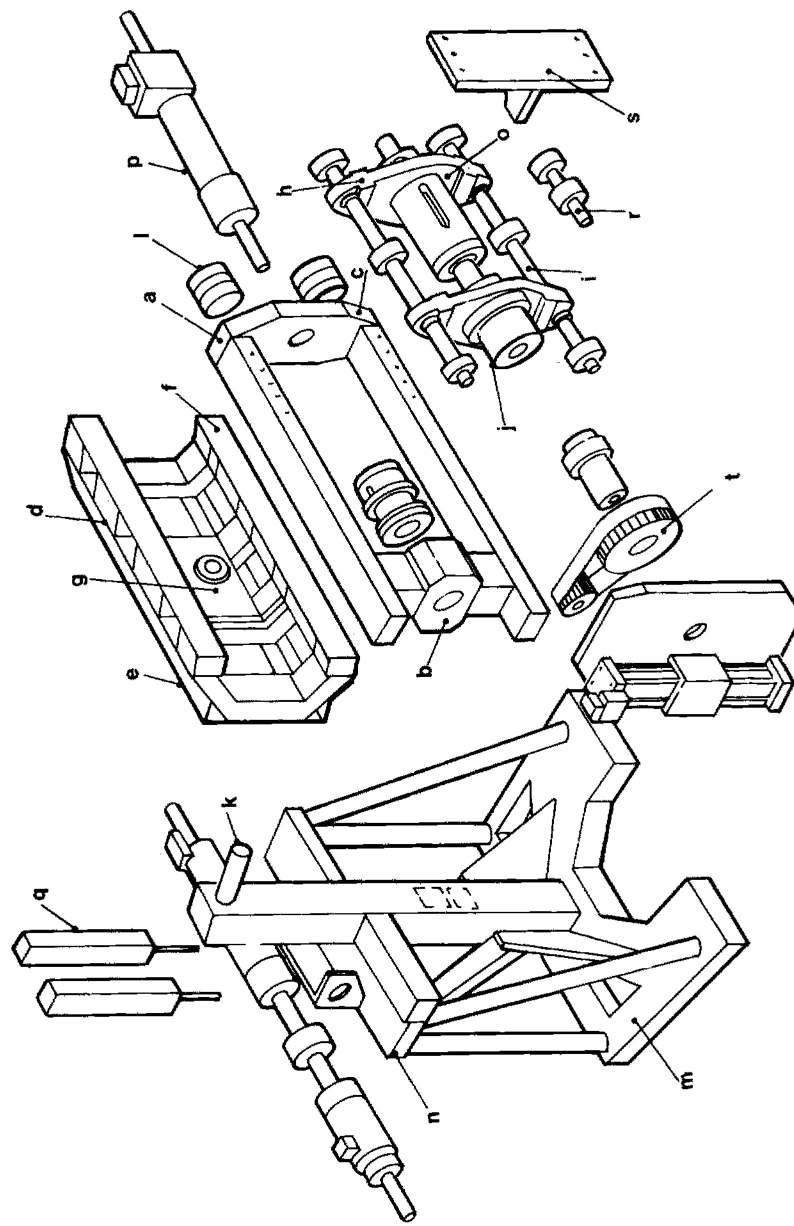

FIG. 2—*Exploded view of apparatus showing major elements of the construction. Finer detail has been ommitted for clarity.*

the frame. The runout was found to be better than 0.02 mm over the entire stroke.

The main bearing (*b*) consisted of two angular contact ball bearings preloaded beyond the design load of 30 kN. This headstock bearing permitted rotation but was effectively rigid in every other respect. The mainshaft through the bearing was hollow to allow access to the end of the specimen. The shaft extended beyond the main bearing and was made to accept a large toothed wheel which was the final wheel in a toothed belt drive system for the torque mode.

The tensile/compressive modes are applied via the thrust-blocks and stabilizer crossheads. These are held on line by linear bearings (recirculatory ball). The bearing tracks (*i*) are mounted on the ground surface of the subframe with an intermediate packing plate which was selectively ground on assembly.

The linear bearing tracks are kept as wide apart as is possible to lessen the effects of the torsional load on the bearings and consequently to reduce the axial frictional restraint. The stabilizer (*j*) is an addition to conventional test machines. It performs a number of functions; principally it constrains the specimen on the centerline of the machine, but also allows the stress transducer to operate free from bending stress and the use of supportive gaging (horizontal operation).

One of the innovations of this machine is the facility to operate at positions between vertical and horizontal (see Fig. 1). The main frame is pivoted about the visual center of the frame so that the operator is able to work and observe at a comfortable height. Some attention was paid at the design stage to arrange the pivot (*k*) to be at the approximate center of gravity with the final balance made with counterweights (*l*). This final balancing allows one person to set the operation position. A static mounting frame (*m*) was constructed to give overhang stability, swing clearance, and a mounting for the pressurization mode. The spars and struts of the frame were crossbraced. A platform (*n*) was welded to the back of the frame to carry the coupling housing for the pressurization cylinders and the associated valves, reservoirs, and pipework, etc. as well as the hydraulic oil supply manifold.

Axial Loading System

A double-rodded, flange mounted, 75-mm-diameter servohydraulic cylinder was used to apply the tensile/compressive load. This cylinder was attached to the thrustblock (*o*) via a floating coupling. The choice of the double-rodded cylinders (*p*) was to ensure that the response, load, and other characteristics of the tension and compression were the same. The stroke was plus and minus 150 mm. The cylinders were specially adapted to take a servovalve, and the seals were all low friction.

Internal Pressurization System

The internal pressurization system is the most complex both in terms of physical arrangement and control. The system (*q*) is shown more fully in Fig. 3 as

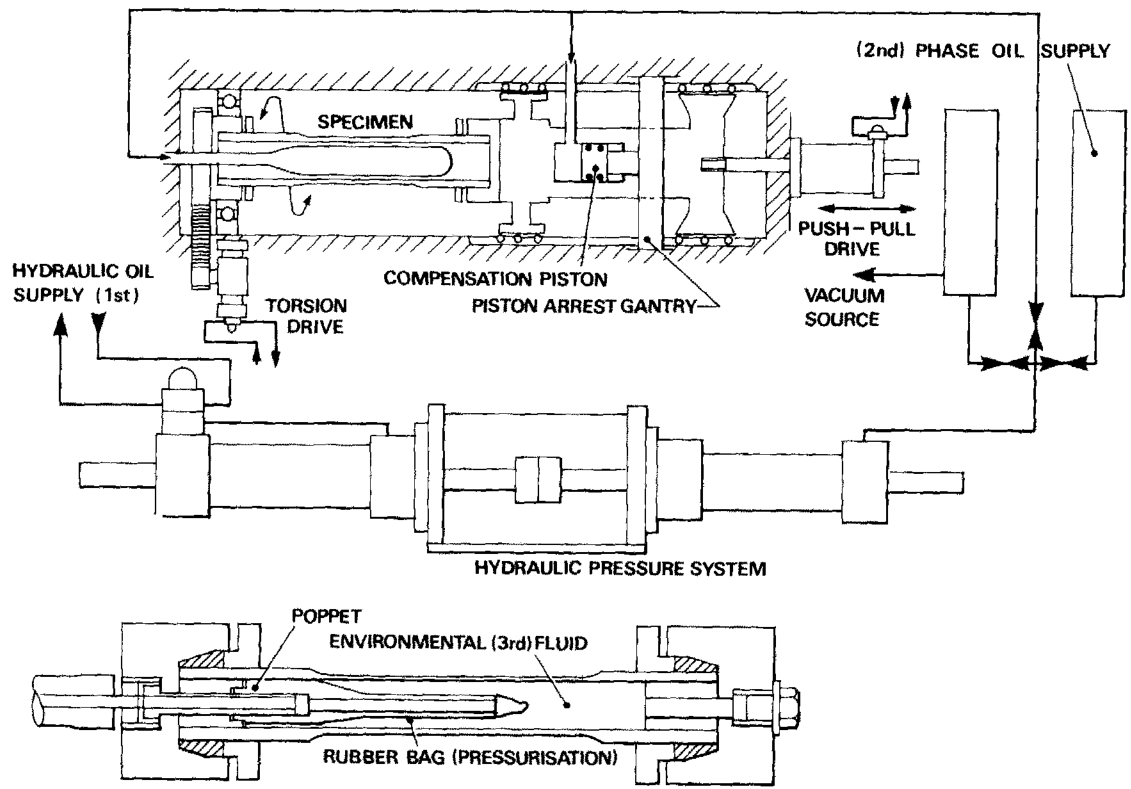

FIG. 3—*Schematic of machine showing the three loading systems, all under servohydraulic control. Enlargement shows hydrostatic chucks.*

a schematic of the three-phase system where the pressurizing fluid is kept remote from the fluid in contact with the wall of the specimen.

There are several reasons for adopting this method, but the principal reason is the need to control the fluid in contact with the specimen under test. The majority of common plastics would be affected adversely by hydraulic fluid at high pressure, but this quality of oil is essential for the effective running of hydraulic servovalves, and consequently a two phase system is the least requirement. The simplest method is to separate the primary source altogether by using two pistons. This technique has the further advantage of scaling both up and down by interchanging the roles of the pistons. Two other disadvantages of using hydraulic oil in the system directly are that it has to be kept clinically clean and it can be injurous to health, and so it is best kept as a conservative unit. The intermediate fluid considerably simplifies the actual pressurization because the fluid that is required at the specimen may not be compatible with the slave cylinder. The diaphragm separates the two fluids, and a choice of rubber can be usually found. For a number of reasons natural rubber is found to be best for this application [*5*]. The choice of intermediate fluid is restricted by the foregoing considerations to a natural oil such as a nut oil, silicone oil, and air. Silicone oil is the obvious choice as it does not oxidize readily, has a low and consistent viscosity, is not a health hazard, and does not affect most other materials. This latter claim is disputed by some workers which means that the three phase system is essential if the findings are to be accepted universally, the control of environment is important since something as apparently innocuous as water can greatly modify the performance of some plastics. The natural rubber does not limit the pressurization in any way. Pressures of 500 MN/m^2 have been applied using this technique, provided there is sufficient elasticity in the diaphram. Because of the diaphram's sealing effect, the specimen can be taken to complete rupture even though the specimen has failed functionally by seepage [*6*]. To avoid air entrapment the specimen assembly procedures are designed to be carried out on a bench so that the specimen can be loaded vertically and the air purged by gravity. The whole chucking system can be sealed prior to loading. The pressurizing fluid system is charged by first pulling a vacuum. This technique can be used on two-phase systems quite successfully with the residual air only a fraction of a millilitre.

The problem of finding a mathematical model for internal pressurization tests that is simple has led, in many cases, to a very liberal interpretation of the term "thin cylinders." The attraction of this method is that a closed cylinder has a simple 2:1 ratio of stress under these conditions. The difficulty with the method when applied to plastic specimens is that for manufacturing and safety reasons the walls are made comparatively "thick." The machines in this series are designed to remove this end effect to zero by taking this load on a floating piston (*r*) which is arrested by a spigot attached to a gantry (*s*) mounted on the main frame. This technique allows the applied axial stress to take any value of tension or compression without having to first compensate for the induced axial load. This method also allows total control of the hoop stress.

Torsional Loading System

The torsional load is applied through a toothed belt system (*t*). This method of transmission was chosen to avoid the backlash that is found in geared and chain transmissions. Various pulley configurations are used to optimize the load and strain range. For simplicity of control a hydraulic rotary actuator is used, but this limits the strain range at the specimen to plus and minus 90° of rotation. This is usually more than sufficient, but, for elastomers, a secondary attachment has been developed using a large stepper motor which gives "limitless" strain potential. However, to get the torque requirement this system has to have its own computer control which adds to the cost as well as complicating the control function.

Specimen Geometry

Such is the diversity of possible test regimes that it is impossible to specify a unique specimen shape. The specimen used in the various programs to date range from very carefully machined polymethylmethacrylate to commercial pipe simply sawn and trimmed to length with no other preparation. Because each program has involved pressurization (hoop strain) at some stage, all the specimens have been tubular, but hollow specimens are not essential.

Control

There are two systems of servocontrol on the machine. Proportional control is used for loading and some simple tests. The combined and dynamic system have psuedoderivative feedback control (PDF) [7]. The PDF technique in outline has proportional and derivative control in the inner loop with integral control in an outer loop. The model is based on the assumption that the outer loop control is achieved by a simple change of force. However flow control valves are complex, but have an overall integrating effect; consequently, in this application, the outer loop controller is used to supplement only. With this type of controller it was found possible to accommodate the differing response of the various modes. The "tuning" of the control is done electronically and not via the valve. The PDF system was used because of the differing dynamic response of the various modes, and it enables the system to be tuned with each other electronically. If for operational reasons there is an inherent phase lag in a particular mode but the frequencies must be matched, then the output from the lagging mode can be used to drive the second, provided that the phaselag in the second system is insignificantly small, which can be arranged usually. The control valves are obtained commercially (MOOG series 76). These valves are controlled by analogue-current dependent-signals. These signals are derived from control units that are driven by a loading signal from say a signal generator. All the modes can be operated with a steady load (dc level) with a superimposed dynamic load.

The interactions between creep and dynamic fatigue are considerable especially in the more ductile polymers, and, since the machine can work at extremely low-cycle rates as well as static loads, crack propagation studies are possible. However, crack propagation tests are usually carried out against a particular program requirement which is specifically instrumented for such observation. No such experiments have been done to date except fatigue tests with static offset in another mode or supplementing the fatigue load. End data (complete severance of the material) has been used since for many polymers, and the penultimate cycle is indistinguishable from the cycles preceding it. As the tests run day and night it is difficult to arrange constant surveillance of such a fracture.

Just as the machine was designed for a comprehensive range of test and materials, so also were the chucks. They are based on the hydrostatic principle described by Lawrence [3] and shown schematically in Fig. 3.

Again the diversity of loading and specimen geometry requires the gaging to be matched to the types of tests. As an example of the range possible, in the four tests requiring an indication of hoop strain, the methods used were wide-gap air gaging, travelling microscope, strain gages adhered to the surface and overall volumetric change. The wide gap air gaging and strain gages were available for the control of the rig. The stresses at the grips and the internal pressure were measured by built-in load cells, but it must be stressed that polymers do not respond in the comparatively simple way observed in metals, and in a dynamic test the stress-strain patterns within the specimen are equally dynamic and almost certainly out of phase with the applied load. Consequently there is considerable difficulty in determining a stress-strain distribution by simple observation of overall stress or strain or surface displacement. Therefore the gaging has to be of the type that best suits those parameters important to any particular test, this is not unlike the choices an experimenter has to make when using a conventional machine such as an Instron.

Test Procedures

There can be no specific description of the test procedures since there is such a wide range of options. It is primarily the limitations of the material under dynamic load that determine the envelope of test possibilities. The bounds of the individual modes have been outlined, but the additional constraints are:

1. The ability to present data in a continuous form if other than function generated.
2. The response demanded from any part of the data in (i) must not exceed the capability of the control system.
3. The extensometry must be capable of working under the complex strain configuration.
4. The energy/rate input must not cause the material to degradate or to mask favorable characteristics, such as creep recovery.

5. It should be possible for the test to proceed without specimen geometry change and undue influence from the gripping system.

Data from typical tests, specialized extensometry, and other pertinent factors to meet the above requirements are given elsewhere [*3*]. However, it should not be inferred from this that these matters are unimportant. On the contrary, the tests are only good as are the systems gaging, controlling, and monitoring the experiment.

Conclusions and Future Work

A machine has been developed that can apply a multiaxial load to the gage length of a specimen in a way that is representative of the stress patterns observed in an actual component undergoing complex loading. Procedures to accelerate quality evaluation are currently under development. These tests include the effects of various environmental fluids and at differing temperatures.

Acknowledgments

I wish to thank the Polymer Engineering Directorate of the Science and Engineering Research Council of Great Britain for their encouragement and financial support and my own technical staff for their considerable assistance in the work.

References

[*1*] Lawrence, C. C., *British Polymer Journal*, Vol. 10, March 1978, pp. 93–97.
[*2*] Crawford, R. J. and Benham, P. P., *Journal of Materials Science*, Vol. 9, 1974, pp. 1297–1304.
[*3*] Lawrence, C. C., *Journal Strain Analysis*, Vol. 15, No. 3, 1980, pp. 159–173.
[*4*] Robertson, A. and Newport, A. J., Report Memoranda Aero M56, Committee London No. 1161, pp. 1–7.
[*5*] "Natural Rubber Puts the Pressure on Plastic Pipe Report," *Rubber Developments*, Vol. 34, No. 4, 1981, pp. 107–109.
[*6*] Choo, V. and Lawrence, C., "Glass Wound Pipes under Multiaxial Stress," to be published.
[*7*] Phelan, R. M., "Automatic Control System" Cornell University Press, Ithaca, NY.

Deformation Behavior and the Stress Analysis of Cracks

Stanley J. Harvey,[1] Amrit P. Toor,[1] and Paul Adkin[1]

The Use of Anisotropic Yield Surfaces in Cyclic Plasticity

REFERENCE: Harvey, S. J., Toor, A. P., and Adkin, P., "**The Use of Anisotropic Yield Surfaces in Cyclic Plasticity,**" *Multiaxial Fatigue, ASTM STP 853,* K. J. Miller and M. W. Brown, Eds., American Society for Testing and Materials, Philadelphia, 1985, pp. 49–63.

ABSTRACT: An anisotropic plasticity approach is used to determine the plastic strains developed in two mechanical ratchetting processes, (*a*) thin-walled tubes subjected to cyclic plastic shear strain and a sustained axial stress, and (*b*) thin-walled tubes subjected to cyclic plastic tension and compression with a sustained steady hoop stress. The anisotropic plastic potential includes linear terms which enables Bauschinger effects to be incorporated in the general approach. The coefficients, representing the state of anisotropy, are expressed in terms of the uniaxial and shear yield stresses of the material and can be easily determined from simple tests.

Results are presented showing the cyclic properties developed, together with the results of uniaxial tests showing the development of anisotropic material properties due to axial and hoop strain accumulation.

Using the anisotropic material data, yield surfaces are developed and used to predict the axial and hoop strain within a cycle of plastic strain for the mechanical ratchetting processes. The justification for using equi-plastic strain surfaces is discussed, and the results are compared with those obtained using current or instantaneous yield surfaces.

The results presented indicate that the latter approach is more appropriate, but more material data are required in order to test its validity for other loading systems.

The problems associated with developing realistic yield surfaces for the period immediately after cyclic stress reversal is discussed together with the influence of micro residual stresses.

KEY WORDS: anisotropic, plasticity, plastic potential, cyclic properties, Bauschinger effects, yield surfaces, loading surfaces, residual stresses

Nomenclature

$a_1 \ldots a_{12}$	Material constants
σ_{rr}	Radial stress
$\sigma_{\theta\theta}$	Hoop stress
σ_{zz}	Axial stress
Z_1, Z_2	Tensile and compressive yield stresses in the axial direction
R_1, R_2	Tensile and compressive yield stresses in the radial direction
θ_1, θ_2	Tensile and compressive yield stresses in the hoop direction

[1]Head, experimental officer, and research assistant, respectively, Department of Combined Engineering, Coventry (Lanchester) Polytechnic, Coventry, U.K.

Copyright© 1985 by ASTM International www.astm.org

$\left.\begin{matrix} S_1, S_2 \\ T_1, T_2 \\ V_1, V_2 \end{matrix}\right\}$ Shear yield stresses corresponding to the Z, R, and θ directions

$\hat{\sigma}$	Maximum axial stress during a cycle
σ_z, ϵ_z	Axial stress and axial strain, respectively
σ_θ, ϵ_θ	Hoop stress and hoop strain, respectively
τ, γ	Shear stress and shear strain, respectively
$d\epsilon_z$, $d\epsilon_\theta$	Increments of axial and hoop strain, respectively
$d\gamma$	Increment of shear strain

$$\bar{\sigma} = \frac{1}{\sqrt{2}} \{(\sigma_z - \sigma_\theta)^2 + (\sigma_\theta - \sigma_r)^2 + (\sigma_r - \sigma_z)^2 + 6\,(\gamma_{z\theta}{}^2 + \gamma_{\theta r}{}^2 + \gamma_{rz}{}^2)\}^{1/2}\text{: von Mises equivalent stress}$$

$$d\bar{\epsilon}p = \sqrt{2/3}\,\{(d\epsilon_z{}^p - d\epsilon_\theta{}^p)^2 + (d\epsilon_\theta{}^p - d\epsilon_r{}^p)^2 + (d\epsilon_r{}^p - d\epsilon_z{}^p)^2 + 6\,[(d\epsilon_{z\theta}{}^p)^2 + (d\epsilon_{\theta r}{}^p)^2 + (d\epsilon_{rz}{}^p)^2]\}^{1/2}\text{: von Mises equivalent plastic strain}$$

The analysis of multiaxial cyclic plasticity problems has received considerable attention in recent years. A particular problem where the prediction of plastic strains is of importance is that of structural ratchetting or cyclic strain accumulation. Plastic strain accumulation in the direction of a steady load can be induced by multiaxial cyclic loading, and this can often result in failure by gross deformation before fatigue failure occurs. The analytical approaches adopted have been developed from plasticity theories used for more simple loading systems, but the general requirements necessary to fully describe the plastic behavior of a material undergoing cyclic plastic deformation remain the same, namely (*a*) a yield criterion which specifies the states of stress at which plastic flow begins, (*b*) a flow rule which relates the plastic strain increment with the stress and stress increment, and (*c*) a hardening rule which describes the changes in the yield criterion with plastic flow.

If the growth and development of the yield surface within a cycle of plastic strain can be established, then the nature and magnitude of the plastic strains can be determined, assuming that the yield surface also represents the plastic potential and the equivalent plastic strain increment is normal to the yield surface. The yield surfaces relevant to multiaxial cyclic plasticity problems can be only realistically developed by fitting yield surface models to experimental data, and notable contributions to this approach have been made by Yoshida et al [*1*] and Shiratori et al [2] who subjected thin-walled tubes to combinations of cyclic plastic torsion with steady axial loads and cyclic push-pull with steady internal pressure. Similar experiments were carried out by Bright and Harvey [*3*] and Harvey et al [*4*] for a range of larger cyclic plastic strains, and by Moreton and Moffat [*5*] for a range of small plastic strains which resulted in shakedown. Other attempts to model material behavior for cyclic loading have been made by Mroz [*6*] and Dafalias and Popov [*7*]. Mroz introduced the concept of a collection of yield surfaces and a range of work-hardening moduli, and Dafalias and Popov used a bounding surface to define their work hardening law.

One of the major problems in developing an appropriate yield surface model in cyclic loading is the presence of Bauschinger effects and attempts to use the simple kinematic hardening models developed by Prager [*8*], modified by Ziegler [*9*] and Shield and Ziegler [*10*], have not been successful, since they tend to predict a limit to the strain accumulation and this is not observed experimentally. The anisotropic plastic potential, defined by equi-plastic strains, used by Shiratori et al [*2*] models the yield surface extremely well for the materials and strain ranges investigated. However, a large amount of material data is required to define the potential surfaces which are shown to expand towards a limiting isotropic yield surface at the end of a half cycle of plastic strain. An approach using the anisotropic yield criterion developed by Hill [*11*], but modified by including linear stress terms to allow for Bauschinger effects, has been developed by Jeans [*12*] and Harvey et al [*13*], and forms the basis of the present paper. It is felt that this approach offers advantages over the other methods because the material properties which control the shape of the yield surface are easily identifiable and may be readily obtained from simple tests.

Anisotropic Yield Criterion

The criterion which describes the yielding of many materials is that of von Mises, and the simplest yield criterion for materials which develop anisotropic properties would be one which reduced to the von Mises isotropic form when the anisotropy was negligibly small. This anisotropy may develop due to cyclic or monotonic loading, and in order to allow for Bauschinger effects as well as anisotropy then linear stress terms must be included in the yield criterion. Following the approach of Hill [*11*], this can be expressed in polar co-ordinates as

$$\begin{aligned} a_1 (\sigma_{rr} - \sigma_{\theta\theta})^2 + a_2 (\sigma_{rr} - \sigma_{zz})^2 + a_3 (\sigma_{\theta\theta} - \sigma_{zz})^2 + a_4 \tau_{\theta z}{}^2 + a_5 \tau_{r\theta}{}^2 \\ + a_6 \tau_{rz}{}^2 + a_7 (\sigma_{rr} - \sigma_{\theta\theta}) + a_8 (\sigma_{rr} - \sigma_{zz}) + a_9 (\sigma_{\theta\theta} - \sigma_{zz}) \\ + a_{10} \tau_{\theta z} + a_{11} \tau_{r\theta} + a_{12} \tau_{rz} = 1 \end{aligned} \tag{1}$$

The coefficients of this equation can be easily related to the uniaxial yield stresses [*12*] and are

$$a_1 = \tfrac{1}{2} \left[\frac{1}{Z_1 Z_2} - \frac{1}{R_1 R_2} - \frac{1}{\theta_1 \theta_2}\right]$$

$$a_2 = \tfrac{1}{2} \left[\frac{1}{\theta_1 \theta_2} - \frac{1}{R_1 R_2} - \frac{1}{Z_1 Z_2}\right]$$

$$a_3 = \tfrac{1}{2} \left[\frac{1}{R_1 R_2} - \frac{1}{\theta_1 \theta_2} - \frac{1}{Z_1 Z_2}\right]$$

$$a_4 = \frac{-1}{S_1 S_2}, \qquad a_5 = \frac{-1}{T_1 T_2}$$

$$a_6 = \frac{-1}{V_1 V_2}, \qquad a_7 + a_8 = \frac{R_1 + R_2}{R_1 R_2}$$

$$a_9 - a_7 = \frac{\theta_1 + \theta_2}{\theta_1 \theta_2}, \qquad -a_8 - a_9 = \frac{Z_1 + Z_2}{Z_1 Z_2}$$

$$a_{10} = \frac{S_1 + S_2}{S_1 S_2}, \; a_{11} = \frac{T_1 + T_2}{T_1 T_2}, \; a_{12} = \frac{V_1 + V_2}{V_1 V_2} \tag{2}$$

where Z_1, Z_2, R_1, R_2, θ_1, θ_2 represent the uniaxial tensile and compressive yield stress in the axial, radial, and hoop directions, respectively, and S_1, S_2, T_1, T_2, V_1, V_2 represent the shear yield stresses in the three corresponding shear directions.

From the relations for the coefficients of the linear terms of the direct stress components, it can be seen that

$$\frac{R_1 + R_2}{R_1 R_2} + \frac{\theta_1 + \theta_2}{\theta_1 \theta_2} + \frac{Z_1 + Z_2}{Z_1 Z_2} = 0 \tag{3}$$

For the particular case of thin-walled tubes subjected to a cyclic shear stress τ and an axial stress σ_z, Eq 1 reduces to

$$\frac{-\sigma_z^2}{Z_1 Z_2} + \frac{(Z_1 + Z_2)\sigma_z}{Z_1 Z_2} - \frac{\tau^2}{T_1 T_2} + \frac{(T_1 + T_2)\tau}{T_1 T_2} = 1 \tag{4}$$

If Eq 4 represents the plastic potential then the axial plastic strains will be given by

$$d\epsilon_z = \left[\frac{-2\sigma_z + (Z_1 + Z_2)}{-2\tau + (T_1 + T_2)} \times \frac{T_1 T_2}{Z_1 Z_2}\right] d\gamma \tag{5}$$

For the case of tubes subjected to cyclic push-pull with steady internal pressure we have, assuming $R_1 R_2 \simeq \theta_2 \theta_2$

$$\frac{\sigma_\theta^2}{\theta_1 \theta_2} - \frac{\sigma_z^2}{Z_1 Z_2} + \frac{\sigma_\theta \sigma_z}{Z_1 Z_2} + \frac{\sigma_\theta (\theta_1 + \theta_2)}{\theta_1 \theta_2} + \frac{\sigma_z (Z_1 + Z_2)}{Z_1 Z_2} = 1 \tag{6}$$

and the hoop plastic strains are given by

$$d\epsilon_\theta = \frac{-2\sigma_\theta (Z_1 Z_2) + \sigma_z (\theta_1 \theta_2) + (\theta_1 + \theta_2)(Z_1 Z_2)}{-2\sigma_z (\theta_1 \theta_2) + \sigma_\theta (\theta_1 \theta_2) + (Z_1 + Z_2)(\theta_1 \theta_2)} d\epsilon_z \tag{7}$$

All the foregoing equations reduce to those given by Hill [*11*] when Bauschinger effects are not considered and further reduce to the von Mises criterion when the degree of anisotropy becomes negligibly small.

Experimental Program

In order to effectively test the proposed anisotropic plasticity model, tests should be carried out using thin-walled tubes. Two different ratchetting mechanisms can be identified.

(a) Cyclic plastic torsion of thin-walled tubes subjected to sustained axial loads—For this loading system the direction of principal stress and strain change throughout a cycle of shear strain. The cumulative axial strains will be controlled essentially by the material properties in the axial direction and also by any changes in these properties due to the cumulative strains and any interaction caused by the cyclic shear strains.

(b) Cyclic tension-compression of thin-walled tubes subjected to a sustained internal pressure—For this loading system the directions of the principal stresses and strains remain fixed, and, since the slip directions associated with the follow up stresses are the same as the cyclic stresses, then considerable interaction between the material properties in the axial and hoop directions might be expected.

The experimental equipment and procedures have been described fully elsewhere [*4*]. Two test materials were used, both of which rapidly cycled to a steady-state condition. For the cyclic torsion tests a low-carbon steel EN 32B (Cl115) was used and for the cyclic tension-compression tests a similar low-carbon steel EN 32M (Cl114) was used. The composition of these materials was

	C	Si	S	P	Mn
EN 32B	0.10 to 0.18	0.05 to 0.35	0.6 to 1.0	0.070	0.05 max
EN 32M	0.10 to 0.18	0.05 to 0.35	0.9 to 1.2	0.10 to 0.15	0.05 max

All tests were carried out in the annealed condition; therefore, the materials exhibited initial cyclic hardening characteristics.

The tubes were subjected to a range of cyclic strains between ± 0.01 and ± 0.03. For the cyclic torsion tests several axial stresses were used between 0 and 272 MN/m^2, and, for the cyclic tension-compression tests, hoop stresses up to 62.6 Mn/m^2 were applied. The results presented in this paper concentrate on the cyclic strain range of ± 0.03.

Results

Cyclic Torsion/Axial Tension

The material parameters which exert a controlling influence on the shape and movement of the yield surface are the uniaxial material properties Z_1 and Z_2 and the cyclic material properties given by the τ-γ relationship. For the material tested, a steady-state cyclic τ-γ relationship was quickly established, and this is shown in Fig. 1, expressed in equivalent stress-strain terms and compared with the uniaxial stress-strain curves obtained after cycling to the steady-state condition. It can be seen that the tensile yield stress is always greater than the compressive yield stress, indicating a degree of anisotropy is being developed due to the axial strain accumulation. Also, the axial stresses are greater than the equivalent cyclic stresses. This would suggest that for this material and cyclic strain range the concept of a limiting yield surface based on isotropic hardening, used by Shiratori et al [2], does not hold.

In order to examine whether this relationship between axial and shear properties was more general, further data were obtained [14] for other materials, shear cycled without end loads, and this is shown in Fig. 2 for two 300 series austenitic stainless steels. It can be seen that, although the axial stress-strain relationships have not been extended very far into the plastic range, they always lie well above the cyclic stress-strain curve. For reasons of clarity, only part of the cyclic stress-strain hysteresis curve is shown.

It has been also shown [3] that the presence of a moderate steady axial stress does not greatly influence the cyclic τ-γ relationship when the cyclic strains are large (>2%). Therefore, Curve 3 of Fig. 1 represents the cyclic material data for the range of axial stresses considered.

The type of material data shown in Fig. 1 can be used, together with Eq 5, to predict the axial plastic strain increment for thin-walled tubes subjected to shear-strain controlled cyclic torsion with static axial stress. Following the method used by Shiratori et al [2] and Yoshida et al [1], the strains in the previous half cycle are considered to be a prestrain. The starting point for defining the material properties is at the beginning of the next half cycle of shear strain. In the

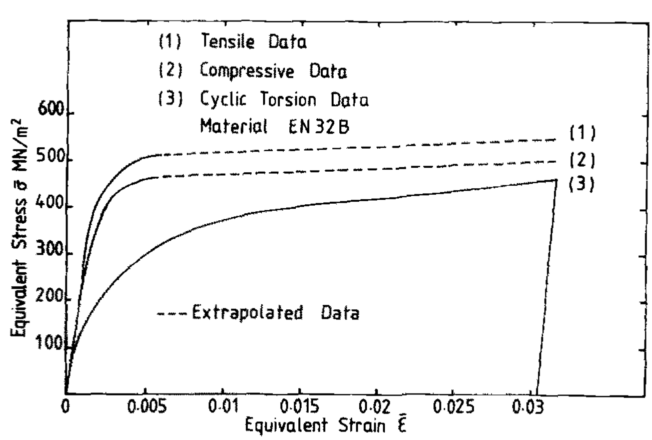

FIG. 1—*Cyclic shear stress strain curve and tension and compression properties after shear strain cycling, low-carbon steel.*

anisotropic model, the material properties needed to construct the yield surfaces are Z_1, Z_2, T_1, and T_2. For the zero axial load condition this process is straightforward since all the required parameters can be obtained from Fig. 1. The values of Z_1 and Z_2 for any particular equivalent strain can be defined, together with T_1 and T_2. The equivalent strain yield surfaces can be then fitted to points Z_1, Z_2, T_1, and T_2 by varying σ_z between Z_1 and Z_2 and calculating the corresponding values from Eq 4. This enables the full yield surfaces to be drawn, as shown in Fig. 3. The material properties, together with Eq 5 define the curvature of the yield surface at the loading point.

For other loading conditions, a different set of material properties would be required. For example, with a static axial stress of 94.5 MN/m^2, the material properties are evaluated as shown in Fig. 4. Values of Z_1 and Z_2 can be obtained directly for a range of equivalent strains. The appropriate values of T_1 and T_2 then have to be calculated using the data available, that is, X_1 and X_2.

By algebraic manipulation of Eq 4 it can be shown that

$$T_1 = X_1 + X_2 - T_2$$

and

$$T_2 = \frac{P\,(X_1 + X_2) + \sqrt{P^2\,(X_1 + X_2)^2 + 4P\,X_1\,X_2}}{2\,P}$$

where

$$P = \frac{\tau^2}{T_1 T_2} - \frac{(T_1 + T_2)\tau}{T_1 T_2} = -1 - \frac{\sigma_z^2}{Z_1 Z_2} + \frac{(Z_1 + Z_2)}{Z_1 Z_2}\,\sigma_z$$

T_1 and T_2 = shear yield stresses, and
X_1 and X_2 = shear yield stresses at a static axial load of 94.5 MN/m^2.

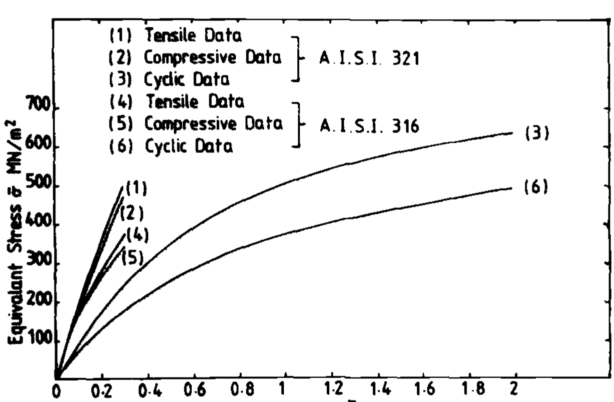

FIG. 2—*Comparison of cyclic shear and tension and compression properties after shear strain cycling, stainless steels.*

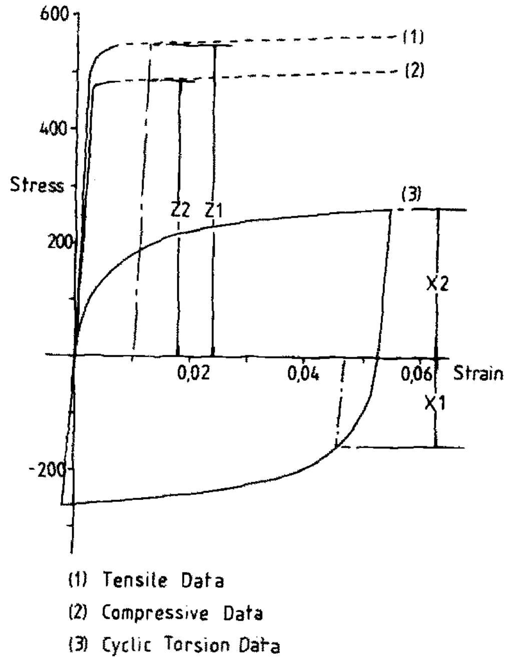

FIG. 3—*Cyclic shear strain curve and tension and compression properties after shear strain cycling with a static axial load, low-carbon steel.*

This calculation simplifies the implementation of the model, specified in Eq 4 to enable it to be fitted to the four points on the axial stress and shear stress axes.

The yield surfaces developed using these data are shown in Fig. 3, and a comparison of the theoretical and experimental axial strains is shown in Fig. 5. Also shown in Fig. 5 are the experimental and theoretical strains for an axial

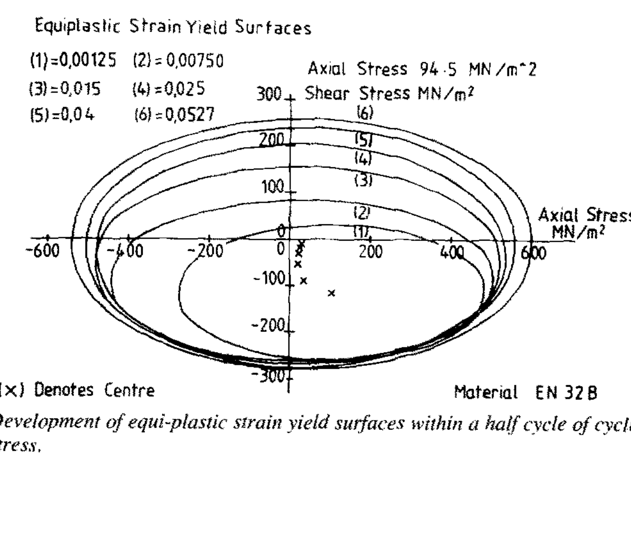

FIG. 4—*Development of equi-plastic strain yield surfaces within a half cycle of cyclic shear with static axial stress.*

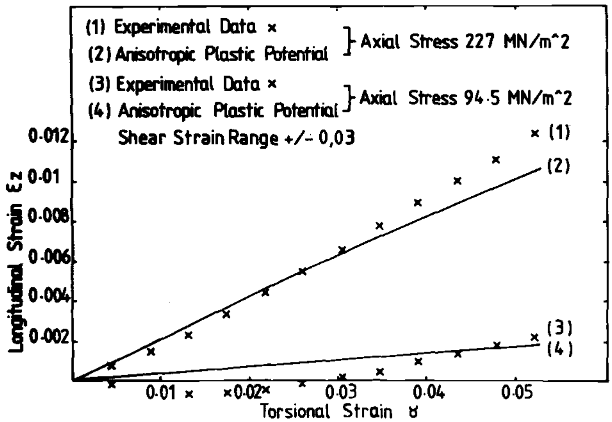

FIG. 5—*Comparison of predicted and experimental strains within a half cycle for large and small axial stresses.*

stress of 227 MN/m^2. Generally, the predictions are quite good for the larger axial stresses, but overestimate the axial strains for small axial stresses.

Cyclic Push-Pull-Internal Pressure

For the material tested, a steady-state cyclic condition was reached after four or five cycles with the peak tensile stress always greater than the peak compressive stress when an internal pressure was applied. The changes in the peak cyclic stresses are shown in Fig. 6 for cyclic axial strains of ± 0.01 and ± 0.03 with a steady hoop stress of 62.6 MN/m^2. The differences in the peak tension and compression values are seen to decrease with increases in the cyclic strain range. The steady-state values with no internal pressure are up to 5% lower than

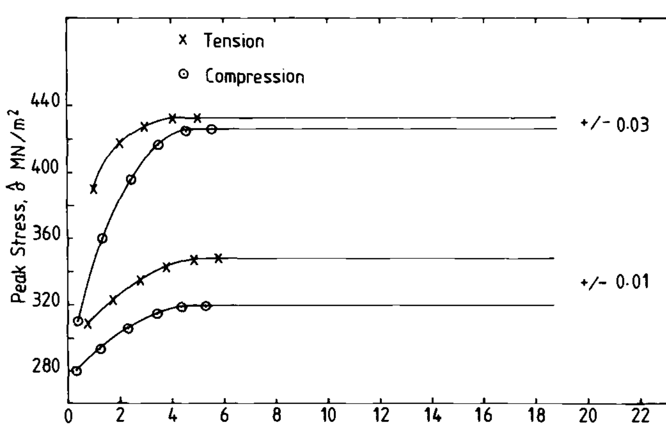

FIG. 6—*Variation of peak cyclic stresses in push-pull. Hoop stress 62.6 MN/m^2.*

when hoop stresses are present, and the cyclic properties are relatively insensitive to small changes in the hoop stress. Reducing the hoop stress from 62.6 to 21 MN/m^2 makes negligible difference in the cyclic behavior for cyclic strains of ± 0.03, and there is only 5% difference at cyclic strains of ± 0.01.

The material properties which control the yield surface are the axial properties Z_1 and Z_2, and the circumferential properties θ_1 and θ_2. The properties in these directions might be expected to be more closely related than in the cyclic torsion-tension case because the principal stresses remain fixed in direction, and the slip planes associated with the hoop and axial strains are essentially the same. Material data in the form of cyclic σ_z-ϵ_z curves are readily available, but data relating to the properties in the hoop direction are more limited. The results of internal pressure tests after push-pull cycling are shown in Fig. 7 together with the cyclic data. There is clearly a difference in the hoop stress-strain relationship obtained at the end of the tension and compression cycles. The internal pressure tests were not extended very far into the plastic range, and the hoop stress-strain relations have been linearly extrapolated in Fig. 7 for the plastic strains above 0.01. The test equipment was not suitable for determining the hoop compression characteristics, but it would be reasonable to assume from the nature of the deformation that at the end of the tension stroke the hoop compression stress-strain curve lies above that obtained at the end of the compression stroke.

Discussion

The anisotropic yield model provides a simple method of constructing yield surfaces but will obviously only produce sensible results when appropriate material data is used. For the cyclic torsion-tension system the predictions appear to be satisfactory for the larger axial stresses, but overestimate the axial strain

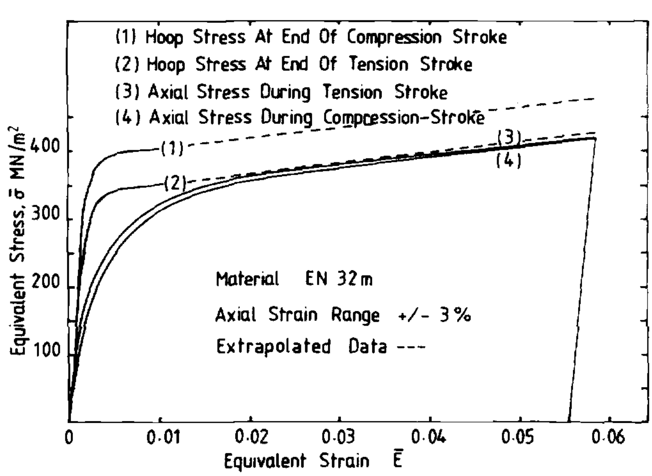

FIG. 7—*Comparison of cyclic push-pull and hoop stress-strain data.*

for the lower axial stresses. The experimental results show that considerable anisotropy is developed by the cyclic process, and there would appear to be no justification for assuming that a bounding yield surface could be constructed on the basis of isotropic hardening. There would also appear to be no physical reason why the yield surfaces should be constructed on the basis of equi-plastic strains for the cyclic plasticity problems, apart from the fact that many previous investigations have used this approach to consider the effects of prestrain and it has been used extensively for other noncyclic yield surface investigations. To use equi-plastic strain for cyclic loading means we are often equating cyclic strains with noncyclic strains, and, as was shown in Fig. 1, they do not always result in the same equivalent stress levels which would be predicted by an isotropic bounding surface. For any element of material undergoing plastic deformation there must exist an instantaneous yield surface which will be modified as plastic straining proceeds. If the plastic strain increment is normal to this yield surface then the plastic strains can be determined by defining a series of instantaneous yield surfaces. Although the physical justification for this is obvious, there are clearly many problems associated with defining in mathematical terms a yield surface which may be severely distorted and with corners or regions of apparent large curvature at the loading point.

Philips and Lee [*15*] have shown that yield surfaces, defined by extremely small plastic strains, are enclosed by loading surfaces. The yield surface is generally tangential to the loading surface at the loading point with the strain increment vectors normal to both surfaces. The problem may be simplified if we consider that all that is required to predict the plastic strains is a knowledge of the curvature of the yield surface at the loading point.

Other points on the yield surface may help to define the curvature at the loading point and are necessary in order to predict the plastic strain response to any changes in the load path. However, it is obvious that the instantaneous curvature at this loading point may be described by other means, for example, equi-plastic strain surfaces, but this may be fortuitous and could lead to problems if applied generally. There is no reason to presuppose that for cyclic problems an increment of strain in one direction should automatically lead to any change of material properties in other directions. The absence of cross effects have been frequently reported, and it is likely that for cyclic problems material properties in particular directions attain certain values which remain constant throughout a strain cycle. This would be a distinct possibility if the plastic strains in a particular direction remain uniaxial and plastic unloading does not occur. This approach can be examined by considering the cyclic torsion-tension problem together with the material data from Fig. 1.

The effect of the cumulative axial strains will be to induce some anisotropy. When plastic flow is established within a cycle of shear strain, that is, the effects of residual stresses become negligible, the anisotropy is reflected in the values of the tension and compression yield stresses. The tensile yield stress is seen to be greater than the compressive yield stress for the range of strains measured.

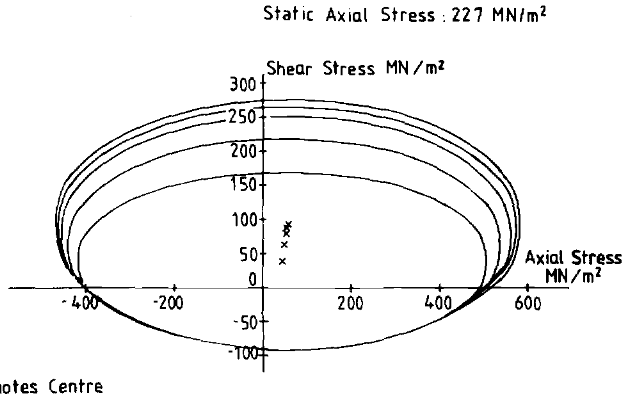

FIG. 8—*Proposed current yield surfaces: cyclic shear with axial stress.*

The instantaneous shear stresses in the forward and reverse directions would necessarily vary at some stages throughout the cycle, with the reverse value decreasing rapidly as the forward shear stress increases. These conditions would result in a yield surface of fixed width along the σ-axis and of varying depth along the τ-axis, moving upward and downwards with the loading point as shown in Fig. 8.

The axial strain predictions using this approach are as good as when using equi-plastic strains. The method can be used to predict the axial shortening observed for the smaller axial loads, but requires more precise interpretation of the material data. It can be also seen that if there are differences in the tension and compression properties due to strain accumulation or heat treatment etc., then length changes will occur when a shear strain is applied, even in the absence of an axial stress.

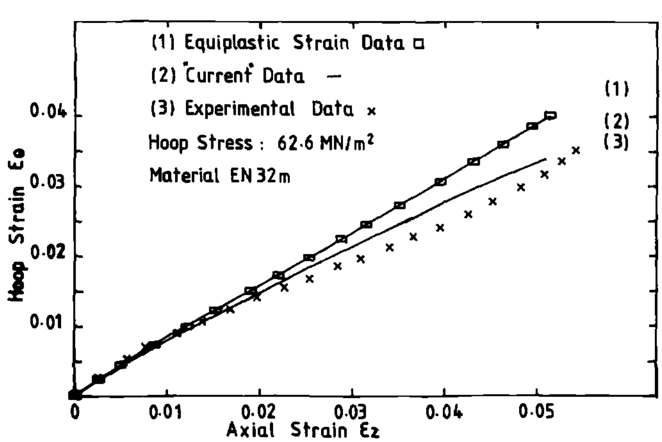

FIG. 9—*Proposed current yield surfaces: push-pull with internal pressure, tension stroke.*

For cyclic push-pull with steady internal pressure, the cumulative hoop strain should result in gradual increase in the hoop tensile yield stress (θ_1), which should be numerically greater than the hoop compressive yield stress (θ_2). However, this needs to be confirmed experimentally, and much more material data are required before the anisotropic approach can be used more generally. Due to Poisson's effects, the hoop strains will be cyclic with a super-imposed tensile hoop stress, and there will be some interaction between the properties developed in the hoop and axial directions. An increase in the axial compressive yield stress (Z_2) should result in a reduction in the hoop compressive yield stress (θ_2) and an increase in the hoop tensile yield stress (θ_1).

Using the material data shown in Fig. 7, a series of yield surfaces have been constructed based on instantaneous or current values of the yield stresses, some of which have had to be estimated, and these are shown in Fig. 9. Predictions of the hoop strains using these surfaces are shown in Figs. 10 and 11, and it can be seen that there is reasonably good agreement with the experimentally observed strains. The centers of the yield surfaces are also shown, and the final yield surface at the end of the tension stroke also defines the first surface at the start of the compression stroke. Using the same material data, the predicted strains based on equi-plastic strain yield surfaces are also shown in Fig. 9, and it can be seen that they compare less favorably than when using current yield surfaces, particularly during the tension stroke.

Conclusions

The anisotropic approach can be used to construct yield surfaces for cyclic plasticity problems using the minimum of material data. However, much more material data are required in order to test its general use for multi-axial cyclic plasticity problems. The anisotropic yield criterion cannot be used to fully describe severely distorted yield surfaces observed [16] in the early stages of

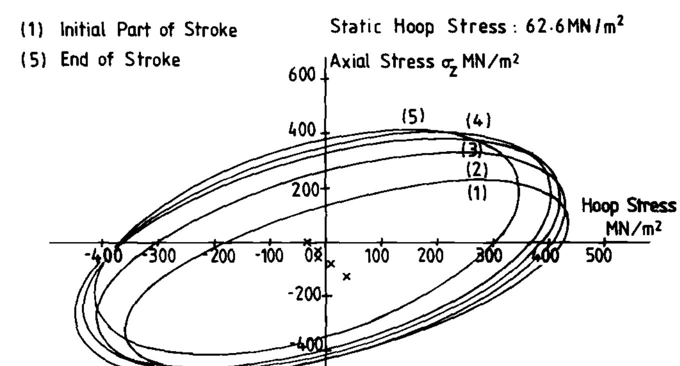

FIG. 10—*Strain predictions using equi-plastic strain and current (or instantaneous) yield surfaces for cyclic push-pull, compression stroke.*

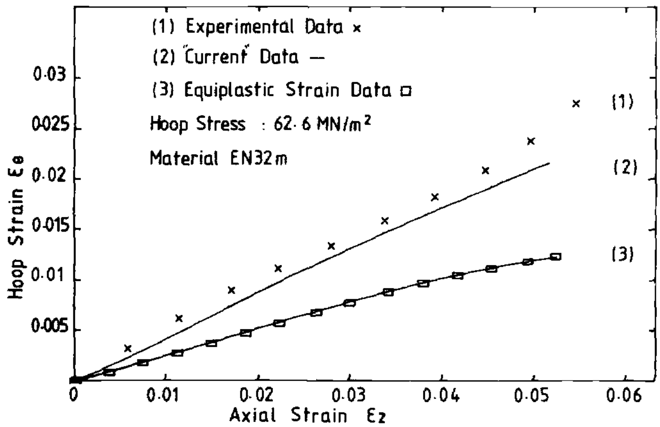

FIG. 11—*Strain predictions using equi-plastic strain and current (or instantaneous) yield surfaces for cyclic push-pull, tension stroke.*

inelastic deformation in torsion tension after a prestrain but will adequately describe the shape and position of the elliptical yield surface developed for other stress systems. A major problem arises in attempting to develop a generalized plasticity approach for cyclic problems when the cyclic strains are of elastic order. The inelastic deformation immediately after stress reversal is controlled to a large extent by microresidual stresses, and it could be argued that the use of anisotropic von Mises type surfaces only become applicable when these stresses have become negligible and plastic flow is established.

The results presented would indicate that the use of current or instantaneous material properties might be more appropriate for construcitng yield surfaces rather than using equi-plastic strain surfaces.

References

[1] Yoshida, F., Tajima, N., and Ikegami, K., Japan Society of Mechanical Engineers, Vol. 12, No. 153, 1978, pp. 389–397.
[2] Shiratori, E., Ikegami, K., and Yoshida, Y., *Journal of the Mechanics and Physics of Solids,* Vol. 27, 1979, pp. 213–229.
[3] Bright, M. R. and Harvey, S. J. in *Non Linear Problems in Stress Analysis,* P. Stanley, Ed., Applied Science Publishers, London, 1977.
[4] Harvey, S. J., Bright, M. R., and Breckell, T. H., "Deformation Modes in Cyclic Plasticity," 4th International Conference on Pressure Vessel Technology, London, 1980.
[5] Moreton, D. N. and Moffat, D. G., "Shakedown of 3 Stainless Steel Pressure Vessel Components," 3rd International Conference on Pressure Vessel Technology, Tokyo, 1977, pp. 233–245.
[6] Mroz, Z., *Acta Mechanical,* Vol. 1, 1969, pp. 199–212.
[7] Dafalias, Y. and Popov, E., *Acta Mechanical,* Vol. 21, 1975, pp. 173–192.
[8] Prager, W., *Journal of Applied Mechanics, Transactions,* American Society of Mechanical Engineers, Vol. 78, 1956, pp. 493–496.
[9] Ziegler, H., *Quarterly Applied Mathematics,* Vol. 17, 1959, pp. 55–65.
[10] Shield, R. T. and Ziegler, H., *Zeitschrift für Angewandte Mathematik und Physik,* Vol. 9a, Part 3, 1958, pp. 260–276.

[*11*] Hill, R., *The Mathematical Theory of Plasticity,* 1st Edition, 1950, Oxford University Press, Oxford, U.K.
[*13*] Harvey, S. J., Jeans, P. J., and Adkin, P., *Journal of Fatigue of Engineering Materials and Structures,* Vol. 6, No. 1, 1983, pp. 89–100.
[*14*] Breckell, T. H., "The Effect of Martensitic Transformations on the Fatigue Behaviour of Stainless Steel in Cyclic Plastic Torsion," Ph.D. thesis, 1976, Coventry (Lanchester) Polytechnic, Lanchester, U.K.
[*15*] Phillips, A. and Lee, C. W., *International Journal of Solid Structures,* Vol. 15, 1979, pp. 715–729.
[*16*] Williams, J. F. and Svenson, N. L., *International Strain Analysis,* Vol. 6, No. 4, 1970, pp. 263–272.

David L. McDowell[1] *and Darrell F. Socie*[2]

Transient and Stable Deformation Behavior Under Cyclic Nonproportional Loading

REFERENCE: McDowell, D. L. and Socie, D. F., "**Transient and Stable Deformation Behavior Under Cyclic Nonproportional Loading,**" *Multiaxial Fatigue, ASTM STP 853,* K. J. Miller and M. W. Brown, Eds., American Society for Testing and Materials, Philadelphia, 1985, pp. 64–87.

ABSTRACT: The transient hardening behavior of metals subjected to nonproportional cyclic loading, including the corresponding cyclically stable state, is dependent on plastic strain range in addition to the "degree" of nonproportionality. Experiments were performed on thin-walled tubular specimens of stainless steel 304 in combined tension-compression and torsion to investigate sequence effects, memory of prior loading, and rate changes of cyclic hardening under complex, nonproportional, strain-controlled cyclic loading. The material was observed to remember cyclic hardening achieved under the most severe nonproportional loading case. Effective stress states achieved by cycling at increasingly severe nonproportionality of loading increased correspondingly and tended to "wash out" the effects of less severe nonproportional paths. For several complex nonproportional paths, the actual intermediate cyclically stable (or near stable) effective stress states were correlated accurately using a path-dependent integral. Only uniaxial and 90° out-of-phase sinusoidal test results are required by this integral representation.

KEY WORDS: multiaxial, biaxial, nonproportional, cyclic hardening, cyclic plasticity, cyclic stress-strain curve

Nomenclature

D_o, D_i	Specimen outside and inside diameters
E	Young's modulus
F	Rotation factor
G	Shear modulus
$\bar{g}, \bar{h}$	Step functions
$k, \bar{k}, k^*, \bar{k}_{90}$	Cyclic strength coefficients
$L(\theta)$	Hardening distribution for loading for which $Q \geq Q_o$ always

[1] Assistant professor, School of Mechanical Engineering, Georgia Institute of Technology, Atlanta, GA 30332.

[2] Associate professor, Department of Mechanical and Industrial Engineering, University of Illinois at Urbana-Champaign, Urbana, IL 61801.

Copyright© 1985 by ASTM International www.astm.org

l,m	Material constants
$n,\bar{n},\bar{n}^*,\bar{n}_{90}$	Cyclic strain hardening exponents
P	Axial load
Q	Measure of instantaneous deviation from proportionality
Q_o	Threshold value of Q
T	Torque
u	Step function
β	A phase angle
γ_{max}	Maximum engineering shear strain
γ,γ_a	Engineering shear strain and shear strain amplitude
$\Delta\gamma_{max}{}^P$	Maximum range of plastic shear strain for all planes in a cycle
$\Delta\overset{*}{\gamma}_{max}{}^P$	Maximum range of plastic shear strain in incremental step test (history)
$(\Delta\gamma_{max})_i$	Range of shear strain on i^{th} set of maximum shear strain planes in a cycle
$\Delta\tau_{max}$	Maximum range of shear stress for all planes in a cycle
ϵ,ϵ_a	Axial strain and strain amplitude
$\boldsymbol{\epsilon}$	Total strain tensor
$\epsilon_a{}^P$	Axial plastic strain amplitude
ϵ_1,ϵ_3	Largest and smallest principal strains
$(\dot{\boldsymbol{\epsilon}})_1,(\dot{\boldsymbol{\epsilon}})_3$	Largest and smallest principal values of the strain rate tensor
$\dot{\bar{\epsilon}}$	Effective strain rate
θ,θ_i	Angles from reference axis
μ	Poisson's ratio
σ	Axial stress
σ_a	Axial stress amplitude
σ_1,σ_3	Largest and smallest principal stresses
τ	Shear stress
τ_{max}	Maximum shear stress
ϕ_1,ϕ_2,ϕ	History-dependent measures of nonproportional hardening state
ω	Frequency

The cyclic hardening and softening response of metals has been the subject of a number of experimental studies [*1–5*]. Information from these tests has been largely used to evaluate proposed cyclic plasticity models [*6–9*] or to determine a cyclic stress-strain curve used to predict steady-state deformation response [*10–12*].

Most previous investigations have centered on uniaxial cyclic hardening or softening. These studies have resulted in a considerable body of knowledge and established analytical techniques [*13,14*] for predicting local cyclic stress-strain response at notches and other "stress-raisers." Often these methods base stress-strain response on cyclic stress-strain curves determined from uniaxial tests. At first glance, it might appear that a multiaxial generalization of these analytical techniques based on an effective stress-strain approach would be sufficient to correlate cyclic hardening or softening behavior. This is not the case, however, for nonproportional loading where the principal axes of strain rotate during cyclic plastic flow. In this case, the cyclic stress-strain curve based on effective stress and strain is not unique but depends on the degree of nonproportionality of loading. A number of cases of practical design interest fall into this category.

Rotation of the maximum plastic shear strain planes leads to additional cyclic hardening. For a given octahedral shear strain amplitude, for example, the octahedral shear stress amplitude may increase significantly during completely reversed, nonproportional cyclic plastic straining. Furthermore, this increase in effective stress amplitude is observed to exceed the stable cyclic stress-strain response for uniaxial or proportional loading. Proportional loading may be defined by

$$\dot{\epsilon}_{ij} = \dot{\eta}\epsilon_{ij}^{o} \tag{1}$$

where

ϵ_{ij}^{o} = a constant, nonzero strain tensor,
$\dot{\eta}$ = a scalar proportionality factor, and
$\dot{\epsilon}_{ij}$ = total strain rate tensor.

For nonproportional loading, the equality in Eq 1 does not hold. This paper will be concerned with the case where the principal axes of total and plastic strain rotate as in strain-controlled, nonproportional, axial-torsional tests on thin-walled tubular specimens.

Several previous experimental investigations have been conducted to study transient deformation behavior of metals subjected to nonproportional loading. Some studies have concentrated on the shape changes of yield surfaces during loading and unloading [*4,15–17*]. Others have considered the cyclic increase or decrease of stress component amplitudes to characterize cyclic hardening or softening [*5,18*]. In all of these studies, the effect of nonproportional loading was to cyclically harden the material above the cyclically stable state obtained for proportional loading at the same effective strain amplitude. This phenomenon was observed for materials which cyclically soften or harden during uniaxial loading.

In the present study, correlations for cyclic hardening of metals subjected to complex nonproportional loading are investigated.

Correlating Parameters

Kanazawa, Miller, and Brown [*18*] showed for 1% Cr-Mo-V steel that the additional hardening for sinusoidal axial-torsional strain paths could indeed be correlated using the maximum shear stress-strain (Tresca) theory. Consider axial-torsional straining of thin-walled tubular specimens defined by

$$\begin{aligned} \epsilon_{11} &= \epsilon = \epsilon_a \sin \omega t \\ \epsilon_{22} &= \epsilon_{33} = -\mu\epsilon_{11} \\ 2\epsilon_{12} &= \gamma = \gamma_a \sin(\omega t - \beta) \\ \epsilon_{23} &= \epsilon_{13} = 0 \end{aligned} \tag{2}$$

where

ω = frequency,
μ = Poisson's ratio, and
β = phase angle.

Here, the subscripts 1, 2, 3 on the strain tensor denote the axial, circumferential, and radial directions of the tubular test specimen.

Brown and Miller defined a "universal" stable cyclic stress-strain curve as

$$\tau_{max} = k(\gamma_{max}/2)^n(1 + lF) \tag{3}$$

where

$$\tau_{max} = (\sigma_1 - \sigma_3)/2, \text{ and } \gamma_{max} = \epsilon_1 - \epsilon_3$$

The maximum and minimum principal stresses and strains are denoted by σ_1, ϵ_1, and σ_3, ϵ_3, respectively. The material constant l reflects the sensitivity of the cyclic hardening response to nonproportional loading. The strength coefficient, k, and strain hardening exponent, n, are determined by linear regression of in-phase test data. Constant l is chosen to fit out-of-phase results.

The rotation factor, F, is defined as

$$F = \frac{\text{shear strain range at 45° to maximum shear plane}}{\text{maximum shear strain range}} \tag{4}$$

The rotation factor may take on any value between 0 and 1. If $\beta = 0°$ or $\beta = 180°$, then $F = 0$. For the experimentally observed maximum hardening case of $\gamma_a/\epsilon_a = (1 + \mu)$ and $\beta = 90°$, $F = 1$. When $\beta = 0$ or $180°$, the maximum shear strain planes are fixed with respect to the material. When $\beta = 90°$ and $\gamma_a/\epsilon_a = (1 + \mu)$, the maximum shear strain planes rotate at a constant rate, and every plane is a maximum shear strain plane at some point during the loading cycle. This leads to maximum dislocation interaction which maximizes impediment of cyclic plastic flow.

Other values of β lead to values of F which accurately correlate sinusoidal loading according to Eq 3. Therefore, F is a variable indicative of the potential stable state. For the restricted case of sinusoidal loading the rotation factor is easy to calculate and the potential state described by Eq 3 is eventually reached by continued cycling.

The cyclic stress-strain curve in Eq 3, based on effective stress and strain, is a useful analytical tool for predicting deformation response during cyclic nonproportional loading [*19,20*]. The isotropic hardening parameters and plastic moduli in cyclic plasticity models can be based on such stress-strain curves [*19*].

The Brown and Miller correlation is useful for two reasons: it requires only knowledge of the applied strains, and it fits experimental data for sinusoidal axial-torsional paths satisfactorily. The quantity F, which varies between 0 and 1, need not be defined by Eq 4. Another possibility for a metallurgical definition is the size and shape of the dislocation cell structures obtained from tests of varying degrees of nonproportionality [*21*].

For arbitrary nonproportional loading, calculation of F in Eq 4 is somewhat inefficient for implementation in constitutive models for deformation since the shear strain ranges on all material planes in a history must be known. Hence, the following development is motivated by a desire for a parameter, analogous to F, which depends only on the strain rate history through a minimum number of path-dependent integrals. For any loading path, including nonproportional cases where the principal axes of strain rotate, the following path-dependent, incremental approach is introduced. Define two quantities

$$\dot{\gamma}_{\max}(\boldsymbol{\epsilon}) = \frac{d}{dt}(\epsilon_1 - \epsilon_3) \tag{5}$$

$$\gamma_{\max}(\dot{\boldsymbol{\epsilon}}) = (\dot{\boldsymbol{\epsilon}})_1 - (\dot{\boldsymbol{\epsilon}})_3 \tag{6}$$

where ϵ_1, ϵ_3 = largest and smallest principal strains, respectively, $(\dot{\boldsymbol{\epsilon}})_1$, $(\dot{\boldsymbol{\epsilon}})_3$ = largest and smallest principal values of the strain rate tensor, and $\boldsymbol{\epsilon}$ is the total strain tensor. For $\dot{\epsilon}_{ij}\dot{\epsilon}_{ij} > 0$, the quantity

$$Q = \left| \frac{\dot{\gamma}_{\max}(\boldsymbol{\epsilon})}{\gamma_{\max}(\dot{\boldsymbol{\epsilon}})} \right| \tag{7}$$

provides an instantaneous measure of the deviation of the strain increment from proportionality. For the strain state in a thin-walled tubular specimen defined in Eq 2

$$Q = |(\epsilon_{11}\dot{\epsilon}_{11}(1 + \mu)^2 + 4\epsilon_{12}\dot{\epsilon}_{12})/[(\epsilon_{11}^2(1 + \mu)^2 + 4\epsilon_{12}^2)(\dot{\epsilon}_{11}^2(1 + \mu)^2 + 4\dot{\epsilon}_{12}^2)]^{1/2}| \tag{8}$$

If the loading is proportional as defined in Eq 1, then $Q = 1$. For $\beta = 90°$ and $\gamma_a/\epsilon_a = (1 + \mu)$ in Eq 2, $Q = 0$. For all other nonproportional loading,

$0 < Q < 1$. In fact, obtaining these values of Q for $\beta = 0°$ and $\beta = 90°$ with $\gamma_a/\epsilon_a = (1 + \mu)$ was the motivation for the definition in Eq 7. Physically, an increase of Q is representative of a decrease in rotation of maximum shear planes, and a corresponding decrease in dislocation interaction. The actual stable state achieved during axial-torsional cycling is a path-dependent function of Q. Define ϕ_1 for a given cyclic loading path in direct analogy to F as

$$\phi_1 = u\left(\int_{t_o}^{t} u(Q_o - Q)(\dot{\epsilon}:\dot{\epsilon})^{1/2}dt'\right) \frac{\int_{t_o}^{t} u(Q_o - Q)(\dot{\epsilon}:\dot{\epsilon})^{1/2}Q\,dt'}{g\left(\int_{t_o}^{t} u(Q_o - Q)(\dot{\epsilon}:\dot{\epsilon})^{1/2}dt'\right)} \tag{9}$$

where Q_o is a threshold constant, and $\dot{\epsilon}:\dot{\epsilon} = \dot{\epsilon}_{ij}\dot{\epsilon}_{ij}$; $u(x) = 1$ if $x >$, $u(x) = 0$ otherwise. The function g is defined by $g(x) = 1$ if $x = 0$; $g(x) = x$ if $x \neq 0$. The ϕ_1 function may be interpreted as a weighted or "average" value of the degree of nonproportionality over the loading cycle. The $u(Q_o - Q)$ function of Eq 9 is introduced to omit contributions from loading which are radial in strain space. Thus, Eq 9 allows contributions only from those portions of axial-torsional loading paths for which the maximum shear strain planes rotate continuously. This is consistent with the mechanisms responsible for additional nonproportional hardening, since changes in direction of the applied shear stress within each grain can be associated with increased slip and dislocation interaction. A suitable value of Q_o might range from 0.85 to 0.95; ϕ_1 is relatively insensitive to the actual value used, particularly if the loading is moderately or severely nonproportional in each cycle. Note that ϕ_1 is nonzero only if $Q < Q_o$ at some point in the loading cycle.

Sinusoidal, out-of-phase, axial-torsional loading is an example of continuous rotation of the maximum shear strain planes. For sinusoidal paths in axial-torsional strain space defined by Eq 2, it is informative to compare ϕ_1 in Eq 9 with F of Eq 4. Values of F and ϕ_1 computed for a variety of loading cases appear in Table 1 for $Q_o = 0.9$. Note that for $\beta = 0°$ and $\beta = 90°$ with γ_a/

TABLE 1—*Stable values of ϕ_1 and F for various phase angles and strain ratios.*

μ	γ_a/ϵ_a	β, deg	F	ϕ_1
0.5	1.5	60	0.577	0.664
0.3	1.5	60	0.566	0.654
0.5	1.5	30	0.268	0.322
0.3	1.5	30	0.265	0.319
0.5	1.5	0	0.000	0.000
0.5	1.5	90	1.000	1.000
0.5	1.0	90	0.667	0.746
0.5	2.0	90	0.750	0.819
0.5	4.0	45	0.247	0.297
0.5	4.0	90	0.375	0.451
0.5	4.0	135	0.247	0.297
0.5	∞	...	0.000	0.000
0.5	0	...	0.000	0.000
0.5	1.5	45	0.414	0.494

$\epsilon_a = (1 + \mu)$, ϕ_1 and F are both exactly 0 and 1, respectively. For intermediate phase angles and γ_a/ϵ_a ratios, ϕ_1 is slightly greater than F. The ϕ_1 approach tends to correlate data for phase angles between 0 and 90° reported in Ref *18* as good or better than the rotation factor, F, in Eq 4. For phase angles between 0 and 90°, ϕ_1 oscillates due to the variation of Q and settles down to a stable value within 10 cycles. These stable values after 10 cycles are those reported in Table 1. Note that ϕ_1 is insensitive to changes in Poisson's ratio. The ϕ_1 function is plotted in Fig. 1 for several sinusoidal cyclic loading paths for $Q_o = 0.9$.

Since Q in Eq 7 may be determined at each time instant, calculation of ϕ_1 for any arbitrary cyclic path requires only that the integrals in Eq 9 be computed. Computation of ϕ_1 is, in general, more efficient than that of F, which requires knowledge of shear strain ranges on all material planes. Hence, ϕ_1 is of an appropriate form for use in an isotropic hardening rule [*22*].

It is possible to conceive of paths in ϵ-γ space where $Q = 1$ yet the loading is nonproportional. A path consisting of a discrete number of sets of maximum shear strain planes is shown in Fig. 7. For this type of path, $\phi_1 = 0$ since $Q > Q_o$ always. It is necessary to define a function ϕ_2, analogous to ϕ_1 and F, which correlates the hardening state. Define each direction of the i sets of maximum shear strain planes by an angle measured from a reference axis fixed in the specimen wall, θ_i, such that $0 \leq \theta_i < \pi/2$. Then consider a distribution, $L(\theta)$, of the range of shear strain on each of these maximum shear strain planes that is representative of dislocation interaction effects due to switching between discrete sets of maximum shear strain planes (cross effects)

$$L(\theta) = \max_{\text{all } i} \left\{ \sum_{n=-1}^{1} \left[(\Delta\gamma_{\max})_i \left| \frac{\theta - \theta_i + n\pi/2}{\pi/4} \right|^{2m} h \times \left(1 - \left| \frac{\theta - \theta_i + n\pi/2}{\pi/4} \right| \right) \right] \right\} \tag{10}$$

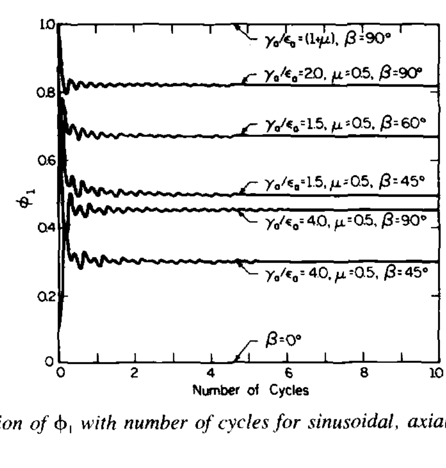

FIG. 1—*Variation of ϕ_1 with number of cycles for sinusoidal, axial-torsional loading.*

where

$(\Delta\gamma_{max})_i$ is the range of shear strain on the i^{th} set of maximum shear strain planes during a loading cycle,

m = material constant, and

$h(x) = 1$ if $x \geq 0$; $h(x) = 0$ otherwise.

The angle θ is measured from the same reference axis as θ_i.

Then, ϕ_2 is defined as

$$\phi_2 = \frac{\min(L(\theta))}{\max(L(\theta))} \tag{11}$$

for $0 \leq \theta < \pi/2$.

For cyclic loading paths for which $Q < Q_o$ at some points in each cycle the definition of $\phi = \phi_1$ in Eq 9 is appropriate. If $Q \geq Q_o$ at all points in the loading cycle, then we can define $\phi = \phi_2$. The parameter ϕ, based on these definitions, is analogous to the rotation factor F. For any given strain cycle, only one of these definitions for ϕ can hold.

As an example, consider a cycle consisting of axial straining followed by torsional straining as shown in Fig. 2*a*. Assuming the maximum shear strain amplitude on each set of maximum shear planes is equal, the resulting hardening distribution, $L(\theta)$, for a variety of m and μ values is shown in Fig. 2*b*. In this case $Q = 1$ always, and the reference axis is the axial tube direction. The parameter $\phi = \phi_2$ is reported in Fig. 2*b* for several m and μ values. Note that ϕ is insensitive to changes in Poisson's ratio.

The material constant m can be found from the test of Fig. 2 by fitting the observed increase in the strength coefficient in an expression such as Eq 3. Such an expression, of course, does not attempt to correlate the anisotropic deformation of yield or loading surfaces [*15–17*], but must be viewed as relevant to the isotropic portion of a combined isotropic-kinematic cyclic plasticity theory [*9,23,24*].

Hence, a ϕ-parameter has been introduced, motivated by the experiments of Kanazawa, Miller, and Brown [*18*], with superior computational efficiency and similar correlation capability for nonproportional cyclic hardening to the rotation factor F. It is useful to investigate whether or not ϕ can correlate the stable cyclic hardening states for histories other than sinusoidal loading, and for histories consisting of successive blocks of nonproportional cycles. Such histories are reported in the next section.

Experimental Results

The material chosen for this cyclic deformation study was stainless steel 304 because of its appreciable hardening and Masing-type behavior. This material undergoes a plastic strain range dependent transformation from metastable austenite to martensite during cycling [*25*] which renders a Ramberg-Osgood cor-

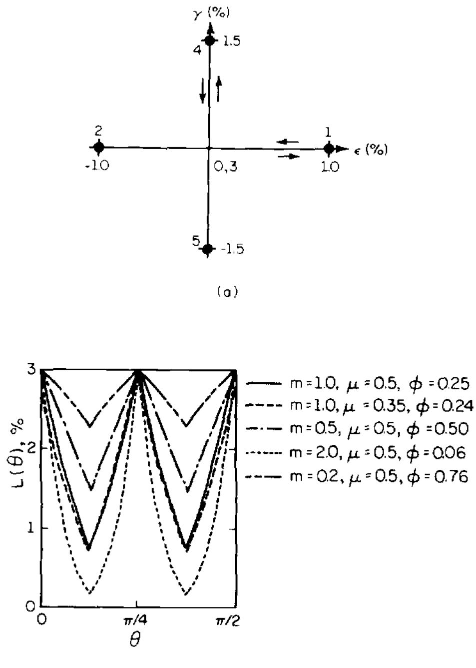

FIG. 2—*Hardening distribution for two discrete sets of maximum shear planes:* (a) *strain path with numbered loading sequence,* (b) *resulting hardening distributions for various* m *and* μ *values.*

relation with single-valued strength coefficient and strain hardening exponent inaccurate over a wide range of maximum plastic strain amplitudes. To determine the cyclic stress strain curve under proportional ($\phi = 0$) loading, four uniaxial strain-controlled incremental step tests [*12*] at maximum strain amplitudes ranging from 0.003 to 0.01 and $\dot{\epsilon} = 0.002\ s^{-1}$ were run to determine the stable effective cyclic strength coefficient and strain hardening exponent in the expression

$$\Delta\tau_{max} = \bar{k}(\Delta\gamma_{max}{}^{P}/2)^{\bar{n}} \tag{12}$$

where $\Delta\tau_{max}$ and $\Delta\gamma_{max}{}^{P}$ are the maximum ranges of shear stress and plastic shear strain, respectively, for all planes in the material in each cycle. For uniaxial tests, $\Delta\tau_{max} = \sigma_a$ and $\Delta\gamma_{max}{}^{P} = 3\epsilon_a{}^{P}$, where σ_a and $\epsilon_a{}^{P}$ are the axial stress and plastic strain amplitudes, respectively. All uniaxial specimens were heat treated at 1100°C for 40 min in a vacuum and furnace cooled to achieve the relatively isotropic grain structure shown in Fig. 3 with an ASTM grain size number of 4. Fortuitously, changes in $\bar{n}$ were found to be negligible in comparison to changes in $\bar{k}$ as a function of maximum range of plastic shear strain in the

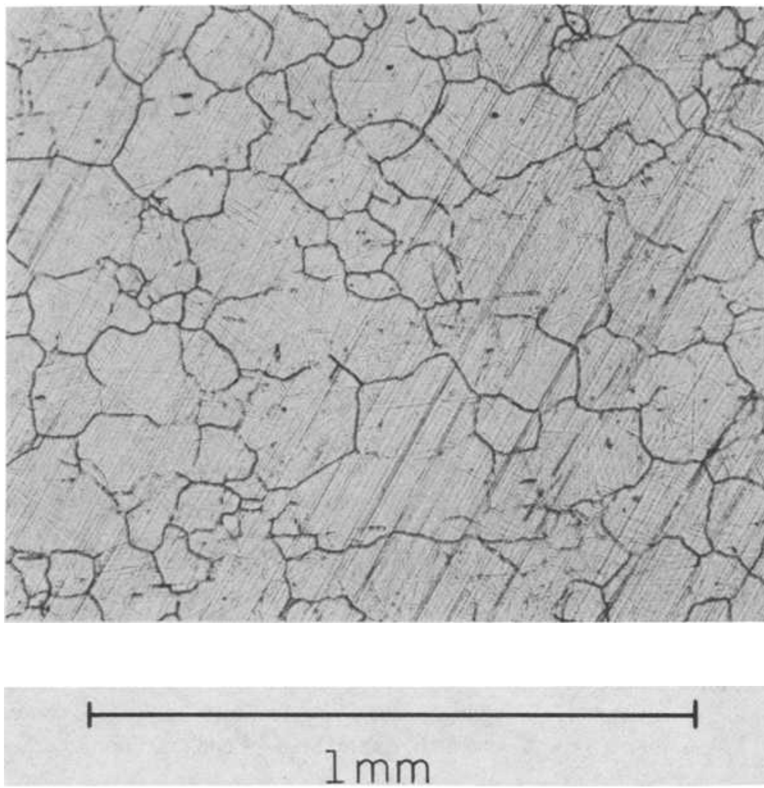

FIG. 3—*Grain structure of heat-treated stainless steel 304.*

incremental step test, $\Delta\overset{*}{\gamma}_{max}{}^{P}$, and the dependence on $(\Delta\overset{*}{\gamma}_{max}{}^{P}/2)$ was approximated with enough accuracy by

$$\bar{k} = (585 + 473\,(\Delta\overset{*}{\gamma}_{max}{}^{P}/2) + 572\,727\,(\Delta\overset{*}{\gamma}_{max}{}^{P}/2)^2)\ \text{MPa} \tag{13}$$

where

$$\bar{n} = 0.145$$

This representation of $\bar{k}$ was selected by performing a best fit of $\bar{k}$ in Eq 12 with $\bar{n} = 0.145$ to the hysteresis loop response from incremental step tests at several $\Delta\overset{*}{\gamma}_{max}{}^{P}$ levels. Due to the amplitude dependent transformation of austenite to martensite, the maximum plastic strain range in a history must be known. Then, $\bar{k}$ and $\bar{n}$ in Eq 13 can be considered as constant for subsequent cycling such that $\Delta\gamma_{max}{}^{P} \leq \Delta\overset{*}{\gamma}_{max}{}^{P}$.

In this investigation, the stress-strain response after 40 to 50 cycles was considered cyclically stable since the cyclic stress amplitudes increased only by a few percent for 50 additional cycles. This definition of cyclic stability is also useful for correlation of hardening for the three histories to be reported in this study, since each loading block is of the order of 20 to 50 cycles.

Tension-torsion tests were performed on tubular specimens with the same material and heat treatment (same grain size). The wall-thickness to outside diameter ratio of 0.11 was found necessary from experience to prevent buckling for cyclic loading at significant plastic strain levels. From finite element analysis and strain gage work, the variation in axial strain along the gage length was less than 3%. There were approximately 25 grains across the wall thickness. A diagram of the specimen appears in Fig. 4.

Collets were used to grip the specimen on its round ends. An internal extensometer was placed inside the specimen with a gage length of 25.4 mm. A linear variable differential transformer (LVDT) was used to measure axial displacement between contact points at the gage length, while a rotary variable differential transformer (RVDT) measured the relative angle of twist. The LVDT and RVDT were decoupled by a bellows on the output shaft. See Ref *26* for further details of extensometry.

The biaxial tests were performed on a computer controlled, closed-loop, servohydraulic test machine. A computer program was written so that any combination of line segments in strain space could be joined end-to-end to define a loading cycle. A block was defined as an arbitrary number of identical cycles. Furthermore, the program allows the user to define any number of blocks, each containing a different cycle loading path. The effective strain rate ($\dot{\bar{\epsilon}} = (\dot{\epsilon}^2 + \dot{\gamma}^2/3)^{1/2}$ assuming $\mu = 0.5$) was kept approximately constant along each segment.

Axial stress, σ, and shear stress, τ, were calculated from the axial load, P, and torque, T, as

$$\sigma = 4P/(\pi(D_o^2 - D_i^2)) \tag{14}$$

$$\tau = 12T/(\pi(D_o^3 - D_i^3)) \tag{15}$$

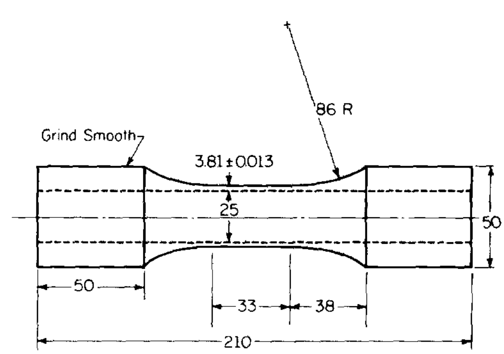

FIG. 4—*Tubular biaxial specimen. Dimensions in millimetres.*

with the assumption that the stresses are uniform across the wall thickness. D_o and D_i are the gage section outside and inside diameters, respectively. This assumption obviously involves some error, but the deformation theory of plasticity cannot be used to estimate the stress distribution for nonproportional loading. Brown and Miller [*11,18*] showed that the error in maximum shear stress

$$\tau_{max} = [\tau^2 + (\sigma/2)^2]^{1/2} \tag{16}$$

is small for proportional loading and assumed small for nonproportional loading, particularly if there is significant cyclic plasticity present.

The shear strain was obtained by dividing the angle of twist by the gage length and multiplying by the mean radius.

Strain Histories and Predictions

Nonproportional, strain-controlled axial-torsional tests were conducted to investigate the path dependence of cyclic hardening, memory of prior hardening, load sequence effects, and correlation potential of the ϕ approach with regard to the actual stable effective stress state achieved during cycling. For nonproportional loading, the stable cyclic stress-strain curve is given as

$$\Delta\tau_{max} = \bar{k}^*(\Delta\gamma_{max}{}^P/2)^{\bar{n}^*} \tag{17}$$

where

$\bar{k}^* = \bar{k} + \phi(\bar{k}_{90} - \bar{k})$,

$\bar{n}^* = \bar{n} + \phi(\bar{n}_{90} - \bar{n})$, and

$\bar{k}_{90}$ and $\bar{n}_{90}$ = the strength coefficient and strain hardening exponent, respectively.

This provides a fit to the stable cyclic stress-strain curve obtained from sinusoidal tests with $\beta = 90°$ and $\gamma_a/\epsilon_a = 1.5$ at three $\Delta\overset{*}{\gamma}_{max}{}^P/2$ values [*18,22*] from 0.0045 to 0.015. Assuming $\mu = 0.5$, $\phi = 1$ for these tests. Three tests were conducted in which the strain amplitudes were successively increased or decreased after reaching stability at each previous level. It was found that the maximum stable range of shear stress in a cycle and the corresponding maximum range of plastic shear strain for $\Delta\gamma_{max}{}^P \leq \Delta\overset{*}{\gamma}_{max}{}^P$ were described with sufficient accuracy by

$$\Delta\tau_{max} = 1304(\Delta\gamma_{max}{}^P/2)^{0.145} \tag{18}$$

Thus, $\bar{k}_{90} = 1304$ MPa and $\bar{n}_{90} \simeq 0.145$. The value $\bar{n} = \bar{n}_{90} = 0.145$ was chosen for convenience since only slight variations in $\bar{n}$ and $\bar{n}_{90}$ about 0.145 were observed for $\beta = 0$ and 90° tests at several $\Delta\overset{*}{\gamma}_{max}{}^P$ ranges. In contrast, $\bar{k}^*$

experienced significant variation, justifying the current approximation. For $\Delta\overset{*}{\gamma}_{max}{}^{P}/2$ ranging from 0.0045 to 0.015, $\bar{k}_{90}$ was reasonably constant.

To facilitate computation of plastic strain ranges necessary for Eqs 13 and 17, load-displacement data were acquired for the first ten cycles of each block. Then the increments of plastic strain were computed using suitable numerical analysis. The maximum plastic shear strain ranges and planes for nonproportional loading were also computed for each block of loading.

Results of three separate strain-controlled tension-torsion tests are reported in this investigation. The initial values of Young's modulus and the shear modulus were determined as E = 188 GPa and G = 77 GPa, respectively.

Specimen SS09: History 1—To investigate the sequence effects, path dependence of the stable cyclic state, and material response to a sudden increase in the degree of nonproportionality, the specimen was subjected to 10 cycles of a proportional, 10 level incremental step test with maximum strain amplitudes of $\epsilon_a = 0.007$, $\gamma_a = 0.0105$ and a strain rate $\dot{\epsilon} = 0.001\ s^{-1}$. The strain amplitudes were increased and decreased within each cycle. Then three successive blocks of sinusoidal loading shown in Fig. 5 were applied with phase angles of $\beta = 0°$ (16 cycles), 30° (25 cycles), and 60° (25 cycles), respectively. For all three blocks, $\epsilon_a = 0.005$ and $\gamma_a = 0.0075$.

The stress-space response for the 16th cycle of block 1 and the first ten cycles of blocks 2 and 3 is shown in Fig. 6. Notice that the maximum effective stress in a cycle, the maximum value of $(\sigma^2 + 4\tau^2)^{1/2}$, increases in each block even though calculations based on the data reveal that $\Delta\gamma_{max}{}^{P}$ actually decreases for each successive block. Hence, this increase in effective stress must be associated with increased resistance to cyclic plastic flow via dislocation interaction, etc. Interestingly, as shown in Ref *22*, the rate of increase of the effective stress in each block due to an increase in the degree of nonproportionality of loading is the same as the cyclic rate of increase of stress amplitude due to a sudden increase in strain amplitude in a uniaxial test for stainless steel 304. This indicates that the same physical processes govern hardening during proportional and nonproportional loading for this material but to different degrees.

After applying these three loading blocks, the specimen was cycled proportionally with $\epsilon_a = 0.005$, $\gamma_a = 0.0075$, and $\beta = 0°$. Subsequently, virtually no decrease of the maximum effective stress was observed. This result suggests that the "state" of resistance to plastic flow achieved by prior cyclic hardening is nonfading or slowly fading for this particular material at room temperature where annealing mechanisms are not activated. However, generalizations cannot be made regarding memory loss of prior nonproportional hardening states; the microstructural mechanisms responsible for increased or decreased resistance to plastic flow must be considered.

Another auxiliary experiment considered the sequence effects of loading. A different specimen was subjected from its virgin state to the strain path of block three in Fig. 5. The stress-space response after 25 cycles was virtually the same as that of block three of Specimen SS09 at 25 cycles. One can infer that the

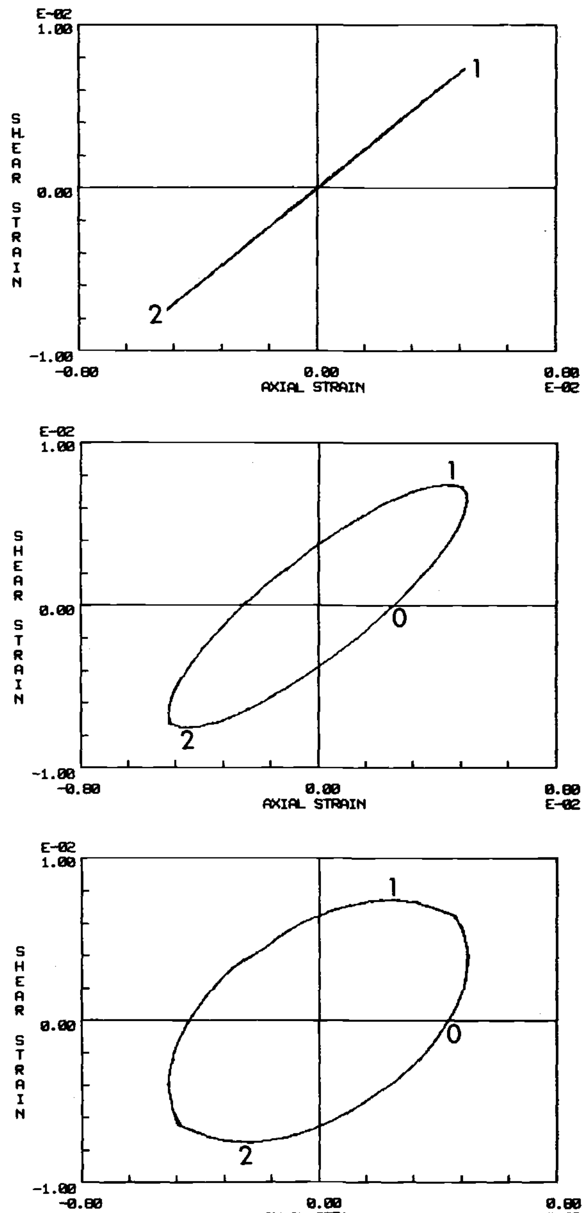

FIG. 5—*Strain paths for history 1:* (top) *block 1, 16 cycles,* (center) *block 2, 25 cycles, and* (bottom) *block 3, 25 cycles.*

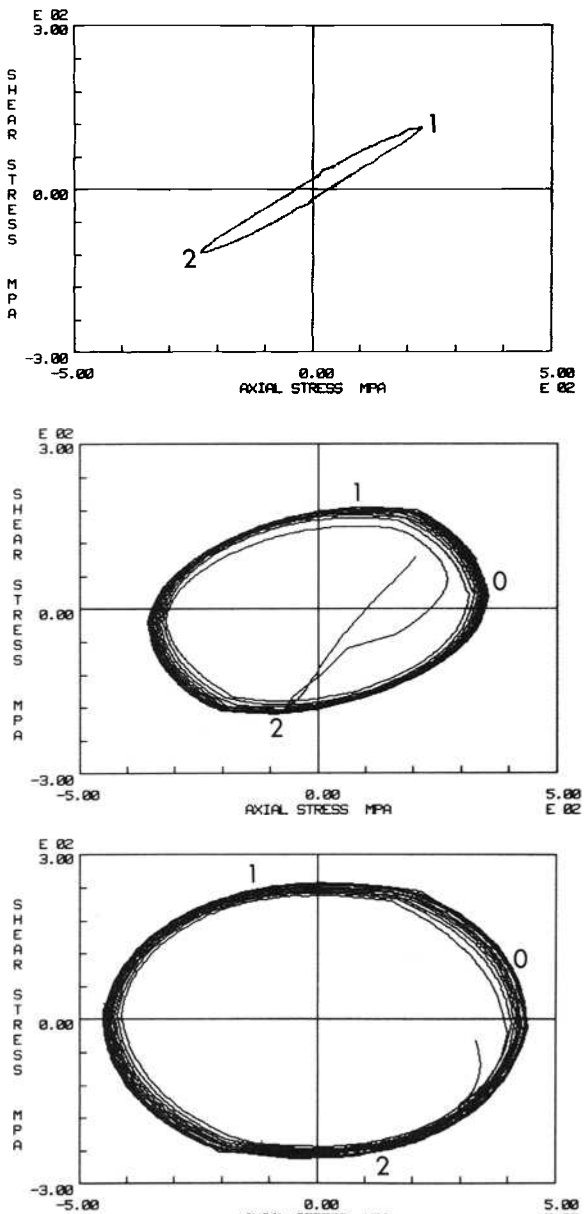

FIG. 6—*History 1 stress-space response:* (top) *block 1, cycle 16,* (center) *block 2, first 10 cycles, and* (bottom) *block 3, first 10 cycles.*

highest degree of nonproportionality of loading in a block of cycles, in analogy to the maximum plastic strain range in uniaxial tests, "washes out" the effects of loadings involving less dislocation interaction. This observation lends some credibility to the application of correlative functions such as ϕ to complex loading sequences with the constraint that the material remembers the maximum degree of nonproportionality of loading in addition to maximum plastic strain range. In other words, although the final cyclically stable effective stress-strain state differs significantly from the uniaxial cyclic stress-strain curve, correlations such as Eq 17 should be successful if independently applied to each block in a sequence of successively increasing degrees of nonproportionality. For arbitrary loading, however, fading memory of the effects of high nonproportionality due to an increase in dislocation mobility, changes in cyclic dislocation cell structure, etc., precludes the possibility that $\Delta\tau_{max}$ is a potential function of ϕ. Yet, the potential for empirical correlation using such functions is not diminished, particularly if the path dependence is defined by a set of suitable constitutive equations [*22*].

Specimen SS04: History 2—To investigate hardening due to a number of discrete sets of maximum shear planes, a specimen was subjected from its initial state to 50 cycles of the strain history shown in Fig. 7. For this history, $\dot{\epsilon} = 0.002$ s^{-1}. The endpoints are numbered to denote loading sequence in the overall cycle. There are six discrete sets of maximum shear strain planes in the plane of the specimen. The locus of tips of each path lie on an ellipse of constant octahedral shear strain of 0.0086 with the assumption that $\mu = 0.5$. This path represents the exceptional case of tension-torsion loading where the maximum shear strain planes do not rotate continuously with time. Note that $Q = 1$ for each linear path segment. The loading is definitely nonproportional, though, and considerable cyclic hardening is observed as seen in Fig. 8, which illustrates the transient hardening in stress space for only the first 10 cycles. The maximum effective stress in each cycle after 40 cycles is significantly higher (~50%) than

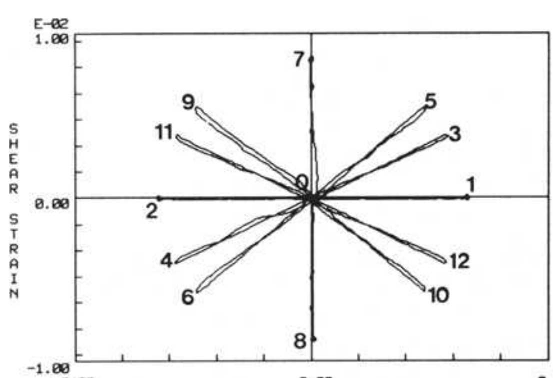

FIG. 7—*Strain path for history 2 applied for 50 cycles.*

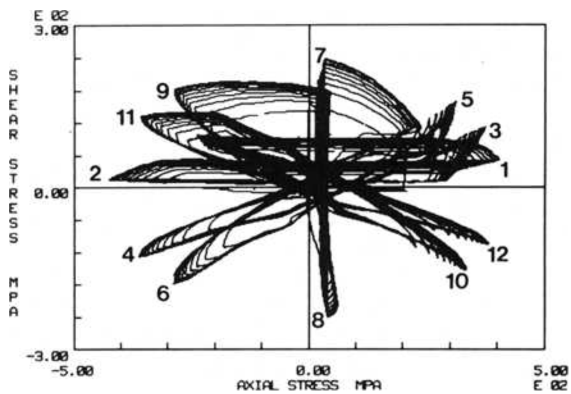

FIG. 8—*History 2 stress-space response; first 10 cycles.*

the stable stress amplitude for uniaxial loading at the same $\Delta\overset{*}{\gamma}_{max}{}^{P}$, again reflecting the effects of nonproportionality.

Specimen SS01: History 3—To investigate sequence effects of more general types of loading than sinusoidal, a virgin specimen was subjected from its initial state to the strain history shown in Fig. 9; $\dot{\epsilon} = 0.003\ s^{-1}$. The first block consisted of proportional loading for 25 cycles at $\epsilon_a = 0.0041$ and $\gamma_a = 0.006$. The second block consisted of another radial path in strain space at the same ϵ and γ amplitudes for 25 cycles, which led to nonproportional loading with additional cyclic hardening (cross effects). Finally, each cycle in the third block consisted of the paths from the first two blocks joined sequentially at the endpoints. The third block consisted of 25 cycles. The endpoints of each path are numbered in Fig. 9 to denote the sequence in each cycle. The stress-space response for each block is shown in Fig. 10 for the 24th cycle of the first two blocks, and the first 10 cycles of the third block.

Note that even though the maximum range of total shear strain is the same for each block, block three involves a considerably higher cyclically hardened effective stress state. Apparently the effect of continuous rotation of maximum shear planes along the portions of the path where $\epsilon \approx$ constant is to substantially increase resistance to plastic flow.

Again, from Fig. 10, an approach to a complex, cyclically stable stress state is observed. In this case, however, the loading sequence has resulted in a nonsymmetric stress-space response.

Since the maximum degree of nonproportionality (highest ϕ) for a loading block appears to erase the effects of prior loading of a lesser degree of nonproportionality at approximately the same plastic strain range, one might expect ϕ values calculated for each block independently to correlate cyclic hardening if indeed ϕ is a valid parameter. Such correlations will be discussed in the next section.

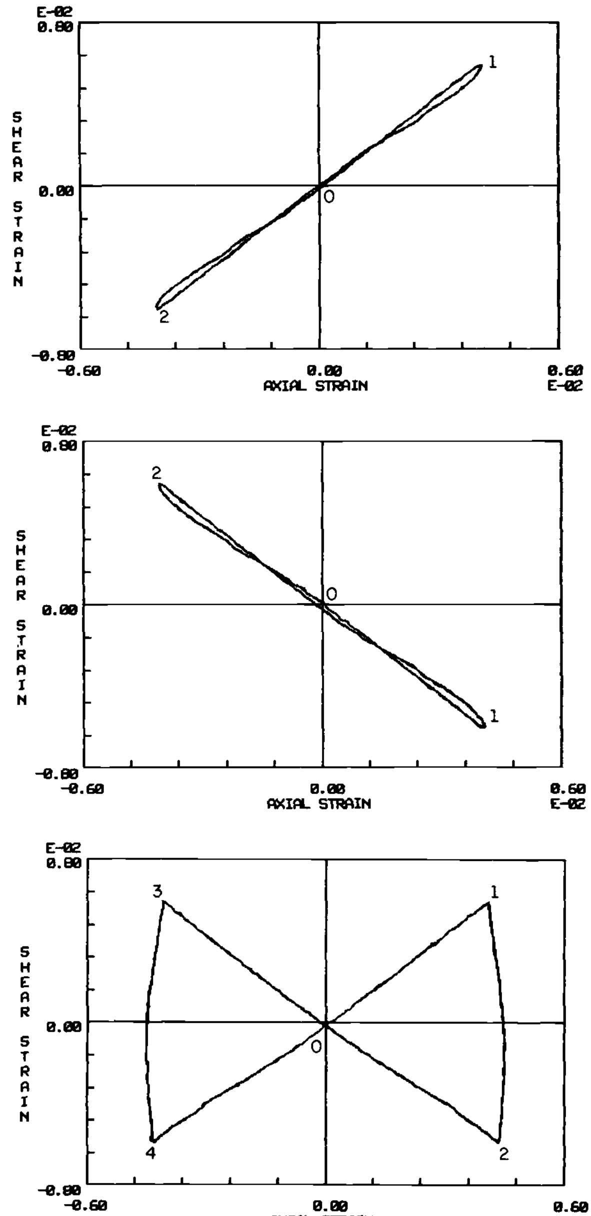

FIG. 9—*Strain paths for history 3:* (top) *block 1, 25 cycles,* (center) *block 2, 25 cycles, and* (bottom) *block 3, 25 cycles.*

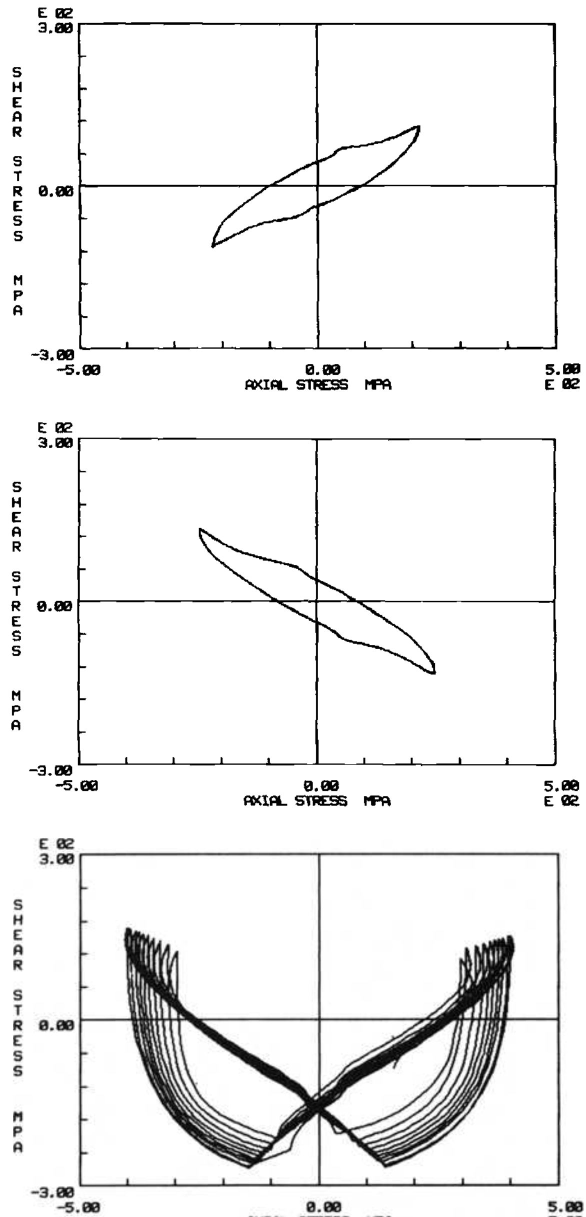

FIG. 10—*History 3 stress-space response:* (top) *block 1, cycle 24,* (center) *block 2, cycle 24, and* (bottom) *block 3, first 10 cycles.*

Correlations of "Stable" States

The comparison of the effective stress computed from Eq 17 with the maximum effective stress in a cycle requires justification from previous research in cyclic plasticity. Comparison of predicted and experimental results is not a trivial matter, since predicting the path in stress-space requires a flow rule and a kinematic-isotropic hardening rule. However, the work of Shiratori et al [17] indicates that yield surfaces defined by large offset strains (>0.8% or so) from the last unloading point experience isotropic hardening almost exclusively. This limit behavior has been observed in a number of experimental studies and is often included in constitutive relations for cyclic plasticity.

In the three histories of the current study, limit behavior [5] was also observed at the maximum effective stress levels with the isotropic limit surface apparently somewhere between a Tresca and von Mises form. Since all histories were of a reversed and symmetric nature in stress and strain space, the maximum actual values of

$$\bar{\sigma}_{\text{max,actual}} = (\sigma^2 + 4\tau^2)^{1/2}$$

in each cycle are expected to correlate fairly accurately with

$$\bar{\sigma}_{\text{max,predicted}} = \bar{k}^*(\Delta\gamma_{\text{max}}{}^P/2)^{\bar{n}*}$$

where $\Delta\gamma_{\text{max}}{}^P$ is the maximum range of plastic shear strain on all material planes in a cycle.

Of course, some error is introduced in this correlation since the limit surface is not necessarily of a Tresca form. These errors, though, are small considering the extent of nonproportional hardening exhibited by this material.

In Table 2, the comparisons of the maximum effective stress observed in a cycle, $\bar{\sigma}_{\text{max,actual}}$, with predicted results, $\bar{\sigma}_{\text{max,predicted}}$, are given for the last sampled cycle in each block of each history. Two points are noteworthy. Relatively good agreement is obtained for the effective stress state for each history at the end of each loading block. This agreement is quite good in view of the tremendous degree of cyclic hardening experienced for this material under nonproportional loading with $\beta = 90°$, $\gamma_a/\epsilon_a = (1 + \mu)$. The error between predicted and actual results is at most 7%, and typically less than 4%. It should be noted that the number of cycles used to define cyclic stability in determining $\bar{k}^*$ and $\bar{n}^*$ should be adequate to correlate the intermediate saturated state attained in each block, since each block contains 16 to 50 cycles. For history 2 and block 3 of history 3, $\bar{\sigma}_{\text{max,actual}}$ was computed as the average of the maxima of $(\sigma^2 + 4\tau^2)^{1/2}$ in the last sampled data cycle, even though the variation in maxima was 5% or less.

It should be noted that the $\bar{k}^*(\Delta\gamma_{\text{max}}{}^P/2)^{\bar{n}*}$ values in Table 2 for blocks 2 and 3 of histories 1 and 3 can truly be considered as predicted values, not just matchings, since the forms of $\bar{k}^*$ and $\bar{n}^*$ in Eq 17 are assumed functions of ϕ

TABLE 2—*Comparison of experimental and predicted maximum effective stress amplitudes in each loading block.*

History	Block No.	Cycle No. in Block	$\Delta\gamma_{max}^{p}$	ϕ^{a}	Actual, MPa $\max(\sigma^2 + 4\tau^2)^{1/2}$	Predicted, MPa $\bar{k}^*(\Delta\gamma_{max}^{p}/2)^{\bar{n}*}$
1	1	16	0.0166	0	325	314
1	2	24	0.0159	0.322	430	419
1	3	24	0.0146	0.664	519	527
2	1	40	0.0126	0.546	469	474
3	1	24	0.0136	0	308	298
3	2	24	0.0132	0.243	368	378
3	3	24	0.0123	0.593	528	489

[a] $\mu = 0.5$ was assumed.

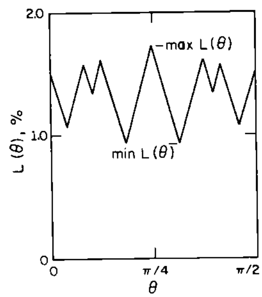

FIG. 11—*Hardening distribution for loading of history 2;* $\mu = 0.5$, m $= 1$, *and* $\phi_2 = 0.546$.

and $\bar{k}$, $\bar{k}_{90}$, $\bar{n}$, and $\bar{n}_{90}$, which are obtained entirely from uniaxial and 90° out-of-phase tests.

In Fig. 11 the hardening distribution from Eq 10 for history 2 is shown. For this distribution, $\mu = 0.5$ was assumed. From a test consisting of alternating blocks of pure axial loading and pure torsional loading, $m = 1$ was selected to fit the hardening response based on Eq 17. Again, since this history is different from history 2, the $\bar{k}^*(\Delta\gamma_{max}{}^P/2)^{\bar{n}^*}$ value in Table 2 for history 2 is a predicted value, and not a matching. In all analyses, $Q_o = 0.9$ was assumed.

It should be noted that the $\Delta\overset{*}{\gamma}_{max}{}^P$ value used to compute the appropriate constant value of $\bar{k}$ in Eq 13 for each history corresponded to the maximum range of plastic shear strain in the first block.

Conclusions

For room temperature, nonproportional, cyclic loading of annealed stainless steel 304 specimens, the following observations are pertinent.

1. An increase in the nonproportionality of cyclic loading is analogous to an increase in plastic strain range with regard to cyclic hardening behavior.
2. The memory of prior hardening is washed out by more severe nonproportional loading.
3. The stable state reached during cyclic loading appears to be a function of the most severe nonproportional loading block in a history consisting of a number of blocks of varying degrees of nonproportionality.
4. For a given heat treatment (initial state), the cyclically stable effective stress state achieved during nonproportional cycling is not unique, but a function of the loading path.
5. Path-dependent correlations have the potential to predict cyclically stable states to within bounds of acceptable engineering accuracy for the axial-torsional loading of this paper. Nonproportional loading under different strain states such as axial-torsional with internal-external pressure should be investigated to determine the more general validity of correlations and concepts.

6. The sensitivity of the material's transient response to nonproportional loading depends on structure, number of activated slip systems, initial heat treatment, etc. Consequently, no sweeping generalization can be made for all materials regarding significance of nonproportional hardening to designers. Regardless, this phenomenon is real and deserves consideration when selecting materials for applications involving nonproportional loading.

Acknowledgments

The support of this work by a fellowship from the International Harvester Corporation is gratefully acknowledged.

References

[*1*] Lamba, H. S. and Sidebottom, O. M., *Journal of Testing and Evaluation,* Vol. 6, No. 4, July 1978, pp. 260–267.
[*2*] Tuler, F. R. and Morrow, J. D., "Cycle-Dependent Stress-Strain Behavior of Metals," TAM Report No. 239, Department of Theoretical and Applied Mechanics, University of Illinois at Urbana-Champaign, Urbana, 1963.
[*3*] Ellyin, F., Neale, K. W., and Bouveret, M., "Effect of Cyclic Loading on the Yield Surface," Department of Civil Engineering Report, University de Sherbrooke, Quebec, Canada, 1976.
[*4*] Liu, K. C. and Greenstreet, W. L. in *Proceedings,* Winter Annual Meeting of ASME, "Constitutive Equations in Viscoplasticity: Computational and Engineering Aspects," New York, Dec. 1976, pp. 35–55.
[*5*] Lamba, H. S., "Nonproportional Cyclic Plasticity," TAM Report No. 413, Department of Theoretical and Applied Mechanics, University of Illinois at Urbana-Champaign, Urbana, 1976.
[*6*] Jackson, M. S., Cho, C. W., Alexopoulos, P., and Li, Che-Yu, *Journal of Engineering Materials and Technology, Transactions,* American Society of Mechanical Engineers, Vol. 103, Oct. 1981, pp. 314–325.
[*7*] Wu, H. C. and Yip, M. C., *Journal of Engineering Materials and Technology, Transactions,* American Society of Mechanical Engineers, Vol. 103, July 1981, pp. 212–217.
[*8*] Chaboche, J. L., Dang Van, K., and Cordier, G., *Proceedings,* Fifth International Conference on Structural Mechanics in Reactor Technology, Berlin, 1979.
[*9*] Dafalias, Y. F. and Popov, E. P., *Acta Mechanica,* Vol. 21, 1975, pp. 173–192.
[*10*] McDowell, D. L., "Multiaxial Nonproportional Cyclic Deformation," Report No. 102, Design and Materials Division, Department of Mechanical and Industrial Engineering, University of Illinois at Urbana-Champaign, Urbana, 1981.
[*11*] Brown, M. W. and Miller, K. J., *Fatigue of Engineering Materials and Structures,* Vol. 1, 1979, pp. 93–106.
[*12*] Landgraf, R. W., Morrow, J. D., and Endo, T., *Journal of Materials,* Vol. 4, No. 1, March 1969, pp. 176–188.
[*13*] Socie, D. F. and Morrow, J. D. in *Risk and Failure Analysis for Improved Performance and Reliability,* J. J. Burke and V. Weiss, Eds., Plenum, New York, 1980, Chapter 8, pp. 141–194.
[*14*] Martin, J. F., "Fatigue Damage Analysis for Irregular Shaped Structures Subjected to Representative Loads" FCP Report No. 10, College of Engineering, University of Illinois at Urbana-Champaign, Urbana, 1973.
[*15*] Hecker, S. S., *Proceedings,* Winter Annual Meeting of ASME, "Constitutive Equations in Viscoplasticity: Computational and Engineering Aspects," New York, Dec. 1976, pp. 1–32.
[*16*] Phillips, A. and Sierakowski, R. L., *Acta Mechanica,* Vol. 6, 1968, pp. 29–35.
[*17*] Shiratori, E., Ikegami, K., and Yoshida, F., *Journal of the Mechanics and Physics of Solids,* Vol. 27, 1979, pp. 213–229.

[18] Kanazawa, K., Miller, K. J., and Brown, M. W., *Fatigue of Engineering Materials and Structures*, Vol. 2, 1979, pp. 217–228.
[19] McDowell, D. L., Socie, D. F., and Lamba, H. S. in *Low-Cycle Fatigue and Life Prediction, ASTM STP 770*, American Society for Testing and Materials, Philadelphia, 1982, pp. 500–518.
[20] Dittmer, D. F., "Characterization and Simulation of Cyclic Stress-Strain Behavior," M.S. thesis, Department of Theoretical and Applied Mechanics, University of Illinois at Urbana-Champaign, Urbana, 1980.
[21] Pratt, J. E., *Acta Metallurgica*, Vol. 15, Feb. 1967, pp. 319–327.
[22] McDowell, D. L. in *Proceedings*, International Conference on Constitutive Laws for Engineering Materials: Theory and Application, Desai and Gallagher, Eds., Tucson, Ariz., Jan. 1983, pp. 125–132.
[23] Mroz, Z., *Acta Mechanica*, Vol. 7, 1967, pp. 199–212.
[24] Krieg, R. D., *Journal of Applied Mechanics*, Sept. 1975, pp. 641–646.
[25] Landgraf, R. W. in *Proceedings*, Symposium on Work Hardening in Tension and Fatigue, American Institute of Mining, Metallurgical, and Petroleum Engineers, Cincinnati, Nov. 1975, pp. 240–259.
[26] Socie, D. F., Waill, L. A., and Dittmer, D. F., this publication, pp. 463–481.

Alex P. Kfouri[1] *and Keith J. Miller*[1]

Crack Separation Energy Rates for Inclined Cracks in a Biaxial Stress Field of an Elastic-Plastic Material

REFERENCE: Kfouri, A. P. and Miller, K. J., "**Crack Separation Energy Rates for Inclined Cracks in a Biaxial Stress Field of an Elastic-Plastic Material,**" *Multiaxial Fatigue, ASTM STP 853,* K. J. Miller and M. W. Brown, Eds., American Society for Testing and Materials, Philadelphia, 1985, pp. 88–107.

ABSTRACT: Elastic-plastic finite element analyses are described for plates containing inclined cracks and subjected to biaxial loads given by λ equal to σ_Q/σ_P where σ_P is the main principal tensile stress and σ_Q is the second in-plane principal stress. Three loading modes, λ equal to -0.5, -1, and 0.5 are considered and are compared also with previous results for the uniaxial mode $\lambda = 0$ and the equibiaxial mode $\lambda = 1$. Qualitative and quantitative information is presented on crack-tip opening displacements, on plastic strains and on maximum stresses near the crack tip. The analyses include calculations of J contour integrals and of crack separation energy rates G^Δ for coplanar crack extension. Estimates of G^Δ for nonplanar crack growth applicable to cases where the plastic flow is small are also made and used in conjunction with a fracture criterion based on maximum G^Δ. The implications of these analyses for fatigue crack growth, in terms of plastic zone sizes, shapes, and orientation, are discussed with regard to (*a*) modes of cracking, (*b*) stress biaxiality, and (*c*) crack inclinations, and are then related to experimental results under mixed mode (I and II) loading conditions in stainless steel.

KEY WORDS: biaxiality, crack growth step, crack-tip opening displacement, crack-tip plasticity, crack-tip plastic zone, crack-tip stresses and strains, crack separation energy rate, elastic-plastic fracture mechanics, finite element method, Griffith's energy release rate, inclined crack, J-contour integral, mixed mode loading, nonplanar crack growth

Nomenclature

a	Half crack length
E	Modulus of elasticity
G	Griffith's energy release rate
G_o	Griffith's energy release rate at incipient yielding when $\theta = \lambda = 0$
$G^\Delta(\alpha)$	Crack separation energy rate in direction given by branch angle α
G_I, G_{II}	Mode I and Mode II components of G for coplanar crack extension
$G_I^\Delta, G_{II}^\Delta$	Mode I and Mode II components of G^Δ for coplanar crack extension
H	Linear hardening tangent modulus

[1]Senior research fellow and professor, respectively, Department of Mechanical Engineering, University of Sheffield, Sheffield, U.K.

Copyright© 1985 by ASTM International www.astm.org

J	Rice's path independent integral
K_I, K_{II}	Mode I and Mode II components of Irwin's stress-intensity factor
K_{I_o}	Value of K_I at incipient yielding when $\theta = \lambda = 0$
K_{ij}	Quadrature coefficients
K^*	Nondimensional stress-intensity factor
l	Length of branch in crack extension
r_p	Crack-tip plastic zone size
T_L	Lateral stress coefficient ($= \sigma_T/\sigma_o$)
u, v	Displacements in x and y directions, respectively
x, y	Co-ordinates
α	Branch angle giving direction of crack extension
α_M	Value of α making $G^\Delta(\alpha)$ a maximum
θ	Crack inclination angle
δ	Distance separating upper and lower nodes adjacent to crack tip node
δ_I, δ_{II}	Mode I and Mode II components of δ
Δa	Crack growth step
ϵ	Strain
$\bar{\epsilon}_{AV}$	Average equivalent strain in element containing the crack-tip node
λ	Biaxiality parameter ($= \sigma_Q/\sigma_P$)
ν	Poisson's ratio
ρ	Constant of proportionality
σ	Stress
σ_{1M}	Maximum value of main principal stress
σ_P	Applied main tensile principal stress on crack
σ_Q	Second in-plane applied principal stress on crack
σ_N	Applied normal stress on crack
σ_L	Applied laterial stress on crack
σ_T	($= \sigma_L - \sigma_N$)
σ_o	Value of σ_P at incipient yielding when $\theta = \lambda = 0$
σ_{Po}	0.95 of value of σ_P at incipient yielding
σ_y	Yield stress in uniaxial tension
τ	Applied shear stress on crack

The very complex nature of cracks in real structures has made it necessary to use much simplified models for the study of dominant factors affecting fracture behavior. As the data accumulate and more powerful methods of analysis become available, so also is attention focussed on new aspects of interest in the continuing quest for information of greater general applicability. In the past two decades the inclined crack shown in Fig. 1*a* has served as a useful configuration for the study of asymmetrical mixed mode loading of cracks. The literature on inclined and branched cracks is extensive, for example, Ref [*1–26*] to mention but a few. Nearly all the studies have been in the context of linear elastic fracture mechanics (LEFM). Perhaps the most notable exception is the small-scale yield-

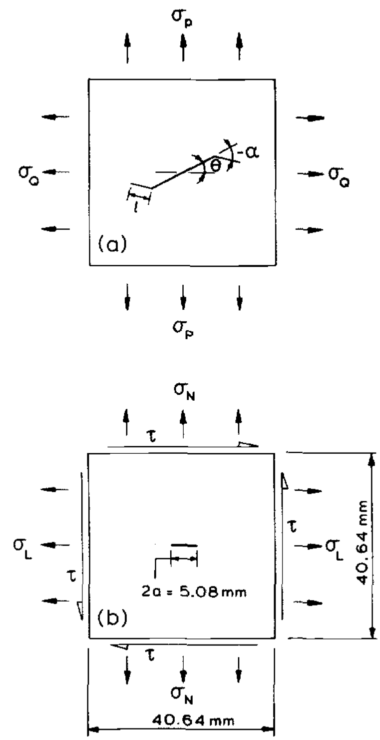

FIG. 1—*An inclined crack* (a) *in a biaxial stress field and* (b) *a center-cracked plate loaded by an equivalent stress system.*

ing analysis by Shih on materials obeying power law hardening [*27*], based on the Hutchinson-Rice-Rosengren (HRR) dominant singularity solutions [*28–30*]. Also, in the majority of cases, inclined cracks in a uniaxial tensile stress field were examined. Inclined cracks under biaxial tensile modes of loading were studied by Ueda et al [*31*] in the context of LEFM but recently elastic-plastic analyses have been also carried out [*32*].

A crack under pure Mode I loading extends in its own plane, that is, the crack extension is coplanar, but a special feature of mixed mode loading is the effect of the antisymmetric shear load which causes nonplanar crack extension. A number of different fracture criteria have been proposed to predict both the direction of crack extension and the fracture load in a linear elastic material, details of which can be found in the cited literature. Briefly, the main criteria are: (*a*) the maximum tangential stress criterion [*2,5–7*], (*b*) the criterion of local symmetry [*15,16*], (*c*) the minimum strain energy criterion [*10,11*], and (*d*) the maximum energy release rate criterion [*3,4,9*]. A criterion based on the maximum normal strain has been proposed [*33*], and another uses the crack-tip opening displacement (CTOD) to predict the direction of the onset of crack extension [*32*].

In a previous paper [1] inclined cracks in an elastic-plastic material under uniaxial tension were examined in the context of elastic-plastic fracture mechanics (EPFM), and the results of finite element analyses were reported. However since biaxiality of the applied load influences crack-tip plasticity parameter [34–42] further analyses on a center-cracked plate (CCP) have been carried out to investigate the response to biaxial modes of loading, including lateral compressions, and these studies are now described.

Problem

The medium considered is a two-dimensional elastic-plastic material in plane strain with the following properties: modulus of elasticity $E = 207$ GN/m^2; Poisson's ratio $\nu = 0.3$; yield stress $\sigma_y = 310$ MN/m^2, and linear strain hardening takes place with a tangent modulus $H = 4830$ MN/m^2. The material obeys von Mises' yield criterion. A biaxial state of stress, with at least one tensile component is considered. Figure 1*a* shows the main principal tensile stress acting vertically and the second, in-plane, principal stress σ_Q, which can be negative, acting in a horizontal direction. The crack of length $2a$ is inclined at an angle θ measured counterclockwise from the plane normal to σ_P. A crack extension angle α measured counterclockwise from the plane of the crack is also shown. For convenience the analyses are carried out on the CCP in Fig. 1*b* using a coordinate system with axes x, y parallel and normal to the plane of the initial crack, respectively. The corresponding applied stresses are σ_N and σ_L normal and parallel to the plane of the crack, respectively, but, in addition, there is a shear stress τ with positive sign as indicated in the figure. The stresses in the two configurations are related as follows

$$\sigma_N = \tfrac{1}{2}(\sigma_P + \sigma_Q) + \tfrac{1}{2}(\sigma_P - \sigma_Q)\cos 2\theta \tag{1a}$$

$$\sigma_L = \tfrac{1}{2}(\sigma_P + \sigma_Q) - \tfrac{1}{2}(\sigma_P - \sigma_Q)\cos 2\theta \tag{1b}$$

$$\tau = \tfrac{1}{2}(\sigma_P - \sigma_Q)\sin 2\theta \tag{1c}$$

The loads on the crack can be expressed in the form of applied Mode I and Mode II stress-intensity factors K_{I} and K_{II} where

$$K_{\mathrm{I}} = \sigma_N K^* \sqrt{a};\ K_{\mathrm{II}} = \tau K^* \sqrt{a};\ (K_{\mathrm{III}} = 0) \tag{2}$$

Here $K^* = \sqrt{\pi}$ for the infinite medium of Fig. 1*a* and $K^* = 1.785$ for the CCP in Fig. 1*b*. Since σ_L does not of course appear in Eq 2, K_{I} and K_{II} on their own provide an adequate characterization of the crack tip field only when the lateral stress σ_L is irrelevant to fracture phenomena. For a linear elastic material the path independent J-integral calculated on a contour surrounding the right hand side crack tip in Fig. 1*b* is related to the stress-intensity factors by

$$J = (K_{\mathrm{I}}^2 + K_{\mathrm{II}}^2)/E' \tag{3}$$

where

$$E' = E/(1 - \nu^2)$$

Griffith's energy release rate $G(\alpha)$ (which is equal to the crack separation energy rate $G^\Delta(\alpha)$ [*43,44*] when the material is elastic) depends on the direction of the crack extension given by the angle α. When the extension is coplanar ($\alpha = 0$) and the material is elastic we have

$$J = G(0) = G^\Delta(0) \tag{4}$$

The energy rates $G(\alpha)$ and $G^\Delta(\alpha)$ can be expressed as the sum of the Mode I and Mode II components

$$G(\alpha) = G_{I}(\alpha) + G_{II}(\alpha);\ \text{and}\ G^\Delta(\alpha) = G_{I}{}^{\Delta}(\alpha) + G_{II}{}^{\Delta}(\alpha) \tag{5}$$

Estimates of $G^\Delta(\alpha)$ for nonplanar crack extension may be obtained from values of $G_I{}^\Delta(0)$ and $G_{II}{}^\Delta(0)$ calculated by finite-element analyses on cracks of different orientations undergoing coplanar extension. Use was made of the quadrature coefficients $K_{ij}(\alpha)$, $i, j = 1, 2$ [*15,16,19,45*]. Thus

$$[G_I{}^\Delta(\alpha)]^{1/2} = K_{11}(\alpha)\,[G_I{}^\Delta(0)]^{1/2} + K_{12}(\alpha)\,[G_{II}{}^\Delta(0)]^{1/2} \tag{6a}$$

$$[G_{II}{}^\Delta(\alpha)]^{1/2} = K_{21}(\alpha)\,[G_I{}^\Delta(0)]^{1/2} + K_{22}(\alpha)\,[G_{II}{}^\Delta(0)]^{1/2} \tag{6b}$$

Equations 6*a* and *b* are not exact when the material is elastic-plastic but they provide a working approximation for moderate crack-tip plasticity as occurs in fatigue. Note that values of G^Δ obtained directly from finite-element analyses involving nonplanar crack extensions may be compared with values obtained by using equations 6 but these will be reported subsequently.[2] A maximum G^Δ fracture criterion is applicable both to linear elastic and elastic-plastic materials.

Analyses

The plate in Fig. 1*b* is symmetric, but the load on the plate is not symmetric since it includes the shear stress τ. However, by taking advantage of the fact that the configuration in Fig. 1*a*, including the loading, is unchanged when it is viewed upside down, it was possible to confine the analyses to the right half of the CCP in Fig. 1*b*. The finite-element idealization is shown in Fig. 2*a*, and the region of interest near the crack tip is shown to a larger scale in Fig. 2*b*. Thus, the displacements of Nodes 1 to 8 are equal in magnitude but opposite in direction to those of Nodes 16 to 9, respectively. Three loading cases with different biaxial ratios λ ($= \sigma_Q/\sigma_P$) were analyzed with λ taking the values -0.5, -1, and 0.5. For $\lambda = -0.5$ and $\lambda = 0.5$ five crack inclinations were examined, namely, $\theta = 0°$, 11.25°, 22.5°, 33.75°, and 45°. For $\lambda = -1$ the inclinations were $\theta = 0°$, 11°, 22.5°, and 33.75°; the case corresponding to a

[2]See Ref *50*.

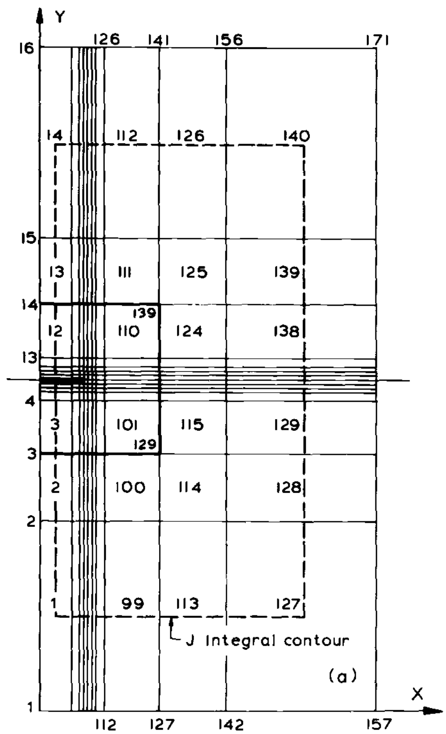

FIG. 2a—*Finite element idealization of one half of the plate.*

crack inclination angle θ equal to 45° coincides with the pure shear loading mode already analyzed [*1*]. Comparisons will be made with this latter case and also for the uniaxial loading mode and the equibiaxial loading mode [*36*] noting that when $\lambda = 1$ only pure Mode I loading occurs irrespective of the orientation of the crack.

In each case the analyses started with an elastic solution which adjusted automatically the loads to values $\sigma_P = \sigma_{P_0}$ and $\sigma_Q = \lambda\sigma_{P_0}$ equal to 95% of the load required to cause incipient yielding at the crack tip. This was followed by the iterative incremental-load elastic-plastic analyses using loading steps of 0.08 σ_{P_0} and 0.08 $\lambda\sigma_{P_0}$. At the end of each loading step information was obtained on the development of the crack-tip plastic zones, the distribution of plastic strains within the zones, the nodal displacements, the Mode I and Mode II crack-tip opening displacements and the stress at the centers of the elements. The J-integral was calculated around the contour shown in Fig. 2a. The two components G_{I}^{Δ} and G_{II}^{Δ} of the crack separation energy rates G^{Δ} were evaluated by the consecutive uncoupling in six release steps of the pairs of tied nodes numbered 56 and 57 at the crack tip and then numbers 72 and 73 and finally 88 and 89 in the crack plane beyond the crack front. Crack extension in growth steps of

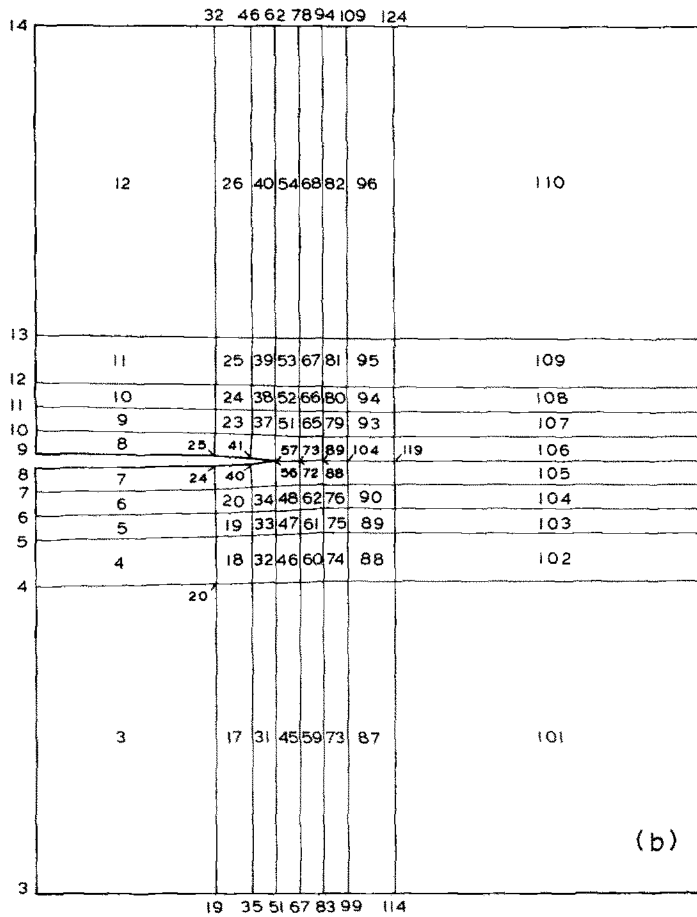

FIG. 2b—*The node and element numbers in the region of the crack tip of the opening crack.*

size $\Delta a = 0.254$ mm were made at constant load at one of the values of σ_P given by σ_{P_o}, 1.56 σ_{P_o}, 2.12 σ_{P_o}, and 3.24 σ_{P_o} with corresponding values of σ_Q equal to $\lambda\sigma_P$.

Results

Figures 3, 4, and 5 show the crack-tip plastic zones for values of λ equal to -0.5, -1, and 0.5, respectively, for the different crack inclination angles indicated on the figures. The deformations are shown with an exaggerated factor of 50, and the numbers in the elements indicate the average equivalent strains in the elements, namely, $\bar{\epsilon}_{av} \times 10^4$. The figures show the plastic zones before crack extension with the exception of Figs. 3*f*, 4*e*, and 5*f* which show the crack-tip plastic zones after two coplanar crack growth steps. The value of σ_p at incipient yielding when λ and θ are both nil was found to be $\sigma_o = 75.22$ MN/m^2. At this value of the load $K_I = K_{Io} = \sigma_o K^*\sqrt{a}$, and Griffith's energy release rate takes the value $G_o = 0.2315$ N/mm, also equal to the contour integral J_o.

In the remaining Figs 6 to 11 the abscissae represent the normalized load, $(\sigma_P/\sigma_o)^2$. The crack-tip opening displacements (CTOD) are given here by the vertical and horizontal distances, δ_I and δ_{II}, separating the nodes adjacent to the crack tip on the lower and upper crack surfaces, respectively. Initially these two nodes coincide and are at a distance Δa from the crack-tip node.

Figures 6*a* and 7*a* give the CTOD before crack extension for different values of θ, corresponding to the cases $\lambda = -0.5$ and $\lambda = -1$, respectively, while Figs. 6*b* and 7*b* give the CTOD values after two crack growth steps. Figures 8 to 11 refer to the same crack inclination angle $\theta = 22.5°$, but the curves on each figure correspond to different values of the load mode parameter λ. Figure 8 gives the CTOD before crack extension (solid lines) and after two crack growth steps (broken lines). Figure 9 gives the maximum stress σ_{1M}, Fig. 10 gives the maximum normalized crack separation energy rate $G^{\Delta}(\alpha_M)/G_o$, and, finally Fig. 11 gives $J/G(O)$. More detailed information in tabular form is contained in Ref *46*.

Discussion

The limitations of K_I and K_{II} have been referred to concerning their inability to characterize by themselves the fracture events at crack tips. In LEFM this also occurs when the branch length/crack length ratio $(1/a)$ is not infinitesimal; see Fig. 1*a*—or generally when a finite process zone is considered in which fracture processes occur [*5–7,11,15*]. An improved characterization is obtained by taking into account the first nonsingular term of Williams' eigenfunction expansion [*47*] for the stresses near the tip of a crack. This term takes the form of a lateral stress $\sigma_T = (\sigma_L - \sigma_N)$ for the CCP in Fig. 1*b*. In elastic-plastic materials the effect of σ_T on fracture behavior is much more dramatic since the crack-tip plastic zone size and other associated crack-tip plasticity parameters are strongly influenced by load biaxiality [*34–36*]. In order to reduce to a minimum the influences of the mesh sizes and of the values of the yield stress used in the analyses, the results can be given greater generality by normalizing σ_T with respect to σ_o, that is, using $T_L = \sigma_T/\sigma_o$. From the relation between σ_o, σ_y and the mesh size Δa, namely, $\sigma_o(a/\Delta a)^{1/2} = \rho\sigma_y$, based on the assumption that at incipient yielding the normal stress at the center of the leading element ahead of the crack tip is of the order of the yield stress, we have

$$T_L = (\sigma_L - \sigma_N)\,(a/\Delta a)^{1/2}/\rho\sigma_y \tag{7}$$

where ρ takes the value of 0.82. The load on the inclined crack can be then characterized by three parameters, namely, $\sigma_N/\sigma_o(= K_I/K_{Io})$, $\tau/\sigma_o(= K_{II}/K_{Io})$ and T_L. Note that T_L varies with the load and also that the final state of

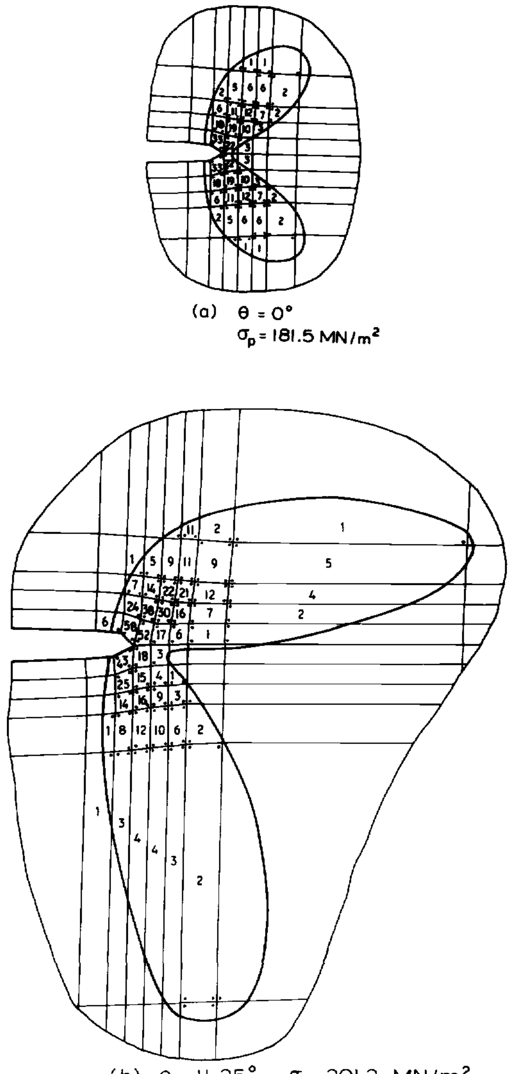

FIG. 3—*Plastic zones for different crack inclinations for the* $\lambda = -0.5$ *loading mode;* (a *to* e) *before and* (f) *after, the release of crack-tip nodes.*

the crack-tip plasticity depends on the loading path. This is easily seen if one considers the trivial example of the CCP containing a crack at zero inclination and loaded in the equibiaxial mode $\lambda = 1$. This will cause a crack-tip plastic zone of modest size r_p when the final applied loads σ_P and σ_Q $(= \sigma_P)$ are attained. On the other hand the same final load can be arrived at by first loading in the shear mode $\lambda = -1$ with $\sigma_Q = -\sigma_P$ followed by the application of a

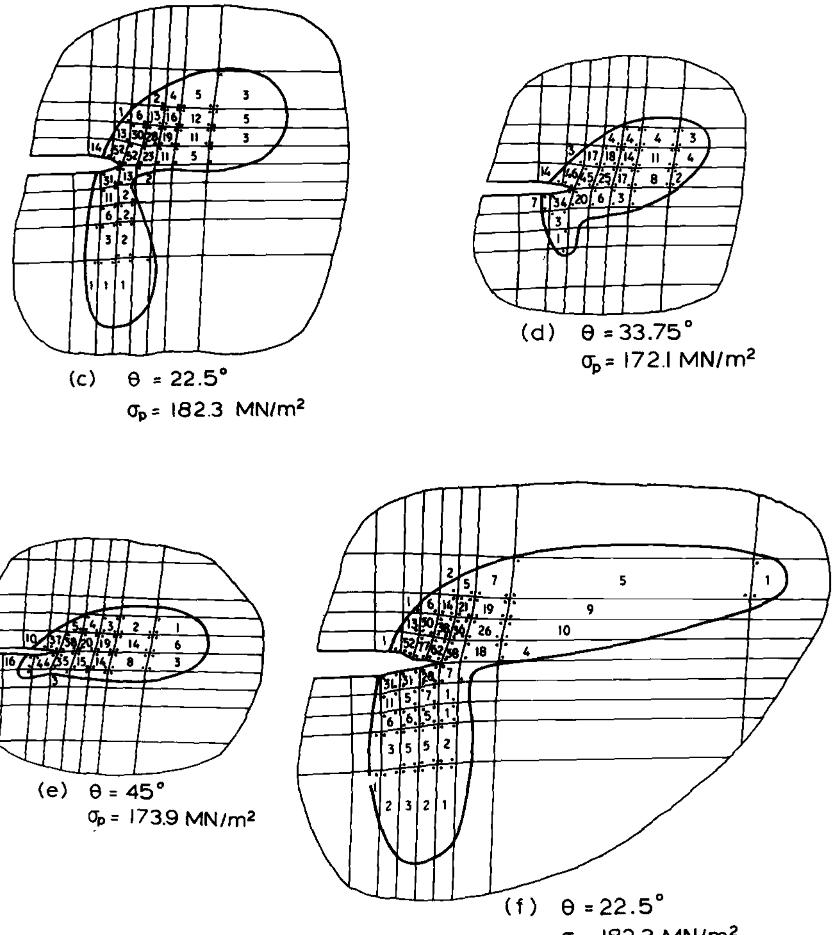

FIG. 3—*Continued.*

lateral stress from $\sigma_Q = -\sigma_P$ to $\sigma_Q = \sigma_P$, at the same time keeping the normal stress σ_P constant. This second loading path will result in a very much larger value of r_p than in the previous case, the large plastic zone being incurred during the shear mode part of the loading.

The various loading patterns of the CCP corresponding to the different loading modes λ and crack inclination angle θ are given in Table 1. Generally the (algebraic) values of τ/σ_N and σ_T/σ_N increase (or do not decrease) with increasing values of θ. An increase in τ/σ_N tends to increase the values of r_p and δ. However, an increase in σ_T/σ_N has the opposite effect of decreasing r_p, $\bar{\epsilon}_{av}$ and δ. This was already known in the uniaxial mode. An example in mixed-mode loading is obtained by comparing the two cases (*a*) $\lambda = -1$, $\theta = 11°$, $\sigma_N = 144.6$

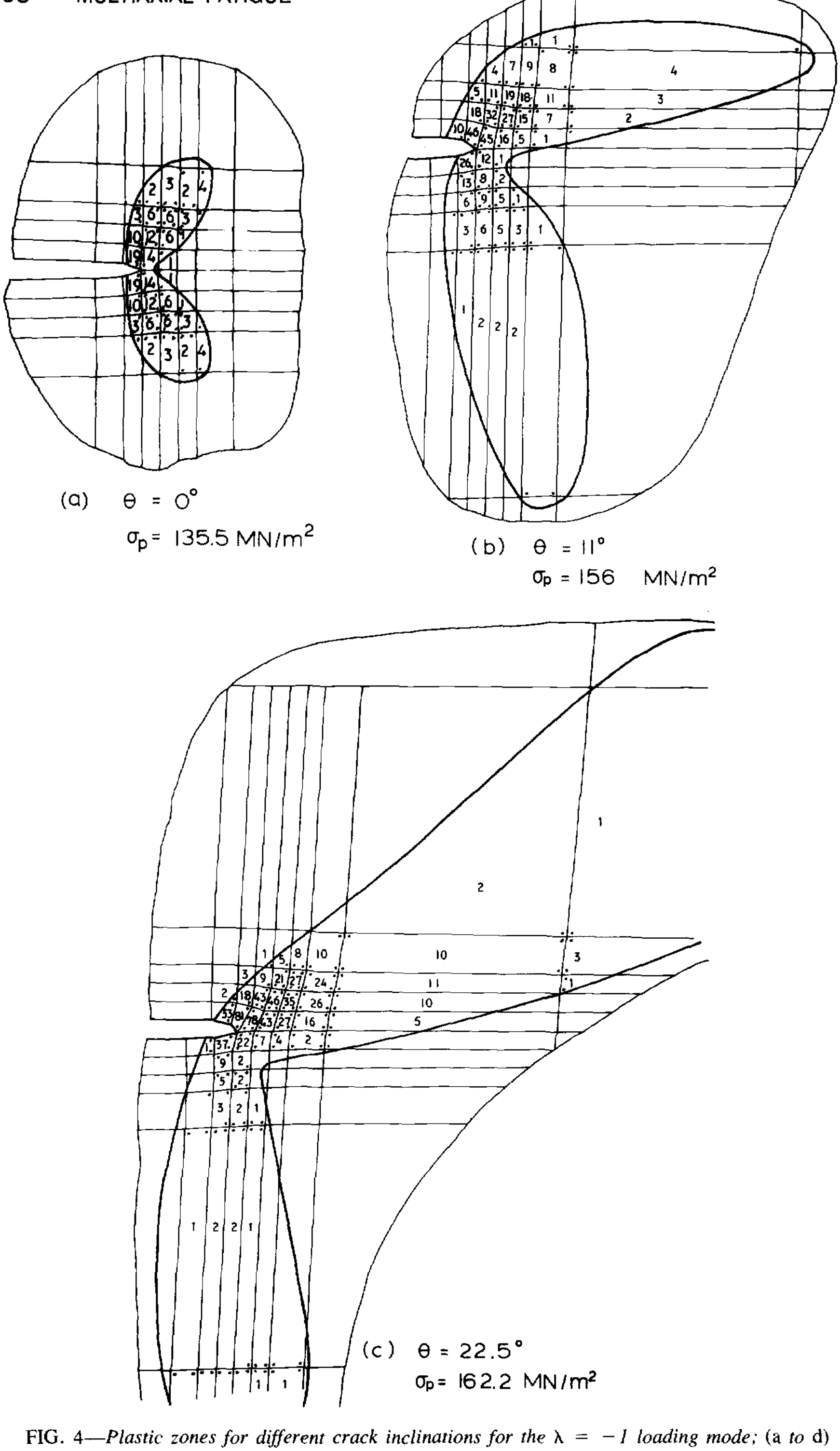

FIG. 4—*Plastic zones for different crack inclinations for the* $\lambda = -1$ *loading mode;* (a *to* d) *before and* (e) *after, the release of the crack-tip nodes.*

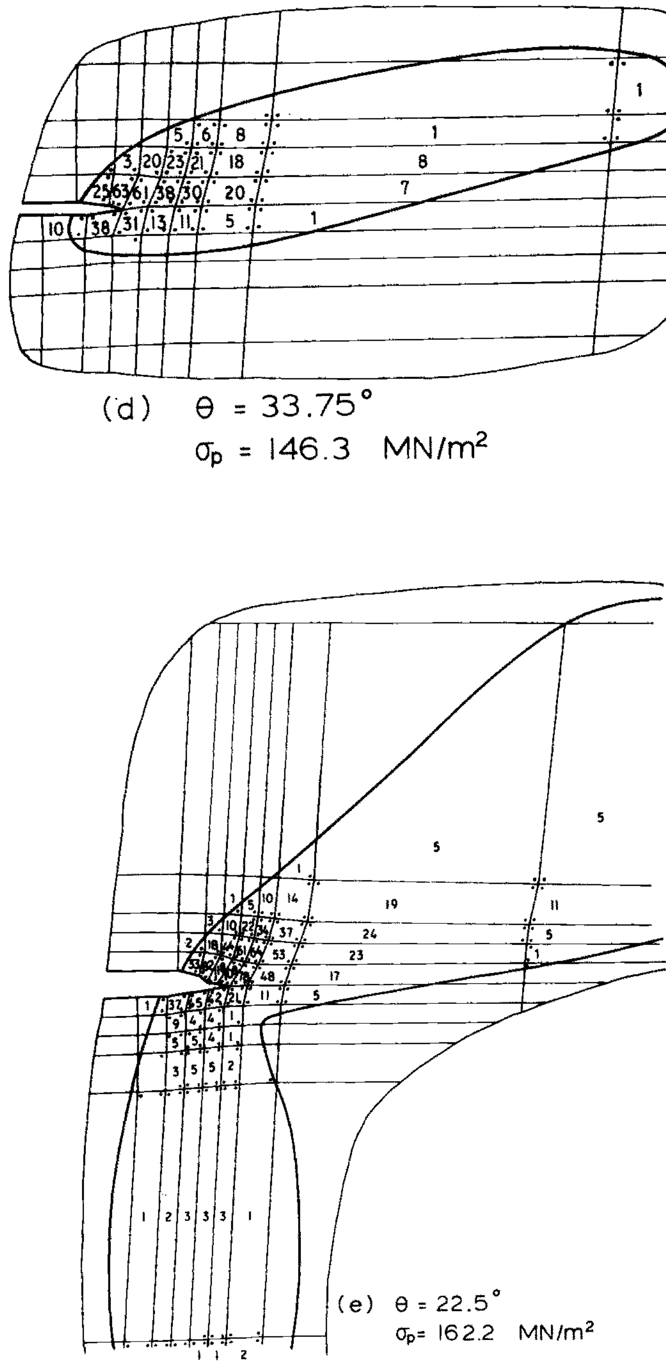

FIG. 4—*Continued.*

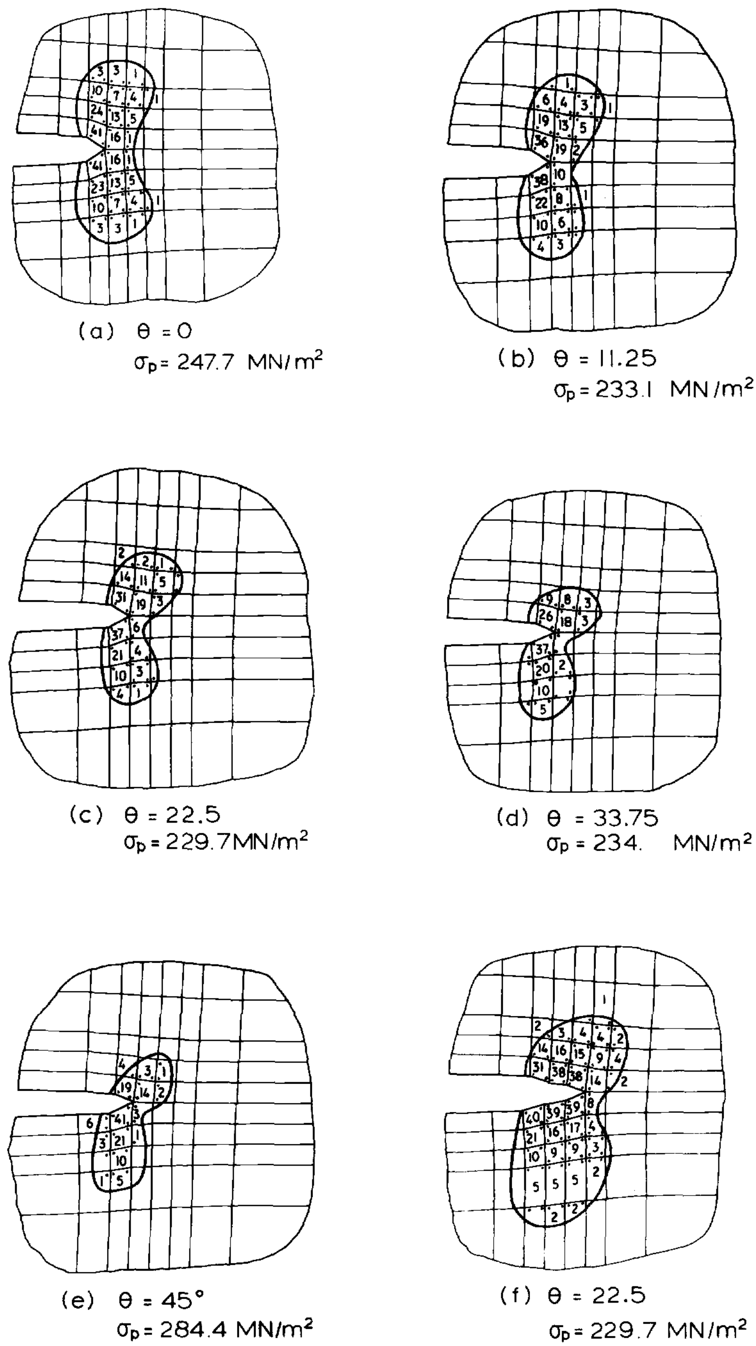

FIG. 5—*Plastic zones for different crack inclinations for the* λ = *0.5 loading mode;* (a *to* e) *before and* (f) *after, the release of crack-tip nodes.*

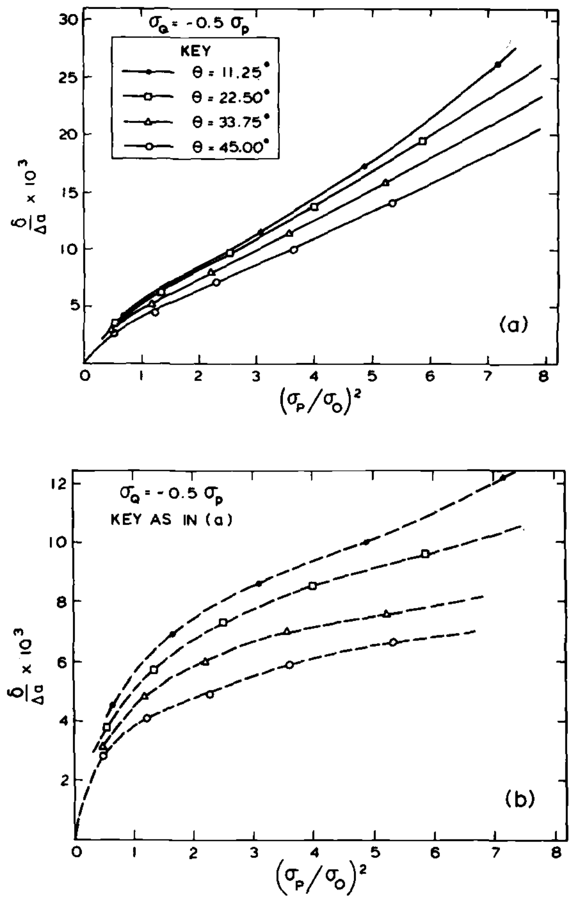

FIG. 6—*The effect of applying loading mode* $\lambda = -0.5$ *on the crack-tip opening displacement for different crack inclinations* (a) *before and* (b) *after, crack extension.*

MN/m^2, τ = 58.5 MN/m^2, σ_T = -289.2 MN/m^2, and (*b*) λ = 0, θ = 22.5°, σ_N = 144.9 MN/m^2, τ = 60.0 MN/m^2, σ_T = -120.0 MN/m^2, since K_I and K_{II} are approximately the same in both cases but σ_T differs appreciably. Following static loading, the average values of $\bar{\epsilon}_{av}$ in crack-tip elements 35 and 36 are 36.0 and 22.3 for cases *a* and *b*, respectively, while the values of $\delta/\Delta a$ are 18.8 and 13.6. On the other hand respective values of σ_{1M} are 339.1 MN/m^2 and 432.2 MN/m^2, while those for $G^{\Delta}(\alpha_M)/G_o$ are 2.348 and 2.796. The resulting state of crack-tip plasticity is, therefore, the outcome of conflicting influences which can sometime cancel one another as shown in Fig. 7*a* which corresponds to a state of pure shear at an inclination of 45° to σ_P. At the inclination θ = 22.5°, Fig. 8 shows that for the stationary crack $\delta/\Delta a$ increases as λ decreases while the opposite is true of $\delta/\Delta a$ after two crack-tip node releases. The latter is

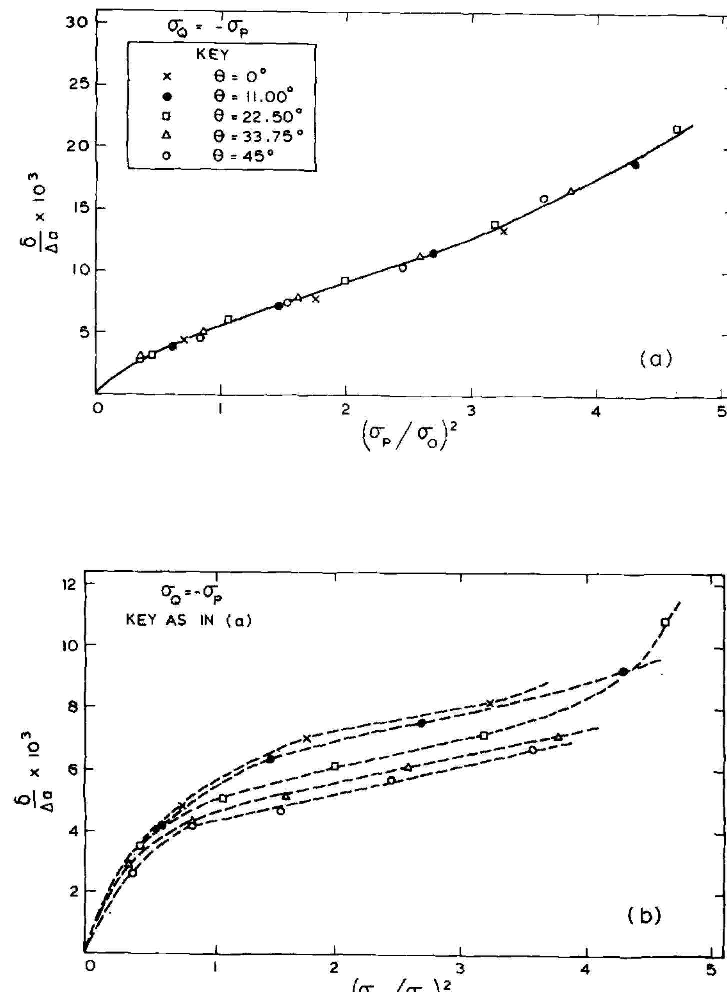

FIG. 7—*The effect of applying loading mode* $\lambda = -1$ *on the crack-tip opening displacement for different crack inclinations* (a) *before and* (b) *after, crack extension.*

consistent with an increase in G^{Δ} with λ. Figures 9 and 10 show that σ_{1M} and $G^{\Delta}(\alpha_M)/G_o$ increase with λ, which in turn is related to the hydrostatic component of the applied stress. The direction of maximum $G^{\Delta}(\alpha_M)$, making an angle $(\theta + \alpha_M)$ with the normal to the principal applied stress σ_P, seems to vary from approximately 0° for $\lambda = 0.5$ to $-35°$ for $\lambda = -1$. Figure 11 shows that at low values of the applied load J is approximately equal to $G(0)$. However, J is related to the crack-tip plastic zone size r_P and as r_P increases $J/G(0)$ also increases.

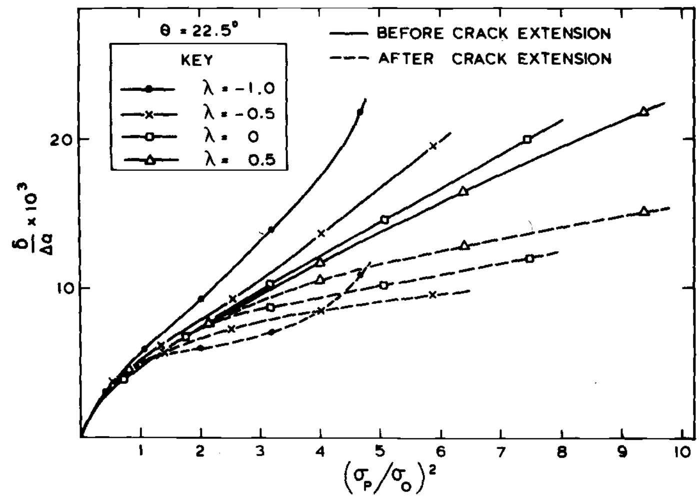

FIG. 8—*Comparisons of the effects of different applied loading modes on the crack-tip opening displacement for an inclination angle* $\theta = 22.5°$ *before* (———) *and after* (------) *crack extension.*

Implications to Fatigue Crack Propagation

The responses to different loading patterns on an inclined crack in a biaxial stress field present a very complex picture, but it is hoped that this type of analysis may help throw some light on those aspects capable of affecting the rate, mode, and direction of fatigue crack propagation (FCP). For instance, if the extent and intensity of crack-tip plasticity as reflected by the CTOD or other

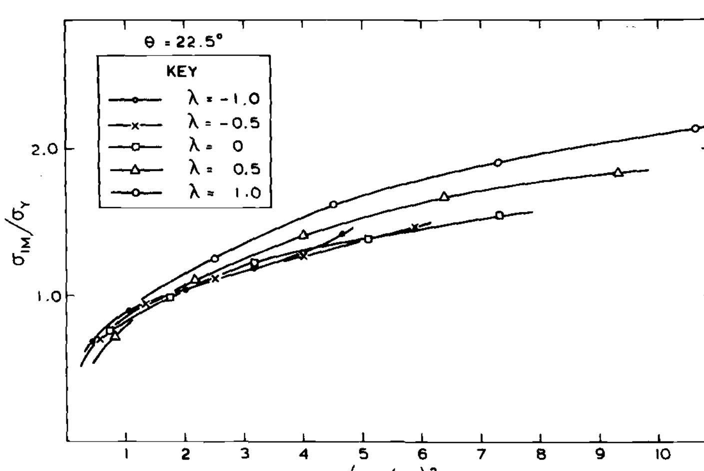

FIG. 9—*Largest principal stress at the center of crack-tip elements against applied load for different biaxial loading modes for an inclination angle* $\theta = 22.5°$.

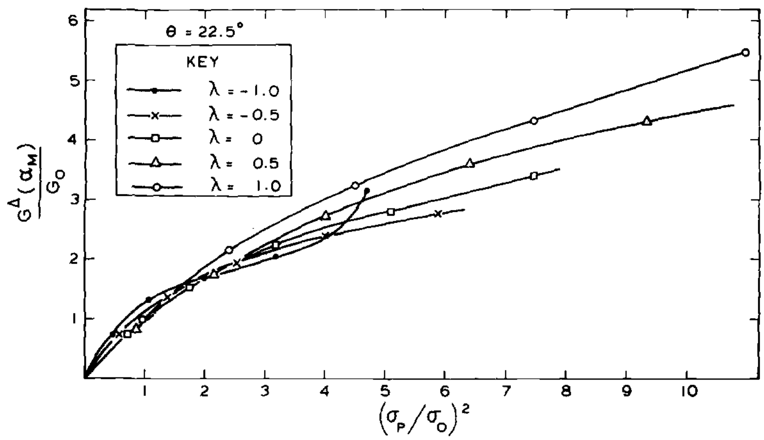

FIG. 10—*Estimates of maximum crack separation energy rates for nonplanar crack extension against applied load when the inclination angle θ is equal to 22.5°, for different biaxial loading modes.*

plasticity parameters are dominant, then it would appear that increasing negative values of λ or σ_T would tend to enhance FCP in spite of their inherently stabilizing effect on monotonic crack propagation. One might be tempted to try to correlate such quantities as threshold values, crack growth rates, and directions of crack growth with some measure of intensity of crack-tip plasticity such as the severe strain zone size [*48*]. For negative values of σ_T the values of $\delta/\Delta a$ are usually largest at nil (or possibly small) values of the inclination angle θ. This would suggest that if the cyclically growing crack tends to adjust to a direction giving

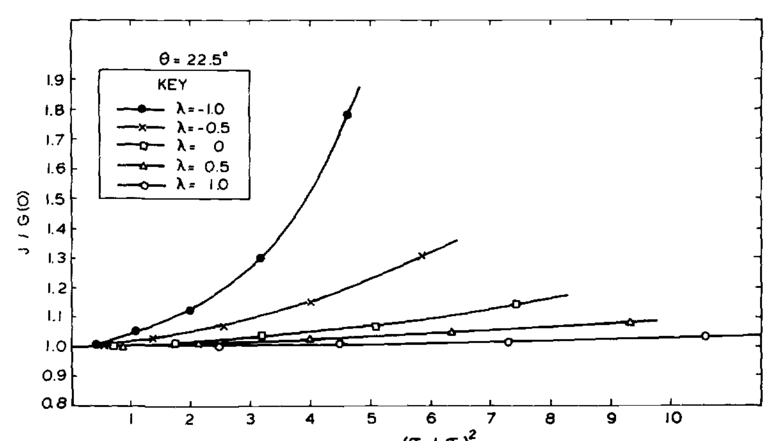

FIG. 11—*Values of* J/G(O) *against applied load when* θ = *22.5°, for different biaxiality loading modes* λ.

TABLE 1—*Value of σ_P/σ_N, τ/σ_N and σ_T/σ_N for variously inclined cracks under different loading modes.*

λ	$\theta°$	0	11.25	22.5	33.75	45
−1	σ_P/σ_N	1	1.082	1.414	2.613	∞
	τ/σ_N	0	0.414	1	2.414	∞
	σ_T/σ_N	−2	−2	−2	−2	undefined
−0.5	σ_P/σ_N	1	1.061	1.282	1.862	4
	τ/σ_N	0	0.304	0.680	1.290	3
	σ_T/σ_N	−1.5	−1.470	−1.359	−1.069	0
0	σ_P/σ_N	1	1.040	1.172	1.447	2
	τ/σ_N	0	0.199	0.414	0.688	1
	σ_T/σ_N	−1	−0.960	−0.828	−0.554	0
0.5	σ_P/σ_N	1	1.019	1.079	1.183	1.333
	τ/σ_N	0	0.098	0.191	0.273	0.333
	σ_T/σ_N	−0.5	−0.471	−0.382	−0.226	0
1	σ_P/σ_N	1	1	1	1	1
	τ/σ_N	0	0	0	0	0
	σ_T/σ_N	0	0	0	0	0

maximum CTOD it will eventually assume a path normal to σ_P, that is, Mode I growth. This is not incompatible with experimental evidence [*49*].

Conclusions

1. In order to characterize the effects of a biaxial load on the tip of a crack a description of the laterally applied stress σ_T must be included in addition to the applied loads K_I and K_{II}. Increasingly negative values of σ_T tend to increase the crack-tip plastic zone size and the CTOD, but they have an opposite effect on the maximum crack-tip stress and on the crack separation energy rate.
2. If the rate of FCP increases with the extent of crack-tip plasticity characterized by the CTOD then with increasingly negative values of σ_T and λ, the FCP rate will increase although the applied load at the onset of unstable monotonic crack propagation may also increase.
3. If the crack path tends to adjust itself so that the CTOD is a maximum, this maximum value usually corresponds to zero or small values of the crack inclination angle θ, that is, to Mode I crack propagation. This agrees with experimental observation.

Acknowledgments

The authors acknowledge the assistance given by the Nuclear Regulatory Commission of the United States of America who, in collaboration with the Science Research Council of the United Kingdom, gave financial assistance towards this and other work concerned with theoretical and experimental studies on crack growth in biaxial/multiaxial stress fields.

References

[*1*] Kfouri, A. P. and Miller, K. J. in *Three-Dimensional Constitutive Relations and Ductile Fracture,* S. Nemat-Nasser, Ed., *Proceedings,* Conference, Dourdan, France, 2–5 June 1980, International Union of Theoretical and Applied Mechanics, 1981, p. 83.
[*2*] Erdogan, F. and Sih, G. C., *Journal of Basic Engineering,* Vol. 85D, 1963, p. 519.
[*3*] Anderson, G. P., Ruggles, V. L., and Stibor, G., *International Journal of Fracture Mechanics,* Vol. 7, 1971, p. 63.
[*4*] Palaniswamy, K. and Knauss, W. G. in *Mechanics Today,* S. Nemat-Nasser, Ed., Vol. 4, Pergamon, Oxford and New York, 1976, pp. 87–148.
[*5*] Williams, J. G. and Ewing, P. D., *International Journal of Fracture Mechanics,* Vol. 8, 1972, p. 441.
[*6*] Ewing, P. D. and Williams, J. G., *International Journal of Fracture,* Vol. 10, 1974, p. 135.
[*7*] Finnie, I. and Saith, A., *International Journal of Fracture,* Vol. 9, 1973, p. 484.
[*8*] Hussain, M. A., Pu, S. L., and Underwood, J. in *Fracture Analysis, ASTM STP 560,* American Society for Testing and Materials, Philadelphia, 1974, p. 2.
[*9*] Wu, C.-H., *Journal of Applied Mechanics,* Vol. 45, Sept. 1978, p. 553.
[*10*] Sih, G. C., *International Journal of Fracture,* Vol. 10, 1974, p. 305.
[*11*] Sih, G. C. and Kipp, M. E. (discussion on paper in Ref *5*) *International Journal of Fracture,* Vol. 10, 1974, p. 261.
[*12*] Liu, A. F., "Crack Growth and Failure of Aluminum Plate under In-Plane Shear," presented at AIAA 11th Aerospace Sciences Meeting, Washington, DC, Jan. 1973.
[*13*] Toor, P. M., *International Journal of Fracture Mechanics,* Vol. 7, 1975, p. 321.
[*14*] Swedlow, J. L. in *Cracks and Fracture, ASTM STP 601,* American Society for Testing and Materials, Philadelphia, 1976, p. 506.
[*15*] Bilby, B. A. and Cardew, G. E., *International Journal of Fracture,* Vol. 11, 1975, p. 708.
[*16*] Bilby, B. A., Cardew, G. E., and Howard, I. C. in *Fracture 1977,* Vol. 3, D. M. R. Taplin, Ed., University of Waterloo Press, Ont., 1978, p. 197.
[*17*] Kitagawa, H. and Yuuki, R. in *Fracture 1977,* Vol. 3, D. M. R. Taplin, Ed., University of Waterloo Press, Ont., 1978, p. 201.
[*18*] Chiang, W. T. in *Fracture 1978,* Vol. 4, D. M. R. Taplin, Ed., University of Waterloo Press, Ont., 1979, p. 135.
[*19*] Howard, I. C., *International Journal of Fracture,* Vol. 14, 1978, p. R307.
[*20*] Theocaris, P. S. and Ioakimidis, N. I., *Zeitschift für Angewandte Mathematik und Physik,* Vol. 27, 1976, p. 810.
[*21*] Theocaris, P. S., *Journal of Applied Mechanics,* Vol. 44, 1977, p. 611.
[*22*] Andersson, H., *Journal of the Mechanics and Physics of Solids,* Vol. 17, 1969, p. 405 (see also Vol. 18, 1970, p. 437).
[*23*] Vitek, V., *International Journal of Fracture,* Vol. 13, 1977, p. 481.
[*24*] Lo, K. K., *Journal of Applied Mechanics,* Vol. 45, 1978, p. 797.
[*25*] Bergkvist, H. and Guex, L., *International Journal of Fracture,* Vol. 15, 1975, p. 429.
[*26*] Amestoy, M., Bui, H. D., and Dang-Van, K., C. R., *Academie des Sciences,* Paris, Vol. 289, 1979, B-99.
[*27*] Shih, C. F. in *Fracture Analysis, ASTM STP 560,* American Society for Testing and Materials, Philadelphia, 1974, p. 187.
[*28*] Hutchinson, J. W., *Journal of the Mechanics and Physics of Solids,* Vol. 16, 1968, p. 137.
[*29*] Hutchinson, J. W., *Journal of the Mechanics and Physics of Solids,* Vol. 16, 1968, p. 337.
[*30*] Rice, J. R. and Rosengren, G. F., *Journal of the Mechanics and Physics of Solids,* Vol. 16, 1968, p. 1.
[*31*] Ueda, Y., Ikeda, K., Yao, T., Aoki, M., Yoshie, T., and Shirakura, T., *Fracture 1977,* Vol. 2, D. M. R. Taplin, Ed., University of Waterloo Press, Ont., 1978, p. 173.
[*32*] Ueda, Y., Ikeda, K., Yao, T., Aoki, M., Shibasaki, S., and Shirakura, T. in *Advances in Fracture Research,* Vol. 4, Pergamon, Oxford and New York, 1981, p. 1741.
[*33*] Chang, K. J., *Engineering Fracture Mechanics,* Vol. 14, 1981, p. 107.
[*34*] Miller, K. J. and Kfouri, A. P., *International Journal of Fracture,* Vol. 10, 1974, p. 393.
[*35*] Kfouri, A. P. and Miller, K. J., *Fracture 1977,* Vol. 3, D. M. R. Taplin, Ed., University of Waterloo Press, U.K., 1978, p. 241.

[36] Miller, K. J. and Kfouri, A. P. in *Elastic-Plastic Fracture, ASTM STP 668,* American Society for Testing and Materials, Philadelphia, 1977, p. 214.
[37] Eftis, J., Subramonian, N., and Liebowitz, H., *Engineering Fracture Mechanics,* Vol. 9, 1977, p. 189.
[38] Eftis, J. and Subramonian, N., *Engineering Fracture Mechanics,* Vol. 10, 1978, p. 43.
[39] Hilton, P. D., *International of Journal Fracture,* Vol. 9, 1973, p. 143.
[40] Larsson, S. G. and Carlsson, A. J., *Journal of Mechanics and Physics of Solids,* Vol. 21, 1973, p. 263.
[41] Rice, J. R., *Journal of the Mechanics and Physics of Solids,* Vol. 22, 1974, p. 17.
[42] Kfouri, A. P., *Journal of the Mechanics and Physics of Solids,* Vol. 27, 1979, p. 135.
[43] Kfouri, A. P. and Miller, K. J., *Proceedings, Institute of Mechanical Engineers,* Vol. 190, (paper 48/76), p. 571.
[44] Kfouri, A. P. and Rice, J. R., *Fracture 1977,* Vol. 1, D. M. R. Taplin, Ed., University of Waterloo Press, Ont., 1978, p. 43.
[45] Khrapkov, A. A., *International Journal of Fracture Mechanics,* Vol. 7, 1971, p. 373.
[46] Kfouri, A. P. and Miller, K. J., "Crack Separation Energy Rates for Inclined Cracks in a Biaxial Stress Field of an Elastic-Plastic Material," Departmental Report No. 114, Mechanical Engineering Department, University of Sheffield, Sheffield, 1983.
[47] Williams, M. L., *Journal of Applied Mechanics,* Vol. 24, p. 109.
[48] Brown, M. W., Liu, H. W., Kfouri, A. P., and Miller, K. J., "An Analysis of Fatigue Crack Growth Under Yielding Conditions," in *Advances in Fracture Research,* D. François et al, Ed., Conference Proceedings, ICF5, Pergamon, Oxford and New York, 1980.
[49] Gao Hua, Brown, M. W., and Miller, K. J., *Fatigue of Engineering Materials and Structures,* Vol. 5, 1982, pp. 1-17.
[50] Kfouri, A. P., "A Finite Element Analysis of Nonplanar Crack Growth in a Linear Elastic and in an Elastic-Plastic Material," *Proceedings,* ICF International Symposium on Fracture Mechanics, Beijing, China, 22-25 Nov. 1983, pp. 76-81.

Propagation of Long Fatigue Cracks

Edward W. Smith[1] *and Kenneth J. Pascoe*[2]

Fatigue Crack Initiation and Growth in a High-Strength Ductile Steel Subject to In-Plane Biaxial Loading

REFERENCE: Smith, E. W. and Pascoe, K. J., "**Fatigue Crack Initiation and Growth in a High-Strength Ductile Steel Subject to In-Plane Biaxial Loading,**" *Multiaxial Fatigue, ASTM STP 853*, K. J. Miller and M. W. Brown, Eds., American Society for Testing and Materials, Philadelphia, 1985, pp. 111–134.

ABSTRACT: Flat cruciform-shaped specimens of HY100 steel were tested in fatigue under biaxial stress states. For Mode I crack growth, a tensile component of stress parallel to the crack decreased crack growth rate; a compressive component had the opposite effect. These changes in growth rate are explained in terms of the material's differing cyclic stress-strain response under shear and equibiaxial loading.

Studies of Mode II growth were found difficult to perform, due to a critical balance between Mode II and Mode I growth. Mode II crack growth rates were much greater than for the equivalent Mode I crack. The growth rate increased with increasing ΔK_{II} but did not follow the Paris relationship due to the occurrence of incipient or undeveloped bifurcation which prevented continued and undisturbed Mode II growth.

KEY WORDS: fatigue crack initiation, fatigue crack growth, biaxial loading, cyclic stress/strain behavior, Mode I crack growth, Mode II crack growth

Nomenclature

1,2	Axes of applied loading
a	Half length of center crack
C	Material constant in Paris equation
$K_{\mathrm{I}}, K_{\mathrm{II}}$	Modes I and II stress intensity factors
$K_{\mathrm{Ic}}, K_{\mathrm{IIc}}$	Modes I and II critical stress intensity factors
ΔK	Range of stress-intensity factor
ΔK_{II}	Range of Mode II stress intensity factor
n	Material constant in Paris equation
N	Number of cycles
P	Cyclic load
P_1, P_2	Loads in orthogonal directions

[1]Lecturer, Department of Production Technology, Massey University, Palmerston North, New Zealand.
[2]University lecturer, Department of Engineering, Cambridge University, Cambridge, U.K.

Copyright© 1985 by ASTM International www.astm.org

P_{1m},P_{2m}	Mean values of P_1,P_2
$\Delta P_1,\Delta P_2$	Semi-ranges of P_1,P_2
R	$\sigma_{min}/\sigma_{max}$ in fatigue cycle
δ	Displacement
ϵ_1,ϵ_2	Strains in orthogonal directions
$\Delta\epsilon_1,\Delta\epsilon_2$	Semi ranges of ϵ_1,ϵ_2
$\Delta\epsilon_t$	Total strain range
λ	Load range biaxiality $\Delta P_1/\Delta P_2$
ν	Poisson's ratio
ξ	Ratio of principal strain ranges $\Delta\epsilon_2/\Delta\epsilon_2$
σ	Stress
$\sigma_{max},\sigma_{min}$	Maximum and minimum values of σ
$\Delta\sigma$	Stress range
τ	Shear stress

Fatigue crack initiation arises from the accumulation of slip bands into slip zones: these slip bands will occur on the planes of maximum shear. So, in the idealized case of uniaxial loading of an isotropic bar or structure of simple geometry the direction of slip bands, and hence crack initiation will be 45° to the free surface. As crack growth continues, the growth direction does not remain at 45° but turns normal to the loading direction. These two distinct regimes of crack propagation are called Stage I and Stage II, respectively.

Parsons and Pascoe [*1*] showed that the direction of crack initiation was dependent on the applied stress state. Biaxial fatigue tests were carried out for five different ratios, ξ, of principal strain range, that is, $\Delta\epsilon_2/\Delta\epsilon_1$. For low-cycle fatigue, where the whole fatigued region may be plastic and Poisson's ratio can be considered as 0.5, the biaxial state of $\xi = 0.5$ corresponds to uniaxial tension. Cracks were found to initiate along planes of maximum shear. These initial or Stage I cracks were seen to appear at the surface in directions as given in Table 1.

This extensive work considered only crack initiation and Stage I growth. Because the specimens were essentially plain, there was no unique site for crack initiation. Many microcracks were found to initiate, referred to as primary cracks, which then joined up to form secondary cracks. The newly formed secondary

TABLE 1—*Angle of crack on surface as function of strain state.*

Applied Strain State, ξ =	Crack Angles from Principal Axis
−1 (shear)	45 and 135°
−0.5	55 and 125°
0 (plane strain)	90°
+0.5 (uniaxial tension)	between 45 and 135°
+1 (equibiaxial)	any angle

cracks behaved in a similar manner to the primary cracks, and the two can be grouped together as Stage I. No attempt was made to study Stage II growth, either in form or in a quantitative measure of propagation rates.

In the terminology of linear elastic fracture mechanics cracks may deform and grow in three ways, namely, Mode I: opening, Mode II: in-plane shear, and Mode III: anti-plane shear. Consequently, Stage I growth and Mode II growth often are considered as synonymous; as are Stage II and Mode I growth.

The ease with which Stage II/Mode I growth can be isolated from the two earlier stages of initiation and Stage I, and the general validity of the Paris equation, $da/dN = C(\Delta K)^n$, where a is crack half-length of a center-cracked plate, N is the number of cycles of applied load, ΔK is the range of stress-intensity factor (SIF), C and n are constants, has led to a preponderance of data on uniaxial Mode I fatigue crack propagation. However, there is not a lot of data available on crack propagation under stress biaxiality. A review of the behavior of fatigue cracks subject to applied biaxial stress is presented by the authors elsewhere [*2*]. The experimental evidence that can be gained from the few published papers is not conclusive; indeed, comparing experimental data from different sources can lead to contradictions.

The purpose of this work is to show that the cyclic stress/strain response of a material is dependent on stress biaxiality so that the extent of cyclic softening, hardening, or ratchetting under different stress states can influence crack growth rates and behavior. The starting point was the five biaxial strain ratios used by Parsons, and the primary crack directions which he found from initiation studies. Natural crack growth directions for the most critical initiation states were found and then attention devoted to those particular cases.

Experimental Equipment and Method

The biaxial fatigue testing rig developed by Parsons and Pascoe [*3*] was used for all the fatigue initiation and crack propagation tests. This testing rig consists of two pairs of 20 kN tension/compression hydraulic loading rams which are set on orthogonal axes. Flat cruciform-shaped specimens were used with a thinned-down center section (thickness 1.25 mm). For crack initiation studies, dished centers of 100 and 50 mm radius of curvature were used because a plain center was liable to buckle under compressive loading. On the other hand, for the propagation studies, a flat center section was essential. Testing was then restricted to a positive stress ratio, R (= minimum stress level/maximum stress level). A value of $R = 0.1$ was taken as the norm for the present studies. More details of the specimen geometry, strain measurement, and testing philosophy are given in Ref *4*.

Fatigue crack initiation and propagation have been carried out on one material—a high yield-strength weldable steel, HY100. Specimen blanks, supplied in a quenched and tempered condition, measured 200 by 200 by 6.35 mm^3. The composition and tensile stress-strain properties of the material are given in Ref

4. There was no significant difference in properties between the longitudinal and transverse directions. Nevertheless, specimens were always loaded so that the rolling direction was aligned with the major principal load.

Studies of fatigue crack initiation were made by controlling the cyclic strains. Crack initiation was observed by optical microscope. Wherever possible, specimens for fatigue crack growth were machined from specimens that had been used for fatigue crack initiation. When cracked initiation specimens were not available or a prescribed crack direction was required, specimens with a prenotch cut by electric discharge machining were used. For notched specimens used at high load levels and negative biaxial ratios, cracks grew from the corners of the notch along planes of maximum shear. The result was two cracks growing from each end of the notch. This was overcome by prefatiguing under equibiaxial load. Crack propagation tests were made by controlling the cyclic loads. Crack growth was monitored using two travelling microscopes, one on each side of the specimen, the position of the crack tip being measured in both x- and y-directions. Measurement was tedious and required holding the cyclic load stationary; but no other simple automated method could be used to monitor direction as well as length.

Presentation of Results

The test results to be presented can be split into three distinct regimes:

1. Cyclic stress-strain behavior and fatigue crack initiation under cyclic biaxial straining.
2. Mode I fatigue crack growth, where growth is normal to the major principal stress direction.
3. Mode II and combined-mode fatigue crack growth, the crack growth direction may differ from that of an initial flaw or crack.

Fatigue Crack Initiation and Cyclic Behavior

From Parsons' work [5] on fatigue crack initiation using QT35 and AISI 304 steels, the biaxial strain ratios of $\xi = +1$ and $\xi = -1$ would appear to represent the most severe and least severe conditions, respectively. Only these two biaxial strain ratios with constant strain ranges were tested for HY100 steel. For each case the principal cyclic strains were controlled using strain extensometers with a nominal gage length of 6.35 mm.

Plots of total strain range, $\Delta\epsilon_t$, versus cycles to primary cracking are presented in Fig. 1. As in previous tests, equibiaxial cyclic strain proved more damaging than shear cyclic strain.

The cyclic load-strain histories for the two loading conditions are plotted in Figs. 2 through 4. Under equibiaxial straining, cyclic softening is seen; this was first evident in the compressive half cycle. Shear straining also shows cyclic softening, but more discernible is the pronounced cyclic ratchetting, giving a

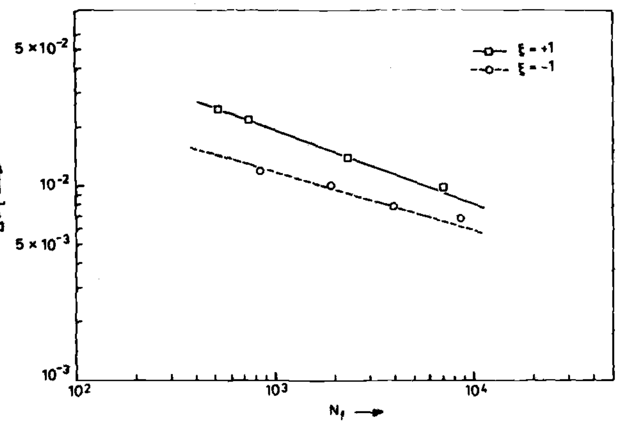

FIG. 1—*Major surface strain range versus cycles to primary cracking.*

$\xi = \Delta\epsilon_{t1}/\Delta\epsilon_{t2}$.

marked shift of mean load into tension. Indeed, this shift, when approaching the limits of endurance, is such that the maximum cyclic load exceeds the monotonic shear failure load despite cyclic softening.

Fatigue Crack Growth Normal to the Major Principal Stress Direction

The ratio of load range biaxiality, λ, is defined as $\Delta P_2/\Delta P_1$ where ΔP_1 and ΔP_2, respectively, are the variations from the mean values P_{1m} and P_{2m} of the orthogonally applied loads P_1 and P_2. Tests under constant load ranges were made for three ratios of λ, namely, $+1$, ν, and -1 as defined in Fig. 5*a*. P_{1m} and P_{2m} were kept approximately constant at 13.5 kN for all these tests.

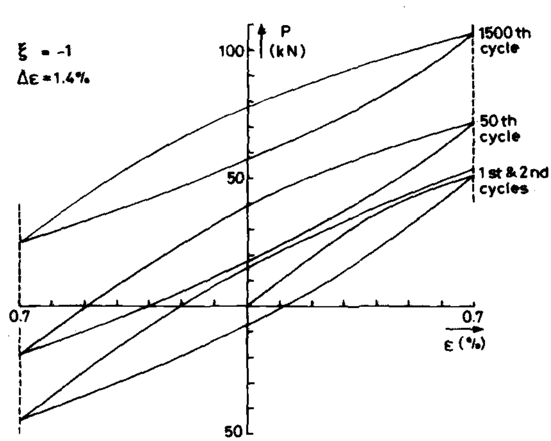

FIG. 2—*Cyclic load versus strain hysteresis loops under applied shear strain. Constant strain range.*

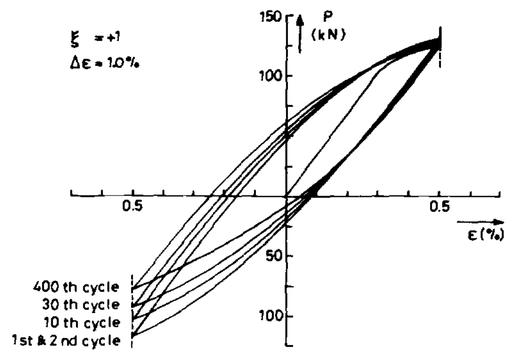

FIG. 3—*Cyclic load versus strain hysteresis loops under applied equibiaxial strain. Constant strain range.*

For $\lambda = +1$, a load range from 3 to 30 kN ($R = 0.1$) gave a useful life of 100 000 cycles. Crack growth followed the same direction as the initiation crack or notch. When the same load range was used for $\lambda = -1$, large "shear ears" emanating from the crack tip caused two cracks to grow from each notch tip along the shear zones (see Fig. 6). The result was mixed Mode I/Mode II growth with Mode II predominant. Crack growth was so rapid that the test had to be abandoned after little more than 400 cycles. This large increase in shear zone size for $\lambda = -1$ confirms the theoretical work of Miller and Kfouri [*6*]. To restrict the size of the yield zone to realistic proportions (and yet keep test times to less than one week) all further tests were set up using the same strain range and same mean strain across the working section. Tests were then load controlled in the usual way. For $\lambda = -1$, the minimum and maximum loads were +11 and +20 kN, respectively, for a strain range from 0.015 to 0.15%, that is, R equaled 0.55 and not 0.1 as originally planned. This is at a variance from $\lambda = -1$ as defined by other workers. In fact, for a true $\lambda = -1$ stress state then $R = -1$;

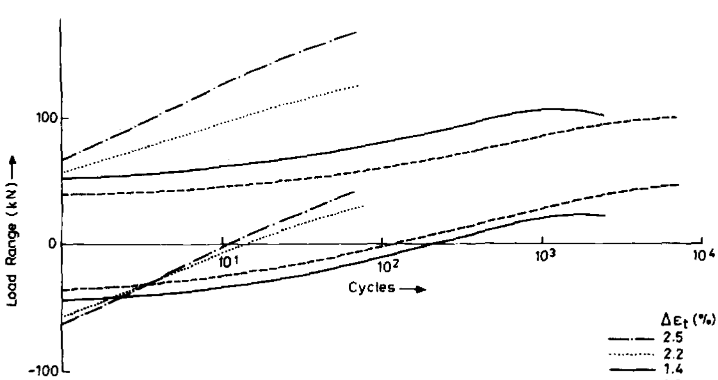

FIG. 4—*Load range variation with cycles; strain control under shear ($\xi = -1$).*

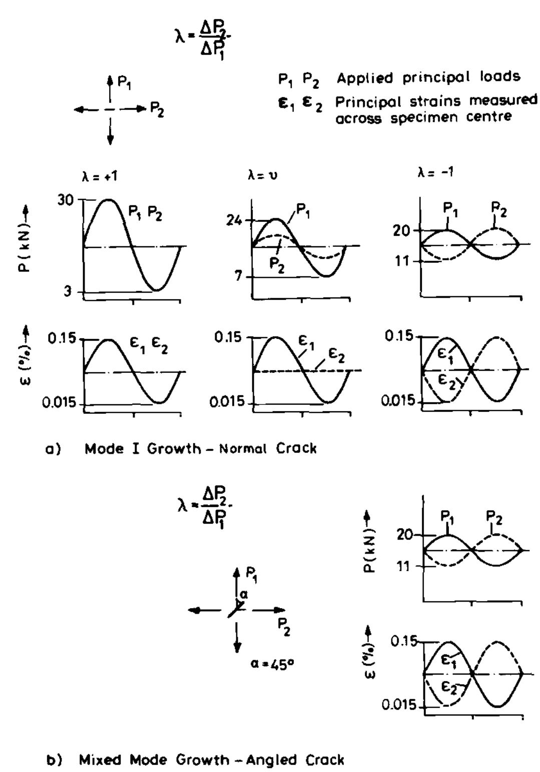

FIG. 5—*Test parameters for crack propagation studies.*

but this is difficult to achieve in a flat-centered cruciform specimen because of the risk of buckling.

Results for normal fatigue crack growth (Mode I) are shown in Fig. 7. Barsom [7] presented fatigue crack growth rates for a full range of materials under uniaxial loading: his upper and lower boundaries for high yield-strength steels (which include HY80 and HY130) are superimposed on Fig. 7.

Mode II and Mixed-Mode Fatigue Crack Growth

All Mode II and mixed-mode tests were made with one experimental setup. This is depicted in Fig. 5*b* and is the combination of crack angle, $\alpha = 45°$ to the principal load axes, stress biaxiality, $\lambda = -1$, and stress level ratio, $R = 0.55$. It is exactly the same test situation as for Mode I growth and $\lambda = -1$, except that the crack now lies along the plane of maximum shear. Ideally, fully reversed loading, $R = -1$, should be used for Mode II growth, but, to prevent buckling due to the compressive load component, it was found best, in practice, to set R positive. However, positive R leads to further problems if Mode II growth alone

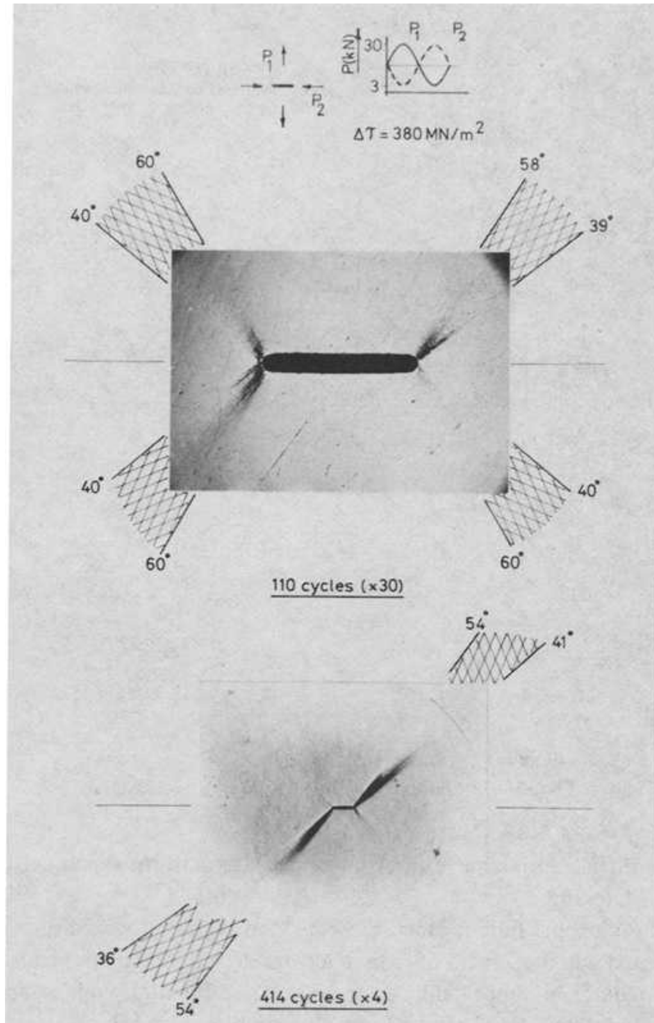

FIG. 6—*Shear zones and crack growth for* $\lambda = -1$ *loading at high stress range, on a crack perpendicular to one principal stress.*

is required; transition to mixed mode or even Mode I growth will occur. A number of tests with stress biaxiality set at $\lambda = -1$ showed that transition and interaction between Mode I, Mode II and mixed mode growth was very critically balanced. Figure 8 shows, for $\lambda = -1$ loading, the crack patterns for a number of tests; except for (*a*) and (*c*), the test parameters were as in Fig. 5*b*.

Configuration (*a*) shows the situation arising when a true shear ($\xi = -1$) initiated fatigue crack is propagated. Crack initiation was made in a plain dished-center specimen subject to high-strain fatigue ($\Delta\epsilon = 2.2\%$). After 760 cycles

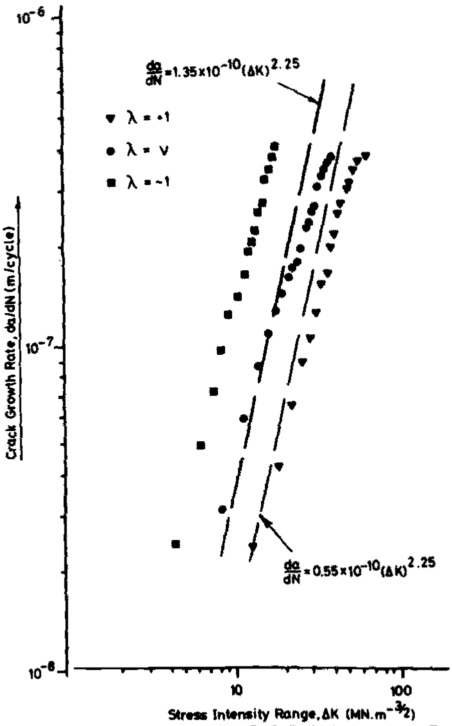

FIG. 7—*Mode I crack growth rate versus stress-intensity range. Scatter bands for uniaxial crack propagation of martensitic steels taken from Barsom* [7].

the specimen was removed from the rig and machined to give a flat center. The test was continued with an elastic shear stress range of 155 MN/m^2 (R = O). During the initiation phase two or three sufficiently large cracks had grown, but one of these dominated as soon as the propagation phase was established. This one crack grew in Mode II, but the effect of the other small initiated cracks was to cause crack bifurcation leading to a complicated crack path and mixed mode growth, though still dominantly Mode II. This behavior did not lend itself to quantitative measurement of crack growth. It did show that Mode II propagation is not a particularly stable mode of growth.

Configuration (*b*) shows the situation arising when Mode II propagation is attempted directly from a machined notch. Two pairs of cracks are initiated; one pair from each rounded end of the notch. Each crack propagates in mixed mode, but predominantly Mode I. Pairs of cracks, rather than single ones, form due to the alternating shear load. They lie at −60 to −66° to the crack. Ironically, the first attempts to propagate a Mode I crack from a 90° notch subject to shear (λ = −1) resulted in Mode II growth; and the first attempt to propagate a Mode II crack from a 45° notch resulted in predominantly Mode I.

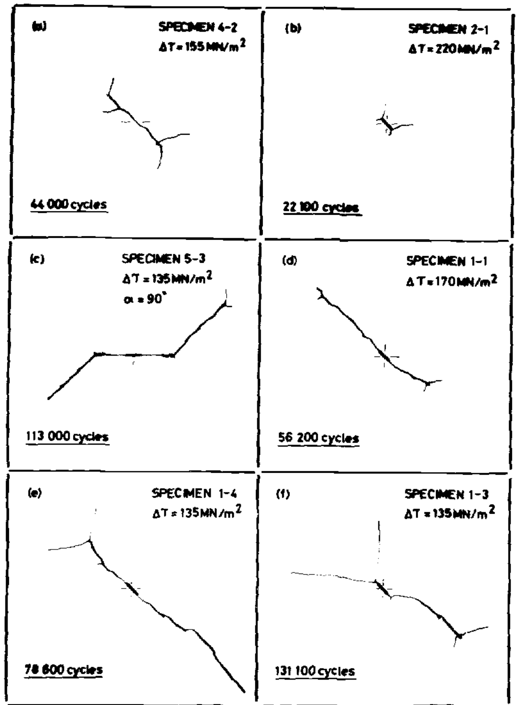

FIG. 8—*Crack growth paths for $\lambda = -1$ (shear) loading showing evidence of Mode I, Mode II, and Mixed Mode growth $\Delta\tau$ = shear stress range in absence of crack.*

By using equibiaxial loading ($\lambda = +1$) it was possible to propagate single sharp cracks aligned with the starter notch. Once the influence of the starter notch was overcome, the loading could be changed to $\lambda = -1$. This procedure was used with configurations (*c*) to (*f*).

Configuration (*c*) shows, for $\lambda = -1$ loading, that Mode I crack growth can change to Mode II, even once a sharp Mode I crack has propagated under $\lambda = -1$ loading. Configurations (*d*) to (*f*) show crack growth paths for three $\lambda = -1$ tests made under identical conditions. The starter notch is set at 45° and initial growth is Mode II. The Mode II cracks of configurations (*d*) and (*e*) show transition to Mode I at around $\Delta K_{\text{II}} = 6$ MN m$^{-3/2}$ where ΔK_{II} is the range of Mode II SIF. In constrast, the Mode II cracks of configuration (*f*) show transition to Mode I at a much lower stress intensity.

Macrographs (approximately $\times 3$) of configurations (*e*) and (*f*) are shown in Fig. 9 where the Mode II, mixed mode and Mode I cracks are annotated. Mode II cracks are easily recognized by their greater width due to troughs of the shear zone pushing ahead of the propagating crack. Mode I cracks are sharply defined and run normal to the principal load axes. Because there is no major principal

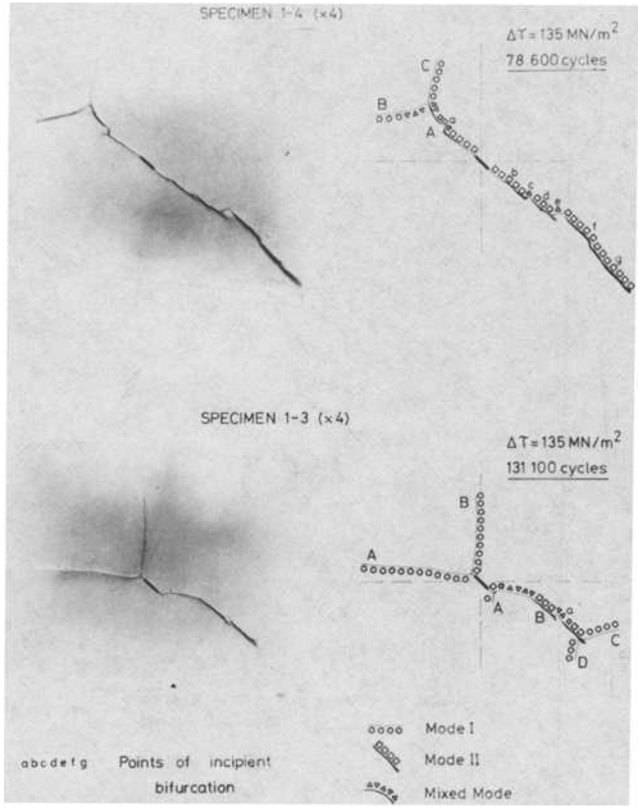

FIG. 9—*Modes of crack growth for cracks with bifurcation under* $\lambda = -1$ *(shear) loading.*

direction, two Mode I cracks will always occur at the transition from Mode II to Mode I—this is termed crack "bifurcation".

Crack propagation data for configurations (*c*) to (*e*) prior to any bifurcation are shown in Fig. 10, from which a comparison of Mode I and Mode II growth rates can be made. In configuration (*f*), the Westward Crack *B* changes from Mode I to Mode II by a slow transition in path direction. Mixed mode growth occurs during this transition. Figure 11 compares crack growth rates for the transition and final bifurcation.

Discussion of Results

The previous section presented the experimental results in three divisions; the same divisions will be used now. Though the findings of each division show distinct conclusions, these conclusions must not be treated in isolation. In particular, consideration of the material's cyclic stress/strain properties is necessary to understand the effects of stress biaxiality on crack propagation.

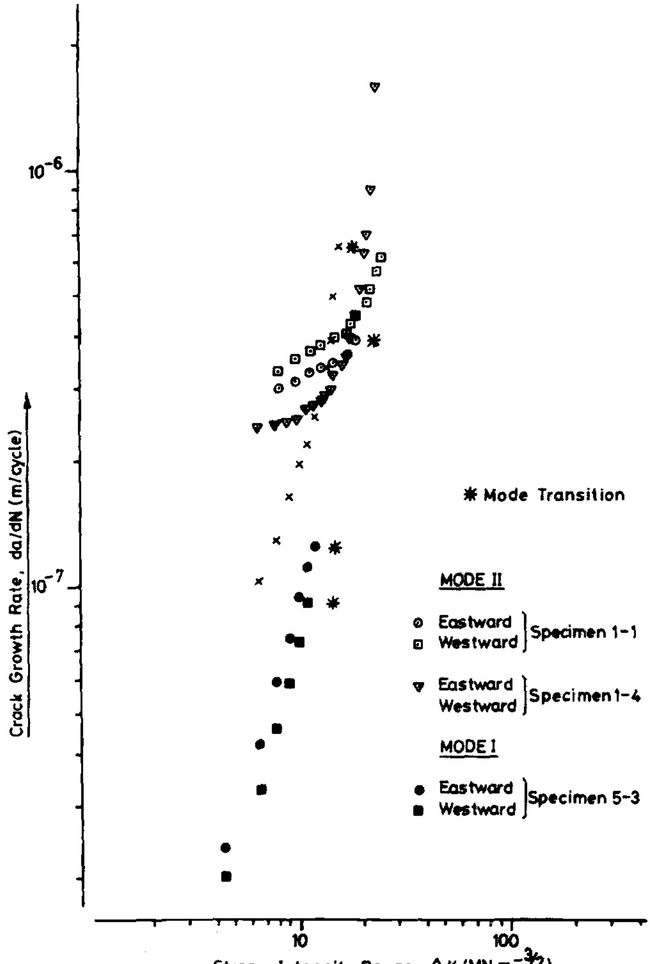

FIG. 10—*Crack propagation plotted as stress intensity range versus crack growth rate to compare Mode I and Mode II growth (crack configuration shown in Fig. 8c,* d, *and* e).

Fatigue Crack Initiation and Cyclic Behavior

Cyclic softening is apparent for both the strain conditions of $\xi = +1$ and $\xi = -1$. For equibiaxial strain the softening is most evident in the compressive half cycle, but both states of strain show similar extents of softening.

The pronounced cyclic ratchetting or axial strain accumulation evident under reversed shear strain was not witnessed in the two steels (QT35 and AISI 304) tested by Parsons and Pascoe [*5*]. Evidence of axial strain accumulation due to torsional loading is documented by Swift [*8*] and by Bright and Harvey [*9*].

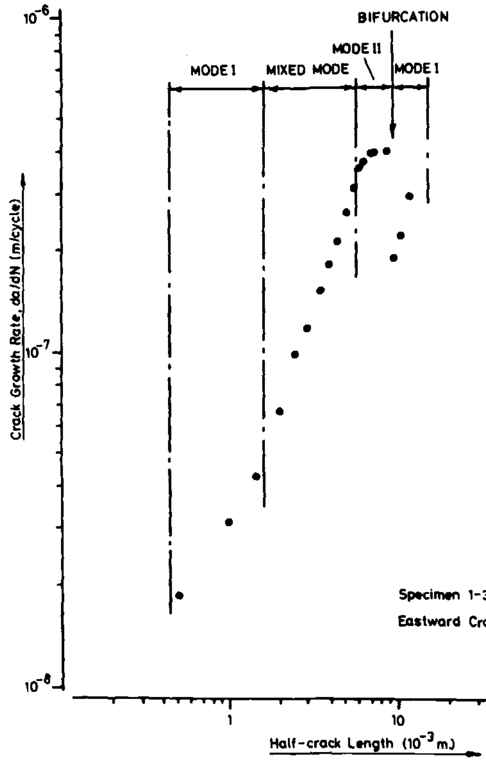

FIG. 11—*Crack propagation plotted as crack length versus crack growth rate to compare Mode I, Mixed-Mode, and Mode II growth (crack configuration shown in Fig. 8*f*).*

Mainly, static torsional strains were used, but a number of different materials were tested to very high shear strains. Axial elongation was witnessed for the work-hardening materials; only lead showed axial compression. It was deduced that axial elongation was brough about by continued slip of suitably orientated grains off set by work hardening of other less suitably oriented grains. Materials with large numbers of possible slip planes, for example, body-centered cubic structures, would be least prone to preferred slip and anisotropic hardening and so show least elongation. This was indeed the case for mild steel and plain carbon steels showed elongations of less than 0.03, whereas the face-centered curbic structures of stainless steel, aluminum, and copper-based alloys showed elongations of up to 0.11. Swift did not carry out true fatigue cycling, but he did show that reversal of the torsional strains could lead to further axial elongation.

The HY100 steel has a martensitic/bainitic structure, with hardness of 275 to 285 VHN as tested. Taking into account the resistance of martensite to slip, the initial anisotropic structure will slip only in suitably positioned and oriented bainitic regions. This will lead to a progressively more anisotropic structure as some bainite regions are allowed to slip and others are resisted by the rigid martensite. Axial elongation will then be more marked in martensitic-bainitic steels than with plain carbon steels as work-hardening is not a prerequisite. However, the rate of axial strain accumulation does not build up, but in fact falls off with cycling until a steady state is reached.

Fatigue Crack Growth and the Normal Crack

Figure 7 shows that a compressive cyclic transverse stress causes a significant increase in crack growth rate. The plane-strain state line falls inside the upper and lower boundary lines for high yield-strength steels set by Barsom [*7*], but the $\lambda = -1$ line is shifted well to the left of the upper boundary line and the $\lambda = +1$ line is shifted just outside the lower boundary line.

A cyclic transverse stress should affect Mode I crack growth by altering:

(*a*) shear distribution about the crack tip, and

(*b*) size of the plastic zone.

Further variables are seen to change uniaxial crack growth rates, which become dependent variables when changing applied stress biaxiality; these are:

(*c*) crack opening displacement and crack closure,

(*d*) mean stress/strain level, and

(*e*) cyclic stress/strain behavior.

The size of the cyclic plastic zone differs considerably between $\lambda = -1$ and $\lambda = +1$ loadings. The approximate extent of the plastic zone can be seen simply by using slightly oblique lighting during microscopic observation of the crack tip. Comparing Figs. 6 and 12*a* highlights the extent of the difference between the two cases. After 110 cycles of $\lambda = -1$ loading, that is even before crack propagation of a notch of half length 0.8 mm, the width of the cyclic plastic zone track is of the order of 1.4 mm. In comparison, after 63 000 cycles of $\lambda = +1$ loading and a semicrack length of 1.4 mm, the width of the cyclic plastic zone track is less than 0.1 mm. The cyclic (or reversed) plastic zones, that is, those still apparent after stress removal, will be smaller than the monotonic plastic zone at the crack tip during loading.

The crack propagation process in ductile materials is one of slip. Neumann [*10*], in testing single crystals of copper, showed that slip occurred along successive planes which were in the near vicinity of the crack vertex. As the vertex moved along under coarse slip, so would the active slip planes. Obviously in a complicated polycrystal structure this mechanism will not exist in such a simple and reproducible manner. However, in a polycrystalline anisotropic material the size of the plastic zone will reflect the extent of slip occurring at the crack tip since:

1. More slip planes will be activated in larger plastic zones.
2. The extent of slip on each plane will be greater if the "ears" of the plastic zone are long.

Thus, large plastic zones at the crack tip, that is, the case for $\lambda = -1$, would be expected to increase crack growth rate.

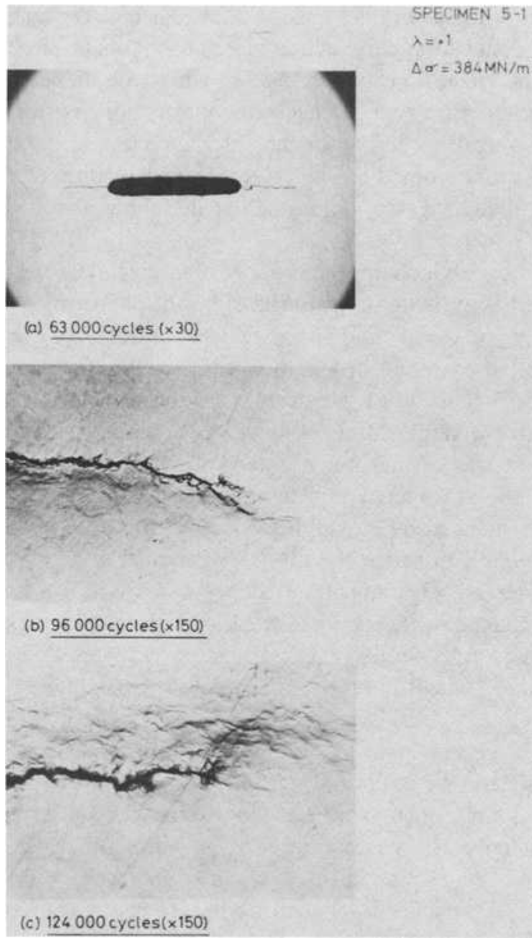

FIG. 12—*Macrographs of the crack tip area for equibiaxial loading. Specimen 5–1,* $\lambda = +1$, $\Delta\sigma = 384$ *MN/m*^{2}.

The plastic zone induced at the crack tip for $\lambda = +1$ is relatively small and the microphotographs of Fig. 12*b* and *c* show that the plastic zone plays a part in the formation of the crack path. Not only is surface rumpling evident above and below the crack behind the crack tip, but evidence of forking of the crack can be seen at a number of points. Indeed, the actual crack tip on both micrographs appears forked with severe surface distortions ahead of the visible crack. Coarse slip from the crack tip could cause this premature forking, and the slip induced per cycle will not be enough to turn the crack along either of the forks. Miller and Kfouri [6] showed for equibiaxial loading of a non-work-hardening material that the plastic zone is squat with an inclination of 100° to the crack axis (compared to 65° for uniaxial loading and 50° for shear). Though the plastic zone protrudes ahead of the crack tip, it presents a blunt profile. Alternative reasoning for the forked and rather chaotic appearance of the crack tip region is the formation of dislocation cells which have no dominant direction. Slip and microgrowth at the crack tip can then take any direction dictated by the microstructure within the plastic zone. Because the plastic zone is small, square, and squat there is no overall incentive for the crack direction to deviate. The result is that the overall crack direction under equibiaxial loading ($\lambda = +1$) is extremely straight, though it can, on a small scale, show a zig-zag growth (see Fig. 12*a*).

The large shear ears which appeared under high levels of stress for $\lambda = -1$ loading caused crack growth along tracks splayed out between 40 and 60° to the notch axis (Fig. 6). As cycling progressed, these tracks or ears did not grow in angular extent but extended in length to form well-defined channels. Crack growth and further extension of the shear tracks occurred on diametrically opposite zones so that a single Mode II crack developed. As the Mode II crack from either end of the normal notch extended so the influence of the notch became less and the tracks tended to move to a 45° plane, the maximum shear stress direction as dictated by the applied loading. More will be said about the transition from Mode I to Mode II and vice versa later.

There is considerable experimental evidence to show that a change in mean stress, that is, a change in R, can alter crack growth rates (for example, [*11*]). In biaxial stressing, unless fully reversed loading ($R = -1$) is used, altering the load range ratio, λ, will alter the mean strain experienced by the cracked area. Tanaka et al [*12*] considered nine stress states. The normal cyclic stress range and mean were the same for each state: the transverse stress range and mean were changed to give different values of λ. The transverse stress was cyclic in only four cases, and a change in mean stress was the only difference between two of these. In only one case were two tests directly comparable without interference from mean stress changes ($\lambda = 0$ and $\lambda = +1$). Undoubtedly Tanaka's results are influenced as much by the mean stress effects (change in R) as by stress biaxiality (change in λ). Four of their test situations show no change at all in cyclic stress biaxiality from the standard uniaxial case, but give wide variations in crack growth rates.

In setting up the three test parameters of $\lambda = +1$, ν, and -1 some thought has been given to the question of true cyclic stress biaxiality and the consequence of mean stress-strain changes. The ideal would have been to use a zero mean stress level for both normal and transverse stresses. In the early days of testing cruciform specimens, great difficulty was experienced with specimen center buckling when a flat center of small area was used in initiation studies. A 40 mm diameter flat center with a long crack would be prone to buckling under small (20 kN) compressive loads unless lateral movement was constrained by mechanical guides. A further consequence of fully reversed cyclic loading is the effect of the compressive half cycle on crack growth. When a crack is closed (faces under compressive load) it it accepted that no contribution is made to crack growth though as will be discussed later the conclusion may be inadequate for the purpose of testing for stress biaxiality. It was planned to use a mean stress ratio of $R = 0.1$, but, in setting up tests, it became evident that this would lead to complications. If one chooses $R = 0.1$ then negative λ can induce compressive strains normal to the crack even though the normal applied stress is still tensile. For example, in Fig. 13 the case for $\lambda = -1$ is compared with $\lambda = +1$ where both the normal and transverse maximum to minimum stress ratios are set for $R = 0.1$. For this setting of $\lambda = -1$, the compressive strains will induce compressive stress at the crack tip and hence crack closure when the normal applied stress is still tensile. The stress intensity range will be reduced accordingly. For the case of Fig. 13 and using elastic calculations, ΔK will be reduced to 28%. Thus, in order to compare like with like and measure cyclic stress biaxiality changes uninfluenced by mean stress changes, tests were best set up over a constant strain range.

The concept of crack closure during crack propagation under tensile normal loading is not restricted to biaxial loaded cracks. Elber [13] showed that under uniaxial loading the cyclic plastic zone behind the crack tip can induce compressive residual stress, and hence crack closure before the applied normal stress drops to zero. He related the magnitude of crack closure to the plastic zone size and the stress ratio R. Can the cyclic plastic stress-strain behavior of a material affect the extent and continuance of crack closure? Elber in his experiments showed that crack closure tended to remain constant as cycling progressed, unless overloads were introduced. Small plastic zones allow minimal reversed plasticity at the crack so that residual tensile strains will be produced (Fig. 14*a*). On the other hand, if the applied stress cycle is fully reversed ($R = -1$), then the plastic strain in the shear zone at the crack tip will be able to undergo full reversal, that is, no residual strains will be induced and the crack growth will not be affected (Fig. 14*b*). When the plastic zone is large ($\lambda = -1$ for instance) plasticity may show some reversibility even under nonreversed tensile loading ($R + ve$), then the magnitude of the induced compressive stress will be reduced accordingly (Fig. 14*c*).

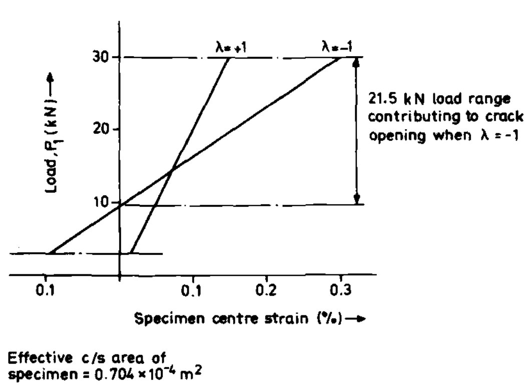

FIG. 13—*Plots of load versus strain on principal stress axes for* $\lambda = +1$ *and* $\lambda = -1$ *loading.*

If reversed plasticity is free to occur then transient cyclic stress-strain behavior can complicate the foregoing. Cyclic softening, as witnessed in HY100, will tend to prohibit high residual strain levels (Fig. 14*d*). Cyclic strain ratchetting, as measured under reversed shear loading, will tend to promote crack opening due to the accumulation of tensile residual strains (Fig. 14*e*). Crack growth will then be accelerated. It is expected that ratchetting will not need fully reversed plasticity to have a marked effect. In fact, the extent of ratchetting should be exaggerated by nonreversed loading so long as some reversed plasticity is present.

Mode II and Mixed-Mode Fatigue Crack Growth

Even without measuring the direction of crack face displacements it is possible to identify the mode of crack growth from the crack profile. Predominantly Mode II cracks show deep shear tracks either side and ahead of the crack; under a low power microscope the crack appears as a wide track with no distinct crack tip. Though the crack front is wide and ill defined, an undisturbed Mode II crack will be straight with a gradually widening track as K_{II} increases. On the other hand, predominantly Mode I cracks are well defined but may show slight di-

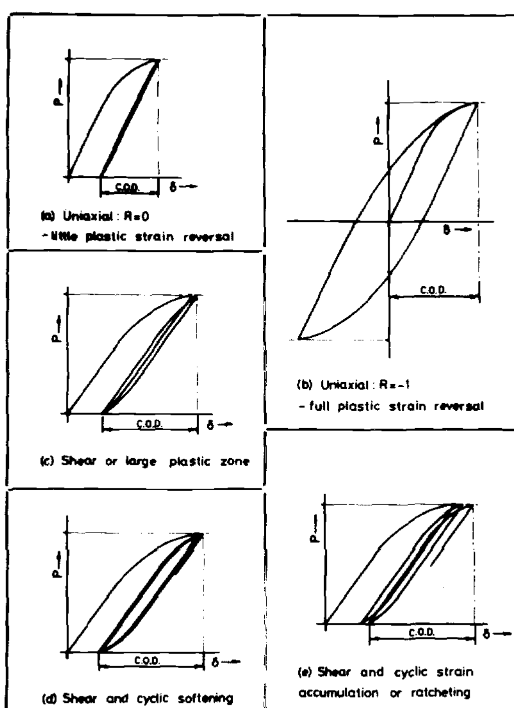

FIG. 14—*Graphs of cyclic load,* P, *versus displacement,*δ, *in the vicinity of the crack tip showing effect upon fatigue crack-opening displacement (COD).*

rectional instabilities. In a shear stress field ($\lambda = -1$) a Mode I orientated crack can bifurcate to give Mode II growth, and vice versa a Mode II orientated crack can bifurcate to give Mode I growth. The initial shear ears or tracks at the tip of a Mode I notch are orientated between 40 and 60° (see Fig. 6). This correlates well with the shear zone angle of 50° predicted by Miller and Kfouri [6]. But as the tracks deepen and cracks are initiated, the tracks tend to a mean angle approaching 45° or the maximum shear plane: the track is seen to span from 36 to 54° after 414 cycles. The longer pair of diametrically opposite tracks will gradually form into a Mode II crack. In contrast, Mode I cracks growing from a Mode II notch are well defined from their start. Cracks are seen to originate at angles of between −61 and −66° to a 45° notch. This is shown in the bifurcating crack after 122 500 cycles of Fig. 15.

As these cracks propagate, they gradually rotate to align normal to the applied principal stress directions. This compares agreeably with Iida and Kobayashi

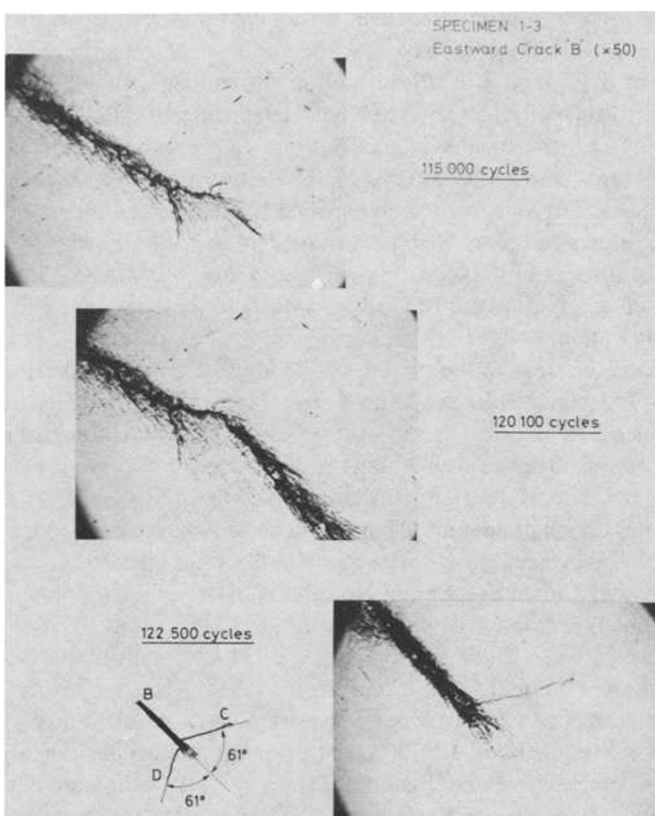

FIG. 15—*Mode II growth with mixed mode forking and final bifurcation into two predominantly Mode I cracks.*

[14] who found that inclined cracks subject to uniaxial loading grew in a direction which tended to reduce the Mode II stress intensity to zero, that is, to a direction normal to the principal stress direction.

The original crack growth angles of -61 and $-66°$ do not tally with available theory. Predicting the crack growth angle using maximum tensile hoop stress gives $-74°$ [15], minimum strain energy density gives $-82°$ [16]. The "roundness" of the crack tip may be thought to have some bearing on this variance, but similar behavior is witnessed for a sharp crack initiated using biaxial loading.

The crack growth mode is not wholly dependent on the applied stress state. Figure 9 shows the crack paths resulting from two identical tests; Mode I, Mode II, and mixed mode growth can be recognized. The crack growth behavior is not identical: Mode I/Mode II growth seems to be dependent on microstructure as well as applied stress state. Specimen 1–4 has shown almost undisturbed Mode II growth up to 64 000 cycles, when the Westward crack has bifurcated into two Mode I cracks. The Westward crack of Specimen 1–3 shows bifurcation after 28 000 cycles, the Eastward crack after 39 000 cycles. The Westward cracks have quickly rotated to grow normal to the applied principal stress directions. However, the Eastward cracks have not shown the same rotation: crack B has gradually turned to align with the maximum shear plane, thus continuing in Mode II. This Mode II crack has grown at the expense of the other bifurcated arm (crack A), which, though aligned normal to an applied principal stress direction, has arrested. At 120 000 cycles, the Eastward Mode II crack has again bifurcated, this time propagating as two Mode I cracks C and D.

The crack bifurcation process appears to be very unstable. Figure 9 shows up four points of distinct bifurcation, but there are other points where bifurcation has interrupted straightforward Mode II growth, and these are discernible even at $\times 4$ magnification.

Figure 15 shows steps in the growth of the long Eastward Mode II crack of Specimen 1–3: designated Eastward crack B in Fig. 9. As ΔK_{II} increases so the yield track increases in size. At 115 000 cycles, slight bifurcation at the crack tip has induced mixed-mode growth, but the crack angle at the fork is not enough to cause predominant Mode I growth. One arm of the fork still favors Mode II growth and after a small amount of mixed-mode growth the crack continues in Mode II (120 100 cycles). After further growth the yield track increases in size: the crack tip is effectively becoming more blunt. The yield track now behaves like a blunt notch and crack growth favors Mode I bifurcation.

The balance between Mode II continuation or Mode I transition appears critical. Bifurcation of Mode II cracks occurs over a range of stress intensity. Otsuka et al [17] found that Mode II to Mode I transition was controlled by $K_\sigma(\theta)$, the opening mode SIF. Tests on HY100 do not support this supposition. Figure 8 illustrates that crack growth configurations for $\lambda = -1$ loading are not repeatable: possibly microstructure has a major influence. HY100 steel has a high sulfide inclusion count and inclusion interaction with crack path profile has been reported [*18*]. In particular, Specimen 1–4, illustrated in Fig. 9, draws evidence of at least seven points of incipient bifurcation (marked as *a* to *g*).

Bifurcation causes a distinct change in crack mode, which is accompanied by an equally distinct change in crack growth rate. A single specimen may show Mode I, Mode II, and mixed-mode growth, but the direct comparison of crack growth rates for each mode is not easily assessed. A single Mode II crack can usually bifurcate into two Mode I cracks. The calculation of stress intensity after bifurcation is not easy. Further, two cracks are growing concurrently in place of one, though it may be argued in the case of shear loading that when bifurcated Mode I cracks are running normal to the applied principal stress directions one crack will be experiencing opening, while the other is closing or closed, and vice versa during the other half cycle.

Crack growth rates are difficult to compare after bifurcation, but Fig. 10 presents plots of da/dN versus ΔK to allow Mode I/Mode II comparison prior to bifurcation. The Mode II curves lie to the left of the Mode I line. This tallies with the results of Otsuka et al [*19*] but not with Roberts and Kibler [*20*]. Plotted on log/log scales, the Mode II results do not show straight line plots over the whole range of crack length. Either the Paris relationship does not hold for Mode II growth or alternatively the three proportional regions seen for Mode I growth are not so distinct in Mode II. The combination of crack length and stress range may put the plot near the upper limits of ΔK, but this is unlikely as K_{IIc} is likely to be greater than K_{Ic}. Here K_{IIc} and K_{Ic} are respectively the Mode II and Mode I critical SIFs.

The most likely explanation for the invalidity of the relationship

$$\frac{da}{dN} = C\Delta K_{\text{II}}{}^{n}$$

can be explained by incipient bifurcation. The bifurcation process destroys continuity of crack growth, partly because a new mode of growth must be initiated and partly because crack growth direction is changed. Crack formation at bifurcation, therefore, will tend to be a slower process than is straightforward growth. All the Mode II cracks considered in Fig. 10 show evidence of incipient or arrested bifurcation. Consider the two cracks of Specimen 1–4 (see Fig. 9). The Westward crack is least prone to incipient bifurcation: only one distinct point is apparent. On the other hand, the Eastward crack has six points of likely bifurcation which have not propagated into Mode I. This is reflected in the two da/dN versus a lines for the respective cracks. The Westward crack line is the straighter; the Eastward crack line shows a gradient at short crack lengths which only approaches that of the smoother running Eastward crack at much longer crack lengths.

The mixed mode, Mode II, Mode I crack running Eastward in Specimen 1–

3 (see Fig. 9) is represented in a plot of da/dN versus semicrack length in Fig. 11. Just as three distinct regions of crack growth are recognizable in the micrograph, so three divisions can be seen in the rate plots. Changing from Mode I to mixed-mode shows an increase in the Paris law exponent, but as Mode II growth predominates there is only minimal increase in da/dN with increase in crack length. Again, incipient bifurcation is the probable cause of breakdown in the Paris relationship. After bifurcation the Mode I growth rate falls to a point which is a continuation of the early Mode I Paris line. Prolonged or stable mixed-mode growth was never witnessed. The stable conditions of crack growth were Mode I and Mode II and undoubtedly even under shear loading the former appeared to be the more stable of the two. Because of the instability of mixed-mode growth it is surprising to see the da/dN versus a plot obeying an exponential relationship. As the crack propagated so the angle changed, in this case rotating to the plane of maximum shear: ΔK_I would be decreasing while ΔK_{II} would be increasing.

Conclusions

Knowledge of the elastic stress state at the tip of a propagating crack goes only a little way towards understanding the problem of biaxial stress effects on fatigue crack propagation. In a real material, it is apparent that crack-tip plasticity must play a vital role, and a material's cyclic stress/strain behavior is of first importance. Tests on HY100 steel show that when a material exhibits high strength and ductility the effects of applied stress biaxiality can be marked.

Considering firstly fatigue crack initiation the following is concluded:

1. Shear loading tends to be the most damaging in-plane cyclic stress state.
2. Cyclic stress-strain behavior can differ with stress state; in particular, longitudinal tensile strain accumulation or ratchetting is found to be a dominant characteristic of HY100 steel under reversed cylic shear straining. Microstructural anisotropy due to the steel's martensitic/bainitic structure is believed to account for this phenomenon.

Looking next at normal fatigue crack growth, but not isolating the foregoing findings:

3. Cyclic loads transverse to a normal or Mode I crack can affect crack growth rate, but usually not the crack path. Out-of-phase biaxial stress, producing cyclic shear ($\lambda = -1$) is found to increase crack growth rate; conversely, equibiaxial stress ($\lambda = +1$) is found to decrease the growth rate.
4. Changes in crack growth rate under different cyclic stress conditions are a consequence of changes in crack tip plasticity. In particular, changes in crack-tip shear-stress distribution, plastic zone size, cyclic stress-strain behavior and opening displacement and closure occur with changes in applied stress biaxiality.

Finally, Mode II and mixed-mode growth studies show the following conclusions:

5. Cyclic shear stress ($\lambda = -1$) can cause Mode I, Mode II, or mixed-mode crack growth. Mode I and Mode II are stable forms of growth, on the other hand mixed-mode growth will change quickly, by crack rotation, to either Mode I or Mode II.

6. The occurrence of Mode I or Mode II growth is dictated by crack angle, but the occurrence of any one mode is believed to be dependent on both stress state and microstructure.

7. Mode I growth can change to Mode II growth by cracks turning and following the path of the Mode I crack shear ears.

8. Mode II growth changes to Mode I growth by crack bifurcation. Two Mode I cracks will usually propagate, each in a direction normal to the applied principal stress directions. The balance between Mode II to Mode I transition appears to be very critical. Bifurcation can lead straight into Mode I growth, alternatively incipient or arrested bifurcation can cause continued, but disturbed, Mode II growth.

9. Mode II growth is characterized by a yield track either side and ahead of the propagating crack.

10. A crack propagating in Mode II can be considered more dangerous than the equivalent Mode I crack. Prior to bifurcation

$$\left[\frac{da}{dN}\right]_{\text{Mode II}} > \left[\frac{da}{dN}\right]_{\text{Mode I}}$$

for a given range of stress intensity factor. If, in a structure, conditions favor Mode II crack growth, then available Mode I crack growth data must be considered inadequate.

Acknowledgments

The authors wish to thank colleagues at the Cambridge University Engineering Department for their assistance.

This work has been carried out with the support of the Procurement Executive, Ministry of Defence.

References

[1] Parsons, M. W. and Pascoe, K. J., *Materials Science and Engineering*, Vol. 22, 1976, pp. 31–50.

[2] Smith, E. W. and Pascoe, K. J., *Fatigue of Engineering Materials and Structures*, Vol. 6, 1983, pp. 201–224.

[3] Parsons, M. W. and Pascoe, K. J., *Journal of Strain Analysis*, Vol. 10, 1975, pp. 1–9.

[4] Smith, E. W. and Pascoe, K. J., "Fatigue Crack Initiation and Growth in HY100 Steel Subject to In-plane Biaxial Loading," Technical Report CUED/C-MAT/TR. 95, Cambridge University Engineering Department, Cambridge, 1982.

[5] Parsons, M. W. and Pascoe, K. J., *Proceedings*, Institution of Mechanical Engineers, Vol. 188, 1974, pp. 657–671.
[6] Miller, K. J. and Kfouri, A. P., *International Journal of Fracture*, Vol. 10, 1974, pp. 393–404.
[7] Barsom, J. M., *Transactions*, American Society of Mechanical Engineers, *Journal of Engineering Industries Series B*, Vol. 93, 1971, pp. 1190–1196.
[8] Swift, H. W., *Engineering*, Vol. 163, 1947, pp. 253–257.
[9] Hancell, P. J. and Harvey, S. J., *Fatigue of Engineering Materials and Structures*, Vol. 1, 1979, pp. 271–279.
[10] Neumann, P., *Acta Metallurgica*, Vol. 22, 1974, pp. 1155–1165.
[11] Frost, N. E., Pook, L. P. and Denton, K., *Engineering Fracture Mechanics*, Vol. 3, 1971, pp. 109–126.
[12] Tanaka, K., Hoshide, T., Yamada, A., and Taira, S., *Fatigue of Engineering Materials and Structures*, Vol. 2, 1979, pp. 181–184.
[13] Elber, W. in *Damage Tolerance in Aircraft Structures, ASTM STP 486*, American Society for Testing and Materials, Philadelphia, 1971, pp. 230–242.
[14] Iida, S. and Kobayshi, A. S., *Transactions*, American Society of Mechanical Engineers, *Journal of Basic Engineering*, Vol. 91, 1969, pp. 764–769.
[15] Eftis, J. and Subramonian, N., *Engineering Fracture Mechanics*, Vol. 10, 1978, pp. 43–67.
[16] Sih, G. C., *International Journal of Fracture*, Vol. 10, 1974, pp. 305–321.
[17] Otsuka, A., Mori, K., and Miyata, T., *Engineering Fracture Mechanics*, Vol. 7, 1975, pp. 429–439.
[18] Fields, A., from discussion of Rhines, F. N. in *Fatigue Mechanisms, ASTM STP 675*, American Society for Testing and Materials, Philadelphia, 1979, pp. 23–46.
[19] Otsuka, A., Mori, K., Okshima, T., and Tsuyama, S., *Advances in Fracture Research, Proceedings of 5th International Conference on Fracture*, Pergamon, Oxford, 1981, pp. 1851–1858.
[20] Roberts, R. and Kibler, J. J., *Transactions*, American Society of Mechanical Engineers, *Journal of Basic Engineering*, Vol. 93, 1971, pp. 671–680.

Michael W. Brown[1] *and Keith J. Miller*[1]

Mode I Fatigue Crack Growth Under Biaxial Stress at Room and Elevated Temperature

REFERENCE: Brown, M. W. and Miller, K. J., "**Mode I Fatigue Crack Growth Under Biaxial Stress at Room and Elevated Temperature,**" *Multiaxial Fatigue, ASTM STP 853*, K. J. Miller and M. W. Brown, Eds., American Society for Testing and Materials, Philadelphia, 1985, pp. 135–152.

ABSTRACT: Fatigue crack growth rates have been measured in different biaxial stress fields for a variety of stress ranges at two temperatures. It is shown that a negative *T*-stress accelerates the crack propagation, the increase in growth rate being greater for high stresses. Different methods of determining plastic zone size are compared, and a crack growth correlation with crack-tip plasticity is proposed for remote loads not greater than the yield stress.

KEY WORDS: biaxial stresses, crack propagation, fatigue (materials), plastic deformation, stress intensity, stainless steels

Nomenclature

a	Crack length
c	Crack plus plastic zone size
C,m	Constants
E	Young's modulus
K	Stress intensity factor
N	Number of cycles
r	Distance from crack tip
R	K_{min}/K_{max}
T	T-stress
W^*	Specimen width for K-calibration
γ_{max}	Maximum shear strain amplitude
$\Delta\sigma$	Range of stress
ϵ_n	Normal strain amplitude to maximum shear plane
θ	Polar coordinate
Λ	Biaxial stress ratio

[1]Senior research fellow and professor, respectively, Department of Mechanical Engineering, University of Sheffield, Sheffield, U.K.

Copyright© 1985 by ASTM International www.astm.org

ν	Poisson's ratio
σ	Stress

Subscripts

f,o	Final and initial values
p	Plastic
u	Ultimate tensile strength
x,y,z	Cartesian coordinates
ys	Yield stress
1	Value for $\Lambda = 1$

Since the introduction of linear elastic fracture mechanics (LEFM) many studies of fatigue crack propagation have invariably demonstrated that the rate of growth of cracks is controlled by the crack-tip stress intensity factor. Although there may be differences between materials in their sensitivity to mean stress, which is characterized by the ratio $R = K_{min}/K_{max}$, the use of fracture mechanics equations has led to a wide acceptance of the LEFM approach in all situations involving nominally elastic loading, for example, the power law relationship due to Paris

$$da/dN = C(\Delta K)^n \quad (1)$$

relating crack growth rate to range of stress intensity factor.

The Paris law has been developed from empirical considerations, together with the knowledge that the stress intensity factors describe adequately the stress conditions at the tip of a crack. However, the experimental results supporting this approach have been obtained almost exclusively from uniaxial loading situations, and to ensure that true LEFM conditions exist, stresses have been well below yield stress. An important prediction of the Paris equation is that only the stresses which contribute to the crack tip singularity can affect fatigue crack growth. This has been upheld in later biaxial studies, but only where long cracks and low stress levels have been used to ensure that the LEFM conditions are strictly maintained.

However, when stresses are increased, particularly for the short crack growth regime, marked deviations from LEFM predictions have been found. A number of studies of Mode I fatigue crack propagation have been conducted in recent years for biaxial stress conditions, and these have been reviewed elsewhere [*1,2*].

Unfortunately the results are in conflict, a fact which does not appear to be related solely to the different properties of the various materials studied. A compressive stress parallel to the plane of the crack has been shown to increase, to decrease, and to leave unaffected the rate of growth of cracks in carbon steels [*3*]. Reasons for such discrepancies are difficult to ascertain when comparing results from different laboratories; nevertheless, the foregoing effect of stress range on the magnitude of the biaxial influence is apparent. The importance of plasticity is also underlined by low-cycle fatigue studies, which show a far greater dependence of strength on multiaxial strain state compared to crack propagation tests.

An investigation of biaxial Mode I fatigue crack growth, therefore, has been conducted over a wide range of cyclic loads to examine the dependence on stress range, at both room and elevated temperature. The results emphasize the importance of plasticity to fatigue crack growth, showing a distinct correlation between crack-tip plastic zone size and propagation rate.

Biaxial Test System

A servohydraulic biaxial test facility has been developed for fatigue and creep crack growth studies. Tensile or compressive loads may be applied to each pair of arms of a cruciform specimen (Fig. 1), developing a biaxial stress field in the working section. The loads are controlled such that equal forces are produced on opposing arms. Crack propagation may be observed in the uniform thickness portion of the plate, with growth initiated at a central slot formed by spark erosion. A five zone heater enables elevated temperature testing, giving a uniform temperature distribution over the specimen and avoiding thermally induced stresses [*4*].

The specimen depicted in Fig. 1 is complex and expensive to produce, but it is designed to ensure that a constant, controlled biaxial stress field can be maintained over a wide range of crack lengths. The array of slots machined along each edge of the working area serves two purposes. First, they allow a uniform distribution of applied stress along the edge, as each "finger" experiences the same extension (or compression) under tensile (or compressive) load. Second, they eliminate cross sensitivity between the two axes, because, as the load is

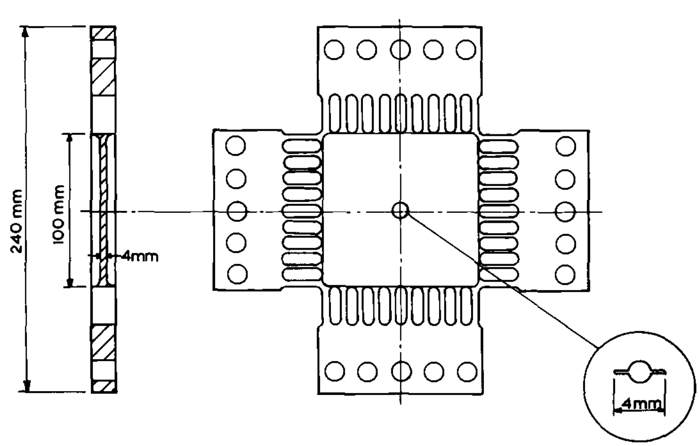

FIG. 1—*Cruciform specimen geometry.*

applied along one axis deforming the gage area, the individual fingers on the other loading axis are able to flex freely, thereby allowing the gage section to deform without restraint along the edges. Since the edge constraint is small, a uniform distribution of strain is readily obtained over the working section of uncracked specimens from the separate loads applied to each axis, irrespective of their sense. The elastic strain distribution was observed in a photoelastic study, verifying both the uniformity of strain and the bending behavior of the fingers. This was subsequently checked by a finite-element analysis, revealing a stress variation of 2% over the central 70% of the working section for equibiaxial loading, and 5% deviation at the base of the fillet radius.

The applied stress was determined from applied load for each axis, divided by the cross-section area of the working region (421 mm^2), assuming that a negligible proportion of the load was required to bend the fingers of the second axis. This procedure was verified by the finite-element analysis, indicating better than 1% accuracy for the stress on the central axis of the specimen.

Strains were measured with a biaxial extensometer enabling one strain controlled test to be conducted. All other tests were under load control with a sinusoidal waveform. Mode I crack extension was monitored using a d-c potential drop technique, although the room-temperature tests were checked using a traveling microscope. Crack growth rates were determined by a least squares fit of a parabola to groups of five crack length readings, differentiated to give the extension per cycle according to ASTM Test Method for Constant-Load-Amplitude Fatigue Crack Growth Rates Above 10^{-8} m/Cycle (E 647-83).

Specimen Material and Test Conditions

All tests were conducted on AISI 316 austenitic stainless steel, taken from two different heats. The composition and tensile properties are given in Table 1. Both heats were solution annealed, although Material A showed a higher yield stress probably due to a number of small size grains remaining in the plate. The

TABLE 1—*Chemical Composition and Mechanical Properties.*

Material	C	Mn	P	S	Si	Cr	Ni	Mo
A	0.06	1.88	0.023	0.020	0.62	17.30	13.40	2.34
B	0.049	1.36	0.023	0.018	0.54	17.26	11.20	2.15

Material	Temperature, °C	0.2% Proof Stress, MPa	Tensile Strength, MPa	Elongation, %	Reduction in area, %
A	20	395	611	55	71
	550	268	489	39	54
B	20	243	597	68	71
	550	133	474	44	55

tensile tests at 550°C for both materials showed marked serrated flow at a strain rate of $10^{-4}s^{-1}$.

Three stress states were examined, equibiaxial ($\Lambda = +1$), uniaxial ($\Lambda = 0$) and pure shear ($\Lambda = -1$), where $\Lambda = \sigma_x/\sigma_y$ is a measure of biaxiality, σ_y being normal to the crack plane. Loading was proportional, the value of Λ being held constant throughout the load controlled cycle. Stresses were chosen to cover the full range from threshold (corresponding to the 2 mm initial crack) up to the yield stress. Cyclic hardening was observed at the start of the tests above the yield point. An R ratio of -1 was chosen to avoid ratchetting, except at the lowest stress level where zero to tension cycling was employed to reduce crack closure effects in measuring threshold. Frequencies were 1 Hz at high-stress levels and 20 Hz for threshold tests.

Results

The crack growth results are presented in Figs. 2 to 6 in terms of crack growth rate plotted against ΔK, where

$$\Delta K = \Delta\sigma \sqrt{(\pi a \sec (\pi a/W^*))} \tag{2}$$

Here $\Delta\sigma$ is the stress range normal to the crack, including the compressive portion. The term W^* ($= 101.9$ mm) is the equivalent width of the specimen (nominally 100 mm) which allows for the stiffening of the edges, see Appendix. Equation 2 is used only as a convenient parameter in plotting the results at the highest stresses, even though LEFM is strictly not applicable, since it provides a suitable correction factor for the effects of finite plate width. As each figure corresponds to a fixed stress range $\Delta\sigma$ normal to the crack plane, the results show relative crack growth rates for different biaxialities corresponding to each crack length a, given by Eq 2.

Figure 2 shows crack growth from threshold, defined here as a growth rate of 0.1 nm/cycle. Although there is a small variation in the threshold values, this is probably within experimental error, disguising any influence of stress state on the threshold. These thresholds are for growth from an initial crack of root radius 0.08 mm, giving higher values than might be expected from a sharper crack [5]. A slightly higher crack growth rate is observed in shear loading, the results obeying the Paris law with $m = 2$.

Figure 3 presents similar data to Fig. 2, but for $R = -1$ and with stress range increased by a factor of 3. The shear cracks clearly propagate more rapidly than in the equibiaxial case. The anomalous uniaxial points for low ΔK correspond to nonsymmetrical growth early in the test where only one fatigue crack was growing from the notch. Below 10 nm/cycle the shear and equibiaxial tests give $m = 2$, rising to 3.5 above 10 nm/cycle.

Figure 4 shows the effect of doubling the stress range, giving a very clear effect of biaxial stress state on fatigue crack growth. Here the Paris law exponent

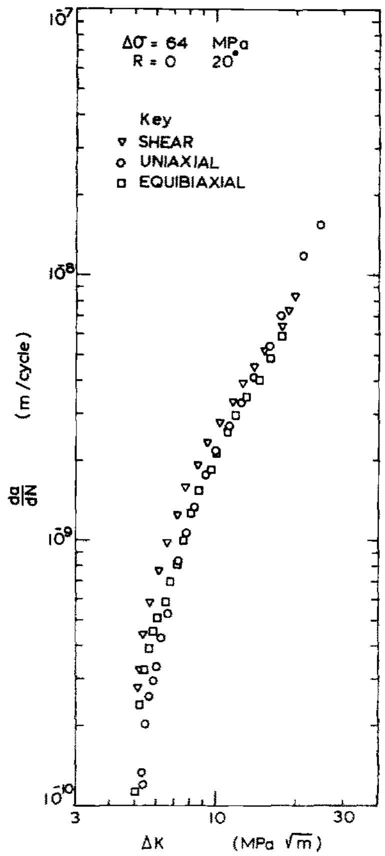

FIG. 2—*Fatigue crack growth close to threshold* (R = 0) *for Material A at 20°C.*

is approximately 2.8, increasing sharply when ΔK exceeds 100 MPa $\sqrt{m}$. Also included in this figure is a shear test conducted under strain control, giving very much lower propagation rates. The strain range $\Delta\epsilon$ of 0.25% was chosen to give the same initial stress range as the load controlled tests. The shear tests are of note because both at this stress level and in the elevated temperature tests two pairs of cracks were produced. The first pair formed at the initial slot in the expected manner, following the Mode I direction closely along the horizontal plane. However, a pair of vertical cracks also nucleated at the initial notch, growing at a similar rate to the horizontal cracks since they experienced a similar stress field with $\Lambda = -1$.

Figures 5 and 6 show elevated temperature results, both at 550°C, but for the two different materials. The clear biaxial effect of faster growth when Λ is negative is again observed. However, the slope of the power law equation, m, has reduced to about 1, increasing sharply to $m = 6$ at about 33 MPa$\sqrt{m}$ for

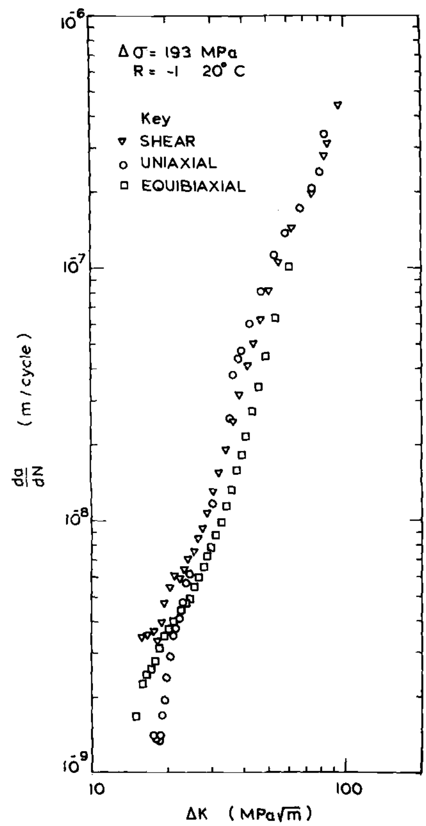

FIG. 3—*Biaxial fatigue crack growth for $\Delta\sigma$ = 193 MPa for Material A at 20°C.*

Material B, 48 MPa$\sqrt{m}$ for Material A. This change in slope corresponds with a transition to slant mode growth, introducing a Mode III component at the crack tip. Similar changes in slope have been observed particularly in Type 316 stainless steel [*6,7*], related to the influence of thermal aging. The low value for *m* of unity reflects the steadily increasing resistance of the material to fatigue crack growth as cyclic aging proceeds at this temperature, strengthening the microstructure ahead of the crack tip [*8,9*]. As Mode I growth becomes difficult, Mode III is favored, and the cracks turns to a slant mode, leading rapidly to failure.

Crack-Tip Plasticity and Crack Growth Rate

At low stresses with very small-scale yielding, crack-tip plasticity is very limited, and plastic zone size is governed by the stress intensity factor, irrespective of biaxiality. But at higher stresses, above the very small-scale yield

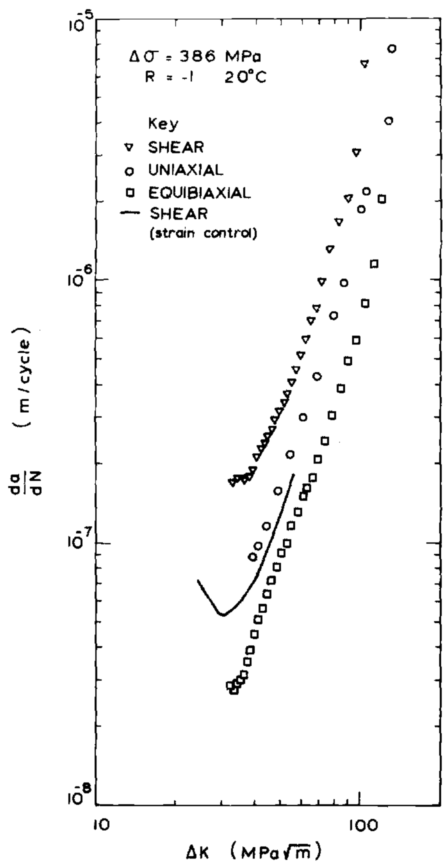

FIG. 4—*Biaxial fatigue crack growth for* $\Delta\sigma$ = *386 MPa for Material A at 20°C.*

regime, larger plastic zone sizes are found for shear loading compared to uniaxial [*10,11*]. For small-scale yielding, the plastic zone size may be estimated from the elastic stress distribution, but it is important to include the second term in the series expansion of σ_{xx}, the stress parallel to the plane of crack, as follows

$$\sigma_{yy} = \frac{K_I}{\sqrt{2\pi r}} \cos\frac{\theta}{2}\left(1 + \sin\frac{\theta}{2}\sin\frac{3\theta}{2}\right) + 0(r^{1/2})$$

$$\sigma_{xx} = \frac{K_I}{\sqrt{2\pi r}} \cos\frac{\theta}{2}\left(1 - \sin\frac{\theta}{2}\sin\frac{3\theta}{2}\right) + (\Lambda - 1)\sigma + 0(r^{1/2}) \qquad (3)$$

$$\tau_{xy} = \frac{K_I}{\sqrt{2\pi r}} \left(\sin\frac{\theta}{2}\cos\frac{\theta}{2}\cos\frac{3\theta}{2}\right) + 0(r^{1/2})$$

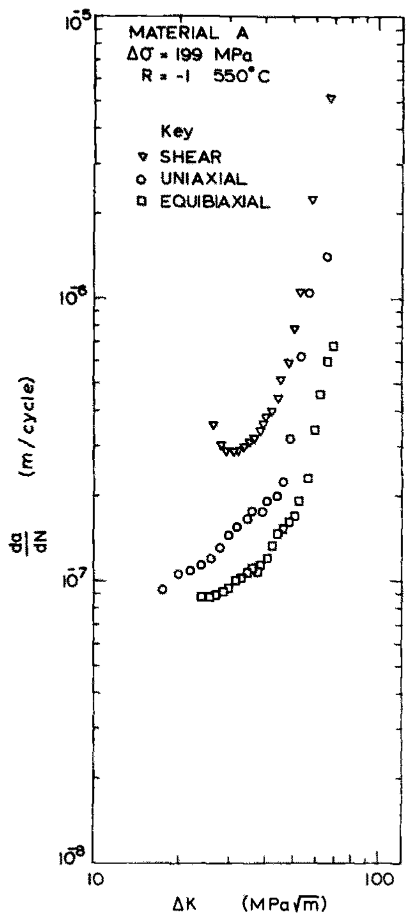

FIG. 5—*Elevated temperature crack growth for Material A at 550°C.*

where $K_I = \sigma\sqrt{\pi a}$ and σ is the stress normal to the crack of length a. The term $(\Lambda - 1)\sigma$ is frequently called the T-stress, and it is clearly determined in biaxial stress tests by the load applied parallel to the crack. Since the stress $(\Lambda\sigma)$ is parallel to the crack, it contributes nothing to the crack tip singularity, defined by the initial terms in Eq 3; therefore, K_I takes the usual form of $\sigma\sqrt{\pi a}$, for a wide center cracked panel.

By using the von Mises yield criterion with the stresses in Eq 3, and neglecting terms of order $r^{1/2}$ and above, a quadratic equation for plastic zone radius r_p in terms of θ is derived for the plane stress case. For plane strain an additional stress

$$\sigma_{zz} = \nu(\sigma_{xx} + \sigma_{yy}) \tag{4}$$

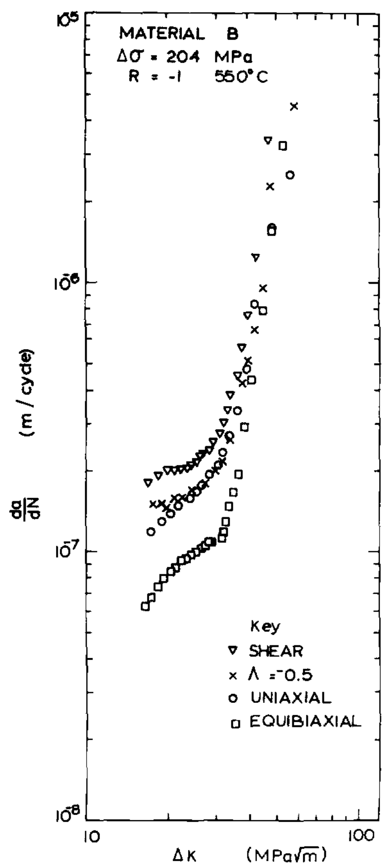

FIG. 6—*Elevated temperature crack growth for Material B at 550°C.*

is required for the yield criterion. The quadratic may be solved for r_p, choosing θ to give the maximum value for plastic zone size. For plane stress θ is always close to 71° for the K-values covered by the tests, but for plane strain θ reduces from a maximum value of 87 to 71° as K is increased. Values for reversed plastic zone sizes are given in Table 2, showing that as Λ decreases, plasticity is more widespread. To obtain the reversed plastic zone size, observed in cyclic loading, ΔK was used in Eq 3 for K, and twice the monotonic yield stress was used in the yield criterion, following the suggestion of Rice [*12*], assuming that a kinematic hardening rule is applicable. In view of the high degree of cyclic hardening found in austenitic stainless steels, the monotonic yield stress may appear to be too low for cyclic conditions, giving an overestimate of plastic zone size. However, the error will offset to some extent by the use of the elastic stress distribution to define r_p, which always gives a lower bound value because equilibrium will not be strictly satisfied with an elastic-plastic stress-strain law.

TABLE 2—*Crack growth rates and plastic zone sizes.*

Material	A		A		A		A		B	
Temperature, °C	20		20		20		550		550	
$2Y$, MPa	790		790		790		536		266	
$2\sigma_u$, MPa	1222		1222		1222		978		948	
$\Delta\sigma$, MPa	64		193		386		199		204	
ΔK, MPa$\sqrt{m}$	10.0		32.2		52.5		32.5		25.5	
da/dN_1, nm/cycle	2		10		100		100		100	
Λ	0	−1	0	−1	0	−1	0	−1	0	−1
$(da/dN)/(da/dN_1)$	1.03	1.28	1.63	1.63	1.95	3.70	1.55	2.90	1.68	2.18
r_p/a plane stress	0.005	0.005	0.048	0.068	0.272	22.6	0.129	0.344	1.66	GY[a]
r_p/r_{p1} plane stress	1.05	1.11	1.20	1.71	1.71	142	1.40	3.75	4.24	∞
r_p/a plane strain	0.003	0.003	0.035	0.060	0.242	3.55	0.105	0.344	1.66	GY
r_p/r_{p1} plane strain	1.11	1.24	1.42	2.43	2.43	35.8	1.83	6.00	6.76	∞
r_p/a DBCS	0.009	0.010	0.110	0.195	1.50	GY	0.388	9.80	GY	GY
r_p/r_{p1} DBCS	1.09	1.21	1.40	2.49	3.86	∞	1.96	49.5	∞	∞
r_p/a Eq 11	0.004	0.004	0.038	0.050	0.226	0.724	0.069	0.103	0.080	0.124
r_p/r_{p1} Eq 11	1.06	1.12	1.21	1.57	1.65	5.28	1.30	1.94	1.33	2.07

[a]GY = general yield.

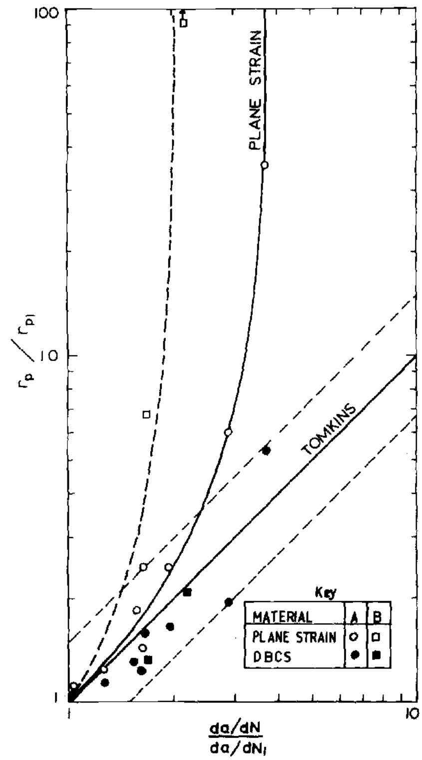

FIG. 7—*Normalized biaxial crack growth rate as a function of plastic zone size.* da/dN_l *and* r_{pl} *refer to the equibiaxial test.*

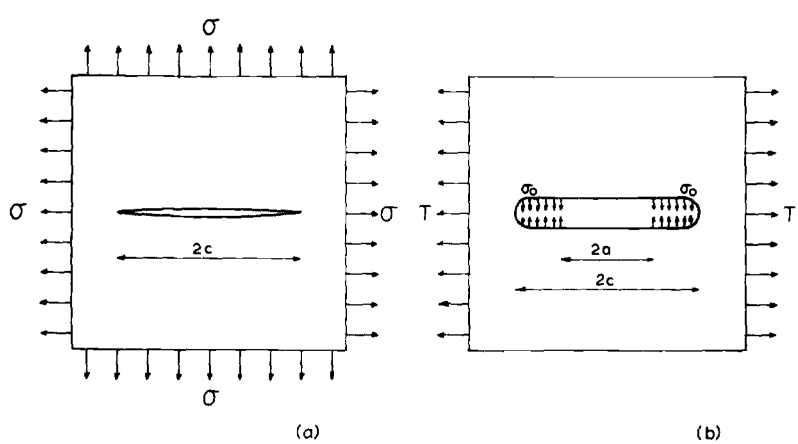

FIG. 8—*Elastic crack loading for DBCS analysis.*

The increase in plastic zone size with biaxiality Λ, defined as (r_p/r_{p1}) where r_{p1} corresponds to equibiaxial loading ($\Lambda = 1$), is compared with the increase in crack growth rate in Table 2, showing a fair correlation at the lower stress levels. However, as the applied stresses become close to the yield stress, the plastic zone size becomes infinite, corresponding to general yield, and the correlation breaks down. The plane-strain results are plotted in Fig. 7 showing this trend, and also showing the difference between the two materials tested. The normalization of r_p and da/dN with the equibiaxial values has a distinct advantage in that crack closure has no effect on the curves in Fig. 7, if closure stress is a function of the applied stress σ.

Another estimate for plastic zone size can be made from the Dugdale Bilby Cottrell Swinden (DBCS) model [13,14]. Dugdale divided the stresses applied to a crack into two components, sketched in Fig. 8. For a crack of length $2a$, a notional crack $2c$ was defined to include two strip yield plastic zones. For the elastic loading of Fig. 8*a*, Westergaard [15] has provided an elastic solution for a crack in an infinite plate under equibiaxial stress, giving

$$K = \sigma\sqrt{\pi c} \tag{5}$$

It is a feature of the Westergaard solution that along the faces of the crack, σ_{xx}, σ_{yy}, and τ_{xy} are all zero. For the open crack in Fig. 8*b* the stress intensity factor for the stress σ_o alone is

$$K = 2\sigma_o\sqrt{c/\pi}\,\cos^{-1}\left(\frac{a}{c}\right) \tag{6}$$

Dugdale equated σ_o to the yield stress, σ_{ys} and superposing these two solutions, he made K equal to zero to ensure that yield stress was not exceeded outside the plastic zone, by elimination of the singularity. This gave a plastic zone size

$$r_p = c - a = a\left(\sec\left(\frac{\pi\sigma}{2\sigma_{ys}}\right) - 1\right) \tag{7}$$

The Dugdale solution may be extended to biaxial loading of a Mode I crack by adding the T-stress in Fig. 8*b*, as shown. Clearly the T-stress does not affect the crack-tip singularity, so Eq 6 remains unchanged. However, along the crack face $\sigma_{xx} = T$ and $\sigma_{yy} = \sigma_o$ where the cohesive stresses are applied. It is no longer possible to equate σ_o to σ_{ys}, but rather using the von Mises yield criterion for plane-stress conditions

$$\sqrt{\{(\sigma_o - T)^2 + \sigma_o^2 + T^2\}} = \sqrt{2}\,\sigma_{ys}$$

whence

$$\sigma_o = \frac{1}{2}\left(T \pm \sqrt{(4\sigma_{ys}^2 - 3T^2)}\right) \tag{9}$$

If $\sigma > 0$, we take the positive sign in Eq 9, and for $\sigma < 0$, we take the negative sign, since σ_o and σ have the same sign. Replacing σ_{ys} by σ_o in Eq 7, the plastic zone size is given by

$$r_p = a\left(\sec\left(\frac{\pi}{(\Lambda - 1) + \sqrt{(4\sigma_{ys}^2/\sigma^2 - 3(\Lambda - 1)^2)}}\right) - 1\right) \quad (10)$$

where $T = (\Lambda - 1)\sigma$. Clearly the plastic zone size depends not only on (σ/σ_{ys}) as in Eq 7, but also on $(\Lambda - 1)$. Values of r_p for the modified DBCS model are also given in Table 2, replacing σ by $\Delta\sigma$ and σ_{ys} by $2\sigma_{ys}$ as previously shown. Note that Eq 10, which is very much easier to solve than the preceding numerical solution for plane-strain plastic zone size, gives similar results for (r_p/r_{p1}). The values of (r_p/a) are higher, however, because the DBCS solution is an elastic plastic solution that does satisfy equilibrium conditions.

When attempting to correlate fatigue crack growth rate with plastic zone size, it is inevitable that plastic zone size will become infinite as the applied loads approach yield conditions. However finite crack growth rates are still obtained, as can be observed in low-cycle fatigue tests. This problem was overcome by Tomkins [*16*], who replaced σ_{ys} in Eq 7 by the tensile strength, σ_u, assuming that σ_u was a better estimate of the cyclic flow stress near the crack.

Since the Tomkins crack growth equation has found wide applicability, the same approach has been tried here for comparative purposes. The results are plotted in Fig. 7, showing that the predicted crack growth rates fall into line with the experimental ones, even when general yield occurred for material B in the shear test. Therefore, within the limits of scatter $\pm(\times 1.5)$ crack growth rate may be related to the equibiaxial value da/dN_1 by

$$\frac{da/dN}{da/dN_1} = \frac{\sec\{\pi/[\sqrt{((4\sigma_u/\Delta\sigma)^2 - 3(\Lambda - 1)^2)} + (\Lambda - 1)]\} - 1}{\sec(\pi\Delta\sigma/4\sigma_u) - 1} \quad (11)$$

This is at best only an empirical formula since replacing σ_{ys} by σ_u in Eq 10 contravenes the condition of elastic deformation outside the strip yield zone in the preceding derivation. Its usefulness lies in (*a*) the ability of the Tomkins' crack growth equation to predict low-cycle fatigue behavior and (*b*) the correlation of multiaxial fatigue test data.

Discussion

The results have shown that the application of a negative T-stress increases fatigue crack propagation rates, but, for $\Delta\sigma << 2\sigma_{ys}$, this increase will be negligible. This is in broad agreement with the effect of stress range discussed in the introduction, and it also implies that in some studies where the crack growth showed no dependence on biaxiality the stresses may have been low. However, there are still a few reports of reduced growth rates in shear loading which are incompatible with Eq 11. The strain controlled test result was included in Fig. 4 to show that very different results can arise. This highlights the importance of specimen design [*4*], which must ensure not only that the calculated stress field is correct, but also that it will be maintained (*a*) as the crack extends, and (*b*) as plasticity becomes apparent. Elastic stress calculations can be only used for small-scale yielding situations. As plasticity spreads, residual stress fields may be set up in the working area of the specimen if it is contrained by rigid loading arms or grips operating at a lower stress. It is therefore suggested that the results showing a beneficial effect of a negative *T*-stress may be due to geometry effects, associated with the particular specimen design and stress measurement technique.

The improved correlation of results with Eq 11 compared to true plastic zone size suggests that plastic zone size itself is not the important parameter, but rather the intensification of strain around the tip of an advancing fatigue crack. Strain hardening will clearly play an important role inside the plastic zone, particularly above general yield, and so the concept of a severe-strain zone [*17*] rather than a plastic zone was proposed, related to the plastic stress singularity rather than yield conditions far from the crack tip. In replacing σ_{ys} by tensile strength σ_u in Eq 11, some kind of instability zone is apparently being defined, since tensile strength is related to instability of plastic deformation. This zone, within which plastic deformation is not constrained by strain hardening, appears to be more closely related to severe-strain zone size than plastic zone size.

Taking the crack growth equation developed in Ref *17* and assuming that Eq 10 with $\sigma_{ys} = \sigma_u$ represents severe strain zone size, we find

$$da/dN = 18\,(\sigma_u/E)^2\,a \times \frac{1}{2}\left[\frac{\pi}{\Lambda - 1 + \sqrt{16(\sigma_u/\Delta\sigma)^2 - 3(\Lambda - 1)^2}}\right]^2 \qquad (12)$$

using only the first two terms for the secant series expansion. Equation 12 may be integrated between initial and final crack lengths, a_o and a_f, to determine crack propagation life, N_p. Thus for elastic loading

$$\left(\frac{1}{2}\gamma_{max}\right)^2 [D^2 + 2D\,(1 - \Lambda) + 4(1 - \Lambda)^2] = \left[\frac{\sigma_u}{E}\,(1 + v)\,(1 - \Lambda)^x\right]^2$$

and

$$D = 3\pi\left(\frac{\sigma_u}{E}\right)\sqrt{\left(N_p/\ln\left(\frac{a_f}{a_o}\right)\right)} \qquad (13)$$

$x = 0$ for Case B, 1 for Case A. This is a relationship that defines Γ-plane contours, described elsewhere in this publication [8], because for Case B [18],

$$\frac{2\epsilon_n}{\gamma_{max}} = (1 - \nu - 2\nu\Lambda)/(1 + \nu) \qquad \Lambda > 0 \tag{14}$$

and for Case A

$$\frac{2\epsilon_n}{\gamma_{max}} = (1 + \Lambda)(1 - \nu)/((1 - \Lambda)(1 + \nu)) \qquad \Lambda < 0 \tag{15}$$

The Γ-plane is a graph with axes $\frac{1}{2}\gamma_{max}$ and ϵ_n, the shear and normal strains on the plane experiencing maximum shear deformation, on which contours of constant endurance may be plotted.

Since a slope m of 2 was found in Fig. 2, stainless steel can be represented by Eq 12, which predicts $C = 4.4 \times 10^{-11}$ in the Paris equation, compared to 2.2×10^{-11} in Fig. 2. The Γ-plane for N_p of 10^6 cycles is plotted in Fig. 9, showing the familiar shape observed in multiaxial fatigue tests [19].

Equation 13 also provides a useful prediction for Case B behavior, which is difficult to obtain experimentally. However, the equation should not be used for shear strain $\frac{1}{2}\gamma_{max}$ in excess of yield, as the DBCS formula breaks down with general strain hardening far from the crack tip. Secondly, N_p does not include initiation cycles, which will be a significant proportion of life at these low-strain amplitudes, making Eq 13 conservative in estimating total endurance. No account has been taken of crack shape factors or growth direction. Thumbnail cracks develop in smooth specimen multiaxial tests, which imply a dimensionless geometry correction factor for Eq 12.

A similar dependence of crack growth rate on the T-stress through plastic zone size has been observed by Gao et al [20], for small-scale yield conditions and

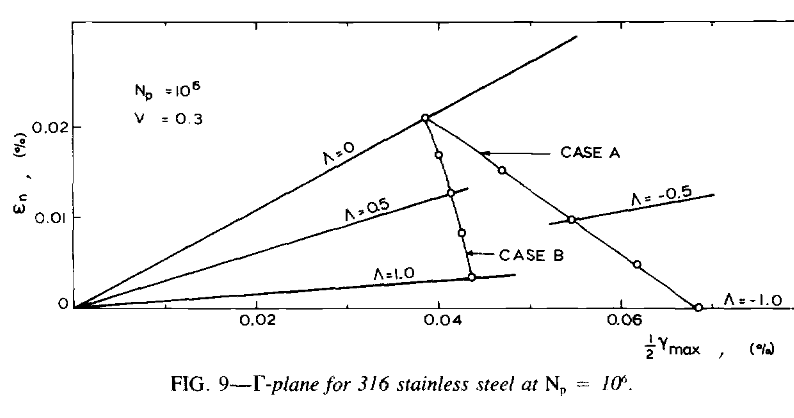

FIG. 9—Γ-plane for 316 stainless steel at $N_p = 10^6$.

mixed-mode loading. Thus endurance predictions on these lines may be extended to shear mode or Stage I cracking situations.

Conclusions

1. Biaxial fatigue crack propagation tests have shown that Mode I cracks are accelerated by a negative T-stress in 316 stainless steel, the magnitude of this effect depending on the stress amplitudes.
2. In biaxial fatigue, there is a correlation between reversed plastic zone size and crack growth rate.
3. A crack growth equation is proposed, based on the crack tip severe-strain zone size, from which high-cycle fatigue life predictions can be made.

Acknowledgments

The authors are grateful to the United States Nuclear Regulatory Commission and the Science and Engineering Research Council for their support, and to Oak Ridge National Laboratory and the Electric Power Research Institute for supplying the materials. Dr. M. W. Brown is a Central Electricity Generating Board Research Fellow.

APPENDIX

Estimation of Stress Intensity Factors

It was shown previously that in the absence of a crack, the stress in the gage section is substantially uniform across the width, and that a negligible proportion of the load in the x-direction is transmitted by bending of the "fingers" on the y-axis (less than 2%). Since there is virtually no cross sensitivity of stress between the x- and y-axes of this particular specimen geometry, the specimen is equivalent to a center-cracked panel, and the K calibration for a Mode I crack of length $2a$ is given in ASTM Method E 647 as

$$K = \sigma\sqrt{[\pi a \sec (\pi a/W)]} \tag{16}$$

for a specimen of width W, where $W = 100$ mm.

The geometry factor should be adjusted to account for (a) the fillet radius at the edge of the specimen and (b) the finite height of the specimen. Since the correction is small in both cases, this may be achieved conveniently by altering the value of W to W^*, giving Eq 2.

The fillet radius at the edge of the specimen stiffens the edge, and solutions have been provided by Isida [*21*]. The stiffening is equivalent to putting $W = (421/4)$ mm in Eq 16, for $a/W \leq 0.7$, that is, increasing the specimen width in proportion to the cross-section area.

The finite height of center cracked panels has been studied by Isida [*22*], for conditions of (a) uniform stress along the top edge and (b) uniform displacement without transverse shear restraint. This specimen exhibits boundary conditions lying between (a) and (b), (a) being applicable for compliant fingers and (b) being applicable for axially stiff fingers. The K-calibration for the cruciform specimen was determined by a weighted average of

Isida's solutions (*a*) and (*b*) with respect to the compliance of the central section and the compliance of the fingers.

Finally the two solutions were combined to give an overall *K*-calibration, which was characterized adequately by Eq 2 with $W^* = 101.9$ mm. In view of the assumptions made in the derivation, the accuracy should be better than 3% for $a/W \leq 0.7$.

References

[*1*] Charvat, I. M. I. and Garrett, G. G., *Journal of Testing and Evaluation*, Vol. 8, 1980, pp. 9–17.

[*2*] Smith, E. W. and Pascoe, K. J., *Fatigue of Engineering Materials and Structures*, Vol. 6, No. 3, 1983, pp. 201–224.

[*3*] Brown, M. W. and Miller, K. J. in *Defects and Fracture*, G. C. Sih and H. Zorski, Eds., Martinus Nijhoff, The Hague, 1982, pp. 29–38.

[*4*] Brown, M. W. in *Measurement of High Temperature Mechanical Properties of Materials*, Her Majesty's Stationary Office, London, 1982.

[*5*] Gao Hua, Brown, M. W., and Miller, K. J., *Fatigue of Engineering Materials and Structures*, Vol. 5, No. 1, 1982, pp. 1–17.

[*6*] Shahinian, P., Smith, H. H., and Watson, H. E., *Journal of Engineering for Industry, Transactions*, American Society of Mechanical Engineers, Vol. 93B, 1971, pp. 976–980.

[*7*] James, L. A., *Metallurgical Transactions*, Vol. 5, 1974, pp. 831–838.

[*8*] Kandil, F. A., Brown, M. W., and Miller, K. J., this publication, pp. 651–668.

[*9*] de los Rios, E. R., Kandil, F. A., Brown, M. W., and Miller, K. J., this publication, pp. 669–687.

[*10*] Eftis, J., Subramonian, N., and Liebowitz, H., *Engineering Fracture Mechanics*, Vol. 9, 1977, pp. 189–210.

[*11*] Miller, K. J. and Kfouri, A. P., *International Journal of Fracture*, Vol. 10, 1974, pp. 393–404.

[*12*] Rice, J. R. in *Fatigue Crack Propagation, ASTM STP 415*, American Society for Testing and Materials, Philadelphia, 1967, pp. 247–309.

[*13*] Dugdale, D. S. *Journal of the Mechanics and Physics of Solids*, Vol. 8, 1960, pp. 100–104.

[*14*] Bilby, B. A., Cottrell, A. H., and Swinden, K. H. *Proceedings*, Royal Society, Series A, Vol. 272, 1963, pp. 304–314.

[*15*] Westergaard, H. M., *Journal of Applied Mechanics*, Vol. 6, 1939, pp. 49–53.

[*16*] Tomkins, B., *Philosophical Magazine*, Vol. 18, 1968, pp. 1041–1066.

[*17*] Brown, M. W., Liu, H. W., Kfouri, A. P., and Miller, K. J. in *Advances in Fracture Research*, D. François, Ed., Pergamon, Oxford, 1980, Vol. 2, pp. 891–898.

[*18*] Brown, M. W. in *High Temperature Fatigue*, R. P. Skelton, Ed., Applied Science, London, 1983, pp. 97–113.

[*19*] Brown, M. W. and Miller, K. J., *Proceedings*, Institution of Mechanical Engineers, Vol. 187, 1973, pp. 745–755.

[*20*] Gao, H., Alagok, N. Brown, M. W., and Miller, K. J., this publication, pp. 184–202.

[*21*] Isida, M. in *Mechanics of Fracture, Methods of Analysis, and Solutions of Crack Problems*, G. C. Sih, Ed., Noordhoff International, Leyden, The Hague, 1973, Vol. 1, pp. 56–130.

[*22*] Isida, M., *International Journal of Fracture Mechanics*, Vol. 7, 1971, pp. 301–316.

David Rhodes[1] *and John C. Radon*[2]

Effect of Local Stress Biaxiality on the Behavior of Fatigue Crack Growth Test Specimens

REFERENCE: Rhodes, D. and Radon, J. C., "**Effect of Local Stress Biaxiality on the Behavior of Fatigue Crack Growth Test Specimens,**" *Multiaxial Fatigue, ASTM STP 653*, K. J. Miller and M. W. Brown, Eds., American Society For Testing and Materials, Philadelphia, 1985, pp. 153–163.

ABSTRACT: Fatigue crack growth rates have been measured for aluminium alloys, using compact type (CT) specimens, and the results compared with published data from the same materials, obtained from center-cracked tension (CCT) specimens. There is a general trend for CCT specimens to exhibit higher crack growth rates, even at identical stress intensity factor ranges. This result is explained in terms of the difference in the nonsingular component of stress, parallel to the crack faces, which influences both the plastic zone size, and, in the case of very thin specimens, the buckling behavior.

KEY WORDS: stress biaxiality, fatigue, crack growth rate, plastic zone, buckling

There is considerable evidence in the literature to demonstrate that the nonsingular component of stress, parallel to the line of a crack, has an influence on the fatigue crack growth rate, even though it does not influence the stress intensity factor. This has been observed in aluminium alloys [*1*], steels [*2*], and polymers [*3*]. In the selection of standard fatigue crack growth test specimens, this nonsingular component is not normally considered, but it may in fact vary significantly between one specimen geometry and another [*4*]. This stress component influences the crack growth in two ways:

1. The plastic zone size is influenced by the biaxial (or, strictly, triaxial) stress state, and this may be demonstrated to affect the fatigue crack growth rate.
2. Thin specimens may buckle, due to the presence of local compressive stresses, and this may introduce a Mode III (out-of-plane shear) component to the stress intensity factor.

[1]Research engineer, Institut für Werkstofftechnologie, GKSS Firschungszentrum, Geesthacht, West Germany.
[2]Research fellow, Department of Mechanical Engineering, Imperial College, London, U.K.

Copyright© 1985 by ASTM International www.astm.org

There is an additional effect, in that the crack path stability may be influenced by the biaxial stress state [5]. This does not affect the growth rate, provided that standard procedures are followed in assessing the validity of results from assymmetrically cracked specimens. It may, however, influence specimen design, if steps are to be taken to avoid invalid results. Figure 1 shows the compact type (CT) specimen idealized as three beams. Neglecting the local stress concentration effect of the crack tip and using engineers bending theory as a first approximation, the bending moments in the figure are given by

$$M_1 = P_{yy} \times a \text{ and } M_2 = P_{yy} \frac{W + a}{2} \tag{1}$$

The values of σ_{xx} and σ_{yy} may be estimated [5]. Under an applied tensile load, both σ_{xx} and σ_{yy} are always tensile

$$\sigma_{xx} = 6P_{yy}\, a/BH^2 \tag{2}$$

and

$$\sigma_{yy} = \frac{P_{yy}(2W + a)}{B(W - a)^2} \tag{3}$$

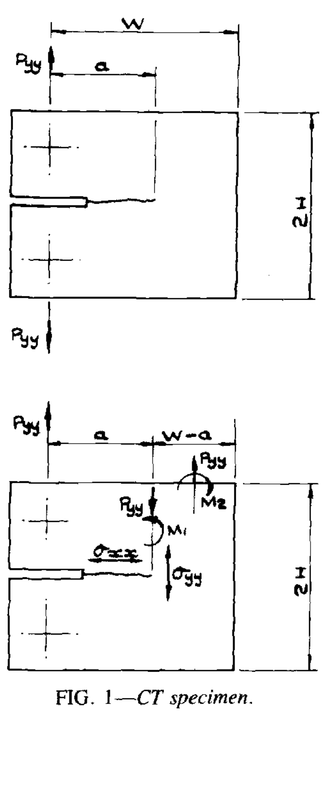

FIG. 1—*CT specimen.*

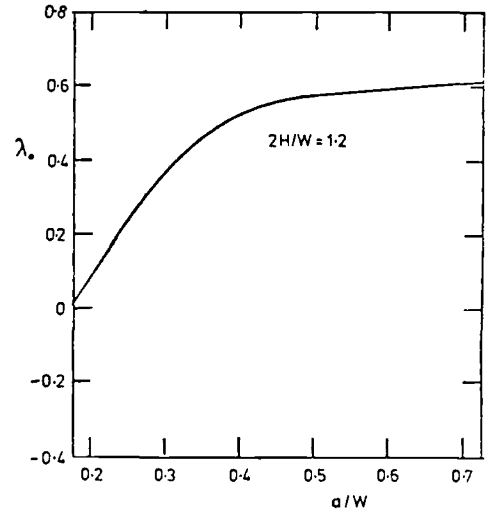

FIG. 2—*Inherent biaxiality factor for CT specimens* [6].

More exact analyses show that the σ_{xx} component decrease to zero at the very tip of the crack, but this simple approximation is still expected to provide a useful insight into the local stress distribution. Leevers [7] has used a computational technique to obtain more reliable values for the "inherent biaxiality ratio," λ_o, defined by

$$\lambda_o \equiv \sigma_{xx}/\sigma_{yy} \text{ when } P_{xx} = 0, P_{yy} > 0 \tag{4}$$

that is, the ratio of nominal stress parallel to, and normal to the crack, when no load is applied other than that normal to the crack faces. Leevers' results are shown in Fig. 2, for ASTM Test Method for Constant-Load-Amplitude Fatigue Crack Growth Rate Above 10^{-8} m/Cycle (E 647-83) compact type specimen, with $2H/W = 1.2$. The value of λ_o increases with crack length, a/W, but decreases with increasing specimen depth, $2H/W$.

For the center crack tension (CCT) specimen, the stress along the crack is compressive, under external tensile loading, and similar in magnitude to the remote tensile stress, that is, $\lambda_o \simeq -1$ [8]. Once again, Leevers' results are shown (Fig. 3).

If an external load, P_{xx}, is applied, parallel to the crack direction, the applied biaxiality ratio, λ_{app}, is defined simply as

$$\lambda_{app} \equiv P_{xx}/P_{yy} \tag{5}$$

The actual biaxiality ratio, λ, is then obtained by simple superposition

$$\lambda \equiv \lambda_{app} + \lambda_o \tag{6}$$

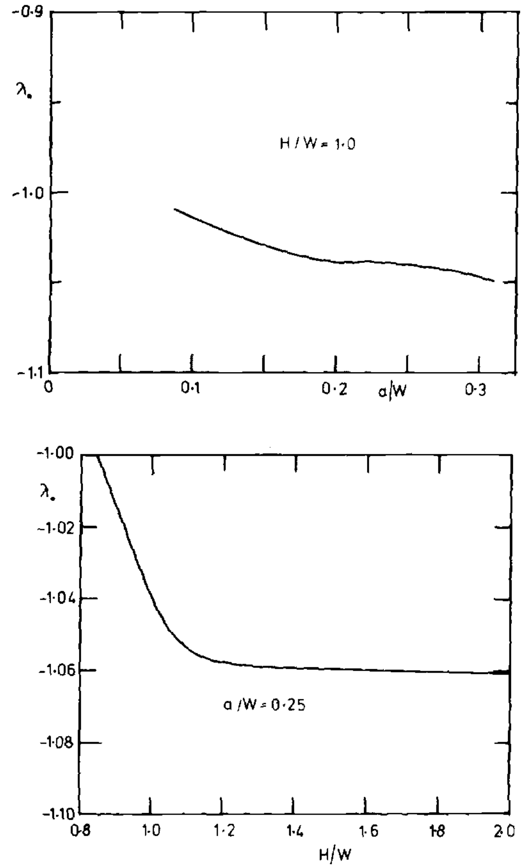

FIG. 3—*Inherent biaxiality factor for CCT specimens* [6].

Testing

Fatigue crack growth tests have been carried out on CT specimens of aluminium alloys 2024-T3 (as clad sheet, to British Standard L109) and 7010-T7X51 (as rolled plate, to U.K. Ministry of Defence standard DTD5120, using an Alcan-Booth proprietary heat treatment [*6*]) of various thicknesses (9 to 11 mm), in particular, tests on 6-mm-thick specimens of the 7010 alloy were carried out on conventional CT specimens [*10*] in a Dowty, 60 kN capacity, servohydraulic fatigue test machine, at a frequency of 10 Hz. The thin, 0.9-mm 2024 specimens were made with the ratio $2H/W = 1.9$, in order to reduce λ_o and thereby avoid any crack path instability problems, to which thin specimens may be more prone [5,*12*]. These specimens were tested between steel face plates, lubricated with molybdenum grease (Fig. 4.). The test frequency was, in this case, 1 Hz.

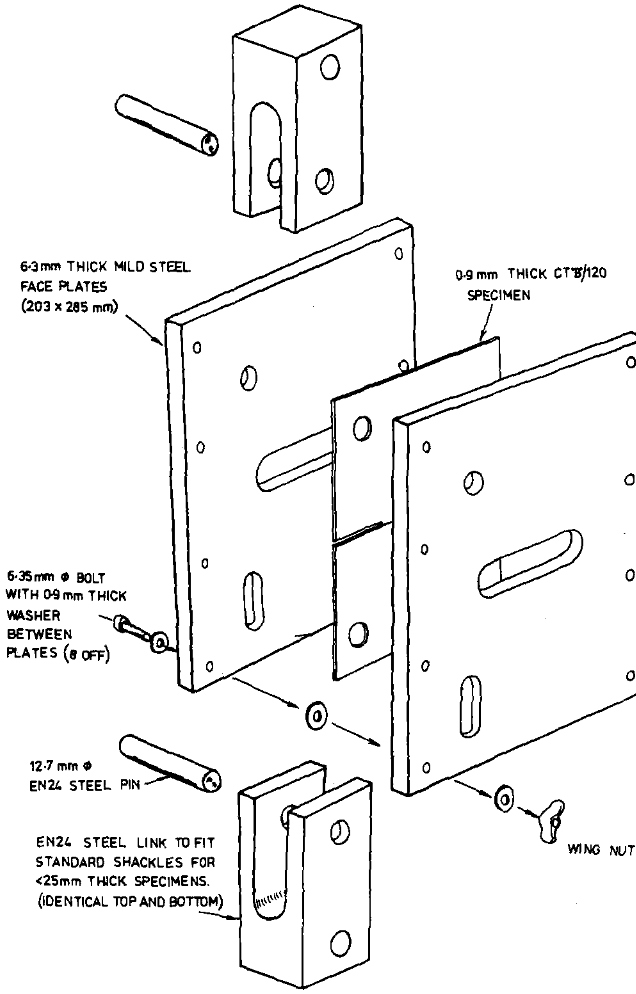

FIG. 4—*Anti-buckling plates for CT B/120 specimens.*

The test results are shown in Figs. 5 and 6, where they are compared with published data on CCT specimens of 6.35-mm (0.25-in.) thick DTD 5120, and various thin sheet clad 2024-T3 specimens, respectively [*6,13*]. Both show that growth rates obtained from CT specimens are around one half of those obtained for CCT specimens, for $da/dN \gtrsim 10^{-4}$ mm/cycle. This difference is less than the scatter for either specimen, but there is a systematic shift in the data.

Discussion

It has been shown both analytically [*14*] and numerically [*15,16*] that the size of the plastic zone decreases with increasing biaxiality factor, λ, at constant

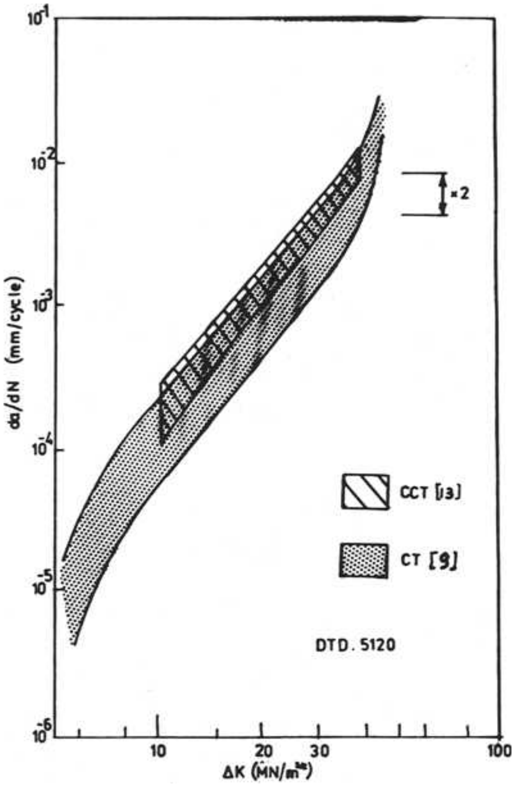

FIG. 5—*Comparison of CT and CCT test results for DTD 5120.*

stress intensity factor, K. At the same time, Rice [*17*] and others have related fatigue crack growth rate to crack-tip opening displacement, which is related, in turn, to plastic zone size. Qualitatively, this provides an explanation for the effect of λ on da/dN. There is, however, one apparent anomaly in this approach: when comparing specimens of different thickness, a change from plane-stress to plane-strain conditions results in a reduction in plastic zone size, but if any change in da/dN is noted, it is an increase, especially in the high growth rate ($da/dN > 10^{-4}$ mm/cycle) regime. As this, too, is a problem relating to multiaxial stress-strain fields—specifically, the effect of constraint in the through thickness direction. It is clear that neither the stress intensity range, nor the plastic zone size, are unambiguous correlating parameters for fatigue crack growth.

In the region of interest, fatigue crack growth in high-strength aluminium alloys occurs by a combination of two processes: alternate blunting and resharpening of the crack tip, and microvoid coalescence [*11*]. This first process results in a crack growth rate which is closely related to the cyclic COD, which may be calculated as

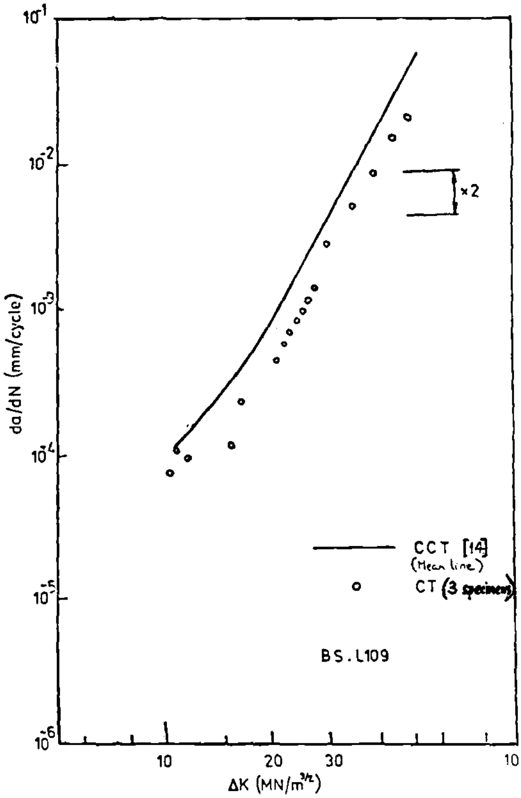

FIG. 6—*Comparison of CT and CCT test results for BS L109.*

$$\frac{da}{dN} \propto \theta \equiv 2 \int_{o}^{\Delta r_p} \Delta\gamma_p \times dr \qquad (7)$$

where $\Delta\gamma_p$ is the plastic shear strain range at a distance, r, from the crack tip. The integration is carried out along the maximum shear plane, and Δr_p, the cyclic plastic zone size, is defined as the value of r such that when $r \geqslant \Delta r_p$, $\Delta\gamma_p = 0$. Notice that elastic components of strain do not contribute to permanent crack extension. Under uniaxial linear-elastic fracture mechanics (LEFM) conditions this is equivalent to Rice's analysis [*17*] for COD, which reduces to

$$\frac{da}{dN} \propto \Delta r_p \propto \Delta K^2 \qquad (7a)$$

The second process, ductile tearing, depends on the total strain applied to material very close to the crack tip. Voids form at inclusions or other microstructural features, and the ligament between the crack front and the void fails by tensile instability ("necking") when the total strain is high enough [10]. The mean spacing of void nucleation sites in commercial aluminium alloys is of the order of 10 μm, so that this mechanism depends on crack-tip strains rather than strains over the entire plastic zone.

Considering the case of a biaxially loaded specimen, under plane stress conditions, from von Mises' criterion, yielding will occur when

$$\sigma_{xx}{}^2 - \sigma_{xx}\sigma_{yy} + \sigma_{yy}{}^2 = \sigma_{yt}{}^2 \tag{8}$$

where σ_{xx} and σ_{yy} are components of the applied stress, and σ_{yt} is the yield stress in uniaxial tension. This may be rearranged to show that yielding occurs when

$$\frac{\sigma_{yy}}{\sigma_{yt}} = \left\{1 - \frac{\sigma_{xx}}{\sigma_{yy}} + \left(\frac{\sigma_{xx}}{\sigma_{yy}}\right)^2\right\}^{-1/2} \tag{9}$$

This function shows the value of σ_{xy}/σ_{yt} at which yielding occurs increases with σ_{xx}/σ_{yy} for all negative, or small positive ratios (Fig. 7). The implication is that the amount of strain which can be accommodated elastically in the y-direction increases as the ratio σ_{xx}/σ_{yy} increases. If the stress intensity factor is specified for a cracked specimen, it is assumed that the distribution of total strains is correspondingly fixed, so that an increase in elastic strain implies a decrease in plastic strain. In the biaxially loaded, plane stress case, σ_{xx} is uniform due to the applied load, P_{xx}, but σ_{yy} varies with $P_{yy}r^{-1/2}$ according to the usual LEFM conditions. Thus the magnitude of σ_{xx}/σ_{yy} increases with r. Close to the tip of the crack, the normal strain is very high, and the component parallel to the crack may not be significant. Further away from the crack tip, the local biaxiality ratio does have a significant effect, resulting in the well-known variation of Δr_p with λ. This affects the crack growth rate by blunting, via equation [7], but has little effect on the tearing process. Correspondingly, crack growth rate is expected, and observed to increase with increasing plastic zone size.

Turning to the effect of specimen thickness, the situation is quite different. Under plane-strain conditions, a component of stress, σ_{zz}, must exist in the "through-the-thickness" direction, to prevent transverse deformation, and this stress must increase as the normal stress increases. Consequently, the σ_{zz} (and σ_{xx}) components of stress must be highest close to the crack tip. Changing to plane stress, crack growth by the blunting process is expected to increase with increasing plastic zone size, but relief of the high degree of triaxial constraint at the crack tip allows, for example, shear lip formation, resulting in an increase in "toughness" and a decrease in crack growth rate due to tearing. Under some circumstances it has been shown [10] that substitution of appropriate monotonic fracture toughness data into a fatigue crack growth equation is sufficient to account for the effect of thickness.

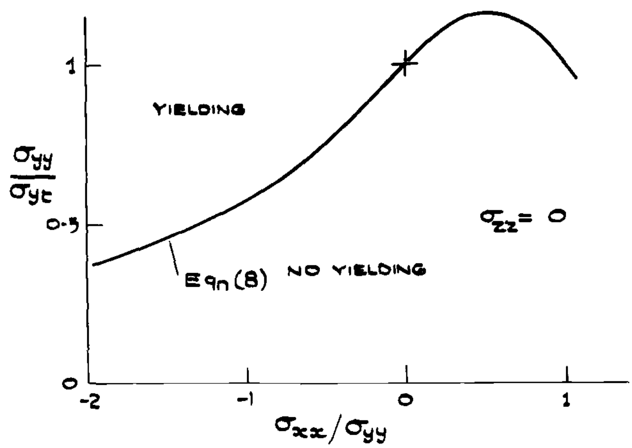

FIG. 7—σ_{yy}/σ_{yt} *versus* σ_{xx}/σ_{yy}.

Buckling Behavior

When thin sheet specimens are tested, nominally in tension, local compressive stresses do occur and may give rise to buckling instability problems. Figure 8 shows CCT and CT specimens. In order to obtain reproducible test results, buckling must be prevented by clamping "face plates" or "anti-buckling" bars over those areas of the specimen. Although this presents no real problems for CT specimens (Fig. 4 and Ref *12*), it is impossible to obtain effective clamping on CCT specimens and yet allow direct observation of the crack [*18*]. The problem is particularly severe with wide specimens, long cracks, and high loads. The CCT data in Fig. 6. was obtained with anti-buckling bars spaced so that the immediate vicinity of the crack tip was unsupported. This could lead to an unwanted K_{III} component, especially at the higher values of ΔK, so that the difference between CT and CCT results is exaggerated.

Comparison of CT and CCT Results

By simple superposition (Eq 6) one would expect a CCT specimen with $\lambda_o = -1$ and $\lambda_{app} = +1$ to exhibit the same crack growth rate for a given value of ΔK, as a CT specimen containing a crack of length $a/W \simeq 0.2$ ($\lambda_o \simeq \lambda_{app} = 0$).

Elastic-plastic finite-element analyses tend to support this view. Kfouri [*19*] has studied the case where $a/W = 0.5$. From Fig. 2 this gives $\lambda \simeq 0.55$. Under these conditions, the plastic zone size for the CT specimen was found by Kfouri to be some 15% smaller than that for a CCT specimen with $\lambda_{app} = +1$.

Hopper and Miller [*1*] showed da/dN decreasing by a factor of about 1.4 when λ_{app} is increased from 0 to +1 at high crack growth rates in CCT specimens of a 2618-T651 alloy. Anstee and Morrow [2] used stiffened panels of thin

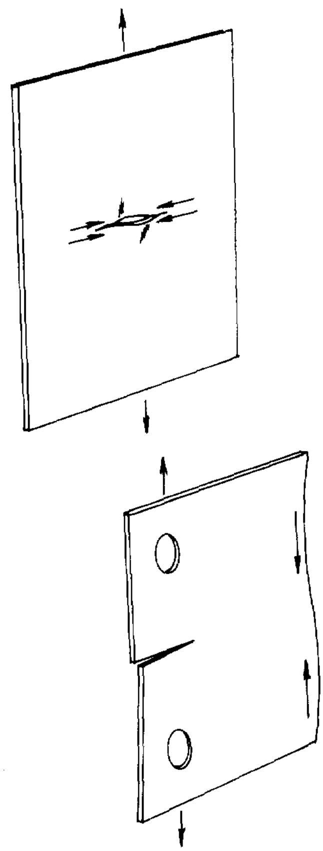

FIG. 8—*Buckling behavior of unsupported CCT and CT specimens.*

sheets of the same alloy and found that the crack propagation life increased 1.5 times when λ_{app} increased from 0 to +0.5, or 2.2 times when λ_{app} increased from 0 to +1. If the difference in results is due to the difference in buckling behavior, one might expect the 6-mm 7010 specimens in the present study to show crack growth rates in CCT specimens around 50% higher than in CT specimens, but in the 0.9 mm 2024 specimens perhaps 100% higher. These estimates are in close agreement with the data of Figs. 5 and 6.

Conclusions

Fatigue crack growth rates obtained from specimens of various geometries may differ if the nonsingular component of stress, parallel to the crack direction differs. The changes in inherent stress biaxiality factor may be compared with changes in applied load biaxiality in tests on one particular type of specimen. Consideration of such tests implies that tests on CCT specimens of aluminium alloys will give growth rates some 50% higher than tests on CT specimens. The difference may be greater where buckling of thin specimens is not fully constrained.

The effect of stress biaxiality on fatigue crack growth rate is explained in terms of the distribution of plastic strain near to the crack tip, and the micromechanisms of crack growth. Neither the stress-intensity factor, nor the plastic-zone size, provide unambiguous one-parameter descriptions of this strain field.

References

[*1*] (a) Hopper, C. D. and Miller, K. J., *Journal of Strain Analysis,* Vol. 12, 1977, pp. 23–28. (b) Anstee, R. F. W. and Morrow, Sarah, M. in *Proceedings,* 10th Symposium of the International Committee on Aircraft Fatigue (ICAF), Brussels, 1979.

[*2*] Kitagawa, H., Yuuki, R., and Tohgo, K., *Fatigue of Engineering Materials Structures,* Vol. 2, 1979, pp. 195–206.

[*3*] Leevers, P. S., Radon, J. C., and Culver, L. E., *Polymer,* Vol. 17, 1976, pp. 627–632.

[*4*] Knott, J. F., *Fundamentals of Fracture Mechanics,* 1973, Butterworth, London, p. 133.

[*5*] Cottrell, B., *International Journal of Fracture Mechanics,* Vol. 6, 1970, pp. 189–192.

[*6*] Reynolds, M. A., Fitzsimmons, P. E., and Harris, J. G. in *Proceedings,* Symposium on Aluminium Alloys for the Aircraft Industry, Turin, 1976, Technicopy, London.

[*7*] Leevers, P. S. and Radon, J. C., *International Journal of Fracture,* Vol. 19, 1982, pp. 311–325.

[*8*] Dixon, J. R. and Strannigan, J. S. in *Fracture 1969,* Chapman and Hall, London, pp. 105–108.

[*9*] Rhodes, D., Radon, J. C., and Culver, L. E., *Fatigue of Engineering Materials and Structures,* Vol. 4, 1981, pp. 49–63.

[*10*] Rhodes, D. and Radon, J. C. in *Fracture Mechanics: Fourteenth Symposium, ASTM STP 791,* American Society for Testing and Materials, Philadelphia, 1983, pp. II-33–II-46.

[*11*] Rhodes, D., Nix, K. J., and Radon, J. C. in *Proceedings,* 4th European Conference on Fracture, Leoben, Austria, 1982, pp. 443–448.

[*12*] Bradshaw, F. J. and Wheeler, C., TR73191, Royal Aircraft Establishment, Farnborough, 1974.

[*13*] ESDU Data Item No. 73021 Amendment C, Engineering Sciences Data Unit, London, 1977.

[*14*] Liebowitz, H., Lee, J. D. and Eftis, J., *Engineering Fracture Mechanics,* Vol. 10, 1978, pp. 315–355.

[*15*] Miller, K. J. and Kfouri, A. P., *International Journal of Fracture,* Vol. 10, 1974, pp. 393–403.

[*16*] Tanaka, K., Hoshide, T., Yamada, A., and Taira, S., *Fatigue of Engineering Materials and Structures,* Vol. 2, 1979, pp. 181–194.

[*17*] Rice, J. R. in *Fatigue Crack Propagation, ASTM STP 415,* American Society for Testing and Materials, Philadelphia, 1966, pp. 247–309.

[*18*] Schwalbe, K.-H. in *Proceedings,* 3rd European Conference on Fracture, London, 1980, pp. 267–276.

[*19*] Kfouri, A. P., *Journal of Strain Analysis,* Vol. 18, 1983, pp. 69–75.

Hideo Kitagawa,[1] *Ryoji Yuuki*,[2] *Keiichiro Tohgo*,[3] *and Masato Tanabe*[4]

ΔK-Dependency of Fatigue Growth of Single and Mixed Mode Cracks Under Biaxial Stress

REFERENCE: Kitagawa, H., Yuuki, R., Tohgo, K., and Tanabe, M., "**ΔK-Dependency of Fatigue Growth of Single and Mixed Mode Cracks Under Biaxial Stresses,**" *Multiaxial Fatigue, ASTM STP 853,* K. J. Miller and M. W. Brown, Eds., American Society for Testing and Materials, Philadelphia, 1985, pp. 164–183.

ABSTRACT: A comprehensive fracture mechanics study has been carried out on the fatigue crack growth under various biaxial stress conditions. Fatigue tests have been conducted on a high-cycle biaxial fatigue test facility and a cruciform flat specimen of a weldable structural steel with a center crack parallel to one load axis or a slant crack.

The effects of biaxial stresses have been investigated on the fatigue crack growth properties ΔK_I-da/dN, the threshold conditions ΔK_{Ith}, and the crack closure behavior.

If a crack is large and stress level is low, no effect of biaxial stress appears. However significant effects of biaxial stress appear where a crack is small and stress level is high.

The mixed mode cracks were realized by a series of fatigue tests started from a slant crack in a cruciform specimen, where a longer bent crack or a branched crack appeared. It is found that such a nonstraight crack follows along the direction where $\Delta K_{II} = 0$ and the ΔK_I-da/dN relations coincide with those for a straight crack under single K_I mode.

KEY WORDS: biaxial loading, fatigue crack propagation, fracture mechanics, structural steel, mixed modes, stress intensity, stress ratio, branched cracks

Most structural components suffer biaxial/multiaxial cyclic loadings, and most fatigue cracks in them propagate in biaxial stress or mixed mode conditions. There are now many arguments for and against the ΔK-dependency of the fatigue crack growth under biaxial stresses [*1–12*] and also in mixed mode state [*13–16*]. That is, the effects of biaxial stress or nonsingular stress on fatigue crack propagation have been investigated theoretically [*17–21*] and experimentally [*1–12*] by many researchers and various conclusions have been reached on the ΔK-dependency of the fatigue crack growth under biaxial stresses. Few data [*13–16*] have been obtained on the fatigue crack growth properties under mixed mode

[1]Professor, Yokohama National University, Yokohama, Japan.
[2]Associate professor, Institute of Industrial Science, University of Tokyo, Tokyo, Japan.
[3]Research assistant, Department of Iron and Steel Engineering, Nagoya University, Nagoya, Japan.
[4]Toyota Motor Co., Ltd., Toyota, Japan.

Copyright© 1985 by ASTM International www.astm.org

conditions where a crack follows a nonstraight path. It is an important problem in fracture mechanics whether the fatigue crack growth behavior in such a complex stress field can be predicted directly from uniaxial fatigue data for a pure K_I mode in a simple specimen or not.

In the present study, a comprehensive fracture mechanics study has been carried out on fatigue crack growth under various in-plane biaxial stress conditions, using a high-cycle biaxial fatigue test facility and a cruciform flat specimen of weldable structural steel with a center crack parallel to one load axis or a slant crack. The crack at every stage was analyzed by an analytical method and a finite element method, taking geometry of the specimen and nonlinear crack path into consideration.

The effects of stress biaxiality have been investigated on the fatigue crack growth properties both at lower and higher stress levels and also the threshold conditions ΔK_{Ith}. Moreover the fatigue growth behavior for a slant crack was investigated under biaxial stress conditions. The applicability and limitations of linear fracture mechanics to such fatigue crack growth are discussed.

Specimens and Experimental Procedure

Two kinds of a cruciform flat specimen were used for biaxial fatigue tests as shown in Fig. 1. A large specimen in Fig. 1*a* is used for the fatigue tests at lower stress levels and also for mixed mode fatigue crack growth tests, and a small one in Fig. 1*b* is for the fatigue tests at higher stress levels. The material used is a weldable structural steel sheet with the thickness of 4.5 mm. There is a little difference in the mechanical properties of weldable structural steels (Welten 60) used for the two kinds of specimens. The mechanical properties and chemical composition of the materials are shown in Table 1.

Fatigue tests have been performed on the new high-cycle biaxial fatigue testing machine specially developed for the present study. This machine has four electric-hydraulic servoactuators and load cells, arranged perpendicular to each other on a horizontal plane in a rigid circular frame and can control with high accuracy the mean and amplitude of load for both axes as well as the phase difference ϕ between the loads of both axes at high frequency. The load capacity is ± 98 kN. The details of the machine and the testing procedures were reported in other papers [*10,22*].

Analysis of the Cruciform Specimen

In advance of experiments, it is important to evaluate the stress intensity and the stress distribution in cruciform specimens because of the complication of the specimen shape. Since the specimens are flat, it can be dealt with as a two-dimensional elastic problem. The stress intensity factors for a center crack in a cruciform specimen were analyzed exactly by a modified mapping collocation method, which used special complex stress functions [*10,23*]. The solutions obtained were checked by finite-element method (FEM) analysis. Figure 2 shows

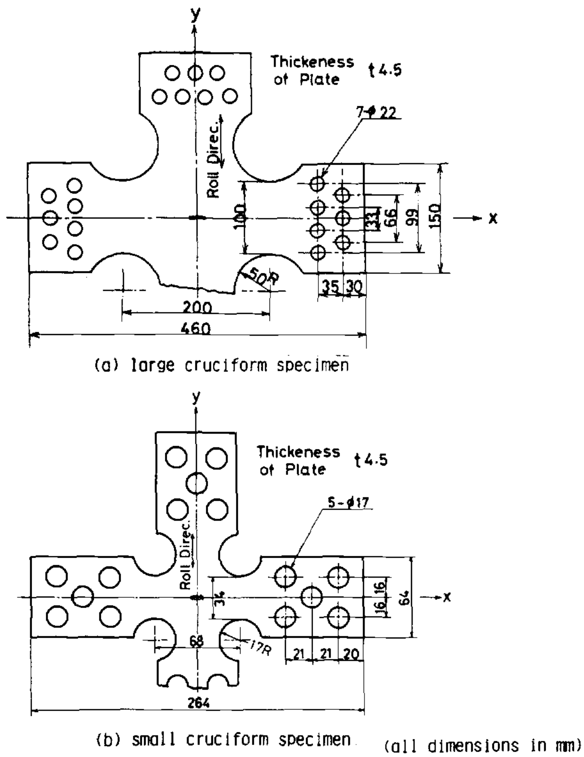

FIG. 1—*Configurations of two cruciform biaxial specimens.*

TABLE 1—*Mechanical properties and chemical composition of the materials.*

Chemical Composition, %						
C	Si	Mn	P	S	Cr	Specimen
0.10	0.39	1.36	0.021	0.007	0.01	Fig. 1*a*
0.09	0.16	1.01	0.014	0.005	0.01	Fig. 1*b*

Mechanical Properties			
Yield Strength, MN/m^2	Tensile Strength, MN/m^2	Elongation, %	Specimen
480	620	28	Fig. 1*a*
539	646	20	Fig. 1*b*

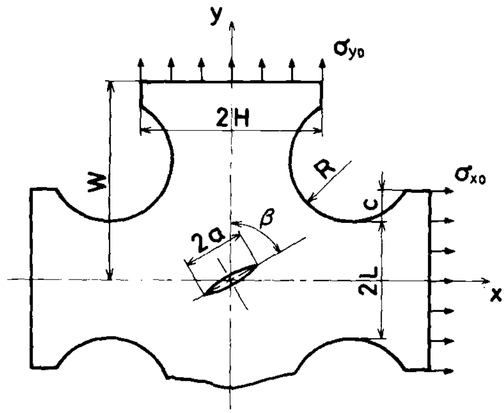

FIG. 2—*Nomenclature for analysis.*

the model of this analysis. Here, σ_{y0} and σ_{x0} are nominal stresses applied to the gripped parts of specimen. In the case of a crack parallel to x-axis ($\beta = \pi/2$), K_I can be calculated as follows

$$K_I = F_{Iy}\delta_{y0}\sqrt{\pi a} + F_{Ix}\sigma_{x0}\sqrt{\pi a} \tag{1}$$

where F_{Iy} and F_{Ix} are the correction factors of K_I, which is induced by tension stress σ_{y0} in y-direction and σ_{x0} in x-direction, respectively.

From the analytic results, the values of F_{Iy} and F_{Ix} can be polynomially approximated as follows

$$\begin{aligned} F_{Iy} = &\begin{Bmatrix} 1.1906 \\ 1.4890 \end{Bmatrix} + \begin{Bmatrix} 0.0076 \\ -0.0077 \end{Bmatrix}(a/L) \\ &+ \begin{Bmatrix} 0.2051 \\ 0.2713 \end{Bmatrix}(a/L)^2 - \begin{Bmatrix} 0.0042 \\ 0.0184 \end{Bmatrix}(a/L)^3 \end{aligned} \tag{2}$$

$$\begin{aligned} F_{Ix} = &\begin{Bmatrix} -0.2589 \\ -0.3227 \end{Bmatrix} + \begin{Bmatrix} 0.0253 \\ 0.0062 \end{Bmatrix}(a/L) \\ &- \begin{Bmatrix} 0.0459 \\ 0.0114 \end{Bmatrix}(a/L)^2 + \begin{Bmatrix} 0.0665 \\ 0.0547 \end{Bmatrix}(a/L)^3 \end{aligned} \tag{3}$$

($0.1 \leq a/L \leq 1.0$, within 0.1%), (upper row for Fig. 1*a* and lower row for Fig. 1*b*).

It is noteworthy that F_{Ix} in these specimens represents a relatively large negative value. This means that the tension stress σ_{x0} parallel to a crack causes a decrease in K_I-value.

In the biaxial fatigue tests of these specimens controlling the applied stresses

σ_{y0} and σ_{x0}, the values of stress intensity range ΔK_I and the stress ratio R_k can be defined as follows in the cases of phase difference $\phi = 0$ and π.

$$\Delta K_I = 2\sqrt{\pi a}\,(F_{Iy}\sigma_{ya} \pm F_{Ix}\sigma_{xa}) \tag{4}$$

$$R_k = \frac{K_{I\min}}{K_{I\max}} = \frac{F_{Iy}(\sigma_{ym} - \sigma_{ya}) + F_{Ix}(\sigma_{xm} \mp \sigma_{xa})}{F_{Iy}(\sigma_{ym} + \sigma_{ya}) + F_{Ix}(\sigma_{xm} \pm \sigma_{xa})} \tag{5}$$

(upper sign for $\phi = 0$, lower sign for $\phi = \pi$)

where σ_{ym} or σ_{ya} is mean or amplitude of applied stress σ_{y0} in y-direction and σ_{xm} or σ_{xa} is in x-direction.

The value of R_k is different in general from the stress ratio of applied loads $R_y = \sigma_{y\min}/\sigma_{y\max}$ and $R_x = \sigma_{x\min}/\sigma_{x\max}$. For actual fatigue tests, the changes in ΔK_I and R_k must be taken into consideration.

If a crack is slant with respect to the x-axis, as shown in Fig. 2, a K_I and K_{II} mixed mode state appears. The stress intensity for a slant crack in the specimen of Fig. 1*a* was also analyzed by the analytical method mentioned before [*23*]. The values of K_I can be calculated by Eq 1, and K_{II} is as follows

$$K_{II} = F_{IIy}\,\sigma_{y0}\sqrt{\pi a} + F_{IIx}\sigma_{x0}\sqrt{\pi a} \tag{6}$$

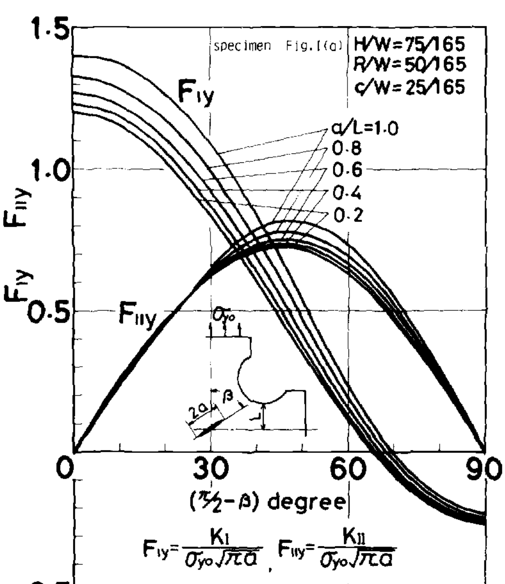

FIG. 3—*Stress intensity factors for a slant crack in a cruciform specimen under tension stress in* y*-direction.*

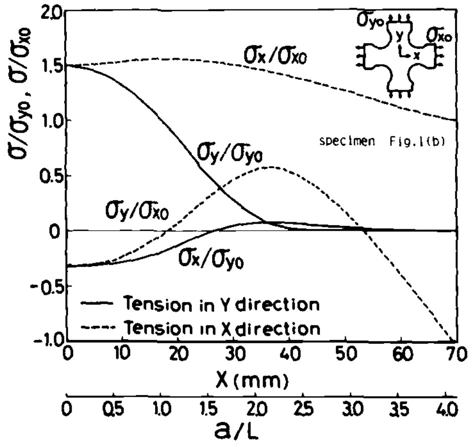

FIG. 4—*Stress distribution along* x-*axis in a cruciform specimen without a crack. (Fatigue tests are carried out where* a/L < *1.0).*

The values of F_{Iy} and F_{IIy} obtained are shown in Fig. 3 as functions of crack length a/L and crack angle $(\pi/2 - \beta)$. Since the specimen is symmetric about the origin, $F_{Ix}(\beta) = F_{Iy}(\pi/2 - \beta)$ and $F_{IIx}(\beta) = -F_{IIy}(\pi/2 - \beta)$. In the case of the equibiaxial stress state ($\sigma_{y0} = \sigma_{x0}$, $\phi = 0$), the value of K_{II} for a crack with any angle β becomes zero and the crack grows straight under pure K_I mode. Using the specimen with a slant crack, any desired K_{II} and K_I combinations can be induced by various biaxial loadings.

The stress distribution in the cruciform specimen without a crack was examined by FEM. Figure 4 shows the stress distribution along x axis in the specimen of Fig. 1*b*.

From these results, the stress σ_L in the y-direction and σ_T in x-direction at the center of the specimen (Fig. 1*b*) without a crack can be represented by

$$\left.\begin{aligned}\sigma_L &= \alpha\sigma_{y0} + \beta\sigma_{x0}\\ \sigma_T &= \beta\sigma_{y0} + \alpha\sigma_{x0}\end{aligned}\right\} \qquad \left.\begin{aligned}\alpha &= 1.49\\ \beta &= -0.32\end{aligned}\right\} \tag{7}$$

These stress components σ_L and σ_T correspond to the uniform biaxial stresses in the y- and x-direction for a crack in a infinite plate. Therefore the nonsingular term T in a stress field near a crack tip and biaxial stress ratio C can be defined approximately as follows

$$T = \sigma_T - \sigma_L = -(1 - C)\sigma_L \tag{8}$$

$$C = \frac{\sigma_T}{\sigma_L} \tag{9}$$

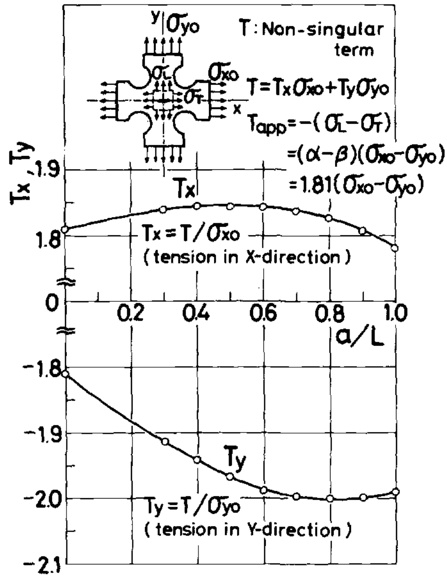

FIG. 5—*Nonsingular term* T_x *and* T_y *in a cruciform specimen.*

These equations are effective only for a small crack. The exact values of T in a cruciform specimen were calculated by FEM according to Larsson and Carlson [*24*]. Figure 5 shows the values of T_x and T_y analyzed. The values of T_x are almost constant for any crack length, and the values of T_y decrease only by 10%. In the fatigue tests, the required σ_{y0} and σ_{x0} corresponding to any desirable σ_L, and σ_T combination are calculated by solving Eq 7.

Experimental Results and Discussions

Fatigue Crack Growth Properties for Wide ΔK_I Range and Threshold Conditions

To obtain the fatigue crack growth properties for wide ΔK_I range under various biaxial loading conditions, both constant load and decreasing load biaxial fatigue tests were carried out for a large crack parallel to one load axis in the specimen of Fig. 1*a*. In the present tests, the applied stresses σ_{y0} and σ_{x0} were controlled, and the stress ratio $R_y = \sigma_{y0min}/\sigma_{y0max}$ was kept constant for a series of biaxial fatigue tests. Four kinds of biaxial loading conditions were selected; uniaxial stress ($\sigma_{x0} = 0$), static lateral stress ($\sigma_{xm} = \sigma_{ym}$, $\sigma_{xa} = 0$), equibiaxial stress ($\sigma_{x0} = \sigma_{y0}$, $\phi = 0$) and out-of-phase equibiaxial stress ($\sigma_{xm} = \sigma_{ym}$, $\sigma_{xa} = \sigma_{ya}$, $\phi = \pi$). In decreasing load tests, the loads of both axes are gradually decreased by 3%, keeping the stress ratio R_y and R_x constant, after crack growth is observed by a surface replica method.

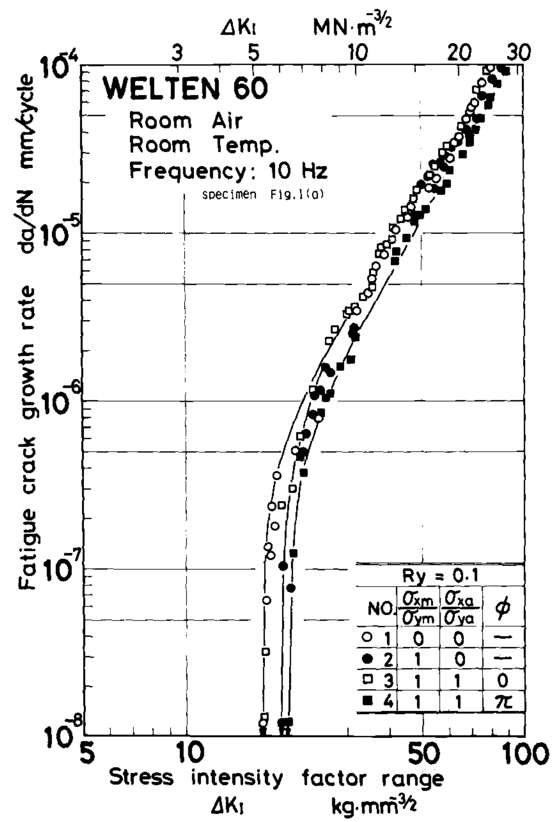

FIG. 6*a*—*Crack growth rate versus stress intensity range for various biaxial loads* (R_y = *0.1*).

Figure 6*a* and *b* represent the fatigue crack growth rates da/dN for various biaxial loadings against exact ΔK_I-values calculated by Eqs 2 through 4 in the cases of R_y = 0.1 and 0.3, 0.5, respectively. Figure 6 shows that there are some difference in the ΔK_I-da/dN relations for various biaxial loadings, and this tendency is remarkable at low ΔK_I range. The reason for this tendency can be explained as follows. In present fatigue tests, R_y was kept constant, the real stress ratio $R_k = K_{\mathrm{I}min}/K_{\mathrm{I}max}$ defined in Eq 5 is different from R_y in the cases of static lateral stress and out-of-phase biaxial stress conditions. In these cases the R_k-value is smaller than R_y, and therefore the fatigue crack growth rates apparently decrease. It is well known that the fatigue crack growth properties in high-strength steels are insensitive to stress ratio in the middle ΔK_I range and become very sensitive at lower ΔK_I ranges. It is known that the effect of stress ratio can be well explained by crack closure concept [*25*].

The crack closure was measured by a strain gage method in the tests at R_y = 0.3 and 0.5. Figure 7 shows the effective stress intensity range $\Delta K_{\mathrm{I}eff}$-da/dN relations, which fall within a narrow scatterband above da/dN of 5×10^{-7}

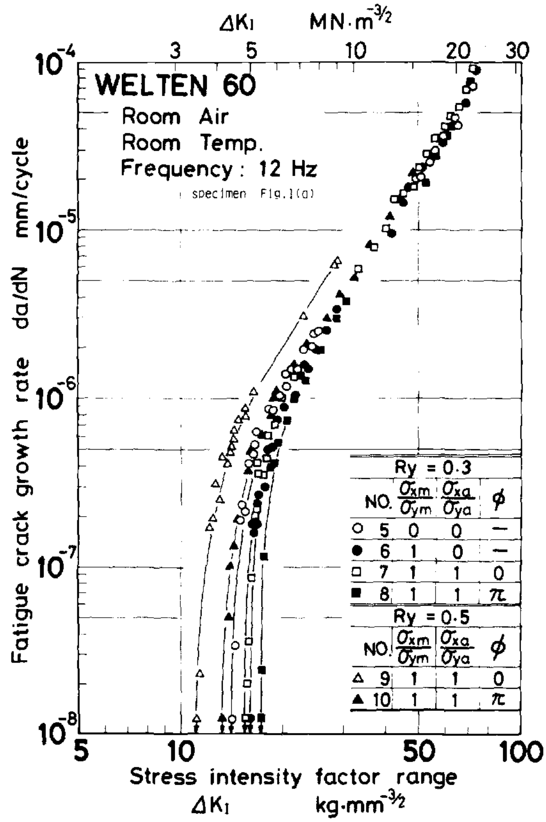

FIG. 6*b*—*Crack growth rate versus stress intensity range for various biaxial loads* (R_y = *0.3, 0.5*).

mm/cycle. This means that no effects of biaxial stresses on the crack closure phenomenon appear in the present tests, and the effects of R_k mentioned previously can be well explained by effective stress intensity range.

Figure 8 represents the threshold conditions ΔK_{Ith} obtained for various biaxial loading conditions as a function of stress ratio R_k exactly calculated by Eq 5. Here the ΔK_{Ith} was defined as the ΔK_I-value where the da/dN was below 5×10^{-8} mm/cycle. The values of ΔK_{Ith} obtained follow single ΔK_{Ith}-R_k relation in a manner similar to that of uniaxial fatigue data [*26,27*] and agree with the uniaxial data obtained by a center cracked plate specimen (CCP) of same material.

From these results, it is found that the ΔK_I-da/dN relations including ΔK_{Ith} for various biaxial loading conditions can be characterized by exact values of ΔK_I and R_k or uniformly by ΔK_{Ieff}. Biaxial stresses or the nonsingular term do not affect the fatigue crack growth properties and also crack closure behavior within the present study. The reason for these results is that the present experimental condition adequately satisfy small-scale yielding conditions at a crack

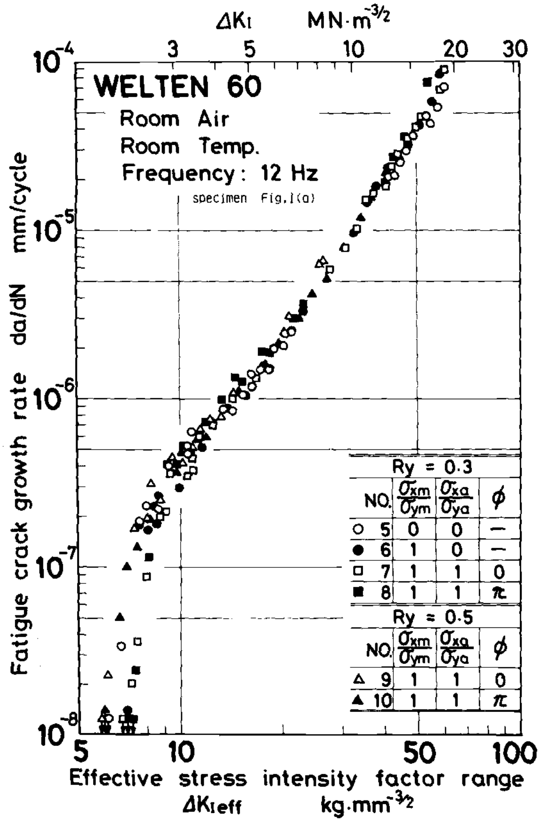

FIG. 7—*Crack growth rate versus effective stress intensity range for various biaxial loads at* R_y = *0.3 and 0.5.*

tip where one parameter of stress intensity prescribes the stress field near a crack tip.

Effect of Biaxial Stresses

To examine the effects of stress biaxiality on the fatigue crack growth, another series of biaxial fatigue tests were carried out at higher stress level and for a smaller crack than in previous work. In the present tests, a smaller specimen as shown in Fig. 1*b* was used for nearly the same material and the stress ranges $\Delta\sigma_L$ and $\Delta\sigma_T$ defined in Eq 7 and the stress ratio R_k were kept constant throughout a series of biaxial tests. Four kinds of typical biaxial stress conditions were selected; uniaxial (No. 1), equibiaxial (No. 2), shear stress (No. 3), and out-of-phase equibiaxial (No. 4) stress conditions. A buckling protector was used in the tension-compression biaxial fatigue tests (shear stress, No. 3).

Figures 9 and 10 show the ΔK_I-da/dN relations obtained for various biaxial

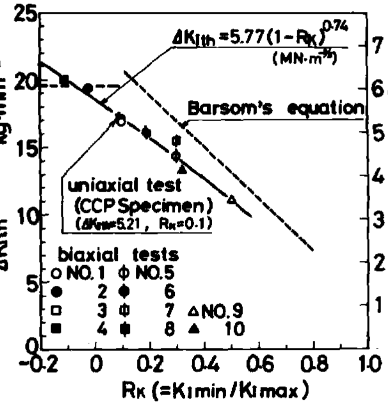

FIG. 8—*Threshold conditions* ΔK_{lth} *versus stress ratio* R_k *for various biaxial loads.*

stresses at two stress levels in the cases of $R_k = 0.1$ and 0.3, respectively. The data in Fig. 9 at lower stress level reveal negligible effect of stress biaxiality and fall within a narrow scatterband. But the data in Fig. 9 at a higher stress level have some differences in ΔK_I-da/dN relations and show a significant effect of biaxial stresses. This tendency becomes remarkable at $R_k = 0.3$ as shown in Fig. 10. From these data, it is found that the difference in the ΔK_I-da/dN relations is remarkable at low ΔK_I range where a crack is small. Compared with each

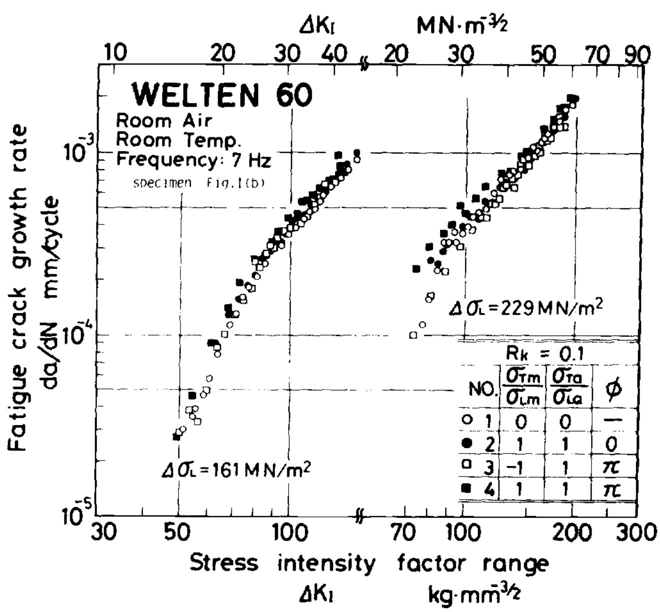

FIG. 9—*The* ΔK_I-da/dN *relations for various biaxial stress conditions at* $R_k = 0.1$.

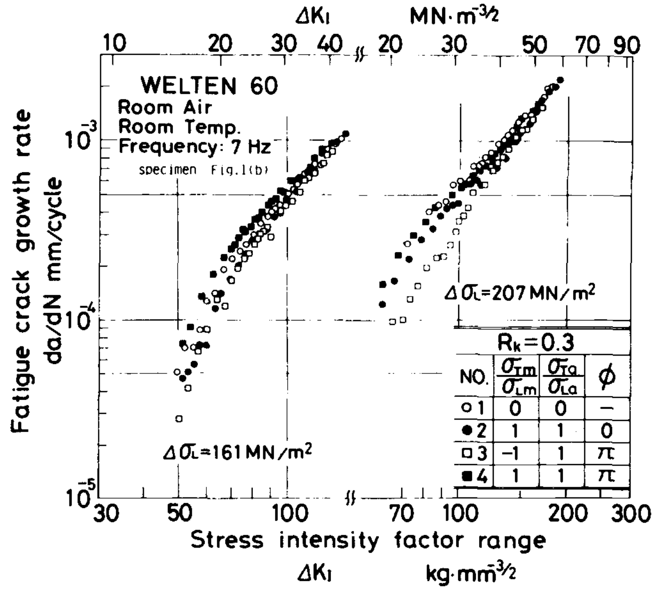

FIG. 10—*The* ΔK_I-da/dN *relations for various biaxial stress conditions at* R_k = *0.3.*

data set for various biaxial stress conditions, it is found that the data for the shear stress condition (No. 3) deviate from the other data on the decreasing side of crack growth rate. Tanaka et al [*12*] reported the same tendency in the biaxial fatigue tests of mild steel at $R = 0$. However Miller [*8*] and others have reported results contradictory to the present results. It seems to depend on the material whether the data for the shear stress condition deviate on the decreasing side or the increasing side. In our tests of stainless steel, results different from the present study in weldable steel have been obtained and the *da*/*dN* for shear stress becomes higher than that for uniaxial data [*28*].

It is important that the effect of biaxial stresses does appear only at higher stress levels and at higher stress ratio, and the effects are remarkable at low ΔK_I range where a crack is small. Focusing on these points, the experimental conditions for the present biaxial fatigue tests are rearranged in Fig. 11, including those for our tests not reported here [*10,28*], and also for recent papers on cyclic biaxial fatigue of cruciform specimen by Miller [*7,8*], Tanaka [*11,12*], and Liu [*9*].

In Fig. 11, the vertical axis is one half of the crack length measured, and the horizontal axis is stress level $\sigma_{L\max}/\sigma_{ys}$, where σ_{ys} is a yield strength of material and $\sigma_{L\max}$ is maximum applied stress in *y*-direction at a center of specimen.

This figure shows that the effect of biaxial stress appears only in the tests for a relatively small crack and at higher stress level, and its limitation line seems to exist at $\sigma_{L\max}/\sigma_{ys} = 0.4$ to 0.5. This fact can be considered as follows. It is known that the yielding condition and the plastic zone at crack tip under biaxial stresses are quite different from those under uniaxial stress. Some theoretical analyses [17–21] show that the plastic zone under equibiaxial tension stresses is small and that under tension-compression biaxial stress or shear stress it becomes large. Therefore large scale yielding at a crack tip can occur under some biaxial stresses at a lower stress level than under uniaxial stress, where not only the stress intensity but also nonsingular term T seem to prescribe the stress field near a crack tip, and the effect of biaxial stress should appear.

In many previous works on biaxial fatigue, stress intensity and biaxial stress ratios were described explicitly, however such experimental conditions as a crack length and stress level were usually not taken into consideration. Therefore some confusion seems to occur as to the ΔK dependency of fatigue crack growth under biaxial stresses. The limitations of linear fracture mechanics must be investigated by further researches of both systematic biaxial fatigue tests and theoretical studies on the effect of nonsingular term.

Mixed Mode Fatigue Crack Growth

A series of fatigue tests were carried out on fatigue crack growth behavior using a cruciform specimen (Fig. 1*a*) with a slant crack. The experimental conditions are listed in Table 2. A slant crack with various angle β propagated without deviation under equibiaxial stresses until the total crack length 2α reached to about 20 mm. Then the applied stress conditions were changed to uniaxial or out-of-phase equibiaxial stress conditions. The values of ΔK_{I} and ΔK_{II} at this stage were calculated by Eqs 1 and 6 and shown in Table 2. Mixed mode fatigue cracks under various combinations of ΔK_{I} and ΔK_{II} have been realized in the present tests, where a large bent or branched crack was observed.

Figure 12 shows the initial fracture angles at the tip of a slant crack against the ratio $\Delta K_{\text{II}}/\Delta K_{\text{I}}$ or $\Delta K_{\text{I}}/\Delta K_{\text{II}}$ and also theoretical curves after various criteria

TABLE 2—*Experimental conditions for mixed mode fatigue cracks.*

Specimen No.		1	2	3	4	5	6
Material		Welten 60					
Slant angle, β°		31.5	43.5	61.0	75.3	45.0	43.5
Initial crack length, $2a_i$ (mm)		20.02	19.67	19.96	20.31	20.35	20.20
Mean and amplitude of stress	σ_{ym}	43.54	43.54	43.54	43.54	43.54	43.54
in y-direction, MN/m^2	σ_{ya}	35.60	35.60	35.60	35.60	35.60	35.60
Mean and amplitude of stress	σ_{xm}	0	0	0	0	43.54	43.54
in x-direction, MN/m^2	σ_{xa}	0	0	0	0	0.0	35.60
Stress ratio of applied load,	R_y	0.1	0.1	0.1	0.1	0.1	0.1
$R = \sigma_{min}/\sigma_{max}$	R_x	—	—	—	—	1.0	0.1
σ_{xm}/σ_{ym}		0	0	0	0	1	1
σ_{xa}/σ_{va}		0	0	0	0	0	1
Phase difference, radius	0	0	0	0	0	0	π
ΔK_{I} at initial stage, MN/m$^{3/2}$		1.89	5.59	10.89	14.08	6.08	0.84
ΔK_{II} at initial stage, MN/m$^{3/2}$		8.18	9.05	7.71	4.32	9.25	18.38
$\Delta K_{\text{II}}/\Delta K_{\text{I}}$ at initial stage		4.33	1.62	0.72	0.31	1.52	21.88

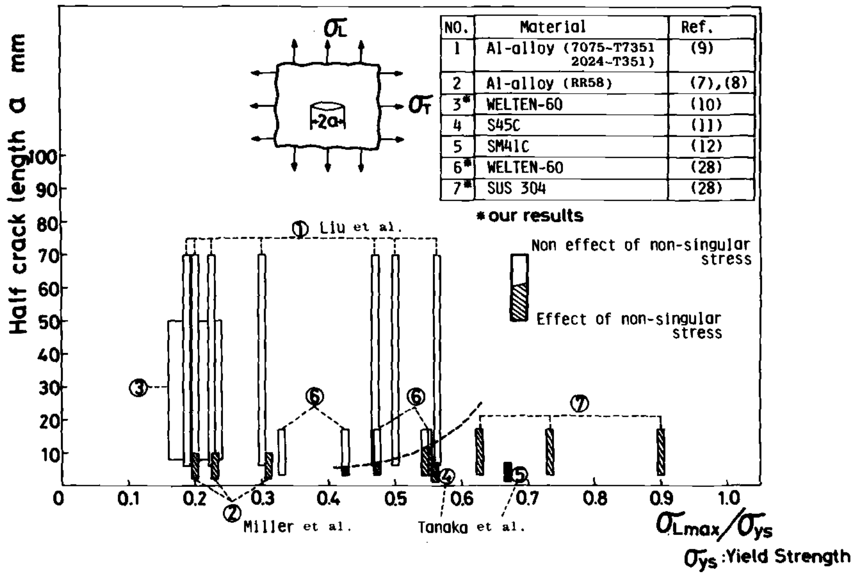

FIG. 11—*Experimental conditions for various biaxial fatigue tests.*

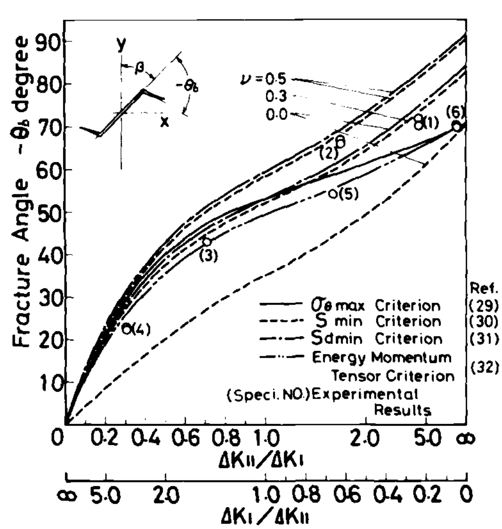

FIG. 12—*Initial fracture angle versus the ratio of stress intensity ranges* ΔK_{II} *and* ΔK_I. ($\sigma_{\theta max}$ . . . *circumferential stress maximum criterion by Erdogan and Sih* [29], S_{min} . . . *strain energy minimum criterion by Sih* [30], S_d . . . *distortion strain energy minimum criterion by Jayatilaka* [31], *energy momentum tensor criterion by Tirosh* [32]).

for brittle fracture under mixed mode conditions [29–32], in which the K_I and K_{II} are replaced by ΔK_I and ΔK_{II}, respectively. Experimental results seem to agree with maximum cucumferential stress $\sigma_{\theta max}$ criterion by Erdogan and Sih [29]. However compared with the fracture angles of No. 2 and No. 5 for the same $\Delta K_{II}/\Delta K_I$ value, a little difference is observed. This is because the stress ratio R_k is different.

Figure 13 shows the fatigue growth rate da_x/dN for a crack projected onto the x-axis versus the apparent stress intensity range ΔK_{Iapp} for a straight crack with the crack length of $2a_x$. This figure shows that these ΔK_{Iapp}-da_x/dN relations for various nonstraight cracks fall within relatively narrrow scatterband except the data just after a crack starts to grow, and they almost agree with the data for a straight crack under single K_I mode. Figure 14 shows schematically two typical crack paths observed in No. 2 and No. 6 specimens. In the case of No. 2, a slant crack with an angle of nearly 45° changed direction gradually at initial stage to grow perpendicularly to the loading direction as shown in Fig. 14*a*. In the case of No. 6, a particular crack path was observed under out-of-phase equibiaxial stress conditions, where $\Delta K_I = 0$ and reversed Mode II loading was applied. A symmetric branched crack with a half branched angle of about 70° was observed as shown in Fig. 14*b*.

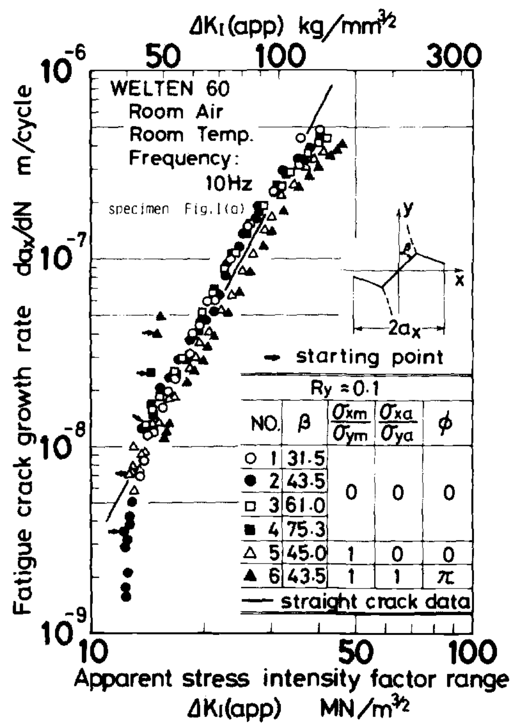

FIG. 13—*Crack growth rate of nonstraight cracks versus apparent stress intensity range* ΔK_{Iapp} *for a straight crack.*

To investigate the ΔK-dependency of fatigue growth behavior for such a nonstraight crack, K_I and K_{II} for a bent and a branched crack shown in Fig. 14 were analyzed at every stage of crack growth by FEM [33] and an analytical method [34,35]. The details of these analyses are omitted in this paper and only numerical results are shown in Fig. 15. Figure 15 shows the variations of ΔK_I and ΔK_{II} normalized by $\Delta\sigma\sqrt{\pi\alpha_x}$ with the crack length projected to x-axis (a_x). The normalized stress intensity F_I (bent) for a bent crack (No. 2) gradually approaches to that for a straight crack under same stress conditions. But F_I (branch) for a branched crack (No. 6) has higher value than that for a straight crack. This is because this stress intensity is analyzed on the assumption that crack edges of branched cracks are stress free. However, it is found that one of branches is closed for a large portion of load cycling as shown in Fig. 15*a*. Fig. 15*a* shows the variation of K_I for branched crack with time. Taking this crack closure effect, the normalized stress intensity for a branched crack becomes F_I^C (branch) or F_I^{CP} (branch) as shown in Fig. 15*b*. F_I^C (branch) is the normalized stress intensity range, assuming that F_I-values for branched crack are approximated by those for bent crack when one of the branches is closed.

F_I^{CP} (branch) is the normalized stress intensity range correspond to the portion of positive K_I-variation, assuming that the negative region of K_I-variation does not contribute to fatigue crack growth. The F_I^{CP} (branch) gradually approaches to that for a straight crack in the same manner as F_I (bent). These results of F_I (bent) and F_I^{CP} (branch) well explain the fatigue crack growth properties shown in Fig. 13 where the fatigue crack growth rates for a bent or branched crack were uniformly characterized by ΔK_{Iapp}.

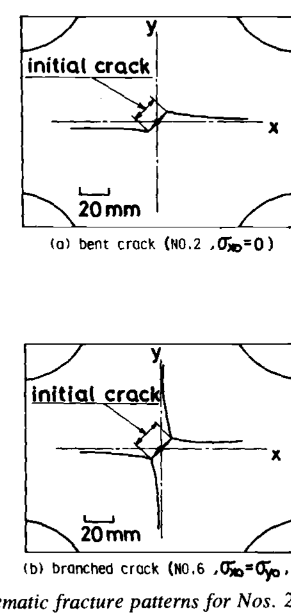

(a) bent crack (NO.2, $\sigma_{x0}=0$)

(b) branched crack (NO.6, $\sigma_{x0}=\sigma_{y0}$, $\phi=\pi$)

FIG. 14—*Schematic fracture patterns for Nos. 2 and 6 specimens.*

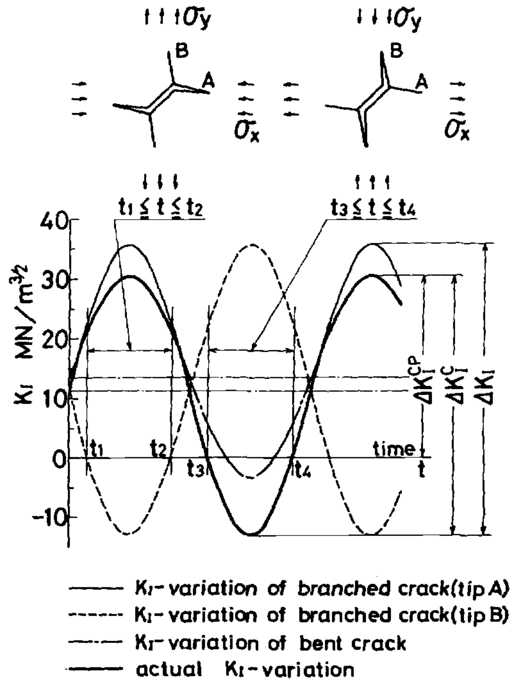

FIG. 15*a*—*Variation of* K_I *for branched crack with time.*

In Fig. 15*b*, it is found that Mode II stress intensity ΔK_{II} for a bent crack (F_{II} (bent)) or a branched crack ($F_{II}{}^C$ (branch)) is negligibly small. This means that such a nonstraight crack grows along the direction where $\Delta K_{II} = 0$, which was proposed by us in another paper [*34*]. Therefore the ΔK_I-da/dN relations for such a crack follow the same properties as those for a straight crack under pure K_I mode, if the exact K_I-value for a nonstraight crack is evaluated. It is so difficult to evaluate the stress intensity for such a crack at every stage that various conclusions have been drawn on fatigue crack growth under mixed mode conditions. In practical application, the fact is also important that the ΔK_{Iapp}-da_x/dN relations approximately coincide with ΔK_I-da/dN relations for a straight crack under Mode I condition.

Thus it is found that the ΔK-dependency of the fatigue crack growth is effective even under biaxial loadings and in mixed mode state, if the small-scale yielding condition is satisfied and stress intensity is exactly evaluated.

Conclusions

A series of fatigue tests and analyses has been conducted on the fatigue crack growth in a weldable structural steel under various cyclic biaxial stress conditions

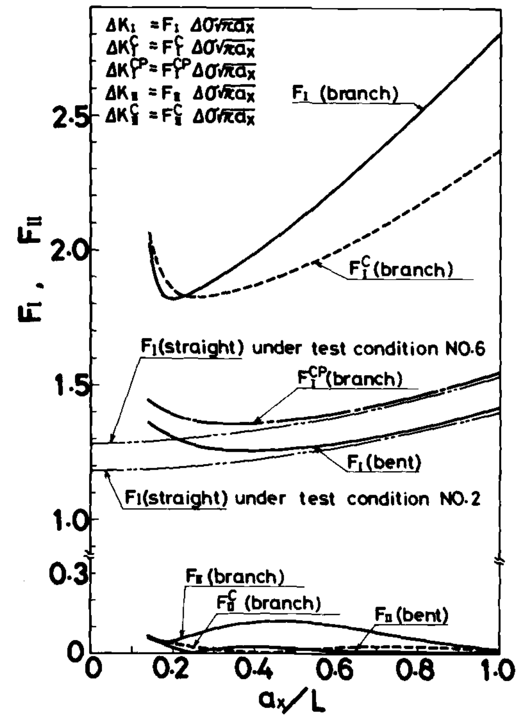

FIG. 15b—*The variation of stress intensity range with crack length for a bent or a branched crack.*

both in the cases that a crack parallel to one load axis grows straight and that a slant crack follows along a nonstraight crack path. The main results obtained in the present study are as follows.

1. Stress intensity factors for a straight crack and also a bent or branched crack and nonsingular terms in cruciform specimen have been analyzed by both analytical and finite element methods.
2. The ΔK_I-da/dN relations for a wide ΔK_I range including the threshold ΔK_{Ith} under various biaxial loading conditions can be characterized by exact values of ΔK_I and stress ratio R_k or uniformly by effective stress intensity range ΔK_{Ieff}. No effect of stress biaxiality has appeared in the ΔK_I-da/dN relations or the crack closure behavior, if a crack is adequately large and the stress level is low. However significant effect of stress biaxiality has appeared in the case where a crack is relatively small and stress level is relatively high.
3. The experimental conditions for the present biaxial fatigue tests and some papers reported are rearranged, focused on crack length and stress level. The critical region where the effect of biaxial stresses appear is clarified.
4. The mixed mode fatigue cracks were realized by a series of fatigue tests

started from a slant crack in a cruciform specimen where a bent crack or a branched crack is observed.

5. It is found that such a nonstraight crack path follows along the direction where $\Delta K_{II} = 0$ and the ΔK_I-da/dN relations coincide with those for a straight crack under single K_I mode.

References

[1] Christensen, R. H. and Harmon, M. B. in *Fatigue Crack Propagation, ASTM STP 415,* American Society for Testing and Materials, Philadelphia, 1967, p. 5.
[2] Kilber, J. J. and Roberts, R., *Transactions,* American Society of Mechanical Engineers, *Journal of Engineering for Industry,* Vol. B-92, 1970, p. 727.
[3] Joshi, S. R. and Shewchuk, J., *Experimental Mechanics,* Vol. 10, 1970, p. 727.
[4] Pook, L. P. and Denton, K., *International Journal of Fracture,* Vol. 8, No. 1, 1972, p. 118.
[5] Leevers, P. S., Radon, J. C., and Culver, L. E., *Polymer,* Vol. 17, No. 3, 1976, p. 627.
[6] Leevers, P. S., Culver, L. E., and Radon, J. C., *Engineering Fracture Mechanics,* Vol. 11, 1979, p. 487.
[7] Hopper, C. D. and Miller, K. J., *Journal of Strain Analysis,* Vol. 12, No. 1, 1977, p. 23.
[8] Miller, K. J., *Metal Science,* Vol. 11, 1977, p. 432.
[9] Liu, A. F., Allison, J. E., Dittner, D. F., and Yamane, J. R., *Fracture Mechanics, ASTM STP 677,* American Society for Testing and Materials, Philadelphia, 1979, p. 5.
[10] Kitagawa, H., Yuuki, R. and Tohgo, K., *Fatigue Engineering and Materials Structure,* Vol. 2, 1979, p. 195.
[11] Tanaka, K., Hoshide, T., Yamada, A., and Taira, S., *Fatigue Engineering and Materials Structure,* Vol. 2, 1979, p. 181.
[12] Hoshide, T., Tanaka, K., and Yamada, A., *Fatigue Engineering and Materials Structure,* Vol. 4, No. 4., 1981, p. 355.
[13] Iida, S. and Kobayashi, A. S., *Transactions,* American Society of Mechanical Engineers, Series D 91, 1969, p. 764.
[14] Roberts, R. and Kibler, J. J., *Transactions,* American Society of Mechanical Engineers, Series D 93, 1971, p. 671.
[15] Tanaka, K., *Engineering Fracture Mechanics,* Vol. 6, 1974, p. 493.
[16] Otsuka, A., Mori, K., and Miyata, T., *Engineering Fracture Mechanics,* Vol. 7, 1975, p. 671.
[17] Hilton, P. D., *International Journal of Fracture,* Vol. 9, No. 2., 1973, p. 149.
[18] Smith, S. H. in *Prospects of Fracture Mechanics,* G. C. Sih, Ed., Noordhoff International, Leyden, The Netherlands, 1974, p. 367.
[19] Miller, K. J. and Kfouri, A. P., *International Journal of Fracture,* Vol. 10, No. 3, 1974, p. 393.
[20] Rice, J. R., *Journal of the Mechanics and Physics of Solids,* Vol. 22, 1974, p. 17.
[21] Adams, N. J. I., *Engineering Fracture Mechanics,* Vol. 5, 1973, p. 983.
[22] Kitagawa, H., Yuuki, R., Tohgo, K., and Kakuta, Y., *Transactions, Journal of the Society of Mechanical Engineers,* (in Japanese) Vol. 45, No. 395, 1979, p. 707.
[23] Kitagawa, H., Yuuki, R., and Tohgo, K., *Monthly Journal of the Institute of Industrial Science,* University of Tokyo, Vol. 30, No. 10, 1978, p. 395.
[24] Larsson, S. G. and Carlsson, A. J., *Journal of the Mechanics and Physics of Solids,* Vol. 21, 1973, p. 263.
[25] Elber, W., *Damage Tolerance in Aircraft Structures, ASTM STP 486,* American Society for Testing and Materials, Philadelphia, 1971, p. 230.
[26] Barsom, J. M., Welding Research Council Bulletin, No. 194, 1974.
[27] Klesnil, M. and Lukas, P., *Material Science and Engineering,* Vol. 9, 1972, p. 231.
[28] Yuuki, R., Kitagawa, H., Tohgo, K., and Tanabe, M., Preprint of Japan Society of Mechanical Engineers, No. 820-2, 1982, p. 164.
[29] Erdogan, R. and Sih, G. C., *Transactions,* American Society of Mechanical Engineers, Series D 85, 1963, p. 519.
[30] Sih, G. C., *International Journal of Fracture,* Vol. 10, No. 3, 1974, p. 305.
[31] Jayatilaka, A. de S, Jenkins, I. J., and Prasad, S. V., *Fracture,* Vol. 3, International Conference on Fracture, No. 4, Waterloo, 1977, p. 15.

[32] Tirosh, J., *Engineering Fracture Mechanics*, Vol. 9, No. 3, 1977, p. 607.
[33] Ishikawa, H., Kitagawa, H., and Okamura, H., *Fracture*, Vol. 3, International Conference on Fracture, No. 3, 1979, p. 447.
[34] Kitagawa, H., Yuuki, R. and Ohira, T., *Engineering Fracture Mechanics*, Vol. 7, 1975, p. 515.
[35] Kitagawa, H. and Yuuki, R., *Fracture*, Vol. 3, International Conference on Fracture, Waterloo, 1977, p. 201.

Gao Hua,[1] *Nejat Alagok,*[2] *Michael W. Brown,*[3] *and Keith J. Miller*[3]

Growth of Fatigue Cracks Under Combined Mode I and Mode II Loads

REFERENCE: Gao, H., Alagok, N., Brown, M. W., and Miller, K. J., "**Growth of Fatigue Cracks Under Combined Mode I and Mode II Loads,**" *Multiaxial Fatigue, ASTM STP 853,* K. J. Miller and M. W. Brown, Eds., American Society for Testing and Materials, Philadelphia, 1985, pp. 184–202.

ABSTRACT: Although the majority of fatigue crack propagation studies have been concerned with pure Mode I loading situations, in practice many cracks in components may initially extend by fatigue under a combination of all three crack growth modes, and this initial period may predominate during the fatigue lifetime. In this paper, the threshold and growth behavior of cracks under various combinations of Mode I and Mode II crack tip displacements are studied, showing the effect of the *T*-stress in the biaxial specimen. Four materials (AISI 316 stainless steel, DTD 5120 aluminium alloy, Ti-6A1-4V, and 1Cr-Mo-V steel) have been tested. Two different experimental procedures, four-point bending and biaxial loading of a plate, are employed.

An expression is derived for fatigue crack growth under combined mode load conditions relating growth to crack-tip reversed plastic deformation, which depends on the Mode I and Mode II crack-tip stress-intensity factors and also the *T*-stress. A secondary but important factor is the fracture ductility of the material around the crack tip, which itself is a function of biaxial stress state.

KEY WORDS: biaxial stresses, crack propagation, crack initiation, fatigue (materials), plastic deformation, ductility, stress intensity, stress ratio

Nomenclature

a	Crack length
a_o	Initial crack length
B	Specimen thickness
E	Young's Modulus
k	Material constant
K	Stress intensity factor
$\tilde{K}$	Branch crack tip stress intensity factor
N	Number of cycles

[1]Research fellow, Institute of Mechanics, Academia Sinica, Beijing, China.

[2]Research assistant, Mechanical Engineering Department, Middle East Technical University, Ankara, Turkey.

[3]Senior research fellow and professor, respectively, Mechanical Engineering Department, University of Sheffield, Sheffield, U.K.

Copyright© 1985 by ASTM International www.astm.org

P	Applied load
R	P_{min}/P_{max}
T	T-stress
r, θ, z	Polar coordinates
r_p	Maximum radius of crack tip plastic zone
W	Half specimen width
α	Measured inclined crack angle (Figs. 4 and 5)
γ	Fracture shear strain
Δ	Range of stress or K
θ_c	Measured branch cracking angle
θ^*	Angle of maximum plastic zone extent
Λ	Biaxial load ratio (Fig. 4)
ν	Poisson's ratio
ρ	Initial slit root radius
σ	Normal stress
τ	Shear stress

Subscripts

eff	Effective value
ft	Torsional fracture strain
fu	Uniaxial fracture strain
I	Mode I
II	Mode II
max	Maximum
th	Threshold
x, y, z	Cartesian coordinates
ys	Yield stress
θmax	Maximum hoop stress direction

Linear elastic fracture mechanics (LEFM) has been used successfully for analyzing fatigue crack growth leading to many improvements in fatigue design procedures. First, by relating propagation rate to crack-tip stress-strain fields, the Paris law can be used for estimating the fatigue life of cracked structures. Second, as an alternative design route for infinite life components containing crack like flaws, a tolerable defect approach based on the fatigue threshold has been developed. While many papers have been published dealing with the pure Mode I case, only a few investigations have been concerned with fatigue crack growth under mixed-mode loading conditions and in particular mixed-mode fatigue threshold behavior [*1–5*]. In real engineering situations, however, since there are a variety of structures, flaw geometries, and complex applied loads, the majority of fatigue cracks may extend under a combination of all three crack growth modes. Unfortunately, if pure Mode I results and existing LEFM criteria are used directly in the fatigue design of a component subject to complex applied loads, the design will not be safe in some circumstances. For instance, the crack may grow sufficiently to cause failure even below the estimated thresholds. In addition the real crack growth rate may be larger than that estimated, so that early failure may occur.

In this paper, the threshold and growth of cracks under various combinations of Mode I and Mode II crack-tip displacements are studied from both theoretical and experimental viewpoints. By considering both the plasticity and the local fracture ductility of material around the crack tip, a new expression of fatigue crack growth under mixed mode loading is derived, which gives a satisfactory prediction for the mixed mode threshold curve.

Experimental Method

Two experimental procedures have been used to study mixed mode behavior, (*a*) four-point bend tests on rectangular specimens with skew symmetric application of the loads together with cracks displaced from the axis of symmetry, and (*b*) inclined cracks in cruciform shaped specimens subject to biaxial cyclic stresses.

Details of the two methods for conducting biaxial fatigue crack propagation experiments are given in Refs *5* and *6*, respectively.

Four materials have been tested, namely, AISI 316 stainless steel, DTD 5120 aluminium alloy, Ti-6A-4V, and 1Cr-Mo-V steel. Their mechanical properties are listed in Table 1.

All tests were conducted in laboratory air at room temperature on servohydraulic fatigue machines, operating under load control in the frequency range 15 to 80 Hz (sine wave). Load ratios $R = \sigma_{min}/\sigma_{max}$ of 0.2 and 0.5 were employed. A load increasing technique was used to determine threshold values with crack extension being monitored visually with a $\times 40$ travelling microscope, and simultaneously with a d-c potential drop system. Crack growth increments of 0.02 mm could be discerned readily by these methods.

Two types of starter crack were used. In "slit" specimens, a slot was formed by spark erosion, giving an initial crack of finite width, 0.16 mm. In some tests a fatigue crack was grown from this slot under pure Mode I conditions prior to mixed mode loading, using a load reducing technique down to threshold, to minimize residual stress effects [5]. In both cases, plane-strain conditions existed at the crack tip, since the monotonic plastic zone size was less than one fortieth of the specimen thickness.

Crack Propagation Close to Threshold

Although the mechanical properties of the four materials tested varied considerably, and, in the case of stainless steel, the specimen geometry and the loading system employed were quite different, good agreement between the experimental results has been obtained. Tests have been conducted to evaluate the fatigue thresholds for (*a*) coplanar, mixed mode growth, and (*b*) the formation of a pure Mode I branch crack. These two thresholds may be characterized by lower and upper bound curves, respectively, as shown in Fig. 1, drawn to show the general trend of the data presently available.

TABLE 1—*Mechanical properties.*

Material	Yield Stress (0.2% offset), MPa	Tensile Strength, MPa	Elongation (on 5d), %	Reduction of Area, %	γ_{fu}	γ_{ft}	Mode I Fatigue Threshold (R = 0.2), MN m$^{-3/2}$ ΔK_{thI}	$\Delta K_{thI\rho}$
316 stainless steel	246	595	67	66	1.62	2.50	4.34	5.81
DTD 5120 aluminium alloy	500	560	13	37	0.69	0.7	2.33	2.57
Ti-6Al-4V	930	1032	15 (on 4d)	38	0.72		6.60	4.61
1Cr-Mo-V steel	940	1260	14				6.52	9.84

NOTE—γ_{fu} = fracture ductility in the monotonic tension test.
γ_{ft} = fracture ductility in the monotonic torsion test.
$\Delta K_{thI\rho}$ = threshold for growth from a slot of root radius ρ = 0.08 mm.

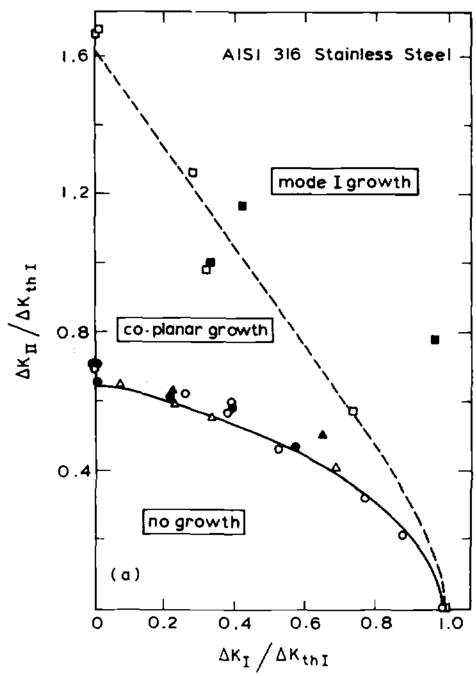

(i) Initiation of coplanar growth △ (bending) ▲ (cruciform), (ii) Mode I branch crack formation in precracked specimen □ (bending) ■ (cruciform), (iii) Initiation of crack growth from a slit ○ (bending) ● (cruciform).
(*a*) stainless steel.
(*b*) DTD 5120 aluminium alloy.
(c) Ti-6Al-4V.
(*d*) 1Cr-Mo-V steel.

FIG. 1—*Mixed mode threshold conditions.*

Below the lower bound no crack growth was detected. Between the curves coplanar growth occurred, although subsequently crack arrest and oxide debris blocking of the crack tip were observed. A Mode I branch appeared when the apparent values of ΔK_I and ΔK_{II} (that is, with no allowance for closure) corresponded to the upper bound curve. However, this line appears to be dependent strongly on crack-tip closure, crack surface contact, rubbing, and oxide blocking [*5*]. In some situations the influence of these effects becomes less important, that is, when the load ratio R is high or the crack surface is quite smooth, so that the upper bound curve approaches the lower bound (Fig. 2). In the case of slit specimens, since both closure and crack surface rubbing effects are minimized, the upper and lower bound curves apparently coincide. This unique curve is then dependent intrinsically on the crack-tip stress-strain field and the fatigue resistance of the material.

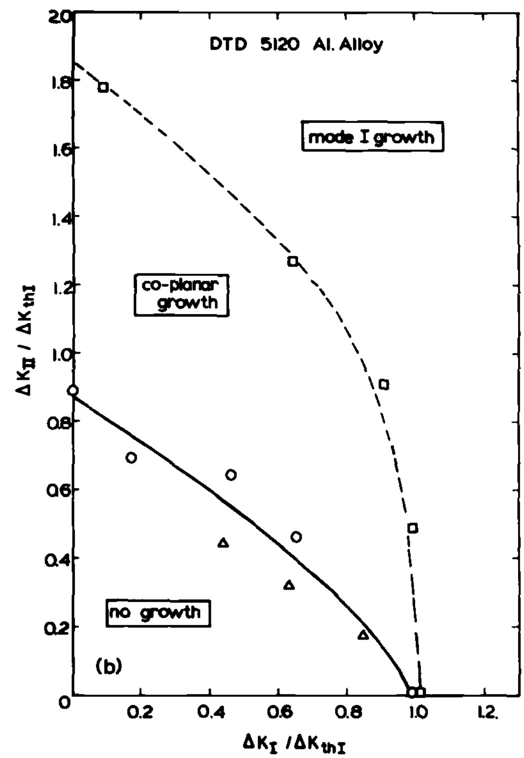

FIG. 1—*Continued.*

Theoretical Analysis of Mixed Mode Thresholds

The Mode I branch crack always initiated on the plane normal to the maximum stress σ_θ, within the original crack tip stress field, once the applied load exceeded a critical value. However, the value of threshold was governed not only by the Mode I displacement, but also by the Mode II component.

In the present paper we define the threshold as a crack growth rate of 2.5×10^{-7} mm/cycle, that is, an average of approximately one atomic spacing per cycle over the crack front. In order to predict the mixed mode threshold curve, it is necessary to understand how crack growth rate changes with the $\Delta K_{II}/\Delta K_I$ ratio.

First, fatigue crack growth is a function of crack-tip reversed plastic deformation. It may be shown from dimensional analysis that, if there is no size effect which may arise from specimen geometry or microstructural features, the crack growth rate is governed by the crack-tip reversed plastic zone size [7]. However, close to threshold the crack grows discontinuously in each individual grain, but

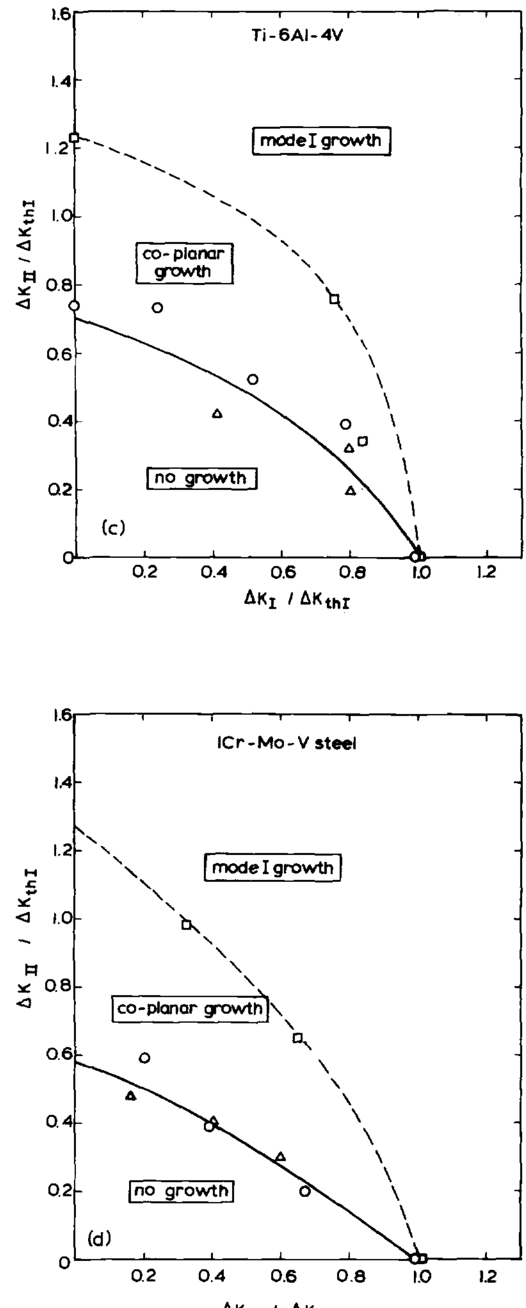

FIG. 1—*Continued.*

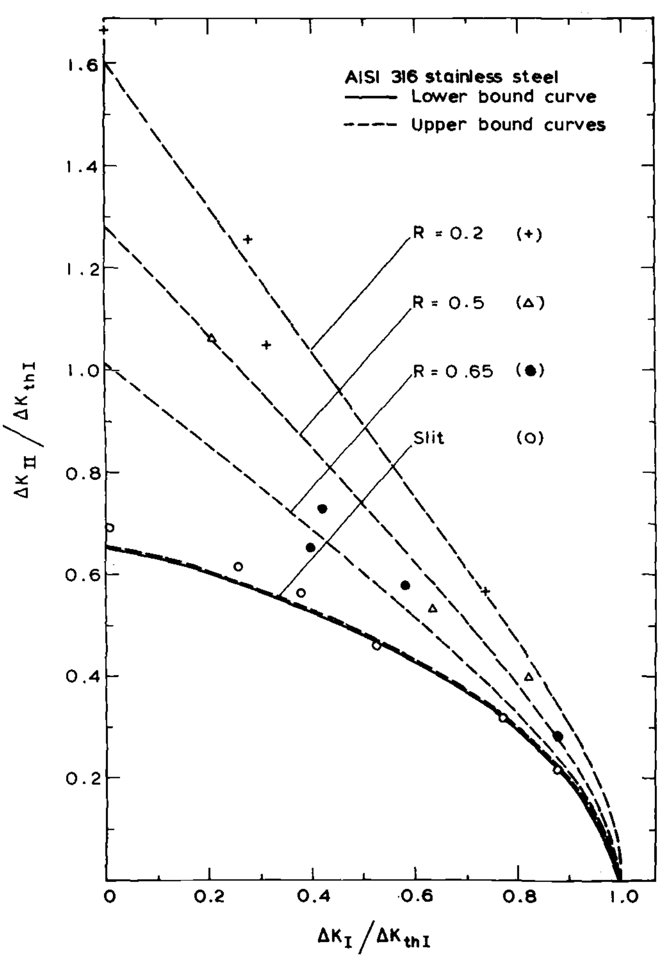

FIG. 2—*The upper bound dependence of mixed mode crack growth on the load ratio* R, *for stainless steel. (Data for* R = *0.65 from Tanaka* [1] *on aluminium).*

for the purpose of assessing the average growth rate across many differently orientated grains, it is still possible to employ a continuum mechanics approach to determine relative plastic zone sizes.

Second, the ductility ahead of the crack tip is an important parameter [*8,9*]. Crack growth rate is believed to be inversely proportional to the true fracture ductility (γ_f), which itself is a linear function of stress state [*10,11*]. In case of fatigue crack growth, we have chosen the ratio of normal stress to shear stress on the plane of maximum shear deformation emanating from the crack tip, that is, $\sigma_\theta(\theta^*)/\tau_{r\theta}(\theta^*)$ [*12,13*], to characterize the crack-tip stress state; this is the plane that provides the greatest contribution to fatigue damage. Thus, the crack growth rate at threshold (2.5×10^{-7} mm/cycle) under combined mode loading conditions can be represented by the equation (see Ref 5)

$$\frac{da}{dN} = k\,\frac{r_p(\theta^*)}{\gamma_f} \tag{1a}$$

where

$$\gamma_f = \gamma_{ft} + (\gamma_{fu} - \gamma_{ft})\,\frac{\sigma_\theta(\theta^*)}{|\tau_{r\theta}(\theta^*)|} \tag{1b}$$

and

$$\begin{aligned} r_p(\theta) = \frac{1}{2\pi\sigma_{ys}^2}\Bigg\{ & \Delta K_I^2 \cos^2\frac{\theta}{2}\left[(1-2\nu)^2 + 3\sin^2\frac{\theta}{2}\right] \\ & + \Delta K_I \Delta K_{II} \sin\theta \left[3\cos\theta - (1-2\nu)^2\right] \\ & + \Delta K_{II}^2\left[3 + \sin^2\frac{\theta}{2}\left((1-2\nu)^2 - 9\cos^2\frac{\theta}{2}\right)\right]\Bigg\} \end{aligned} \tag{1c}$$

where K is a constant that depends on the cyclic deformation behavior of the material alone. The term $r_p(\theta^*)$ is the maximum extent of crack-tip reversed plastic zone, θ^* being chosen to give the maximum value for r_p in Eq 1c. For ideal plasticity, σ_{ys} will be twice the cyclic yield stress, being the effective yield stress following a stress reversal. Parameters γ_{fu} and γ_{ft} are the true fracture ductilities measured as maximum shear strain from monotonic tensile and torsional tests, respectively. In the case of combined Mode I and Mode II loading, according to LEFM close to the crack tip, for $-\pi \leq \theta \leq \pi$

$$\sigma_\theta(\theta) = \frac{K_I}{\sqrt{2\pi r}}\left(\frac{3}{4}\cos\frac{\theta}{2} + \frac{1}{4}\cos\frac{3\theta}{2}\right) + \frac{K_{II}}{\sqrt{2\pi r}}\left(-\frac{3}{4}\sin\frac{\theta}{2} - \frac{3}{4}\sin\frac{3\theta}{2}\right) \tag{2a}$$

$$\tau_{r\theta}(\theta) = \frac{K_I}{\sqrt{2\pi r}}\left(\frac{1}{4}\sin\frac{\theta}{2} + \frac{1}{4}\sin\frac{3\theta}{2}\right) + \frac{K_{II}}{\sqrt{2\pi r}}\left(\frac{1}{4}\cos\frac{\theta}{2} + \frac{3}{4}\cos\frac{3\theta}{2}\right) \tag{2b}$$

If ΔK_{thI}, γ_{fu} and γ_{ft} can be measured, then the mixed mode threshold corresponding to any $\Delta K_{II}/\Delta K_I$ ratio can be estimated [5] by solving Eqs 1 and 2. The theoretical curve calculated shows agreement with experimental results, as shown in Fig. 3. Aluminum alloy has a very low resistivity, so some measured

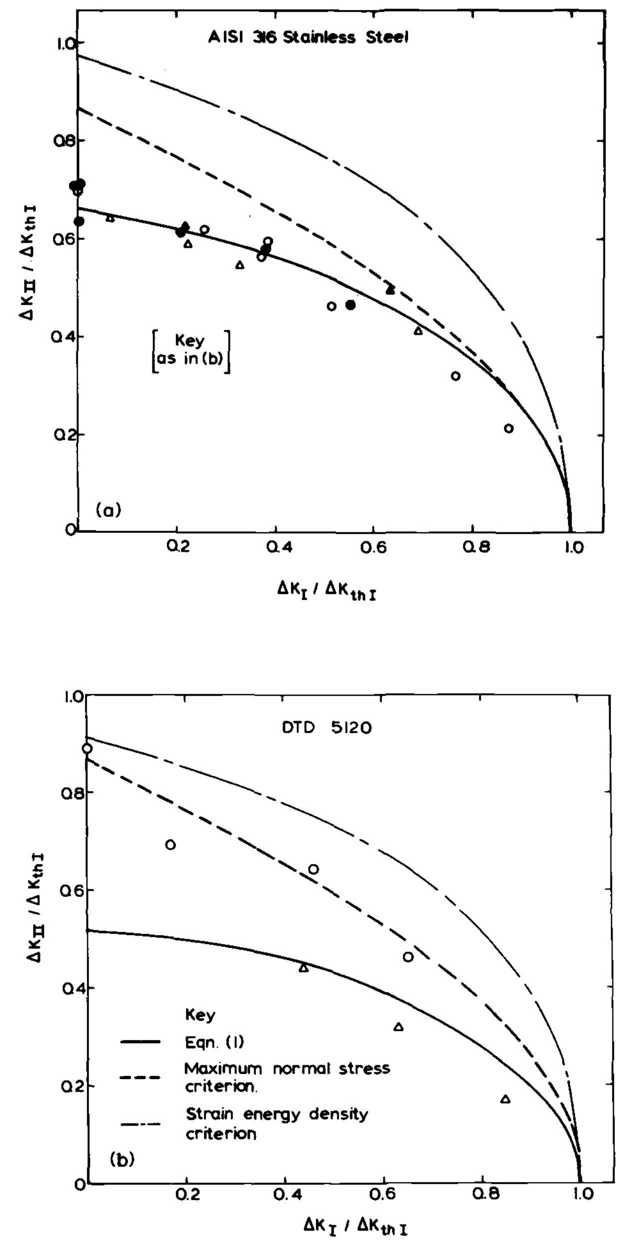

(i) Initiation of coplanar growth in precracked specimens △ (bending) ▲ (cruciform).
(ii) Crack initiation from a slit ○ (bending) ● (cruciform).
(*a*) Stainless steel (ν = 0.29).
(*b*) DTD 5120 aluminium alloy (ν = 0.33).

FIG. 3—*A comparison of theoretical predictions with experimental results.*

points are high because of the difficulty of detecting crack growth from the specimen surface. For design purposes, this approach gives a safer prediction than other theories previously used, for example, the minimum strain energy density and maximum normal stress criteria [2,5]. For the maximum normal stress, the value of θ in Eq 2*a* is determined from $\partial\sigma_\theta/\partial\theta = 0$, which gives, for a critical value of ($\sqrt{2\pi r} \cdot \sigma_\theta$), a predicted threshold for mixed mode loading as plotted in Fig. 3.

Compared to the plane-strain conditions used here, the theoretical curve for the case of plane stress may be higher, since the increase of crack-tip plastic zone with $\Delta K_{II}/\Delta K_I$ is not so great. As shown in Table 2, if $\Delta K_{II} = \Delta K_I$, in the plane-strain case $r_{pII}(\theta^*)$ is 3.7 times larger than $r_{pI}(\theta^*)$, while in the plane-stress case the difference between $r_{pII}(\theta^*)$ and $r_{pI}(\theta^*)$ is 2.25. As an example, for AISI 316 stainless steel, in plane-strain $\Delta K_{thII} = 0.65\ \Delta K_{thI}$ (Fig. 1*a*) so that one would expect $\Delta K_{thII} = 0.89\ \Delta K_{thI}$ for plane stress.

Inclined Crack Growth Under Biaxial Loading

The rate of crack growth was studied for the stainless steel over a range of stress conditions in biaxially loaded plates with a central inclined crack, as illustrated in Fig. 4 and listed in Table 3. It was always observed that the branch crack appeared in the direction corresponding to the maximum normal stress, σ_θ, in the crack-tip stress field. However, as it grew the direction changed because the crack followed the path of maximum ΔK_I (and $\Delta K_{II} \rightarrow 0$), eventually becoming a pure Mode I crack normal to the maximum principal stress range axis of the applied stress field.

In order to calculate the stress-intensity factors (SIF) of the branch crack, an appropriate method has been developed. First of all, the observed propagating path is divided into several linear segments (Fig. 5*a*). The calculation procedure is as follows:

1. Estimate the inclined crack SIF ΔK_{I0} and ΔK_{II0} (Fig. 5*b*, crack *C*-0) from

$$\Delta K_I = \Delta\sigma\ (\sin^2\alpha + \Lambda\cos^2\alpha)\sqrt{\pi a} \tag{3a}$$

$$\Delta K_{II} = \Delta\sigma\ (1 - \Lambda)\sin\alpha\cos\alpha\sqrt{\pi a} \tag{3b}$$

2. Calculate the kinked crack (*C*-0-1) tip SIF $\Delta\tilde{K}_{I1}$ and $\Delta\tilde{K}_{II1}$, by using Chatterjee's method [*14*] (Fig. 5*c*) for a short branch crack.

3. Derive an equivalent crack a_{effi} ($i = 1$) with the SIF $\Delta\tilde{K}_{Ii}$, $\Delta\tilde{K}_{IIi}$ and normal stress $\Delta\sigma_{\alpha i}$ (Fig. 5*d*),

$$a_{effi} = \frac{1}{\pi}\left(\frac{\Delta\tilde{K}_{Ii}}{\Delta\sigma_{\alpha i}}\right)^2 \tag{4a}$$

TABLE 2—*A comparison of plane-stress and plane-strain cases for $\nu = 1/3$.*

Conditions		θ^*	$\tau_{max}(\theta^*)$	$\sigma_\theta(\theta^*)/\tau_{r\theta}(\theta^*)$	$r_p(\theta^*)$
Pure Mode I	plane stress	70.5°	$0.645 \frac{K_I}{\sqrt{2\pi r}}$	1.415	$1.333 \left(\frac{\Delta K_I^2}{2\pi\sigma_{ys}^2}\right)$
	plane strain	87.88°	$0.5 \frac{K_I}{\sqrt{2\pi r}}$	1.037	$0.8066 \left(\frac{\Delta K_I^2}{2\pi\sigma_{ys}^2}\right)$
Pure Mode II	plane stress	0°	$\frac{K_{II}}{\sqrt{2\pi r}}$	0	$3\left(\frac{\Delta K_{II}^2}{2\pi\sigma_{ys}^2}\right)$
	plane strain	0°	$\frac{K_{II}}{\sqrt{2\pi r}}$	0	$3\left(\frac{\Delta K_{II}^2}{2\pi\sigma_{ys}^2}\right)$

$$\Delta\sigma_{\alpha i} = \Delta\sigma\,(\sin^2 \alpha_i + \Lambda \cos^2 \alpha_i) \tag{4b}$$

where α_i is the measured crack angle. The term a_{eff} is decided by $\Delta\tilde{K}_{Ii}$ alone since $\Delta\tilde{K}_{IIi}$ was always a small quantity.

4. Calculate kinked crack (C_I-1-2) tip SIF $\Delta\tilde{K}_{I2}$ and $\Delta\tilde{K}_{II2}$ (Fig. 5*d*).
5. Repeat Steps 2 to 4 for $i = 2, 3, \ldots n$.
6. Multiply $\Delta\tilde{K}_{Ii}$ and $\Delta\tilde{K}_{IIi}$ by the width correction factor $\sqrt{\sec(\pi x/2W)}$ where x is the distance of the crack tip from the centerline of the specimen.
7. Calculate $r_{pi}(\theta^*)$ corresponding to each crack increment using Eq 1*c*.

The stress-intensity factors obtained from this approximate method were compared with those from two separate finite element calculations, one based on the energy release rate (G^Δ) estimation and the other performing a least squares analysis using the Williams terms of the displacement distribution in the neighborhood of the crack tip. These showed that agreement was within 10% error.

The relationship between crack growth rate da/dN and $r_p(\theta^*)$, as illustrated in Fig. 6, shows that for the same value of $r_p(\theta^*)$ different crack speeds are obtained under various biaxial stresses, and the differences become greater as the crack extends. This phenomenon may be interpreted in terms of the T-stress effect, as shown next.

T-stress Effect

According to LEFM, at low levels of stress the stress field close to a crack tip can be described with sufficient accuracy in terms of the stress-intensity factors. However, at moderate levels of stress, the T-stress becomes significant in the crack-tip field and should not be omitted arbitrarily [*15*]. The T-stress [*16*], the final term in Eq 5*b*, is the next most significant term in the series expansion for σ_x after the singular terms, where σ_x is the stress parallel to the crack. If terms of order $r^{1/2}$ and greater are omitted, crack-tip stresses are given

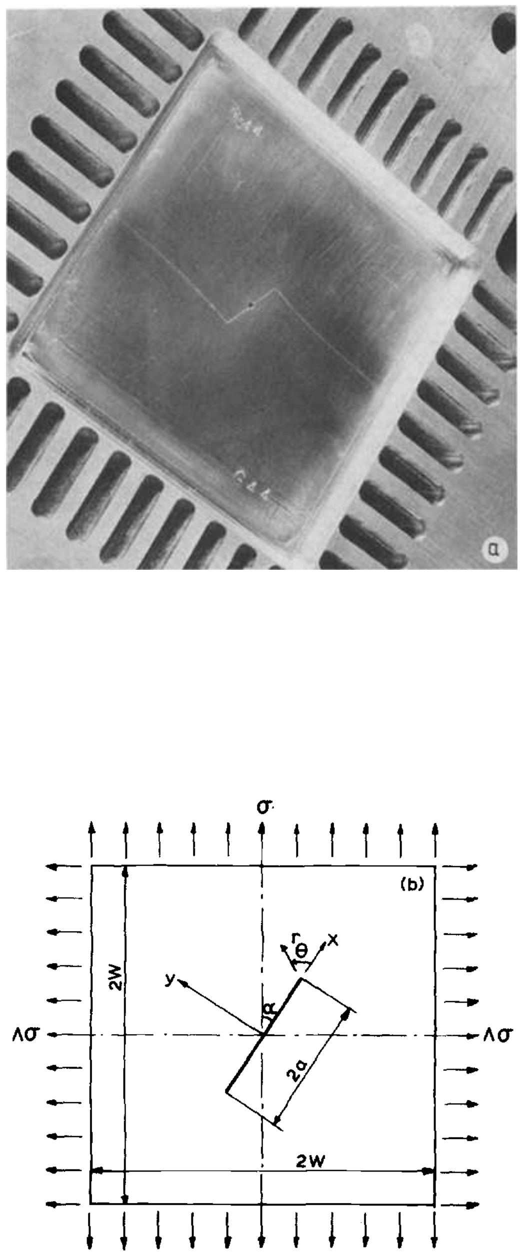

(*a*) Broken specimen.
(*b*) Applied stresses.

FIG. 4—*Biaxially loaded plate with a central inclined crack.*

TABLE 3—*Testing conditions of inclined crack growth in Type 316 stainless steel, for* R = *0.2.*

	Specimen			Loading						At a_o Tip			
Test	B, mn	a_o, mm	α, deg	Phase angle ϕ, deg	Λ	σ_{xmax}, MPa	σ_{xmin}, MPa	σ_{xmax}, MPa	σ_{xmin}, MPa	ΔK_{IO}, MN m$^{-3/2}$	ΔK_{IIO}, MN m$^{-3/2}$	$\Delta K_{IIO}/\Delta K_{IO}$	θc, deg
1	4.05	5.01	45	180	−1	−12.22	−61.11	61.11	12.22	0	6.18	∞	−74
2	3.94	7.52	45	180	−0.5	−6.13	−30.57	61.11	12.22	1.88	5.63	3	−65
3	4.17	8.26	22.5	180	−0.1716	−2.89	−14.46	84.24	16.85	0	4.54	∞	−77
4	4.15	8.20	22.5	0	0.082	7.67	1.54	93.53	18.71	2.62	3.93	1.5	−67
5	4.08	4.67	45	0	0.1	11.34	2.26	113.42	22.57	6.08	4.98	0.82	−52

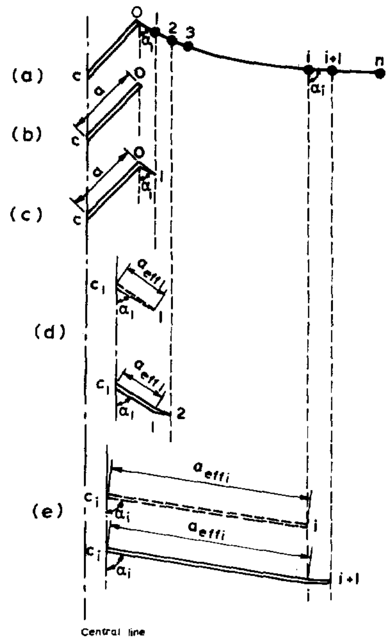

FIG. 5—*A diagrammatic sketch of the approximate* K-*calculation method.*

by

$$\sigma_y = \frac{K_I}{\sqrt{2\pi r}} \cos\frac{\theta}{2}\left[1 + \sin\frac{\theta}{2}\sin\frac{3\theta}{2}\right] + \frac{K_{II}}{\sqrt{2\pi r}} \sin\frac{\theta}{2}\cos\frac{\theta}{2}\cos\frac{3\theta}{2} \quad (5a)$$

$$\sigma_x = \frac{K_I}{\sqrt{2\pi r}} \cos\frac{\theta}{2}\left[1 - \sin\frac{\theta}{2}\sin\frac{3\theta}{2}\right] - \frac{K_{II}}{\sqrt{2\pi r}} \sin\frac{\theta}{2}\left[2 + \cos\frac{\theta}{2}\cos\frac{3\theta}{2}\right] + \sigma(1 - \Lambda)\cos 2\alpha \quad (5b)$$

$$\tau_{xy} = \frac{K_I}{\sqrt{2\pi r}} \sin\frac{\theta}{2}\cos\frac{\theta}{2}\cos\frac{3\theta}{2} + \frac{K_{II}}{\sqrt{2\pi r}} \cos\frac{\theta}{2}\left[1 - \sin\frac{\theta}{2}\sin\frac{3\theta}{2}\right] \quad (5c)$$

Although the *T*-stress has no influence on the SIF, since it is a nonsingular stress parallel to the crack plane (Eq 5*b*), it does affect the crack-tip plasticity [*17*]. For equibiaxial loading the *T*-stress contribution is zero ($\Lambda = 1$), but as Λ decreases to -1 for pure shear, the plastic zone size increases above that predicted by Eq 1*c*. Since larger plastic zones give higher growth rates, a spread of data is observed in Fig. 6, with the shear loading giving the highest growth rates. However, no such dependence on *T*-stress was shown for the threshold values, as listed in Table 4. In Table 4, tests 1 to 4 give the Mode II threshold

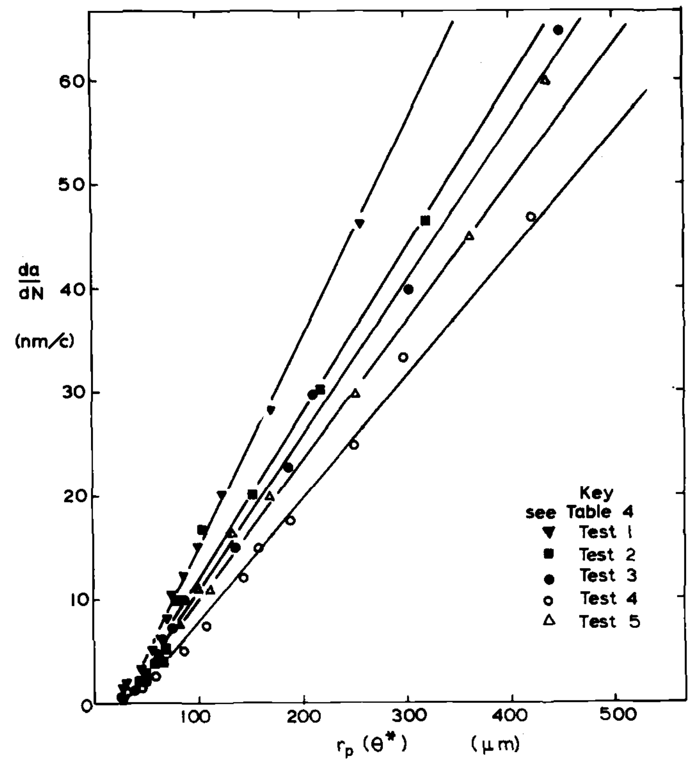

FIG. 6—*Relationship between crack growth rate and crack-tip reversed plastic zone size calculated from SIF alone.*

for this material, but the Mode I threshold values are derived from a different batch of Type 316 stainless steel [*6*]. For either mode, threshold is constant within experimental error.

The increased effect of *T*-stress in the crack propagation tests is due to the higher stress levels employed (Table 3). In this case a new equation should be derived in place of Eq 1*c*, which will include additional terms for the *T*-stress. This is readily obtained from Eq 5 by using the von Mises yield criterion for plane-strain conditions

$$(\sigma_x + \sigma_y)^2 (1 - \nu + \nu^2) - 3\sigma_x\sigma_y + 3\tau_{xy}{}^2 = \sigma_{ys}{}^2 \qquad (6)$$

and may be solved numerically to obtain $r_p'(\theta^*)$, for any given value of *T*-stress. The resultant plastic zone size, $r_p'(\theta^*)$ is plotted in Fig. 7, showing that much of the divergence in results in Fig. 6 is actually due to the *T*-stress.

Equation 1*a* suggests that one should obtain a single straight line in Fig. 7, passing through the origin, if r_p' is the true plastic zone size. This equation was previously suggested for Mode I plane-stress cracking [*7*], based on a model proposed by Pook and Frost [*18*], and it may be rewritten for plane-strain

TABLE 4—*Thresholds of AISI 316 stainless steel under different T-stresses for crack growth from a slit.*

Specimen				Loading, MPa						Thresholds			*T*-Stress, MPa	
Test	B, mm	a_o	α, deg	Phase angle ϕ, deg	Λ	σ_{xmax}	σ_{xmin}	σ_{ymax}	σ_{ymin}	ΔK_{thI} MN m$^{-3/2}$	ΔK_{thII}, MN m$^{-3/2}$	θc, deg	T_{max}	T_{min}
1	3.93	8.20	22.5	180	−0.172	−2.51	−12.56	72.95	14.59		3.88	−73	60.46	12.09
2	4.17	8.26	22.5	180	−0.178	−2.69	−13.47	76.14	15.68		4.22	−77	63.36	12.99
3	4.30	8.90	33.75	180	−0.447	−4.19	−20.95	46.90	9.38		4.20	−72	25.97	5.19
4	4.05	5.02	45	180	−1.0	−8.31	−41.50	41.50	8.31		4.20	−74	0	0
10	4.00	2.02	90	0	0.090	5.37	−0.61	66.70	0.08	5.69		0	−61.33	−0.69
11	3.96	2.06	90	0	0.997	62.64	0.06	62.58	−0.16	5.23		0	0.06	0.22
12	4.10	1.98	90	180	−0.992	62.90	0.27	62.94	−0.17	5.09		0	−62.67	63.07

NOTE—For $\phi = 0$: $T_{max} = (\sigma_{ymax} - \sigma_{xmax}) \cos 2\alpha$, and $T_{min} = (\sigma_{ymin} - \sigma_{xmin}) \cos 2\alpha$.
For $\phi = 180°$: $T_{max} = (\sigma_{ymax} - \sigma_{xmin}) \cos 2\alpha$, and $T_{min} = (\sigma_{ymin} - \sigma_{xmax}) \cos 2\alpha$.

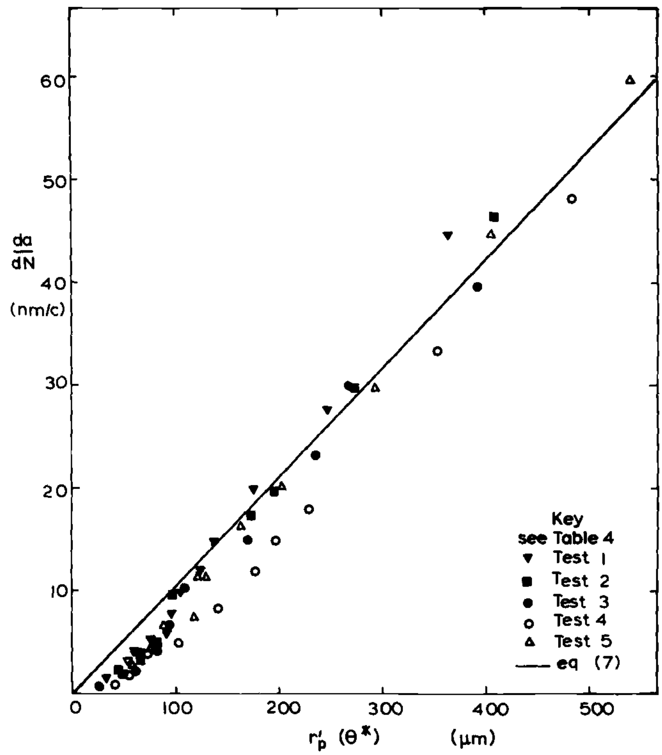

FIG. 7—*Relationship between crack growth rate and the true plastic zone size.*

conditions using $r_p'(\theta^*)$ as defined in Table 2,

$$\frac{da}{dN} = \frac{14}{0.8066}\left[\frac{\sigma_{ys}}{E}\right]^2 r_p'(\theta^*) \tag{7}$$

This equation is plotted in Fig. 7 with a Young's modulus of 200 GPa and σ_{ys} taken as twice the monotonic yield stress. Clearly the experimental points approximate to a straight line equation of this form, indicating that the true plastic zone size is a useful parameter for relating mixed mode crack propagation data to the results of standard Mode I tests.

Fracture ductility does not appear in Eq 7 because it only applies to Mode I crack extension. Close to the crack tip the *T*-stress is insignificant in determining the biaxial state on the shear plane, so that the dependence of crack growth rate on biaxiality is governed by plastic zone size alone.

Conclusions

1. Two types of fatigue threshold are found for mixed mode loading, (*a*) for coplanar, mixed mode growth, and (*b*) for the formation of a Mode I branch crack.

2. Cracks follow a path that gives the maximum Mode I component once a Mode I branch has formed.

3. T-stress has no obvious effect on threshold, but, at higher stresses, a negative T-stress gives faster crack propagation rates in fatigue.

4. The rate of crack growth is proportional to the true plastic zone size, modified by a fracture ductility term when coplanar mixed mode growth takes place.

Acknowledgments

The authors would wish to thank Professor B. A. Bilby and Professor T. C. Wang for their advice in developing the K-calculation method, and also G. E. Cardew and M. R. Goldthorpe for their finite element analyses. Thanks are due to the Electric Power Research Institute, Royal Aeronautical Establishment, Rolls Royce, and Central Electricity Generating Board (CEGB) for supplying the materials, and to the Nuclear Regulatory Commission and Science and Engineering Research Council for financial support for the project. Dr. Gao Hua and N. Alagok are visitors in the University of Sheffield under exchange agreements with the Royal Society/Chinese Academy of Sciences, and the British Council, respectively. Dr. M. W. Brown is a CEGB Research Fellow.

References

[1] Tanaka, K., *Engineering Fracture Mechanics*, Vol. 6, No. 3, Oct. 1974, pp. 493–507.
[2] Sih, G. C. and Barthelemy, B. M., *Engineering Fracture Mechanics*, Vol. 13, No. 3, 1980, pp. 439–451.
[3] Pook, L. P., *International Journal of Fracture*, Vol. 13, No. 6, Dec. 1977, pp. 867–869.
[4] Pook, L. P. in *Proceedings*, International Symposium on Fatigue Thresholds, Stockholm, 1981, Vol. 3, pp. 46:1–46:29.
[5] Gao, H., Brown, M. W. and Miller, K. J., *Fatigue of Engineering Materials and Structures*, Vol. 5, No. 1, 1982, pp. 1–17.
[6] Brown, M. W. and Miller, K. J., this publication, pp. 135–152.
[7] Brown, M. W., Liu, H. W., Kfouri, A. P., and Miller, K. J. in *Proceedings*, 5th International Conference on Fracture, Pergamon, Oxford, 1981, Vol. 2, pp. 891–898.
[8] McClintock, F. A., *Fracture of Solids*, Wiley, New York, 1963, p. 65.
[9] McEvily, A. J. Jr., and Johnston, T. L. in *Proceedings*, 1st International Conference on Fracture, Japan Society for Strength and Fracture of Materials, 1965, Vol. 2, p. 515.
[10] Bridgman, P. W., *Studies in Large Plastic Flow and Fracture*, Metallurgy and Metallurgical Engineering Series, McGraw-Hill, New York, 1952.
[11] Brandes, M. in *Mechanical Behaviour of Materials under Pressure*, Elsevier, London, 1970, pp. 236–298.
[12] Laird, C. in *Fatigue Crack Propagation, ASTM STP 415*, American Society for Testing and Materials, Philadelphia, 1967, pp. 131–168.
[13] Tomkins, B., *Philosophical Magazine*, Vol. 18, No. 155, 1968, pp. 1041–1066.
[14] Chatterjee, S. N., *International Journal of Solids and Structures*, Vol. 11, No. 5-A, 1975, pp. 521–538.
[15] Eftis, J. and Subramonian, N., *Engineering Fracture Mechanics*, Vol. 10, No. 1, 1978, pp. 43–67.
[16] Rice, J. R., *Journal of Mechanics and Physics of Solids*, Vol. 22, 1974, pp. 17–27.
[17] Kfouri, A. P. and Miller, K. J. in *Three Dimensional Constitutive Relations and Ductile Fracture*, S. Nemat-Nasser, ed., North Holland, Amsterdam, 1981, pp. 83–109.
[18] Pook, L. P. and Frost, N. E., *International Journal of Fracture*, Vol. 9, 1973, pp. 53–61.

Robert O. Ritchie,[1] *Frank A. McClintock,*[2] *Elmar K. Tschegg,*[3] *and Hamid Nayeb-Hashemi*[4]

Mode III Fatigue Crack Growth Under Combined Torsional and Axial Loading

REFERENCE: Ritchie, R. O., McClintock, F. A., Tschegg, E. K., and Nayeb-Hashemi, H., "**Mode III Fatigue Crack Growth Under Combined Torsional and Axial Loading,**" *Multiaxial Fatigue, ASTM STP 853,* K. J. Miller and M. W. Brown, Eds., American Society for Testing and Materials, Philadelphia, 1985, pp. 203–227.

ABSTRACT: An investigation has been made into the propagation of fatigue cracks in Mode III (anti-plane shear) in circumferentially notched cylindrical specimens subjected to cyclic torsion with and without small superimposed static tension loading. Studies were performed in a range of low-alloy steels of yield strengths varying from 310 to 1625 MN/m^2, with the objective of characterizing both constant amplitude and variable amplitude Mode III crack growth behavior. Rates of fatigue crack propagation in Mode III were found to be characterized uniquely by the Mode III cyclic crack tip displacement (ΔCTD_{III}) or the plastic strain intensity range ($\Delta\Gamma_{III}$) for elastic/plastic and fully plastic conditions, *only* if allowance was made for friction, rubbing, and interlocking between sliding crack surfaces (crack surface interference) through superposition of small axial loads. Such Mode III crack advance is envisaged in terms of Mode II shear coalescence of microcracks initiated at inclusions in the immediate vicinity of, and parallel to, the main crack front, consistent with micromechanical modelling studies incorporating either instantaneous crack tip displacement or damage accumulation arguments. The application of such models to the prediction of Mode III fatigue crack propagation behavior under both constant amplitude and simple variable amplitude loading spectra is briefly reviewed.

KEY WORDS: fatigue (materials), cracking (fracturing), crack propagation, Mode III, torsional loading, alloy steels, crack tip displacement, plastic strain intensity, damage accumulation, elastic/plastic fracture mechanics, mean tension

Nomenclature

A Constant in Coffin-Manson law (Eq 9)

b Length of crack step during Mode II linkage of voids

[1]Formerly, associate professor, Massachusetts Institute of Technology, Cambridge, MA 02139; currently, professor, Materials and Molecular Research Division, Lawrence Berkeley Laboratory, and Department of Materials Science and Mineral Engineering, University of California, Berkeley, CA 94720.

[2]Professor, Department of Mechanical Engineering, Massachusetts Institute of Technology, Cambridge, MA 02139.

[3]Formerly, visiting associate professor, Massachusetts Institute of Technology, Cambridge, MA 02139; currently, Technical University Vienna, Institute of Applied and Technical Physics, A-1040, Vienna, Austria.

[4]Formerly, research assistant, Massachusetts Institute of Technology, Cambridge, MA 02139; currently, assistant professor, Department of Mechanical Engineering, Northeastern University, Boston, MA 02115.

Copyright© 1985 by ASTM International www.astm.org

c	Total crack length (including notch)
C_{III}	Material constant in Mode III crack growth relationship (Eq 8)
CTD_i	Crack tip displacement in Mode i = I, II, III
ΔCTD_i	Range of crack tip displacement in Mode i = I, II, III
d	Exponent in Coffin-Manson law (Eq 9)
$(dc/dN)_i$	Fatigue crack growth increment per cycle in Mode i = I, II, III
e_i	Exponent relating displacement increment across an inclusion to its aspect ratio (Eq 7)
F_{II}	Constant relating Mode II growth rate to ΔCTD_{II} (Eq 6)
G	Shear modulus
K_i	Stress intensity factor in Mode i = I, II, III
ΔK_i	Range of stress-intensity factor in Mode i = I, II, III
k	von Mises shear yield strength
L	Distance grown by inclusion cracks before coalescence
l_i	Length of inclusion crack
ΔM	Applied torque range
M_L	Limit torque
N	Number of cycles
N_{II}	Number of cycles to linkup inclusion cracks
N_{IIb}	Number of cycles to grow Mode II crack across crack step b
R	Load ratio, ratio of minimum to maximum load (or torque)
r	Radial coordinate measured from specimen axis (Fig. 3)
r_N	Uncracked ligament radius of specimen (Figs. 2 and 3)
r_0	External radius of specimen
r_p	Radius from specimen axis to boundary of plastic zone (Fig. 3)
r_y	Cyclic plastic zone size
Q	Strain concentration, defined as exp(Q)
UTS	Tensile strength
v_f	Volume fraction of inclusions
w	Width of inclusion crack
Y	Tensile yield strength (monotonic)
Y_c	Tensile yield strength (cyclic)
Γ_{III}	Plastic strain intensity (Eq 2)
$\Delta\Gamma_{III}$	Plastic strain intensity range
γ	Shear strain
γ_f	Monotonic fracture strain
$\Delta\gamma$	Shear strain range
$\Delta\phi$	Crack mouth rotation
τ	Nominal shear stress
ρ	Characteristic microstructural dimension

Compared to the large volume of information on the growth of fatigue cracks under Mode I (tensile opening) conditions (for a recent review, see Ref *1*), experimental studies on fatigue crack propagation in Mode III (anti-plane shear) are comparatively rare in the literature. Early analytical work by McClintock and co-workers [*2–6*] on the problem of longitudinal cracks in torsionally loaded samples under fully plastic and elastic-plastic conditions led to the development of damage accumulation models for Mode III crack advance, where the crack was considered to grow at a rate consistent with the damage, or fraction of life expended, remaining at unity at some microstructural distance ρ (related to the mean inclusion spacing) ahead of the crack tip [*5*]. Later studies generalized these models to predict Mode III growth rates as a function of plastic zone size, utilizing failure criteria based either on accumulated strain or Coffin-Manson damage at the critical microstructural distance ρ [*6*].

More recently the question of Mode III fatigue crack growth has been reexamined in the context of fracture mechanics where experimental crack propagation behavior has been principally examined as the radially inward concentric cracking of circumferentially notched cylindrical bars loaded in cyclic torsion [*7–16*]. Based on studies on several low-alloy steels [*8,9*] and a 6061-T6 aluminum alloy [*10*] it appeared that the rate of Mode III crack extension $(dc/dN)_{III}$ could be power-law related to the stress intensity range ΔK_{III}. However, the uniqueness and generality of such correlations may be questioned in terms of (*a*) the problem of rubbing and interlocking between sliding fracture surfaces in anti-plane shear (termed crack surface interference) [*11–13*] and (*b*) the validity of a linear elastic (that is, ΔK_{III}) characterization for Mode III cracking, which is a fracture mode promoted by extensive plasticity [*8,12*].

In the present paper, the role of superimposed axial loads in influencing Mode III fatigue crack growth in cyclic torsion is examined in the light of experimental crack growth data on 4340, 4140, A469, and A470 low-alloy steels, ranging in yield strength from 310 to 1625 MN/m^2. Particular attention is paid to the characterization of Mode III crack growth rates in terms of fracture mechanics concepts and the associated role of crack surface interference with respect to the fracture morphologies involved. The experimental crack growth behavior is described in terms of recent micromechanical models for Mode III crack advance which incorporate either instantaneous crack tip displacements or damage accumulation arguments. Crack extension in Mode III is considered to occur via the Mode II coalescence of microcracks initiated at inclusions in the immediate vicinity of, and parallel to, the main Mode III crack front. The success of these models in predicting rates of Mode III crack advance under constant amplitude and simple variable amplitude loading spectra is briefly discussed.

Experimental Measurement of Mode III Crack Growth Rates

Figure 1 indicates the state of stress and the corresponding modes of failure of a cylindrical bar loaded in cyclic torsion. In the long-life/low-stress regime (typically for applied shear stresses τ less than 70% of yield k) helical failures occur in Mode I at ±45° to the axis of the shaft along surfaces of maximum tensile stress (akin in the monotonic sense to the torsional fracture of chalk). In

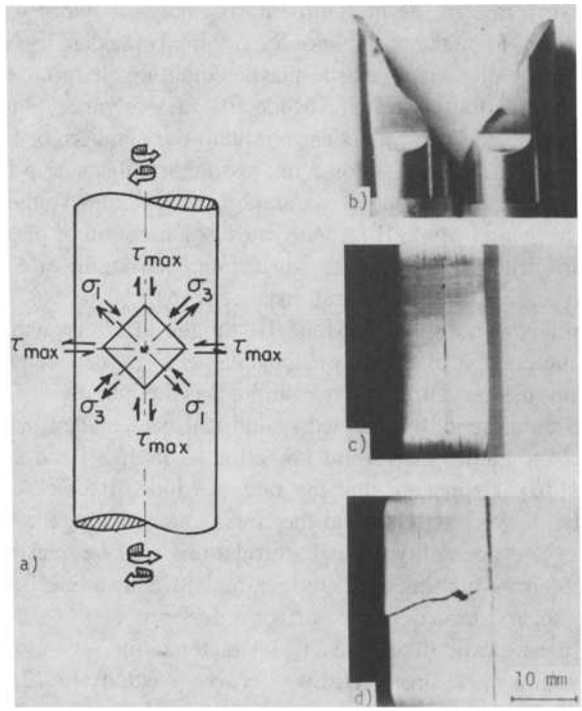

FIG. 1—(a) *State of stress and modes of failure for a torsionally loaded unnotched solid cylindrical bar, showing* (b) *Mode I tensile cracking at* $\tau/k \approx 0.5$, (c) *Mode III + II longitudinal shear cracking at* $\tau/k \approx 1$, *and* (d) *Mode III + II radial shear cracking at* $\tau/k \approx 0.9$.

the short-life/high-stress regime (typically $\tau/k \gtrsim 0.85$), failures occur along transverse or longitudinal shear surfaces which are Mode II on the surface and Mode III in the interior (akin to the torsional fracture of plasticene) [*8*]. Accordingly, to promote crack growth in Mode III and facilitate the process of crack monitoring, most recent studies [*7–9,11–17*] have been performed with circumferentially notched cylindrical specimens where the radially inward concentric growth is Mode III in torsion and Mode I in tension.

In the present study, such specimens of AISI 4340, AISI 4140, ASTM A469, and ASTM A470 steels (of composition and mechanical properties listed in Tables 1 and 2, respectively) were cycled on a computer-controlled Instron tension-torsion servohydraulic testing machine at zero mean torque (load ratio $R = -1$) with a frequency of 1 Hz (sine wave).[5] Specimen dimensions are shown in Fig. 2. Although simple in geometry, the circumferentially notched specimen is extremely prone to misalignment problems which induce undesired bending moments and hence cause asymmetrical crack growth. Since the typical alignment

[5]Additional data for Figs. 5 and 6 were obtained with a Baldwin rotating mass testing machine operating under constant torsional amplitude at 30 Hz [*13*].

TABLE 1—*Chemical composition in weight percent of low-alloy steels investigated.*

	C	Mn	Ni	Cr	Mo	Si	P	S	Cu	V
AISI 4340	0.40	0.78	1.77	0.81	0.25	0.26	0.007	0.013	0.14	...
AISI 4140	0.40	0.80	...	1.00	0.20	0.20	0.010	0.015	...	...
ASTM A469	0.25	0.30	3.25	1.75	0.40	0.10	0.015	0.015	...	0.11
ASTM A470	0.26	0.28	3.47	1.73	0.39	0.07	0.006	0.003	...	0.09

TABLE 2—*Monotonic and cyclic strength levels for low-alloy steels at ambient temperatures. Numbers in parentheses ( ) derived from Mises yield criterion.*

Steel	Yield Strength, MN/m^2			Maximum Stress at Ultimate Tensile Strength, MN/m^2	
	Monotonic Tensile, Y	Cyclic Tensile, Y_c	Monotonic Shear, k	Monotonic Tensile	Monotonic Shear
AISI 4340 (T200)[a]	1625	...	(938)	2080	(1201)
AISI 4340 (T650)[a]	956	589	(552)	1076	(621)
AISI 4140	310	250	(179)	590	(340)
ASTM A469	621	...	(358)	721	(416)
ASTM A470	764	...	(441)	879	(507)

[a]Quenched and tempered at 200 and 650°C, respectively.

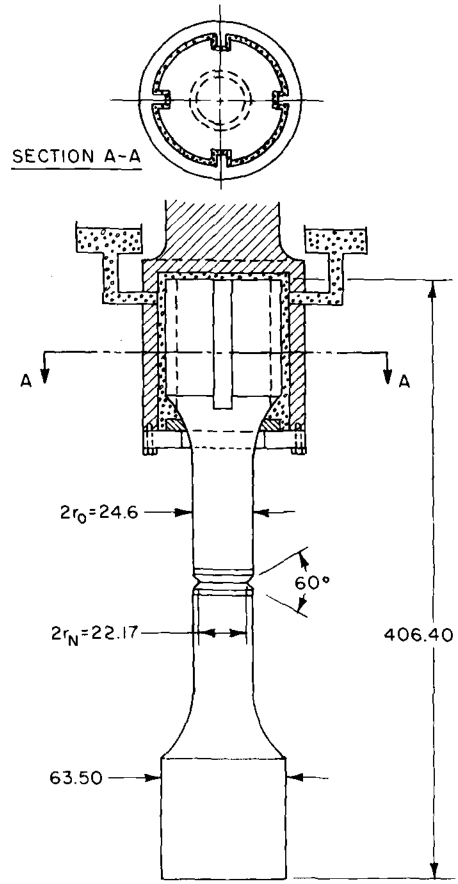

FIG. 2—*Circumferentially notched solid cylindrical torsion specimen for Mode III fatigue crack propagation tests, showing torsional Wood's metal pot for alignment. Dimensions in millimetres.*

accuracy in standard testing machines (that is, to within ~0.02–0.05 mm) is insufficient to prevent such problems, test specimens in the current study were loaded through specially designed torsional Wood's metal grips. A schematic diagram of the grips and actual test geometry is shown in Fig. 2, and, with such an arrangement, symmetrical radial cracking was consistently obtained.

Radial crack extension was continuously monitored using d-c electrical potential methods [*17*]. Once again problems can arise with this test geometry in torsion due to electrical shorting between sliding fracture surfaces in the wake of the crack tip. This problem, however, was minimized in the current work by superposition of the applied axial load to the cyclic torques. For tests under pure cyclic torsion, a small axial load was applied periodically, while the test was stopped, to permit electrical potential crack length measurements. Full details of these procedures are described in Ref *17*.

To provide a wide range of loading conditions to assess the validity of various crack growth parameters, tests were performed under a variety of conditions, namely, at a constant torque range (ΔM), at variable torque range where ΔM was changed periodically, at a constant ratio of torque range to net section limit torque, based on the cyclic yield strength ($\Delta M/M_L$), and at constant range of crack mouth rotation ($\Delta\phi$), monitored using a twist meter of 25.4 mm gage length. Crack growth rates were computed by applying finite difference procedures to data for crack length, c at various numbers of cycles, N.

After testing, specimens were broken open at $-196°C$ and examined optically and in the scanning electron microscope.

Fracture Mechanics Characterization of Mode III Crack Growth Rates

For small-scale yielding, Mode III crack growth rates were characterized in terms of the stress-intensity range (ΔK_{III}) and the cyclic crack tip displacements (ΔCTD_{III}). The respective solutions for the circumferentially notched cylindrical geometry were obtained from Refs [*18,19*], and are listed elsewhere [*8,12,14*]. Where required, the Mode I solutions for the stress intensity and crack tip displacement (CTD) were also taken from these sources [*18,19*]. However, since crack extension in anti-plane shear is promoted in general by extensive plasticity, characterization in terms of elastic-plastic fracture mechanics is necessary. This was achieved by considering analytical solutions [*20*] for the plastic strain distribution, γ, in the plane of the crack of a circumferentially cracked solid cylinder, with net section radius r_N, of an elastic perfectly plastic material, with shear modulus G and shear yield stress k, yielding to a radius from the axis r_p (Fig. 3)

$$\gamma = \frac{k}{G}\left(\frac{r}{r_p}\right)^2\left(\frac{r_N - r_p}{r_N - r}\right) \tag{1}$$

Note all radii are defined from the axis. Although the plastic strain γ is infinite at the crack tip ($r = r_N$), the parameter $\gamma(r_N - r)$ is clearly finite and defines the intensity of plastic strain in the crack plane, in the limit as $r_N - r \rightarrow 0$

$$\Gamma_{III} = \gamma(r_N - r) = \frac{k}{G}\frac{(1 - r_p/r_N)}{(r_p/r_N)^2}\, r_N \tag{2}$$

$$\text{at } r \rightarrow r_N$$

Γ_{III} is the so-called plastic strain intensity [*7,12*] and, as defined in Eq 2, can be used for the circumferentially notched test geometry as the governing parameter for Mode III crack extension in the presence of extensive plasticity ($0 \leq M/M_L \leq 1$) [*12,14*]. Computation of Γ_{III} for this specimen involves determining

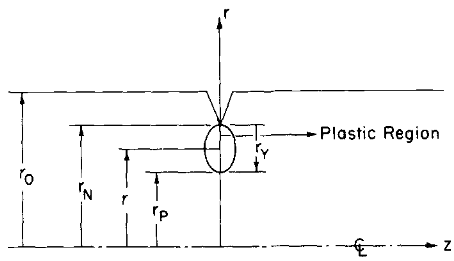

FIG. 3—*Nomenclature for plastic zone and respective radii in cylindrically notched test specimen.*

analytical expressions for r_p/r_N. Limiting cases for $M/M_L \rightarrow 0$ (elastic) and $M/M_L \rightarrow 1$ (fully plastic) are given in Ref *20*, and interpolated solutions for the range of M/M_L between these limits have been recently derived [*12,21*].

Crack extension also was characterized in terms of the cyclic crack-tip displacement. By considering the functional form of the plastic zone size (r_y) in Mode III [*3*], and integrating to determine the CTD_{III}, it may be shown [*14*] that the plastic strain intensity Γ_{III} is related to the CTD_{III} via the simple expression for small scale yielding

$$\text{CTD}_{\text{III}} \simeq 2\Gamma_{\text{III}} \tag{3}$$

Equation 3 tends to overestimate CTD_{III} for large-scale yielding but is generally correct within a factor of no more than 2.

Experimental Mode III Crack Growth Data

Initial results for radial Mode III crack growth $(dc/dN)_{\text{III}}$ behavior in 4340 steel (650°C temper), representing tests at constant torque amplitude (increasing $(dc/dN)_{\text{III}}$ with increasing crack length), are compared in Fig. 4 with equivalent behavior in Mode I. Mode III and Mode I growth rates in this figure are plotted as a function of their respective crack-tip displacements (derived from small-scale yielding solutions [*19*]). Similar to the well documented Mode I results, propagation rates in Mode III appear to be related to the cyclic crack tip displacement (and hence the stress-intensity range), although the crack increment per cycle is a much smaller fraction of the ΔCTD.

However, when subsequent tests were performed at different torque levels, specifically with decreasing and then increasing $(dc/dN)_{\text{III}}$ with increasing crack length, a marked hysteresis effect was observed in the dependence of $(dc/dN)_{\text{III}}$ on ΔK_{III} (or $\Delta\text{CTD}_{\text{III}}$), as shown for 4340 steel (200°C temper) in Fig. 5. This was particularly evident for tests at a constant ΔK_{III} where growth rates were observed to steadily decay with increasing crack length (Fig. 6), implying no unique dependence of $(dc/dN)_{\text{III}}$ on ΔK_{III}. The effect was even more pronounced in the lower strength 4140 steel where tests in pure cyclic torsion (that is, with zero axial load) at constant and variable torque range, at constant $\Delta M/M_L$, and

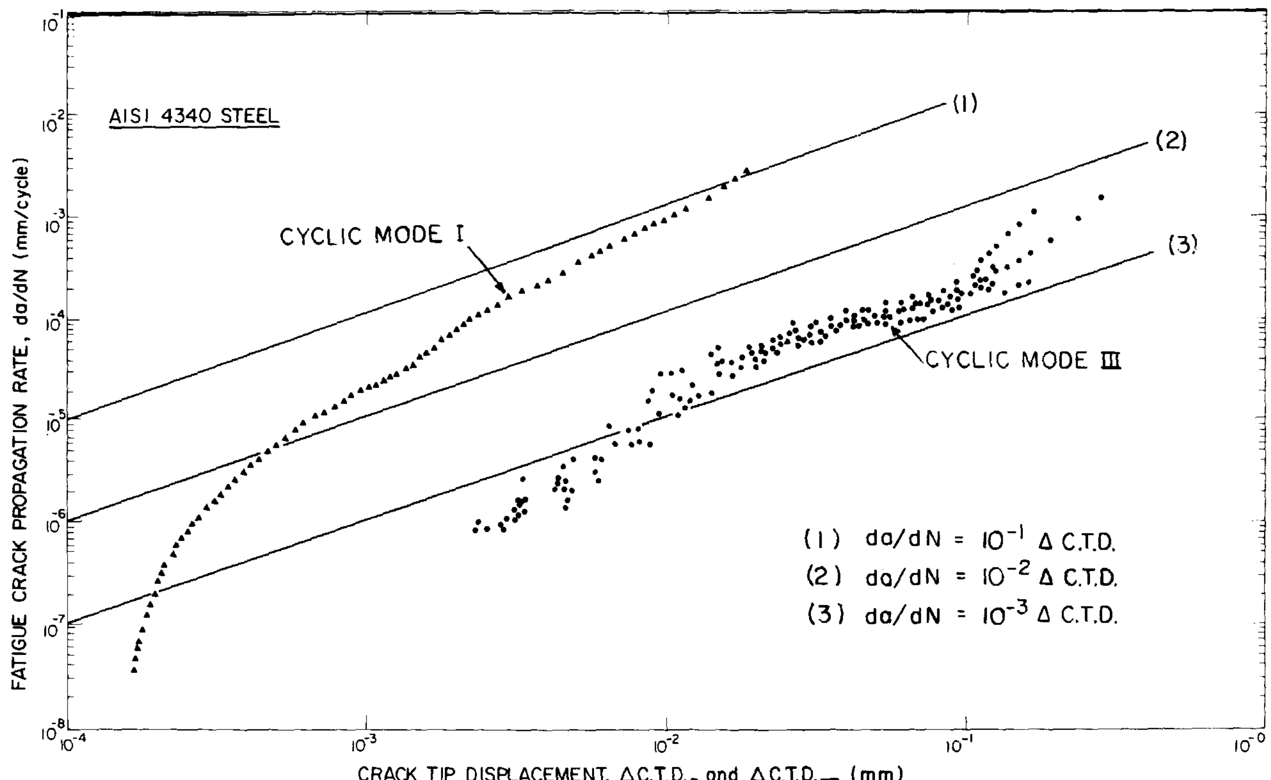

FIG. 4—*Comparison of Mode III and Mode I fatigue crack propagation rates at* R = −*1 in 4340 steel (650°C temper) as a function of their respective crack tip displacement ranges.*

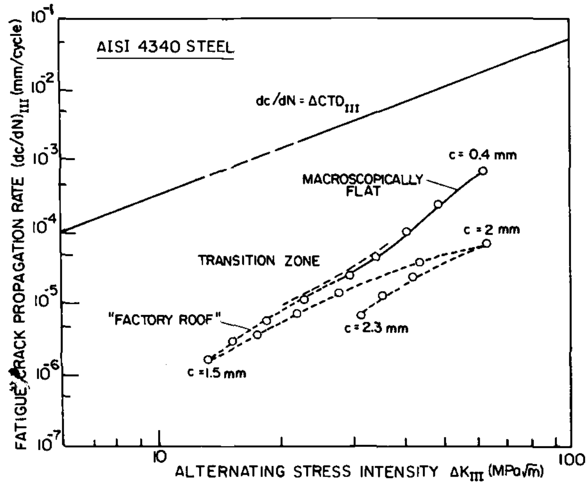

FIG. 5—*Mode III fatigue crack propagation data at* R $= -1$ *in 4340 steel (200°C temper) as a function of the stress-intensity range* (ΔK_{III}).

at constant $\Delta\phi$ yielded no apparent correlation between $(dc/dN)_{\text{III}}$ and ΔK_{III} over the range $\sim 10^{-6}$ to 10^{-3} mm/cycle (Fig. 7*a*).

At first glance this nonuniqueness in the Mode III data appeared to be associated with the invalidity of the linear elastic fracture mechanics characterization (that is, in terms of ΔK_{III}), since cyclic plastic zone sizes (r_y) at higher growth rates were comparable with specimen dimensions. However, when the data were reassessed in terms of the plastic strain intensity range $\Delta\Gamma_{\text{III}}$ (Eq 2) using elastic-

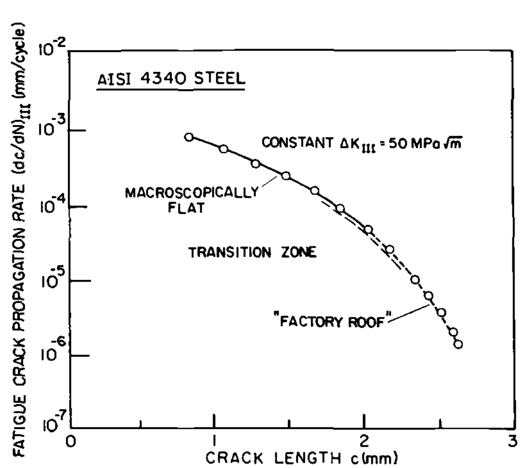

FIG. 6—*Mode III fatigue crack growth behavior at* R $= -1$ *in 4340 steel (650°C temper) as a function of crack length* c *for tests at a constant* ΔK_{III} *of 50 MPa*$\sqrt{m}$.

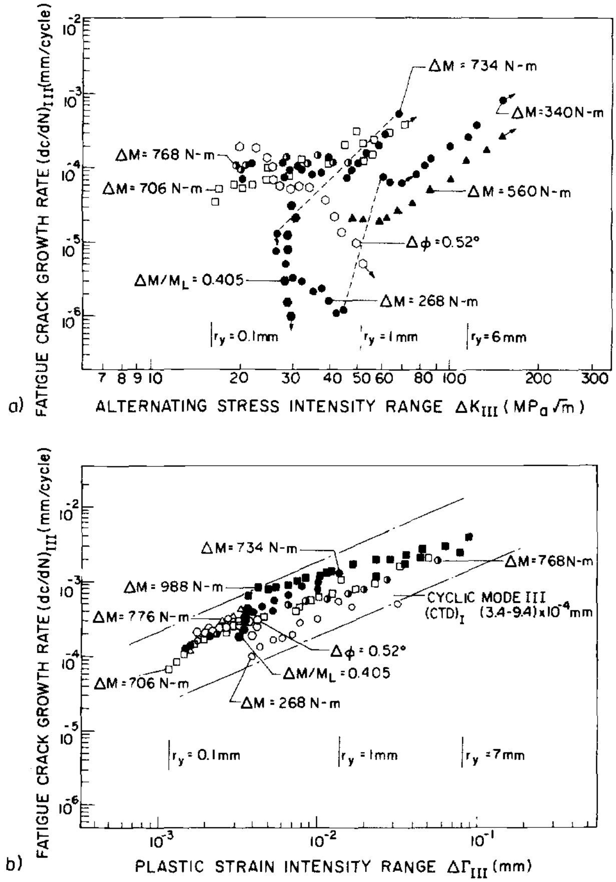

FIG. 7—*Mode III fatigue crack growth rates* $(dc/dN)_{III}$ *at* $R = -1$ *in annealed 4140 steel* ($Y = 310\ MN/m^2$) *for various test procedures of constant and variable* ΔM *levels, constant* $\Delta M/M_L$ *and constant* $\Delta\phi$ *conditions, showing* (a) *behavior as a function of* ΔK_{III} *for tests under pure cyclic torsion* ($K_I = 0$) *and* (b) *behavior as a function of the plastic strain intensity range* $\Delta\Gamma_{III}$ *for tests under cyclic torsion with a small superimposed axial load* ($K_I \approx 6$ *to* $11\ MPa\sqrt{m}$, $CTD_I \approx 0.3$ *to* $0.9\ \mu m$). *Key to data points similar in each figure. Arrows indicate increasing or decreasing growth rate tests.*

plastic fracture mechanics, again no unique correlation was found although the amount of scatter in Fig. 7*a* was reduced somewhat.

The solution to this problem was realized by examining pure cyclic torsion experiments in 4140 steel [*12*], where specimens cycled at constant $\Delta M/M_L$ levels were found to be able to withstand torque levels (computed on the unbroken cross section) in excess of three times the limit torque without total failure. Clearly in pure Mode III tests, the sliding crack surfaces remain in contact to such an extent that the broken ligament of the specimen is still able to carry torque. The effect is somewhat analogous to crack closure during Mode I fatigue crack growth [*22–24*] in that the effective torque actually experienced at the

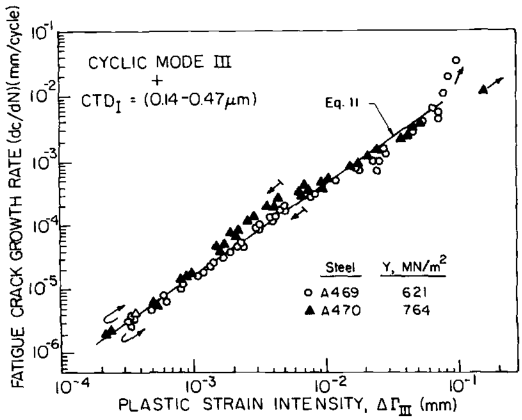

FIG. 8—*Mode III fatigue crack growth rates* $(dc/dN)_{III}$ *at* $R = -1$ *as a function of plastic strain intensity range* $\Delta\Gamma_{III}$ *in A469 and A470 rotor steels* ($Y = 621$ *and* 764 MN/m^2, *respectively) under cyclic torsion with a small superimposed axial load* ($K_I \approx 6$–11 $MPa\sqrt{m}$, $CTD_I \approx 0.14$ *to* 0.47 μm). *Arrows indicate increasing or decreasing growth rate tests. Prediction from damage accumulation model (Eq 11).*

crack tip is significantly less than the nominally applied value, although unlike Mode I closure, it acts over the entire loading cycle. Mechanisms for such sliding crack surface interference, which is promoted by longer crack depths and rough fracture surfaces, are discussed in detail next in terms of the morphology of Mode III failures.

Accordingly, to minimize such interference, small static axial loads were superimposed onto the cyclic torsional loads to separate the sliding crack surfaces. Specifically, the same series of tests on 4140 steel shown in Fig. 7*a* were repeated with a *small* axial load superimposed, corresponding to a static K_I of 6 to 11 $MPa\sqrt{m}$ (that is, a $CTD_I \approx 0.3$ to 0.9 μm, which is small compared to the ΔCTD_{III} of 2 to 200 μm). The results, shown in Fig. 7*b* in terms of $(dc/dN)_{III}$ as a function of $\Delta\Gamma_{III}$, now show a reasonable correlation of growth rates for a wide range of test conditions, with scatter reduced to within a decade in $(dc/dN)_{III}$.

Similar results were obtained in A469 and A470 rotor steels where growth rate data for pure cyclic torsion (that is, zero axial load) were again unreproducible. However, with the superposition of an axial load corresponding to $K_I = 6$ to 11 $MPa\sqrt{m}$ ($CTD_I \approx 0.14$ to 0.47 μm) for tests under both increasing and decreasing $(dc/dN)_{III}$ conditions, a unique relationship between Mode III propagation rates and $\Delta\Gamma_{III}$ was found with minimal scatter over a wide range of growth rates from $\sim 10^{-6}$ to 10^{-1} mm/cycle (Fig. 8).

Fractography of Mode III Crack Growth

Mechanisms for the occurrence of sliding crack surface interference, which so markedly affects Mode III behavior, can be appreciated by examining the fractography of Mode III failures. Scanning electron microscopy of such radial fractures in 4340, 4140, A469, and A470 steels revealed several distinct morphologies. At higher growth rates and short crack lengths, surfaces in all materials were microscopically flat (pure Mode III) and "smeared-out," with evidence of severe rubbing, abrasion, and fretting oxide formation (Fig. 9*a*). Specimens were observed to become hot to the touch during testing with wear-like debris emerging from the crack opening. Although this fracture mode was observed at all growth rates in the A469 and A470 rotor steels, at lower growth rates and larger crack lengths in the 4140 and 4340 steels a marked transition occurred to a rough failure mode consisting of ridges and valleys (termed "factory-roof" fracture [*25*]). In 4340, this nominally Mode III failure, which is commonly

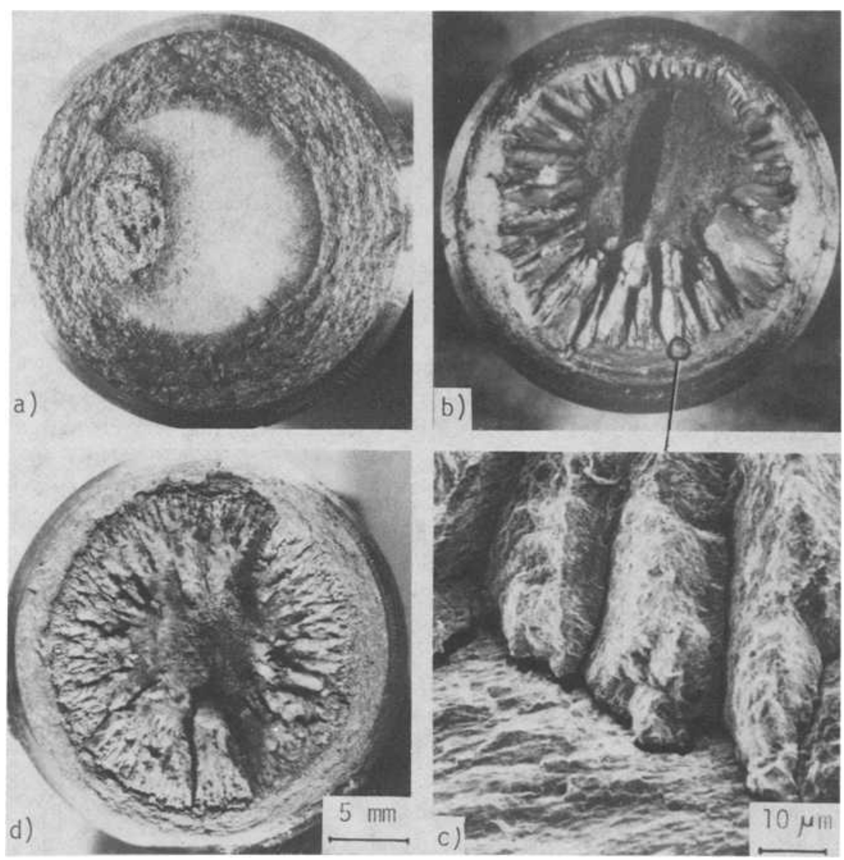

FIG. 9—*Fractography of torsional fatigue failures showing* (a) *macroscopically-flat mode (pure radial Mode III) in 4140 steel at* $\Delta M = 734$ *N m* ($\Delta CTD_{III} \approx 100–200$ μm), (b) *factory-roof fracture (radial Mode III with 45° Mode I branch cracks) in 4340 steel,* (c) *enlargement of* (b) *at* $\Delta CTD_{III} \approx 12$ μm, *and* (d) *factory-roof fracture (radial Mode III with longitudinal Mode III branch cracks) in 4140 steel at* $\Delta M = 409$ *N m* ($\Delta CTD_{III} \approx 6$ *to* 120 μm).

observed in torsion [*8,9,11,12,25–27*], had local mixed-mode character consisting of a radial shear surface with marked 45° Mode I branch cracks (Fig. 9*b*,*c*). In the lower strength 4140, similar factory-roof fractures were seen with branch cracks now perpendicular to the radial Mode III surface indicating additional longitudinal shear cracks (Fig. 9*d*). The transition in fracture mode as a function of crack length is illustrated for 4340 in Figs. 5 and 6. Interestingly, the factory-roof mode, although favored at lower torque levels, does not revert to the macroscopically flat mode in tests where torque levels were raised again to previous levels.

Under the sliding contact imposed by pure cyclic torsional loading such fracture morphologies clearly give rise to marked crack surface interaction effects. This is evident from signs of heating, abrasion, and fretting oxidation on Mode III surfaces (Fig. 9) and from the fact that electrical potential measurements of crack length in pure torsion ($K_I = 0$) suffer from severe shorting problems [*17*]. Probable mechanisms for such interference involving rubbing, abrasion, debris formation, and interlocking of asperities are illustrated schematically in Fig. 10, and clearly all enable the broken portion of the specimen to carry part of the applied torque. As might be expected, Mode III fracture surfaces for tests conducted with a superimposed axial load showed significantly less abrasion [*8*] and little evidence of fretting oxide formation [*12*].

Micromechanical Modelling of Mode III Crack Growth

From the preceding discussion, it is apparent that Mode III fatigue crack growth rates can be characterized by $\Delta\Gamma_{III}$ or ΔCTD_{III} for large-scale yielding,

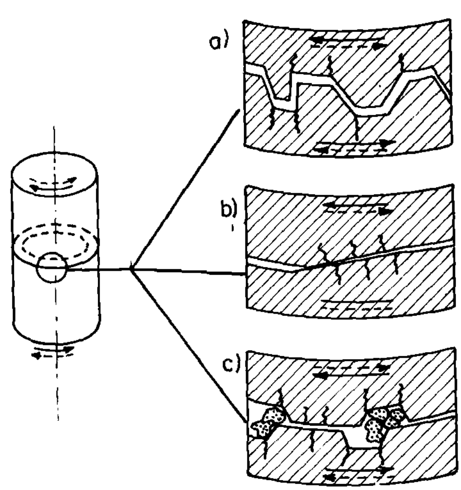

FIG. 10—*Schematic illustration of mechanisms of sliding crack surface interference for Mode III fatigue cracks under pure cyclic torsion showing* (a) *interlocking,* (b) *friction and abrasion and* (c) *fretting debris formation.*

only if small axial loads are superimposed on the cyclic torsion to minimize rubbing and interlocking between sliding crack surfaces. Based on such experimental data (Figs. 7 and 8), Mode III crack growth relationships for 4140 and the two rotor steels are given by

4140 steel

$$\left(\frac{dc}{dN}\right)_{\mathrm{III}} = (0.01 - 0.10)\Delta\mathrm{CTD}_{\mathrm{III}} = (0.01 - 0.10)2\Delta\Gamma_{\mathrm{III}} \quad (4a)$$

A469 and A470

$$\left(\frac{dc}{dN}\right)_{\mathrm{III}} = (0.1 - 0.2\ mm^{-1/2})\Delta\mathrm{CTD}_{\mathrm{III}}{}^{1.5}$$

$$= (0.1 - 0.2\ mm^{-1/2})(2\Delta\Gamma_{\mathrm{III}})^{1.5} \quad (4b)$$

indicating a dependence of growth rates on $\Delta\mathrm{CTD}_{\mathrm{III}}$ to the 1 to 1.5 power.

Such dependencies of Mode III growth rates on the cyclic crack-tip displacements can be predicted through simple micromechanical modelling of the anti-plane shear crack extension process [*8,14*].

Based on the experimental observations of Tipnis and Cook [*28*], Ritchie *et al* [*8*] proposed a mechanistic model for radial Mode III crack growth on the premise that crack advance in anti-plane shear occurs through the coalescence, by Mode II shear parallel to the crack front, of voids initiated at inclusions just ahead of the crack tip (Fig. 11). The mechanism is consistent with their observations [*8*] that microscopic sections through Mode III cracks reveal occasional forks from the main crack (as depicted in Fig. 11*a*), and with fractographic evidence of somewhat elongated voids formed in the *immediate vicinity* of the main crack front[6] (Fig. 12).

By neglecting damage beyond the first inclusion, expressions for the Mode III growth rate $(da/dN)_{\mathrm{III}}$ can be derived by determining the number of reversals N_{II} for such voids to elongate and link up by reversing Mode II shear. Assuming the voids to be elliptical with length l_i and width w, at link up where they have grown to a length $l_i = L$, the original Mode III crack can be considered to have advanced an average distance w, as shown in Fig. 11, such that

$$\left(\frac{dc}{dN}\right)_{\mathrm{III}} = \frac{w}{N_{\mathrm{II}}} \quad (5)$$

Evaluation of Eq 5 involves determining the number of cycles N_{II} for the Mode II coalescence of voids parallel to the Mode III crack front, which can be achieved

[6]Such fractographic details are largely obscured in the wake of the crack front by rubbing and abrasion between sliding fracture surfaces.

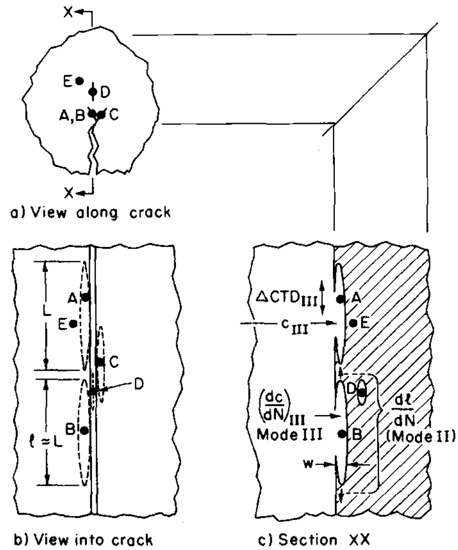

FIG. 11—*Schematic illustration of model for fatigue crack propagation in anti-plane shear showing orthographic views of Mode III crack extension occurring by microscopic Mode II shear growth, parallel to the crack front, of voids initiated at inclusions just ahead of the main crack front.*

by estimating the local Mode II growth rates of the voids either in terms of their instantaneous crack tip shear displacements [*8*] or in terms of Coffin-Manson damage accumulation [*14*]. A brief summary of the two formulations follows. Full derivations are given in Refs *8* and *14*.

The crack-tip displacement model [*8*] assumes the local Mode II growth rates of the voids to be related to their crack-tip shear displacements via expressions of the form

$$\left(\frac{dl_i}{dN}\right)_{\text{II}} = \left(\frac{dc}{dN}\right)_{\text{II}} = F_{\text{II}}\,\Delta\text{CTD}_{\text{II}} \tag{6}$$

where F_{II} is an experimentally determined constant for Mode II crack advance (above the near-threshold region). By noting that the volume fraction of inclusions along a given line, v_f, is given by w/L and by assuming that no appreciable damage is accumulated beyond the first inclusion, solutions for N_{II} can be determined which on substitution into Eq 5 yields an expression for the Mode III growth rate of the form

$$\left(\frac{dc}{dN}\right)_{\text{III}} = F_{\text{II}}(1 + e_i)v_f^{\,1+e_i}\,\Delta\text{CTD}_{\text{III}} \tag{7}$$

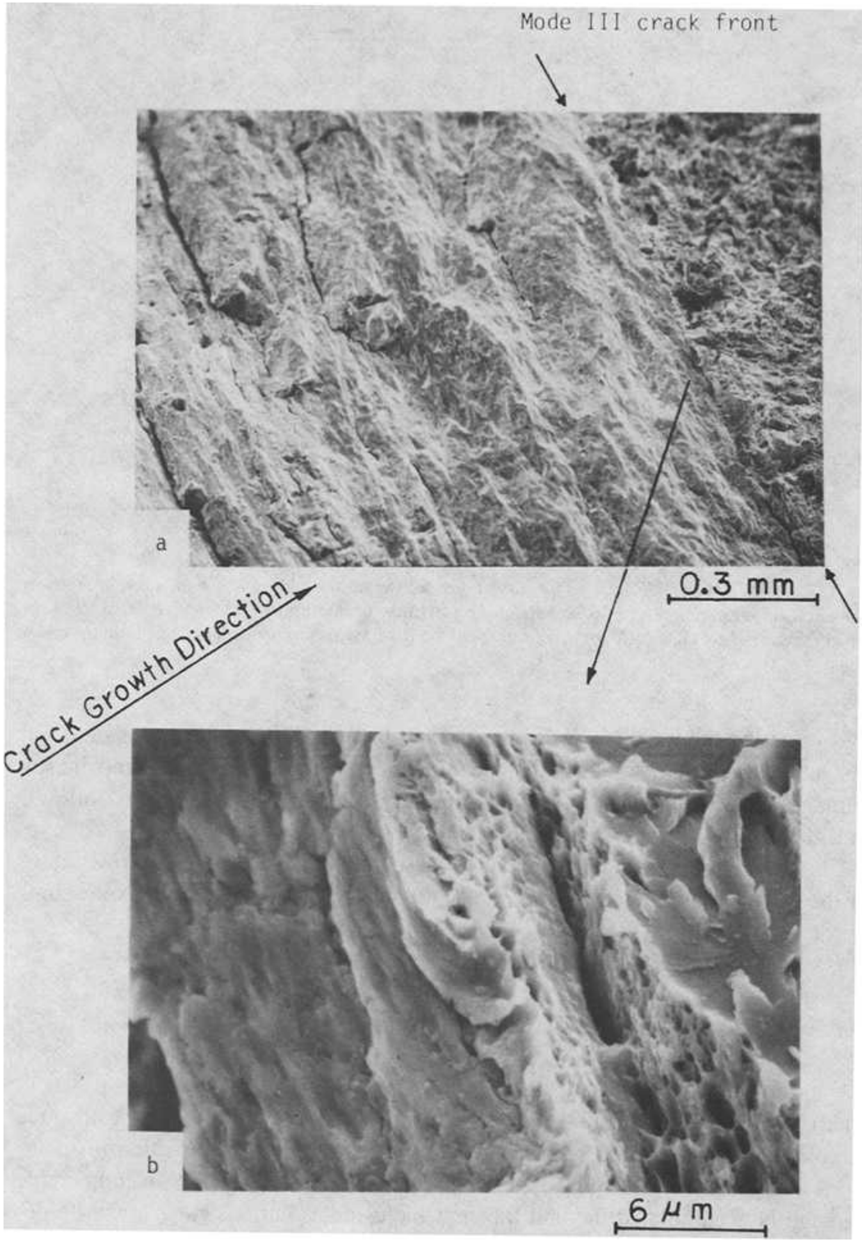

FIG. 12—*Micrographs of torsional fatigue fracture surface in A469 rotor steel at* $\Delta\Gamma_{III}$ = *0.0075 mm* ($\Delta CTD_{III} \approx$ *15* μ*m), showing elongated voids formed parallel to the crack front. Note the highly localized damage in the immediate vicinity of the crack tip, revealed by breaking the specimen open in liquid nitrogen.*

where e_i is an exponent which relates the displacement increment across an inclusion crack to its aspect ratio (w/l_i). The model can be extended [7] to include high applied torques through the strain-intensity concept by invoking Eq 3 such that the Mode III growth rate is predicted to be proportional to the first power of the reversed strain intensity of cyclic crack-tip displacement

$$\left(\frac{dc}{dN}\right)_{\mathrm{III}} = C_{\mathrm{III}}(2\Delta\Gamma_{\mathrm{III}}) = C_{\mathrm{III}}\ \Delta\mathrm{CTD}_{\mathrm{III}} \tag{8}$$

where the constant C_{III} is a function of v_f, F_{II}, and e_i.

The damage accumulation model [14], on the other hand, computes the local Mode II coalescence rates in terms of accumulated damage in elements (of length b) along the crack front. If each element is subjected to an average strain $\Delta\gamma(l_i)$, then the number of cycles for the Mode II crack to propagate across each element $N_{\mathrm{II}b}$ can be estimated by the Coffin-Manson relationship

$$N_{\mathrm{II}b} = A\left(\frac{\gamma_f}{\Delta\gamma(l_i)}\right)^d \tag{9}$$

where d and A are the Coffin-Manson constants, and the strain range is normalized with respect to the monotonic fracture strain γ_f. Thus the local Mode II growth rate can be expressed as

$$\left(\frac{dl_i}{dN}\right)_{\mathrm{II}} = \left(\frac{dc}{dN}\right)_{\mathrm{II}} = \frac{b}{N_{\mathrm{II}b}} = \frac{b}{A\left(\dfrac{\gamma_f}{\Delta\gamma(l_i)}\right)^d} \tag{10}$$

Using the Walsh and Mackenzie solution [20] for the distribution of shear strain in a torsionally loaded circumferentially notched cylindrical bar, and integrating Eq 10 up to the point of coalescence when $l_i = L$ (Fig. 11), yields an expression for N_{II}, which on substitution into Eq 5 gives a second expression for the Mode III growth rate

$$\left(\frac{dc}{dN}\right)_{\mathrm{III}} = \frac{Qd}{1 - \exp(-Qd)}\ \frac{2b}{A}\ v_f \left(\frac{2\Delta\Gamma_{\mathrm{III}}}{w\gamma_f}\right)^d \tag{11a}$$

or in terms of crack-tip displacements

$$\left(\frac{dc}{dN}\right)_{\mathrm{III}} = \frac{Qd}{1 - \exp(-Qd)}\ \frac{2b}{A}\ v_f \left(\frac{\Delta\mathrm{CTD}_{\mathrm{III}}}{w\gamma_f}\right)^d \tag{11b}$$

where $\exp(Q)$ is the strain concentration at the tip of the inclusion crack.

Thus, based on a mechanism of Mode III cyclic crack extension involving Mode II shear coalescence of voids in the immediate vicinity of the crack front, the dependence of the Mode III crack growth rate $(dc/dN)_{III}$ on ΔCTD_{III} or $\Delta\Gamma_{III}$ is seen to be linear for the instantaneous crack-tip shear displacement model (Eq 7) and a function of the Coffin-Manson exponent d for the Mode II crack tip strain accumulation model (Eq 11). Such dependencies are consistent with experimental data for 4140 steel (Fig. 7*b*) and the two rotor steels (Fig. 8) where the superposition of small axial loads has removed problems associated with crack surface interference. 4140 steel shows a linear dependence of $(dc/dN)_{III}$ on ΔCTD_{III} or $\Delta\Gamma_{III}$ (compare Eq 4*a*), whereas in A469 rotor steel, recent torsional low-cycle fatigue tests [*29*] show the Coffin-Manson exponent to be approximately 1.5 (with $A(\gamma_f)^{1.5} = 1.72$) indicating a dependence of $(dc/dN)_{III}$ on ΔCTD_{III} or $\Delta\Gamma_{III}$ to the 1.5 power (compare Eq 4*b*). Whereas materials in general are likely to show experimentally either type of behavior, this result is strikingly analogous to the well-known analytical models for Mode I fatigue crack growth. Here models for Mode I crack extension based on instantaneous crack-tip opening displacements yield a growth rate dependence on ΔK_I^2 (that is, proportional to the first power of ΔCTD_I) [for example, *6,30*], whereas Mode I damage accumulation models yield a dependence on ΔK_I^{3-4} (that is, proportional to $\Delta CTD_I^{1.5-2}$) [for example, *6,31*].

Despite these similarities in the dependence of Mode I and Mode III behavior in terms of their dependence on ΔCTD, the growth rates per cycle in absolute terms are very different in that Mode III cracks advance at a much smaller proportion of the crack tip displacements per cycle (compare Fig. 4). As with Mode I behavior, though, *a priori* prediction of the absolute magnitude of such growth rates from idealized models is extremely difficult in view of the many other factors involved in the fatigue process (for example, near-threshold effects, crack closure, environmental effects on Mode I behavior) [*1*]. However, by assigning reasonable values for the constants in Eqs 7 and 11 one can obtain close agreement with the experimental data. For example, taking $v_f = 0.001$, $b = 2\ \mu m$, $w = 1\ \mu m$, and $Q = 1$ for A469 rotor steel, where the Coffin-Manson relationship has been determined as $A(\gamma_f)^{1.5} = 1.72$ [*29*], Eq 11 reduces to

$$\left(\frac{dc}{dN}\right)_{III} \approx 0.4(mm^{-1/2})(\Delta\Gamma_{III})^{1.5} \tag{12}$$

which with reference to Fig. 8 and Eq 4*b* provides excellent agreement between theory and experiment. However, with regard to the utilization of such crack growth relationships for in-service defect-tolerant life-time predictions we would advise at this time the use of the physical form of the fundamental models (Eqs

7 and 11) with the constants determined by curve-fitting to relevant experimental data.[7]

Mode III Crack Growth under Variable Amplitude Loading

Recent studies [*32*] on A469 rotor steel have also focussed on the behavior of radial Mode III fatigue cracks under simple variable amplitude loading spectra (with small superimposed axial loads to minimize crack surface interference). Specifically, transient crack growth behavior was monitored following single (positive) and fully reversed single overloads and for high-low block loading sequences and results compared to equivalent tests for Mode I fatigue cracks. It was found that the transient growth rate response following such loading histories was almost exactly the opposite for Mode III as opposed to Mode I cracks. Whereas Mode I cracks showed a pronounced transient *retardation* following single overloads (in excess of 50% of the baseline stress intensity), Mode III cracks showed a corresponding acceleration (FIg. 13). The effect of single fully reversed overloads on Mode III crack rates was greater (that is, larger acceleration) than for single positive overloads, whereas the generally observed behavior for Mode I cracks is that fully reversed overloads (with the positive portion first) significantly lessen the retarding influence of single positive overloads [*33*]. Furthermore, high-low block loading sequences resulted in transient Mode III crack growth rates which were *greater* than the steady-state velocity corresponding to the lower (current) load level, whereas Mode I cracks showed a transient growth rate which was lower.

Such contrasting types of behavior may be understood by considering the various crack-tip mechanisms at play during Mode I and Mode III crack advance. Although single positive overloads can cause increased crack-tip damage for Mode I cracks, a post-overload retardation (or arrest) generally is observed due to more significant crack-tip blunting, branching, and crack closure processes which reduce the effective stress-intensity range at the crack tip [for example, *34,35*]. Similar arguments have been used to rationalize the analogous effects for fully reversed overloads and block loading sequences [*35*]. The overloaded Mode III crack, however, is not subjected to such blunting and experiences no premature closure other than the rubbing and abrasion between sliding crack surfaces. The phenomenon is thus somewhat less complex in Mode III, and the influence of variable amplitude loading sequences observed for Mode III cracks can be thus analyzed in terms of the damage (in the form of an instantaneous crack-tip displacement or Coffin-Manson damage accumulation) within the reversed plastic zones for each individual load reversal in the loading history [*7*].

[7]Current practice in defect-tolerant design procedures for Mode I fatigue is often simply to derive the entire crack growth relationship by empirical curve fits to experimental data such that extrapolation outside the range of the original data becomes highly questionable.

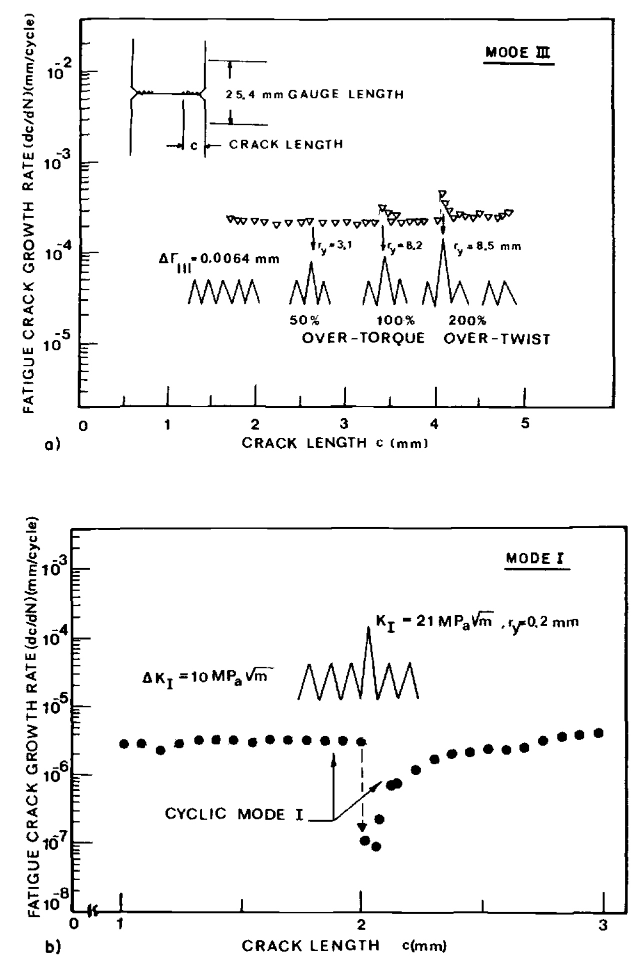

FIG. 13—*Experimental growth rate data in A469 rotor steel showing the differing transient response of* (a) *Mode III and* (b) *Mode I fatigue cracks to single positive overloads. Note the post-overload acceleration of Mode III cracks compared to the retardation of Mode I cracks.*

Based on the assumption of Mode III crack extension involving Mode II coalescence of voids parallel to the crack front (Fig. 11) and the damage accumulation model for computing the rate of coalescence described previously, such analyses have been performed for single positive and fully reversed overloads by estimating the damage increment for each torque reversal (N_{II} = ½) and integrating over the entire loading history [*32*]. Using a parametric model where the damage was considered over distances comparable with an inclusion spacing ahead of the crack tip [*32*], agreement with the transient post-overload behavior in A469 rotor steel was found to be extremely close (Fig. 14).

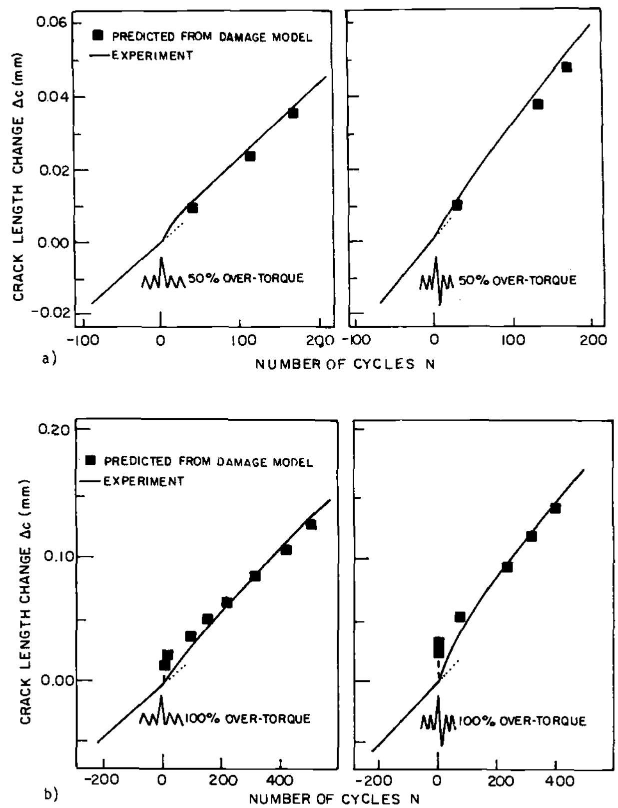

FIG. 14—*Comparison of experimental results and parametric damage model predictions* [15] *for the effects of* (a) *50% single and fully reversed overloads and* (b) *100% single and fully reversed overloads on Mode III fatigue crack growth in A469 rotor steel. Baseline conditions are* $\Delta\Gamma_{III}$ *= 0.0064 mm* ($\Delta CTD_{III} \approx 13$ *μm*) *with* (a) c = *2.6 mm,* r_y = *3.1 mm, and* (b) c = *3.5 mm,* r_y = *8.2 mm.*

Conclusions

Based on a study of radial Mode III fatigue crack propagation rates, spanning $\sim 10^{-6}$ to 10^{-1} mm/cycle, derived from cyclic torsion tests using circumferentially notched cylindrical specimens on a series of low-alloy steels, the following conclusions can be made:

1. Mode III crack growth rates were found to be related to the cyclic crack-tip displacement (ΔCTD_{III}) or the plastic strain intensity range ($\Delta\Gamma_{III}$) provided friction, abrasion, and interlocking between sliding fracture surfaces was minimized by the application of a small superimposed tensile mean load.

2. No unique correlation was found between Mode III growth rates and ΔCTD_{III} or $\Delta\Gamma_{III}$ for tests under pure cyclic torsion (that is, $K_I = 0$), where crack surface interference limited the effective torque range at the crack tip.

3. Based on a comparison at equivalent crack-tip displacements, Mode III

cracks were observed to propagate at significantly slower rates than Mode I cracks with the crack advance per cycle being a much smaller proportion of the cyclic crack-tip displacement.

4. In the rotor steels and in 4340 and 4140 at higher growth rates, torsional fatigue fracture surfaces were macroscopically flat and smeared out. At lower growth rates and larger crack lengths in 4140 and 4340 steels, transitional fracture modes were observed in the form of factory-roof failures containing 45° (Mode I) branch cracks in 4340 and longitudinal (Mode III) branch cracks in 4140.

5. Crack extension in anti-plane shear was considered to occur via the coalescence, by Mode II shear parallel to the crack front, of voids initiated at inclusions in the immediate vicinity of the Mode III crack tip.

6. Micromechanical models for Mode III crack extension were presented based on this mechanism where the coalescence of voids was estimated either in terms of the instantaneous crack tip displacements (ΔCTD_{II}) or Coffin-Manson damage accumulation. Mode III growth rates were predicted to be dependent upon the first power of ΔCTD_{III} (or $\Delta\Gamma_{III}$) from the former model, consistent with experimental behavior in 4140 steel, and to be dependent upon $\Delta CTD_{III}{}^{1.5}$ (or $\Delta\Gamma_{III}{}^{1.5}$) from the damage model, consistent with behavior in the rotor steels.

7. The transient response of Mode III cracks to single positive and fully reversed overloads and high-low block loading sequences was found to be markedly different to that observed for Mode I cracks. For example, whereas Mode I cracks showed a post-overload retardation in growth rates, Mode III cracks showed a corresponding acceleration. Such effects were attributed primarily to the absence of crack closure in Mode III and were rationalized in terms of damage accumulation arguments.

Acknowledgments

The work was supported by the U.S. Department of Energy, Division of Energy Conservation, under Contract No. W-7405-ENG-26, through Subcontract 9062 from the Oak Ridge National Laboratory to the Massachusetts Institute of Technology. Additional support for one of the authors (R. O. Ritchie) was provided by the Materials Science Division, Office of Basic Energy Sciences of the Department of Energy under Contract No. DE-AC03-76SF0Q098. Thanks are due to Drs. A. S. Argon, J. J. Blass, J. de Castro, and M.-Y. He for helpful discussions and to Drs. R. Williams and N. E. Dowling of the General Electric and Westinghouse Electric Companies, respectively, for supplying the rotor steels. The detailed and constructive comments of the reviewers are also appreciated.

References

[1] Ritchie, R. O. in *Encyclopedia of Materials Science and Engineering,* M. B. Bever, Ed., Pergamon Press, Oxford and New York, 1985.

[2] McClintock, F. A. in *Proceedings,* International Conference on Fatigue of Metals, Institution of Mechanical Engineers, London, U.K., 1956, p. 538.

[3] Hult, J. A. and McClintock, F. A. in *Proceedings*, Ninth International Congress of Applied Mechanics, University of Brussels, Vol. 8, 1956, p. 51.
[4] Hult, J. A., *Transactions of Royal Institute of Technology*, Stockholm, Sweden, No. 119, 1958.
[5] Kayan, I., *Bulletin of the Technical University of Istanbul*, Vol. 14, 1961, p. 45.
[6] McClintock, F. A. in *Fracture of Solids*, D. C. Drucker, and J. J. Gilman, Eds., Interscience, New York, TMS-AIME Conference Series 20, 1963, p. 65.
[7] McClintock, F. A. and Ritchie, R. O. in *Mechanics of Fatigue*, T. Mura, Ed., American Society for Mechanical Engineers, New York, AMD Vol. 47, 1981, p. 1.
[8] Ritchie, R. O., McClintock, F. A., Nayeb-Hashemi, H., and Ritter, M. A., *Metallurgical Transactions A*, Vol. 13A, 1982, p. 101.
[9] Hurd, N. J. and Irving, P. E. in *Design of Fatigue and Fracture Resistant Structures, ASTM STP 761*, American Society for Testing and Materials, Philadelphia, 1982, p. 212.
[10] Wright, R. P. and Queeney, R. A., *International Journal of Fatigue*, Vol. 4, 1982, p. 27.
[11] Tschegg, E. K., *Materials Science and Engineering*, Vol. 54, 1982, p. 127.
[12] Nayeb-Hashemi, H., McClintock, F. A., and Ritchie, R. O., *Metallurgical Transactions A*, Vol. 13A, 1982, p. 2197.
[13] Tschegg, E. K., Ritchie, R. O., and McClintock, F. A., *International Journal of Fatigue*, Vol. 5, 1983, p. 29.
[14] Nayeb-Hashemi, H., McClintock, F. A., and Ritchie, R. O., *International Journal of Fracture*, Vol. 23, 1983, p. 163.
[15] Pook, L. P. and Sharples, J. K., *International Journal of Fracture*, Vol. 15, 1979, p. R223.
[16] Pook, L. P., *International Journal of Fatigue*, Vol. 4, 1982, p. 175.
[17] Ritter, M. A. and Ritchie, R. O., *Fatigue of Engineering Materials and Structures*, Vol. 5, 1982, p. 91.
[18] Tada, H., Paris, P. C., and Irwin, G. R. in *Stress Analysis of Cracks Handbook*, Del Research Corporation, Hellertown, PA 1973.
[19] Rice, J. R. in *Fracture: An Advanced Treatise*, H. Liebowitz, Ed., Academic Press, New York, Vol. 2, 1968, p. 191.
[20] Walsh, J. B. and Mackenzie, A. C., *Journal of Mechanics and Physics of Solids*, Vol. 7, 1959, p. 247.
[21] McClintock, F. A. and Tschegg, E. K., *International Journal of Fracture*, Vol. 26, 1984, p. R11.
[22] Elber, W. in *Damage Tolerance in Aircraft Structures, ASTM STP 486*, American Society for Testing and Materials, Philadelphia, 1972, p. 280.
[23] Suresh, S., Zamiski, G. F., and Ritchie, R. O., *Metallurgical Transactions A*, Vol. 12A, 1981, p. 1435.
[24] Suresh, S. and Ritchie, R. O., *Metallurgical Transactions A*, Vol. 13A, 1982, p. 1627.
[25] Hourlier, F., McLean, D., and Pineau, A., *Metals Technology*, Vol. 5, 1978, p. 154.
[26] Ritchie, R. A., S.M. thesis, Department of Mechanical Engineering, Massachusetts Institute of Technology, Cambridge, Jan. 1971.
[27] Hourlier, F. and Pineau, A. in *Advances in Fracture Research*, D. François, Ed., Pergamon Press, New York, Vol. 4, 1981, p. 1833.
[28] Tipnis, V. A. and Cook, N. H., *Journal of Basic Engineering, Transactions*, American Society of Mechanical Engineers, Series D, Vol. 89, 1967, p. 533.
[29] Placek, R., Williams, R., Klufas, O., and Adams, S. in *EPRI-GE Workshop on Torsional Fatigue Strength of Large Turbine-Generator Shafts*, G.E. Technical Report, Contract RP1531, General Electric Company, Schenectady, NY, Sept. 1980.
[30] Lardner, R. W., *Philosophical Magazine*, Vol. 17, 1968, p. 71.
[31] Weertman, J., *International Journal of Fracture Mechanics*, Vol. 2, 1966, p. 460.
[32] Nayeb-Hashemi, H., McClintock, F. A., and Ritchie, R. O., *Engineering Fracture Mechanics*, Vol. 18, 1983, p. 736.
[33] Schijve, J. and Broek, D., *Aircraft Engineering*, Vol. 34, 1962, p. 314.
[34] Lankford, J. and Davidson, D. L. in *Advances in Fracture Research*, D. François, Ed., Pergamon Press, New York, Vol. 2, 1981, p. 899.
[35] Suresh, S., *Engineering Fracture Mechanics*, Vol. 18, 1983, p. 577.

François Hourlier,[1] Hubert d'Hondt,[1] Michel Truchon,[2] and André Pineau[1]

Fatigue Crack Path Behavior Under Polymodal Fatigue

REFERENCE: Hourlier, F., d'Hondt, H., Truchon, M., and Pineau, A., **"Fatigue Crack Path Behavior Under Polymodal Fatigue,"** *Multiaxial Fatigue, ASTM STP 853*, K. J. Miller and M. W. Brown, Eds., American Society for Testing and Materials, Philadelphia, 1985, pp. 228–248.

ABSTRACT: The study is devoted to the prediction of crack path direction in polymodal fatigue. First experimental and theoretical results published in the literature are reviewed. It is shown that proportional and nonproportional loading conditions should be distinguished. Then, the experimental results obtained in cyclic Mode III and biaxial nonproportional Modes I + II loading are presented. These tests were carried out on two alloy steels and an aluminum alloy. The biaxial tests were performed on cruciform type specimens.

In Mode III loading, it is shown that, at low applied torque, the crack surface adopts a "factory-roof" appearance with facets characteristic of local Mode I extension. It is suggested that the flat surfaces corresponding to apparent macroscopic Mode III extension observed in this study as in other ones might be an artefact. In Modes I + II loading, it is shown that the two investigated materials exhibit very different crack bifurcation angles. The results are discussed in terms of possible extended forms of the maximum tangential stress criterion, $\Delta k_{\mathrm{Imax}}{}^*$, $k_{\mathrm{Imax}}{}^*$ and $(da/dN)_{\max}$. It is shown that, as a general rule, the latter criterion gives results in better agreement with the experiments. The difficulties associated with crack closure effect are also shortly discussed.

KEY WORDS: fatigue crack propagation, polymodal fatigue, Modes I and II loading

A large number of studies dealing with fatigue crack propagation behavior have been devoted to Mode I loading. For this type of loading, many examples have shown that linear elastic fracture mechanics can be successfully applied to practical engineering problems. Unfortunately, many service failures occur from cracks which were subjected to polymodal loadings, usually Modes I + II or Modes I + III. For instance, turbine shafts are usually submitted both to bending and torsion stresses. In these conditions a crack initiated in a transverse plane experiences a combination of Modes I + II + III displacements. Despite the practical importance of polymodal fatigue, there exists only a limited number of investigations devoted to this problem. Two aspects must be distinguished

[1]Researchers and professor, respectively, Centre des Matériaux, Ecole des Mines, Evry, France.
[2]Research group leader, Centre de Recherches d'Unieux, Creusot Loire, France.

Copyright© 1985 by ASTM International www.astm.org

(*a*) crack path determination and (*b*) crack growth rate behavior. Although these two aspects are related, the present study is devoted essentially to the first one.

As a general rule a crack loaded under mixed mode branches, that is, grows in a direction different from the initial crack plane. The determination of the stress intensity factors corresponding to a branched crack has received the attention of many authors. Exact, analytical solutions are available for two dimensional Modes I + II infinitesimaly small cracks [*1*]. For finite extension the stress intensity factors can be calculated numerically using Chatterjee's results [*2*]. An approximate analytical solution can be obtained by assuming the continuity of the tangential stress for Mode I and that of the shear stress for Mode II in noncolinear propagation. However this method becomes increasingly inaccurate as the bifurcation angle increases [*3*]. Most often, Modes I + III crack propagation is more complex. Usually Modes I + III tests are carried out on notched round bars loaded both in tension and torsion. This configuration is three dimensional, but, because of its axisymmetry, it may be treated as a bidimensional problem. However, if crack branching occurs as shown later the problem is strictly three dimensional, and, in particular, two angles are necessary to define the branched cracks. In these conditions, the stress intensity factors can be calculated by approximate solutions [*4*].

As far as the loading conditions are concerned, two different cases must be distinguished corresponding respectively to proportional and nonproportional loading.

Loadings

Proportional Loading

The cracked structure is subjected to one load or to several proportional loads giving rise to mixed mode fatigue. The ratios of stress intensity factors K_I/K_{II}, K_I/K_{III}, and K_{II}/K_{III} are kept constant during the cycle. The stresses at the crack tip are given by

$$\sigma_{ij} = \frac{1}{\sqrt{2\pi r}} [K_I f_{ij}^{I}(\theta) + K_{II} f_{ij}^{II}(\theta) + K_{III} f_{ij}^{III}(\theta)] = \frac{K_I(t)}{\sqrt{2\pi r}} \text{gij } (\theta) \quad (1)$$

where r and θ are polar coordinates. This configuration is very similar to pure Mode I loading. Most studies on polymodal fatigue deal with this type of loading [*5–8*]. As a general rule these studies showed that a crack initially under Modes I + II loading bifurcates in a direction where the stress intensity factor on the branched crack k_I^* is maximum.[3] This corresponds to the situation encountered also under monotonic loading. Here it must be kept in mind that several criteria have been proposed to account for these observations: (*a*) the maximum tangential

[3]In order to be consistent with the notations of other authors, the stress intensity on a branched crack are denoted by an asterisk and written with minor character.

stress criterion proposed by Erdogan and Sih [*9*], modified by Ewing and Williams [*10*] to account for the effect of nonsingular terms; (*b*) the maximum strain energy density criterion [*11*]; and (*c*) the maximum energy release rate criterion [*12*]. Usually the bifurcation angles predicted from these criteria are very close.

In fewer cases, it was observed that a fatigue crack could grow in a direction strongly different from the ones predicted by these criteria. Hua et al [*13*] have shown recently that in AISI 316 stainless steel cracks loaded in Modes I + II could grow over a short distance in the same plane as the initial precrack instead of branching. These observations were made in the near-threshold regime. Other observations of coplanar crack extension in mixed mode fatigue have been also made by Tanaka [*6*] in Modes I + II, Hurd and Irving [*14*] and Ritchie et al [*15*] in Modes I + III loading. In particular the two latter groups of investigators have carried out tests on notched round bars loaded in cyclic torsion (Mode III) and steady tension (Mode I). They observed two different crack surface morphologies depending on loading conditions. First, at high torques and short crack length, the fracture surfaces appeared flat and smeared with severe abrasion. The plane of the fracture surface was perpendicular to the axis of the torsion bar. It was claimed that this morphology was associated to macroscopic Mode III crack extension. Second, at smaller applied torques and at longer crack lengths, fracture surfaces with a "factory-roof" appearance were observed, having local Mode I character. From this short review of the literature, it appears that, even for simple proportional loading, the factors influencing the fatigue crack path behavior, especially the stability of macroscopic Modes I + II or Mode III crack extension are not yet fully understood.

Nonproportional Loading

The problem of cracks subjected to several nonproportional loads leading to polymodal fatigue is different in many respects. In particular the criteria presented previously cannot be easily applied to predict the crack growth direction. To illustrate the situation, consider a crack in a plane structure subjected to two in phase loads at the same frequency

$$P_1(t) = p_1 \cos t + p_{10} \tag{2}$$

and

$$P_2(t) = p_2 \cos t + p_{20} \tag{3}$$

The stress intensity factors k_I^* and k_{II}^* on a branched crack with angle θ can be expressed as

$$k_I^* = F(a,w)\,[P_1(t)\,f_1(\theta) + P_2(t)\,f_2(\theta)] \tag{4}$$

and

$$k_{\rm II}^* = F(a,w)[P_1(t)\, g_1(\theta) + P_2\,(t)\, g_2(\theta)] \tag{5}$$

where the geometry is characterized by $F(a,w)$, a and w being lengths associated to the crack length and the specimen dimension, respectively.

The direction θ where $k_{\rm I}^*$ is maximum when θ is varying is a root of the equation

$$P_1(t)\,f'_1(\theta) + P_2(t)\,f'_2(\theta) = 0 \tag{6}$$

As a general rule, this direction is time dependent contrary to the situation corresponding to proportional loading (for example, see Fig. 1*a*). One possible solution for the direction corresponding to the maximum of $k_{\rm I}^*$ when both θ and t are varying is given by the solution of the equation

$$(\pm\, p_1 + p_{10})f'_1(\theta) + (\pm\, p_2 + p_{20})f'_2(\theta) = 0 \tag{7}$$

The latter direction is usually different from the direction where $\Delta k_{\rm I}^*$ is maximum, which corresponds to a root of the equation

$$p_1 f'_1(\theta) + p_2 f'_2(\theta) = 0 \tag{8}$$

This is the case when the loads P_1 and P_2 are not proportional, that is, when $P_1/P_{10} \neq P_2/P_{20}$.

It appears therefore necessary to define new criteria or to extend the previous ones when dealing with polymodal fatigue. Considering the maximum tangential stress criterion, it can be assumed that the crack propagates either in the direction corresponding to $\Delta k_{\rm Imax}^*$ or in the direction associated with $k_{\rm Imax}^*$. Both extensions raise a number of difficulties. In particular the $\Delta k_{\rm Imax}^*$ criterion does not take into account the effect of mean stress which is known to influence the fatigue crack behavior. The $k_{\rm Imax}^*$ criterion which is an extension of a criterion for monotonic loading is expected to be applicable only at very high crack growth rates approaching final rupture.

In order to solve partly these difficulties, we have proposed recently another extension of the maximum tangential stress criterion [*16*]. The modified criterion states essentially that the fatigue cracks propagate in a direction in which the crack growth rate is maximum. The crack growth rate is calculated from pure Mode I results, assuming that $k_{\rm II}^*$ and $k_{\rm III}^*$ have no effect on crack path behavior. To illustrate the latter approach let us consider a crack submitted to Modes I + II loading which bifurcates in a direction θ. Assuming that the stress intensity factor $k_{\rm I}^*$ on the branched crack can be evaluated, the crack growth rate is calculated as $da/dN(\theta) = f[k_{\rm Imax}(\theta), \Delta k_{\rm I}^*(\theta)]$ using conventional $da/dN = f(K_{\rm Imax}, \Delta K_{\rm I})$ curves established under pure Mode I loading (Fig. 1*b*). The predicted bifurcation

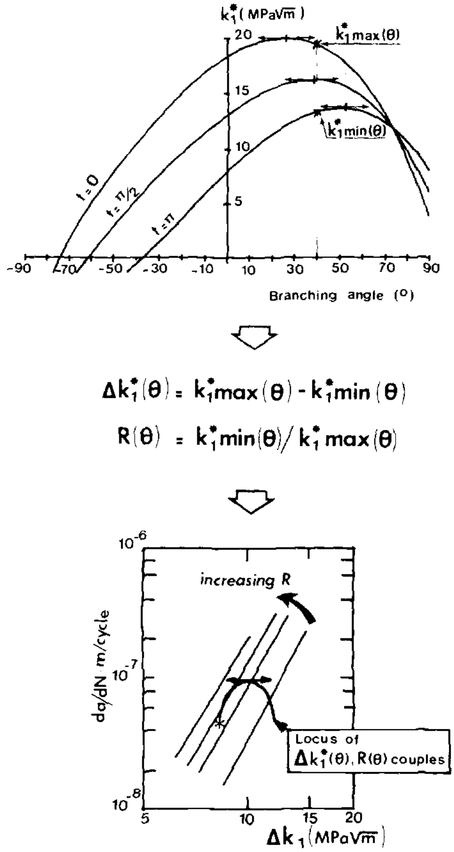

(*a*) Derivation of Δk_I^* (θ) and R (θ) for any value of the branching angle for three different values of the phase angle t.

(*b*) Determination of da/dN corresponding to Δk_I^* (θ) and R (θ).

The locus of the couples (Δk_I^* (θ), R (θ)) exhibits a maximum in terms of fatigue crack growth rate: the angle θ at this point is the branching angle.

FIG. 1—*Presentation of the* da/dN_{max} *criterion.*

angle, θ, corresponds to that one giving the maximum calculated crack growth rate. It can easily be shown that:

1. If the applied loads are proportional, the $(da/dN)_{max}$ criterion predicts the same crack bifurcation angle as the maximum tangential stress approach.
2. If the material does not exhibit any influence of R ratio $= K_{Imin}/K_{Imax}$ in pure Mode I the proposed criterion is the same as the Δk_I^* criterion.
3. If, at the other extreme, the crack growth rate is only dependent on maximum stress, which is very unusual except at very high crack growth rates, the $(da/dN)_{max}$ approach is the same as k_{Imax}^* criterion.

To test the applicability of these approaches there are few experimental results. It is worth mentioning the study by Truchon and Amestoy [17] who observed in a structural steel that the crack path direction in Modes I + II was reasonably well predicted by $k_{\mathrm{I}max}{}^*$ criterion. Otsuka et al [18] carried out cyclic Mode I + steady Mode II tests in mild steel and aluminum alloys. They indicated that in some cases the crack propagated in a direction coplanar with the precrack while in other cases the crack bifurcated. Finally, two of the authors [19] have also conducted cyclic Mode I + steady Mode II or Mode III tests on two steels, an aluminum alloy and two titanium alloys. In these tests it was observed that the crack path direction was strongly dependent on the material, suggesting that both the effect of mean stress and maximum stress should be taken into account in the derivation of a criterion for crack path behavior under polymodal fatigue.

The present study was instigated to clarify a number of aspects in this field. First tests were carried out under cylic Mode III loading in order to contribute to the understanding of crack path behavior associated with this type of loading. Second, cyclic Modes I + II experiments were conducted on cruciform type specimens subjected to nonproportional loading. The aim of this part of the study was a comparison between the three possible extensions of the maximum tangential stress criterion, that is, $k_{\mathrm{I}max}{}^*$, $\Delta k_{\mathrm{I}max}{}^*$ and $(da/dN)_{max}$ criteria.

Material and Experimental Procedures

Materials

Fatigue tests in cyclic Mode III were carried out on 26NCDV14 steel (AFNOR Standard). Modes I + II tests materials were 35NCD16 steel and AU4G aluminum alloy. The specimens for Modes I + II tests were cut from 300-mm-diameter bar. They were sectioned in a transverse plane in order to reduce as much as possible the effect of anisotropy.

The chemical compositions and the tensile properties of the materials are given in Tables 1 and 2, respectively. 35NCD16 steel was used in the annealed condition. The aluminum alloy exhibits a "duplex" structure formed by coarse grains with a mean size of 40 μm surrounded by smaller grain of 8 μm, as illustrated in Fig. 2. It was noticed that the metallurgical structure was isotropic in a plane transverse to the axis of the bar.

Mode III Fatigue Tests

Mode III fatigue crack propagation tests were conducted on circumferentially notched, torsionally loaded specimens (Fig. 3*a*). The crack length was monitored

TABLE 1—*Composition in weight percent of steels.*

Materials	C	Mn	Ni	Cr	Mo	P	S
26NCDV14	0.23	0.29	3.4	1.7	0.42	0.009	0.01
35NCD16	0.36	0.34	3.5	1.6	0.28	0.008	0.003

TABLE 2—*Ambient temperature tensile properties.*

Materials	Yield Stress, MPa	Ultimate Tensile Strength, MPa	Elongation, %
26NCDV14	789	875	18
35NCD16	570	840	22
2024T651	280	410	7

using d-c potential drop technique. The experiments were performed on a uniaxial servohydraulic tensile machine, by using a special apparatus, with zero minimum torque. The stress intensity factors K_{III} were calculated with Bueckner's calibrations [*20*]. After testing, the specimens were broken in liquid nitrogen and the fracture surfaces were examined by optical and scanning electron microscopy. The nominal shear stresses were limited to 300 MPa to prevent extensive plasticity. Thus, with $K_{III\min} = 0$, the range of ΔK_{III} investigated was limited to 50 MPa $\sqrt{m}$. For this value, the monotononic plastic zone size can be evaluated as

$$r_y = \frac{1}{2\pi}\left(\frac{K_{III}^2}{\tau_y^2}\right) = 1.9 \text{ mm} \tag{10}$$

Cyclic Modes I + II Tests

In order to characterize Mode I fatigue crack propagation behavior, tests were conducted on ASTM compact tension (C-T) type specimens (W = 56 mm, B = 6 mm) for different values of R ratio = $K_{I\min}/K_{I\max}$ between 0.1 and 0.7. The influence of anisotropy in the aluminum alloy was investigated using specimens loaded in the RT and TR directions, where R and T denote the radial and the tangential direction, respectively.

The geometry used for cyclic Modes I + II tests was a biaxially stressed cruciform type specimen (Fig. *3b*). Full details of experimental procedure are given elsewhere [*7*]. Strain gages were employed to determine stresses in the center of the uncracked specimen. The transfert matrix which determines stresses as a function of applied loads was the same for both alloys. In these tests the crack was first extended from the notch in Mode I by equibiaxial loading until crack length reaches 21 mm. During the precracking phase, the applied loads were set in such a way ΔK_I should not exceed the anticipated $\Delta k_I{}^*$ of the branched crack. Then nonproportional biaxial loading was applied which leads to cyclic Modes I + II displacement. Five steels and two aluminum alloy specimens were tested. The testing program is given in Table 3. The loading conditions were adjusted in order to reach after the onset of crack bifurcation approximately the same ΔK_I as at the end of precracking. The range of crack

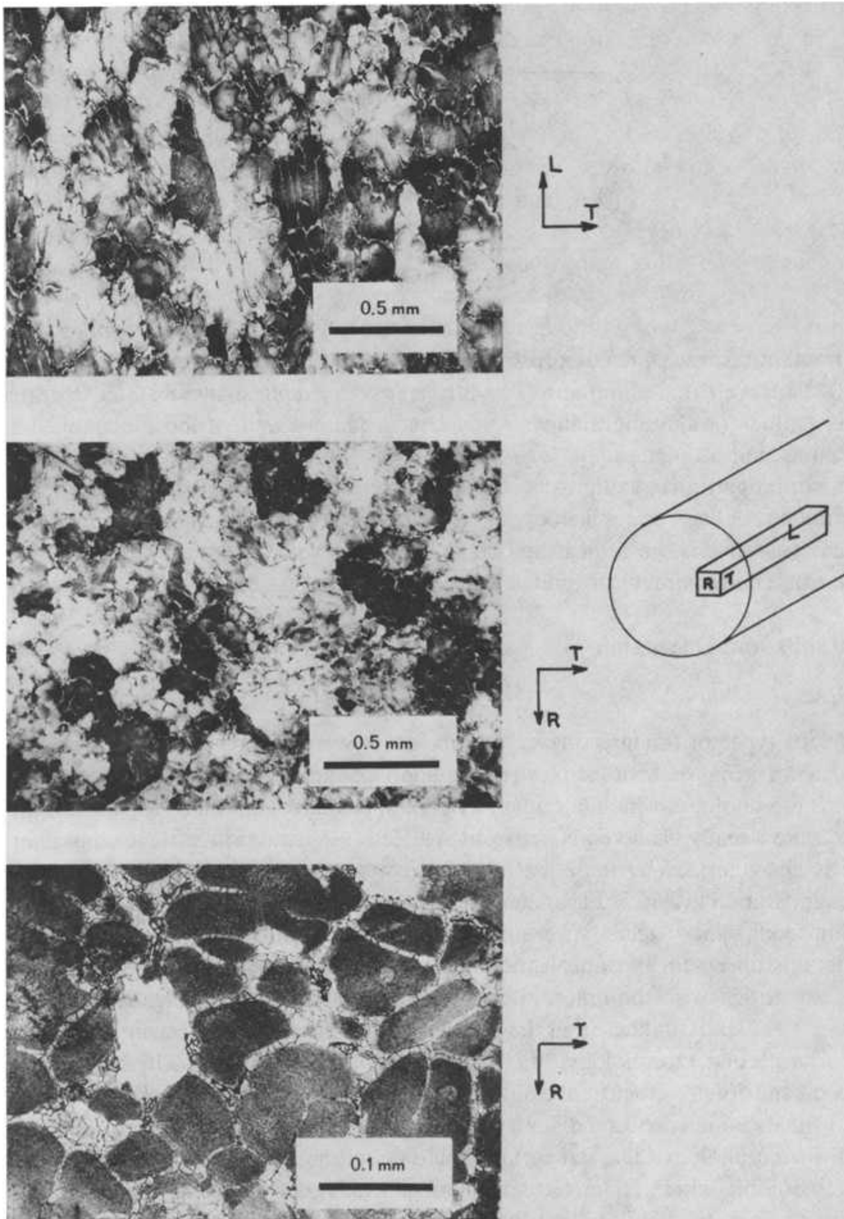

FIG. 2—*Microstructure of the aluminum alloy AU4G.*

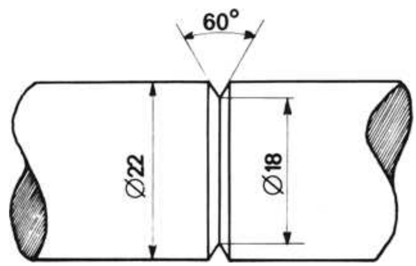

FIG. 3(*a*)—*Mode III test specimen.*

growth rates investigated correspond to 10^{-8}–10^{-7} m/cycle for steel and 10^{-7}–10^{-6} m/cycle for aluminum alloy. It is worth emphasizing that the loading conditions for aluminum alloys specimens are homothetic of those employed in Tests 1 and 5 on steel.

Nonproportional loading usually gave rise to crack bifurcation. The crack paths were observed with an optical microscope at a magnification of ten. Crack deviation angles were measured (face up and down, crack forward and backward). The maximum difference between the four angles was less than 6°.

Results and Discussion

Mode III Loading

Two types of fracture surface morphologies were observed, as shown in Fig. 4*a* and *b*. Figure 4*a* illustrates the situation encountered at low applied torque. This morphology, which has a factory-roof appearance, has many aspects similar to those already observed under cyclic Mode I + steady Mode III loading [*19*]. It is characterized by the existence of two types of facets, as shown at higher magnification in Fig. 5. Facets A contain features characteristic of fatigue fracture (Fig. 5*a*), while Facets B were formed by ductile rupture (Fig. 5*b*). Transverse sections observed by optical microscopy showed that Facets A make an angle of about 45° with the notch plane. The orientation and the fracture aspect of Facets A clearly indicate that they correspond to local Mode I fatigue extension.

The second morphology shown in Fig. 4*b* was observed at higher applied loads and longer crack lengths. In this figure a flat and smeared surface with severe abrasion is observed from the notch before the appearance of the "factory roof" morphology. The flat surface could be interpreted as resulting from either macroscopic Mode III crack extension or as the consequence of the rubbing effect of a previously existing factory-roof morphology. The second hypothesis is supported by the fact that in our observations and in those reported by other investigators [*14,15*] the extent of the apparent Mode III propagation was promoted by high applied torques.

The existence of ductile rupture features suggests that under Mode III loading the crack front morphology is very complex. Relatively long Facets A are de-

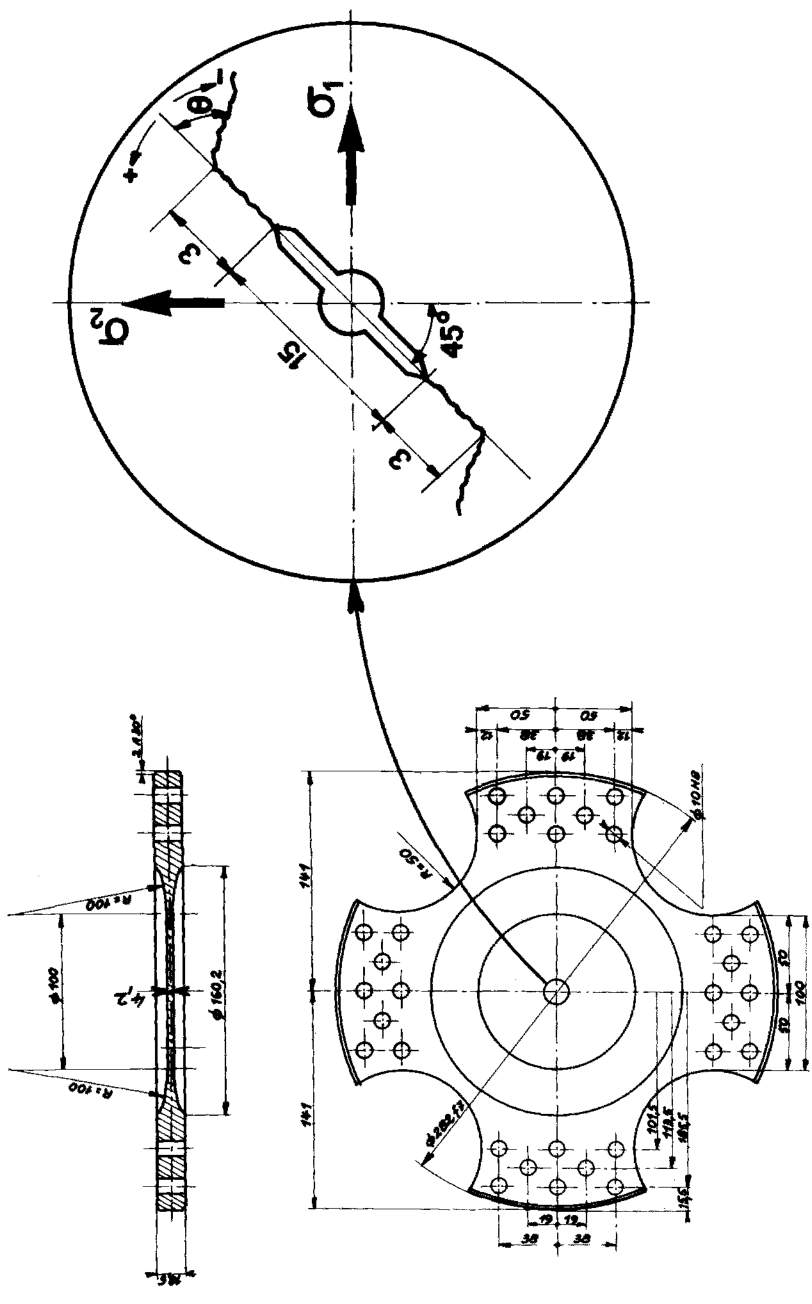

FIG. 3(b)—Cruciform specimen for Modes I + II tests under nonproportional loading.

TABLE 3—*Modes I + II loading conditions.*

Test Number	Loading Conditions, MPa	Observed Angles, Mean Value, deg
	35NCD16	
1	$\sigma_1 = 183.3 + 36.8 \sin(t)$ $\sigma_2 = 63.3 + 63.5 \sin(t)$	−27
2	$\sigma_1 = 167.2 + 33.9 \sin(t)$ $\sigma_2 = 60.8 + 55.9 \sin(t)$	0
3	$\sigma_1 = 156.7 + 34.8 \sin(t)$ $\sigma_2 = 124.3 + 104.5 \sin(t)$	−42
4	$\sigma_1 = 176.5 + 46.6 \sin(t)$ $\sigma_2 = 61.3 + 55.8 \sin(t)$	−10
5	$\sigma_1 = 79.4 + 73.0 \sin(t)$ $\sigma_2 = 184.9 + 38.1 \sin(t)$	31
	AU4G	
1	$\sigma_1 = 86.7 + 17.4 \sin(t)$ $\sigma_2 = 30.0 + 30.0 \sin(t)$	0
2	$\sigma_1 = 40.0 + 36.8 \sin(t)$ $\sigma_2 = 93.2 + 19.2 \sin(t)$	2

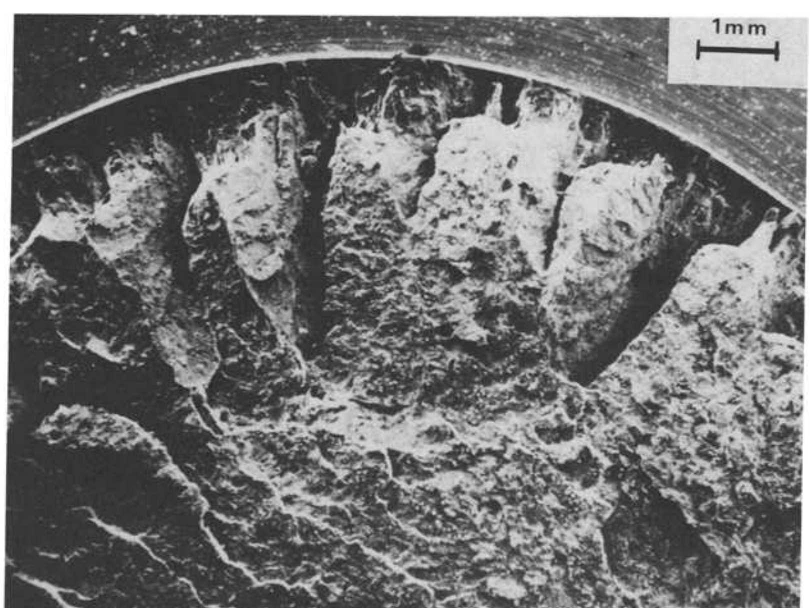

FIG. 4(*a*)—*Steel 26NCDV14. Mode III fracture surface at low torque amplitude.*

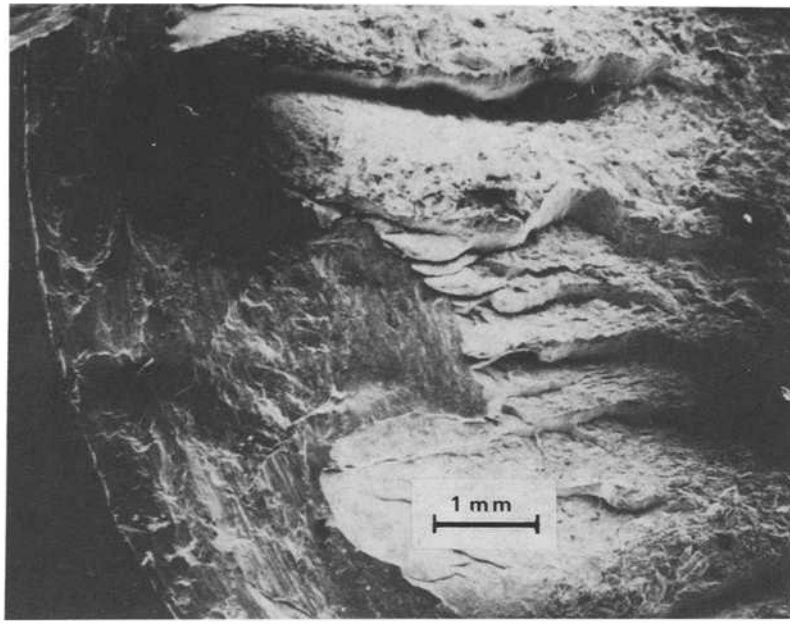

FIG. 4(*b*)—*Steel 26NCDV14, Mode III, fracture surface at high torque amplitude.*

veloping radially in Mode I, leaving in between them uncracked ligaments, as already observed in a previous study [*16*]. These uncracked parts can be subjected to very high stresses giving rise to ductile rupture far behind Facets A crack front. It is suggested that the rupture of the material behind the crack tip might be responsible for the apparent Mode III crack extension. Therefore, in the absence of other investigations, it is felt that, under Mode III loading, the fatigue crack path corresponds systematically to local Mode I extension.

Modes I + II Loading

Mode I Fatigue Crack Growth Rate Measurements—The results of pure Mode I experiments conducted to characterize the two investigated materials are given in Fig. 6*a* and *b*. In the range of crack growth rates examined, it is noticed that the fatigue behavior of 35NCD16 is only slightly dependent on R-ratio. In particular there is no influence of mean stress between $R = 0.3$ and $R = 0.7$. This slight influence was found to be associated with a crack closure phenomenon, as proven by crack closure measurements [*21*]. On the other hand, in the aluminum alloy it is observed that the crack growth rates are significantly dependent on mean stress. In this type of material and in the range of crack propagation rates investigated which corresponds to the upper part of the Paris law, it is likely that the R effect is mainly related to static fracture modes which

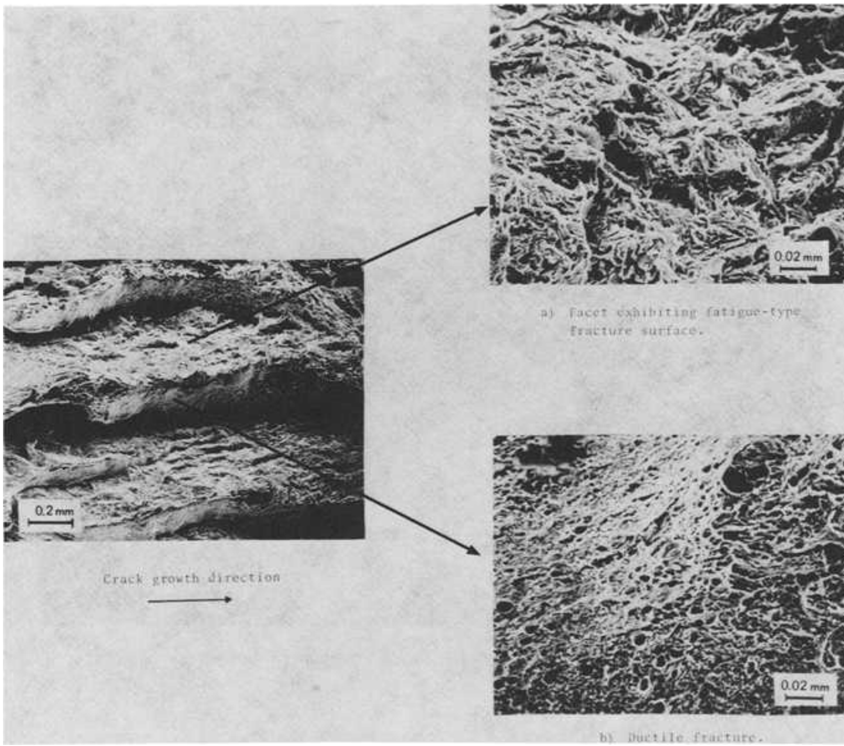

FIG. 5—*Steel 26NCDV14—Factory-roof fracture surface.* (a) *Facets A and* (b) *Facets B.*

are superimposed on fatigue fracture mechanism. It is also worth noting that the fatigue crack growth behavior of the aluminum alloy is isotropic.

Polymodal Experiments—The results of nonproportional loading giving the bifurcation angle defined in Fig. 3*b* are reported in Table 3. In order to make a comparison between observed angles and those predicted by the three criteria, $k_{\mathrm{Imax}}{}^*$, $\Delta k_{\mathrm{Imax}}{}^*$ and $(da/dN)_{\max}$, the stress intensity factors on branched cracks were calculated using Chatterjee formulation [2]. The deviation angles derived from $(da/dN)_{\max}$ criterion were numerically calculated using da/dN-ΔK_{I} data reported in Fig. 6. The loading conditions indicated in Table 3 were chosen in order to derive large differences between the angles predicted from the various criteria. The comparisons are made in Fig. 7 for 35NCD16 steel and in Table 4 for the aluminum alloy. Before discussing these comparisons and although the object of the present study was not the investigation of fatigue crack growth rates under nonproportional loading, here it is worth mentioning that the crack propagation rates measured after crack bifurcation were very similar to those corresponding to pure Mode I loading. This is illustrated in Fig. 8 which is related to the aluminum alloy. In this alloy the biaxial loads were chosen in order to avoid crack bifurcation (see Table 4).

In 35NCD16 steel, it is noticed that, as expected, $\Delta k_{\mathrm{Imax}}{}^*$ and $k_{\mathrm{Imax}}{}^*$ criteria

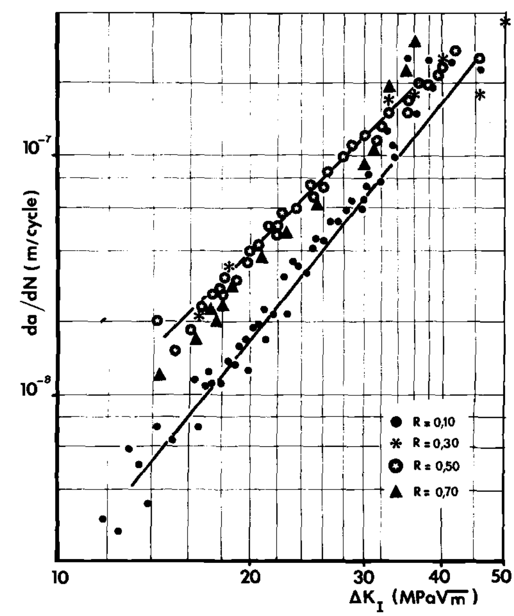

FIG. 6(*a*)—*Basic fatigue crack growth kinetics of steel 35NCD16, as a function of* R*-ratio.*

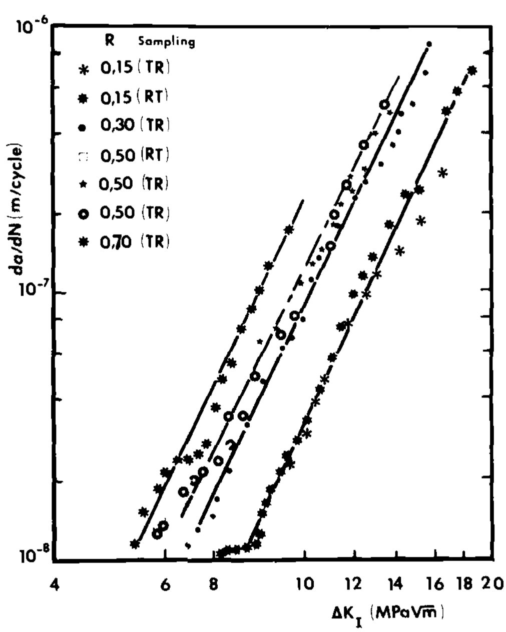

FIG. 6(*b*)—*Basic fatigue crack growth kinetics of aluminum alloy AU4G, as a function of* R*-ratio.*

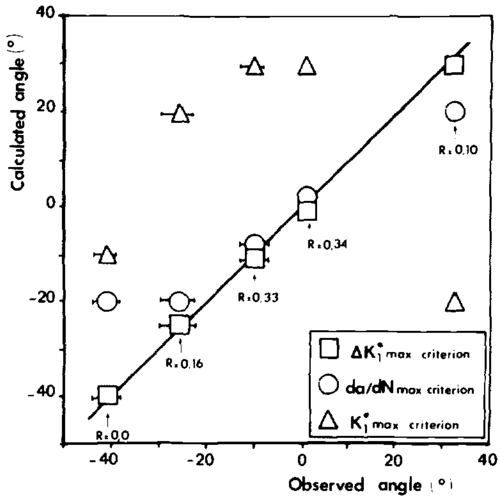

FIG. 7—*Steel 35NCD16. Comparison between the observed branching angles and those predicted by three different criteria. The reported* R*-values refer to stress ratio values as defined by Fig. 1.*

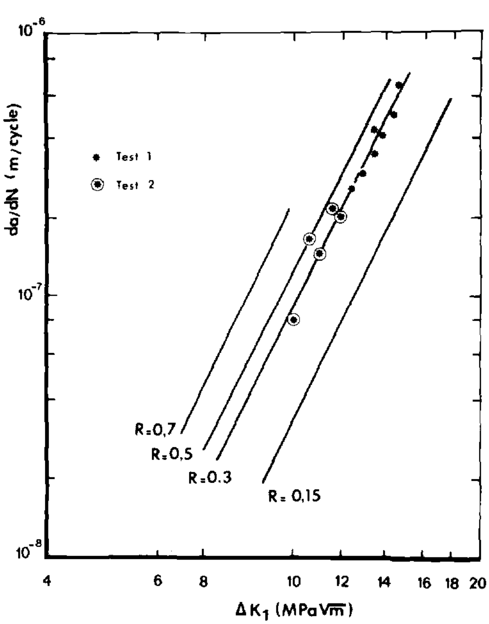

FIG. 8—*Aluminum alloy AU4G. Fatigue crack growth kinetics of branched cracks, in condition where* R = *0.4.*

TABLE 4—*Comparison of predicted angles and observed ones in aluminum alloy (in degrees).*

Test Number	Experiment	da/dN_{max}	Δk_{Imax}*	k_{Imax}*
1	≃0°	0°	−25°	+25°
2	≃0°	0°	+30°	−20°

lead to widely different angles. For this material it appears that Δk_{Imax}* criterion gives the best prediction. The $(da/dN)_{max}$ criterion predicts right angles for three tests corresponding to high values of the $k_{Imin}*/k_{Imax}*$ ratio. For the two other tests with lower R-values, the observed angles are larger than those derived from $(da/dN)_{max}$ criterion. For these two specific tests the predictions from Δk_{Imax}* criterion are different from those derived from $(da/dN)_{max}$ approach because the effect of mean stress observed in pure Mode I (Fig. 6*a*) was taken into account. On the other hand, for R-ratio larger than 0.3, Mode I crack growth rates were found to be independent on mean stress. Therefore, in these conditions, as already discussed in the introduction, the two criteria give identical predicted angles.

In the aluminum alloy, Table 4 shows that the angles derived from the three investigated criteria are very different. It is noticed that only $(da/dN)_{max}$ criterion can account for the experimental results. It is worth noting that the homothetic loading conditions adopted for Test 5 on steel and Test 2 on aluminum alloy lead to widely different bifurcation angles as illustrated in Fig. 9. Test 5 on steel

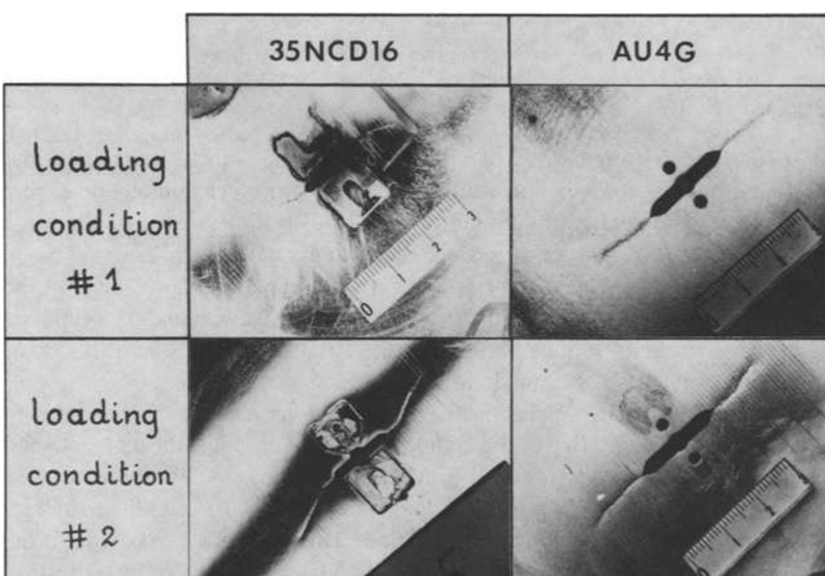

FIG. 9—*Comparison between the branching angles observed in steel 35NCD16 and AU4G alloy, for similar loading conditions as defined in Table 3.*

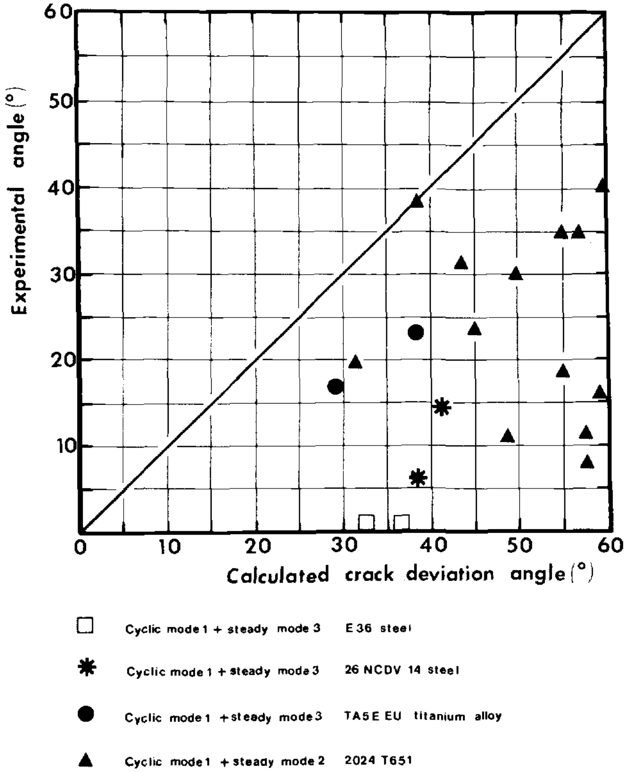

FIG. 10(*a*)—*Comparison between crack deviations angles which are predicted by* k_{Imax}* *criterion and the observed ones.*

gives rise to a crack angle of 32 to 34°, while in the homothetic one carried out on aluminum alloy no deviation is observed. The two other homothetic experiments (Test 1 on steel and aluminum alloy) lead to a difference of the same order. These experiments clearly indicate that a purely mechanical criterion based either on $\Delta k_{\mathrm{Imax}}{}^*$ or $k_{\mathrm{Imax}}{}^*$ cannot account for the experimental results. In the derivation of a criterion for predicting crack path behavior under polymodal fatigue, it is necessary to incorporate also the fatigue response characteristic of the material, which is partly made in the $(da/dN)_{\mathrm{max}}$ approach.

The comparison between the three investigated criteria can be extended to other results obtained by two of the authors [*19,22*]. These results were obtained in cyclic Mode I + steady Mode II or Mode III loading, as already mentioned in the introduction. For this particular loading condition it is clear that $\Delta k_{\mathrm{Imax}}{}^*$ criterion always predicts no crack bifurcation. This does not correspond to the situation observed in most materials investigated; except in a mild steel (E36 steel) which showed no mean stress effect on Mode I crack growth rate in the range of da/dN examined. Figure 10*a* indicates that the $k_{\mathrm{Imax}}{}^*$ criterion cannot

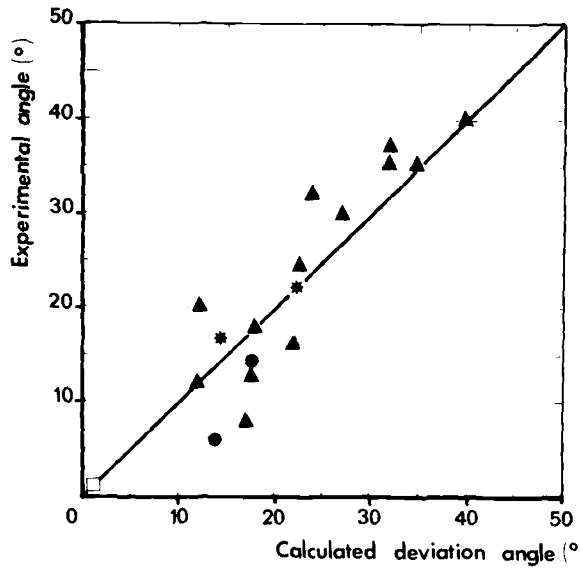

FIG. 10(*b*)—*Comparison between observed crack deviations angles and those predicted by* da/dN_{max} *criterion. For those loading conditions,* $\Delta k_{Imax}{}^*$ *criterion always predict no crack deviation, that is zero angles.*

also account for the experimental results, while Fig. 10*b* shows that the $(da/dN)_{max}$ approach is in better agreement with the experiments. However in a number of cases the differences between the predicted and the observed angles are still large. It is believed that these discrepancies are largely associated with the crack closure phenomenon. The crack closure effect was reflected in the fact that the crack growth rates calculated from the straightforward application of the (da/dN) criterion were usually different from the observed ones [*19*]. Therefore, it can be concluded that an improvement of the approaches to predicting crack path behavior under polymodal fatigue requires a better knowledge of the crack closure phenomenon, which is far from being achieved when one considers that even under conventional Mode I loading, in spite of the large number of studies initiated by Elber's concept [*23*], we are still very far from the goal.

Conclusions

1. When a cracked structure is subjected to several nonproportional loads leading to polymodal fatigue, the criteria usually employed for predicting crack

path direction under monotonic loading are no longer valid. They may be extended in various ways. In this study three possible extensions were examined, assuming that the crack propagates either in the direction where k_I^* or Δk_I^* are maximum, or in the direction corresponding to the maximum crack growth rate ($(da/dN)_{max}$ criterion).

2. In the range of fatigue crack growth rates corresponding to Paris law, crack extension occurs essentially by local Mode I. This situation is observed either in biaxial Modes I + II loading or even in cyclic Mode III.

3. Based on the investigation of cyclic Modes I + II crack growth in 35NCD16 steel, in AU4G alloy, and previous studies in cyclic Mode I + steady Mode II or Mode III, the following conclusions can be drawn.

(*a*) Tests with homothetic loading conditions applied to two different materials giving rise to different crack path, it appears that a criterion based uniquely on the analysis of nominal values of stress intensity factors is unable to predict correctly the crack path behavior for a wide range of materials.

(*b*) In materials such as mild steel or structural steels exhibiting a small influence of R-ratio on Mode I crack growth rate, crack path in polymodal fatigue is reasonably well predicted by Δk_{Imax}^* criterion. The predictions obtained from the application of $(da/dN)_{max}$ criterion are also reasonable. On the other hand, k_{Imax}^* criterion cannot account for the experimental results.

(*c*) In materials such as high-strength aluminum alloys for which Mode I crack growth rates are largely influenced by mean stress, the crack path direction is governed not only by the amplitude of stress-intensity factor Δk_I^* but also by its maximum value. In these conditions, the application of $(da/dN)_{max}$ criterion leads to better results.

Acknowledgments

This study was partly financially supported by the Délégation Générale à la Recherche Scientifique et Technique. The assistance of R. Locicero and P. Clement from the Ecole des Mines and C. Vallet from Institut de Recherches de la Siderugie for conducting the experimental program is also gratefully acknowledged.

References

[1] Amestoy, M., Bui, H. D., and Dang-Van, K., Comptes Rendus Academic des Science, Paris, Vol. 289, Series B, 1979, pp. 99–102.
[2] Chatterjee, S. N., *International Journal of Solids and Structures*, Vol. 11, 1975, pp. 521–538.
[3] Nuismer, R. J., *International Journal of Fracture*, Vol. 11, 1975, pp. 245–250.
[4] Lawn, B. R. and Wilshaw, T. R., *Fracture of Brittle Solids*, Cambridge University Press, Cambridge, U.K., 1975.
[5] Iida, S. and Kobayashi, A. S., *Journal of Basic Engineering, Transactions*, American Society of Mechanical Engineers, 1969, p. 764.
[6] Tanaka, K., *Engineering Fracture Mechanics*, Vol. 6, 1974, pp. 493–507.

[7] Truchon, M., Amestoy, M., and Dang-Van, K., *5th International Conference on Fracture*, Vol. 4, 1981, pp. 1841–1849.
[8] Pook, L. P., "Mixed Mode Threshold behavior of mild steel," in *Fatigue Thresholds*, Proceeding of the 2nd International Conference on Fatigue and Fatigue Thresholds, Stockholm, 1–3 June, 1981.
[9] Erdogan, F. and Sih, G. C., *Journal of Basic Engineering*, Vol. 4, 1963, pp. 519–527.
[10] Ewing, P. D. and Williams, J. C., *International Journal of Fracture*, Vol. 10, 1974, pp. 537–544.
[11] Sih, G. C., "Strain Energy Density Factor Applied to Mixed Mode Crack Problems," *International Fracture*, Lehigh University, Bethlehem, PA, 1972.
[12] Palaniswany, K. and Knauss, W. G., *International Journal of Fracture*, Vol. 8, 1972, p. 114.
[13] Hua, G., Brown, M. W., and Miller, K. J., *Fatigue of Engineering Materials and Structures*, Vol. 5, 1982, pp. 1–17.
[14] Hurd, N. J. and Irving, P. E. in *Design of Fatigue and Fracture Resistant Structures, ASTM STP 761*, American Society for Testing and Materials, Philadelphia, 1982, pp. 212–233.
[15] Ritchie, R. O., McClintock, F. A., Nayeb-Hashemi, H., and Ritter, M. A., *Metallurgical Transactions*, Vol. 13A, 1982, pp. 101–110.
[16] Hourlier, F., These de doctorat, Université de Technologie, Compiegne, France.
[17] Truchon, M. and Amestoy, M., Etude Théorique et Expérimentale de la Fissuration par Fatigue sous Sollicitations Biaxiales," RE 872, 1981, Institut de Recherches de la Siderugie, Saint-Germain-en-Laye, France.
[18] Otsuka, A., Mori, K., Ohshima, T. and Tsuyama, S., *5th International Conference on Fracture*, Vol. 4, 1981, pp. 1851–1858.
[19] Hourlier, F. and Pineau, A., *5th International Conference on Fracture*, Vol. 4, 1981, pp. 1833–1840.
[20] Tada, H., Paris, P., and Irwin, G., *The Stress Analysis of Cracks Handbook*. Del Research Corp., Hellertown, PA, 1973.
[21] Dhondt, H. and Truchon, M., "Etude du Branchement des Fissures sous Sollicitations Bimodales non Proportionnelles," Institut de Recherches de la Siderugie, Saint-Germain-en-Laye, France, 1982.
[22] Hourlier, F., McLean, D., and Pineau, A., *Metals Technology*, 1978, pp. 154–158.
[23] Elber, W., in *Damage Tolerance in Aircraft Structures, ASTM STP 486*, American Society for Testing and Materials, Philadelphia, 1971, pp. 230–242.

DISCUSSION

K. N. Akhurst,[1] *R. C. Lindley,*[1] *and K. J. Nix*[1] *(written discussion)*—Rotors in modern turbogenerators are monitored routinely for changes in vibration characteristics in order to give early warning of cracking. If these measurements suggest the presence of a crack, then the rate of crack propagation is of paramount importance in order to avoid the substantial secondary damage which might result from complete failure of the rotor shaft. The rate of crack growth can be assessed in different ways. For example, a fracture mechanics based analysis may be used which requires a knowledge of the K-solutions for the cracked shaft, together with experimentally derived fatigue crack growth laws. In the event of a cracked shaft being removed from service, the failure investigation invariably includes a "beach mark" analysis. Pronounced beach marks are produced on a fracture surface by significant changes in the applied mechancial loading such as startup/shutdown. The rate of crack development can then be found by comparing the beach mark spacings and the turbogenerator operational records. The beach mark analyses can be used to check the accuracy of the fracture mechanics based analysis. Earlier appraisals used a fracture mechanics analysis in which only the Mode I cyclic stress intensity factor ΔK_I (from rotor self-weight bending) was considered. However, parts of the turbogenerator train experience significant torsional loading. More recently, the Ecole des Mines data of Hourlier and Pineau has been employed. These workers noted that the application of a steady Mode III torsion to a crack growing under a cyclic ΔK_I could significantly retard crack growth. By using the data of Hourlier and Pineau,[2] greatly improved correlation was found between the beach-mark and fracture mechanics analyses during a recent failure investigation.

F. Hourlier, H. d'Hondt, M. Truchon, and A. Pineau (authors' closure)—Two of the present authors (F. Hourlier and A. Pineau) are pleased to learn that their results obtained on specimens tested in the laboratory have been useful for the analysis of an in-service failure of a component. They would like to thank K. N. Akhurst, R. C. Lindley, and K. J. Nix for their comments on one part of their work, which was originally devoted to the effect of a permanent torque giving rise either to steady Mode III or steady Mode II on Mode I fatigue crack growth rate behavior.[2,3,4] This is the situation frequently observed for thumbnail cracks initiated in rotors, as indicated by K. N. Akhurst, R. C. Lindley, and K. J. Nix. In the present paper an extension of the criterion proposed earlier for the determination of crack path under polymodial fatigue is presented.

[1]Central Electricity Research Laboratories, Leatherhead, Surrey, U.K.

[2]Hourlier, F. and Pineau, A., *Memoires Scientifiques de Revue de Métallurgie*, 1979, pp. 175–185.

[3]Hourlier, F., McLean, D., and Pineau, A., *Metals Technology*, 1978, pp. 154–158.

[4]Hourlier, F. and Pineau, A., *Fatigue of Engineering Materials and Structures*, Vol. 5, 1982, pp. 287–302.

Leslie P. Pook[1]

Comments on Fatigue Crack Growth Under Mixed Modes I and III and Pure Mode III Loading

REFERENCE: Pook, L. P., "**Comments on Fatigue Crack Growth Under Mixed Modes I and III and Pure Mode III Loading,**" *Multiaxial Fatigue, ASTM STP 853*, K. J. Miller and M. W. Brown, Eds., American Society for Testing and Materials, Philadelphia, 1985, pp. 249–263.

ABSTRACT: Some features of fatigue crack growth under pure Mode III and mixed Modes I and III loading were examined, including two cases where the Mode III displacements are not proportional to the Mode I displacements. Information obtained under nominally elastic conditions for various commercial alloys was reanalyzed and discussed in the light of theoretical considerations to see whether consistent patterns of behavior could be identified. Despite some inconsistencies and anomalies it was found that a reasonably consistent pattern of behavior was beginning to emerge. In particular a tentative upper bound for the rate of fatigue crack growth was identified, but it does not apply to slant crack growth in thin sheets.

KEY WORDS: fatigue crack growth, metals, complex loading and fracture mechanics

Nomenclature

a	Crack length or depth
C	Constant in Eq 1
K	Stress intensity factor; subscripts I, II, and III denote mode
K_A	Apparent value of K_I for inclined crack
K_{max}	Maximum value of K_I in fatigue cycle
k	K for small-scale feature (Figs. 5, 6, and 12)
$k_I{}^*$	Value of k_I for pure or predominantly Mode I facet
m	Exponent in Eq 1
N	Number of cycles
R	Stress ratio: ratio of minimum to maximum stress in fatigue cycle
Y	Correction factor in Eq 9
α	Initial crack path angle (Fig. 1)
β	Crack inclination (Fig. 1); exponent in Eq 4
γ	Exponent in Eq 4

[1]Senior principal scientific officer, National Engineering Laboratory, East Kilbride, Glasgow, Scotland.

Copyright© 1985 by ASTM International www.astm.org

ν Poisson's ratio
ϕ Inclination of small-scale feature (Figs. 5 and 12)
ϕ^* Value of ϕ corresponding to k_I^*

For situations where the crack-tip stress field can be characterized by a linear elastic fracture mechanics analysis based on stress-intensity factors it is a matter of observation that in isotropic materials Stage II [*1*] fatigue cracks, viewed macroscopically, tend to grow in Mode I [2]. At and above the onset of general yielding stress-intensity factors are not strictly valid, and crack growth often takes place on planes of maximum shear stress.

Conventional specimens used to determine fatigue-crack-growth data for analysis using stress-intensity factors are therefore designed so that only Mode I crack surface displacements are present and the crack grows in a self-similar manner. However, when Mode III displacements are present then a preferred plane for crack growth only intersects the initial crack front at one point, and behavior becomes complex [*3–5*].

Some features of fatigue crack growth under pure Mode III, and mixed Modes I and III loading are examined, including two cases where the Mode III displacements are not proportional to the Mode I displacements. Information obtained under nominally elastic conditions for various commercial alloys is reanalyzed and discussed in the light of theoretical considerations to see whether consistent patterns of behavior can be identified.

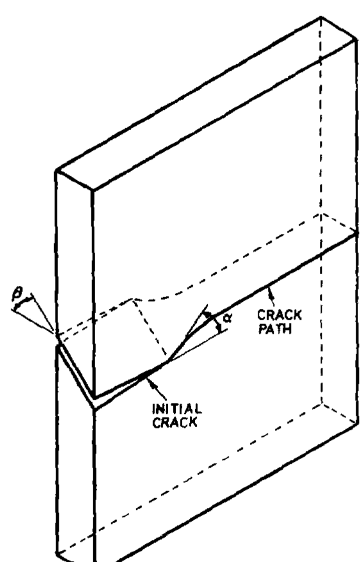

FIG. 1—*Inclined crack.*

Irregular surfaces, such as fracture surfaces, cannot be adequately characterized unless the scale at which measurements are to be made is first specified in some way [6]. A scale of 1 mm has been suggested [7], but, in the analysis of fatigue-crack-growth data obtained under Mode I loading, it is not usually necessary to be so specific. However in the case of pure Mode III or mixed Modes I and III loading more care is needed. In this paper the following conventions are used. The modes of crack surface displacement, and associated stress-intensity factors, refer to a macroscopic scale of 1 mm unless otherwise noted. Characterization of modes of crack surface displacement at the slightly smaller scale of 0.1 mm is also used; associated stress-intensity factors, expressed in terms of macroscopic stress-intensity factors (see Appendix), are distinguished by the use of lower case k. Upper case K is otherwise used for stress-intensity factor. In both cases subscripts I, II, III are used to denote mode, and the prefix Δ to denote range in fatigue cycle. However, at zero mean load ΔK_{III} denotes the alternating Mode III stress-intensity factor.

Some Fractographic Aspects

At macroscopic scales, where irregularities of less than the order of, say, 1 mm are ignored, behavior depends on whether or not the crack front forms a closed curve. In a thick plate with a crack inclined at an angle β (Fig. 1) so that Modes I and III are present, the crack front rotates as a crack grows (Figs. 1 and 2) until the crack is perpendicular to the applied stress, and therefore growing in Mode I. At the start of crack growth the crack trace on the plate surface makes an angle α with the initial direction, suggesting the possible presence [3,4] of

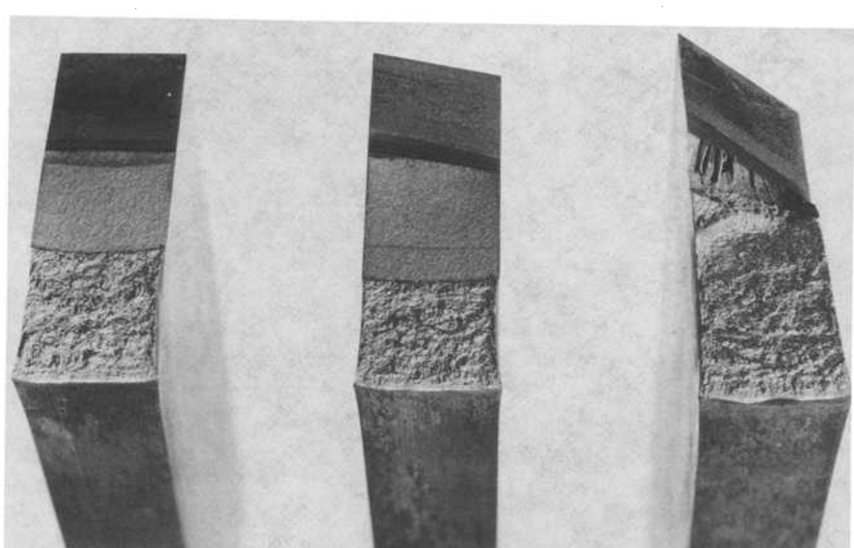

FIG. 2—*Fracture surfaces of 25-mm-thick mild steel bend specimens.* β = *0, 15, and 45°.*

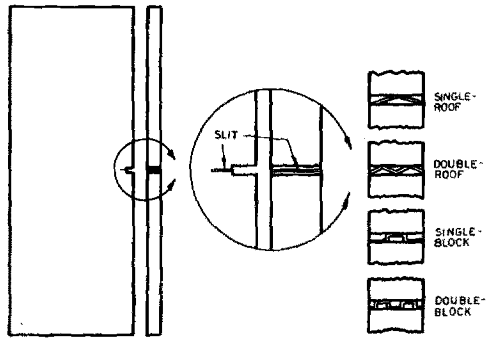

FIG. 3—*Edge notch plate specimen with spark eroded slit.*

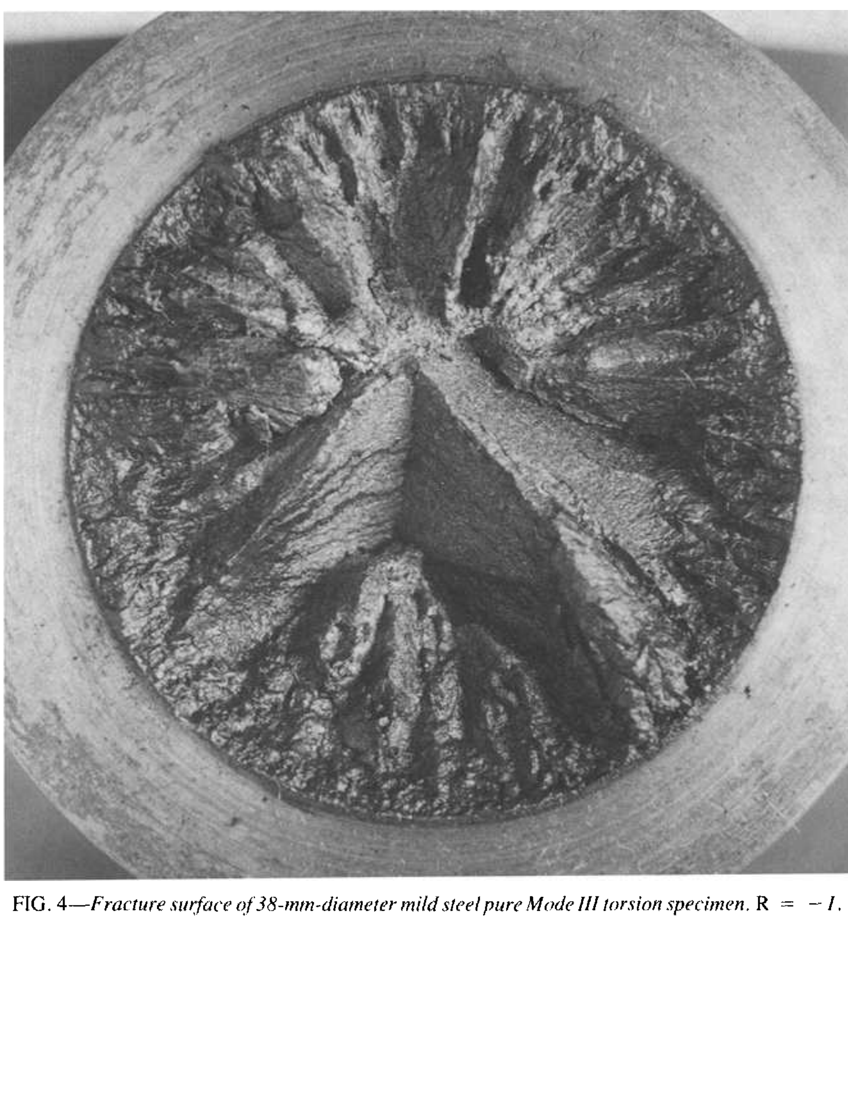

FIG. 4—*Fracture surface of 38-mm-diameter mild steel pure Mode III torsion specimen.* R = *−1.*

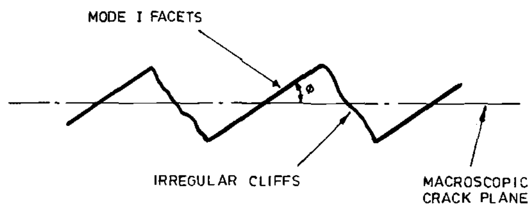

FIG. 5—*Schematic section through twist crack perpendicular to crack-growth direction.*

Mode II as well as Modes I and III. For the mild steel specimens shown in Fig. 2 average values of α are 22 and 61° for β equal to 15 and 45°, respectively. (These specimens are being tested as part of a program [*8*] to determine the mixed mode threshold behavior of mild steel.) A similar effect has been observed [*9*] for crack growth from the "single-roof" and "double-roof" slits shown in Fig. 3.

Examination at the slightly smaller scale of 0.1 mm usually reveals long narrow facets of Mode I crack growth aligned in the overall crack-growth direction (Figs. 2 and 4). Observed facet widths vary from about 0.1 mm [*10*] to about 2½ mm [*11*]. Under mixed Modes I and III displacements the initially separate Mode I facets become connected by irregular cliffs of predominantly Mode III as crack growth proceeds. When fully developed this has been called a "twist" crack [*5*]; a schematic section is shown in Fig. 5. Crack configurations related to twist cracks have been obtained [*9*] for cracks in 7075-T6 aluminum alloy growing from the spark machined "single-block" and "double-block" initial slits shown in Fig. 3. The cliffs separating the blocks gradually disappeared as a crack grew, the cracks eventually becoming normal Mode I.

Pure Mode III is most readily obtained experimentally using circumferentially notched cylindrical specimens loaded in torsion, and the use of such specimens is virtually universal. The crack front is a closed curve, and this means that the crack front cannot rotate and remain continuous. In a macroscopic sense the crack remains confined [*10–13*] to its initial plane (Fig. 4). Some tests using a special plate specimen [*14*] were later shown [*15*] not to be reasonably pure Mode III. Side grooves confined the crack to its initial plane; in effect the crack front was "almost" a closed curve.

For pure Mode III a twist fracture surface is sometimes observed; at zero mean load this consists of intersecting Mode I facets on complementary planes at ±45°

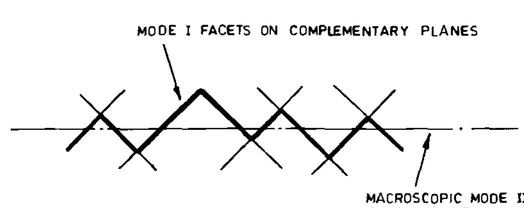

FIG. 6—*Schematic section through Mode III crack perpendicular to crack-growth direction.*

to the macroscopic crack plane (Figs. 4 and 6). "True" Mode III crack growth in which the fracture surfaces have a rubbed, featureless appearance is otherwise observed. It is not clear whether Mode I facets do not form, or they form and are subsequently destroyed by rubbing; the former is assumed in Refs *10,12*, and *13*. The type of fracture surface depends on the material, level of ΔK_{III}, and value of the stress ratio R, which is the ratio of minimum to maximum load in the fatigue cycle. At zero mean load ($R = -1$) Mode I facets were always observed [*8*] on mild steel with a 0.2% proof stress of 450 MN/m^2. For AISI 4340 steel [*10*], 0.2% proof stress 956 MN/m^2, $R = -1$, no Mode I facets were observed over a wide range of ΔK_{III}, but Mode I facets were very common on a lower strength AISI 4140 steel; more recent work [*13*] on the AISI 4340 steel showed that Mode I facets were observed on deep cracks but not shallow cracks. It was found [*12*] for BS 970 605H32 steel heat treated to 0.2% proof stresses of 891, 1294, and 1556 MN/m^2 that Mode I facets were more commonly observed as the strength level increased, ΔK_{III} was decreased, and R was changed from -1 to 0.08.

The slant ($\beta = 45°$) crack growth often observed in thin sheets [*2,16,17*] is mixed Modes I and III at both scales; Mode I facets are not observed. It is an exception to the general observation that fatigue cracks tend to grow in Mode I. In the analysis of fatigue-crack-growth rate data it is conventionally treated as if it were Mode I.

Analysis of Fatigue-Crack-Growth Rate Data

Conventional Mode I fatigue-crack-growth rate data are usually analyzed in terms of ΔK_I. For many metals data can be represented by [*2*]

$$\frac{da}{dN} = C(\Delta K_I)^m \tag{1}$$

where

a = a crack length,
N = number of cycles, and
C and m = material constants; m is usually around 3.

In mean stress sensitive materials crack-growth rates also depend on R. A similar relationship holds for pure Mode III, but at equal values of ΔK_{III} and ΔK_I crack-growth rates in Mode III are generally slower. For twist cracks analysis in terms of Δk_I^*, the value of ΔK_I for a Mode I facet (see Appendix) permits direct comparison with Mode I data. If it be assumed that true Mode III crack-growth results when Mode I facets are destroyed by rubbing then the same comparison is possible. For pure Mode III $k_I^* = K_{III}$ (Eq 7).

Some pure Mode III data are summarized in Table 1 which shows values of Δk_I^* normalized by ΔK_I for the same crack-growth rates. Subjective judgments are involved in the reanalysis of published data, and the third significant figure

TABLE 1—*Summary of Mode III fatigue-crack-growth data.*

Ref	Material	0.2% Proof Stress, MN/m^2	Specimen Type	ϕ^*, deg	R	$\Delta k_I^*/\Delta K_I$	Remarks
8	mild steel	270	cylindrical pure Mode III	45	−1	1.28	Mode I facets, based on threshold
11	AISI 4340 steel	956	cylindrical pure Mode III	45	−1	1.37	no Mode I facets
13	AISI 4340 steel	956	cylindrical Mode III plus small Mode I ($\Delta K_I = 3\ MN/m^{3/2}$)	45	−1	~1	crack-growth rate $>5.10^{-5}$ mm/c no Mode I facets (shallow cracks), Mode I component of load has little effect
13	AISI 4340 steel	956	cylindrical Mode III plus small Mode I ($\Delta K_I = 3\ MN/m^{3/2}$)	45	−1	1.53	crack-growth rate $<5.10^{-5}$ mm/c Mode I facets (deep cracks), Mode I component of load has little effect
12	BS 970 605H32 steel	891	cylindrical pure Mode III	45	−1	1.68	some Mode I facets
12	BS 970 605H32 steel	891	cylindrical pure Mode III	45	0.08	2.15	Mode I facets
12	BS 970 605H32 steel	1294	cylindrical pure Mode III	45	0.08	3.55	Mode I facets
12	BS 970 605H32 steel	1556	cylindrical pure Mode III	45	0.08	2.75	Mode I facets
9	7075-T6 aluminum		single-roof (Fig. 3) $\beta = 18°$ $K_I/K_{III} = 3.08$	31.4	0.2	1.08	
9	7075-T6 aluminum		double-roof (Fig. 3) $\beta = 26°$ $K_I/K_{III} = 2.05$	35.6	0.2	1.21	
9	7075-T6 aluminum		single-block (Fig. 3)	...	0.2	1.12	
9	7075-T6 aluminum		double-block (Fig. 3)	...	0.2	1.23	

is not really justified; it is included to avoid excessive rounding errors. Also shown is the predicted Mode I facet angle, ϕ^*, (Fig. 5) calculated from Eq 8. Values of $\Delta k_I^*/\Delta K_I$ for the results in Refs *10,12,* and *13* were obtained from graphical data. Data from Ref *13* for crack lengths of less than 1 mm were discarded on the grounds that the crack was still within the influence of the crack starter notch. The result for mild steel [*8*] was based on the fatigue-crack-growth threshold. Values of $\Delta k_I^*/\Delta K_I$ cover a wide range from one upwards, with a broad correlation between high values and the appearance of Mode I facets. Data for tests [*13*] carried out at constant ΔK_{III} on the AISI 4340 steel, replotted in Fig. 7, show that the crack-growth rate decreases with increasing crack depth, with concomitant increase in $\Delta k_I^*/\Delta K_I$. A transition from true Mode III crack growth to a twist fracture takes place when the crack-growth rate drops below 5.10^{-5} mm/cycle. It has been suggested [*12*] that there is a threshold for true Mode III crack growth which is substantially higher than that [*8,11*] for Mode I facet growth. The results in Fig. 7 suggest that some of the high values of $\Delta k_I^*/\Delta K_I$ are the result of the interlocking of Mode I facets on complementary planes (at $R = -1$) and of friction between opposite crack surfaces in true Mode III crack growth. In both cases the value of Y in Eq 9 would be reduced. Both effects are difficult to quantify [*10,12*]; an attempt is made in Ref *13* using an extrapolation technique. Another problem is that Mode I facets are sometimes too large for Eqs 5 to 9 to be valid (for example Fig. 4). Also, crack-tip plastic zones are relatively large in the presence of Mode III [*18*]; this makes the use of stress-intensity factors doubtful at higher values of ΔK_{III} [*10,12*].

Table I also shows results for tests [9] on 7075-T6 aluminum alloy specimens

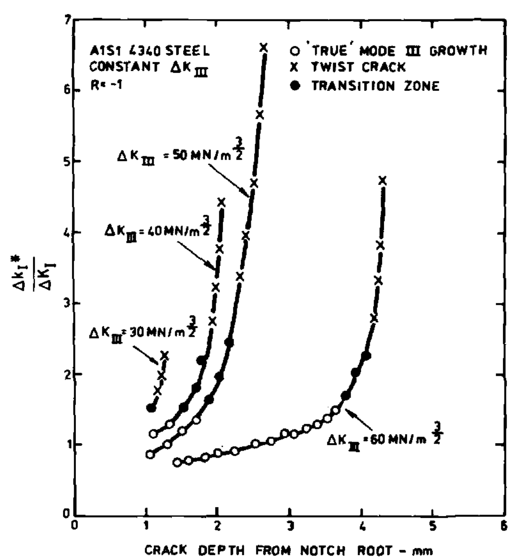

FIG. 7—*Relationship between* $\Delta k_I^*/\Delta K_I$ *and crack depth.*

with the single-roof, double-roof, single-block, and double-block slits shown in Fig. 3. For the roof specimens values of K_I and K_{III} were first calculated from K_A (the apparent value of K_I calculated as if the slits were straight) using the approximate equations [*18*]

$$K_I = K_A \cos^2\beta \tag{2}$$

$$K_{III} = K_A \sin\beta \cos\beta \tag{3}$$

Δk_I^* and ϕ^* were then calculated from Eqs 7 and 8 with Poisson's ratio, ν, taken as one third. Growth rate comparisons were made for crack growth near the initial slits. For the block specimens Δk_I^* was taken as the value of ΔK_I calculated ignoring the intervening cliffs and is therefore analogous to Δk_I^* for a twist crack. Comparison was again for crack growth near the initial slits. Similar values of $\Delta k_I^*/\Delta K_I$ were obtained in each case.

Two Examples of Nonproportional Loadings

In a nonproportional loading, the ratio K_I/K_{III} varies during a fatigue cycle, and there is no facet angle (Fig. 5) for which a facet is pure Mode I throughout the fatigue cycle.

Some tests have been carried out [*19–21*] using circumferentially notched cylindrical specimens cyclically loaded in tension ($R = 0.1$) with superimposed steady-state torsion to give Mode I fatigue plus steady-state Mode III. The materials tested were mild steel, which is not mean stress sensitive, and 26 NCDV rotor steel (3.5 Ni-Cr-Mo-V) and TA5E titanium alloy (5 Al-2.5 Sn) which are both mean stress sensitive. Mode I fatigue-crack-growth data for these two latter materials were fitted to a modified form of Eq 1

$$\frac{da}{dN} = C(\Delta K_I)^{\beta}(K_{max})^{\gamma} = \frac{C(\Delta K_I)^{\beta+\gamma}}{(1 - R)^{\gamma}} \tag{4}$$

where

K_{max} = maximum value of K_I in the fatigue cycle, and
β and γ = material constants.

For the rotor steel $\beta = 2.55$ and $\gamma = 0.55$ ($5.10^{-6} < da/dN < 2.10^{-4}$ mm/cycle) and for the titanium alloy $\beta = 3.05$ and $\gamma = 1.75$ ($10^{-6} < da/dN < 5.10^{-3}$ mm/cycle). As a crack front was a closed curve crack growth, at a macroscopic scale, remained in the initial plane.

For the mild steel crack growth at a smaller scale was also in the initial plane, but twist cracks were produced in the other two materials. (The tips of the cliffs joining the facets lagged several millimetres behind the tips of individual facets.) It was found that the value of ϕ was about that (ϕ^*) for which the combination of Δk_I and the maximum value of k_I, calculated from Eq 5 (see Appendix) corresponded to the fastest expected fatigue-crack-growth rate as calculated from Eq 4. For the mild steel $\beta = 3.04$ and $\gamma \approx o$ which indeed predicts that crack growth should remain in the initial plane.

Figure 8 shows the relationship between relative crack-growth rate (the value at $\phi = 0°$ is taken as one) and ϕ for the titanium alloy. The results are fairly sensitive to Poisson's ratio, and as with some other critical crack directions [*3,4,22*], ϕ^* is not sharply defined. Also shown is the effective R, calculated from Δk_I and the maximum value of k_I. A similar criterion has been suggested [*4*] for fatigue-crack-growth threshold behavior.

In all three materials the superimposition of steady-state Mode III reduced fatigue-crack-growth rates [*21*]. Crack-growth data for the rotor steel and the titanium alloy are summarized in Figs. 9 and 10, which are based on graphical data given in Refs *19* and *20*, respectively. The crack-growth ratio was calculated first and then converted to $\Delta k_I^*/\Delta K_I$ using Eq 4, where Δk_I^* is now the value of Δk_I corresponding to the redefined ϕ^*. In calculations the stress ratios were taken into account, Poisson's ratio was taken as one third, and data which fell outside the validity range of Eq 4 were discarded. There is a broad correlation in each case between $\Delta k_I^*/\Delta K_I$, which can reach high values, and ϕ^*.

The same sort of criterion would be expected to hold for the converse case of a Mode III cyclic loading plus steady-state Mode I. Figure 11 shows the predicted effect of $K_I/\Delta K_{III}$ on $\Delta k_I^*/\Delta K_{III}$ and ϕ^* at $R = -1$. As the material was assumed to be nonmean stress sensitive this simply involved finding the value of ϕ for which Δk_I has its maximum. In calculations it was assumed that a facet closes at $k_I = 0$. Discontinuities appear as K_I becomes large enough for

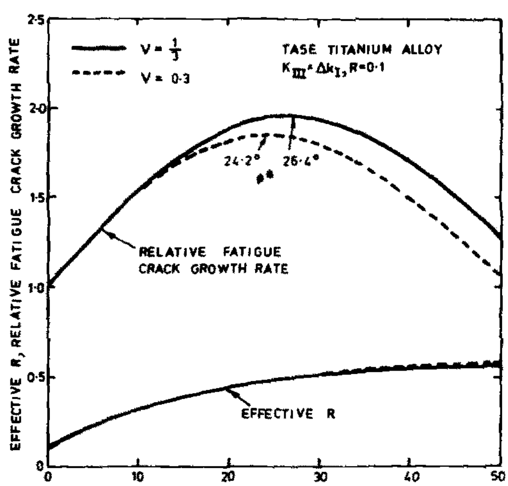

FIG. 8—*Relationship between ϕ, relative fatigue-crack-growth rate and effective value of* R.

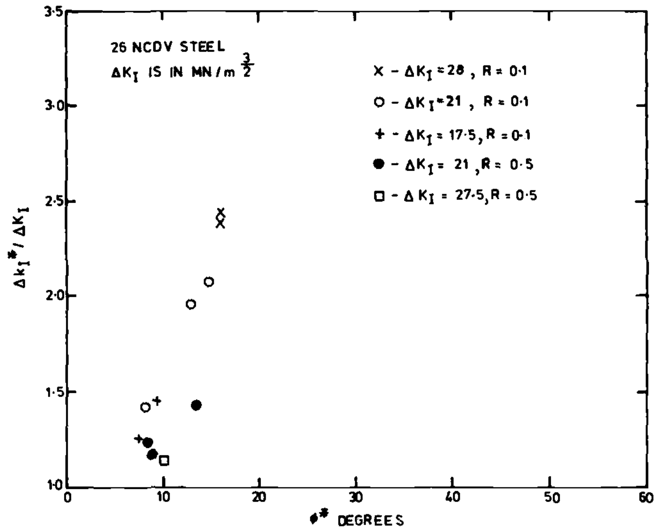

FIG. 9—*Relationship between* ΔK_I, R, ϕ^* *and normalized* Δk_I^*.

a facet to be open throughout the fatigue cycle. The results imply that superimposed steady-state Mode I has relatively little effect on ϕ^* and is roughly equivalent to a superimposed mean K_{III} of the same numerical value. Limited experimental data [*10*] for the AISI 4340 steel mentioned earlier show that, for this type of loading, the tendency to facet formation increased as K_I was in-

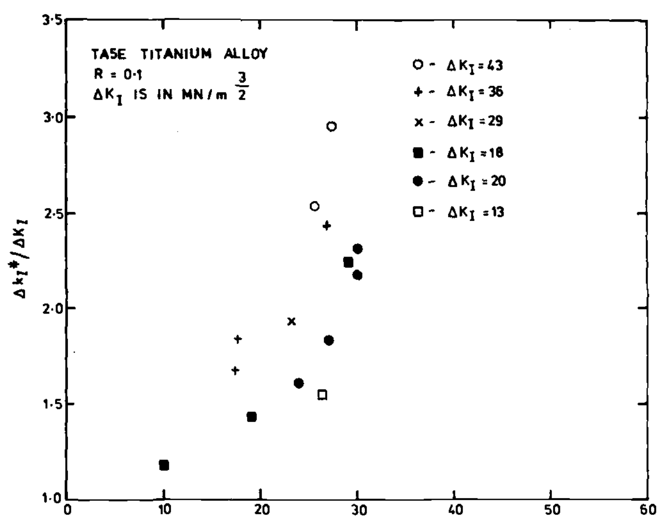

FIG. 10—*Relationship between* ΔK_I, ϕ^* *and normalized* Δk_I^*.

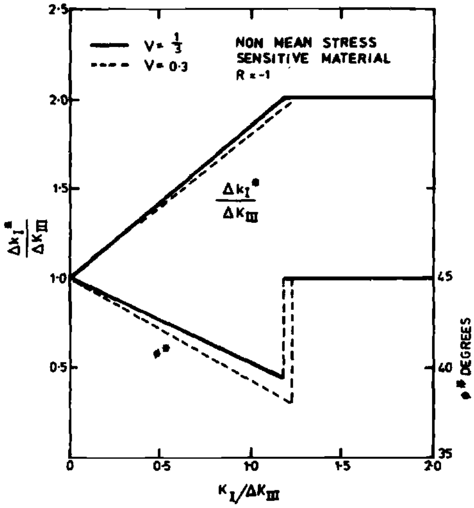

FIG. 11—*Relationship between* $K_I/\Delta K_{III}$, $\Delta k_I^*/\Delta K_{III}$ *and* ϕ^*.

creased, and there was some evidence of the expected increase in crack-growth rates.

Discussion

When this work was started, attention was confined to nominally elastic situations, in the hope that analysis using linear elastic fracture mechanics would reveal reasonably consistent behavior from which useful generalizations could be extracted. In particular it was hoped to relate results for twist cracks (Fig. 5) to those for block slits (Fig. 3). It was felt that experimental values of Y in Eq 9, derived from values of the ratio $\Delta k_I^*/\Delta K_I$ at constant crack-growth rate, ought to follow a consistent pattern. In practice values of $\Delta k_I^*/\Delta K_I$ and hence Y show wide variations (Table 1 and Figs. 7, 9, and 10); Fig. 7 indicates that Y must be a complex function of crack depth and stress-intensity factor. Variations remain wide even if data for true Mode III growth, which perhaps should not be analyzed by this method, are excluded. From the data presented it is only possible to note that $\Delta k_I^*/\Delta K_I$ has a lower bound value of about one; Y has a corresponding upper bound value also of about one. The situation is somewhat analogous to that for the fatigue-crack-growth threshold under mixed mode loading where it is only possible [*8*] to define a lower bound value for the threshold. For pure Mode III it is usual [*10,12,13*] to ascribe low crack-growth rates (with concomitant low values of Y) to the effects of friction between opposing crack surfaces, to facet interlocking, or to both, but quantitative analysis does not seem possible.

The tendency for fatigue cracks to grow in Mode I is an observation [*2*] which does not appear capable of proof in any strict sense of the word [*23*]. It is confirmed here for proportional loadings at both a macroscopic (1 mm) scale and a smaller (0.1 mm) scale. At the macroscopic scale the tendency appears to be suppressed if the crack front is a closed curve. For nonproportional loadings there may be no direction which is pure Mode I throughout the fatigue cycle. For tests where a twist crack forms, the facet angle ϕ^* (Fig. 5) tends to be that for which the expected crack-growth rate is a maximum.

Under pure Mode III loading, Mode I facets are not always observed. There are two possible explanations for true Mode III crack growth where Mode I facets are not observed at the smaller scale. First, Mode I facets may be formed and then destroyed by rubbing. This may account for the data shown in Fig. 7. Second, it may be by a similar mechanism to that for Stage 1 fatigue crack growth [*1*] which takes place on planes of maximum shear stress under conditions of localized general yielding. The evidence for this view is as follows. Mode III fatigue crack growth by a mechanism analogous to that for Mode I (Stage II) fatigue crack growth does not appear to be possible [*2*]. Under Mode III crack-tip plastic zones are relatively large; true Mode III crack growth is only observed at high values of ΔK_{III}, which would provide the necessary yielded region with a plane of maximum shear stress in the appropriate direction. Crack growth is commonly observed [*2*] on planes of maximum shear stress at around and above general yield, especially under torsion [*10*]. At the risk of circularity it could be argued that the occurrence of true Mode III crack growth shows that yielding is too extensive for stress-intensity factors to be used in the analysis of fatigue-crack-growth rate data.

Under mixed Modes I and III predominantly Mode I facets are observed for both proportional and nonproportional loadings. Slant crack growth in thin sheets is the major exception. The reasons for the occurrence of slant crack growth are not clear [*2,16,17*], but it is associated with through thickness yielding on 45° planes. It could be therefore regarded as fatigue crack growth on a plane of maximum shear stress under conditions of localized general yielding. On the other hand, crack growth by a mechanism analogous to that for Mode I crack growth does appear to be possible [2].

General Conclusion

Some features of fatigue crack growth under pure Mode III and mixed Modes I and III loading were examined, including two cases where the Mode III displacements are not proportional to the Mode I displacements. Information obtained under nominally elastic conditions for various commercial alloys was reanalyzed and discussed in the light of theoretical considerations to see whether consistent patterns of behavior could be identified. Despite some inconsistencies and anomalies it was found that a reasonably consistent pattern of behavior was beginning to emerge. In particular a tentative upper bound for the rate of fatigue crack growth was identified, but it does not apply to slant crack growth in thin sheets.

Acknowledgments

This paper is published by permission of the Director, National Engineering Laboratory, United Kingdom Department of Industry. It is British Crown copyright. The work was partly supported by the Engineering Materials Requirements Board of the United Kingdom Department of Industry.

References

[1] Forsyth, P. J. E., *Proceedings*, Crack Propagation Symposium, Cranfield, 1961, Vol. 1, pp. 76-94.
[2] Pook, L. P., "The Role of Crack Growth in Metal Fatigue," Metals Society, London, 1983.
[3] Pook, L. P., "Mode I Branch Cracks and Their Implications for Combined Mode Failure," NEL Report 667, National Engineering Laboratory, East Kilbride, Glasgow, April 1980.
[4] Pook, L. P. in *Fracture and Fatigue. Elastoplasticity, Thin Sheet, and Micromechanism Problems*, J. C. Radon, Ed., Pergamon, Oxford, 1980, pp. 143-153.
[5] Lawn, B. R. and Wilshaw, T. R., *Fracture of Solids*, Cambridge University Press, Cambridge, 1975.
[6] Mandlebrot, B. M., *Fractals, Form, Chance and Dimension*, W. A. Freeman and Co, San Francisco, 1977.
[7] McClintock, F. A. and Irwin, G. R. in *Fracture Toughness Testing and Its Applications, ASTM STP 381*, American Society for Testing and Materials, Philadelphia, 1965, pp. 84-113.
[8] Pook, L. P. in *Fatigue Thresholds Fundamentals and Engineering Applications*, J. Bäcklund, A. F. Blom, and J. C. Beevers, Eds., Engineering Materials Advisory Services Ltd. Warley, West Midlands, 1982, Vol. 2, pp. 1007-1032.
[9] Schijve, J., *Engineering Fracture Mechanics*, Vol. 14, No. 3, 1981, pp. 467-475.
[10] Ritchie, R. O., McClintock, F. A., Hashemi, H. N., and Ritter, M. A., *Metallurgical Transactions A*, Vol. 13A, No. 1, Jan. 1982, pp. 101-110.
[11] Pook, L. P. and Sharples, J. K., *International Journal of Fracture*, Vol. 15, No. 6, Dec. 1979, pp. R223-R225, Vol. 16, No. 3, June 1980, p. R147.
[12] Irving, P. E. and Hurd, N. J. in *Design of Fatigue Resistant Structures*, P. R. Abelkis and C. M. Hudson, Eds., *ASTM STP 761*, American Society for Testing and Materials, Philadelphia, 1982, pp. 212-233.
[13] Tschegg, E. K., *Materials Science and Engineering*, Vol. 54, No. 1, June 1982, pp. 127-136.
[14] Wright, R. P. and Queeney, R. A., *International Journal of Fatigue*, Vol. 4, No. 1, Jan. 1982, pp. 27-30.
[15] Pook, L. P., *International Journal of Fatigue*, Vol. 4, No. 3, July 1982, pp. 175-176.
[16] Pook, L. P., *Metal Science*, Vol. 10, No. 9, Sept. 1976, pp. 334-335.
[17] Schijve, J., *Engineering Fracture Mechanics*, Vol. 14, No. 3, 1981, pp. 467-475.
[18] Pook, L. P., *Engineering Fracture Mechanics*, Vol. 3, No. 3, Oct. 1971, pp. 205-218.
[19] Hourlier, F. and Pineau, A., *Memoires Scientifiques de la Revue de Metàllurgie*, Vol. 76, No. 3, March 1979, pp. 175-186.

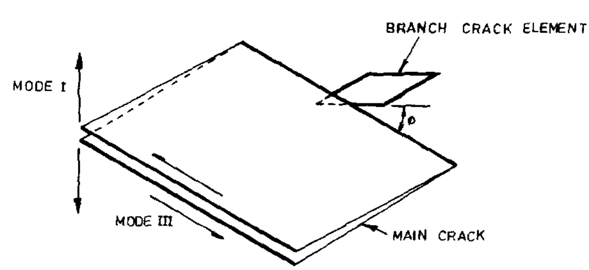

FIG. 12—*Branch crack element at main crack tip.*

[20] Hourlier, F., McLean, D., and Pineau, A., *Metals Technology,* Vol. 5, No. 5, May 1978, pp. 154–158.
[21] Hourlier, F. and Pineau, A. in *Advances in Fracture Research,* D. François, Ed., Pergamon, Oxford, 1981, Vol. 4, pp. 1833–1840.
[22] Swedlow, J. L. in *Cracks and Fracture, ASTM STP 601,* American Society for Testing and Materials, Philadelphia, 1976, pp. 506–521.
[23] Ayer, A. J., *The Problem of Knowledge,* Penguin Books, Harmondsworth, 1956.

APPENDIX

Stress-Intensity Factors for Twist Cracks

For an inclined branch crack element (Fig. 12) Modes I and III stress-intensity factors K_I and K_{III} are given approximately [3–5] by

$$k_I = K_I(\cos^2\phi + 2\nu \sin^2\phi) + K_{III} \sin 2\phi \tag{5}$$

$$k_{III} = -\tfrac{1}{2}K_I(1 - 2\nu)\sin 2\phi + K_{III} \cos 2\phi \tag{6}$$

where

K_I and K_{III} = initial (main) crack stress-intensity factors and
ν = Poisson's ratio.

The maximum value of k_I, k_I^* is given [3,4] by

$$k_I^* = \frac{K_I(1 + 2\nu) + \{K_I^2(1 - 2\nu)^2 + 4K_{III}^2\}^{1/2}}{2} \tag{7}$$

This maximum occurs when k_{III} is zero and the corresponding value of ϕ, ϕ^* is given by

$$\tan 2\phi^* = 2K_{III}/\{K_I(1 - 2\nu)\} \tag{8}$$

If K_I and K_{III} are taken as macroscopic stress-intensity factors on a scale of, say, 1 mm then the equations also provide a first approximation for the facets on a twist fracture surface (Fig. 5). This presumes that the surface irregularity due to the facets is small enough to be considered as within the crack tip stress field. No account is taken of the effect of the intervening cliffs; the effect on k_I can be accounted for by writing Eq *5* in the form

$$k_I = Y\{K_I(\cos^2\phi + 2\nu \sin^2\phi) + K_{III} \sin 2\phi\} \tag{9}$$

where Y is a correction factor for the effect of the cliffs and other irregularities. Using an argument based on possible facet shapes, Y has been deduced to be 0.74 for the initial stages of twist crack growth where the individual facets are not yet connected by cliffs [3,4]. Experimental values could be derived from the data given in Table 1 and Figs. 7, 9, and 10 by noting that $Y = 1/(\Delta k_I^*/\Delta K_I)$.

Formation and Growth of Short Cracks

Nicholas J. Hurd[1] *and Philip E. Irving*[1]

Smooth Specimen Fatigue Lives and Microcrack Growth Modes in Torsion

REFERENCE: Hurd, N. J. and Irving, P. E., "**Smooth Specimen Fatigue Lives and Microcrack Growth Modes in Torsion,**" *Multiaxial Fatigue, ASTM STP 853*, K. J. Miller and M. W. Brown, Eds., American Society for Testing and Materials, Philadelphia, 1985, pp. 267–284.

ABSTRACT: Constant amplitude torsional fatigue tests have been performed on smooth specimens of quenched and tempered steel at two strength levels. Both unidirectional and fully reversed tests have been performed. It was found that there was no detectable effect of mean strain upon fatigue life of either strength level material, both at short and at long lives. Observations on microcrack behavior during the tests has demonstrated that initial crack growth always occurs on a shear plane, even if subsequent propagation is on a tensile Mode I plane at 45°.

As in the uniaxial situation, short lives are dominated by microcrack growth. However, in torsion crack growth dominates over an extended range of life, and, in addition, surface crack lengths are longer than uniaxial at similar fractions of life. It is concluded that whereas crack initiation on shear planes is relatively easy in torsion, the Stage I/Stage II transition, which occurs in tension at crack lengths of one or two grains, is extremely difficult in torsion.

KEY WORDS: torsional fatigue, mean strain, microcrack growth, overstrain

The local strain-life approach has been widely applied in recent years in the automotive industry for the prediction of the fatigue durability of components [*1*]. The approach has been validated [*2*], and the application is essentially routine, within fairly well-defined limits of applicability [*3*]. One of the limitations of the technique is that the loading at the critical location should be approximately uniaxial. This is unfortunate in that automotive components are frequently subjected to more complex, multiaxial loadings. Torsion can be considered a special case of these. Typical examples would be halfshafts, torsion bars in suspension systems, and drive-shafts. Therefore, it would be of considerable benefit if the strain-life approach could be extended first to torsional loadings and then to more complex cases. The underlying aim of this work is, therefore, the development of a life prediction methodology in torsion similar to the local strain-life approach.

[1]Metallurgist and Head of Materials Studies, respectively, GKN Technology Ltd., Wolverhampton, U.K.

Copyright© 1985 by ASTM International www.astm.org

Considerable work has been done to date on torsional and multiaxial loadings. In spite of this there is as yet no consensus on the appropriate fatigue criterion to be employed, although the cyclic shear strain range and the stress normal to the crack path have been identified as important parameters [*4*]. Regarding the case of pure torsional loadings, a number of further advances have been made. The presence of a strain-gradient has been identified as a factor which complicates the derivation of stresses, and hence fatigue testing has involved the use of thin-walled tubes [*5*]. This is somewhat unrealistic in that the majority of engineering components are solid, and bar specimens are more appropriate. In the case of the latter, the use of the construction due to Nadai has been proposed as a possible means of generating the true surface stress [*6,7*].

The significance of the various possible definitions of failure in these tests has been evaluated by other workers and assessed in the light of definitions used in the uniaxial case [*5,7*]. It has been shown that, in the short life regime, plastic shear-strain range is related to life by a powerlaw expression [*6,8*]. Various possible correlations of torsional and uniaxial data have been investigated and reviewed [*5,9*]. Correlations based on octahedral shear stress have enjoyed some success (at long lives), although good correlations have not been consistently achieved [*10*]. Similarly, octahedral shear strain has been used to correlate data in the short-life regime, again with some, but not consistent success [*8,11*]. Miller and Chandler [*7*] have highlighted the importance of failure definition and geometry on these correlations. At present, work is continuing in order to generate more sophisticated descriptions of fatigue performance [*9*].

The work done to date has highlighted some important differences in behavior compared with trends observed in uniaxial fatigue. Thus, mean shear stress has been found to have little effect on life at long lives, in contrast with the effects observed in the uniaxial case [*12*]. A similar insensitivity to mean shear strain has also been noted in the short-life regime [*13*]. Mean strain effects are of obvious importance to a life prediction methodology. Thus, one object of this work is to investigate mean shear-strain effects. In addition to this, the influence of a number of cycles of high strain at the start of the test, that is, an overstrain test, was also evaluated. Considerable overstrain effects are observed in uniaxial testing [*14*], and it is important to determine whether this effect is carried over into torsion.

Different modes of crack extension have been observed during torsional fatigue testing. Propagation has been observed along the longitudinal shear planes [*6*], along the circumferential shear planes [*7*] and normal to the 45° tensile stress planes, which results in a helical fracture [*10*]. Hence, it was also decided to

TABLE 1—*Chemical composition of 605H32 steel.*

C	Si	Mn	P	S	Ni	Cr	Mo
0.38	0.21	1.62	0.035	0.045	0.16	0.15	0.26

investigate the propagation modes in some detail, in order to assess the effect of the propagation mode on the proportion of life spent in initiation and subsequent growth. This could then be compared with existing uniaxial data. In addition, such observations may throw some light on the observed mean strain effects.

Experimental

The material employed for this investigation was BS 970 605H32 (EN16) steel. This quenched and tempered low-alloy steel is typical of those commonly used in torsionally loaded components. The chemical composition is given in Table 1. The steel was austenitized at 850°C, followed by oil quenching. Two tempering temperatures were then employed, 300 and 600°C, which produced the tensile properties given in Table 2. A tempered martensitic microstructure was obtained in each case.

Specimens were machined out of rolled bar in the longitudinal direction; hence, the elongated manganese sulfide inclusions present in the material were parallel to the longitudinal axis of the specimen. Uniform gage fatigue specimens (gage length 12 mm, diameter 7 mm) were employed for the uniaxial testing, failure being identified with separation of the specimen. Solid, cylindrical specimens were employed during the torsional fatigue testing. The specimens had a parallel sided gage section of 20 mm diameter. Final machining was carried out after heat treatment in order to eliminate any decarburization, and the specimen surface was longitudinally polished to 600 grit after final machining.

Torsional fatigue testing was performed on a 2000 Nm capacity servohydraulic tension-torsion machine operating in shear strain control. Axial load was held at zero during the tests. Torque response was monitored throughout the test, and specimen failure was identified with the catastrophic drop off in torque response, which was defined here as the number of cycles at which the torque amplitude dropped by 25% of the initial value. The cyclic stress-strain curve was generated by constructing a plot of apparent surface stress (at halflife, where stable conditions were reached), against shear strain. The true surface shear stress against shear-strain curve was then generated using the construction due to Nadai or Upton [*6,7,15*].

Tests were conducted in which the shear strain was fully reversed, and also in which shear strain was unidirectional (that is, zero to some maximum value).

TABLE 2—*Mechanical properties of 605H32 steel.*

Tempering Temperature, °C	Proof Strength, MPa	Ultimate Tensile Stress, MPa	Reduction in Area, %
600	891	972	63
300	1556	1696	49

In addition, a small number of overstrain tests were conducted on the material tempered at 600°C. In these tests, ten cycles (fully reversed) at a shear strain amplitude of 0.0172 were first applied (such a strain amplitude would cause failure in ~1500 cycles). The specimen was then unloaded to zero strain and stress and then cycled to failure under a second, lower fully reversed strain amplitude.

In each test, the cracks were monitored visually during testing, and the mode of crack extension thus identified. In addition, a small number of replica tests were conducted in order to better assess the initiation and growth behavior.

The replica tests were conducted on tubes of the tempered 600°C material. The internal diameter was 25 mm and the wall thickness 3.81 mm. Specimen strain was monitored using an internal extensometer mounted in the bore of the tube. The external surface was hence free for easy replication of the specimen. Cellulose acetate replicas were taken at regular cycle intervals; these varied with applied strain amplitude but were approximately 5% of specimen life, giving about 20 replicas per test. The replicas were examined under transmitted light and the length of the microcracks measured using a calibrated graticule. Further work was performed by sectioning the specimens after a test and measuring lengths and depths of the cracks thus revealed. In this way the relation between surface length and crack depth could be established.

Results

1. Material Tempered at 600°C

1.1 Torsion Fatigue Data—The fully reversed torsional fatigue test results for the material tempered at 600°C are given in Figs. 1 and 2. The method of curve fitting the shear-strain amplitude versus reversals to failure plot is essentially the same as that used to fit uniaxial data [*1,2*]. Thus, the shear strain amplitude $\Delta\gamma/2$ has been divided into elastic $\Delta\gamma_e/2$ and plastic $\Delta\gamma_p/2$ components and linear log-log relations have been assumed to exist for $\Delta\gamma_e/2$ and

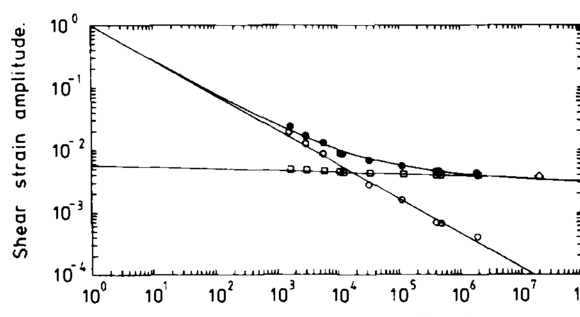

FIG. 1—*Shear strain amplitude against reversals to failure for the material tempered at 600°C. (● Total strain, ○ plastic strain, and □ elastic strain).*

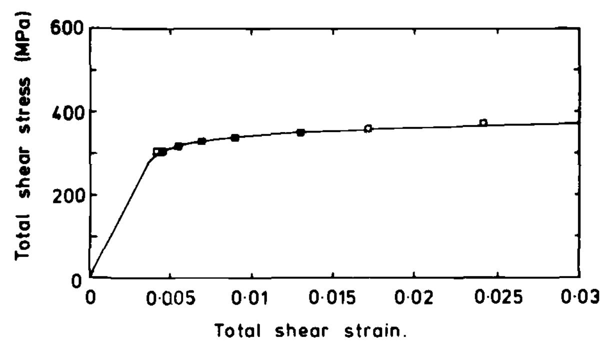

FIG. 2—*Cyclic shear stress-shear strain curve for the material tempered at 600°C.*

$\Delta\gamma_p/2$ with fatigue life in reversals ($2N_f$). The following equation can then be used to fit the data

$$\frac{\Delta\gamma}{2} = \frac{\Delta\gamma_e}{2} + \frac{\Delta\gamma_p}{2} = \frac{\tau_f'}{\mu}(2N_f)^b + \gamma_f'(2N_f)^c \tag{1}$$

Here, μ is the shear modulus and τ_f', b, γ_f', and c are the torsional equivalents of the coefficients and exponents used to fit uniaxial data. Thus, τ_f' and b are the torsional equivalents of the fatigue strength coefficient and exponent and γ_f' and c are the equivalents of the fatigue ductility coefficient and exponent.

The cyclic stress-strain curve has been characterized by the following relation

$$\frac{\Delta\tau}{2} = K'\frac{(\Delta\gamma_p)^{n'}}{2} \tag{2}$$

Again, K' and n' are the torsional equivalents of the cyclic strength coefficient and the cyclic strain hardening exponent.

Numerical values of the material constants in Eqs 1 and 2 are given in Table 3.

The existence of a large amount of strain-life data (appropriate to uniaxial loadings) in materials data banks represents an incentive for the assessment of how well the torsional data may be correlated with the uniaxial. The torsional data in Eqs 1 and 2 has therefore been compared directly with uniaxial strain-

TABLE 3—*Cyclic material constants.*

Tempering Temperature, °C	τ_f', MPa	b	γ_f'	c	K', MPa	n'	μ, GPa
600	455	−0.03	1.02	−0.557	453	0.053	80
300	1277	−0.078	0.382	−0.561	1328	0.124	78

life data for this material. To this end, the strain-life and cyclic stress-strain curves were compared on the basis of actahedral shear stress and strain, defined here as

$$\tau_{OCT} = \frac{1}{3}\{(\sigma_1 - \sigma_2)^2 + (\sigma_2 - \sigma_3)^2 + (\sigma_3 - \sigma_1)^2\}^{1/2} \tag{3}$$

where σ_1, σ_2, and σ_3 are the principal stresses and

$$\gamma_{OCT} = \frac{2}{3}\{(\epsilon_1 - \epsilon_2)^2 + (\epsilon_2 - \epsilon_3)^2 + (\epsilon_3 - \epsilon_1)^2\}^{1/2} \tag{4}$$

where ϵ_1, ϵ_2, and ϵ_3 are the principal strains.

For each data set, the total strain was divided into elastic and plastic components for the purposes of correlation. Octahedral shear stress was used to correlate the elastic components since this has been used with some (but not total) success to correlate results at long lives [*10*]. Similarly, octahedral shear strain was used to correlate the plastic components, since this approach has again yielded some success in the short-life regime [*5,8,11*]. The approach employed here is, therefore, in accord with previous work. The correlation obtained is shown in Fig. 3, while the cyclic stress-strain curve correlation is shown in Fig. 4. As shown in Fig. 3, a correlation within a factor of two on life has been obtained at short and intermediate lives, but there is a considerable discrepancy at long lives, where there is a discrepancy of approximately 30% on the fatigue limit, with corresponding large differences in life at a given octahedral shear strain amplitude. The cyclic stress-strain curves are correlated within approximately 10% on stress.

1.2 Mean Strain and Overstrain Tests—The mean strain and overstrain test results are presented in Fig. 5. The results are plotted, together with the results of the fully reversed baseline data, in terms of the shear strain amplitude against life. It can be seen from this figure that there is little or no effect of mean shear strain on the fatigue life of this material.

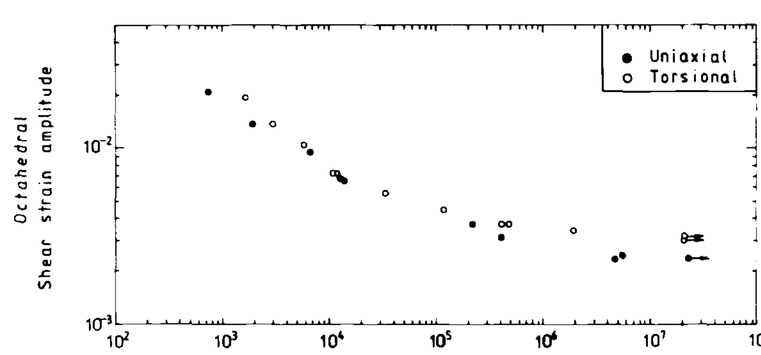

FIG. 3—*Correlation of uniaxial and torsional fatigue data in terms of octahedral shear strain.*

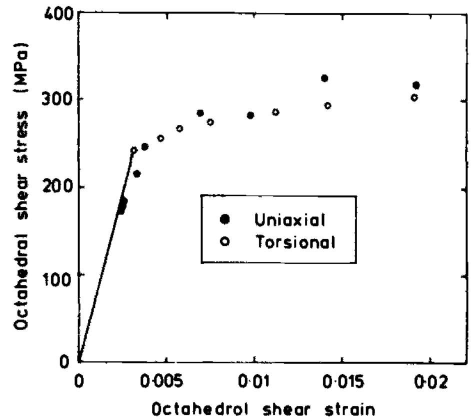

FIG. 4—*Cyclic stress-strain curves from uniaxial and torsional loadings expressed in terms of octahedral shear stress and strain. The solid line represents the elastic modulus.*

It should be noted that, at long lives, a mean shear stress was present throughout the test together with the mean shear strain. However, at larger strain amplitudes, due to the cyclic plasticity, the stress quickly became approximately fully reversed, so there was little mean stress present.

Regarding the overstrain tests, as shown in Fig. 5, there was little effect on the subsequent life of ten cycles of relatively high strain imposed at the start of the test.

1.3 Macroscopic Failure Modes—Failure at shear strain amplitudes of 0.005 and greater was found to be due to the propagation of shear cracks along the longitudinal shear planes. Crack extension, therefore, occurred by Mode II along the specimen surface and by Mode III into the specimen. This was the case for

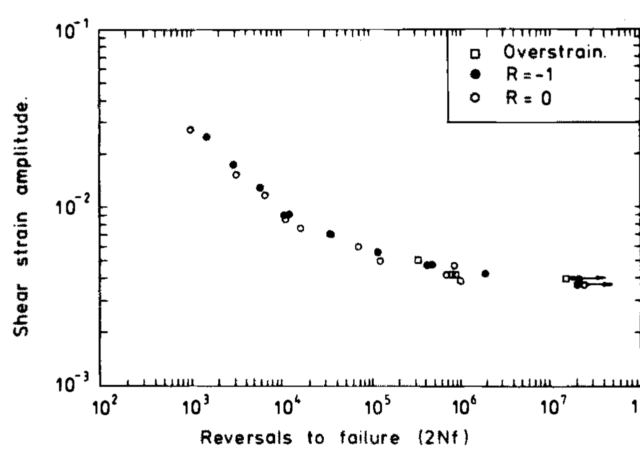

FIG. 5—*Fully reversed* (R = *−1*)*, mean strain* (R = *0*)*, and overstrain fatigue test results for the material tempered at 600°C.*

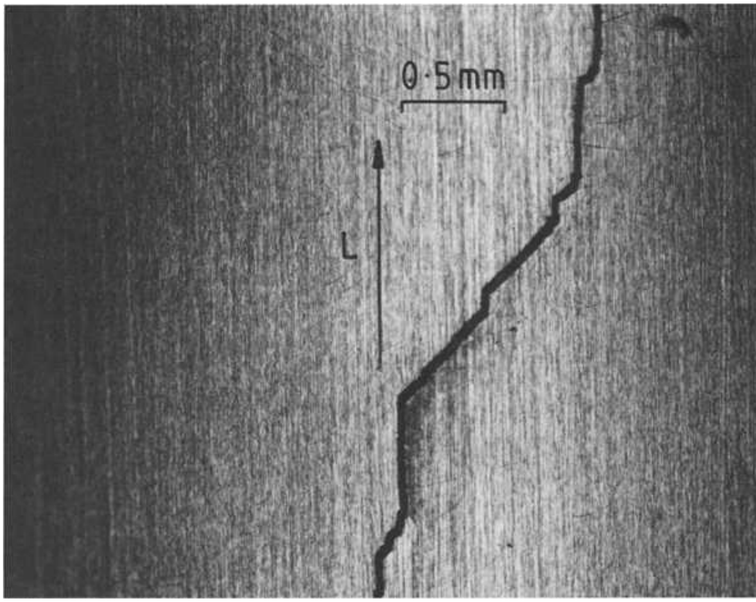

FIG. 6—*Small amounts of growth on 45° tensile stress planes, together with growth on longitudinal shear planes. Material tempered at 600°C (at* $\Delta\gamma/2 < 0.005$*). The longitudinal axis is marked (L).*

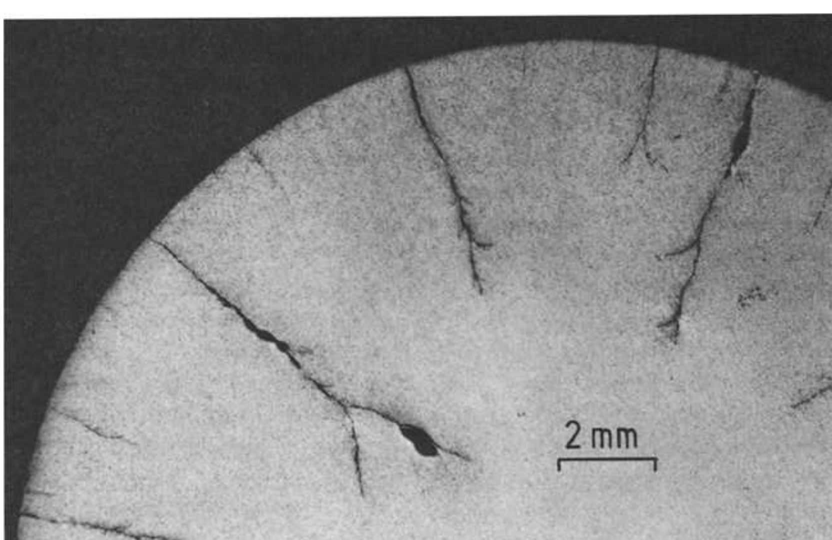

FIG. 7—*Transverse section through a failed specimen, showing multiple cracks around the circumference.*

both the fully reversed and the mean stress tests. Typically, multiple cracks were observed at the end of the test (that is, at failure defined by ~25% drop in torque response). The occurrence of longitudinal shear cracks rather than transverse shear cracks would be expected to be favored by the longitudinal polishing direction employed and the presence of elongated manganese sulfide aligned in the longitudinal direction.

At strain amplitudes less than 0.005, some small amounts of growth were observed to occur on the 45° tensile-stress planes, together with growth on the longitudinal shear planes. Subsequent propagation then occurred exclusively by longitudinal shear (Fig. 6).

1.4 Replica and Sectioning Work—Sectioning the failed specimens showed that failure definition employed here (25% drop in torque response) corresponded to the growth of at least one, and usually several cracks into the specimen. The cracks were of a depth approaching the specimen radius, and their length was of the order of the gage length (Fig. 7).

Replica examination revealed that cracks of 100 μm in length were present at strain amplitudes of 0.006 within 7% of total life, and cracks of 1 mm in length were present at about 50% life. Hence for these strain amplitudes, producing lives in excess of 10^4 cycles, 50% of the life is spent growing cracks in excess of 1 mm length.

At lives of 10^5 cycles, fractional life to produce 100 μm cracks could still be as low as 15%, while 30 to 40% of the life was occupied growing cracks in excess of 1 mm. These results are illustrated in Fig. 8.

The initiation site was always a group of longitudinal inclusions (Fig. 9). A frequent feature of early crack growth was that initiation occurred simultaneously at a number of locations. Initiated cracks that were in the same longitudinal shear plane coalesced and grew on as a larger crack (Fig. 10). Transverse cracks, although they were observed, were never prominent, and dominant cracks were

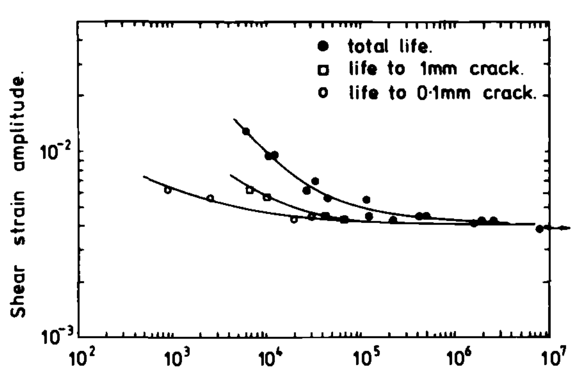

FIG. 8—*Plot of shear strain amplitude against reversals to* (a) *a crack of 0.1 mm surface length,* (b) *1 mm surface length, and* (c) *failure.*

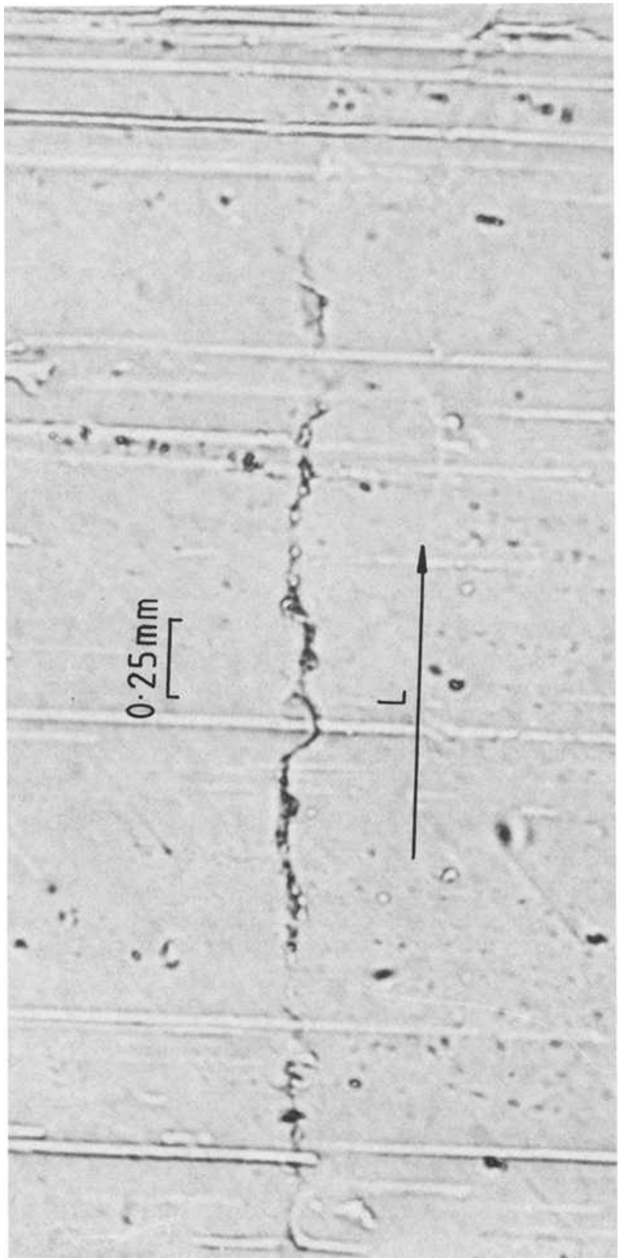

FIG. 9—*Detail of the initiation from surface inclusions. The longitudinal axis is marked (L).*

always longitudinal. There was occasional evidence that cracks produced microfacets at 45° to the specimen axis (Fig. 10), but the general direction was always in the shear mode.

Sectioning experiments revealed that for cracks about 100 μm in surface length, the depth (c) to half surface length (a) ratio was about 0.15, indicating that at lengths less than this, either the crack had initiated from an inclusion of this aspect ratio, or that initial growth was more rapid on the surface than inwards. By the time crack lengths of 1 mm were achieved, the c/a ratio was near 0.4 to 0.45.

2. *Material Tempered at 300°C*

2.1 Fatigue Data—The fully reversed torsional fatigue test data are shown in Figs. 11 and 12. The same curve fitting routine previously discussed has

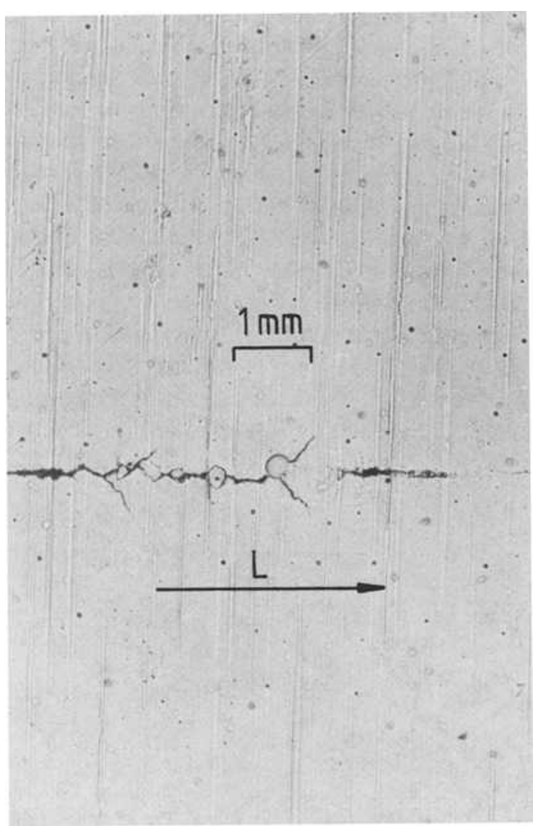

FIG. 10—*Two longitudinal shear cracks on the point of coalescence. Note the microfacets at 45° to the longitudinal axis, which is marked (L).*

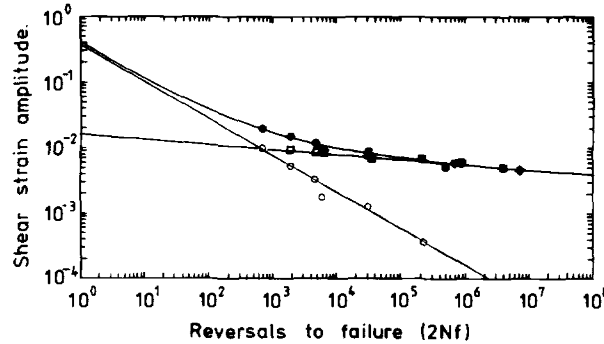

FIG. 11—*Shear strain amplitude against reversals to failure for the material tempered at 300°C.* (● *Total strain,* ○ *plastic strain, and* □ *elastic strain*).

been employed, and the values of the material constants obtained are given in Table 3.

The mean strain test results are presented in Fig. 13. Again, little effect of mean shear strain was observed, despite the occurrence of a variety of macroscopic failure modes. As in the case of the material tempered at 600°C, tests with a large strain amplitude reached a state of approximately fully reversed stress early in life. Those at lower amplitudes maintained a mean stress throughout the test.

2.2 *Macroscopic Failure Modes*—Failure was now observed to occur by the propagation of shear cracks along the longitudinal shear planes at shear strain amplitudes of 0.007 and higher. Faceted failures (that is, those containing some propagation on both the 45° tensile stress planes and on the longitudinal shear planes (as already described in Section 1.3) were found to occur down to shear stain amplitudes of 0.006. Below this, the macroscopic failure mode was by propagation solely along the 45° tensile stress planes, giving the classical helical fracture. The mode of propagation is now exclusively Mode I in fracture mechanics terminology.

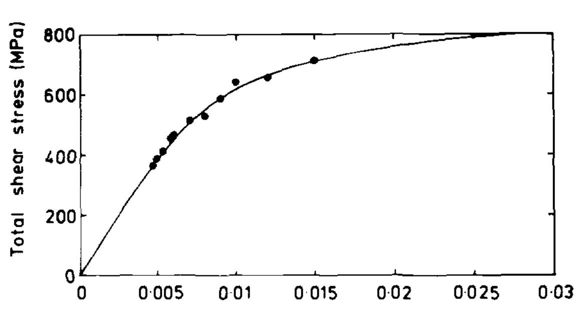

FIG. 12—*Cyclic shear stress versus shear strain curve for the material tempered at 300°C.*

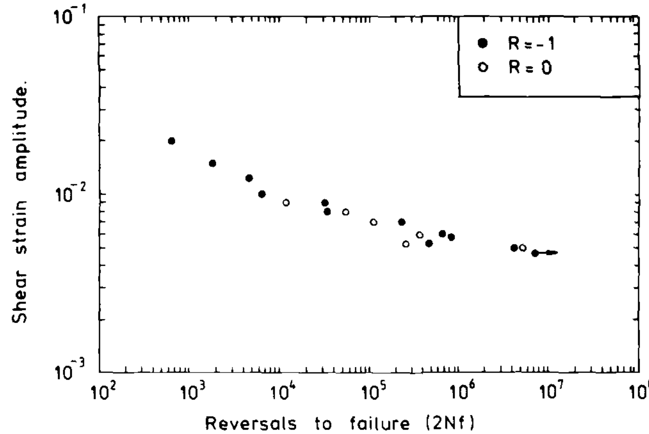

FIG. 13—*Fully reversed* (R = −1) *and mean strain* (R = 0) *fatigue test results for the material tempered at 300°C.*

The micromechanism of crack initiation in a specimen exhibiting the latter failure mode was investigated by scanning electron microscopy. On the spiral fracture surface, at the initiation site, was found a small (100 μm surface length) region of shear crack growth (Fig. 14). That this occurred along the longitudinal shear plane can be seen from the orientation of this shear crack with respect to the spiral Mode I cracking (Fig. 15). Initiation and initial microcrack growth,

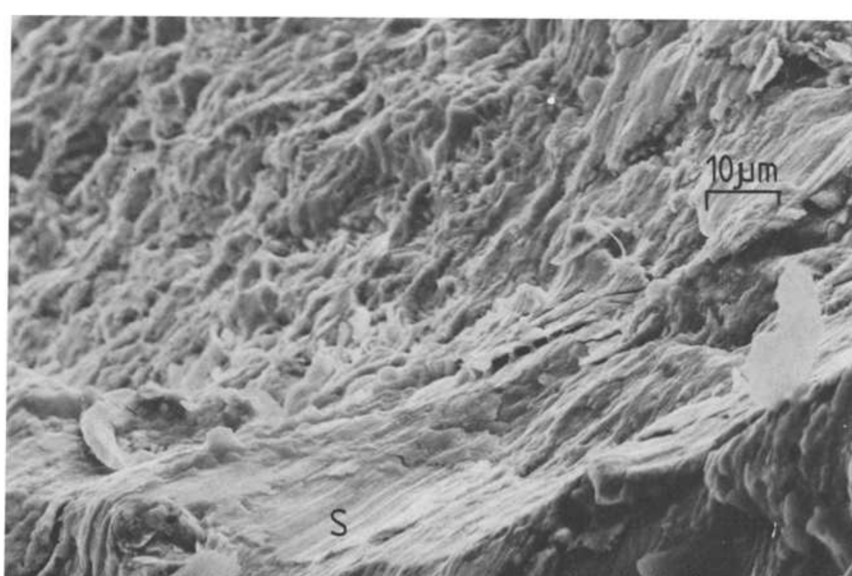

FIG. 14—*Initiation site showing a small region of shear (marked S) on the longitudinal shear plane and subsequent Mode 1 propagation.*

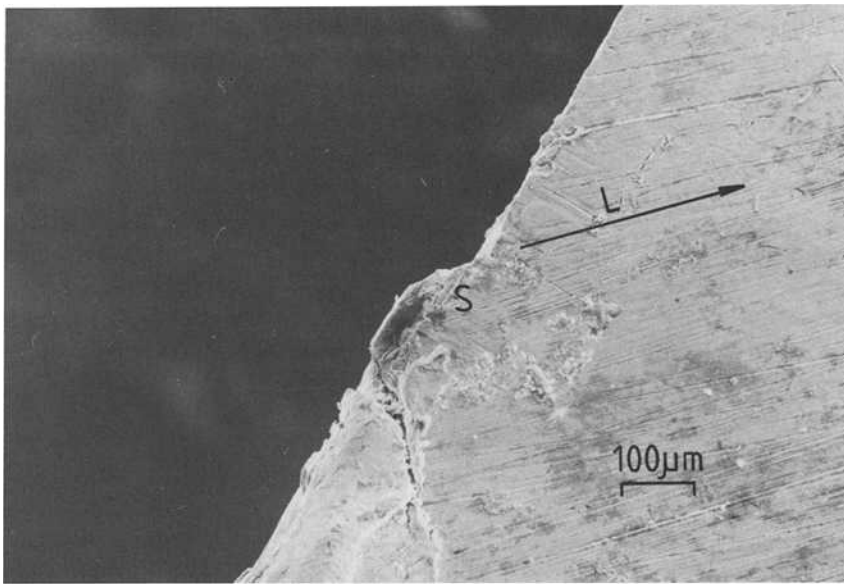

FIG. 15—*Orientation of initiation site (marked S) with respect to the subsequent crack propagation along 45° tensile-stress planes. The longitudinal axis is marked (L).*

therefore, appear to have occurred on a shear plane, even though subsequent micro- and macrocrack growth was by Mode I, under the action of the tensile stress on the 45° planes.

Discussion

Torsional Fatigue

A comparison of the fatigue performance in torsion of the two strength levels is shown in Fig. 16. The effect of strength level on life was different in the high- and low-cycle regimes, a cross over in the shear strain versus life curves occurring at $\sim 10^4$ reversals. The higher strength material was greatly superior at long lives. Such crossovers are of course observed in uniaxial fatigue, where they are thought to reflect the inverse variation of strength and ductility [*16*]. It is interesting that the crossover occurs at somewhat longer lives ($10^4 \times 10^3$ reversals) that in tension-compression [*17*].

The replica observations showed that most of the lifetime was spent in crack propagation at lives up to at least $\sim 10^5$ cycles. Crack propagation has been found to be equally dominant in uniaxial fatigue [*18*], albeit up to somewhat shorter lives. However, the manner of growth in torsion is considerably different. For example, uniaxially, initiation and initial growth up to a few grains, occur by a shear process, termed Stage I by Forsyth [*19*]. A transition then occurs and growth proceeds perpendicular to the normal stresses (Stage II by Mode I in fracture mechanics terminology). Torsional crack growth also occurs initially

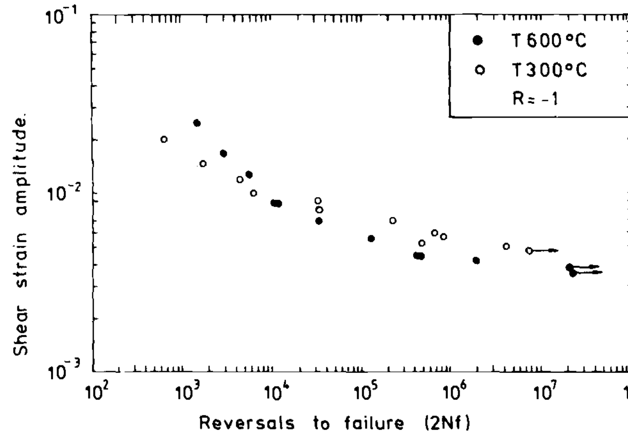

FIG. 16—*Comparison of strain-life data for 300°C and 600°C materials.*

by shear (Stage I growth). However, in the majority of specimens tested this process continues throughout the test, and the transition to Stage II never occurs. In fracture mechanics terms, the growth is by Mode II along the specimen surface and by Mode III into the specimen. That no transition to Stage II has occurred reflects the absence of a stress normal to the shear plane and geometric difficulties associated with growth from the shear plane into the 45° plane in Stage II [*20*].

It can be also noted that in the region $N_f < 10^5$ cycles, surface crack lengths in torsion are longer than in tension at corresponding values of fractional life. This is illustrated in Fig. 17 where crack lengths are plotted as a function of $N/$

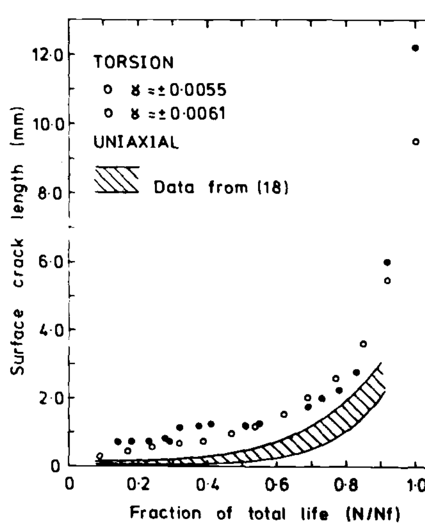

FIG. 17—*Comparison of surface crack length against fractional life for torsion and for uniaxial tension (data from Dowling* [18] *for lives between* 10^3 *and* 10^4 *cycles).*

N_f for the present work and for tension from Dowling [*18*]. This can imply either that surface crack growth rates are faster in torsion than in tension or that initiation occurs earlier in life. At present it is not clear which of these two explanations is correct.

The correlation based on octahedral shear strain between uniaxial and torsional smooth specimen data for the material tempered at 600°C is within a factor of two on life in the short and intermediate life regime. It is surprising that this correlation is achieved in this crack growth dominated regime given the large differences, for example, in macroscopic growth rates measured in Modes I and III [*21*]. There is, however, a considerable discrepancy in the correlation at long lives. It is, therefore, only possible to obtain initial, approximate estimates of torsional fatigue behavior from uniaxial materials data banks. Since these correlations have not in general found to be consistently successful [*5*], and it is possible that metallurgical factors may have different influences in the two cases [*10*], precise evaluation of a components performance under torsional fatigue requires the appropriate data.

Effect of Mean Strain and Overstrain

The absence of a significant effect of mean shear strain on the torsional fatigue life confirms the previous experimental evidence [*12,13*]. The absence of an effect may be rationalized in terms of the mechanisms of failure which occur. At short and intermediate lives (for both materials), initiation and growth occur along the longitudinal shear planes, with the majority of the life being spent in growth. Growth thus occurs by Mode III into the center of the specimen, and this is the Mode that causes failure. A number of reasons can be advanced as to why this Mode should be independent of mean shear strain. Shear Mode III growth rates have been found to be relatively insensitive to stress ratio effects [*21*], which is thought to be due to the absence of the closure effects invariably present in Mode I growth. Furthermore, the nature of the stress state in torsion (with no direct stress perpendicular to the relevant shear plane) prevents any mean strain effect due to normal stress acting across the shear plane.

At long lives, in both materials, the situation is slightly more complicated if viewed in terms of the macromechanisms of growth, which contain 45° facets in the material tempered at 600°C and which occurs solely in the Mode I 45° planes in the material tempered at 300°C. However, fractographic evidence shows that initiation does in fact occur on a plane of maximum shear (longitudinal shear plane) even if the subsequent propagation is completely by Mode I.

In this long-life regime the majority of life is spent in firstly initiating a shear microcrack and secondly growing it over a few grains. For tension-compression cycling the process will be aided by the normal stress operating on all shear cracks, which will increase with increasing mean stress and will aid the decohesion process. In torsion, this normal component is entirely absent, and creation and early growth of shear cracks cannot be aided in this way. Increased mean torque for constant torque amplitude will only produce increased shear stresses. This will not be as helpful in crack creation as it is the range of shear stress which is important.

The lack of a mean strain effect in torsion means that a somewhat different life prediction methodology is appropriate to cases of pure torsional loadings. Now, it is solely the strain amplitude that is significant, at least over the R-ratios considered here. This is in contrast to the uniaxial case where the parameter $(\sigma_{max}\epsilon_a E)^{1/2}$ is often used [22] to account for mean stress effects. (Here σ_{max} is the maximum stress, ϵ_a the strain amplitude, and E is Young's modulus). Further work is required to assess whether this conclusion may be extended to more positive strain ratios.

The negligible effect of overstrain in the tests conducted here is again of significance regarding the assessment of fatigue performance. The behavior is in contrast with that observed for uniaxial loadings where a marked effect of overstrain is generally observed, and it has been postulated [*14*] that overstrains reduce fatigue life by accelerating the crack-initiation process. The reason for the different behavior require further investigation but may be related to the changed proportions of initiation cycles and microcrack growth cycles which make up total life.

Conclusions

1. Torsional fatigue tests have been performed on smooth specimens of quenched and tempered steel at two strength levels.
2. It is found that there is little effect of mean strain or of overstrain on torsional fatigue lives at either strength level.
3. Observations of failure modes have revealed that initial crack growth is always on a shear plane, even though subsequent macroscopic growth continues in shear or changes to a tensile mode crack.
4. Replication of the specimen surface during testing shows that surface crack lengths are longer for a given fraction of life than for uniaxial tension, and that the balance between initiation and propagation cycles comprising total life is shifted towards propagation.
5. Crack initiation is found to be very easy in torsion, but subsequent crack growth is generally constrained to remain on shear planes and the Stage I/Stage II transition always occurs late in life and is often suppressed completely.

Acknowledgments

Thanks are due to V. Kumar for his invaluable assistance with the experimental work. Thanks are also due to many colleagues at GTC for their helpful comments, particularly Dr. S. J. Hill and Dr. P. Watson.

Specimen replication tests were performed at the University of Illinois, and the authors would like to thank Professor D. F. Socie and Mr. J. Fash for many valuable discussions and assistance with replication techniques.

The paper is published by permission of Dr. P. Watson, general manager, Product Development, GKN Technology Limited.

References

[1] Watson, P. and Hill, S. J. in *Design of Fatigue and Fracture Resistant Structures, ASTM STP 761*, American Society for Testing and Materials, Philadelphia, 1982, pp. 5–27.

[2] Wetzel, R. M., Ed., "Fatigue Under Complex Loading: Analysis and Experiments," Society of Automotive Engineers, Warrendale, PA, 1977, *Advances in Engineering*, Vol. 6.

[3] Morrow, JoDean and Socie, D. F. in *Materials, Experimentation and Design in Fatigue*, Sherratt, F. and Sturgeon, J. B., Eds., IPC Science and Technology Press Limited, Guildford, England, 1981, pp. 3–21.

[4] Brown, M. W. and Miller, K. J., *Proceedings*, The Institution of Mechanical Engineers, London, Vol. 187, No. 65/73, 1973, pp. 745–755.

[5] Krempl, E. in *The Influence of State of Stress on Low-Cycle Fatigue of Structural Materials: A Literature Survey and Interpretive Report, ASTM STP 549*, American Society for Testing and Materials, Philadelphia, 1974, pp. 1–46.

[6] Halford, G. R. and Morrow, JoDean, *Proceedings*, Vol. 62, American Society for Testing and Materials, Philadelphia, 1962, pp. 695–707.

[7] Miller, K. J. and Chandler, D. C., *Proceedings*, The Institution of Mechanical Engineers, London, Vol. 184, Part 1, No. 25, 1969–1970, pp. 433–448.

[8] MacKenzie, C. T., Burns, D. J., and Benham, P. P., *Proceedings*, Institution of Mechanical Engineers, London, Vol. 180, Part 131, 1965–1966, pp. 414–423.

[9] Brown, M. W. and Miller, K. J. in *Low-Cycle Fatigue and Total Life Prediction, ASTM STP 770*, American Society for Testing and Materials, Philadelphia, to be published.

[10] Frost, N. E., Marsh, K. J. and Pook, L. P., *Metal Fatigue*, Clarendon Press, Oxford, U.K., 1974.

[11] Kikukawa, M., Ohji, K., Kotani, S., and Yokoi, T., *Bulletin*, Japan Society of Mechanical Engineers, Vol. 15, 1972, pp. 889–898.

[12] Sines, G. and Ohgi, G., *Transactions*, American Society of Mechanical Engineers, *Journal of Engineering Materials and Technology*, Vol. 103, 1981, pp. 82–90.

[13] Yokobori, T., Yamanouchi, H., and Yamamoto, S., *International Journal of Fracture Mechanics*, Vol. 1, 1965, pp. 3–13.

[14] Watson, P. and Topper, T. H., *Experimental Mechanics*, Society for Experimental Stress Analysis, 1972, pp. 11–17.

[15] *Manual on Design and Manufacture of Torsion Bar Springs*, SAE J796a, Society of Automotive Engineers, Warrendale, PA, 1966.

[16] Landgraf, R. W. in *Fatigue and Microstructure*, American Society for Metals, Metal Park, Ohio, 1979, pp. 439–466.

[17] Mitchell, M. R. in *Fatigue and Microstructures*, American Society for Metals, Metals Park, Ohio, 1979, pp. 385–437.

[18] Dowling, N. E. in *Cyclic Stress-Strain and Plastic Deformation Aspects of Fatigue Crack Growth, ASTM STP 637*, American Society for Testing and Materials, Philadelphia, 1977, pp. 97–121.

[19] Forsyth, P. J. E., Cranfield Symposium, September 1961.

[20] Pook, L. P. in *Fracture and Fatigue*, Radon, J. C., Ed., Permagon, Oxford, U.K., 1980, pp. 143–153.

[21] Hurd, N. J. and Irving, P. E. in *Design of Fatigue and Fracture Resistant Structures, ASTM STP 761*, Abelkis, P. R. and Hudson, C. M. Eds., American Society for Testing and Materials, Philadelphia, 1982, pp. 212–233.

[22] Smith, K. N., Watson, P., and Topper, T. H., *Journal of Materials*, Vol. 5, No. 4, 1970, pp. 767–778.

Bernard Jacquelin,[1] François Hourlier,[1] and Andre Pineau[1]

Crack Initiation Under Low-Cycle Multiaxial Fatigue

REFERENCE: Jacquelin, B., Hourlier, F., and Pineau, A., "**Crack Initiation Under Low-Cycle Multiaxial Fatigue,**" *Multiaxial Fatigue, ASTM STP 853,* K. J. Miller and M. W. Brown, Eds., American Society for Testing and Materials, Philadelphia, 1985, pp. 285–313.

ABSTRACT: This study is devoted to the determination of a criterion for predicting crack initiation under low-cycle multiaxial fatigue. Here crack initiation, N_i, is defined as the number of cycles needed by the final microcrack to reach one grain size. The tests which were carried out at room temperature on Type 316L stainless steel and Inconel 718 alloy included (*a*) reversed tension-compression (*b*) reversed tension-compression with a superimposed steady torque, (*c*) pulsated tension-compression with a stress ratio R_σ such that $-0.5 < R_\sigma < 0$ and (*d*) reversed torsion. Scanning electron microscope (SEM) observations were used to determine the number of cycles corresponding to crack initiation and the orientation of the microcracks.

From these observations a criterion combining the plastic shear strain range for the crack initiation plane, $\Delta\gamma_p$, and the maximum of the shear stress on this plane, τ, is proposed. It is shown that the predictive capability of this criterion is satisfactory for various experimental results featuring both Types A and B crack initiation. Using the proposed criterion and the experimental relation between N_i and the number of cycles at failure, N_f, in conjunction with a double linear damage rule, it is shown that this approach accounts for previously published experimental results involving two level loadings.

KEY WORDS: fatigue crack initiation, fatigue crack propagation, multiaxial loading, cyclic stress-strain behavior, microcrack orientation

Nomenclature

N_i	Number of cycles to crack initiation
N_p	Number of cycles spent in crack propagation
N_f,N_f*	Number of cycles to failure
$\Delta\epsilon_p$	Plastic tensile strain range
$\Delta\gamma_p$	Plastic shear strain range
ϵ_1,ϵ_2,ϵ_3	Maximum principal strains
σ_n	Normal tensile stress
τ	Shear stress
$\Delta\tau$	Shear stress range

[1]Doctor, doctor, and professor, Centre des Matériaux, Ecole des Mines de Paris, Evry, France.

Copyright© 1985 by ASTM International www.astm.org

R_γ	$\gamma_{min}/\gamma_{max}$ shear strain ratio
R_ϵ	$\epsilon_{min}/\epsilon_{max}$ tensile strain ratio
R_σ	$\sigma_{min}/\sigma_{max}$ stress ratio
σ_o^M	Maximum load/initial cross section area
ϵ	$(l - l_o)/l_o$ where l is the gage length
ϵ^M	Ln $(1 + e)$
σ^M	$\sigma_o^M (1 + e)$
$\alpha,\beta,N_o,k_1,k_2,k_3$	coefficients
λ	Slope of the constant initiation life curves in the $\Delta\gamma_p - \tau$ plane
μ	Manson-Coffin type law exponent
ν	Strain hardening exponent

Most components and structures are subjected to complex loading conditions, that may eventually lead to fatigue crack initiation and crack propagation. For a long time, studies dealing with fatigue damage have been predominantly concerned with uniaxial, mainly tensile, situations, and most of the multiaxial fatigue studies have been carried out in the regime corresponding to the fatigue limit. In the last past two decades the regime associated with low-cycle fatigue (LCF) has received increased attention (for a review, see Ref *1*). Nevertheless, important difficulties are still encountered when predicitng fatigue life due to complex loading.

We have already exposed elsewhere [*2,3*] why it seems necessary to distinguish crack initiation and crack propagation when modeling LCF life. The socalled Stage I and Stage II phases have been defined from simple reversed tensile fatigue observations. For such a simple loading configuration, both stages have been found to depend on very different mechanisms [*4–8*]. When dealing with complex loading configurations, the Stage I and Stage II concepts may have to be reconsidered. Moreover the very early stage of fatigue cracking, that is crack initiation, and the subsequent crack propagation, may have to be studied separately. The present paper is devoted to the assessment of a LCF criterion for crack initiation. Crack initiation is defined here as the number of cycles, N_i, required by the principal crack, that is, the crack that will bring the specimen to rupture, to reach the size of one grain.

Several authors have already proposed LCF criteria for application to complex loading. In particular, the approach followed by Miller and Brown [*9–12*] is related in some respects to the physical aspects of crack initiation and propagation. For these authors, the critical parameters governing fatigue life are the maximum shear strain range ($\Delta\gamma_{max}$) and the tensile strain ϵ_n normal to the plane experiencing $\Delta\gamma_{max}$. The principal strains are labelled ϵ_1, ϵ_2, ϵ_3 ($\epsilon_1 > \epsilon_2 > \epsilon_3$). In tests such as pure torsion, the strains ϵ_1 and ϵ_3 are parallel to the surface plane, and thus the maximum shear strain is also parallel to the surface (Type A). But for tests with positive biaxial stresses, the strain ϵ_3 is normal to the free surface, and the maximum shear strain is oriented in-depth from the surface of the material (Type B). Type B loading configurations are found to bring shorter fatigue lives than Type A. Therefore, a specific criterion was developed for both of these situations by Lohr and Ellison [13] who, adopting the same approach, proposed a modification. Considering that fatigue life is controlled by in-depth growing cracks, they replaced ϵ_3 by the strain normal to the specimen surface and suggested the use of a single criterion for both Types A and B loading configurations.

LCF tests corresponding to a fatigue life range between 10^3 and 10^5 cycles were carried out at room temperature on one heat of 316L austenitic stainless steel by the authors of the present paper [3]. These tests included (*a*) reversed tension-compression, (*b*) reversed tension-compression with a superimposed steady torque, (*c*) pulsated tension-compression, with a stress ratio (R_σ) such that $-0.5 < R_\sigma < 0$ and (*d*) pulsated tension-compression with a superimposed steady internal pressure. Scanning electron microscope (SEM) observations were used to determine the number of cycles corresponding to Stage I crack initiation as here defined and the orientation of shear microcracks. For that program and material, it was observed that in-depth growing Type B microcracks were the most damaging for every loading configuration mentioned. A simple crack initiation criterion was proposed

$$N_i = N_o\,(\Delta\gamma_p{}^B)^\alpha \cdot (\sigma_n{}^B)^\beta \tag{1}$$

where

$\Delta\gamma_p{}^B$ = range of plastic shear strain on Type B planes,
$\sigma_n{}^B$ = maximum normal stress acting on these planes, and
N_o, α, and β = parameters determined from the Manson-Coffin law and the reversed cyclic stress-strain curve.

Some exploratory reversed torsion tests carried out on the same material suggested that crack initiation could be fully controlled in some cases by the Type A shear strain component. Moreover, preliminary complex fatigue tests on a nickel-base superalloy, Inconel 718, reinforced this conviction and strongly suggested that the extension of the criterion given by Eq 1 to other materials or loading configurations than those described in Ref *3* was questionable. The present paper reports further critical experiments and observations carried out on both 316L stainless steel and Inconel 718 in order to get a better understanding of the LCF failure mechanisms. Equation 1 is then modified and its applicability extended to a wider range of test conditions.

Materials and Experimental Procedure

The materials used for this study are a low-carbon Type 316L stainless steel and Inconel 718 alloy. The chemical compositions of these materials are given in Table 1. The stainless steel has been solution treated at 1070°C for 1 h and then water quenched. This heat treatment provides grain sizes from 10 to 100 μm, with an average size of 30 μm. Manganese sulfide inclusions are also observed, lying parallel to the longitudinal direction. Inconel 718 alloy was given

TABLE 1—*Chemical compositions (weight percent).*

Type 316L Stainless Steel

C	Mn	Si	S	P	Ni	Cr	Mo	N	Cu	Co
0.029	1.80	0.50	0.012	0.032	12.60	17.54	2.38	0.077	0.26	0.18

Inconel 718

C	Mn	Si	S	P	Cr	Ni	Mo	Co	Cu	Al	Ti	Fe	B	Ta + Nb
0.035	0.13	0.09	0.002	0.009	18.25	52.26	3.06	0.25	0.05	0.54	1.02	19.00	0.039	5.3%

the standard heat treatment, that is, 955°C/1 h − air cooling + 720°C/8 h + 620°C/8 h + air cooling. In this material the resulting grain size of 30 μm was rather homogeneous. The tensile properties of both materials at room temperature are given in Table 2.

All the experiments were carried out at room temperature, and loads and strains were continuously recorded. We performed the following tests: On both materials: strain controlled reversed torsion ($R_\gamma = -1$). On Inconel 718 only:

1. Strain controlled reversed tension-compression ($R_\epsilon = -1$).
2. Strain controlled reversed tension-compression with a superimposed steady torque.
3. Stress controlled pulsated tension-compression ($R_\sigma = 0$ and $R_\sigma = -0.5$).

Two types of specimens were employed:

1. Cylindrical solid specimens were used in tests (1, 2, 3). They have an 8 mm diameter and a 12.5 mm gage length.
2. Tubular specimens with a 19.5 mm outer diameter, 1.5 mm thickness, and a 12 mm gage length were used for reversed torsion tests.

Type 316L stainless steel specimens were electrochemically polished. Inconel 718 specimens were carefully mechanically polished (3-μm diamond paste). Both internal and external surfaces of tubular specimens were polished.

The shear strain definition we used throughout this study is the engineering shear strain, that is

$$\gamma_{13} = \epsilon_1 - \epsilon_3 \tag{2}$$

It was observed previously [3] that the fatigue lives of tensile tubular specimens were shorter by a factor of two than the fatigue lives of solid specimens tested under similar conditions. This difference was believed to be related to a size effect. In torsion tubular specimens, Miller and Chandler [14] have also shown that the fatigue life was dependent on specimen geometry. In the present study because of the determined specimen size effect, the number of cycles to failure given in mechanical test result tables (N_f*) corresponds to the experimental value

TABLE 2—*Room temperature tensile properties.*

Material	0.2% Yield Stress, MPa	Ultimate Tensile Stress, MPa	Elongation, %	Reduction of Area, %
Type 316L stainless steel	283	590	51.6	89
Inconel 718	1165	1375	20.5	

of N_f for solid specimens and to twice this experimental value for tubular specimens. In all cases, N_f and N_f^* are included in the tables. In the tests incorporating a tensile load, N_f was defined as corresponding to a drop of the maximum load by 25%. This definition will not be adopted for torsion tests. In this case, N_f was defined as corresponding to the number of cycles when an external crack of about 10 mm was observed on to the specimen surface.

Results and Observations

Mechanical Tests

Type 316L Stainless Steel—The results of the reversed torsion tests carried out on this material are given in Table 3. A comparison of the cyclic behavior of this material for reversed tension and reversed torsion is shown in Fig. 1 for both fatigue lives and cyclic strain hardening. This comparison is based on the Tresca equivalence for stress and strain. For simple tension, the plastic strains are

$$\epsilon_r^p = \epsilon_\theta^p = -\epsilon_z^p/2$$

The engineering plastic shear strain range is, therefore

$$\Delta\gamma^p = (3/2)\,\Delta\epsilon_z^p \tag{3}$$

The shear stress τ can be easily deduced from the tensile stress σ_z

$$\tau = \sigma_z/2 \tag{4}$$

Transcribing the reversed tensile fatigue test results of Ref *3* by using these parameters, a close correspondence of the strain hardening curves is observed. However, torsion fatigue lives are longer than for the tension tests by a factor at least equal to five. Furthermore, the fatigue life curves are not parallel.

Inconel 718: Strain Controlled Reversed Tension-Compression Tests. Superposition of a Steady Torque—The results of these tests are given in Table 4. A nonproportional complex loading configuration was achieved by superimposing a steady torque to the solid specimens, such that the elastic shear stress induced

TABLE 3—*Type 316L stainless steel. Strain controlled reversed torsional fatigue experiments: stabilized stress-strain behavior and fatigue lives.*

Test	Specimen, electropolished	$\Delta\gamma_p$, %	$\Delta\tau/2$, MPa	τ^M, MPa	N_f	N_f^*
6	tubular	2.8	240	240	2 850	5 700
3	tubular	2.42	225	225	4 400	8 800
4	tubular	2	199	199	9 600	19 200
2	tubular	1.65	183	183	17 200	34 400
5	tubular	1.3	165	165	48 000	96 000

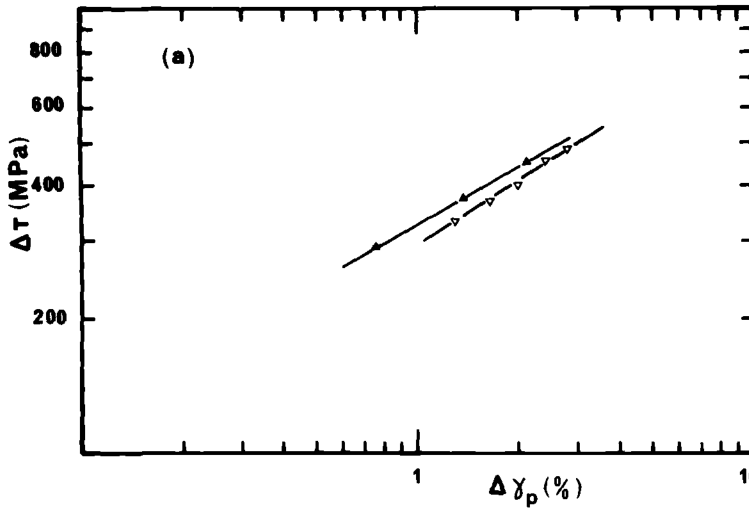

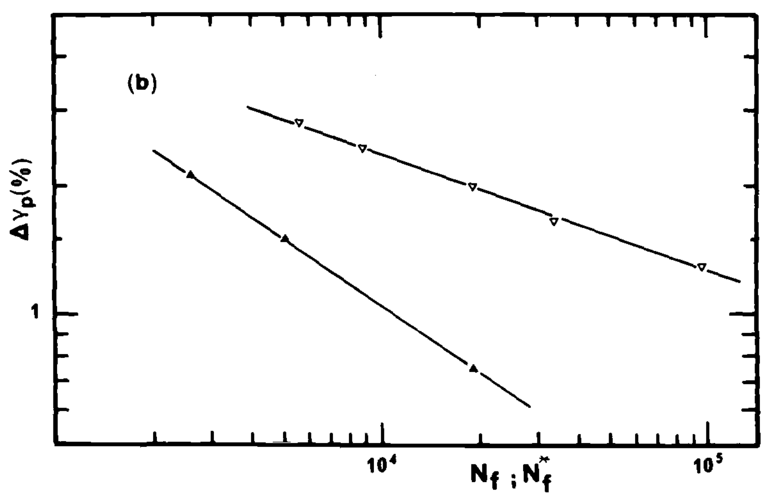

▲ Reversed Tension (solid specimens).
▽ Reversed Torsion (hollow specimens).

FIG. 1—*Type 316L stainless steel. Comparison of tensile and torsional LCF behavior* (a) *cyclic stress-strain response; and* (b) *fatigue life.*

at the specimen free surface was equal to 408 MPa (525 MPa for one test). As described for Type 316L stainless steel in Ref *3*, a strong torsional ratchetting effect was observed when applying the torque. Table 4 shows that the application of a steady torque leads to a significant reduction in fatigue life.

Inconel 718: Stress Controlled Pulsated Fatigue Tests—The results of these experiments are given in Table 5. During these tests, the accumulation of tensile

TABLE 4—*Inconel 718. Strain controlled reversed tensile fatigue experiments, superposition of a permanent shear* (τ_p)*: stabilized stress-strain behavior and fatigue lives.* N_p *is measured from striation spacings.*

Test	Specimen, mechanically polished	τ_p, MPa	$\Delta\epsilon_p/2$, %	$\Delta\gamma_p$, %	$\Delta\sigma/2$, MPa	τ^M, MPa	Torsion at Fracture	N_i	N_i^*	N_p	N_f
5	solid	0	2	6	1236	618	0	200	200		35
3	solid	0	1	3	1136	568	0	530	530	290	240
1	solid	0	0.5	1.5	1030	515	0	1660	1660	1000	660
2	solid	0	0.3	0.9	990	495	0	2660	2660		1250
12	solid	0	0.25	0.75	966	483	0	3420	3420		1700
4	solid	0	0.15	0.45	925	462	0	6080	6080	2100	4000
6	solid	0	0.1	0.3	905	452	0	8250	8250	3450	4800
17	solid	408	1	3	1340	670		155	155		25
1	solid	408	0.4	1.2	1225	612	35°	600	600		170
15	solid	408	0.1	0.3	950	475	5°	4480	4480	2780	1700
16	solid	525	0.1	0.3	1045	522	23°	3150	3150		1300

TABLE 5—*Inconel 718. Stress controlled pulsated tensile fatigue experiments.*

			1st Cycle		Stabilized Behavior, $N_i/2$							
Test	Specimen	R_σ	σ_o^M, MPa	ϵ_o^M, %	σ^M, MPa	τ^M, MPa	$\Delta\epsilon_p$, %	$\Delta\gamma_p$, %	N_f	N_f^*	N_p	N_i
11	solid	0	1320	1	1335	667	0.012	0.018	16 600	16 600		13 800
13	solid	0	1340	2.2	1365	682	0.015	0.022	15 400	15 400	2400	13 000
8	solid	−0.5	1200	<1	1200	600	0.069	0.103	4 840	4 840		2 600
9	solid	−0.5	1140	<1	1140	570	0.025	0.075	10 850	10 850		7 000

strain due to the positive mean stress (which was recorded on 316L stainless steel [3]) is not observed for Inconel 718. The plastic strain amplitudes are very small when compared with the elastic strains, especially with $R_\sigma = 0$.

Inconel 718: Strain Controlled Reversed Torsion Tests—The results of these experiments are given in Table 6. A comparison of the tensile and torsional behavior of Inconel 718 has been carried out by using the Tresca equivalence. We can see in Fig. 2 that the cyclic strain hardening curves are still very close, whereas there is a factor of four between the torsion and tension fatigue lives.

Observations

Striation Spacing Measurements—From direct SEM observation of the fatigue fracture surfaces, striation spacings have been measured on Inconel 718 LCF specimens. The results we obtained on four specimens tested under the reversed tensile condition are plotted as a function of the crack depth in Fig. 3. Let us note the typical broken shape of these curves, where the striation spacings are first constant before suddenly exponentially raising. Similar observations were made on Type 316L stainless steel [2,15]. On Inconel 718, striation spacings were also measured from one specimen tested with a superimposed torque and one specimen tested under pulsated tensile condition, both specimens providing the same curve shape as described previously.

We tried to carry out striation observations from specimens tested under reversed torsion, but, on both Type 316L stainless steel and Inconel 718, the fracture surfaces were heavily smeared.

Microcrack Orientation: Inconel 718 Under Reversed Tensile Loading. Influence of a Permanent Torque—SEM observations of the external surface of Inconel 718 specimens tested under reversed tensile LCF and with a permanent torque show a strong influence of a steady load on the statistical orientation of fatigue microcracks (Fig. 4). These types of histograms were determined using SEM X320 maps covering areas of about 1 mm^2. When superimposing a torque, the crack distribution is shifted towards one of the 45° directions. A simple elastic stress analysis can help explain this phenomenon. The normal stress to planes enduring a maximum in-depth shear strain, that is, case B planes, is not modified by the torque. On the contrary, case A planes, which are the planes

TABLE 6—*Inconel 718. Strain controlled reversed torsional fatigue experiments: stabilized stress-strain behavior and fatigue lives.*

Test	Specimen, mechanically polished	$\Delta\gamma_p$, %	$\Delta\tau/2$, MPa	τ^M, MPa	N_f	N_f*
T5	tubular	2.6	601	601	1 070	2 140
T2	tubular	1.8	555	555	2 000	4 000
T1	tubular	1.5	533	533	2 700	5 400
T3	tubular	1.0	518	518	5 500	11 000
T4	tubular	0.75	480	480	6 600	13 200
T7	tubular	0.5	438	438	13 000	26 000

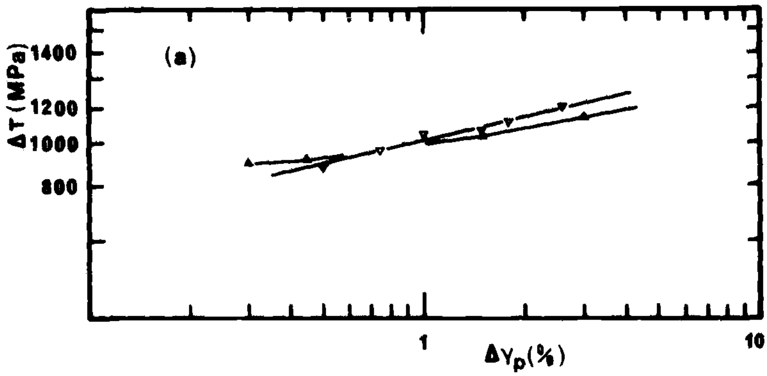

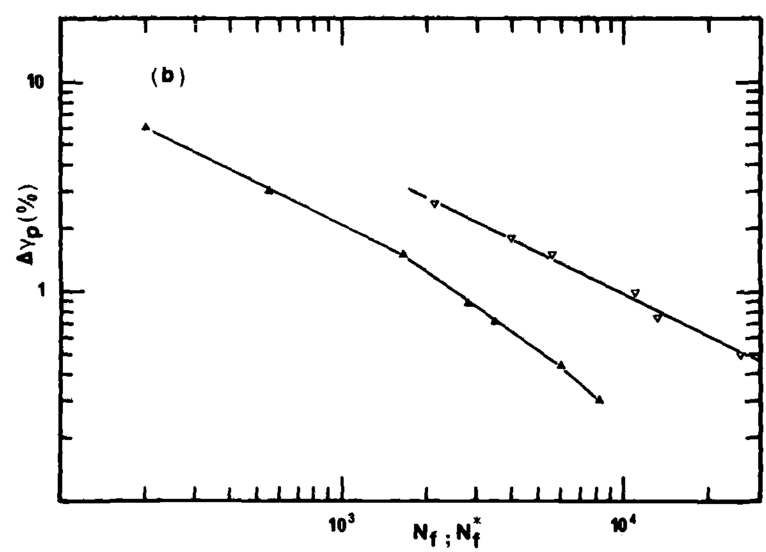

▲ Reversed tension (solid specimens).
▽ Reversed torsion (hollow specimens).

FIG. 2—*Inconel 718 alloy. Comparison of tensile and torsional behavior* (a) *cyclic stress-strain response, and* (b) *fatigue life.*

enduring a surface shear strain, are either overloaded or compressed by the torque. The observed distribution movement towards the direction "opened" by the torque was thus predictable.

An observation of the sharp edge between a cross section and the specimen surface (Fig. 5) confirmed that crack nucleation occurs most often on maximum

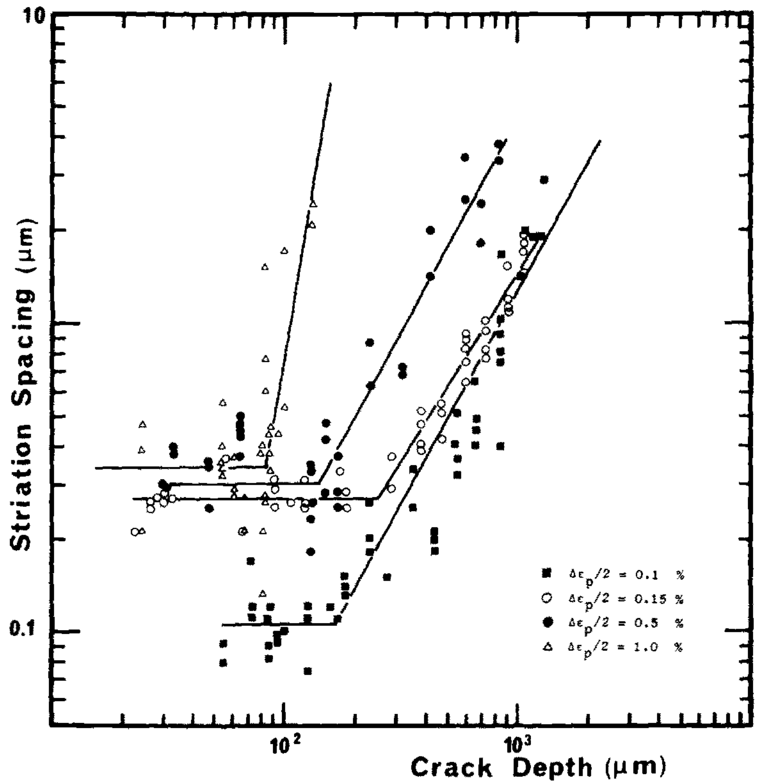

FIG. 3—*Inconel 718 alloy. Striation spacing versus crack depth.*

shear strain planes. Under simple reversed tensile fatigue, Type B cracks are found to be deeper and propagating faster than Type A cracks: Case B cracks are felt to control fracture in this case. On the contrary, when superposing a torque, Type A cracks are predominant and seem to be the most harmful. It should be noticed that under this loading configuration, cracks in Inconel 718 were observed to propagate macroscopically in planes inclined at 45° of the tensile axis, that is on case A planes. Nevertheless, case B cracks were still observed, eventually propagating in classical Stage II.

Microcracks Orientation: 316L Stainless Steel and Inconel 718 Under Reversed Torsional LCF—From SEM maps (Fig. 6*a*) and from cross-section observations, it has been deduced that in both materials microcracking occurs on Type A pure shear planes. Histograms (Fig. 6*b*) show that for Inconel 718 both Type A directions are equally damaged, whereas in Type 316L stainless steel crack initiation is preferentially observed in the longitudinal direction. This is certainly connected with the orientation of the inclusions in this material. For both materials, cracks are observed to propagate several millimetres along the initiation planes, which are pure shear planes.

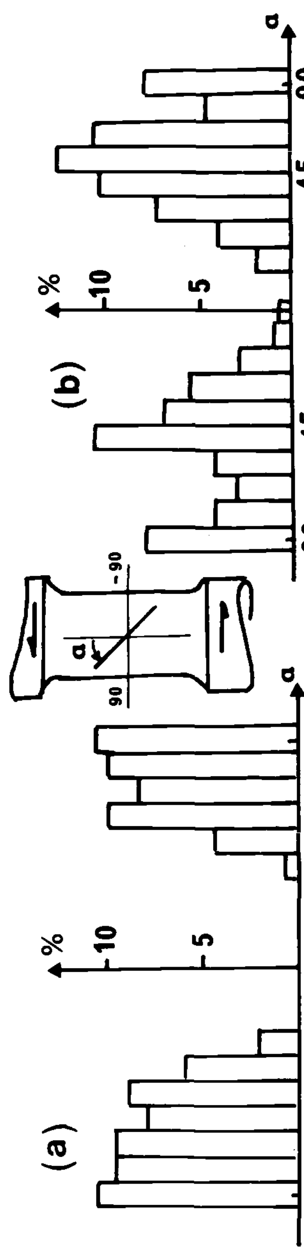

FIG. 4—*Inconel 718. Distribution of crack traces observed onto the specimen surface* (a) *reversed tensile fatigue,* (b) *reversed tensile fatigue with a steady torque. The angle* α *is defined.*

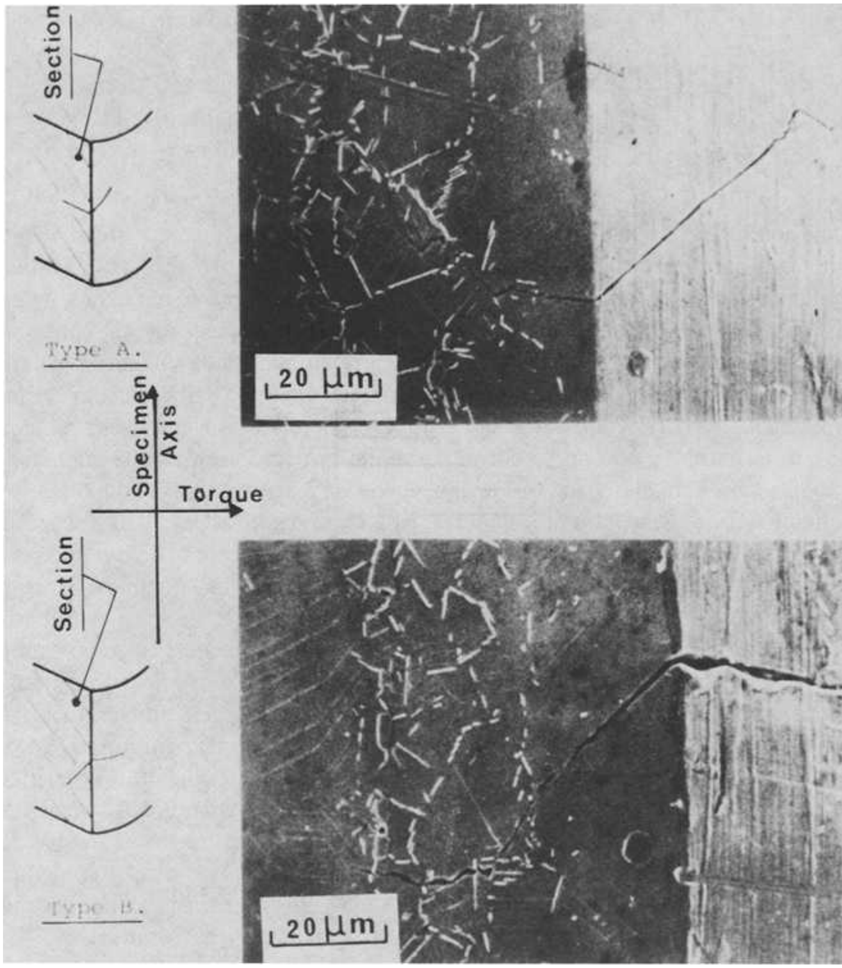

FIG. 5—*Inconel 718. Types A and B microcracks observed on the specimen surface and on a section parallel to the specimen axis. Reversed tensile fatigue with a steady torque.*

Discussion

Experimental Analysis of the Number of Cycles to Crack Initiation

Type 316L Stainless Steel—Several investigators [*7,16,17*] have shown that for Type 316 stainless steel and within the crack propagation rate range usually encountered in LCF (that is, 0.1 to 10 μm per cycle) a one to one relationship between striations and fatigue cycles can be assumed. Recent observations [*18*] have been also carried out on high temperature LCF specimens of Type 316L stainless steel. For different strain amplitudes and fatigue life fractions, the authors have measured on every fatigue specimen the depth of numerous small cracks. A good prediction of these experimental statistical crack depth distributions has been achieved by using a simple model taking into account the crack propagation rates as measured from striation spacings.

A correct estimate of the number of cycles spent propagating the cracks can thus be obtained by plotting striation spacing versus crack depth and by integrating along the fitting curve between the initial value of crack length, a_o, corresponding to the end of Stage I and a_f corresponding to the final crack length. In this integration, a_o was taken as 20 μm and a_f as 2 000 μm.

Inconel 718—Clavel and Pineau [*21*] have shown that in the case of Inconel 718 and within the 0.1 to 10 μm per cycle crack propagation rate range, it can be assumed that the correspondence between striations and fatigue cycles is the same as for Type 316L stainless steel. The value of N_i was estimated for six Inconel 718 LCF specimens, tested mostly under reversed tensile conditions, but including one test with a superimposed permanent torque and another one under pulsated tensile condition. Plotting these results along with the stainless steel data in Fig. 7, it is observed that the fraction of fatigue life spent initiating cracks can be fitted by a single curve for all materials and testing conditions reported here. In the present work and for both stainless steel and Inconel 718, the value of N_i was determined using this correlation. Reversed torsion tests are of course excepted.

Assessment of a LCF Initiation Criterion

Crack Initiation Orientation—From the observations carried out on Inconel 718 (reported in the present paper) and on Type 316L stainless steel (reported in Ref *3*) the following summary can be written. In all cases and for both materials, microcracks can be observed in every high shear strain amplitude orientation. Some of these microcracks exhibit a stronger trend to propagation.

In the case of 316L stainless steel, for all tensile LCF configurations, crack initiation takes place on Type B, in-depth growing shear planes, with a subsequent classical Stage II propagation. For both materials under reversed torsion, microcracking takes place on Type A pure shear planes, and microcracks macroscopically propagate in their own plane.

For Inconel 718 under reversed tensile LCF, Type B microcracks followed by classical Stage II propagation are still controlling the rupture, whereas the superimposition of a steady torque may lead to a different fracture mode. In this case Type A microcracks may be predominant and propagate in the crack initiation plane. It is felt here that classical Stage II propagation, observed for example on Fig. 5, is slowed down by crack closure effects due to ratchetting torsion. Crack propagation becomes faster in Type A planes, and thus Type A microcracks are controlling the fracture process. Let us note that Type A propagation is most probably governed by crack opening modes, as shown by the sharp striations we observed and the propagation rates we measured from them. This propagation mechanism is thus very different from the one observed for

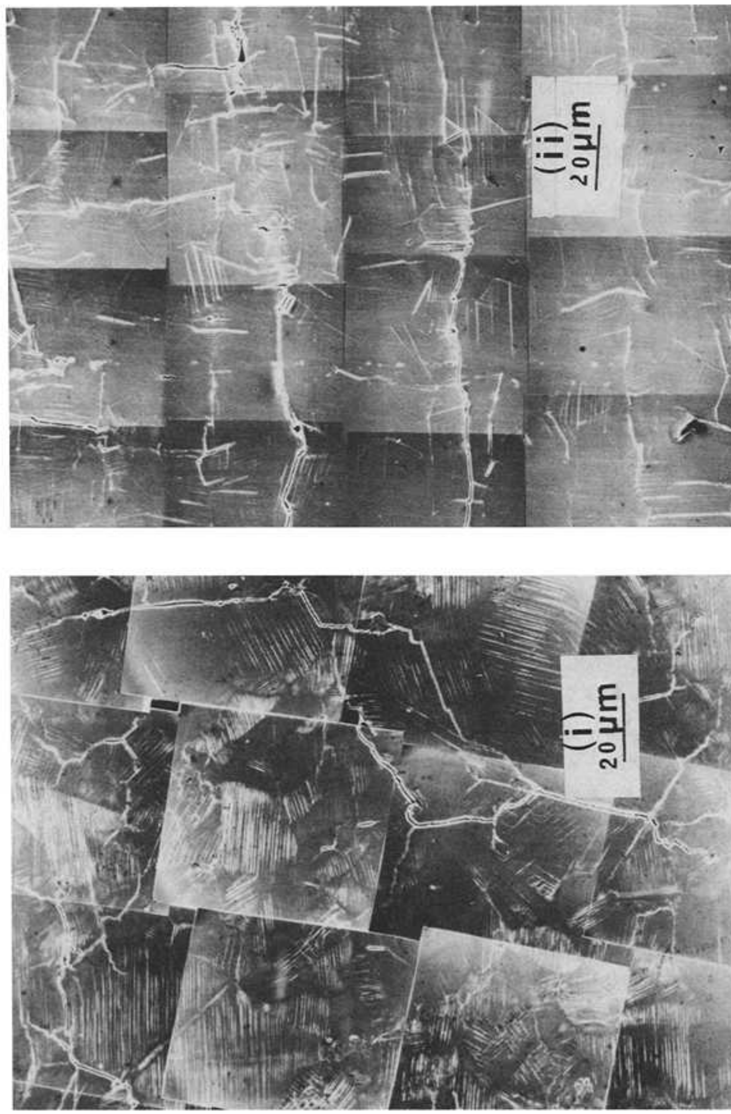

(a)

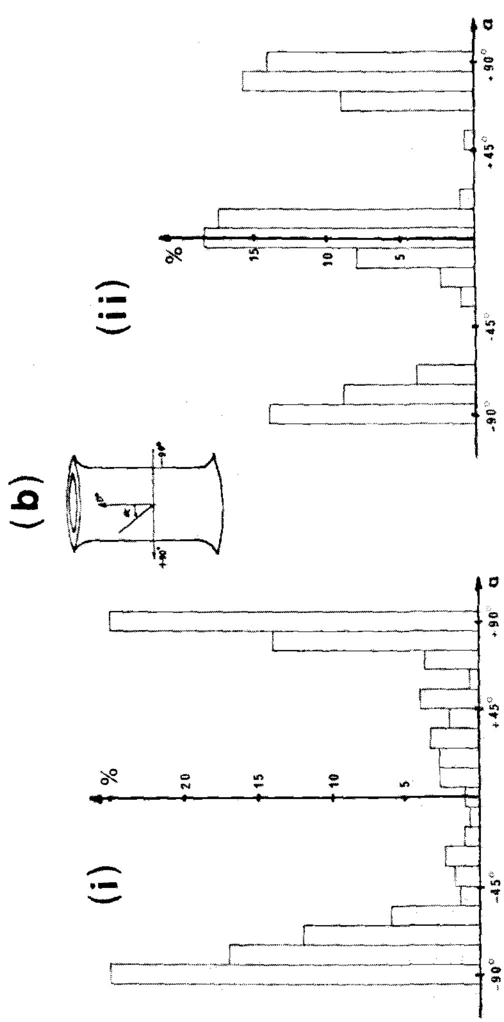

(*a*) Specimen surfaces.
(*b*) Surface crack orientation.

FIG. 6—*Reversed torsional low cycle fatigue for* (i) *Type 316L stainless steel and* (ii) *Inconel 718 alloy.*

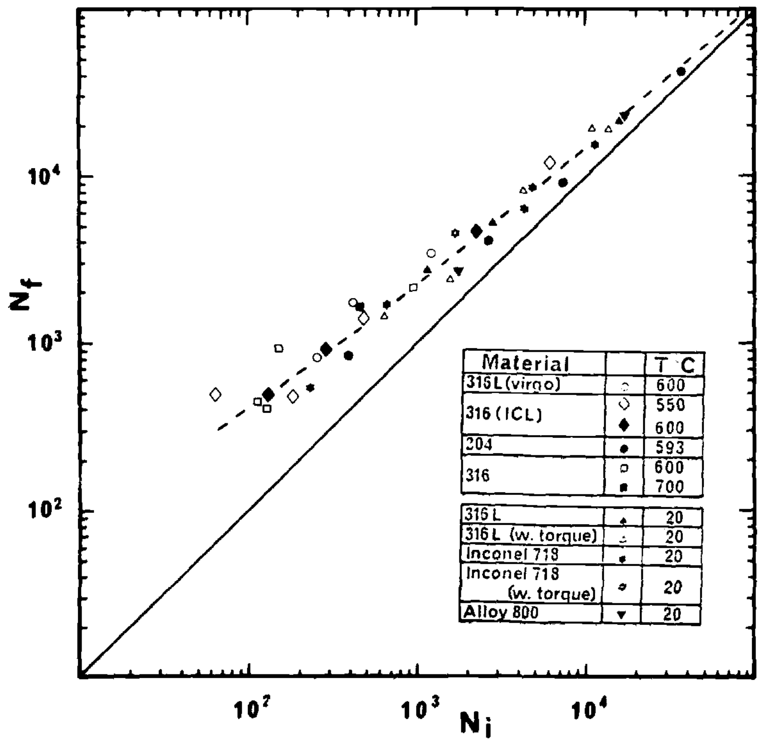

FIG. 7—*Total fatigue life,* N_f, *as a function of the number of cycles for crack initiation,* N_i.

reversed torsional LCF. In spite of its orientation, it can be hardly labelled Stage I, but it is certainly not Stage II.

From all these remarks, it is concluded that the orientation of the initiation plane of the final crack is strongly connected with the orientation of the plane of fastest propagation. When this propagation is classical Stage II, Type B microcracking controls failure. In some cases the fastest propagation can be oriented otherwise, leading to the control of failure by Type A cracks.

Number of Cycles for Crack Initiation—It is clear that it is necessary to use at least two parameters to describe fatigue crack initiation, as already proposed by other investigators [*1,2,3,12,13*]. We mentioned that Types A and B microcracks were simultaneously present when the applied loads on their planes were not too different. This observation suggests that the number of cycles for initiation does not strongly depend on the shear strain orientation. This remark is clearly conflicting with the classical concept of Type B shear being more damaging than Type A. Furthermore, it means that the kind of criterion we formerly proposed for Type B initiation (Eq 1) should be also efficient for Type A, if using the correct mechanical parameters.

Applying Eq 1 to the Inconel 718 results, the effect of the normal stress on Type A planes (σ_n^A) for tensile fatigue with a superimposed torque would predict an important decrease in fatigue life. Furthermore, for reversed torsion tests, σ_n^A is always equal to zero. For these two reasons, we replaced σ_n by the maximum of the shear stress, τ, applicable to the crack initiation plane. The parameter τ is just as complementary as σ_n of the first parameter, $\Delta\gamma_p$, but seems to have a wider applicability.

An attempt at correlating the experimental results was thus carried out using the following relationship

$$N_i = N_o\, \Delta\gamma_p{}^{\alpha}\, \tau^{\beta} \tag{6}$$

where

$\Delta\gamma_p$ = plastic shear strain range applying on the crack initiation plane and
τ = maximum of the shear stress that is applied on the same plane.

The term N_o is a parameter fitted from reversed tensile LCF results, α and β are calculated for every material by using the following procedure. The experimental results are plotted in the ($\Delta\gamma_p$ versus τ) plane for both materials (Fig. 8). In this diagram, iso-initiation life curves appear to be parallel straight lines, that is

$$\tau = k_1\, (\Delta\gamma_p)^{\lambda} \tag{7}$$

k_1 is an empirical function of N_i only. Considering the reversed tensile fatigue tests, a Manson-Coffin type relationship for initiation life can be written as

$$N_i = k_2\, (\Delta\gamma_p)^{\mu} \tag{8}$$

The cyclic stress-strain curve can be fitted by the equation

$$\tau = k_3\, (\Delta\gamma_p)^{\nu} \tag{9}$$

The following equations are easily derived

from Eqs 6 and 7

$$-(\alpha/\beta) = \lambda \tag{10}$$

from Eqs 6, 8, and 9

$$\alpha + \beta\nu = \mu \tag{11}$$

Solving this system, α and β are determined. The numerical values of λ, μ, ν, α, β, and N_o for both Type 316L stainless steel and Inconel 718 are given in Table 7.

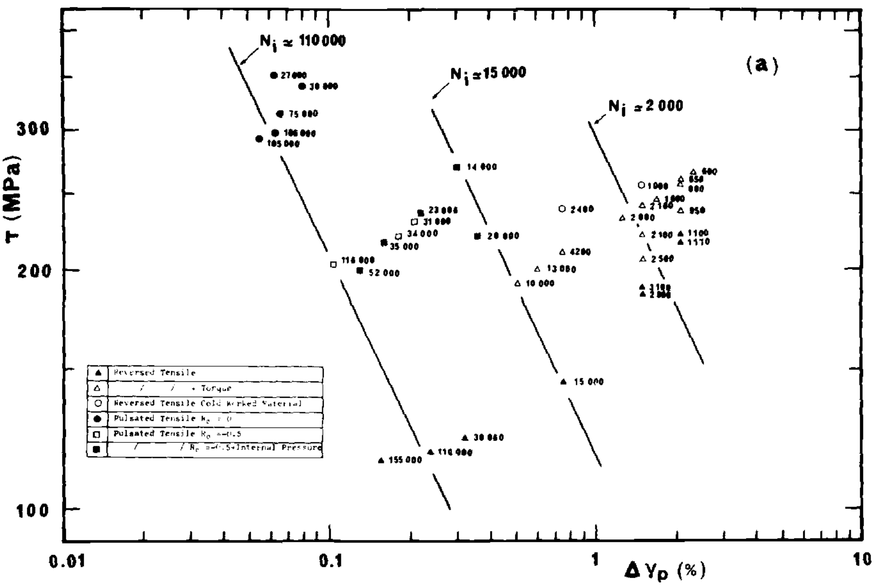

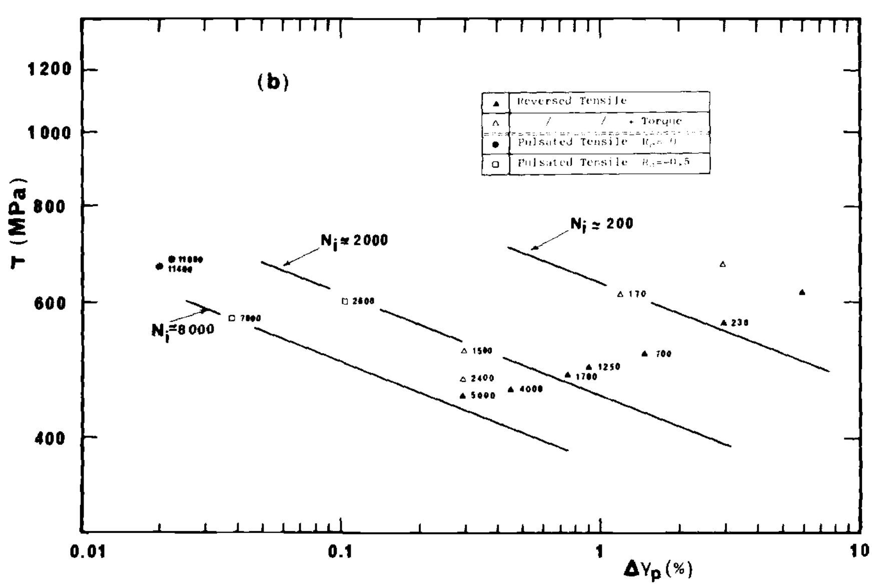

(*a*) Type 316L stainless steel.
(*b*) Inconel 718.

FIG. 8—*Initiation life in the* (τ *versus* $\Delta\gamma_p$) *plane.*

TABLE 7—*Parameters of the crack initiation criterion.*

Material	λ	μ	ν	α	β	N_o
Type 316L stainless steel	-0.7	-2.1	0.38	-1.4	-1.9	9×10^7
Inconel 718	-0.125	-1.55	0.095	-0.88	-7	7.2×10^{21}
316L steel [*23*]	-0.74	-2.36	0.25	-1.75	-2.36	7.5×10^8

Application of the Criterion to Experimental Results

Application to Type 316L Stainless Steel and Inconel 718 Results, Excepting Reversed Torsion Tests—The application of the criterion proposed previously to every result, for which an experimental estimate of N_i could be obtained (that is all experiments excepting reversed torsion tests) has shown a rather satisfactory predictive capability of the criterion for both 316L stainless steel and Inconel 718 (Fig. 9).

Application to 316L Stainless Steel and Inconel 718 Reversed Torsion Tests—The number of cycles at crack initiation predicted by the criterion (N_{ic}) was calculated from reversed torsional LCF data for both materials. The value of N_{ic} is plotted as a function of N_f in Fig. 10 where the experimental $N_i - N_f$ correlation obtained from tensile fatigue results (Fig. 7) is also shown by a dashed curve. This diagram indicates that for a given initiation life, the criterion proposed in this study predicts a much slower crack propagation under reversed torsional loading than under tensile LCF.

With respect to this issue, interrupted reversed torsion experiments were carried out on both materials. Tests were interrupted at fatigue lives corresponding to crack initiation as calculated from the criterion, and the resulting fatigue damage was then studied by SEM. Extrusions and evidence of transgranular decohesion was observed on the surface of the Type 316L stainless steel specimen and Type A microcracks were revealed in Inconel 718 (Fig. 11). This observed damage corresponds to crack initiation as defined previously. Furthermore these few experiments are reinforced by the observations of other workers. Socie et al [22] reported fatigue life fractions for initiation of 100 μm defects in Inconel 718 under reversed torsion similar to those predicted by the proposed criterion. The same trend was observed by Hurd and Irwing [*23*] on a quenched and tempered steel. All these results suggest that the ($\Delta\gamma_p,\tau$) criterion can apply to reversed torsional LCF.

Application to LCF Experiments Carried Out at Two Levels—Following the procedure reported in this study, we analyzed an important batch of experimental results from the literature [*24*]. About 60 tests carried out on a Type 316L stainless steel, including pulsated LCF and LCF after large prestrain (up to 30%), were readily correlated. The correlating parameters are given in Table 7. Some LCF tests carried out on the same material at two successive stress amplitude levels are also reported in Refs *24,25* (Table 8). A prediction of the number of

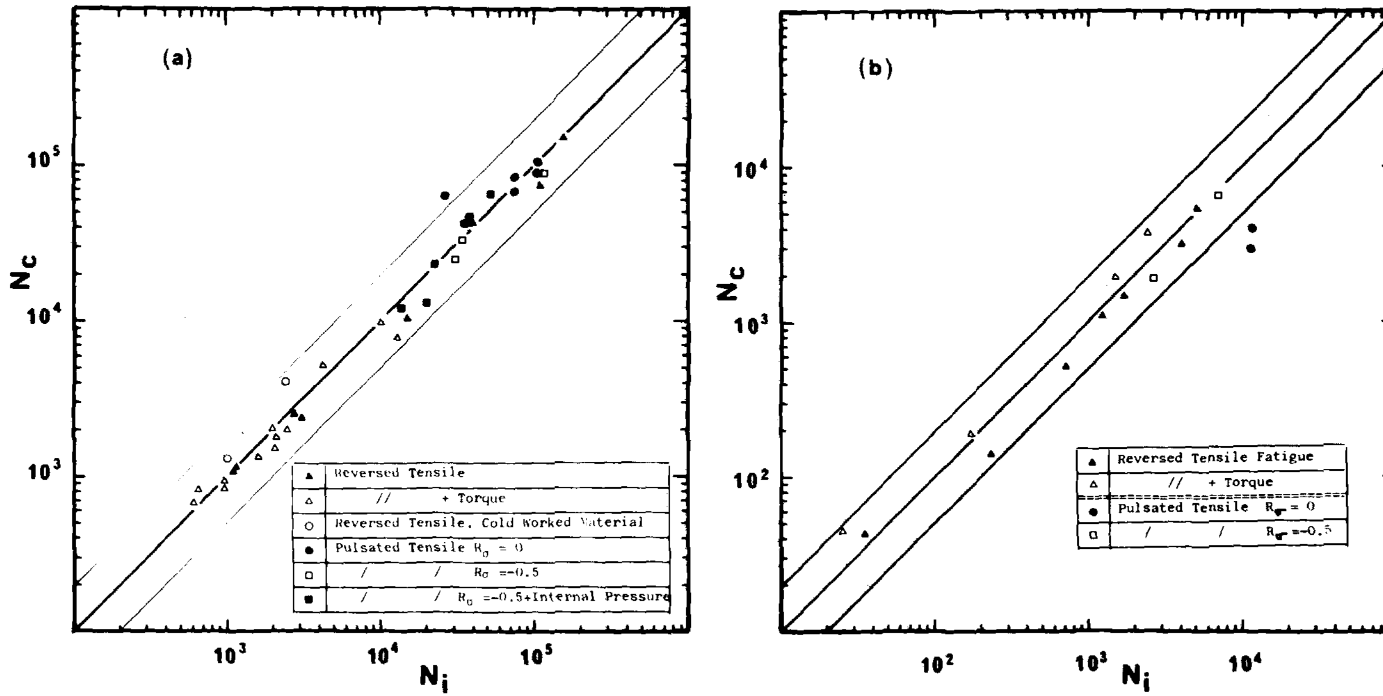

(*a*) Type 316L stainless steel.
(*b*) Inconel 718.

FIG. 9—*Experimental results correlation.*

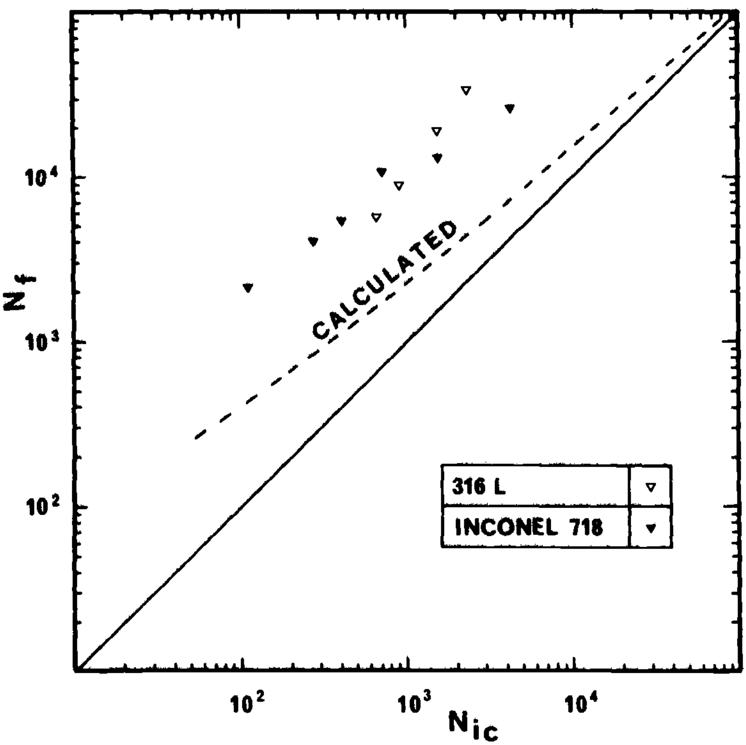

FIG. 10—*Reversed torsion. Experimental fatigue life,* N_f, *as a function of the calculated number of cycles for crack initiation,* N_{ic}.

cycles spent at the second level before final fracture (N_2) was attempted by using the ($\Delta\gamma_p$, τ) crack initiation criterion and the N_i versus N_f curve of Fig. 7. The detail of the procedure is given in Table 9. The terms N_{i1} and N_{i2} are the number of cycles for initiation as predicted from the ($\Delta\gamma_p$, τ) criterion for both test levels, which are considered as distinct, and N_{p1} and N_{p2} are the number of cycles for propagation deduced from N_{i1} and N_{i2} by using the N_i versus N_f correlation. The calculated number of cycles at the second fatigue level (N_{2c}) is derived from the number of cycles spent at the first level (N_1) as follows

for $N_1 < N_{i1}^*$

$$N_{2C} = N_{i2}^* \, (1 - N_1/N_{i1}^*) + N_{p2}^* \tag{12}$$

for $N_1 > N_{i1}^*$

$$N_{2C} = N_{p2}^* \, [1 - (N_1 - N_{i1}^*)/N_{p1}^*] \tag{13}$$

Equation 12 is obtained by applying the Miner linear cumulative damage rule to initiation lives. In Eq 13 the propagation lives are calculated by the same simple rule. In Table 9, it is noticed that in all cases but one Eq 12 applies. A

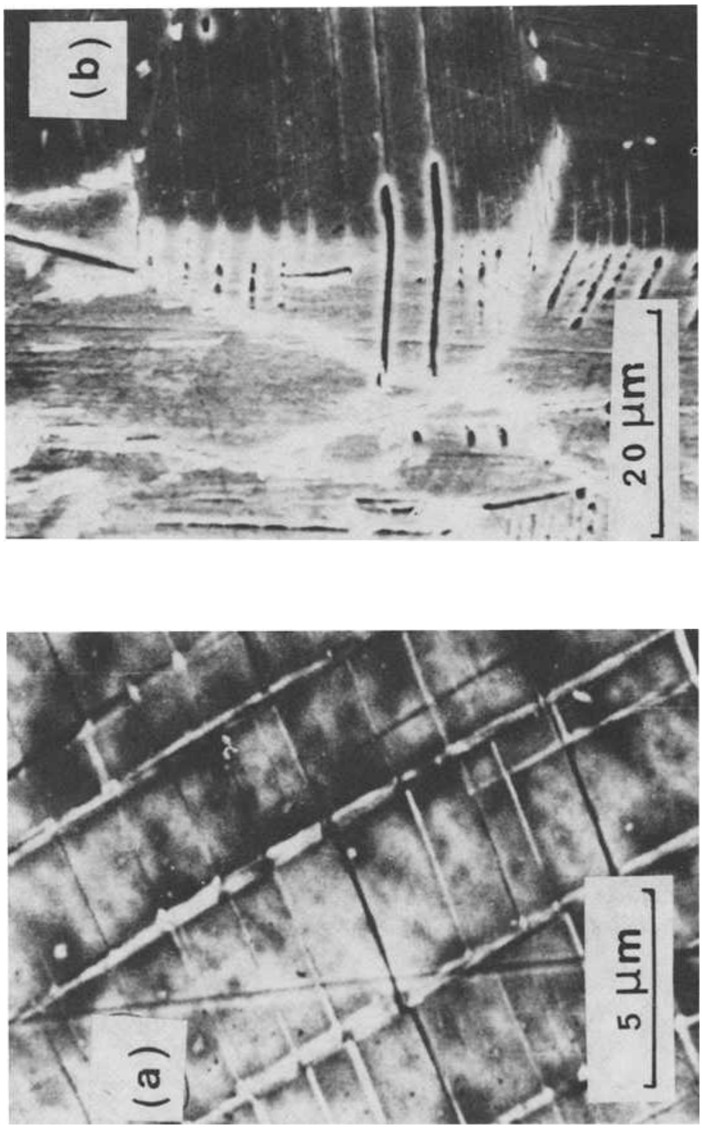

(*a*) Type 316 Stainless steel; $\Delta\gamma_p = 1.3\%$, $N = 2000$ cycles ($N_f = 48\,000$ cycles).
(*b*) Inconel 718 alloy; $\Delta\gamma_p = 1\%$, $N = 1000$ cycles ($N_f = 5500$ cycles).

FIG. 11—*Reversed torsion. Interrupted experiments.*

TABLE 8—*Type 316L stainless steel* [24]. *Two level reversed tensile fatigue experiments: stabilized stress-strain behavior and number of cycles.*

	1st Fatigue Level					2nd Fatigue Level				
Test	$\Delta\epsilon_p$, %	$\Delta\gamma_p$, %	$\Delta\sigma/2$, MPa	τ^M, MPa	N_1	$\Delta\epsilon_p$, %	$\Delta\gamma_p$, %	$\Delta\sigma/2$,, MPa	τ^M, MPA	N_2
47	1.16	1.74	382	191	635	0.74	1.11	339	170	3 253
48	1.32	1.98	382	191	635	0.74	1.11	322	161	4 300
49	1.30	1.95	378	189	635	0.47	0.70	302	151	5 200
50	1.38	2.07	378	189	635	0.166	0.25	269	134	35 000
51	0.65	0.97	286	143	6150	1.37	2.05	378	189	970
52	0.58	0.87	286	144	6150	0.74	1.11	303	152	5 808
0.16	1.98	2.97	430	215	20	0.64	0.96	304	152	7 657
0.19	1.96	2.94	429	214	300	0.615	0.92	329	164	5 060
0.21	0.66	0.99	300	150	4000	1.93	2.89	433	216	398
0.27	2.92	4.38	513	256	20	0.57	0.85	360	180	2 640
1.12	2.96	4.44	535	267	30	0.66	0.99	348	174	6 000
1.16	2.92	4.38	574	287	225	0.58	0.87	413	206	2 510

TABLE 9—*Type 316L stainless steel (24). Analysis of the two level fatigue experiments.*

Test	N_1	N_{i1}*	N_{p1}*	N_{i2}*	N_{p2}*	N_{i2}	N_{p2}	N_2	N_{2r}
47	635	1173		3 446	2 500	1 580	2 500	3 253	4 300
48	635	936		3 918	2 850	1 260	2 850	4 300	4 100
49	635	994		10 055	4 500	3 630	4 500	5 200	8 100
50	635	895		87 000	10 000	25 300	10 000	35 000	35 000
51	6150	6300		895	1 100	20	1 100	970	1 100
52	6150	7700		4 500	3 000	906	3 000	5 808	3 900
0.16	20	350		5 700	3 500	5 375	3 500	7 657	8 900
0.19	300	360		5 130	3 000	855	3 000	5 060	3 850
0.21	4000	5470		360	640	97	640	398	740
0.27	20	116		4 600	3 000	3 800	3 000	2 640	6 800
I.12	30	100		3 900	2 700	2 700	2 700	6 000	5 400
I.16	225	90	290	3 370	2 600	0	1 400	2 510	1 400

good correlation of the experimental results (Fig. 12) was achieved by using this procedure. The double linear damage approach was first introduced by Manson [29], but here it is worth emphasizing that it is applied to specific fatigue life stages as assessed from direct observations.

Summary and Conclusion

Low-cycle fatigue crack propagation is mostly controlled by macroscopic mechanical parameters, while crack initiation is strongly sensitive to physical aspects such as microstructural details and environment. Therefore, the two stages have to be studied separately. From experiments on Type 316L stainless steel and Inconel 718 alloy involving: (*a*) reversed tension-compression, (*b*) reversed tension-compression with superimposition of a steady torque, (*c*) pulsated tension-compression, and (*d*) reversed torsion, the following conclusions can be made.

1. The number of cycles needed by the final crack to reach an initiation size of one grain was determined for tests (*a, b, c*) just mentioned. These results plus others from the literature yield a simple relationship for crack initiation in austenitic stainless steels tested at temperatures ranging from 20 to 700°C and for Inconel 718 at room temperature.
2. Depending on the material and on the loading configuration, cracks controlling the fatigue fracture were observed to initiate as either Types A or B. In all cases, microcracking occurs for every plane orientation corresponding to high shear strain amplitudes. The orientation of the initiation plane of the principal

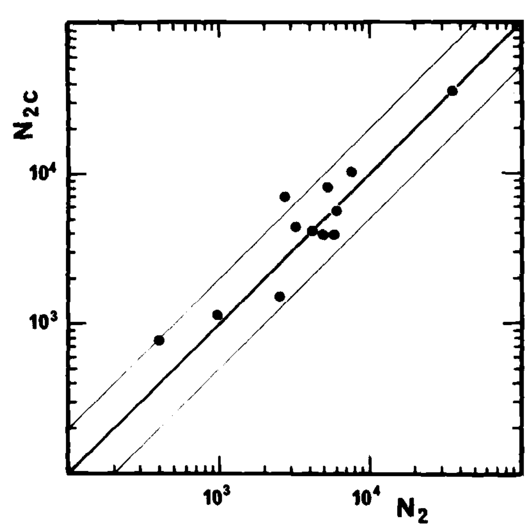

FIG. 12—*Correlation of cumulative damage experiments.*

crack is always strongly connected with the orientation of the plane of fastest propagation, which is not necessarily classical Stage II.

3. Combining the plastic shear strain range on the crack initiation plane, $\Delta\gamma_p$, and the maximum of the shear stress on this plane, τ, a modified LCF crack initiation criterion is proposed

$$N_i = N_o \, (\Delta\gamma_p)^\alpha \, \tau^\beta$$

where N_o, α, β are parameters fitted from the Manson-Coffin type law and the reversed cyclic stress-strain curve.

4. The predictive capability of this criterion was found satisfactory for various experimental results, featuring both Types A and B crack initiation (for example, reversed torsion and reversed tension). Types A and B shear seem thus to have the same effect on crack initiation. Differences in fatigue lives arise only from variations in propagation rates, connected with the propagation orientation or mode.

5. Using the N_i versus N_f correlation and the $(\Delta\gamma_p,\tau)$ criterion, a simple method is applied for evaluating cumulative fatigue damage. Experimental data from the literature are successfully correlated.

Acknowledgments

This study was conducted as part of the program of the French research group "Grandes Déformations et Endommagement Groupe de Recherche Concertée, Centre National de la Recherche Scientifique." Financial support from the Societé Nationale d'Etude et de Construction de Moteurs d'avions and from the Bureau de Contrôle des Centrales Nucleaires is gratefully acknowledged.

References

[1] Brown, M. W. and Miller, K. J. in *Low Cycle Fatigue and Life Prediction, ASTM STP 770,* American Society for Testing and Materials, Philadelphia, 1982, pp. 169–193.

[2] Jacquelin, B., Hourlier, F., and Pineau, A., 3rd International Post-SMIRT Seminar on Inelastic Analysis and Life Prediction in High-Temperature Environment, Paris, France, 24–25 August 1981.

[3] Jacquelin, B., Hourlier, F., and Pineau, A., *Transactions,* American Society of Mechanical Engineers, *Journal of Pressure Vessel and Technology,* Vol. 105, 1983, pp. 138–143.

[4] Baudry, G. and Pineau, A., *Materials Science and Engineering,* Vol. 28, 1977, pp. 229–242.

[5] Petrequin, P. and Pineau, A. in *l itigue des Matériaux et des Structures,* C. Bathias and J. P. Bailon, Eds., Maloine Edi . Paris, 1980, pp. 107–161.

[6] Levaillant, C., Rezgui, B., and Pineau, A., *ICM3 Conference,* Cambridge, England, Aug. 1979, Vol. 2, p. 163.

[7] Mahonney, M. W. and Paton, N. E., *Nuclear Technology,* Vol. 23, 1974, pp. 53–62.

[8] Graf, M. and Hornbogen, E., *Scripta Metallurgica,* Vol. 12, 1978, pp. 147–150.

[9] Brown, M. W. and Miller, K. J., *Proceedings,* Institute for Mechanical Engineering, Vol. 187, 1973, p. 745.

[10] Miller, K. J. and Pascoe, K. J., Conference on the Mechanics and Physics of Fracture, Institute of Physics, Cambridge, England, 1975.

[11] Kanazawa, K., Miller, K. J., and Brown, M. W., *Journal of Engineering Materials and Technology,* Vol. 99, 1977, p. 222.

[*12*] Brown, M. W. and Miller, K. J., *Fatigue of Engineering Materials and Structures*, Vol. 1, 1979, pp. 93–106.
[*13*] Lohr, R. D. and Ellison, E. G., *Fatigue of Engineering Materials and Structures*, Vol. 3, 1980, pp. 19–37.
[*14*] Miller, K. J., and Chandler, D. C., *Proceedings*, Institute of Mechanical Engineers, Vol. 184, 1969–70, pp. 433–440.
[*15*] Levaillant, C. and Pineau, A. in *Low Cycle Fatigue and Life Prediction, ASTM STP 770*, American Society for Testing and Materials, Philadelphia, 1982, pp. 482–499.
[*16*] Wareing, J. and Vaughan, H. G., *Metallurgical Science*, Vol. 11, 1977, pp. 439–446.
[*17*] Wareing, J., Vaughan, H. G., and Tomkins, B., Northern Division UKAEA Report, NDR 447 (S), Sept. 1980.
[*18*] Levaillant, C., Masuda, S., and Pineau, A., Report CEA, Contract CEA SA 7387-SA 7389-SA 8389, Dec. 1980.
[*19*] Maiya, P. S., *Scripta Metallurgica*, Vol. 9, 1975, pp. 1141–1146.
[*20*] Yamaguchi, K., Kanazawa, K., and Yoshida, S., *Materials Science and Engineering*, Vol. 33, 1978, pp. 175–181.
[*21*] Clavel, M. and Pineau, A., *Materials Science and Engineering*, Vol. 55, 1982, pp. 157–171 and pp. 173–180.
[*22*] Socie, D. F., Waill, L. A., and Dittmer, D. F., this publication, pp. 463–481.
[*23*] Hurd, N. J. and Irving, P. E., this publication, pp. 267–284.
[*24*] Chaboche, J. L., Kaczmarek, H., and Raine, P., La Recherche Aérospatiale, Vol. 3, 1980, pp. 177–196.
[*25*] Chaboche, J. L., Cailletaud, G., Policella, H., Kaczmarek, H., Lieurade, H. P., Ribes, A., Marquis, D., Dufailly, J., and Bollinger, E., "Interaction de l'écrouissage et de l'endommagement sous sollicitations complexes dans un acier inoxydable austénitique," Rapport Directions Générale de la Reserche Scientifique et Technique, 1983.
[*26*] Manson, S. S., *ICM3 Conference*, Cambridge, England, Vol. 1, Aug. 1979, pp. 13–45.

Brian N. Leis,[1] *Jalees Ahmad,*[1] *and Melvin F. Kanninen*[2]

Effect of Local Stress State on the Growth of Short Cracks

REFERENCE: Leis, B. N., Ahmad, J., and Kanninen, M. F., "**Effect of Local Stress State on the Growth of Short Cracks,**" *Multiaxial Fatigue, ASTM STP 853,* K. J. Miller and M. W. Brown, Eds., American Society for Testing and Materials, Philadelphia, 1985, pp. 314–339.

ABSTRACT: This paper examines the extent to which local state stress contributes to observed short crack growth rate behavior. Local crack-tip stress state effects are explored in terms of data developed at notch roots in notched plates of various thicknesses. Experimental data and fractography coupled with the results of stress intensity solutions show that a part of the so-called short crack effect may be rationalized by three-dimensional considerations.

KEY WORDS: notches, local stress state, crack initiation, microcrack growth, mechanics, plasticity, metallurgy, fractography, short crack effect

Nomenclature

K_t	Theoretical elastic stress concentration factor
ϕ	Diameter
t	Thickness
$\sigma_1,\sigma_2,\sigma_3$	Principal stresses, at a notch root
$\epsilon_1,\epsilon_2,\epsilon_3$	Principal strains, at a notch root
S_{mx}	Maximum far field (gross section) stress
S_{mn}	Minimum far field (gross section) stress
R	Stress ratio, S_{mn}/S_{mx}
a	Crack length, from notch root on transverse net section
w	Width, across transverse net section
$F(a/w)$	Function of geometry and crack length
K,K_{mx}	Stress intensity factor, corresponding to maximum stress
σ_y	Yield stress
r_p	Plastic zone size
ΔK_{eff}	Effective stress intensity factor range, range of K for which the crack is open

[1] Senior scientist and principal scientist, respectively, Battelle-Columbus Laboratories, Columbus, OH 43201.
[2] Institute scientist, Southwest Research Institute, San Antonio, TX 78284.

Copyright© 1985 by ASTM International www.astm.org

N Cycles
da/dN Crack growth rate per cycle

It is well known that the fatigue resistance of metals depends on the state of stress at the fatigue critical location. Data in the literature indicate that octahedral measures as well as differences between maximum principal stresses or strains have been invoked to relate fatigue in various states of stress and strain (for example [*1*]). Once a macrocrack develops, the literature suggests that a maximum principal stress criterion including crack length is appropriate. For example, Liu et al [*2*] show that for cracking under mixed modes the crack rotates from its initial orientation onto a plane perpendicular to the maximum principal stress as the crack extends. Yet another study shows that the degree of crack closure depends on the inplane nonsingular stress [*3*]. Given these observations, criteria which control multiaxial fatigue would depend at least on the length of the crack. In turn, the initiation and early growth of cracks at notch roots will depend on the local stress state—that is, on the thickness to notch root diameter ratio [*4*].

The purpose of this paper is to explore the growth of cracks from notch roots under various levels of local biaxiality. Results developed from tests of notched plates made of 2024-T351 aluminum, AISI 1080 steel, and SAE 4340 steel are presented and discussed. Crack growth behavior and fractography are presented to illustrate the effects of stress state in terms of linear elastic fracture mechanics (LEFM) analysis. The results are discussed in light of limitations of fracture mechanics and interpreted in regard to observed discrepancies in the LEFM analysis of growth rate behavior from notch roots—one aspect of the so-called short crack effect.

Experimental Aspects

Materials

Tests have been conducted on a range of notched plate geometries made from materials which exhibit cyclic hardening (2024-T351 aluminum), cyclic softening (4340 steel at R_c45), and softening at low strains and hardening at high strains (1080 steel at R_c19).

Typical microstructures in the longitudinal-longitudinal transverse (L-LT) plane for these materials are shown in Fig. 1. The scale of the microstructures indicates the aluminum has the coarsest grain size (ASTM 3.5). The grain size of the 1080 steel (ASTM 6) is somewhat refined from that of the aluminum, while that for the 4340 steel is very much refined as compared to both the aluminum and the 1080 steel (ASTM 12.5). The aluminum is a precipitation-hardened material, the 4340 steel is a martensitic structure, and the 1080 steel is fully pearlitic.

Study of the microstructures indicates that the grains of the aluminum are pancaked due to the heavy rolling of the sheet. Those of the 1080 steel are

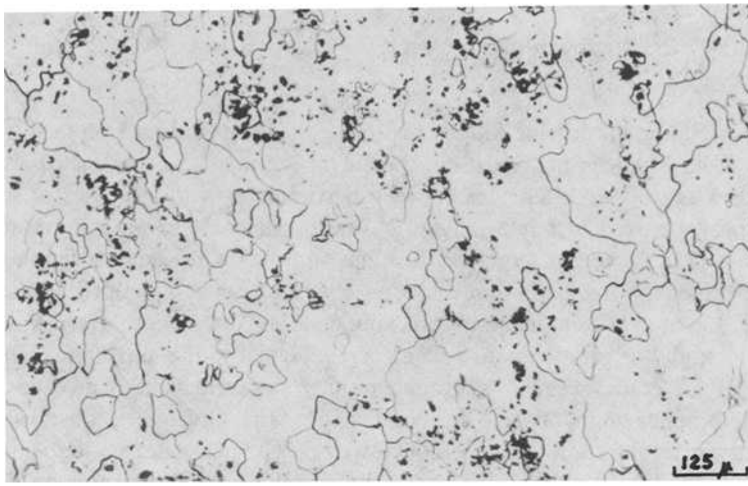

(a)

(b)

(*a*) 2024-T351 aluminum.
(*b*) AISI 1080 steel.
(*c*) SAE 4340 steel.

FIG. 1—*Typical microstructure for materials studied.*

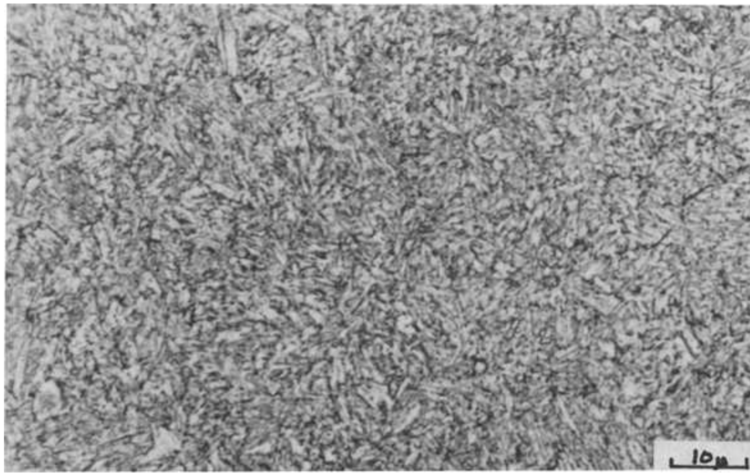

(c)

FIG. 1—*Continued.*

slightly elongated also due to rolling, while those for the 4340 tend to be equiaxed. The aluminum alloy is rather dirty, containing clusters of sometimes large intermetallics. Both steels contain elongated inclusions identified by energy dispersive X-ray analysis as being the manganese sulfide (MnS) variety.

The aluminum alloy 0.2% offset yield strength is 358 MPa with an ultimate strength of 482 MPa. Corresponding data for the 1080 steel are 359 and 820 MPa, while results for the 4340 steel indicated a yield of 1378 MPa and an ultimate of 1426 MPa. The endurance limit stress amplitude for the aluminum alloy is ±172 MPa, while that for the 1080 steel is ±224 MPa, and that for 4340 steel is ±603 MPa, based on $R = S_{mn}/S_{mx} = -1$ cycling. Estimates of the threshold stress intensity based on K increasing near threshold growth rate data from $R = -1$ cycling are $K_{mx} = 5$, 16, and 10 MPa $\sqrt{m}$, for the aluminum alloy, the 1080 steel, and the 4340 steel, respectively.

Specimens

Centrally notched flat plate specimens employed in this investigation embraced thickness, t, to notch root diameter, ϕ, ratios of 0.2 to 2.0 for the 4340 steel, 0.18 to greater than 2.0 for the aluminum alloy, and 0.40 for the 1080 steel. The net section notch acuity is $K_t = 2.50$ for the circularly notched 4340 steel and the 1080 steel specimens. For the 2024 T351 aluminum alloy, net section K_t-values include: 2.56 and, 2.68 for circularly notched plates, and 4.60 and 6.40 for elliptically notched plate specimens.

Three-dimensional analysis (for example, see [*4*]) indicates that, for plates with circular holes, values of t/ϕ equal to 0.2 or less approach the limiting condition of plane stress ($\sigma_z = \sigma_3 = 0$) at the notch root. Values of t/ϕ in excess of 1.5 are therein indicated as approaching the limiting condition of plane strain ($\epsilon_3 = 0$) at the notch root. On this basis, the lower t/ϕ values for the 4340 steel and the aluminum alloy represent plane-stress conditions, whereas the data for $t/\phi \geq 1.5$ reflect plane-strain conditions. Results for the 1080 steel at $t/\phi = 0.40$ and results for similar t/ϕ-values ($0.3 \leq t/\phi \leq 1.0$) for the aluminum alloy and the 4340 steel represent a transition condition beyond plane stress, but well removed from a plane-strain condition. Data generated for the elliptically notched aluminum plates with $K_t = 6.40$ represent a plane-strain condition.

In the case of the 2024 T351 aluminum alloy, data available include: cycles to form a 125-μm-long crack, crack growth measurements for cracks on the order of 125 μm long up to the critical size, and strain measurements throughout the plate. Crack size measurements have been made visually, at up to ×40 magnification, as well as through the use of a photographic technique at ×40 magnification. The same type of data are available for the 1080 steel. However, for this material the crack growth data all have been obtained using a photographic technique at ×40 magnification. Data for the 4340 steel include cycles to form a 125-μm-long crack and crack growth data from cracks of that size up to the critical crack size. Additional details for the aluminum alloy may be found in Refs *5* and *6*, while that for the 1080 steel may be found in Ref *7*.

Results

Metallographic and fractographic results are presented in Figs. 2 through 9. Figures 2 and 3 present data for the aluminum alloy developed under conditions ranging from plane stress to plane strain. Figure 4 characterizes macroscopic deformation patterns anticipated under the limiting conditions of plane stress and plane strain. Figure 5 presents fractographic features that develop with plane stress conditions in 4340 steel, while Fig. 6 contrasts the metallographic aspects of cracking in the aluminum alloy and the 4340 steel. Figure 7 presents typical evidence of multiple initiation and branching that occurs in corner cracking associated with conditions approaching plane stress, while Fig. 8 in contrast to Fig. 7 shows similar results for midthickness cracking for the 1080 steel. Figure 9 further characterizes features of plane-stress corner cracking.

Crack growth data corresponding to the metallographic and fractographic results are shown in Figs. 10 through 12. Crack growth data are presented on length versus cycles coordinates, and as analyzed on growth rate—K_{mx} coordinates. Growth rate is calculated as the slope between two points and reported as a function of the maximum stress intensity factor, K_{mx}, corresponding to the average crack length for a given growth rate. K_{mx} is defined in the usual fashion

$$K_{mx} = F(a/w)\, S_{mx} \sqrt{\pi a} \tag{1}$$

where

S_{mx} = maximum gross section stress in the cycle,
a = surface crack length measured from the notch root,
$F(a/w)$ = a function of the geometry and crack length, and
w = width of the specimen across the crack plane.

Equation 1 is a general description of the crack driving force provided that $F(a/w)$ is known for the crack and specimen/notch geometry. Specific forms of $F(a/w)$ are discussed later.

Discussion

Metallographic and Fractographic Aspects

The fractographs in Figs. 2 and 3 and 5 through 9 present typical views of the crack morphology for the aluminum alloy and the two steels for conditions approaching plane stress ranging up to plane strain. For the plane-stress case, initiation is traced to the corner region while for plane strain initiation typically occurs at (multiple) midthickness sites. Thus, plane-strain cracking in the corner region involves the breakthrough of a long-fronted but shallow crack. Observed trends in the initiation locations follow the behavior predicted based on results of detailed three-dimensional stress analysis in conjunction with an octahedral form of multiaxial equivalence criterion [*4*].

Figures 2 and 3, parts (*a*) and (*b*), show that, for the aluminum alloy and near plane stress conditions, the early crack growth from the corner is on planes other than normal to the free surfaces. At the origin of initiation where the notch field affects the local stress state, cracking involves a mixture of stepped cracking planes and directions and appears to be Mode II and somewhat crystallographic. On the other extreme, Figs. 2*c*, 3*c*, and 3*d* which present typical results for the initiation site and the corner region for cases approaching plane strain, early growth is on a plane normal to the free surface throughout the cracking process, with evidence of striation-like features very near the initiation site.

Differences in morphology in Figs. 2 and 3 may be argued to develop because the surface breaking crack length is comparable to the scale of microstructure. However, these different morphologies develop for comparable physically small cracks in the same microstructure. Evidently microstructural size is not the only factor as the only difference is the local stress state.

At the macromechanics scale, a through thickness macroshear mode of deformation is operative under plane stress while planar macroshear bands develop in plane strain as indicated schematically in Fig. 4. At the microlevel, the 45° slip evident for plane stress in Fig. 4*a* is manifest in the Mode II/III components of corner cracking, because the double free surface of the corner results in easier slip on planes with components of slip normal to the free surfaces. The plane-strain midthickness initiation is observed to produce a Mode I crack whose growth

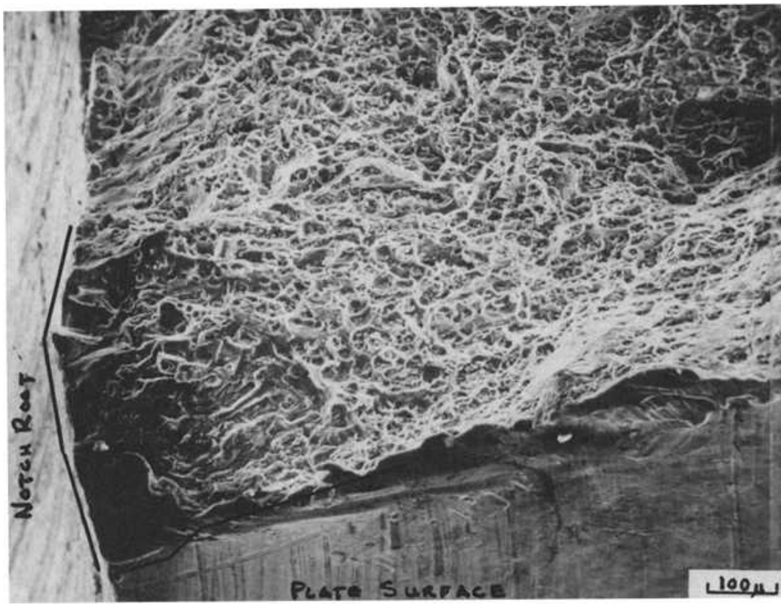

(a)

(b)

(a) Approaching plane stress; $t/\phi = 0.25$, $t = 2.5$ mm, $K_tS_{mx} = 300$ MPa.
(b) Intermediate state; $t/\phi = 1.06$, $t = 2.5$ mm, $K_tS_{mx} = 385$ MPa.
(c) Approaching plane strain; $t/\phi = 2.38$, $t = 2.5$ mm, $K_tS_{mx} = 401$ MPa.

FIG. 2—*Typical character of the fatigue at the notch corner as a function of degree of local biaxiality: 2024 aluminum,* R = *−1.*

(c)

FIG. 2—*Continued.*

is planar, and normal to the single free surface. This behavior is similar to that evident in Fig. 4*b*, with little evidence of Mode II crystallographic cracking. Furthermore, for midthickness initiation, the double-free surface effect of the corner appears to be suppressed by the plane-strain controlled portion of the crack, as the crack breaks the corner. That is, while the crack may be small as seen on the plate's surface it is actually a long crack in that its depth at mid-thickness or length on the opposite surface or both are substantial.

Schijve's work [8] implies that the more stepped crystallographic faces of the plane-stress crack would depress growth rates (perhaps due to ill-defined crack fronts, mixed growth directions, and microcrack closure) as compared to the more planar situation that develops for plane strain. But, the easier slip and larger plastic zone developed in the near notch root plane stress field would enhance growth rates as compared to plane strain. Thus, counteracting mechanics forces are in action in the transition from plane stress to plane strain depicted in Figs. 2 and 3 as the crack grows from the notch-induced local stress state.

The effect of local stress state depends on the material's deformation behavior because the plastic zone size, r_p, depends on the yield stress, σ_y as $r_p \propto \sigma_y^{-2}$. For a given K-level, strong materials would exhibit a smaller zone of plane-stress behavior at the crack tip for the same t/ϕ ratio. As evident in Fig. 5, which presents results corresponding to Fig. 2 for the case of plane stress for the 4340 steel, this trend does indeed develop. For the data considered, r_p for the aluminum alloy is about 15 times that for the 4340 steel. Likewise, for a

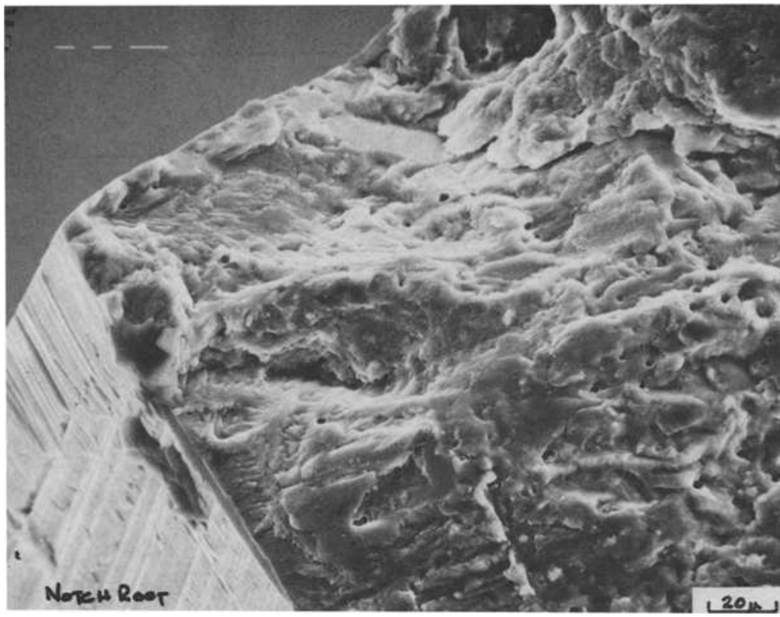

(a)

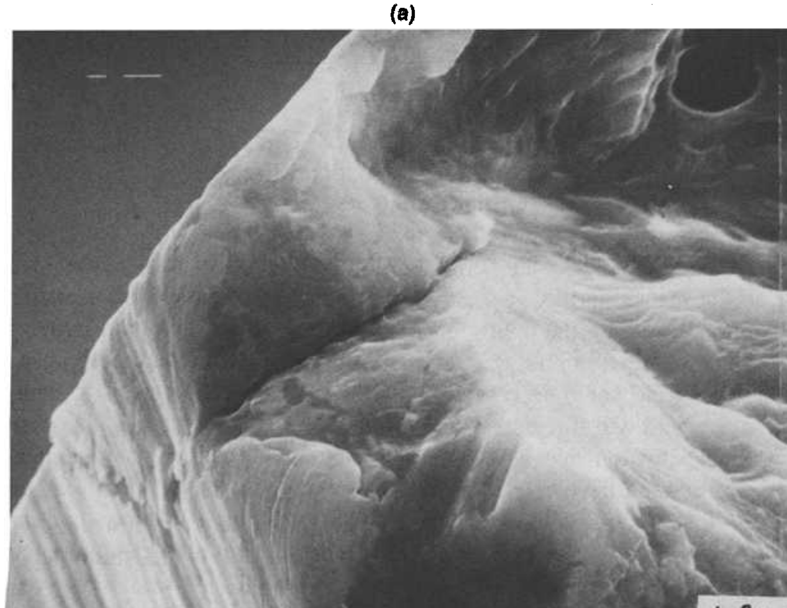

(b)

(a) Notch corner after corner initiation: $t/\phi = 0.18$, $t = 2.25$ mm, $K_tS_{mx} = 444$ MPa.
(b) Notch corner after corner initiation: $t/\phi = 0.18$, $t = 2.25$ mm, $K_tS_{mx} = 444$ MPa.
(c) Midthickness origin of initiation: $t/\phi = 1.06$, $t = 2.5$ mm, $K_tS_{mx} = 385$ MPa.
(d) Corner crack after initiation at midthickness and on opposite face: $t/\phi = 1.06$, $t = 2.5$ mm, $K_tS_{mx} = 385$ MPa.

FIG. 3—*Typical fractographic features at crack origins and notch corners: 2024 aluminum. R = −1.*

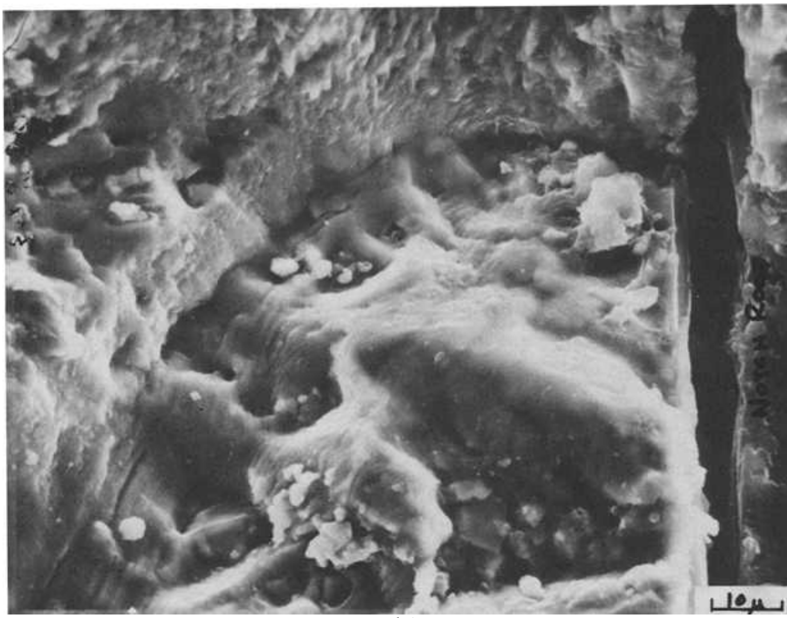

(c)

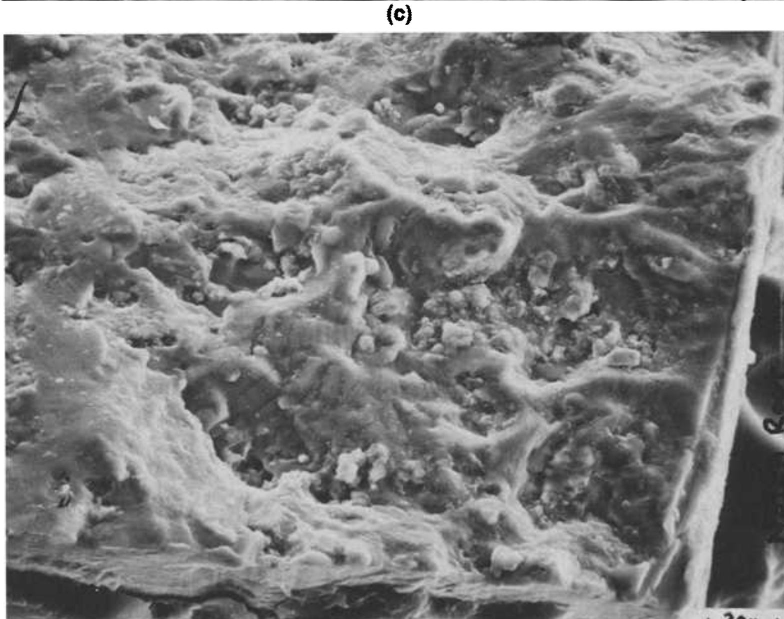

(d)

FIG. 3—*Continued.*

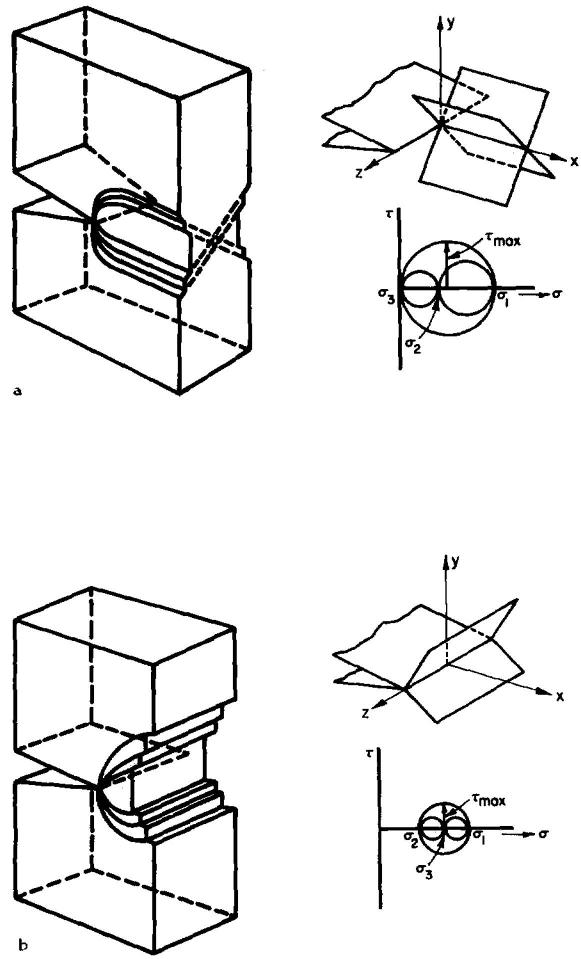

(*a*) Plane stress with shear through the thickness and out of the crack plane.
(*b*) Plane strain with shear across the plate and parallel to the crack plane.

FIG. 4—*Deformation patterns in plane stress and plane strain.*

comparable crack size, a, the ratio of r_p/a is about 15 times greater in the aluminum alloy than in the steel. The absolute $r_p \doteq 150$ μm and $r_p/a \doteq 1$ for the aluminum alloy, whereas for the 4340 steel $r_p \doteq 10$ μm and $r_p/a \doteq 0.07$. For the data examined, r_p is on the order of the grain size for both materials. Consequently, in both materials the microstructural features of the reversed plasticity crack advance process are considered to be similar. Microstructural size, therefore, is not directly a factor in the data being compared. But because the scale of the microstructure is inherently tied to the yield stress, which influences r_p, microstructural scale remains an indirect consideration.

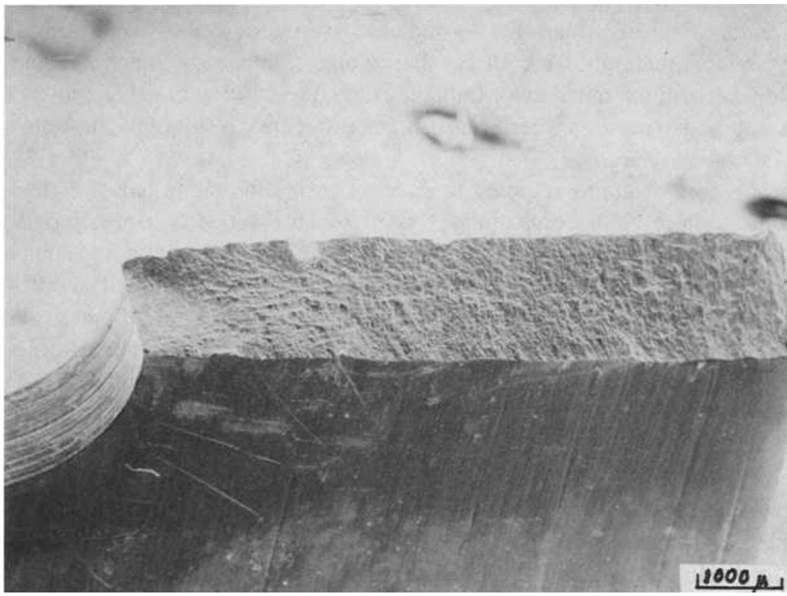

(a)

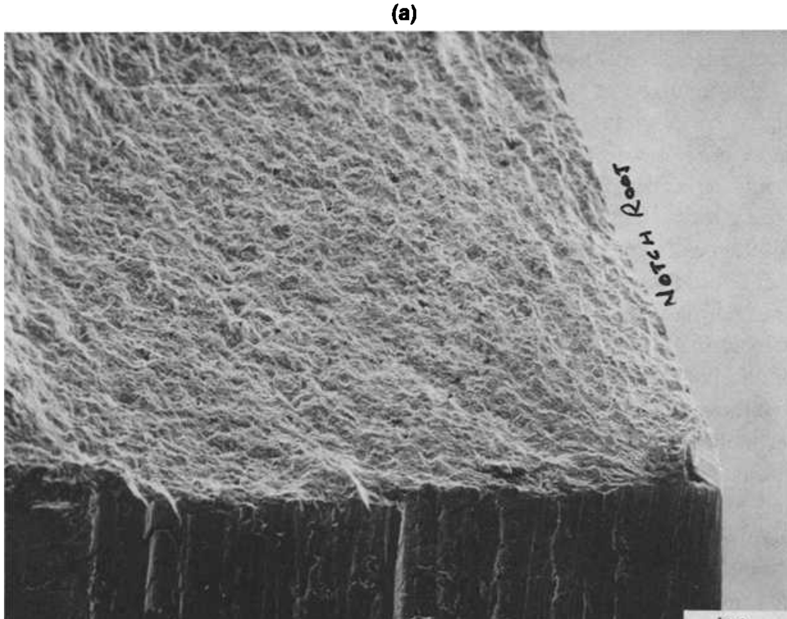

(b)

(*a*) Overview of cracked ligament showing corner thumbnail.
(*b*) Details of notch corner crack region.

FIG. 5—*Fractographic features of notch corner crack initiation typical of SAE 4340 steel:* $R = -1$, $t/\phi = 0.2$, $t = 0.75$ *mm*, $K_tS_{mx} = 969$ *MPa.*

In the case of Figs. 2 and 5, the 4340 results satisfy the confined flow requirement for LEFM, but that for the aluminum alloy does not. More importantly, microstructural size controls the volume (number of grains) needed to develop the continuum behavior implicit in fracture mechanics calculations, and often assumed to develop when comparing fractographic results and crack growth data.

The number of grains required to develop such continuum behavior (homogeneous grain-to-grain compatibility) is reasonably set at 5 to 10, based on matching constitutive behavior [*9*]. On the basis of 5 grains, continuum behavior would develop in the aluminum alloy at a crack length (depth) of about 470 μm. In contrast, continuum behavior develops in the 4340 steel for cracks about 20 μm long (deep). Comparison of early crack growth behavior in the aluminum alloy and the 4340 steel as is done in comparing Figs. 2 and 3 with Fig. 5 thus amounts to comparison of noncontinuum and continuum behavior. Control over continuum versus noncontinuum behavior traces directly to grain-to-grain compatibility, and differences in the absolute crack length to develop a continuum compatibility condition. Differences in fracture morphology evident in Fig. 5 as compared to Figs. 2 and 3 and as well in metallographic sections in Fig. 6, therefore, can be traced directly to differences in the mechanics (compatibility) controlling the cracking process. While microstructural differences have been shown to alter the growth of small cracks (for example, [*10,11*]), such cases involved differences in constraint of crystallographic slip as a function of grain size. Also involved in such data are radical differences in the scale of crack tip plasticity (r_p α yield stress^{-2} for the same K). Therefore, the results in the literature are not conclusive as to the significance of the scale of the microstructure. Further experiments which alter the scale of the structure while holding the strength constant (not too easy) would help clarify this controversial point.

Differences in material deformation response further complicate interpreting differences in the cracking process at a given K-level for notched plates because K is not normalized to the yield stress of the material. Significant differences in the size of the notch field thus can develop at comparable K-levels in different materials. For the aluminum alloy, the bulk of the cracking occurs in the inelastic field of the notch. But for the 4340 steel, virtually none of the cracking develops in the inelastic field (because this field is very small, ≤ 10 μm). Given this situation, K can hardly be expected to provide a unique measure of the crack driving force for the aluminum alloy in the same way it does for the 4340 (or the 1080) steel. Likewise, as noted earlier, continuum fracture mechanics can hardly be expected to characterize the growth of the aluminum alloy at crack lengths much less than about 500 μm. Equal values of K therefore do not infer comparable conditions for cracking in some cases. It is for this reason that measures of the crack driving force should include normalized stress level, as suggested elsewhere [*12*].

Figure 6, which is a polished section 10 to 15 μm below the surface, indicates only a limited interaction of cracks with the microstructure. It also indicates the

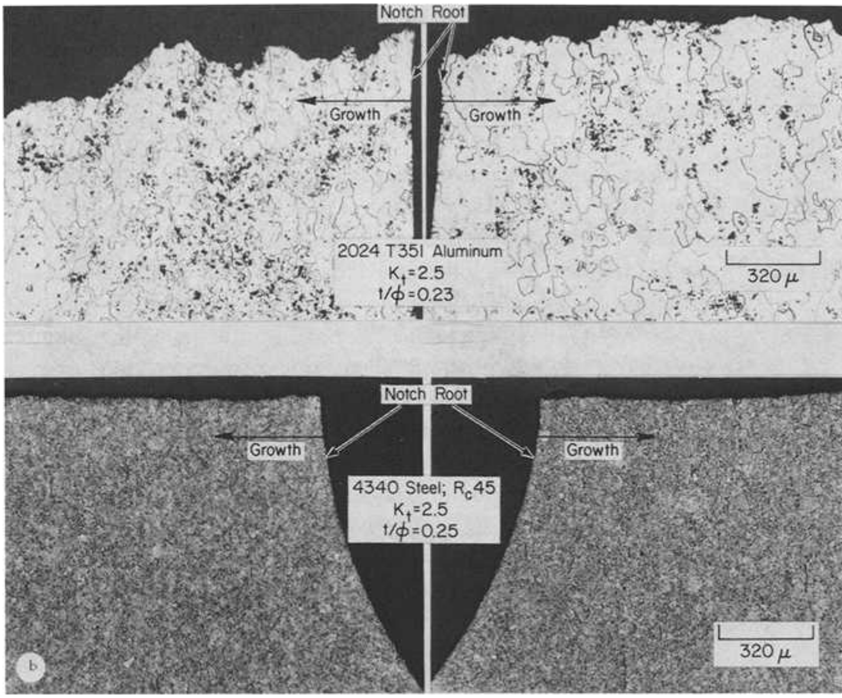

FIG. 6—*Typical metallographic aspects of the cracking of 2024 aluminum and SAE 4340 steel:* R = -1; K_tS_{mx} = *320 and 960 MPa, respectively.*

presence of a dominant crack and thus suggests that a single crack initiates and grows. In the case of the 4340 steel, the microstructural features are very refined so that, in the absence of inclusion stringers, limited interaction is expected. More importantly, significant interaction between the microstructure and the fatigue process is most probable for cracks whose size is on the order of the microstructure. In the case of the 4340 steel, this suggests interactions would not be evident at crack lengths (depths) greater than 20 μm, but are most likely at lengths on the order of the grain size—or about 4 μm. Cracks of this size are below the observation threshold of most laboratories and as such go undetected even if they occur. The absence of obvious interaction in the steel thus is not surprising. For the case of the aluminum, observations of crack interaction with the microstructure at initiation and during microcrack growth are expected given the larger grain size and presence of intermetallics. However, demonstrating such interaction is not easy without doing serial sections. The absence of interaction, therefore, should not be taken to infer that interaction does not occur.

Regarding the formation of a dominant crack, metallographic studies indicate the presence of multiple corner crack initiation at a notch root in the near plane-stress aluminum specimens tested at intermediate and high stress, as shown for example in Fig. 7. Data for $t/\phi > 0.25$ did not exhibit such behavior. Frac-

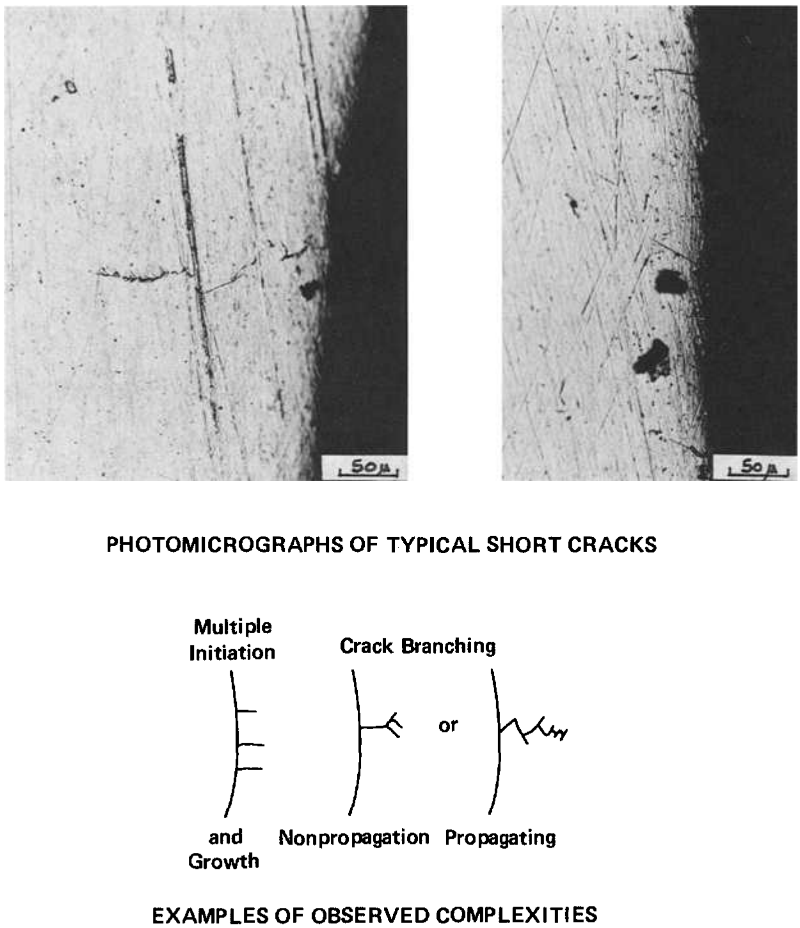

FIG. 7—*Multiple corner cracking and branching typical of 2024 aluminum approaching plane stress:* $R = -1$, $K_tS_{mx} = 300$ *MPa,* $t/\phi = 0.18$ ($t = 2.25$ *mm) and* 0.25 ($t = 2.5$ *mm).*

tography of the 1080 steel ($t/\phi = 0.40$) indicated both corner and midthickness cracking, with a trend toward multiple midthickness cracking resulting in early plane fronted cracks. Typical of this behavior are the results presented in Fig. 8. Observations of cracking in the 4340 steel failed to indicate multiple cracking, regardless of the value of t/ϕ, over the range of stresses explored. But, the small grain size of the 4340 steel virtually precludes casual observation of multiple cracking, and makes it difficult to observe such even at high magnifications. Thus the absence of multiple cracks in the 4340 steel does not preclude their occurrence.

Photographic tracking suggests that crack initiation in the aluminum alloy is associated with a burst of growth. When multiple initiation is observed, the first to initiate cracks are contained within a grain. The initial burst appears to be either blunted by extensive plasticity at the crack tip or constrained by grain boundaries which retard crystallographic Mode I/Mode II growth. In cases checked, fractographic and metallographic examination indicates cracking bursts at initiation tend to be feature free, reminiscent of crystallographic cracking. Successive cracking bursts occur along the corner in the vicinity of the transverse net section, typically with a length greater than the preceding cracks. Finally, one of the bursts attains a length which either is not blunted because the extensive cracking has increased the local compliance or the crack has sufficient driving force to pass through the containing effect of the grain boundary or both. In any event, the behavior is consistent with the observation of Seika et al [*13*] that a minimum size region (volume) of slip must develop before propagation could continue.

Sequential metallographic examination indicates that corner cracks remain open so long as they are crystallographic, as shown for example in Fig. 9. In such cases the effective value of ΔK is larger than for their closed pure Mode I counterparts, suggesting higher initial growth rates would develop. Given the fact that ΔK_{eff} is decreasing with increased crack length, this decreasing ΔK_{eff} coupled with the constraint of Mode II by grain boundaries serves to explain the dormancy of the first to initiate cracks in this study. It may be also invoked to explain the phenomenon of nonpropagating cracks [*14*], although this requires further study before it can be demonstrated conclusively.

Multiple initiation also has implications related to the mechanics controlling initiation and microcrack growth. First, if an inelastic notch field develops, the behavior within that enclave is largely displacement controlled and not adequately characterized by K [*15,16*]. Second, the value of K calculated in the presence of multiple unconnected cracks overestimates the driving force if a single crack is assumed to exist. But, in cases where cracks linkup as shown for example in Fig. 3*b*, the joining of cracks (particularly if they are midthickness cracks) may serve to elevate the driving force by developing a single ''plane fronted'' crack. Even in the presence of these complications, K remains the popular measure of the crack driving force.

Crack Growth Behavior

Figure 10 (supported by data presented elsewhere [5]) presents crack growth as a function of cycles for the aluminum alloy for fully reversed as well as zero tension cycling for a range of stress levels. Figure 10*a* presents results for low stress for a high notch acuity which leads to very limited notch plasticity with a plane-strain initiation. The growth trend evident is typical of the usual ''long crack'' Mode I growth in the compact tension (CT) or center-cracked panels (CCP) studied extensively in the literature. Figures 10*b* and *c* present results for two other combinations of t/ϕ and stress level for the aluminum alloy.

Figure 10*b* characterizes the case of high-stress with plane-stress corner crack

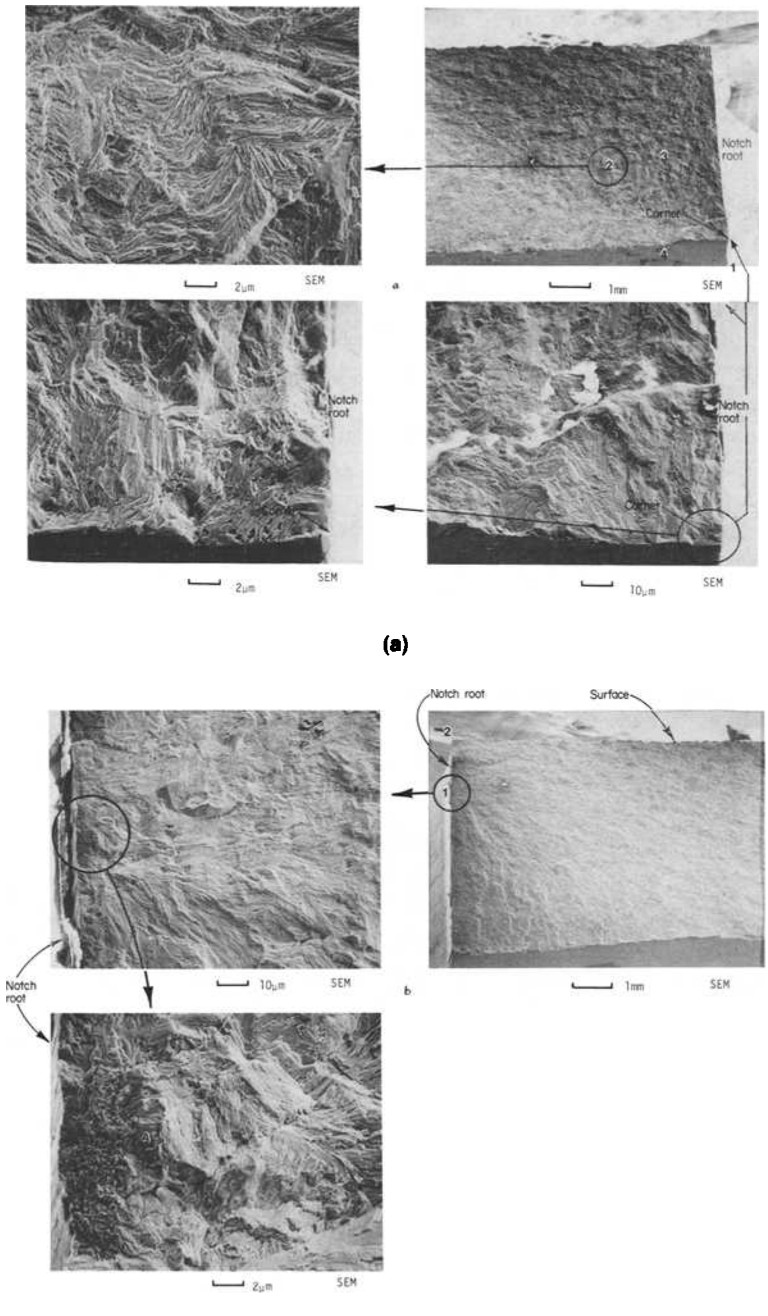

(*a*) For corner initiation, K_tS_{mx} = 830 MPa.
(*b*) For midthickness initiation, K_tS_{mx} = 723 MPa.

FIG. 8—*Typical fractographic features of corner and midthickness cracking in AISI 1080 steel:* R = -1, t/ϕ = *0.4*, t = *5 mm.*

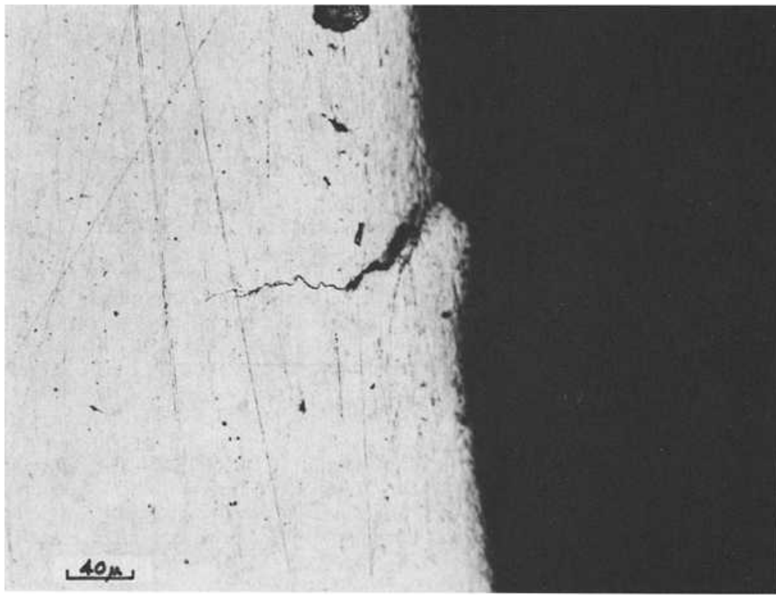

FIG. 9—*Plane-stress initiation indicates Mode II/Mode I cracking which changes to Mode I as the crack grows: note that the shear portion of the crack is not closed;* R = *−1,* t/ϕ = *0.18,* t = *2.25 mm,* K_tS_{mx} = *440 MPa.*

initiation. The initial cracking occurs in the inelastic field of the notch for which early growth is combined Mode II/Mode I cracking, followed by a transition to Mode I growth. Instead of the gradually increasing *a-N* trend evident in Fig. 10*a*, Fig. 10*b* shows an initially steeper slope after which the usual *a-N* trend develops. Back extrapolation of the *a-N* trend to zero length in Fig. 10*b* indicates that a finite crack developed at about 1500 cycles, whereas separation occurs at about 2200 cycles. In contrast, such back extrapolation in Fig. 10*a* could be traced to near zero cycles for zero crack length, with separation occurring near 225 000 cycles.

Results for the case of an intermediate stress level under zero tension cycling with plane-stress corner crack initiation are presented in Fig. 10*c*. In contrast to parts (*a*) and (*b*) of Fig. 10, which present averaged trends for all four notch roots, this figure presents trends for each initiated surface crack. The first to initiate crack, denoted *A*, indicates a steeper initial slope, particularly if the growth trend is back extrapolated to the life at which the detection threshold crack size could not be observed.[3] Thereafter, two steps are apparent in the *a-N* trend for the first to initiate crack as this crack grows through the thickness. Asymmetric extension of this through thickness crack further concentrates strain

[3]The threshold for reliable optical detection for these data (×40 magnification) is on the order of 10 to 20 μm.

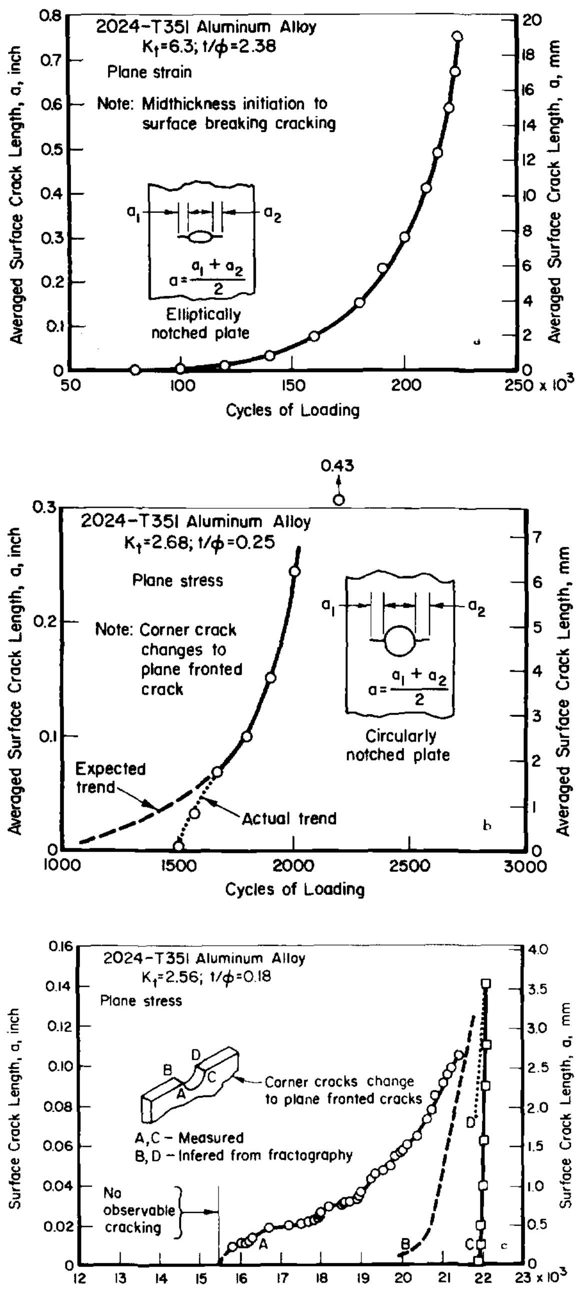

(*a*) Midthickness initiation: $R = -1$, $t/\phi = 2.38$, $t = 2.5$ mm, $K_tS_{mx} = 454$ MPa.
(*b*) Corner initiation: $R = -1$, $t/\phi = 0.25$, $t = 2.5$ mm, $K_tS_{mx} = 670$ MPa.
(*c*) Corner initiation: $R = 0.01$, $t/\phi = 0.08$, $t = 2.25$ mm, $K_tS_{mx} = 630$ MPa.

FIG. 10—*Crack length versus cycles behavior for 2024 aluminum.*

at the second notch root, prompting initiation of a second corner crack. Observe that when the second to initiate corner crack, denoted *D*, breaks through the surface after growing through the thickness, denoted as crack *C*, it appears to grow very rapidly. However, this apparently high growth rate correlates with so-called long crack behavior when analyzed in terms of LEFM. If this trend is averaged with that for crack *A*, the initially high growth rate and the steps evident in the *a-N* trend for crack *A* would smooth somewhat. This averaging tends to smooth discontinuities, but it is unlikely that averaging accounts for continuous growth rate trends, such as evident for example in Fig. 10*a*.

The process of crack initiation and microcrack growth for plane-stress corner cracking may be complicated by crack interaction through the formation of multiple corner cracks [*5*]. Data in Ref *5* indicate early initiation and dormancy of cracks which form on opposite faces of the notch root, whereafter new cracks initiate and grow to failure. Reference *5* also reports data which show early growth at rates in excess of subsequent behavior that cannot be simply correlated by LEFM. Additional results for this material detailed in Ref *5* clearly illustrate (1) interaction between cracks located on the same face of one notch root, (2) steps in crack growth, and (3) the initially rapid growth as cracks break the corner after traversing the thickness of the specimen. Similar trends are evident in earlier reported data for similar plane-stress initiation and microcrack growth in this material [*17*], but the implications went unexplored.

Crack growth versus cycles behavior for the 1080 steel are shown in Fig. 11*a* and *b*. Results for the 1080 steel show many of the trends evident in the results for the aluminum alloy. In other ways, data for the 1080 steel differ from that for the aluminum alloy because corner cracking is not the dominant site of initiation for $t/\phi = 0.40$. Instead, initiation is expected to occur more or less equally across the thickness of the notch root [*4*], a tendency supported by fractography (compare Fig. 8). Also the 1080 steel contained large inclusions which often clustered in stringers along the rolling direction. The 1080 steel also contained a pearlitic phase which if suitably oriented could initiate early (multiple) cracks or result in high initial growth rates or cause step increases in growth rate even for long cracks or all three.

Figure 11*a* presents *a-N* results for multiple midthickness and near corner initiations leading to an essentially plane-fronted crack for the 1080 steel when tested at a low stress level. This trend is similar to that for long cracks developed in compact tension geometries and for the plane-strain initiated cracks in the aluminum alloy (Fig. 10*a*). However, the curves tend to be somewhat stepped particularly at longer crack lengths. The steps in one curve tend to parallel those for the second crack, perhaps because rapid advances at one tip increase the stress intensity at the second tip [*18*] thereby increasing the growth rate. Fractography indicates macroscopic bands of mixed planar (interlamellar delamination-cleavage)/striation formation growth mechanism at crack lengths corresponding to these steps. While it is not clear what triggers these steps, this material contains large clusters of brittle inclusions and a lamellar (pearlitic) structure which periodically may be oriented favorably along a major segment of the crack front

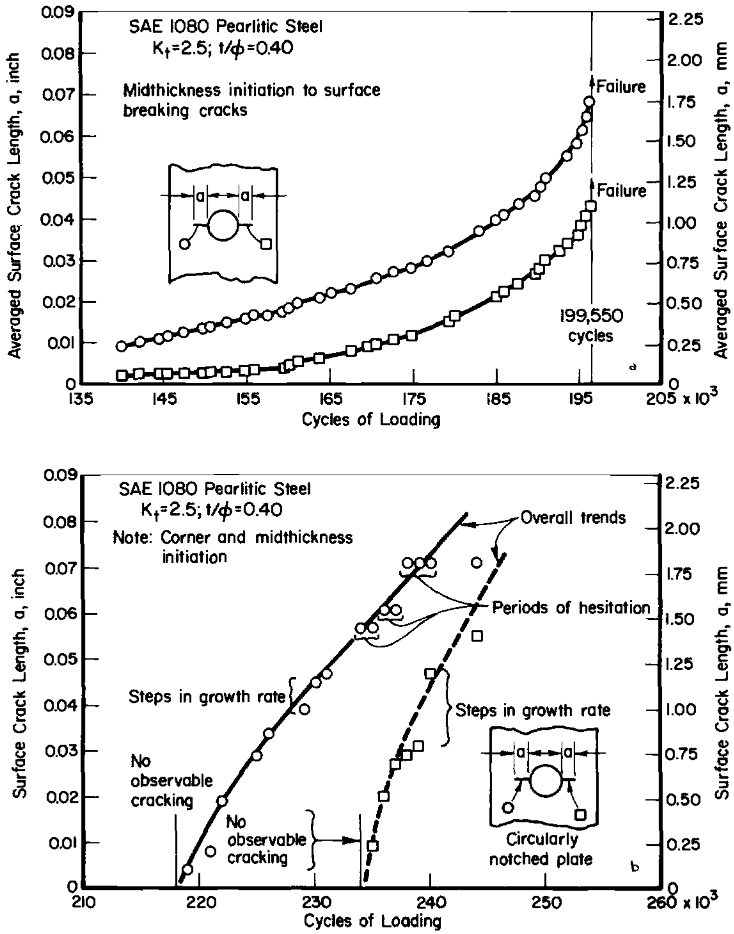

(*a*) Midthickness initiation: $R = -1$, $t/\phi = 0.40$, $t = 5$ mm, $K_tS_{mx} = 440$ MPa.
(*b*) Corner and midthickness initiation at low stress: $R = -1$, $t/\phi = 0.40$, $t = 5$ mm, $K_tS_{mx} = 465$ MPa.

FIG. 11—*Crack length versus cycles behavior for SAE 1080 steel.*

and develop a very sharp tip activating cleavage or interlamellar cracking or both. Thus, even for longer cracks, this material can be expected to exhibit discontinuous growth related to the microstructure.

Figure 11*b* presents typical crack growth behavior for corner cracks that developed under conditions comparable to that for the results shown in Fig. 11*a*. Observe that the growth rate, from the threshold for detection and for several readings beyond, shows a trend to decreasing rates as the crack extends. In this respect, Fig. 11*b* shows trends associated with so-called short cracks. As with Fig. 11*a*, significant rate steps are apparent, as are periods of hesitation. Examination of the fractography for short cracks presented in Fig. 8 suggests these steps may be associated with microstructural features such as favorably oriented lamellar fields and inclusions, in addition to the influence of the doubly free surface at the corner. However, because the conditions (geometry, loading) which produced these data also produced the "long" crack trend of Fig. 11*a*, one could conclude that the double-free surface of corner cracks enhances the affect of the microstructure. Indeed, the only difference between the "long" and "short" cracks of Fig. 11*a* and *b* is the location of the initiation that produces either "plane-fronted" or "corner crack" growth. The $t/\phi = 0.40$ condition resides between the limits for plane stress and plane strain. The balance between mechanics parameters that control the location of initiation is tipped to either corner or corner/multiple midthickness or multiple midthickness initiation by microstructure. Thus, microstructure may be argued to control whether the behavior of Fig. 11*a* or 11*b* develops. Data developed at high stresses indicated the significant influence of the double-free surface through the formation of multiple corner initiations similar to that observed and discussed for the aluminum alloy. In the case of the 1080 steel, the initial high growth rates are no doubt influenced by brittle-like delamination in favorably oriented lamellar regions, an inference supported by fractography (compare Fig. 8).

Results generated for the 4340 steel tested at an intermediate stress level for both fully reversed and zero tension cycling also show the significant influence of corner crack free surface effects. The trend for surface corner crack initiation was similar to that illustrated for a surface crack initiation for the aluminum alloy and the 1080 steel. Initially high growth rates were observed for corner cracks as large as about 150 μm long. This length is substantially greater than any of the microstructural features of this material. Again, as with the aluminum alloy, plane-stress and plane-strain initiated microcracks develop in the same microstructure, yet show radically different behavior related to the longer surface breaking midthickness initiated cracks and the shorter corner initiated cracks.

The crack length versus cycles data presented indicate that corner crack initiation is common for plane-stress conditions and that midthickness cracking is anticipated under plane-strain conditions. Midthickness initiation tends to be associated with near plane-fronted cracks, particularly in multiple initiation cases, and so justifies the use of a surface crack measurement in conjunction with a one-dimensional characterization of the crack. Corner cracking, however, often leads to a two-dimensional crack for which one-dimensional analysis may be questionable.

Study of K-solutions for corner cracks at circular notches [*18–22*] indicates that values of K do not differ significantly for small normalized surface crack lengths, a/ϕ. For example, for a/ϕ less than about 0.6, $F(a/w)$ in Eq 1 is essentially independent of crack length for surface-to-thickness crack aspect ratios, a/c, of 1 [*20*], a value which is typical of short corner cracks. However, as the crack approaches break through, K increases toward the through crack limit. For $a/c > 1$, K is observed to depend strongly on a/ϕ [*20*]. Analyses [*18*] also show that asymmetric growth does not influence K much for cracks whose length is small compared to the notch radius. Experimental results [5,17] indicate that the driving force for physically small corner cracks is reasonably described by only one dimension (surface length). In one experimental study, symmetric corner cracking occurred with some intermittent midthickness cracking [5], and corner cracks quickly changed to near plane-fronted cracks. Analysis based on Ref *20* indicated less than 10% average influence on K due to the two-dimensional effect during the transition period.

Fractography in the present study is consistent with trends anticipated based on existing K-solutions. Corner cracks quickly changed to near plane-fronted geometries, whereas midthickness cracks were nearly plane fronted by the time they broke the surface of the plate. Based on the analysis reported in Ref *20*, errors in K averaged over the transition period are less than 10%. This means that simpler forms of $F(a/w)$ can be used to analyze the data for this study. It does not mean that such simpler forms of $F(a/w)$ which do not embody crack aspect ratio can be used in general.

Crack growth rate data for the aluminum alloy, the 1080 steel, and the 4340 steel are reported as a function of K_{mx} in an extended version of this paper available as a Battelle report [24]. Suffice it here to discuss results for the 1080 steel which reflects the influence of local stress state on early crack growth for corner (plane-stress) and midthickness (plane-strain) initiation.

Figure 12 presents results for the case of fully reversed cycling at a high stress level for the intermediate stress state $t/\phi = 0.40$. Both corner and midthickness cracking occurred. The figure shows an initial decrease in rate, followed by an increase to a plateau, and then a decrease to the long crack (plane-strain) trend. This trend is consistently observed for tests at high stress in this material and is similar to other results developed at high stresses [6]. Clearly such decreases and increases in the growth rate for this material could be argued as to random microstructural effects on cracking. However, the pattern is repeated for a given specimen as well as across the range of specimens tested and as such is not a random microstructural effect.

The initial growth behavior for corner cracks shown in Fig. 12 combines the effect of the double-free surface at the corners, with the effects of increased closure as the crack extends (compare Fig. 9) and an ill-defined discontinuous crack front. The balance between these effects may be controlled by grain boundaries in that the initial period of declining rates occurs for crack lengths on the order of the average grain size. Beyond the initial grain boundary, local closure coupled with a decreasing stress gradient and an increasing $\sqrt{a}$ contribution to the stress intensity control the crack driving force.

For Fig. 12, all of the anomalous growth takes place within the inelastic field of the notch. Analysis reported elsewhere accounts for the coupled effect of closure and local displacement control that develops because of the inelastic action of the notch [16]. That analysis indicates that the driving force for the crack increases to a plateau then decreases and eventually matches the long crack behavior at the inelastic-elastic boundary of the notch field. This trend matches

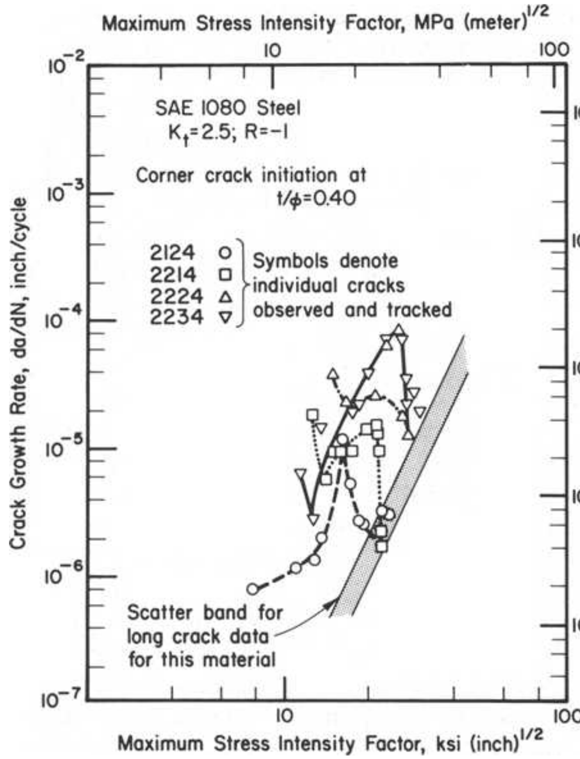

FIG. 12—*Typical crack growth versus* K_{mx} *behavior for the AISI 1080 steel:* R = −*1*, t/ϕ = *0.40*, t = *5 mm*, K_tS_{mx} = *828 Mpa*.

the trend of Fig. 12 suggesting that growth is controlled by closure and the inelastic action at the root beyond the first (few) grains. Microstructure is not a factor of consequence except for the effects of grain boundaries on short cracks because the plane-strain midthickness data lie in the scatterband noted here as "long crack" trend.

Summary and Conclusions

This paper has examined the nucleation and microcrack growth behavior of notched aluminum and steel specimens, to establish the effect of local stress state and assess to what extent local stress state leads to a short crack effect. For plane strain, midthickness initiation dominated cracking behavior. Corner breaking cracks growing from (multiple) midthickness initiation when tracked on the surface developed a smooth increasing trend on *a-N* coordinates for the aluminum alloy and the 4340 steel. Likewise, corner breaking physically small cracks developed from midthickness plane-strain initiation at low stresses in the aluminum alloy and at intermediate stresses for the 4340 steel showed *da*/*dN*-

K_{mx} trends comparable to that for the macrocrack results. However, cracking in the 1080 steel showed growth steps that may be associated with combined cleavage/interlamellar delamination and striation mechanisms, as compared to the lower growth rate reference long crack condition involving a striation forming mechanism. Macrocracks beyond the inelastic notch field showed a correlation in terms of linear elastic fracture mechanics for the materials and geometries studied. Corner crack initiation under plane-stress conditions consistently showed higher initial growth rates which could not be explained by the weak dependence of the stress intensity factor on crack aspect ratio for very short cracks. Occasionally, plane-strain initiated midthickness cracks showed initially high growth rates when these long nearly planar-fronted cracks broke through the remaining corner ligament.

The *a-N* results and fractography presented suggest that linear elastic fracture mechanics analyses do not adequately portray the driving force for cracking when plane-stress initiation and crystallographic Mode II/Mode I growth occurs. This is not the fault of LEFM. Rather this situation arises because (1) the continuum assumed in fracture mechanics analysis does not exist for cracks less than a few grains long or (2) the LEFM requirement of confined crack tip plasticity is violated, or (3) inelastic action in the notch field not handled by LEFM develops or all three. However to overcome these problems requires nonlinear analysis to make deterministic estimates of the crack driving force. Such detailed analyses still ignores the probabilistic aspects of grain orientation that would influence microcrack growth when noncontinuum behavior controls the tracking process.

The results of this study lead to a number of significant conclusions, including:

1. Local stress state has a significant influence on the crack initiation and microcrack growth behavior at notches, apparently because of its effect on the mode of growth.
2. Observations of nonconsolidated growth rate behavior of microcracks at notches (and in unnotched specimens), often referred to as a short crack effect, can be explained in part in terms of differences in the stress states controlling physically long and short cracks.
3. Microstructural effects appear to be confined to one grain diameter and associated with the constraint of the grain boundary to slip.

Acknowledgments

Preparation of this paper has been supported in part by the Mechanics Section of Battelle's Columbus Laboratories.

References

[1] Krempl, E., *The Influence of State of Stress on Low-Cycle Fatigue of Structural Materials, ASTM STP 549*, American Society for Testing and Materials, Philadelphia, 1974.

[2] Liu, A. F. and Dittmer, D. F., *Effect of Multiaxial Loading on Crack Growth*, Northrop Corporation Report to the Air Force Flight Dynamics Laboratory AFFDL-TR-78-175, Dec. 1978.
[3] Hoshide, T. et al, *Fatigue of Engineering Materials and Structures*, Vol. 2, 1979, pp. 181–194.
[4] Leis, B. N. and Topper, T. H., *Journal of Engineering Materials and Technology*, Transactions, American Society of Mechanical Engineers, Vol. 99, No. 3, July 1977, pp. 215–221.
[5] Leis, B. N. and Galliher, R. D. in *Low Cycle Fatigue and Life Prediction, ASTM STP 770*, American Society for Testing and Materials, 1982, pp. 399–421.
[6] Leis, B. N. and Forte, T. P. in *Fracture Mechanics, 13th Symposium, ASTM STP 743*, American Society for Testing and Materials, Philadelphia, 1982, pp. 100–124.
[7] Leis, B. N., in *Fracture Mechanics, 15th Symposium, ASTM STP 833*, American Society for Testing and Materials, Philadelphia, 1984, pp. 449–473.
[8] Schijve, J., *Engineering Fracture Mechanics*, Vol. 14, 1981, pp. 467–475.
[9] McGregor-Tegart, W. J., *Elements of Mechanical Metallurgy*, MacMillan, New York, 1967, pp. 154–174.
[10] Morris, W. L., *Metallurgical Transactions*, Vol. 11A, July 1980, pp. 1117–1123.
[11] Taylor, D. and Knott, J. F., *Fatigue of Engineering Materials and Structures*, Vol. 4, 1981, pp. 147–155.
[12] Ahmad, J., Leis, B. N., and Kanninen, M. F., "Analysis of Fatigue Crack Propagation Under Biaxial Loading Using an Inclined Strip Yield Representation of Crack Tip Plasticity," *Fatigue of Engineering Materials and Structures*, to appear.
[13] Seika, M., Kitaoka, S., and Ko, H., "Change of Material Properties at the Tips of Fatigue Cracks Subjected to Macroscopic Tensile and Shear Stresses for Propagation (in Rotary Bending and Cyclic Torsion)," *Bulletin of the JSME*, Vol. 19, Oct. 1976.
[14] Frost, N. E., "Notch Effects and the Critical Alternating Stress Required to Propagate a Crack in an Aluminum Alloy Subject to Fatigue Loading," *Journal Mechanical Engineering Science*, Vol. 2, 1960.
[15] Leis, B. N., *International Journal of Pressure Vessels and Piping*, Vol. 10, 1982, pp. 141–158.
[16] Leis, B. N., "Displacement Controlled Fatigue Crack Growth in Elastic-Plastic Notch Fields and the Short Crack Effect," *Engineering Fracture Mechanics*, Vol. 21, 1985.
[17] Sova, J. A., Crews, J. H., Jr., and Exton, R. J., "Fatigue Crack Initiation and Growth in Notched 2024-T3 Specimens Monitored by a Video Tape System," NASA Technical Note No. D-8224, Aug. 1976.
[18] Tada, H., Paris, P. C., and Irwin, G. R., *The Stress Analysis of Cracks Handbook*, Del Research Corp., Hellertown, PA, revised, 1977.
[19] Hall, L. R. and Finger, R. W., in *Proceedings*, Air Force Conference on Fatigue and Fracture of Aircraft Structures and Materials, H. A. Wood, R. M. Bader, W. J. Trapp, R. F. Hoener, and R. C. Donat, eds., AFFDL-TR-70-144, U.S. Air Force, Dec. 1970, pp. 235–262. (Available from DDC as AD 719–756).
[20] Newman, J. C., Jr., "Predicting Failure of Specimens with Either Surface Cracks or Corner Cracks at Holes," NASA TN D-8244, National Aeronautics and Space Administration, Washington, DC, 1976.
[21] Shah, R. C. in *Mechanics of Crack Growth, ASTM STP 590*, American Society for Testing and Materials, Philadelphia, 1976, pp. 429–459.
[22] Smith, S. H., "Fatigue-Crack Growth Behavior of C-5A Wing Control Points," ASD-TR-74-18, U.S. Air Force, May 1974. (Available from DDC as AD-A002 553.)
[23] Leis, B. N., Ahmad, J., and Kanninen, M. F., "Local Stress State and the Short Crack Effect," International Battelle Report, available by written request.

Trevor C. Lindley[1] *and Kevin J. Nix*[1]

The Role of Fretting in the Initiation and Early Growth of Fatigue Cracks in Turbo-Generator Materials

REFERENCE: Lindley, T. C. and Nix, K. J., "**The Role of Fretting in the Initiation and Early Growth of Fatigue Cracks in Turbo-Generator Materials,**" *Multiaxial Fatigue, ASTM STP 853*, K. J. Miller and M. W. Brown, Eds., American Society for Testing and Materials, Philadelphia, 1985, pp. 340–360

ABSTRACT: The reduction in fatigue strength due to fretting has been measured for various combinations of materials used for components in turbo generators. With the range of pad contact pressures and pad spans employed, fretting fatigue strength reduction factors of up to 3.5 were found for 3.5Ni-Cr-Mo-V ferritic steel, 2.5 for 18Mn-4Cr, and 18Mn-18Cr austenitic steels and 11 for 2014A aluminum alloy. Metallography and strain gage methods (to monitor frictional forces) revealed that small cracks could develop by fretting early in fatigue life, and a fracture mechanics approach is developed to describe crack growth.

KEY WORDS: fretting fatigue, turbo-generator materials, fatigue strength reduction, frictional forces, fracture mechanics, growth of short cracks

Fretting is the oscillatory sliding motion between two contacting surfaces and can occur as fretting wear or fretting fatigue. Fretting is promoted by high-frequency, low-amplitude vibratory motion and commonly occurs in clamped joints and "shrunk-on" components.

In the present study, the various important fretting variables which may adversely affect fatigue performance were established by generating *S-N* curves, with and without fretting, for various combinations of contacting materials. Metallographic and strain-gage techniques were used to follow crack development.

Experimental Procedure

Fatigue specimens of the type shown in Fig. 1*a* were machined from material released from (*a*) a 3.5Ni-Cr-Mo-V steel generator rotor, (*b*) an 18Mn-4Cr austenitic end ring steel, and (*c*) an 18Mn-18Cr austenitic end ring steel. Flats

[1]Research officers, Technology Planning and Research Division, Central Electricity Generating Board, Central Electricity Research Laboratories, Materials Branch, Leatherhead, Surrey, U.K.

Copyright© 1985 by ASTM International www.astm.org

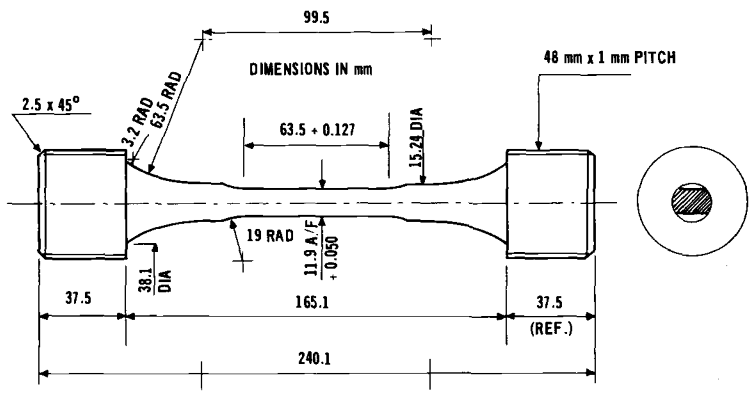

FIG. 1*a*—*Fatigue specimen.*

had been machined on opposite sides of the specimen gage length. These flats were polished down to 600 grade silicon carbide (SiC) and degreased. Flat plate specimens of a similar gage section pattern to that shown in Fig. 1*a* were machined from 2014A aluminum alloy. All specimens were machined such that their axial orientations were coincident with the rotor axis.

Bridge type contact pads (Fig. 1*b*) having a span of 24.1 mm and narrow, rectangular feet were machined from either 1Cr-Mo steel or 3.5Ni-Cr-Mo-V steel. The pad contact feet were also polished down to 600 grade SiC and degreased. The chemical compositions and mechanical properties of the various fatigue specimen and contact pad materials are given in Tables 1 and 2.

Two distinct test methods were used to achieve the controlled fretting between two contacting surfaces. In the present research program, earlier experiments involved the traditional route of clamping contact pads against the flats of a

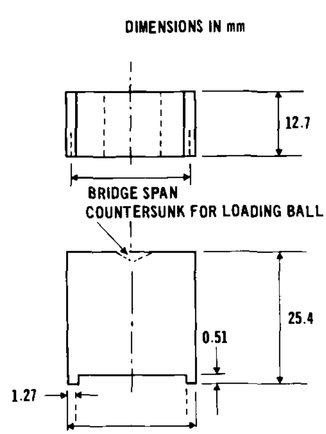

FIG. 1*b*—*Bridge type contact pad.*

TABLE 1—*Chemical composition of the fatigue specimen and contact pad materials.*

Material	C	Si	Mn	S	P	Ni	Cr	Mo	V	Fe	Cu	Mg
3.5Ni-Cr-Mo-V	0.21	0.25	0.30	0.006	0.010	3.43	1.57	0.41	0.12			
1Cr-Mo	0.42	0.30	0.59	0.022	0.030	0.29	1.42	0.75	...			
18Mn-4Cr	0.48	0.44	18.50	...	...	0.12	5.38	...	...			
18Mn-18Cr	0.086	0.26	19.03	0.002	0.040	...	19.0	...	...			
2014A	...	0.5	0.5	...	...					0.2	5.0	0.4

TABLE 2—*Mechanical properties at room temperature of the various materials.*

Material	0.2% Proof	Tensile Strength, MPa	Elongation, %	Reduction in Area, %	Hardness, VPN
3.5Ni-Cr-MoV	600	733	25	70	222
1Cr-Mo	841	999	21	59	340
18Mn-4Cr	1000	1180	29	42	429
18Mn-18Cr	1000	1050	29	68	359
2014A (Longitudinal orientation)	458	504	9.8		155

fatigue specimen using a load calibrated steel proving ring (Fig. 2). More recently, a second more sophisticated method has been used which allows for improved control of the "slip" displacement during the complete test duration and allows easy test interruption for periodic inspection of accumulated fretting damage, by using a biaxial test rig with two pairs of actuators on horizontal and vertical axes. The clamping load was transmitted via steel ball bearings to give the desired contact pressure. With the proving ring assembly, fatigue tests were carried out in an Amsler Vibrophore machine typically resonating at about 150 Hz. The servohydraulic biaxial test rig was usually cycled at 90 Hz.

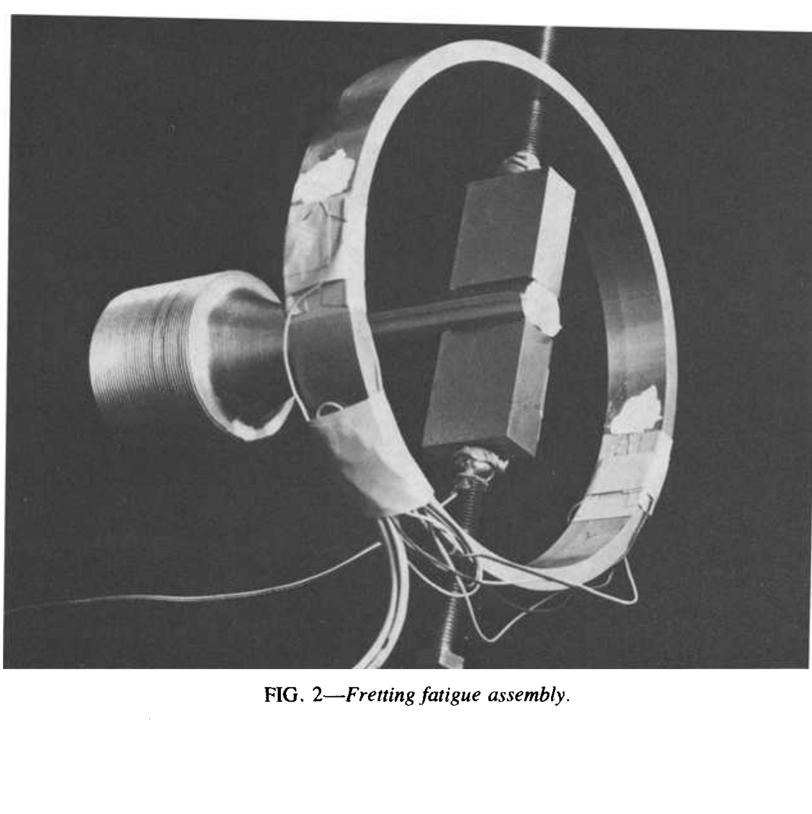

FIG. 2—*Fretting fatigue assembly.*

The frictional forces produced at the fretting feet were measured by straingaging the undersides of the bridge contact pads and monitoring the corresponding sinusoidal signal on an oscilloscope after suitable amplification. A permanent record could be obtained by feeding the signal through a transient recorder into a pen recorder. Initial calibration was by a split specimen technique as described by Edwards and Cooke [1].

All the tests were carried out in air at about 20°C and 40 to 60% relative humidity.

Results and Discussion

3.5Ni-Cr-Mo-V Steel

Baseline *S-N* fatigue data were accumulated from tests on polished unfretted specimens of similar pattern to those in Fig. 1*a* but without machined flats. Various mean stress values were used including 0 and 300 MPa. Fretting results using 1Cr-Mo contact pads at contact pressures of 30 and 300 MPa are compared with baseline data at zero mean stress in Fig. 3. Fretting reduces the fatigue strength from 300 MPa to approximately 140 MPa, a fatigue strength reduction factor of about 2. At a mean stress of 300 MPa, the fatigue strength is reduced by fretting from 215 MPa to about 60 MPa, a fatigue strength reduction factor of about 3.6 (Table 3). At short endurances of 10^5 to 10^6 cycles, Fig. 2 indicates that the higher pad contact pressure of 300 MPa gives a lower fatigue strength compared to the low contact pressure of 30 MPa. However, there is little dif-

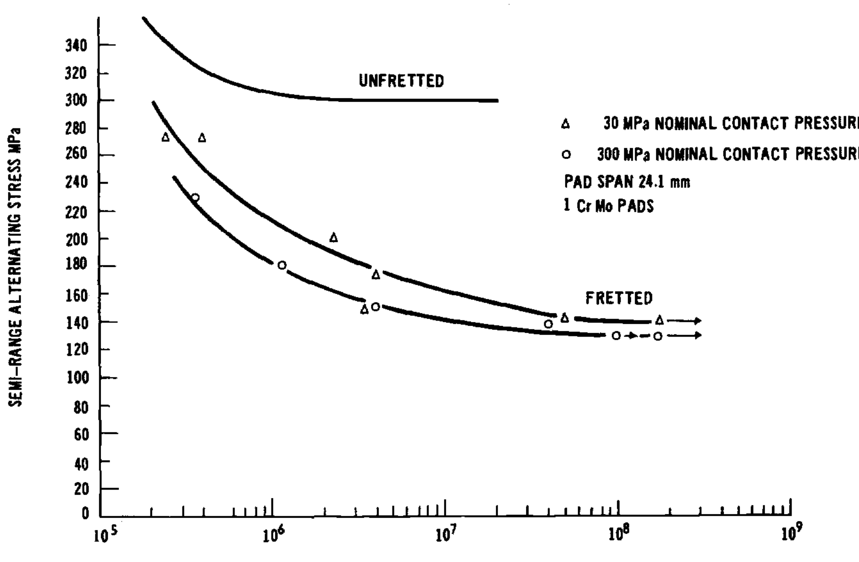

FIG. 3—*Fatigue* S-N *curves with and without fretting for 3.5Ni-Cr-Mo-V rotor steel (zero mean stress). (Arrows represent tests running out at endurance indicated).*

TABLE 3—*Fatigue strength reduction factors due to fretting.*

Fatigue Specimen	Contact Pad	Contact Pressure, MPa	Fatigue Mean Stress, MPa	Fatigue Strength (unfretted), MPa	Fatigue Strength (fretted), MPa	Reduction Factor
3.5Ni-Cr-Mo-V	1Cr-Mo	30	0	±300	±140	2.1
3.5Ni-Cr-Mo-V	1Cr-Mo	30	300	±215	±60	3.6
3.5Ni-Cr-Mo-V	1Cr-Mo	300	0	±300	±130	2.3
3.5Ni-Cr-Mo-V	1Cr-Mo	300	300	±215	±60	3.6
18Mn-4Cr	3.5Ni-Cr-Mo-V	20.7	0	±250	±100	2.5
18Mn-4Cr	3.5Ni-Cr-Mo-V	20.7	300	±125	±50	2.5
18Mn-18Cr	3.5Ni-Cr-Mo-V	20.7	0	±250	±165	1.5
18Mn-18Cr	3.5Ni-Cr-Mo-V	20.7	300	±185	±70	2.6
2014A Al	3.5Ni-Cr-Mo-V	30.8	75	±140	±15	9.3
2014A Al	3.5Ni-Cr-Mo-V	30.8	125	±135	±12.5	10.8

ference in fatigue strengths at 10^8 cycles between the two contact pressures for zero mean stress (Fig. 3). Similar features were found for the higher mean stress of 300 MPa. Since turbo generators accumulate more than 10^{10} self weight bending cycles during a typical lifetime of 20 years, the long endurance behavior is more relevant to practice.

The nominal range of slip S at the end of each centrally clamped pad is given by $S = \sigma x/E$ where $\pm\sigma$ is the alternating stress, x the mean span of the bridge fretting pad, and E is Young's modulus. Table 4 indicates that at 10^8 cycles endurance, the nominal slip ranges for a contact pressure of 30 MPa were 16.1 μm (at zero mean stress) and 6.8 μm (at 300 MPa mean stress). True slip ranges obtained by correcting for pad deflection are also given in Table 4. Previous workers [2] have demonstrated that slip in the range 9 to 15 μm commonly produces the maximum reduction in fatigue strength for a wide range of mean stresses. Future work will explore the effect of pad span and hence slip range on fretting fatigue strength reduction factor.

Austenitic Steels

The end ring steels presently of interest are of the austenitic type 18Mn-4Cr and 18Mn-18Cr. Unlike the well-established 18Mn-4Cr alloy, the 18Mn-18Cr has been recently developed as a new generation end ring material. The properties of 18Mn-18Cr including tensile strength, fracture toughness, environmental cracking susceptibility, etc., are currently being evaluated. Here, a direct comparison is being made between the fretting fatigue properties of 18Mn-4Cr and 18Mn-18Cr steel specimens. The chemical compositions and mechanical properties of the two steels are given in Tables 1 and 2. Fatigue specimens were fretted against contact pads of 3.5Ni-Cr-Mo-V steel at a contact pressure of about 20 MPa.

TABLE 4—*Relative slip ranges at each pad foot and at the fatigue limit for the various fretting combinations.*

Fatigue Specimen	Contact Pad	Contact Pressure, MPa	Fatigue Mean Stress, MPa	Nominal Slip Range, μm/ft	True[a] Slip Range, μm/ft
3.5Ni-Cr-Mo-V	1Cr-Mo	30	0	16.1	15.0
3.5Ni-Cr-Mo-V	1Cr-Mo	30	300	6.8	6.2
3.5Ni-Cr-Mo-V	1Cr-Mo	300	0	16.1	11.7
3.5Ni-Cr-Mo-V	1Cr-Mo	300	300	6.8	4.0
18Mn-4Cr	3.5Ni-Cr-Mo-V	20.7	0	11.6	10.0
18Mn-4Cr	3.5Ni-Cr-Mo-V	20.7	300	5.8	4.5
18Mn-18Cr	3.5Ni-Cr-Mo-V	20.7	0	19.2	17.4
18Mn-18Cr	3.5Ni-Cr-Mo-V	20.7	300	8.1	6.7
2014A Al	3.5Ni-Cr-Mo-V	30.8	75	5.0	2.0
2014A Al	3.5Ni-Cr-Mo-V	30.8	125	4.1	1.5

[a]Range corrected for pad deflection and load redistribution from specimen to pad.

Fretting fatigue results are compared with baseline (nonfretting) data at zero mean stress in Fig. 4 (for 18Mn-4Cr) and Fig. 5 (for 18Mn-18Cr). Table 3 gives fatigue strength reduction factors at 10^8 cycles endurance. It can be seen that at zero mean stress, fretting against 3.5Ni-Cr-Mo-V steel has only a modest effect on the fatigue strength of 18Mn-18Cr, although the fretting wear produces large amounts of debris. In some cases failures at stresses close to the fatigue limit occurred at points remote from the fretting feet, demonstrating the relatively small effect of fretting in these particular circumstances. However, at high mean stresses more appropriate to end ring applications, fatigue strength reduction factors K_{ff} of 2.6 for 18/18 and 2.5 for 18/4 were observed and from the viewpoint of fretting fatigue, 18/18 compares favorably with 18/4 steel.

Aluminium Alloy 2014A

The aluminum alloy 2014A is based on Al-4Cu, the chemical composition and mechanical properties being given in Tables 1 and 2. The present study involved fretting 3.5Ni-Cr-Mo-V steel contact pads against machined surfaces of 2014A aluminum. It can be seen that the fatigue strength reduction factor due to fretting is ~10 (Fig. 6).

Metallography of Fretting Damage

The fretting damage on the fatigue specimen surface under the contact bridge feet varied between the different contacting materials and the different applied load conditions.

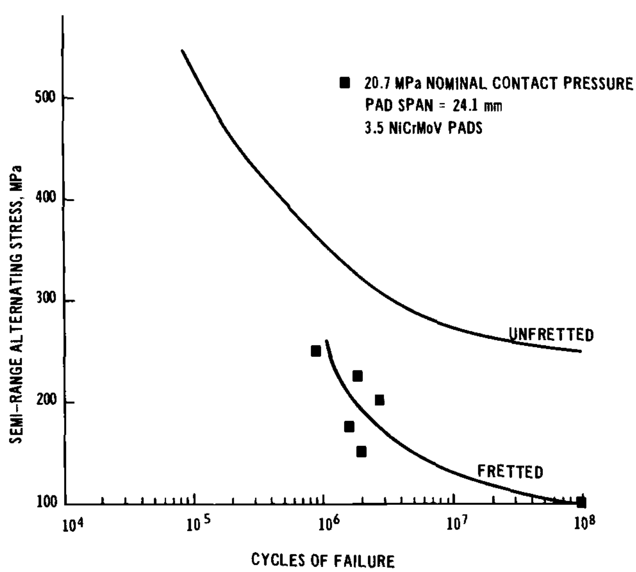

FIG. 4—*Fatigue* S-N *curves with and without fretting for 18Mn-4Cr end ring steel (zero mean stress).*

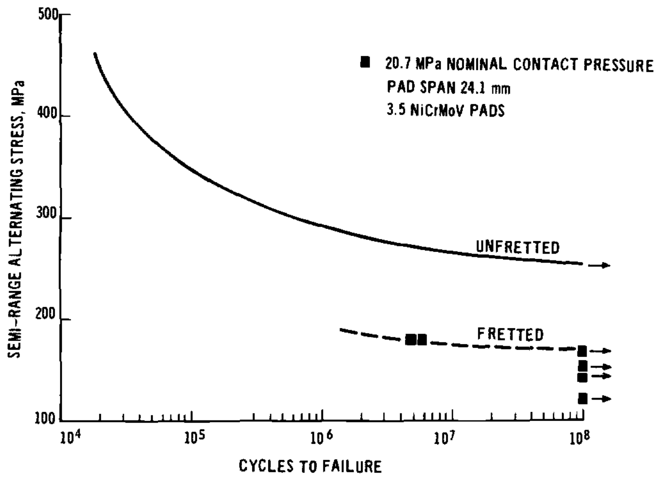

FIG. 5—*Fatigue* S-N *curves with and without fretting for 18Mn-18Cr end ring steel (zero mean stress).*

3.5Ni-Cr-Mo-V Steel

At low contact pressure (30 MPa), slip and fretting damage occurs over all of the contact area, Fig. 7, showing a typical wear scar and associated fretting cracks. By contrast at the high-contact pressure of 300 MPa, slip and associated fretting damage were confined to the edges of the contact strip. The surface damaged regions had an overlay of brown debris, identified by X-ray diffraction

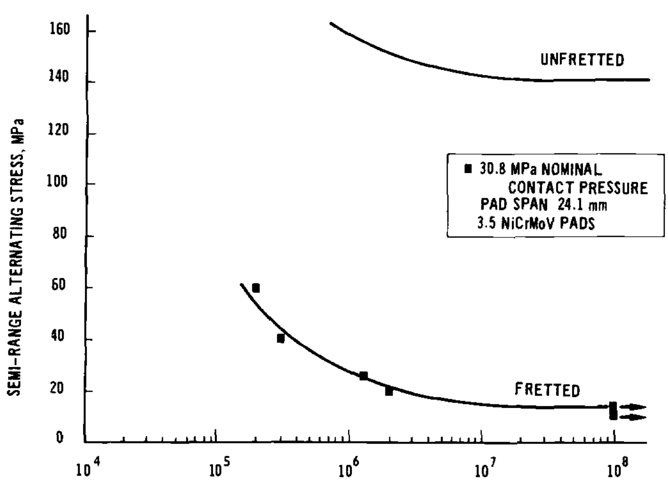

FIG. 6—*Fretting fatigue* S-N *curve for 2014A aluminum alloy (75 MPa mean stress).*

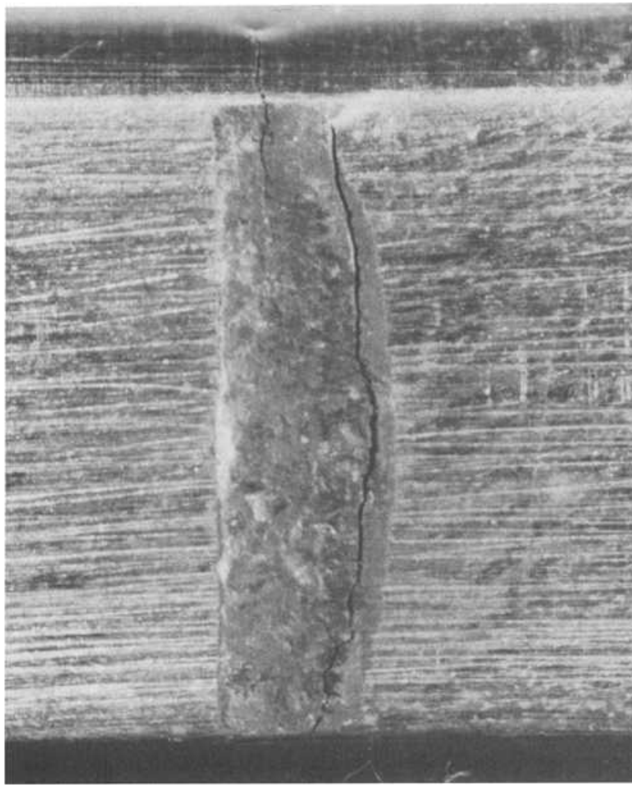

FIG. 7—*Wear scar and associated fretting fatigue crack in 3.5-Ni-Cr-Mo-V rotor steel (1Cr-Mo pad and contact pressure 30 MPa. Applied mean stress 0 MPa).* × *10.*

analysis as α and γ Fe_2O_3 and particulate iron. After nickel plating the fatigue specimen surface, metallographic examination of a longitudinal section taken through a fretting scar revealed the presence of typical fretting fatigue cracks (Fig. 8). Measured in the direction of propagation, these shallow angle fretting cracks were up to 250 μm long. Tracing back to the crack origin on the fracture surface revealed the small shallow angle crack initiation feature characteristic of fretting fatigue (Fig. 9). The crack had initiated at a shallow angle to the fracture surface before turning (at depths typically 100 to 250 μm) and propagating transverse to the applied stress. In order to follow the development of the fretting cracks, some tests were periodically interrupted in order to take acetate film replicas of the fretted regions. Many specimens were broken open at the end of fatigue testing to reveal the fracture surfaces. For 3.5Ni-Cr-Mo-V steel, it was found that small fatigue cracks up to 250 μm deep were present at an early stage (up to 20%) of fatigue life. Small, nonpropagating cracks were sometimes found in fretted specimens running out at 10^8 cycles, when tested just below the fretting fatigue limit as found by other investigations [*3*].

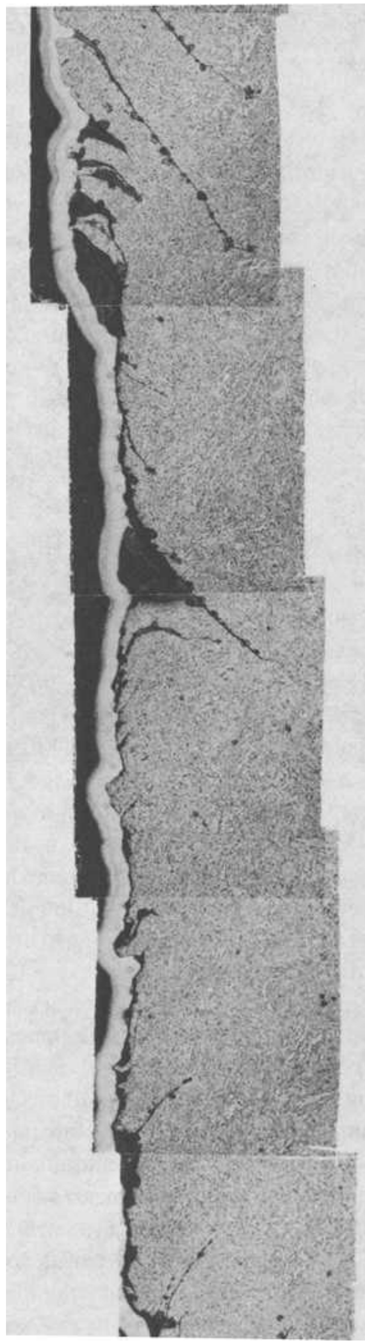

FIG. 8 *Longitudinal section through fretting scar showing shallow angle fatigue cracks in 3.5Ni-Cr-Mo-V rotor steel (1Cr-Mo pad and 30 MPa contact pressure. Applied mean stress 0 MPa).* $\times 180$.

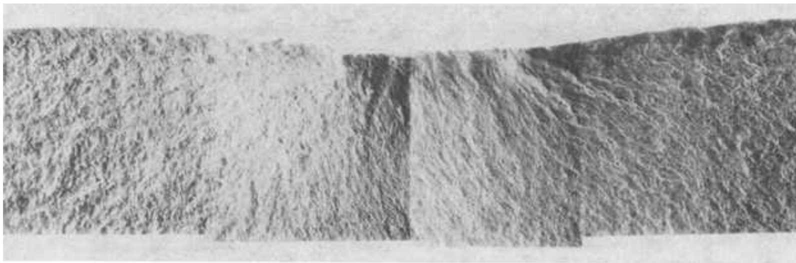

FIG. 9—*Fretting fatigue crack initiation site in 3.5Ni-Cr-Mo-V steel. (1Cr-Mo pad and 300 MPa contact pressure. Applied mean stress 0 MPa).* $\times 20$.

A failed fretting fatigue specimen was broken open in liquid nitrogen to reveal cracks on each side of the specimen (Fig. 10). Note that the left hand side crack shows multiple crack initiation while the right hand side crack in the photomicrograph has developed with a semi-circular shape.

18Mn-18Cr and 18Mn-4Cr Austenitic Stainless Steels

A contact pressure of 20.7 MPa was used throughout the tests on the two austenitic steels. For 18Mn-18Cr at zero mean stress and a slip range of about 17 μm, a great deal of wear was apparent, large amounts of black-brown debris being produced. Much of the wear was incurred by the contact pad since the austenitic steels were much the harder in the fretting combination (compare, VPN 18Mn-18Cr 359; 18Mn-4Cr 429; and 3.5Ni-Cr-Mo-V 222). The wear scar on the fatigue specimen surface was very smooth with little evidence of microcracking. Under these high-wear conditions either cracks do not form or alternatively embryo cracks are worn away before they can develop, resulting in only a modest fatigue strength reduction factor due to fretting for the 18Mn-18Cr steel (Table 3). At a fatigue mean stress of 310 MPa and an estimated slip range of about 5 to 8 μm corresponding to the fatigue limit, much less fretting wear occurred. The fretting scars were patchy rather than being well-developed with evidence of adhesion between specimen and pad, and a small amount of delamination at the specimen surface.

2014A Aluminium Alloy

Despite the large fatigue strength reduction factor (Table 3), little fretting wear resulted from the small-slip ranges. However, there was much evidence of microcracking and multiple crack initiation (Fig. 11). Figure 12 shows a stage in the formation of a pit in 2014A aluminium by the linking of two orthogonal cracks.

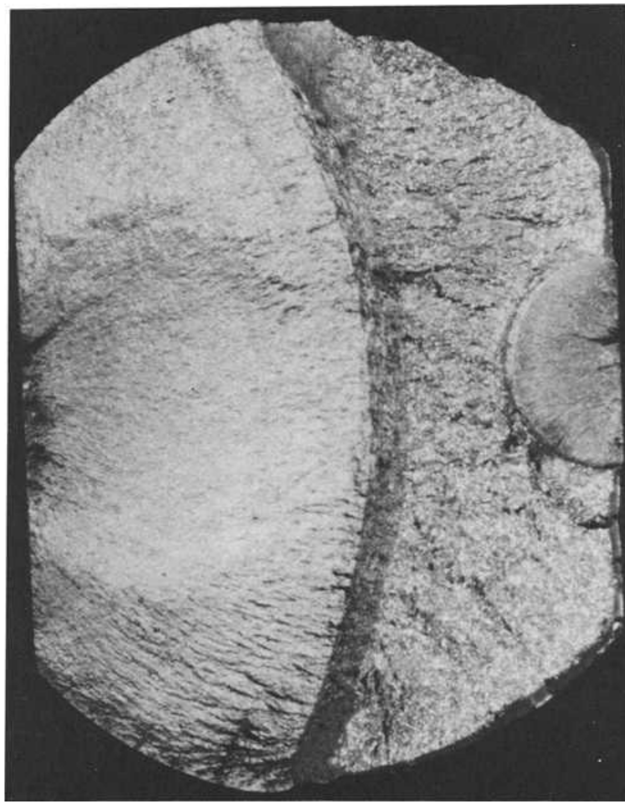

FIG. 10—*Fretting fatigue fracture surface 3.5Ni-Cr-Mo-V showing:* (a) *multiple crack initiation* (left hand side) *and* (b) *semi-circular crack development* (right hand side). *1Cr-Mo pad at 300 MPa contact pressure. Applied mean stress 0 MPa.*

Frictional Force Measurements

Strain gages bonded to both contact pad and fatigue specimens were used to fulfill the following objectives (*a*) to detect the initiation of the fretting fatigue crack, (*b*) to monitor subsequent development of the crack, and (*c*) to measure the frictional forces between pad and specimen for use in a fracture mechanics treatment of crack growth.

Clearly the strain in the specimen below the fretting pad will decrease when a crack initiates underneath the outer point of contact of the pad foot. Such an effect is illustrated in Fig. 13 for the aluminum alloy where frictional force begins to decrease early in the test, consistent with crack initiation at an early stage in fatigue life. By contrast, Fig. 14 shows the changes in frictional force during a long endurance test on the aluminum alloy where an initial rise is observed as the fretting scar develops. This is followed by a narrow plateau,

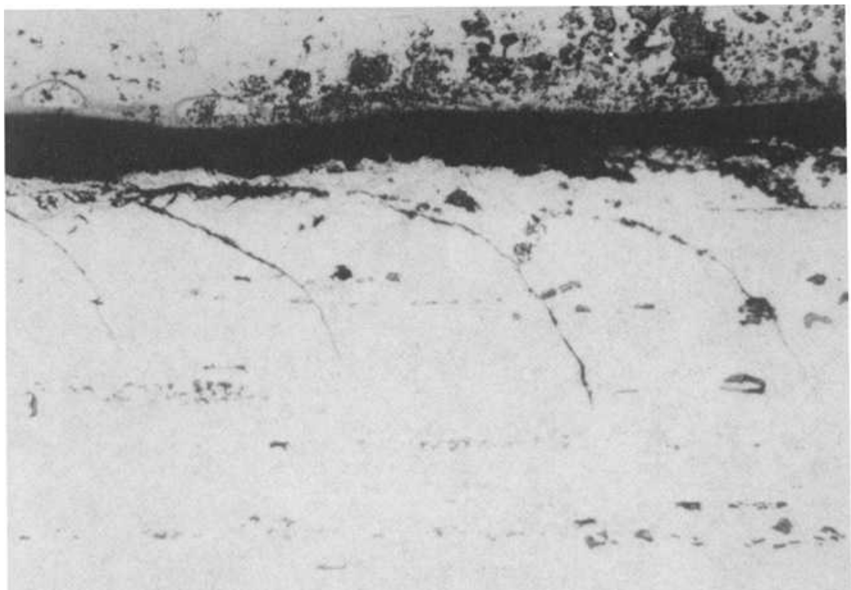

FIG. 11—*Multiple crack initiation due to fretting in 2014A aluminum (3.5Ni-Cr-Mo-V steel pad at 30.8 MPa contact pressure. Applied mean stress 125 MPa).* ×500.

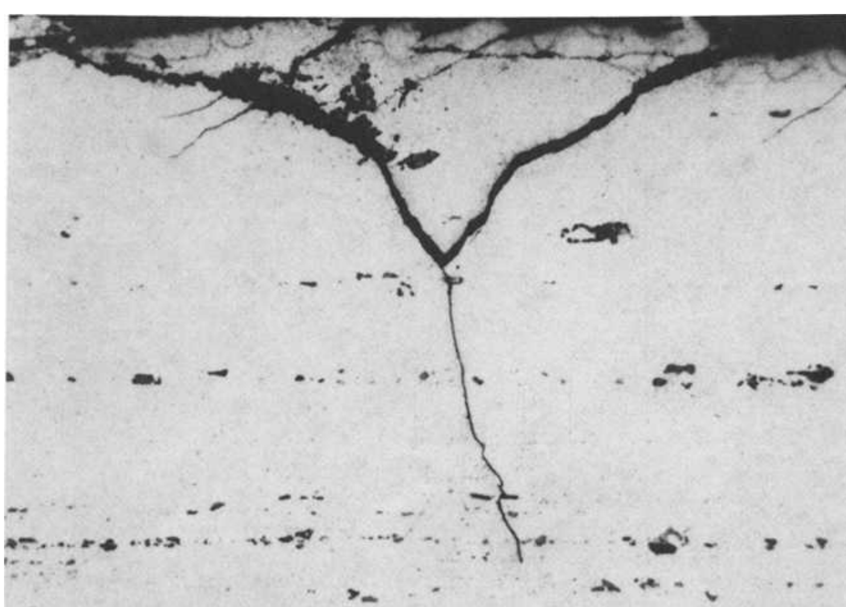

FIG. 12—*Linking of two orthogonal fretting cracks in 2014A aluminum. (3.5Ni-Cr-Mo-V steel pad at 30.8 MPa contact pressure. Applied mean stress 125 MPa).* ×500.

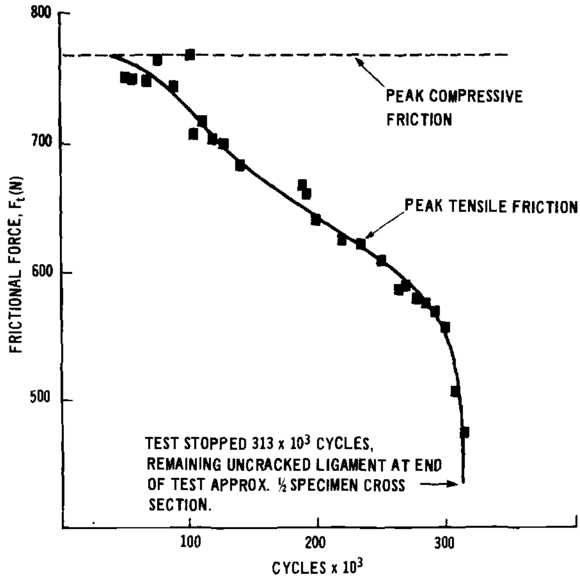

FIG. 13—*Crack initiation detection by monitoring of fretting frictional force changes with endurance in 2014A aluminum.*

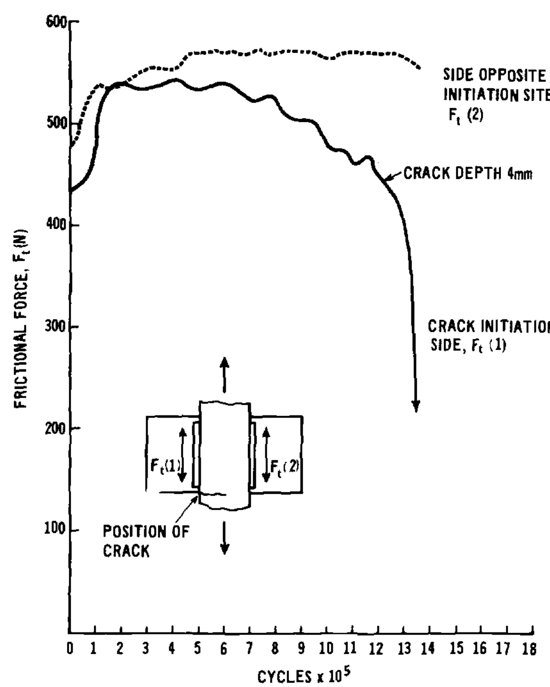

FIG. 14—*Frictional force variation with endurance in 2014A when crack initiation occurs at long endurance.*

and then eventually a fall in frictional force corresponding to the delayed crack initiation event.

It is relatively easy to follow the crack development in the aluminum alloy which exhibits large fatigue strength reductions due to fretting associated with small slip ranges and little wear. Behavior is much more complex under conditions of macroslip or high rates of fretting wear or both. Figure 15 shows the behavior of the 18Mn-18Cr austenitic alloy tested at zero mean stress where the large slip range corresponds to high rates of wear of the 3.5Ni-Cr-Mo-V contact pads. The large amounts of debris generated have a profound effect as shown by comparison of the test machine load cell output and the pad strain gage outputs, the latter being markedly distorted (Fig. 15). More directly, Fig. 15 shows the change in frictional force as the test progresses, and the sudden large drops in output are possibly associated with surface delamination effects. Similar features have been recently observed by Gaul and Duquette [*4*] for a tempered martensite steel. Heilmann and Rigney [*5*] also observed abrupt changes in frictional forces in tests on cupronickel.

Present work is attempting to correlate the frictional force versus time (or cycles) relationship with crack growth.

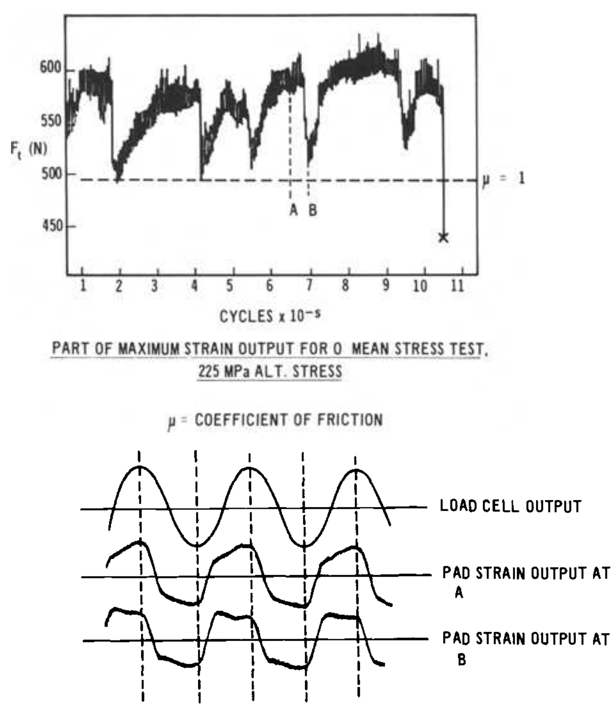

FIG. 15—*Frictional force variation associated with high rates of wear in 18Mn-18Cr austenitic stainless steel.*

Conditions for Crack Propagation

Since the present and earlier studies [*6,7*] have demonstrated that small cracks are commonly initiated at an early stage in fretting fatigue life, it is worthwhile to explore the possibility of using fracture mechanics concepts as a possible route to describe the growth of such cracks. In addition to accelerating crack initiation significantly, it is recognized that fretting can also affect crack growth [*6,7*]. In particular, small cracks which are nonpropagating without fretting might be able to grow through the near-surface region due to an elevation of crack-tip stress-intensity factor provided by the contact pads. Short crack growth behavior and, in particular, the validity of application of linear elastic fracture mechanics is currently receiving much attention. Here, the extent of crack tip plasticity will be clearly of paramount importance. An inspection of fatigue crack growth data in the literature relating to short cracks suggests that for medium strength steels tested near threshold (small stresses at long endurances), linear elastic fracture mechanics (LEFM) can be used down to crack sizes of about 100 μm [for nonfretting conditions].

The basis for such a conclusion has recently been the subject of a detailed study by Lindley, McIntyre, and Trant [*8*]. With fretting, behavior will be even more complex. The stress-intensity factor at the tip of a crack growing beneath a fretting pad will stem not only from the body stresses but also from components arising from the tangential and vertical forces due to the fretting pads. The

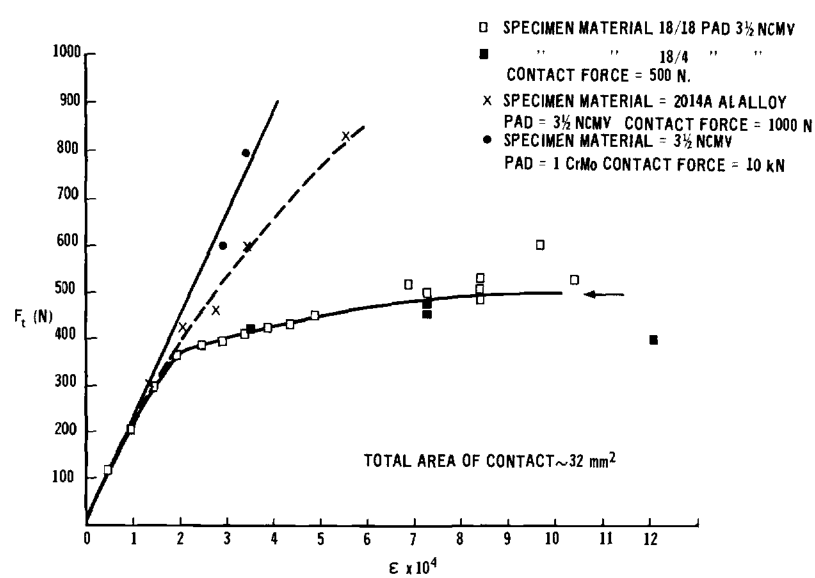

FIG. 16—*Frictional force as a function of specimen strain measured in a series of tests using constant amplitude loading with pad span of 24.1 mm.*

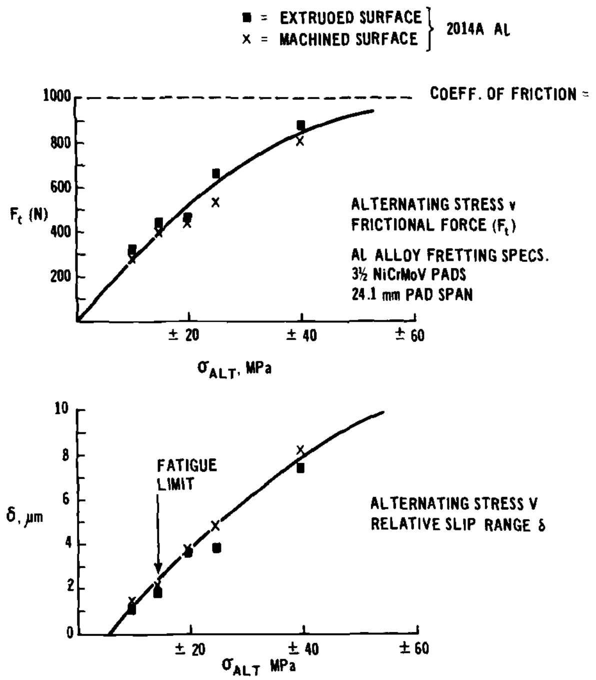

FIG. 17—*Frictional forces (measured in a series of tests using constant amplitude loading) as a function of semirange alternating stress.*

composite applied stress-intensity factor can be evaluated by several distinct methods, namely, (*a*) finite element stress analysis which might be necessary for the complex assemblies found in practice and (*b*) by using opening (and shear mode in more sophisticated analyses) stress-intensity factors arising from tangential and normal forces at the fretting position which have been computed by Rooke and Jones [*9*]. This latter method requires the measurement of frictional forces by strain-gaging the underside of the pad clamped to the fatigue specimen, a procedure [*1,10*] which is described in detail elsewhere.

Frictional forces measured for constant amplitude loading with a pad span of 24.1 mm and with the contact forces indicated are shown for the materials of interest as a function of semirange strain (Fig. 16) and semirange alternating stress (Fig. 17). Similar measurements can be made for other fretting pad span, contact pressure, and fatigue loading conditions. Following the method of Edwards and Cooke [*11*], the alternating stress intensity factor ΔK_{app} is given by the components due to alternating body stresses σ_a and frictional force F_t (and A is the specimen cross-sectional area)

$$\Delta K_{app} = Y\,\sigma_a\sqrt{\pi a} + F_t\,K_{tp} - Y\frac{F_t}{A}\sqrt{\pi a} \qquad (1)$$

The mean stress-intensity factor K_m due to mean stress σ_m and normal force F_n is given by

$$K_m = Y\,\sigma_m \sqrt{\pi a} + F_n K_{np} \tag{2}$$

where a is the crack length and Y is a surface and crack shape correction factor. The stress-intensity factor components due to frictional (F_t) and normal (F_n) loads (per unit load) are K_{tp} and K_{np}, respectively. K_{tp} and K_{np} depend on the distribution of stresses beneath the fretting pad foot. The measured frictional forces (Figs. 16 and 17) are required in order to scale K_{tp} and K_{np} as indicated in Eqs 1 and 2. In principle, it is then possible to use this fracture mechanics approach in which the applied ΔK_{app} is compared with the experimentally measured threshold ΔK_o at the appropriate value of stress ratio R. When $\Delta K_{app} < \Delta K_o$ the crack will arrest, whereas if $\Delta K_{app} > \Delta K_o$ growth will be sustained. In particular, the near-threshold stress-intensity factor of a small crack will be increased by the fretting, possibly enabling propagation when the crack would remain dormant in a nonfretting situation. Such a situation is illustrated in Fig. 18 for the case of the aluminum alloy at a stress close to the fatigue limit. The details of the fracture mechanics calculations are presented elsewhere, Nix, Lindley, and King [12]. Here a uniform distribution of normal pressure and frictional shear stress is assumed beneath the pad foot. Note that the stress ratio (R) varies greatly under fretting conditions and hence so does ΔK_o. The relationship employed in this case between ΔK_o and R was: $\Delta K_o = 2.9 - 2.2\,R$

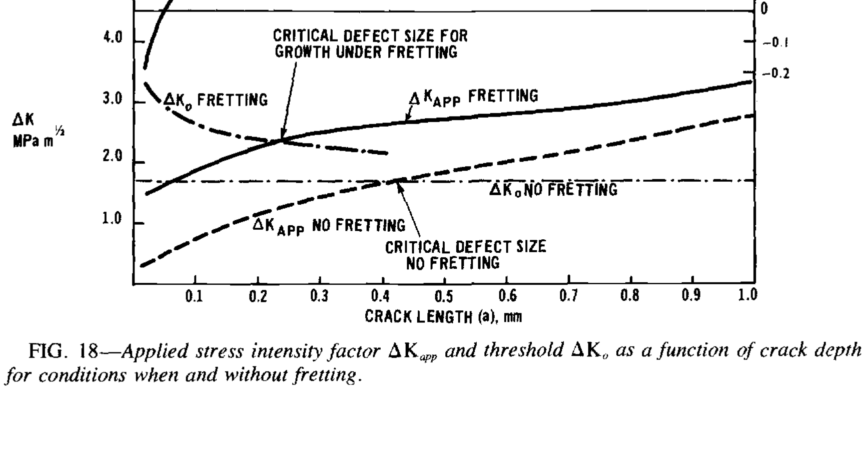

FIG. 18—*Applied stress intensity factor* ΔK_{app} *and threshold* ΔK_o *as a function of crack depth for conditions when and without fretting.*

(in MPa $m^{1/2}$). The present fracture mechanics model requires development in view of the simplications which are currently made. For example, although Mode II stress-intensity factors are clearly present under fretting conditions and can be readily calculated using the analytical data of Rooke and Jones [9], very limited Mode II near-threshold fatigue crack growth data are available for the materials of interest. Multiple crack initiation and deformation due to pad contact are further complications. Nevertheless, the application of fracture mechanics concepts might provide a means of placing the treatment of fretting fatigue on a more quantitative basis than is presently available.

Conclusions

1. Fretting fatigue experiments have been carried out on various combinations of materials used in turbo generators. Fatigue S-N curves, generated with or without fretting, gave fatigue strength reduction factors of up to about 3.5 for ferritic 3.5Ni-Cr-Mo-V steel, 2.5 for austenitic 18Mn-4Cr and 18Mn-18Cr steels, and 11 for 2014A aluminum alloy.
2. Monitoring of fretting damage by both metallography and strain gaging (measurement of the change in frictional forces between specimen and pad with endurance) demonstrated that small cracks were produced by fretting at an early stage in fatigue life.
3. A fracture mechanics approach is developed to predict the growth or arrest of fretting cracks. Here the frictional force measurements are used to compute an applied stress-intensity factor (composed of both body stress and frictional pad stress components) which is then compared with the experimentally measured fatigue threshold parameter ΔK_o at the appropriate value of stress ratio R. Preliminary analysis suggests that this method provides a means of assessing fretting fatigue on a more quantitative basis than is presently available.

Acknowledgments

The work was carried out at the Central Electricity Research Laboratories, and the paper is published by permission of the Central Electricity Generating Board.

References

[1] Edwards, P. R. and Cooke, R., Technical Report 78019, Royal Aircraft Establishment, 1978.
[2] Fenner, A. J. and Field, J. E., *Review of Metallurgy,* Vol. 55, 1958, pp. 475–478.
[3] Nishioka, K. and Hirakawa, K., *Proceedings,* International Conference on Mechanical Behaviour, Kyoto, Japan, 1971.
[4] Gaul, D. J. and Duquette, D. J., *Metallurgical Transactions,* Vol. 11A, 1980, p. 1581.
[5] Heilmann, P. and Rigney, D. A., *Metallurgical Transactions,* Vol. 12A, 1981, pp. 686–688.
[6] Edwards, P. R., Ryman, R. J., and Cooke, R., Technical Report 77056, Royal Aircraft Establishment, 1977.
[7] Endo, K. and Goto, H., *Wear,* Vol. 38, 1975, pp. 311–324.
[8] Lindley, T. C., McIntyre, P., and Trant, P. J., *Metals Technology,* Vol. 9, 1982, pp. 135–142.

[9] Rooke, D. P. and Jones, D. A., *Strain Analysis,* Vol. 14, 1979, pp. 1–6.
[10] Endo, K., Goto, H., and Fukunaga, T., *Bulletin,* Japan Society of Mechanical Engineers, Vol. 17, 1974.
[11] Edwards, P. R. and Cooke, R. in *Proceedings,* 11th Congress of International Council of Aeronautical Sciences, Lisbon, 1978, pp. 505–517.
[12] Nix, K. J., Lindley, T. C., and King, R. N., Central Engineering Research Laboratories, note in preparation.

Ignaas Verpoest,[1] *Budy D. Notohardjono,*[2]
and Etienne Aernoudt[1]

Fatigue of Steel Wire Under Combined Tensile and Shear Loading Conditions

REFERENCE: Verpoest, I., Notohardjono, B. D., and Aernoudt, E., "**Fatigue of Steel Wire Under Combined Tensile and Shear Loading Conditions,**" *Multiaxial Fatigue, ASTM STP 853,* K. J. Miller and M. W. Brown, Eds., American Society for Testing and Materials, Philadelphia, 1985, pp. 361–377.

ABSTRACT: Combined tension and torsion fatigue tests were performed on low- and high-carbon steel wires in the annealed (namely, patented) and drawn condition. It is shown how, with increasing shear to tensile stress ratio, a maximum tensile stress criterion dictates the orientation of the Mode I fatigue cracks in the annealed specimens. This is also the case in drawn wires when the tensile loading component predominates. However, when shear loading predominates and in heavily drawn material where structural and crystallographic anisotropy are well pronounced, easy paths for crack propagation parallel to the wire axis are created and correspondingly Mode II cracks occur.

KEY WORDS: multiaxial fatigue, carbon steel wire, anisotropy, texture, pearlite, ferrite

Nomenclature

σ,τ	Applied normal stress and shear stress
κ	Ratio τ/σ
σ_1,τ_1	Maximum principal normal stress and shear stress
$\bar{\sigma}_1,\bar{\tau}_1$	Mean value of principal stresses for a given number of cycles to failure
$S_{\bar{\sigma}_1},S_{\bar{\tau}_1}$	Standard deviations
$N_f,\bar{N}_f,S_{\bar{N}_f}$	Number of cycles to failure, its mean value and standard deviation
α_p	Angle of the pearlite lamellae in drawn wire
α_c,α_m	Calculated and measured angles of the crack plane (Fig. 4)
$\sigma_y(\sigma_{0.2})$	Yield stress in uniaxial tension test
$\tau_{\gamma=0.004}$	Yield stress in torsion test
τ_y	Shear flow stress
r_p	Plastic zone size

[1]Research associate and professor, respectively, Departement Metaalkunde, K. U. Leuven de Croylaan, Leuven, Belgium.
[2]Research assistant, Mechanical Engineering Department, University of Wisconsin Madison, Madison, WI 53706.

Copyright© 1985 by ASTM International www.astm.org

K	Stress-intensity factor
K_I^*, K_{II}^*	Normalized stress-intensity factors
β_I, β_{II}	Constants in plastic zone size calculation
δ	Plastic zone size ratio
ϵ or ϵ_{wd}	Wire drawing strain

For many years, it has been a challenge to materials scientists to correlate multiaxial fatigue data with the more conveniently obtained uniaxial data. Initially, combined tension and torsion (or bending and torsion) loads were applied on solid, smooth specimens, since it was the opinion at that time that the fatigue limit was mainly controlled by crack initiation. Thus, it was obvious that empirical models which correlate uniaxial and multiaxial fatigue data at least should contain shear stress as a parameter. Gross plastic yielding criteria, such as the maximum shear stress criterion of Tresca or the strain energy criterion of von Mises, contain shear stresses, so it was logical that early relations were directly derived from these yielding criteria, that is, Gough [1] and Guest [2]. Eventually, attention turned to the low-cycle fatigue ($N_f \leq 10^4$ cycles) regime in which crack growth predominated. These tests were mostly performed under plane stress conditions (hollow cylinders or plates), on ductile materials or at high temperatures or both. Hence, it is not surprizing that new relations were expressed in strain terms; the maximum shear strain (most efficient if not parallel to the surface), and the tensile strain normal to the plane of maximum shear are found to be controlling parameters (for example, Brown and Miller [3] and Lohr and Ellison [4]).

Most of the previous studies were carried out on isotropic materials. The aim of our work was to make a preliminary study of the influence of anisotropy on fatigue properties under combined loading conditions, and to investigate which of the models just mentioned would apply to anisotropic materials.

Cold drawn wires were studied. In this material, two kinds of anisotropy have to be distinguished: on the one hand, structural anisotropy is linked with elongated grains or cells or with aligned pearlite. Figure 1 shows how initially random oriented pearlite lamellae (at zero deformation $\epsilon = 0$) gradually align parallel with the wire axis ($\alpha_p \rightarrow 0°$) as the deformation increases ($\epsilon \rightarrow 4$). On the other hand, crystallographic anisotropy is linked with a preferred orientation induced by cold working. The pole figure in Fig. 2 shows a {110} texture after cold drawing ($\epsilon \simeq 2.6$) of a pearlitic steel wire (0.85% carbon).

Experimental

In order to study the effect of anisotropy on fatigue behavior under combined loading four different materials were tested: low-carbon (0.06%) annealed (LCA), and 78% cold-drawn (LCD) steel wire, and high-carbon (0.83%) steel wire in patented (HCP) and 75% cold-drawn (HCD) conditions. The annealed and pat-

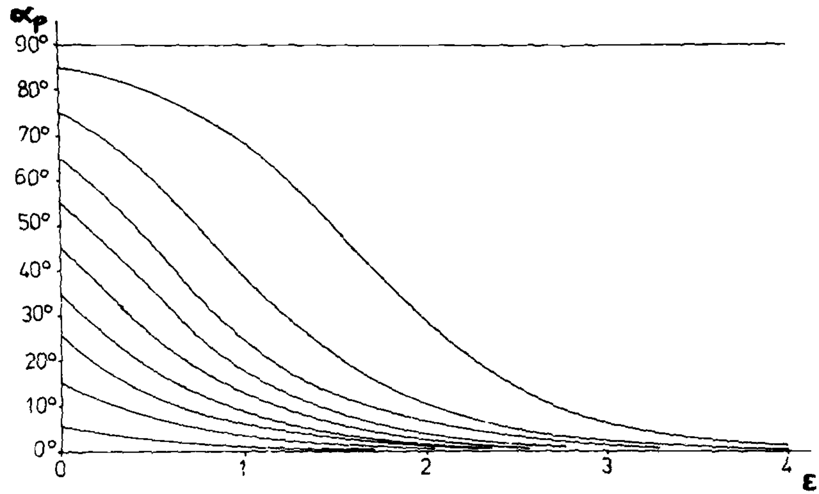

FIG. 1—*The effect of wire drawing deformation* (ϵ) *on pearlite alignment* (α_p *is the angle between the lamellae and the wire axis*).

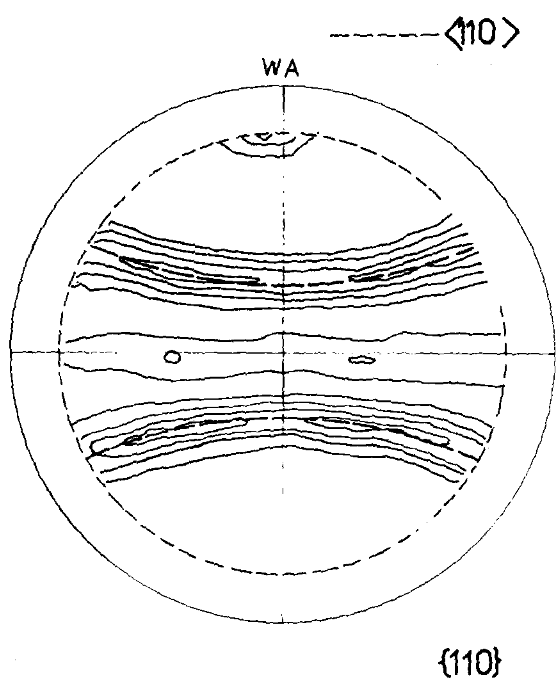

FIG. 2—*A pole figure for a high-carbon (0.85% carbon), cold-drawn* (ϵ = 2.6) *steel wire.*

TABLE 1—*Mechanical properties.*

Property	LCA, low-carbon, annealed	LCD, low-carbon, drawn	HCP, high-carbon, patented	HCD, high-carbon, drawn
$\sigma_{0.2}$, MPa	251	715	812	1347
σ_u, MPa	354	743	1309	1708
$\tau_{\gamma=0.004}$, MPa	211	540	690	900
τ_u, MPa	416	598	841	1055

ented steel wires have only a weak texture, and the pearlite is randomly oriented. Hence, this material can be considered isotropic. The cold-drawn wires are anisotropic. The structural anisotropy is formed by elongated cells and grains in the low carbon steel wire and by an axially oriented lamellar structure in the nearly eutectoidic (pearlitic) steel wire. In both materials, the ferrite shows additionally a {110} fiber texture. The mechanical properties of these materials are listed in Table 1. From the final drawing diameter of 8 mm, the materials were machined down to 6 mm diameter at the gage length. The detailed dimensions of the fatigue specimens are given in Fig. 3. Fatigue tests were carried out on a Schenck servohydraulic fatigue testing machine which has the capability to perform combined tension-compression (± 160 kN, ± 50 mm) and torsion (± 200 Nm, $\pm 140°$). All of the solid cylindrical specimens were subjected to a sinusoidal pulsating tension or torsion loading with a minimum value of zero or both. Each test is specified by the parameter κ, the ratio of the applied shear stress to the applied tensile stress (which are in phase). Seven values of κ were chosen, ranging from $\kappa = 0$ (pure tensile) to 0.25, 0.50, 1, 2, 5, and ∞ (pure torsion).

At each κ-value, appropriate σ- and τ-values were chosen so that two distinct numbers of cycles to failure N_f could be obtained (Table 2). This was done by a trial and error method; hence, a relative standard deviation on N_f of 20% could not be avoided. Furthermore, because the LCA steel wires showed too much

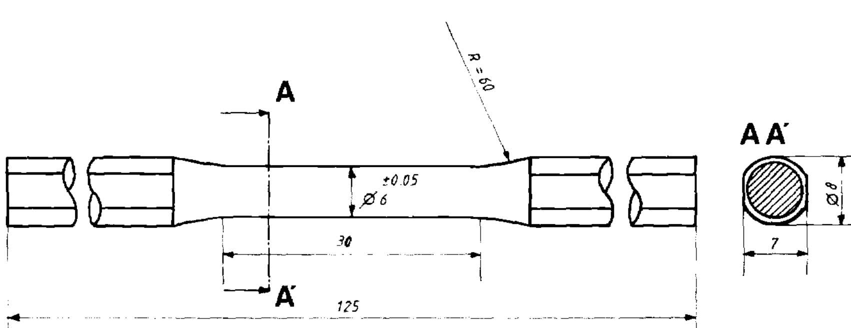

FIG. 3—*Fatigue specimen geometry: dimensions in millimetres.*

TABLE 2—*Fatigue properties.*

Property	LCA, low-carbon, annealed	LCD, low-carbon, drawn		HCP, high-carbon, patented		HCD, high-carbon, drawn	
$\bar{N}_f$	. . .	139 600	383 300	39 000	94 000	59 800	11 750
$S_{\bar{N}_f}$	. . .	28 000	70 500	8 000	21 500	10 700	14 200
S_{N_f}/N_f, %	. . .	18.6	18.4	20.5	23.0	17.8	12.1
σ_1, MPa	. . .	584	555	831	768	985	902
$S_{\bar{\sigma}_1}$, MPa	. . .	75	72	24	24	49	46
$S_{\bar{\sigma}_1}/\sigma_1$, %	. . .	12.8	13.0	2.8	3.1	5.0	5.0
$\bar{\tau}_1$, MPa	. . .	430	373	568	545	707	640
$S_{\bar{\tau}_1}$, MPa	. . .	60	56	175	132	198	176
$S_{\bar{\tau}_1}$, %	. . .	14.0	14.9	30.8	24.2	28.0	27.5

cyclic plasticity, crack initiation was enhanced by a small notch (produced by spark erosion); the depth of this notch varied considerably (0.5 ± 0.2 mm). The N_f-data were not reliable, and so they are not included in Table 2.

Results

Orientation of Fatigue Cracks

The angle between the fatigue crack growth plane and the plane perpendicular to the wire axis has been measured on stereo light micrographs (at a magnification between ×10 and ×40). These measured crack orientations are represented schematically in Fig. 4.

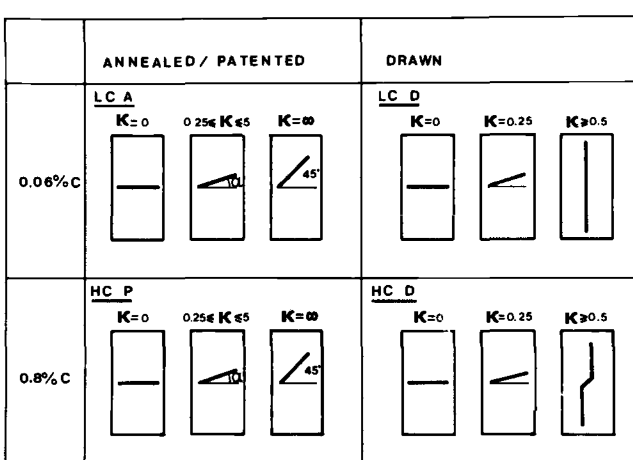

FIG. 4—*Fatigue crack orientation at different torsion-to-tension ratios.*

Isotropic Steel Wires—In annealed low-carbon and patented high-carbon steel wires, which are both isotropic, the fatigue crack growth plane gradually turns over from a 0°-orientation (that is, perpendicular to the wire axis) at pure tension loading to a 45°-orientation at pure torsion loading. In Fig. 5, two such cracks in LCA steel wires are shown, one at almost pure tension (κ = 0.25), the other at almost pure torsion (κ = 5). Note the small needle-like notches, from which the fatigue cracks started at low applied loads; cyclic macroplasticity could be avoided in these low yield stress wires. At almost pure torsion (κ = 5) the final fracture is clearly a torsional fracture (in the transverse, maximum torsion stress plane); whereas, in the harder, HCP wires we find at κ = 5 a typical spiral fracture, which follows the plane of maximum tensile stress; Fig. 6*d*.

Figure 6 shows clearly the gradually changing crack orientation for the HCP steel wire.

Anisotropic Steel Wires—For low κ-values (0 and 0.25) similar crack orientations can be found in anisotropic, drawn steel wires (Fig. 4). However when torsion becomes more important (that is, κ increases), a shear type crack appears parallel to the wire axis. In the *low-carbon drawn* steel wires, no tensile type cracks can be found for $\kappa > 0.5$, and one or more cracks parallel to the wire axis cause delamination and final fracture (Fig. 7). In the *high-carbon drawn* steel wires, however, the tensile type cracks always remain present, but they

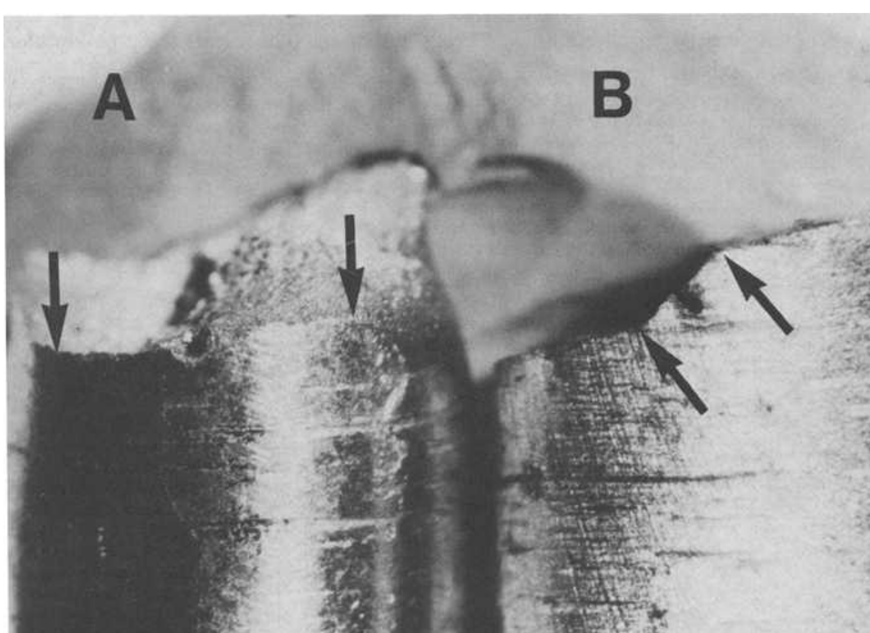

FIG. 5—*Side view of fatigue cracks (between arrows) in LCA steel wires at* κ = *0.25 (A) and* κ = *5 (B) (×6).*

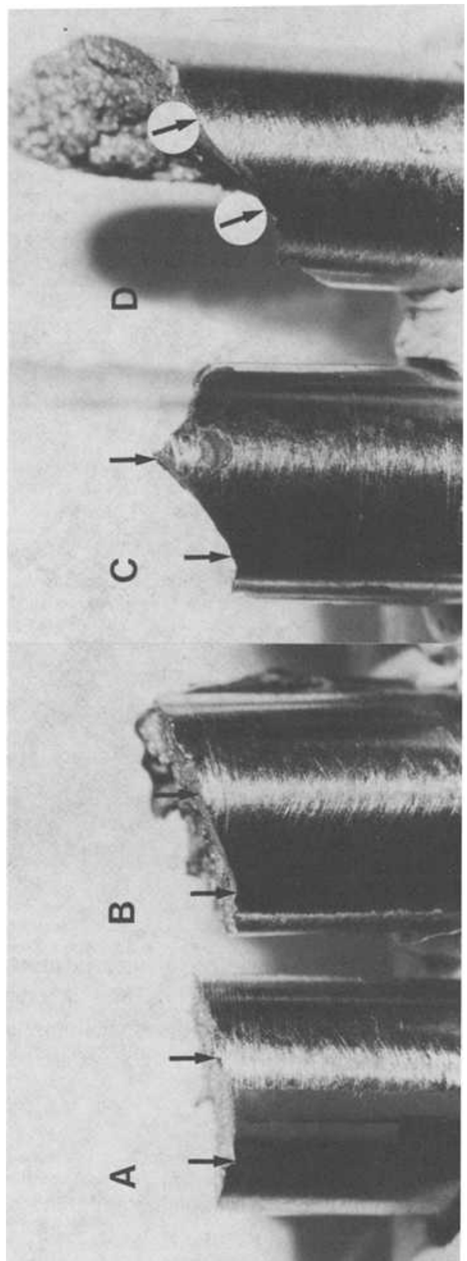

FIG. 6—*Side views of fatigue cracks (between arrows) in HCP steel wires at* κ = *0.25 (A), 0.50 (B), 2 (C), and 5 (D) (×6).*

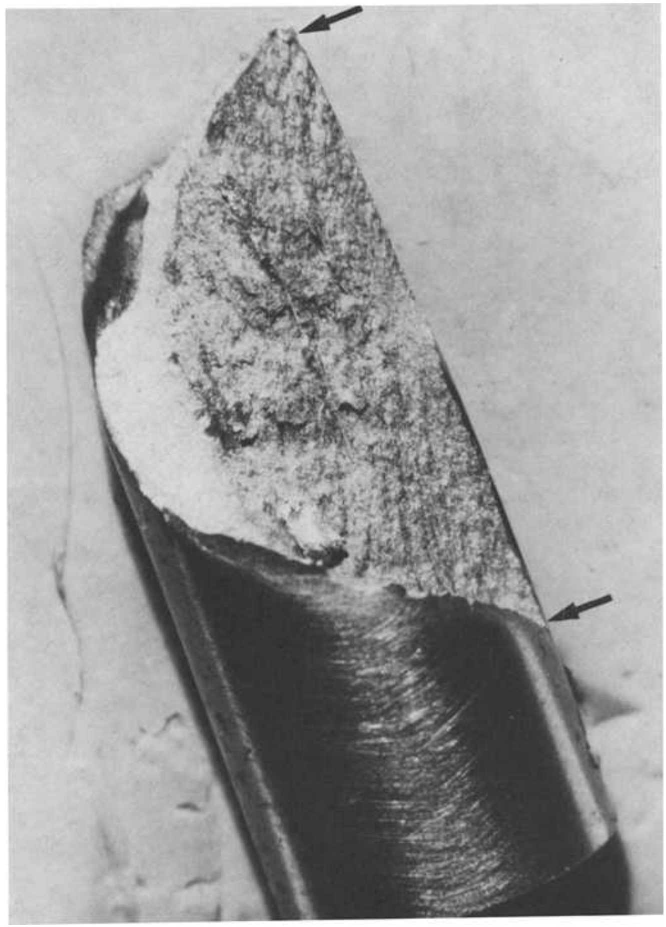

FIG. 7—*Longitudinal fatigue crack (between arrows) in LCD steel wire at* $\kappa = 0.5$ $(\times 6)$.

become smaller and smaller, compared with the shear type cracks which develop subsequently as soon as $\kappa > 0.5$ (Fig. 8). In Fig. 8*a*, the crack surface A has been removed from his counterpart B during the final, longitudinal fracture. It is important to point up that the shear type cracks always are parallel to the wire axis.

Fatigue Life Controlling Parameters

For monotonic, combined tension, and torsion loading, the stress state at which yielding occurs is usually represented in a σ versus τ graph. In a similar way, the data points in Fig. 9 show the combined stress states which lead to the same number of cycles to failure N_f, for the HCP and HCD, and for the LCD steel wires. As we had to notch the LCA specimens, the number of cycles to failure N_f is influenced by the variable depth of the notches. Hence, N_f becomes unreliable, and no σ versus τ graph at constant N_f can be presented.

Discussion

Isotropic Steel Wires

There are two sets of evidence available in the current tests to state that fatigue crack growth in isotropic steel wires is controlled by the principal normal stress σ_I. First, if the principal normal stress σ_I should be the controlling parameter, then for a certain number of cycles to failure σ_I should be constant, independent of the applied stresses σ and τ or of the κ-value.

In order to study the validity of this statement, for each N_f a line of constant σ_I has been plotted in the σ versus τ graphs (Fig. 9). These lines have the following equations

$$\sigma_I = \frac{\sigma}{2} + \frac{1}{2}\sqrt{\sigma^2 + 4\tau^2} \tag{1}$$

For the reasons mentioned previously, this could not be done for the LCA wires. For the HCP specimens (Fig. 9*a*) we see an excellent agreement between the calculated σ_I curve and the σ versus τ data points. Moreover, for all the stress states or κ-values the principal normal stress varies by only 3%, even if the relative standard deviation on N_f is about 20%. However, the maximum shear stress τ_I changes by 100% (from 400 to 800 MPa), and the standard deviation is considerably higher (Table 2).

Second, we can compare the fatigue crack orientation α_m (the measured angle between the fatigue crack plane and the plane perpendicular to the wire axis) with the calculated angle of the plane of maximum normal stress α_c, according to the formula

$$\alpha_c = \frac{1}{2}\tan^{-1}\frac{2\tau}{\sigma} \tag{2}$$

Figure 10 shows that there is an excellent agreement between the measured and the calculated angles, for both isotropic wires. As we want to describe fatigue crack growth, we have to translate the statement that the principal normal stress σ_I is the controlling parameter (in isotropic steel wires) into fracture mechanics terms. If we calculate, for the cracks emerging at the wire surface, K_I and K_{II}, according to the formula mentioned by Smith and Pascoe [5], we find that $K_{II} = 0$ and that K_I is not affected by the stress ratio κ. Hence, for all torsion-tension combinations fatigue cracks are pure Mode I cracks in isotropic materials.

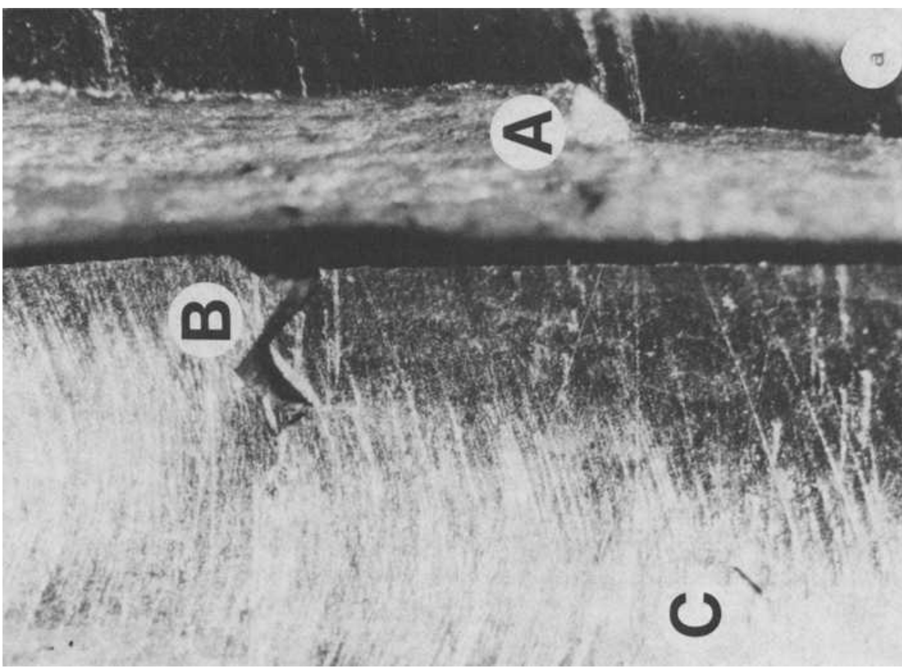
A
B
C

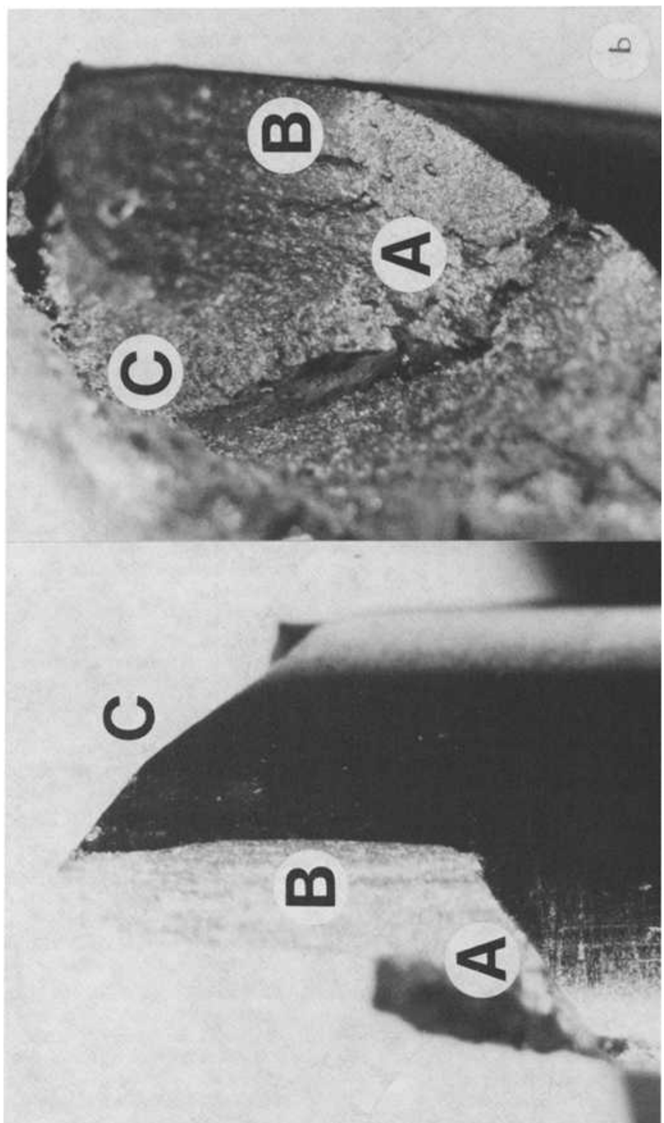

FIG. 8—*Fracture surface characteristics,* (a) *General view of fatigue cracks in HCD steel wire under pure torsion* ($\kappa = \infty$) ($\times 20$). *A. Mode I fatigue crack (45°) with adjacent Mode II cracks parallel to the wire axis. B. Group of Mode I cracks ("factory proof"), and C. Small Mode I crack, at which no Mode II crack yet developed.* (b) *Semicircular Mode I crack* (A) *with adjacent Mode II crack* (B) *and final spiroidal fracture path* (C) ($\kappa = 0.5$) ($\times 10$).

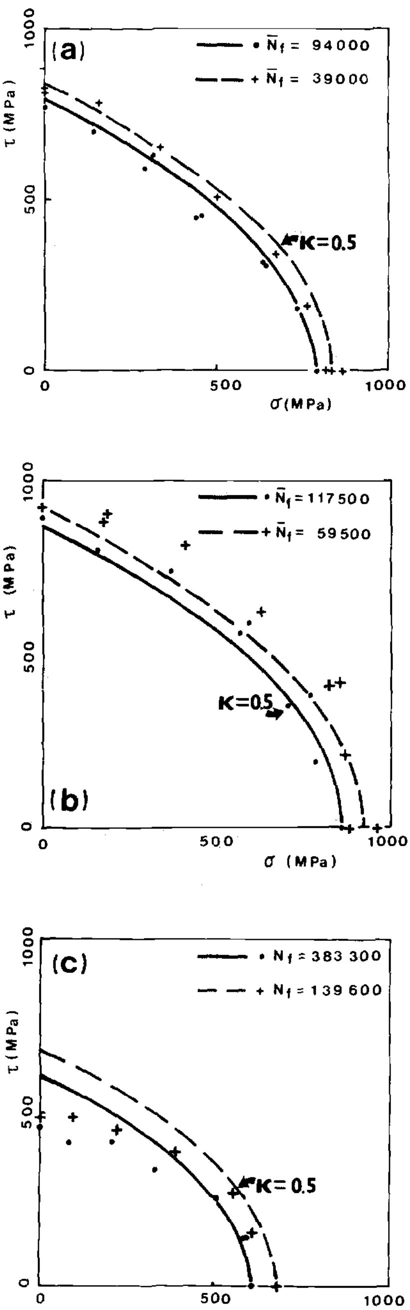

FIG. 9—*Constant fatigue life data points and constant σ_I-lines at different κ-values for* (a) *HCP steel wire,* (b) *HCD steel wire, and* (c) *LCD steel wire.*

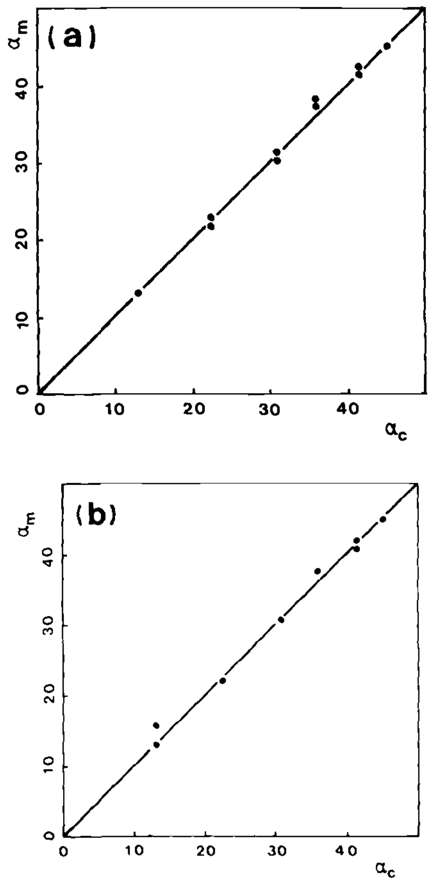

FIG. 10—*Comparison of the calculated* (α_c) *and measured* (α_m) *angle between the normal to the fatigue crack plane and the wire axis, for* (a) *LCA steel wire, and* (b) *HCP steel wire.*

Anisotropic Steel Wires

In low- as well as in high-carbon drawn steel wires longitudinal cracks appear as soon as the applied shear stress becomes equal to or larger than half of the applied tensile stress, $\kappa \geqslant 0.5$. As these longitudinal cracks could not be found in isotropic steel wires, it can be expected that anisotropy plays a major role in this phenomenon. Moreover, it seems to be doubtful that the principal normal stress σ_1 will remain the controlling parameter.

High Carbon, Drawn Steel Wires—The photographs in Fig. 8 clearly show that, even for pure torsion, small inclined cracks are present, together with the long longitudinal ones. Again, the orientation of these small inclined (Mode I) cracks, coincides with the plane of maximum normal stress σ_1. So, it is not unexpected that, for a given number of cycles to failure N_f, σ_1 is almost constant (relative standard deviation of 5%, Table 2) and that the experimental data points in the σ,τ graph (Fig. 9*b*) coincide quite well with the calculated constant σ_1 lines. Nevertheless, a small deviation to higher σ,τ-values can be observed in the intermediate range ($0.5 < \kappa < 5$).

Low Carbon, Drawn Steel Wires—As for high-carbon, drawn steel wires, longitudinal cracks appear as soon as $\kappa \geqslant 0.5$, but no inclined (Mode I) cracks are present (Fig. 7). Hence, σ_1 no longer controls fatigue life: the experimental data in Fig. 9*c* deviate from the constant σ_1-curves and the σ_1 standard deviation goes up to 13%.

Explanation of the Presence of Longitudinal Cracks

Both low- and high-carbon anisotropic steel wires show longitudinal cracks as soon as $\kappa \geqslant 0.5$. If we calculate for these cracks the stress-intensity factors, we find that

$$K_{\rm I} = 0$$
$$K_{\rm II} = \frac{\sigma_1\sqrt{\pi a}}{2}\left[1 - \frac{1 - \sqrt{1 + 4\kappa^2}}{1 + \sqrt{1 + 4\kappa^2}}\right]\frac{2\kappa}{\sqrt{1 + 4\kappa^2}} \tag{3}$$

Normalized K-values are listed in Table 3 as a function of κ. This means that these longitudinal cracks, although they do not coincide with the plane of maximum shear stress, are pure Mode II cracks (at least where these cracks emerge at the wire surface).

To answer the question why, in anisotropic steel wires at a certain κ-value, inclined Mode I cracks are replaced by longitudinal Mode II cracks, and why this does not happen in isotropic steel wires, we have to compare the magnitude of the driving forces for crack growth. In their review, Smith and Pascoe [5] listed five theories to explain crack growth direction. All but one fail to clarify the Mode I-Mode II changeover observed in anisotropic materials, as they do

TABLE 3—*Normalized stress intensity factors and plastic zone size ratios.*

Stress State		Inclined Mode I Cracks,	Longitudinal Mode II Cracks,		$\left(\frac{r_{p,\rm II}}{r_{p,\rm I}}\right)$ ANISO	
$\kappa = \frac{\tau}{\sigma}$	$\lambda = \frac{\sigma_2}{\sigma_1}$	$K_{\rm I}^* = \frac{K_{\rm I}}{\sigma_1\sqrt{\pi a}}$	$K_{\rm II}^* = \frac{K_{\rm II}}{\sigma_1\sqrt{\pi a}}$	$\left(\frac{r_{p,\rm II}}{r_{p,\rm I}}\right)$ ISO	$\frac{\tau_{y,\rm I}}{\tau_{y,\rm II}} = 2$	$=3$
0	0	1	0	0	0	0
0.25	−0.06	1	0.23	0.20	0.80	1.80
0.50	−0.17	1	0.42	0.64	2.58	5.80
1	−0.38	1	0.61	1.39	5.55	12.5
2	−0.61	1	0.78	2.26	9.07	20.4
5	−0.82	1	0.91	3.10	12.4	27.8
∞	−1	1	1	3.72	14.9	33.5

not take into account material properties (only linear elastic fracture mechanics (LEFM) parameters are introduced). A fifth one implicitly accounts for material properties (that is, crack growth rate data), but could not be used as these data are not yet available for the materials treated in this study. Another theory to explain crack growth direction has been presented recently by Gao Hua, Brown, and Miller [*6*]. It states that crack growth rate is controlled by the ratio of the maximum plastic zone size over the true fracture ductility. The same group described in an earlier publication [*7*] a similar but simpler model, presenting the "severe strain zone size" as a unique crack growth rate controlling parameter. For local yielding conditions, this zone can be replaced by the maximum plastic zone size. According to Gao Hua et al [*6*], plastic zones for both Mode I and Mode II cracks can be calculated using the formula

$$r_p = \beta \frac{K^2}{\sigma_y^2} \tag{4}$$

where

$\beta = 0.128$ for Mode I, inclined cracks, and
$\beta = 0.477$ for Mode II, longitudinal cracks.

These maximum dimensions can be found, respectively, at 88 and 0° relative to the crack plane.

To explain the changeover from Mode I to Mode II, one can calculate the $r_{p,\mathrm{II}}/r_{p,\mathrm{I}}$ ratio as a function of the applied torsion-to-tension stress ratio κ (Table 3).

For *isotropic* steel wires, σ_y is independent of the orientation relative to the wire axis; hence, the plastic zone ratio reduces to

$$\delta = \frac{r_{p,\mathrm{II}}}{r_{p,\mathrm{I}}} = \frac{\beta_{\mathrm{II}}}{\beta_{\mathrm{I}}} \cdot K_{\mathrm{II}}^{*2}$$

where

$$K_{\mathrm{II}}^* = \frac{K_{\mathrm{II}}}{\sigma\sqrt{\pi a}} \tag{5}$$

Figure 11 and Table 3 show that this ratio changes in a sigmoidal way from 0 for pure tension to 3.72 for pure torsion. For *anisotropic* steel wires, however, σ_y (or more exactly the shear flow stress τ_y) is orientation dependent. Hence, for Mode I cracks we introduce $\tau_{y,\mathrm{I}}$ (in a direction almost perpendicular to the Mode I crack plane), and $\tau_{y,\mathrm{II}}$ (in the Mode II crack plane, and thus parallel to the wire axis), which results in the formula

$$\delta = \frac{r_{p,\mathrm{II}}}{r_{p,\mathrm{I}}} = \frac{\beta_{\mathrm{II}}}{\beta_{\mathrm{I}}} \left(\frac{K_{\mathrm{II}}^* \, \tau_{y,\mathrm{I}}}{\tau_{y,\mathrm{II}}}\right)^2 \tag{6}$$

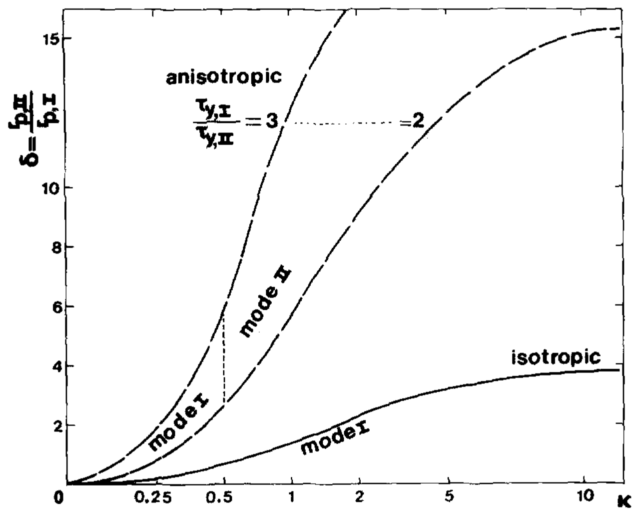

FIG. 11—*Plastic zone size ratio δ as a function of the torsion-to-tension stress ratio κ for isotropic and anisotropic materials.*

The anisotropy of the shear flow stress and hence the $\tau_{y,I}/\tau_{y,II}$ ratio in drawn steel wires is a product of two factors: on the one hand, a {110} fiber texture is formed in the ferrite during wire drawing (Fig. 2). Using a theoretical model elaborated in our department [*8*], one can calculate that the shear flow stress ratio equals 1.25 at a wire drawing strain $\epsilon = 1.2$ [*9*]. On the other hand, a structural anisotropy is developing in the low-carbon (narrow, elongated cells in the ferrite) as well as in the high-carbon (oriented cementite lamellae in the pearlite) steel wires. Hence, free slip length for dislocations is highly influenced by the aforementioned geometry of the microstructure. Calculations, analogous to those published by Gil Sevillano et al [*10*] show that the shear flow stress ratio in drawn pearlite, due to structural anisotropy, lies between 1.5 (for $\kappa = 0.5$) and 3 (for $\kappa = \infty$, pure torsion). For drawn ferrite, containing longitudinal cells, which are not as narrow as ferrite lamellae in pearlite, the microstructural anisotropy will be less important. Nevertheless a careful examination of the ratio of the yield stresses in tension ($\sigma_{0.2}$) and torsion ($\tau_{\gamma=0.004}$) in Table 1 shows that the anisotropy in drawn ferrite is only 15% lower than in drawn pearlite. These preliminary calculations show that crystallographic (texture) and structural anisotropy will lead to a shear flow stress ratio

$$2 < \frac{\tau_{y,I}}{\tau_{y,II}} < 3$$

Introducing this ratio into formula [*6*], Table 3 and Fig. 11 clearly show that the plastic zone size ratio increases very rapidly. From our observations we know that the changeover of Mode I to Mode II happens at $\kappa = 0.5$; the plastic zone ratio has then a mean value of 4.2, which is clearly higher than ever could be reached in isotropic wires. Hence, we conclude that once the ratio of the plastic zones of the Mode II over the Mode I crack reaches a critical value of about 4, Mode II cracks appear. Because in isotropic steel wires this value can never be reached (maximum is 3.72), no Mode II cracks can develop.

It is quite logical that the Mode II crack plastic zone has to be much larger ($\times 4$) than a Mode I crack plastic zone. One has to take into account not only rubbing effects between the crack surfaces, but also the absence of stresses perpendicular to the Mode II cracks, which influences the true fracture ductility, as pointed up recently by Gao Hua et al [*6*].

Conclusions

Under all loading conditions, in isotropic steel wires, fatigue cracks have been shown to be Mode I cracks perpendicular to the principal normal stress σ_1. In anisotropic steel wires, however, longitudinal Mode II cracks appear as soon as the torsion to tension stress ratio equals 0.5. This changeover has been explained using the plastic zone size ratio δ of the two crack modes: in anisotropic materials, δ quite easily attains high values (>4), whereas in isotropic materials the maximum value is 3.72 at pure torsion. From calculations using this model for different anisotropies, it could be predicted at which stress state Mode II crack will appear.

References

[*1*] Gough, H. J. and Pollard, H. V. in *Proceedings,* Institution of Mechanical Engineers, London, Vol. 13, 1935, p. 3.

[*2*] Guest, J. J., *Engineering,* Vol. 155, 1943, p. 21.

[*3*] Brown, M. W. and Miller, K. J. in *Proceedings,* Institution of Mechanical Engineers, Vol. 187, No. 65, 1973, pp. 745–755.

[*4*] Lohr, R. D. and Ellison, E. G., *Fatigue of Engineering Materials Structures,* Vol. 3, No. 1, 1980, pp. 1–17.

[*5*] Smith, E. W. and Pascoe, K. J., *Fatigue of Engineering Materials Structures,* Vol. 6, No. 3, 1983, pp. 201–224.

[*6*] Gao Hua, Brown, M. W., and Miller K. J., *Fatigue of Engineering Materials Structures,* Vol. 5, No. 1, 1982, pp. 1–17.

[*7*] Brown, M. W., Liu, H. W., Kfouri, A. P., and Miller, K. J. in *Proceedings ICF-5,* Pergamon, London, 1981, pp. 891–898.

[*8*] Gil Sevillano, X., Van Houtte, P., Aernoudt, E., *Progress in Materials Science,* Vol. 25, Nos. 2–4, 1980, p. 410.

[*9*] Van Houtte, P., private communication.

[*10*] Gil Sevillano, X., Van Houtte, P., and Aernoudt, E. in *Proceedings,* 5th International Conference on Textures of Materials, Aachen, West Germany, Vol. II, 1978, pp. 495–503.

Damage Accumulation in Composite Materials

Michael S. Found[1]

A Review of the Multiaxial Fatigue Testing of Fiber Reinforced Plastics

REFERENCE: Found, M. S., "**A Review of the Multiaxial Fatigue Testing of Fiber Reinforced Plastics,**" *Multiaxial Fatigue, ASTM STP 853*, K. J. Miller and M. W. Brown, Eds., American Society for Testing and Materials, Philadelphia, 1985, pp. 381–395.

ABSTRACT: A number of multiaxial fatigue systems employed for the testing of fiber reinforced plastics (FRP) composites are discussed, and how they may be used to evaluate failure theories. The effects of anisotropy and end fittings are examined for different specimen geometries. A conservative failure criterion is suggested for predicting the biaxial static and fatigue strength of FRP based on limited test data.

KEY WORDS: biaxial stresses, triaxial stresses, fatigue strength, failure theory, specimen geometry, fiber orientation, anisotropy

Nomenclature

$\sigma_x,\sigma_y,\sigma_s$	Normal stresses and in-plane shear stress
$\sigma_1,\sigma_2,\sigma_6$	Stresses in the principal material directions and the in-plane shear stress
F_1,F_2,F_6	Strengths in the principal material directions and the in-plane shear strength
F_{1t},F_{2t}	Tensile strengths in the principal material directions
F_{1c},F_{2c}	Compressive strength in the principal material directions
F_{12}	Interaction component of strength tensor
θ	Orientation of the stress axes to the principal material axes
$\lambda = \sigma_x/\sigma_y$	Biaxial stress ratio

While fiber reinforced plastics (FRP) materials have been used for engineering structures and components for over 40 years it is only during the past decade that they have received wider attention and recognition, mainly due to the need to save weight and conserve energy. Glass reinforced plastics (GRP) are the largest group of FRP composites and are found extensively in the automotive and railway industries, building and construction industries, chemical and marine industries, and in domestic appliances, sports, and leisure equipment. Carbon

[1]Lecturer, Department of Mechanical Engineering, University of Sheffield, Sheffield, U.K.

Copyright© 1985 by ASTM International www.astm.org

fiber, mixed carbon, and glass fiber and aramid fiber (for example, Kevlar) composites are employed in more specialist applications where higher performance is required and higher cost is tolerated such as in aerospace components, helicopter rotor blades, and automotive drive shafts and springs. FRP components and structures are produced by a variety of manufacturing techniques, and it must be recognized that the design and manufacturing process have a significant effect on the final properties of a composite. With the continuing growth of the FRP industry in terms of both output and applications it is of increasing importance that safe-life design procedures are evolved for these materials so that their full potential is realized.

Safe-life design in FRP requires the development of analytical or empirical rules to cover a range of materials of varying degrees of anisotropy subjected to various loading and environmental conditions. The majority of engineering structures and components are subjected to long-term loading under variable complex stresses; however, most fatigue testing of FRP has involved the uniaxial loading of laboratory specimens in the direction of material orthotropy [*1*]. A significant reduction in strength or fatigue life results if either the applied stresses or the material axes change in orientation. The failure of FRP composites is known to be progressive and that damage in the form of debonding, resin cracking, delamination, or fiber fracture may occur before rupture. Furthermore it has been shown that damage under fatigue loading is more severe than for static loading for both uniaxial [*2*] and biaxial [*3,4*] stress conditions. Therefore, it is necessary for the designer to establish what amount of damage, if any, may be tolerated for a particular application. Visible damage is not normally tolerated by designers, and there is a tendency to over-design in order to avoid it.

An important phase of the design procedure is the selection of a suitable failure criterion which will enable the designer to predict failure under various service loading conditions. Many theories have been proposed for predicting the static strength [*5–18*] of FRP under complex stress conditions, and some of these have been applied to fatigue loading conditions [*4,15,17,19–22*]. In order to take account of possible different types of failure of the fiber, matrix, and interface a few micromechanical theories have been proposed [*23,24*]. These are generally more applicable to unidirectional and filament wound composites and more suitable for predicting first-ply failure. Failure theories for FRP are necessarily more complicated than yield theories developed for isotropic materials because the material strengths change with the direction and mode of loading and because of the various possible failure modes and damage states.

Failure theories are mathematical functions of the stresses and strengths which supposedly represent failures under all stress conditions. Many of the failure theories applied to FRP are extensions of those developed for isotropic metals which were extended to describe the failure of homogeneous, orthotropic materials, and have since been modified to account for quasi-homogeneous, anisotropic materials. Two theories based on strength tensors have been postulated to account for general anisotropy exhibited by FRP [*13,14*]. The theories generally fall into two distinct groups [*4,21*], one in which only direct substitution of the uniaxial strengths and in-plane shear strength is required and the other which in addition requires an interaction coefficient to be evaluated under complex stress conditions. The theories based on strength tensors permit the strength components to be transferred to the stress axes, all the other theories require the stresses to be transformed to the principal material axes before the failure theory can be applied.

A few theories have been particularly proposed in order to predict fatigue failure under complex stress conditions. Griffith and Baldwin [*15*] attempted to predict complex stress failures under static and fatigue loading by treating incipient yielding, fracture, and fatigue as separate failure conditions for a general state of stress. However, their theory requires the use of compliances and, therefore, assumes that the material is linearly elastic to failure. Hashin and Rotem [*24*] have suggested a failure criterion allowing for failure of fiber and matrix which for fatigue loading conditions is expressed in terms of three fatigue curves obtained from fiber, transverse, and shear loading. While the theory is essentially for first laminar failure, it is suggested that it can be extended to give plane stress fatigue of laminates. Both of these theories were supported by off-axis fatigue tests under uniaxial loading conditions. Francis et al [*22*] applied the Hill criterion [*7*] to fatigue failure which enabled the fatigue curve for thin-walled tubes subjected to combined stress states to be predicted from fatigue data for the uniaxial loading modes. The results of biaxial fatigue tests on cruciform specimens were used by Smith and Pascoe [*17*] to support a theory to account for different observed failure modes. However, it does not allow for differences in tensile and compressive strength and requires elastic constants as well as a uniaxial strength and in-plane shear strength to evaluate the theory.

Owen and Found [*4*] and Owen et al [*19–21*] using various failure theories have shown that it is possible to predict damage and rupture of thin-walled GRP cylinders subjected to biaxial static and fatigue loading conditions. From the results of several hundred tests on glass mat, fabric, and woven roving fabric cylinders it is still not possible to select a failure theory which will predict various stages of failure for all materials and stress conditions [*20*].

This paper reviews the various multiaxial fatigue systems employed for the testing of FRP and examines the effects of anisotropy on the choice of specimen geometry and associated test fittings. Existing multiaxial static and fatigue test data for FRP are presented, and a new failure criterion is suggested for predicting the biaxial static and fatigue strength of FRP.

Multiaxial Test Systems

With the development of servohydraulic testing machines and associated closed loop control systems it is now possible to perform fatigue tests under complex stress-strain conditions by various means. It is intended here to mention some of the loading systems employed in the fatigue testing of FRP and also to mention briefly other systems that have been mainly used for static testing to date. There are two principal methods of studying the complex stress behavior of FRP in order to evaluate failure theories under static and fatigue loading conditions, one utilizing flat specimens and the other using cylindrical specimens both with various means of applying the loads. Clearly flat specimens using hand layup or compression molding techniques are easier and cheaper to manufacture than cylinders. The latter are best made by filament winding to a mandrel. The more common forms of reinforcement may be also made into cylinders by wrapping on to a mandrel, but this is likely to result in some form of overlap or discontinuity in the reinforcement.

The simplest and most widely used method for evaluating failure theories is the off-axis test (Fig. *1a*). Here the applied stress, which may be tensile or compressive, is the principal stress σ_y, and the stresses with respect to the fiber axes depend on the fiber orientation. Most of the failure theories have been supported by data obtained from static off-axis tests to rupture [*8,10,11,14*]. Several workers [*15,25,27,28*] have reported off-axis fatigue tests but only Owen and Found [*28*] and Griffith and Baldwin [*15*] have used them to evaluate failure theories. Although this method is often used it has two serious limitations. For most off-axis orientations the applied stress induces bending and shear in the stress field when conventional clamping methods are used. For tensile loading it is suggested [*29*] that the problem can be overcome by using rotating grips and by the use of specimen with adequate length/width ratio. Clearly for compression testing the effects on end constraint are more severe since these specimens are relatively shorter in order to prevent buckling. Secondly, the use of the off-axis test only permits a very limited exploration of the failure surface as discussed later.

Bert et al [*30*] and Smith and Pascoe [*17*] used flat cruciform specimens (Fig. *1b*) as a means of simultaneously applying two principal stresses σ_x and σ_y. With this method it is relatively easy to produce specimens with different fiber orientations relative to the principal stress axes. Bert et al conducted static biaxial tension tests using a cable and pulley system reacted by a rigid frame to load the specimen. For biaxial static and fatigue tests Smith and Pascoe used a servohydraulic rig with the applied loads varied by actuators thus permitting the full range of biaxial ratio (λ) to be covered. In addition it was possible to vary the mean stress and stress amplitude on both loading axes for fatigue tests. With this specimen, stress and strain measurements are difficult, and sometimes it is not possible to prevent failures from initiating at the corner fillets. Other means of applying biaxial stresses to flat specimens include combined axial and shear loading (Fig. *1c*) using a hydraulic jack and shear links as described by Thor [*31*] and a diametrically loaded disk with asymmetric cutouts (Fig. *1d*) as used by Arcan et al [*32*] for static purposes. With both these methods there are difficulties in obtaining a uniform stress in the gage area.

A variety of methods have been used for applying biaxial stresses to cylinders such as (*a*) internal pressure and axial load, (*b*) external pressure and axial load, (*c*) torsion and axial load, and (*d*) combinations of all three by means of torsion,

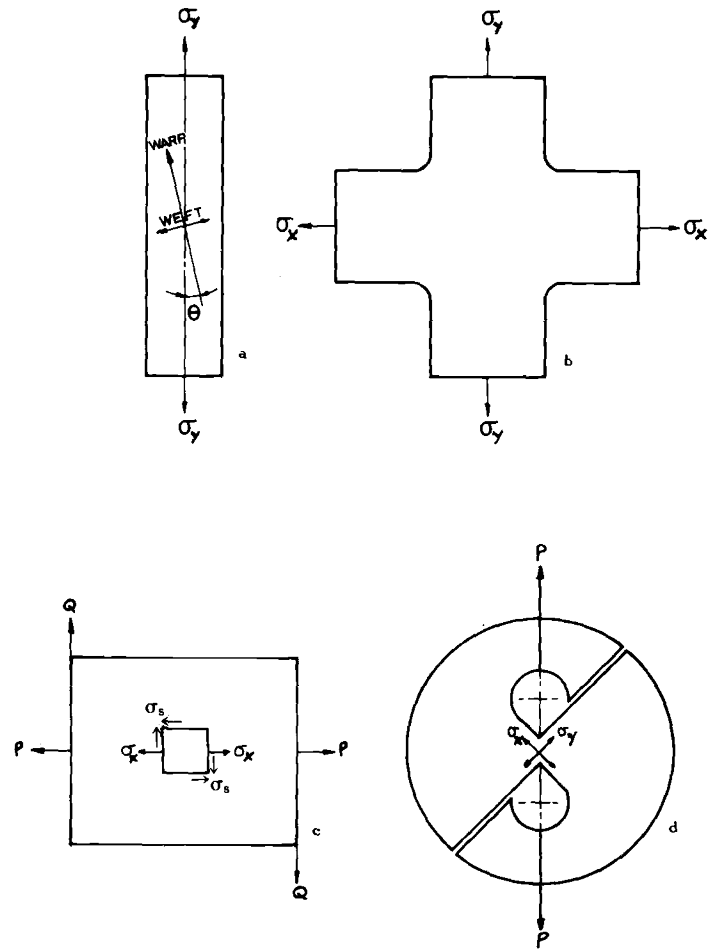

(*a*) Uniaxial specimen
(*b*) Cruciform specimen
(*c*) Plate specimen
(*d*) Disk specimen
FIG. 1—*Flat specimens.*

pressure, and axial load as shown in Fig. 2. With the exception of method (*c*) all these involve direct fluid pressure on the specimen. Fatigue endurance will be reduced due to the hydrowedge effect, and there may be also an environmental influence on crack initiation and propagation due to the fluid. However these effects may be minimized by the use of a suitable protective sleeve. For fatigue loading triaxial stress systems ($\sigma_z \neq 0$) are rarely considered, and, in the majority of cases, the pressure contribution to the stress field is insignificant unless the pressure is high enough to cause fatigue damage or failure. Clearly the cylinder is the most versatile specimen since it is possible to apply any desired biaxial

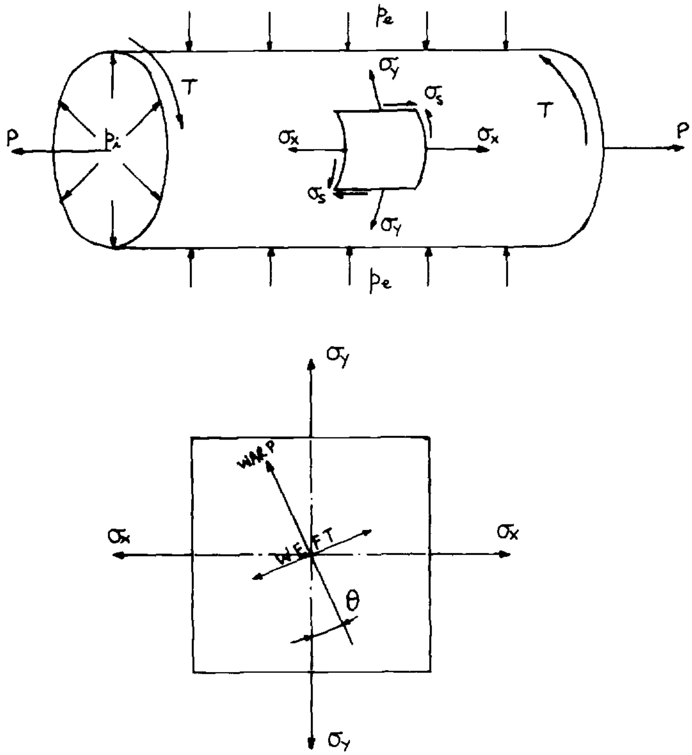

FIG. 2—*Cylindrical specimen.*

state of stress with or without proportional loading. The generalized state of plane stress can be achieved by independent application of axial loads, internal or external pressure, and torque, and such a fatigue testing facility for metals has been described by Found et al [*33*].

Much of the early biaxial stress fatigue data for FRP was obtained using thin-walled cylinders subjected to internal pressure [*34*] with values of $\lambda = 0.5$ or 0 depending on whether the cylinder ends were free or restrained, and on thick-walled cylinders subjected to external pressure [*35*] with similar stress ratios. Owen and Found [*4*] and Owen et al [*19–21*] tested various GRP thin-walled cylinders subjected to internal pressure and differing combinations of axial load to cover the range $\lambda = 1$ to -1 in a rig designed by the author [*3*]. The principal stresses are varied by use of a set of nine interchangeable rams of different diameters. Under fatigue loading conditions the ram friction is low enough to permit rotation of the pistons to accommodate the torsional displacements which occur in cylinders with off-axis fiber orientations. Damage and rupture tests were performed under static and fatigue loading, the latter using pulsating pressure. Francis et al [*22*] have described a biaxial testing facility using a biaxial actuator to apply axial load, internal pressure, or torsion or all three. The biaxial actuator is closed-loop, servocontrolled and can be driven in one of three modes for either or both axial or torsional loading. They performed fatigue tests on graphite epoxy thin-walled tubes containing a circular hole penetrating one wall midway along the tube length.

Protasov and Kopnov [*36*] have conducted static tests on GRP cylinders using different combinations of internal and external pressure, tensile, or compressive axial load and torsion. The oil is supplied from a single pump and the ratio σ_x:σ_y:σ_s is varied by using interchangeable cylinders of different diameters. Wu [*37*] has described similar static tests on graphite epoxy tubes using separate closed-loop rigs to apply internal pressure-axial load and tension-torsion.

It is well known that there may be significant heating effects in FRP under fatigue loading conditions. The heating effect depends on a number of factors including frequency, stress level, and specimen thickness. For biaxial fatigue tests Owen et al [*19–21*] and Smith and Pascoe [*38*] used frequencies less than 2 Hz while Francis et al [*22*] used frequencies up to 5 Hz.

Failure Surfaces

Many of the strength theories for anisotropic materials based on the distortional energy theory are particular cases of strength tensor theories [*13,14*] which are of the form

$$F_i \sigma_i + F_{ij} \sigma_i \sigma_j = 1 \tag{1}$$

and for plane stress conditions reduces to

$$F_1 \sigma_1 + F_2 \sigma_2 + F_{11} \sigma_1^2 + F_{22} \sigma_2^2 + 2 F_{12} \sigma_1 \sigma_2 + F_6 \sigma_6^2 = 1 \tag{2}$$

For plane-stress conditions the failure theories can be represented as failure surfaces by plotting the stresses σ_1, σ_2, and σ_6 in Cartesian space as shown in Figs. 3 and 4. It is assumed that the origin of the stress space should lie within the failure surface and that the surface should be closed for all combinations of stress. In order to ensure that the surface is closed, Tsai and Wu [*14*] introduced a stability criterion of the form

$$F_{ii} F_{jj} - F_{ij} \geq 0 \tag{3}$$

which for plane-stress conditions reduces to

$$F_{12} = \sqrt{F_{11} F_{22}} \tag{4}$$

While much of the experimental data used to support the failure theories was obtained from static off-axis tests to rupture it has since been shown [*28,37,39,40*]

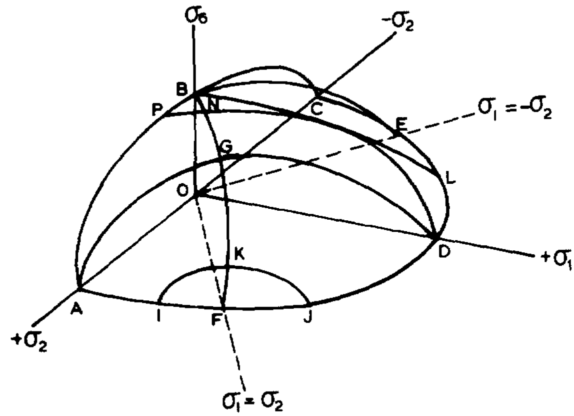

FIG. 3—*Partial failure surface.*

that off-axis tests do not discriminate between failure theories because only a small part of the failure surface is examined. For off-axis tension testing it is only possible to explore the curve DGA in Fig. 3 and a comparable curve in the compressive quadrant. Furthermore small differences in the observed strengths make considerable differences to the shape of the failure surface. The predicted surfaces are often unaccepted because they are either open ended or they appear to intersect [*28*].

Clearly the use of thin-walled cylinders with various means of producing biaxial stresses as shown in Fig. 2 offers the most comprehensive way of exploring the complete failure surface. For example, for internal pressure and axial load ($\sigma_6 = 0$ and $\theta = 0°$) the boundary AFDEC (Fig. 3) can be defined. For external pressure and axial load the boundary is given by AD′C (Fig. 4) and for torsion by BE (Fig. 3). With combinations of axial load, pressure, and torsion, the complete surface can be explored. For tubular specimens Wu [*37*] has recommended optimum principal stress ratios for evaluating the interaction coefficient F_{12}.

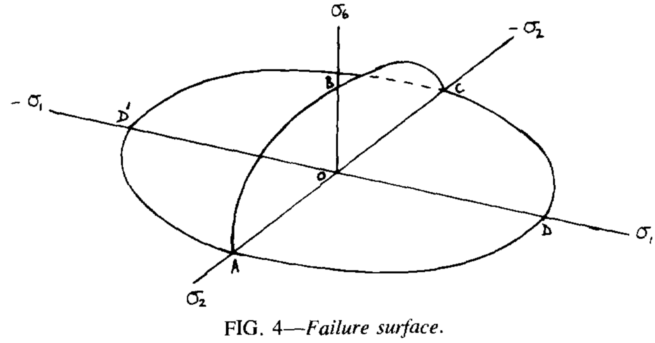

FIG. 4—*Failure surface.*

Specimen Geometry

In order to carry out meaningful tests of FRP it is necessary that the specimen be designed to produce a reasonably uniform stress field in the gage section. The effects of anisotropy must be fully understood, since they can give rise to nonuniform stress fields, stress gradients, end effects, and size effects in both flat and cylindrical specimens. Furthermore Puppo and Evensen [*41*] have indicated that the same stress field is not developed in these two specimens even though the loading and laminate configuration are identical. They likened a cylinder to an infinite laminate such that the interlaminar shear stress would be zero everywhere, while for a flat specimen the interlaminar shear stresses reach a finite maximum value at the edges. Axial fatigue tests [*42*] on glass/epoxy and boron/epoxy specimens with three different geometries each with fiber orientations of $\pm 45°$ showed differences of more than 4 to 1 on fatigue strength.

Pagano and Halpin [*43*] have presented an analytical solution and Rizzo [*44*] a finite-element solution to determine the effects of rigid clamping on off-axis flat specimens with and without end rotation. By reinforcing the ends with a compliant material Richards et al [*45*] have shown that the analysis can be used to design suitable specimens. For long specimens ($l/w > 10$) good accuracy can be obtained, regardless of end conditions and method of calculation. Schneider [*39*] has suggested that the variation in off-axis tensile strength may be due to ineffective loading of fibers which are discontinuous within the gage length, and Endo et al [*27*] have observed apparent size effects under similar fatigue loading conditions.

To eliminate bending and twisting effects induced by in-plane loading of cruciform specimens development tests were carried out by Bert et al [*30*] and Smith and Pascoe [*38*]. In order to obtain a uniform biaxial stress field Bert used a reduced center section with a circular profile for $\lambda = 1$ and an elliptical profile for $\lambda = 0.5$ and 2. Both groups of workers used metal tabs as a means of transferring the load from the machine to the specimen.

For cylindrical specimens there are a number of requirements which must be met in order to have confidence in the test results. The cylinder may be treated as being thin-walled provided the stresses are reasonably uniform in the gage section. The length must be sufficient to overcome end effects and yet prevent buckling under compressive loads. The specimen must be stable under internal pressure or torsion. For cylinders it is usually necessary to reinforce the ends of the specimen in order to attach grips and prevent end failures. Lockett [*46*] has examined the effects of anisotropy and inhomogeneity on GRP pipe and suggested that wall thickness effects are more significant than material anisotropy. Inhomogeneities due to fabrication and joining techniques can induce bending strains as large as the primary strains due to pressure.

A number of workers [*36,47,48*] have analyzed the design requirements of anisotropic cylinders and have suggested limiting diameter/thickness ratios and relationships between gage length and transition length in order to achieve an almost uniform stress in the gage section. Indeed Pagano et al [*49*] have shown by elastic analysis that a uniform state of stress cannot exist in a helical wound tube unless the shear coupling compliance S'_{16} is zero. In order to try to minimize the many problems, special end fittings have been employed and complex specimen geometries have been evolved. Miller [*50*] used contoured end plugs for cylinders under external pressure in order to prevent high interlaminar shear stresses at the ends and reduce bending stresses in the cylinder. This probably offers the cheapest and most practical solution, since it applies to all configurations although different contours may be required for different loading conditions. Daniel et al [*51*] conducted finite element analyses to study the load transfer at the ends of cylinders with tabs. To minimize the effects of tab constraints, compensating pressures were applied to the tabs. They concluded that it was possible to conduct valid biaxial tests with properly designed tubular specimens and load transfer system. This is a rather complex and expensive method and needs modifying for each different material configuration. Duggan and Bailie [*52*] have suggested the use of a constant compliance specimen as a means of achieving uniform biaxial stress distributions in laminated cylinders. In their specimen the laminate plies are reduced to zero thickness the further into the tab they go, while corresponding increase in thickness of the tab material is made. This is probably the most effective solution, since it is possible to provide a stiffness smoothing in the critical transition region and also offers a more compliant tabbing material for embedding in rigid machine grips.

Failure Modes

Since failure theories are mathematical functions of stresses and strengths which do not account for mechanisms or modes of failure, it is necessary to consider the progression of damage in order to understand possible anomalies in the failure surface. Progressive failure may not be confined to one mode and is affected by the properties of the fiber, resin and interface, and the structure of the reinforcement. For static tensile loading it usually takes the following form. Debonding occurs within fibers normal to the applied load, resin cracking progresses from transverse fiber groups into resin rich areas, the cracks cross aligned fibers permitting the aligned fibers to debond, leading to fiber fracture and rupture [*3*]. Compressive loading of woven fabrics produces damage at ply crossovers leading to delamination or local buckling of unsupported surface fibers. Compressive failure may occur on a single or multiple shear-type plane [*3*]. Damage under fatigue loading conditions is more intense than for static loading [*2*].

For cylindrical specimens subjected to complex stress different damage modes may exist which interact with each other to produce a complex final fracture. It is also possible for damage to be initiated in say the tensile mode and final fracture to be in the compressive mode. The failure of GRP cylinders has been shown [*3*] to be stress ratio dependent and is governed by the mode of the axial stress, a tensile stress is more damaging than a compressive stress of the same magnitude. Failure is governed by the severity of resin cracking and is most severe when the biaxial stresses are both tensile.

Discussion

In the published literature there are several references relating to the biaxial static failures of FRP and relatively few references on biaxial fatigue tests. For the purposes of this paper it is only intended to examine the results where both static and fatigue data are available for the same material. While this is rather restrictive it readily permits comparison of failure theories under both static and fatigue loading conditions and for design purposes there are advantages in being able to apply the same theory for both conditions.

The data examined include cylinders made with glass mat, fabric, and woven roving fabric [*4,19–21*], and cruciform specimens made with woven roving fabric [*17,53*]. Various polyester resin systems have been used, and some of the materials exhibit different tensile and compressive strengths. For the fabric and woven roving fabric specimens, all results are for tests in which the material and stress axes are coincident. The biaxial static data are presented in Fig. 5 and the stresses in the principal material axes have been normalized to the appropriate uniaxial strengths. Similarly in Fig. 6 the fatigue stresses at 10^6 cycles have been normalized to the uniaxial fatigue data at 10^6, with the exception of the cruciform tests for which data are given for 10^5 cycles [*17*]. In Figs. 5 and 6 the failure stresses are for catastrophic failure. At the present time there is only very limited data for damage under biaxial stress conditions [*4,19,20*]. In some cases the data in Fig. 5 represent single tests, in others they are an average of a few tests. The fatigue results in Fig. 6 represent the fatigue strengths picked off from the best fit line of the fatigue curves at 10^6 cycles (or at 10^5 cycles [*17*]).

It is not practicable here to compare the results for each material with each of the failure theories. However the significance of the results is that much of it falls within the boundary of the maximum stress theory. In the tension/tension quadrant a circular arc has been drawn and a straight line drawn in the tension/compression quadrant. For the static test data shown in Fig. 5 only one point in each quadrant lies within these boundaries. Therefore, the boundaries would represent for design purposes a conservative estimate of failure for a number of materials.

The data shown in Fig. 6 for fatigue loading show similar trends to the static case except, as is usual for fatigue loading, there is much more scatter. Furthermore, there are two points in the tension/tension quadrant well within the circular arc boundary, and a single point is well within the boundary of the tension/compression quadrant. The offending points in the tension/tension quadrant are those for a glass mat [*4,19*] and showed excessive resin cracking. Some of this may have been caused by joints necessary in the manufacture of cylinders, which has little effect under static loading but has a significant effect under fatigue loading [*19*]. The single offending result in the lower quadrant is probably

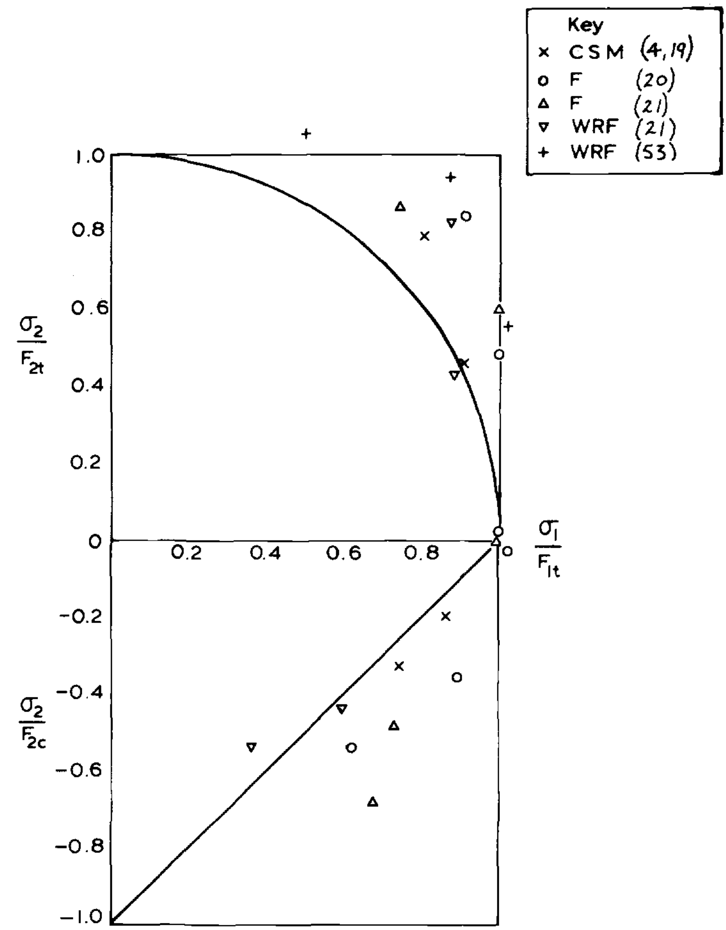

CSM = chopped strand mat.
F = fabric.
WRF = woven roving fabric.

FIG. 5—*Normalized biaxial static results.*

caused by variations in the failure mode and may have shown some signs of buckling [*21*].

Allowing for the preceding factors it is suggested that the boundaries provide a reasonably conservative estimate of failure for design purposes for most materials, for both biaxial static and fatigue loading conditions. The boundaries can be expressed in the following mathematical form for the tension/tension quadrant

$$\left(\frac{\sigma_1}{F_{1t}}\right)^2 + \left(\frac{\sigma_2}{F_{2t}}\right)^2 = 1 \tag{5}$$

(which is the Norris interaction theory [*9*])

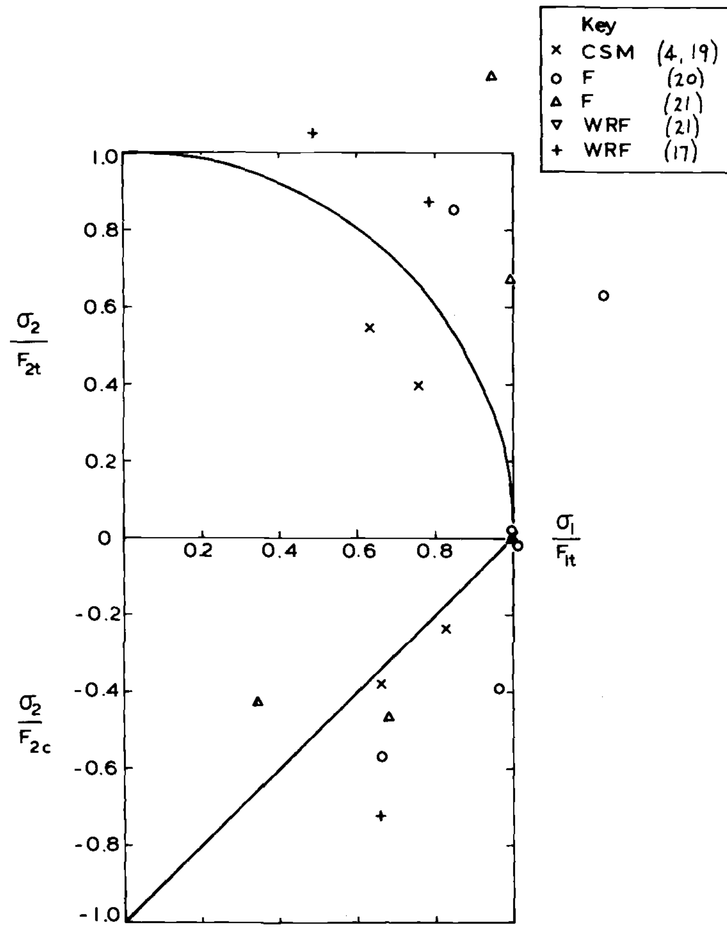

CSM = chopped strand mat.
F = fabric.
WRF = woven roving fabric.

FIG. 6—*Normalized biaxial fatigue results.*

and for the tension/compression quadrant

$$\frac{\sigma_1}{F_{1t}} - \frac{\sigma_2}{F_{2c}} = 1 \tag{6}$$

(which is the maximum shear stress theory)

Clearly further work is needed to investigate this apparently simple failure theory and it should be extended to cover various damage states.

Conclusions

This paper has attempted to review the multiaxial fatigue testing of fiber reinforced plastics and has discussed various test methods and specimen geometries used for such tests. A limited amount of test data have been examined for biaxial stress tests under static and fatigue loading conditions. It is suggested that a conservative estimate for design purposes is that failure in the tension/tension quadrant is given by a circular arc and by a straight line in the tension/compression quadrant such that failure is governed respectively by

$$\left(\frac{\sigma_1}{F_{1t}}\right)^2 + \left(\frac{\sigma_2}{F_{2t}}\right)^2 = 1$$

and

$$\frac{\sigma_1}{F_{1t}} - \frac{\sigma_2}{F_{2c}} = 1$$

Further work is necessary in order to confirm these proposals, and it should be extended to cover various damage states.

References

[*1*] Owen, M. J. in *Glass Reinforced Plastics*, 1st edition, B. Parkyn, Ed., Iliffe Books, London, 1970, Chapter 18, p. 253.
[*2*] Smith, T. R. and Owen, M. J., *Proceedings*, 6th International Reinforced Plastics Conference, Paper 27, British Plastics Federation, London, 1968.
[*3*] Found, M. S., "Biaxial Stress Fatigue of Glass Reinforced Plastics," Ph.D. thesis, University of Nottingham, U.K., 1972.
[*4*] Owen, M. J. and Found, M. S., Faraday Special Discussions of the Chemical Society, No. 2, 1972, pp. 77–89.
[*5*] Stowell, E. Z. and Liu, T. S., *Journal of Mechanics and Physics of Solids*, Vol. 9, 1961, p. 242.
[*6*] Waddoups, M. E., "Advanced Composite Material Mechanics for the Design and Stress Analyst," Report FZM 4763, General Dynamics, Forth Worth Division, 1967.
[*7*] Hill, R., *Proceedings*, Royal Society, Series A., Vol. 193, 1948, p. 281.
[*8*] Azzi, V. D. and Tsai, S. W., *Experimental Mechanics*, Vol. 5, No. 9, 1965, p. 283.
[*9*] Norris, C. B. and McKinnon, P. F., "Compression, Tension and Shear Tests on Yellow-Poplar Plywood Panels of Sizes that do not Buckle with Tests Made at Various Angles to the Face Grain," Report No. 1328, U.S. Forest Products Laboratory, 1956.
[*10*] Norris, C. B., "Strength of Orthotropic Materials Subjected to Combined Stresses," Report No. 1816, U.S. Forest Products Laboratory, May 1962.
[*11*] Hoffman, O., *Journal of Composite Materials*, Vol. 1, No. 2, 1967, p. 200.
[*12*] Franklin, H. G., *Fibre Science and Technology*, Vol. 1, No. 2, 1968, p. 137.
[*13*] Gol'denblat, I. I. and Kopnov, V. A., *Polymer Mechanics*, Vol. 1, No. 2, 1965, p. 54.
[*14*] Tsai, S. W. and Wu, E. M., *Journal of Composite Materials*, Vol. 5, 1971, p. 58.
[*15*] Griffith, J. E. and Baldwin, W. M., *Proceedings*, 1st Southeastern Conference on Theoretical and Applied Mechanics, Gatlinburg, TN, 1962, pp. 410–420.
[*16*] Puppo, A. H. and Evensen, H. A., *Journal of the American Institute of Aeronautics and Astronautics*, Vol. 10, No. 4, 1972, pp. 468–474.
[*17*] Smith, E. W. and Pascoe, K. J., *Proceedings*, 2nd International Conference on Mechanical Behaviour of Materials, Boston, 1976, pp. 941–945.
[*18*] Soden, P. D., Leadbetter, D., Griggs, P. R., and Eckold, G. C., *Composites*, Vol. 9, 1978, pp. 247–250.

[19] Owen, M. J., Griffiths, J. R., and Found, M. S., *Proceedings*, International Conference on Composite Materials, Vol. 2, American Institute of Mining, Metallurgical, and Petroleum Engineers, 1976, pp. 917–941.
[20] Owen, M. J., Rice, D. J., Griffiths, J. J., and Found, M. S., 35th Annual Technical and Management Conference, Reinforced Plastics/Composites Institute, Society of the Plastics Industry, Paper 23 F, 1980.
[21] Owen, M. J. and Rice, D. J., *Composites*, Vol. 12, No. 1, 1981, pp. 13–25.
[22] Francis, P. H., Walrath, D. E., Sims, D. F., and Weed, D. N., *Journal of Composite Materials*, Vol. 11, 1975, pp. 488–501.
[23] Puck, A. and Schneider, W., *Plastics and Polymers*, Vol. 37, No. 127, 1969, pp. 33–44.
[24] Hashin, Z. and Rotem, A., *Journal of Composite Materials*, Vol. 7, 1973, p. 448.
[25] Werren, F., "Supplement to Fatigue Tests on Glass Fabric Base Laminates Subjected to Axial Loading," No. 1823B, U.S. Forest Products Laboratory, 1956.
[26] Endo, K. and Watanabe, M., 14th Japanese Congress on Materials Research—Non Metallic Materials, 1971, p. 120.
[27] Endo K., Yano, A., and Okuda, Y., 9th Japanese Congress on Testing Materials—Non Metallic Materials, 1966, p. 104.
[28] Owen, M. J. and Found, M. S., *Journal of Physics D: Applied Physics*, Vol. 8, 1975, pp. 480–497.
[29] Pagano, N. J. and Halpin, J. C., *Journal of Composite Materials*, Vol. 2, No. 1, 1968, p. 18.
[30] Bert, C. W., Mayberry, B. L., and Ray, J. O. in *Composite Materials Testing and Design, STP 460*, American Society for Testing and Materials, 1969, pp. 362–380.
[31] Thor, S. E., *Proceedings*, 3rd International Conference on Composite Materials, Vol. 1, Paris, 1980, pp. 866–874.
[32] Arcan, M., Hashin, Z., and Voloshim, A., "A Method to Produce Uniform Plane-Stress with Application to Fibre Reinforced Materials," *Experimental Mechanics*, Vol. 18, No. 4, April 1978, pp. 141–146.
[33] Found, M. S., Fernando, U. S., and Miller, K. J., this publication, pp. 11–23.
[34] Hanson, M. P., "Tensile and Cyclic Fatigue Properties of Graphite Filament Wound Pressure Vessels at Ambient and Cryogenic Temperatures," Technical Report TND 5354, National Aeronautics and Space Administration, Washington, DC, 1969.
[35] Cornish, R. H., Nelson, H. R., and Dally, J. W., *Proceedings*, 19th Annual Technical Conference, Society of the Plastics Industry, 1964, Section 9E.
[36] Protasov, V. D. and Kopnov, V. A., *Polymer Mechanics*, Vol. 1, No. 5, 1965, p. 26.
[37] Wu, E. M., *Journal of Composite Materials*, Vol. 6, 1972, p. 472.
[38] Smith, E. W. and Pascoe, K. J., *Composites*, Vol. 8, 1977, pp. 237–243.
[39] Schneider, G. J., *Fibre Science and Technology*, Vol. 5, 1972, pp. 29–35.
[40] Pipes, R. B. and Cole, B. W., *Journal of Composite Materials*, Vol. 7, 1973, pp. 246–256.
[41] Puppo, A. H. and Evensen, H. A., *Journal of Composite Materials*, Vol. 4, 1970, p. 204.
[42] Lucas, J. J. and Sainsbury-Carter, J. B., *Journal of Materials*, Vol. 4, No. 7, 1972, pp. 586–589.
[43] Pagano, N. J. and Halpin, J. C., *Journal of Composite Materials*, Vol. 2, No. 1, 1968, pp. 18–31.
[44] Rizzo, R. R., *Journal of Composite Materials*, Vol. 3, 1969, pp. 202–219.
[45] Richards, G. L., Airhart, T. P., and Ashton, J. E., *Journal of Composite Materials*, Vol. 3, 1969, pp. 586–589.
[46] Lockett, F. J., *Composites*, Vol. 11, No. 4, 1980, pp. 209–216.
[47] Rizzo, R. R. and Vicario, A. A., *Journal of Composite Materials*, Vol. 4, 1970, pp. 344–359.
[48] Pagano, N. J. and Whitney, J. M., *Journal of Composite Materials*, Vol. 4, July 1970, p. 360.
[49] Pagano, N. J., Halpin, J. C., and Whitney, J. M., *Journal of Composite Materials*, Vol. 2, 1968, p. 154.
[50] Miller, R. J., *Composite Materials Testing and Design, STP 460*, American Society for Testing and Materials, 1969, pp. 150–159.
[51] Daniel, I. M., Liber, T., Vanderby, R., and Koller, G. M., *Proceedings*, 3rd International Conference on Composite Materials, Vol. 1, Paris, 1980, pp. 840–855.
[52] Duggan, M. F. and Bailie, J. A., *Proceedings*, 3rd International Conference on Composite Materials, Vol. 1, Paris, 1980, pp. 900–913.
[53] Smith, E. W., "Cyclic Biaxial Deformation and Failure of a Glass Fibre Reinforced Composite," Ph.D. thesis, University of Cambridge, U.K., 1976.

John C. Radon[1] and Christopher R. Wachnicki[1]

Biaxial Fatigue of Glass Fiber Reinforced Polyester Resin

REFERENCE: Radon, J. C. and Wachnicki, C. R., "**Biaxial Fatigue of Glass Fiber Reinforced Polyester Resin,**" *Multiaxial Fatigue, ASTM STP 853,* K. J. Miller and M. W. Brown, Eds., American Society for Testing and Materials, Philadelphia, 1985, pp. 396–412.

ABSTRACT: Fatigue crack growth tests were carried out on chopped strand mat polyester resin under biaxial tensile stress. Center-notch specimens were used to measure the effects of the load biaxiality factor, B, defined as the ratio of the load acting normally to the crack line and that acting parallel to it. A compliance calibration technique was used to measure the crack growth so as to overcome difficulties with visual measurement when using conventional stress-intensity factors in order to present the fatigue results on a fracture mechanics basis. An adaptation of the compliance technique was also used to extend the applicability of the stress-intensity factor concept to planar composite materials by proposing a K-equation that takes into account the effects of reinforcement geometry and biaxial stress. This allows a safe life crack growth criterion to be used more effectively to assess damage tolerance, taking account of a number of detrimental intrinsic effects due to the nature of the composite reinforcement. The Paris power relationship was found to be applicable to the results, the analysis of which shows that nonsingular stresses do affect the behavior of a crack subjected to plane stress cyclic loading. Biaxial stresses were found to produce a shift in the fatigue crack propagation rates, notably a decrease in the Paris exponent with increase in the load biaxiality factor, B. Analysis of the fatigue behavior indicates the failure mechanisms are influenced by the reinforcement geometry of the composite material, together with the Poisson's ratio of the material under biaxial stress. It would seem that the fatigue behavior is governed by the fiber-resin interface at low stress levels, while at higher stresses the Poisson's ratio of the composite determines the biaxial influence.

KEY WORDS: fatigue crack growth, polyester resin, biaxiality factor, biaxial fatigue, corrosion fatigue, fatigue damage zone, moiré fringe technique

The influence of stress biaxiality on crack growth and toughness has received considerable interest especially where certain isotropic materials have shown a significant biaxiality effect [*1*]. However, no explanation is available as yet within the framework of linear elastic fracture mechanics which is normally applicable to these materials. Since the linear elastic theory indicates that stresses applied parallel to the crack do not produce a stress singularity, it has generally

[1]Research fellows, Department of Mechanical Engineering, Imperial College of Science and Technology, London, U.K.

Copyright© 1985 by ASTM International www.astm.org

been assumed that the fatigue and fracture properties of a material are independent of biaxial stresses.

Real materials such as composites do not exhibit linear elastic behavior near a crack tip so that fracture mechanics investigations have met with mixed results mainly because most current approaches simply mimic the applications of linear elastic fracture mechanics to conventional engineering materials. This suggests that there are still many unanswered questions concerning the fundamental mechanisms which control fatigue and fracture in fiber reinforced plastics. The use of glass fiber-reinforced resins in the manufacture of pipes, storage tanks, and pressure vessels for the chemical process industries, which are generally under a state of biaxial stress, has highlighted their capability for strength and corrosion resistance. There is concern that the performance of such materials may suffer from the biaxiality effects of stress especially under dynamic loading conditions in the presence of inherent cracks. The present work is part of a program to study biaxiality effects on fatigue crack propagation in a fiber-reinforced plastic subjected to corrosive environments.

The experimental study indicates for the material and the specimens considered that biaxial stresses do affect the behavior of a crack to a certain extent. The fatigue model examined in this paper to determine whether the biaxial effects observed experimentally could be explained analytically was that of conventional fracture mechanics, so that a relationship was sought between the crack growth rate, da/dN, and the stress-intensity factor range, ΔK.

Stress Analysis

Linear elastic analysis indicates that stresses applied parallel to a crack do not contribute to the stress-intensity factor, and so it has been assumed that there is no difference between the fracture properties of biaxially and uniaxially stressed plates. However, analysis of the problem of a plane infinite elastic body with a centrally located crack subjected to a uniform biaxial load along the remote outer boundaries, indicates that loads applied parallel to the crack influence the value of the critical tensile load applied perpendicularly to it. The Poisson's ratio of the material determines the characteristics of this influence [*2*]. Sih [*3*] has considered the Griffith energy criterion for an elliptical crack in an elastic plate under biaxial loading, for which a sharp crack indicated the critical fracture stress to be independent of the stress applied parallel to the crack line. An alternative approach would be to consider fracture as a function of crack opening displacement [*4*], which can be related directly to the stress-intensity factor and the strain energy release rate. The physical model utilized in this study was that illustrated in Fig. 1. A straight crack of length $2a$ in a square plate of width W is subjected to stresses σ_y and $\sigma_x = B\sigma_y$ on the boundaries parallel to and normal to the crack line, respectively, where B is the stress biaxiality factor. The effect of biaxial stresses on the crack opening displacement could be examined by assuming that a crack opens under σ_y and then is constrained by σ_x which

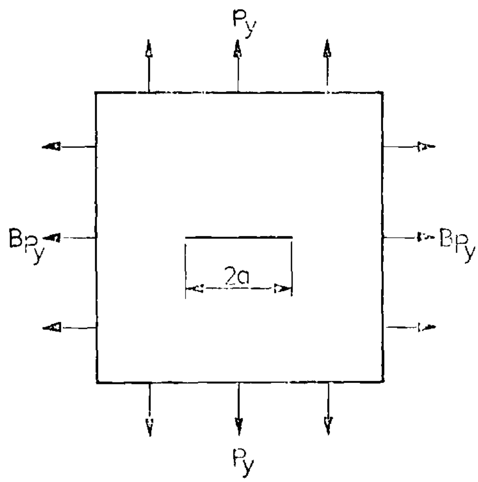

FIG. 1—*Centrally-notched plate under biaxial stress.*

produces only a higher order effect on the resulting crack opening displacement. Thus, elastic analysis indicates that biaxial stresses would produce at best only a second-order effect on the fracture properties of ideally elastic materials.

An exact analysis of the crack-tip stress, strain, and displacement fields is not available due to the complexity of the elastic-plastic problem. Many studies report measurements of critical stress-intensity factors for composite materials [*5,6*]. It is significant to note that, in general, reasonable agreement exists between different measurements for similar materials, in spite of the numerous reinforcement geometries, the different stress intensity factor-calibration functions, and the various test specimens employed. Stress distributions in the crack tip vicinity for anisotropic bodies have been calculated [*7*] and would seem to form the basis of a natural extension of the theory to composite materials. Unfortunately it is impossible here to distinguish a single invariant material parameter having the same significance as the stress intensity factor in the fracture of isotropic materials. Wu [*8*] has investigated the conditions under which linear elastic fracture mechanics (LEFM) may be applied to composites. He found that the approach was valid provided that: (*a*) the orientation of the crack is fixed with respect to the principal axes of symmetry; (*b*) the crack growth coincides with one of the principal axes of symmetry; (*c*) the stress intensity factors defined for the anisotropic case are consistent with those of the isotropic case in terms of stress distribution and crack displacement modes. While these conditions may appear quite restrictive, the fact is that in many practical cases the loading direction of crack growth coincides with one of the principal elastic axes, and hence LEFM may be applied.

The significance and limitations of the stress intensity factor K as a crack-tip stress field characterizing parameter in the present context are best explained by reference to the Williams stress field solution for a semi-infinite crack [9]. This yield stresses as

$$\sigma_{ij} = \sum_{n=1}^{\infty} (a_n \, r^{(n/2-1)} f_n (\theta) + b_n \, r^{(n/2-1)} g_n (\theta)) \tag{1}$$

where

r, θ = a coordinate system based on crack tip and line of prolongation,
a_n = coefficients determining the symmetrical part of the stress field, and
b_n = those fixing the anti-symmetrical part.

At $r = 0$ only a_1 and a_2 contribute to the stress field; a_1 is directly related to K_1 and a_2 to $\sigma_x = B\sigma_y$, but the former dominates due to the $r^{-1/2}$ singularity. As r increases $a_1 r^{1/2}$ falls to a value comparable to that of a_2, while a_3 and subsequent terms increase. A radius can be specified bounding an inner region, the form of whose stress field is independent of the particular boundary conditions, and so it is fully characterised by K and independent of stress biaxiality.

In real materials this solution is modified by plastic flow during loading, which blunts the crack and smooths out the stress singularity. If the size of the crack-tip plastic zone, r_p is small compared to the characteristic dimensions of the specimens, the applicability of LEFM is normally justified on the basis that r_p will lie well within the inner region. Although such a plastic zone develops near the crack tip in the resin matrix of composite materials, the dominant phenomenon in a cracked loaded composite is the development of a damage zone, also sometimes termed a debonding zone. The creation of a damage zone has been reported for chopped strand mat composites [*10*], and is commonly considered analogous to a plastic zone in homogenous materials. The plastic flow patterns within the damage zone must be controlling the separation mechanisms within the inner region and allow primary features such as the biaxiality parameter B of the outer stress field to penetrate the plastic zone, thus modifying the mechanics of crack extension and undermining the characterizing power of K. Since the true fatigue crack extension is a direct result of elastic-plastic crack tip deformation, this seems to be the best method for studying the effects of stress biaxiality on composite materials.

The conditions near the crack tip are quite complicated especially in a composite material, and the mechanics which control fatigue are not yet well understood. Investigations on a more theoretical basis have tried to use simplified plasticity models so as to provide some useful information on the dependence of various crack-tip quantities on stress biaxiality. Applying von Mises criterion to the inner region stress field solution it can be shown that if the stress normal to the crack line is held constant the estimated plastic zone size increases as the stress parallel to the crackline is increased. Irwin's estimate [*11*] of the plastic zone dimension, r_y used to account for crack-tip plasticity in the calculation of stress intensity factor K is

$$r_y = K^2/2\pi\sigma_{yp}^2 \tag{2}$$

where σ_{yp} is the yield stress of the material. If it is assumed that the applied biaxial stresses σ_y and σ_x simply modify the uniaxial yield strength of the material, then σ_{yp} may be assumed to be a function of the external stress system. However, these analyses do not adequately explain the effect of biaxial stresses on plane stress fracture as the models are extreme simplifications of the complicated state which exists at the crack tip.

It has been shown [*12*] that cracks grown in polymers under biaxial stress, whose transverse component σ_x exceeds the normal component σ_y, do so in an S-shaped curve centered on the original straight crack. Stress intensity factors for such a crack are estimated by superposition of related known solutions. On the assumption that crack extension takes place with opening displacements only at the crack tip the dependence of the crack path on the stress biaxiality can be explained. Cotterell [*13*] developed a theoretical analysis to explain cases in which the fracture path deviated from its expected direction. In his work he defined two classes of fracture: Class I, fractures which return to their original direction after any small deviation—path stable; Clase II, fractures which never return to their original direction after deviations—path unstable. For a biaxially loaded plate with a rectilinear crack (Fig. 1), the coefficient a_2 of William's expansion [*14*] becomes $(B - 1)\,\sigma_y$. Therefore according to Cotterell's criterion, it follows that at $B < 1$ the rectilinear crack propagation should be path-stable and at $B > 1$ path unstable.

Analysis of Fatigue Crack Growth Data

Fracture mechanics concepts have been used successfully in describing the behavior of cracks in composite materials [*15*] where the stress intensity factor, K, was employed to model the crack propagation data obtained from the fatigue tests. In the present work Irwin's tangent formula [*15*] was used in a fourth order polynomial form

$$Y = 1.772 - 0.057\lambda + 1.405\lambda^2 - 1.317\lambda^3 + 3.087\lambda^4 \tag{3}$$

for the solution

$$\Delta K = \Delta\,\sigma\,Y\,a^{1/2} \tag{4}$$

where

σ = gross stress,
Y = finite width (CN) correction factor, and
λ = normalized crack length $2a/W$.

The fatigue cycle is usually described by ΔK, which is equated to $(K_{max} - K_{min})$ where K_{max} and K_{min} are values of the opening mode stress intensity factor K_I, calculated from the maximum and minimum stress, respectively, during the fatigue cycle for a stress ratio of $R = K_{min}/K_{max}$. It has been conventional to express fatigue crack growth results as a log (da/dN) versus log (ΔK) curve using the Paris relationship [16]

$$da/dN = C\,(\Delta K)^m \tag{5}$$

where

N = number of cycles,
a = crack length,
C = material constant, and
m = exponent.

Experimental Method

The cruciform specimens for biaxial fatigue testing were molded individually using the "hand layup" technique, the laminates being impregnated with an E glass fiber chopped strand mat reinforcement. To minimize edge-wicking effects the external surfaces of the laminate were molded integrally with a C-glass reinforcement gel coat. The matrix was Atlac 382-05A bis-phenol resin supplied by Imperial Chemical Industries (ICI) and catalyzed with 4 g of benzoyl peroxide (lucidol CH50) and 0.3 mL of dimethylanaline accelerator per 100 mL of resin. After lamination had been completed the molded specimens were left to cure for 24 h at room temperature and then post-cured for a further 3 h at 80°C. The cruciform specimen blanks were then machined to the dimensions presented in Fig. 2, which shows a modified center notched biaxial specimen of 3.4 mm nominal thickness. This design is the fourth of a series of such specimens initiated by a previous photoelastic investigation [17], the biaxial specimen was designed to minimize interaction between two orthogonally applied loads; this was kept to below 3% over a load biaxiality range of $0 < B < 2$.

Fatigue tests were carried out on a specially built biaxial fatigue rig [18], a horizontal testing machine of an electrohydraulic type cycling from zero to a maximum load amplitude of 30 kN at a cyclic frequency range of 0.1 to 1 Hz (Fig. 3). The biaxial fatigue rig is based on a single double-acting actuator dividing a single uniaxial force into two orthogonal components of known and controllable magnitude. The arrangement of linkages and levers provide direct tension stresses for a range of load biaxiality ratios from $B = 0$ to 4. To study the effects of stress biaxiality, fatigue tests were carried out at a constant load range and biaxiality factor B until they fractured in dilute sulfuric acid of 5% concentration at room temperature. To obtain fatigue data at high biaxiality ratios and high fatigue loads, the use of an acidic environment was necessary due to the physical limitations of the test facility and the inherent high toughness and

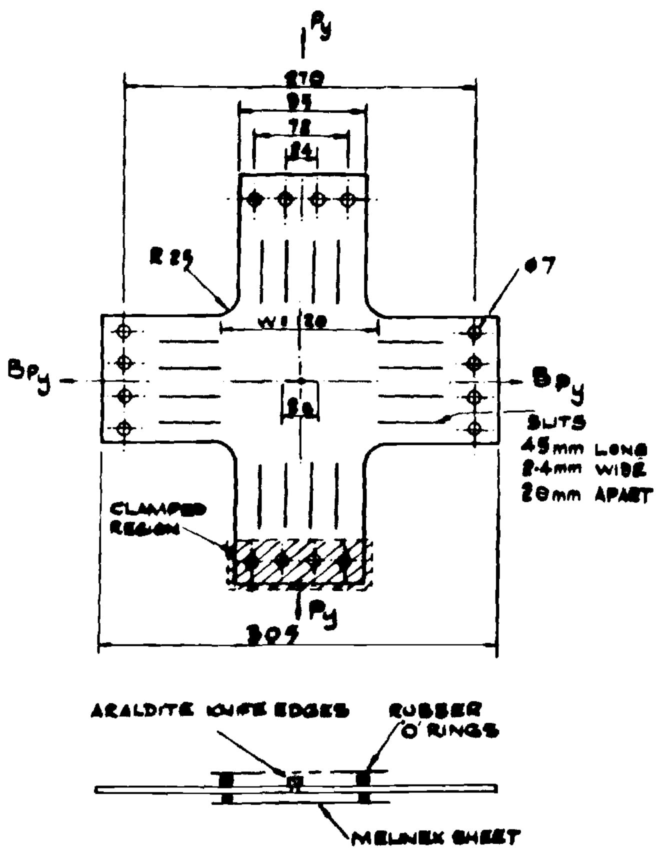

FIG. 2—*Biaxial fatigue specimen geometry with side profile of environment chamber.*

low yield strength of the fiber reinforced composite. The experimental program consisted of fatigue crack growth tests for nominal biaxial ratios of $B = 0, 0.5, 1, 1.5$, and 2. The stress ratio, R, equivalent to K_{min}/K_{max} equaled 0.1, and the cyclic frequency at 0.5 Hz were kept constant throughout the tests. The environmental chamber was made of rubber O-ring material and Melinex sheet sealed together with silicone rubber adhesive to both sides of the specimen, as shown in Fig. 2. The 5% diluted sulfuric acid was introduced into the chamber using an industrial plastic hypodermic syringe via an aperture in the top section of the environmental chamber. As the composite material showed crack path instability (that is, Class II fracture as defined in Ref *13*) for load biaxiality ratios of 1.5 and 2, a different approach was taken in determining their respective crack growth rates. For the first series of tests, fatigue loading was continued at a constant load range and biaxiality factor B (for $B = 0$, 0.5, and 1) until fracture. This ensured that steady-state fatigue crack growth rates were recorded free from transient effects. From these tests it became clear that the effects of variations

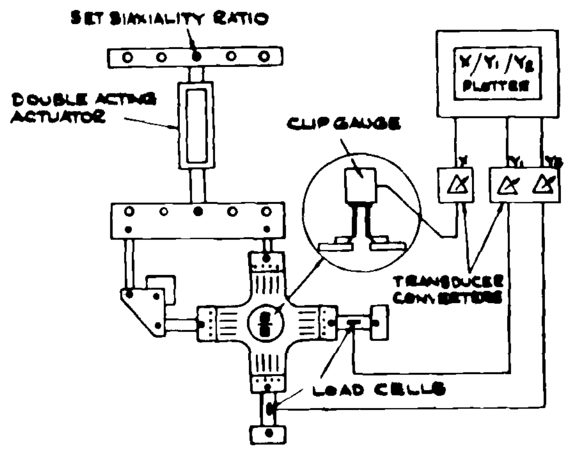

FIG. 3—*Test system used with biaxial fatigue specimen.*

in B were small and could be masked by composite material inconsistencies between specimens. It was necessary to develop a technique to test for corresponding uniaxial and biaxial crack growth rates on identical material and under identical control conditions. The revised test routine evaluated a growth rate under uniaxial stress over a total crack length increment of about 5 mm and then changed the biaxiality ratio to 1.5 or 2, holding the normal load range constant. Testing was then resumed until the crack had grown a further 5 mm or until the crack path deviation prevented valid testing at which point the procedure was repeated to set up the next uniaxial test. This procedure was developed further by varying one of the two parameters—normal load range or stress biaxiality factor at each subsequent step.

The measurement of crack length, $2a$, under fatigue loading is difficult in glass reinforced plastics because of the large amount of irreversible damage which occurs around the crack tip. Two techniques, namely, the compliance method [*19*] and the moiré fringe technique [*20*] were used to determine the effective crack length, $2a$. The compliance technique determined the effective crack length in relation to the biaxial center-notch specimen compliance. Araldite knife edges were attached to the specimen surface with Araldite rapid adhesive as stress raisers may be formed using a bolt-on knife edge in the biaxial mode. The highest biaxiality factor that could be used with this method was $B = 1$, as above this value the crack path stability is affected, thus invalidating the compliance technique. The biaxial specimen was positioned in the test system and the clip gage with associated instrumentation connected and balanced as shown diagrammatically in Fig. 3. The experimental determination of compliance was made by extending a slot in the specimen with a fine fret saw by a small increment and for each crack length of $2a$ measuring the displacement per unit of applied load. Calibration curves for biaxiality ratios $B = 0$, 0.5, and 1 are shown in Fig. 4, where the compliance ϕ is defined as the quotient of the product

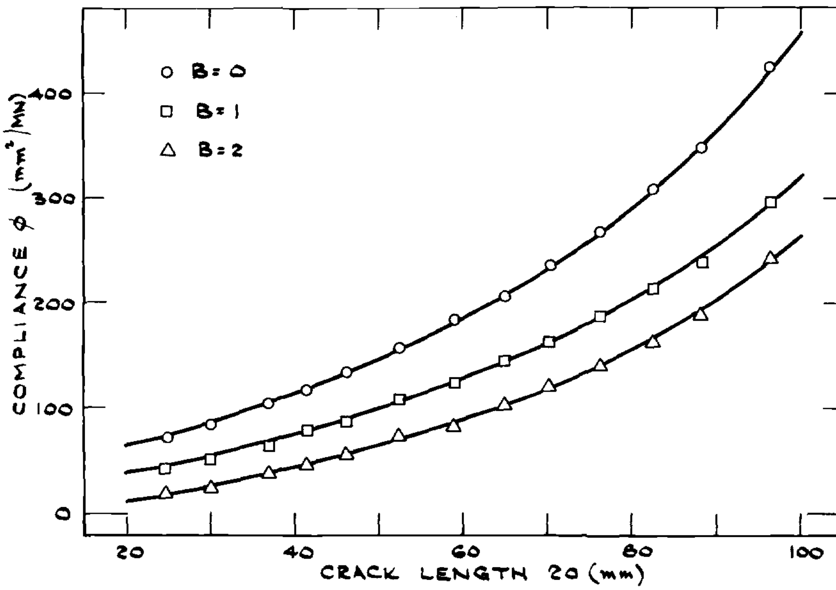

FIG. 4—*Compliance calibration curves for* B = *0, 1, and 2.*

of crack opening displacement and specimen thickness divided by a corresponding load increment. During fatigue testing graphs of load range versus crack opening displacement were plotted on the X/Y plotter, analysis of which leads to the determination of crack length $2a$. The graphs also give information about the development of the damage zone and a comparison of the amount of irreversible damage that occurs around the crack tip with respect to stress biaxiality, and modification of the damage zone with respect to environment.

For the moiré fringe technique orthogonal gratings of 500 lines/in. were used, that is, a pitch of approximately 0.05 mm. The gratings were supplied by Graticules Ltd. in the form of a film deposited on an acetate base. The grating was cut to an appropriate size and stripped of its protective backing, coated with strain gage cement and attached to the specimen. A second grating of the same pitch was superimposed on the fixed grating producing an interference pattern due to the misalignment of the gratings. Assuming that the specimen and reference gratings are coincident before deformation, the moiré fringes represent the loci of points of constant displacement. If there are no dislocations such as cracks, present, the moiré fringes are smooth continuous curves, the displacement field being a single-valued function. During a fatigue test the development of a crack disrupts the fringe patterns causing local kinks because displacement is not single-valued at the crack opening tip. By adjusting the rotational mismatch between the specimen and reference gratings crack visibility was increased because a greater number of fringes could be exhibited. Also the crack length measurements could be made directly by using an optical microscope or in the case of unstable crack paths by taking photographs of them. To help in the measurement of the crack in the stable path mode, a measuring grid graduated in millimetres was fixed 5 mm below the crackline and along it to one face of the specimen. The location of the crack tips using moiré fringes on this grid (Letraset Letratone Type T159) was judged to be accurate to ±0.1 mm, or better, if corrected by grid calibration.

Once the crack length measurement, $2a$, was made, the half crack length, a, could be calculated and plotted as a function of the number of cycles N. The test points were plotted on a large scale and smooth curves were drawn through them, some subjective judgment was necessary in deciding on the best fit. Values of crack growth data, da/dN and the corresponding values of stress-intensity factor range, ΔK, were derived from the a versus N graphs by drawing tangents to the curve at various points from which the shape was found. Then by determining the corresponding value of ΔK from the K-calibration (Eq 4) using the value of a at the point of shape measurement. Summation of the errors from the various sources involved for the determination of da/dN and ΔK would not exceed ±3%.

Results and Discussion

The log da/dN versus log ΔK graphs (see Eq 5) for all the fatigue crack growth rate data were plotted for comparison. It was noted that in the investigated region all the results showed a small decrease in the exponent m and corresponding increase in coefficient C with increasing biaxiality ratio B, Table 1. The fatigue crack propagation data are plotted in Fig. 5 for a range of constant fatigue loads for $0 \leqslant B \leqslant 1$, and for a number of different fatigue load values using a simple specimen for $0 \leqslant B \leqslant 2$. The testing procedures employed showed only a little scatter due to transient effects compared with the inherent scatter due to the material inconsistencies. These results clearly indicate the influence of the stress biaxiality.

The specimen geometry, the material of the composites, and the loading conditions used in this study leave some doubts as to whether the K-factor remains truly independent of the transverse stress. It should be remembered that the Paris

TABLE 1—*Paris law parameters* m *and* C *for a chopped strand mat composite in 5%* H_2SO_4.

Cyclic Stress Ranges,[a] $\Delta\sigma$ (MPa)	Biaxiality, B	Exponent, m	Coefficient, C (mm/c) MPa $m^{1/2}$
(12.0), (10.4), (8.6)	0	6.07	2.27×10^{-6}
(12.7), (9.6)	0.5	5.76	3.38×10^{-6}
(11.3), (9.2), (6.5)	1	5.53	4.91×10^{-6}
(7.1 to 11.4)[b]	1.5	5.39	5.69×10^{-6}
(7.4 to 10.8)[b]	2	5.27	6.48×10^{-6}

[a]Individual specimens shown in brackets.
[b]Numerous intermediate constant load levels.

law, Eq 5, does not predict the crack propagation rate approaching the region of fast fracture, (Regime III), or the instability of the crack growth [*21*]. Assuming the validity of the current fracture/mechanics theory, a correct crack growth law should show the crack growth rate close to infinity as K_{max} approaches the critical stress intensity for fracture. This definition leaves considerable latitude in the choice of K_c, since for plane stress K_c is not a property of the material, but strongly geometry dependent, as well as being a function of biaxial loading.

It is not the purpose of this study to redefine the stress-intensity factor used in Eq 5 but merely to point up an inherent limitation of this approach as discussed earlier [*22*]. In that report computations of the K-calibration curves were made using the compliance technique [*23*]. The results obtained indicated that the stress intensity factors were not only influenced by the reinforcement geometry of the composite material, but also significantly affected by the biaxiality factor. The calculated finite width correction factors Y_B for a given crack length showed a tendency to decrease in magnitude with increasing biaxiality. Though the methods for calculating Y_B were fraught with difficulty, qualitative information

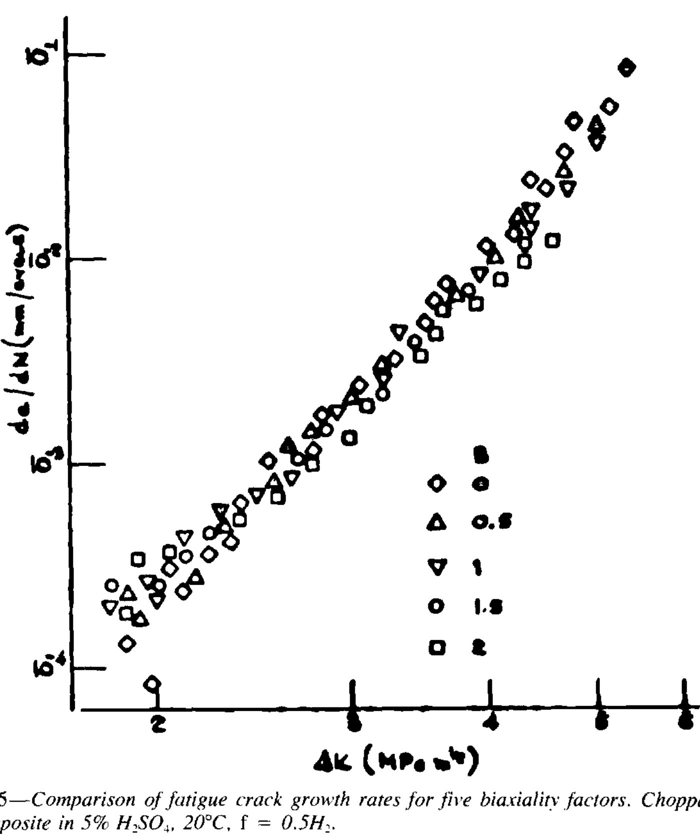

FIG. 5—*Comparison of fatigue crack growth rates for five biaxiality factors. Chopped strand mat composite in 5% H_2SO_4, 20°C, f = 0.5Hz.*

was obtained on the biaxiality effects which still showed the characteristic decrease in exponent m with increase in biaxiality B. The difference between this crack growth model and the one just cited (Eq 5), may explain the shift of the fatigue data to the left of the log (da/dN) versus log (ΔK) curves due to the stress biaxiality. This shift corresponds to an effective increase of the Paris coefficient C with increasing biaxiality factor B. The results obtained in this analysis suggest a detrimental effect of biaxial fatigue on structures as well as higher crack growth rates for corresponding values of ΔK. The main difficulty in providing a positive explanation of stress biaxiality effects is the varied characterizations of the stress-intensity parameters at the crack tip.

Accepting that there is a direct biaxiality effect on ΔK, it can be shown that the crack closure may provide a suitable explanation. Fatigue crack growth rates are therefore assumed to be a function of ΔK_{eff} which is equal to $K_{max} - K_{cl}$. Also ΔK_{eff} directly modifies the stress ratio R equation. During the unloading part of a cycle, at the minimum load level represented by K_{cl} the crack faces will close at the tip, thus eliminating the stress singularity. Closure at nonzero load occurs due to the plastic deformation at the crack tip incurred under cyclic loading. Introducing the stress biaxiality factor may increase the closure level and thus reduce ΔK_{eff} [*26*]. Preliminary observations (Fig. 6) of the crack closure effect in the fiber reinforced plastic using the moiré fringe technique showed

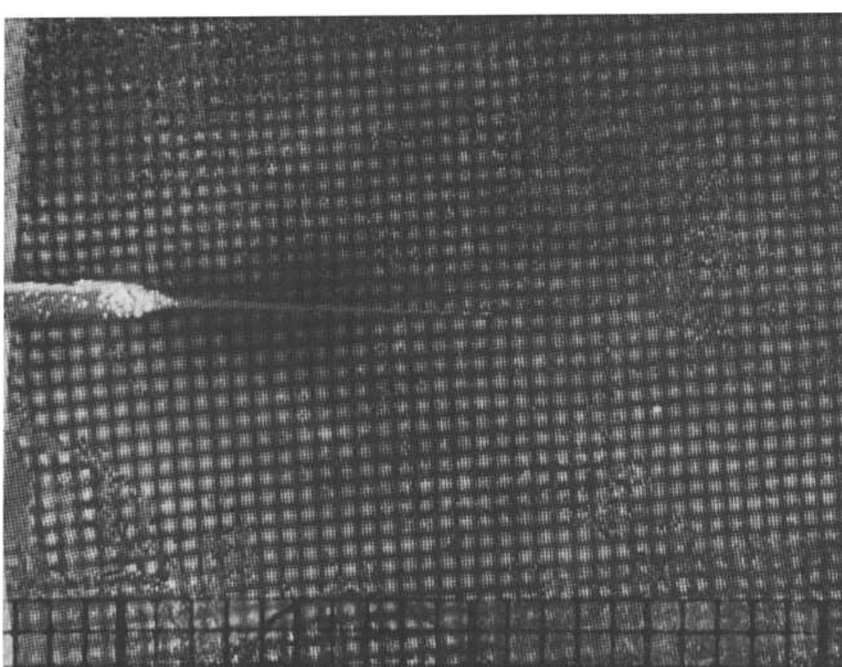

FIG. 6—*Crack measurement using moiré technique.*

small reductions in ΔK_{eff} and therefore correspondingly small increases in the coefficient C. Further refinement of the moiré technique is required before accurate measurements of crack closure levels can be made.

The development of the damage zone (Fig. 7) in the notched biaxial fatigue specimens have been examined microscopically, and the appearance of the damage has been described previously [*21,22*]. In reality plastic deformations at the crack tip of any composite material are not one-dimensional but at least two-dimensional. It may be that the constraint produced by the biaxial stress component in some way changes the available energy within the damage zone for the mechanisms of crack extension. Initial damage is caused by the debonding mechanism where fibers lying normal to the loading axis ($B = 0$) are revealed as closely spaced black lines by transmitted light. Not until large biaxiality ratios are used ($B \geq 1$), do strands lying parallel as well as normal to the principal loading axes show signs of debonding; the damage is progressive until it reaches fibers angled at 45° to the principal loading direction. This debonding process is able to spread along the fibers in both directions from the crack tip thus producing secondary cracks. These secondary cracks deviate from the main crack path broadening the crack front; and the broadening effect is further increased with the increasing biaxiality ratio. There is also a large amount of fiber pullout

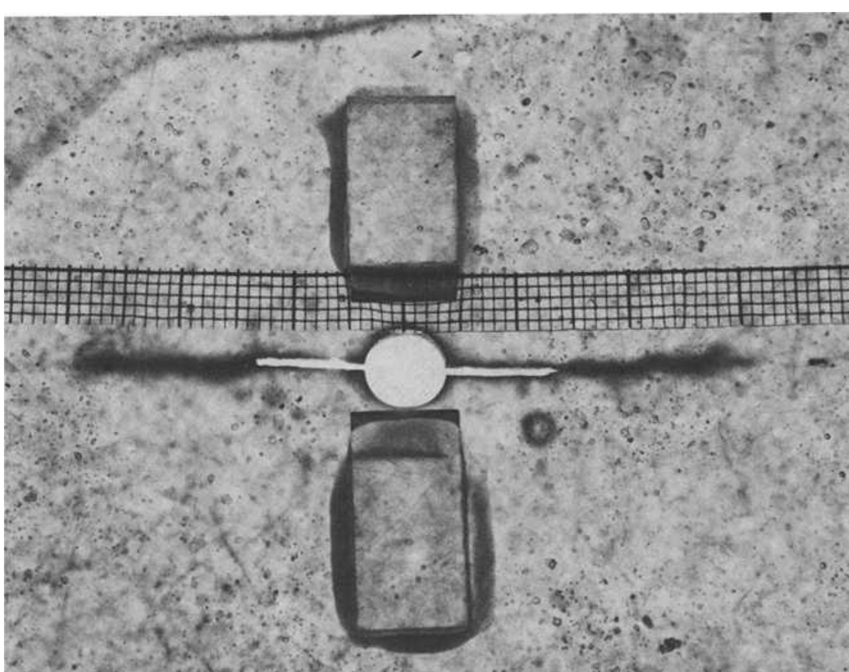

FIG. 7—*Damage zone development in 5% H_2SO_4 under fatigue.*

except when the crack is bathed in dilute sulfuric acid, as discussed earlier [*21*]. In this way the glass fibers are directly attacked by the corrosive environment, thus reducing the crack blunting mechanism and causing an increase in crack growth rate compared to that in air.

Debonding can, for $B > 1$, lead to a large-scale deviation of the crack tip, and cracking may then proceed on some other plane, remote from the original plane, with a resultant increase in the complexity of the fracture surface. This process may have important implications for path stability. It has been predicted in the previous study [*25*] that if the transverse stress is increased, there is an increasing tendency for the crack trajectory to deviate from this line, a marked path instability occurring above the equibiaxial condition ($B = 1$). Figure 8 shows that tests carried out at biaxiality ratios less than 1.5 give good crack path stability, with fatigue tests above $B = 1$ showing a tendency to deviate into *S*-shaped cracks. For biaxiality ratios $B = 0$ and 0.5, the effective crack length measured by the compliance technique was greater than the damage zone length (Fig. 6); for $B = 1$ both lengths were about the same; for $B = 1.5$ and 2 the equivalent crack lengths were much smaller than the damage zone length. This suggested that the point of crack path instability has a value of stress biaxiality slightly greater than one.

The stress intensity factor will continue to be a powerful engineering tool for predicting the behavior of a crack. However, a more fundamental understanding of the fracture process in composite materials is needed before a general crack growth model for plane stress fracture can be developed. The application of fracture mechanics to glass reinforced plastics is in its infancy compared with

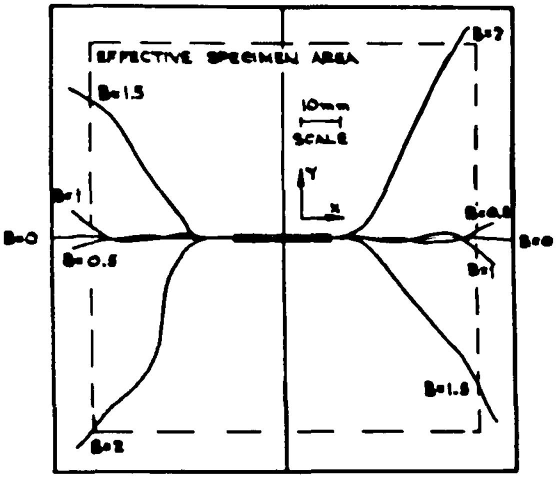

FIG. 8—*Fracture trajectories for a chopped strand mat composite in 5% H_2SO_4 under biaxial stress.*

metals. It is normally assumed [8] that in composite materials with cracks parallel to the principal specimen axis, stress intensity factors for isotropic materials can be used. This may be true for composite materials where the damage zone is small. The damage zone is not strictly comparable with the plastic zone in metals, but it does not follow that the existence of a damage zone invalidates a LEFM approach. Observations at the crack opening displacement tip using moiré fringes has shown little evidence of a substantial plastic zone. Also, within the range of the crack growth rates tested, a good agreement was achieved using a conventional crack growth model, and the range of cyclic loads was small compared to the ultimate strength of the composite material, 10 to 25% of the ultimate tensile strength. Problems with fast fracture were not considered as it is this rapid acceleration of crack growth leading to instability which defines the failure life as observed in composites [22], rather than gradual crack growth causing a steady increase of the ΔK range, finally reaching the critical crack-tip stress intensity factor K_c. The authors are studying many of the aforementioned problems and feel that most of them could be solved and that an effective model of crack-propagation rate in composite materials under biaxial stress could be developed.

Conclusions

Fatigue crack growth rates were measured as a function of the stress-intensity factor range ΔK for a random oriented glass fiber-reinforced polyester resin composite at various stress biaxiality ratios. The present study demonstrated a satisfactory application of fracture mechanics concepts in characterising biaxial fatigue crack propagation in composite materials with the use of compliance and moiré fringe techniques. Several proposals are made for modifying the Paris law crack propagation model to take into account stress biaxiality, composite reinforcement, environmental effects, specimen geometry, specimen thickness, elastic-plastic effects, and loading conditions.

The conclusions to be drawn from this investigation may be summarized as follows:

1. Analysis of the crack growth data shows that nonsingular stresses do affect the fatigue behavior of a crack subjected to plane stress loading, with the Poisson ratio of the material indirectly causing the characteristic of this influence.
2. Biaxial stresses appear to produce a shift in the fatigue crack propagation rates, notably a decrease in the exponent m when calculated using conventional finite width geometry factors.
3. Using the linear elastic fracture mechanics concepts presently available does not explain the fatigue behavior of a chopped strand mat composite in a specimen loaded under biaxial stress. The present study has shown evidence that conventional fracture mechanics techniques underestimate the value of crack growth rates in cracked specimens subjected to biaxial stresses. The compliance

and moiré and fringe methods show promise in developing proposals for overall design usage especially when they can provide K-values interpreted as being a function of stress biaxiality loading and the nature and geometry of the glass fiber-reinforcement.

4. The path stability problem for fatigue propagation of a rectilinear crack in a biaxially stressed plate has been investigated. The observations show that cracks have a strong tendency to follow along the principal axis of the specimen normal to the applied load, for biaxiality ratios up to one even if the initial notch is slightly misoriented. For stress biaxiality greater than one, there is a tendency for the crack trajectory to curve away from the original direction towards a line parallel to the direction of maximum load.

Acknowledgments

The authors acknowledge the support received by Imperial Chemical Industries Ltd.

References

[*1*] Kibler, J. J. and Roberts, R., *Journal of the Engineering Industry,* Vol. 92, 1970, p. 727.
[*2*] Swedlow, J. L., *International Journal of Fracture Mechanics,* Vol. 1, No. 3, 1965, p. 210.
[*3*] Sih, G. C., *International Journal of Solid Structures,* Vol. 3, 1967, p. 1.
[*4*] Burdekin, F. M. and Stone, D. E. W., *Journal of Strain Analysis,* Vol. 1, No. 2, 1966, p. 145.
[*5*] Mandell, J. F., McGory, E. J., Wang, S. S., and Im, J., *Journal of Composite Materials,* Vol. 8, 1974, p. 106.
[*6*] Bornby, J. T. and Spencer, B., *Journal of Materials Science,* Vol. 11, 1976, p. 78.
[*7*] Sih, G. C., Paris, P. C., and Irwin, G. C., *International Journal of Fracture Mechanics,* Vol. 1, 1965, p. 189.
[*8*] Wu, E. M. in *Composite Materials Workshop,* S. W. Tsai, J. C. Halpin, and N. J. Pagano, Eds., Technionic Press, Stamford, 1968, p. 20.
[*9*] Williams, M. L., *Transactions,* American Society of Mechanical Engineers, *Journal of Applied Mechanics,* Vol. 28, 1961, pp. 78–83.
[*10*] Owen, M. J. and Dukes, R., *Journal of Strain Analysis,* Vol. 2, 1967, p. 272.
[*11*] Irwin, G. E., *Transactions,* American Society of Mechanical Engineers, *Journal of Basic Engineering,* Vol. 82, 1960, p. 417.
[*12*] Leevers, P. S., Radon, J. C., and Culver, L. E., *Journal of the Mechanics and Physics of Solids,* Vol. 24, 1976, pp. 381–395.
[*13*] Cotterell, B., *International Journal of Fracture Mechanics,* Vol. 1, 1965, p. 96.
[*14*] Williams, M. L., *Transactions,* American Society of Mechanical Engineers, *Journal of Applied Mechanics,* Vol. 24, 1957, p. 109.
[*15*] Owen, M. J. and Rose, R. G., *Journal of Physics D: Applied Physics,* Vol. 6, 1973, pp. 42–53.
[*16*] Paris, P. C. and Erdogan, F., *Transactions,* American Society of Mechanical Engineers, *Journal of Basic Engineering,* Vol. 85, 1963, pp. 528–534.
[*17*] Wachnicki, C. R. and Radon, J. C., *Proceedings ECF2,* Darmstadt, Verein Deutscher Ingenieure, Dusseldorf, 1979, pp. 36–64.
[*18*] Leevers, P. S., Radon, J. C., and Culver, L. E., *Polymer,* Vol. 17, 1976, pp. 627–632.
[*19*] Irwin, G. R. and Kies, J. A., *Welding Journal Supplement,* Vol. 33, 1954, pp. 193s–198s.
[*20*] Chiang, Fu-Pen, *Journal of Composite Materials,* Vol. 7, Jan. 1973, pp. 134–137.
[*21*] Radon, J. C. and Wachnicki, C. R., "Fatigue Damage in Glass Reinforced Plastics," presented at International Conference on Fracture Mechanics Technology, Melbourne, Aug. 1982, in print.

[22] Wachnicki, C. R., "Fatigue Crack Growth in Atlac 382-05A Polyester Resin Reinforced With Chopped Strand Mat Under Biaxial Stress," Report No. 7, July 1981, Imperial College, Mechanical Engineering Department, London.
[23] Horel, H., Marom, G., Fischer, S., and Roman, I., *Composites*, Vol. 11, April 1980, pp. 69–72.
[24] Elber, W., *Damage Tolerance in Aircraft Structures, ASTM STP 486*, American Society for Testing and Materials, Philadelphia, 1971, pp. 230–242.
[25] Leevers, P. S., Radon, J. C., and Culver, L. E., *Journal of the Mechanics and Physics of Solids*, Vol. 24, 1976, pp. 381–395.
[26] Radon, J. C., *Advances in Fracture Research*, Vol. 2, pp. 1109–1126.

Douglas L. Jones,[1] P. K. Poulose,[1] and H. Liebowitz[1]

Effect of Biaxial Loads on the Static and Fatigue Properties of Composite Materials

REFERENCE: Jones, D. L., Poulose, P. K., and Liebowitz, H., "**Effect of Biaxial Loads on the Static and Fatigue Properties of Composite Materials,**" *Multiaxial Fatigue, ASTM STP 853*, K. J. Miller and M. W. Brown, Eds., American Society for Testing and Materials, Philadelphia, 1985, pp. 413–427.

ABSTRACT: This paper presents the results of several series of tests performed primarily to determine the effect of biaxial loads on the mechanical properties of specimens made from four graphite/epoxy laminates. Static strength, fatigue life, and residual strength tests were performed on a cruciform type of specimen containing a center hole. The parameters varied in these tests were the applied load biaxiality, hole diameter, and laminate layup.

The test results showed that the hole diameter had a limited influence on the static strength, when the strength was based on the net section area. The applied load biaxiality appeared to have a significant influence on both the fracture path and the magnitude of the failure load. For the quasi-isotropic $[0,\pm45,90]_{ns}$ laminates, the static strength increased by a factor of 1.44 as the biaxiality was increased from zero to unity and the fracture path rotated from 90° to the principal loading axis to approximately 45° to it. Although fewer tests were performed on the anisotropic $[0_2,\pm45]_{ns}$ laminates, the biaxial influence appeared to be insignificant. For some fatigue tests, increasing the biaxiality decreased the fatigue life, while for others the fatigue life was increased. This behavior appears to be governed by material anisotropy, in which certain directions (that is, perpendicular to each layer) exhibit increased sensitivity to fatigue damage. The decreasing lifetimes appeared to be associated with the rotation of the primary failure plane to coincide with one of the relatively weaker directions.

KEY WORDS: biaxial loads, composite materials, static strength, fatigue life, residual strength, fatigue damage

The widespread utilization of composite materials in aerospace structures, which are typically subjected to biaxial loadings, has led to the initiation of several theoretical and experimental research programs. The occurrence of holes and the importance of free edge effects in composite laminates have provided incentives for studying composites with holes and, to a lesser extent, cracks. The theoretical studies have emphasized linear anisotropic elasticity or the finite-element method, while the experimental studies have involved static and fatigue testing of cruciform shaped specimens containing circular holes and cracks.

[1]Professor, associate research professor, and dean, School of Engineering and Applied Science, The George Washington University, Washington DC 20052.

Copyright© 1985 by ASTM International www.astm.org

Although the formalism of linear elasticity for anisotropic materials has existed for many years, applications to composite materials have become practical only through use of the finite-element method. However, the complexities associated with multilayered composites have rendered such finite-element studies impractical until very recently [1,2]. As part of the study into biaxial loading effects on composites with holes at The George Washington University, Lee [3,4] performed an extensive finite-analysis of multiply graphite/epoxy composites subjected to varying biaxial loads. Experimental studies into the effect of biaxial applied loads on graphite/epoxy laminates with holes were also performed as part of this study [5]. An additional testing program on the biaxial effects of graphite/epoxy laminates with holes has been performed by Daniel [6,7]. The purpose of this paper is to present the results of a number of static and fatigue tests on graphite/epoxy specimens containing center holes. In these tests the center hole diameter, biaxiality ratio, and composite layup were varied, and conclusions were drawn as to the significance of these parameters on the breaking strength, fatigue life, and residual strength.

Experimental Procedure

The biaxial loading system used for these tests is comprised of a special, lightweight test frame having a 222 kN capacity on the horizontal axis, and a 444 kN capacity on the vertical axis. Both static and dynamic loads could be applied to either axis by servohydraulic actuators. The control system has the capability of controlling both axes without interaction between the two channels. Since only two hydraulic actuators were used, the center of the specimen would not remain stationary but would move in response to each actuator. In order to prevent this motion from introducing side loads onto the specimen the horizontal axis was suspended in its working position by elastic ropes. The deformation and pendulum action permitted by the ropes allowed slight movement in both the vertical and horizontal directions. Although the motion of the frame under rapid cycling transmits dynamic inertial loads to the specimen, their magnitudes were calculated for the expected worst-case conditions and were found to be small enough to be neglected.

The biaxial test specimen geometry used in this program is shown in Fig. 1. This design is a modification of similar specimen configurations used elsewhere [6–9]. Since the basic cruciform shape was necessary for flat plate biaxial testing, some variations in specimen configuration were examined photoelastically for the purpose of optimizing the size of the uniform biaxial stress field. Most of the photoelastic results were not photographed since the final specimen configuration and photoelastic results were very similar to those published in Ref 8.

A typical specimen is shown in Fig. 2, where it is seen that a reinforcing aluminum sheet was bonded to each side of the specimen in the area around the loading tabs. The direction of the 0° fibers was marked by the manufacturer on all specimens, as shown in Fig. 2, and the other laminate directions are measured

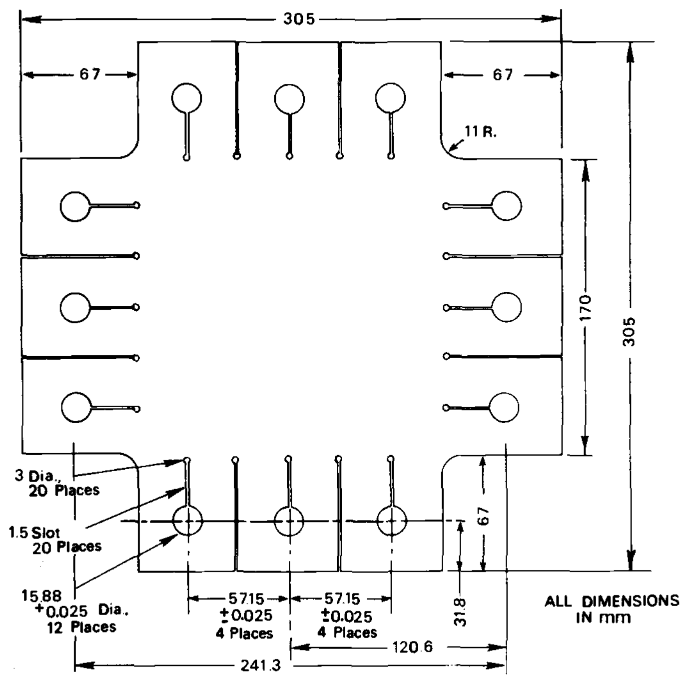

FIG. 1—*Biaxial specimen profile.*

from this axis. For example, the designation $[0,\pm45,90]_s$ refers to an 8-ply laminate in which the angular orientations of the first 4 plies are indicated and the subscript s means that the remaining 4 plies are the mirror image, resulting in a symmetric laminate. The 0° direction was always treated as the principal loading axis and oriented vertically in the test system. A total of 30 specimens, all made of Thornel 300/Narmco 5208 graphite/epoxy lamina, were prepared and tested under this program. All of the laminates were comprised of either 8- or 16-plies of Thornel 300 with the fiber content ranging from 62.6 to 66.1%. The characteristics and test conditions for these specimens are shown in Table 1. The biaxiality ratio, k, defined as the ratio of the horizontal force to the vertical force, was limited to the range $0 \leq k \leq 1.0$ for two reasons: (*a*) the quasi-isotropic $[0,\pm45,90]_{ns}$ configuration (ns indicating s for 8-ply and $2s$ for 16-ply) is symmetric with respect to the horizontal and vertical axes, so that the reciprocal biaxiality ratios, $1.0 < k \leq \infty$ are also included in these tests, and (*b*) tests on the $[0_2,\pm45]_{ns}$ configuration was limited to ratios of $0 \leq k \leq 0.5$, because of its reduced strength in the 90° orientation.

The specimen design shown in Fig. 2 created one type of difficulty that had considerable influence on some of the test parameters. The problem was caused by the tendency of some specimens to fail by tearing off one or more of the loading tabs, resulting in the lack of failure through the central test section.

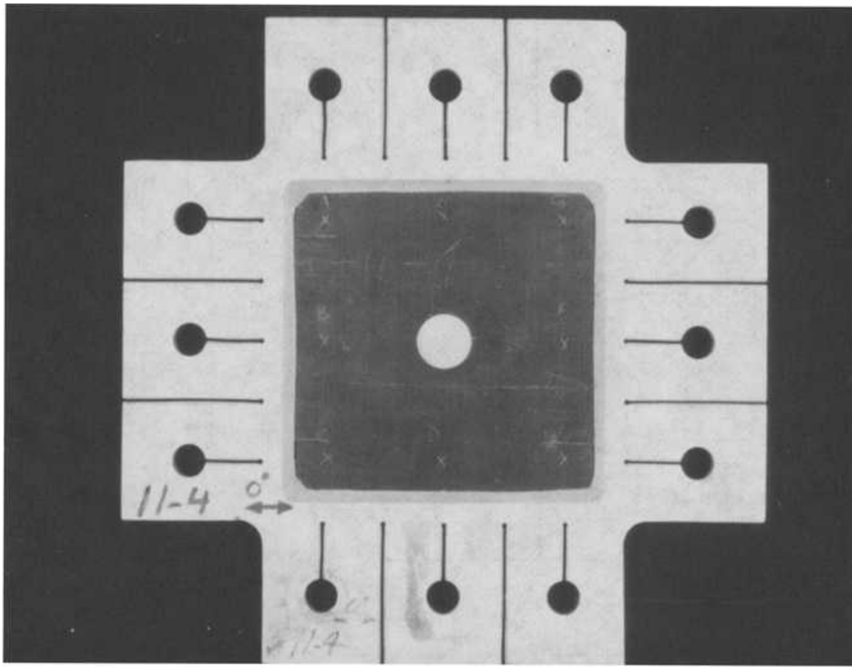

FIG. 2—*Photograph of typical specimen prior to testing, for test series 1 and 2.*

These tests could not provide valid results, so certain modifications were introduced into the specimen design to reduce the tendency for tab failures. The problem was particularly bothersome in the $[0_2, \pm 45]_{ns}$ specimens because the tabs in the 90° or horizontal orientation would fail under quite low biaxiality ratios. In order to reduce the strength of the center section, most of the later tests employed nominal hole diameters of 50.8 mm. This modification was still inadequate for several tests, so further modifications were introduced. The most successful approach employed was to machine away the reinforcing aluminum beyond where the individual tabs were separated. The problem of tab tearoff was also greater for the fatigue tests than for the static tests.

The 30 tests were divided into five groups of static and fatigue tests, and the test characteristics unique to each series are discussed next.

Test Series (1)

This test series was comprised of four static strength tests on the quasi-isotropic laminates involving variations in thickness (8- and 16-ply laminates with average thicknesses of 1.09 and 2.22 mm, respectively), hole diameter (D = 12.75 and 50.98 mm), and biaxiality ratio (k = 0 and 1.0). The loads were applied as in-phase ramp functions with ramp rates of either 297 or 741 N/s. The ramp functions were interrupted periodically to record data manually from digital

TABLE 1—*Characteristics and test conditions of T300/5208 graphite/epoxy biaxial specimens.*

Test Series	Specimen Number	Lamina	Thickness, mm	Biaxiality Ratio	Hole Size D, mm	Type of Test[a]
1	5-1	$[0,\pm45,90]_s$	1.11	0	12.75	1
	5-2	$[0,\pm45,90]_s$	1.09	0	50.98	1
	9-4	$[0,\pm45,90]_{2s}$	2.29	1.0	50.98	1
	9-5	$[0,\pm45,90]_{2s}$	2.15	1.0	12.75	1
2	9-2	$[0,\pm45,90]_{2s}$	2.25	1.0	25.53	1
	9-3	$[0,\pm45,90]_{2s}$	2.26	1.0	25.53	1
	5-3	$[0,\pm45,90]_s$	1.08	0	25.53	1
	5-4	$[0,\pm45,90]_s$	1.10	0.50	25.53	1
	5-5	$[0,\pm45,90]_s$	1.10	1.0	25.53	1
	11-1	$[0_2,\pm45]_{2s}$	2.20	0	25.55	1
	11-2	$[0_2,\pm45]_{2s}$	2.20	0.50	25.55	1
3	11-3	$[0_2,\pm45]_{2s}$	2.19	0	25.48	3
	11-4	$[0_2,\pm45]_{2s}$	2.21	0.50	25.53	2
	11-5	$[0_2,\pm45]_{2s}$	2.23	0.25	25.53	2
	7-1	$[0_2,\pm45]_s$	1.11	0.25	25.55	3
	7-3	$[0_2,\pm45]_s$	1.09	0.25	50.80	2
	7-4	$[0_2,\pm45]_s$	1.09	0.25	25.53	2
	7-5	$[0_2,\pm45]_s$	1.14	0.25	50.93	2
4	23-1	$[0,\pm45,90]_s$	1.10	0	25.47	1
	23-2	$[0,\pm45,90]_s$	1.10	0	25.45	2
	23-3	$[0,\pm45,90]_s$	1.10	0	50.80	2
	23-4	$[0,\pm45,90]_s$	1.10	0.50	50.80	2
	23-5	$[0,\pm45,90]_s$	1.09	0.50	50.80	3
	23-6	$[0,\pm45,90]_s$	1.08	1.0	50.80	2
5	24-1	$[0_2,\pm45]_s$	1.09	0.25	50.80	4
	24-2	$[0_2,\pm45]_s$	1.07	0.25	50.80	3
	24-3	$[0_2,\pm45]_s$	1.09	0.25	50.80	3
	24-4	$[0_2,\pm45]_s$	1.09	0.25	50.80	2
	24-5	$[0_2,\pm45]_s$	1.07	0.10	50.80	2
	24-6	$[0_2,\pm45]_s$	1.08	0	50.80	2

[a]NOTES—
1 = Static strength test at low load rate.
2 = Fatigue life test.
3 = Residual strength test after 10^6 fatigue cycles.
4 = Static strength test at high load rate.

multimeters. Five channels of data were recorded, including load and stroke on each axis and the hole opening displacement in the primary (largest load) direction. Load-displacement curves in the primary direction were also recorded using an x-y recorder. All specimens failed through the center hole, although it was not certain whether the final fractures initiated at the center hole or the specimen boundary.

Test Series (2)

Upon satisfactory completion of the first four tests, seven additional static tests were performed on both the quasi-isotropic and the $[0_2,\pm45]_{2s}$ configurations. The first two tests were performed to examine the influence of fabrication damage, which existed in a number of the specimens, around the central hole. The most extensively damaged specimen was 9-2 and the extent of the damage is indicated in Fig. 3*a*. Identical test conditions were applied to Specimens 9-2 and 9-3 (which had negligible damage around the hole), with the test results indicating that the initial damage did not influence the strength. Although the breaking strength was slightly lower for Specimen 9-2, the final fracture did not appear to be influenced by the initial damage, as seen in Fig. 3*b*. As a result of these tests, the existing initial damage was not taken into consideration in the subsequent testing.

Specimens 5-3, 5-4, and 5-5 represented a subseries in which only the biaxial load ratio was varied. The material was quasi-isotropic and biaxial ratios of 0, 0.5, and 1.0 were selected. The tests were performed using in-phase ramp functions on each axis, and all failures traversed through the center holes.

Specimens 11-1 and 11-2 also represented a biaxial static strength series for the $[0_2,\pm45]_{2s}$ configuration. Biaxial ratios of $k = 0$ and 0.5 were employed for these tests and the failures traversed through the center holes.

Test Series (3)

This test series was comprised of seven fatigue tests on the $[0_2,\pm45]_{2s}$ and $[0_2,\pm45]_s$ configurations. All fatigue tests were conducted at a frequency of 10 Hz and a load ratio, $R = \sigma_{min}/\sigma_{max} = 0.1$. The purpose of these tests was to determine whether damage accumulation due to cyclic loading at low biaxiality ratios would have any significant influence on the strength in the 0° fiber orientation. However, during the fatigue life or residual strength determinations, two of the first three specimens (11-4 and 11-5) failed along the tabs away from the center holes. Hence, the next four tests (Specimens 7-1, 7-3, 7-4, and 7-5) were employed primarily for determining a modified specimen design capable of eliminating tab failure. In the design chosen from these tests, the specimens had a nominal hole diameter of 50.8 mm, and the depth of the 20 slots between individual loading tabs was increased to the edge of the reinforcing aluminum plate. This reduced the net section of the specimen through the center hole and prevented initial cracking of the aluminum plate which apparently contributed to tab failures. A photograph of Specimen 7-5 modified in this fashion is shown in Fig. 4.

Test Series (4)

This test series was comprised of one static and five fatigue tests on specimens having the quasi-isotropic $[0,\pm45,90]_s$ configuration. The first test was a static test for the purpose of comparing the strength with prior tests of the same configuration. The test conditions for this specimen, 23-1, were identical to Specimen 5-3, and the ultimate loads were in quite good agreement with each other. For the remaining specimens the nominal center hole diameter was in-

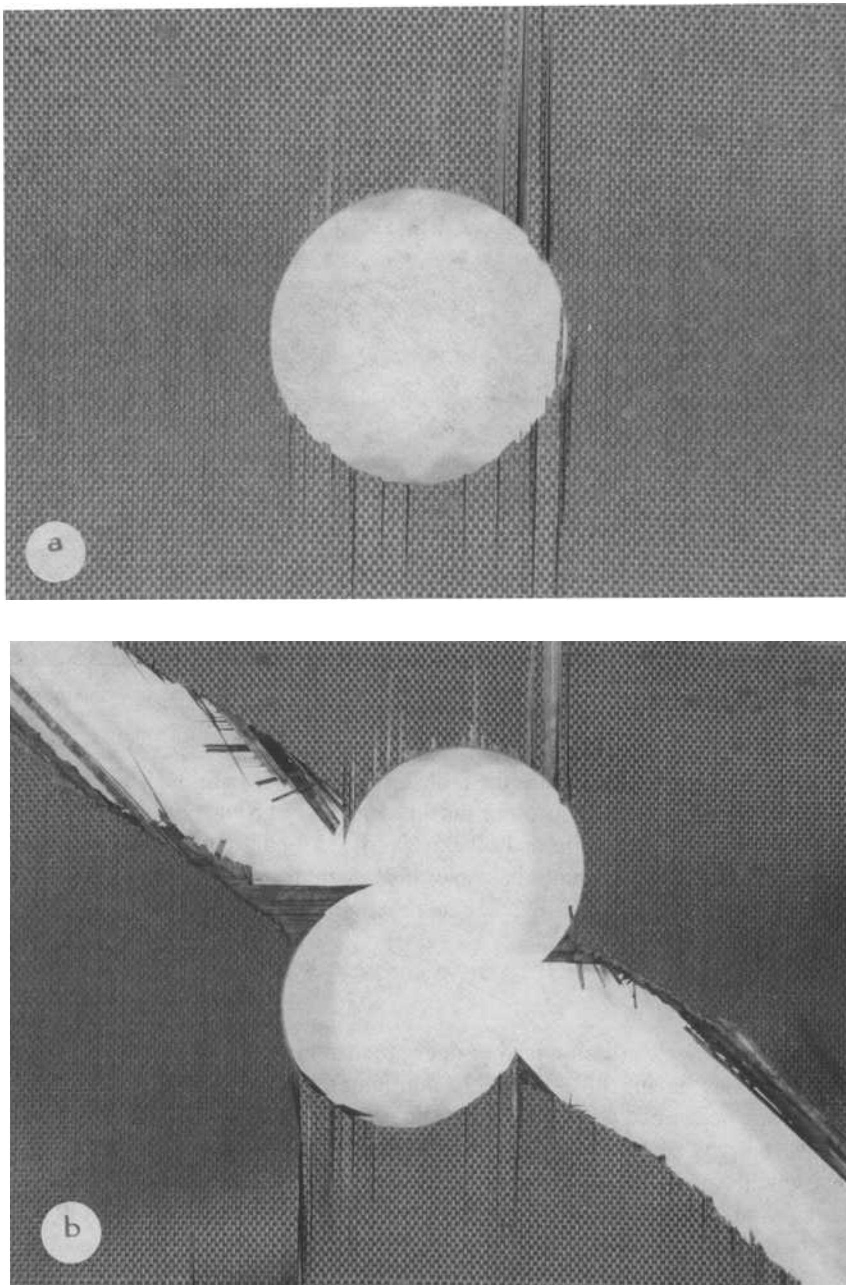

FIG. 3—*Close-up photograph of specimen 9-2 showing,* (a) *prior damage, and* (b) *final fracture condition.*

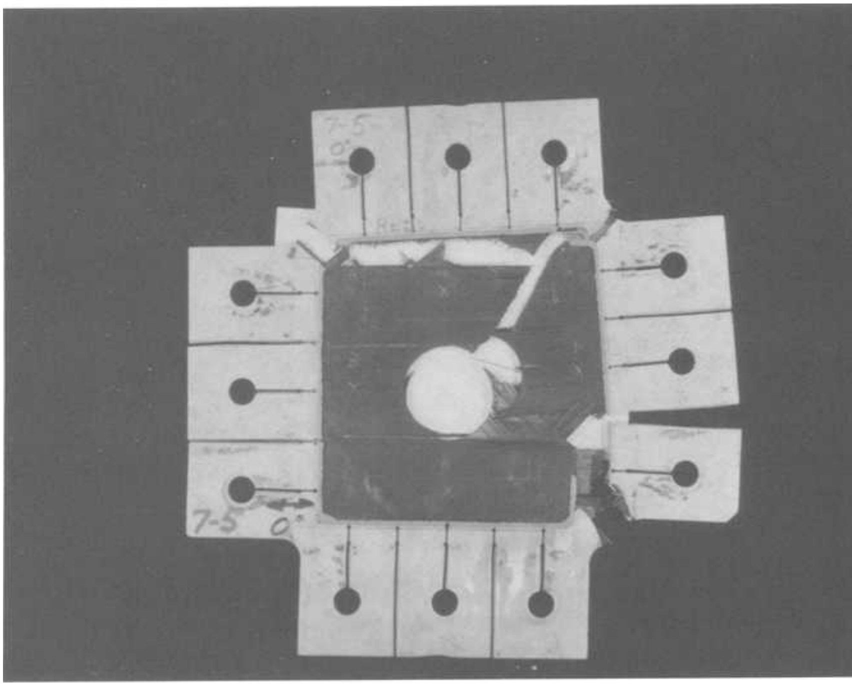

FIG. 4—*Photograph of fractured Specimen 7-5 showing effect of deeper slots on the fracture behavior.*

creased to 50.8 mm to increase the probability of center failures. The next three tests (23-3, 23-4, 23-6) represent the influence of biaxial loads (k = 0, 0.5, and 1.0) on the fatigue life and all three provided valid data. Specimens 23-2 and 23-5 did not fail through the center holes, and the results for Specimen 23-2 were not reported because of a premature fatigue failure induced by a laboratory power failure.

Test Series (5)

This test series was comprised of one static strength test and five fatigue tests on specimens having the $[0,\pm45,0]_s$ configuration. By the time that this test series was performed a DEC PDP 11-03 computer had been added to the system for the purpose of rapid data collection. Therefore, it was decided that the static test would be performed at the same loading rate as the fatigue tests, 10 Hz, rather than at the low rates previously employed. This procedure was followed to eliminate any loading rate effects on the ultimate strength, since the fatigue loads were preselected as a percentage of the ultimate strength. Also, because of the prior problems encountered with tab failure, two modifications of these specimens were made: (a) the nominal hole diameter was increased from 25.4 to 50.8 mm, and (b) the aluminum reinforcing plate was machined away to

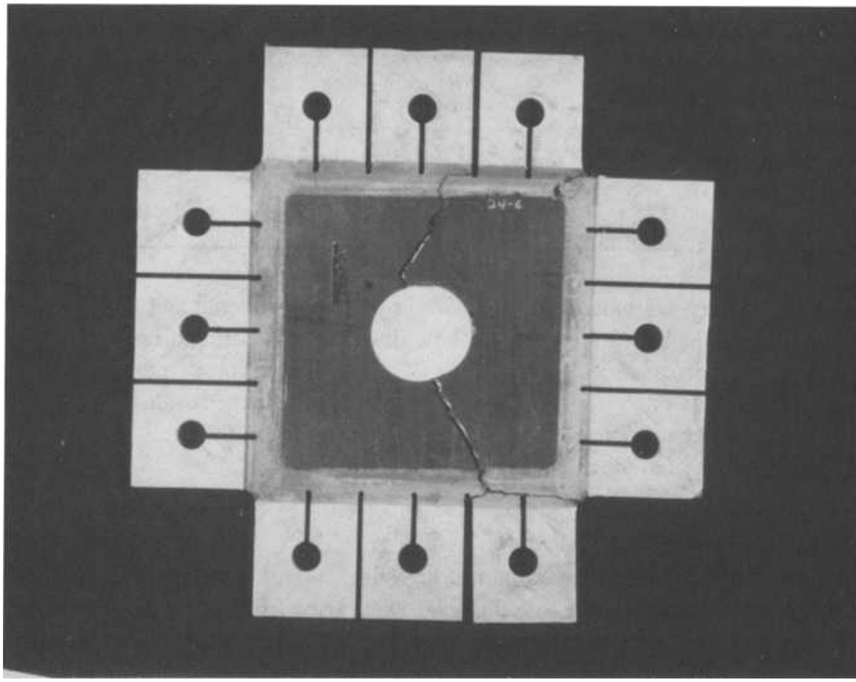

FIG. 5—*Photograph of fractured Specimen 24-6 showing effect of machining away part of the aluminum reinforcing plate on the fracture behavior.*

approximately 6.35 mm beyond the slot tips without disturbing the composite material. These modifications were successful, since all six specimens failed through the center hole. A photograph of one of the modified specimens is shown in Fig. 5. Specimens 24-2 and 24-3 were loaded in fatigue at 82 and 90%, respectively, of the net section strength determined from Specimen 24-1. Both of these specimens sustained 10^6 cycles and provided high residual strengths. The biaxial ratio was 0.25 for all three tests.

The final three tests constituted a series of three fatigue life tests in which the biaxial ratio had the values, k = 0, 0.1, and 0.25. All three specimens were loaded to at least 90% of the static strength obtained from Specimen 24-1, and all failed in less than 10^3 cycles. Thus, the results were not as conclusive as they would have been if there had been a greater spread of fatigue lives. Nevertheless the tests appear to be valid and do provide some measure of the influence of biaxial loads on the fatigue life.

Results and Discussion

The results of the various types of tests and specimen parameter variations have been collected together in tabular form as shown in Tables 2 to 5. These tables illustrate the results of similar tests on each laminate and how the me-

TABLE 2—*Effect of center hole diameter on the static strength of* $[0,\pm45,90]_s$ *laminates.*

Specimen Number	Biaxiality Ratio	Hole Diameter, mm	Breaking Load, kN	Static Strength, MPa
5-1	0	12.75	64.5	366
5-3	0	25.53	55.2	349
23-1	0	25.45	56.9	356
5-2	0	50.98	55.6	429

chanical property examined was influenced by various material and test parameters. The parameters examined were hole diameter, biaxial load factor, thickness, and type of specimen modification. The mechanical properties examined were the static or ultimate strength, the fatigue life, and the residual strength. The details of each property variation will be discussed on the basis of the data in the accompanying tables.

Static Strength Variations

Although it was not a primary part of this study, an initial series of static tests was performed in which the hole diameter was varied from 12.75 to 50.98 mm to examine the influence of hole diameter on the static strength. These tests were performed on the quasi-isotropic configurations in both the 8- and 16-ply thicknesses. Thus, these tests were expected to provide indications of both hole diameter and specimen thickness influence on the static strength of these materials.

All static and residual strength calculations, as well as the applied stress level determinations, are based on the applied force divided by the net section area. The net section width is taken to be the distance between the tips of the stress equalization slots minus the diameter of the center hole. The theoretical stress concentration factor, K_t, was not used for either the center holes or the load equalizing holes, because of several reasons. The K_t-values represent the stress elevation only at the edge of the hole, with the effect diminishing with increasing distances from the hole. The full K_t-values are normally never used because of other irregularities in brittle materials or plastic deformation in ductile materials. The K_t-values are also influenced by load biaxiality. The difficulty in properly

TABLE 3—*Effect of center hole diameter on the static strength of* $[0,\pm45,90]_{2s}$ *laminates.*

Specimen Number	Biaxiality Ratio	Hole Diameter, mm	Breaking Load, kN	Static Strength, MPa
9-5	1.0	12.75	161	473
9-2	1.0	25.53	133	405
9-3	1.0	25.53	144	439
9-4	1.0	50.98	128	472

TABLE 4—*Effect of applied load biaxiality on the static strength of* $[0,\pm45,90]_s$ *and* $[0_2,\pm45]_{ns}$ *laminates.*

Specimen Number	Biaxiality Ratio	Hole Diameter, mm	Breaking Load, kN	Static Strength, MPa
		$[0,\pm45,90]_s$ LAMINATE		
5-3	0	25.53	55.2	349
23-1	0	25.45	56.9	356
5-4	0.5	25.53	64.9	405
5-5	1.0	25.53	81.0	507
		$[0_2,\pm45]_{2s}$ LAMINATE		
11-1	0	25.55	161	505
11-2	0.5	25.55	162	505
		$[0_2,\pm45]_s$ LAMINATE		
24-1	0.25	50.80	48.8	372[a]

[a]Static strength test at high load rate.

quantifying the effects discussed previously and the similarity in geometry of all specimens appears to justify neglecting stress concentration effects in determining the net section stresses.

The influence of hole diameter variation on the static strength of the $[0,\pm45,90]_s$ laminates is shown in Table 2. The biaxial load ratio, k, was equal to zero for all of these tests. It is seen that the static strength decreased slightly as D increased

TABLE 5—*Effect of cyclic load biaxiality on the fatigue life and residual strength of composite laminates.*

Specimen Number	Biaxiality Ratio	Cyclic Stress Level, MPa	Fatigue Life, kc	Residual Strength, MPa
		$[0,\pm45]_{2s}$ LAMINATE		
11-3	0	377	1000	514
11-5[a]	0.25	370	442	...
11-4[a]	0.50	378	23	...
		$[0,\pm45,90]_s$ LAMINATE		
23-3	0	338	29	...
23-4	0.5	339	447	...
23-5[a]	0.5	341	1000	416
23-6	1.0	343	42	...
		$[0_2,\pm45]_s$ LAMINATE		
24-6	0	335	0.15	...
24-5	0.10	338	0.50	...
24-4	0.25	356	0.44	...
24-3	0.25	332	1000	451
24-2	0.25	305	1000	392

[a]Specimen did not fail through center hole.

from 12.75 to 25.50 mm and then increased as D was increased to 50.98 mm. However, the entire variation was less than 20%, so the effect does not appear to be of extreme importance. It is also noted that the two identical tests, 5-3 and 23-1, which were conducted from different specimen lots and several months apart, provided results that were nearly identical.

Daniel [6] has performed tests on similar biaxial specimens with a range of center hole sizes and reported a decrease of approximately 20% in strength as the hole diameter-to-specimen width ratio, D/W, increased from 0.03 to 0.12. However, the ratios employed in the present tests ranged from 0.075 to 0.30 so there is not much overlap for comparison. For the range in which there is substantial overlap, Daniel's results ($0.06 < D/W < 0.12$) show a decrease of approximately 15%, while the present results ($0.075 < D/W < 0.15$) show a decrease of approximately 4%.

A similar series of tests was performed on the 16-ply quasi-isotropic laminate, $[0,\pm45,90]_{2s}$, and the results are seen in Table 3. The biaxial load ratio, k was equal to 1.0 for all of these tests. The same pattern seen in Table 2 also exists in Table 3. The static strength decreased slightly as D/W increased from 0.075 to 0.15 and then increased, so that the breaking strengths for D = 12.75 and 50.98 mm were approximately equal.

Since the primary objective of this research program was the determination of biaxial load effects, attention is drawn to Table 4. These tests show a significant influence of applied load biaxiality on the ultimate strength of the $[0,\pm45,90]_s$ laminates. For these laminates, Table 4 shows that the strength increased by a factor of 1.44 as k increased from 0 to 1.0. These results coincided with a change in fracture path from perpendicular to the primary load axis to approximately 45° to this axis.

These test results can be correlated with the finite-element analysis by Lee [3,4], in which he found that stresses perpendicular to the fiber cause localized matrix failure while longitudinal (σ_L) stresses cause fiber fractures resulting in progressive failures. As expected, the layer in which the maximum σ_L occurred depends on the biaxiality ratio, k. When $k = 0$, the maximum value of σ_L occurred in the 0° fibers (with a stress concentration factor (scf) ≈ 8.0) and failure was predicted at 90° to the load axis. For $k = 0.5$, the fracture direction was still predicted at 90° but at a higher applied load because the stress concentration factor was reduced to 6.5. When k was increased to 1.0, the maximum value of σ_L occurred at eight places, 0, 180, ±45, ±90, and $\pm135°$, since there are two laminae perpendicular to each of these directions. The scf for each of these positions was 5.2, so the fracture load would be slightly higher than for $k = 0.5$. Using a general set of strength parameters for $[0,\pm45,90]_s$ graphite/epoxy, Lee [3,4] predicted fracture stresses of 156, 189, and 193 MPa for k = 0, 0.5, and 1.0, respectively. Thus the biaxial ultimate strength was approximately 1.24 times the uniaxial ultimate strength in comparison to a factor of 1.44 for the experimental results.

Additional comparisons can be also made with test data provided by Daniel

[6] from a very similar series of biaxial tests on $[0,\pm45,90]_s$ laminates. Daniel reported the strength reduction as a function of hole radius for uniaxial and equal biaxial loadings. For comparable D/W ratios, that is, 0.12 and 0.15, the biaxial ultimate strength was 1.42 times the uniaxial strength. For lower D/W ratios the strength increase varied from 1.23 to 1.31. Daniel's results were based on an average of two tests for each configuration.

Two tests which provided an indication of the biaxial effect for the $[0_2,\pm45]_{2s}$ laminates are also included in Table 4. The k variation was limited to the range 0 to 0.5 because of the weakness of this laminate in the 90° orientation. Although the biaxial load had no effect on the breaking strength in these two tests, additional tests would be necessary before any conclusions could be drawn from these data. However, Daniel [7] has also tested similar laminates, $[0_2,\pm45]_s$, and obtained an average strength reduction factor of approximately 0.78 as the biaxiality increased from 0 to 0.5.

Fatigue Tests

A number of fatigue tests have been performed to ascertain the possible extent of cyclic load biaxiality on the fatigue life and residual strength. For these tests the specimens were subjected to in-phase cyclic loads at a frequency of 10 Hz until they failed, or until 10^6 cycles were sustained. Any specimens lasting for 10^6 cycles were then tested for their residual strength. The results of both the fatigue life and residual strength tests are seen in Table 5. In general the objective was to apply cyclic loads at levels of 70 to 80% of the static ultimate strength. However, the results given in Table 5 indicate a considerable amount of scatter in the fatigue results.

The results of the test series on the $[0_2,\pm45]_{2s}$ laminates indicate a very strong and detrimental influence of load biaxiality on the fatigue life. However, as noted in the table, Specimens 11-5 and 11-4 did not fail through the center hole but failed due to the breaking of the loading tabs. Thus, it seems likely that the biaxial effect would not have been nearly as great if the premature tab failures had not occurred.

The results of a series of fatigue tests on the $[0,\pm45,90]_s$ laminates, in which only the biaxial load ratio was varied, are also presented in Table 5. These tests showed that both the uniaxial and equal biaxial tests resulted in relatively short fatigue lives. However, the test with $k = 0.5$ resulted in a cyclic life approximately ten times the $k = 0$ and $k = 1.0$ results. Because of this behavior an additional test, 23-5, was performed with $k = 0.5$, which displayed even greater resistance to fatigue failure. The appearance of the broken specimens suggested that these results may represent a valid biaxial effect. The $k = 0$ and $k = 1.0$ specimens both failed in a rather brittle fashion along planes parallel to one of the layers (the 90 and 45° directions). However, the specimens with $k = 0.5$ failed at an angle between the 90 and 45° directions only after a very extensive amount of damage had been accumulated. It was thus concluded that, when the preferred failure plane coincided with a ply orientation, the failure could occur with relative ease. However, when failure along another plane would be anticipated, a considerable amount of damage accumulation is necessary, thus resulting in a longer fatigue life. These tentative conclusions are also in need of further verification.

The results of the last series of fatigue tests on the $[0_2,\pm45]_s$ laminates are also shown in Table 5. As discussed previously, all of these specimens were modified as shown in Fig. 5. This modification was successful in eliminating the problem of tab failure, but the variations in the results were still too great to justify drawing definite conclusions about the existence of trends in these results.

It is seen from Table 5 that a possible trend of increasing fatigue lives with increasing biaxiality in the range $0 \leq k \leq 0.25$ may exist. However, the differences between tests 24-2 and 24-3 on one hand and 24-4, 24-5, and 24-6 on the other are immense, being more than three orders of magnitude in the fatigue life without taking into consideration the considerable residual strength. One conclusion which may be drawn from these tests is that the fatigue life probably does increase with increasing biaxiality in the range tested. The fractured specimens displayed the same trend as the 23 series, in which the amount of damage accumulated by the specimens was much greater when the failure could not occur along one of the fiber directions. Thus, it is possible that the fatigue life would begin to decrease as the biaxial load ratio increased beyond 0.25.

Conclusions

An experimental research program has been conducted to examine the influence of biaxial applied loads on the mechanical properties of composite materials. Five series of biaxial fracture and fatigue tests, comprised of 30 specimens, have been performed. Whenever the conditions were appropriate, these results have been compared with an associated finite-element analysis, and with other data reported elsewhere.

1. The applied load biaxiality had a significant influence on the static strength of the $[0,\pm45,90]_{ns}$ laminates with the fracture load increasing with increasing biaxiality. Both the direction and magnitude of this trend were in agreement with previous finite-element results and experimental data.
2. The applied load biaxiality did not appear to have any appreciable influence on the breaking strengths of the $[0_2,\pm45]_{ns}$ laminates, since two tests for $k = 0$ and 0.5 gave identical breaking strengths. Additional tests are needed to confirm this behavior.
3. The size of the center hole did not appear to have a significant influence on the net failure stress. However, the number of tests performed was not adequate for a definite conclusion.
4. The biaxial applied stress ratio appeared to have a strong influence on the

fatigue life, although the trends were not always consistent. This inconsistency in behavior may have been due to an inadequate number of specimens tested, since the fatigue life data exhibited greater scatter than the static strength. However, the trends in the data may have been caused by the manner in which the biaxial load altered the orientation of the fracture path with respect to the fiber orientations.

Acknowledgment

The authors gratefully acknowledge support from Grant NSG 1289, from the NASA Langley Research Center.

References

[*1*] Nishioka, T. and Atluri, S. N., *AIAA Journal*, American Institute of Aeronautics and Astronautics, Vol. 18, 1980, p. 1125.
[*2*] Raju, I. S. and Crews, J. H., Jr., *Journal of Computers and Structures*, Vol. 14, 1981, p. 21.
[*3*] Lee, J. D., *Journal of Computers and Structures*, Vol. 12, 1980, pp. 319–339.
[*4*] Lee, J. D., *Journal of Computers and Structures*, Vol. 15, 1982, pp. 335–350.
[*5*] Liebowitz, H. and Jones, D. L., "Biaxial Tests of Flat Graphite/Epoxy Laminates," *NASA Contractors Report 165793*, NASA Langley Research Center, October 1981.
[*6*] Daniel, I. M., *Experimental Mechanics*, Vol. 20, No. 1, 1980, pp. 1–8.
[*7*] Daniel, I. M., *Experimental Mechanics*, Vol. 22, No. 5, 1982, pp. 188–195.
[*8*] Radon, J. C., Leevers, P. S., and Culver, L. E., *Experimental Mechanics*, Vol. 17, No. 6, 1977, pp. 228–232.
[*9*] Hopper, C. D. and Miller, K. J., *Journal of Strain Analysis*, Vol. 12, 1977, pp. 23–28.

Life Prediction Techniques for Plain and Notched Components

Donald L. McDiarmid[1]

Designing for High-Cycle Biaxial Fatigue Using Surface Strain Records

REFERENCE: McDiarmid, D. L., "**Designing for High-Cycle Biaxial Fatigue Using Surface Strain Records,**" *Multiaxial Fatigue, ASTM STP 853,* K. J. Miller and M. W. Brown, Eds. American Society for Testing and Materials, Philadelphia, 1985, pp. 431–439.

ABSTRACT: A method of designing for high-cycle biaxial fatigue using surface strain records is proposed. The irregular strain records are first idealized to cycles of constant amplitude to enable a first estimate of long-life capability to be made from allowable surface strain envelopes. These are developed from a criterion of failure under biaxial fatigue based on material bending and twisting fatigue properties. Methods of determining likely crack growth directions are also proposed. Important parameters to be considered in refining the initial approximate analysis are discussed.

KEY WORDS: fatigue (materials), stresses, strains, damage, predictions, service, crack initiation, crack propagation

Nomenclature

b	Fatigue strength in bending
t	Fatigue strength in twisting
f	Mathematical function
ϵ	Strain amplitude
$\epsilon_1,\epsilon_2,\epsilon_3$	Principal strains ($\epsilon_1 \geqslant \epsilon_2 \geqslant \epsilon_3$)
ϵ_m	Mean strain
ϵ_{ae}	Equivalent strain amplitude
ϵ_{TS}	Strain at tensile strength
ϵ_A	Strain at uniaxial reversed fatigue strength
σ	Normal stress amplitude
$\sigma_1,\sigma_2,\sigma_3$	Principal stresses ($\sigma_1 \geqslant \sigma_2 \geqslant \sigma_3$)
σ_A	Uniaxial reversed fatigue strength
σ_τ	Normal stress amplitude on plane of maximum range of shear stress
τ	Shear stress amplitude
τ_a	Shear stress amplitude on plane of maximum range of shear stress
λ	σ_2/σ_1 (λ + *ve*), = σ_3/σ_1 (λ − *ve*)
ν	Poisson's ratio
Q	t/b

[1]Senior lecturer, Department of Mechanical Engineering, The City University, London, U.K.

Copyright© 1985 by ASTM International www.astm.org

The designer often does not know with any degree of confidence the state of multiaxial stress or strain which will exist in a complex shaped component subjected to irregular loading. Service testing of the component, suitably fitted with electrical resistance strain gages in the regions of greatest strain, will provide surface strain records. An analysis of these surface strain records can be made to obtain a record of the principal surface strains which will be also irregular and nonstationary in direction.

If the design requirement is for long life, that is, essentially the prevention of fatigue crack initiation, it is necessary to determine from the surface strain records whether a fatigue problem is likely to exist. It is convenient to have a fairly simple method of answering this broad question, using available uniaxial fatigue data for the material, especially if a more extensive fatigue analysis may be thought necessary.

This paper proposes a method of idealizing the strain records to equivalent alternating principal strains which can be then examined following Brown and Miller [*1*] to determine which mode of crack growth is the more likely, cracks growing inwards being more severe than cracks growing along the surface. A multiaxial stress/strain criterion of fatigue failure, already found to give good correlation with multiaxial constant amplitude strain test data is developed to obtain allowable surface strain envelopes for high-cycle fatigue, in terms of the bending and twisting fatigue strengths of materials, properties which are readily available in the literature [*2–5*].

Idealization of Surface Strains

The surface strain records obtained from the service testing of a component suitably fitted with electrical resistance strain gages in the regions of greatest strain can be analyzed using plane-strain analysis methods to give the principal surface strain records at positions of interest on the surface of the component as shown in Fig. 1. The directions of the principal strains will generally vary with time. It will be conservative to assume that these principal strains always do occur in the same directions so that one particular set of planes will be critical,

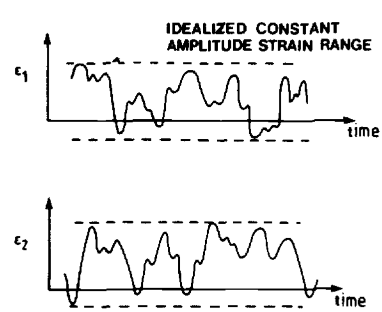

FIG. 1—*Principal surface strains.*

whereas in fact a number of possible critical planes will be subjected to less severe conditions in the same period.

For an initial estimate of whether the component is satisfactory for long life these principal strains are idealized, by inspection of the irregular principal strain records, to constant amplitude fluctuating variations in phase as shown in Fig. 1. Again it is conservative in the first instance to consider strain amplitudes based largely on an outer envelope of the irregular strains.

These fluctuating strains can be adjusted to equivalent alternating strain amplitudes by using the Booth [6] mean stress equation which would give

$$\epsilon_{ae} = \epsilon \left[1 - \frac{\epsilon_m}{\epsilon_{TS}} \right]^{1/2} \tag{1}$$

This equation deals with both tensile and compressive mean strains in a more satisfactory manner than the more commonly used Goodman line or Gerber parabola.

Crack Growth Cases

Brown and Miller [1] have shown that there are two possible cases of crack growth under biaxial fatigue conditions. Case A arises for negative values of $\lambda = \sigma_2/\sigma_1$ (actually σ_3/σ_1), where the cracks propagate *along* the surface and the surface strains are ϵ_1 and ϵ_3 as shown in Fig. 2. Case B arises for positive values of $\lambda = \sigma_2/\sigma_1$ where the cracks propagate *inwards* and the surface strains are ϵ_1 and ϵ_2 as shown in Fig. 2. Case B is more severe than Case A.

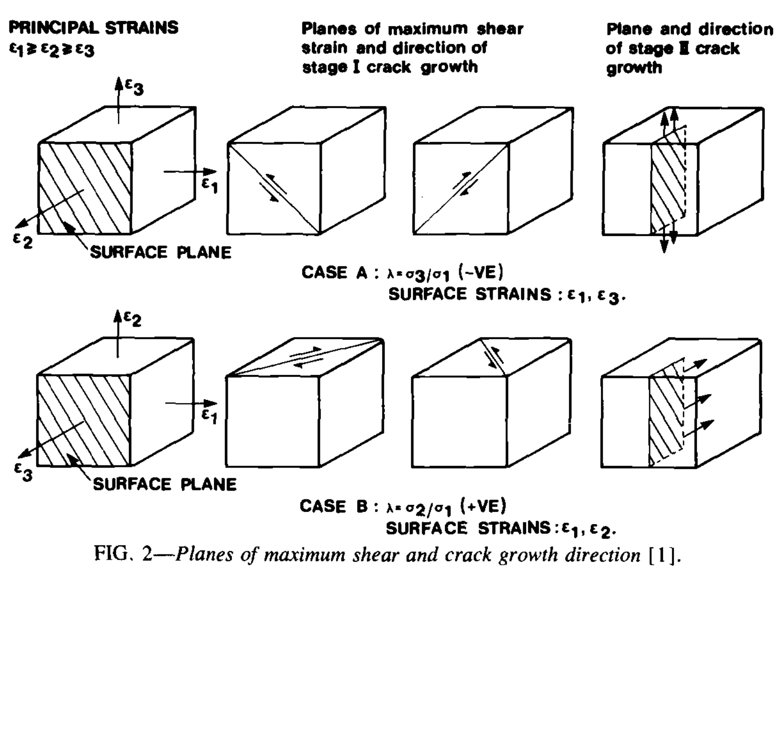

FIG. 2—*Planes of maximum shear and crack growth direction* [1].

Brown and Miller suggest that

$$\frac{\epsilon_1 - \epsilon_3}{2} = f\left[\frac{\epsilon_1 + \epsilon_3}{2}\right] \tag{2}$$

but do not attempt to quantify the function.

The designer does not as yet know whether his measured surface strains are ϵ_1 and ϵ_2 (potential Case B) or ϵ_1 and ϵ_3 (potential Case A).

Using the three-dimensional elastic stress-strain relationships

$$\epsilon_1 = \frac{1}{E}[\sigma_1 - \nu(\sigma_2 + \sigma_3)] \text{ etc} \tag{3}$$

with $\nu = 0.3$, the three principal strains can be found as functions of σ_1/E for a range of positive and negative values of λ as shown in Fig. 3.

If the surface strains are both positive then we have Case B. If one surface strain is positive and the other negative then we could have Case A or Case B. If the ratio of the lesser/greater surface strain is greater than $(-\nu)$, positively, then we have Case B; if the ratio is less than $(-\nu)$, negatively, then we have Case A.

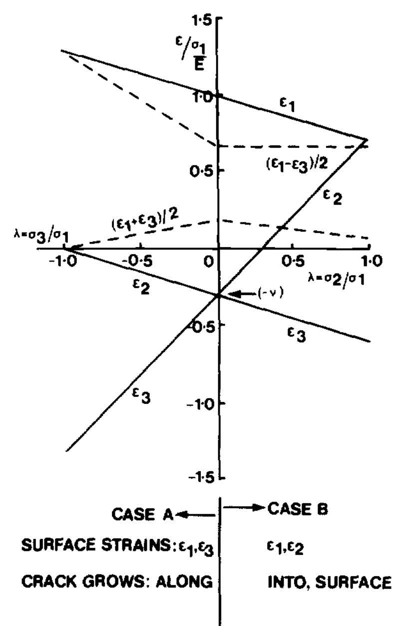

FIG. 3—*Principal strains as functions of* σ_1/E.

Criterion of Failure

Many criteria of fatigue failure under multiaxial stress-strain conditions have been proposed. Such theories are reviewed in [*7–10*] and many are listed in Ref *1*. As already shown in Eq 2 Brown and Miller [*1*] proposed a generalized theory based on maximum shear strains and normal direct strain. This paper was important in that physical cracking processes were considered, and the conclusion was reached that behavior was divided into two distinct cases, A and B, already described, so that classical failure criteria were inappropriate.

Findley [*11*] concluded that life was primarily influenced by the maximum shear stress but modified by the complementary normal direct stress, such that

$$\tau_a = \text{constant} - f(\sigma_\tau) \tag{4}$$

Other researchers [*10,12,13*] have proposed similar relationships. The Brown and Miller [*1*] theory is similar but in strain terms.

The relationship

$$\tau_a = t - [(t - 0.5\sigma_A)/(0.5\sigma_A)^{1.5}]\ \sigma_\tau^{1.5} \tag{5}$$

from Ref *10*, where the constants in Eq 4 have been expressed in terms of the torsion fatigue strength t, and the uniaxial fatigue strength σ_A has been found to give good correlation with high-cycle biaxial fatigue test data [*10,14*].

Where $\sigma_A = b$ and $t/b = Q$ with $\nu = 0.3$, Eq 5 can be expressed in terms of the surface strains ϵ_1 and ϵ_2 for $\lambda = \sigma_2/\sigma_1$ (positive) and $\sigma_3 = 0$, that is, Case B, as

$$\frac{\epsilon_1}{\epsilon_A} + 0.3\frac{\epsilon_2}{\epsilon_A} = 1.82\,Q - \{2.1Q - 1.05\}\left[\frac{\epsilon_1}{\epsilon_A} + 0.3\frac{\epsilon_2}{\epsilon_A}\right]^{1.5} \tag{6}$$

and in terms of the surface strains ϵ_1 and ϵ_3 for $\lambda = \sigma_3/\sigma_1$ (negative) and $\sigma_2 = 0$, that is, Case A, as

$$\frac{\epsilon_1 - \epsilon_3}{2\epsilon_A} = 1.3Q - (6.28Q - 3.14)\left[\frac{\epsilon_1 + \epsilon_3}{2\epsilon_A}\right]^{1.5} \tag{7}$$

For λ = positive, $\tau_a = \sigma_\tau = \sigma_1/2$ in Eq 5. Also it can be shown that $\sigma_1 = E(\epsilon_1 - \epsilon_3)/(1 + \nu)$ and as $(\epsilon_1 - \epsilon_3)$ is constant for λ positive as shown in Fig. 3, then the allowable strains are independent of Q, the ratio t/b. Allowable values of the surface strains ϵ_1 and ϵ_2 can be found from Eq 6 or more simply from

$$\epsilon_2 = \left(\frac{\lambda - \nu}{1 - \nu\lambda}\right)\epsilon_1 \tag{8}$$

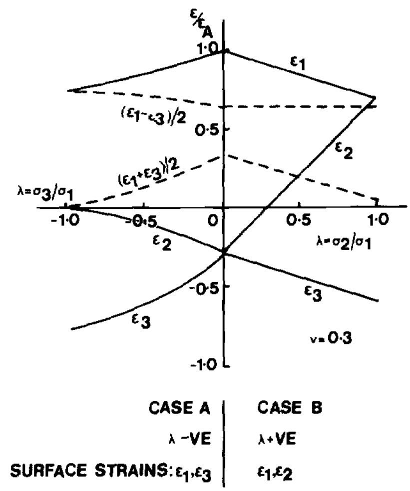

FIG. 4—*Allowable principal strains for* Q = *0.58 over* $-1 > \lambda < 1$.

where at $\lambda = +1$, $\epsilon_2 = \epsilon_1$ and $\epsilon_1/\epsilon_A = (1 - \nu)$ and at $\lambda = 0$, $\epsilon_2 = -\nu\epsilon_1$ and $\epsilon_1/\epsilon_A = 1$ with a linear variation between these values of λ.

Solving Eqs 6 and 7 for $Q = 0.58$, an average value for wrought steels [*4*] and also the value predicted by the shear-strain energy theory of failure, over $-1 > \lambda < 1$, gives strain values as shown in Fig. 4.

Solving the equations over a range of Q-values gives allowable surface strains as indicated in Fig. 5. The allowable values of maximum shear strain amplitude as a function of the tensile strain amplitude normal to the plane of maximum shear, both rationalized against the uniaxial reversed fatigue strength are shown in Fig. 6.

Discussion

Repeated stress test data [*10,15*] obtained from tests on thin-wall tubes subjected to repeated (zero to maximum) longitudinal load and repeated internal oil pressure, have been idealized as suggested earlier and show good agreement with the design envelopes as shown in Fig. 7. McDiarmid [*10*] conducted tests on 2L65 aluminum alloy cylinders of 22.2 mm internal diameter and 0.51 mm wall thickness over a range of transverse stress to longitudinal stress ratios of 0, 0.5, 1.0, 2.0, 7.9, −2.0, −1.0, −0.5, and −0. Ros and Eichinger [*15*] tested two steels (Rohrstahl and Stahlguss), two weld metals (Arcos Stabilend and Arcos Ductilend), and two aluminum alloys (Reinealuminum and Avional D) over a range of transverse stress to longitudinal stress ratios of 0, 0.5, 1, 2, 0, −1, and −0. These tests were all conducted in air at room temperature with the stresses in phase. Figure 7 shows that the test data for the cases where λ is positive fall close to the Case B predicted straight line. The several cases of

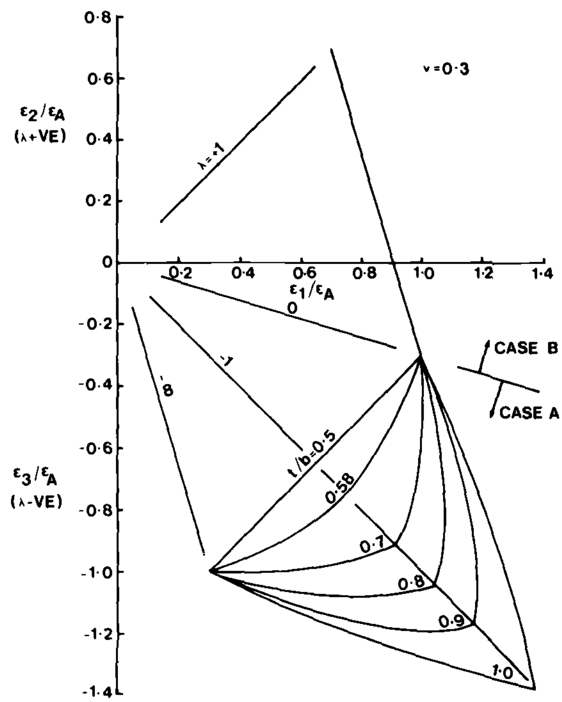

FIG. 5—*Allowable principal surface strains.*

positive ratio of transverse to longitudinal stress tested fall into two categories where either the longitudinal or transverse stress predominates, allowing for material anisotropy. Most of the Case A test data give reasonably good agreement with the predictions for the various t/b ratios except for $\lambda = -\infty$, that is, the repeated compression only case. It has been stated [10,15] that these test data are approximate due to practical difficulties experienced in the compression only

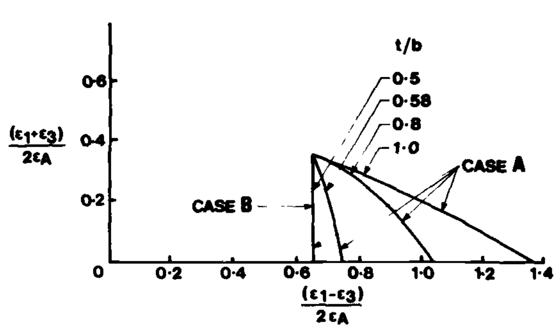

FIG. 6—*Allowable principal surface strains on* $\Gamma[(\epsilon_1 - \epsilon_3)/2$ *versus* $(\epsilon_1 + \epsilon_3)/2]$ *plane* [1].

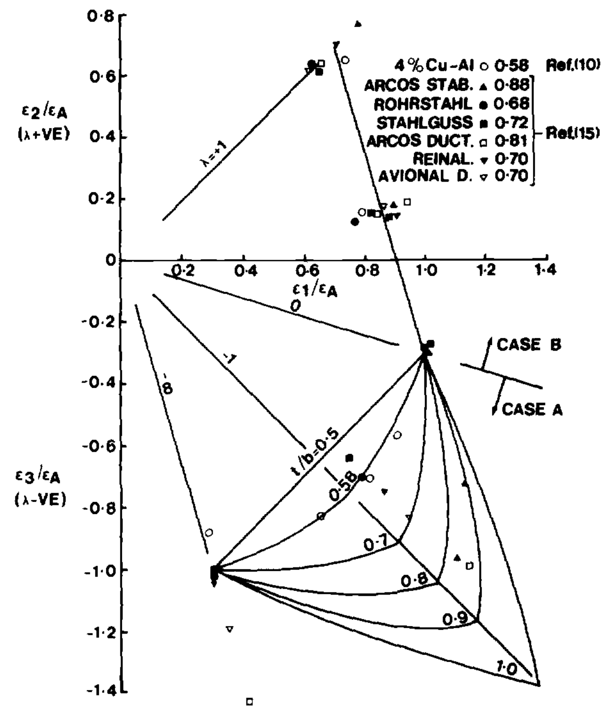

FIG. 7—*Test data correlation.*

case. The longitudinal or transverse value of ϵ_A, whichever is appropriate, has to be used to allow for the material anisotropy found in these tests. It is important in designing for biaxial fatigue that due allowance is made for material anisotropy as the transverse fatigue strengths of some steels and aluminum alloys can be up to 30% lower than their longitudinal fatigue strengths [*4,5*]. Combined bending and twisting data [*10*] have already been found to be in excellent agreement with Eq 7. This type of analysis could be also used for shorter lives as long as the bulk strain conditions are predominantly elastic, using the appropriate uniaxial endurance strain.

If this initial coarse analysis indicates that a potential fatigue problem does exist then a more "accurate" analysis could be attempted using a cycle counting method such as the rainflow method [*16*] and a cumulative damage law derived from the linear damage rule of Miner [*17*]. Such methods are discussed in Ref *18*. A closer assessment of the broad initial assumptions can be also made giving due regard to parameters such as amplitude ratio, mean strain, out-of-phase effects, frequency effects, rotating principal axes, crack growth directions, material anisotropy, sequence effects in cumulative damage, and the effects of low- and high-strain cycles.

Conclusions

1. Allowable surface strain envelopes have been found for high-cycle biaxial fatigue.
2. A method of dealing with irregular loading has been proposed, suitable for preliminary design/development calculations.
3. A method of determining the direction of possible crack growth based on the ratio of the surface strains has been proposed.

References

[1] Brown, M. W. and Miller, K. J., *Proceedings*, Institution of Mechanical Engineers, Vol. 187, 65/73, 1973, pp. 745–755.
[2] Gough, H. J., Pollard, H. V., and Clenshaw, W. J., "The Resistance of Metals to Fatigue under Combined Stress," R & M 2522, Aeronautical Research Council, 1951
[3] Nishihara, T. and Kawamoto, M., "The Strength of Metals under Combined Alternating Bending and Torsion," Memoirs College of Engineering, Kyoto Imperial University, Japan, Vol. 10, No. 6, 1941, pp. 177–201.
[4] Forrest, P. G., *Fatigue of Metals*, Pergamon, London, 1962, p. 107.
[5] Frost, N. E., Marsh, K. J., and Pook, L. P., *Metal Fatigue*, Oxford University Press, Oxford, 1974, p. 76.
[6] Booth, S. E. "Fatigue Failure Criteria Using Two Load Systems Out of Phase," M.Sc. thesis, University of London, London, 1970.
[7] Evans, W. J., "Deformation and Failure under Multiaxial Stresses—A Survey of Laboratory Techniques and Experimental Data," Note N.T.833, National Gas Turbine Establishment, U.K., 1972.
[8] Parsons, M. W., "Cyclic Straining of Steels under Conditions of Biaxial Stress," Ph.D. thesis, University of Cambridge, Cambridge, 1971.
[9] Ellison, E. G. and Andrews, J. M. H., *Journal of Strain Analysis*, Vol. 8, 1973, p. 209.
[10] McDiarmid, D. L., "Failure Criteria and Cumulative Damage in Fatigue under Multiaxial Stress Conditions," Ph.D. thesis, The City University, London, 1972.
[11] Findley, W. N., *Transactions*, American Society of Mechanical Engineers, Vol. 79, 1957, p. 1337.
[12] Guest, J. J., *Engineering*, London, 1943, Vol. 155.
[13] Stulen, F. B. and Cummings, H. N., *Proceedings*, American Society for Testing and Materials, Philadelphia, Vol. 54, 1954, p. 822.
[14] McDiarmid, D. L., *Proceedings*, Second International Conference on Pressure Vessel Technology, American Society of Mechanical Engineers, San Antonio, TX, 1973, pp. 851–862.
[15] Ros, M. and Eichinger, A., *Metalle Bericht*, Vol. 173, Sept. 1950.
[16] Matsuishi, M. and Endo, T., "Fatigue of Metals Subjected to Varying Stress," paper presented to Japan Society of Mechanical Engineers, Fukuoka, Japan, March 1968.
[17] Miner, M. A., *Transactions*, American Society of Mechanical Engineers, *Journal of Applied Mechanics*, Vol. 67, Sept. 1945, p. A159.
[18] Fuchs, H. O. and Stephens, R. I., *Metal Fatigue in Engineering*, Wiley, New York, 1980.

Roy A. Williams,[1] Ronald J. Placek,[1] Oleg Klufas,[1] Steven L. Adams,[1] and David C. Gonyea[1]

Biaxial/Torsional Fatigue of Turbine-Generator Rotor Steels

REFERENCE: Williams, R. A., Placek, R. J., Klufas, O., Adams, S. L., and Gonyea, D. C., **"Biaxial/Torsional Fatigue of Turbine-Generator Rotor Steels,"** *Multiaxial Fatigue, ASTM STP 853*, K. J. Miller and M. W. Brown, Eds., American Society for Testing and Materials, Philadelphia, 1985, pp. 440–462.

ABSTRACT: This paper presents the results of a study to develop a methodology for predicting torsional fatigue damage to a turbine-generator rotor subjected to transient electrical disturbances. This methodology used torsional properties obtained from constant amplitude tests on 25.4-mm-diameter specimens. The predictions were verified with constant amplitude and variable amplitude tests of specimens up to 127 mm in diameter.

The constant amplitude tests gave the following results:

1. Fatigue reduction factors for notched specimens were readily estimated from Neuber's rule.
2. Size effect could be approximated by lowering the strain-life curve by a function of the diameter ratio.
3. Uniaxial and torsional fatigue properties and cyclic stress-strain properties correlated on octahedral shear stress and strain using a deformation theory of plasticity.

Variable amplitude loading tests indicated that range pair cycle counting technique and linear damage rule predicted fatigue lives within a factor of two of actual test results. In addition, the predicted lives were generally conservative.

KEY WORDS: fatigue (materials), torsional fatigue, low cycle fatigue, high cycle fatigue, damage accumulation, notch fatigue

Engineering studies in the late 1970s revealed that a wide variety of electrical disturbances can produce transient oscillations in turbine-generator shafts. In many cases, the stresses produced by these oscillations were large enough to produce cumulative fatigue damage. To assess the damage produced, torsional fatigue methodologies were developed using torsional properties which were estimated from uniaxial fatigue properties due to a lack of a torsional fatigue data base.

[1]Engineer, manager of Rotor Design, and engineers, respectively, Steam Turbine-Generator Engineering and Manufacturing Department, General Electric Company, Schenectady, NY 12345.

Copyright© 1985 by ASTM International www.astm.org

For this reason, the Large Steam Turbine-Generator Division of the General Electric Company conducted an extensive torsional fatigue program on steels commonly used for large turbine-generator shafts. Since 1979, this study has been sponsored by the Electric Power Research Institute (EPRI).

A complete description of the experiments and analyses for this extensive program is contained in the EPRI Project RP 1531-1 final report [*1*]. Included also is a complete data base of fatigue properties of the 17 different heats of material tested. This paper presents a synopsis of the program. Test procedures and results of these tests are given for three materials studied. A methodology for predicting torsional fatigue damage in large turbine-generator shafts with variable amplitude loads is described in component form. Each of the methodology components was evaluated singly and in combinations with tests on small and large specimens.

Materials, Specimens, and Test Procedures

Materials

The materials in this program were vacuum treated steels that were representative of rotor materials used by present-day large steam turbine-generator manufacturers. The following three alloy steels were tested:

1. *Ni-Cr-Mo-V*—a low pressure rotor material within the scope of ASTM Specification A 470 [2].
2. *Ni-Mo-V*—a generator field material within the scope of ASTM Specification A 469 [2].
3. *Cr-Mo-V*—a high pressure rotor material within the scope of ASTM Specification A 471 [2].

Material blanks for the small specimens were removed axially from low stress regions of the turbine-generator shafts and the large test specimens. The chemical composition of the various heats of material are given in Table 1. Table 2 presents tension data for the different heats. The austenitizing and tempering temperatures of the final heat treatment for each of the heats are given in Table 3. No additional heat treatment was given to the small specimen blanks.

TABLE 1—*Chemistry.*

Rotor Serial	C	Mn	P	S	Si	Ni	Cr	Mo	V
122H240VA1	0.31	0.72	0.014	0.013	0.24	0.23	0.99	1.28	0.26
121E086VA2	0.23	0.29	0.005	0.010	0.04	3.39	1.70	0.39	0.12
122C311VA1	0.20	0.29	0.009	0.011	0.22	3.60	0.07	0.23	0.10

TABLE 2—*Tension data.*

Rotor Serial	Axial or Transverse	Tensile Strength, MPa (ksi)	0.02% Yield Strength, MPa (ksi)	Elongation, %	Reduction in Area, %
122H240VA1	A	831 (120.5)	662 (96)	19.1	62.1
121E086VA2	A	724 (105)	596 (86.5)	25	77
122C311VA1	A	632 (91.6)	507 (73.5)	27	69

Specimens

The torsional specimens used to obtain the "baseline" data were 25.4-mm-solid and thin-walled circular cylinders. Geometry effects were investigated with 25.4-mm-minimum diameter specimens with fillets (K_t = 1.44, 1.55, and 1.63) and a circular groove (K_t = 1.75). The large specimens were 127 mm in diameter, and the notched geometries were again fillets and grooves with elastic stress concentration factors of 1.5 and 2.0, respectively. Detailed sketches of the specimens are presented in the EPRI Final Report for RP 1531-1 [*1*].

Test Procedures

All tests were performed in servocontrolled electrohydraulic test machines. The torsional tests with linearly elastic stresses and strains on the outer surface of the smooth gage section were run in torque control. The nominal alternating shear stress, τ_a, was calculated from the alternating torque, T_a, with the equation

$$\tau_a = 2T_a/\pi R_0^3 \tag{1}$$

where R_0 is the radius of the specimen. The shear strain, γ_a, corresponding to this stress was calculated to be

$$\gamma_a = \tau_a/G \tag{2}$$

where G is the shear modulus determined from static tests. The tests were terminated when preset stroke limits were reached. When the test was terminated, there were always visible cracks.

For tests in which plastic strains were significant, the control parameter was

TABLE 3—*Final heat treatment temperatures.*

Rotor Serial	Austenitizing Temperature, °C	Tempering Temperature, °C
122H240VA1	968	671
121E086VA2	838	649
122C311VA1	816	638

strain on the outer surface of the specimen nominal section. Descriptions of the extensometers used to measure strains are given in Ref *1*. Torque was monitored and continuously recorded during testing, and the record of torque was used to define failure. The smooth specimen tests were terminated when the torque range dropped off significantly from a stabilized torque range. The notched specimen tests were terminated when a preset stroke limit was reached. Some of the large smooth specimen low cycle fatigue tests were run with torque as the control parameter and strain recorded as the uncontrolled parameter.

Two definitions of failure were used for the torsional fatigue tests of solid specimens in this program. The first definition, called failure, attempted to determine the cycle in which the torsional load carrying capacity of the structure became radically changed. The second definition, defined as engineering crack initiation or cracking, attempted to determine the cycle in which cracks were first observed. The following sections demonstrate how failure and crack initiation were determined.

The torque ranges for strain controlled tests were plotted on semilogarithmic paper with an expanded torque range scale, as shown in Fig. 1. For these strain softening materials, the torque range was found to decrease linearly with the logarithm of accumulated cycles. After a certain number of cycles, there was a

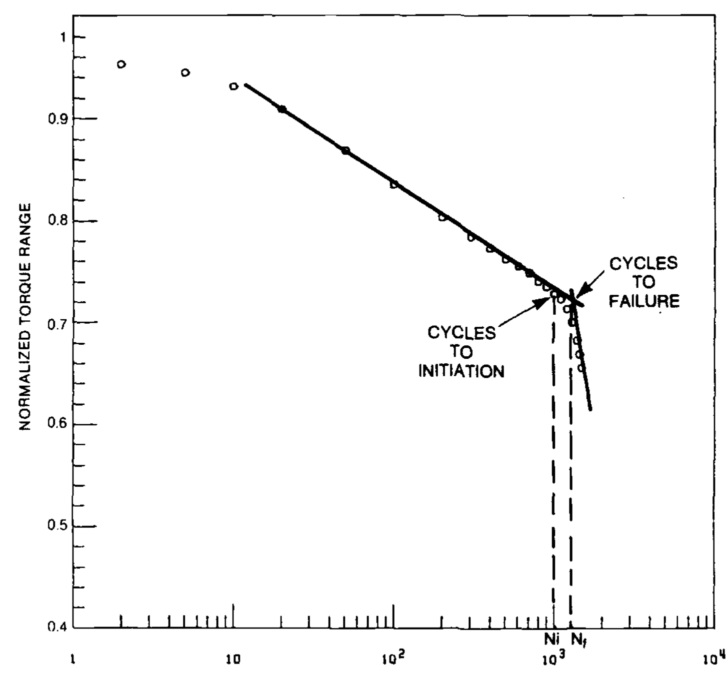

FIG. 1—*Definition of failure and crack initiation.*

change in the slope of the line, that is, the torque range dropped off more quickly with increasing cycles. It appeared possible to describe the increased slope by a second straight line. The intersection of these two straight lines was chosen as a convenient means for defining failure. At this point, the load carrying capacity changed radically due to the presence of a large crack.

An engineering size crack was defined as a crack that was (1) visible, (2) essentially a surface crack, and (3) able to be propagated to failure as defined previously. The initiation of an engineering crack was estimated by noting the earliest detectable deviation from the logarithmic softening of smooth baseline specimens, as shown in Fig. 1. This definition, like the previous definition of failure, attempted to identify a very slight compliance change and correlate this change with a small surface crack. A better correlation requires fracture mechanics analysis and fatigue crack growth rate data that are not available to date. However, it should be noted that no cracks were visible in any smooth specimen prior to the cycle in which initiation or cracking was defined. For notched specimens, cracking was defined with an observed crack.

Analysis of Baseline Material Properties

The torsional fatigue methodology presented later in this report requires baseline cyclic stress-strain and fatigue life properties as input. In this section, procedures for obtaining them are described.

Cyclic Stress-Strain Properties

1. Uniaxial Cyclic Stress-Strain Curves—The materials in this program were cyclic softening materials. During the softening process, the rate of change of the stress level decreases from an initial rapid rate to a rate in which the level may be considered almost stable [*3–6*] at one half the specimen fatigue life. For this assumed stable material, the relationship between stress and strain is called the cyclic stress-strain curve [*7–9*] and is generally represented by the following equation

$$\epsilon_a = \frac{\sigma_a}{E} + \left[\frac{\sigma_a}{H}\right]^{1/s} \tag{3}$$

where

$\epsilon_a = \Delta\epsilon/2$ = strain amplitude,
$\sigma_a = \Delta\sigma/2$ = stress amplitude,
E = elastic modulus,
H = cyclic strength coefficient, and
s = cyclic strain hardening exponent.

The constants H and s are determined from regression analysis. The numerical values for all the material constants are given in Table 4. Figure 2 represents the cyclic stress-strain curve for the nickel-chromium-molybdenum-vanadium

TABLE 4—*Material stress-strain and strain life constants.*

			Materials		
			Ni-Cr-Mo-V	Ni-Mo-V	Cr-Mo-V
Uniaxial	E	(MPa)	200 000	201 000	204 000
Material		(psi)	29.0×10^6	29.2×10^6	29.6×10^6
Constants	H	(MPa)	689.5	726.7	748.8
		(psi)	100 000	105 400	108 600
	S		0.061	0.075	0.060
	A		0.0034	0.0037	0.004
	α		−0.043	−0.055	−0.051
	B		1.14	1.34	2.6
	β		−0.69	−0.71	−0.79
Torsional	G	(MPa)	80 670	82 760	82 760
Material		(psi)	11.7×10^6	12.0×10^6	12.0×10^6
Constants	H'	(MPa)	426	387	451
		(psi)	61 750	56 180	65 430
	S'		0.087	0.074	0.082
	A'		0.0055	0.0048	0.0059
	α'		−0.054	−0.043	−0.052
	B'		1.69	1.24	1.69
	β'		−0.62	−0.59	−0.64
Octahedral	G	(MPa)	77 240	77 931	79 310
Shear		(psi)	11.2×10^6	11.3×10^6	11.5×10^6
Predicted	H'	(MPa)	385	403	418
Torsional		(psi)	55 833	58 396	60 667
Material	S'		0.061	0.075	0.060
Constants	A'		0.0051	0.0055	0.0059
	α'		−0.043	−0.055	−0.051
	B'		1.97	2.32	4.50
	β'		−0.69	−0.71	−0.79

(Ni-Cr-Mo-V) material tested. Shown also are the test data. These results were typical of all the materials tested.

2. *Uniform Shear Cyclic Stress-Strain Relationship*—With suitable test data, cyclic stress-strain curves can be found for stress states other than uniaxial. Halford and Morrow [*10*] found by testing thin-walled tubes in torsion that the cyclic stress-strain curves may be expressed as

$$\gamma_a = \frac{\tau_a}{G} + \left(\frac{\tau_a}{H'}\right)^{1/s'} \tag{4}$$

$$\gamma_{ae} = \frac{\tau_a}{G},\ \gamma_{ap} = \left(\frac{\tau_a}{H'}\right)^{1/s'} \tag{5}$$

where

τ_a = shear stress amplitude,
$\gamma_a, \gamma_{ae}, \gamma_{ap}$ = total, elastic, and plastic shear amplitudes, respectively,
G = elastic modulus in shear,
H' = cyclic shear strength coefficient, and
s' = cyclic shear strain hardening exponent.

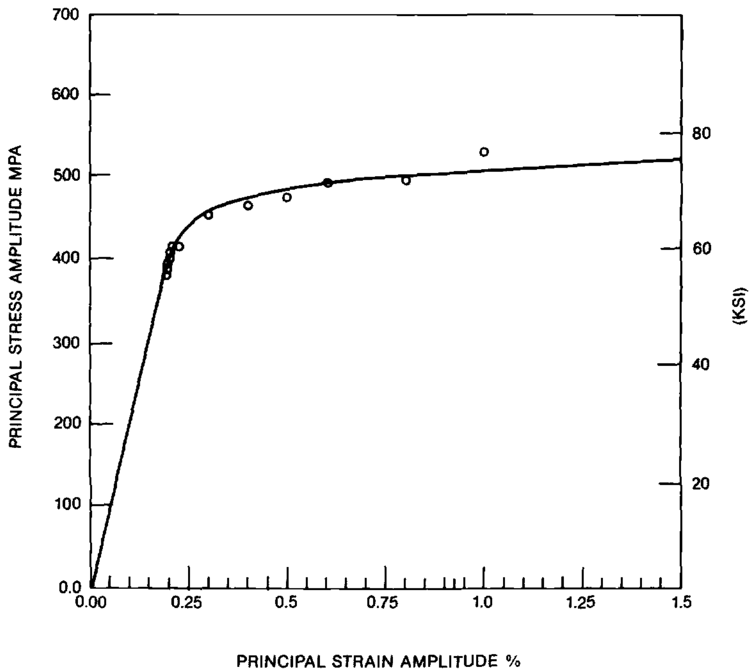

FIG. 2—*Uniaxial cyclic stress-strain results for Ni-Cr-Mo-V.*

Although the test is not a great deal more difficult than the uniaxial test, the number of thin-walled torsion tests performed to date is minuscule compared to the number of uniaxial tests. It is thus advantageous to be able to predict these stress strain properties from uniaxial results. For monotonic loading, the relationship between octahedral shear stress and octahedral shear strain has been found to be independent of the state of stress [*11,12*]. This relationship also appeared to be reasonable for cyclic loading provided the stress state is such that Hencky's deformation theory of plasticity is valid [*13–16*]. In terms of principal stress amplitude components, the octahedral shear stress amplitude, τ_{ag}, is defined by

$$\tau_{ag} = 1/3\ ((\sigma_{a1} - \sigma_{a2})^2 + (\sigma_{a2} - \sigma_{a3})^2 + (\sigma_{a3} - \sigma_{a1})^2)^{1/2} \qquad (6)$$

Likewise, octahedral shear strain, γ_{ag}, is related to principal strain amplitude components by

$$\gamma_{ag} = 2/3\ ((\epsilon_{a1} - \epsilon_{a2})^2 + (\epsilon_{a2} - \epsilon_{a3})^2 + (\epsilon_{a3} - \epsilon_{a1})^2)^{1/2} \qquad (7)$$

The octahedral shear representation of stress and strain in uniaxial and torsional fatigue tests are equated to yield the following relationship between the constants

$$\begin{aligned} s' &= s \\ H' &= H(1/3)^{(s+1)/2} \\ G &= E/2\,(1 + \nu) \end{aligned} \tag{8}$$

In addition to an octahedral shear correlation, a Tresca criteria [13] was examined. In terms of principal stresses and strains, the maximums of shear stress and strain are given by

$$\tau_{\max} = (\sigma_{a1} - \sigma_{a3})/2 \tag{9}$$

$$\gamma_{\max} = \epsilon_{a1} - \epsilon_{a3} \tag{10}$$

The resulting relationships between the constants are

$$\begin{aligned} s' &= s \\ H' &= H/2\,(2/3)^{s'} \\ G &= E/2\,(1 + \nu) \end{aligned} \tag{11}$$

3. Torsional Cycle Stress-Strain Relationship—The basic assumption in torsion of a circular section is that the strain distribution is proportional to the radius at any point in the section. If this assumption is applied to cyclic loading, the results are that relationships developed for stress and strain on the outer surface [18] can be applied to stress and strain ranges or amplitudes. In terms of the angle of twist amplitude per unit length, θ_a, the shear strain amplitude on the outer fiber, γ_{oa}, [18,19] is given by

$$\gamma_{oa} = R_o\theta_a \tag{12}$$

where R_o is the outside radius. The basic relationship between torque amplitude, T_a, and the shear stress amplitude, τ_a, is given by Eq 13 for a solid cylinder

$$T_a = \int_0^{R_0} 2\pi r^2 \tau_a \, dr \tag{13}$$

This integral equation was solved for τ for monotonic loading by Nadai [20]. Extending Nadai's solution to cyclic loading, the surface shear stress amplitude can be expressed similarly as a function of the torque amplitude and angle of twist amplitude per unit length as follows

$$\tau_{oa} = \frac{1}{2\pi R_0^3}\left\{3T_a + \theta_a \frac{dT_a}{d\theta_a}\right\} \tag{14}$$

This analysis was extended to tubular geometries by Brown [21] and resulted in the following approximate expression

$$\tau_{oa} = \frac{1}{2\pi}\left\{\frac{3T_a}{R_0^3 - R_i^3} + \left[\frac{4R_0}{R_0^4 - R_i^4} - \frac{3}{R_0^3 - R_i^3}\right]\theta_a \frac{dT_a}{d\theta_a}\right\} \tag{15}$$

This approximation is exact for elastic and fully plastic stress distributions and for solid cylinders. It also tends toward the exact solution for a thin-walled tube. The slope, $dT_a/d\theta_a$, is best calculated from a curve fit of discrete (T_a, θ_a) data. Normally, these data are taken versus the stable (half-life) values and can be reasonably fitted with the equation

$$\theta_a = \frac{T_a}{JG} + \left[\frac{T_a}{K_0}\right]^{1/n_0} \tag{16}$$

where K_0 and n_0 were constants determined from regression analysis and J is the polar section modulus. In this case

$$\frac{dT_a}{d\theta_a} = \frac{T_a}{\left[\frac{T_a}{JG} + \frac{1}{n_0}\left\{\frac{T_a}{K_0}\right\}^{1/n_0}\right]} \tag{17}$$

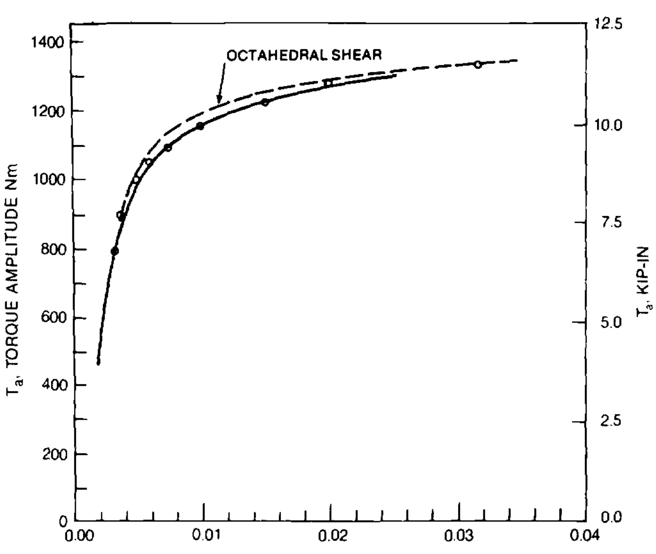

FIG. 3—*Torque strain results for Ni-Cr-Mo-V.*

The cyclic stress-strain equation in torsion is expected to take the same form as Eq 4 and is given by

$$\gamma_{oa} = \gamma_{oae} + \gamma_{oap} = \frac{\tau_{oa}}{G} + \left[\frac{\tau_{oa}}{H'}\right]^{1/s'} \tag{18}$$

where

γ_{oa} = shear strain amplitude on the outer surface,
τ_{oa} = shear stress amplitude on the outer surface,
G = shear modulus,
H' = strength coefficient, and
s' = strain hardening exponent.

Table 4 presents the torsional cyclic shear strength coefficient H' and the shear strain hardening exponent s' for the material studied. To compare the results of this procedure with test data, the elastic and plastic shear strain amplitudes on the surface and the determined constants were substituted in the following equation given by Dowling [17]

$$T_a = 2\pi R^3\tau_{oa}\left\{\frac{1/4 + \dfrac{2s'+1}{3s'+1}\left[\dfrac{\gamma_{oap}}{\gamma_{oae}}\right] + \dfrac{s'+2}{2s'+2}\left[\dfrac{\gamma_{oap}}{\gamma_{oae}}\right]^2 + \dfrac{1}{s'+3}\left[\dfrac{\gamma_{oap}}{\gamma_{oae}}\right]^3}{\left[1+\left(\dfrac{\gamma_{oap}}{\gamma_{oae}}\right)\right]^3}\right\} \tag{19}$$

As shown in Fig. 3, excellent agreement was attained.

Also noted in this study was the near agreement of the strain hardening exponent, s, in both the uniaxial expression and the torsional expression for the cyclic stress-strain curve. This agreement suggested a correlation between the two equations. One such examined correlation was octahedral shear theory in which the relationships between the constants are given in Eq 8. Figure 3 also presents the predicted torque-strain curves for Ni-Cr-Mo-V based on octahedral shear theory. This curve demonstrates that torsional cyclic stress-strain data can be approximated reasonably well from uniaxial data. The results of the other materials tested were equally as good. In addition to octahedral shear correlation, a Tresca correlation as suggested by Brown and Miller [22] was examined. The correlation was reasonable but not as good as octahedral shear.

Fatigue Properties

Low cycle fatigue properties are normally presented as strain life diagrams, which are curves of strain amplitude versus reversals to failure that are fitted to experimental data. In this section, typical uniaxial and torsional fatigue properties

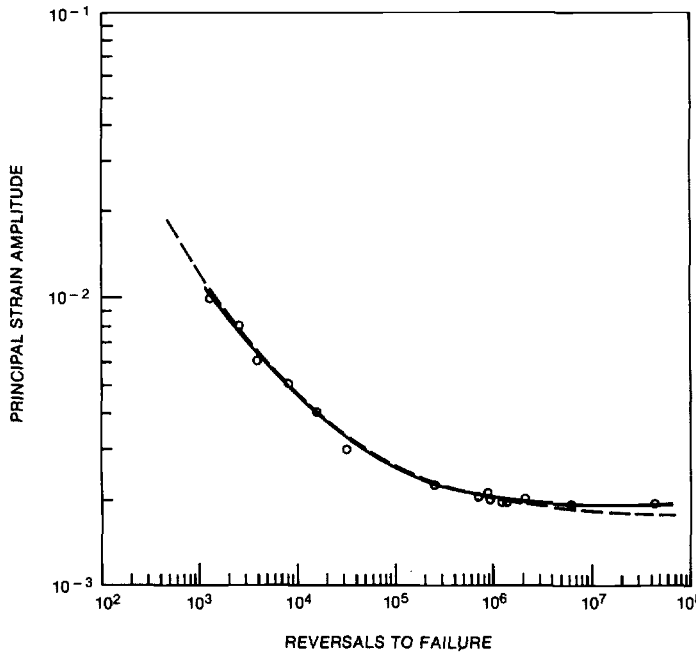

FIG. 4—*Uniaxial strain-life results for Ni-Cr-Mo-V.*

of the program materials are presented. A procedure for estimating torsional fatigue properties from uniaxial tests is also presented.

1. Uniaxial Fatigue Properties—The uniaxial strain life diagram for the Ni-Cr-Mo-V material is given in Fig. 4. The smooth curve is a best fit of the data by eye and is bounded from below by the endurance limit. Another common way to fit the data is with a universal slopes [*4–6*] equation of the form

$$\epsilon_a = A(2N_f)^{\alpha} + B(2N_f)^{\beta} \tag{20}$$

where the constants A, α, B, and β (Table 4) are determined from regression analysis of the elastic and the plastic components of strain. Because the materials exhibit an endurance limit, the universal slopes-type equation resulted in conservative life predictions in the high cycle regime as shown in Fig. 4.

2. Torsional Fatigue Properties—Typical torsional strain life diagrams are presented in Fig. 5 as plots of shear strain amplitude versus reversals to failure. The solid curve again is a best fit of the data set by eye. A fit of the data with a universal slopes-type equation of the form

$$\gamma_a = A'(2N_f)^{\alpha'} + B'(2N_f)^{\beta'} \tag{21}$$

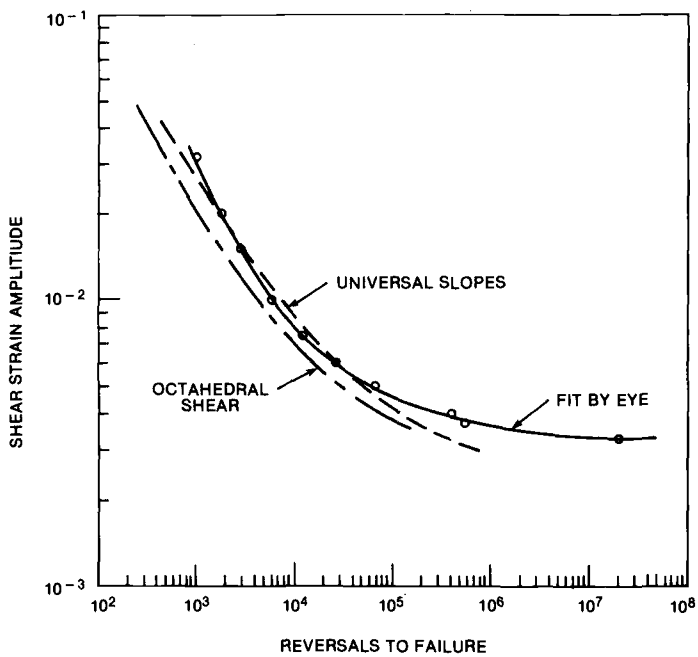

FIG. 5—*Torsional strain-life results for Ni-Cr-Mo-V.*

was examined, and the result is shown also in Fig. 5. This curve demonstrates again that the high cycle portion of the curve is conservatively predicted because of the apparent endurance limit behavior. It was again noted that the exponents for the uniaxial and torsional case were similar. Since octahedral shear theory correlated the cyclic stress-strain results reasonably well, it was examined for application to the strain life results. The following relationships between the constants in Eq 20 and 21 for an octahedral shear correlation were determined by equating octahedral shear strains for the torsional and uniaxial tests.

$$\begin{aligned} A' &= \frac{2}{3^{1/2}}(1 + \nu) A, \qquad \alpha' = \alpha \\ B' &= 3^{1/2} B, \qquad \beta' = \beta \end{aligned} \tag{22}$$

Curves of predicted results are also given in Fig. 5. These curves all predicted the results conservatively.

Correlations other than octahedral shear were also examined. In the low cycle region, where the greatest portion of life is spent on the propagation of cracks, one would expect a correlation based on quantities that control fatigue crack growth. Miller et al [*23–26*] proposed such a criteria which is a function of the maximum shear strain and the tensile strain normal to the plane of maximum shear. Although this failure theory is general and applicable also to other biaxial fatigue tests, the theory is not inconsistent with an octahedral shear strain criteria for torsion.

Methodology

General Description of the Fatigue Methodology

The methodology to predict the torsional fatigue life of large turbine-generator shafts incorporated the local strain approach. This concept makes it possible to calculate fatigue damage at regions of stress concentrations using the results of a notch stress analysis and smooth bar fatigue data. Figure 6 presents an overall flowchart for the methodology. The step-by-step procedure for its use was as follows:

1. The stresses and strains at the shaft nominal section were determined from the input torques.
2. The geometry under consideration was modeled, and the theoretical stress concentration was determined.
3. Material properties, given by the strain life diagram and the cyclic stress-strain diagram, were developed from fatigue tests for the specific materials under consideration. The cyclic stress-strain properties developed for the 25.4-mm specimen were used directly. However, the fatigue curves were modified for size effect using the equation

$$\gamma_{a1}/\gamma_{a2} = (D_1/D_2)^{-0.093} \tag{23}$$

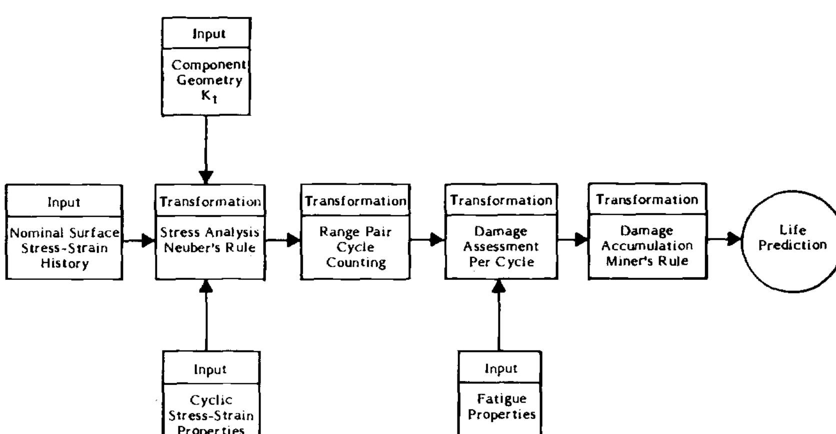

FIG. 6—*Schematic of cumulative fatigue procedure.*

where the subscript 1 and 2 refer to the rotor diameter and the reference diameter of the smooth baseline fatigue data, respectively. This relationship was obtained from regression analysis of high cycle torsional and bending fatigue tests on specimens ranging from 7.62 mm (0.3 in.) to 228.6 mm (9.0 in.) in diameter [27–29]. Although this relationship was obtained from high cycle fatigue data, it was shown to be applicable over all regimes of the strain life diagram. In Fig. 7, the smooth fatigue curve for the 25.4-mm-diameter specimens was adjusted to predict the 127-mm-diameter curve. The superimposed data were the first observed cracks in the 127-mm-diameter specimen tests.

4. The stress-strain behavior at the specified stress concentrated location was evaluated from stress analysis of the geometry under consideration. Since detailed finite element analysis of all notched geometries would not be feasible, an approximate method for estimating the stresses and strains in a notch was used. This method was Neuber's rule [*30*]

$$K_t^2 = \tau_a \gamma_a / \tau_{oa} \gamma_{oa} \tag{24}$$

where τ_a and γ_a are, respectively, the maximum shear stress and shear strain amplitudes in the notch, τ_{oa} and γ_{oa} are the shear stress and shear strain amplitudes, respectively, on the outer surface of the nominal section, and K_t is the theoretical stress concentration factor. Elastic-plastic finite element analyses were performed on a fillet and a groove geometry. The results of the analyses were compared to results which used Neuber's rule in terms of von Mises effective stress and strain. Excellent agreement was found.

5. Since fatigue damage is assessed on a closed hysteretic loop basis, the notch strain history was analyzed with a cycle counting technique which identifies closed hysteretic loops. In reviewing cycle counting techniques, Dowling [*31,32*] concluded that only the range pair and rain flow methods gave satisfactory cycle

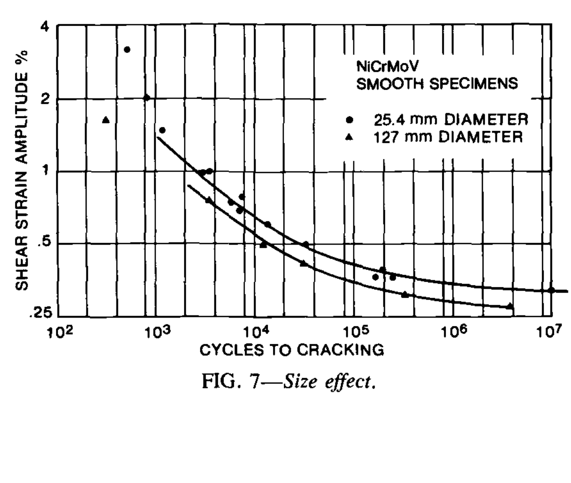

FIG. 7—*Size effect.*

counts. All other techniques such as peak counting, mean crossing peak, and level crossing neglect sequence and, therefore, underestimate the fatigue damage. The range pair method was used in this methodology.

6. The fatigue damage done during each closed hysteretic loop was determined from constant amplitude strain life diagrams. For each cycle of strain amplitude, γ_{a1}, the fatigue life expended was $(2N_{f1})^{-1}$ where $2N_{f1}$ represents the number of reversals to failure for the material tested at a constant strain amplitude γ_{a1}.

7. The fatigue damage for each reversal must be summed to obtain the cumulative damage. Linear damage techniques were used for damage summation in the form of Palmgren-Miner [33] rule given by

$$\sum_{1}(n/N)_1 = 1 \tag{25}$$

where

n = number of applied cycles at a specified deformation level, and
N = number of cycles to produce a failure at the same deformation level.

Results

The correlation between theory and experimental results for each step of the cumulative fatigue damage assessment procedure was individually and collectively evaluated through appropriate tests. Exponential decay, high-low, and low-high sequence tests on smooth specimens were used to evaluate linear cumulative damage rules. The range pair cycle counting technique in combination with the linear damage rule was evaluated with tests on smooth specimens with complex simulated line fault loadings. Neuber's rule to correlate notched specimen fatigue data with smooth specimen data was evaluated with constant amplitude tests in both small and large diameter specimens. Finally, the overall methodology was evaluated with complex load history tests on notched speci-

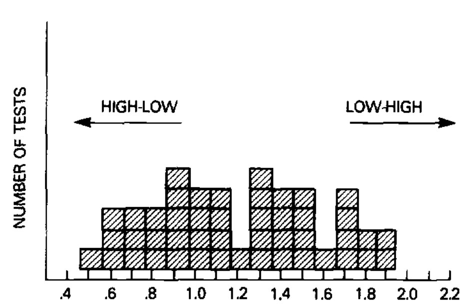

FIG. 8—*Distribution of damage summation ratios.*

mens. The following sections present the results of the methodology evaluation tests.

Damage Accumulation

The applicability of linear cumulative damage theory to torsional fatigue problems was evaluated with several different load histories. The simplest load history was a high-low sequence in which the specimen was subject to large constant amplitude deformation for 25 to 50% of its estimated fatigue life and then tested at a lower constant amplitude until failure. This procedure was then reversed, that is, the testing started out with low constant amplitude deformation and was followed by large constant amplitude deformation. The order in which cyclic loads are applied to a fatigue specimen normally affects its fatigue life. It has been shown in uniaxial fatigue that the high-low sequence is more damaging than the low-high sequence. The results shown in Fig. 8, in general, confirm that this sequence effect also holds for torsional fatigue. Linear damage rules were also evaluated with loading histories in the form of a decaying exponential function. The results of these tests are presented in Fig. 9 for the Ni-Cr-Mo-V material. Very good correlation between prediction and test results was obtained for this waveform.

Cycle Counting

To evaluate the cycle counting procedure, six smooth specimens of each material were subject to a complex strain history shown in Fig. 10. This complex history contained 394 reversals and was considered representative of the multi-

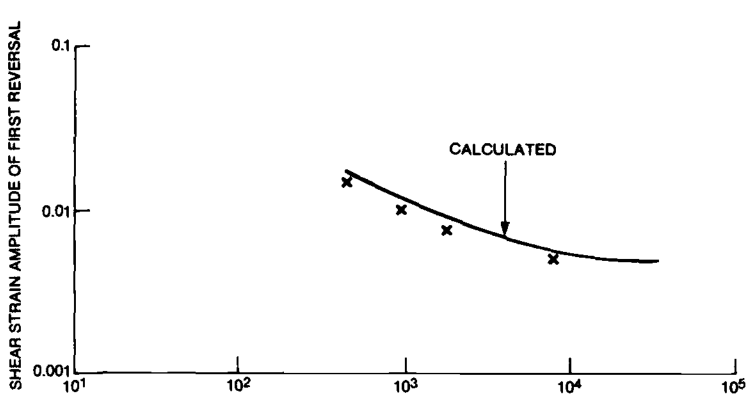

FIG. 9—*Exponential history smooth bar fatigue tests on Ni-Cr-Mo-V.*

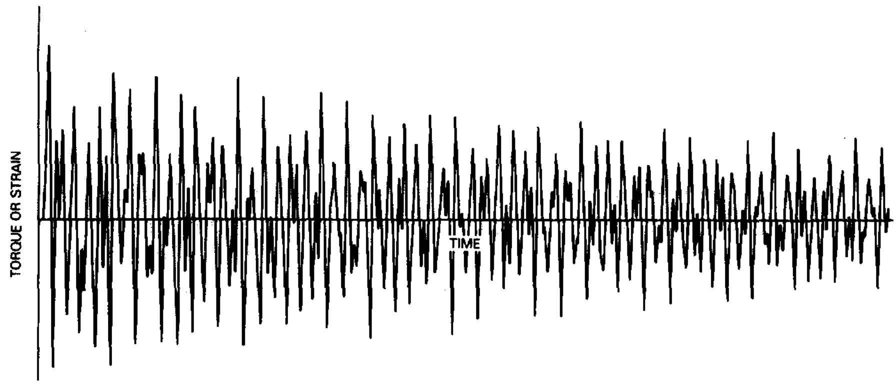

FIG. 10—*Simulated line-fault history.*

model response observed in turbine-generator shafts during torsional disturbances. A comparison of the experimental and analytical results showed that, in general, the calculated results were within a factor of two of the measured results. The results also indicated the following:

1. The analytical predictions improved with decreasing blocks to failure.
2. The calculated results generally overestimated the fatigue capability.
3. The data were fairly consistent and not scattered.
4. All the alloys exhibited the same trends on plots of initial strain amplitude versus cycles to failure, as shown in Fig. 11 for Ni-Cr-Mo-V.

Stress Analysis

The use of Neuber's rule to characterize the deformation and fatigue response of notches was evaluated with constant amplitude tests on both small and large diameter specimens. Two groove and three fillet small specimen geometries and one groove and one fillet large specimen geometry were tested. Analytical predictions were made from Eq 24 with the appropriate cyclic stress-strain curve. Typical results of the small specimen analyses and tests are shown in Fig. 12. In general, the calculated lives were conservative compared to the measured lives. In particular, analytical predictions became more conservative with increasing cycles to cracking, as shown in Fig. 13. One reason for this conservatism could be the use of K_t in place of a fatigue reduction factor, K_f, in Eq 24.

The results of Neuber's rule verification tests on large specimens are shown in Fig. 14. The predicted results correlated very well for the groove geometry tests and for all but one test for the fillet geometry. This specimen which failed in 200 cycles appeared to exhibit gross plasticity in the notch which may have accounted for the nonconservative results.

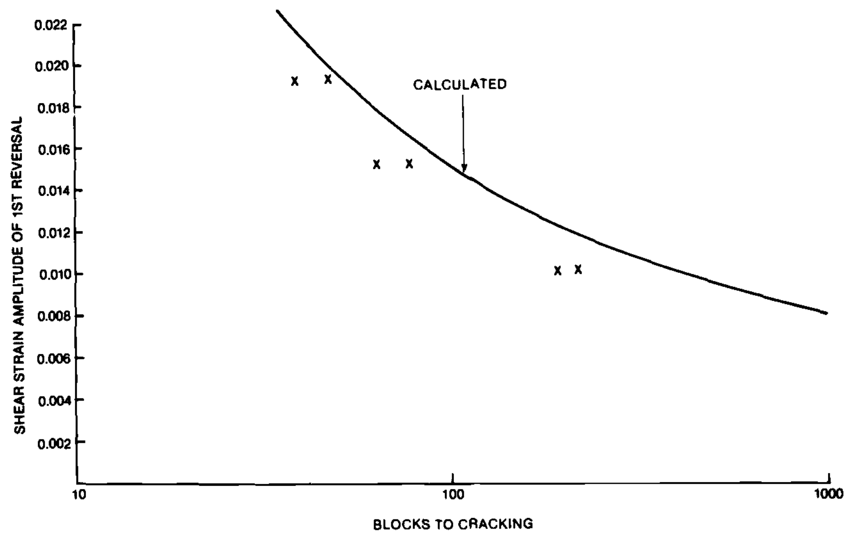

FIG. 11—*Complex history smooth bar fatigue tests on Ni-Cr-Mo-V.*

Methodology Evaluation

The overall methodology was evaluated with a series of tests on both large and small specimens containing stress concentrations. The methodology was evaluated first with the series of tests on small notched specimens. Exponential decay and complex waveform tests were run on grooved specimens. The results are shown in Fig. 15 of the complex waveform test. The results indicate that the methodology conservatively predicted the life. The final evaluation of the methodology was made with large fillet specimens. The results for the fillet

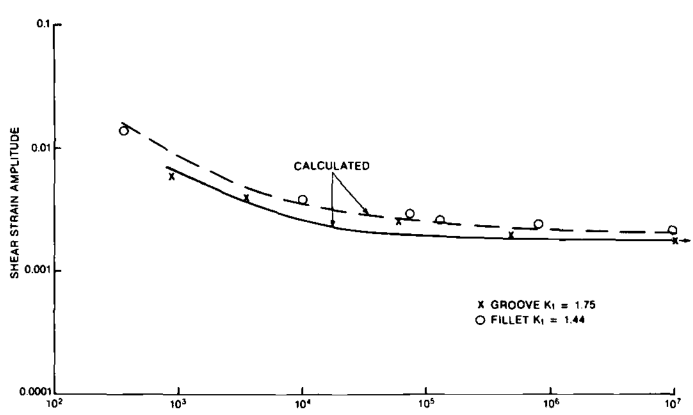

FIG. 12—*Constant amplitude fatigue tests on notched Ni-Cr-Mo-V specimens.*

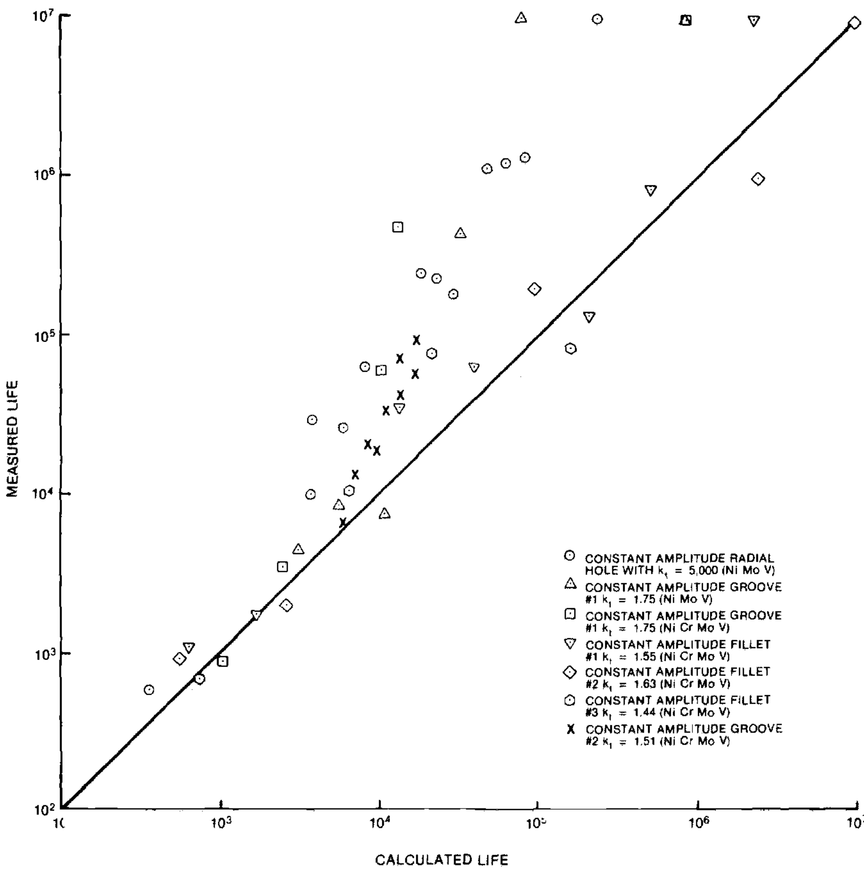

FIG. 13—*Measured versus calculated lives for the various constant amplitude fatigue tests on specimens with stress concentration factors.*

specimen tests are shown in Fig. 16 as a function of torque amplitude of first reversal versus blocks to cracking. The test results agree excellently with the calculated results. Also, except for the high torque test, the predicted results are conservative.

Discussion and Conclusions

The objective of this work was to generate a data base and to develop a methodology that will predict the torsional fatigue damage in turbine-generator shafts subjected to a variety of torsional transients. The methodology developed was made as simple as possible. It was reasoned that, given a formidable body of torsional fatigue data, more than one methodology with satisfactory predictive capability could be developed. Thus, primary emphasis was placed on generation of sufficient data for the development and verification of such methodologies.

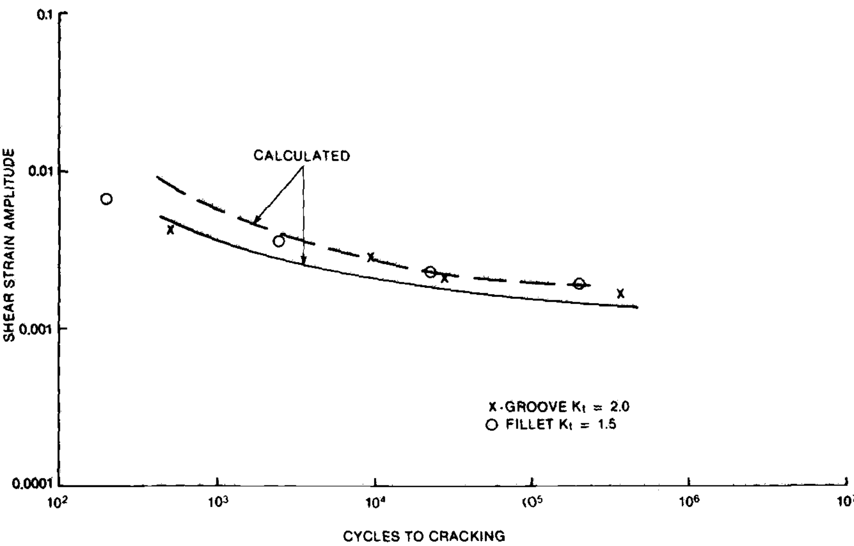

FIG. 14—*Verification tests—constant amplitude fatigue tests on large Ni-Cr-Mo-V specimens.*

The test program was set up to permit evaluation of various parameters on torsional fatigue strength. In general, the influences were understood in terms of smooth 25.4-mm-diameter cylindrical specimen data. The influence of geometry, other stresses, loading sequence, and specimen size on torsional fatigue strength was investigated. In the evaluation of the range of test geometries, it

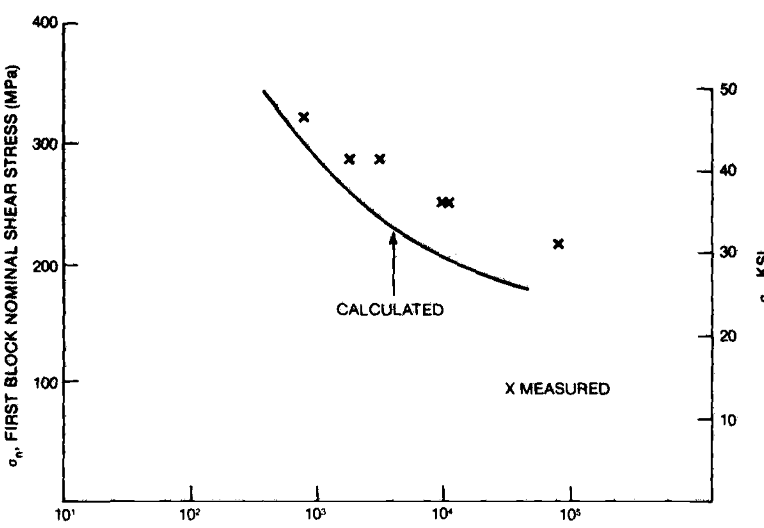

FIG. 15—*Complex history fatigue tests on Cr-Mo-V specimens with a groove,* k_t = *1.75.*

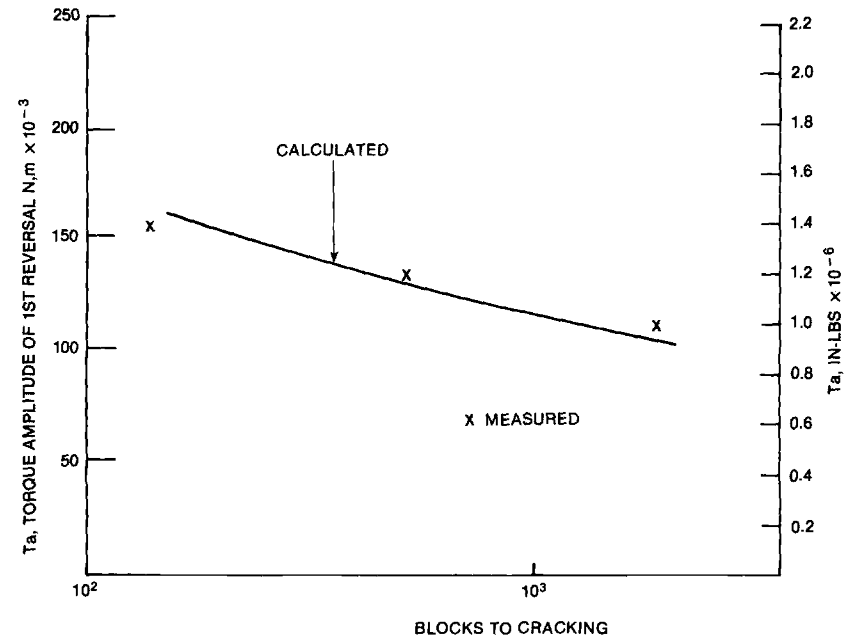

FIG. 16—*Verification test—complex history fatigue on large Ni-Cr-Mo-V specimen with shoulder filler,* k_t = *1.50.*

quickly became apparent that grooves and fillets in small diameter regions of turbine-generator rotors would generally result in stress concentration factors of less than two. It was surmised that this narrow range of stress concentrations factors would also result in a fairly narrow range of elasto-plastic strain concentration. This supposition was supported by test results and finite element analysis.

The Neuber notch simulation was also tried, and it was decided that this simple approach was sufficiently accurate within the scope of other uncertainties. Size effect, reduced fatigue strength of large over small specimens at the same number of cycles to failure, was observed in specimens with grooves and fillets as well as in smooth specimens. It was accounted for by reducing the strain by the ratio of specimen diameters raised to a power. Damage accumulation methods previously developed for axial fatigue were applied successfully to torsional fatigue. Basically, the concept used the average specimen strain-life representation, the stress at specimen half-life, linear damage accumulation, and the range-pair cycle counting method. The torsional testing in combination with other steady and alternating stresses was, in general, exploratory in nature. Mean torsional loading showed no effect on torsional fatigue life up to the point where combined mean and alternating loading exceeded the gross section yield stress and resulted in rachetting. The mean torsional loading was limited to 103.4 MPa (15 ksi). The onset of ratchetting was noted, but ratchetting was not studied per se due to rotational limitations of the test machine.

The need to explore effects of axial stresses on torsional fatigue strength was recognized. Axial stresses at or near turbine-generator journals could be caused by centrifugal, thermal, and gravity bending effects. While centrifugal and thermal stresses could be treated with fatigue diagrams as mean stresses with respect to torsional transients, the gravity bending stress is an alternating stress and poses a more complex problem. Indeed, some of the tests under combined torsion and axial fatigue indicated a significant effect of axial components. However, detailed analysis of these last effects was outside of the scope of this project.

The foregoing discussion has described the scope and limitations of information developed under this program. The limitations of the developed methodology are similar. It is believed that the predictive method is accurate if the damaging cyclic strain amplitudes are in the low cycle region of the strain-life curve (500 to 100 000 cycles to failure). Cycles with strain magnitudes larger than that can result in local heating, elastic hinge instability, ratchetting, or shaft bending. The damage from cycles in the high cycle fatigue region may be significant; however, this damage will be highly dependent on surface finish and will be difficult to assess because the life curves have a very shallow slope in this region.

Acknowledgments

The authors would like to show their appreciation to EPRI and the project manager, Dr. D. K. Sharma, for support of this work and to Messrs. A. L. Gallo and S. C. Heitkamp for the experimental work.

References

[*1*] Placek, R. J., Williams, R. A., Adams, S. L., and Klufas, O. "Torsional Fatigue Strength of Large Turbine-Generator Shafts—Project RP 1531-1," Final Report, EL3083, Electric Power Research Institute, Palo Alto, CA.

[*2*] *1982 Annual Book of ASTM Standards, Part 5,* American Society for Testing and Materials, Philadelphia.

[*3*] Smith, R. W., Mirschberg, M. H., and Manson, S. S., "Fatigue Behavior of Materials Under Strain Cycling in Low and Intermediate Life Range," NASA TN D-1574, National Aeronautics and Space Administration, Washington, DC, April 1963.

[*4*] Morrow, J. in *Internal Friction, Damping, and Cyclic Plasticity, ASTM STP 378,* American Society for Testing and Materials, Philadelphia, 1965, pp. 45–87.

[*5*] Landgraf, R. W., "Cyclic Deformation and Fracture of Hardened Steels," *International Conference on Mechanical Behavior of Materials,* Kyoto, Japan, 1972.

[*6*] Landgraf, R. W. in *Achievement of High Fatigue Resistance in Metals and Alloys, ASTM STP 467,* American Society for Testing and Materials, Philadelphia, 1970, pp. 3–36.

[*7*] Raske, D. T. and Morrow, J. in *Manual on Low Cycle Fatigue Testing, ASTM STP 465,* American Society for Testing and Materials, Philadelphia, 1969, pp. 1–26.

[*8*] Landgraf, R. W., Morrow, J., and Endo, T., *Journal of Materials,* Vol. 4, No. 1, March 1969, pp. 176–188.

[*9*] Coffin, L. F., Jr., and Tavernelli, J. F., *Transaction of the Metallurgical Society,* American Institute of Mining, Metallurgical, and Petroleum Engineers, Vol. 215, October 1959, pp. 794–807.

[*10*] Halford, G. R. and Morrow, J. *ASTM Proceedings,* Vol. 62, 1962, pp. 695–707.
[*11*] Havard, D. G. and Topper, T. H., *Experimental Mechanics,* Society for Experimental Stress Analysis, Dec. 1969, pp. 550–557.
[*12*] Dieter, G. E., Jr., *Mechanical Metallurgy,* McGraw-Hill, New York, 1961, pp. 17–77 and 279–281.
[*13*] Smith, J. O. and Sidebottom, O. M., *Inelastic Behavior of Load-Carrying Members,* Wiley, New York, 1965, pp. 51–102.
[*14*] Benham, P. P., *Journal of the Institute of Metals,* Vol. 91, 1962, pp. 404.
[*15*] Havard, D. G. and Topper, T. H., *First International Conference on Structural Mechanics in Reactor Technology,* Berlin, Sept. 1971. See also *Ontario Hydro Research Quarterly,* Vol. 23, No. 4, Fourth Quarter, 1971.
[*16*] Miller, J., *Journal of Material,* Vol. 7, No. 3, Sept. 1971, pp. 307–314.
[*17*] Dowling, N. E., *Journal of Engineering Materials and Technology, Transactions,* American Society of Mechanical Engineers, Vol. 100, April 1978.
[*18*] Timoshenko, S., *Strength of Materials, Part I, Elementary Theory and Problems,* Van Nostrand, New York, 1940, pp. 261–269.
[*19*] Timoshenko, S., *Strength of Materials, Part II, Advanced Theory and Problems,* Van Nostrand, New York, 1941, pp. 383–388.
[*20*] Nadai, A., *Theory of Flow and Fracture of Solid,* Vol. 1, McGraw-Hill, New York, 1950.
[*21*] Brown, M. W., *Journal of Strain Analysis,* Vol. 13, No. 1, 1978.
[*22*] Brown, M. W. and Miller, K. J., "Biaxial Cyclic Deformation Behavior of Steels," *Fatigue of Engineering Materials and Structures,* Vol. 1, 1979.
[*23*] Brown, M. W. and Miller, K. J., *Proceedings of the Institution of Mechanical Engineers,* Vol. 187, 1972, pp. 745–755.
[*24*] Miller, K. J. and Chandler, D. C., *Proceedings of the Institute of Mechanical Engineers,* 1969–1970, Vol. 184, Part I, p. 433.
[*25*] Miller, K. J., "Fatigue Under Complex Stress," *Metal and Science,* August/September 1977.
[*26*] Liddle, M. and Miller, K. J., "Multiaxial High Strain Fatigue," *Proceedings Third International Conference on Fracture,* 1973, Munich.
[*27*] Dorey, S. F. and Smedley, G. P., "Influence of Fillet Radius on the Fatigue Strength of Large Steel Shafts," *Transactions,* Institute of Mechanical Engineers, 1956.
[*28*] Mailander, R. and Bauersfeld, W., "Einfluss der Prabengrosse und Probenform auf die Dreh-Schwingungsfestigkeit von Stahl," *Technische Mitteilungen Krupp,* 1934.
[*29*] Kudryavtsev, I. V. and Andrenko, V. M., "Torsional Fatigue Resistance of Large Steel Shafts," *Russian Engineering Journal,* 1964.
[*30*] Neuber, H., Stress Concentration for Shear-Strained Prismatical Bodies with Arbitrary Non-linear Stress-Strain Law," *Journal of Applied Mechanics,* American Society of Mechanical Engineers, December 1961.
[*31*] Dowling, N. E., *Journal of Materials,* Vol. 7, No. 1, March 1972, pp. 71–87.
[*32*] Dowling, N. E., *Fatigue Life and Inelastic Strain Responses Under Complex Histories for an Alloy Steel,* T&AM Report No. 354, Department of Theoretical and Applied Mechanics, University of Illinois, Urbana, IL, April 1972.
[*33*] Miner, M. A., *Journal of Applied Mechanics, Transactions,* American Society of Mechanical Engineers, Vol. 67, Sept. 1974, pp. A149–A164.
[*34*] Krempl, E., *The Influence of State of Stress on Low Cycle Fatigue of Structural Materials, ASTM STP 549,* American Society for Testing and Materials, Philadelphia, 1974.

Darrell F. Socie,[1] *Linda A. Waill,*[1] *and Dennis F. Dittmer*[1]

Biaxial Fatigue of Inconel 718 Including Mean Stress Effects

REFERENCE: Socie, D. F., Waill, L. A., and Dittmer, D. F., "**Biaxial Fatigue of Inconel 718 Including Mean Stress Effects,**" *Multiaxial Fatigue, ASTM STP 853,* K. J. Miller and M. W. Brown, Eds., American Society for Testing and Materials, Philadelphia, 1985, pp. 463–481.

ABSTRACT: Biaxial fatigue tests were conducted on Inconel 718 specimens at room temperature. Thin-walled tubular specimens were subjected to tension, torsion, and combined tension and torsion loading in strain control. Two strain ratio's, $R_\epsilon = 0$ and $R_\epsilon = -1.0$, were investigated. Effective strain amplitudes of 1.0 and 0.5% were employed and resulted in fatigue lives ranging from 10^3 to 10^4 cycles. Fatigue lives were determined in terms of life to 0.1 and 1.0-mm cracks as well as specimen failure. Fatigue lives were correlated in terms of the Lohr and Ellison parameter for plastic strain which is based on the plane of maximum shear strain that causes the crack to grow into the thickness of the specimen and the normal strain to that plane. Good correlation was also obtained for the Kandel, Brown, and Miller parameter which is based on maximum shear strain and the normal strain to the maximum shear plane. Mean stress effects for the $R_\epsilon = 0$ tests were observed. These data could be correlated with the $R_\epsilon = -1$ data by introducing a mean stress term in the parameters which were then combined with the Coffin-Manson equation for estimating fatigue lives. Data on 24 tests correlated within a factor of 1.5 on life when fatigue lives were determined on the basis of 1-mm cracks.

KEY WORDS: biaxial fatigue, mean stress effects, cyclic deformation

Nomenclature

b	Fatigue strength exponent
c	Fatigue ductility exponent
E	Elastic modulus
N_f	Cycles to failure
$N_{0.1}$	Life to 0.1-mm crack
$N_{1.0}$	Life to 1.0-mm crack
R_ϵ	Strain ratio, $\bar{\epsilon}_{min}/\bar{\epsilon}_{max}$
ϵ	Axial strain amplitude
$\epsilon_1, \epsilon_2, \epsilon_3$	Principal strains
$\overline{\Delta\epsilon}/2$	Effective axial strain amplitude
ϵ'_f	Fatigue ductility coefficient

[1]Associate professor, research assistant, and research engineer, respectively, Department of Mechanical Engineering, University of Illinois at Urbana-Champaign, Urbana, IL 61801.

Copyright© 1985 by ASTM International www.astm.org

ϵ_p	Axial plastic strain amplitude
$\hat{\epsilon}_n$	Strain amplitude normal to $\hat{\gamma}$-plane
ϵ_n^*	Strain amplitude normal to γ^*-plane
$\hat{\epsilon}_{np}$	Plastic amplitude strain normal to $\hat{\gamma}$-plane
ϵ_{np}^*	Plastic amplitude strain normal to γ^*-plane
γ	Shear strain amplitude
γ_{max}	Maximum shear strain
γ^*	Shear strain amplitude on critical plane for growth into specimen surface
$\hat{\gamma}$	Shear strain amplitude on maximum shear plane
$\hat{\gamma}_p$	Plastic shear strain amplitude on $\hat{\gamma}$-plane
γ_p^*	Plastic shear strain amplitude on γ^*-plane
λ	Biaxial strain ratio γ/ϵ
σ	Axial stress
$\sigma_1,\sigma_2,\sigma_3$	Principal stresses
σ_o	Axial mean stress
σ'_f	Fatigue strength coefficient
σ_{no}^*	Mean stress normal to γ^*-plane
τ_o	Torsional mean stress
$\hat{\sigma}_{no}$	Mean stress normal to $\hat{\gamma}$-plane

Several strain based multiaxial fatigue theories have been proposed, each one with its advantages and limitations. A number of review papers exist [1–3]. Early work involved correlations based on maximum principal strain range, maximum shear strain range, and maximum octahedral shear strain range. More recent approaches are based on the critical plane for crack initiation and growth. Major advantages of the critical plane approaches are reasonable reliability, physical interpretation of the theory, ability to predict the plane on which cracks occur, and the construction of constant life plots which may prove to be of convenience to designers.

Brown and Miller [2] proposed that the maximum shear strain $\gamma_{max} = (\epsilon_1 - \epsilon_3)/2$ governed plastic deformation and hence crack initiation. Once the crack had initiated on the maximum shear plane, they reasoned that it would be assisted in propagation by the normal strain on maximum shear planes, $\epsilon_n = (\epsilon_1 + \epsilon_3)/2$. For a given fatigue life, they postulated that

$$\gamma_{max} = f(\epsilon_n) \tag{1}$$

Two specific cases of loading were identified for biaxial loading. In case A, ϵ_1, and ϵ_3 are parallel to the surface and cracks propagate in a shallow manner along the surface normal to ϵ_1. In Case B, ϵ_3 is normal to the free surface and cracks propagate away from the surface.

Lohr and Ellison [4] propose similar parameters: γ^*, the shear strain driving the crack through the thickness; and ϵ_n^*, the normal strain to that plane. This differs from the previous approach in the exact definition of the shear strain parameter. They proposed the following relationship

$$\gamma^* + k\,\epsilon_n^* = \text{constant} \tag{2}$$

and suggest a value of $k = 0.4$ which showed good correlation with test data for three steels. An advantage of this formulation is that material properties could be obtained from simple uniaxial tests.

In an extension of the original theory [2] Kandil, Brown, and Miller [5] present a more general equation for the equivalent strain range of the form $\Delta\gamma + S\Delta\epsilon_n$ which, for the present study could be reduced to the simple equation

$$\hat{\gamma} + \hat{\epsilon}_n = \text{constant} \tag{3}$$

They propose a value of 1.0 for S when Eq 3 is written in terms of shear amplitude rather than strain ranges. For loading situations involving only tension and torsion, both theories can be written directly in terms of the applied axial and torsional strains. In terms of plastic strains, Eq 2 can be expressed as

$$\gamma_p^* + k\,\epsilon_{np}^* = \frac{k+1}{2}\,[(1.5\,\epsilon_p)^2 + \gamma_p^2]^{1/2} + \frac{3-k}{4}\,\epsilon_p \tag{4}$$

and Eq 3 expressed as

$$\hat{\gamma}_p + S\hat{\epsilon}_{np} = [(1.5\epsilon_p)^2 + \gamma_p^2]^{1/2} + \frac{S}{4}\,\epsilon_p \tag{5}$$

Both theories should fit the data equally well if the constants k or S are fit to each data set. The equations can be combined with the Coffin-Manson equation relating axial plastic strain amplitude to fatigue life to evaluate the constant term. For the Lohr and Ellison theory, this results in the following relationship

$$\gamma_p^* + 0.4\,\epsilon_{np}^* = 1.6\,\epsilon'_f(2N_f)^c \tag{6}$$

and the results for the Kandil, Brown, and Miller parameter, are given by

$$\hat{\gamma}_p + \hat{\epsilon}_{np} = 1.75\,\epsilon'_f(2N_f)^c \tag{7}$$

Mean stress or mean strain effects have not yet been considered in the critical plane approaches. From a physical viewpoint, it seems appropriate to modify the normal strain term to account for mean stress effects. Tensile mean stresses normal to the crack surface should hold the crack open and assist in Mode II growth.

Correlation of multiaxial fatigue data from different laboratories is not good. This is usually attributed to differences in specimen design, testing system, and definition of failure. The latter is particularly important and often overlooked. In an axial test, the specimen separates into two pieces at final fracture. Separation is not observed in a torsion test of a thin-walled tubular specimen. Failure is often defined as the point where the specimen no longer supports the torsional loads. At this point very large cracks equal to the gage length are observed. It seems reasonable that fatigue data should be reported in terms of some specific crack size rather than final failure. In this investigation, both mean stress effects and the definition of failure are considered.

Material Description

Specimens were cut from a forged ring of Inconel 718 purchased to Aerospace Material Specification, AMS 5663. The ring (800 mm outside diameter, 650 mm inside diameter) was sectioned into 75 x 75 x 225 mm blocks with the long dimension parallel to the axis of the ring. The microstructure is shown in Fig. 1. A mixture of grain sizes was observed ranging from small clusters where the typical diameter was 0.01 mm to areas with grains as large as 0.2 mm. There are at least 10 grains through the specimen thickness for the largest grains. Tensile properties are given in Table 1.

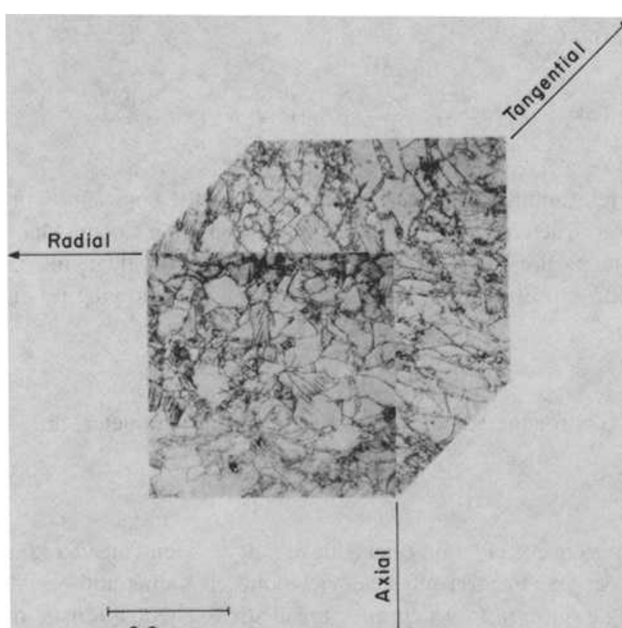

FIG. 1—*Microstructure of Inconel 718.*

TABLE 1—*Mechanical properties.*

MONOTONIC PROPERTIES	
Modulus	209 GPa
Yield stress 0.2 percent	1160 MPa
Fracture stress	1850 MPa
Fracture strain	0.33
Percent reduction in area	28
Strength coefficient	1910 MPa
Strain hardening exponent	0.08
CYCLIC PROPERTIES	
Fatigue strength coefficient	1640 MPa
Fatigue strength exponent	−0.06
Fatigue ductility coefficient	2.67
Fatigue ductility exponent	−0.82
Cyclic strength coefficient	1530 MPa
Cyclic strain hardening exponent	0.07

The specimens were heat treated at 600°C for 12 h after rough machining to prevent distortion during the final machining operations.

Experimental Procedure

Uniaxial Tests

A limited number of tests was performed using standard 6.3-mm-diameter low-cycle fatigue specimens [ASTM Recommended Practice for Constant Applitude Low-Cycle Fatigue Testing (E 60680)] with a 25 mm gage length. These specimens were cut from both the axial and tangential directions of the forging and were used to check for anisotropy in the material. All tests were conducted in strain control employing an MTS computer controlled test system. Hysteresis loop data were stored on disks for analysis and plotting. The tests were periodically interrupted so that an acetyl cellulose film replica of the surface topography could be made and the size of small cracks determined. Details of the replicating procedure are described later. At a prescribed number of cycles, the computer halted the test when the hysteresis loop reached zero stress or load.

The testing system was switched from strain to load control so that the extensometer could be removed for replicating the surface. After reinstalling the extensometer, the computer rezeroed it to the previous strain level before changing to strain control. Hysteresis loops taken before and after this procedure were identical, indicating that rest periods did not influence the test.

Biaxial Tests

Biaxial tests were conducted using the tubular specimen shown in Fig. 2. Elastic-plastic finite element analysis showed that the axial strain gradient along

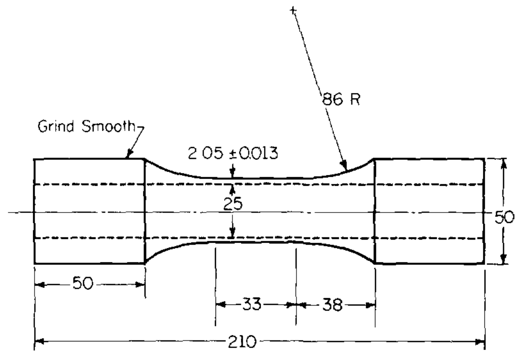

FIG. 2—*Specimen dimensions, in millimetres.*

the gage length was less than 2%. The torsional strain gradient along the surface was nearly zero, and the torsional gradient between the inner and outer surfaces was 15%. Standard machine collets are used to grip the ends of the specimens. An internal extensometer, shown in Fig. 3, was designed so that the outside surface of the specimen could be easily replicated with acetyl cellulose film to monitor crack formation and growth. Axial displacements were measured and controlled with a linear variable differential transducer (LVDT) located on the centerline of the specimen and rotations with a rotary variable differential transducer (RVDT). Coupling between the two measurements was less than 1%. Tests were conducted on an MTS Model 809 tension-torsion machine that was modified to increase the torsional stiffness. An MTS Model 463 processor/interface was used for computer control and data reduction of the tests.

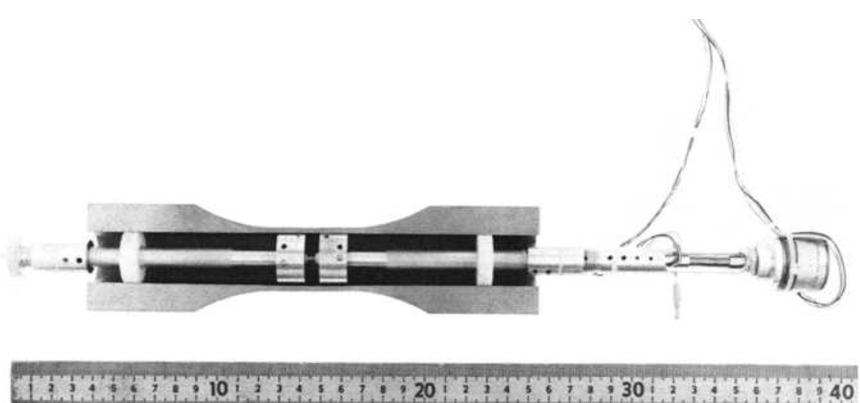

FIG. 3—*Specimen and extensometer assembly.*

Replicating Technique

Specimens were polished to eliminate scratches that might be interpreted as small cracks. Final polishing was done with 0.5-μm alumina. Standard metallographic acetyl cellulose film was used to record the surface of the specimens during fatigue. Acetone was applied to the surface with a syringe and the film placed around the gage length of the specimen. Considerable improvement in the quality of the replica can be obtained by using high grade methyl acetate rather than distilled acetone. After removing the replica from the specimen, it was placed between glass slides. Several techniques were attempted to observe the details of the replicas including scanning electron microscopy (SEM) observation incorporated with evaporation or sputtering of conductive films. The easiest and most reliable method for observation of the replicas is using an optical microscope and illuminating through the replica.

Results

Axial Tests

Results of uniaxial tests, employing solid smooth specimens, are shown in Fig. 4. Additional test data are included in determining the constants in Table 1 but not shown here for clarity so that the 1 mm and failure lives can be distinguished. Cracks 0.1 mm long form in 10 to 20% of the total fatigue life of the specimen. Cracks 1 mm long are formed at 80 to 90% of the life. These cracks are small compared to the dimensions of the specimen.

A comparison of fatigue lives of specimens taken from both axial and tangential directions is shown in Fig. 5. Data for 0.1 and 1-mm cracks were available and show the same trends but are omitted here for clarity. Also included are data from axial tests on the tubular specimen. Correlation between the three sets of test data is good, indicating that anisotropic effects are small. Also, no difference

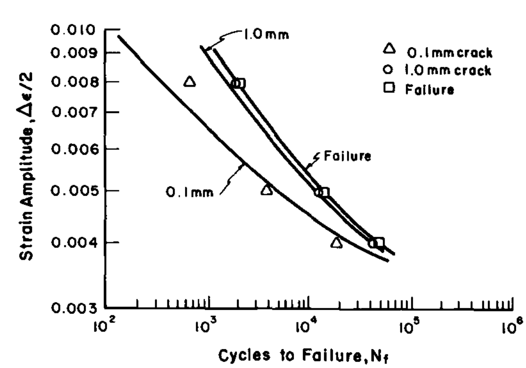

FIG. 4—*Uniaxial test results from solid specimens.*

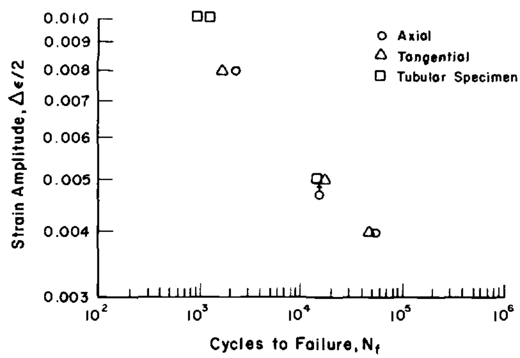

FIG. 5—*Fatigue test results from solid and tubular specimens taken from the axial and tangential directions.*

in total fatigue lives was observed for the solid and tubular specimen, because the fatigue life from a 1-mm crack to specimen separation is small.

The strain life equation

$$\Delta\epsilon/2 = \sigma'_f/E\,(2N_f)^b + \epsilon'_f\,(2N_f)^c \quad (8)$$

was fitted to the axial fatigue data from 11 tests. Constants are listed in Table 1 and were obtained by fitting the elastic and plastic strains separately. These tests as well as those of Dowling [*6*] suggest that the plastic strain-life term can be modified for crack lengths other than failure. The fatigue ductility exponent remains constant, and the plastic strain-life line is shifted to the left. A simple way to incorporate this behavior is to reduce the fatigue ductility coefficient. For example, 0.1 and 1.0-mm cracks can be estimated from Eq 8 using the following modifications: ϵ'_f for a 0.1-mm crack equals 0.15 ϵ'_f at failure and ϵ'_f for a 1.0-mm crack equals 0.9 ϵ'_f at failure. These modifications were made and shown as the solid lines in Fig. 4.

Biaxial Tests $R_\epsilon = -1$

Two nominal effective strain amplitudes were selected for these tests, 1 and 0.5%. At 1%, the elastic and plastic strains are nearly equal. The strains are initially elastic at a strain amplitude of 0.5%. Three biaxial loading conditions were employed: axial loading, $\lambda = 0$; torsional loading, $\lambda = \infty$; and combined tension and torsion with a biaxial strain ratio of $\lambda = 3^{1/2}$. Cyclic softening was observed for all loading conditions for both strain amplitudes. Torsional stresses on the outside surface were estimated by extrapolating the average torsional stress-strain hysteresis loop to the strain level on the surface.

Fatigue test results are summarized in Table 2. Total strains are reported in terms of the axial and average torsional strains which were controlled. Plastic

TABLE 2—*Fatigue test results for* $R_\epsilon = -1$.

Specimen	Nominal Strain Amplitudes		Maximum Plastic Strain Amplitude		Fatigue Life		
	ϵ	γ	ϵ_p	γ_p	$N_{0.1}$	$N_{1.0}$	N_f
			AXIAL				
B 33	0.010	0	0.00478	0	100	1 000	1 225
B 14	0.010	0	0.00483	0	200	1 050	1 330
B 06	0.005	0	0.00050	0	2000	13 500	14 174
B 12	0.005	0	0.00050	0	2000	11 000	13 364
			COMBINED				
B 35	0.007	0.012	0.00342	0.00756	200	1 000	1 374
B 11	0.007	0.012	0.00362	0.00770	300	1 200	1 581
B 04	0.0035	0.0063	0.00038	0.00140	3000	7 000	12 125
B 26	0.0035	0.0063	0.00045	0.00140	2000	8 000	12 899
			TORSION				
B 07	0	0.017	0	0.01109	200	890	1 625
B 13	0	0.017	0	0.01106	100	800	1 674
B 03	0	0.0085	0	0.00232	...	...	10 600
B 08	0	0.0085	0	0.00233	2000	7 000	12 942

strains are computed on the outside surface of the specimen. Failure was defined as 0.1 and 1-mm surface cracks as well as specimen separation or the inability to sustain the torsional loads. Tests were interrupted at 5 to 10% of the expected fatigue life to make a replica of the surface. The lives in Table 2 represent the replicating interval closest to the crack size of interest. Cracks always initiated on the outside surface of the specimen. Hundreds of cracks formed on the specimen surface during these tests. The lives reported are for the crack that eventually led to final failure. During the early stages of life, cracks longer than the crack that leads to final fracture are often observed. Reporting fatigue lives to greater precision than that shown in Table 2 would be misleading.

Crack directions for these tests are shown in Figs. 6 and 7 for effective strain amplitudes of 1 and 0.5%, respectively. Cracks form on the surface on planes of maximum shear strain in all cases.

Biaxial Tests $R_\epsilon = 0$.

A second series was conducted at the same strain amplitudes but with a strain ratio of 0 rather than -1. In addition to transient cyclic softening, mean stress relaxation was also observed in all of the tests. At an effective strain amplitude of 1%, the initial mean stress is only 5% of the stress amplitude and relaxes to zero during $R_\epsilon = 0$ loading. The initial mean stress is 30% of the stress amplitude for the lower effective strain amplitude during $R_\epsilon = 0$ loading. It relaxes to 20% of the stress amplitude at the half-life of the specimen.

Mean stresses are reported at the half-life of each test. Fatigue test results are

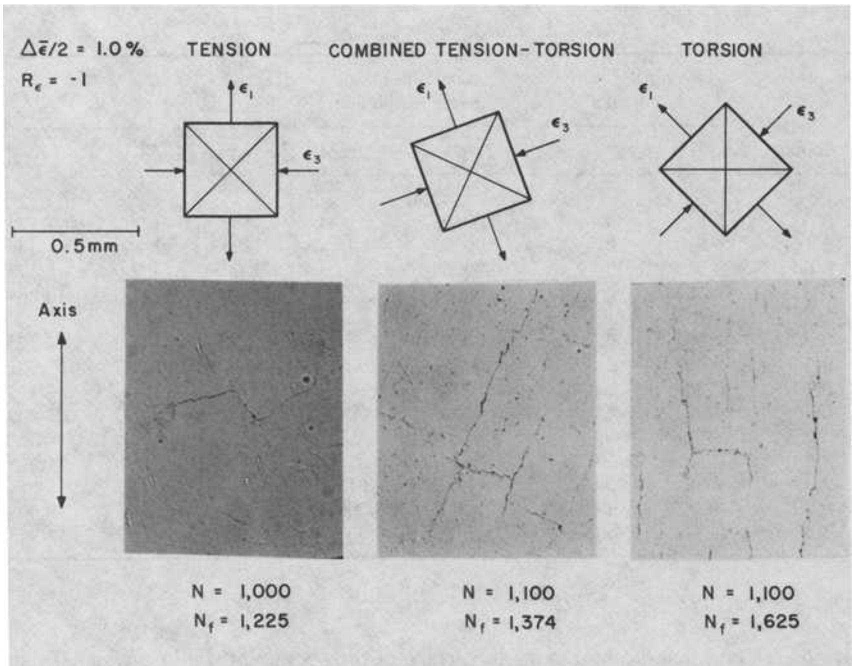

FIG. 6—*Crack directions for* $\overline{\Delta\epsilon}/2 = 1.0\%$ *and* $R_\epsilon = -1$.

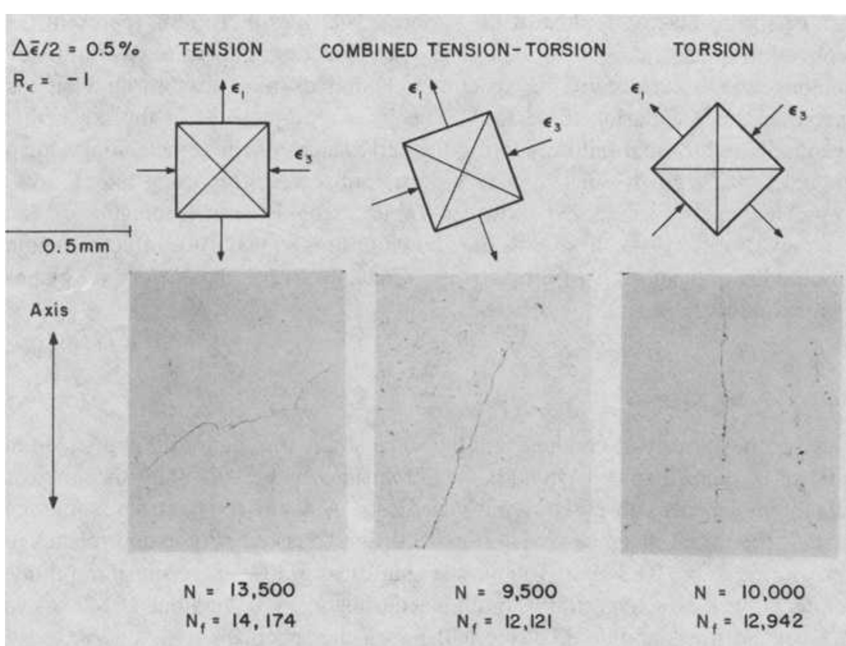

FIG. 7—*Crack directions for* $\overline{\Delta\epsilon}/2 = 0.5\%$ *and* $R_\epsilon = -1$.

shown in Table 3 for these test conditions. Crack directions are shown in Figs. 8 and 9. Again, cracks always initiate and grow along planes of maximum shear. The planes are identical with those shown in Figs. 6 and 7.

Discussion

Data for crack directions suggest that correlations based on maximum shear strain are appropriate [2]. In this work, cracks always formed on planes of maximum shear strain on the surface of the specimens. Crack growth along planes of maximum principal strain was never observed in the combined tension and torsion loading or in the torsion tests. It was only observed very late in the fatigue life of the axial tests.

Figure 10*a* shows the $R_\epsilon = -1$ failure data normalized in terms of plastic shear strain amplitude on the outside surface of the specimen. The solid line represents the estimate using the uniaxial data from Table 1 converted into plastic shear strain. Most investigators have reported similar trends, namely, torsion data lying above the tension data, for example, Ref 7. Final failure during torsion tests occurs only when the cracks have grown through the wall thickness. Shallow surface cracks are found on the surface early in the life of the specimen.

Correlations based on the Lohr and Ellison parameter are shown in Fig. 10*b* where the solid line is the estimate from Eq 6. They argue that the strains that cause cracks to grow into the specimen are more important than the strains that cause cracks to grow along the surface. This parameter is computed from Mohr's circle of strain for ϵ_1 and ϵ_2 for the combined tension and torsion loadings considered here. Maximum shear strain is computed from Mohr's circle of strain for ϵ_1 and ϵ_3. Several specimens were sectioned to look for cracks oriented 45° to the specimen surface (γ^*-plane) to provide supporting evidence for this theory.

TABLE 3—*Fatigue test results for* $R_\epsilon = 0$.

	Nominal Strain Amplitudes		Maximum Plastic Strain Amplitude		Mean Stress		Fatigue Life		
Specimen	ϵ	γ	ϵ_p	γ_p	σ_1, MPa	σ_3, MPa	$N_{0.1}$	$N_{1.0}$	N_f
				AXIAL					
B 5	0.01	0	0.00463	0	19	0	240	800	936
B 9	0.01	0	0.00483	0	22	0	100	800	959
B 36	0.005	0	0.00051	0	215	0	2400	7000	7 029
B 15	0.005	0	0.00044	0	215	0	1500	6000	8 000
				COMBINED					
B 98	0.007	0.012	0.00337	0.00763	46	−72	225	1050	1 333
B 10	0.007	0.012	0.00320	0.00738	12	−4	200	1000	1 502
B 34	0.0035	0.0063	0.00041	0.00114	177	−8	2200	4800	5 963
B 17	0.0035	0.0063	0.00050	0.00141	134	−66	2000	7500	9 500
				TORSION					
B 99	0	0.017	0	0.01088	14	−14	50	1000	1 687
B 16	0	0.017	0	0.01116	14	−14	200	800	1 738
B 32	0	0.0085	0	0.00242	76	−76	500	4500	9 526
B 25	0	0.0085	0	0.00248	81	−81	1000	6500	10 772

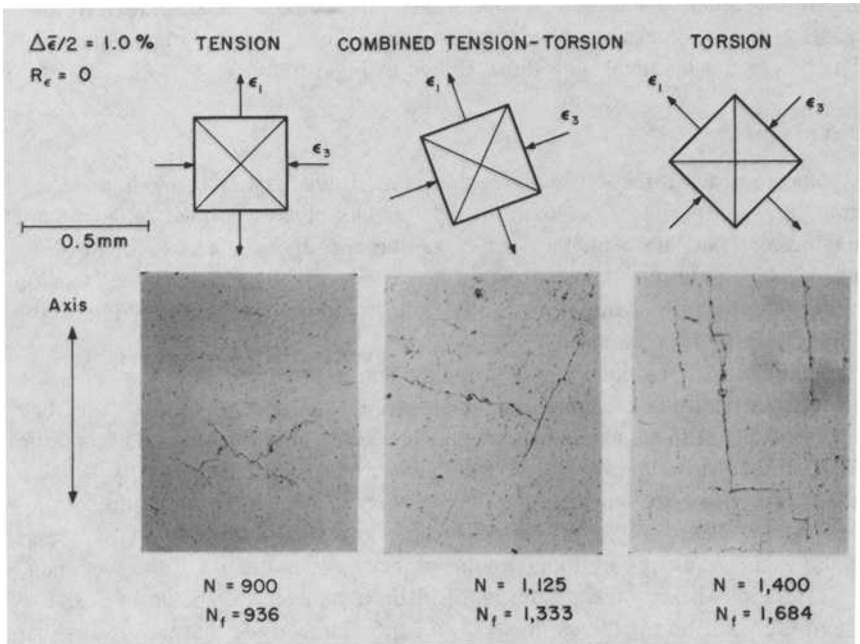

FIG. 8—*Crack directions for* $\overline{\Delta\epsilon}/2$ = *1.0% and* R_ϵ = *0.*

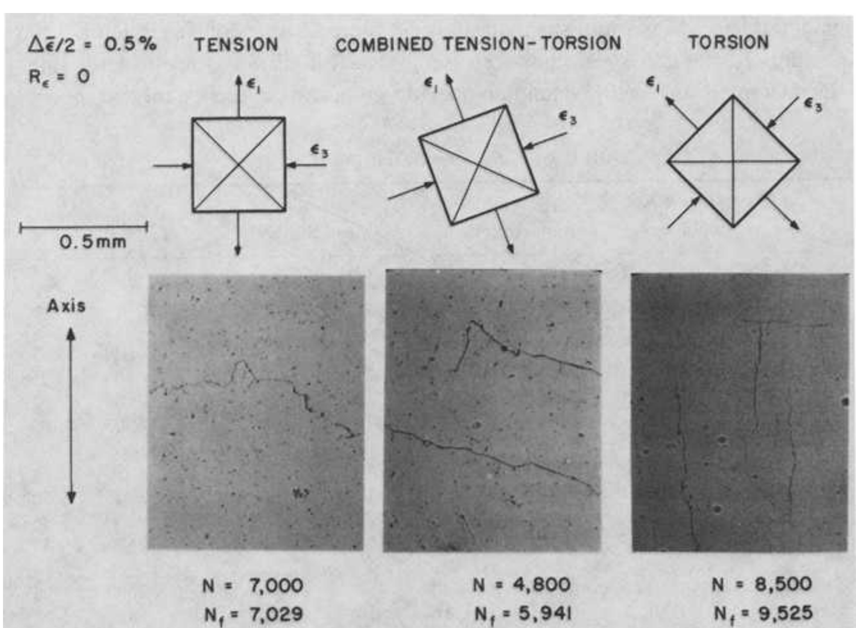

FIG. 9—*Crack directions for* $\overline{\Delta\epsilon}/2$ = *0.5% and* R_ϵ = *0.*

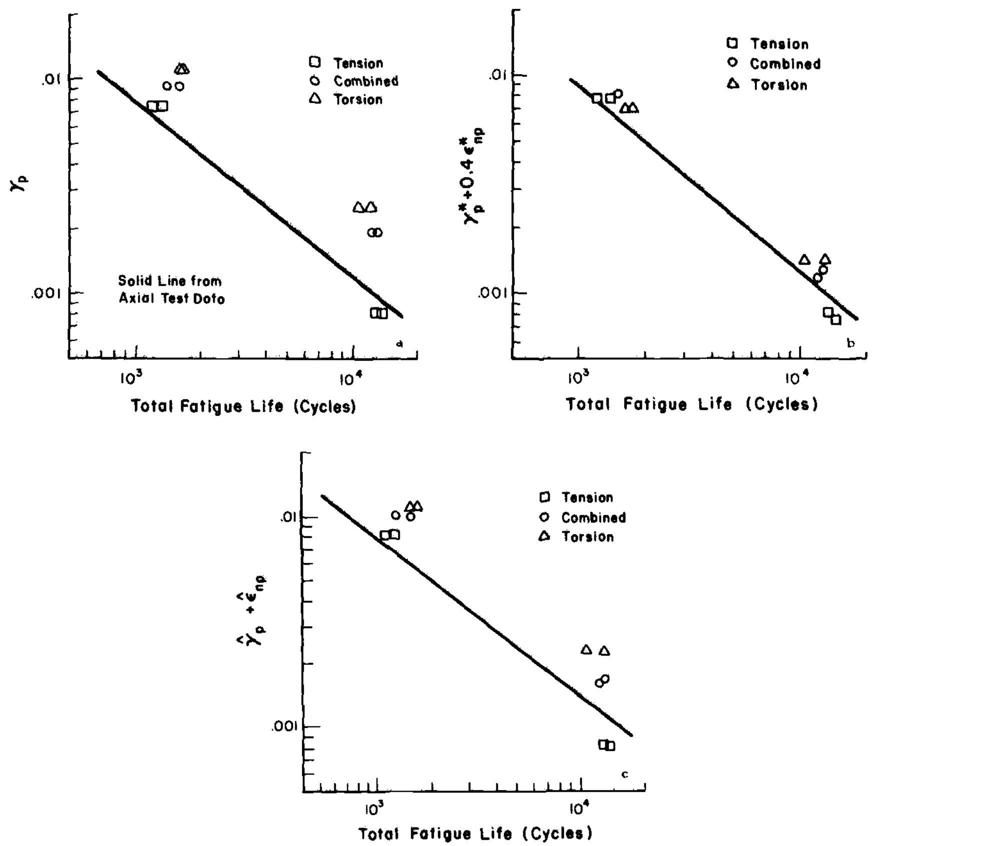

FIG. 10—*Correlation of test data for* $R_\epsilon = -1$ *(a) maximum plastic shear strain amplitude;* (b) *Lohr and Ellison parameter;* (c) *Kandil, Brown, and Miller parameter.*

Cracks along the γ^*-plane were found in tension and combined tension and torsion but not in torsion loading. In torsion, cracks initiate and grow on maximum shear strain planes. Correlations based on the maximum shear strain parameter proposed by Kandil, Brown, and Miller are shown in Fig. 10*c*. The solid line is the estimate from Eq 7. Although better correlation is observed for the Lohr and Ellison parameter even though cracks were not found on the γ^*-planes, both approaches could be made to fit the data equally well by adjusting the constants k $(=0.4)$ and S (unity) used in formulating Eqs 2 and 3, respectively.

Better correlation can be obtained if the life to the formation of a 1-mm crack is used rather than final failure. The growth of cracks from 1 mm to specimen failure is quite different in the tension and torsion tests. Beer [*8*] has shown that the cracking mode (for example, Mode II) and crack shape are nearly the same for all of the tests until the crack reaches a length of 1 mm.

Correlations based on final fracture may be acceptable for engineering estimates where a factor of 2 in life is considered good. They are not, however, adequate for tests to discriminate between fatigue theories. The comparison should be made on an equal basis and that basis should be similar cracking modes and size. These cracks grow to final failure in different modes and should be treated with a separate analysis for each mode.

The data presented in Fig. 11 are for the plastic shear strain versus cycles to the formation of a 1-mm crack. Both the Lohr and Ellison and the Kandil, Brown, and Miller parameters provide good estimates of the life to form a 1-mm crack as shown in Fig. 11. Correlation is better than the total fatigue life estimates in Fig. 10.

Mean stress or strain effects are observed when comparing the lives reported in Tables 2 and 3 for final failure and 1-mm crack lives. The effect is not observed for the formation of a 0.1-mm crack. At the higher strain amplitude,

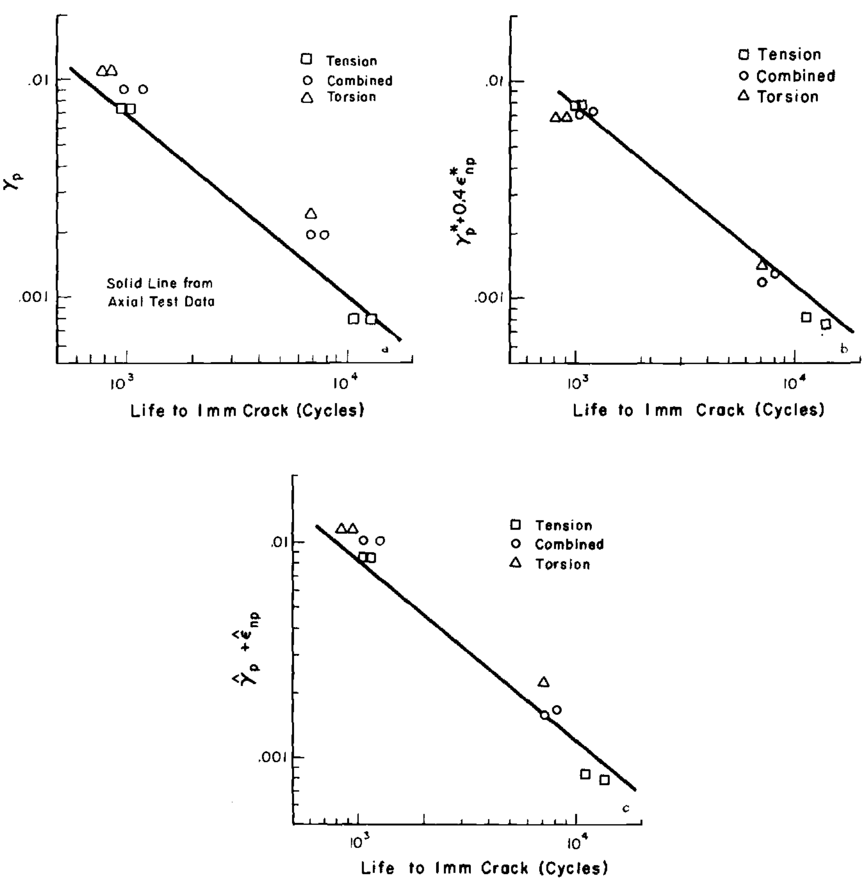

FIG. 11—*Correlation of test data based on 1-mm crack size* (a) *maximum plastic shear strain amplitude;* (b) *Lohr and Ellison parameter;* (c) *Kandil, Brown, and Miller parameter.*

the mean stress in both tension and torsion relaxes to zero, and no effect on life is observed for any of the life criteria. From these data, one can conclude that mean stress rather than mean strain is the controlling variable. Mean stresses for the lower strain amplitude do not completely relax, and an effect on fatigue life is observed.

One possible method for including mean stress effects would be to modify Eqs 2 and 3 to include a mean stress term. Plastic shear strain amplitude is the dominant parameter in determining the fatigue life. Normal strain across the shear plane has a smaller effect. Mean stresses across the shear plane should have also effects similar to the normal strain. Findley [9] proposed that the normal stress on the critical shear plane would have a linear influence on the allowable alternating shear stress. A similar modification for the Lohr and Ellison parameter can be expressed as

$$\gamma_p^* + 0.4\,\epsilon_{np}^* + \sigma_{no}^*/E = 1.6\,\epsilon'_f(2\,N_f)^c \tag{9}$$

where σ_{no}^* represents the mean stress across the γ^*-plane and is determined from Mohr's circle of stress for σ_1 and σ_2 similar to the calculation of ϵ_n^*. The modification for the Kandil, Brown, and Miller parameter can be expressed as

$$\hat{\gamma}_p + \hat{\epsilon}_{np} + \hat{\sigma}_n/E = 1.75\,\epsilon'_f(2N_f)^c \tag{10}$$

This equation is consistent with the observations of the crack directions. That is, crack directions do not change when mean stresses are present. Mean stress only influences fatigue life. Correlations based on the two parameters are shown in Fig. 12 for life to a 1-mm crack. Agreement for both parameters is good for the limited amount of data available.

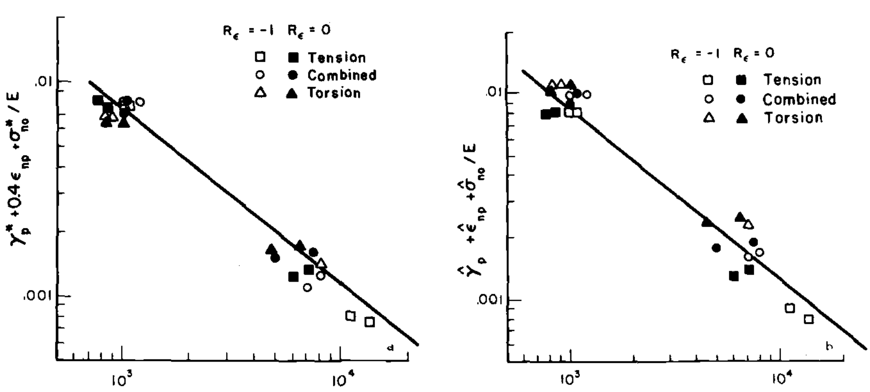

FIG. 12—*Correlation of test data including mean stress effects* (a) *Lohr and Ellison parameter; and* (b) *Kandil, Brown, and Miller parameter.*

Mohr's circle of strain shows that a mean stress can exist on the γ^*-plane but not the $\hat{\gamma}$-plane during torsion testing. The low amplitude torsion tests show a small influence of torsional mean stress. Much work still needs to be done in the area of multiaxial mean stress effects.

Summary

1. The Lohr and Ellison parameter provided the best correlation of the data for total fatigue lives and can be combined with uniaxial material properties to estimate lives in biaxial loading.

2. Improvement in multiaxial fatigue correlations can be obtained by defining life as a 1-mm crack rather than specimen failure because of the differences in macroscopic crack growth lives in tension and torsion.

3. Both Lohr and Ellison and Kandil, Brown, and Miller parameters provide good correlation for the life to the formation of a 1-mm crack.

4. Mean stresses effects observed in $R_\epsilon = 0$ testing were accommodated by modifying the shear strain parameters to include the mean stress acting normal to the shear plane.

Acknowledgments

These tests were conducted in the Materials Engineering Research Laboratory at the University of Illinois at Urbana-Champaign. T. Shield assisted in conducting the tests. Financial support was provided by Detroit Diesel Allison Division of General Motors.

References

[1] Krempl, E., *The Influence of State of Stress on Low Cycle Fatigue of Structural Materials, ASTM 549,* American Society for Testing and Materials, Philadelphia, 1974.

[2] Brown, M. W. and Miller, K. J., *Proceedings,* Institute of Mechanical Engineers, Vol. 187, 1973, pp. 745–755.

[3] Garud, Y. S., *Journal of Testing and Evaluation,* Vol. 9, No. 3, 1981, pp. 165–178.

[4] Lohr, R. D. and Ellison, E. G., *Fatigue of Engineering Materials and Structures,* Vol. 3, 1980, pp. 1–17.

[5] Kandil, F. A., Brown, M. W., and Miller, K. J., *Biaxial Low-Cycle Fatigue Fracture of 316 Stainless Steel at Elevated Temperatures,* Book 280, The Metals Society, London, 1982, pp. 203, 210.

[6] Dowling, N. E. in *Cyclic Stress-Strain and Plastic Deformation Aspects of Fatigue Crack Growth, ASTM STP 637,* American Society for Testing and Materials, Philadelphia, 1977, pp. 97–121.

[7] Yokobori, T., Yamanouchi, H., and Yamamoto, S., *International Journal of Fracture Mechanics,* Vol. 1, 1965, pp. 3–13.

[8] Beer, T. A., "Crack Shapes During Biaxial Fatigue," M.S. thesis, Department of Mechanical and Industrial Engineering, University of Illinois at Urbana-Champaign, 1983.

[9] Findley, W. N., *Journal of Engineering for Industry, Transactions,* American Society of Mechanical Engineers, Series B, Vol. 81, 1959, pp. 301–306.

DISCUSSION

W. N. Findley[1] (*written discussion*)—The authors' experiments were confined to low-cycle fatigue. In common with other investigators of low-cycle fatigue they appear to assume that low-cycle fatigue is a different phenomena from high-cycle fatigue and thus draw no comparisons and cite no references to similar work on high-cycle fatigue. Thus, I would like to take this opportunity to point up some of the relevant features of prior work on high-cycle fatigue under multiaxial loading and mean stressing.

Early work on fatigue under combined bending and torsion included the extensive results reported by Gough and Pollard in 1935[2]. More recent works by the writer and others were reported.[3-9] These report fatigue tests well into the yield region and failures after as little as 2×10^4 cycles. Footnotes 3 and 4 contain a review and extensive bibliography.

Fatigue Fractures

It was gratifying to note that the authors found the initiation of fatigue cracks to occur on or near principal shear planes. This was also observed in footnote 4 and reviewed in footnote 8. The following paragraphs are quoted from footnote 4, which is not readily available.

> Fractures of fatigue specimens representing various loading conditions are illustrated in (Figure 14 of footnote 4.) The entire group of fractured specimens was assembled in an orderly sequence according to stress amplitude, mean stress, and state of stress for examination. It was observed that there were from one to three long cracks lengthwise of the specimen in the torsion specimens having highest stress amplitudes. Some of these cracks were as deep as the center of the specimen. The final fractures, however, occurred as transverse

[1]Brown University, Providence, RI 02912.

[2]Gough, H. J. and Pollard, H. V. in *Proceedings*, International Mechanics E., London, Vol. 131, Nov. 1935, pp. 1–103.

[3]Findley, W. N. in *Proceedings*, American Society for Testing and Materials, Philadelphia, Vol. 52, 1952, pp. 818–832.

[4]Findley, W. N., "Combined Stress Fatigue Strength of 76S-T61 with Superimposed Mean Stresses and Corrections for Yielding," Technical Note 2924, National Advisory Committee for Aeronautics, May 1953.

[5]Findley, W. N., *Journal of Applied Mechanics*, Vol. 74, 1953, pp. 365–374.

[6]Findley, W. N. in *Proceedings*, American Society of Testing and Materials, Philadelphia, Vol. 54, 1954, pp. 836–852.

[7]Findley, W. N., Coleman, J. J., and Hanley, B. C. in *Proceedings*, International Conference on Fatigue of Metals, London, 1956, pp. 150–157.

[8]Findley, W. N. in *Transactions*, American Society of Mechanical Engineers, Vol. 79, 1957, pp. 1337–1347.

[9]Findley, W. N., *Journal of Engineering for Industry*, Vol. 81, 1959, pp. 301–306.

cracks. As the stress amplitude decreased the extent of the longitudinal cracking decreased and at the lower stress amplitudes the final fractures changed to a spiral or stairstep pattern.

Examination of torsion specimens having mean stresses greater than zero showed that the transition from a final fracture of the transverse type to the spiral type occurred at higher stresses (from 17 000 to 25 000 psi) and smaller numbers of cycles (from 23×10^6 to 77×10^3) as the mean stress increased from 0 to 45 000 psi.

After cracks had formed in the fatigue tests, a black powder exuded from the cracks (especially in torsion). The fractured specimens also showed that fractured surfaces on which shear stresses had acted were blackened, except in some of the torsion specimens in which the transverse planes had been considerably gouged as a result of the large relative movements during the final stages of the test.

In the tests having a state of stress such that $\tau = 1.207$ the two highest-stressed specimens had long longitudinal cracks which were at angles of 3°, 8° and 11° to the axes of the specimens. These angles are in approximate agreement with the angle (11.3°) of the plane of maximum shearing stress. At lower stresses the general fracture is of the spiral type.

The specimens fractured in bending showed that all fractures were essentially transverse with small areas of black markings. The extent of the black markings decreased with decrease in alternating stress and with increase in mean stress. At the highest amplitudes of stress, cracks appeared to form at several points. At zero mean stress and high amplitude, cracks formed on both top and bottom surfaces.

Microscopic examination of the fractures indicated that blackened areas were surfaces which would have been subjected to shear stress. It was also observed that the point of initiation of the fatigue cracks contained surfaces of fracture which were shear planes either at an angle to the axis and to the surface of the specimen or at an angle to the axis and perpendicular to the surface of the specimen.

The fractures under other combinations of bending and twisting were helical or diagonal fractures with some black markings as in the bending fatigue specimens. The angle of the helix or diagonal plane was roughly that of the plane of maximum principal stress, except that this angle decreased (tended to become a transverse plane) as the mean stress was increased in the tests for a state of stress such that $\tau = 0.5\sigma$."

Effect of Normal Stress Acting on the Critical Shear Plane

A theory of the effect of the normal stress acting on a critical shear plane (not necessarily the principal shear plane) was described by Stulen and Cummings[10] and by Findley, Coleman, and Hanley[7] in which the effect of the normal stress is to decrease fatigue strength when tensil and increase it when compressive. The degree of effect of the normal stress depended on the material through a

[10]Stalen, F. B. and Cummings, H. N. in *Proceedings*, American Society for Testing and Materials, Philadelphia, Vol. 54, 1954, p. 822.

parameter k. An extension of this theory to include mean stresses under combinations of stresses by Findley[9] showed the following relation for the orientation θ of the critical shear plane on which cracks initiated

$$\tan 2\theta = \left[\frac{(2a - k\tau_M/f)^2}{(1 + 4a^2)\,(k\tau_M/f)} - 1\right]^{1/2} \tag{1}$$

where $\tau_A/\sigma_A = \tau_M/\sigma_M = a$, M, and A refer to maximum and alternating stresses, k is the degree of influence of the normal stress, f is the critical shear stress when the normal stress is zero, and θ is the angle of the critical plane with respect to the principal stress direction.

Equation 1 shows that the critical shear plane for zero mean stress is a few degrees from the principal shear plane for small k and a few degrees from the principal plane for large k (k is small for ductile metals). It was noted that when the maximum stress was zero (entire cycle in compression) θ was 45° for all values of k. Equation 1 was reported to be in reasonable agreement with most available observations.

D. F. Socie, L. A. Waill, and D. F. Dittmer (*authors' closure*)—The authors would like to thank Prof. Findley for his valuable contribution. Equation 1 indicates that the cracking direction will be affected by mean tensile and shear stresses. Additional testing with this material[11] for a wide variety of mean stresses has shown that the cracking direction is only dependent on cyclic shear strain.

[11]Socie, D. F. and Shield, T. W., "Mean Stress Effects in Biaxial Fatigue at Inconel 718," *Journal of Engineering and Materials Technology*, Vol. 106, 1984, pp. 227–232.

Gail E. Leese[1] *and JoDean Morrow*[2]

Low Cycle Fatigue Properties of a 1045 Steel in Torsion

REFERENCE: Leese, G. E. and Morrow, J., "**Low Cycle Fatigue Properties of a 1045 Steel in Torsion,**" *Multiaxial Fatigue, ASTM STP 853,* K. J. Miller and M. W. Brown, Eds., American Society for Testing and Materials, Philadelphia, 1985, pp. 482–496.

ABSTRACT: A method of performing torsional low cycle fatigue tests on thin-walled tubular specimens is described. Shear strains are measured and controlled using an internally mounted rotary variable differential transducer (RVDT). Test results for a 1045 hot-rolled and normalized steel are discussed.

As in the case of uniaxial fatigue analysis, power law relationships are assumed in the elastic strain-life, plastic strain-life, and stress-plastic strain functions. From this analysis, the fatigue strength and ductility exponents and coefficients in torsion are determined, as well as the cyclic strain hardening exponent and strength coefficient in torsion. These properties are compared to those obtained in uniaxial fatigue tests of the same steel. The question of whether the cyclic strain hardening, fatigue strength, and fatigue ductility exponents are stress state dependent is specifically addressed. This is one of the fundamental issues that must be resolved if uniaxial fatigue properties are to be used to analytically predict multiaxial fatigue behavior.

KEY WORDS: fatigue (materials), fatigue tests, low cycle fatigue, shear stress, shear strain, torsion tests, shear properties

The local stress-strain approach for estimating fatigue lives is currently used by the ground vehicle industry on a worldwide basis. While this approach is well documented [*1,2*] for the uniaxial fatigue of wrought metals, there is no general agreement on how to deal with multiaxial fatigue. Given the effort and resources previously devoted to determining axial baseline fatigue properties, it would be advantageous if one could apply or extrapolate or both the axial properties to other loading modes. Most proposed multiaxial fatigue life prediction schemes attempt to do so. A fundamental issue to be resolved in such an approach is whether or not the exponents of the strain-life relationships are stress state independent.

While many investigators have performed shear strain controlled fatigue tests, there is little experimental data published containing both axial and torsional

[1]Formerly, engineer, Deere & Company Technical Center, Moline, IL 61265; presently, TRW, Inc., Cleveland, OH 44117.

[2]Professor, Theoretical and Applied Mechanics, University of Illinois, Urbana, IL 61801.

Copyright© 1985 by ASTM International www.astm.org

fatigue data, allowing one to specifically address the question of stress state dependency of the fatigue life exponents. Dowling [3] recently concluded that torsional cyclic stress-strain and strain-life response can be adequately predicted from axial properties for a Ni-Cr-Mo-V steel. Earlier work by Yokobori [4] shows conflicting results with a mild steel. Engineers who must predict multiaxial fatigue lives are often forced to make an assumption one way or the other.

In this paper, results of shear strain controlled torsional fatigue tests of a common industrial shaft steel are presented. Torsional fatigue properties are obtained in a manner analogous to the reduction of axial fatigue data, allowing comparisons of axial fatigue properties with those obtained in a nonaxial loading mode. These comparisons are offered as an extension of the localized stress-strain approach and are directed towards current industrial applications.

Experimental Program

Material

All of the material used in this investigation was obtained from the stock of 1045 hot-rolled and normalized steel used in the Society of Automotive Engineers (SAE) biaxial fatigue research program. Inland Steel provided eight tons of 63.5-mm-diameter bar stock from the same heat for use in the SAE biaxial program, and LaSalle Steel performed the normalizing treatment. Availability aside, this material was chosen to complement the SAE biaxial research effort.

Chemical composition of the steel is shown in Table 1. Brinell hardness measurements from all specimens fell within the range of 192 to 201. The microstructure consisted of fine grained pearlite and ferrite, but also contained thin inclusions along the rolling direction up to 0.1 mm in length. Figure 1 shows the microstructure.

Tables 2 and 3 list the axial monotonic and fatigue properties, respectively, from 6-mm-diameter specimens. Axial strain-life curves are shown graphically in Fig. 2. Failure in the axial tests was defined as an 80% drop in load. The associated cyclic stress-strain curve superimposed on the monotonic, shown in Fig. 3*a*, shows cyclic softening at low strain amplitudes and cyclic hardening at high strain amplitudes.

TABLE 1—*Chemical composition of 1045 steel. Chemical analysis, percent by weight, obtained from Ref 9.*

C	Mn	P	S	Si	Ni	Cr	Mo	Cu	Al
0.44	0.70	0.019	0.046	0.23	0.03	0.05	nil	0.03	0.05

B	V	Nb	Pb	Ti
0.0002	0.002	0.008	0.005	0.002

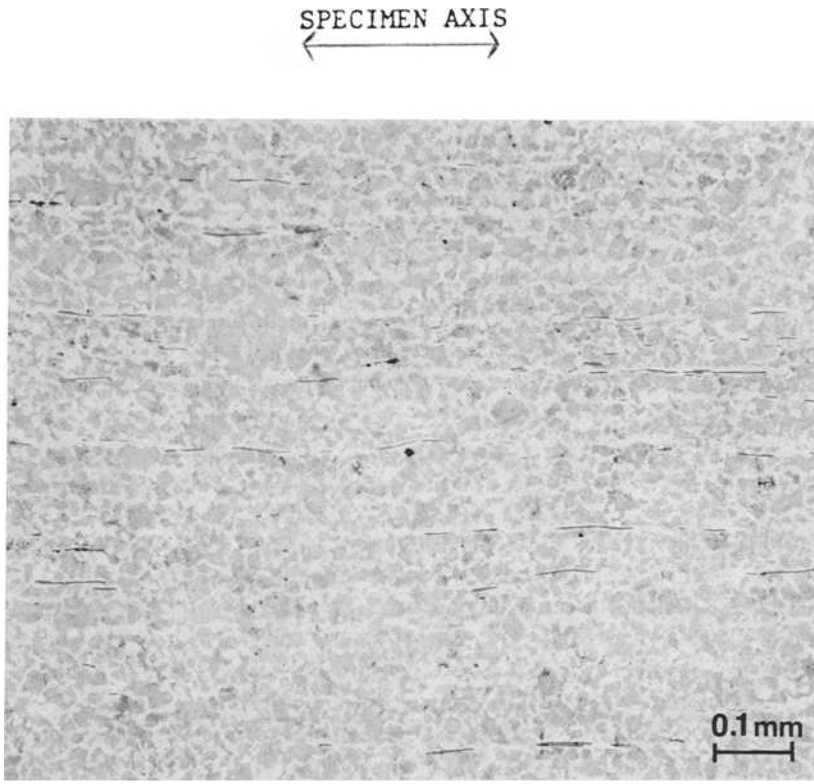

FIG. 1—*Microstructure of the 1045 HR and normalized steel used. (Picture courtesy of D. Brodd, Deere & Company Technical Center, Moline, IL.)*

Test and Specimen Design

There were two basic requirements considered in establishing the torsional fatigue test method:

1. Control of the total shear strain range within the gage length of deformation.
2. Capability of measuring total shear strain, shear stress amplitude, shear modulus, and cycles to failure.

TABLE 2—*Axial monotonic properties of 1045 steel. Obtained from Ref* 9.

Inside Diameter	BHN	σ_y, MPa	σ_f, MPa	ϵ_f	Reduction in Area, %	E, MPa
M022	157	384	992	0.71	51	203 350
M104	148	379	977	0.71	51	201 400
Average	153	382	985	0.71	51	202 375

TABLE 3—*Axial fatigue data and properties. Raw data obtained from Ref 9.*

	E = 202 375 MPa K' = 1258 MPa n' = 0.208	σ'_f = 948 MPa b = −0.092 ϵ'_f = 0.260 c = −0.445	
Total Strain Amplitude	Stress Amplitude, MPa	Plastic Strain Amplitude	Reversals to Failure
0.0200	524	0.01741	514
0.0150	499	0.01253	770
0.0100	452	0.00777	3 054
0.0100	465	0.00770	2 922
0.0080	445	0.00581	6 088
0.0080	440	0.00583	4 093
0.0060	400	0.00402	13 344
0.0060	420	0.00393	13 650
0.0050	372	0.00316	25 826
0.0040	351	0.00227	35 970
0.0040	353	0.00226	40 398
0.0030	315	0.00144	73 860
0.0025	298	0.00103	234 268
0.0020	270	0.00067	523 222
0.0020	269	0.00067	762 902
0.0015	241	0.00031	4901 750

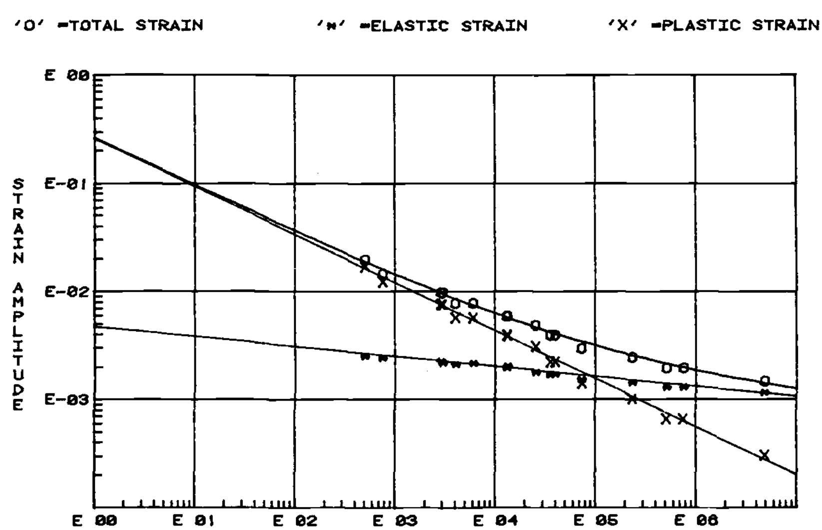

FIG. 2—*Axial total strain versus reversals to failure.*

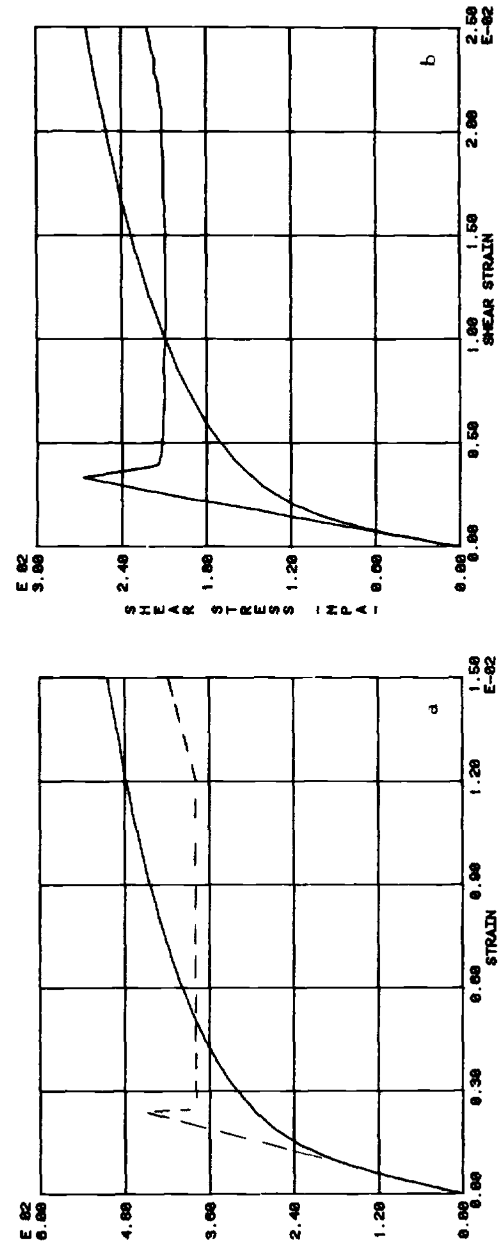

(*a*) Axial stress versus strain.
(*b*) Shear stress versus strain.

FIG. 3—*Cyclic and monotonic stress versus strain curves.*

It was the second consideration that dictated specimen geometry. A direct stress calculation from acquired load data can be made for a thin-walled tubular specimen, assuming that the stress is constant across the thickness and that the thickness of the wall is constant. Hence, a specimen with a thin-walled gage length was used. The ratio of wall thickness to the outer and inner diameter was 0.1 and 0.125, respectively. Note that the 4 mm wall thickness is of a dimension comparable to the axial specimens, which were 6 mm in diameter. Figure 4 shows the geometry and dimensions of the test specimen.

Each specimen had a honed surface on the interior and a ground outer surface. Thus, the surfaces were not as finely polished as would be a smooth, round axial fatigue specimen. However, the grinding marks were circumferential on the specimen and were subsequently found to be perpendicular to the direction of crack growth.

The basic test system was that designed by Galliart and Downing [5] for use in the SAE biaxial fatigue program. It included two independent linear actuators with two 45-kN load cells. The specimen was clamped into the test frame with a wedge-type fixture and into the load arm with a collet. Most of the hardware was adapted from MTS materials test systems, including a computer interface to a PDP 11/04 allowing computer control of the two rams. In the SAE biaxial program, this test setup is used for load controlled combined bending/torsion tests. Hence, some hardware and software modifications were necessary to perform strain controlled tests in torsion.

To reduce the possibility of undesired bending, the load cell on actuator number two was slaved to the inverted signal from actuator number one directly through the internal hardware. Hence, at any point in time, each ram theoretically imparted loads of equal amplitude but opposite sign on the specimen to achieve pure torsional loading. In actuality, there was a slight time lag between the measuring of the load signal of ram number one and execution of the inverted signal by ram number two. Any continued resultant difference in load amplitudes between the rams would produce a cyclic bending stress. Typically, the bending stress computed from the two measured loads was less than 2% of the shear stress range and considered negligible.

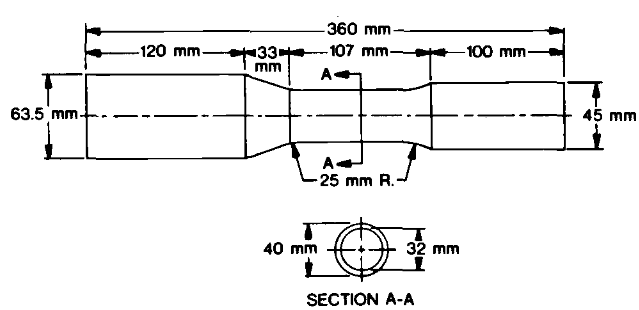

FIG. 4—*Torsional fatigue specimen.*

A method was needed for measuring the shear strain over the gage length which could be also used as the feedback signal in the closed-loop control. The "shear strain extensometer" devised [6] consisted of a Schaevitz R30D rotary variable differential transducer (RVDT) set into two sleeves, one holding the body of the RVDT and the other attached to the shaft. Each sleeve consisted of two pieces separated by an O-ring. By tightening the two pieces together, each O-ring could be expanded against the inside diameter of the specimen, thus internally mounting the RVDT between the two O-rings, within the gage length of the specimen.

The RVDT produced a voltage output as a function of the angular position of the shaft. In this test procedure the RVDT output indicated the relative angular displacement between the O-rings. Since the angle of twist is directly proportional to the shear strain, control of the angle of twist constituted control of the shear strain over that same gage length.

Each specimen was strain gaged with a three-legged rosette, placed approximately in the middle of the gage length. Prior to the fatigue tests each specimen underwent several single cycle tests at $\gamma_a \simeq 0.001$ to compare the RVDT and the rosette readings. Any initial disparity was due to the gage length input parameter used with the relative angle of twist to calculate the shear strain measured by the RVDT. In a sense, this method experimentally "calibrated" the RVDT with the rosette.

There were predetermined intervals during the fatigue tests at which data acquisition was performed and written to disk so that the stress-strain response could be regenerated at a later time. These intervals were at 1, 17, 33, 65, 129, 256 . . . etc., cycles, although immediate mode data acquisition could be performed on demand at any time. Intermittently, during most fatigue tests, cellulose film replicas were made that were later examined under an ordinary light microscope for studying surface cracking. In all tests the life to failure, as determined by a drop in the load required to enforce the given strain amplitude, was recorded.

Three specimens were tested at each of the following shear strain amplitudes: $\gamma_a = \pm 0.0250, \pm 0.0150, \pm 0.0080, \pm 0.0050$, and ± 0.0040. One specimen was tested at $\gamma_a = \pm 0.0060$ before the strain amplitudes for testing were firmly established and the remaining specimen was tested at $\gamma_a = \pm 0.003$ to represent long life behavior.

Data Reduction

The elastic strain-life, plastic strain-life, and cyclic stress-strain equations can be expressed in terms of torsional fatigue parameters as follows

$$\frac{\Delta\gamma_e}{2} = \frac{\tau'_f}{G}(2N_f)^{b_o} \tag{1}$$

$$\frac{\Delta\gamma_p}{2} = \gamma'_f\,(2N_f)^{c_o} \tag{2}$$

$$\tau_a = K'_o\,(\gamma'_p)^{n'_o} \tag{3}$$

where

$\Delta\gamma_e$ = elastic shear strain range,
$\Delta\gamma_p$ = plastic shear strain range,
τ_a = true torsional stress amplitude,
τ'_f = torsional fatigue strength coefficient,
γ'_f = torsional fatigue ductility coefficient,
K'_o = cyclic torsional strength coefficient,
b_o = torsional fatigue strength exponent,
c_o = torsional fatigue ductility exponent, and
n'_o = cyclic torsional strain hardening exponent.

Assuming that in pure torsion, the total shear strain is the summation of the elastic and plastic shear strain, one arrives at the following relationships between total shear strain and life

$$\frac{\Delta\gamma}{2} = \frac{\tau'_f}{G}\,(2N_f)^{b_o} + \gamma'_f\,(2N_f)^{c_o} \tag{4}$$

and cyclic shear stress and shear strain

$$\frac{\Delta\gamma}{2} = \frac{\tau_a}{G} + \left(\frac{\tau_a}{K'_o}\right)^{1/n'_o} \tag{5}$$

Results

There were two distinctly different modes of failure observed in all tests: a shearing mode where longitudinal cracks parallel with the specimen axis formed, followed by a mode where the faces of the longitudinal cracks opened and closed. Either mode in itself could be described in terms of initiation and propagation, with the propagation of longitudinal cracks in shear preceding the initiation of opening and closing across the faces of the same cracks. Hence, defining the fatigue life to crack initiation cannot be done without qualifying the mode of cracking.

For the purpose of comparing fatigue properties between axial and shear strain controlled conditions, like modes of failure must be considered. Therefore, for this discussion, failure in the torsional tests is defined as that point where a crack exists that is opening and closing. This appeared to coincide with the occurrence of a through thickness (4 mm) crack, causing a drop in the load amplitude required to maintain strain levels. Although the actual percentage of load drop at the point considered failure varied slightly for each specimen, it was typically between 10 and 20%. Any error introduced by this variance is slight since the drop in load is rapid after its onset.

Table 4 lists the results of all torsional fatigue tests. In all cases the stress amplitude was measured at the half-life where it was assumed that the stress-strain response was stable. Where possible, the shear modulus, G, was calculated with the data acquired in the first ramp to yield. The average shear modulus for the 17 tests was 79 100 MPa. Elastic strain was calculated by dividing the shear modulus into the shear stress amplitude, and then subtracted from the total shear strain to obtain the plastic shear strain. The fatigue properties were obtained by linear regression of Eqs 1 to 3. Figure 5 shows the results graphically. The cyclic stress-strain curve in torsion is superimposed on the monotonic curve in Fig. 3*b*. Mixed mode cyclic softening and hardening behavior is observed in torsion as it is in axial conditions.

Table 5 shows a comparison of the fatigue properties in the axial and torsional cases. Included in this table are the transition fatigue lives, where the elastic and the plastic strains are equal.

TABLE 4—*Torsional fatigue data and properties.*

τ'_f = 505 MPa, γ'_f = 0.413, K'_o = 615 MPa, G = 79100 MPa

b_o = −0.097, c_o = −0.445, n'_o = 0.219

Shear Strain	Shear Stress, MPa	Shear Modulus, MPa	Plastic Shear Strain	Reversals to Load Drop Off	Specimen No.
0.0250	272	80 200	.0216	940	20
0.0251	270	78 200	.0216	990	18
0.0250	259	80 100	.0218	1 082	16
0.0150	232	78 400	.0120	2 538	1
0.0150	237	78 200	.0120	2 758	6
0.0150	232	78 100	.0120	2 934	13
0.0150	235	78 400	.0120	...	2[a]
0.0082	198	81 200	.0058	11 010	12
0.0082	200	80 400	.0057	14 264	3
0.0082	194	79 100	.0057	16 716	4
0.0060	186	78 400	.0036	22 146	5
0.0050	161	78 000	.0029	60 746	11
0.0050	165	78 000	.0029	70 036	14
0.0050	168	78 300	.0029	72 234	15
0.0041	160	81 200	.0021	83 678	7[b]
0.0040	159	78 000	.0020	145 928	10
0.0039	154	78 200	.0019	190 536	9
0.0030	148	80 700	.0012	1092 006	8

[a]Test aborted due to hydraulics failure.
[b]Test interrupted due to lack of agreement between RVDT and rosette. Specimen and RVDT reset.

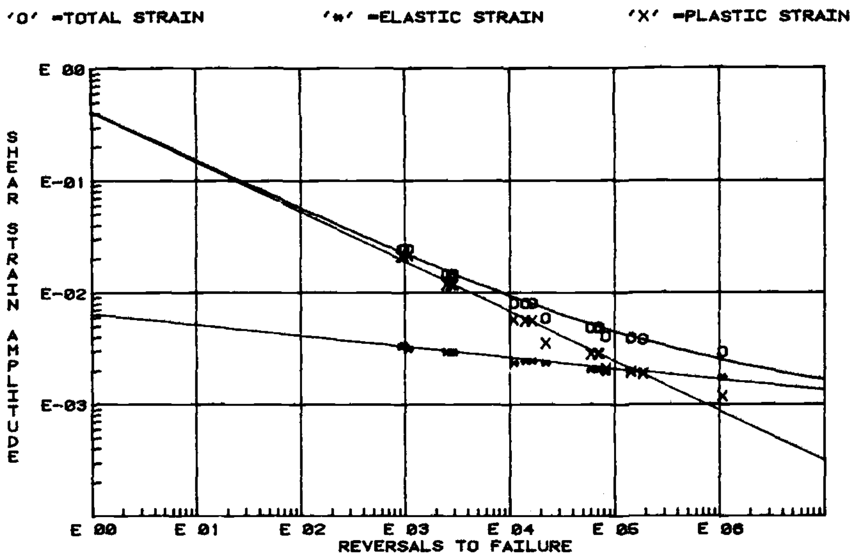

FIG. 5—*Total shear strain versus reversals to failure.*

The reporting of torsional fatigue tests results would not be complete without describing the surface cracking phenomena that occur long before any load drop can be detected. Small (0.25 mm) longitudinal cracks were detected on the surface throughout the gage length early in each test. As the early cracks grew to approximately 1 mm in length, many other smaller cracks continued to appear. However, the majority of these cracks remained small while relatively few continued to grow to the 2 and 3 mm lengths. Near the end of a test, many of the cracks joined, greatly increasing the apparent crack propagation rate. Finally, a crack would propagate through the wall thickness.

TABLE 5—*Summary of fatigue properties.*

Fatigue Property	Stress State	
	Axial	Torsional, 17 test points
b	-0.092	-0.097
n'	0.208	0.219
c, as regressed	-0.445	-0.445
$c = b/n'$	-0.442	-0.443
K' or K'_o, MPa, as regressed	1258	615
σ'_f or τ'_f (MPa)	948	505
ϵ'_f or γ'_f	0.260	0.413
$2N_t$	87 382	159 790

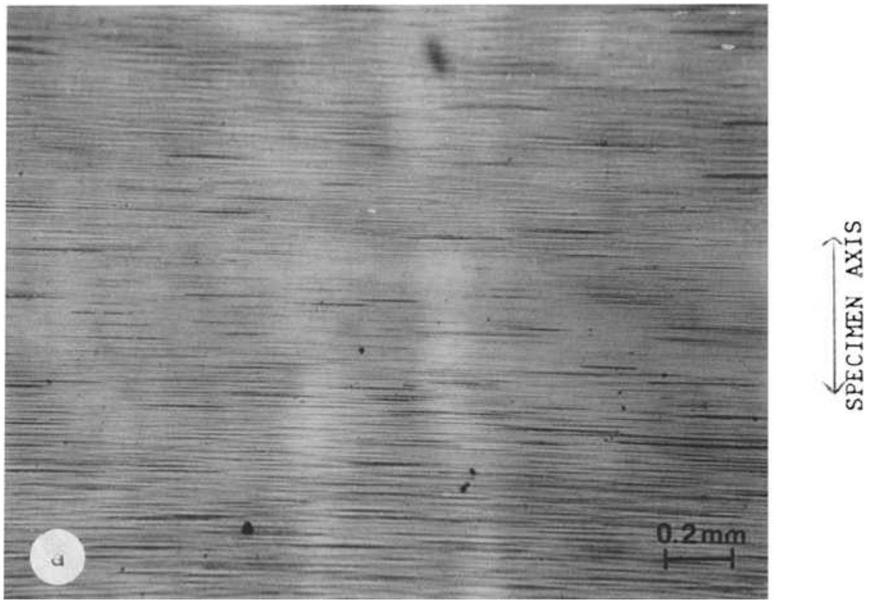

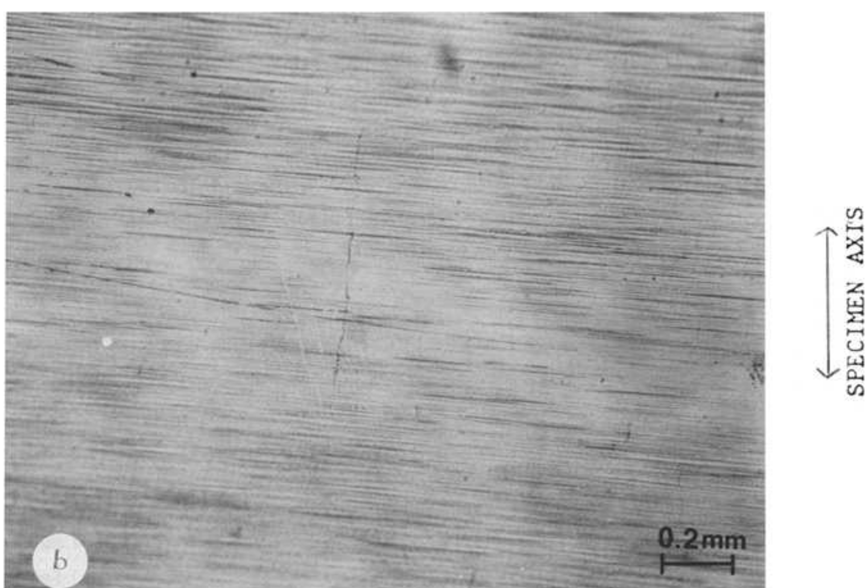

(*a*) $N = 0$.
(*b*) $N = 259$, $N_f = 5505$.
(*c*) $N = 4633$, $N_f = 5505$.

FIG. 6—*Replicas of specimen #12*, $\gamma_a = \pm 0.008$.

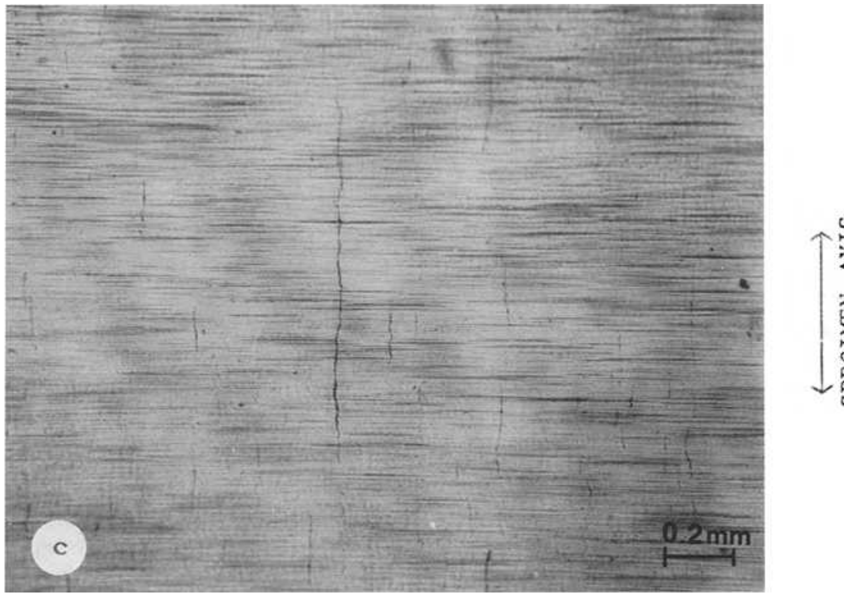

FIG. 6—*Continued*

Figure 6 shows the progression of surface cracking at one specific location for a specimen tested at $\gamma_a = \pm 0.008$. These pictures were taken from the replicas made during the test. The horizontal streaks are grinding marks, while the primarily vertical lines are the longitudinal fissures. Note that the alignment of the cracks is along a plane of maximum shear stress, which also coincides with the rolling direction of the material. Any tensile stress normal to this plane is negligible. Note also the similarity in alignment of the surface cracks seen in Fig. 6*b* to that of the inclusions present in the microstructure seen in Fig. 1.

One would expect that the presence of cracks would cause a drop in load. Actually the shear stress amplitude increased as the surface cracking became more extensive. In the particular example shown in Fig. 6, the material cyclically softened between $N = 1$ and $N = 259$, with the shear-stress range decreasing from approximately 415 to 383 MPa. Coincident with the detection of cracks at $N = 259$, the shear-stress range began to increase until it reached 401 MPa at $N = 5195$. Failure of this specimen was recorded at $N = 5505$ ($2N = 11\ 010$) due to a detected drop in load. Note that the life to detection of a significant surface crack in shear was only 5% of the total failure life. This pattern of surface cracking was exhibited by all the specimens, although the degree of surface cracking and when it was detected relative to total life may be dependent on the shear strain amplitude. It appeared that as the shear strain amplitude increased, the surface cracks were detected earlier in life, with the small cracks joining to form a predominant crack. Also, the surface cracks were often long compared to the wall thickness. A surface crack on specimen number 14 (tested at

$\gamma_a = \pm 0.005$) was directly observed through a microscope growing from 5 to 23 mm in total length before any load drop occurred.

Discussion

The shear strain controlled data presented here show a good fit to the power law fatigue relationships as written in terms of a torsional stress state. This result alone enhances the prospect of extrapolating the axial strain-based fatigue methodology into multiaxial situations. Even more promising is the quantitative comparison of the three fatigue exponents between torsional and axial stress states.

Within the context of normal scatter of fatigue data, the exponents in the torsional and axial states are essentially equal. It is important to realize that including or excluding any one data point will somewhat change the numerical values of b, c, and n'. However, the change should be slight if enough good data covering an adequate life range for analysis are used.

While consistency within any one analysis is important, it appears that b, c, and n' would not be affected if failure was defined differently in terms of crack dimensions. Dowling [7] showed constant exponents when measuring life to various crack lengths in the axial fatigue of a pressure vessel steel. Similar results are also obtained with Inconel 718 when the torsional data for various failure definitions reported by Socie et al [8] are fitted to Eqs 1 to 3. However, the coefficients of the power law relationships certainly depend on the final crack size. In this investigation, the torsional specimen wall thickness and the axial specimen radius are of roughly the same dimensions. Hence, one might try to predict torsional fatigue response using fatigue shear ductility and shear strength coefficients derived from the axial properties and an equivalent stress criterion. Using the Tresca ($\tau'_f = \sigma'_f/2$ and $\gamma'_f = 1.5\ \epsilon'_f$) or the von Mises ($\tau'_f = \sigma'_f/\sqrt{3}$ and $\gamma'_f = \sqrt{3}\ \epsilon'_f$) criterion, the predicted shear strength and ductility coefficients would envelope the values determined from the actual torsional fatigue data. The cyclic shear stress-shear strain curve and the total shear strain-life curve obtained from these criteria are shown graphically in Figs. 7*a* and *b*, along with the torsional fatigue raw data points.

The presence of longitudinal surface cracks with no corresponding load drop suggests that more attention must be given to establishing and defining failure criteria for multiaxial fatigue than for uniaxial. For the higher shear strain amplitudes tested here, surface cracks existed for nearly the entire life of the specimen. Yet, a crack propagation approach seems impractical to apply at the early stages due to the vast number of cracks apparently growing at different rates. One is reminded that the nucleation and growth of very small cracks consumes most of the life of axial specimens as well. This similitude is essential in the comparison of axial and torsional response within the confines of the local stress-strain approach.

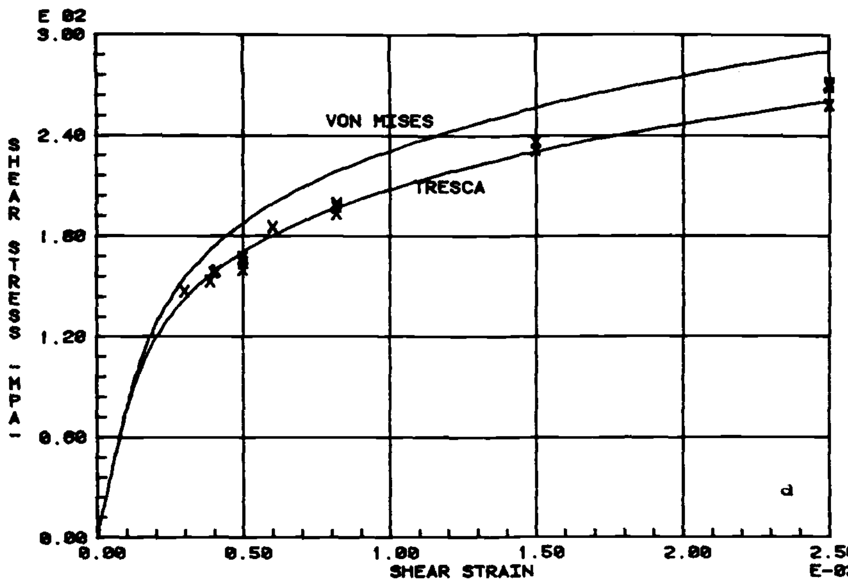

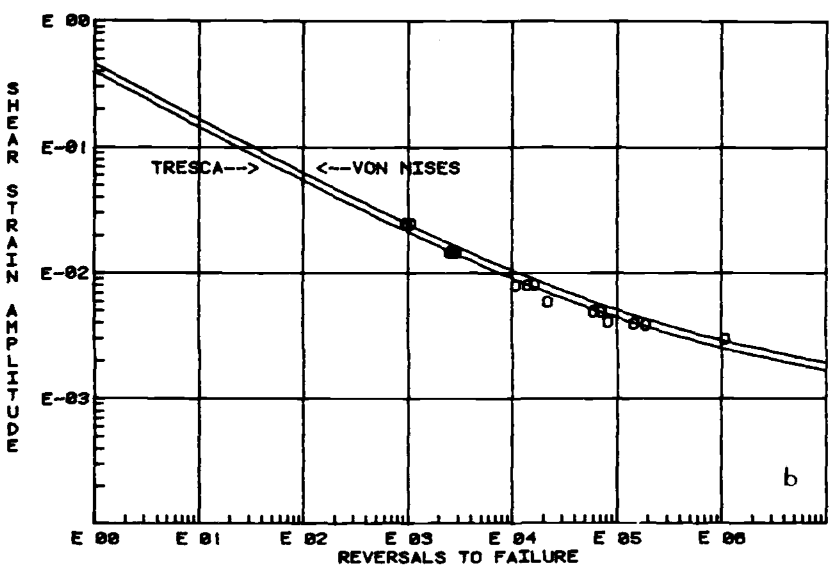

(*a*) Cyclic shear stress versus strain.

(*b*) Total shear strain versus reversals to failure.

FIG. 7—*Torsional fatigue response as predicted from axial properties using von Mises and Tresca criteria.*

Conclusions

The experimental results presented here support the following conclusions:

1. Shear strain controlled fatigue data may be reduced with the same power law relationships as in the axial case.
2. The steel tested exhibits cyclically mixed mode behavior in torsional fatigue, that is, it cyclically softens at low strain amplitudes and cyclically hardens at high strain amplitudes.
3. The fatigue strength exponent, b, cyclic strain hardening exponent, n', and the fatigue ductility exponent, c, are independent of the stress states tested for like modes of failure for 1045 HR and normalized steel.
4. The inclusions in this steel probably act as initiation sites for the longitudinal shear cracks.
5. Relatively large surface cracks in shear exist during a significant portion of the full load carrying lifetime.

Acknowledgment

The research culminating in this paper was conducted as partial fulfillment of the Master of Science requirements in Theoretical and Applied Mechanics, University of Illinois, Urbana, with Professor R. T. Shield as department head. The experimental portion of this investigation was conducted at the Deere & Company Technical Center, Moline, Illinois. Partial financial support was provided by the Fracture Control Program, College of Engineering, University of Illinois.

The authors gratefully acknowledge the constructive conversations, ideas, and advice offered by D. R. Galliart, S. D. Downing, and G. L. Curless throughout this investigation. Professor D. F. Socie is thanked for his constructive review of the manuscript.

References

[1] "Fatigue Under Complex Loading: Analysis and Experiments," *Advances in Engineering*, Vol. 6, Society of Automotive Engineers, Warrendale, PA, 1977.
[2] Socie, D. F. and Morrow, JoDean, "Review of Contemporary Approaches to Fatigue Damage Analysis," FCP Report No. 24, College of Engineering, University of Illinois, Urbana, IL, Dec. 1976.
[3] Dowling, N. E., "Torsional Fatigue Life of Power Plant Equipment Rotating Shafts," DOE/RA/29353-1, U.S. Department of Energy, Washington, DC Sept. 1982.
[4] Yokobori, T., Yamanouchi, H., and Yamamoto, S., *International Journal of Fracture Mechanics*, Vol. 1, No. 1, March 1965, pp. 3–13.
[5] Galliart, D. R. and Downing, S. D., this publication, pp. 24–32.
[6] Curless, G. L., Deere & Company Technical Center, Moline, IL, personal communication, 1982.
[7] Dowling, N. E., *Cyclic Stress-Strain and Plastic Deformation Aspects of Fatigue Crack Growth, ASTM STP 637*, American Society for Testing and Materials, Philadelphia, 1977, pp. 97–121.
[8] Socie, D. F., Waill, L. A., and Dittmer, D. F., this publication, pp. 463–481.
[9] Deere & Company Technical Center, Internal Report T-1676, Moline, IL, 5 Feb. 1982.

James W. Fash,[1] Darrell F. Socie,[1] and David L. McDowell[2]

Fatigue Life Estimates for a Simple Notched Component Under Biaxial Loading

REFERENCE: Fash, J. W., Socie, D. F., and McDowell, D. L., "**Fatigue Life Estimates for a Simple Notched Component Under Biaxial Loading,**" *Multiaxial Fatigue, ASTM STP 853*, K. J. Miller and M. W. Brown, Eds., American Society for Testing and Materials, Philadelphia, 1985, pp. 497–513.

ABSTRACT: Three-dimensional stress-strain fields are routinely determined for complex components using elastic and elastic-plastic finite element models. Although the local stress-strain response can be easily determined, the proper approach to strain based multiaxial fatigue analysis is not clear. Several multiaxial fatigue theories have been suggested, but there exists a lack of consensus on which model is most appropriate. To clarify the situation, experiments have been performed on two different multiaxial specimen geometries. Results are compared with theoretical predictions.

Thin-walled tube specimens have been tested using combined in-phase tension-torsion loading. This specimen geometry has a simple uniform stress-strain state. Tests were also performed using a solid notched shaft specimen subjected to inphase torsion-bending loads. Stress-strain gradients exist in the notch root. Local multiaxial stress-strain fields were determined using an elastic-plastic finite element model.

Five current multiaxial strain based fatigue theories have been developed to correlate the experimental results. Fatigue life estimates were based upon uniaxial strain controlled fatigue data.

Correlations for the thin-walled tube test series were within a factor of 3 in fatigue life. For the notched shaft specimen with the more complex stress-strain state, life estimates were in error by a factor of 10 in fatigue life. This suggests that the effects of geometry are as important as the selection of the fatigue theory. Much additional work needs to be done to understand the effect of notches in multiaxial fatigue before these methods can be routinely implemented by designers.

KEY WORDS: biaxial fatigue, notch fatigue, stress analysis, life prediction

Nomenclature

$\epsilon, \Delta\epsilon$	Axial strain and axial strain range, respectively
$\epsilon_1, \epsilon_2, \epsilon_3$	Ordered principal strains
$\Delta\epsilon_1$	Maximum principal strain range
$\bar{\epsilon}, \Delta\bar{\epsilon}$	Effective strain and effective strain range, respectively

[1]Research assistant and associate professor, respectively, Department of Mechanical Engineering, University of Illinois at Urbana-Champaign, Urbana, IL 61801.

[2]Assistant professor, School of Mechanical Engineering, Georgia Institute of Technology, Atlanta, GA 30332.

Copyright© 1985 by ASTM International www.astm.org

$\gamma_{max}, \Delta\gamma_{max}, \epsilon_n$	Maximum shear strain, maximum shear strain range, and normal strain, respectively
$\gamma^*, \Delta\gamma^*, \epsilon_n^*$	Lohr-Ellison shear strain, shear strain range, and normal strain, respectively
σ'_f	Fatigue strength coefficient
b	Fatigue strength exponent
ϵ'_f	Fatigue ductility coefficient
c	Fatigue ductility exponent
N_f	Cycles to failure
E	Young's modulus
ν	Poisson's ratio
k	Constant

Strain-based fatigue analysis is routinely employed to assess the fatigue resistance of components in the ground vehicle industry [*1*]. Unfortunately, these methods are restricted to uniaxial loading situations such as simple notches in plate-like structures. Many components are subjected to multiaxial stresses and strains. Examples include axles, frames, shafts, and springs. Analytical stress analysis techniques are available in which elastic and elastic-plastic models are routinely employed to determine three-dimensional stress and strain states in complex components. Analytic procedures for multiaxial fatigue analysis have been slow to develop due to the complexity of the subject and the difficulty in obtaining experimental data. As a result, no consensus exists as to the most appropriate multiaxial fatigue theory. Designers have relied on extensions of static yield criteria such as maximum principal strain, maximum shear strain, and octahedral shear strain for making judgments about the fatigue resistance of their components.

Five strain based multiaxial fatigue theories have been investigated. A relationship between the applicable strain parameter and the number of cycles to failure has been developed for each theory. Results of two series of biaxial fatigue tests are analyzed using these relationships. Thin-walled tube specimens have been tested under strain controlled completely reversed combined tension-torsion loading.

The Society of Automotive Engineers (SAE) Fatigue Design and Evaluation Committee established a testing program to provide experimental data for assessing the reliability of existing multiaxial fatigue design procedures and to stimulate research and development of improved analytical methods [*2*]. A simple notched shaft that would simulate an engineering component was selected as the test specimen. Experiments have been performed by applying combinations of cyclic torsion and bending loads to the shaft. Local multiaxial stress-strain states in the notch were calculated using a three-dimensional elastic-plastic finite element model.

If fatigue life is a function only of the local strain, similar correlations of test results should be obtained by applying the same strain-based theories to both types of specimens.

Fatigue Theories

A number of good reviews on multiaxial fatigue exist [3–5] and will not be repeated here. Three commonly used approaches based on extensions of static yield criteria and two new theories based on critical damage planes were selected for this investigation. Extensions of static criteria are the maximum principal strain, the effective strain, and the maximum shear strain. The critical plane approaches have been proposed by Lohr and Ellison [6] and by Kandil, Brown, and Miller [7]. A shared characteristic of all five approaches is that the required material properties can be determined from standard uniaxial fatigue test data.

Uniaxial fatigue data are commonly reported in terms of strain-life curves. The relationship between fatigue life and applied strain amplitude is given by

$$\frac{\Delta\epsilon}{2} = \frac{\sigma'_f}{E}(2N_f)^b + \epsilon'_f(2N_f)^c \tag{1}$$

In the uniaxial test, the maximum principal strain amplitude is equal to the axial strain amplitude. Life estimates based on the range of maximum principal strain are obtained using Eq 2.

$$\frac{\Delta\epsilon_1}{2} = \frac{\sigma'_f}{E}(2N_f)^b + \epsilon'_f(2N_f)^c \tag{2}$$

Effective strain also may be used to correlate the fatigue data. Effective strains normalized to the axial case are given by

$$\bar{\epsilon} = \frac{2^{1/2}}{3}[(\epsilon_1 - \epsilon_2)^2 + (\epsilon_2 - \epsilon_3)^2 + (\epsilon_1 - \epsilon_3)^2]^{1/2} \tag{3}$$

This equation is often employed even though it is derived for Poisson's ratio of 0.5. The amplitude of effective strain can be computed by substituting the amplitudes of principal strains into Eq 3. The effective strain amplitude is equal to the axial strain amplitude during uniaxial testing.

$$\frac{\Delta\bar{\epsilon}}{2} = \frac{\sigma'_f}{E}(2N_f)^b + \epsilon'_f(2N_f)^c \tag{4}$$

Equation 4 then may be used to estimate fatigue lives based on effective strains.

Correlations based on maximum shear strain can be obtained by converting uniaxial data into shear strains

$$\frac{\Delta\gamma_{max}}{2} = (1 + \nu)\frac{\Delta\epsilon}{2} \tag{5}$$

For combined loading, maximum shear strain is computed using ϵ_1 and ϵ_3 from Mohr's circle

$$\frac{\Delta\gamma_{max}}{2} = \Delta(\epsilon_1 - \epsilon_3), \qquad \epsilon_1 \geq \epsilon_2 \geq \epsilon_3 \tag{6}$$

Substituting the appropriate Poisson's ratio for elastic and plastic components of strain leads to the life relationship given in Eq 7

$$\frac{\Delta\gamma_{max}}{2} = 1.30\frac{\sigma'_f}{E}(2N_f)^b + 1.50\,\epsilon'_f\,(2N_f)^c \tag{7}$$

Lohr and Ellison [*6*] have proposed a theory based on the maximum shear strain γ^* which occurs on planes intersecting the free surface at 45° for tension-torsion loading of thin-walled tubes. The normal strain to this plane ϵ_n^* has a modifying influence. They argue that the strains that cause cracks to grow into the specimen are more important than the strains that cause cracks to grow along the surface. This parameter is computed from Mohr's circle of strain for ϵ_1 and ϵ_2

$$\begin{aligned} \frac{\Delta\gamma^*}{2} &= \Delta(\epsilon_1 - \epsilon_2) \\ \epsilon_n^* &= \frac{\Delta(\epsilon_1 + \epsilon_2)}{2} \end{aligned} \tag{8}$$

Substituting the appropriate Poisson's ratio for elastic and plastic strains gives

$$\frac{\Delta\gamma^*}{2} + 0.4\,\epsilon_n^* = 1.44\frac{\sigma'_f}{E}(2N_f)^b + 1.60\,\epsilon'_f\,(2N_f)^c \tag{9}$$

The coefficient of ϵ_n^* in Eq 9 was found to be nearly constant for several materials by Lohr and Ellison and is used here.

Kandil, Brown, and Miller [*7*] proposed a critical plane theory based on the maximum shear strain range $\Delta\gamma_{max}$ modified by the normal strain to the plane of maximum shear, ϵ_n. Maximum shear strain is given by Eq 6 and the normal strain is

$$\epsilon_n = \frac{\Delta(\epsilon_1 - \epsilon_3)}{2} \tag{10}$$

Again substituting appropriate values of Poisson's ratio results in

$$\frac{\Delta\gamma_{max}}{2} + k\epsilon_n = 1.65 \frac{\sigma'_f}{E}) (2N_f)^b + 1.75\ \epsilon'_f(2N_f)^c \tag{11}$$

The constant k has been taken as unity.

Equations 2, 4, 7, 9, and 11 can be used with material properties determined from uniaxial fatigue tests to estimate fatigue endurance for more complex states of strain.

Test Program

Material

Hot-rolled 1045 steel (63.5-mm-diameter bars) in the normalized condition was used for all tests in this investigation. The unetched microstructure is shown in Fig. 1. Note the sulfide inclusions in the direction of rolling which are approximately 0.1 mm long. Mechanical properties are given in Table 1. Fatigue specimens 45 mm long with a 2.5-mm-diameter gage section were cut from both axial and tangential directions of the bar. Tangential specimens were cut halfway

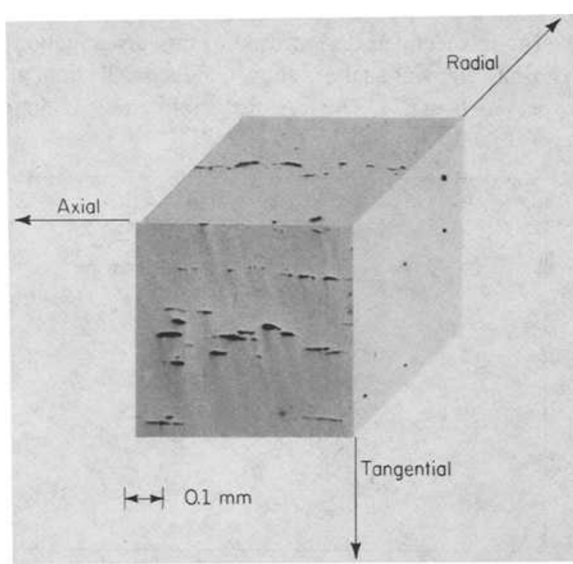

FIG. 1—*Unetched microstructure showing sulfide inclusions.*

TABLE 1—*Mechanical properties of 1045 steel.*

MONOTONIC PROPERTIES		
Yield stress (0.2%)	380	MPa
Fracture stress	620	MPa
Fracture strain	0.71	
Percent reduction in area	50	
Strain hardening exponent	0.23	
Strength coefficient	1185	MPa
Modulus of elasticity	205	GPa
CYCLIC PROPERTIES		
Fatigue ductility coefficient	0.20	
Fatigue ductility exponent	−0.43	
Fatigue strength coefficient	980	MPa
Fatigue strength exponent	−0.11	

between the center and outside surface of the bar. Smooth specimen completely reversed tension-compression fatigue test results are shown in Fig. 2 for both axial and tangential directions. Specimens cut from the tangential direction have a lower fatigue life by a factor of 2 to 3. This anisotropy in fatigue life is due to the sulfide inclusions. In the tangential tests, the inclusions are normal to the applied stress and aid in crack initiation. Inclusions are parallel to the applied stress in the axial tests and do not act to raise local stresses. This material exhibits cyclic softening below 0.5% axial strain and hardening at larger strains.

Thin-Walled Tube Tests

The thin-walled tube specimen design used in this investigation is shown in Fig. 3. Results of finite element analysis show that the axial strain gradient along the gage length was less than 2%. The torsional strain gradient along the surface

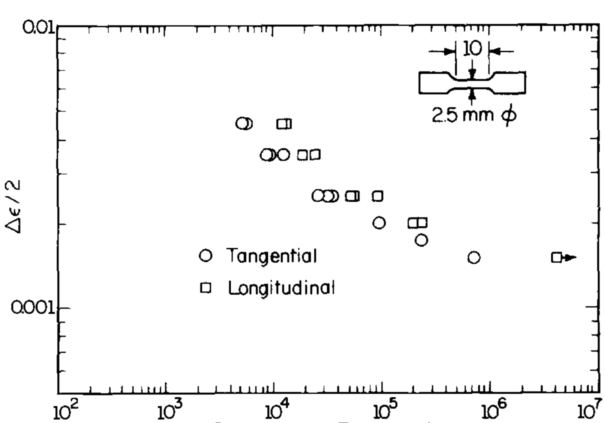

FIG. 2—*Strain-life comparison of axial and tangential smooth specimen tests.*

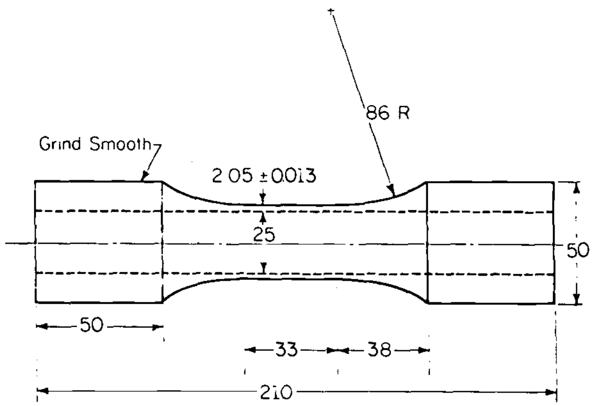

FIG. 3—*Thin-walled tube tension-torsion specimen. Dimensions in millimetres.*

was nearly zero, and the torsional gradient between the inner and outer surfaces was 15%. Standard machine collets are used to grip the ends of the specimen. Axial displacements were measured and controlled with a linear variable differential transformer (LVDT) located on the centerline of the specimen and rotations with a rotary variable differential transformer (RVDT). Coupling between the two measurements was less than 1%. Tests were conducted on an MTS Model 809 tension-torsion machine that was modified to increase the torsional stiffness. An MTS Model 463 processor-interface was used for computer control, data acquisition, and data reduction of the tests. Failure was defined as 10% load drop in all of the tests. Results are summarized in Table 2. Axial strains are controlled to the values reported in Table 2. In torsion there is a small strain gradient between the inside and outside surfaces of the specimen. The controlled torsional strain values reported are the average of midthickness values. These values have been extrapolated to the outside surface for the values used in the fatigue life predictions discussed in a later section.

Notched Shaft Specimen Tests

The notched shaft specimen is shown in Fig. 4. Combined torsion and bending loads were applied with two linear servohydraulic actuators operated in load control. Any combination of bending and torsion loads are possible by adjusting the amplitude and phase of each actuator. Crack initiation was detected with an ultrasonic transducer, and the initiation life was defined as a crack of approximately 1 mm surface length for the SAE test program [*8*]. Test results are summarized in Table 3 for tests conducted at the University of Illinois at Urbana-Champaign. Bending moments at the notch root radius are reported.

Finite-Element Analysis

An elastic-plastic finite-element model [*9*] was employed in this study to determine the notch root stresses and strains for the shaft specimen. Twenty

TABLE 2—*Thin-wall tube specimen test results.*

Axial Strain	Shear Strain	Axial Stress	Shear Stress	Life[a], cycles		
0.0015	0.0000	234.4	0.0	. . .[b]		
0.0021	0.0000	266.1	0.0	142 541		
0.0022	0.0000	273.1	0.0	78 271	94 525	
0.0043	0.0000	344.7	0.0	7 839		
0.0050	0.0000	355.1	0.0	4 959		
0.0055	0.0000	375.8	0.0	4 600		
0.010	0.0000	450.7	0.0	1 137	1 107	
0.0014	0.0007	224.6	43.8	611 780		
0.0021	0.0011	266.0	52.7	115 462	91 000	
0.0041	0.0021	338.0	54.8	11 777		
0.0096	0.0048	427.7	79.2	1 258		
0.0013	0.0013	212.8	80.3	595 613	393 633	
0.0019	0.0019	238.0	87.9	123 544	103 000[c]	
0.0037	0.0037	305.0	107.0	11 611	10 377	
0.0087	0.0087	381.4	131.9	1 616	1 229	
0.0010	0.0020	147.5	111.0	545 840		
0.0014	0.0029	179.8	126.5	98 779	101 000[c]	
0.0026	0.0061	234.4	153.2	20 031	16 887	
0.0065	0.0131	288.0	195.6	1 758		
0.0000	0.0026	0.0	146.9	1010 210		
0.0000	0.0038	0.0	168.2	102 083	57 369	93 052
0.0000	0.0072	0.0	197.0	8 710		
0.0000	0.0173	0.0	251.8	890	889	

[a]Multiple results indicate test replication.
[b]Runout.
[c]Test stopped after a visible crack (1 to 3 mm) was detected. Values reported for life are estimated to 10% load drop.

noded solid elements with a biquadratic interpolation function for displacement were employed. The mesh is shown in Fig. 5 and contains 729 nodes and 128 elements.

The cyclic stress-strain curve obtained from uniaxial tests was used for the plasticity analysis to obtain an estimate of the stabilized stresses and strains. A comparison of the finite-element strains (solid line) and experimental data (open symbols) from strain gages measured by several laboratories for the bending load case is shown in Fig. 6. Stabilized strain gage measurements have been examined in detail in Ref *8*. Good correlation is obtained between strain gage

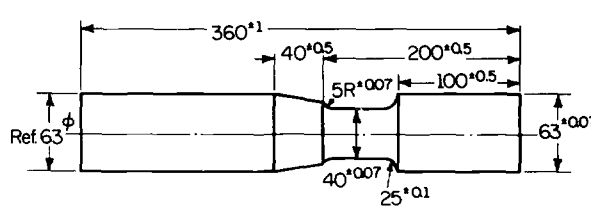

FIG. 4—*SAE notched shaft specimen. Dimensions in millimetres.*

TABLE 3—*Notched shaft fatigue test results.*

Bending moment, nm	Torsion Moment, nm	Life[a], N_i cycles			
1400	0	. . .[b]			
1475	0	230 000	430 000	463 976	
1708	0	163 770			
1730	0	60 000	30 000	130 000	
2600	0	3 000	8 111	14 000	7930
2800	0	2 571			
1250	880	60 000			
1550	1090	97 500	80 000		
2325	1350	3 000			
915	880	. . .[b]			
1135	1090	. . .[b]	. . .[b]		
1720	1350	17 065	21 450		
990	1390	933 000			
1220	1710	72 000			
1850	2550	2 200			
725	1390	. . .[b]			
1355	2550	5 500			
625	1760	. . .[b]			
780	2180	70 000			
1150	2700	3 000			
460	1760	. . .[b]			
570	2180	76 100	99 560		
840	2700	9 000	10 000		
0	2000	1584 000	750 000		
0	2400	75 700			
0	3000	7 000	4 057		

[a]Multiple results indicate test replications.
[b]Runout.

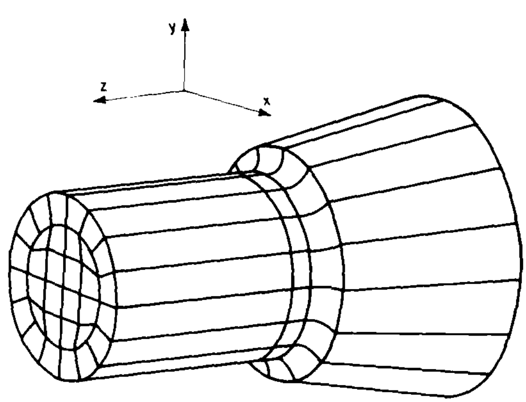

FIG. 5—*Finite element mesh for notched shaft specimen.*

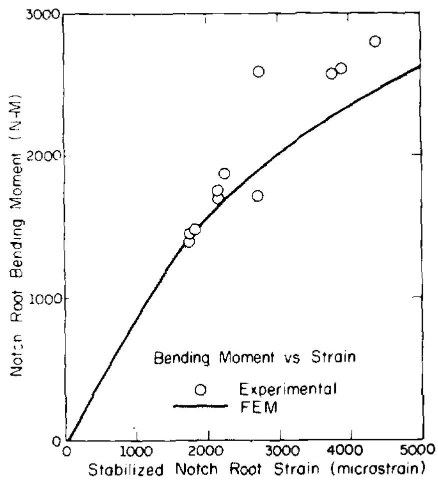

FIG. 6—*Comparison of computed and measured notch root strains for bending loads only.*

TABLE 4—*Notched shaft strain analysis from finite-element model.*

Moments		Strains					
Bending	Torsion	ϵ_{xx}	ϵ_{yy}	ϵ_{zz}	γ_{xy}	γ_{xz}	γ_{yz}
1400	0	218	611	−1675	0	0	571
1730	0	295	867	−2165	0	0	757
2600	0	758	2802	−4877	0	0	1749
990	1390	154	432	−1184	−249	1917	403
1220	1710	206	643	−1561	−335	2532	544
1850	2550	847	2548	−4358	−1040	7343	1574
725	1390	113	316	−867	−249	1917	295
894	1720	148	442	−1116	−320	2479	384
1355	2550	457	1404	−2604	−838	6115	948
1250	880	195	546	−1495	−157	1214	510
1550	1090	265	790	−1953	−205	1584	685
2325	1350	679	2327	−4228	−368	2927	1516
915	880	143	400	−1096	−158	1214	373
1135	1090	181	509	−1369	−192	1516	465
1703	1350	391	1333	−2613	−319	2441	942
625	1760	97	273	−747	−315	2428	254
770	2180	132	414	−995	−437	3279	347
1150	2700	409	1216	−2224	−928	6553	829
458	1760	71	200	−547	−315	2428	186
568	2180	96	300	−729	−434	3256	252
842	2700	156	487	−1130	−583	4380	397
0	2000	0	0	0	−360	2759	0
0	2400	0	0	0	−492	3668	0
0	3000	0	0	0	−809	6031	0

results and finite-element results. The actual component exhibited more stiffness than the model since the stabilized cyclic stress-strain curve was used and the material cyclically softens at small strain amplitudes. Measured strains for all load cases were within 10% of the computed values. Strains for all of the load cases in this investigation are listed in Table 4. The local Cartesion coordinate system used in Table 4 to define strain components is a right-handed xyz system with the xz plane corresponding to the specimen surface. The z-axis is the primary bending axis. Computed stresses normal to the surface are less than 20% of the maximum normal stress component. These surface stresses result from load tolerances during the iteration process of the finite-element method.

Results and Discussion

Estimated fatigue lives versus experimental lives based on crack initiation for the thin-walled tube specimens are shown in Figs. 7 through 11 for the five theories considered. Perfect correlation would lie along the 45° line. Correlations based on plastic strains were essentially the same as those based on total strains and are not reported here. Predictions were made during the early stages of the test program to avoid fitting test results.

Correlation for all five methods is within a factor of three in life except for the torsion data. Scatter of the data is about the line of perfect correlation for the principal strain, effective strain, and the Lohr and Ellison theories. Both theories based on maximum shear strain parameters result in conservative predictions. Torsion test data should not correlate because of the anisotropy shown in Fig. 2. Only the Lohr and Ellison parameter shows this. When material

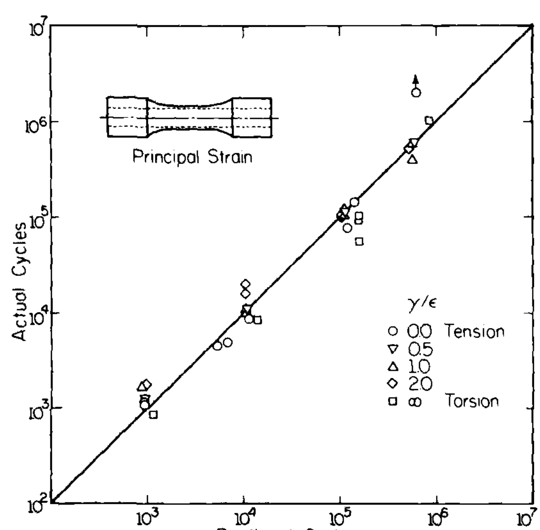

FIG. 7—*Actual versus predicted lives: maximum principal strain theory.*

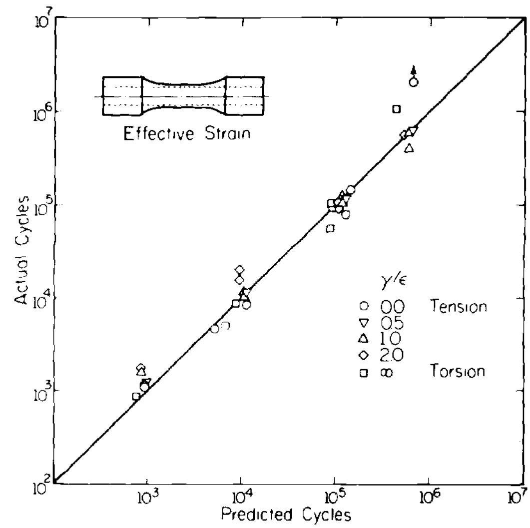

FIG. 8—*Actual versus predicted lives: effective strain theory.*

properties determined from specimens taken in the tangential direction are employed for torsional predictions, the torsion data fall in the same scatterband as the other data for the Lohr and Ellison parameter.

Estimates for the notched shaft fatigue crack initiation lives are shown in Figs. 12 through 16. Again, predictions were made prior to obtaining most of the actual test results. Correlations for the notched member are not as good as those

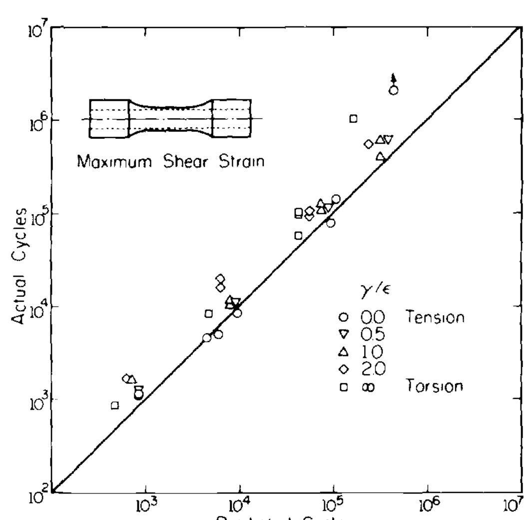

FIG. 9—*Actual versus predicted lives: maximum shear strain theory.*

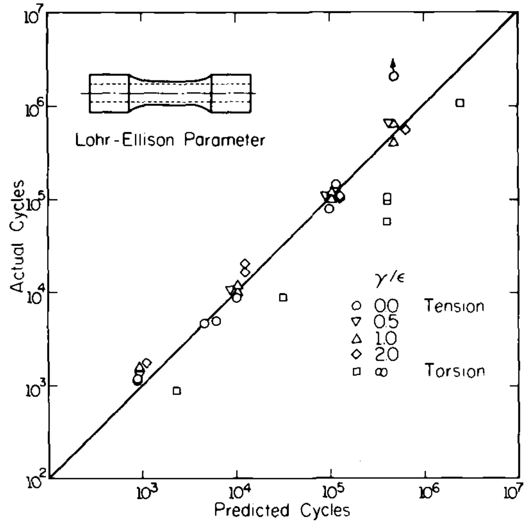

FIG. 10—*Actual versus predicted lives: Lohr and Ellison theory.*

for the thin-walled tube. All prediction methods result in scatter of a factor of ten or more. Bending results are in general about the line of perfect correlation. Torsion results are at the extremes of the scatter. The slope of the torsion data differs from the 45° slope of perfect correlation. Strain gage results for the notched specimen show that the finite element results are within 10% of the measured strains. At the longer lives, this would result in an error in fatigue life predictions

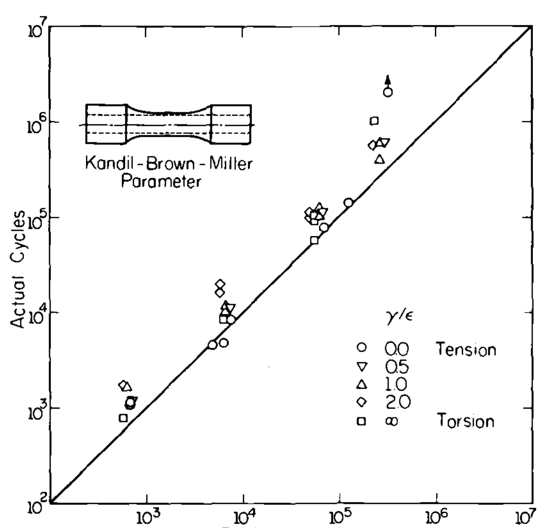

FIG. 11—*Actual versus predicted lives: Kandil, Brown, and Miller theory.*

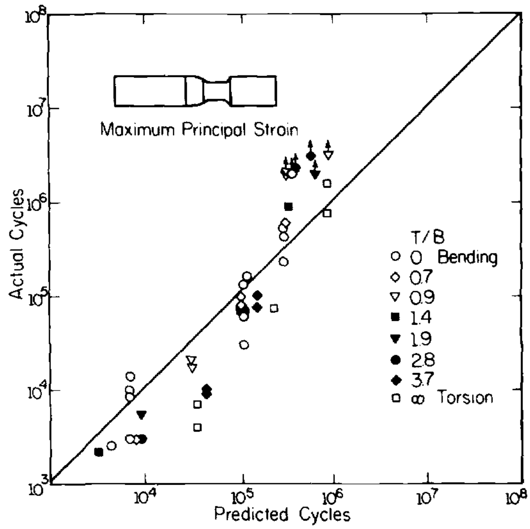

FIG. 12—*Actual versus predicted lives: maximum principal strain theory.*

of a factor of 2. Scatter is noticeably less at shorter lives. These small errors in computed strains cannot explain the significant lack of correlation of the notched shaft test results. This anomaly is apparently related to the effect of the notch on the local stress-strain field and actual damage mechanisms.

From the comparison of tests on smooth and notched specimens, it is clear that the choice of a biaxial fatigue theory is considerably less important than understanding biaxial notch effects. When notches are present under biaxial

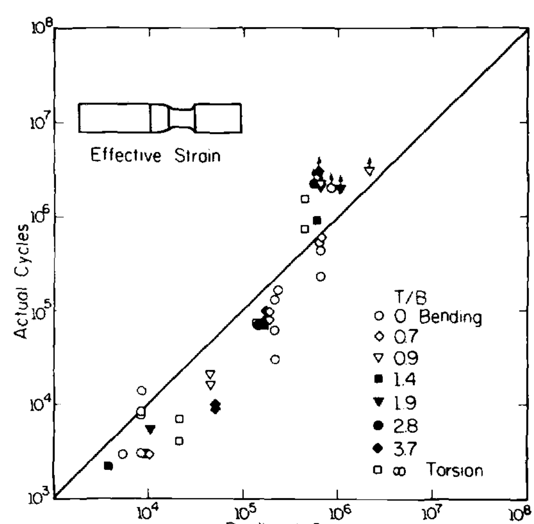

FIG. 13—*Actual versus predicted lives: effective strain theory.*

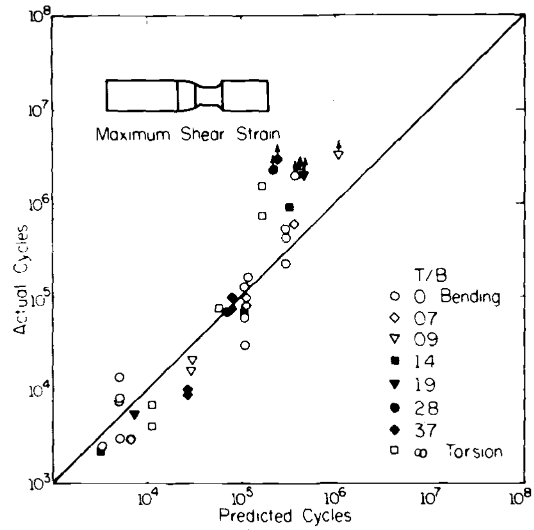

FIG. 14—*Actual versus predicted lives: maximum shear strain theory.*

loading, the local strain approach must be refined or re-examined to conform with actual test results. In this regard, the methods based upon the maximum shear strain led to the least scatter for notched specimen results.

Conclusions

1. For combined tension and torsion loading, the maximum principal strain, octahedral shear strain, maximum shear strain, Lohr and Ellison and Kandil,

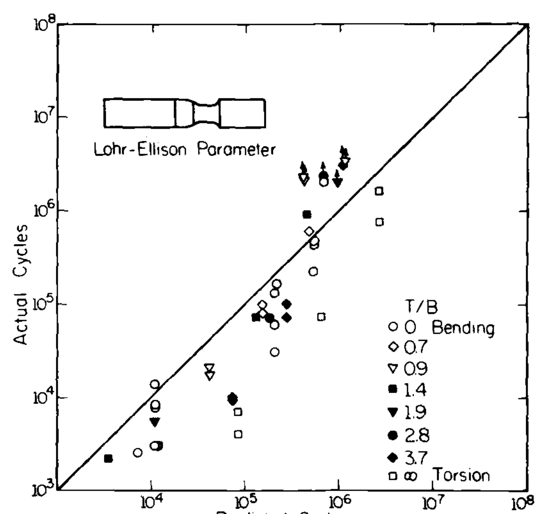

FIG. 15—*Actual versus predicted lives: Lohr and Ellison theory.*

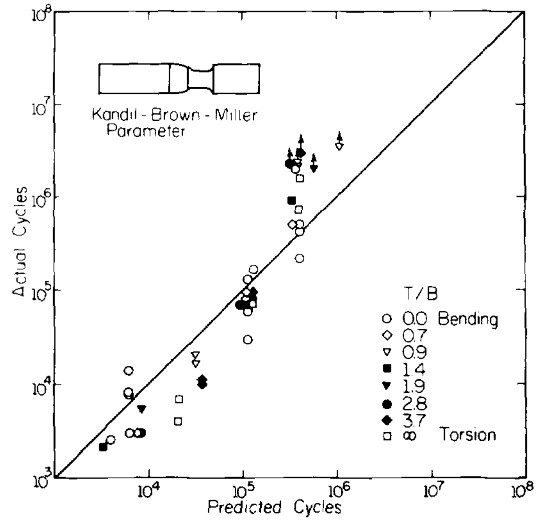

FIG. 16—*Actual versus predicted lives: Kandil, Brown, and Miller theory.*

Brown, and Miller approaches yield essentially equivalent correlations of thin-wall tube specimen fatigue life.

2. For the notched shaft specimens, the aforementioned approaches offer considerably less correlation based on computed notch root strains. Bending tests results are scattered about the line representing perfect correlation. Correlation of torsion results differed from the line of perfect correlation with predictions being nonconservative at short lives and becoming more conservative in the long-life region.

3. Emphasis should be placed on understanding the influence of notches in biaxial fatigue.

Acknowledgments

The support of this work by the U.S. National Science Foundation Grant MEA-81-11282 is gratefully acknowledged. Laboratory assistants T. Shield and J. Koch are acknowledged for their experimental assistance.

References

[1] *Fatigue Under Complex Loading*, Society of Automotive Engineers, Vol. 6, 1977.

[2] Tucker, L. E. and Galliart, D. R., "A Fatigue Test Program for a Notched Round Component," Symposium on Biaxial Multiaxial Fatigue, San Francisco, 15–17 Dec. 1982.

[3] Krempl, E., *The Influence of State of Stress on Low-Cycle Fatigue of Structural Materials, ASTM STP 549*, American Society for Testing and Materials, Philadelphia, 1974.

[4] Garud, Y. S., *Journal of Testing and Evaluation*, Vol. 9, No. 3, 1981, pp. 165–178.

[5] Brown, M. W., and Miller, K. J., *Low-Cycle Fatigue and Life Prediction, ASTM STP 770*, American Society for Testing and Materials, Philadelphia, 1982, pp. 482–499.

[6] Lohr, R. D. and Ellison, E. G., *Fatigue of Engineering Materials and Structures*, Vol. 3, 1980, pp. 1–17.
[7] Kandil, F. A., Brown, M. W., and Miller, K. J., *Biaxial Low-Cycle Fatigue Fracture of 316 Stainless Steel at Elevated Temperatures*, Book 280, The Metals Society, London, 1982, pp. 203–210.
[8] Downing, S. D. and Galliart, D. R., this publication, pp. 24–32.
[9] ABAQUS Finite Element Code, Hibbitt, Karlsson, and Sorenson, Inc. Providence, RI, 1980.

Steven M. Tipton[1] *and Drew V. Nelson*[1]

Fatigue Life Predictions for a Notched Shaft in Combined Bending and Torsion

REFERENCE: Tipton, S. M. and Nelson, D. V., "**Fatigue Life Predictions for a Notched Shaft in Combined Bending and Torsion,**" *Multiaxial Fatigue, ASTM STP 853,* K. J. Miller and M. W. Brown, Eds., American Society for Testing and Materials, Philadelphia, 1985, pp. 514–550.

ABSTRACT: As part of a cooperative research program on biaxial fatigue of the Society of Automotive Engineers (SAE), this paper reports progress to date in the evaluation of methods for predicting fatigue life of a round-bar specimen (1045 steel) with a shoulder fillet, subjected to fully reversed bending, torsion and combined bending and torsion, in-phase and 90° out of phase.

First, test data from the literature on multiaxial fatigue behavior of notched specimens are reviewed. Factors influencing that behavior (for example, notch stress state and type of notch geometry) are discussed, as are approaches for correlating the data.

Next, a number of different methods for predicting life to "crack initiation" (millimetre sized cracks) are compared with test data for the SAE specimen. The methods are: (*a*) elastically calculated notch maximum shear and octahedral shear stress criteria based on nominal stresses and fatigue notch factors, (*b*) maximum shear and octahedral shear strain criteria, (*c*) a cyclic plastic work approach, and (*d*) a criterion based on amplitudes of maximum shear strain and of normal strain on the plane of maximum shear. Methods (*b*) through (*d*) utilize measured notch strains. Advantages and shortcomings of the methods are discussed.

Measured notch bending and torsional shear strains are compared to values estimated by simplified elastic-plastic analyses which investigate both use of Neuber's rule and the assumption of total strain invariance (that is, notch strain concentration factor equal to an elastic stress concentration factor.)

KEY WORDS: multiaxial fatigue, notches, life prediction, combined bending-torsion fatigue, fatigue notch factor, out-of-phase loadings, notch strain analysis, strain gradient, crack initiation, nonpropagating cracks

The past two decades have witnessed significant advances in development of methods for predicting fatigue life of notched components under uniaxial loading. Most methods assume that maximum principal stress or strain governs behavior. Many notched components experience multiaxial fatigue (in some cases even when the loading is uniaxial), and there is a strong need to develop improved methods for predicting their life. The SAE Fatigue Design and Evaluation Committee has recently established a cooperative industry-university research pro-

[1]Research assistant and associate professor, Mechanical Engineering Department, Stanford University, Stanford, CA 94305.

Copyright© 1985 by ASTM International www.astm.org

gram to generate fatigue test data for a round-bar specimen with a shoulder fillet subjected to various combinations of bending and torsion and to develop better life prediction techniques for this commonly encountered notch geometry and type of multiaxial loading.

This paper has two purposes. First, previous studies of multiaxial fatigue in notched specimens will be reviewed and discussed. Second, various methods for predicting life to crack initiation (millimetre sized cracks) for the SAE specimen will be compared with test data currently available in the research program. Relative advantages and shortcomings of the methods will be discussed.

Review of Multiaxial Fatigue of Notched Specimens

Several comprehensive reviews of multiaxial fatigue, based on smooth specimen behavior, are available [*1–3*]. In this section, multiaxial fatigue in notched specimens will be considered, a topic where current knowledge is very limited.

Notched Specimens Under Uniaxial Loading

To predict life to crack initiation (millimetre sized cracks) of notched specimens and structural components experiencing uniaxial loading, the following approaches are often used. When elastic analysis is conducted, maximum principal stress at a notch, or a lower "effective" value based on a fatigue notch factor, K_f, is used to enter a smooth specimen *S-N* curve to assess damage per cycle. When Neuber analysis is performed, maximum principal notch strain estimated with K_f in Neuber's rule [*4*] is used with smooth specimen ϵ-*N* data to predict damage. Both approaches utilize input data generated in a uniaxial stress state. Neither approach explicitly takes into account the possible influence of multiaxial stresses present in many notches. Neither do they account for the influences of notch strain gradient, notch sensitivity, etc., except through K_f factors, but those influences are not primary subjects of this paper.

For mild notches in thin plates, the stress state is uniaxial on the notch surface, but biaxial below the surface, as illustrated in Fig. 1*a*. In thicker plates, a transverse component of stress develops due to constraint on straining in the thickness direction, Fig. 1*b*. For circumferentially notched round bars, the stress state is biaxial at the notch root and triaxial in depth, as shown in Fig. 1*c*. The influence of multiaxial stress state at a notch can be twofold. First, the same geometrical factors which produce notch biaxial or triaxial stresses also influence the value of maximum principal strain. Second, for a given maximum principal strain, a multiaxial stress state may cause fatigue behavior to differ from that determined in uniaxial stressing.

In notch geometries with constraint on plastic flow, maximum principal strain is overestimated by Neuber's rule using the elastic stress concentration factor, K_t. Notch strain generally falls between Neuber estimates and those based on the assumption that strain concentration factor, K_ϵ, remains equal to K_t with plastic straining [*5–7*].

Walker [*8*] proposed that equally good predictions of fatigue life of uniaxially

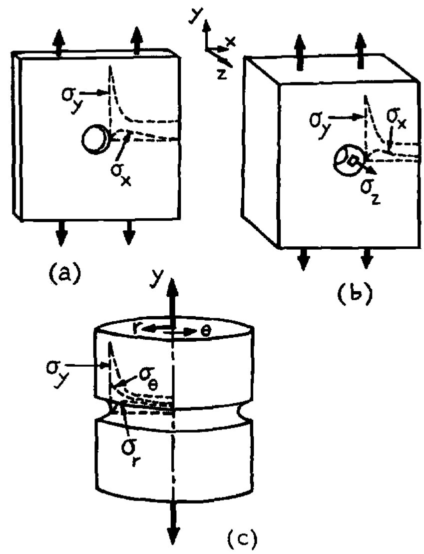

FIG. 1—*Schematic of elastically calculated stresses in several types of notched specimens under uniaxial loading.*

loaded notched specimens could be obtained by using Neuber analysis with K_f and a uniaxial cyclic stress-strain curve or by using Neuber analysis with K_t and a cyclic stress-strain curve modified to account for notch multiaxial stress state. The modified curve reflects an effectively higher modulus of elasticity and greater resistance to plastic flow resulting from hydrostatic tension. Walker's approach gives estimates of maximum principal strain similar to those based on $K_\epsilon = K_t$ for levels of plastic straining typically encountered in intermediate to long-life fatigue (that is, lives beyond about 10^3 cycles). Wundt [*9*] reviews other methods for estimating cyclic notch strain under "plane-stress" and "plane-strain" conditions.

Leis and Topper [*10*] have suggested that the discrepancy between K_t and K_f when notch straining is elastic and only "crack initiation" is considered may result from the influence of notch stress biaxiality. In particular, they proposed a theoretical fatigue notch factor given by

$$K_f^{th} = K_t\,(1 - \alpha + \alpha^2)^{1/2} \tag{1}$$

where

$\alpha = \Delta\sigma_2/\Delta\sigma_1$, and
$\Delta\sigma_1, \Delta\sigma_2$ = ranges of maximum principal and transverse stress, respectively.

The K_f^{th} factor is equal to the von Mises equivalent stress range divided by the range of maximum principal stress. This approach produced good estimates of long-life fatigue strength for thick plates with central holes and circumferentially notched round bars. It could not and was not intended to account for the influence of nonpropagating cracks on the difference between K_t and K_f for sharp notches.

In his review of low-cycle fatigue, Wundt [9] discusses Krempl's tests [11] of uniaxially loaded, circumferentially notched round bars of 2.25Cr-1Mo steel with a K_t of 3.3. Measured transverse strains were less than one tenth of axial strains, indicating the presence of biaxial tension at the notch root. For lives between 10^2 and 10^4 cycles, and for the same values of maximum principal strain range, the notched specimens cracked earlier than smooth ones, with the difference in behavior diminishing at lives approaching 10^4 cycles. Little improvement in correlation of behavior was achieved through use of either Tresca or von Mises equivalent strain criteria. In smooth specimens, biaxial tension has been observed in many cases to reduce low-cycle fatigue strength relative to uniaxial strength [12]. In Krempl's tests, it is difficult to know if the presence of biaxial tension at the notch root was responsible for the earlier cracking because of discrepancies in failure definition between the smooth and notched specimens. In the smooth specimens, a drop-off in load was taken as failure, while in the notched ones, it was appearance of cracks with surface lengths of 0.1 to 0.4 mm, a somewhat earlier definition of failure.

To summarize, many notched specimens and structural components subjected to uniaxial loading represent cases of multiaxial fatigue. The hydrostatic stress state developed at notch geometries with constraint on straining from surrounding material may influence fatigue behavior, but it is difficult to evaluate the possible significance of this influence based on the limited data currently available for notched specimens. Maximum principal notch strain is also strongly affected by the notch geometry and constraint.

High Strain Torsional Fatigue of Notched Specimens

Takahara and co-workers [13] tested circular bar specimens with several different types of notches in fully reversed, angle-of-twist controlled torsion. Notch shearing strain was computed assuming that the ratio of notch strain to nominal strain determined by elastic analysis would be preserved when plastic straining occurred at the notch. This is analogous to the assumption of $K_\epsilon = K_t$ for uniaxial loading. To check the assumption, smooth specimen cyclic shear stress-strain data were used to predict the torque versus angle-of-twist relation for the notched specimens; agreement with measurements was good, providing indirect evidence that the assumption was reasonable. Figure 2 shows the correlation between smooth and notched specimen fatigue data, for an alloy similar to aluminum 2024-T4 and for a number of different circumferential notch severities. In this figure, the shear strain amplitude for the notched specimens is the value computed at the notch root. Figure 3 shows a similar comparison for longitudinally grooved specimens made of pure copper. In both cases, excellent correlations of life to crack initiation were obtained. (The exact definition of initiation was not reported

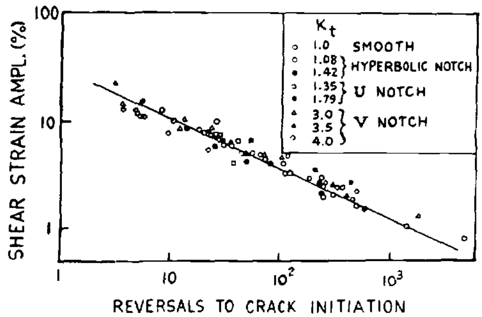

FIG. 2—*Correlation by maximum shear strain amplitude of torsional fatigue life of smooth and circumferentially notched specimens* [13].

in Ref *13* but did correspond to a crack of surface length of less than 0.2 mm, at least for the data in Fig. 3).

Combined Bending and Torsion (In-Phase)

Gough [*14*] reported the results of an extensive test program in which four different types of notched specimens were subjected to in-phase combined bending and torsion at fatigue limit stress levels. The first series of tests utilized circumferentially V-notched specimens made of seven different steels. Tests were fully reversed. Specimens with K_t factors in bending ranging between 7.2 and 18 and with K_t factors in torsion between 3.8 and 7 were investigated. The corresponding K_f factors in bending varied between 1.6 and 2.4 and in torsion between 1.2 and 1.8. Gough found that an ellipse arc provided good correlation of test results. The arc is given by

$$\frac{\tau^2}{t_n^2} + \frac{\sigma^2}{b_n^2}\left(\frac{b_n}{t_n} - 1\right) + \frac{\sigma}{b_n}\left(2 - \frac{b_n}{t_n}\right) = 1 \qquad (2)$$

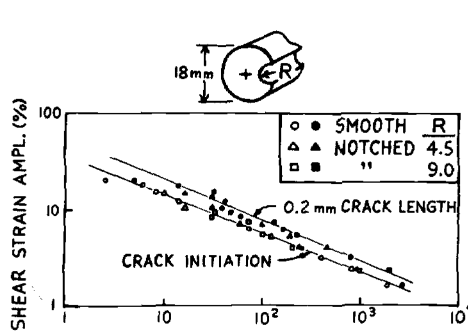

FIG. 3—*Correlation by maximum shear strain amplitude of torsional fatigue life of smooth and longitudinally notched specimens* [13].

where

τ = torsional shear stress amplitude,
σ = bending stress amplitude,
b_n = fatigue limit of notched specimens in bending, and
t_n = fatigue limit of notched specimens in torsion.

In order to apply this criterion requires, of course, that tests be conducted to determine t_n and b_n. Gough did not ascribe any physical interpretation to the ellipse arc. Guest [15] noted that it was equivalent to a criterion based on amplitude of maximum shear stress modified by a fraction of normal stress amplitude, which, for combined bending and torsion, becomes

$$t_n = \frac{1}{2}\left[\sqrt{\sigma^2 + 4\tau^2} + \left(\frac{2t_n}{b_n} - 1\right)\sigma\right] \tag{3}$$

Figure 4 compares test data for a V-notched specimen made of 0.4% carbon normalized steel with correlations given by three different approaches. (The data are typical of trends for the other V-notched specimens and the other steels.) The first approach is the von Mises criterion with notch stress amplitudes taken as nominal stress amplitudes in bending and torsion multiplied by respective K_t factors, that is

$$b = [(K_{t,\ \mathrm{bend}}\, S_{\mathrm{bend}})^2 + 3\ (K_{t,\ \mathrm{tors}}\, S_{\mathrm{tors}})^2]^{1/2} \tag{4}$$

where

b = smooth specimen fatigue limit in bending,
$K_{t,\ \mathrm{bend}}, K_{t,\ \mathrm{tors}}$ = elastic stress concentration factors in bending and torsion, and
$S_{\mathrm{bend}}, S_{\mathrm{tors}}$ = nominal stress amplitudes in bending and torsion.

The second approach is the von Mises criterion with experimentally determined K_f instead of K_t, and the third is the Guest criterion (Eq 3). The von Mises criterion was investigated because it gives fairly good correlations of long-life, in-phase biaxial fatigue strength for smooth specimens [16] and may do so for certain types of notched specimens. It is also commonly employed in design of shafts and axles [17]. The use of K_t factors in the criterion was investigated because K_f factors cannot be known in advance of testing unless one is willing to place confidence in empirical relations between K_t and K_f. The Guest criterion was investigated because similar strain-based criteria [1,18] have shown promise in correlating multiaxial fatigue data, at least for low-cycle fatigue of smooth specimens.

As shown in Fig. 4, the von Mises criterion using K_t is unduly conservative for the sharply V-notched specimen. The same criterion with K_f is slightly

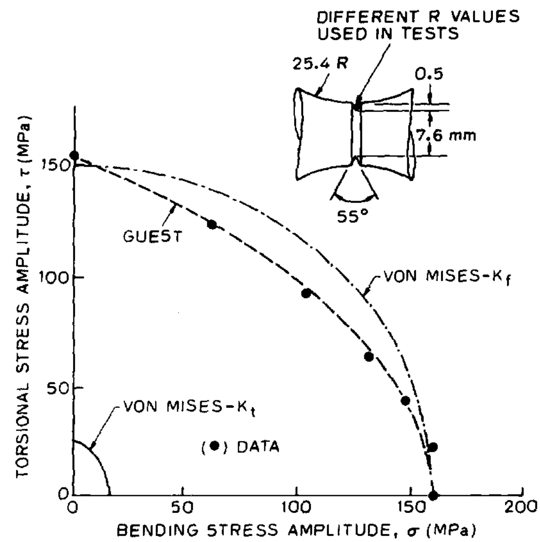

FIG. 4—*Comparison of predicted combined bending-torsion fatigue limit with test data* [14] *for a circumferentially notched round-bar specimen.*

nonconservative. The Guest criterion produces an excellent correlation. One reason for the failure of the von Mises criterion with K_t for this notch geometry is the extremely low ratio of K_f/K_t, likely owing to the occurrence of nonpropagating cracks, a phenomenon not checked in Gough's tests. There may be other reasons as well, such as a basic inadequacy of the criterion.

Gough also reported results of tests of specimens with (*1*) a shoulder fillet, (*2*) six splines, and (*3*) a radial hole. All specimens were made from a nickel-chromium-molybdenum-vanadium (Ni-Cr-Mo-V) steel treated to have a monotonic yield strength of 850 MPa and ultimate tensile strength of 895 MPa. Fully reversed tests were supplemented by tests with mean bending and mean torsion.

The shouldered specimens had a K_t in bending of 2.1 and K_t in torsion of 1.6, with corresponding K_f factors (for fully reversed cycling) of 1.66 and 1.36, respectively. As shown in Fig. 5, the von Mises criterion with K_t provides a conservative estimate of the combined bending-torsion fatigue limit strength. The same criterion with K_f and the Guest criterion both give excellent correlations of strength. For this notch geometry and for the stress combinations used, cracks propagated readily to fracture on transverse planes.

The splined specimens had virtually no stress concentration in bending but a K_t in torsion of 2.1. At higher ratios of applied bending to torsional stress amplitude, σ/τ, specimens failed by transverse cracking which originated at the crest of splines, and fatigue strength approached that of smooth specimens, due to lack of bending stress concentration. With increasing torsion, a transition in cracking behavior occurred at an undetermined ratio of σ/τ. Cracks started at inner corners of splines and propagated in shear along the longitudinal direction for some distance before changing to grow transversely to fracture. The von

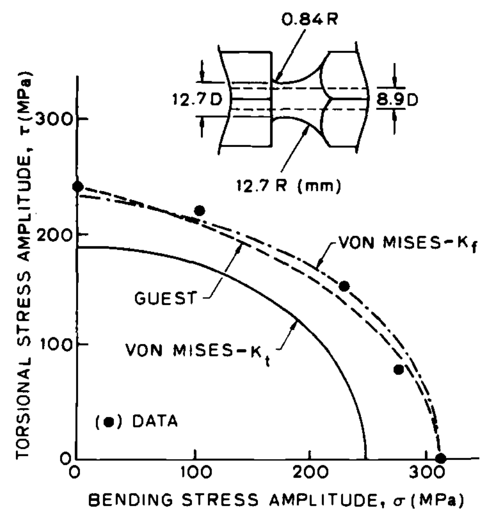

FIG. 5—*Comparison of predicted combined bending-torsion fatigue limit with test data* [14] *for a round-bar specimen with a shoulder fillet.*

Mises criterion with K_t or K_f provides a somewhat conservative correlation of fatigue strength, as shown in Fig. 6. The Guest criterion provides a better correlation, but neither criterion is able to account for the change in cracking behavior. These test results suggest that the particular type of notch and its influence on cracking behavior, in turn, may have a significant influence on multiaxial fatigue strength, and that criteria such as those considered here will not be sufficient to account for those influences.

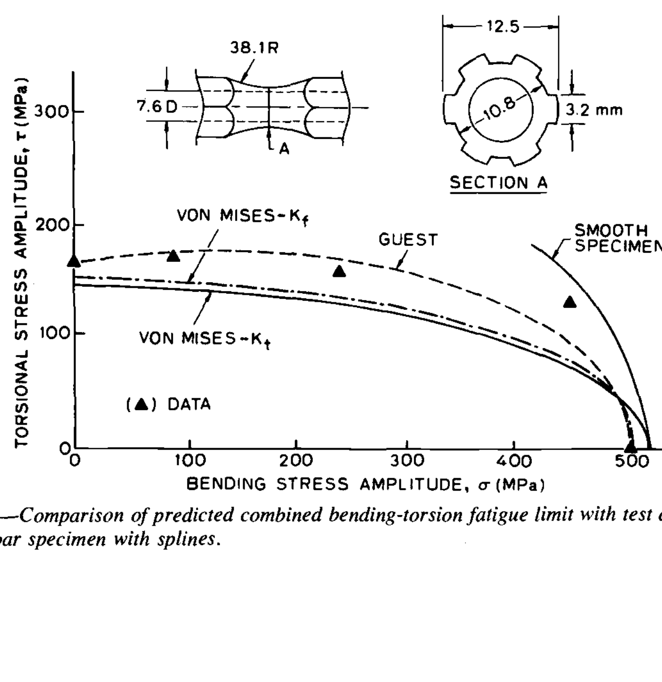

FIG. 6—*Comparison of predicted combined bending-torsion fatigue limit with test data* [14] *for a round-bar specimen with splines.*

Specimens with a radial hole had a K_t in bending of 2.6 and K_t in torsion of 2.0. In this case, K_t in torsion is taken as the ratio of the maximum shear stress at the edge of the hole to the nominal torsional shear stress. (An alternative definition would be the ratio of the maximum principal stress at the hole edge to the nominal shear stress.) The corresponding fully reversed K_f factors were 2.26 in bending and 1.96 in torsion. Gough observed that maximum principal stress appeared to govern both the location of crack formation on hole boundaries and the planes on which cracks propagated to fracture. As shown in Fig. 7, the von Mises criterion with either K_t or K_f and the Guest criterion provide reasonably good correlations of the fatigue limit.

Frost and co-authors [*19*] also discuss the combined bending fatigue behavior of specimens with a radial hole, noting that a maximum principal stress range fatigue criterion is mathematically equivalent to the ellipse arc when (t_n/b_n) is 0.75. In Gough's tests of specimens with a hole, that ratio was approximately 0.7. They also cite test results by Thurston and Field [*20*] of specimens with radial holes, made of seven different wrought steels. Again, an ellipse arc provided a good correlation of fatigue strength, with an average (t_n/b_n) of 0.8 for the steels tested.

Stulen and Cummins [*21*] also evaluated Gough's data for the four different notch types using the proposed criterion

$$\sigma_{1a} - \lambda_N \sigma_{3a} = b_n \tag{5}$$

where

$\lambda_N = (b_n/t_n) - 1$, and

σ_{1a},σ_{3a} = largest and smallest nominal principal stress amplitudes, respectively.

They found that this criterion gave excellent correlations of the data. Algebraic manipulation of Eq 5 shows that it reduces to the Guest criterion (Eq 3).

The previous summary and discussion of Gough's test results pertained to fully reversed loading. Tests with mean bending or mean torsion for all three notch types (shoulder fillet, hole, and splines) revealed very little if any effect. However, neither did mean stress tests of smooth specimens of the same metal. In general, a minimal mean stress influence in smooth specimens does not necessarily imply a similarly small influence in notched ones. For example, mean torsion does not significantly affect the torsional or bending fatigue limits of smooth specimens, based on available data [*16*]. In torsional fatigue tests of round bars with radial holes, Kakuno and Kawada [22] found that at lower K_t values, there was no appreciable influence of mean torsion on the alternating torsional fatigue limit, but, that at higher values, there was a definite reduction in the fatigue limit.

A more complete discussion of the influence of static torsion on the torsional fatigue behavior of a shaft with a radial hole is given by Sines [*23*]. He points out that the location around the hole most critical for crack initiation will depend

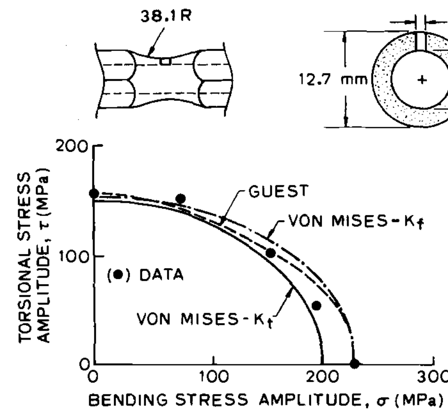

FIG. 7—*Comparison of predicted combined bending-torsion fatigue limit with test data* [14] *for a round-bar specimen with a radial hole.*

on the magnitude of the static torsion, particularly if it produces residual stresses, in which case a detailed analysis of notch stress/strain behavior would be needed to predict life.

Combined Bending and Torsion (*in-phase and out-of-phase*)

Grubisic and Simburger [*24,25*] conducted constant amplitude, cantilevered bending-torsion tests of a round-bar specimen with a shoulder fillet, made of a 0.44% carbon steel treated to have a monotonic yield strength of 810 MPa and ultimate tensile strength of 850 MPa. The specimen had a test section diameter of 25 mm, shoulder radius of 5 mm, and fixed end diameter of 39 mm, with a K_t in bending of 1.49 and K_t in torsion of 1.24. (Its geometry is similar to that of the specimen being used in the SAE research program.) Tests were conducted under deflection control and results presented in terms of elastically calculated notch stresses. In addition to fully reversed testing, the influence of mean bending and of mean torsion was investigated, as well as the effect of different phase angles between applied bending and torsion. Tests were performed at one fixed ratio of torsion to bending stress amplitude, $\tau/\sigma = 0.575$. Failure was taken as life to appearance of millimetre size cracks, detected ultrasonically.

Test results revealed that out-of-phase loading was more damaging than in-phase loading, for lives between 10^4 and 10^6 cycles. The damage increased as phase angle was increased from 0 to 90°. The ability of an equivalent stress parameter, SEQA, based on the ASME Code procedure [*26*] for evaluation of multiaxial fatigue, to correlate the results is shown in Fig. 8. This parameter, derived in Ref *27*, is given for fully reversed loading by

$$\mathrm{SEQA} = \frac{\sigma}{\sqrt{2}}\left[1 + \frac{3}{4}K^2 + \sqrt{1 + \frac{3}{2}K^2\cos 2\phi + \frac{9}{16}K^4}\right]^{1/2} \qquad (6)$$

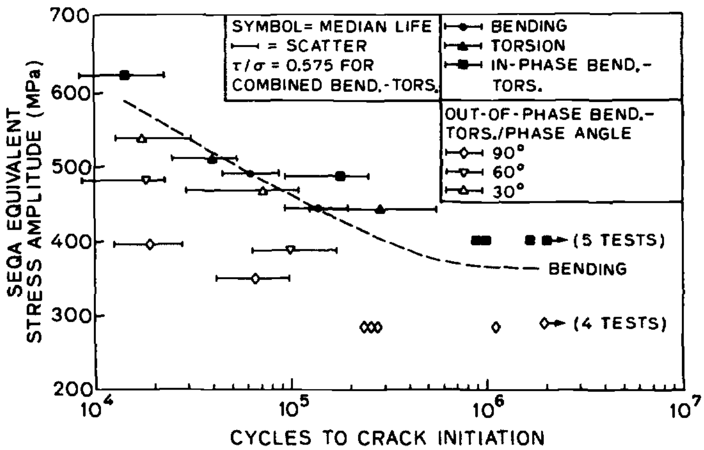

FIG. 8—*Correlation by the SEQA criterion of combined bending-torsion life with bending life for a round-bar specimen with a shoulder fillet, based on data from Ref 25.*

where

σ = elastically-calculated notch bending stress amplitude,
K = $2\tau/\sigma$,
τ = elastically-calculated notch torsional stress amplitude, and
ϕ = phase angle between bending and torsion.

The SEQA parameter reduces to the von Mises criterion for in-phase loading. For these data, it is conservative for pure torsion and in-phase bending and torsion, using notched bending as a reference, but nonconservative for the out-of-phase loadings.

Grubisic and Simburger also performed combined bending and torsion tests with zero-to-maximum bending or zero-to-maximum torsion. Imposition of mean bending reduced life, as might be expected. Mean torsion also reduced life, by approximately a factor of five compared to fully reversed cycling for both in-phase and 90° out-of-phase cases. Thus, while Gough found a minimal influence of mean torsion on the combined bending-torsion fatigue limit of shouldered specimens, these tests showed a significant effect.

Other Factors Influencing Notched Bending-Torsion Fatigue

Tests by Nisitani and Kawano [*28–30*] provide some insight into the role of notch geometry on long-life fatigue under bending and torsion. All of their specimens were made from an annealed 0.39% carbon steel with a monotonic yield strength of 323 MPa and ultimate tensile strength of 570 MPa, and all tests were conducted at fatigue limit stress levels. Figure 9 shows the relation between K_t, K_f and notch radius for shouldered specimens tested separately in torsion and in rotating bending. For relatively mild shoulders (that is, K_t in

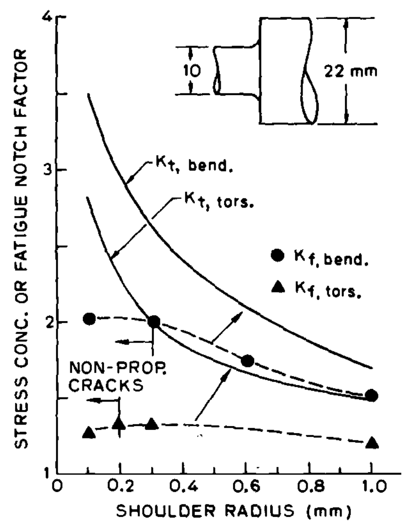

FIG. 9—*Comparison of fatigue notch factors in bending and in torsion with respective stress concentration factors for round-bar specimens with a shoulder fillet, based on data from Refs* 28,30.

bending of 1.7 and K_t in torsion of 1.5), the corresponding K_f/K_t ratios are 0.88 and 0.8, respectively. Use of criteria such as von Mises based on K_t provided relatively good and somewhat conservative correlations of Gough's and Grubisic and Simburger's in-phase data for this type of notch geometry. Only at higher K_t values is there a large discrepancy between K_f and K_t, owing to the occurrence of nonpropagating cracks.

For specimens with a radial hole, the relation between K_f, K_t and hole radius for bending and for torsion is given in Fig. 10. (K_t is based on gross area.) For

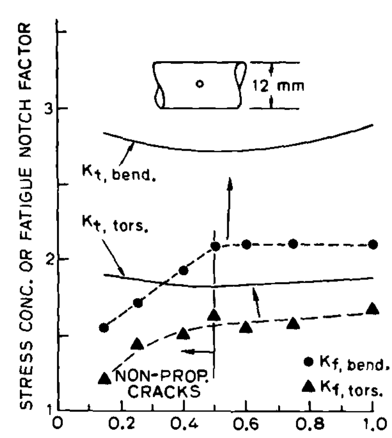

FIG. 10—*Comparison of fatigue notch factors in bending and in torsion with respective stress concentration factors for round-bar specimens with a radial hole, based on data from Ref* 29.

larger radii, the K_f/K_t ratios in bending and torsion are approximately 0.75 and 0.9, respectively. Again, criteria such as von Mises do reasonably well in correlating fatigue limit strength in this case, where cracks are able to propagate readily to fracture. However, for smaller hole radii, K_t remains about the same, but the stress gradient at the hole steepens, resulting in nonpropagating cracks.

Figure 11 shows the relation between K_t, K_f, and root radius for circumferentially notched specimens. For relatively mild notches (for example, K_t in bending of 2 and in torsion of 1.5), the K_f/K_t ratios in bending and torsion are 0.9 and 0.85, respectively, but even then, nonpropagating cracks are present in torsion. In sharper notches, there is an increasing discrepancy between K_f and K_t, due primarily to the occurrence of nonpropagating cracks. The discrepancy is more pronounced for torsion. In rotating bending, cracks propagate through the minimum section, and thus whether or not cracks are arrested is determined by the stress distribution in that section. In torsion, cracks were observed to grow in a zigzag manner into the larger diameter portion of the specimen, but were arrested after encountering sufficient resistance provided by the notch flanks. For this type of notch, crack propagation behavior and thus specimen fatigue strength is influenced not only by the stress distribution in the minimum section, but also by the constraint on growth presented by material surrounding the notch root. These test results also suggest that the large differences between K_f and K_t in Gough's combined bending and torsion tests of very sharp, circumferentially notched specimens were very likely the result of nonpropagating cracks.

Approaches for predicting the influence of nonpropagating cracks on the fatigue strength of notched specimens under uniaxial loading have been given by Smith and Miller [31] and Dowling [32]. Comparable approaches for multiaxial loadings await development.

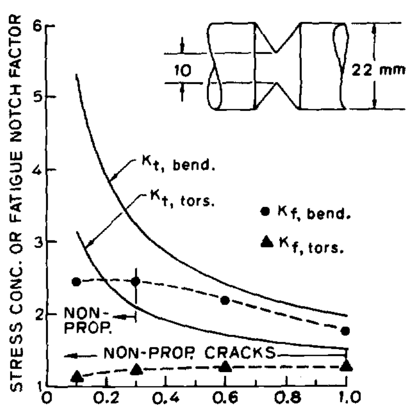

FIG. 11—*Comparison of fatigue notch factors in bending and in torsion with respective stress concentration factors for circumferentially notched round-bar specimens, based on data from Ref* 30.

Bunyan [33] conducted fully reversed torsion tests of shouldered shafts at fatigue limit stress levels. Shafts with diameters (minimum section) ranging from 76 to 248 mm and with different ratios of shoulder radius to diameter, (r/D), were used. Failure was taken as the appearance of cracking. No "size effect" was observed in tests of smooth shafts of varying diameter, but notched ones of the largest diameter had as much as a 35% lower torsional fatigue limit than the smallest diameter ones. The size effect was most pronounced at smaller (r/D). Also, the K_f/K_t ratio increased with shaft size, approaching 0.7 for the largest size tested. Bunyan also observed that for (r/D) greater than 0.1, one or two cracks formed and propagated to fracture in a few hundred cycles, while for smaller (r/D), numerous criss-crossed, nonpropagating cracks occurred. These tests results suggest, of course, that use of multiaxial fatigue data from small smooth specimens to predict long-life fatigue strength of larger notched components may be nonconservative.

Discussion

As shown in the previous review, the bulk of existing multiaxial fatigue data for notched specimens have been generated under long life, combined bending and torsion. Smooth specimens or mildly notched ones tested under uniaxial loading at long life spend most of that life in the formation of millimetre sized cracks [34]. If one assumes the same to be true in multiaxial fatigue and that the mechanisms which cause cracks to form are associated primarily with cyclic shear stresses, it is not surprising that criteria such as von Mises with K_t provide reasonably good and conservative estimates of long life, fully reversed combined bending and torsion fatigue strength, at least for in-phase loadings and for those bluntly notched specimens in which remaining crack growth life is relatively small. Better correlations of fatigue strength are achieved with use of K_f in the von Mises criterion or with use of t_n and b_n in the Guest criterion. In both cases though, testing is necessary to determine K_f or t_n and b_n, thus diminishing the usefulness of the methods in design evaluations.

The limited out-of-phase combined bending and torsion data for a shouldered specimen suggest that the von Mises criterion may be nonconservative for such loadings. A similar observation has been made for low-cycle, out-of-phase axial-torsional fatigue of smooth specimens [18].

In sharper notches, cracks start quickly, even at lower stress levels, and fatigue strength is governed by subsequent crack growth behavior. In many instances, crack propagation is slowed or arrested by a steep notch stress gradient or by resistance offered by material surrounding a notch root or both (for example, circumferentially notched round bars). In such cases, conventional criteria such as von Mises will be unduly conservative.

Obviously, the multiaxial fatigue behavior of notched specimens is complicated, influenced by numerous factors such as those noted in the review. For use in design evaluations, life prediction methods must be developed which represent a compromise between an ability to account for the complications and ease of use and reasonable requirements for experimental input data.

Fatigue Life Predictions for the SAE Specimen

In this section, the ability of a number of different methods for predicting life to crack initiation in the SAE specimen will be assessed based on test data currently available in the research program. (The definition of crack initiation will be discussed shortly.) Each method is either currently used in multiaxial fatigue life evaluations or is considered to hold promise as an improved approach.

The specimen is shown in Fig. 12. According to elastic finite element analysis [*35*], it has a K_t in bending of 1.42 and a K_t in torsion of 1.23. According to Peterson [*36*], it has a K_t in bending between 1.57 and 1.63, depending on assumptions used in modeling the specimen geometry, and a K_t in torsion between 1.29 and 1.32. Based on strain gage readings taken on the specimen, the K_t values in bending and torsion are 1.57 and 1.25, respectively; these values were used in all subsequent life predictions.

Specimens were made from normalized 1045 steel with monotonic and cyclic yield strengths of 379 and 344 MPa, respectively, and an ultimate tensile strength of 622 MPa. All specimens were taken from the same heat and had processing and surface finishes as identical as possible.

To date, all specimens have been tested in load control, under fully reversed torsion or bending or various combinations of bending and torsion (in-phase and 90° out-of-phase). Strains at the shoulder fillet have been monitored by rosettes. Initial and cyclically stable values of axial and shear strain amplitudes have been recorded, along with applied bending moment and torque amplitudes, cycles to "crack initiation," and cycles to fracture. In certain tests, circumferential strains have also been reported. A complete listing of test data is given in Ref *37*. A more detailed description of the SAE test program and facilities is given in Refs *37* and *38*.

The definition and detection of crack initiation in the test program is the source of some possible uncertainty in interpreting test results and in evaluating life prediction methods. The SAE FD&E Committee has selected an "observable crack" as a definition. Some participants in the test program (for example, Deere

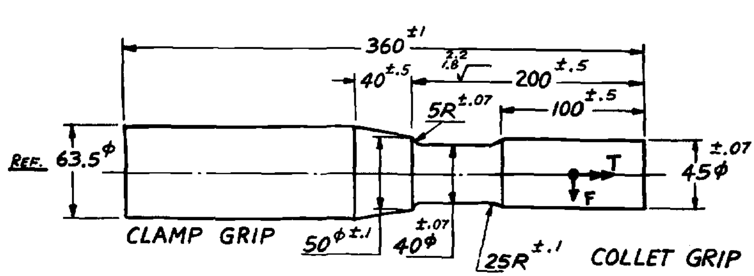

FIG. 12—*SAE Fatigue Design & Evaluation Committee bending-torsion fatigue specimen geometry.*

& Co.) detect crack initiation with an ultrasonic surface acoustic wave transducer calibrated against a sawcut of 0.7 mm depth normal to the specimen longitudinal axis. Other participants, without such instrumentation available, detect cracking visually, in some cases with the aid of a low power microscope. Test experience has shown that cracks with surface lengths of several millimetres can be detected visually. The Deere & Co. tests have indicated that when cracking is detected ultrasonically, often no cracks can be seen on the surface. However, after additional cycling, always less than a few percent of total life, surface cracking of several millimetres length is visible. Thus the discrepancy in detection and definition of crack initiation from laboratory to laboratory should be relatively small compared to other experimental uncertainties and to inherent scatter in fatigue lives. An additional concern about the definition of initiation is that for certain combinations of torsion and bending, multiple cracking occurs, or cracks form and grow on planes different than the plane used in calibrating acoustic detectors or both. This will also cause some discrepancies in the definition of initiation from one test condition to another, but it is difficult to assess the possible significance of such discrepancies based on available test data.

The multiaxial life prediction methods to be considered here utilize as input uniaxial strain amplitude versus fatigue life data generated with smooth specimens of 6 mm diameter, in which failure is taken as a 50% drop-off in load amplitude. The following relation was used to fit the available data

$$\epsilon_a = 0.00481\,(2N_f)^{-0.102} + 0.182\,(2N_f)^{-0.433} \tag{7}$$

where

ϵ_a = strain amplitude, and
$2N_f$ = reversals to failure.

Twelve samples of the uniaxial specimens were examined by the authors. It was observed that a 50% drop-off in load generally corresponded to the propagation of a fatigue crack through roughly half of the cross-sectional area. This fatigued area is somewhat larger than the area at initiation in the SAE specimen when initiation is taken as a crack with surface length of several millimetres. This is an inherent difficulty in the use of conventional uniaxial ϵ-N data to predict behavior in specimens and components with other geometries and sizes. An additional difficulty is that the type of cracking in uniaxial tension may differ substantially from that in other states of strain, such as pure torsion. Although these problems exist with the use of uniaxial ϵ-N data as an input to prediction of multiaxial fatigue life, such data will likely remain the basis for fatigue design evaluations in the near term.

Nominal Stress Life Predictions Methods

These methods reduce a multiaxial stress state to an equivalent uniaxial stress. The elastic portion of the uniaxial ϵ-N curve is multiplied by the modulus of elasticity to produce an *S-N* curve, which is used to predict the SAE specimen crack initiation life for a given equivalent uniaxial stress amplitude.

The application of the following stress-based methods requires assumptions concerning the effect of stress concentration on fatigue behavior. Two limiting assumptions were made. First, the nominal bending and torsional stress amplitudes were multiplied by fatigue notch factors equal to respective stress concentration factors. This is a conservative approach which might be used in design evaluations. Second, the stress concentration effect on fatigue was considered negligible and notch stresses calculated with $K_f = 1$.

With the preceding assumptions, the first multiaxial fatigue criterion to be investigated used the amplitude of maximum shearing stress, SALT, as an equivalent stress amplitude. This criterion was developed by Langer [*39*] and is utilized in the ASME Boiler and Pressure Vessel Code, Section III [*40*]. For fully reversed bending and torsion with a phase angle, ϕ, between bending and torsion, the closed form expression for SALT is

$$\text{SALT} = \frac{\sigma}{\sqrt{2}}[1 + K^2 + [1 + 2K^2\cos(2\phi) + K^4]^{1/2}]^{1/2} \tag{8}$$

where

σ = notch bending stress amplitude,
= $(K_{f,b}S_{\text{bend}})$,
τ = notch torsional shearing stress amplitude,
= $(K_{f,t}S_{\text{tors}})$,
$K_{f,b}$ = fatigue notch factor in bending,
$K_{f,t}$ = fatigue notch factor in torsion, and
K = $2\tau/\sigma$.

A detailed description and derivation of SALT is given in Ref *27*.

A comparison of test data with life estimates based on this method using $K_f = K_t$ is shown in Fig. 13. In this and later figures, the ratios of *B* to *T* denote ratios of von Mises equivalent stresses in bending and in torsion. The extreme conservatism of life estimates indicates that the fatigue notch factors are greatly overestimated. The method also predicts that out-of-phase loading will be less damaging than in-phase loading of the same magnitude.

Another multiaxial stress-based criterion is the SEQA equivalent stress amplitude considered previously (Eq 6). It is much like SALT except that a stress parameter similar to octahedral shearing stress is considered instead of maximum shearing stress. Comparison of test data with life estimates based on SEQA is presented in Fig. 14. SEQA, and SALT yield the same predictions for pure bending, as expected. While being less so than SALT when torsional loading is present, SEQA still underestimates observed life (that is, is too conservative). This again indicates that use of $K_f = K_t$ overestimates the notch influence.

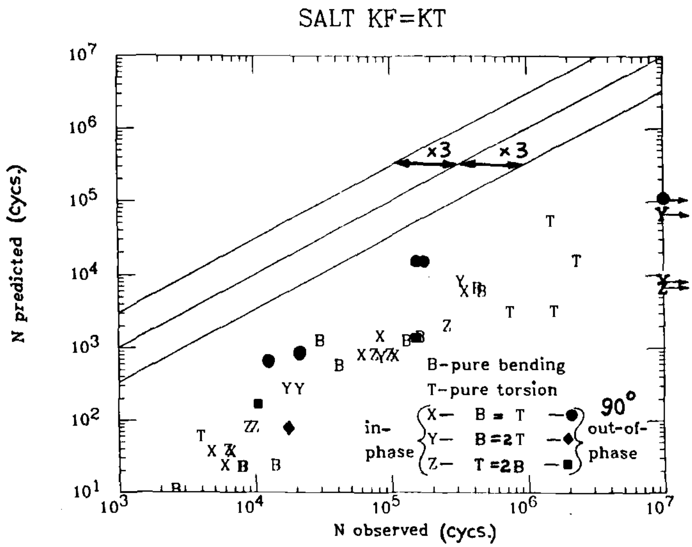

FIG. 13—*Comparison of life predictions based on the SALT equivalent stress approach with SAE test data, taking fatigue notch factors equal to stress concentration factors.*

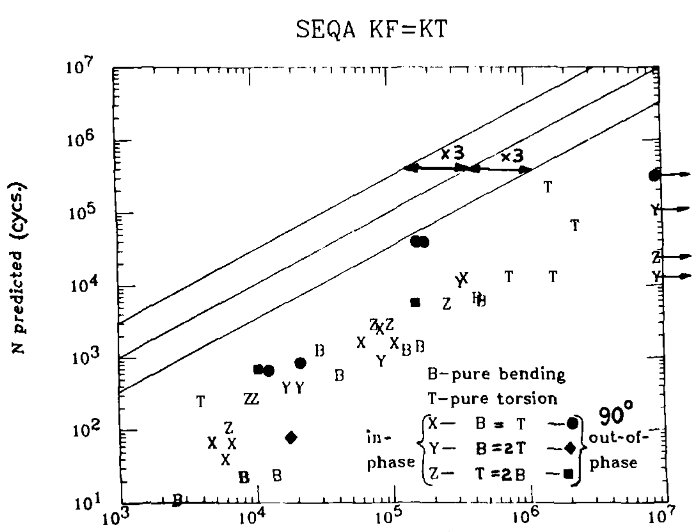

FIG. 14—*Comparison of life predictions based on the SEQA equivalent stress approach with SAE test data, taking fatigue notch factors equal to stress concentration factors.*

Using SALT with bending and torsional notch stresses calculated with $K_f = 1$ gives the life estimates shown in Fig. 15. The estimates are generally better than those in Fig. 13, but the lives of most specimens are still underestimated (that is, conservative predictions). A comparison of test data with SEQA predictions is shown in Fig. 16, with $K_f = 1$. SEQA gives reasonably good life estimates, less conservative than SALT, as anticipated. It tends to underestimate the damage done by out-of-phase loading. All of these stress-based approaches are too conservative for long life (that is, lives greater than 10^7 cycles).

Figure 17 compares life of SAE specimens under pure bending and pure torsion with smooth specimen uniaxial and torsional *S-N* data [*41*], respectively. Stress amplitudes are nominal and computed elastically. In bending, K_f is generally less than 1.1 at long life, then becomes less than unity at shorter lives, indicating notch strengthening in fatigue, a phenomenon often observed when data are plotted in terms of elastic, nominal stress. In torsion, K_f is consistently somewhat less than unity. Thus, it is not surprising that the SALT or SEQA approaches with $K_f = 1$ give better life estimates than with $K_f = K_t$. However, the behavior of K_f in these tests could not be predicted in advance of testing, thereby making the assumption of any K_f values a questionable proposition in design analysis.

Conventional Strain Based Life Prediction Methods

These methods calculate an equivalent uniaxial strain amplitude from a multiaxial strain history. This amplitude is then used with the uniaxial ϵ-*N* curve to predict life to crack initiation. Application of these methods is considerably more

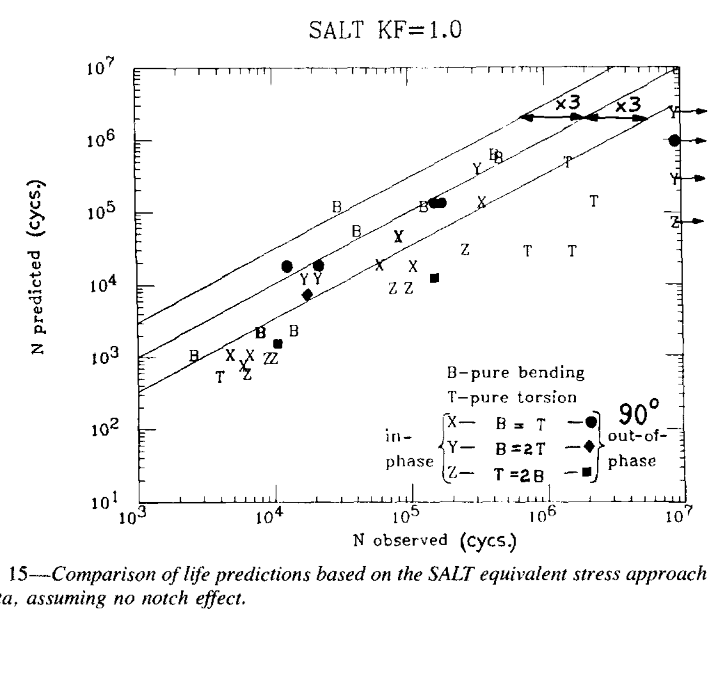

FIG. 15—*Comparison of life predictions based on the SALT equivalent stress approach with SAE test data, assuming no notch effect.*

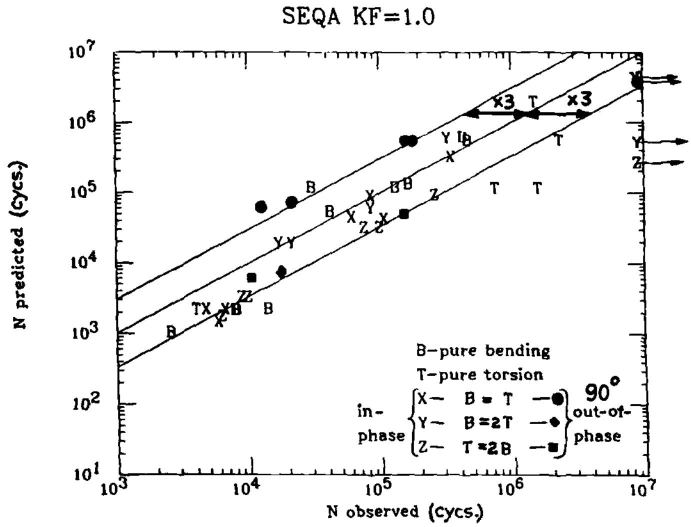

FIG. 16—*Comparison of life predictions based on the SEQA equivalent stress approach with SAE test data, assuming no notch effect.*

involved than the stress-based methods because even when notch strain data are available, estimates or assumptions must be made about variations in Poisson's ratio with strain level. Also, notch constraint on circumferential strain produces values which are a fraction of notch bending strain less than those for full Poisson contraction, with the fraction also varying with strain level. Without measurement, it is difficult to estimate the fractions, except by detailed elastic-plastic

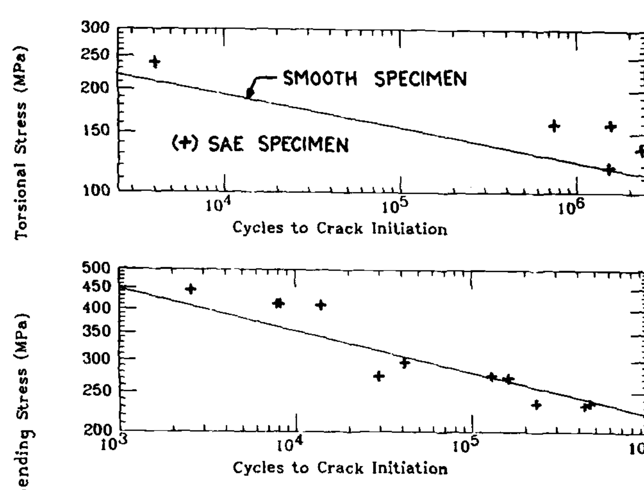

FIG. 17—*Comparison of SAE specimen fatigue strength with smooth specimen strength.*

finite element analysis. The following life prediction methods will utilize measured notch bending and torsional strain amplitudes.

The first method assumes that notch maximum shearing strain amplitude (Tresca criterion) will correlate life with the maximum shearing strain amplitude in uniaxial specimens. In the following analysis, it will be assumed that circumferential strain at the notch equals Poisson's ratio times the stabilized notch bending strain. The maximum shearing strain amplitude will be computed with Poisson's ratio taken as 0.29 and 0.5 to see the influence on life predictions. Based on the strain analysis given in Ref *18*,

$$\gamma_{\max} = (\epsilon_{xx}^2(1 + \nu)^2 + \gamma_{xy}^2)^{1/2} \text{ for in-phase loading} \tag{9a}$$

$$\gamma_{\max} = \text{greater of} \begin{Bmatrix} \gamma_{xy} & \\ \epsilon_{xx} & (1 + \nu) \end{Bmatrix} \begin{array}{l} \text{for } 90^\circ \\ \text{out-of-phase} \\ \text{loading} \end{array} \tag{9b}$$

where

γ_{xy} = stabilized notch torsional shear strain amplitude, and
ϵ_{xx} = stabilized notch bending strain amplitude,
γ_{xy} = stabilized notch torsional shear strain amplitude, and
ν = Poisson's ratio.

The equivalent strain amplitude is found from

$$\epsilon_a = \gamma_{\max}/(1 + \nu) \tag{10}$$

This amplitude is used with the uniaxial ϵ-N relation (Eq 7) to predict life to crack initiation. As shown in Fig. 18, predictions tend to be nonconservative at lives less than 10^5 cycles for pure bending or higher ratios of applied bending to torsion. At longer lives, predictions are conservative, particularly for pure torsion or higher ratios of applied torsion to bending. This method is also nonconservative for 90° out-of-phase loadings, except where torsion is dominant. For pure bending or higher ratios of applied bending to torsion, predictions are unaffected or relatively insensitive, respectively, to assumed Poisson's ratio, as anticipated. On the other hand, for pure torsion and higher ratios of applied torsion to bending, predictions may differ by as much as a factor of two in life.

It should be noted again that the strain analysis leading to Eq 9 does not account for the fact that notch circumferential strain is some fraction of bending strain less than indicated by Poisson contraction. The influence of circumferential strain on $\gamma_{\max}$ will be discussed later.

A second multiaxial fatigue evaluation method is based on octahedral shearing strain amplitude (von Mises criterion). Several assumptions were made concerning Poisson's ratio and circumferential strain to investigate the sensitivity of the equivalent strain amplitude to each. (Circumferential strains have not been re-

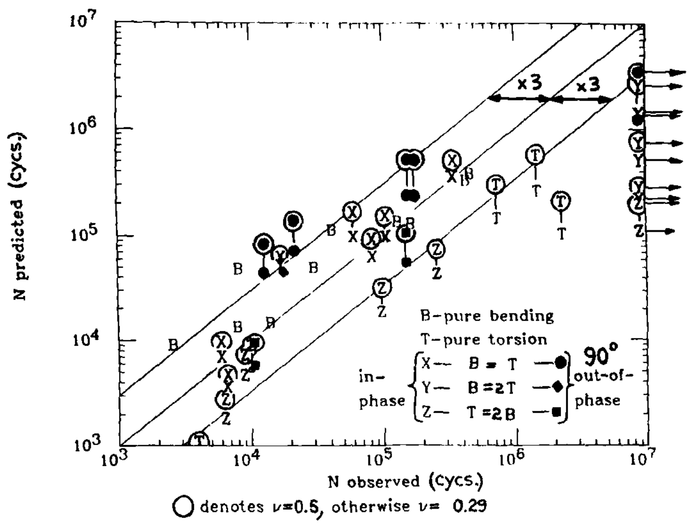

FIG. 18—*Comparison of life predictions based on the Tresca equivalent strain criterion with SAE test data.*

ported for all tests.) For in-phase loading, this amplitude, which is used to enter the uniaxial ϵ-N curve to predict life, is given by

$$\bar{e} = \frac{1}{\sqrt{2(1 + \nu)}} [(\epsilon_1 - \epsilon_2)^2 + (\epsilon_2 - \epsilon_3)^2 + (\epsilon_3 - \epsilon_1)^2]^{1/2} \tag{11}$$

where

$\bar{e}$ = von Mises equivalent strain amplitude,
ν = Poisson's ratio,
$\epsilon_1 = \frac{1}{2}(\epsilon_{xx} + \epsilon_{yy}) + \frac{1}{2}[(\epsilon_{xx} - \epsilon_{yy})^2 + \gamma_{xy}^2]^{1/2}$,
$\epsilon_2 = \frac{1}{2}(\epsilon_{xx} + \epsilon_{yy}) - \frac{1}{2}[(\epsilon_{xx} - \epsilon_{yy})^2 + \gamma_{xy}^2]^{1/2}$,
$\epsilon_3 = -\frac{\nu}{1 - \nu}(\epsilon_1 + \epsilon_2)$,
ϵ_{xx} = stabilized notch bending strain amplitude,
ϵ_{yy} = stabilized notch circumferential strain amplitude,
γ_{xy} = stabilized notch torsional shear strain amplitude, and
$\epsilon_1,\epsilon_2,\epsilon_3$ = principal strain amplitudes.

Taking $\nu = 0.29$ or 0.5, life predictions are compared with test data in Fig. 19 assuming $\epsilon_{yy} = 0$ and in Fig. 20 assuming $\epsilon_{yy} = -\nu\epsilon_{xx}$. There is generally little difference between predictions in the figures for a given value of ν. The most notable difference involves pure bending. Assumption of $\epsilon_{yy} = -\nu\epsilon_{xx}$ causes bending predictions to be unaffected by ν. It also reduces sensitivity to ν for those tests with higher ratios of applied bending to torsion.

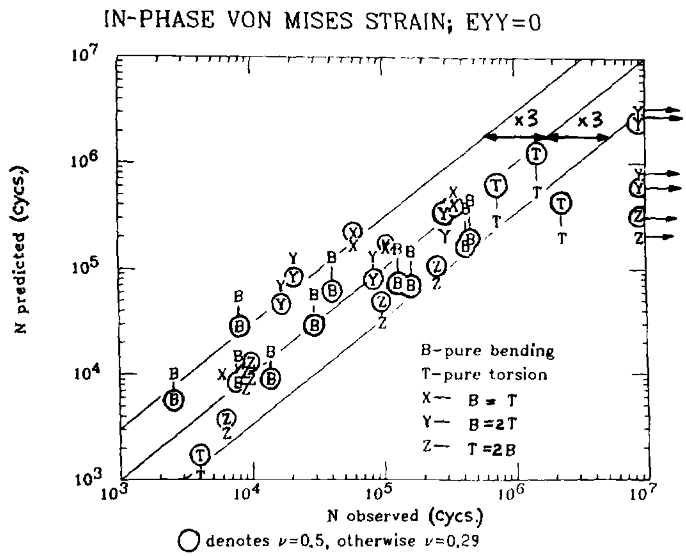

FIG. 19—*Comparison of life predictions based on the von Mises equivalent strain criterion with in-phase SAE test data, taking circumferential notch strain to be zero.*

Predictions were also made using a variable Poisson's ratio, $\bar{\nu}$, found iteratively by the procedure proposed by Gonyea [*42*]. The results are shown in Fig. 21. Use of $\bar{\nu}$ causes the von Mises equivalent strain amplitude to be virtually independent of assumptions concerning ϵ_{yy}. All of the predictions in Fig. 21 fall between the limiting cases shown in Figs. 19 and 20, as expected. Predictions using the von Mises criterion for in-phase loading are comparable to those for the Tresca criterion, perhaps slightly better. They also tend to be conservative for longer lives, but somewhat nonconservative at shorter lives, again for pure bending or higher ratios of applied bending to torsion.

To apply a von Mises type of equivalent strain approach to the 90° out-of-phase tests, the procedure of the ASME Boiler and Pressure Vessel Elevated Temperature Code Case [*26*] was investigated. The approach was used with $\nu = 0.29$ and 0.5 as well as with measured values of ϵ_{yy}, which happened to be available for the out-of-phase tests. It was not possible to compute a variable Poisson's ratio for the nonproportional straining resulting from out-of-phase loading. As shown in Fig. 22, predictions are nonconservative.

Brown and Miller Strain Ellipse

This approach postulates that improved multiaxial fatigue life predictions can be made if one considers not only the amplitude of maximum shear strain, γ_{max}, but also the amplitude of normal strain, ϵ_n acting on the plane of γ_{max}. Brown

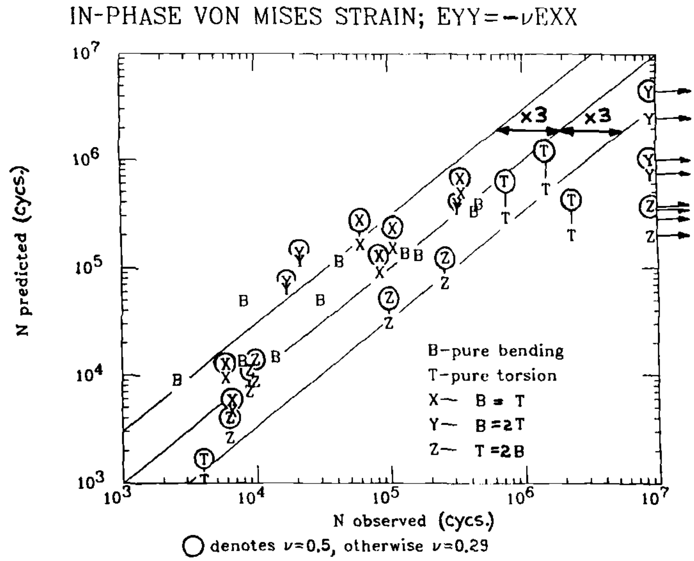

FIG. 20—*Comparison of life predictions based on the von Mises equivalent strain criterion with in-phase SAE test data, taking circumferential notch strain as Poisson's ratio times notch bending strain.*

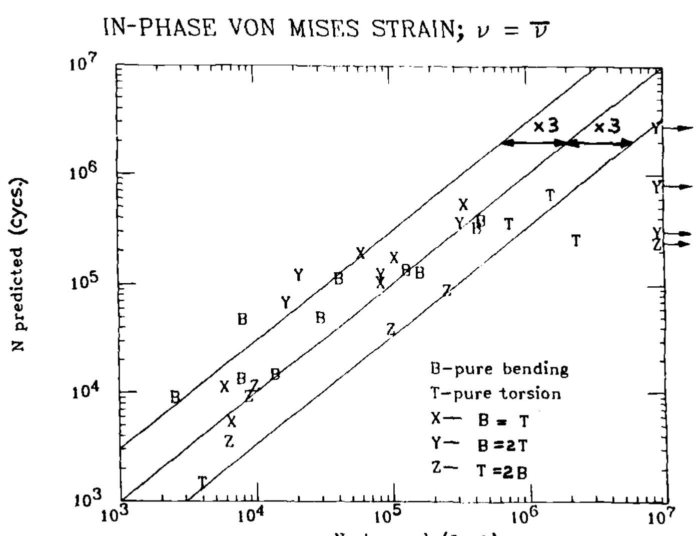

FIG. 21—*Comparison of life predictions based on the von Mises equivalent strain criterion with in-phase SAE test data, using a variable Poisson's ratio.*

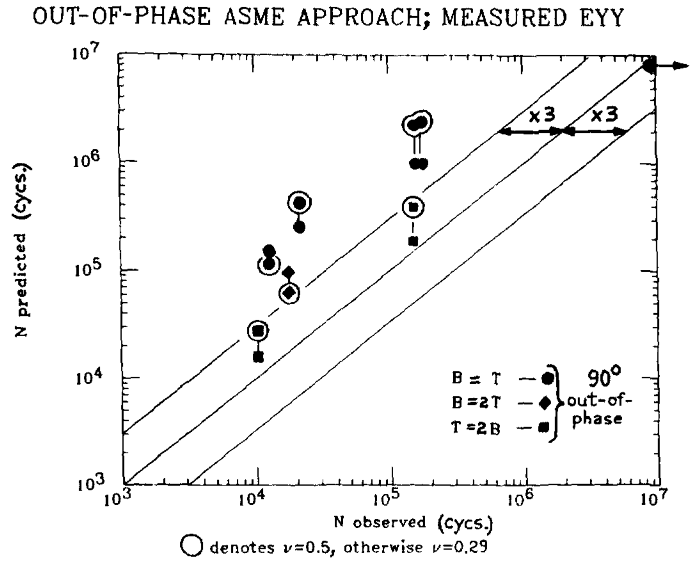

FIG. 22—*Comparison of life predictions based on the ASME multiaxial fatigue approach* [26] *with 90° out-of-phase SAE test data.*

and Miller [*43*] plotted contours of constant life on a graph of γ_{max} versus ϵ_n, called the Γ-plane for brevity. They fitted curves of the form

$$\left(\frac{\gamma_{max}}{g}\right)^j + \left(\frac{\epsilon_n}{h}\right)^j = 1 \tag{12}$$

to points on the Γ-plane determined from strain controlled, in-phase, combined tension and torsion fatigue tests. The constants g, h, and j were found to vary with life. However, it was suggested that a safe and simple design criterion could be established by taking $j = 2$ such that

$$\left(\frac{\gamma_{max}}{g}\right)^2 + \left(\frac{\epsilon_n}{h}\right)^2 = 1 \tag{13}$$

This relation is similar to Gough's ellipse quadrant.

To investigate this approach for the SAE specimen, the constant g in Eq 13 was fitted to smooth specimen torsional strain-life data for 1045 steel [*41*]. The constant h was determined from uniaxial strain-life data (Eq 7) by computing the maximum shear strain and corresponding normal strain amplitudes in the smooth specimens. These computations utilized a variable Poisson's ratio as a function of uniaxial strain amplitude.

In the SAE specimen, γ_{max} and ϵ_n at the notch were calculated assuming $\nu = 0.29$ and 0.5 to assess the sensitivity of the approach to Poisson's ratio.

Based on the strain analysis of Ref *18*, for in-phase straining

$$\gamma_{max} = \sqrt{\epsilon_{xx}^2 (1 + \nu)^2 + \gamma_{xy}^2} \tag{14a}$$

$$\epsilon_n = \frac{\epsilon_{xx}}{2} \sqrt{[2 (1 + \nu) \cos^2 \psi - 2\nu]^2 + [\lambda \sin 2\psi]^2} \tag{14b}$$

where $\lambda = \gamma_{xy}/\epsilon_{xx}$ and ψ is determined from

$$\psi = \frac{1}{4} \tan^{-1} \left[\frac{2\lambda (1 + \nu)}{(1 + \nu)^2 - \lambda^2} \right] \tag{14c}$$

For 90° out-of-phase straining

$$\gamma_{max} = \text{the greater of} \begin{cases} \gamma_{xy} & (15a) \\ (1 + \nu)\, \epsilon_{xx} & (15b) \end{cases}$$

When Eq 15*a* governs

$$\epsilon_n = \epsilon_{xx} \tag{15c}$$

When Eq 15*b* does

$$\epsilon_n = \frac{\epsilon_{xx}}{2} \sqrt{(1 - \nu)^2 + \lambda^2} \tag{15d}$$

Predictions based on this method are compared with test data in Fig. 23. For in-phase tests, predictions are comparable to those based on the von Mises criterion. However, for 90° out-of-phase tests, predictions are much better, tending to be somewhat conservative. Also, the predictions are relatively insensitive to assumed Poisson's ratio, and thus only one set of symbols is shown in Fig. 23.

Plastic Work Approach

This method uses uniaxial cyclic stress-strain data to compute the hysteresis loops resulting from axial and torsional straining for in-phase or out-of-phase loadings. The plastic work per cycle, W_p, is taken as

$$W_p = \int_{cycle} \sigma_{xx} \cdot d\epsilon_{xx}^p + \tau_{xy} \cdot d\gamma_{xy}^p \tag{16}$$

and is assumed to be related to fatigue life, N, by $W_p = AN^a$, where constants A and a are fitted from uniaxial strain-life data. Details of the method are given by Garud [*44*].

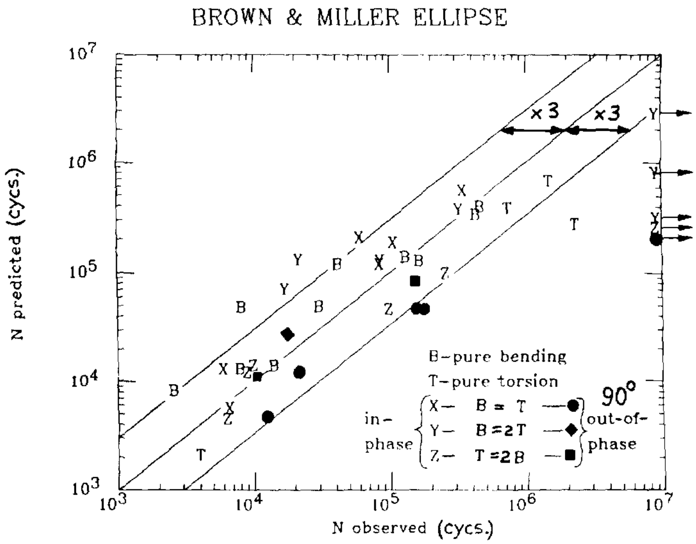

FIG. 23—*Comparison of life predictions based on the Brown and Miller strain ellipse approach with SAE test data.*

From the smooth specimen fatigue data for 1045 steel, the plastic work versus life relation was computed to be

$$W_p\ (\mathrm{MJ/m^3}) = 465\ N^{-0.57} \tag{17}$$

Plastic work at the notch in the SAE specimen was calculated from measured ϵ_{xx} and γ_{xy} and used with Eq 17 to predict life to crack initiation. The current version of the plastic work computer program assumes $\epsilon_{yy} = -\nu\epsilon_{xx}$ and thus the influence of suppressed ϵ_{yy} was not investigated in this study.

Plastic work life predictions are compared with test data in Fig. 24. For the in-phase loadings, predictions are comparable to those of the strain ellipse and von Mises equivalent strain approaches. Predictions are also reasonably good for the out-of-phase loadings, but somewhat less conservative than those of the strain ellipse approach.

Notch Strain Analysis

The previous strain-based life prediction methods utilized notch strains measured by rosettes. For use in design analysis before a prototype is available, notch strains must be estimated. One approach is to perform elastic-plastic finite element analysis, which could become costly and time consuming, particularly for complicated notch multiaxial strain histories. Another approach is to see if notch

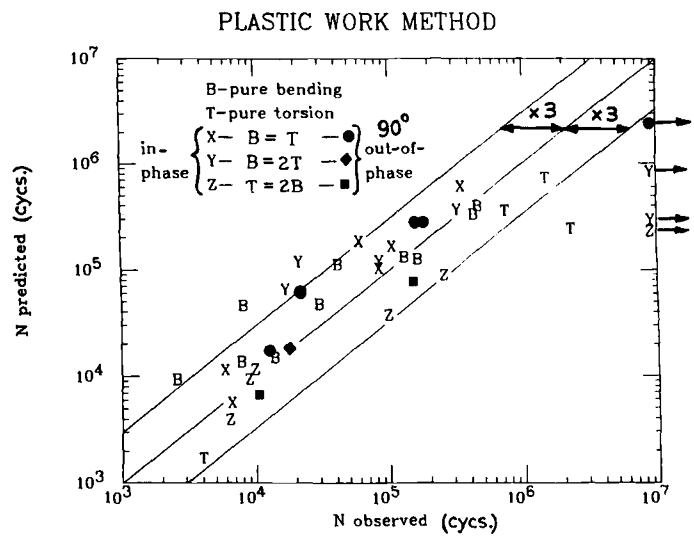

FIG. 24—*Comparison of life predictions based on the plastic work approach with SAE test data.*

strains can be estimated with a simplified elastic-plastic analysis from nominal strains, which are generally elastic and relatively easy to calculate from applied loadings and component geometry. The following analysis will attempt to estimate bending moment versus stabilized notch bending strain and torque versus notch shearing strain for the SAE specimen. Bending and torsional strains are computed separately, and no attempt is made to account for their possible interaction in combined loading cases.

Bending Strain Estimates

In order to develop a relation between bending moment and notch bending strain, the following items are needed: (1) a relation between nominal strain, e_{nom}, and notch strain, ϵ_{notch}, (2) a K_t factor, (3) an estimate of the strain gradient in the specimen, (4) a stabilized uniaxial cyclic stress-strain curve, and (5) an equilibrium relation between bending moment and stress.

Two relations between e_{ncm} and ϵ_{notch} were investigated. The first is a "linear rule," which assumes

$$\epsilon_{notch} = K_{t,\,bend}\, e_{nom} \tag{18}$$

even when plastic straining occurs at a notch. The second is Neuber's rule:

$$(\epsilon\sigma)_{notch} = K_{t,\,bend}^2\, (Se)_{nom} \tag{19}$$

As noted previously, the elastic finite element analysis by Tucker [35] indicated a $K_{t,\ \text{bend}} = 1.42$, while Peterson [36] and strain gage measurements indicated a $K_{t,\ \text{bend}} \simeq 1.57$. Both values were used to observe the sensitivity of notch strain estimates to them.

Two strain gradients were also assumed. One assumption, proposed by Galliart [45], is shown in Fig. 25*a*. The other is a bilinear approximation of the gradient predicted by the elastic finite element analysis, shown in Fig. 25*b*.

The relation between bending moment and notch bending strain was developed with the following procedure. When Neuber's rule was used, first a value of e_{nom} was selected, then S_{nom} determined from

$$e_{\text{nom}} = \left(\frac{S_{\text{nom}}}{E}\right) + \left(\frac{S_{\text{nom}}}{K'}\right)^{1/n'} \tag{20}$$

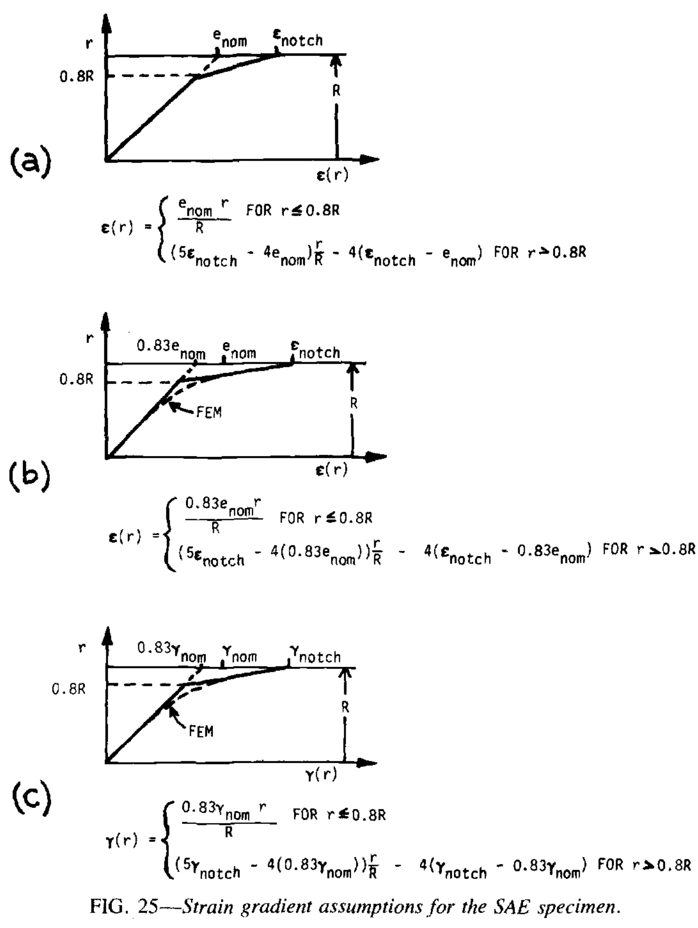

(a)
$$\varepsilon(r) = \begin{cases} \dfrac{e_{nom}\, r}{R} & \text{FOR } r \leq 0.8R \\ (5\varepsilon_{notch} - 4e_{nom})\dfrac{r}{R} - 4(\varepsilon_{notch} - e_{nom}) & \text{FOR } r \geq 0.8R \end{cases}$$

(b)
$$\varepsilon(r) = \begin{cases} \dfrac{0.83e_{nom}\, r}{R} & \text{FOR } r \leq 0.8R \\ (5\varepsilon_{notch} - 4(0.83e_{nom}))\dfrac{r}{R} - 4(\varepsilon_{notch} - 0.83e_{nom}) & \text{FOR } r \geq 0.8R \end{cases}$$

(c)
$$\gamma(r) = \begin{cases} \dfrac{0.83\gamma_{nom}\, r}{R} & \text{FOR } r \leq 0.8R \\ (5\gamma_{notch} - 4(0.83\gamma_{nom}))\dfrac{r}{R} - 4(\gamma_{notch} - 0.83\gamma_{nom}) & \text{FOR } r \geq 0.8R \end{cases}$$

FIG. 25—*Strain gradient assumptions for the SAE specimen.*

where

K' = cyclic strain hardening coefficient, and
n' = cyclic strain hardening exponent.

(The second term in Eq 20 was used because certain tests of the SAE specimen had elastic-plastic nominal straining.) Next, Eq 19 and the following relation were solved simultaneously to determine ϵ_{notch}

$$\epsilon_{\text{notch}} = \frac{\sigma_{\text{notch}}}{E} + \left(\frac{\sigma_{\text{notch}}}{K'}\right)^{1/n'} \tag{21}$$

When the linear rule is used, Eq 18 gives ϵ_{notch} directly.

For the assumed strain gradients, $\epsilon(r)$, the corresponding stress gradients, $\sigma(r)$, were then computed from

$$\epsilon(r) = \frac{\sigma(r)}{E} + \left(\frac{\sigma(r)}{K'}\right)^{1/n'} \tag{22}$$

With $\sigma(r)$ available, a numerical integration of the following integral was performed

$$M = 4 \int_0^R \sigma(r)\, r \sqrt{R^2 - r^2}\, dr \tag{23}$$

where

M = applied bending moment,
r = radial distance from the neutral axis, and
R = outer radius (20 mm).

This procedure was repeated for different values of e_{nom} to establish a relation between ϵ_{notch} and M. Inherent in this analysis is the assumption that the material is cyclically stabilized at all radii. For material at the interior of the specimen, the lower strains may require a larger number of cycles for stabilization than surface strains. In this case, the notch strains for a given applied moment would tend to be somewhat overestimated.

Moment versus notch strain estimated with the linear rule and Neuber's rule are compared with test data in Figs. 26 and 27, respectively, for the different assumptions of strain gradient and $K_{t,\text{ bend}}$. There is considerable scatter in the data, but pure bending strains are estimated conservatively (except for one point) by the linear rule using Galliart's proposed strain gradient and $K_{t,\text{ bend}} = 1.57$ or the finite element gradient and its corresponding $K_{t,\text{ bend}} = 1.42$. However, estimates are rather sensitive to assumed gradient for a fixed $K_{t,\text{ bend}}$. This is unfortunate since assumption of a gradient is the largest uncertainty in the analysis. Estimates based on Neuber's rule are even more conservative for pure

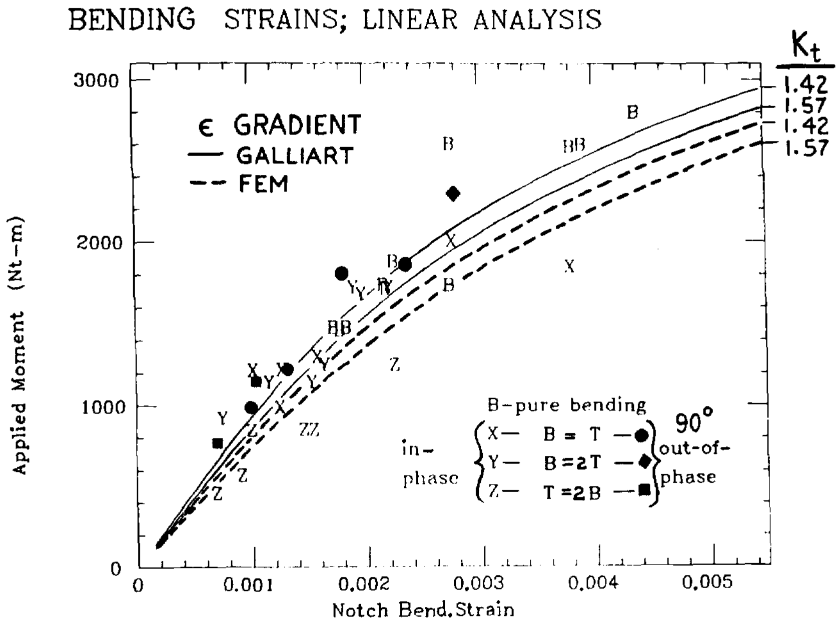

FIG. 26—*Comparison of estimated notch bending strains in the SAE specimen with measured values, based on the linear rule.*

bending, as expected. For combined in-phase loadings, bending strains tend to be comparable to or somewhat less than strains generated by pure bending. A notable exception is those loadings with a higher ratio of applied torsion to bending, the Z-points in Figs. 26 and 27, where considerably larger notch bending strains are developed. However, in those tests, torsional shear strains were three to five times larger than the bending strains, and thus life predictions should not be seriously affected by underestimation of bending strains. Bending strains due to out-of-phase, combined loadings are smaller than those for in-phase loadings and are estimated conservatively by the pure bending analysis.

Torsional Strain Estimate

The procedure to generate an applied torque versus notch shear strain relation is similar to that used for bending. Since the stress concentration factors determined by elastic finite element analysis and from Peterson are about the same, a single value of $K_{t,\mathrm{tors}} = 1.25$ was used in shear stress-strain versions of the linear and Neuber's rule. The torsional shear strain gradient was taken as a bilinear approximation to the finite element result and is shown in Fig. 25*c*. The stabilized cyclic shear stress-strain relation from Ref *41* was used in conjunction with the torque-stress relation

$$T = 2\pi \int_0^R r^2\, \tau(r)\, dr \tag{24}$$

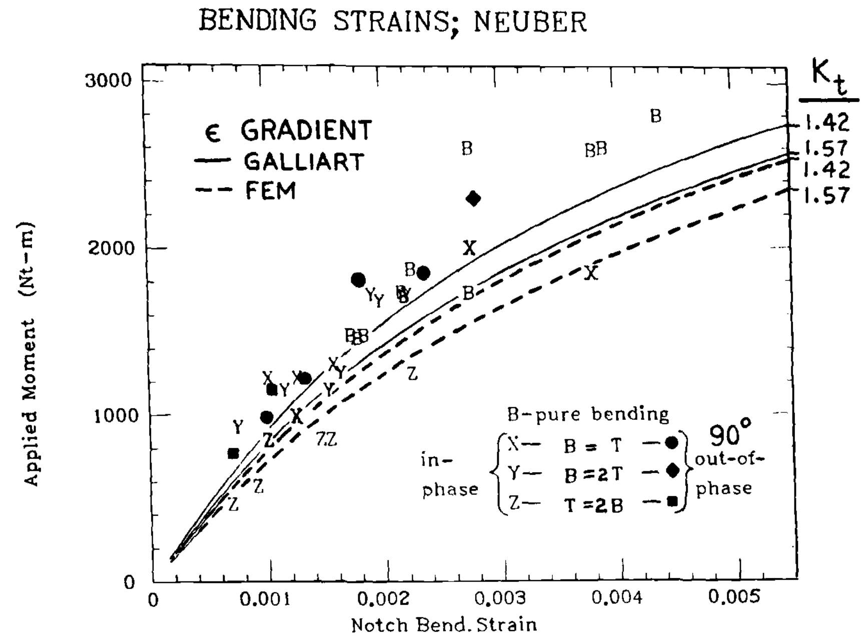

FIG. 27—*Comparison of estimated notch bending strains in the SAE specimen with measured values, based on Neuber's rule.*

where

T = applied torque, and
$\tau(r)$ = shear stress gradient.

Estimates based on the linear and Neuber rules are compared with test data in Fig. 28. The relatively low value of $K_{t,tors}$ causes estimates to be close to each other. Agreement between estimates and data is better than in the bending case. Out-of-phase strains are comparable to in-phase ones, tending to be somewhat smaller for a given applied torque.

Discussion

In the SAE tests conducted thus far, 90° out-of-phase loading was found to be less damaging and to produce smaller stabilized notch strains than in-phase loading for the same applied bending moment and torque and for lives between 10^4 and 2×10^5 cycles. Tests by Grubisic and Simburger cited previously showed out-of-phase loading to be considerably more damaging than in-phase loading for similar lives and for a specimen with a geometry much like that of the SAE specimen and made of a similar steel but treated to have higher monotonic strength. It is not known whether this difference in behavior is a result of differences in material or to the fact that SAE tests have been conducted under

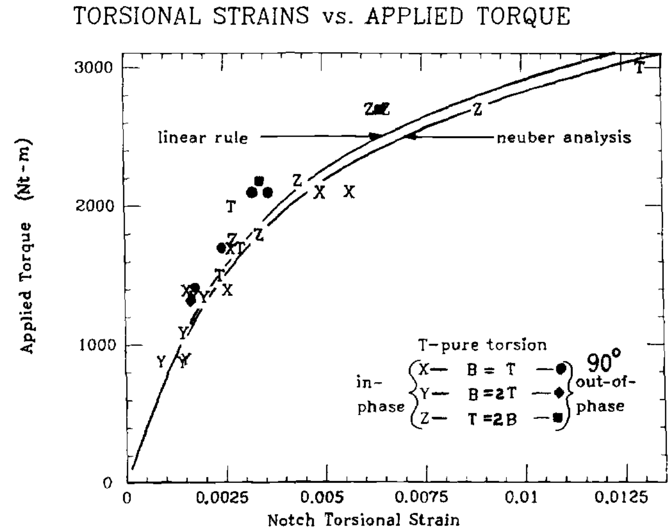

FIG. 28—*Comparison of estimated notch torsional shear strains in the SAE specimen with measured values, based on both linear and Neuber's rules.*

load control, while those of Grubisic and Simburger were performed under deflection control. It would be interesting to see if the multiaxial fatigue criteria considered in this paper, or others which may be developed, could predict the difference.

Measured values of circumferential notch strains, ϵ_{yy}, in the SAE specimen varied widely from close to $-\nu\epsilon_{xx}$ to as small as $-0.07\ \epsilon_{xx}$. There is no apparent trend to the variation. The suppression of ϵ_{yy} indicates that a transverse component of stress was present, the possible significance of which will be discussed shortly.

The nominal stress-based life prediction methods were investigated because they require only elastic calculation of stresses and a minimum of data as an input. The SEQA method, which reduces to the von Mises criterion for in-phase bending and torsion, provided reasonably good estimates of finite life with $K_f = 1$, but was unduly conservative with $K_f = K_t$. The method tended towards nonconservatism for certain out-of-phase loadings and would have been more so had the out-of-phase tests been more damaging than the in-phase tests. A serious drawback to use of the stress-based methods is that K_f behavior cannot be predicted with confidence in advance of testing. The relative lack of fatigue notch effect in the SAE tests could not have been anticipated.

The conventional Tresca and von Mises strain-based approaches are more complicated than the stress-based approaches because notch strains must be determined, either by measurement or by analytical estimates. For in-phase loadings, predictions were reasonably good for finite lives, but sensitive to assumed Poisson's ratio, a disadvantage. Use of a variable Poisson's ratio in the von Mises approach for in-phase loading eliminated this sensitivity as well as sensitivity to assumed circumferential strain. However, a variable Poisson's ratio method could not be applied to out-of-phase loadings. Use of the strain-based approaches tended to be nonconservative for the 90° out-of-phase loadings, as was the case for the similar stress-based SALT and SEQA methods.

By consideration of the influence of both the amplitudes of maximum shear strain and normal strain on the plane of maximum shear, the Brown and Miller strain ellipse approach provided finite life predictions comparable to those of the Tresca and von Mises criteria for in-phase loadings, but had the notable advantage of being both conservative and reasonably accurate for the out-of-phase loadings. It was also relatively insensitive to assumed Poisson's ratio. The approach did require additional input data (that is, smooth specimen torsional γ-N data). A similar stress-based approach (Guest criterion) also provided excellent correlations of in-phase, combined bending-torsion fatigue limits for several different notch types. It was necessary, though, to have data available on notched fatigue strength in bending and in torsion to apply the criterion.

The plastic work approach provided reasonably good predictions for in-phase loadings, being slightly more conservative for pure torsion or loadings with a higher ratio of torsion to bending. It also provided reasonably good predictions for the out-of-phase loadings. The approach has the advantage of requiring only uniaxial fatigue and cyclic stress-strain input data. A drawback to the approach for use in long life fatigue evaluations is that plastic strains are generally so small that slight variations in their computation can lead to large differences in predicted life.

Both the Tresca and Brown and Miller approaches were used assuming $\epsilon_{yy} = -\upsilon\epsilon_{xx}$, in which case planes of maximum shear intersect the surface at 90°. For certain combinations of torsional to bending strain, suppression of ϵ_{yy} (approaching a plane-strain condition) could cause the plane of maximum shear to shift to one intersecting the surface at 45°. Lohr and Ellison [*46*] have proposed a multiaxial fatigue criterion based on shear and normal strains on such 45° planes, applying it to evaluation of low-cycle, in-phase straining tests. It would be interesting to see if such an approach could be extended to out-of-phase straining.

At shorter lives ($N < 10^5$ cycles), all life prediction methods tended to overestimate life for pure bending and for higher ratios of bending to torsion. This could be due to the damaging effect of tensile hydrostatic stress produced by the transverse component of stress at the notch in the SAE specimen. This effect should be more influential at shorter lives and is, of course, not reflected in the uniaxial ϵ-N data used as input to the methods. It could be also due to discrepancies in crack initiation definition between the SAE specimen (crack with 0.7 mm depth and 2 to 3 mm surface length) and uniaxial smooth specimens (50% load drop-off). One approach to investigate the possible significance of this discrepancy would be to estimate the life spent in growing a 0.7 mm deep surface flaw in the uniaxial specimens to the larger size corresponding to a 50% load drop-off. To do so would require a means of estimating crack propagation under elastic-plastic straining, for example a da/dN-ΔJ method. This will be attempted in future work. Such an analysis would not be able to resolve discrepancies between growth behavior of small cracks in the uniaxial specimens and in torsion tests of the SAE specimen or those with higher ratios of torsion to bending.

All prediction methods underestimated the fatigue strength of specimens tested at long life ($N > 10^6$ cycles), particularly those tested in pure torsion or with higher ratios of torsion to bending. When plotted in terms of nominal torsional stress, the notched specimens exhibited a higher strength than thin-walled smooth ones. This discrepancy may be due to differences in crack initiation detection and definition or to the influence of notch shear strain gradient, and will be investigated in future work.

Conclusions

The following conclusions apply to fully reversed, monofrequency, combined bending and torsion and are based on both the literature review and evaluation of SAE tests to date.

1. The ability of nominal stress-based versions of the Tresca and von Mises criteria to predict finite life is highly dependent on knowledge of fatigue notch factor, thus reducing their usefulness in design evaluations.
2. Strain-based versions of the Tresca and von Mises criteria provided reasonably good estimates of finite life for the SAE specimen under in-phase loadings. They tended towards nonconservatism for out-of-phase loadings.
3. The Brown and Miller strain ellipse and the plastic work approaches provided the best life estimates for the SAE tests for both in- and out-of-phase loadings. A stress-based approach similar to the strain ellipse approach (Guest criterion) was successful in correlating combined bending-torsion fatigue limits for several different types of notches.
4. All of the methods gave somewhat more conservative predictions for pure torsion or loadings with higher ratios of torsion to bending. Plastic work predictions might be improved if a weighting factor were applied to the damage attributed to torsional straining.
5. All prediction methods were too conservative at long life and somewhat nonconservative at lower cycles, particularly for bending or loadings with larger ratios of bending to torsion.
6. Using a simplified elastic-plastic analysis, notch strain in bending was estimated conservatively taking $K_\epsilon = K_t$. However, estimates were quite sensitive to assumed strain gradient. Also, the simplified analysis could not conservatively estimate bending strains for in-phase tests with a high ratio of torsion to bending, but the nonconservatism in the strain estimate should not seriously affect life predictions since damage would be dominated by torsional straining.
7. Torsional notch shearing strain was predicted reasonably well by $K_\gamma = K_{t,\mathrm{tors}}$ or by Neuber's rule. For the same torque, shear strains under various combined

loadings were close to those for pure torsion, unlike the situation for bending strains.

8. For sharp notches, long-life multiaxial fatigue strength is governed by crack growth or arrest behavior, and none of the life prediction methods considered here is capable of accounting for that behavior. They are more suitable for application to blunt notches.

9. In general, multiaxial fatigue behavior of notched specimens will depend not only on stress concentration and stress gradient, as in "uniaxial fatigue," but also on the specific type of notch geometry and its influence on cracking behavior.

Acknowledgment

The authors are grateful for the support of the Solid Mechanics and Industrial Programs of the National Science Foundation and for the cooperation, advice, and contribution of materials, specimen fabrication, and testing by other participants in the SAE FD&E research project.

References

[1] Brown, M. W. and Miller, K. J. in *Proceedings,* Institution of Mechanical Engineers, Vol. 187, 1973, pp. 754–755.
[2] Garud, Y. S., *Journal of Testing and Evaluation,* Vol. 9, No. 3, 1981, pp. 165–178.
[3] Jordan, E. H., Chapter 7.6 in *Pressure Vessels and Piping: Design Technology, A Decade of Progress,* American Society of Mechanical Engineers, 1982, pp. 507–520.
[4] Topper, T. H., Wetzel, R. M., and Morrow, J., *Journal of Materials,* Vol. 4, No. 1, March 1969, pp. 200–209.
[5] Kotani, S., Koibuchi, K., and Kasai, K., *Proceedings,* 2nd International Conference on Mechanical Behavior of Materials, Boston, 1976, p. 606.
[6] Kühnapfel, K.-F. and Troost, A., *Konstruktion,* Vol. 31, 1979, 11.5, pp. S183–190.
[7] Wilson, W. K., *Journal of Pressure Vessel Technology, Transactions,* American Society of Mechanical Engineers, Nov. 1974, pp. 293–298.
[8] Walker, E. K., *Journal of Testing and Evaluation,* Vol. 5, No. 2, March 1977, pp. 106–113.
[9] Wundt, B. M., *Effect of Notches on Low-Cycle Fatigue, ASTM STP 490,* American Society for Testing and Materials, Philadelphia, 1972.
[10] Leis, B. N., and Topper, T. H., *Journal of Engineering Materials and Technology, Transactions,* American Society of Mechanical Engineers, July 1977, pp. 215–221.
[11] Krempl, E., "The Influence of Stress-Strain Concentration and Mean Stress on the Low-Cycle Fatigue Behavior of Three Structural Steels at Room Temperature," General Electric Co. Report GEAP-5726, San Jose, CA, Sept. 1968.
[12] Krempl, E., *The Influence of State of Stress on Low-Cycle Fatigue of Structural Materials, ASTM STP 549,* American Society for Testing and Materials, Philadelphia, 1974.
[13] Takahara, M., Kaneshiro, H., and Endo, T., *Memoirs of the Kyushu Institute of Technology,* No. 2, March 1972, pp. 55–98.
[14] Gough, H. J. in *Proceedings,* Institution of Mechanical Engineers, Vol. 160, 1949, pp. 417–440.
[15] Guest, J. J., *Proceedings,* Institute of Automotive Engineers, Vol. 35, No. 3, 1940, p. 33.
[16] Sines, G., "Failure of Materials under Combined Repeated Stresses with Superimposed Static Stresses," NACA Technical Note 3495, National Advisory Committee for Aeronautics, Nov. 1955.
[17] Burr, A. H., *Mechanical Analysis and Design,* Elsevier North Holland, Inc., New York, 1982, Chapter 6.

[*18*] Kanazawa, K., Miller, K. J., and Brown, M. W., *Journal of Engineering Materials and Technology, Transactions,* American Society of Mechanical Engineers, Vol. 99, No. 3, 1977, pp. 222–228.
[*19*] Frost, N. E., Marsh, K. J., and Pook, L. P., *Metal Fatigue,* Oxford University Press, London, 1974, pp. 184–187.
[*20*] Thurston, R. C. A. and Field, J. E., DSIR Properties and Mechanics of Materials Committee Report PM No. 53, NPL Engineering Division Report No. 447/50, 1950.
[*21*] Stulen, F. B. and Cummins, H. N. in *Proceedings,* American Society for Testing and Materials, Philadelphia, Vol. 54, 1954, pp. 822–835.
[*22*] Kakuno, H. and Kawada, Y., *Fatigue of Engineering Materials and Structures,* Vol. 2, 1979, pp. 229–236.
[*23*] Sines, G., *Transactions,* American Society of Mechanical Engineers, Vol. 26, No. 170, pp. 1340–1347.
[*24*] Grubisic, V. and Simbürger, A., *Fatigue Testing and Design,* Vol. 2, *Proceedings,* SEE International Conference 5, London, April 1976, pp. 27.1–27.8.
[*25*] Simbürger, A., "Festigkeitsverhalten zaher Werkstoffe bei einer mehrachsigen, phasenverschobenen Schwingbeanspruchung mit Korperfesten und veranderlichen Hauptspannungsrichtungen," Bericht Nr. BR-121, Laboratorium fur Betriebsfestigkeit, Darmstadt, Germany, 1975.
[*26*] ASME Boiler and Pressure Vessel Code, Section III, Code Case N-47-12, American Society of Mechanical Engineers, New York, 1980.
[*27*] Tipton, S. M., "Fatigue Life Predictions for a Notched Shaft in Combined Bending and Torsion," Interim Report No. 1, Mechanical Engineering Department, Stanford University, Stanford, CA, Dec. 1982.
[*28*] Nisitani, H. and Kawano, K. in *The Eleventh Japan Congress on Materials Research-Metallic Materials,* March 1968, pp. 49–51.
[*29*] Nisitani, H. and Kawano, K., *Bulletin,* Japan Society of Mechanical Engineering, Vol. 15, No. 82, pp. 433–438.
[*30*] Kawano, K. and Nisitani, H. in *The Thirteenth Japan Congress on Materials Research-Metallic Materials,* March 1970, pp. 73–76.
[*31*] Smith, R. A. and Miller, K. J., *International Journal of Mechanical Sciences,* Vol. 20, 1978, pp. 201–206.
[*32*] Dowling, N. E., *Fatigue of Engineering Materials and Structures,* Vol. 2, 1979, pp. 129–138.
[*33*] Bunyan, T. W., in *Large Fatigue Testing Machines and their Results," ASTM STP 216,* American Society for Testing and Materials, Philadelphia, 1957, pp. 59–80.
[*34*] Nelson, D. V. and Socie, D. F. in *Design of Fatigue and Fracture Resistant Structures, ASTM STP 761,* American Society for Testing and Materials, Philadelphia, 1982, pp. 110–132. pp. 110–132.
[*35*] Tucker, L. E., "Stress Analysis of SAE Notched Shaft Component," Report EIR-11 Sept. 80-5201-D01, Industrial Equipment Division, Deere & Co., Dubuque, Iowa, Sept. 1980.
[*36*] Peterson, R. E., *Stress Concentration Factors,* Wiley, New York, 1974.
[*37*] Tucker, L. E. and Galliart, D. R., "A Fatigue Test Program for a Notched Round Component," paper presented at ASTM Symposium on Biaxial/Multiaxial Fatigue, Dec. 1982.
[*38*] Galliart, D. R. and Downing, S. D., this publication, pp. 24–32.
[*39*] Langer, B. F. in *Pressure Vessel Engineering Technology,* Elsevier, Amsterdam-London-New York, 1971, pp. 59–100.
[*40*] ASME Boiler and Pressure Vessel Code, Sec. III, Div. 1, Subsection NA, American Society of Mechanical Engineers, New York, 1974.
[*41*] Leese, G. E. and Morrow, J. D., this publication, pp. 482–496.
[*42*] Gonyea, D. C. in *Fatigue at Elevated Temperatures, ASTM STP 520,* American Society for Testing and Materials, Philadelphia, 1973, pp. 678-687.
[*43*] Brown, M. W. and Miller, K. J., *Fatigue of Engineering Materials and Structures,* Vol. 1, 1979, pp. 217–229.
[*44*] Garud, Y. S., *Journal of Engineering Materials and Technology, Transactions,* American Society of Mechanical Engineers, Vol. 103, April 1981, pp. 118–125.
[*45*] Private communication, D. R. Galliart to D. V. Nelson, Dec. 1981.
[*46*] Lohr, R. D. and Ellison, E. G., *Fatigue of Engineering Materials and Structures,* Vol. 3, 1980, pp. 1–17.

Nonproportional Loading Effects

Soon-Bok Lee[1]

A Criterion for Fully Reversed Out-of-Phase Torsion and Bending

REFERENCE: Lee, S.-B., "**A Criterion for Fully Reversed Out-of-Phase Torsion and Bending,**" *Multiaxial Fatigue, ASTM STP 853,* K. J. Miller and M. W. Brown, Eds., American Society for Testing and Materials, Philadelphia, 1985, pp. 553–568.

ABSTRACT: This paper presents a new design criterion for fully reversed out-of-phase torsion and bending fatigue. This criterion, similar in spirit to that proposed by Kanazawa, Miller, and Brown, is derived as an extension of Gough's ellipse quadrant.

Theories and tests under "in-phase" torsion and bending fatigue are briefly reviewed. A few commonly used fatigue theories for "out-of-phase" multiaxial loadings are critically evaluated. Tests were performed with cantilever type SM45C structural steel specimens under fully reversed out-of-phase combined torsion and bending loadings in the intermediate cycle regime. Available fatigue data under high-cycle out-of-phase torsion and bending are plotted on constant life diagrams calculated according to the new criterion.

For multiaxial out-of-phase loadings, generated by fully reversed combined torsion and bending, both the present test results and data in the literature are in good agreement with the new fatigue criterion. The criterion predicts fatigue life under fully reversed bending with out-of-phase or in-phase torsion at intermediate to high cycles.

KEY WORDS: multiaxial fatigue, nonproportional, out-of-phase loadings, fatigue life prediction, equivalent stress, fatigue tests, bending, torsion

Structures and machine parts are generally subject to repeated multiaxial loadings. Such loadings are often complex, that is, the corresponding principal stresses are nonproportional or principal directions change during a cycle of such loadings. Fatigue life prediction of engineering components under complex multiaxial loadings is essential to their reliable design and failure prevention. Such prediction is often based on simple laboratory data generated under cyclic uniaxial loading and an appropriate multiaxial fatigue theory or criterion. The latter is essentially a method for reducing the multiaxial loading to an "equivalent" uniaxial loading.

Many attempts have been made to extend the classical multiaxial "yield criteria" to multiaxial fatigue problems. Such attempts are limited primarily to simple (proportional, in-phase) multiaxial loading.

Recent evaluation of multiaxial fatigue theories [*1*] showed that different investigators report different conclusions on complex (nonproportional, out-of-

[1]Head, Structural Mechanics Laboratory, Korea Institute of Machinery and Metals, Changwon, KyungNam, Korea; formerly, research assistant, Stanford University, Stanford, CA 94305.

Copyright© 1985 by ASTM International www.astm.org

phase) multiaxial loadings. Among the many cases of complex multiaxial loadings, the case of out-of-phase torsion and bending is commonly encountered in engineering practice, such as crankshafts in automotive industry. A new practical fatigue design criterion for out-of-phase torsion and bending is developed herein and compared with other plausible criteria. Reviews follow of previous criteria for in-phase and out-of-phase torsion and bending.

Review of In-Phase Torsion and Bending

Early investigations [*2–4*] on multiaxial fatigue have been done under combined torsion and bending. Extensive experimental work was performed by Gough, Pollard, and Clenshaw [*5*] who proposed the empirical ellipse quadrant equation for ductile materials and the empirical ellipse arc equation for brittle materials. Gough's criterion, though empirical in nature, correlates excellently data of in-phase torsion and bending and accounts for anisotropic effects as well. Other investigations [*6,7*] also found agreement with the ellipse quadrant equation. Marin [*8*] proposed an expression which was equivalent to Gough's ellipse quadrant equation.

Sines [*9*] suggests that the permissible alternation of octahedral shear stress is a linear function of the sum of orthogonal normal static stresses. Sines' criterion, when applied to fully reversed in-phase torsion and bending, coincides with the von Mises criterion and with Gough's ellipse quadrant when $t/b = 0.577$. Here, t/b is the ratio of torsional fatigue limit to bending fatigue limit. Sines' criterion provides reasonably good correlations for the fatigue life of smooth specimens under high cycle, proportional, constant amplitude loadings. This criterion does not allow for out-of-phase torsion and bending loading, which is common in crankshafts, nor for effects of anisotropy.

Findley [*10–14*] has performed many investigations under combined torsion and bending. He modified theories of failure with t/b to yield the empirical ellipse quadrant proposed by Gough [*5*]. He suggested that the maximum shear stress theory modified for material anisotropy and the normal stress acting on the plane of maximum shear stress, correlates satisfactorily with test data. Findley's [*12*] criterion does not allow for out-of-phase torsion and bending.

McDiarmid [*15,16*] reviewed in-phase multiaxial fatigue and proposed a general criterion of fatigue failure based on the critical range of shear stress modified for the effects of the normal stress acting on the plane of maximum shear stress and of anisotropy. McDiarmid's criterion does not apply to out-of-phase torsion and bending.

Recently, Kakuno and Kawada [*17*] proposed a rather complicated formula by modifying Sines' [*9*] criterion for combined static and repeated torsion and bending and showed that the formula agreed more closely with Gough's [*5*] experimental results than Sines' criterion. However, Kakuno et al's formula is not applicable for out-of-phase torsion and bending loading.

Reviews by Brown and Miller [*18*], Krempl [*19*], and Toor [*20*] are worth mentioning. These reviews also deal exclusively with fixed principal axes and proportional loading.

Review of Out-of-Phase Torsion and Bending

The early experiments on out-of-phase torsion and bending were performed by Manson [*21,22*]. However, no conclusions could be drawn because of the limited number of tests performed. Nishihara and Kawamoto [*23*] performed high-cycle out-of-phase torsion and bending tests on hard steel, mild steel, cast iron, and duralumin. They concluded that fatigue limit increases as the applied phase difference increases. Little [*24*] developed a graphical technique to analyze fatigue stresses from complex loadings. Later, Little [*25*] analyzed Nishihara and Kawamoto's [*23*] data on out-of-phase torsion and bending with respect to "true shear stress amplitude" and showed that fatigue limit actually decreases as the phase difference increases, which is *opposite* to Nishihara et al's claim.

Grubisic and Simbürger [*26*] have proposed an "effective straining" (root mean square expression) which involves examining "all" planes in a body for the most unfavorable combination of mean and alternating shear stress on each. It could be difficult to apply in practical situations. Simbürger [*27*] showed that out-of-phase stresses could be more damaging than in-phase stresses of the same magnitude.

Miller et al [*28*] proposed a "modified octahedral shear stress" theory for out-of-phase loadings. Dietmann and Issler [*29*] conducted out-of-phase tests and correlated data in terms of bearable octahedral stresses, that is, alternating shear stress and mean normal stress acting on the octahedral plane of maximum range of shear stress. Taira et al [*30,31*] investigated the low-cycle, torsion and axial tests at elevated temperature. They developed a modified "equivalent strain-range" based on the von Mises criterion. Zamrik et al [*32*] conducted low-cycle, out-of-phase fully reversed tests on 7075-T6 aluminum alloy and proposed use of maximum total strain to correlate their results. The total strain expression was defined as

$$\epsilon_T = \sqrt{\epsilon_1^2 + \epsilon_2^2 + \epsilon_3^2} \tag{1}$$

where ϵ_1, ϵ_2, and ϵ_3 are principal strains. To maximize the function ϵ_T, a computer program may be needed even for out-of-phase torsion and bending only. The total strain expression reduces to von Mises criterion when Poisson's ratio is 0.5.

Recently, Kanazawa, Miller, and Brown [*33*] have made a significant contribution to the field of out-of-phase multiaxial fatigue. They conducted tests under out-of-phase cyclic axial and torsional straining on a 1% Cr-Mo-V steel and showed that out-of-phase loading was more damaging than in-phase loading in the low-cycle regime. They also found that both the Tresca and von Mises type criteria are not conservative for out-of-phase multiaxial loadings. Finally, they proposed that the shear strain range and normal strain amplitude on the maximum shear plane should govern out-of-phase multiaxial fatigue but offered no functional relationship.

For out-of-phase multiaxial loading, most of the proposed fatigue theories are extensions of the Tresca or von Mises criteria. Langer [*34*] proposed a fatigue evaluation procedure seeking the highest range of shear stress in a multiaxial load history, which has been adopted in 1974 ASME Boiler and Pressure Vessel Code.[2] For fully reversed out-of-phase torsion and bending, the equivalent stress, SALT, based on that procedure can be obtained as

$$\mathrm{SALT} = \frac{B}{\sqrt{2}}\left[1 + K^2 + \sqrt{1 + 2K^2\cos2\phi + K^4}\right]^{1/2} \tag{2}$$

where

B = applied bending stress amplitude,
K = $2T/B$,
T = applied torsional stress amplitude, and
ϕ = phase angle between bending and torsion.

A modification of Langer's method, an extension of von Mises criterion, has been incorporated in ASME Code Case.[3] The equivalent stress, SEQA, based on the modification for out-of-phase torsion and bending can be expressed as following form

$$\mathrm{SEQA} = \frac{B}{\sqrt{2}}\left[1 + \frac{3}{4}K^2 + \sqrt{1 + \frac{3}{2}K^2\cos2\phi + \frac{9}{16}K^4}\right]^{1/2} \tag{3}$$

The expressions in Eqs 2 and 3 were derived in Ref *1* for critical evaluation of plausible multiaxial fatigue theories and presented in Ref *35*.

Inconsistencies with experimental results and difficulties in implementation of most complex multiaxial fatigue criteria have prompted efforts to develop a new criterion for out-of-phase multiaxial loadings.

Development of a New Criterion

For a general complex multiaxial stress field with constant amplitude cyclic loading a fatigue criterion or equivalent stress, S, can be determined by the following functional relations

$$S = f(\tilde{\sigma}_{ij}, \bar{\sigma}_{ij}, w_{ij}, \phi_{ij}), \quad i,j = 1,2,3 \tag{4}$$

[2]ASME Boiler and Pressure Vessel Code, Section III, Division I, Subsection NA, Appendix XIV, American Society of Mechanical Engineers, New York, NY, 1974.

[3]"Cases of the ASME Boiler and Pressure Vessel Code," Code Case N-47-12, American Society of Mechanical Engineers, New York, NY, 1978.

where

f = function of variables in parenthesis,
$\tilde{\sigma}_{ij}$ = 6 components of cyclic stress amplitude,
$\bar{\sigma}_{ij}$ = 6 components of mean stress,
w_{ij} = 6 frequencies, and
ϕ_{ij} = 5 phase differences between cyclic stresses.

twenty-three variables govern the fatigue life under complex multiaxial conditions. No theory has been developed for this case.

When all cyclic stresses are at the same frequency and in-phase, Eq 4 can be reduced to following functional expression

$$S = f(\tilde{\sigma}_{ij}, \bar{\sigma}_{ij}), \quad i,j = 1,2,3 \tag{5}$$

Comprehensive reviews [*18,19*] show that most multiaxial fatigue research is in this category. Sines' criterion [*9*] provides one such example.

When stresses are out-of-phase but of the same frequency, the fatigue criterion can be given in following functional form

$$S = f(\tilde{\sigma}_{ij}, \bar{\sigma}_{ij}, \phi_{ij}), \quad i,j = 1,2,3 \tag{6}$$

Seventeen variables still remain for this complex multiaxial fatigue problem. Many attempts [*24–34*] have been made to propose multiaxial fatigue criteria but none generally accepted. Some attempts lead to contradictory conclusions, which is no surprise considering the complexity of out-of-phase loadings.

Fully reversed out-of-phase torsion and bending loading is an example of a complex multiaxial fatigue loading whose principal directions move through cycling. For this loading, 17 variables in Eq 6 can be reduced to 3 variables without losing the characteristics of complex multiaxial fatigue as follows

$$S = f(\sigma, \tau, \phi) \tag{7}$$

The applied stresses are of the form

$$\sigma = B \sin \omega t \tag{8}$$

$$\tau = T \sin(\omega t + \phi) \tag{9}$$

where

B and T = applied bending and torsional stress amplitudes, respectively, and
ϕ = phase difference between cyclic bending and torsion.

For a special case of Eq 7, that is, in-phase bending and torsion, Gough et al [5] proposed the following ellipse quadrant equation for ductile materials

$$(B/b')^2 + (T/t')^2 = 1 \tag{10}$$

where b' and t' are fatigue limits in bending and torsion, respectively. In general, a fatigue design criterion or formula should: (*a*) have a clearly defined region of validity; (*b*) be easily applied; (*c*) permit prediction; and (*d*) be checked by tests on many engineering materials. Gough's ellipse formula meets all the requirements, and correlates excellently data of in-phase torsion and bending on many engineering steels for high cycles. A sound basis for the new out-of-phase criterion is provided by Gough's ellipse quadrant, which is well supported by other investigations [*6–9,12,15,16*].

Gough's ellipse quadrant Eq 10 can be generalized to out-of-phase torsion and bending loadings by adapting the power as follows

$$(B/b)^\alpha + (T/t)^\alpha = u^\alpha \tag{11}$$

where

b = bending fatigue strength for a given life N,
t = torsional fatigue strength for the same life N,
u = dimensionless unit variable, and
α = a variable power which depends on phase difference and material.

An equivalent stress, SLEE, can be postulated as

$$\text{SLEE} = b \times u \tag{12}$$

Upon substitution of u in Eq 11 into Eq 12, one can obtain the following expression

$$\text{SLEE} = b\,[(B/b)^\alpha + (T/t)^\alpha]^{1/\alpha} \tag{13}$$

Equation 13 can be written as

$$\text{SLEE} = B\,[1 + (bK/2t)^\alpha\,]^{1/\alpha} \tag{14}$$

where $K = 2T/B$. The power α is expressed for ductile materials as

$$\alpha = 2\,(1 + \beta\,\sin\phi) \tag{15}$$

where

β = a material constant and
ϕ = phase angle between applied torsion and bending.

The power α permits allowance for phase angle.

The equivalent stress, SLEE, in Eq 14 along with Eq 15 is one of the detailed functional expressions of Eq 7. SLEE consists of three material parameters; b, t, and β. Here, β can be determined by drawing the best fit constant life curve according to SLEE on data of any out-of-phase fully reversed torsion and bending. When $\phi = 0$, SLEE reduces to Gough's ellipse quadrant. The equivalent stresses, SALT and SEQA in Eqs 2 and 3 are other detailed functional expressions of Eq 7. When $\phi = 0$, SALT reduces to the Tresca criterion and SEQA reduces to the von Mises criterion.

Test Program

Fatigue tests were performed with SM45C structural steel at room temperature and in the intermediate-cycle regime. This material, which is equivalent to SAE 1045, is a commonly used steel for crankshafts which are subject to out-of-phase torsion and bending. The chemical composition and mechanical properties of the material tested are given in Table 1.

Fatigue tests were conducted under alternating torsion and bending separately. The bending specimen and torsion specimen are made according to *ASTM STP 566* [*36*], tested with a Schenck deflection controlled torsion/bending fatigue machine at around 20 Hz. Multiaxial fatigue tests under various combinations of torsion and bending were carried out on a round cantilever type specimen with a deflection-controlled multiaxial fatigue test machine. Detailed description of this multiaxial fatigue test machine may be found elsewhere [*1,37*]. The geometries of specimens tested are shown in Fig. 1. The test section of the cantilevered torsion-bending specimen is the reduced diameter portion of the bar. Stress concentration factors of this test section are less than 1.02 in torsion and bending.

Fatigue life was defined as the number of cycles to 10% load decrease due to cracking of the specimen.

Test Results

Results of fatigue tests of SM45C structural steel under alternating torsion and under alternating bending are plotted as *S-N* curves in Fig. 2. Open circles and open squares in Fig. 2 indicate data obtained with the torsion-bending

TABLE 1—*Chemical composition and mechanical properties of SM45C steel tested.*

Element	C	Si	Mn	P	S	Ni	Cr	Cu
Weight Percent	0.48	0.29	0.68	0.021	0.043	0.14	0.18	0.13
Yield strength						418 MN/m^2		
Ultimate tensile strength						731 MN/m^2		
Area reduction						45%		
Elongation						22%		
Young's modulus						208.6 GN/m^2		
Shear modulus						80.5 GN/m^2		

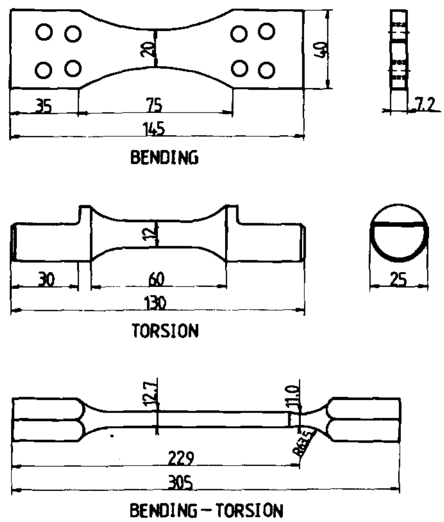

FIG. 1—*Test specimens (dimensions in millimetres).*

specimen. The values of t/b for any given life N can be obtained from Fig. 2. Results of multiaxial fatigue tests under combined torsion and bending are listed in Table 2. The equivalent stresses, SLEE, calculated according to the new criterion for in-phase and out-of-phase torsion and bending are compared with bending data and illustrated in Fig. 3. The constant β for SLEE was found empirically to be 0.15 for SM45C structural steel. Multiaxial data under both in-phase and out-of-phase loadings are very well correlated by the new criterion. Figure 4 shows the multiaxial test data plotted on the constant life curves of SALT, SEQA, and SLEE for 90° out-of-phase torsion and bending. The new criterion correlates data more closely than conventional von Mises or Tresca type criteria.

One of the requirements for a good fatigue criterion is the life prediction

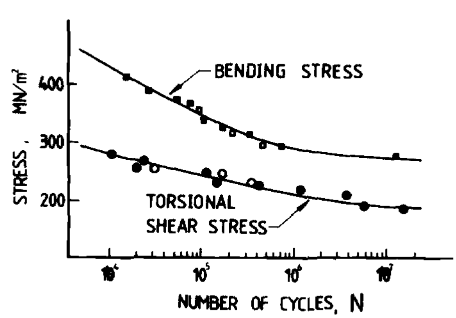

FIG. 2—S-N *curves of SM45C steel under torsion and under bending.*

TABLE 2—*Results of multiaxial fatigue tests under fully reversed combined torsion and bending with SM45C structural steel.*

B^a	T^b	ϕ^c	N^d	B^a	T^b	ϕ^c	N^d
390	151	0°	8.5×10^3	245	216	90°	2.0×10^4
349	148	0°	2.4×10^4	245	211	90°	2.5×10^4
325	153	0°	3.2×10^4	304	186	90°	2.6×10^4
372	93	0°	3.8×10^4	304	152	90°	5.7×10^4
309	134	0°	1.0×10^5	314	127	90°	1.0×10^5
265	225	90°	1.2×10^4	286	143	90°	1.2×10^5
392	118	90°	1.27×10^4	167	211	90°	2.9×10^5
417	78	90°	1.3×10^4	265	132	90°	3.5×10^5
346	173	90°	1.6×10^4				

[a]Applied bending stress amplitude, MN/m^2.
[b]Applied torsional stress amplitude, MN/m^2.
[c]Phase difference between B and T, degree.
[d]Number of cycles to failure.

capability. Figure 5 illustrates the life prediction capability of the various criteria under 90° out-of-phase torsion and bending and several K-values. Predicted lives by the new criterion (SLEE) are very close to actual lives of SM45C steel tested under 90° out-of-phase torsion and bending.

Both the Tresca (SALT) and von Mises type (SEQA) criteria seriously underestimate or overestimate the fatigue danger of SM45C steel under 90° out-of-phase torsion and bending, which depends on the $K(= 2T/B)$ value. Both criteria are not conservative, that is, underestimate the fatigue danger, when K is around 1 or smaller. On the contrary, they considerably overestimate the fatigue danger when $K > 2$, where torsion dominates. Figure 5 clearly indicates that the predictions by SALT and SEQA depend on K.

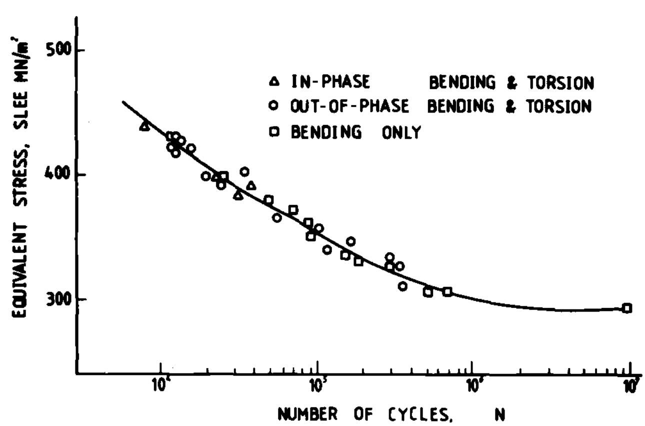

FIG. 3—*Equivalent stress (SLEE)-N curve of SM45C under multiaxial loadings.*

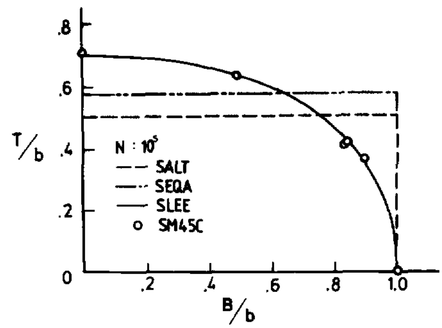

FIG. 4—*Modified test data of SM45C steel for* 10^5 *cycles on the constant life curves of SALT, SEQA, and SLEE for 90° out-of-phase torsion and bending.*

Discussion

Dietmann and Lempp [*38*] pointed up that the effect of phase difference upon fatigue strength depends on the material. None of the conventional criteria up to now correspond to out-of-phase experimental data of different materials. Out-of-phase data for different materials [*23,39,40*] have been successfully correlated by the new criterion with proper empirical constants β. Table 3 lists the constants β for various materials. The value of β can be loosely considered as the degree of sensitiveness to phase difference. The constant β must be determined from tests. However, it is not necessary to make experiments for various phase angles to get β, but sufficient to make tests only for $\phi = 90°$ and preferably at $K = 1$.

A high-strength steel, 42Cr-Mo-4V, tested by Lempp [*39*] showed that out-

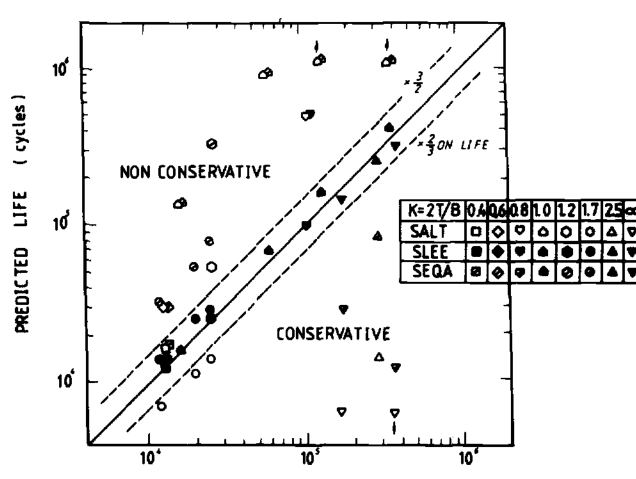

FIG. 5—*Comparison of predicted lives by SALT, SEQA, and SLEE, and actual lives of SM45C under out-of-phase loadings.*

TABLE 3—*Mechanical properties and constant β for various materials tested under out-of-phase torsion and bending.*

Materials	Ultimate Tensile Strength[a]	Endurance[b]	t/b,	N[c]	β for SLEE	Data
SM45C	731	295	0.7	10^5	0.15	present
St35	399	176	0.63	5×10^6	1.25	Lempp [*39*][d]
42Cr-Mo-N	724	254	0.62	2×10^6	0.9	Lempp [*39*]
42Cr-Mo-4V	1025	398	0.67	2×10^6	−0.22	Lempp [*39*]
34Cr-4V	795	411	0.63	2×10^6	0.0	Zenner [*40*]
Mild steel	374	235	0.583	10^7	0.3	Nishihara [*23*]
Hard steel	680	314	0.625	10^7	0.15	Nishihara [*23*]
Duralumin	429	156	0.642	10^7	0.0	Nishihara [*23*]
Cast iron	190	96	0.949	10^7	0.8[e]	Nishihara [*23*]

[a]Ultimate tensile strength, MN/m^2.
[b]Endurance limit in bending, MN/m^2.
[c]Number of cycles tested.
[d]Reference number.
[e]$\alpha = 1.5(1 + \beta \sin\phi)$ for this case.

of-phase loading is more detrimental than in-phase loading of the same magnitude in the high-cycle regime, which is contrary to the predictions of most conventional criteria. Figure 6 illustrates that the new criterion successfully predicted the fatigue behavior of 42Cr-Mo-4V. Here, the value of β is −0.22. In the low-cycle regime, 1Cr-Mo-V steel [*33*] is also shown to be more damaged by out-of-phase loading.

Figure 7 shows the fatigue data at 2×10^6 cycles of 34Cr-4V steel by Zenner [*40*] plotted on the constant life curves according to the new criterion. Phase difference between torsion and bending does not affect the fatigue strength of the 34Cr-4V as shown in Fig. 7. Duralumin by Nishihara et al [*23*] was also insensitive to phase difference. Here, the value of β is zero for both materials.

Figure 8 shows the curves of SLEE for in-phase and 90° out-of-phase torsion

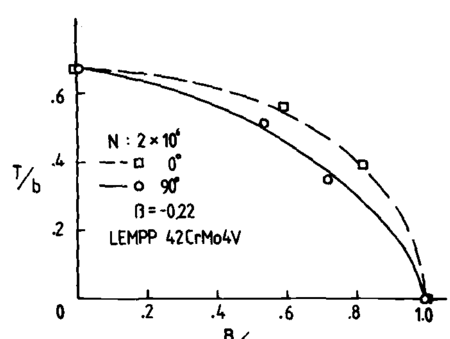

FIG. 6—*Constant life curves of SLEE with* β = −0.22 *and data of 42Cr-Mo-4V* [39] *at* 2×10^6 *cycles.*

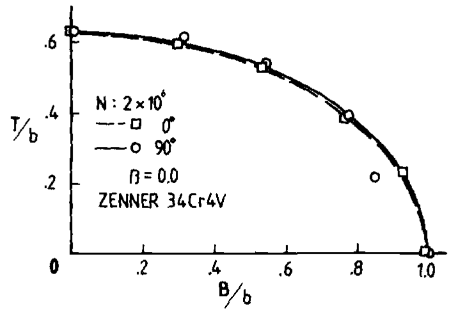

FIG. 7—*Constant life curves of SLEE with* β = *0 and data of 34Cr-4V* [40] *at 2* × *10*^{6} *cycles.*

and bending, and fatigue data at 10^7 cycles of the mild steel by Nishihara et al [*23*]. Nishihara's steels indicate that "in-phase" loading is more harmful than "out-of-phase." Here, the value of β for mild steel is 0.3.

The new criterion with $t/b = 0.6$ and $\beta = 0.3$ can predict fatigue life of Nishihara's steels [*23*] under combined torsion and bending at various phase angles, which is illustrated in Fig. 9. In Fig. 9, constant life curves of conventional criterion (SALT) and new criterion (SLEE) are shown for comparison at phase angles of 0, 30, 60, and 90° against Nishihara's steels. The new criterion correlates data at various phase angles more closely than the conventional Tresca type criterion. For in-phase and 30° out-of-phase, SALT is conservative. At 60° out-of-phase SALT is also conservative for $K > 1$, and close to SLEE for $K < 1$. At 90° out-of-phase and $K > 1.4$, SALT is also conservative. However, at 90° out-of-phase and $K < 1.4$, SALT is no longer conservative, but SALT underestimates the fatigue danger. The underestimation is most pronounced at $K = 1$. The same tendency of underestimation by conventional criteria (both SALT and SEQA) was shown in Fig. 5.

A one parameter concept, such as maximum shear range or octahedral shear

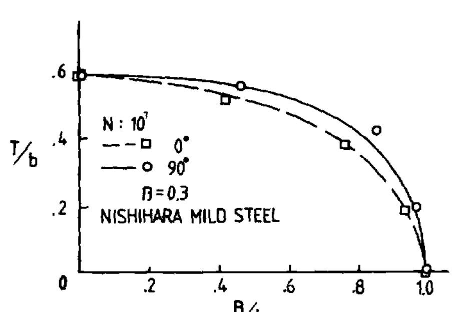

FIG. 8—*Constant life curves of SLEE with* β = *0.3 and data of mild steel* [23] *at 10*^{7} *cycles.*

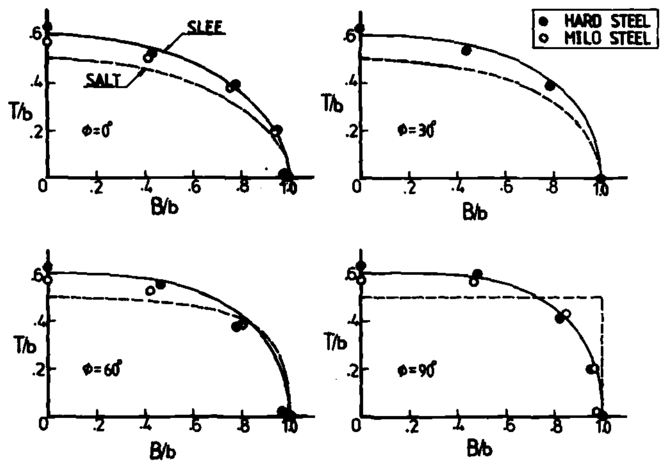

FIG. 9—*Comparison of SALT and SLEE (with* β = *0.3 and* t/b = *0.6) at 0, 30, 60, and 90° out-of-phase torsion and bending and data of Nishihara's steels at* 10^7 *cycles* [23].

range, is not sufficient to predict fatigue danger of out-of-phase multiaxial loadings.

The value of t/b, an ingredient of the new criterion, is readily available for many structural materials in Refs *5,12*, and *16*. The values of t/b for a given material can be obtained with simple fatigue tests as illustrated in Fig. 1.

The region of validity of the new criterion is the constant amplitude, fully reversed multiaxial fatigue, generated by out-of-phase torsion and bending. Emphases are placed on the fatigue strength of ductile materials under intermediate to high-cycle, nonproportional loadings with equal fundamental frequencies in

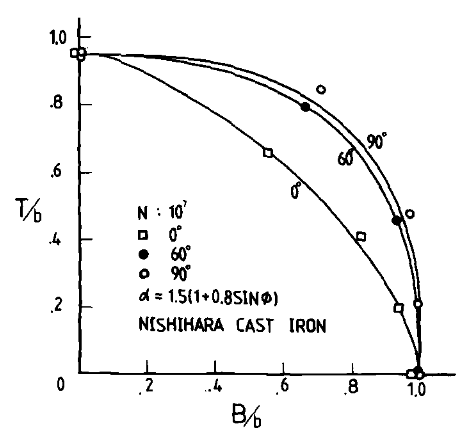

FIG. 10—*Constant life curves of SLEE with* α = *1.5(1* + *0.8 sin*ϕ) *and data of cast iron* [23].

all axes, at room temperature. The present investigation excluded some important problems such as high-temperature behavior and cumulative damage in out-of-phase multiaxial fatigue.

For cast iron which contains voids and microcracks, the power α in SLEE needs some modification. Nishihara's [23] cast iron data can be correlated by SLEE using $\alpha = 1.5\ (1 + \beta \sin\phi)$, which is shown in Fig. 10 with $\beta = 0.8$. However, it may need more cast iron fatigue data to justify the modified α expression.

Conclusions

Commonly used Tresca and von Mises criteria may seriously underestimate or overestimate the fatigue damage under out-of-phase loadings. In 90° out-of-phase torsion and bending loadings, they overestimate the fatigue damage when the applied torsional stress is dominant but underestimate it when the applied bending stress amplitude is larger than torsional stress amplitude.

The new criterion presents a short description which condenses data into a two-parameter-expression with material related constants of t/b and β. For complex multiaxial loadings, generated by fully reversed out-of-phase torsion and bending, both the present medium life test results and long life data in the literature are in good agreement with the new fatigue criterion.

The new criterion can be used for a preliminary fatigue design formula for unnotched machine parts or shafts which are subject to out-of-phase torsion and bending of same frequencies.

Acknowledgment

This research was supported in part by the Electric Power Research Institute in California, and invaluable guidance was given by Professors H. O. Fuchs and D. V. Nelson while the author was at Stanford University.

Mr. H. M. Byun and other members of structural mechanics laboratory in the Korea Institute of Machinery and Metals are affably thanked for conducting fatigue tests.

References

[1] Lee, S. B., "Evaluation of Theories on Multiaxial Fatigue with Discriminating Specimen," *Ph.D. thesis*, Stanford University, Stanford, 1980.
[2] Stanton, T. E. and Batson, R. G., *Engineering*, Vol. 102, 15 Sept. 1916, pp. 269–270.
[3] Lea, F. C. and Budgen, H. P., *Engineering*, Vol. 122, 1926, pp. 242–245.
[4] Gough, H. J. and Pollard, H. V., *Proceeding of the Institution of Mechanical Engineers*, Vol. 132, 1935, pp. 3–103.
[5] Gough, H. J., Pollard, H. V., and Clenshaw, W. J., "Some Experiments on the Resistance of Metals to Fatigue under Combined Stresses," *Aeronautical Research Council*, R&M 2522, 1951.
[6] Narmore, P. B., "A Fatigue Study of Strong Steel under Combined Alternating Stresses," *Ph.D. thesis*, University of Michigan, Ann Arbor, 1957.

[7] Nishihara, T. and Kawamoto, M., "The Strength of Metals under Combined Alternating Bending and Torsion," Memoirs, College of Engineering, Kyoto Imperial University, Vol. 10, No. 6, 1941, pp. 177-201.
[8] Marin, J., *Proceeding of the International Conference on Fatigue of Metals,* Institution of Mechanical Engineers, London, 1956, pp. 184-194.
[9] Sines, G., "Failure of Materials under Combined Repeated Stresses with Superimposed Static Stresses," TN 3495, National Advisory Committee for Aeronautics, 1955.
[10] Findley, W. N., "Combined Stress Fatigue Strength of 76S-T61 Aluminum Alloy with Superimposed Mean Stresses and Corrections for Yielding," TN 2924, National Advisory Committee for Aeronautics, 1953.
[11] Findley, W. N., Mitchell, W. I., and Strohbeck, D. D., *Transactions,* American Society of Mechanical Engineers, Vol. 78, No. 7, 1956, pp. 1481-1487.
[12] Findley, W. N., *Transactions,* American Society of Mechanical Engineers, Vol. 79, 1957, pp. 1337-1348.
[13] Findley, W. N., *Transactions,* American Society of Mechanical Engineers, Series B., Vol. 81, No. 4, Nov. 1959, pp. 301-306.
[14] Findley, W. N., Mathur, P. N., Szcepanski, E., and Temel, A. W., *Transactions,* American Society of Mechanical Engineers, Series D, Vol. 83, 1961, pp. 10-14.
[15] McDiarmid, D. L., *Proceedings of the Second International Conference on Pressure Vessel Technology,* American Society of Mechanical Engineers, San Antonio, TX, 1973, pp. 851-862.
[16] McDiarmid, D. L., *Aeronautical Journal,* 1974, pp. 325-329.
[17] Kakuno, H., Kawada, Y., *Fatigue of Engineering Materials and Structures,* Vol. 2, Pergamon Press, New York, London, 1979, pp. 229-236.
[18] Brown, M. W. and Miller, K. J., *Proceeding of the Institution of Mechanical Engineers,* Vol. 187, 1973, pp. 745-755.
[19] Krempl, E. in The Influence of State of Stress on Low-Cycle Fatigue of Structural Materials, *ASTM STP 549,* American Society for Testing and Materials, Philadelphia, 1974.
[20] Toor, P. M., *Engineering Fracture Mechanics,* Vol. 7, 1975, pp. 731-741.
[21] Manson, W., *Proceeding of the Institution of Mechanical Engineers,* London, 1917, pp. 121-196.
[22] Manson, W., "Alternating Combined Stress Experiments," Reports of the British Association for the Advancement of Science, 1921, pp. 329-341.
[23] Nishihara, T. and Kawamoto, M., "The Strength of Metals Under Combined Alternating Bending and Torsion with Phase Difference," Memoirs, College of Engineering, Kyoto University, Vol. 11, 1945, pp. 145-149.
[24] Little, R. E., *Machine Design,* Vol. 38, 6 Jan. 1966, pp. 145-149.
[25] Little, R. E., *Aeronautical Quarterly,* Vol. 20, 1969, pp. 57-60.
[26] Grubisic, V. and Simbürger, A., "Fatigue under Combined Out-of-phase Multiaxial Stresses," *International Conference on Fatigue Testing and Design,* Society of Environmental Engineers, London, 1976, pp. 27.1-27.8.
[27] Simbürger, A., "Festigkeitsverhalten zäher Werkstoffe bei einer mehrachsigen phasenverschobenen Schwingbeanspruchung mit körperfesten und veränderlichen Hauptspannungsrichtungen," *Laboratorium für Betriebsfestigkeit,* Darmstadt, Bericht Nr. FB-121, 1975.
[28] Miller, W. R., Ohji, K., and Marin, J., *Transactions,* American Society of Mechanical Engineers, Series D, Vol. 89, March 1967, pp. 76-80.
[29] Dietmann, H. and Issler, L., "Strength Calculation under Multiaxial Out-of-phase Fatigue Loading," *Sixth Congress on Materials Testing,* Budapest, 1974, pp. II 388-399.
[30] Taira, S., Inoue, T., and Takahashi, M., *Proceedings of the 10th Japan Congress on Testing Materials,* 1967, pp. 18-23.
[31] Taira, S., Inoue, T., and Yoshida, T., *Proceedings of the 11th Japan Congress on Materials Research,* 1968, pp. 60-65.
[32] Zamrik, S. Y. and Frishmuth, R. E., *Experimental Mechanics,* Vol. 13, May 1973, pp. 204-208.
[33] Kanazawa, K., Miller, K. J., and Brown, M. W., *Transactions,* American Society of Mechanical Engineers, Series H., Vol. 99, July 1977, pp. 222-228.
[34] Langer, B. F. in *Pressure Vessel Engineering,* R. W. Nichols, Ed., Elsevier Publishing Co., Amsterdam, 1971, pp. 59-100.

[35] Fuchs, H. O., *Fatigue of Engineering Materials and Structures*, Vol. 2, Pergamon Press, New York, London, 1979, pp. 207–215.
[36] Swanson, S. R., Ed., *Handbook of Fatigue Testing, ASTM STP 566*, American Society for Testing and Materials, Philadelphia, 1974, pp. 85–102.
[37] Lee, S. B., *Proceedings of the first ROK-ROC Joint Workshop on Fracture of Metals*, Seoul, 1983, pp. 135–149.
[38] Dietmann, H. and Lempp, W., "Untersuchengen zum Festigkeitsverhalten von Stählen bei mechrachsiger phasenverschobener Dauerschwingbeansprunchung," *Konstruktion*, Vol. 31, H.5, Spring-verlag, 1979, pp. 191–200.
[39] Lempp, W., "Festigkeitsverhalten von Stählen bei mehrachsiger Dauerschwingbeanspruchung durch Normalspannungen mit ueberlagerten phasengleichen und phasenverschobenen Schubspannungen," Dissertation, University, Stuttgart, 1976.
[40] Zenner, H. and Richter, I., "Eine Festigkeitshypothese für die Dauerfestigkeit bei beliebigen Beanspruchungskombinationen," *Konstruktion*, Vol. 29, Heft 1, 1977, pp. 11–18.

Eric H. Jordan,[1] *Michael W. Brown,*[2] *and Keith J. Miller*[2]

Fatigue Under Severe Nonproportional Loading

REFERENCE: Jordan, E. H., Brown, M. W., and Miller, K. J., "**Fatigue Under Severe Nonproportional Loading,**" *Multiaxial Fatigue, ASTM STP 853,* K. J. Miller and M. W. Brown, Eds., American Society for Testing and Materials, Philadelphia, 1985, pp. 569–585.

ABSTRACT: In order to extend our understanding to more generalized and practical cyclic loading conditions, severe nonproportional loading has been studied. Tension-torsion, low-cycle fatigue tests were performed on 1Cr-Mo-V steel at room temperature by applying intermittent axial half cycles. Tests with different loading paths but the same amplitudes of maximum shear strain and normal strain across the maximum shear plane were conducted. Different fatigue lives resulted from different loading paths even when amplitudes were held constant. Additional tests showed that the elimination of the compressive half cycles did not change fatigue life which suggest that the compressive half cycles were nondamaging. The principal implication of the work is that successful methods for predicting nonproportional loading must be selected from models which can show loading path sensitivity. Several models with this feature are discussed, and a procedure for predicting endurance from continuous cycling tests is proposed.

KEY WORDS: biaxial stresses, cyclic loads, ductility, fatigue life, fatigue (materials), plastic deformation, steels, stress analysis, torsion tests

Nomenclature

- h Phase measure
- j Constant
- N_f Fatigue life
- R σ_2/σ_1
- S Constant
- t Time
- W Hysteresis energy
- W^* Modified hysteresis energy
- α Coffin-Manson exponent
- γ Shear strain
- Δ Prefix denoting range of a stress or strain

[1]Assistant professor, Department of Mechanical Engineering, University of Connecticut, Storrs, CT 06268; formerly, NATO research scholar, University of Sheffield, Sheffield, U.K.

[2]Senior research fellow and professor, respectively, Department of Mechanical Engineering, University of Sheffield, Sheffield, U.K.

Copyright© 1985 by ASTM International www.astm.org

ϵ	Axial strain
ϵ_n	Normal strain on maximum shear plane
ζ	$2\epsilon_n/\gamma_{max}$
λ	$\Delta\gamma/\Delta\epsilon$
ν	Poisson's ratio
σ	Normal stress
τ	Shear stress
ϕ	Phase angle
ψ	Shear plane angle
ω	2π/(torsional strain cycle period)
ω'	2π/(axial strain cycle period)

Subscripts

ap	Applied
max	Maximum shear
np	Peak value of ϵ_n
p	Plastic component
t	Total strain
1,2,3	Principal values

Many common engineering components experience cyclic loading that results in states of stress more complex than the simple uniaxial state which exists in standard fatigue tests. Three recent reviews [*1–3*] describe much of the work which has been done with a view to predicting fatigue lives for components suffering complex stress states utilizing fatigue data derived from simpler uniaxial stress state tests. The majority of published work deals with proportional loading only [*1–3*]. This paper describes an experimental study of the low-cycle fatigue behavior of hollow tubes subjected to combined tension-torsion loading where the strains are applied in a severely nonproportional manner. Severe nonproportional loading was employed because it offered a good method by which to highlight and examine certain effects that might be expected to occur under generalized service conditions. It is of practical importance when, for example, shock loads are superimposed on steadily loaded structures, or when intermittent cycles of one loading mode (for example, bending) are added to the strain generated by another (for example, torsion).

Experiments involving nonproportional loading can be traced back at least as far as 1921 [*4*]. In these early tests it was shown that life predictions were nonconservative when applied to such loading conditions. The tendency to obtain nonconservative life predictions under nonproportional loading has been reinforced by a number of more recent investigations [*5,6*], giving nonproportional loading studies an engineering significance.

Experimental results from nonproportional loading are very limited [*4–8*] and they are reviewed elsewhere [*1–3,6*]. Therefore, only selected relevant aspects of prior work will be discussed here.

The first problem encountered in nonproportional loading fatigue is that of selecting representative stress or strain amplitudes to use in correlating results. The choice of a representative stress or strain is made difficult by the fact that stresses not only change magnitude but also that the principal axes may rotate. For a particular type of loading, fatigue failure can occur with constant magnitude (that is, zero amplitude) maximum shear stress if the principal axes are made to rotate [*6*]. An additional factor in low-cycle fatigue is that the principal stress and strain axes are not always coincident. A number of different approaches to the problem of choosing representative stress or strain values for nonproportional loading have been developed, which may be divided into two categories. The first category considers stress, strain, or energy variation without regard to how these quantities are distributed with respect to specific planes and crack growth directions, while the second category considers the variation of some quantity on a critical plane related to crack growth.

Taira et al [*9*], Zamrik and Frishmuth [*8*], and Garud [*10*] have proposed methods in the first category. Taira et al integrated the octahedral shear strains throughout a cycle, in order to avoid the problem of changing stress direction. Zamrik and Frishmuth [*8*] found ϵ_t the maximum value of "total strain" without regard for direction was useful in correlating data. The definition used for total strain is the following

$$\epsilon_t = \sqrt{\epsilon_1^2 + \epsilon_2^2 + \epsilon_3^2} \tag{1}$$

where ϵ_1, ϵ_2, and ϵ_3 are principal strains.

Garud [*10*] has used the plastic work per cycle independent of material planes as a measure of damage. For the special case of tension-torsion, his general expression of plastic work reduces to

$$W_p = \oint [\sigma d\epsilon_p + \tau d\gamma_p] \tag{2}$$

In order to improve the correlation of experimental data, a modified version of plastic work was also used by Garud, which for the special case of tension-torsion reduces to

$$W_p{}^* = \oint [\sigma d\epsilon_p + 0.5\tau d\gamma_p] \tag{3}$$

The weighting factor of 0.5 in Eq 3 was determined empirically.

The second category of methods used to characterize nonproportional loading considers conditions on a critical plane. Dietmann et al [*7*], also Hull and Miller [*11*], and Miller et al [*12*] have employed an approach that considers shear and normal stresses, both alternating and mean, on the plane experiencing the largest octahedral shear stress. Kanazawa et al [*6*] have developed a similar approach by considering the maximum shear plane, looking at the physical processes of deformation and fatigue crack growth in order to choose the most suitable parameters. They also found that two independent parameters are required to char-

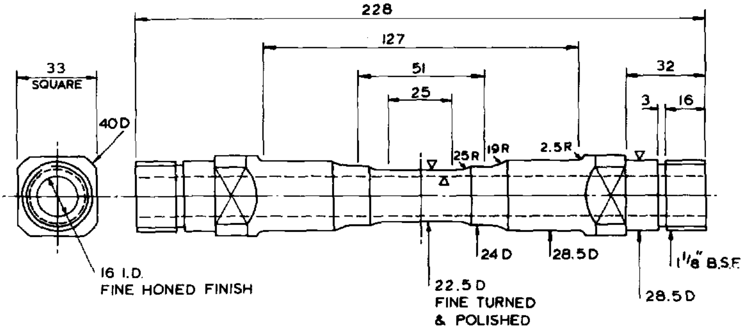

FIG. 1—*Specimen geometry (all dimensions in millimetres).*

acterize multiaxial failure, being (*a*) the range of maximum shear strain, which governs the reversed plastic flow of the material that causes crack propagation, and (*b*) the largest positive normal strain on the maximum shear plane, which influences the fatigue ductility coefficient [*13*]. Since only low-cycle fatigue conditions with fully reversed loading were analyzed, the resulting method considered the amplitude of shear strain and the amplitude of normal strain acting on the plane of maximum shear strain. This method is also applicable to high-cycle fatigue.

All of the methods in each category have shown some success for at least some data sets.

Experimental Program

The test machine, extensometer, specimen design, and material were identical to those used previously [*6,14*]. Briefly, the tests were carried out on tubular specimens of a 1Cr-Mo-V steel at room temperature. The specimen geometry is shown in Fig. 1, and the material composition and monotonic properties are given in Tables 1 and 2. The heat treatment was designed to give a midbainite structure, and the production of the steel was carefully controlled to give isotropic properties [*15*].

The strains in the specimen gage length were monitored continuously with the extensometer shown in Fig. 2, the strain signals being derived from the axial and torsional transducers. The applied loads were governed by two independent closed-loop servocontrol systems operating on the two strain signals. A more detailed description of the fatigue machine may be found elsewhere [*14*].

Four different types of strain cycle were used (see Fig. 3). All waveforms of

TABLE 1—*Chemical composition, %.*

C	Si	Mn	Ni	Cr	Mo	V	S	P
0.24	0.29	0.64	0.21	1.02	0.57	0.29	0.010	0.016

TABLE 2—*Monotonic properties.*

	Tension	Torsion
0.5% proof stress, MPa	698	378
Tensile strength, MPa	800	. . .
True shear fracture stress, MPa	524	532
Reduction in area, %	64	. . .
True shear strain at fracture, %	153	160

the axial and torsional strain cycles were sinusoidal. For cycles of Type I both torsional and axial sine waves have the same period (286 s), while for cycles of Types II *a*, *b*, and *c*, the duration of the axial cycle is one tenth that of the torsional cycle. For Type I cycles the phase of the applied shear strain relative to the axial strain is represented by a phase angle ϕ. For Type II cycles the relative phase is less ambiguously represented by the parameter *h* shown in Fig. 3. This parameter is the nondimensional torsional strain value which occurs at the axial strain peak. All three variations of the Type II cycle indicated in Fig. 3 were used, with $\Delta\gamma$ = 3%, while $\Delta\epsilon$ was 1.4% in Cycles I and II*a* and 0.7% in Cycles II*b* and II*c*. Failure was defined as the first measurable drop in the torque amplitude after saturation and prior to rupture.

The test data are summarized in Table 3. A notable feature of the program was that the specimens tested were from the same batch used earlier by Kanazawa et al [*6*]. The data in this investigation were found to be comparable to that of Kanazawa et al, and therefore the in-phase and out-of-phase Type I data of Ref *6* provided an invaluable baseline for the present investigation.

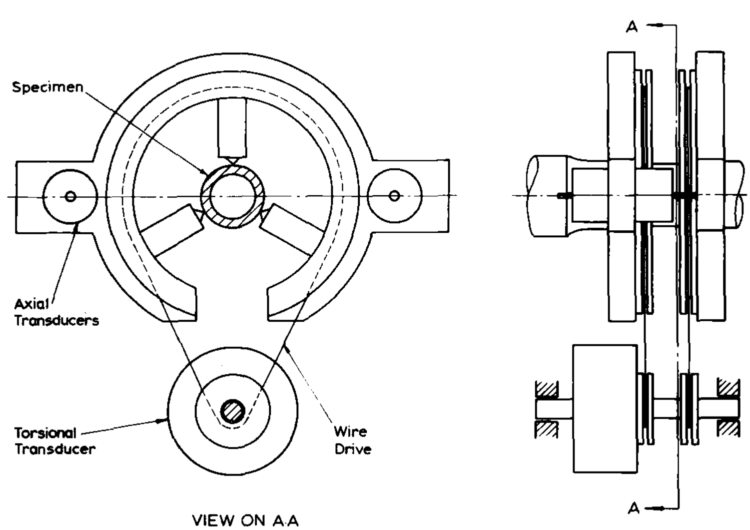

FIG. 2—*Biaxial strain extensometer.*

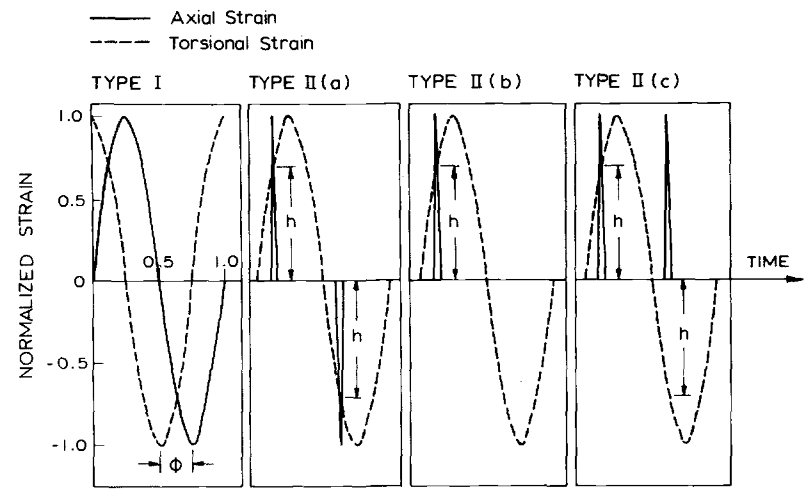

FIG. 3—*Definition of cyclic types, phase angle* ϕ *and phase measure* h (*for* $\phi = 90°$, h $= 0$).

Strain Anaıysis

It is necessary to calculate from the imposed strains the range of the maximum shear strain and the maximum positive value of the normal strain across the plane of maximum shear. For Type I cycles a closed form expression for these quantities was found previously [*6*], but, for the Type II*a* cycles, no closed form expression has been found. When thin-walled tubes are subjected to axial and torsional straining the applied strains are given by the strain tensor

$$\begin{bmatrix} \epsilon_{ap} & 1/2\gamma_{ap} & 0 \\ 1/2\gamma_{ap} & -\nu\epsilon_{ap} & 0 \\ 0 & 0 & -\nu\epsilon_{ap} \end{bmatrix}$$

The basic procedure was to solve for the principal strains and principal directions at a given time. The numerical procedure used was available as a commercial subroutine developed for finding eigenvalues and eigenvectors based on Householder reduction. From the principal strains at a given time the maximum shear strain may be easily determined. These quantities were solved repeatedly to develop a time history of the maximum shear strain. From this time history, the largest and smallest maximum shear strains were determined. It was found for the particular cases considered that the largest positive and the largest negative maximum shear strain always occurred on the same plane. With the maximum shear strain amplitude and orientation of the maximum shear plane known, the time history of the normal strain across that plane was easily generated using

TABLE 3—*Test results.*

Test Number	Cycle Type	h	$\Delta\epsilon$, %	$\Delta\gamma$, %	σ, MPa	τ, MPa	$\Delta\epsilon_p$, %	$\Delta\gamma_p$, %	W_p, MJ/m^3	W_p^*, MJ/m^3	N_f, life	N_f, corrected
46	II*a*	0.000	1.396	3.03	643.2	350.1	0.803	2.214	17.7	12.5	420	417
52	II*a*	+0.324	1.437	3.165	649.7	347.3	0.771	2.198	17.6	11.7	332	377
53	II*a*	−0.324	1.40	3.00	662.4	356.8	0.709	2.053	17.2	11.9	353	353
54	II*a*	−0.500	1.372	3.045	661.9	351.3	0.705	2.099	16.8	11.5	344	340
57	II*a*	+0.550	1.387	2.97	621.0	345.6	0.733	2.160	16.1	10.6	409	389
59	II*a*	+0.675	1.379	3.024	641.1	352.8	0.737	2.213	17.3	11.7	359	354
55	I		0.0	3.023	0	338.2	0.0	2.06	10.9	5.4	1473	1483
66	I-90°	0.00	1.379	3.03	657.4	362.8			23.6	16.9	208	206
60	II*c*	0.00	0.6895	2.88	546	364.7	0.288	1.938	14.2	9.4	433	402
61	II*b*	0.00	0.70	3.038	578	372.6	0.288	2.006	14.2	8.4	395	403
62	II*b*	0.00	0.686	3.045	594.6	396.5	0.281	2.001	14.6	8.6	445	448
64	II*c*	0.00	0.6895	3.045	554.0	368.4	0.273	2.03	15.3	9.7	462	445

the time history of the strain tensor, the unit vector normal to the maximum shear plane, and appropriate inner products.

In carrying out this procedure, 720 time steps were used for each complete cycle analyzed. The results of the computer analysis are shown for Poisson's ratio equal to 0.4 in Figs. 4 and 5. This value of Poisson's ratio is the approximate effective value at peak strain for these tests.

Experimental Results

The experiments were planned to investigate three questions. First, in two tests where the maximum shear strain amplitude and the amplitude of ϵ_n are held constant, will a different straining path give different fatigue lives? Second, will the phase of the applied maximum shear strain relative to the normal strain acting normal across the plane of maximum shear (ϵ_n) affect the fatigue life? Third, will the constant reintroduction of mean strain and associated mean stress affect fatigue life? The importance of the answers to these questions and the results will be used collectively to discuss the merits of various life prediction methods.

The tests conducted and the resulting fatigue lives are given in Table 3. It is

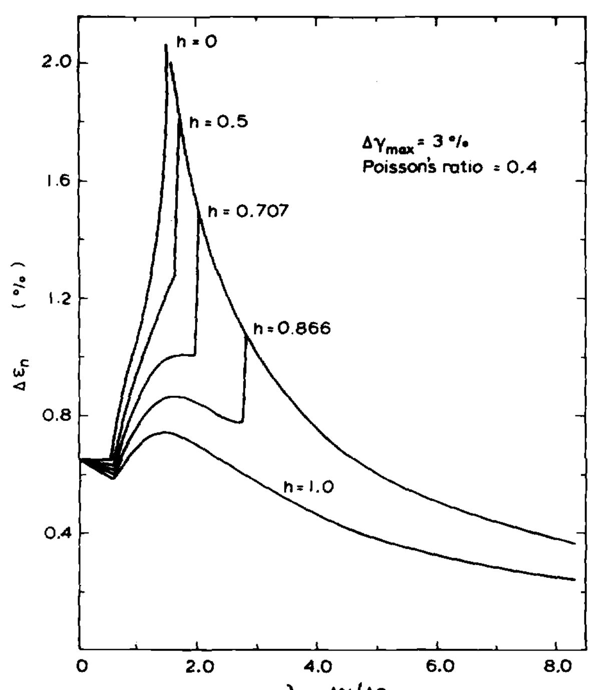

FIG. 4—*Variation of normal strain range, $\Delta\epsilon_n$, for constant maximum shear strain range.*

worth noting that the stresses given were calculated by treating the specimen as a thin-walled tube. The plastic strain and plastic work ranges were determined from the hysteresis loops at approximately midlife, and the corrected fatigue lives were determined by scaling the actual fatigue lives to the life expected for $\Delta\gamma_{max} = 3\%$, $\Delta\epsilon_n = 0.7\%$ using graphs from the Type I tests of Kanazawa et al [6], since it was difficult to obtain the desired test parameters precisely.

Effect of Strain Path

Figure 6 shows fatigue life as a function of the normal strain acting across the plane of maximum shear for tests run with a maximum shear strain range of 3%. The open symbols show the results for Type I strain cycles, while the solid symbols show the results for Type II cycles. Most of the Type I data are from tests of the work of Kanazawa et al [6] who used the same batch of specimens. The data from Type II cycles fall consistently above the Type I data indicating an effect of straining path on fatigue life when the straining path is changed from Type I to Type II.

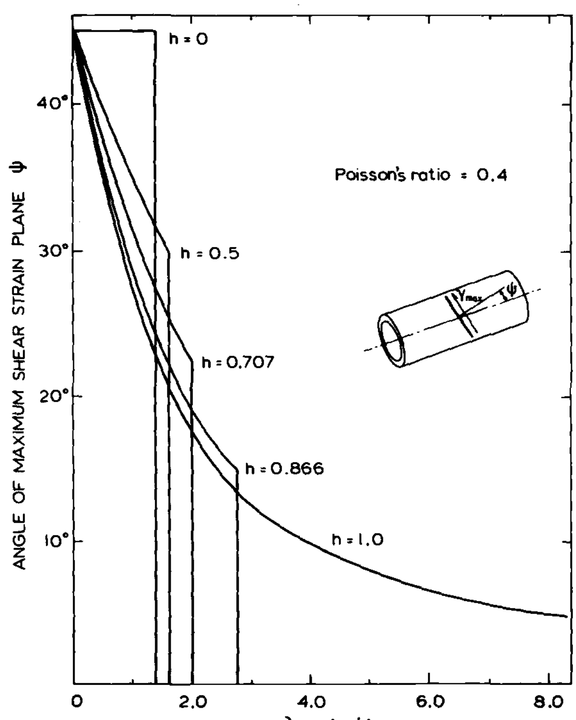

FIG. 5—*Orientation of the maximum shear plane as a function of* λ *and* h.

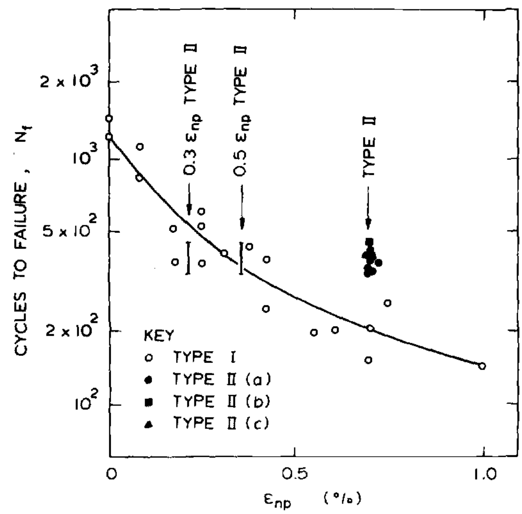

FIG. 6—*Fatigue life as a function of normal strain amplitude,* ϵ_{np}, *for* $\Delta\gamma_{max} = 3\%$.

Effect of the Relative Phase of γ_{max} *and* ϵ_n

It has been suggested that the normal strain across the maximum shear plane affects ductility and influences the damaging process on the maximum shear strain plane [*13*]. It is important to know whether the relative phase of these two strain components affects fatigue endurance for general nonproportional cycles if crack growth models are to be based on these two components.

Tests were run to show the effect of the relative phase of γ_{max} and ϵ_n independent of other factors. To do this it is desirable to keep the following quantities constant.

$\Delta\gamma_{max}$ = maximum range of shear strain,
$\Delta\epsilon_n$ = range of normal strain across the plane of maximum shear,
$\Delta\gamma$ = range of applied torsional strain, and
$\Delta\epsilon$ = range of applied axial strain.

Noting that λ equals $\Delta\gamma/\Delta\epsilon$, Type II tests were run with the value of λ fixed at 2.14. As indicated by Fig. 4, if the phase h is restricted to $-0.7 < h < +0.7$ then all these quantities can be held constant because $\Delta\epsilon_n$ has a unique value of 1.4%, irrespective of h. In addition, the orientation of the maximum shear plane ψ will be constant at 0° (see Fig. 5). The tests were run with the values of the applied torsional strain range and the applied axial strain range as close as possible to 3% and 1.4%, respectively. In Fig. 7 the corrected fatigue life versus the phase h is plotted, and it is apparent that phase has no significant effect on fatigue life.

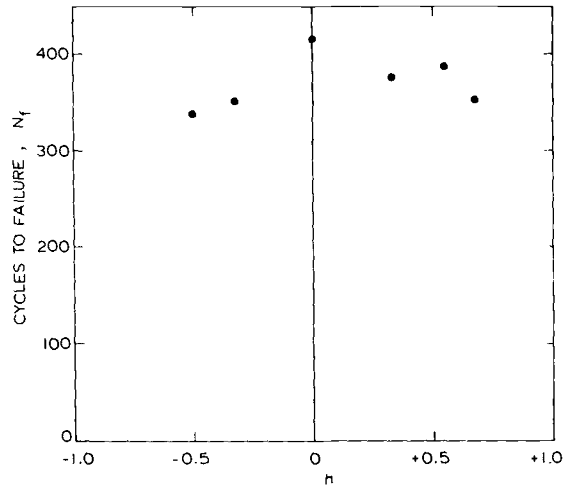

FIG. 7—*Fatigue life as a function of phase,* h, *for Type II*a *cycles, with* $\Delta\gamma_{max} = 3\%$.

Effect of Mean Normal Strain

Two Type II*b* tests (tests 61 and 62) were run with a shear strain range of 3%, $h = 0.0$, and $\Delta\epsilon_n = 0.7\%$ with only the tensile half cycles of normal strain applied. These two tests resulted in lives that were not significantly different from tests which included both tensile and compressive going half cycles (see Fig. 6), suggesting that the compressive going half cycle was nondamaging. A test with only compressive going half cycles was attempted, but, unfortunately, it resulted in a cyclic-buckling failure of the specimen. It is worth noting that the elimination of the compressive going half cycle cut the overall axial strain range in half without affecting life.

Two additional tests were run at 3% torsional strain range with two, rather than one, tensile going axial strain cycles per torsion cycle (Type II*c*). As can be seen in Fig. 6 these tests resulted in lives essentially the same as tests involving only a single tensile half cycle.

Discussion

It is important to consider how the fatigue lives obtained for both Types I and II loading may be predicted by a single theory. Octahedral shear stress theory is normally only applied to cases of elastic deformation and will not be further discussed.

Fatigue Damage in Terms of Strain Amplitude

The traditional and generally accepted approach to fatigue life prediction is formulated in terms of strain ranges, whether elastic, plastic, or total. A typical example is Eq 1 where the greatest value of "total" strain, ϵ_t, is used as an effective strain amplitude to find the endurance. For all Type I and II tests and the torsion test run in this program, the value of ϵ_t is $(\sqrt{2} \times 0.75)\%$, which predicts the same life for all of these tests. However, the lives ranged from 1483 cycles for test 55, which was pure torsion, to 206 cycles for test 66, a Type I test.

The ASME Boiler and Pressure Vessel Code Case N47 recommends design for nonproportional cyclic loading using the greatest range of octahedral shear strain. Similarly, this calculation predicts identical lifetimes for both the Type I tests conducted and all the Type II tests, if $-0.83 \leq h \leq +0.83$. Reference to uniaxial baseline data [*6*], as recommended by the code, gives an estimated endurance of 489 cycles, which is an unsafe prediction in all cases tested except pure torsion.

The approach of Kanazawa et al [*6*] was also based on peak strain values and is unable to correlate the Type II data in Fig. 6. It does however give a satisfactory representation of all Type I results and is conservative.

Thus, it is apparent that fatigue assessment techniques based on strain amplitudes cannot accommodate severely nonproportional loading paths because strain path influences endurance (Section on Effect of Strain Path). Therefore, the accumulation of damage, that is, crack extension, should be assessed throughout the cycle. The mechanism of low-cycle fatigue failure by crack propagation suggests that a gradual buildup of damage during a cycle is physically more realistic than a sudden, discontinuous crack extension on reaching the peak strain condition. This conclusion may be deduced from Fig. 6 also, since the Type II results can be correlated with the main curve by plotting a reduced value of normal strain by a factor of about 0.3 to 0.5 corresponding to the observed proportion of the loading half cycle in which axial strain affects the torsional stress in the hysteresis loop. This factor in some sense reflects the fraction of the torsional cycle over which the axial cycle enhances the damage due to shearing.

Fatigue Damage in Terms of Integrated Strains

Taira et al [*9*] devised an integral damage theory, integrating over one cycle the octahedral shear strain raised to the power $1/\alpha$, where α is the Coffin-Manson exponent. Although quantitative prediction is not good, the test types are separated out in the correct manner. Their theory predicts, using $\alpha = 0.5$, that the respective lives for torsion, Type II*a* and Type I ($\phi = 90°$) tests are 1483, 1300, and 540 cycles, while the current experiments gave 1483, 393, and 206 cycles.

The plastic work approach of Garud [*10*] is also an integral theory using both stress and strain, being based on hysteresis loop area. The results are plotted in Fig. 8 in terms of plastic strain energy density (Eq 2), together with data from

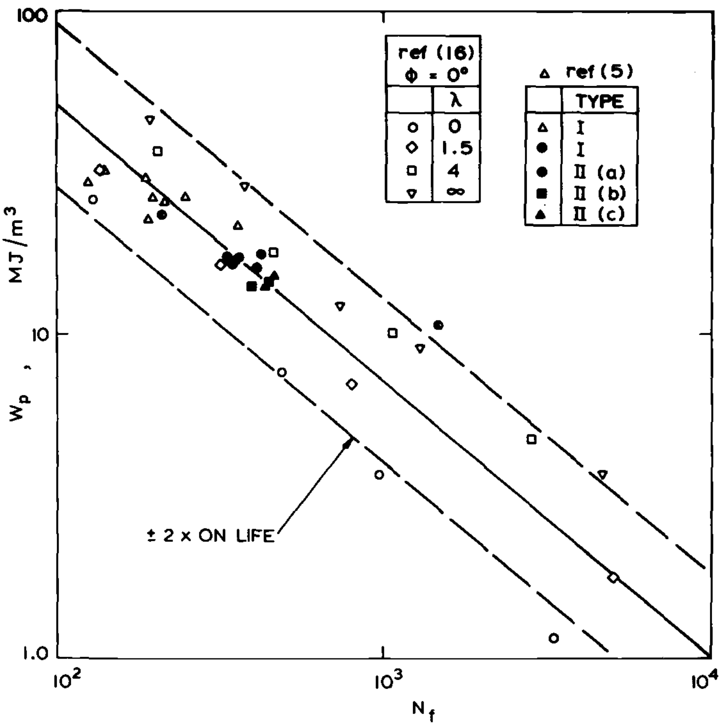

FIG. 8—*Fatigue life as a function of plastic strain energy density,* W_p.

Refs *6* and *16*. This figure shows considerable scatter of the points, but the use of the modified strain energy formula (Eq 3) gives a closer correlation in Fig. 9. It is perhaps worth noting that although the same data sets were analyzed and plotted by Garud [*10*], Figs. 8 and 9 differ in some details from Garud's figures because here actual hysteresis loop areas were measured to determine W_p, rather than estimating energy from cyclic hardening and flow rules. In particular, for out-of-phase loading, lower energies were observed than those estimated by Garud. In general, actual areas gave improved correlation for W_p^* at low lives, but the data diverge in the longer endurance region.

Thus, integral theories yield a much closer representation of experimental results than strain-amplitude based theories, and they also predict correctly the observation that there will be no significant effect of the relative phase, h, on endurance (see Section on Effect of the Relative Phase of γ_{max} and ϵ_n).

Maximum Shear Strain Theory

Kanazawa's analysis was formulated in terms of strain amplitude since the integral and amplitude based equations are equivalent for continuous fully reversed sinusoidal loading. A mathematical expression has been proposed by Kandil et al [17] which may be written in terms of total strains as

$$\Delta\bar{\gamma} = \Delta\gamma_{max}(1 + S\zeta^j)^{1/j} \tag{4}$$

where the strain state parameter ζ is $2\epsilon_n/\gamma_{max}$ and S and j are empirical constants. In Fig. 6 the influence of the parameter ζ on life can be seen, the curve being adequately represented by Eq 4. Fitting the equation to three points (torsional, uniaxial, and, for maximum ϵ_{np}, $\lambda = 1.5$, $\phi = 90°$) gives $j = 0.55$, $S = 0.675$.

In the analysis of Type II tests the critical plane is assumed to be the plane experiencing the largest degree of plasticity in the nominal uncracked specimen, that is, maximum shear strain range. It is further observed that the maximum positive value of normal strain acting on the plane of maximum shear influences fatigue life [13]. There is some analytical support for the idea that the microscopic normal strain ϵ_n affects the normal strain on the local crack tip shear planes and then influences ductility [18]. In any case the analysis of the test data is based on the notion that ϵ_n enhances fatigue damage during that part of the shear strain cycle during which the value of ϵ_n is positive. The notion of damage enhancement leads to an effective value of ϵ_n in integral form. A simple form consistent with the experimental results obtained is the following

$$\begin{aligned}\bar{\epsilon}_n &= \sqrt{\left\{\frac{\omega}{\pi}\left[\int_0^{\pi/\omega'}\left(\frac{\Delta\epsilon_n}{2}\,sin\omega'\,t\right)^2 dt + \int_{\pi/\omega'}^{\pi/\omega'} 0.dt\right]\right\}} \\ &= \epsilon_{np}\sqrt{}\ (\omega/2\omega')\end{aligned} \tag{5}$$

where ω' is the effective frequency for the axial strain. Since integration is made only for half a cycle, Types II*a*, *b*, and *c* will have identical $\bar{\epsilon}_n$-values, which is in agreement with the experimental facts (see Section on Effect of Mean Normal Strain). By redefining ζ in terms of the root mean square value, Eq 5 gives

$$\zeta = \sqrt{\omega/\omega'}\ 4\ \epsilon_{np}/\Delta\gamma_{max}) \tag{6}$$

so that Eq 4 may be used for both types of cycle with the same constants, S and j. The results are presented in Fig. 10, to show a similar predictive capability to the $W_p{}^*$ correlation.

This analysis of these results leads to three important conclusions.

(*a*) Stage I cracks will develop in the maximum shear plane for which $\bar{\epsilon}_n$ is greatest. This was observed to be the case for all tests, cracks being normal to the tensile axis, $\psi = 0$.

(*b*) In low-cycle fatigue with reversed plasticity there is no effect of mean strain (see Section on Effect of Mean Normal Strain). Mean strain should be

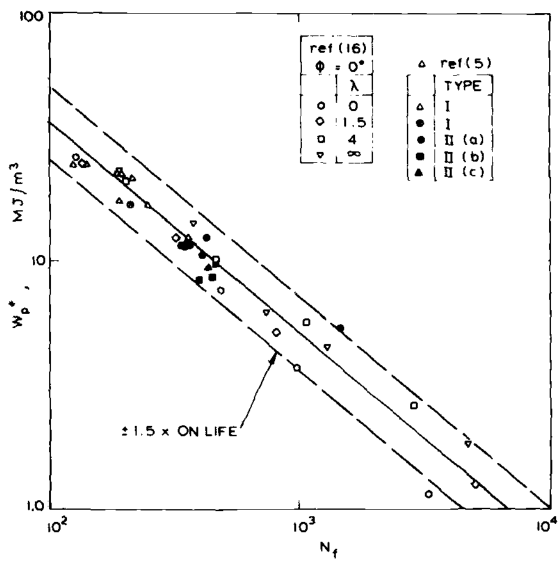

FIG. 9—*Fatigue life as a function of modified plastic strain energy density,* W_p^*.

excluded from the integral $\bar{\epsilon}_n$, as mean stresses will shakedown to zero. Therefore, there should be no effect of moderate mean strain on life except under elastic high-cycle fatigue conditions. Equation 5 should be used for low-cycle fatigue only, and substantial mean components of the full ϵ_n cycle should not be assessed by this technique [*12*].

(*c*) The normal strain on the maximum shear plane in the unloading half cycle where ϵ_n is negative has no effect on endurance. This is an important conclusion, because where there are normal strains throughout the cycle, the half cycle of shear strain should be selected to give the greater damage, or value of ϵ_n, in Eq 5 since this will be naturally selected by the material as giving more rapid crack propagation.

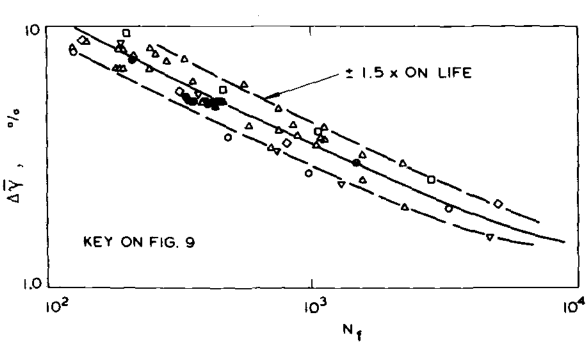

FIG. 10—*Fatigue life correlation by the equivalent shear strain range,* $\Delta\bar{\gamma}$.

Comparison of Predictive Procedures

Equally good predictions of endurance are provided by the W_p^* and $\Delta\bar{\gamma}$ parameters. Although the former has less scatter at low life, it differentiates between the similar results of Type II*a*, *b*, and *c* tests. It is therefore valuable to compare some of the shortcomings of each approach. For the plastic strain energy density, W_p^*, these are:

(*a*) The need for a good constitutive equation for making predictions under multiaxial loading limits the application of the theory in the near term. This is chiefly because suitable constitutive equations and associated constants are not available to most designers and for most materials.

(*b*) The basic form of the theory could be generalized to any type of loading; however, the method of generalizing the modified plastic work version of the theory has not been presented or proven.

(*c*) No method for handling mean stress has been proposed for the theory.

(*d*) It predicts no effect of hydrostatic pressure on endurance, contrary to experiment [*19*].

(*e*) For lives in excess of 2000 cycles, the results appear to diverge, making life assessment difficult when plastic strain energies are small.

For the $\Delta\bar{\gamma}$ formula, outstanding difficulties are:

(*a*) Equation 4 is not a precise representation of fracture behavior, since for in-phase results alone, $j = 2.5$ [*16*]. Data scatter is therefore inevitable, and extrapolation may be dangerous.

(*b*) Out-of-phase predictions cannot be determined from in-phase results alone.

(*c*) Three biaxial conditions must be tested to find the constants j and S.

(*d*) For very rapid axial strain cycles of Type II, the theory predicts that life will tend to the torsional value. This may not prove to be true in practice.

(*e*) No method of handling mean stress has been developed.

Conclusions

1. The reduction of the duration of the axial cycle compared to the period of the torsion cycle increased fatigue life by about a factor of 2. This result shows that fatigue is not only a function of strain amplitude but also of straining path. Therefore, effective strain formulae for nonproportional loading should consider the integration of the strain path throughout a cycle.

2. The relative phase of maximum shear strain and normal strain across the plane of maximum shear (ϵ_n) did not affect fatigue life in any tests.

3. The elimination of the compressive part of the axial cycle did not affect fatigue life, indicating that the compressive half of a fatigue cycle is nondamaging.

4. Life estimates based on amplitude of strain are unsatisfactory for nonproportional straining.
5. The modified strain energy density and the effective shear strain theory developed in the paper are equally good at life prediction in the low-cycle fatigue regime.

Acknowledgments

E. H. Jordan was supported by a NATO postdoctoral fellowship and M. W. Brown by a Central Electricity Generating Board (CEGB) research fellowship. The support of the United States Nuclear Regulatory Commission is gratefully acknowledged. The material was provided by the CEGB.

References

[1] Garud, Y. S., *Journal of Testing and Evaluation,* Vol. 9, 1981, pp. 165–178.
[2] Brown, M. W. and Miller, K. J. in *Low-Cycle Fatigue and Life Prediction, ASTM STP 770,* American Society for Testing and Materials, Philadelphia, 1982, pp. 482–499.
[3] Jordan, E. H. in *A Decade of Progress,* American Society of Mechanical Engineers, New York, pp. 507–518.
[4] Mason, W. and Delaney, W. J., "Alternating Combined Stress Experiments," *Reports of the British Association for the Advancement of Science,* 1921, pp. 329–341.
[5] Little, R. E., *The Aeronautical Quarterly,* Vol. 20, Part 1, Feb. 1969, pp. 57–60.
[6] Kanazawa, K., Miller, K. J., and Brown, M. W. *Transactions,* American Society of Mechanical Engineers, Series H, *Journal of Engineering Materials and Technology,* Vol. 99, July 1977, pp. 222–228.
[7] Dietmann, H. and Issler, L. in *Proceedings,* Fifth Conference on Dimensioning and Strength Calculations, and the Fifth Congress of Material Testing. Budapest, 28 Oct.–1 Nov. 1974, Vol. II, Akademiai Kiado, Budapest, 1974, pp. 388–399.
[8] Zamrik, S. Y. and Frishmuth, R. E., *Experimental Mechanics,* No. 5, Vol. 13, 1973, pp. 204–208.
[9] Taira, S., Inoue, T., and Yoshida, T. in *Proceedings,* Eleventh Japan Congress on Materials Research, 1968, pp. 60–65.
[10] Garud, Y. S., *Journal of Engineering Materials and Technology, Transactions,* American Society of Mechanical Engineers, Series H, Vol. 103, 1981, pp. 118–125.
[11] Hull, W. C. and Miller, W. R., *Proceedings,* Second International Conference on the Mechanical Behaviour of Materials, Boston, 1976, pp. 860–864.
[12] Miller, W. R., Ohji, K., and Marin, J., *Journal of Basic Engineering, Transactions,* American Society of Mechanical Engineers, Series D, Vol. 89, 1967, pp. 76–80.
[13] Brown, M. W. and Miller, K. J., *Proceedings,* Institution of Mechanical Engineers, Vol. 187, 1973, pp. 745–755.
[14] Brown, M. W. and Miller, K. J., *Journal of Testing and Evaluation,* Vol. 9, 1981, pp. 202–208.
[15] Darlaston, B. J., Miller, K. J. and Stanley, P., "Some Aspects of Elevated Temperature Behaviour of a 1% Cr-Mo-V Steel" *Proceedings,* International Conference on Creep and Fatigue in Elevated Temperature Applications, Institution of Mechanical Engineers' Conference, Publication 11, Paper 232/73, 1973.
[16] Brown, M. W. and Miller, K. J., *Fatigue of Engineering Materials and Structures,* Vol. 1, 1979, pp. 217–229.
[17] Kandil, F. A., Brown, M. W. and Miller, K. J. in *Proceedings,* International Conference on Mechanical Behaviour and Nuclear Applications of Stainless Steel at Elevated Temperature, Metals Society, London, 1982, pp. 203–209.
[18] Gao Hua, Brown, M. W., and Miller, K. J., *Fatigue of Engineering Materials and Structures,* Vol. 5, 1982, pp. 1–17.
[19] Krempl, E., *The Influence of State of Stress on Low-Cycle Fatigue of Structural Materials, ASTM STP 549,* American Society for Testing and Materials, Philadelphia, 1974.

Cetin M. Sonsino[1] and Vatroslav Grubisic[1]

Fatigue Behavior of Cyclically Softening and Hardening Steels Under Multiaxial Elastic-Plastic Deformation

REFERENCE: Sonsino, C. M. and Grubisic, V., "**Fatigue Behavior of Cyclically Softening and Hardening Steels Under Multiaxial Elastic-Plastic Deformation,**" *Multiaxial Fatigue, ASTM STP 853*, K. J. Miller and M. W. Brown, Eds., American Society for Testing and Materials, Philadelphia, 1985, pp. 586–605.

ABSTRACT: To investigate the fatigue behavior of cyclically softening and hardening steels under multiaxial elastic-plastic strains, axial strain, and shear strain controlled fatigue tests under constant amplitude loading were carried out. *S-N* curves under axial strain and torsional pure shear as well as under combined axial strain and shear, in and out of phase, were obtained for the cyclically softening high-strength steel 30Cr-Ni-Mo 8 (similar to AISI Type 4340) and the cyclically hardening stainless steel X 10Cr-Ni-Ti 18 9 (AISI Type 321) in the region of low-cycle fatigue.

For both steels, used for vessels, pipings, shafts, etc., the fatigue life to crack initiation (crack depth $a < 1$ mm) is reduced by an out-of-phase ($\delta = 90°$) loading of the specimens in comparison to in-phase loading.

The decrease of fatigue life under out-of-phase strains is caused by the changing direction of principal strains resulting in an interaction of the deformations in all directions on the surface. This interaction is taken into account by the arithmetic mean value of shear amplitudes acting in all interference planes of the surface. The equivalent strain is then calculated according to the octahedral shear strain hypothesis. Using this equivalent strain and the *S-N* curve for uniaxial strain, the fatigue life under combined strain is predicted. For the multiaxial strain evaluation it is important to know if the local strains and shears are deformation or load controlled.

KEY WORDS: low-cycle fatigue, cyclic softening, cyclic hardening, stress-strain/shear-curves, axial strain, torsional shear strain, combined strain, in phase, out of phase, multiaxial strain state, equivalent strain, fatigue life prediction, computer program

Nomenclature

Stresses

σ_a, τ_a	Stress (tensile, shear) amplitude
σ_{eq}	Equivalent stress
K	Stress coefficient

[1]Research engineer and head of department, respectively, Stress Analysis and Strength Evaluation Department, Fraunhofer-Institut für Betriebsfestigkeit (LBF), Darmstadt, Federal Republic of Germany.

Copyright© 1985 by ASTM International www.astm.org

Strains

ϵ_R,γ_R	Strain (normal, shear) at fracture
$\epsilon_x,\epsilon_y,\epsilon_z,\gamma_{xy}$	Strains (normal, shear)
$\epsilon_1,\epsilon_2,\epsilon_3$	Principal strains
$\epsilon_{xa,\mathrm{tot}},\epsilon_{xa,\mathrm{el}},\epsilon_{xa,\mathrm{pl}}$	Total, elastic and plastic strain amplitudes
$\gamma_{xya,\mathrm{tot}},\gamma_{xya,\mathrm{el}},\gamma_{xya,\mathrm{pl}}$	Total, elastic and plastic shear strain amplitudes
$\epsilon(\phi),\gamma(\phi),\epsilon(\phi)_a,\gamma(\phi)_a$	Strain and shear in an interference plane ϕ, amplitudes
$\gamma_{a,\mathrm{effective}},\gamma_{a,\mathrm{arithmetic}}$	Effective and arithmetic mean values of $\gamma(\phi)_a$
$\epsilon_{\mathrm{eq},a}$	Equivalent strain amplitude

Other Symbols

N_c,N_f	Fatigue life to crack initiation, total life
T,t,S,s	Constants of the strain-life relationship
R_ϵ,R_γ	Strain (normal, shear) ratio, for example, $\epsilon_{\min}/\epsilon_{\max}$
F_x,M_{xy}	Axial load, torsional moment
K_t	Stress concentration factor
P_s	Probability of survival
f	Frequency
ω	Angular frequency $2\lambda f$
S,S_γ	Phase angle between ϵ_x and γ_{xy}
ϕ	Angle of an interference plane, fracture plane
t	Time
m	Number of tests

The low-cycle fatigue design of vessels, piping, and shafts has to consider local elastic-plastic strains which are due to complex loading or structural discontinuities, often multiaxial. For a strain-based fatigue evaluation, a multiaxial strain-state is generally converted into an "equivalent" uniaxial strain state using a suitable failure hypothesis. The most commonly used hypotheses [*1,2*] in the design of multiaxially strained structural parts manufactured with ductile materials do not take into account cyclic hardening or softening. Moreover, the influence of changing principal strain directions induced for example by an out-of-phase straining under a multiaxial strain state is not properly considered. For example, the distortion energy hypothesis of von Mises, used in several design codes [*3*], or the shear stress hypothesis of Tresca produce a lower equivalent strain for out-of-phase straining than for in-phase straining, indicating an increase of fatigue life to crack initiation in comparison to the in-phase straining. Several experimental results obtained in the fatigue life region between 2×10^4 and 5×10^5 cycles to crack initiation [*4,5*] contradict this prediction. The lack of reliability of these hypotheses for complex loading conditions led to several investigations in the low-cycle fatigue region [*6–11*], surveyed in Refs *12–14*, proposing different parameters such as maximum principal strain, octahedral shear strain, maximum shear strain acting on the surface or on a plane 45° to the surface, etc. to derive an equivalent strain.

This paper refers to a study on the mechanics of cyclic softening and hardening materials under multiaxial straining and on the influence of changing principal strain directions on the fatigue life to crack initiation in which an important phenomenon governing the multiaxial fatigue behavior was observed. This phenomenon results from an interaction of deformation in different directions on the surface; a phenomenon which is not covered by the parameters previously mentioned. For this investigation in- and out-of-phase tests were carried out in combined axial and torsional straining in the low-cycle fatigue region ($N_c < 5 \times 10^4$ cycles to crack initiation). This loading mode often occurs in service of structural parts.

Multiaxial Strain Evaluation in Practical Cases

For the conversion of a multiaxial strain state to an equivalent uniaxial strain state, the distortion energy hypothesis of von Mises is often recommended, which is also equivalent to the octahedral shear stress hypothesis. In the case of a triaxial strain state with normal strains ϵ_x, ϵ_y, ϵ_z and shear strains γ_{xy}, γ_{xz}, γ_{yz} the distortion energy hypothesis gives [3]

$$\epsilon_{eq} = \frac{1}{\sqrt{2}\,(1 + \mu)} \left[(\epsilon_x - \epsilon_y)^2 + (\epsilon_y - \epsilon_z)^2 + (\epsilon_z - \epsilon_x)^2 + \frac{3}{2} (\gamma_{xy}{}^2 + \gamma_{xz}{}^2 + \gamma_{yz}{}^2) \right]^{1/2} \tag{1}$$

where ϵ_{eq} is the "equivalent" strain. This hypothesis is proposed for ductile materials, and predicts that the ratio between shear strain and axial strain amplitudes in torsional and axial fatigue tests at equal life will be

$$\gamma_{xy}/\epsilon_x = 2(1 + \mu)/\sqrt{3} \tag{2}$$

If the shear strain components are zero the strains ϵ_x, ϵ_y, and ϵ_x are equal to the principal strains ϵ_1, ϵ_2, and ϵ_3.

For the frequently occurring case of an in-phase strain state adjacent to a free surface with constant principal strain directions and known principal strains ϵ_1 and ϵ_2, then with $\epsilon_3 = -\mu(\epsilon_1 + \epsilon_2)/(1 - \mu)$, the equivalent strain is [15]

$$\epsilon_{eq} = \frac{\epsilon_1}{1 - \mu^2} \left[(1 - \mu + \mu^2) \left(1 + \left(\frac{\epsilon_2}{\epsilon_1} \right)^2 \right) - \frac{\epsilon_2}{\epsilon_1} (1 - 4\mu + \mu^2) \right]^{1/2} \tag{3}$$

The Poisson's ratio μ has to be obtained in the elastic-plastic range from the cyclic stress strain curve using the elastic Poisson's ratio μ_{el}, Young's modulus E, and the secant modulus E_s [16]

$$\mu = 0.5 - (0.5 - \mu_{el}) \frac{E_s}{E} \tag{4}$$

The equivalent stress amplitude σ_{eq} is determined by relating the equivalent strain amplitude to the uniaxial cyclic stress strain curve derived from hysteresis loops at $N_c/2$ cycles.

Low-cycle fatigue tests on planar and cylindrical specimens having high strain concentration and triaxial strain states with constant principal strain directions indicated that the fatigue life to crack initiation N_c can be predicted with fatigue data from unnotched specimens [15] by means of the equivalent strain amplitude according to the Eq 3.

As reported in Ref 14 several suggestions have been made to account for changing principal strain directions in deriving an equivalent strain. Because of the complexity of multiaxial fatigue, a general solution to this problem cannot be given. But here a simplified suggestion for ductile material is described that takes into account the mentioned interaction of deformations on different surface planes due to a change of principal strain directions. The original suggestion [4] led to imaginary solutions.

According to the von Mises yield criterion, failure of ductile materials is induced mainly by the effective shear strain. In most cases the fatigue failure starts on the surface, with a triaxial strain state having at least one constant direction of principal strain. The effective shear strain amplitude can be calculated from the following relation [4]

$$\gamma_{eff} = \left[\frac{1}{\pi} \times \int_o^{\pi} [\gamma(\phi)]^2 \times d\,\phi \right]^{1/2} \tag{5}$$

where $\gamma(\phi)$ is the shear strain amplitude on an interference plane ϕ on the surface (refer to Fig. 6). According to the effective stress hypothesis [4] the equivalent strain is then

$$\epsilon_{eq} = \frac{5}{4(1 + \mu)} \times \gamma_{eff} \tag{6}$$

For an in-phase strain state the effective shear strain amplitude is

$$\gamma_{eff} = \frac{4}{5} \left[\epsilon_x^2 + \epsilon_y^2 + \epsilon_z^2 - \epsilon_x \times \epsilon_y - \epsilon_x \times \epsilon_z - \epsilon_y \times \epsilon_z + \frac{3}{4} (\gamma_{xy}^2 + \gamma_{xz}^2 + \gamma_{yz}^2) \right]^{1/2} \tag{7}$$

For a uniaxial strain state with $\epsilon_y = \epsilon_z = -\mu \times \epsilon_x$ and $\gamma_{xy} = \gamma_{xz} = \gamma_{yz} = 0$ the equivalent strain reduces to $\epsilon_{eq} = \epsilon_x$. Equation 6 is derived from Eq 7 for uniaxial strain state. Further details of this procedure will be discussed after presenting the test results. In this paper the fatigue life evaluation considers only the life to crack initiation and not crack propagation life. Concepts for multiaxial fatigue assuming cracks from the beginning of the fatigue life [*13*] are not discussed.

Materials, Specimen Test Performance, and Program

The investigations were carried out with the cyclically softening quenched and tempered steel 30Cr-Ni-Mo 8 (similar to AISI Type 4340) and the cyclically hardening quenched austenitic steel X 10Cr-Ni-Ti 18 9 (similar to AISI Type 321), both used for vessels, piping, shafts, etc. The material properties are given in Tables 1 and 2.

Figure 1 shows the test specimen and its fixture. The axial load was applied by a 100 kN actuator and the torsional moment by a 25 kN servohydraulic

TABLE 1—*Material properties of the steel 30Cr-Ni-Mo 8, quenched and tempered (similar to AISI Type 4340).*

	Chemical Composition		
C = 0.26 to 0.33%	P ≤ 0.035%		Mo = 0.30 to 0.50%
Si = 0.15 to 0.40%	S ≤ 0.035%		Ni = 1.80 to 2.20%
Mn = 0.30 to 0.60%	Cr ≤ 1.80 to 2.20%		
	Monotonic Properties		
True tensile strength	σ_f'	[MPa]	2405
Tensile strength	S_u	[MPa]	1030
Tensile yield stress	$S_{y,monotonic}$	[MPa]	835
Stress coefficient	$K_{\sigma,monotonic}$	[MPa]	1313
Strain hardening exponent	$n_{\sigma,monotonic}$		0.075
Elongation	e		0.16
Area reduction	RA		0.66
Young's modulus	E	[GPa]	212
Poisson's constant	μ_{el}		0.28
Shear strength	τ_m	[MPa]	715
Shear yield stress	$\tau_{y,monotonic}$	[MPa]	580
Shear stress coefficient	$K_{\tau,monotonic}$	[MPa]	879
Shear hardening exponent	$n_{\tau,monotonic}$		0.064
Shear modulus	G	[GPa]	82
	Cyclic Properties		
Yield stress	$S_{y,cyclic}$	[MPa]	710
Stress coefficient	$K_{\sigma,cyclic}$	[MPa]	1013
Strain hardening exponent	$n_{\sigma,cyclic}$		0.055
Shear yield stress	$\tau_{y,cyclic}$	[MPa]	496
Shear stress coefficient	$K_{\tau,cyclic}$	[MPa]	567
Shear hardening exponent	$n_{\tau,cyclic}$		0.020

actuator described in Ref *4*. The axial strain and shear strain control for a gage length of 25 mm was performed using an extensometer, calibrated by strain gages on the test specimen. The reason for the axial and shear strain control is that the local strains in critical areas of most structural components are also deformation controlled because of inhomogenous deformation distributions, multiaxial strain states, and resulting constraints [*15*].

After the basic constant amplitude fatigue tests under pure axial strain and pure torsional shear strain, fatigue tests were conducted under combined in- and out-of-phase strain control. For all tests the frequency was 1 Hz, and the strains were completely reversed: $R_\epsilon = R_\gamma = -1$.

For an adequate determination of the *S-N* curves the fatigue tests were carried out at four strain levels in the range 5×10^2 to 2×10^5 cycles to crack initiation. Each level was covered by at least three tests. The fatigue life to crack initiation N_c was defined as the fatigue life for which a crack depth of a ≤ 1 mm with an area of about 1 mm^2 was reached. At this crack depth, fixed as a practical failure criterion, the continuously registered axial load range and the torsional moment range, respectively, began to decrease significantly. During each test the load-deformation curves were plotted periodically.

TABLE 2—*Material properties of the austenitical stainless steel X 10Cr-Ni-Ti 18 9, quenched (AISI Type 321).*

Chemical Composition			
$C \leq 0.10\%$	Cr = 17.0 to 19.0%	Ni = 9.0 to 11.5%	$Ti \geq 0.50\%$
Monotonic Properties			
True tensile strength	σ_f'	[MPa]	1320
Tensile strength	S_u	[MPa]	605
Tensile yield stress	$S_{y,\text{monotonic}}$	[MPa]	198
Stress coefficient	$K_{\sigma,\text{monotonic}}$	[MPa]	455
Strain hardening exponent	$n_{\sigma,\text{monotonic}}$		0.126
Elongation	e		0.59
Area reduction	RA		0.74
Young's modulus	E	[GPa]	200
Poisson's constant	μ_{el}		0.28
Shear strength	τ_m	[MPa]	426
Shear yield stress	$\tau_{y,\text{monotonic}}$	[MPa]	150
Shear stress coefficient	$K_{\tau,\text{monotonic}}$	[MPa]	260
Shear hardening exponent	$n_{\tau,\text{monotonic}}$		0.084
Shear modulus	G	[GPa]	79.1
Cyclic Properties			
Yield stress	$S_{y,\text{cyclic}}$	[MPa]	280
Stress coefficient	$K_{\sigma,\text{cyclic}}$	[MPa]	1014
Strain hardening exponent	$n_{\sigma,\text{cyclic}}$		0.199
Shear yield stress	$\tau_{y,\text{cyclic}}$	[MPa]	196
Shear stress coefficient	$K_{\tau,\text{cyclic}}$	[MPa]	713
Shear hardening exponent	$n_{\tau,\text{cyclic}}$		0.196

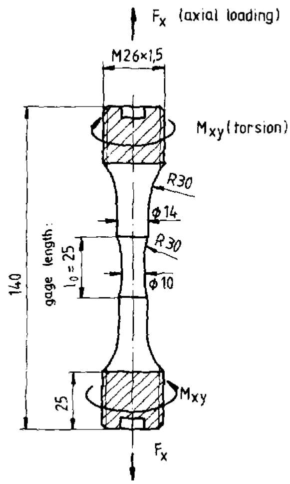

a. Test Specimen (dimensions in mm)

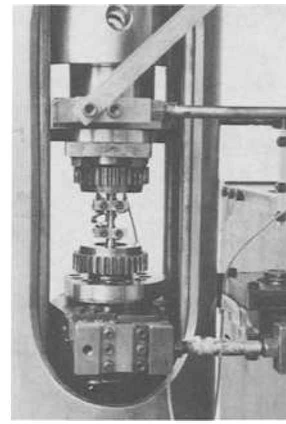

b. Specimen in Test Fixture with Extensometer for Axial Strain and Shear Strain Control

FIG. 1—*Test specimen and fixture.*

Experimental Results

Monotonic and Cyclic Material Properties for Pure Axial Strain and Pure Shear Strain

The conventional monotonic properties as well as cyclic properties are given in Tables 1 and 2. The stress coefficients K and strain-hardening exponents n [17] are derived from monotonic stress-strain curves and cyclic stress-strain curves obtained in deformation controlled tests for the stabilized state at $N_c/2$ (Fig. 2). With these constants the relations between stresses and strains are given by

$$\sigma_a = K \times (\epsilon_{xa,\mathrm{pl}})^n \tag{8}$$

and

$$\epsilon_{xa,\mathrm{tot}} = \frac{\sigma_a}{E} + 0.002 \times \left(\frac{\sigma_a}{S_y}\right)^{1/n} \tag{9}$$

For pure shear the stresses, strains, and Young's modulus are substituted by the shear stress, shear, and shear modulus. The low-cycle fatigue behavior (Figs. 3 and 4) is described by the strain-life relation [17]

$$\epsilon_{xa,\mathrm{tot}} = \epsilon_{xa} = \epsilon_{xa,\mathrm{el}} + \epsilon_{xa,\mathrm{pl}} \tag{10}$$

with

$$\epsilon_{xa,\mathrm{el}} = S \times N_c^{-s} \quad \text{and} \quad \epsilon_{xa,\mathrm{pl}} = T \times N_c^{-t} \tag{11}$$

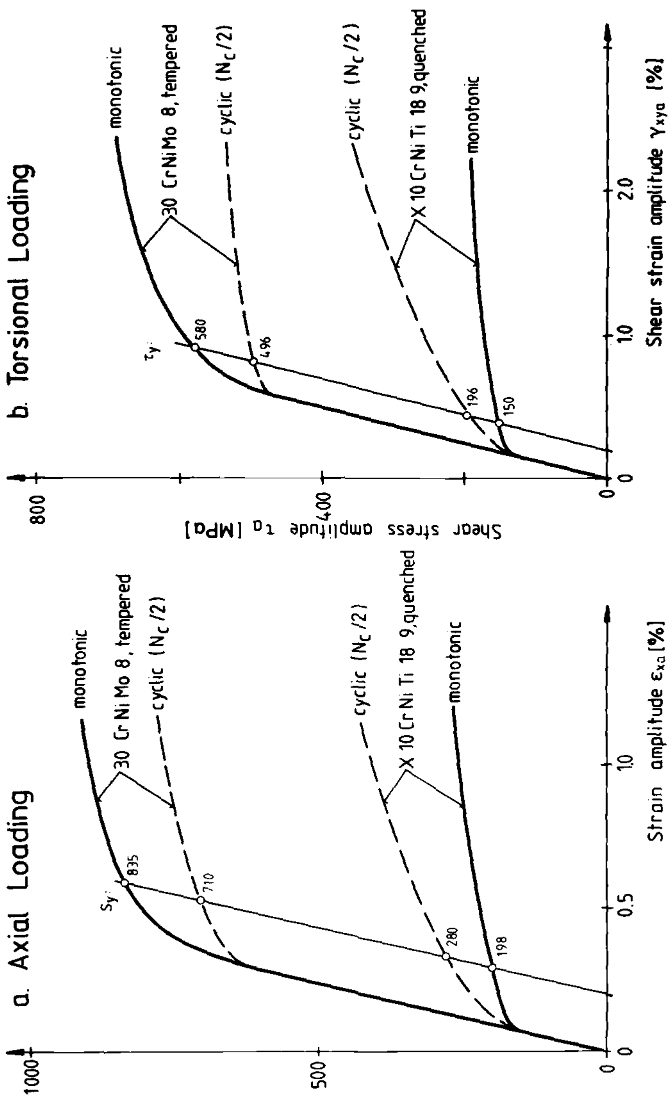

FIG. 2—*Monotonic and cyclic stress-strain curves.*

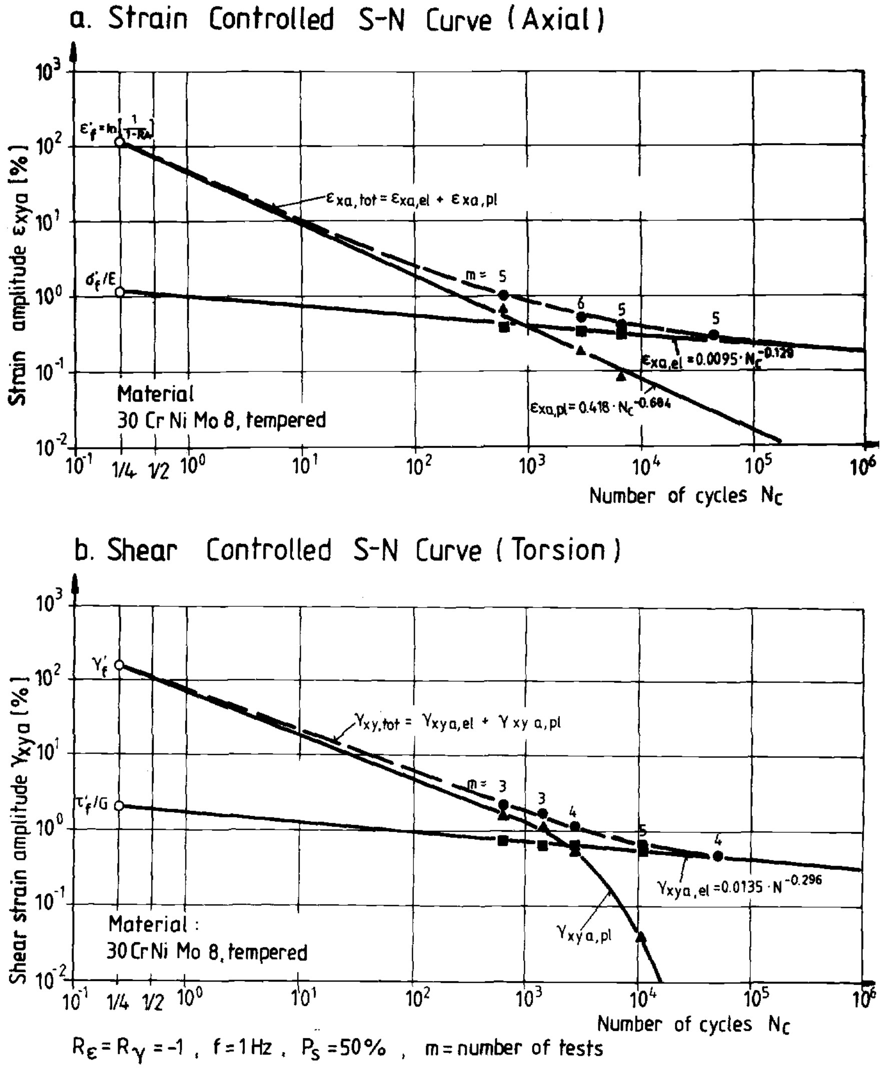

FIG. 3—*Deformation controlled* S-N *curves, failure criterion: initial crack* a $\leq$ *1 mm.*

The constants S, s, T, and t are derivable from Figs. 3 and 4 for the appropriate elastic and plastic portions of the total strain amplitude. These portions are valid for the as-stabilized material state at $N_c/2$. For pure shear the axial strains are substituted by shear strains.

The materials investigated show a very different cyclic strength behavior. While the high-strength steel 30Cr-Ni-Mo 8 shows a cyclic softening (Fig. 2)

$$\frac{S_{y,\mathrm{cyclic}}}{S_{y,\mathrm{monotonic}}} = 0.85 \quad \text{and} \quad \frac{\tau_{y,\mathrm{cyclic}}}{\tau_{y,\mathrm{monotonic}}} = 0.86 \tag{12}$$

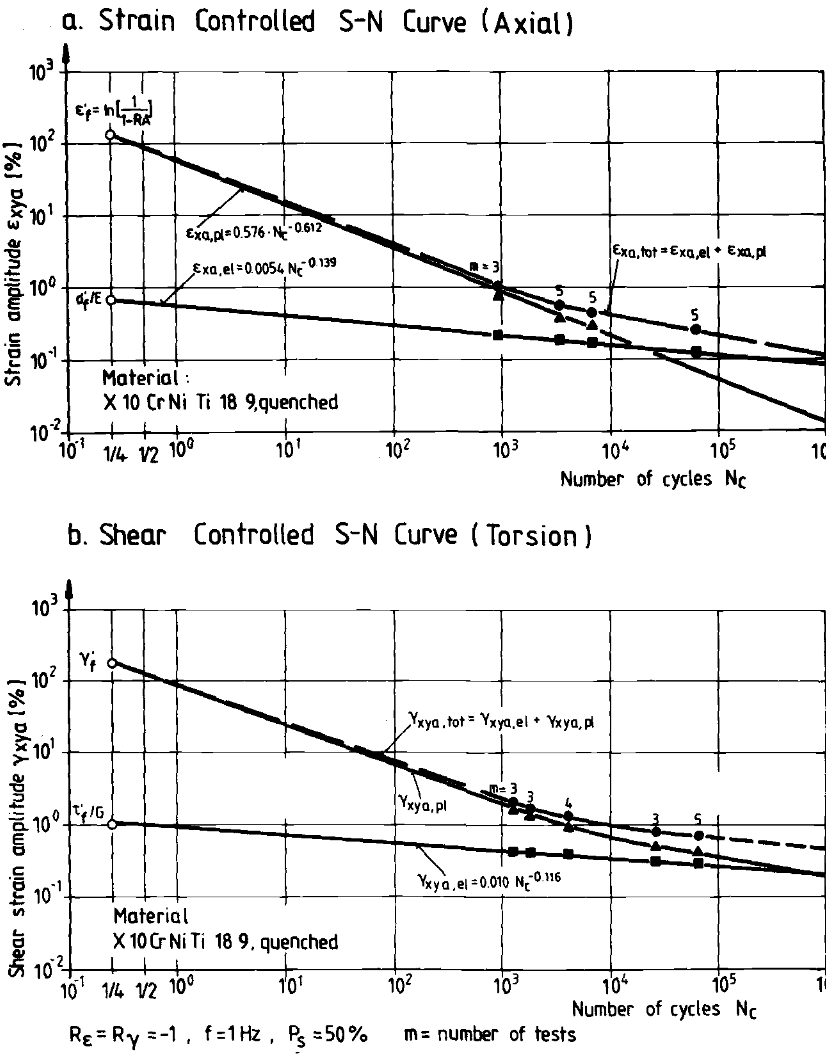

FIG. 4—*Deformation controlled* S-N *curves, failure criterion: initial crack* a $\leq$ *1 mm.*

the more ductile austenitic steel X 10Cr-Ni-Mo 8 cyclically hardens

$$\frac{S_{y,\text{cyclic}}}{S_{y,\text{monotonic}}} = 1.41 \quad \text{and} \quad \frac{\tau_{y,\text{cyclic}}}{\tau_{y,\text{monotonic}}} = 1.31 \tag{13}$$

Even in the biaxial strain state under pure shear nearly the same amount of cyclic softening and hardening as under axial straining is observed. A mean strain sensitivity for tests under strain ratios $R_\epsilon = R_\gamma = 0$ could not be found in the low-cycle region.

Due to its greater ductility the austenitic steel supports higher axial strain amplitudes in the range below 2×10^4 cycles and higher shear strain amplitudes below 2×10^5 cycles compared to the high-strength steel. But beyond these life times the high-strength steel is superior in axial loading because of the greater elastic deformation resulting from its higher strength.

Figure 5 shows the dependence of the ratios γ_{xy}/ϵ_x and τ_a/σ_a, derived from

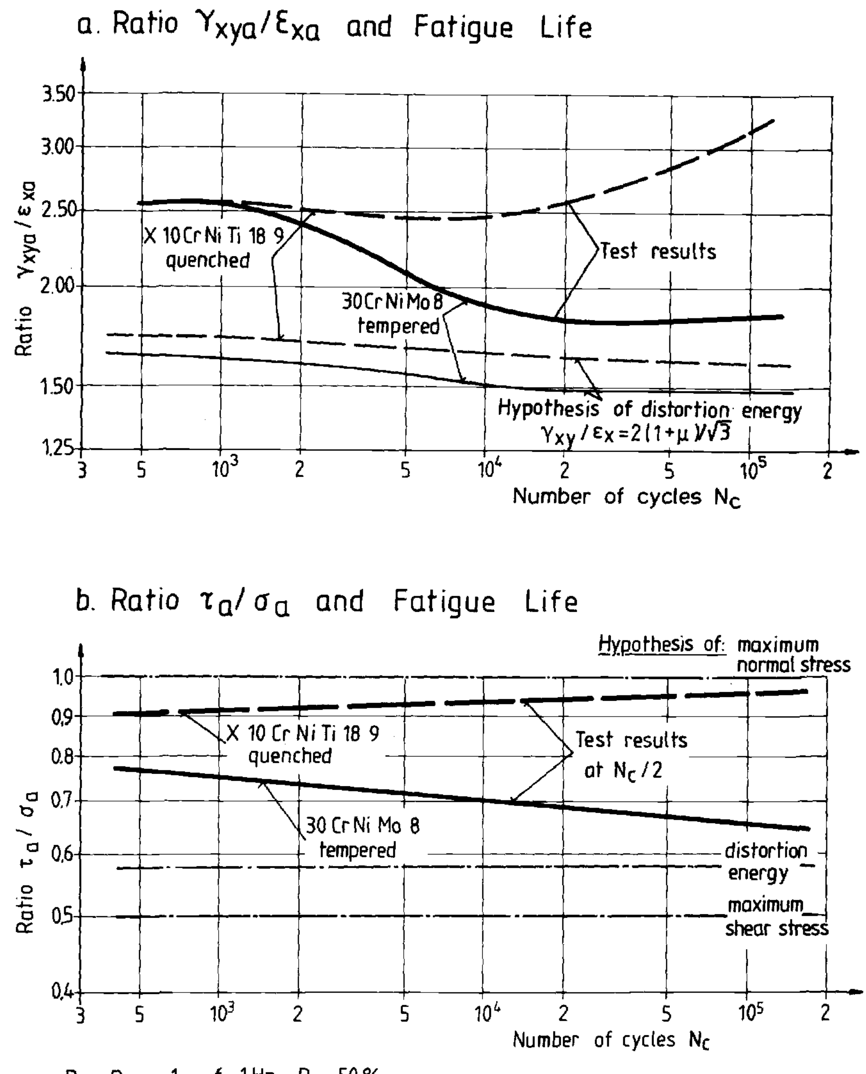

FIG. 5—*Ratios $\gamma_{xya}/\epsilon_{xa}$ and τ_a/σ_a derived from fatigue tests under axial strain and shear strain.*

the tests under pure shear and axial strain, on the number of cycles to crack initiation. They are also compared with hypothetical ratios.

While the ratio γ_{xy}/ϵ_x for the austenitic steel increases, it decreases for the high-strength steel. The higher ratio for the X 10Cr-Ni-Ti 18 9 may result from the greater number of active slip planes due to the austenitic structure. But the theoretical ratios are lower than the experimentally determined ones, indicating that the distortion energy hypothesis overestimates the influence of the torsion induced strains.

The ratio τ_a/σ_a, obtained for the as-stabilized state ($N_c/2$), is from 0.9 to 1.0 for the stainless steel and 0.8 to 0.6 for the 30Cr-Ni-Mo 8. According to [*4,5,18*] the ratio 0.9 to 1.0 indicates brittle material behavior and the applicability of the maximum normal stress hypothesis. At a ratio of 0.8 to 0.6 the material behaves semiductile to ductile when the damage mechanism is influenced both by normal and shear stresses. In this case the distortion energy or shear stress hypotheses should be applied as well as a modification of these hypotheses for semiductile behavior.

The high ductility of the X 10Cr-Ni-Ti 18 9 contradicts the conclusions drawn from the theoretical ratio τ_a/σ_a as the fracture mode shows, Fig. 6*b*. Under pure shear the macroscopic fracture plane is perpendicular to the specimen axis for ductile materials, as the failure is caused by shear; for brittle materials the macroscopic fracture plane lies under 45°, while under pure axial loading the fracture plane has the same position as shown in Fig. 6*a*.

The higher τ_a/σ_a ratio for the austenitic steel may result, as mentioned previously for γ_{xy}/ϵ_x, from its structure, indicating that the conventional hypotheses do not consider features due to the microstructure (number of slip planes, microstructural transformations).

Although the cyclic behavior and the experimental ratios differ for both materials tested, the same macroscopic fracture appearance is obtained indicating same damage mechanisms. The fracture planes in Fig. 6*c* and *d* are planes where the maximum shear strains under the combined loading acted. The determination of the fracture plane will be discussed next.

Tests Under Combined Axial and Torsional Shear Strains

The tests with the unnotched specimens (Fig. 1*a*) were carried out under total strain control, where

$$\epsilon_x(t) = \epsilon_{xa} \times \sin \omega t \tag{14}$$

$$\epsilon_y(t) = \epsilon_z(t) = -\mu \times \epsilon_x(t) \tag{15}$$

$$\gamma_{xy}(t) = \gamma_{xya} \times \sin(\omega t - \delta) \tag{16}$$

$$\gamma_{xz}(t) = \gamma_{yz}(t) = 0 \tag{17}$$

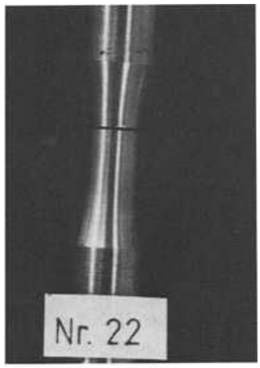

$\varepsilon_{xa} = 0.40$ [%] , $R_\varepsilon = -1$
$N_c = 5100$, $N_f = 5695$
Fracture plane : $\varphi = 0°$

$\gamma_{xya} = 0.50$ [%] , $R_\gamma = -1$
$N_c = 17420$, $N_f = 21120$
Fracture plane : $\varphi = 0°$

c. Combined Axial and Shear Strain

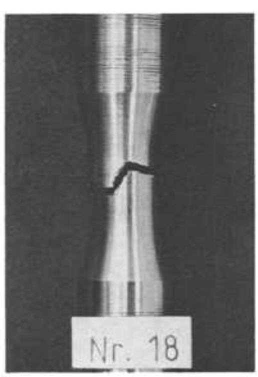

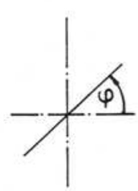

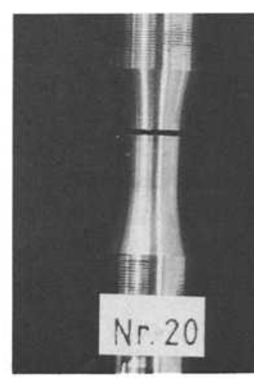

$\varepsilon_{xa} = 0.36$ [%] , $\gamma_{xya} = 0.54$ [%] $R_\varepsilon = R_\gamma = -1$

Phase angle : $\delta = 0°$
$N_c = 3625$ $N_f = 4625$
Facture plane : $\varphi = 70°$

$\delta = 90°$
$N_c = 1330$ $N_f = 1634$
$\varphi = 0°$

Material : 30 Cr Ni Mo 8 tempered

FIG. 6—*Fracture under pure and combined axial strain and shear strain.*

The strain state is triaxial and the stress state biaxial. For the combined tests the shear amplitude was chosen to be

$$\gamma_{xya} = \epsilon_{xa} \times 2(1 + \mu)/\sqrt{3} \tag{18}$$

According to the distortion energy hypothesis it is then assumed that the equivalent strain

$$\epsilon_{\text{eq}} = \left[\epsilon_x^2 + \frac{3}{4(1 + \mu)^2} \times \gamma_{xy}^2\right]^{1/2} \tag{19}$$

since the applied strain state consists of equal deformation in the axial and torsional straining modes. The Poisson's constant is determined according to Eq 4. The out-of-phase tests were carried out mainly with the phase angle $\delta = 90°$ between $\epsilon_x(t)$ and $\gamma_{xy}(t)$, because in several publications this angle is considered as one of the most severe test conditions in comparison to the in-phase situation [*4,5,14*]. In some tests the phase angles $\delta = 45°$ and $135°$ were also applied (see definition of δ on Fig. 9).

Figure 7 shows the test results for the steels 30Cr-Ni-Mo 8 and X 10Cr-Ni-Ti 18 9 comparing them also with the results obtained for the fatigue tests under axial strain and torsion. For axial strain the applied longitudinal strain ϵ_{xa} is identical to the equivalent strain amplitude. For the case of torsional shear, it is transformed into an equivalent strain by Eq 19. For the same number of cycles to crack initiation the equivalent strain derived for torsional shear is higher than the axial strain because the distortion energy hypothesis overestimates the damaging influence of the torsion induced shear. The overestimation for the austenitic steel is more pronounced. An evaluation of pure elastic shear stresses according to the distortion energy hypothesis and the comparison of pure elastic normal stresses with the data obtained in [*4*] for finite fatigue life leads to the same overestimation of the torsion induced shear stresses.

A phase angle of $\delta = 90°$ between axial strain and shear strain decreases the fatigue life for both materials by a factor of two. The reason for this reduction can be recognized from Fig. 8.

Under the same applied deformation the load amplitudes increase so that the stress response in the out-of-phase situation is higher than for the in-phase condition. This implies material hardening due to a higher interference of dislocations, which requires higher loading resulting in earlier crack initiation. A higher interference of dislocations may be explained by the changing principal strain directions

$$\phi(t) = \frac{1}{2} \text{arc tan} \frac{\gamma_{xy}(t)}{\epsilon_x(t) - \epsilon_y(t)} \tag{20}$$

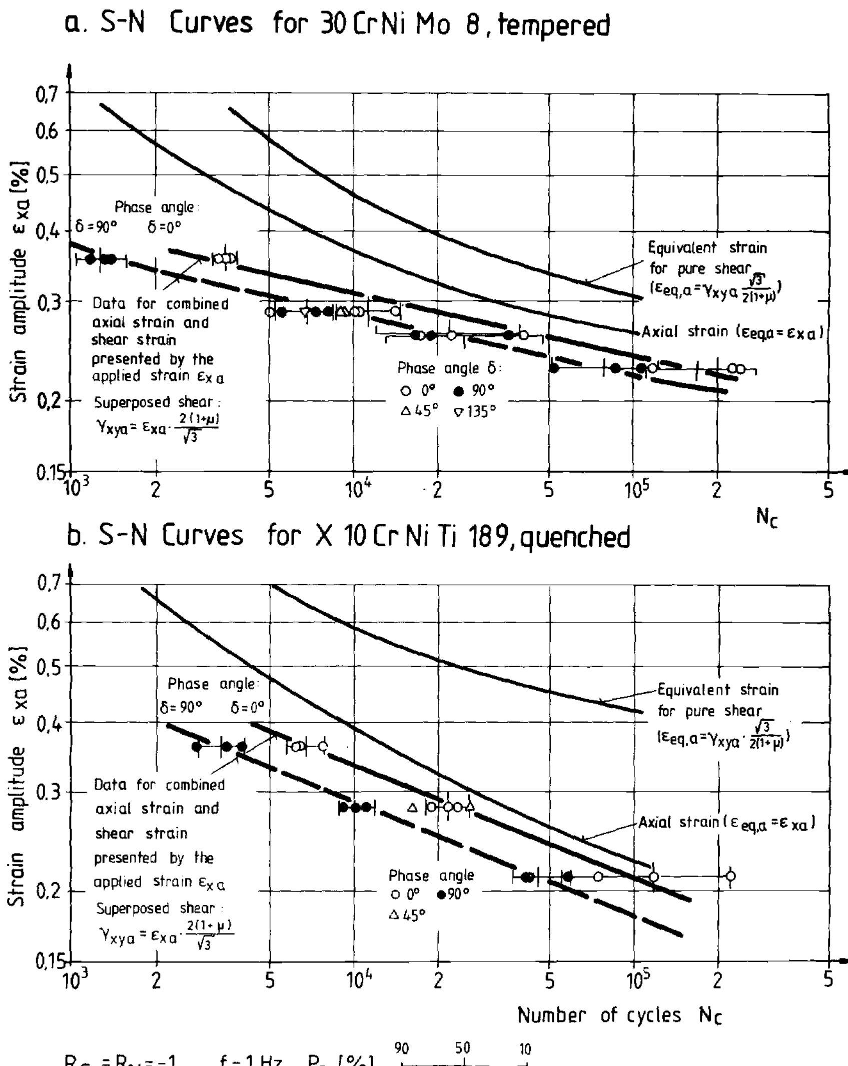

FIG. 7—S-N *curves for combined axial and shear strain, failure criterion: initial crack* a $\leq$ *1 mm.*

According to Eq (20), out-of-phase straining will be likely to activate dislocations in more slip planes than in-phase straining. This phenomenon is demonstrated in Ref *19* by transmission electron microscopy.

A slight cyclic softening under combined straining was only observed at the highest deformation level for the 30Cr-Ni-Mo 8. For all other levels, also for the X 10Cr-Ni-Ti 18 9, the plotted hysteresis loops showed a neutral behavior during the fatigue life to crack initiation.

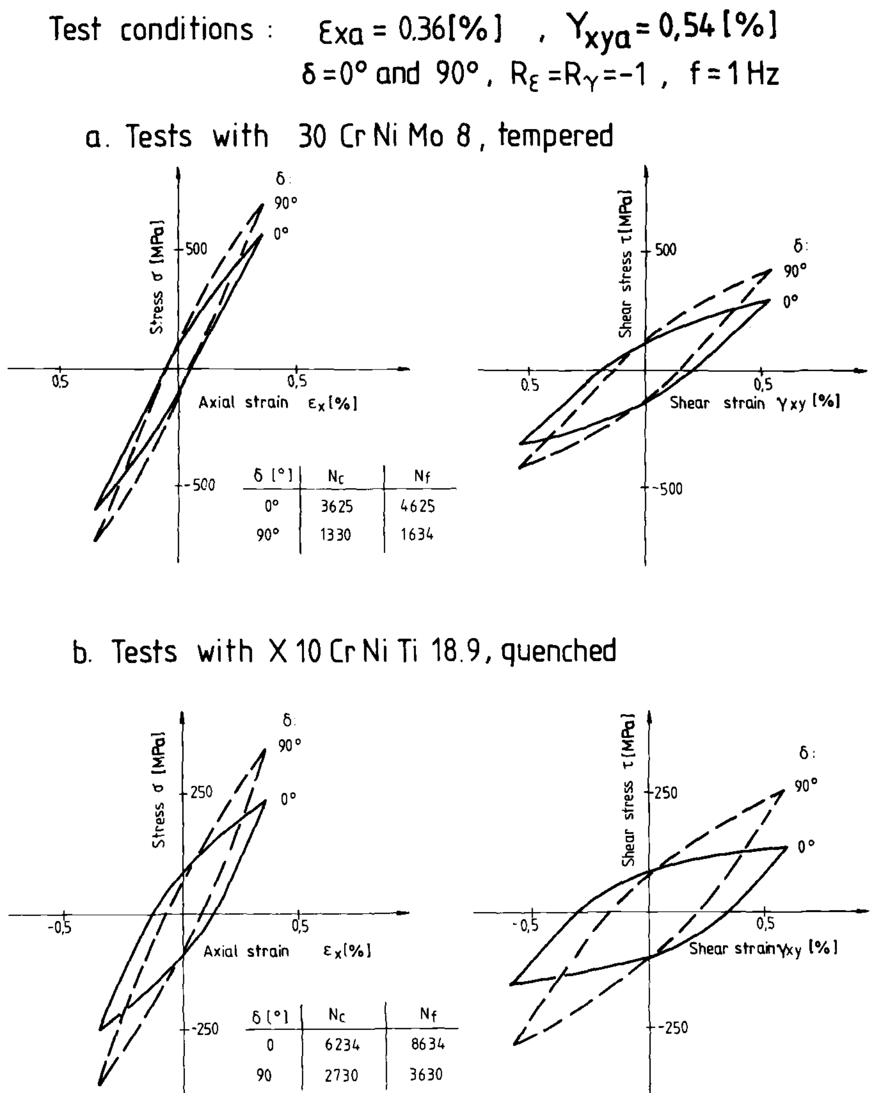

FIG. 8—*Stabilized hysteresis at* $N_c/2$ *for combined axial and shear strain.*

A phase angle of 45° shows a slight reduction of fatigue life compared with the angle of 0° for both materials. The phase angle of 135°, applied only to the 30Cr-Ni-Mo 8 material, decreases the fatigue life, similar to the angle of 90° (Fig. 7).

Despite the cyclic softening of the 30Cr-Ni-Mo 8 steel and the cyclic hardening of X 10Cr-Ni-Ti 18 9 under axial strain or torsion strain, the materials tested behave in a neutral manner under combined deformations. This behavior indicates that material and damage accumulation laws obtained under pure axial loading are not valid for multiaxial loading.

Calculation of the Equivalent Strain

Because of the decisive effect of shear strains on crack initiation several fatigue hypotheses are shear strain-based [*12–14*] and use parameters such as octahedral shear strain, maximum shear-strain acting on the surface or on a plane 45° to the surface, etc. Due to the phenomenon recognized in Fig. 8, the calculation procedure suggested in this paper assumes that the damage for the investigated triaxial strain and biaxial stress state is caused only by the interaction of shear strains

$$\gamma(\phi, t) = [\epsilon_y(t) - \epsilon_x(t)] \times \sin 2\phi + \gamma_{xy}(t) \times \cos 2\phi \tag{21}$$

acting on different interference planes ϕ on the surface (see definition of ϕ on Fig. 6). This interaction is taken into account in the following way

(*a*) for each interference plane the shear amplitudes $\gamma(\phi)_a$ are calculated, and
(*b*) then the arithmetic mean value is determined

$$\gamma_{a,\text{arith}} = \frac{1}{\pi} \int_o^{\pi} \gamma(\phi)_a \times d\phi \tag{22}$$

The equivalent strain amplitude is calculated according to the effective strain hypothesis [*4*]

$$\epsilon_{\text{eq},a} = \frac{5}{4(1 + \mu)} \times \gamma_{a,\text{arith}} \tag{23}$$

With this equivalent strain amplitude the fatigue life can be derived from an *S-N* curve obtained under axial strain.

This calculation procedure does not consider mean strain effects because their influence may be neglected in the range of low-cycle fatigue if they are not greater than the amplitudes being applied. It also does not consider features such as cyclic hardening or softening, which were not observed under multiaxial loading. The arithmetic mean value in the out-of-phase case is higher than for the in-phase case. This results in a higher equivalent strain and a fatigue life reduction in comparison to the in-phase condition. The fracture occurs in the plane in which the maximum shear strain amplitude $\gamma(\phi)_a$ acts. The fracture planes on Fig. 6*c* and *d* were verified by this calculation procedure. As the effective mean shear values according to Eq 5 do not differ for the phase angles investigated, they are not taken into account.

Figure 9 shows the influence of the phase angle on the ratio between the applied strain amplitudes giving $N_c = 10^4$ under combined and uniaxial deformation states. The comparison between experimental and calculated fatigue lives to crack initiation is presented in Fig. 10. The approach in the low-cycle fatigue region is satisfactory. The best results are obtained in the region around 10^4 cycles to crack initiation.

Summary and Conclusions

The deformation controlled tests carried out with the 30Cr-Ni-Mo 8 steel and the X 10Cr-Ni-Ti 18 9 stainless steel, together with a suggested calculation procedure cover practical cases in which local strains due to axial loading or bending and local shears due to torsional loading may occur.

The results obtained under combined multiaxial strain states show that the material cyclic softening or hardening behavior is not the same as under axial deformation. The observed increase of the stresses by an out-of-phase loading may explain the observed fatigue life reduction in comparison to the in-phase situation. This phenomenon is predicted by the arithmetic mean value of the shear amplitudes acting on different interference planes. But as the reasons for this phenomenon are not yet understood, further investigations should be done.

The fatigue life reduction at a phase angle of 90° between axial and torsion induced strains in the low-cycle fatigue region has been also observed in other investigations [*14*]. Load controlled tests under combined axial and torsional loading of unnotched cylindrical specimens give for the phase angle of 90° an increase of the fatigue life [*4*], probably because the uncontrolled deformations are higher in the in-phase conditions. This comparison between deformation and

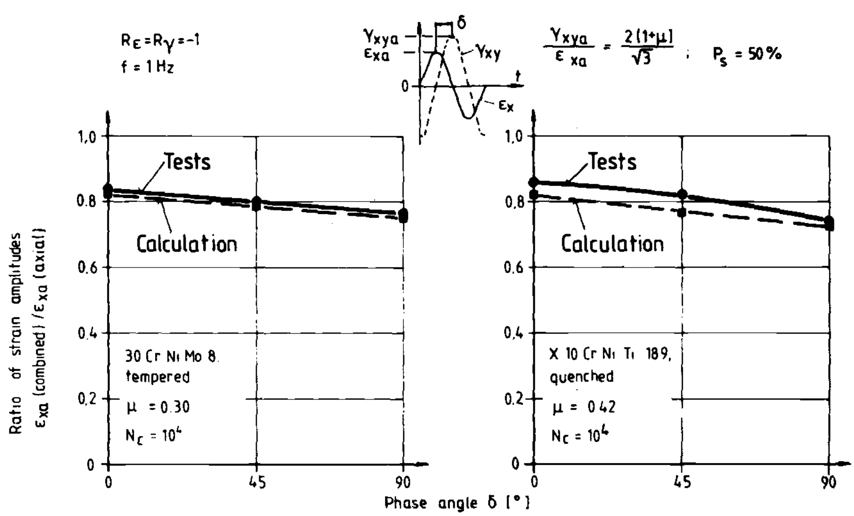

FIG. 9—*Influence of phase angle on the ratio of strain amplitudes.*

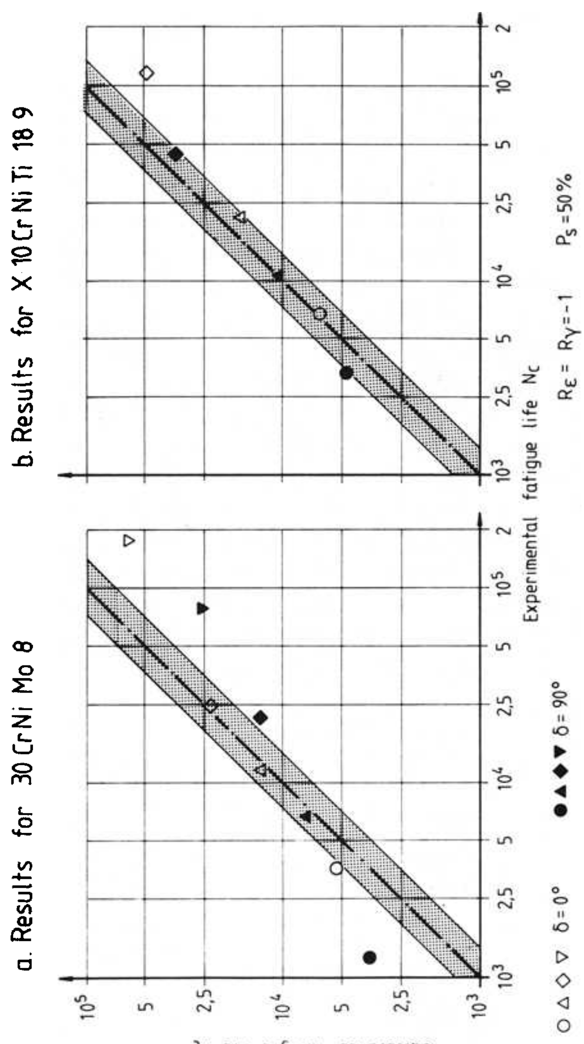

FIG. 10—*Comparison of experimental and calculated fatigue lives.*

load controlled tests shows that for practical applications it must be decided whether the local strains and shears are deformation controlled or not. For such an evaluation further criteria must be developed.

Acknowledgments

The authors acknowledge the German Research Community, Bonn, (DFG) for the financial support and K. Amelung for the test performance.

References

[*1*] Tresca, H., "Mémoires sur l'ecoulement des corps solides," *Mémoires présentés par diverses savants,* Vol. 18, 1868, pp. 733–799; Vol. 20, 1872, p. 169.

[*2*] Mises, R. V. in Mechanik der festen Körper im plastisch deformablen Zustand *Göttinger Nachtuchtenfür mathematisch physikatische Klasse,* 1913, pp. 582–592.

[*3*] ASME Boiler and Pressure Vessel Code, Section III, Code Case N-47-12, Rules for Construction of Nuclear Power Plant Components, 1980.

[*4*] Simbürger, A., "Fatigue Behaviour of Ductile Materials under Multiaxial out of Phase Stresses with Constant and Changing Directions of Principal Stresses," Fraunhofer-Institut für Betriebsfestigkeit (LBF), Darmstadt, Report No. FB-121, 1975, in German.

[*5*] Grubisic, V. and Simbürger, A. in *Fatigue under Combined Out-of-Phase Multiaxial Stresses;* International Conference on Fatigue Testing and Design, Society of Environmental Engineers, London, 1976, pp. 27.1–27.8.

[*6*] Pascoe, K. J. and de Villiers, J. W. R., *Journal of Strain Analysis,* Vol. 2, No. 2, 1967, pp. 117–126.

[*7*] Taira, S., Inoue, T., and Yoshida, T. in *Proceedings,* Twelfth Japan Congress on Materials Research, 1969, pp. 50–55.

[*8*] Zamrik, S. Y. and Frishmuth, R. E., *Experimental Mechanics,* Vol. 6, No. 8, 1973, pp. 204–208.

[*9*] Miller, J., *Journal of Materials,* Vol. 7, 1972, pp. 307–314.

[*10*] Lohr, R. D. and Ellison, E. G., *Fatigue of Engineering Materials and Structures,* Vol. 3, 1980, pp. 1–17.

[*11*] Sines, G. and Ohgi, G., *Transactions,* American Society of Mechanical Engineers, Vol. 103, 1981, pp. 82–90.

[*12*] Krempl, E., *The Influence of State of Stresses on Low-Cycle Fatigue, ASTM STP 549,* American Society for Testing and Materials, Philadelphia, 1974.

[*13*] Brown, M. W. and Miller, K. J. in *Low-Cycle Fatigue Life and Life Predictions, ASTM STP 770,* 1982, pp. 482–499.

[*14*] Garud, Y. S., *Journal of Testing and Evaluation,* Vol. 9, No. 3, 1981, pp. 165–178.

[*15*] Grubisic, V. and Sonsino, C. M., *Low-Cycle Fatigue Life and Life Predictions, ASTM STP 770,* American Society for Testing and Materials, Philadelphia, 1982, pp. 612–629.

[*16*] Gonyea, D. C. in *Fatigue at Elevated Temperatures, ASTM STP 520,* American Society for Testing and Materials, Philadelphia, 1973, pp. 678–687.

[*17*] Raske, D. T. and Morrow, J. D., *Manual of Low-Cycle Fatigue Testing, ASTM STP 465,* American Society for Testing and Materials, Philadelphia, 1969, pp. 1–25.

[*18*] Grubisic, V. and Sonsino, C. M., "Computer Programs to Determine the Material Behaviour under Multiaxial Fatigue with Constant and Changing Directions of Principle Stresses," Fraunhofer-Institut für Betriebsfestigkeit (LBF), Darmstadt, Technical Information No. 79/76, 1976, in German.

[*19*] Ohnami, M., Sakane, M., and Hamada, N., this publication, pp. 622–634.

Donald L. McDiarmid[1]

Fatigue Under Out-of-Phase Biaxial Stresses of Different Frequencies

REFERENCE: McDiarmid, D. L., "**Fatigue Under Out-of-Phase Biaxial Stresses of Different Frequencies,**" *Multiaxial Fatigue, ASTM STP 853*, K. M. Miller and M. W. Brown, Eds., American Society for Testing and Materials, Philadelphia, 1985, pp. 606–621.

ABSTRACT: An analysis of fatigue under out-of-phase biaxial stresses of different frequencies shows that the stress conditions on the critical shear plane are of a nonconstant amplitude nature. A general expression for the allowable principal stresses to give long life fatigue is derived in terms of the uniaxial fatigue strength and the principal stress amplitude ratio, the expression being independent of both phase angle and frequency ratio. A test system to subject thin-wall cylinders to these stress conditions is described, and the results of tests under a range of out-of-phase angles and frequency ratios are given and discussed in relation to the derived theory. It is suggested that the maximum shear stress criterion of failure can be adapted for use in designing for such complex stress conditions.

KEY WORDS: fatigue (materials), stresses, strains, damage, predictions, service, crack initiation, crack propagation

Nomenclature

α	Frequency ratio = frequency of σ_{2a}/frequency of σ_{1a}
λ	Principal stress amplitude ratio = σ_{2a}/σ_{1a}
ϕ	Out of phase angle, σ_2 leading σ_1 (related to σ_2 where 1 cycle of σ_2 is 360°)
$\sigma_1,\sigma_2,\sigma_3$	Principal stresses ($\sigma_1 > \sigma_2 > \sigma_3$)
$\sigma_{1a},\sigma_{2a},\sigma_{3a}$	Principal stress amplitudes
σ_A	Uniaxial reversed fatigue strength
σ_n	Normal stress amplitude on the plane of maximum range of shear stress
$\sigma_{n12},\sigma_{n23},\sigma_{n31}$	Normal stress amplitudes on the 12,23,31 planes of maximum range of shear stress
τ	Shear stress amplitude
$\tau_{12},\tau_{23},\tau_{31}$	Shear stress amplitudes on the 12,23,31 planes of maximum range of shear stress
12,23,31	Planes of maximum range of shear stress associated with the 1,2,3 principal stress directions.

[1]Senior lecturer, Department of Mechanical Engineering, The City University, London, U.K.

Copyright© 1985 by ASTM International www.astm.org

The majority of components in service suffer a two- or three-dimensional stress state and a nonconstant amplitude stress-time history. This general state of stress is difficult to analyze, and most components have to be designed using uniaxial constant amplitude fatigue data only. Fortunately the most severe stress conditions in service components often occur at a free surface, and, hence, a biaxial stress analysis can be of considerable interest and practical value.

Various theories for multiaxial fatigue have been proposed recently [*1–3*] which correlate well with the available experimental data. These theories suggest that for unnotched specimens the important parameters in fatigue are the maximum shear strain and the strain normal to the plane of maximum shear. The Brown and Miller [*1*] theory showed that the orientation and direction of growth of fatigue cracks could be deduced from a knowledge of the three-dimensional strain field and that it was necessary to differentiate between cracks which propagated along the surface plane and those that propagated away from the surface plane. The theory proposed by McDiarmid [*2*] does not deal specifically with crack growth but offers design relationships in terms of the bulk applied stresses to prevent crack initiation.

Both of these theories have been extended for the case of out-of-phase biaxial stresses [*4–6*] where it is shown that the out-of-phase stresses produce shorter fatigue lives than equal in-phase stresses.

The present paper extends the investigation of fatigue behavior under biaxial stress to the case where the stresses are not only out-of-phase but also at different frequencies. A pressure test cell device designed for use with a standard servohydraulic fatigue test machine and able to test thin-walled tubular test specimens under such conditions is described as are tests on steel specimens subjected to a range of conditions of biaxial stress ratio, out-of-phase angles and frequency of cycling ratio. An analysis of fatigue under such conditions leads to the proposal of a relationship for the prevention of fatigue crack initiation.

Experimental Program

A series of fatigue tests were carried out on thin-wall tubular specimens subjected simultaneously to constant amplitude alternating longitudinal load and alternating differential pressure across the wall thickness. These tests covered the range of principal stress amplitude ratio, out-of-phase angle, and frequency ratio shown in Table 1. Note that in the testing $\sigma_1 = \sigma_{\text{longitudinal}}$ and $\sigma_2 = \sigma_{\text{transverse}}$. The frequency of σ_{2a} was the greater and equalled 30 Hz in the tests conducted.

Material and Specimens

The material used in this investigation was EN24T steel, being the most easily obtained material similar in properties to the EN25 used in extensive fatigue tests of thick-walled cylinders under pressure [*7*]. The material was supplied in 3-m-lengths of 40-mm-diameter bar. The percentage chemical composition was 0.35 to 0.45 carbon, 0.10 to 0.55 silicon, 0.45 to 0.70 manganese, 1.3 to 1.8 nickel, 0.90 to 1.40 chromium, 0.20 to 0.35 molybdenum, and 0.05 sulfur and

TABLE 1—*Test conditions. For all tests, σ_1 is longitudinal and σ_2 is transverse.*

Case	$\lambda = \sigma_{2a}/\sigma_{1a}$	ϕ = Phase Angle	$\alpha = \dfrac{\text{Frequency of } \sigma_{2a}}{\text{Frequency of } \sigma_{1a}}$
1	0		
2	∞		
3	1	0	1
4	1	180°	1
5	1	0	2
6	1	90°	2
7	1	0	3
8	1	180°	3

phosphorus; and the mechanical properties were: tensile strength 850 MN/m^2, yield stress 680 MN/m^2, and elongation 18%.

The specimen dimensions are shown in Fig. 1. The outside diameter of the test section was produced with a fine turned finish, and a special reamer was used to produce a good quality finish in the bore. The longitudinal surface roughness from four specimens selected at random was 0.20 to 0.40 μm centerline average (CLA) along the outside diameter and 0.60 and 0.90 μm CLA along the inside diameter. The wall thickness of 0.635 mm used was a compromise between buckling instability problems and pressure required to produce fatigue failure.

Test Equipment

The thin-wall tubular test specimen was mounted in a pressure test cell device shown in Fig. 2, the complete unit being assembled in a standard +250 kN Schenck fatigue test machine, fitted with an additional high pressure pump capable of applying a differential pressure of ± 35 MN/m^2 across the specimen wall. The bore and annular areas of the specimen subject to pressure were arranged to be equal so that a constant longitudinal stress due to pressure acted on the thin-wall test section of the specimen which could be offset by actuator load to obtain alternating differential pressure.

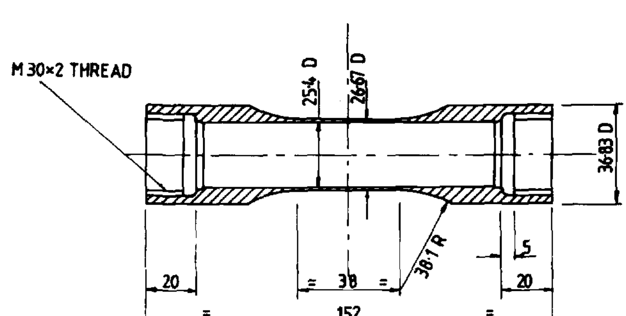

FIG. 1—*The test specimen.*

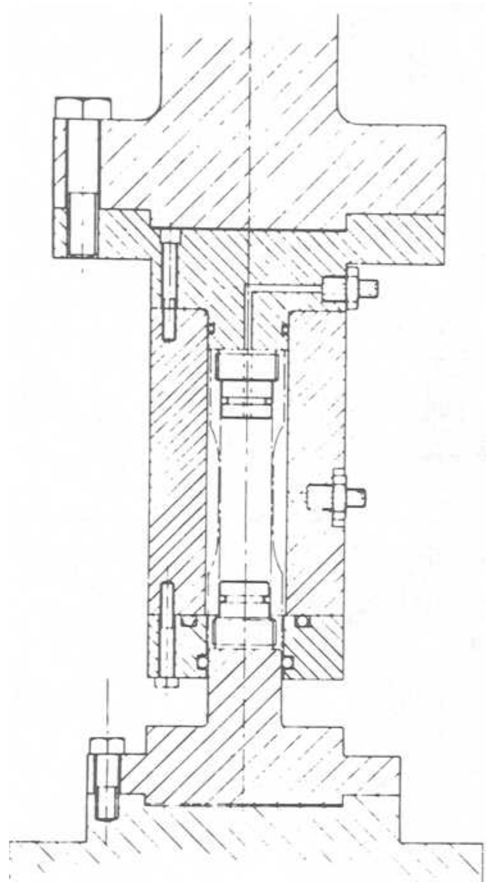

FIG. 2—*The pressure test cell.*

The actuator and pressure cell had independent control units and phase, and frequency ratio could be adjusted using the machine output signals in conjunction with a variable phase function generator and a bandpass filter specially adapted to enable frequency ratios of up to 10 to be obtained, along with a two channel oscilloscope for monitoring purposes.

Specimen failure was detected by the limits on pressure differential tripping out due to leakage through a crack in the specimen wall. Very fine initial cracks, about 3 mm long and difficult to see with the naked eye, were detected by this system. An additional check for maintenance of static differential pressure was carried out before specimens were removed from the test cell.

Test Results

The results of the fatigue tests are shown in Fig. 3. The material is seen to be anisotropic, the transverse fatigue strength being about 65% of the longitudinal

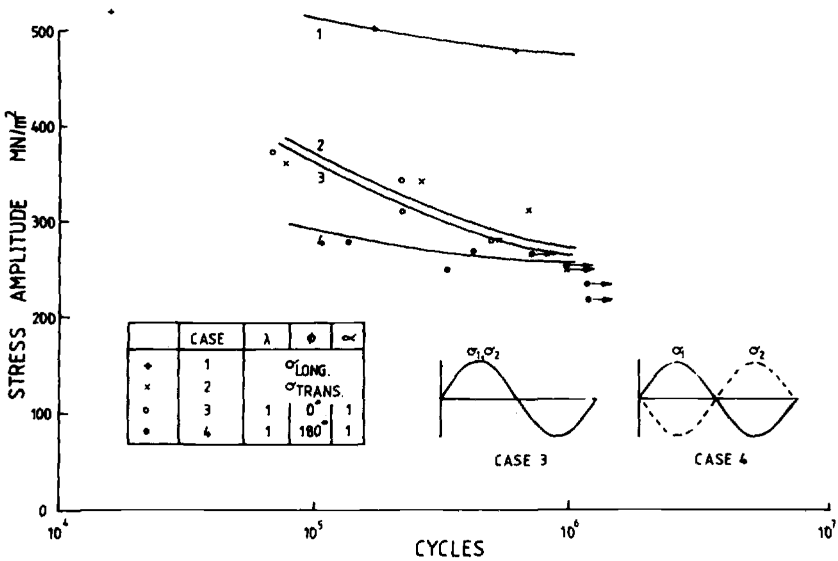

FIG. 3*a*—*Test results, Cases 1 to 4.*

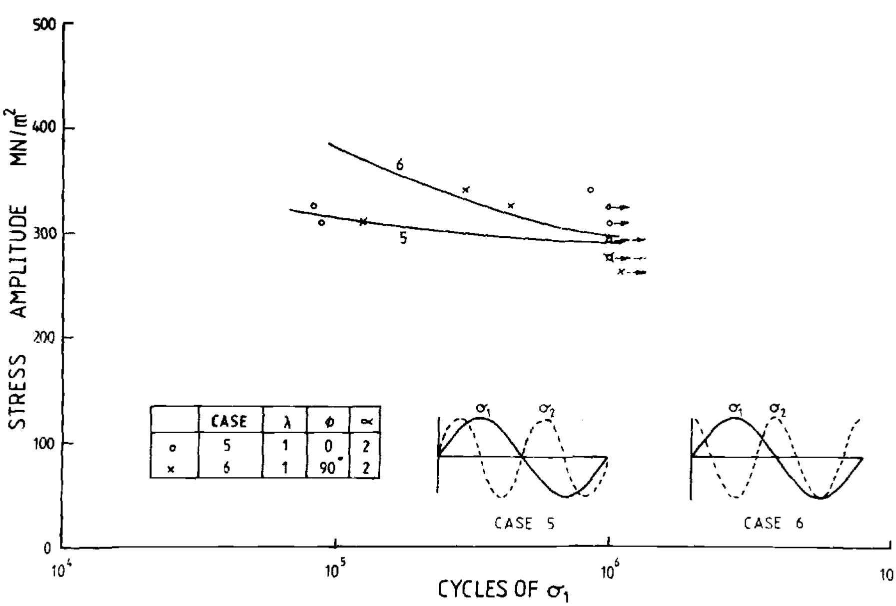

FIG. 3*b*—*Test results. Cases 5 and 6.*

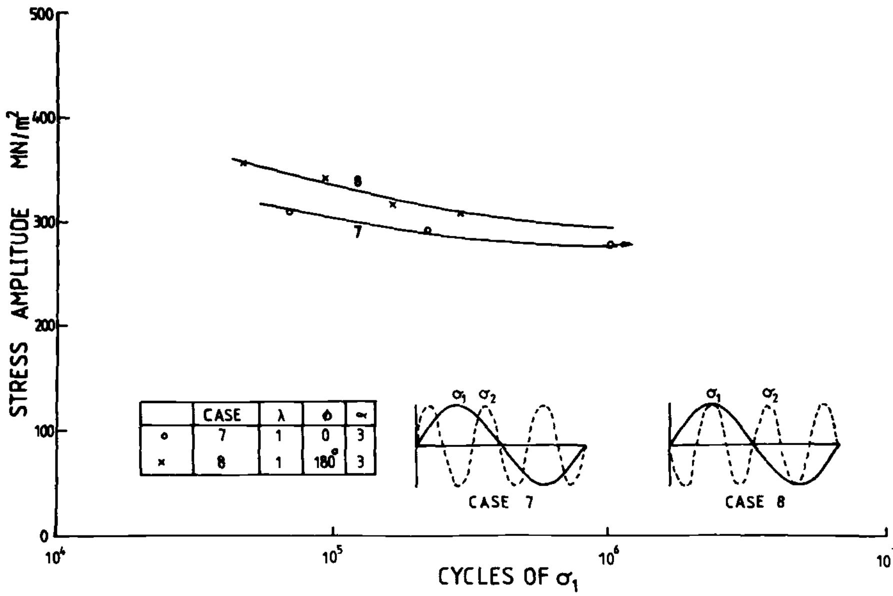

FIG. 3*c*—*Test results, Cases 7 and 8.*

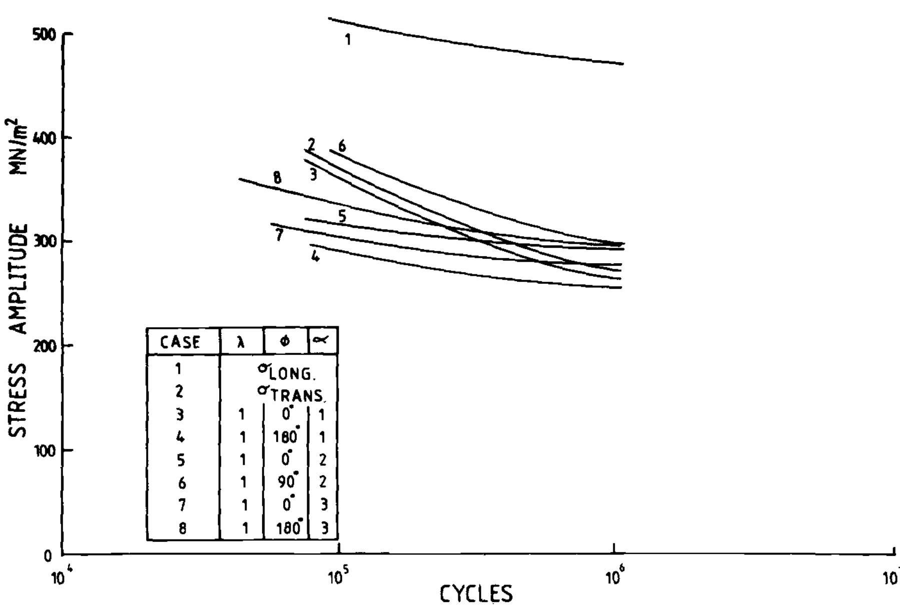

FIG. 3*d*—*Test results, Cases 1 to 8.*

fatigue strength. This is about the limit of the difference found over 40 different steels [8] and a greater effect than the 80% found in the case of EN25 in Ref 7. The test results are discussed later in conjunction with the analysis of the effects of phase difference and frequency of cycling difference in biaxial fatigue.

Analysis of Out-of-Phase Biaxial Stresses at Different Frequencies

To study the effect of phase angle and difference in frequency in fatigue, assume a system in which the principal stress amplitudes $\sigma_{1a} = \sigma_{2a} > \sigma_{3a} = 0$, and that for the principal stresses σ_2 leads σ_1 by an angle of ϕ and that the frequency of cycling of σ_2 is α times the frequency of cycling of σ_1, as shown in Fig. 4 for $\lambda = 1$, $\alpha = 2$, and $\phi = 60°$. Note that ϕ is related to σ_2, where one cycle of σ_2 is equivalent to 360°. It is required to find the variations of the maximum shear stresses τ_{12}, τ_{23}, and τ_{31} and their associated normal stresses σ_{n12}, σ_{n23}, and σ_{n31} for a range of values of amplitude ratio λ, phase angle ϕ, and frequency ratio α.

Using the foregoing notation

$$\tau_{12} = \frac{\sigma_1 - \sigma_2}{2}, \tau_{23} = \frac{\sigma_2 - \sigma_3}{2}, \tau_{31} = \frac{\sigma_3 - \sigma_1}{2} \tag{1}$$

and

$$\sigma_{n12} = \frac{\sigma_1 + \sigma_2}{2}, \sigma_{n23} = \frac{\sigma_2 + \sigma_3}{2}, \sigma_{n31} = \frac{\sigma_3 + \sigma_1}{2} \tag{2}$$

For the case of $\lambda = 1$, $\alpha = 2$, and ϕ_{12} typically 60° as shown in Fig. 4, the variation of shear stress τ_{12} and its associated normal stress σ_{n12} are as shown

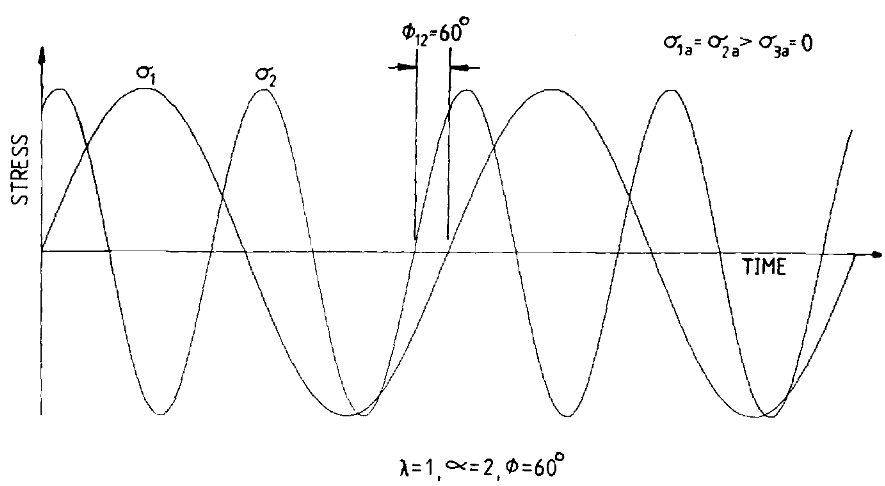

FIG. 4—*Equal amplitude out of phase biaxial stress variation with time at different frequencies.*

in Fig. 5. It should be noted that τ_{12} and σ_{n12} are drawn to a scale twice that of σ_{1a} and σ_{2a} for clarity. The variation of τ_{12} and σ_{n12} for $\lambda = 1$, $\alpha = 3$, $\phi_{12} = 60°$, and $\lambda = 1$, $\alpha = 5$, $\phi_{12} = 60°$ is shown elsewhere [9]. It is clear that although the principal stresses are of constant amplitude the difference in their frequencies is causing τ_{12} and σ_{n12} to have varying amplitude and there is thus a cumulative damage problem. It is also clear that τ_{12} and σ_{n12} are out of phase.

Due to the double complexity of τ_{12} and σ_{n12} not only both being of varying amplitude but also out of phase it is proposed that the various biaxial stress cases of different amplitude ratio, phase, and frequency are compared in the first instance on a maximum shear stress amplitude (Tresca) criterion of failure and the effect of the normal stress variation on the maximum shear stress plane is ignored, although it is known to be a parameter of secondary importance in biaxial equal frequency fatigue [*1,2*].

For the $\lambda = 1$, $\alpha = 2$, $\phi_{12} = 60°$ case considered in Figs. 4 and 5 the other two maximum shear stresses τ_{23} and τ_{31} have amplitudes one half of σ_{2a} and σ_{1a}, respectively, and frequencies equal to those of σ_2 and σ_1, respectively. These shear stress amplitudes are less than that of τ_{12} and are thus considered to be less damaging. It is assumed that the greatest shear stress amplitude will cause the damage leading to fatigue failure.

The variations of τ_{12} and σ_{n12} over a range of λ from 0 to 1 in steps of 0.2, α from 0.5 to 5 in steps of 0.5, and ϕ_{12} from 0 to 180° are shown for two cycles of σ_1 in Ref *10*.

Using the rainflow [*11*] method of cycle counting in the analysis of the τ_{12}

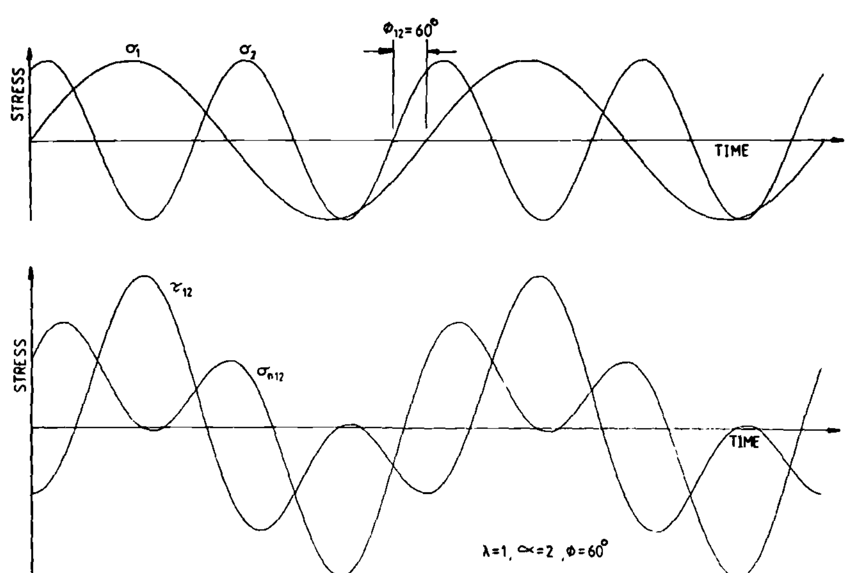

FIG. 5—*Stress variation on the maximum shear plane with time for a frequency ratio of 2.*

stress histories for the various λ, α, ϕ cases gives the resulting shear stress cycles as in Ref *9* and as shown in Fig. 6 for the most damaging cycles only. A few examples are given in Table 2 for the case of $\lambda = 1$ to show that for each cycle of σ_1 we obtain a number of τ_{12} cycles of different amplitude dependent on the value of the frequency ratio. In general cycles of τ_{12} of amplitude less than 0.5 σ_{1a} are taken to be nondamaging. For integer values of α only the largest amplitude τ_{12} cycle is damaging. For $\alpha = 1.5$ and 2.5 the two largest amplitude half cycles of τ_{12} obtained are damaging.

Damage Calculations

Assuming for ease of initial computation that the $\log \tau - \log N$ fatigue curve for a typical material can be represented by a straight line between a shear stress amplitude value of 1.5 σ_A at 10^3 cycles and a fatigue limit value of 0.5 σ_A at 10^7 cycles then the general equation of the $\log \tau - \log N$ line is

$$\log \tau = m \log N + C \tag{3}$$

Substitution of the assumed shear stress values at 10^3 and 10^7 cycles to find the values of m and C gives

$$\log N = -8.382 \log \tau + 8.382 \log (1.5\, \sigma_A) + 3 \tag{4}$$

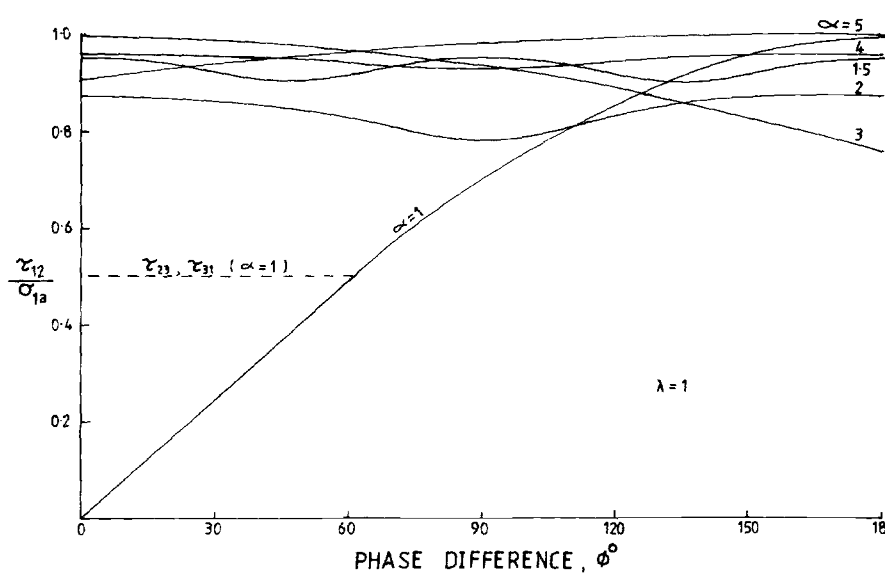

FIG. 6—*Shear stress as a function of maximum principal stress for varying phase difference and frequency ratio.*

TABLE 2—*Shear stress amplitudes resulting from rainflow analysis for one cycle of* σ_1, $\tau_{12} = f(\sigma_{1a})$. *In all cases,* $\lambda = 1$.

α, ϕ°	0	15	30	45	60	75	90	105	120	135	150	165	180
1	0	0.11	0.25	0.38	0.50	0.61	0.71	0.79	0.86	0.92	0.97	0.99	1.00
1.5 (½ cycles)	0.95	0.94	0.92	0.90	0.92	0.94	0.95	0.94	0.92	0.90	0.92	0.94	0.95
	0.60	0.60	0.59	0.58	0.59	0.60	0.60	0.60	0.59	0.58	0.59	0.60	0.60
	0.10	0.11	0.14	0.17	0.14	0.11	0.11	0.11	0.14	0.17	0.14	0.11	0.11
2	0.88	0.88	0.87	0.86	0.84	0.81	0.78	0.81	0.84	0.86	0.87	0.88	0.88
	0.18	0.18	0.19	0.20	0.23	0.25	0.28	0.25	0.23	0.20	0.19	0.18	0.18
2.5 (½ cycles)	0.98	0.97	0.97	0.96	0.97	0.97	0.98	0.97	0.97	0.96	0.97	0.97	0.98
	0.81	0.81	0.81	0.80	0.81	0.81	0.81	0.81	0.81	0.80	0.81	0.81	0.81
	0.28	0.30	0.32	0.34	0.32	0.30	0.28	0.26	0.25	0.24	0.23	0.23	0.22
	0.28	0.26	0.25	0.24	0.23	0.23	0.22	0.23	0.23	0.24	0.25	0.26	0.28
	0.22	0.23	0.23	0.24	0.25	0.26	0.28	0.30	0.32	0.34	0.32	0.30	0.28
3	1.00	1.00	0.99	0.98	0.97	0.95	0.94	0.92	0.89	0.86	0.83	0.79	0.76
	0.28	0.27	0.28	0.28	0.28	0.29	0.30	0.31	0.32	0.32	0.34	0.36	0.38
	0.28	0.27	0.28	0.28	0.28	0.29	0.30	0.31	0.32	0.32	0.34	0.36	0.38
4	0.96	0.96	0.96	0.95	0.94	0.94	0.93	0.94	0.94	0.95	0.96	0.96	0.96
	0.36	0.37	0.38	0.39	0.40	0.41	0.42	0.41	0.40	0.39	0.38	0.37	0.36
	0.36	0.36	0.35	0.35	0.34	0.33	0.33	0.32	0.32	0.32	0.32	0.32	0.32
	0.32	0.32	0.32	0.32	0.32	0.32	0.33	0.33	0.34	0.35	0.35	0.36	0.36
5	0.91	0.92	0.94	0.95	0.96	0.97	0.97	0.97	0.99	0.99	1.00	1.00	1.00
	0.35	0.35	0.35	0.35	0.35	0.36	0.36	0.36	0.36	0.36	0.37	0.38	0.38
	0.35	0.35	0.35	0.35	0.35	0.36	0.36	0.36	0.36	0.36	0.37	0.38	0.38
	0.45	0.44	0.43	0.43	0.42	0.42	0.42	0.41	0.40	0.39	0.39	0.38	0.38
	0.45	0.44	0.43	0.43	0.42	0.42	0.42	0.41	0.40	0.39	0.39	0.38	0.38

Using Eq 4 to find the N-values corresponding to the $\tau_{12} = f(\sigma_{1a})$-values from Table 2 and Ref *9*, N being found as a function of σ_{1a} and σ_A, and using the Miner [*12*] damage sum

$$\sum \frac{n}{N} = 1 \tag{5}$$

we can find the allowable value of σ_{1a}/σ_A for any particular λ, α, ϕ condition as indicated next.

To find the maximum allowable value of σ_{1a} under which fatigue cracks will not initiate in less than 10^7 cycles for equal amplitude biaxial stresses, (*a*) at a frequency ratio $\alpha = 2$ and $\phi = 90°$ out of phase and (*b*) at a frequency ratio $\alpha = 2.5$ and $\phi = 0°$ in phase.

(*a*) For $\lambda = 1$, $\alpha = 2$, $\phi = 90°$ the τ_{12}-values from Table 2 are $0.78\sigma_{1a}$ and $0.28\sigma_{1a}$. For $\tau_{12} = 0.78\sigma_{1a}$ in Eq 4 gives $\log N = 5.380 - 8.382 \log(\sigma_{1a}/\sigma_A)$. Thus when $N = 10^7$ cycles, $\sigma_{1a}/\sigma_A = 0.640$.

(*b*) For each cycle of σ_1, when the frequency ratios are 1.5 and 2.5, Table 2 shows that we obtain 3 and 5 half cycles, respectively, of τ_{12} of different amplitudes. When $\alpha = 2.5$ the two largest half cycles of τ_{12} are damaging. When

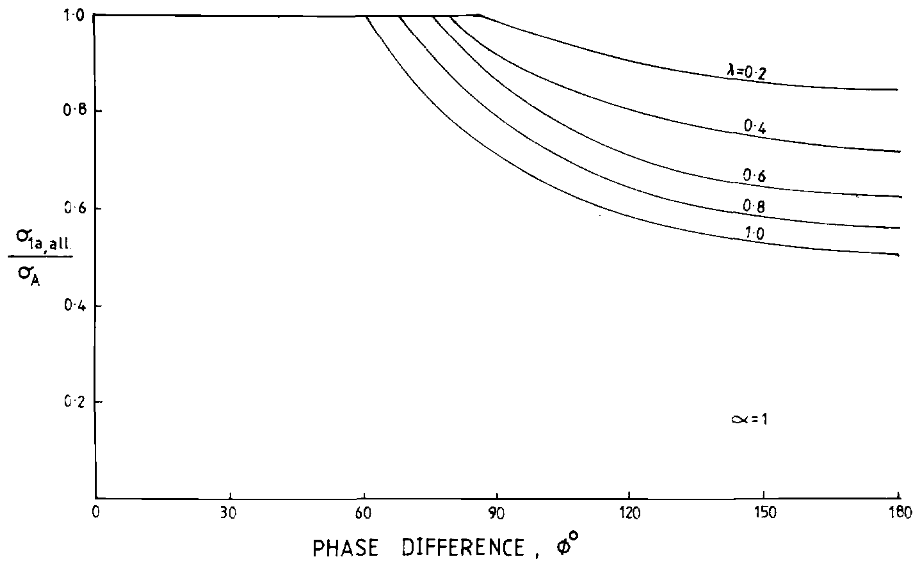

FIG. 7—*Allowable biaxial stresses at the same frequency for varying phase difference and amplitude ratio.*

$\lambda = 1$, $\alpha = 2.5$, $\phi = 0°$ the τ_{12}-values (half cycles) from Table 2 are $(0.98, 0.81, 0.28, 0.28, 0.22)\sigma_{1a}$. Substituting for $\tau_{12} = 0.98\sigma_{1a}$ and $0.81\sigma_{1a}$ in Eq 4 and using Eq 5 gives N-values of 6.01×10^6 and 29.64×10^6, respectively, and hence $\sigma_{1a}/\sigma_A = 0.542$.

Derivation of a General Expression for an Allowable Value of σ_{1a}

Converting the damaging values of τ_{12}/σ_{1a} to σ_{1a} (allowable)/σ_A values as indicated above enables σ_{1a} (allowable)/σ_A versus ϕ_{12} for $\lambda = 0.2$ to 1.0 to be shown as in Fig. 7 for $\alpha = 1$.

From similar plots for $\alpha = 0.5$ to 5.0, σ_{1a} (allowable) can be plotted versus α for $\lambda = 0.2$ to 1.0 as shown in Fig. 8 for any value of ϕ.

Limiting values of σ_{1a}/σ_A are indicated and were found using the maximum shear stress criterion of failure assuming the reversed shear fatigue strength as $\sigma_A/2$.

In general, the maximum shear stress occurs when the biaxial stresses are maximum positive and maximum negative, respectively, at the same time. Thus using the maximum shear stress criterion of failure in fatigue

$$\tau_{12(\text{allowable})} = \frac{\sigma_A}{2} = \frac{\sigma_{1a} - (-\sigma_{2a})}{2}$$

therefore

$$\sigma_A = \sigma_{1a} + \sigma_{2a}$$

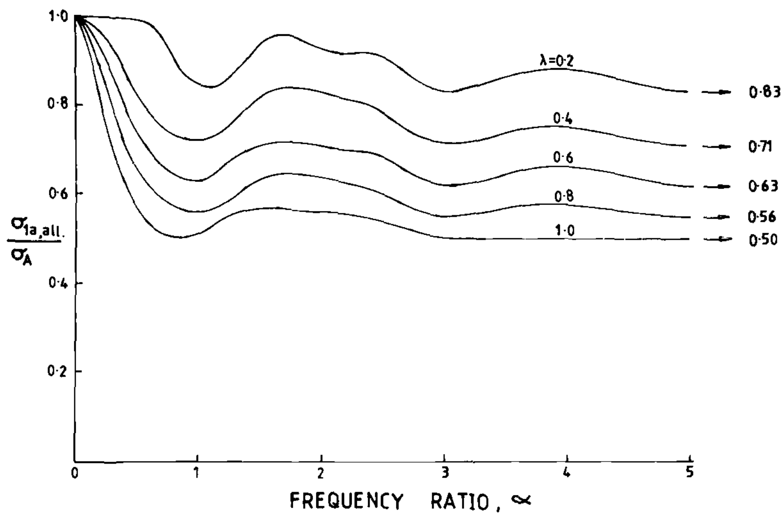

FIG. 8—*Allowable biaxial stresses at varying amplitude ratio and frequency for any phase difference.*

Hence

$$\frac{\sigma_A}{\sigma_{1a}} = 1 + \lambda$$

therefore

$$\sigma_{1a(\text{allowable})} = \sigma_A/(1 + \lambda)$$

as shown in Fig. 9.

Discussion

Figure 7 predicts that, in general, fatigue strength is reduced in the presence of biaxial stresses which are out of phase. In the case of equal amplitude biaxial stresses at the same frequency the predicted fatigue strength is halved when the out of phase angle is 180° (the reversed torsion case), but the reduction in fatigue strength is less severe for $60° < \phi < 180°$, and there is no reduction for $0° < \phi < 60°$ as shown.

A limited amount of test data [*13–16*] is available for long life fatigue under biaxial out-of-phase stress conditions. These tests were conducted using tubes subjected to either pulsating internal pressure and axial load [*13–15*] and are thus subject to the effect of mean stresses, or to combined axial load and torsion [*15,16*] where the principal stress axes rotate according to the relative values of the applied loads. In general these data support the maximum shear stress criterion of failure which indicates a decrease of fatigue strength with out of phase angles greater than 60°. An increase of fatigue strength when the stresses are 60° out

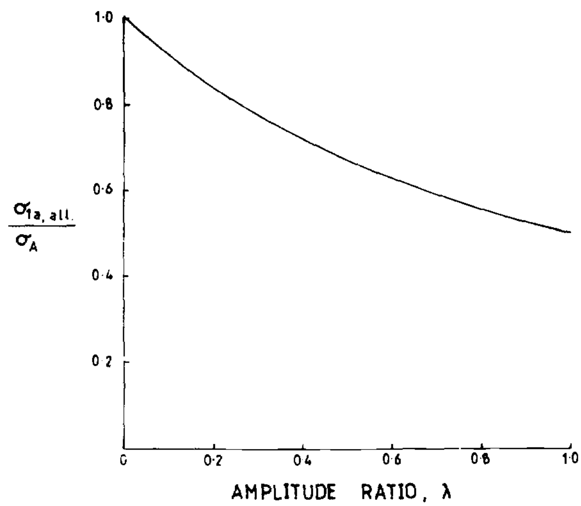

FIG. 9—*Allowable biaxial stresses for any phase difference and frequency ratio.*

of phase has been also found, which could be due to interference of different cracking systems as suggested by Miller [*4*].

Nishihara [*17*] showed that fatigue limits for ductile materials are apparently higher for combined bending and torsion with phase difference than for the conventional in-phase cyclic stressing case. This is true when the out-of-phase fatigue data are stated in terms of the maximum in-phase shear stress amplitudes. However, Little [*18*] showed that this apparent increase in fatigue strength is very misleading, as when the fatigue limit data are expressed in terms of the true shear stress amplitudes it becomes clear that the fatigue limit actually decreases as the phase difference increases. The decrease is of the order of 25% for a shear stress amplitude to bending stress amplitude ratio of 0.5 and a phase difference of 90°. This is a special case as every plane in the surface material is a plane of maximum range of shear stress. This case is further discussed in Ref *6*.

The analysis indicates that the maximum principal stress σ_{1a} is always the dominant parameter regardless of the frequency of cycling of σ_{2a}, even for $\lambda = 1$ and high values of α as only one damaging cycle of τ_{12} occurs per cycle of σ_{1a}. For $\alpha > 3$ the reduction in fatigue strength due to biaxial stress is constant for any value of principal stress ratio λ and effectively independent of out-of-phase angle ϕ and frequency ratio α. For $\alpha < 1$ low values of σ_{2a} having their maximum positive value occurring at the same instant as the maximum negative value of σ_{1a} or vice versa can cause a reduction in fatigue strength as the resulting damaging amplitude of τ_{12} will be greater than the amplitudes of τ_{23} and τ_{31} although at the lower frequency. No record can be found in the literature of any test work where biaxial fatigue stresses are at different frequencies as well as out of phase.

TABLE 3—*Predicted and experimental fatigue limit (10^6 cycles) strengths.*

Case	τ_{12}, $f(\sigma_{1a})$	τ_{23}, $f(\sigma_{1a})$	τ_{31}, $f(\sigma_{1a})$	σ_{1a}/σ_A, predicted	σ_{1a}/σ_A, experimental
1	$\underline{0.5}$	0	$\underline{0.5}$	1	1
2	0.5	$\underline{0.5}$	0		0.65
3	0	$\underline{0.5}$	0.5		0.65
4	$\underline{1.0}$	0.5	0.5	0.5	0.56
5	$\underline{0.88}$	0.5	0.5	0.57	0.62
6	$\underline{0.8}$	0.5	0.5	0.63	0.63
7	$\underline{1.0}$	0.5	0.5	0.5	0.58
8	$\underline{0.85}$	0.5	0.5	0.59	0.62

In discussing the present test results and their relation to the analysis of out-of-phase biaxial stresses at different frequencies given in this paper it is acknowledged that, due to the expensive nature of the test specimens used, only a minimal number of fatigue tests were carried out at each of the eight test conditions considered. Thus any conclusions drawn can only be of a tentative nature indicating whether or not the analysis provides a reasonable basis for a more extensive test program.

Failure cracks were longitudinal in all cases except Case 1 (longitudinal stress only) where cracks were transverse. In Cases 4 to 8 evidence can be seen of the crack originating at 45° to the longitudinal axis in the τ_{12} maximum shear stress plane and then propagating in the longitudinal direction normal to the hoop stress direction, the material being anisotropic and less resistant to fatigue stress in the transverse compared to the longitudinal direction.

The specimen tested under Case 8 conditions at a stress of 315 MN/m^2 was found to have failed from a crack originating at a small material defect just below the surface, and thus the fatigue life is likely to be lower than would be normally expected. Under Case 5 conditions the specimen first tested under a stress of 277 MN/m^2 showed evidence of coaxing to a higher strength finally failing at a stress of 339 MN/m^2.

Table 3 shows the damaging shear stress amplitudes (underlined) occurring in each of the cases tested, considered as functions of the maximum applied principal stress. This table also shows the predicted and experimental fatigue limits as functions of the uniaxial longitudinal fatigue strength. The predicted value is based on the maximum shear stress criterion of failure, and the experimental stress values are taken from Fig. 3 at 10^6 cycles. No predicted values of σ_{1a}/σ_A are given for Cases 2 and 3 as these are affected by the anisotropic nature of the material used, where the τ_{23} critical shear stress planes in these cases is weaker than the τ_{12} or τ_{31} critical shear stress planes in the other cases. Reasonable agreement is found between the predicted and experimental values of the ratio σ_{1a}/σ_{1A}. These results are illustrated in Fig. 10 which shows that the greatest difference between predicted and experimental value is 15%.

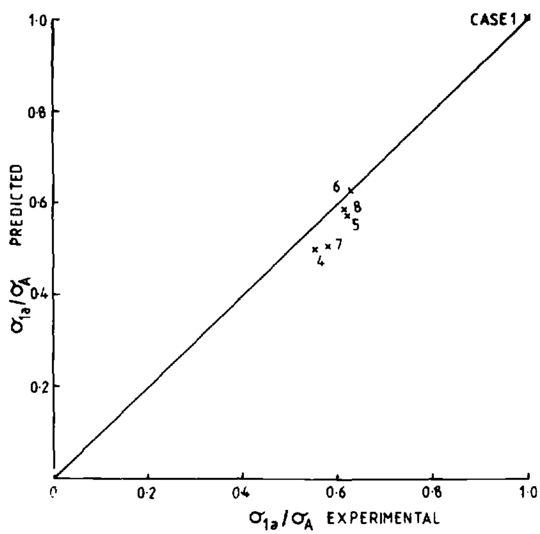

FIG. 10—*Comparison of experimental and predicted allowable maximum principal stress amplitudes.*

In Case 6 the ratio $\tau_{23}/\tau_{12} = 0.5/0.8 = 0.63$ which is approximately equal to the ratio of the transverse to the longitudinal fatigue strength of 0.65 and thus either the 12 or 23 shear stress could be critical, the latter would explain why the *S-N* curves for Cases 2, 3, and 6 are of similar form as shown in Fig. 3*d*.

Conclusions

1. Constant amplitude out-of-phase biaxial fatigue stresses of different frequencies produce nonconstant amplitude maximum shear stress variations.
2. For these conditions the normal stress acting on the maximum shear stress plane is also of nonconstant amplitude.
3. The maximum shear stress criterion of failure using damaging shear stress amplitude appears to be a reasonable basis for the analysis of fatigue under out-of-phase biaxial stresses of different frequencies, based on available test data.
4. For high-frequency ratios the reduction in fatigue strength due to biaxial stress is predicted to be constant for any principal stress amplitude ratio and effectively independent of out-of-phase angle and frequency ratio.
5. For low-frequency ratios low values of secondary principal stress amplitude are predicted to cause a reduction in fatigue strength.
6. Using the proposed criterion the allowable biaxial stresses for long life at any out-of-phase angle and any frequency ratio can be found from σ_{1a} (allowable) $= \sigma_A/(1 + \lambda)$.

References

[1] Brown, M. W. and Miller, K. J., *Proceedings*, The Institution of Mechanical Engineers, Vol. 187, 65/73, 1973, pp. 745–755.
[2] McDiarmid, D. L., "Failure Criterion and Cumulative Damage in Fatigue under Multiaxial Stress Conditions," Ph.D. thesis, The City University, London, 1972.
[3] McDiarmid, D. L. in *Proceedings*, Second International Conference in Pressure Vessel Technology, American Society of Mechanical Engineers, San Antonio, TX, 1973, pp. 851–862.
[4] Miller, K. J., "Multi-axial Fatigue." *Proceedings*, Conference on Fatigue Testing and Design, Society of Environmental Engineers, The City University, London, April 1976.
[5] McDiarmid, D. L., *Proceedings*, Sixth Canadian Congress of Applied Mechanics, Vancouver, Canada, June 1977, p. 245.
[6] McDiarmid, D. L. *The Aeronautical Journal of the Royal Aeronautical Society*, March 1981, pp. 118–122.
[7] Morrison, J. L. M., Crossland, B., and Parry, J. S. C., *Proceedings*, Institution of Mechanical Engineers, Vol. 174, 1960, p. 95.
[8] Love, R. J., Motor Industries Research Association, U.K. Report No. 1950/9, 1950.
[9] McDiarmid, D. L., The City University, London, Research Memo No. ML120, July 1980.
[10] Martin, O. H., "Cumulative Damage in Fatigue Under Multiaxial Out-of-Phase Stresses at Different Frequencies and Amplitudes," M.Sc. project dissertation, The City University, London, 1979.
[11] Matsuiski, M. and Endo, T., "Fatigue of Metals Subjected to Varying Stresses," paper presented at The Kyusha district meeting of the Japan Society of Mechanical Engineers, March 1968.
[12] Miner, M. A., *Journal of Applied Mechanics*, American Society of Mechanical Engineers, Vol. 12, No. 3, 1945, p. 159.
[13] Bodelind, B., "Biaxial Fatigue with Phase Difference." Internal Report, Division of Strength of Materials, Chalmers University of Technology, Gothenberg, Sweden, 1966.
[14] Issler, L., "Strength Relations for Metals under Multiaxial Out of Phase Fatigue Loading," Ph.D. thesis, University of Stuttgart, 1973.
[15] Deitmann, H. and Issler, L., "Strength Calculations under Multiaxial Out of Phase Fatigue Loading," Sixth Congress on Materials Testing, Budapest, 1974.
[16] Lempp, W., "Strength Behaviour of Steels under Multiaxial Long Life Fatigue Loading Consisting of Direct Stress with Superimposed Shear Stresses both In phase and Out of phase," Ph.D. thesis, University of Stuttgart, 1977.
[17] Nishihara, T. and Kawamoto, M., *Memoirs*, College of Engineering, Kyoto Imperial University, Japan, Vol. XI, 1945, pp. 85–112.
[18] Little, R. E., *Aeronautical Quarterly*, Vol. 20, February 1969, pp. 57–60.

Masateru Ohnami,[1] Masao Sakane,[1] and Naomi Hamada[1]

Effect of Changing Principal Stress Axes on Low-Cycle Fatigue Life in Various Strain Wave Shapes at Elevated Temperature

REFERENCE: Ohnami, M., Sakane, M., and Hamada, N., "**Effect of Changing Principal Stress Axes on Low-Cycle Fatigue Life in Various Strain Wave Shapes at Elevated Temperature,**" *Multiaxial Fatigue, ASTM STP 853*, K. J. Miller and M. W. Brown, Eds., American Society for Testing and Materials, Philadelphia, 1985, pp. 622–634.

ABSTRACT: A study on the effect of changing the principal stress axes on low-cycle fatigue lives was carried out in four strain waveforms at 923 K in air using SUS 304 austenitic stainless steel. No effect of alternation of axes on fatigue lives was observed at that temperature. But comparison of this result with a former result at 823 K, in which the alternation of axes is detrimental to fatigue lives, shows that the effect of the alternation of axes is connected closely to the fracture mode, that is, transgranular at 823 K and intergranular at 923 K. When the specimen fractured transgranularly the alternation of axes decreases the fatigue life, but, when the specimen fractured intergranularly, no effect is noted. This phenomenon is not affected by the strain waveform. Detailed discussion on the fatigue life is made from crack initiation and propagation considerations.

KEY WORDS: low-cycle fatigue, elevated temperature, biaxial stress, nonproportional loading, prediction of low-cycle fatigue life

Since all structural materials in elevated temperature applications suffer biaxial/multiaxial stress, it is important that life prediction methods be constructed that are applicable to multiaxial stress conditions. Krempl [*1*] extensively surveyed multiaxial low-cycle fatigue work in 1974, and pointed up some related problems. A number of papers have been published, for example [*2–11*], relating to multiaxial fatigue both in low-cycle and high cycle regimes at ambient temperature, but only a few deal with elevated temperature problems [*3,9,12–19*]. These papers can be classified into three categories.

The first category [*2,3,11–16,18,19*] is connected with parameters which can arrange the low-cycle fatigue data under complex stresses. The equivalent strain range of the von Mises' type is a typical parameter [*3*], but other

[1]Professor, assistant professor, and research student, respectively, Department of Mechanical Engineering, Faculty of Science and Engineering, Tojiin-Kitamachi, Kita-ku, Kyoto, Japan.

Copyright© 1985 by ASTM International www.astm.org

parameters have been proposed [*2,11,16*]; however, no general agreement has been reached on the use of any specific parameters. Papers [*4–6,8–10,14,15,17–19*] which treat the effect of biaxiality of stress on crack behavior are those of the second category. Some papers [*5,6,13–15,17,18*] report that the stress parallel to the crack affects the crack propagation rate, but reference [*10*] shows no effect. The last category covers the effect of nonproportional loading [*7*]. Out-of-phase loading is employed usually as a means of nonproportional loading. Shorter fatigue lives were reported [*7*] compared with those under proportional loading. But a careful discussion is necessary for the results of out-of-phase tests. Usually the mean stress in out-of-phase tests is higher than that in in-phase tests. Therefore, it is necessary that the pure effect of nonproportional loading must be separated from that of mean stress.

In a previous paper [*19*], biaxial low-cycle fatigue tests were carried out on SUS 304 austenitic stainless steel at 823 K in air using five strain waveforms with and without the alternation of principal stress axes. We discovered that the alternation of principal stress axes reduces fatigue lives of the material, resulting from the acceleration of crack propagation rate by the alternation. Transgranular fracture was found in all the tests with and without the change of the stress axes.

This paper examines the effect of the change of principal stress axes on fatigue lives at 923 K in air using four strain waveforms. The reason why the experiments were made at the higher temperature is that an intergranular fracture was expected at that temperature, and a different fracture mode may have a different effect on the alternation of principal stress axes. Also the cyclic work-hardening behavior is studied in relation to the deformation behavior of microstructure due to the alternation.

Test Specimen and Procedure

Test Specimen and Apparatus

A hollow cylindrical specimen of solution annealed SUS 304 austenitic stainless steel with grain size of ASTM No. 3 was used. The specimen has a 1-mm-diameter hole at the midlength to permit easy confirmation of crack initiation. The shape and dimensions of the specimen are illustrated in Fig. 1. The values of stress and strain used in this paper are all nominal values.

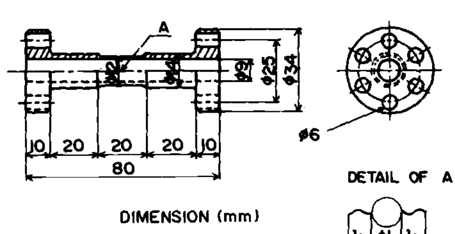

FIG. 1—*The test specimen; dimensions in millimetres.*

The test apparatus used in the study is an original design of an electrohydraulic servocontrolled testing machine which can apply an axial load in combination with a torsional load in various waveforms and shapes. A rotary actuator is attached on top of the apparatus, and an axial actuator is attached under the lower plate. Axial load and torque applied to the specimen are measured separately by load cells. Relative axial displacement and rotation along the gage length of 20 mm are measured by two linear variable differential transducers (LVDTs). A microcomputer was used as a digital function generator.

The specimen was heated by a sheath heater from inside, and a subheater was used to obtain uniform temperature distribution along the gage length. Tests were performed at 923 K in air and controlled by total strain. A camera with an automatic switch was used to monitor fatigue cracks which initiate from the circular hole. Crack length l is defined as $l = (l_1 + l_2)/2$, where l_1 and l_2 are the top and second largest crack length (see Fig. 1). Number of cycles to crack initiation, N_c, is defined as the cycle at which l reaches a length of 100 μm, which corresponds with the grain size. Number of cycles to failure, N_f, is also defined as the cycle at which the tensile stress amplitude decreases to three quarters of the maximum value.

Test Program

Four strain waveforms were employed as shown in Table 1. The solid lines denote axial loading and the dotted lines torsional loading. In three waveforms out of the four, a further test program was employed in which push-pull and reversed torsional load were applied alternately. In this case, a push-pull cycle followed by a torsional cycle was counted as two separate cycles. A push-pull cycle was interchanged to a torsional cycle at null strain. This test program permits the principal stress axes to change while keeping the equivalent total strain range of the von Mises' type constant during the test. The net angular change of the principal stress axes is $\pi/4$ radian per cycle. Total strain ranges and strain rates are also listed in Table 1.

Experimental Results and Discussion

Effect of Changing the Principal Stress Axes on Low-Cycle Fatigue Lives in Various Strain Wave Shapes

The authors previously have carried out low-cycle fatigue tests with the change of principal stress axes at 823 K in air, and these results have been published [*18,19*]. In this study, experiments at 923 K in air are performed, but we discuss the results at both temperatures, in order to assist a global understanding of the phenomenon.

Before proceeding with the current work the main points of the previous results are now stated briefly.

Figure 2*a* shows the experimental results at 823 K in air under five strain

TABLE 1—*Waveforms and symbols.*

WAVE FORM	LOADING MODE	KEY	T=923 K TOTAL STRAIN RANGE, mm/mm	T=923 K STRAIN RATE $\dot{\varepsilon}_{eqt}$, Ks^{-1}	T=923 K STRAIN RATE $\dot{\varepsilon}_{eqc}$, Ks^{-1}	T=823 K TOTAL STRAIN RANGE, mm/mm	T=823 K STRAIN RATE $\dot{\varepsilon}_{eqt}$, Ks^{-1}	T=823 K STRAIN RATE $\dot{\varepsilon}_{eqc}$, Ks^{-1}
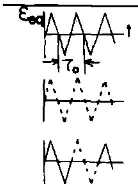	NOT ALTERNATED	○	0.01	2.000	2.000	0.02	4.000	4.000
		●	0.007	1.400	1.400	0.01	2.000	2.000
			0.005	1.000	1.000			
	ALTERNATED	⊕	0.003	0.600	0.600	0.005	1.000	1.000
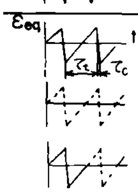	NOT ALTRENATED	□	0.01	0.020	2.000			
		■	0.007	0.014	1.4000	0.01	0.200	2.000
	ALTERNATED	⊞	0.005	0.010	1.000			
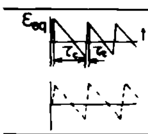	NOT ALTERNATED	◇	...	...	...	0.01	2.000	0.200
		◆						
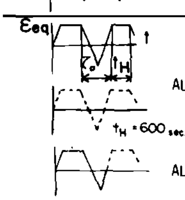	NOT ALTERNATED	○	0.01	2.000	2.000	0.01	2.000	2.000
		●	0.007	1.400	1.400	0.005	1.000	1.000
	ALTERNATED	⊕	0.005	1.000	1.000			
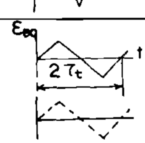	NOT ALTERNATED	△	0.01	0.020	0.020	0.01	0.200	0.200
		▲	0.007	0.014	0.014	0.005	0.100	0.100

NOTE) SOLID LINES DENOTE PUSH-PULL LOADING AND DOTTED LINES TORSIONAL LOADING.
τ_t: TENSION GOING TIME, τ_c: COMPRESSION GOING TIME
τ_o: TIME FOR A CYCLE IN THE FAST-FAST STRAIN WAVE SHAPE

waveforms, that is, fast-fast, fast-slow, slow-fast, slow-slow, and trapezoid, with and without the alternation of principal stress axes. An equivalent total strain range of the von Mises' types, $\Delta\epsilon_{eq}$, was used as the unit of the ordinate. No significant difference in fatigue lives is observed between push-pull and reversed torsion in the same strain waveforms. A noticeable characteristic in the figure is the reduction in fatigue lives by the change of principal stress axes in all the strain waveforms tested. And the observation of the fracture surface by both a scanning electron microscope (SEM) and optical microscope revealed that

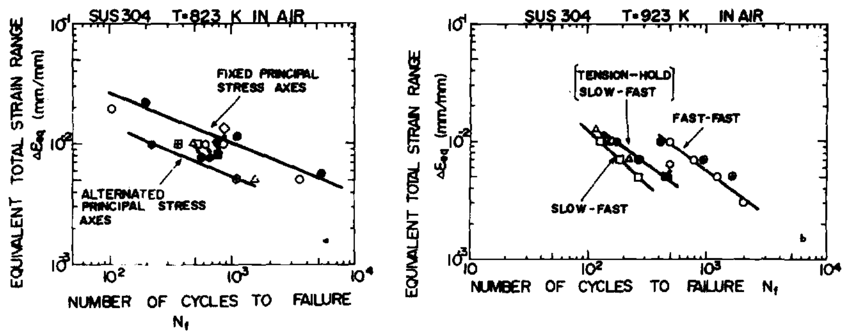

FIG. 2—*Relationship between equivalent total strain range of the von Mises' type and number of cycles to failure for SUS 304 austenitic stainless steel at* (a) *823 K in air and* (b) *923 K in air.*

the fracture mode was transgranular in all the strain waveforms. Especially in the strain waveform of fast-fast, clear striation marks were observed.

Figure 2*b* is similar to Fig. 2*a*, but the test temperature is higher at 923 K. No effect of the alternation of principal stress axes can be observed on the fatigue lives. Comparing this result to that at 823 K, it is seen that the effect of the change of principal stress axes depends on temperature level.

Effect of Changing Principal Stress Axes on Cyclic Work-Hardening Behavior

Figure 3*a* shows the von Mises' equivalent stress versus strain curves by means of the incremental method in the push-pull test and the alternation test of push-pull and reversed torsion at 923 K. Similar curves at 823 K are given in Fig 3*b*. Monotonic tensile and torsional curves on the von Mises' basis are also superimposed on the cyclic curves. Values of strain hardening coefficient, k, and exponent, n, when approximating stress strain relation as $\sigma = \kappa\epsilon^n$ are 526 MPa and 0.25 for monotonic loading, 1572 MPa and 0.38 for cyclic push-pull test, and 7290 MPa and 0.59 for alternated test at 923 K, while they are

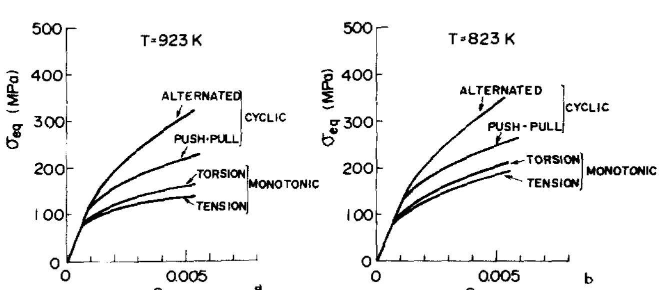

FIG. 3—*The von Mises' equivalent stress versus strain curves of SUS 304 austenitic stainless steel in push-pull and alternation incremental tests at* (a) *923 K and* (b) *823 K in air. Monotonic tensile and torsional curves are also superimposed on the cyclic curves.*

752 MPa and 0.27 for monotonic loading, 3180 MPa and 0.48 for cyclic loading, and 7746 MPa and 0.59 for alternated test at 823 K.

It is well known that SUS 304 austenitic stainless steel is a typical cyclic hardening material, and the same is observed in the present study. About 35% increase in the stress amplitude is found in cyclic push-pull test compared with monotonic tests. Further cyclic hardening is discovered in the alternated test. About 40% increase in stress amplitude is caused by changing principal stress axes at both temperatures. In this regard, Kanazawa et al [*20*] also found the increase in the stress amplitude by rotating the principal stress axes for 1% chromium-molybdenum-vanadium (Cr-Mo-V) steel in out-of-phase tests under somewhat different test condition to the present study.

This larger cyclic work-hardening of SUS 304 austenitic stainless steel due to the alternation of principal stress axes at 823 and 923 K may be related to the increase in the number of activated slip systems in grains. In the tests without the alternation, only two conjugate macroscopic slip systems are expected to operate because of the two directions of the maximum shear stress. On the other hand, in the tests with the alternation, four slip systems would operate because the direction of the maximum shear stress changes by $\pi/4$ radians in each cycle. So, complex interactions of slip systems is expected in the tests with the alternation, which results in a greater degree of work hardening.

Further evidence was provided by means of the SEM and the optical microscope. Figures 4*a* and *b* show examples of intergranular fracture surfaces observed by SEM in the slow-fast test with and without the change of principal stress axes. On the other hand, a transgranular fracture mode was found at 823 K in all the strain waveforms [*19*]. Figures 5*a* and *b* show an example of optical micrographs along the macrocrack in the slow-fast test with and without the change of principal stress axes at 923 K. The fracture mode in Fig. 5 corresponds to that in Fig. 4, but Fig. 5*a* shows a much greater intensity of deformation in

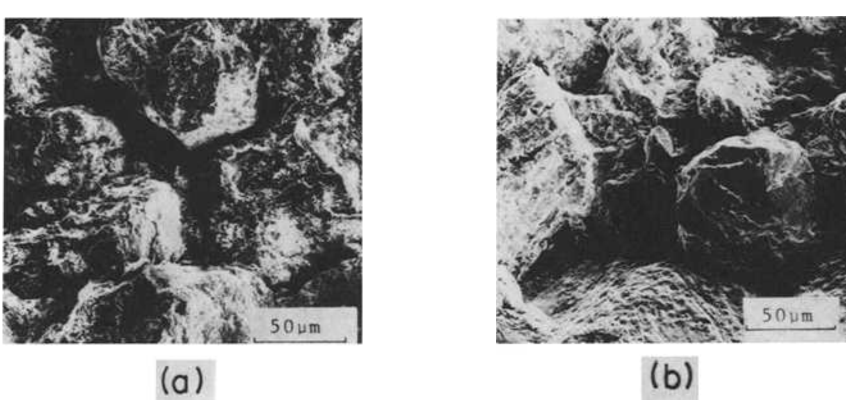

FIG. 4—*Fracture surface observed by SEM in a slow-fast test* (a) *with and* (b) *without the alternation of principal stress axes at 923 K in air.*

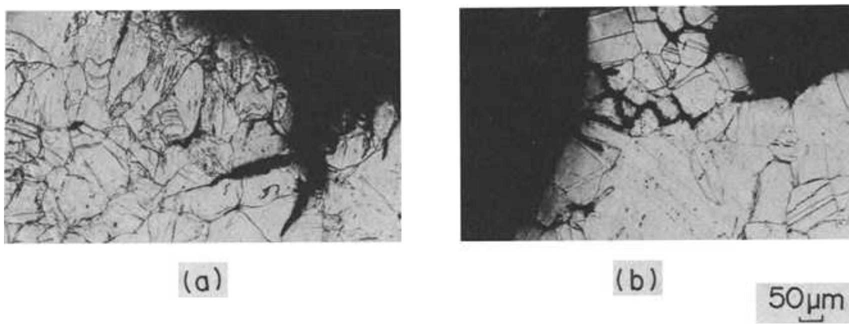

FIG. 5—*Fracture and deformation characteristics observed by optical microscopy in a slow-fast test* (a) *with and* (b) *without the alternation of principal stress axes at 923 K in air.*

the grain than that in Fig. 5*b*. This is evidence to support the observed increase in cyclic work hardening of the material as shown in Fig. 3*a*. From this fact, it can be considered that the greater intensity of the deformation in the test with the change of principal stress axes is witness to the increase in cyclic work hardening, but this does not affect the fatigue lives because of intergranular fracture at 923 K. Regarding deformation in the test at 823 K, Fig. 6 shows an example of fracture surfaces in (*a*) alternated and (*b*) not alternated tension-hold tests. A much greater intensity of deformation is also observed in Fig. 6*a* as compared to Fig. 6*b*. Therefore, we can conclude that, in the case of transgranular fracture at 823 K, the alternation of principal stress axes affects the fatigue lives, but, in the case of intergranular fracture at 923 K, it does not; this phenomenon is not affected by the strain waveforms.

There is one exception. In the test of the nonalternated fast-fast strain waveform at 923 K, clear striation marks were observed on the fracture surface, and this specimen fractured transgranularly. But we could not obtain clear fracture surfaces for the same strain waveform with a change of principal stress axes because of the damage to the surfaces by rubbing of the surfaces during the alternation of principal stress axes. Hence, a definite conclusion could not be obtained.

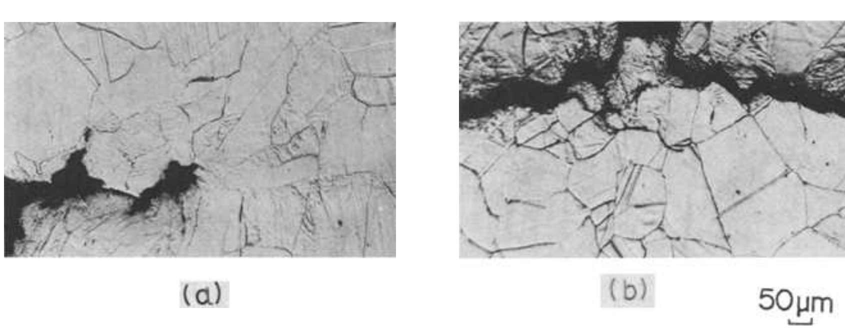

FIG. 6—*Fracture and deformation characteristics by optical microscopy in a tension-hold test* (a) *with and* (b) *without the alternation of principal stress axes at 823 K in air.*

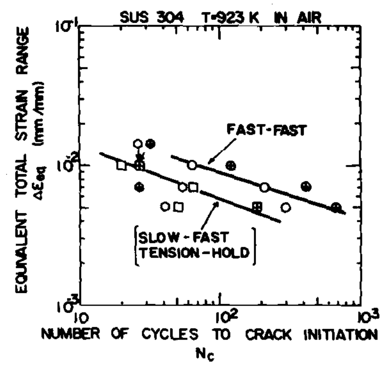

FIG. 7—*Relationship between equivalent total strain range of the von Mises' type and number of cycles to crack initiation at 923 K in air.*

At the end of this section, deviation of the principal stress axes from the principal strain axes is mentioned briefly. In proportional loading tests, the direction of principal stress axes usually agrees with that of principal strain axes [*1,19*], but in nonproportional loading tests, this is not always guaranteed [*19*]. Sometimes disagreement was observed in the present tests where the direction of the principal stress axes almost coincides with that of the principal strain axes programmed in the push-pull cycle, but in the torsional cycle it does not.

Effect of Alternating Principal Stress Axes on Fatigue Crack Propagation Behavior

Figure 7 shows the relationship between equivalent strain range of the von Mises' type, $\Delta\epsilon_{eq}$, and number of cycles to crack initiation, N_c, at 923 K in air. It is seen from the figure that the alternation of principal stress axes is not influential in N_c and it does not reduce N_f at 923 K, but it does at 823 K [*19*].

Figures 8*a* and *b* represent, respectively, the relation between crack propagation rate, dl/dN, and crack length, l, at 923 and 823 K, in air. From Fig. 8*a*, no significant effect at 923 K of the alternation of principal stress axes is found on dl/dN when the data are compared with the same strain waveforms. On the other hand, Fig. 8*b*, which is related to the transgranular fracture mode, shows that the crack propagation rate in the alternated tests is higher than in the not alternated tests in the same strain waveforms. Therefore, the reduction in fatigue lives by the alternation of principal stress axes at 823 K is because of earlier crack initiation and enhancement of the crack propagation rate. At 923 K, both N_c and dl/dN are little affected by the alternation of the stress axes, and this results in no effect on N_f.

Life Prediction

In this section, the applicability of three life prediction methods, that is, Ostergren's method [*21*], frequency separation method [22], and Tomkins' method [*23*] is checked by applying these methods to the experimental data.

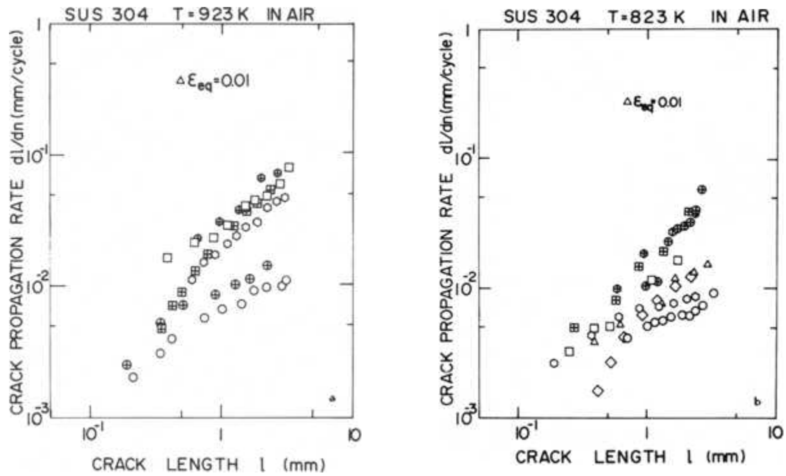

FIG. 8—*Relationship between crack propagation rate,* dl/dN, *and crack length,* l, *at* (a) *923 K and* (b) *823 K in air.*

Ostergren [*21*] modified the frequency modified fatigue life equation [*24*] by adding a tensile stress amplitude and obtained the following equation

$$\Delta\epsilon_p \sigma_t \, \nu^{\beta(k'-1)} N_f^{\beta} = C \tag{1}$$

where

$\Delta\epsilon_p$ = inelastic strain range,
σ_t = tensile stress amplitude in a hysteresis loop at $N = N_f/2$, and
ν = frequency.

In this equation, ν is defined as $1/\tau_o$ for the case of the fast-fast test and is also defined as $\nu = 1/(\tau_c + \tau_t)$ for the cases of the slow-fast, fast-slow and slow-slow tests. Here τ_o is the time for a cycle in the fast-fast test while τ_t and τ_c are the tension and the compression going times (see Table 1). In addition, for the tension-hold tests, ν is defined as $1/(\tau_o + t_H)$, where t_H is the tension hold time. The exponents β and k' in Eq 1 are determined from $\Delta\epsilon_p - N_f$ curves in the push-pull test at specific frequencies.

Concerning the frequency modified fatigue life equation, Coffin [*22*] proposed the following frequency separation method for the prediction of fatigue lives under unsymmetric waveforms

$$\Delta\epsilon_p \left[\left(\frac{\nu_c}{2}\right)^{k_1} + \left(\frac{\nu_t}{2}\right)^{k_1}\right]^{1/n'} \nu_o^{-k'_1 n'} N_f^{\beta} = C \tag{2}$$

where

ν_c = frequency in compression,
ν_t = frequency in tension, and
ν_o = frequency in the fast-fast test.

The exponents k_1 and n' are determined also from $\Delta\sigma$ versus $\Delta\epsilon_p$ curves in the push-pull slow-fast test at specific frequencies. The exponents k'_1 and β correspond to those in Eq 1.

Tomkins [23] proposed the following life prediction method based on crack propagation considerations

$$\Delta\epsilon_p \left(\frac{\Delta\sigma}{\sigma_u}\right)^2 N_f = C \tag{3}$$

where $\Delta\sigma$ denotes stress range in a hysteresis loop at $N = N_f/2$ and σ_u is the tensile strength of the material.

Figure 9 shows the experimental data compared with the three prediction methods. Parts *a*, *b*, and *c* are the results at 923 K, and *d*, *e*, and *f* are those at 823 K in air. Ostergren's parameter is comparatively good for the arrangement of the experimental data at 923 K in which no reduction in fatigue lives occurred by the alternation. All the data fall into the scatterband of a factor of two. But nearly a half of the experimental data drops out of the band of a factor of two in the other prediction methods. Their prediction methods predict the fatigue lives unconservatively. So, frequency separation and Tomkins' method cannot cover the variety of fatigue lives with different strain wave shapes.

On the other hand, all three prediction methods are adequate for the data at 823 K, without the alternation of principal stress axes, but inadequate for the data with the alternation. The data in the tests with the alternation of the stress axes fall well outside of the scatterband. Therefore, it is concluded that an additional safety factor margin is needed for predicting the low-cycle fatigue life in the case of alternated principal stress axes with transgranular fracture.

Now we comment briefly on the notch effect in the low-cycle fatigue under creep-fatigue conditions. A crack starter hole on the specimen in this study causes stress and strain concentration around the notch hole. Inelastic strain and stress concentration factors are necessary in order to convert low-cycle fatigue data of the notched specimen to that of the unnotched specimen. From finite element method (FEM) analyses of the notched specimen used in this paper, values of strain concentration factors in monotonic tension and torsion are 4.0 and 4.5, respectively, while those of stress concentration factors in monotonic tension and torsion are 1.6 and 1.8, respectively, at 923 K. Since the strain and stress concentration factors take almost the same value in both loading modes, the data in Fig. 9 for the notched specimen should be able to be converted to data for an unnotched specimen if the strain and stress ranges are multiplied by

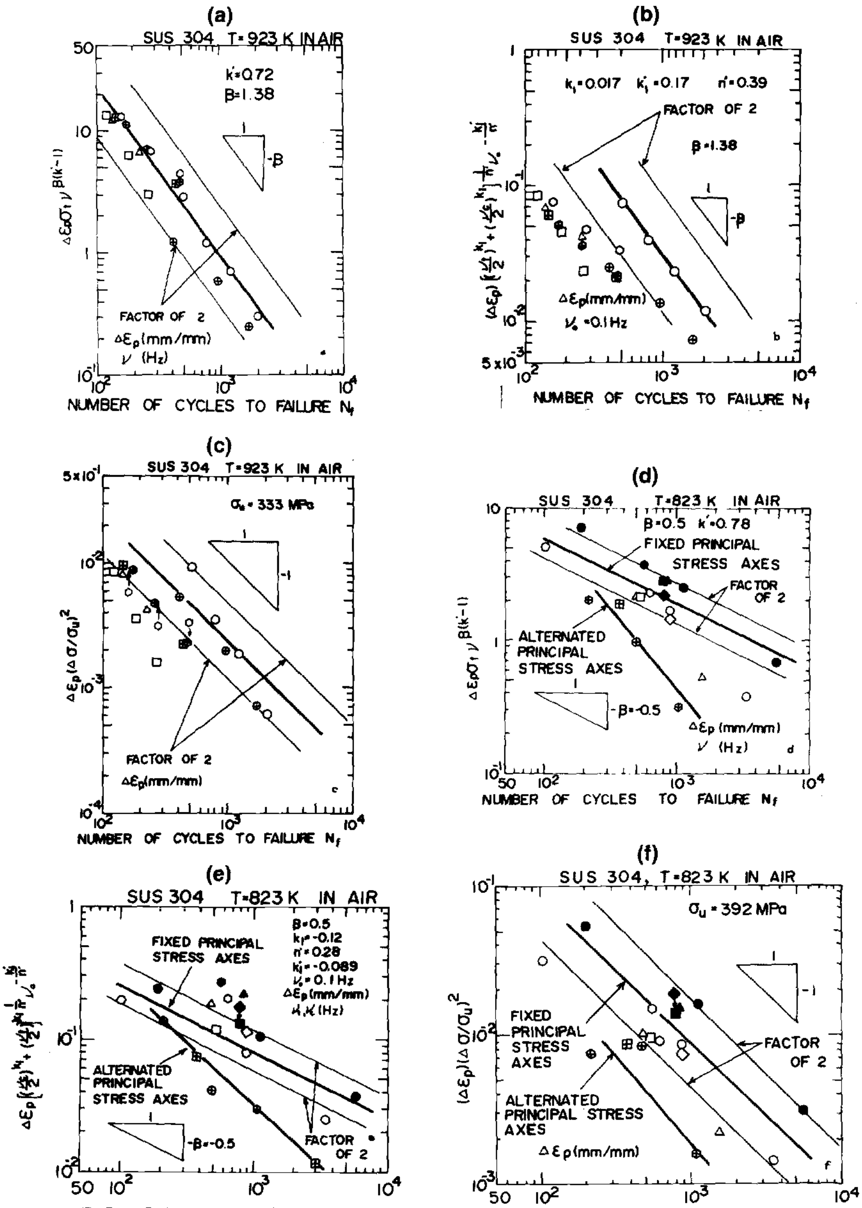

(*a*) Ostergren's method (T = 923 K in air).
(*b*) Frequency separation method (T = 923 K in air).
(*c*) Tomkins' method (T = 923 K in air).
(*d*) Ostergren's method (T = 823 K in air).
(*e*) Frequency separation method (T = 823 K in air).
(*f*) Tomkins' method (T = 823 K in air).

FIG. 9—*Comparison between predicted and actual fatigue lives.*

the inelastic strain and stress concentration factors. It is a formal conversion of the data of notched specimens to that of unnotched specimens. Note that because Tomkins' model was deduced from a crack propagation model careful treatment should be made by splitting the failure life into crack initiation and propagation period when converting rigorously the notched data to the unnotched data.

Conclusions

1. The changing of principal stress axes reduces the low-cycle fatigue life of SUS 304 austenitic stainless steel at 823 K in air, but not at 923 K for the four strain wave shapes tested. Observations of the fracture surfaces by SEM and optical microscopy reveal that specimens fractured transgranularly at 823 K but intergranularly at 923 K. Therefore, the alternation of principal stress axes is detrimental to fatigue in the case of transgranular fracture.
2. Greater cyclic work hardening of the material is observed in the tests with the alternation of the principal stress axes at 823 and 923 K in comparison with not alternated tests. About 40% increase in stress amplitude is observed by changing principal stress axes at the two temperatures in air. From the observations by SEM and optical microscopy, a much greater intensity of deformation in grains occurs in the tests with the change of principal stress axes, which contributes to the increase in cyclic work hardening at the two temperatures.
3. The changing of principal stress axes causes earlier initiation of a fatigue crack and enhances the crack propagation rate at 823 K in air, while it has no effect on initiation and propagation at 923 K.
4. Three prediction methods for low-cycle fatigue lives are applied to the experimental data. No single method is adequate for predicting the low-cycle fatigue life. The best method is that proposed by Ostergren which can arrange the data within a factor of two at 923 K in air, but not at 823 K in air. It predicts the low-cycle fatigue life in the alternated tests unconservatively. Therefore, an additional safety factor margin is needed for predicting low-cycle fatigue life under changing stress axes with transgranular fracture.

Acknowledgment

This work was partly supported by Grant-in-Aid for Developmental Scientific Research, 389007. The authors wish to thank T. Miyaake, H. Yasuda, and I. Yoshimura for carrying out the experiments.

References

[1] Krempl, E., *The Influence of State of Stress on Low-Cycle Fatigue of Structural Materials: A Literature Survey and Interpretive Report, ASTM STP 549,* American Society for Testing and Materials, Philadelphia, 1974.

[2] Brown, M. W. and Miller, K. J., *Proceedings,* Institution of Mechanical Engineers, Vol. 187, 1973, pp. 745–755.

[3] Ellison, E. G. and Andrews, J. M. H., *Journal of Strain Analysis*, Vol. 8, No. 3, 1973, pp. 209–219.
[4] Parsons, M. W. and Pascoe, K. J., *Materials Science and Engineering*, Vol. 22, No. 1, 1976, pp. 31–50.
[5] Hopper, C. D. and Miller, K. J., *Journal of Strain Analysis*, Vol. 12, No. 1, 1977, pp. 23–28.
[6] Miller, K. J., *Metal Science*, Vol. 11, No. 9, 1977, pp. 423–438.
[7] Kanazawa, K., Miller, K. J., and Brown, M. W., *Transactions*, American Society of Mechanical Engineers, *Journal of Engineering Materials and Technology*, Vol. 99, 1977, pp. 222–228.
[8] Liebowitz, H., Lee, J. D., and Subramonian, N., *Theoretical and Experimental Biaxial Studies*, Symposium on Naval Structural Mechanics 10th, Washington, 1978, pp. 593–628.
[9] Brown, M. W. and Miller, K. J., *Fatigue of Engineering Materials and Structures*, Vol. 1, No. 2, 1979, pp. 231–246.
[10] Liu, A. F., Allison, J. E., Dittmer, D. F., and Yamane, J. R. in *Fracture Mechanics*, American Society for Testing and Materials, ASTM STP 677, American Society for Testing and Materials, Philadelphia, 1979, pp. 5–22.
[11] Lohr, R. D. and Ellison, E. G., *Fatigue of Engineering Materials and Structures*, Vol. 3, No. 1, 1980, pp. 1–17.
[12] Miller, K. J. and Pascoe, K. J. in *Conference on Mechanics and Physics of Fracture*, Institute of Physics, 1975, pp. 287–294.
[13] Ohnami, M. and Sakane, M., *Bulletin*, Japan Society of Mechanical Engineers, Vol. 21, No. 157, 1978, pp. 1057–1063.
[14] Ohnami, M. and Sakane, M., *Bulletin*, Japan Society of Mechanical Engineers, Vol. 20, No. 139, 1977, pp. 1–8.
[15] Sakane, M. and Ohnami, M., *3rd International Conference on Pressure Vessel Technology, Part 2*, Tokyo, American Society of Mechanical Engineers, 1977, pp. 779–786.
[16] Brown, M. W. and Miller, K. J., *Fatigue of Engineering Materials and Structures*, Vol. 1, No. 2, 1979, pp. 217–229.
[17] Taira, S., Ohtani, R., and Wada, F., *Transactions*, Japan Society of Mechanical Engineers, Vol. 46, No. 411, 1980, pp. 1213–1219 (in Japanese).
[18] Ohnami, M. and Hamada, N., *Journal of the Society of Materials Science*, Japan, Vol. 30, No. 335, 1981, pp. 822–828 (in Japanese).
[19] Ohnami, M. and Hamada, N., *Proceedings*, 25th Japan Congress on Material Research, 1982, pp. 93–99.
[20] Kanazawa, K., Miller, K. J., and Brown, M. W., *Fatigue of Engineering Materials and Structures*, Vol. 2, No. 2, 1979, pp. 217–228.
[21] Ostergren, W., *Journal of Testing and Evaluation*, Vol. 4, No. 5, 1976, pp. 327–339.
[22] Coffin, L. F., Jr., *4th International Conference on Fracture*, Vol. 1, Waterloo, 1977, pp. 263–292.
[23] Tomkins, B., *Philosophical Magazine*, Vol. 18, No. 104, 1968, pp. 1041–1066.
[24] Coffin, L. F., Jr., *Proceedings*, 2nd International Conference on Fracture, 1969, Brighton, pp. 643–654.

Elevated Temperature Studies

Richard H. Marloff,[1] *Robert L. Johnson,*[1] *and William K. Wilson*[1]

Biaxial Low-Cycle Fatigue of Cr-Mo-V Steel at 538°C By Use of Triaxiality Factors

---

REFERENCE: Marloff, R. H., Johnson, R. L., and Wilson, W. K., "**Biaxial Low-Cycle Fatigue of Cr-Mo-V Steel at 538°C By Use of Triaxiality Factors,**" *Multiaxial Fatigue, ASTM STP 853*, K. J. Miller and M. W. Brown, Eds., American Society for Testing and Materials, Philadelphia, 1985, pp. 637–650.

ABSTRACT: Low-cycle strain-controlled hold-time fatigue tests were performed on 1Cr-1Mo-¼V rotor steel at 538°C under uniaxial and plane-strain biaxial states of stress. Plain strain was produced by use of a blunt notched compact tension specimen. An inelastic finite-element analysis was used to relate strain at the base of the notch to the notch opening displacement. The results showed reasonable correlation by use of von Mises effective elastic and plastic strain components, with the latter modified by a function of the triaxiality factor. Published results for Cr-Mo-V steel at room temperature and elevated temperature for various biaxial stress conditions were examined in terms of the triaxiality factor-effective strain approach. Good correlation was obtained between predicted and measured life.

KEY WORDS: fatigue, biaxial, high temperature, low cycle, steel Cr-Mo-V, creep, hold time, tests, triaxiality, notch, finite element, analysis, cyclic, compact tension specimen

Nomenclature

- A_ϵ Strain A ratio, $\epsilon_{alt}/\epsilon_m$
- E Elastic modulus
- N_f Cycles to fracture
- N_i Cycles to crack initiation
- N_O Cycles to first change in stabilized stress or compliance
- N_T Cycles at termination of test
- P Load
- V Notch opening displacement
- γ Shear strain
- γ Shear strain rate
- Δ Range of variable
- ϵ Strain

[1]Fellow engineer, fellow engineer, and advisory engineer, respectively, Westinghouse R&D Center, Pittsburgh, PA 15235.

Copyright© 1985 by ASTM International www.astm.org

ϵ_{alt} Alternating strain
$\bar{\epsilon}$ Effective strain, $[(\epsilon_1 - \epsilon_2)^2 + (\epsilon_2 - \epsilon_3)^2 + (\epsilon_3 - \epsilon_1)^2]^{0.5}/\sqrt{2}(1 + \mu)$
ϵ_m Mean strain
λ $\Delta\gamma/\Delta\epsilon$
μ Poisson's ratio
ν Frequency
σ Stress
$\bar{\sigma}$ Effective stress
ϕ Principal strain ratio, $\Delta\epsilon_2/\Delta\epsilon_1$

Subscripts

e Elastic component
f Failure
o Uniaxial stress condition
p Plastic component
r Relaxed value
t Total
x,y,z Components in coordinate directions
1,2,3 Principal components

As a result of thermal and mechanical loads, the state of stress at many locations in a turbine rotor is multiaxial. Even under uniaxial loading, the presence of a notch may induce a biaxial stress field as a result of geometric constraints. Life prediction under cyclic loading must include the effect of the state of stress, since, in many cases, the use of uniaxial fatigue data may not be conservative.

In general, multiaxial fatigue is treated by modifying the uniaxial criterion, for example a strain-life equation, in a manner which accounts for the stress state. There is, however, no consensus among various investigators on a single criterion, even for the simplest case of proportional loading at room temperature. Garud [*1*] in a recent review of room-temperature multiaxial fatigue summarizes 24 criteria which have been proposed by various investigators and cites over 75 references on this subject. Other reviews of multiaxial fatigue can be found in Refs *2* and *3*.

A number of investigators have examined the elevated temperature uniaxial behavior of chromium-molybdenum-vanadium (Cr-Mo-V) steels under straight cycling and with various hold times [*4–10*]. Lohr and Ellison [*11*] and Liddle and Miller [*12*] performed biaxial fatigue tests under straight cycling at room temperature, while Brown and Miller [*13*] examined multiaxial fatigue effects at elevated temperatures. There are essentially no results on creep-fatigue interaction for these steels under multiaxial stress conditions available in the literature. This is primarily due to the difficulties associated with performing such tests.

In an earlier paper [*14*] the influence of a biaxial stress state on low-cycle fatigue of 1Cr-1Mo-¼V steel at 538°C was examined using blunt notched compact tension (CT) specimens. Crack initiation results were correlated with uniaxial fatigue data using the Davis-Connelly triaxiality factor. All of these tests were conducted under straight cycling conditions at 1 cpm. An extension of this work to include the effect of a 1 h hold time is presented in this paper. A brief review of the proposed criterion is given, and additional assessment of its predictive capability is made by analyzing published multiaxial fatigue data for Cr-Mo-V steels.

Review of Proposed Method

The role of the state of stress and strain rate of a material at elevated temperature has been discussed by Manjoine [15–17]. For relatively ductile materials, the following empirical relationship between ductility and state of stress has been proposed

$$\frac{\bar{\epsilon}_f}{\epsilon_{fo}} = 2^{(1 - \mathrm{TF})} \tag{1}$$

where $\bar{\epsilon}_f$ and ϵ_{fo} are the effective strain limits for multiaxial and uniaxial stress, respectively, TF is the Davis-Connelly triaxiality factor [18]

$$\mathrm{TF} = \frac{\sigma_1 + \sigma_2 + \sigma_3}{\bar{\sigma}} \tag{2}$$

and $\bar{\sigma}$ is the von Mises effective stress. The measured reduction in ductility for a number of materials and multiaxial stress states has shown good correlation with this expression [16,19].

In low-cycle fatigue under multiaxial stress conditions, we assume a strain-life equation in terms of effective plastic and elastic strain components, with the plastic term modified by Eq 1

$$\Delta\bar{\epsilon}_t = 2^{(1 - TF)}\, C\, N_f^{-b} + G\, N_f^{-g} \tag{3}$$

where the constants are derived from uniaxial fatigue data. The motivation for extending Eq 1 to fatigue is based on the relationship of plastic strain to ductility [20].

Mowbray [21] has suggested a similar criterion for biaxial fatigue based on principal strain ranges. It can be shown that his relation has the form of Eq 3 with the plastic strain modified by a different function of the TF

$$\Delta\bar{\epsilon}_p = \frac{3 - m\,\mathrm{TF}}{3 - m}\, C\, N_f^{-b}$$

where m is an empirically derived material constant.

Experimental Work

Specimens and Test Procedure

Low-cycle uniaxial and biaxial fatigue tests were made on 1Cr-1Mo-¼V rotor steel at 538°C. Test specimens were taken from a section of a turbine rotor forging. The tensile properties and heat treatment of the material are given in Table 1.

The biaxial stress state was produced using a CT specimen containing a 1.19 mm notch root radius, shown in Fig. 1. Dowling and Wilson [*22*] have shown that for a thickness to notch root radius ratio greater than 5, plane-strain conditions are achieved at the notch tip. Under these conditions, the notch tip strain and stress are

$$\epsilon_x : \epsilon_y : \epsilon_z = -\mu/(1-\mu) : 1 : 0$$
$$\sigma_x : \sigma_y : \sigma_z = 0 : 1 : \mu$$

for the coordinate system shown in Fig. 1. Since no equipment for directly measuring notch root strain was available, the notch opening displacement (NOD) was controlled during the fatigue tests.

All fatigue tests were run at a frequency of 1 cpm with a hold time of 60 min at maximum strain. The majority of tests were performed at $A_\epsilon = 1.0$ ($A_\epsilon = \epsilon_{alt}/\epsilon_m$) although a few were run under completely reversed strain cycling at $A_\epsilon = \infty$. Complete details of the test procedure and results of the straight cycling tests at 1 cpm were presented in Ref *14*. Additional results for the hold time tests are given in this paper.

Notch Strain-Displacement Calibration of the CT Specimen

An elastic-plastic plane-strain finite-element analysis was made to determine the local stress-strain response at the notch tip [*14*]. Cyclic stress-strain curves at half life, as determined from the uniaxial fatigue tests, were used as effective (von Mises) stress-strain curves in the analysis. The influence of stress relaxation

TABLE 1—*Tensile properties and heat treatment of 1Cr-1Mo-¼V test specimen material.*

	24°C	538°C
Modulus of elasticity, GPa	200.0	172.4
0.2% yield strength, MPa	643.7	499.9
Ultimate tensile strength, MPa	802.1	545.4
% elongation (in 5.08 cm)	17.0	18.4
% reduction in area	45.8	68.3
Heat treatment		
Austenitize at 954°C		
Air cool		
Temper at 662°C		

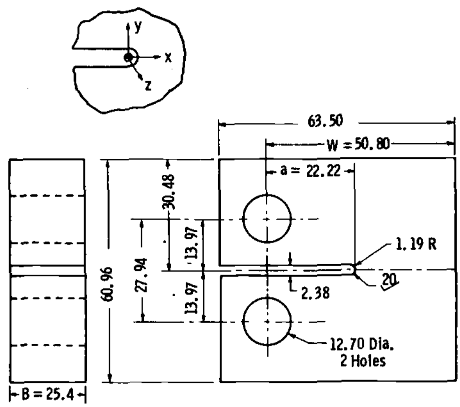

FIG. 1—*Blunt notched compact tension specimen. Dimensions in millimetres.*

due to the hold time was included by using the relaxed stress range at the end of the 60 min hold period. The difference between this curve and that for straight cycling is illustrated in Fig. 2 which also shows the 5 segment piecewise linear representation of the curves used in the analyses. Note that this represents a monotonic loading analysis based on stable cyclic behavior. Reasonable predictions of cyclic strains have been made [*22,23*] by using the stable cyclic stress-strain curve in a monotonic elastic-plastic finite element analysis.

Neglecting time dependent effects, the analysis predicts a unique relation between NOD and notch strain amplitudes. Therefore under these conditions, control of NOD during cyclic tests should be equivalent to strain control. With a hold time at maximum NOD, however, creep may occur at the notch tip

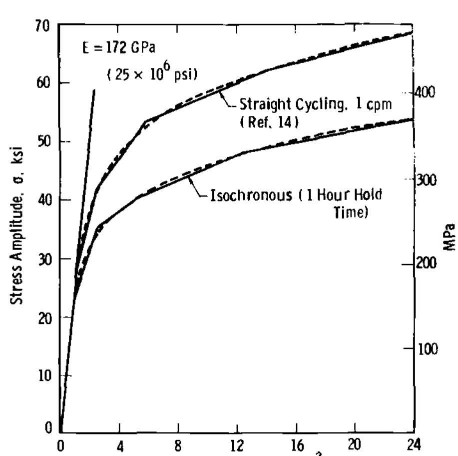

FIG. 2—*Piecewise linear representation of the cyclic stress-strain curves for 1Cr-1Mo-¼V steel at 538°C.*

resulting in a variation in strain and possibly TF. Note that some account of this is taken when the isochronous stress-strain curve is used in the analysis. To further examine these effects, a creep analysis was made using the 1 cpm curve (top curve, Fig. 2) together with a second stage creep law for this material. It was found that during a 1 h hold at maximum NOD and for an initial strain amplitude of 0.02, the strain change was less than 5% while the TF varied less than 2%.

Results

Uniaxial Tests

The frequency-modified life method [*24*] was used to correlate all of the uniaxial test results for this material. A least-squares multiple regression analysis of the strain range and life data for the two frequencies (in the hold time tests the frequency is assumed to be the inverse of the total cycle time, or 0.0167 cpm) gave the following equations for the elastic and plastic components

$$\Delta\epsilon_{eo} = 0.0081\ N_f^{-0.083}\nu^{0.08} \tag{4a}$$

$$\Delta\epsilon_{po} = 1.81\ N_f^{-0.75}\nu^{0.14} \tag{4b}$$

where ν is the frequency in cycles per minute. Figure 3 shows the total strain range versus life data and the corresponding fit of the sum of Eqs 4*a* and 4*b*.

Crack initiation in low-cycle fatigue was discussed in some detail in Ref *14*, where several empirical equations were reviewed. It was shown that under straight cycling conditions, the number of cycles to the first deviation from the stabilized

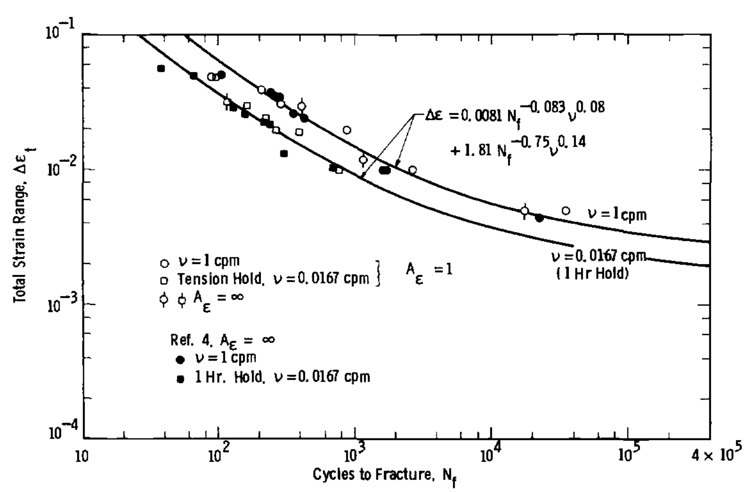

FIG. 3—*Total strain range versus cycles to fracture for uniaxial tests of 1-Cr-1Mo-¼V steel at 538°C showing effect of test frequency or hold time.*

stress versus cycle curve (here, stabilized may imply either a zero or a constant slope), N_O, agrees reasonably well with the expression for crack initiation suggested by Manson and Hirschberg [25]

$$N_i = N_f - 4N_f^{0.6} \tag{5}$$

Here N_i is the number of cycles to produce an "engineering size" crack of 0.15 to 0.25 mm in notched specimens.

A relatively large data base of Cr-Mo-V fatigue data from several investigators was subsequently examined for crack initiation based on N_O as defined previously. Figure 4 shows a plot of N_O versus N_f for the data and a comparison with two empirical expressions, Eq 5 and

$$N_O = N_f - 1.22\, N_f^{0.75} \tag{6}$$

which was obtained from a log-log plot of $(1 - N_O/N_f)$ versus N_f. We assume that Eq 6 can predict initiation of "engineering size" cracks in the CT specimens and that such a point corresponds to the first change in the stabilized compliance, $\Delta V/\Delta P$. Without suggesting a definite crack size we will simply define crack initiation as the early stages of damage. As will be shown, an estimate of this crack size can be made from the test results.

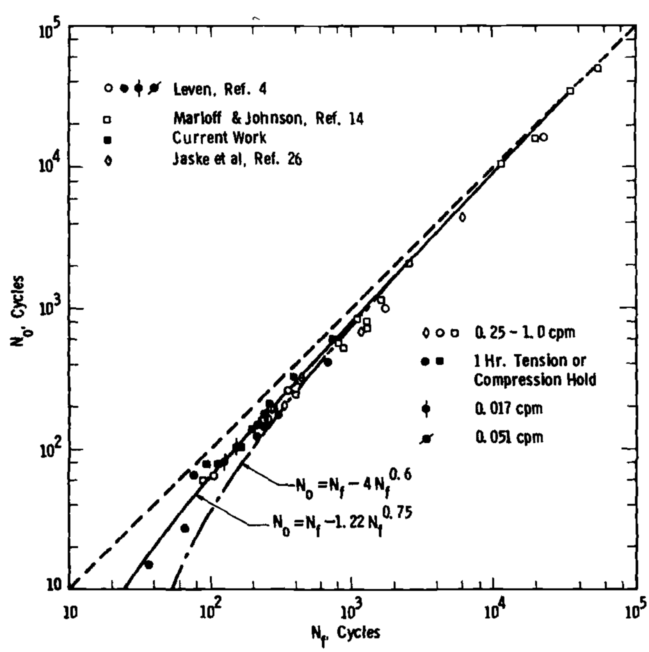

FIG. 4—*Comparison of crack initiation of Cr-Mo-V steel at 538°C based on* N_O *determined from uniaxial specimens with two empirical predictions.*

CT Specimen Test Results

The results of the CT specimen low-cycle fatigue tests with hold times are given in Table 2. The effective strain ranges were obtained from the finite element analysis. The load range, ΔP_r is at the end of the hold period and represents the stabilized value. Tests were terminated at N_T which was well beyond N_O, and the specimens were pulled apart for observation. Except for Test D3 which was deliberately terminated early, most specimens showed evidence of multiple crack initiation.

The largest measured crack depth is given in Table 2. For Tests C9 and D1, the compliance change was essentially continuous so that a definite change in slope was not discernible. However, cracks were observed in both of these tests. In Test D3, the test was stopped at $N_T = 25$ cycles to inspect for cracks. None could be observed under light microscopy in this specimen.

Correlation of Results

For plane-strain conditions, the TF is a function of Poisson's ratio, and for plastic conditions, TF = 1.73. Evaluating Eq 3 using the constants from Eqs 4*a* and 4*b* with $\nu = 0.0167$ cpm, we obtain the proposed strain-life relationship for plane strain

$$\Delta\bar{\epsilon}_t = 0.615\, N_f^{-0.75} + 0.00583\, N_f^{-0.083} \tag{7}$$

This equation cannot apply to fracture of the CT specimen because of strain gradients and differing crack growth rates between uniaxial and CT specimens. However, using Eq 6 with Eq 7, we obtain the crack initiation curve shown as the dashed line in Fig. 5.

The measured values of N_O and N_T at test termination are shown in Fig. 5. For Tests C8, CI0, and D2, N_O shows good agreement with the prediction. Comparison of Tests C9 and D2 for the same strain range shows qualitative agreement in crack size at N_T, although N_O for the former was not discernable.

TABLE 2—*Summary of displacement controlled CT specimen fatigue tests for Cr-Mo-V steel at 538°C.* [ν = *1 cph (1 h hold time)*].

Test No.	ΔV,[a] mm	$\Delta\bar{\epsilon}$	ΔP_r, kN	Cycles N_O	N_T	Maximum Crack Depth, mm
C8	0.434	0.0226	44.2	75	149	0.20
C9	0.330	0.0152	35.1	. . .[b]	320	0.27
C10	0.472	0.0262	48.8	35	138	0.33
D1	0.325	0.0148	33.6	. . .[b]	415	0.58
D2	0.330	0.0152	34.8	180	350	0.41
D3	0.335	0.0156	33.7	. . .[b]	25	none

[a]0 to maximum displacement.
[b]No measurable compliance change.

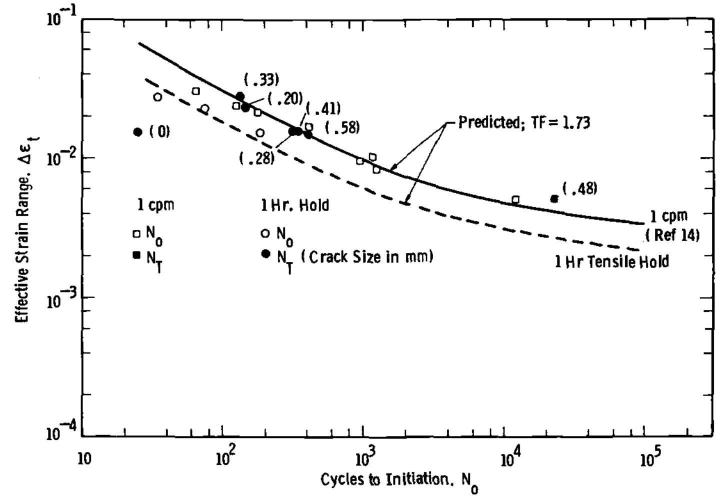

FIG. 5—*Comparison of measured and predicted strain-life behavior for Cr-Mo-V steel at 538°C under plane-strain conditions (TF = 1.73). Data from CT specimens.*

Also shown in Fig. 5 are the results of the straight cycling tests, Ref *14*, and a comparison with the prediction denoted by the solid curve.

Figure 6 shows a plot of the largest crack size measured at termination versus number of cycles to termination, N_T. The latter is normalized with respect to N_i given by Eqs 6 and 7 or the dashed curve in Fig. 5. The open points are the

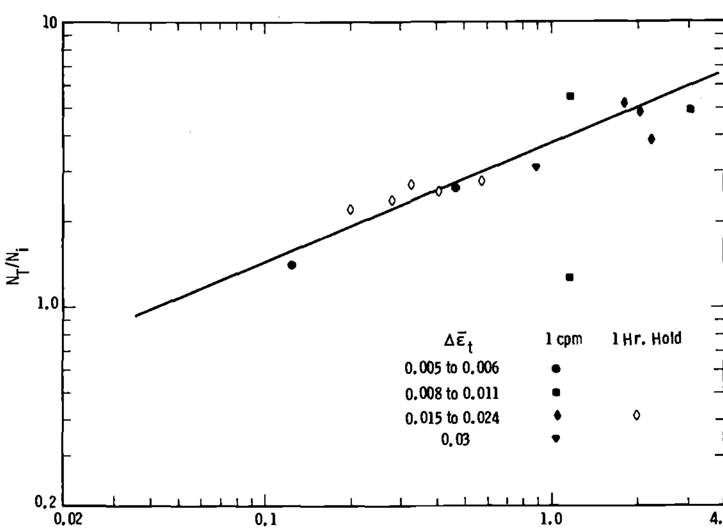

FIG. 6—*Relationship between maximum crack depth and cyclic life for blunt notched CT specimens of Cr-Mo-V steel at 538°C.*

results of the hold time tests from Table 2. In addition, the results from the 1 cpm tests [14] are included as solid points. Strain ranges are also indicated. With one exception, the data correlate reasonably well assuming a linear relationship on this plot. An extrapolation to $N_T/N_i = 1.0$ suggests a crack size on the order of 0.05 mm at our definition of initiation.

Analysis of Other Multiaxial Fatigue Results for Cr-Mo-V Steels

To further assess the predictive capability of the method, some published biaxial fatigue data on Cr-Mo-V steels were analyzed. Unfortunately, such data, particularly at elevated temperatures, are rather limited. Also it is necessary that the elastic and plastic strain components are separable in the results. Only three such references were identified; the work of Brown and Miller [13] at 565°C and investigations by Liddle and Miller [12] and Lohr and Ellison [11], both at room temperature. The materials used in these investigations were similar to the present material in chemistry and tensile properties.

Brown and Miller's tests [13] were made both at 20 and 565°C using combined axial-torsion loading conditions. The tests were conducted at fixed ratios of shear to axial strain ranges. Such stress states produce TFs between 0 and 1.

In the analysis of their results, it was assumed that the von Mises yield criterion together with the Prandtl-Reuss flow rule in total deformation form could characterize the plastic behavior. Because no test points were included in their paper, all analyses were made using data calculated from empirical stress and strain-life relations. Figure 7 shows a correlation of the elevated temperature test results in terms of measured vs. predicted life at 50, 100, 300, 1000, and 2000 cycles.

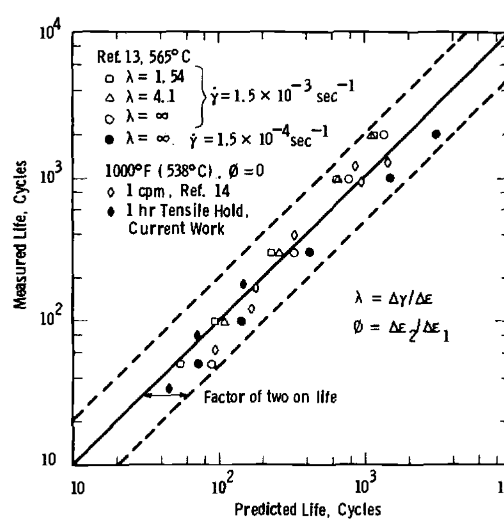

FIG. 7—*Comparison of measured and predicted life for Cr-Mo-V steel under various biaxial stress conditions based on TF.*

The predicted life was based on total strain, Eq 3 using the appropriate uniaxial constants. Also shown in Fig. 7 are the present results and those from Ref *14*. It can be seen that the method results in life predictions within a factor of two.

In the work of Liddle and Miller [*12*], strain controlled axial-torsion tests at 20°C were made using the same test procedure as in Ref *13*. No test points are given, so that, again, the effective plastic strain ranges, stress ratios, and TF were calculated. Predicted versus measured life for these data is shown in Fig. 8 for five arbitrarily selected strain levels. The prediction is based only on the plastic strain component in Eq 3. The scatterband is less than ± 1.5 on life prediction.

Lohr and Ellison [*11*] performed room-temperature biaxial stress fatigue tests on tubular specimens subjected to combined axial loading and internal pressure at fixed ratios of $\phi = \Delta\epsilon_2/\Delta\epsilon_1$. In addition to the uniaxial case, these ratios included equibiaxial (TF = 2), plane strain (TF = 1.73), and pure shear (TF = 0) stress states. From the test points given in Fig. 6 of their paper, and using N_f as the dependent variable [ASTM Practice for Statistical Analysis of Linear or Linearized Stress-Life (*S-N*) and Strain-Life (ϵ-*N*) Fatigue Data (E 739-80)], regression analysis of the uniaxial strain-life data gave

$$\Delta\epsilon_p = 2.50\, N_f^{-0.95}$$
$$\Delta\epsilon_e = 0.0188\, N_f^{-0.149}$$

Based on total strain, Eq 3 gives the predictions shown in Fig. 8. The worst correlation was for $\phi = 1$ where the TF method predicted, on the average, only about 65% of life. Comparing the prediction for plastic strain only, we have $\Delta\bar{\epsilon}_p = 1.25\, N_f^{-\alpha}$ versus the empirical equation $\Delta\bar{\epsilon} = 2.32\, N_f^{-\alpha}$, ($\Delta\bar{\epsilon}_p = 2\Delta\epsilon_{pz}$ for $\phi = 1$) reported by the authors. It is interesting to note that only for the case of $\phi = 1$ does the von Mises or effective strain approach give a better life prediction for these data. Unfortunately, the elastic strain component was dominant in these data for all of the biaxiality ratios; thus, it does not provide a good test of the plastic-strain correlation. Room temperature results from Brown and Miller [*13*] are also shown in Fig. 8.

Note that it has been assumed at the outset that the exponents on life in the strain-life equations are independent of stress state. While the methods of data presentation differed among the various investigators, it was observed that the exponents showed only minor variations with biaxiality ratio for the elastic and plastic-strain components.

Discussion

In the earlier CT specimen test series reported in Ref *14*, it was observed that identification of crack initiation from compliance changes became more difficult as the strain range decreased. Some evidence of this was seen in the present tests also. At the lowest strain range, N_O could be identified in only one of three

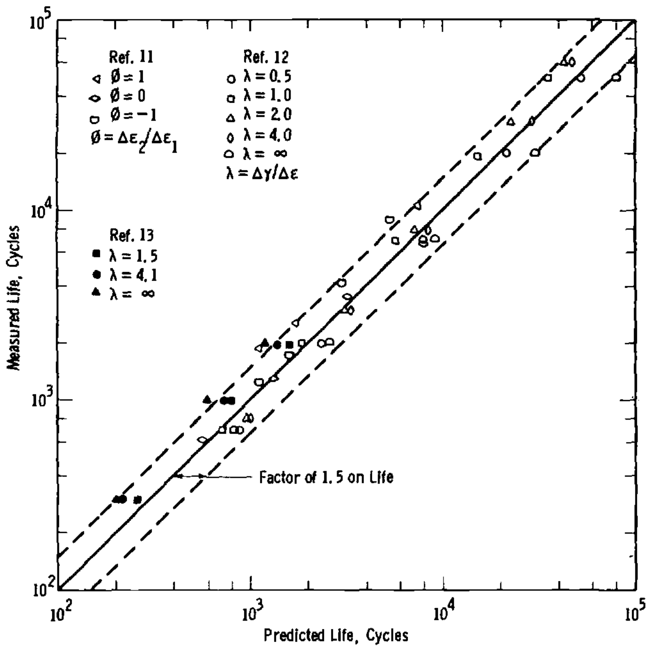

FIG. 8—*Comparison of measured and predicted life of Cr-Mo-V steel under various biaxial stress conditions based on TF. Room-temperature test data from various investigators.*

tests. In general, it was found that N_O was more difficult to determine in these hold time tests than in continuous cycling tests. It is possible that the stability of the compliance versus cycles curve is influenced by the hold period. During additional testing of CT specimens having a larger root radius, no compliance change occurred at crack initiation for all strain ranges. Thus, for these tests, a sacrificial method was used whereby duplicate tests were made, terminating at various number of cycles to measure crack size. Such a procedure is probably the best way to accurately identify crack initiation.

In spite of this difficulty, reasonable correlation was achieved in several tests using the TF approach. This also gives confidence in the use of isochronous cyclic stress strain curve to treat hold time effects. At the same time, however, it is recognized that considerable additional testing is necessary where strain gradients are absent and strains are directly measurable.

In the analysis of the published data where the strain components necessary for application of the method were not given, using total deformation plasticity theory may not be entirely accurate. Also, in most cases, actual test data points were not given so that analyses were based on best-fit empirical equations. Both of these factors make the absolute accuracy of correlations somewhat questionable. However, the trends in the results indicate that the TF approach is promising for life prediction involving proportional loading. The published results together with the present data encompass the full biaxial range of TF from 0 to 2. Further development of the TF method and further testing will be necessary in order to include nonproportional loading.

As indicated in Ref *14*, for greater generality the value 2 in Eq 3 can be changed, if a different relative torsional ductility is more appropriate for a given material. An alternate form was proposed by Manson and Halford. Their multiaxiality factor approach is equivalent to substitution of $2 - TF$ (where $TF \leq 1$) or TF^{-1} (where $TF \geq 1$) for the term $2^{(1 - TF)}$.

Conclusions

1. Use of the TF with the frequency-modified life characterization, shows some promise in treating hold time effects in fatigue.

2. Because of the difficulty in identifying compliance changes for low strain ranges and hold times, crack initiation in the CT specimens might better be determined by running sacrificial tests, measuring crack size at various numbers of cycles.

3. Analysis of published biaxial fatigue data on Cr-Mo-V steel both at room temperature and 565°C gave additional confidence in the predictive capability of the TF based approach. These data covered a range of biaxial stress states from pure torsion to equibiaxial.

Acknowledgments

The support provided for this project by the Steam Turbine-Generator Division of Westinghouse Electric Corporation is gratefully acknowledged. M. J. Manjoine contributed to the development of the multiaxial fatigue theory in numerous discussions. The fatigue tests were performed by J. A. Fratangelo.

References

[*1*] Garud, Y. S., *Journal of Testing and Evaluation,* Vol. 9, No. 3, May 1981, pp. 165–178.
[*2*] Brown, M. W. and Miller, K. J. in *Proceedings,* Institution of Mechanical Engineers, Vol. 187, 1973, pp. 745–755.
[*3*] Krempl, E., *The Influence of State of Stress on Low-Cycle Fatigue of Structural Materials: A Literature Survey and Interpretive Report, ASTM STP 549,* American Society for Testing and Materials, Philadelphia, 1974.
[*4*] Leven, M. M., *Experimental Mechanics,* Vol. 13, No. 9, Sept. 1973, pp. 353–372.
[*5*] Coles, A., Hill, G. J., Dawson, R. A. T., and Watson, S. J. in *Proceedings,* International Conference on Thermal and High Strain Fatigue, The Metals and Metallurgy Trust, London, 1967, pp. 270–294.
[*6*] Krempl, E. and Walker, C. D. in *Fatigue at High Temperature, ASTM STP 459,* American Society for Testing and Materials, Philadelphia, 1969, pp. 75–99.
[*7*] Ellison, E. G. and Paterson, A. J. F. in *Proceedings,* Institution of Mechanical Engineers, Vol. 190, Dec. 1976, pp. 319–348.
[*8*] Curran, R. M. and Wundt, B. M. in *1976 ASME-MPC Symposium on Creep-Fatigue Interaction,* Vol. MPC-3, ASME Publication G00112, 1976, pp. 203–282.
[*9*] Thomas G. and Dawson, R. A. T. in *Proceedings,* International Conference on Engineering Aspects of Creep, Vol. 1, Sheffield, 1980, pp. 167–173.

[10] Priest, R. H. and Ellison, E. G., *Materials Science and Engineering*, Vol. 49, No. 1, June 1981, pp. 7-17.
[11] Lohr, R. D. and Ellison, E. G., *Fatigue of Engineering Materials and Structures*, Vol. 3, 1980, pp. 19-37.
[12] Liddle, M. and Miller, K. J., "Multiaxial High Strain Fatigue," *Proceedings*, Third International Conference on Fracture, Munich, 1973.
[13] Brown, M. W. and Miller, K. J., *Fatigue of Engineering Materials and Structures*, Vol. 1, 1979, pp. 217-229.
[14] Marloff, R. H. and Johnson, R. L., "The Influence of Multiaxial Stress on Low Cycle Fatigue of Cr-Mo-V Steel at 1000°F," Welding Research Council Bulletin No. 264, Dec. 1980.
[15] Manjoine, M. J., *Transactions*, American Society of Mechanical Engineers, *Journal of Engineering Materials and Technology*, Series H, Vol. 97, No. 2, April 1975, pp. 156-161.
[16] Manjoine, M. J. in *Inelastic Analysis and Life Prediction in Elevated Temperature Design*, PVP-Vol. 59, Publication H00216, American Society of Mechanical Engineers, pp. 173-184.
[17] Manjoine, M. J., "Elevated Temperature Mechanics of Metals," 1974 Symposium on Mechanical Behavior of Materials, Kyoto, Japan, Society of Materials Science.
[18] Davis, E. A. and Connelly, F. M., *Transactions*, American Society of Mechanical Engineers, *Journal of Applied Mechanics*, Series E., Vol. 81, No. 1, March 1959, pp. 25-30.
[19] Marloff, R. H., Leven, M. M., and Sankey, G. O., "Creep of Rotors Under Triaxial Tension," *Proceedings*, Joint BSSM-SESA International Conference on Measurements in Hostile Environments, Edinburg, 1981.
[20] Manson, S. S., *Experimental Mechanics*, Vol. 5, No. 7, July 1965, pp. 193-226.
[21] Mowbray, D. F., *Journal of Testing and Evaluation*, Vol. 8, No. 1., Jan. 1980, pp. 3-8.
[22] Dowling, N. E. and Wilson, W. K., "Analysis of Notch Strain for Cyclic Loading," *Transactions*, Fifth International Conference on Structure Mechanics in Reactor Technology, West Berlin, Aug. 1979.
[23] Mowbray, D. F. and McConnelee, J. E. in *Cyclic Stress-Strain Behavior-Analysis, Experimentation and Failure Prediction, ASTM STP 519*, American Society for Testing and Materials, Philadelphia, 1973, pp. 151-169.
[24] Coffin, L. F., Jr. in *Proceedings*, Second International Conference on Fracture, Brighton, Chapman and Hall, Ltd., London, 1969, pp. 643-654.
[25] Manson, S. S. and Hirschberg, M. H. in *Proceedings*, First International Conference on Fracture, Vol. 1, 1965, pp. 479-498.
[26] Jaske, C. E. and Mindlin, H. in *2 1/4 Chrome 1 Molybdenum Steel in Pressure Vessels and Piping*, Publication No. G11, American Society of Mechanical Engineers, 1971, pp. 137-210.

Fathy A. Kandil,[1] *Keith J. Miller,*[1] *and Michael W. Brown*[1]

Creep and Ageing Interactions in Biaxial Fatigue of Type 316 Stainless Steel

REFERENCE: Kandil, F. A., Miller, K. J., and Brown, M. W., "**Creep and Ageing Interactions in Biaxial Fatigue of Type 316 Stainless Steel,**" *Multiaxial Fatigue, ASTM STP 853,* K. J. Miller and M. W. Brown, Eds., American Society for Testing and Materials, Philadelphia, 1985, pp. 651–668.

ABSTRACT: A high-strain, biaxial (tension/torsion) fatigue study has been conducted on Type 316 stainless steel at 550°C. The tests were under strain control, some with dwell periods up to 10 min at the positive strain peaks. The deformation and fracture behavior under these conditions revealed a strengthening effect due to the fast carbide precipitation which extended life in some cases. Also it is shown that the form of the multiaxial fatigue failure criterion, modes, and directions of cracking were functions of hold time. The multiaxial cyclic stress-strain curve is best described in terms of shear stress and strain components on the maximum shear plane for a given hold time.

KEY WORDS: stainless steels, elevated temperature, fatigue life, biaxial stresses, damage, hardening (materials), cracking (fracturing)

Nomenclature

C,S,T,k,m,n',q,z	Constants
A_o	Biaxiality factor
a	Crack length
c	Cavity size
E	Young's modulus
G	Modulus of rigidity
N_f	Number of cycles to failure
t	Time
α,β,η	Constants
γ	Shear strain
$\bar{\gamma}$	Equivalent shear strain
Δ	Range of stress or strain
δ	Standard error of estimate

[1]Research student, professor, and senior research fellow, respectively, Department of Mechanical Engineering, University of Sheffield, Sheffield, U.K.

Copyright© 1985 by ASTM International www.astm.org

ϵ	Strain
$\dot{\epsilon}$	Strain rate
λ	$\Delta\gamma/\Delta\epsilon$
μ	Poisson's ratio
ν	Frequency
σ	Stress
τ	Shear stress
ϕ	Biaxiality factor
ψ	Crack inclination angle

Subscripts

A	Axial
B	Biaxial
c	Compression
e	Elastic
eff	Effective
eq	Equivalent
h	Hold period
m	Maximum
n	Normal strain on maximum shear planes
p	Plastic
T	Torsional
t	Tension
x,y,z	Co-ordinates
1,2,3	Principal values ($\epsilon_1 \geq \epsilon_2 \geq \epsilon_3$)

One of the design methods in Code Case N47 of the ASME Boiler and Pressure Vessel Code deals with multiaxial fatigue in conjunction with creep-fatigue interaction. Experimental studies however have revealed that the accuracy of these design rules is uncertain. Wood et al [*1*], for example, have presented some experimental data for Type 316 stainless steel at 625°C to assess uniaxial creep-fatigue interaction (CFI), showing that the damage rule is very conservative in many instances. It has been also shown that the equivalent strain criterion employed is unsatisfactory for correlating low-cycle fatigue data [*2,3*].

Undoubtedly both designers and materials scientists should be provided with a good mechanistic foundation when considering future developments of such design rules. Consequently, a number of different approaches and extensive experimental studies have been pursued in considering materials deformation behavior and endurance at elevated temperatures [*4–15*]. Recently these have been enhanced by two major factors: (1) advances in structural design methods which permit analyses of inelastic behavior under complex loading conditions, and (2) advances in testing and measuring methods.

Naturally, to deal with a complex problem like CFI, researchers have concentrated on the simpler problem of uniaxial loading. However, for real components, the uniaxial mode is only a special case. Results from an experimental program of biaxial fatigue tests are presented in this paper concerning the deformation and fracture behavior of Type 316 austenitic stainless steel at 550°C.

Brief Review

Detailed reviews of low-cycle biaxial fatigue [*2,3*] and multiaxial CFI [*4*] have been published previously. A variety of techniques have been developed to treat multiaxial CFI [*5–10*], most of which were originally developed to correlate data for uniaxial stress. A limited number of experimental studies have been performed in torsion [*11,12*] and multiaxial CFI [*13–15*].

The ASME Boiler and Pressure Vessel Code incorporates a linear damage summation rule for any sequence of fatigue and creep loading. For computing the design number of cycles N_d under in- or out-of-phase loading as required by the damage equation, an equivalent total strain range is given by

$$\Delta\epsilon_{eq} = \frac{\sqrt{2}}{3}\left[(\Delta\epsilon_x - \Delta\epsilon_y)^2 + (\Delta\epsilon_y - \Delta\epsilon_z)^2 + (\Delta\epsilon_z - \Delta\epsilon_x)^2 + \frac{3}{2}(\Delta\gamma_{xy}{}^2 + \Delta\gamma_{yz}{}^2 + \Delta\gamma_{zx}{}^2)\right]^{1/2} \tag{1}$$

Manson and Halford [*5*] presented a special technique for applying the strain-range partitioning (SRP) method to multiaxial CFI. They suggested the use of the Mises-Hencky equivalent stress and plastic strain, defined in terms of principal values as

$$\sigma_{eq} = \frac{1}{\sqrt{2}}[(\sigma_1 - \sigma_2)^2 + (\sigma_2 - \sigma_3)^2 + (\sigma_3 - \sigma_1)^2]^{1/2} \tag{2}$$

$$\epsilon_{eqp} = \frac{\sqrt{2}}{3}[(\epsilon_{1p} - \epsilon_{2p})^2 + (\epsilon_{2p} - \epsilon_{3p})^2 + (\epsilon_{3p} - \epsilon_{1p})^2]^{1/2} \tag{3}$$

to draw an "equivalent" hysteresis loop to be partitioned in the conventional way. The partitioned strain ranges are then multiplied by a multiaxiality factor chosen to fit observed biaxial fatigue behavior.

Coffin [*7*] also suggested the use of Eq 3 to characterize an equivalent strain parameter to be used in the frequency separation approach. The endurance is related to equivalent plastic strain range by

$$\Delta\epsilon_{eqp} = C' N_f^{-\beta}\left(\frac{\nu_t}{2}\right)^{\beta(1-k)}\left(\frac{\nu_c}{\nu_t}\right)^{\beta\eta} \tag{4}$$

where C', β, k, η are numerical coefficients dependent on material and testing conditions, and ν_t and ν_c are the frequencies during tension and compression, respectively.

None of these approaches have been verified by a complete set of experimental biaxial data. However Zamrik [13] tested Type 304 stainless steel at 649°C under uniaxial, torsional, and biaxial CFI conditions. He applied SRP, but the torsional endurance data were distinctly separated from the uniaxial and the biaxial results, although he did not use Manson's multiaxiality factor. It has been shown that Eq 1 is not suitable for describing fatigue behavior [8,12,16,17] especially in the low endurance regime, which largely accounts for the divergence in Zamrik's data.

Majumdar and Maiya [8,18] have developed a promising mechanistic model for predicting fatigue crack growth rate in the presence of cavities

$$\frac{1}{a} \times \frac{da}{dt} = \left\{\frac{T}{C}\right\} \left(1 + z \ln \frac{c}{c_o}\right) |\epsilon_p|^m \, |\dot{\epsilon}_p|^k \tag{5}$$

where

a = crack length,
c_o and c = initial and current cavity sizes,
$|\epsilon_p|$ = modulus of the current plastic strain, and
T, C, m, k, and z = material parameters.

For multiaxial CFI, Majumdar postulated that the fatigue life for continuous cycling is given by

$$N_f = \frac{m + 1}{2 A_o} (\Delta\epsilon_{\text{eff}})^{-(m + 1)} (\dot{\epsilon}_{\text{eff}})^{1 - k} \tag{6}$$

where

$\Delta\epsilon_{\text{eff}}$ = effective plastic strain range given by Eq 3,
A_o = function of the ratio $(\Delta\epsilon_{np}/\Delta\epsilon_{\text{eff}})$, and
$\Delta\epsilon_{np}$ = plastic normal strain range on the maximum shear strain plane.

This expression leads to an equivalent strain to replace ϵ_p in Eq 5.

In a recent paper [17] the authors derived an equivalent shear strain parameter ($\bar{\gamma}$) for correlating in-phase multiaxial fatigue endurance behavior,

$$\frac{1}{2}\bar{\gamma} = \left[\left(\frac{1}{2}\gamma_m\right)^\alpha + S \times \epsilon_n{}^\alpha\right]^{1/\alpha} \tag{7}$$

where

$$\frac{1}{2}\gamma_m = \frac{\epsilon_1 - \epsilon_3}{2} \tag{8}$$

and

$$\epsilon_n = \frac{\epsilon_1 + \epsilon_3}{2} \tag{9}$$

The parameters α and S are material, temperature, and strain rate dependent, and must be determined experimentally. One of the main features of Eq 7 is its flexibility in describing the variation between different materials and testing conditions. It is worth noting that many of the classical deformation and fatigue criteria could be written in the form of Eq 7 with suitable values of α and S in each case. Collected data under biaxial fatigue show that the parameter α does not have a unique value, although it generally lies between 0.5 and 3. Lower values give safer design predictions. Appendix I shows how the parameters α and S may be determined, for the combined tension/torsion case.

The effect of dynamic strain ageing has received some attention especially for the high-cycle fatigue regime. Hirose et al [19] tested low-carbon steel at room and elevated temperatures. They found that dynamic strain ageing had a significant effect on retarding fatigue crack growth, and the fatigue limit showed a maximum value at about 375°C due to the rapid strain ageing at this temperature. Coffin [7] said that dynamic strain ageing may produce opposite effects to a normal material because of the reversed sensitivity to strain rate associated with this phenomenon—the flow stress increases with decreasing the strain rate.

Material and Testing Details

The material used was Type 316 austenitic stainless steel, solution annealed at 1050°C for 30 min in vacuum followed by air cooling. The chemical composition was 0.06C, 0.49Si, 1.75Mn, 17.68Cr, 12.30Ni, 2.34Mo, 0.021S, 0.035P, 17 ppm B, and 0.040N. The average grain diameter (taking twin boundaries into account) was 32 μm.

The elastic constants were determined from the first quarter cycle of each test and generally agreed favorably with those obtained from monotonic tensile tests (Table 1).

The test specimens were in tubular form having 25 mm gage length with 22 and 16 mm outside and inside diameters, respectively. The bores were honed while the outside surfaces were polished such that cracks should not initiate in polishing marks. Axial and torsional strain were measured over the gage length with a biaxial extensometer. In the uniaxial tests on these specimens, crack growth was observed from the bore. However the same density of cracking was

TABLE 1—*Tensile properties and elastic constants for 316 stainless steel (strain rate = 10^{-3} S^{-1}).*

	Tensile Properties				Elastic Constants		
Temperature, °C	0.2% Proof Stress, MPa	Ultimate Tensile Strength, MPa	Elongation, %	Reduction in Area, %	E, GPa	G, GPa	μ
Room temperature	298	593	61	77	189	...	...
550	136	465	46	65	154	57.9	0.334

found on the outer, polished surface, indicating that for low-cycle fatigue the honed surface did not reduce endurance.

Strain controlled fatigue tests were performed with a triangular waveform and a rate of maximum shear strain of 10^{-3} s^{-1}. Hold periods of 2 and 10 min were included at peak tensile strain, during which the relaxation of both torque and axial stress was recorded. Three biaxial strain states were tested, uniaxial ($\lambda = 0$), torsional ($\lambda = \infty$), and biaxial ($\lambda = 2$), where the biaxiality ratio λ is $\Delta\gamma/\Delta\epsilon$; $\Delta\gamma$ and $\Delta\epsilon$ being torsional and axial total strain ranges, respectively.

A four zone heater was used to give a uniform temperature over the gage section within ±5°C. All tests were conducted at 550°C. A full description of the testing rig is given in Ref [*20*].

Results

Cyclic Stress-Strain Behavior

The deformation behavior of 316 stainless steel at 400 and 550°C has been discussed in Ref [*17*]. At both temperatures the multiaxial cyclic stress-strain curve is adequately represented in terms of maximum shear stress and strain for continuous cycling.

Although the material showed changes in endurance with the insertion of a hold period in the fatigue cycle, the general trend of the deformation response was unaffected. For all loading cases, the material hardened rapidly to a peak value followed by slight softening to a stable cyclic condition. At high strain ranges and longer hold times the material softened slightly from the peak until failure.

Figure 1 shows the cyclic stress-strain curves for 0, 2, and 10 min hold times in terms of maximum shear stress amplitude, $\tau_m = (\sigma_1 - \sigma_3)/2$, and one half of the maximum plastic shear strain amplitude, $\frac{1}{2}\gamma_{pm} = (\epsilon_{1p} - \epsilon_{3p})/2$, plotted on logarithmic scales. A full stress analysis is presented elsewhere [*4,21*]. Values of stresses and strains were determined at midlife, and the plastic strain components were computed at the peak stresses of the hysteresis loops, that is, they do not include creep components due to load relaxation. Tresca's criterion correlates quite successfully the cyclic behavior of the material in all cases (Fig. 1). The insertion of hold times seems to have no effect on the applicability of the criterion.

Within strain limits the cyclic stress-strain curve can be fitted to the equation

$$\tau_m = k' \, (0.5 \, \gamma_{pm})^{n'} \tag{10}$$

where

k' = cyclic strength coefficient and
n' = cyclic strain hardening exponent.

Values of the constants of Eq 10 are given in Table 2, with the limits of applicability. The deviation from linearity at high strain levels, and also for low

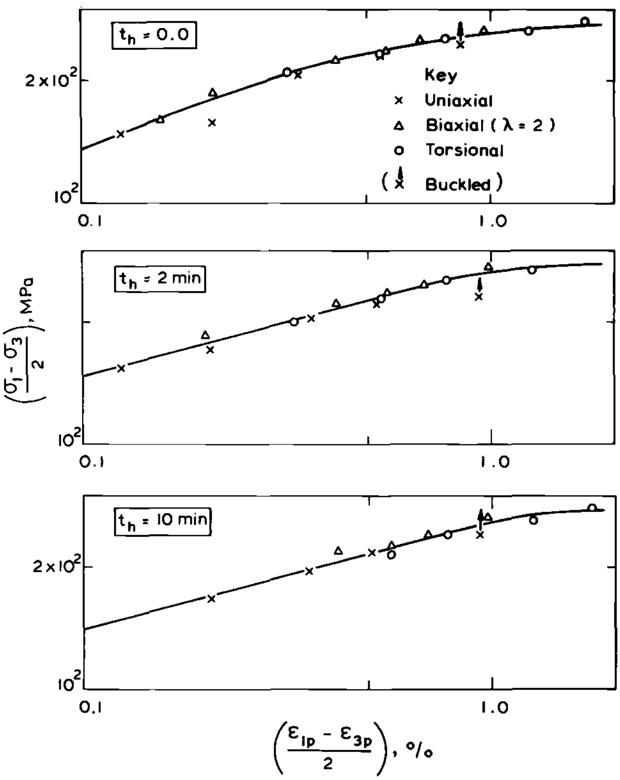

FIG. 1—*Stabilized cyclic stress-strain curves for AISI Type 316 stainless steel at 550°C.*

strain levels in the case of zero hold time, reflects changes in the material hardening characteristics.

Brown and Miller [*21*] found a value of n' equal to 0.24 for 316 stainless steel at 400°C. The same value has been quoted by Coffin [*22*] for 650°C. Table 2 shows similar values irrespective of the hold time. This indicates that the cyclic hardening exponent for this material is constant within the temperature range 400 to 650°C.

Comparing the curves of Fig. 1, one can hardly distinguish between them. At low strain levels ($\frac{1}{2}\gamma_{pm} < 0.3\%$), the 2-min curve shows slightly higher stresses than zero hold which may be due to carbide precipitation during the

TABLE 2—*Cyclic stress strain relationship constants (Eq 10).*

t_h, min	k', MPa	n'	Range of Application of $\Delta\gamma_{pm}$ (%)
0	824	0.240	0.8 to 4
2	853	0.250	0.4 to 4
10	822	0.250	0.8 to 4

long duration of the 2-min tests. The 10-min curve shows the same shape as the 2-min curve but is slightly lower due to recovery during the hold periods.

Wood and Wynn [*23*] found that at low strain levels, near the fatigue limit, the material hardens continuously up to failure. Their result emphasizes the dependency of the cyclic hardening characteristics of this material on stress or strain level. It is therefore not advisable to extend the lines defined in Table 2 to strain levels below the limits given.

Endurance

Since cyclic hardening occupies a small proportion of the total fatigue life, the stress and strain values at midlife may be used to characterize the average plastic strain amplitude during the test.

Figure 2 presents the lives obtained for three hold periods, 0, 2, and 10 min, plotted against maximum plastic shear strain amplitude, $\frac{1}{2}\gamma_{pm}$. This is a viable basis for direct comparison of the three biaxial stress states, since plastic deformation is governed by the Tresca criterion in Eq *10*.

Most results clearly conform to the Coffin-Manson law

$$\tfrac{1}{2}\gamma_{pm} \times N_f^{\beta} = \text{constant} \tag{11}$$

in which β does not vary markedly with biaxiality. However, there are deviations from this power law relationship particularly at the highest strain levels achieved in the torsion tests. Since the exponent β depends primarily on the cyclic strain hardening exponent, n', the flattening of the stress strain curve for $\frac{1}{2}\gamma_{pm} > 1\%$ causes an increase in β, giving the steeper slope to the torsion data in Fig. 2 above the critical strain level. Deviations also occur for $N_f > 4000$ cycles to give longer endurance, as was also observed at 400°C [*17*].

The effect of hold time on endurance may be seen in Figs. 2*b* and *c*. These data are summarized in Fig. 3, where each line corresponds to a fixed plastic shear strain amplitude. These strains were chosen to give lives of 300, 1000, and 3000 cycles at zero hold time, using Fig. 2*a*. The corresponding endurances at 2 and 10 min holds were derived from the fitted lines in Figs. 2*b* and *c*. Clearly, there is some scatter in the experimental data, reflecting the repeatability of fatigue test results. The standard deviation of the differences in endurance between the test results and fitted lines in Fig. 2 is shown in Fig. 3, to indicate the repeatability of the data.

In the uniaxial test, Fig. 3 shows that life is generally reduced by introducing a hold period, but for torsion this trend is reversed to give slightly higher endurance with 2 min hold time. The biaxial results fall between these two extremes. Thus the relative strengths, torsional to uniaxial, vary with hold time as listed in Table 3. The increase in endurance for torsion with 2 min hold period is comparable with the scatter in data at long life, but rising to a 40% enhancement for the test at the highest strain range. All the torsion tests gave increased lives compared to continuous cycling, suggesting that the indicated trend is genuine.

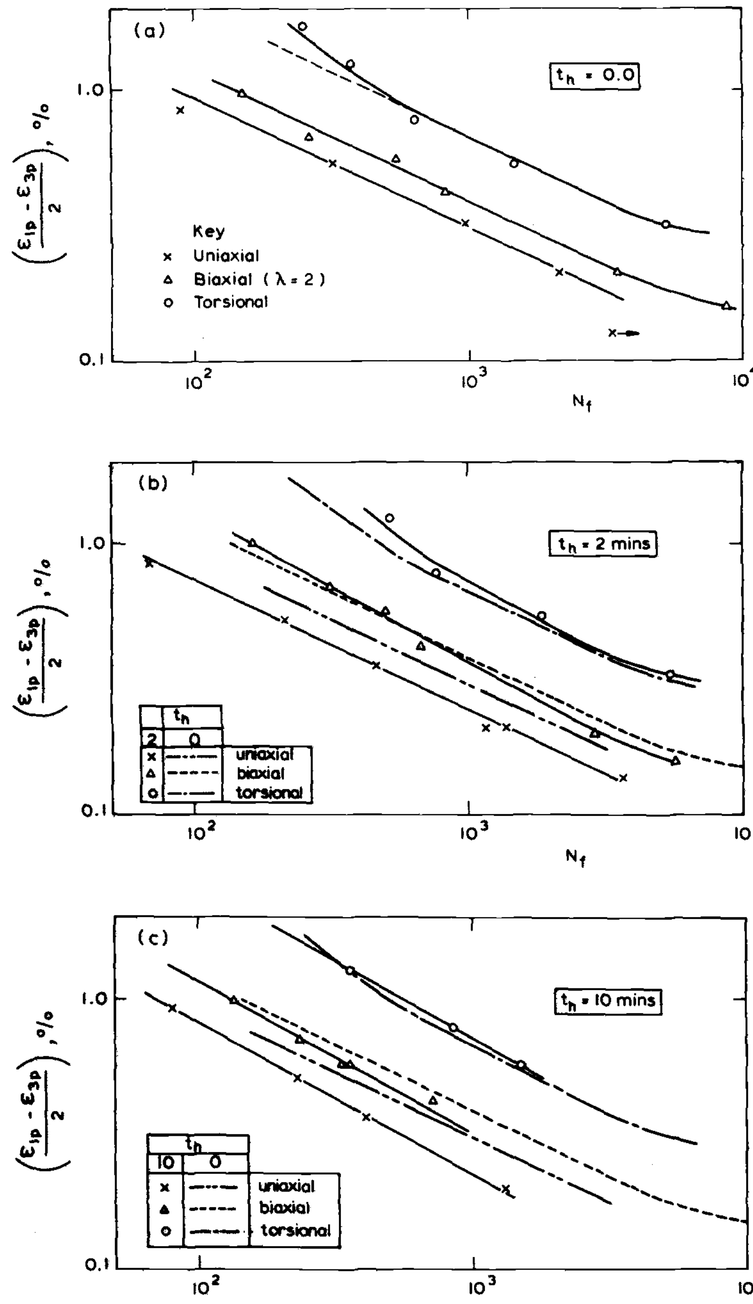

FIG. 2—*Fatigue endurance in terms of maximum plastic shear strain* (a) t_h = *0,* (b) t_h = *2 min and* (c) t_h = *10 min.*

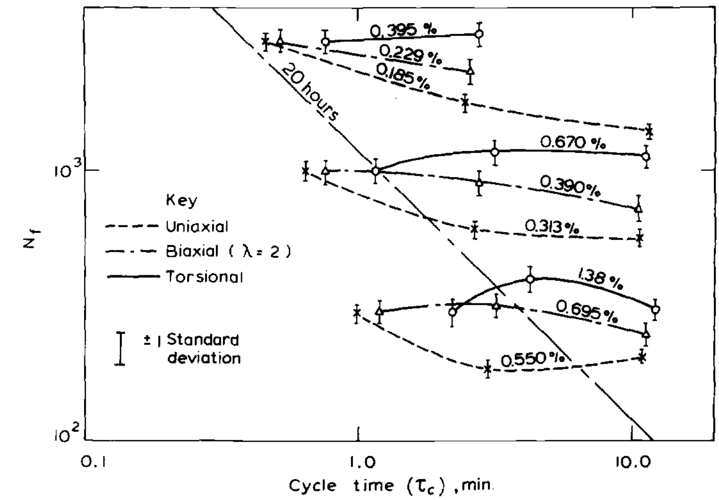

FIG. 3—*Effect of cycle time* (τ_c) *on the number of cycles to failure* (N_f). *Values of* $\frac{1}{2}\gamma_{mp}$, *plastic shear strain amplitude, are shown for each line.*

The average increase measured over four tests was 23%, compared to 10% for the standard deviation of torsional tests, giving a 97% confidence level that a 2 min hold time does enhance LCF endurance, when the results are analyzed using Student's *t* distribution. No significant change can be attributed to the 10 min hold period until more data are available.

Correlation of the Endurance Behavior

The endurance data at zero hold time is presented in Fig. 4. The figure shows three constant life contours (the solid lines) of 500, 1000, and 3000 cycles to

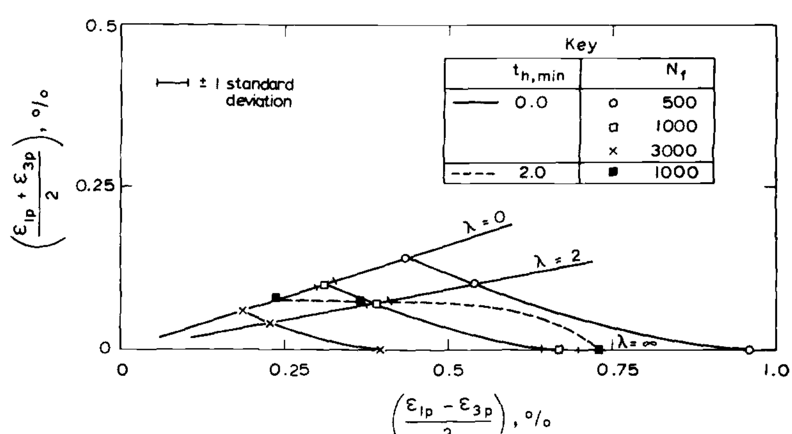

FIG. 4—*Constant life contours on the* Γ*-plane.*

TABLE 3—*Constants of Eqs 7 and 12 for 316 stainless steel at two temperatures.*

Temperature, °C	t_h, min	R^b	α	S	β	C	δ^c
	0	2.2	0.9	2.76	0.53	0.270	0.072
550	2	3.0	1.75	39.37	0.54	0.305	0.063
	10	3.2	1.70	40.28	0.56	0.332	0.040
400[a]	0	2.8	2.0	60.48	0.46	0.244	0.054

[a]Data from Ref *17*.
[b]Torsional/uniaxial strength ratio $R = \frac{1}{2}\gamma_{pmT}/\frac{1}{2}\gamma_{pmA}$ (calculated at $N_f = 1000$).
[c]δ = standard error of estimate for $\log_{10} N_f$ in Eq 12, with $100 < N_f < 4000$.

failure, represented in terms of $\frac{1}{2}\gamma_{pm}$ against ϵ_{pn}, that is, the Γ-plane [*16*]. Unlike the elliptical contours found at 400°C [*17*], those drawn have a concave shape. This change in the shape was accompanied by changes of the observed crack growth modes.

On Fig. 4 a constant life contour for 1000 cycles to failure with $t_h = 2$ min is drawn, which also shows a change in shape due to reduction in the uniaxial strength. The 10-min hold time, which is not shown in the graph, gives a parallel result to the 2 min one but at a slightly lower strength. These changes in constant life contours reflect on the parameters α and S in Table 3. Clearly there is an influence of scatter on the accuracy of these values, but the overall effect of changing shape in Fig. 4 is established from the lines in Fig. 2, each fitted to several data points.

Figure 5 shows the endurance behavior of zero hold time tests correlated by the proposed equivalent plastic shear strain parameter ($\bar{\gamma}_p$). Because $\bar{\gamma}_p$ is directly proportional to γ_{pm}, then any distortion or nonlinearity in Fig. 2*a* will be reflected on Fig. 5. Nevertheless, the figure shows fair correlation for the available data,

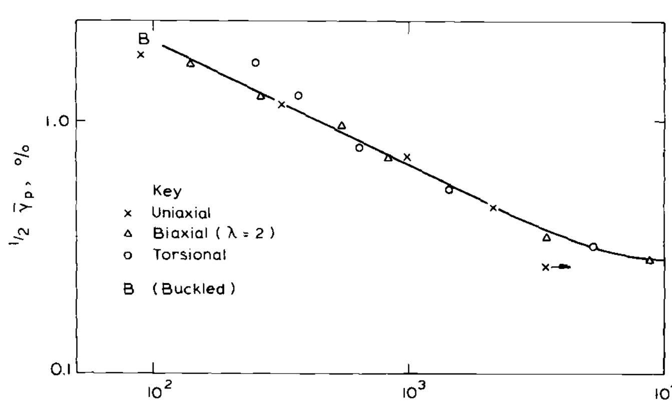

FIG. 5—*Equivalent plastic shear strain correlation for fatigue endurance at 550°C under different biaxial states at zero hold time.*

and the endurance behavior of this material for $100 < N_f < 4000$ can be represented by the equation

$$\tfrac{1}{2}\bar{\gamma}_p \times N_f^{\beta} = C \tag{12}$$

The tests with hold time showed better correlation than those of Fig. 5 in terms of data scatter. Table 3 summarizes the different constants for all cases and gives the standard error of estimate, δ, to indicate the accuracy of correlation.

Since the present data gives a value of $\alpha = 0.9$ for the zero hold time tests, this means that if α is given a fixed value of 2, as suggested by Konter et al [*24*], the prediction will be unconservative for the biaxial case if S is derived from uniaxial and torsional data.

Modes of Crack Growth

Extensive examinations were made on the fractured specimens to study the effect of hold time on the different stages of crack growth. A tool maker's microscope was used for measuring the inclination angle of the cracks on the specimen surface with respect to the specimen axis. Figure 6 shows an example for a biaxial test with 2 min hold time. For biaxial ratio $\lambda = 2$, the expected inclination for Stage I (shear mode) cracks is 18 or 108° compared to 63° for

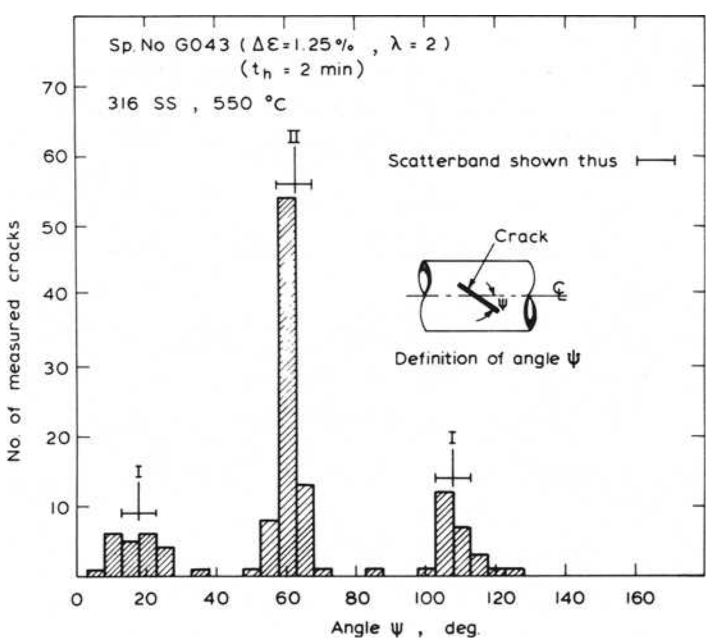

FIG. 6—*Distribution of fatigue crack inclinations on specimen surface.*

Stage II (opening mode). These values are shown in the figure, and cracks within a scatterband of ±5° are classified as Stage I or Stage II, respectively. All the results are summarized in Fig. 7. In all cases the proportion of Stage II cracks decreased as hold time increased up to 1 h because the distribution of crack angles became more diffuse. The Stage I to Stage II ratio increased suddenly from a value of 12% at zero hold time to 44% at 2 min and then gradually decreased with increasing hold time. Only one test was run with a 60 min hold period.

The predominance of the opening mode, particularly at zero hold time, was confirmed for all three biaxial states, for early crack growth.

For torsion, the scanning electron microscope revealed small cracks orientated at ±45° with respect to the specimen axis, covering the entire surface of the specimen. These crossed cracks were in many cases found as strings along the specimen axis [*25*], forming shear mode macrocracks prior to failure.

Increasing hold time from 2 to 10 min showed a decrease in life in most cases. The uniaxial tests at this hold time showed a high proportion of intergranular cracking [*25*]. The biaxial case showed fewer intergranular cracks, whereas growth was transgranular for the torsional loading. Both types of crack are represented in Fig. 6, the more diffuse nature of the distribution of angles ψ being reflected by the onset of intergranular growth with increasing hold period.

Discussion

Cyclic Stress-Strain Behavior

Since both axial and torsional load responses showed significant serration, particularly at high-strain levels, it is of value to discuss Coffin's formulation

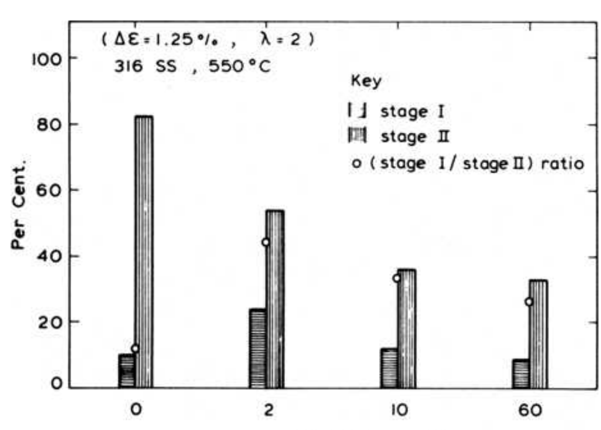

FIG. 7—*Effect of hold time on the proportion of Stage I/Stage II fatigue cracks.*

of Eq 10. He suggested [*22*] that the strain rate dependency of Eq 10 could be represented at a specific temperature by

$$k' = k'' \dot{\gamma}_p{}^q \tag{13}$$

He reported a positive value for the constant q of 0.05, for 304 stainless steel at 650 and 816°C. However at 430°C its value reduced to −0.035 which he related to dynamic strain ageing. This negative strain rate sensitivity was also observed by Kanazawa and Yoshida [*26*] for 316 stainless steel at 450°C and by Abdel Raouf et al [*27–28*] for 304 stainless steel at 470°C and for annealed iron carbon alloy. Since dynamic strain ageing is both temperature and strain rate dependent, one would expect that this negative exponent q should be applicable only within a specific range of strain rates, beyond which it would revert to a positive value. In other words, at temperatures where dynamic strain ageing is expected the exponent q itself should become strain rate dependent.

A strengthening effect can be produced by cyclic ageing associated with the formation of carbides in addition to cyclic hardening due to the multiplication of dislocations. Transmission electron microscope studies showed that well developed dislocation cells formed under cyclic strain [*25*], and for all tests that lasted more than 15 to 20-h carbide precipitation was detected along the dislocation walls as well as the grain boundaries. So the strengthening effect observed by Coffin in austenitic stainless steel could be associated with the formation of a dispersion of carbides nucleated on dislocations, giving rise to the negative exponent q. Once the process is complete, the value of q should become positive again. The process of fast carbide precipitation in fatigue is called here "cyclic ageing" to differentiate it from "dynamic strain ageing."

In conclusion it seems that the insertion of hold time periods in strain cycles has two effects on 316 stainless steel at 550°C. First, the hold time introduces creep recovery, giving a reduction in cyclic stress. Secondly, a beneficial cyclic ageing process can increase the stresses. These two effects oppose each other for the relatively short hold times in Fig. 1, although the stress should be reduced when the period is longer than 10 min.

Endurance

In high-strain fatigue tests, the life is dominated by the crack propagation phase, as has been demonstrated for these tests from fractographic analysis [*25*].

An increase in life with the introduction of hold periods is not allowed for in current approaches to CFI. However, if creep damage is small, as indicated by the lack of intergranular damage in torsion, then any strengthening effect caused by cyclic strain ageing should become apparent. If this was due to the multiplication of dislocations alone, the effect of strengthening on endurance should be apparent for all hold periods, irrespective of biaxiality. But if it was due to carbide precipitation, strengthening would only be found in long-term tests, in which the carbides will have had time to form, that is, in excess of 20 h for the present material, temperature combination.

An additional test was performed in torsion to observe the effect of cyclic ageing. After the first quarter cycle, the specimen was held at constant strain and temperature for 28 h, followed by continuous cycling to failure. During the dwell period, carbides were expected to nucleate on dislocation sites generated in the initial loading. The presence of a dispersion of carbides was confirmed after the test by transmission electron microscopy. In subsequent cycling a life of 2110 cycles was obtained, compared to 1467 cycles in the test on solution annealed material. The 44% increase in endurance suggests that the effects of hold time on torsional tests in Fig. 3 are realistic, in spite of scatter in the data.

Clearly the precipitation is a continuous process, starting as soon as the dislocation cells have formed and continuing well beyond the notional 20 h limit. Nevertheless one may construct a 20 h line on Fig. 3, since this line represents the onset of carbide precipitation of measurable size. All tests falling within a limited band either side of this line were under the effect of three competing processes operating at the same time for a significant proportion of the lifetime. These processes, assuming there are no environmental effects, are:

(*a*) fatigue damage—crack growth due to cyclic strain,
(*b*) creep damage—crack acceleration due to cavitation, and
(*c*) cyclic ageing—crack retardation due to precipitation.

In Fig. 3, the 20 h line corresponds approximately to the increase in torsional fatigue endurance, particularly if at longer lives the time required to form dislocation cells is added to the 20 h period. But in push-pull, creep damage becomes dominant over ageing, giving the reduced endurance observed. Finally for the biaxial tests with $\lambda = 2$, the two processes (*b*) and (*c*) tend to cancel each other, although it is apparent that ageing is completed more rapidly at lower endurances where plastic strains are greater.

Creep Fatigue Interaction Rules

There are two implications from the foregoing discussion for the creep-fatigue rules, listed in the brief review, for materials that exhibit cyclic ageing.

1. Cyclic ageing strengthens the material against fatigue crack propagation. This is indicated not only by the enhanced lives but also by the changes in modes of crack growth to adopt the path of least resistance (Fig. 7). Short-term fatigue test results should not be used to provide baseline data for damage summations, since after ageing one is essentially dealing with a new material that has different fatigue properties.

2. Creep damage, which may be related to the proportion of intergranular cracking, accrues more rapidly in tensile tests than in torsion. Although creep

deformation may be described by equivalent stress and strain formulae (Eqs 2 and 3), the formation of intergranular cracks is dependent on the hydrostatic stress as well as the equivalent strain. A two parameter approach is required in creep damage assessment under biaxial stress, and so the lines in Fig. 3, when extrapolated to longer hold times, may not be parallel. For those materials in which hydrostatic stress plays a dominant role, damage assessments will be over conservative in the torsion case using current procedures.

Conclusions

1. Under biaxial loading with hold times up to 10 min, the cyclic stress strain curve follows a Tresca criterion in Type 316 austenitic stainless steel at 550°C.
2. Creep-fatigue interaction rules should not use short-term baseline data where cyclic ageing has not taken place, if extrapolation to long lives is desired.
3. Fatigue crack growth, creep damage, and cyclic ageing are three contributing processes in creep-fatigue interactions for this material, and this interaction is influenced by multiaxial strain state.

Acknowledgments

The authors would like to acknowledge the assistance of the United Kingdom Atomic Energy Authority UKAEA in providing the material, specimens, and financial support, and helpful discussions with D. S. Wood. E. R. de los Rios provided invaluable help with the metallurgical aspects and microscopy.

APPENDIX

Determination of the Parameters α and S of Eq 7 for the Tension-Torsion Case

Under in-phase loading of combined tension-torsion, the major and minor principal strains are given by

$$\epsilon_1 = \frac{1}{2}(1 - \mu)\epsilon + \frac{1}{2}\sqrt{\gamma^2 + (1 + \mu)^2\epsilon^2} \tag{14}$$

and

$$\epsilon_3 = \frac{1}{2}(1 - \mu)\epsilon + \frac{1}{2}\sqrt{\gamma^2 + (1 + \mu)^2\epsilon^2} \tag{15}$$

where ϵ and γ are axial and torsional semi strain ranges, respectively, and μ is the effective Poisson's ratio which lies between the elastic value and 0.5 for constant volume plastic deformation.

The equivalent shear strain criterion (Eq 7) can be rewritten in the form

$$\frac{1}{2}\bar{\gamma} = \frac{1}{2}\gamma_m\left[1 + S \times \left(\frac{\epsilon_n}{\frac{1}{2}\gamma_m}\right)^{\alpha}\right]^{1/\alpha} \tag{16}$$

where, from Eq 14 and 15, for $\lambda = \gamma/\epsilon$

$$\frac{\epsilon_n}{\frac{1}{2}\gamma_m} = \frac{(1-\mu)}{\sqrt{\lambda^2 + (1+\mu)^2}} \tag{17}$$

Substituting Eq 17 into Eq 16 gives

$$\frac{1}{2}\bar{\gamma} = \frac{1}{2}\gamma_m[1 + S \times \phi]^{1/\alpha} \tag{18}$$

where the biaxiality factor

$$\phi = \left[\frac{(1-\mu)}{\sqrt{\lambda^2 + (1+\mu)^2}}\right]^\alpha \tag{19}$$

To compute the constants α and S of Eq 7 it is easier to use the plastic strains ($\mu = 0.5$), avoiding the problems of determining μ [3].

For any three different biaxial cases, typically uniaxial, biaxial, and torsion, one determines the maximum plastic shear strain components which give the same life. Then

$$S = \left[\left(\frac{\gamma_{mpT}}{\gamma_{mpA}}\right)^\alpha - 1\right] \times \frac{1}{\phi_A} \tag{20}$$

$$S = \left[\left(\frac{\gamma_{mpT}}{\gamma_{mpB}}\right)^\alpha - 1\right] \times \frac{1}{\phi_B} \tag{21}$$

where subscripts A, B, and T refer to axial, biaxial, and torsional cases, respectively, since in torsion ϕ is zero.

Dividing Eq 20 by Eq 21 leads to

$$\left(\frac{\phi_B}{\phi_A}\right)\left[\frac{\left(\frac{\gamma_{pmT}}{\gamma_{pmA}}\right)^\alpha - 1}{\left(\frac{\gamma_{pmT}}{\gamma_{mpB}}\right)^\alpha - 1}\right] = 1 \tag{22}$$

which may be solved for α. The value of S can be obtained from Eq 20 or Eq 21.

References

[1] Wood, D. S., Wynn, J., Baldwin, A. B., and O'Riordan, P., *Fatigue of Engineering Materials and Structures,* Vol. 3, No. 1, 1980, pp. 39–57.

[2] Brown, M. W. and Miller, K. J. in *Low Cycle Fatigue and Life Prediction, ASTM STP 770,* American Society for Testing and Materials, Philadelphia, 1982, pp. 482–499.

[3] Brown, M. W. in *Fatigue at High Temperature,* R. P. Skelton, Ed., Applied Science, 1983, Chapter 3.

[4] Kandil, F. A. "Time Effects on Biaxial Fatigue at Elevated Temperatures," Ph.D. thesis, University of Sheffield, U.K., 1984.

[5] Manson, S. S. and Halford, G. R. in *1976 ASME-MPC Symposium on Creep-Fatigue Interactions,* The American Society of Mechanical Engineers, New York, Dec. 1976, pp. 299–322.

[6] Lobitz, D. W. and Nickell, R. E., "Creep Fatigue Damage Under Multiaxial Conditions," Report No. SAND 76-0720, Sandia Laboratories, Albuquerque, NM, Feb. 1977.
[7] Coffin, L. F. in "Time-Dependent Fatigue of Structural Alloys" Technical Report ORNL 5073, Oak Ridge National Laboratory, Oak Ridge, Tennessee, Jan. 1977, pp. 37–153.
[8] Majumdar, S., *Nuclear Engineering and Design,* Vol. 63, 1981, pp. 121–135.
[9] Fong, J. T. and Penn, R. W. in *Proceedings,* International Conference on Fracture Mechanics and Technology, G. C. Sih, C. L. Shaw, Eds., Sijthoff and Noordhoff, The Netherlands, 1977, Vol. 1, pp. 145–159.
[10] Leis, B. N., *Journal of Pressure Vessel Technology, Transactions,* American Society of Mechanical Engineers, Vol. 99, No. 4, Nov. 1977, pp. 524–533.
[11] Zamrik, S. Y. and Bilir, O. G., *Journal of Engineering Materials Technology, Transactions,* American Society of Mechanical Engineers, Vol. 98, No. 3, July 1976, pp. 244–248.
[12] Wei, K. and Dyson, B. F. in *Mechanical Behaviour and Nuclear Applications of Stainless Steel at Elevated Temperatures,* Book 280, The Metals Society, London, 1982, pp. 136–140.
[13] Zamrik, S. Y., "The Application of Strain Range Partitioning to Multiaxial Creep-Fatigue Interaction," *AGARD Conference Proceedings No. 243,* April 1978, paper No. 16.
[14] Ohnami, M. and Sakane, M., *Bulletin,* Japan Society of Mechanical Engineers, Vol. 21, No. 157, July 1978, pp. 1057–1063.
[15] Ohnami, M. and Hamada, N., "Biaxial Low-Cycle Fatigue of a SUS 304 Stainless Steel at Elevated Temperature," *Proceedings,* 25th Japan Congress on Materials Research, Society of Material Science (Japan), Kyoto, 1982, pp. 93–99.
[16] Brown, M. W. and Miller, K. J., *Proceedings,* Institution of Mechanical Engineering, Vol. 187, 1973, pp. 745–755.
[17] Kandil, F. A., Brown, M. W., and Miller, K. J. in *Mechanical Behaviour and Nuclear Applications of Stainless Steel at Elevated Temperatures,* Book 280, The Metals Society, London, 1982, pp. 203–209.
[18] Majumdar, S. and Maiya, P. S., Journal of Engineering Materials Technology, Transactions, American Society of Mechanical Engineers, Vol. 202, No. 1, Jan. 1980, pp. 159–167.
[19] Hirose, M., Hasegawa, N., and Kato, Y., *Bulletin,* Japan Society of Mechanical Engineers, Vol. 21, No. 158, Aug. 1978, pp. 1201–1207.
[20] Brown, M. W. and Miller, K. J., *Journal of Testing and Evaluation,* Vol. 9, No. 4, July 1981, pp. 202–208.
[21] Brown, M. W. and Miller, K. J., *Journal of Fatigue of Engineering Materials and Structures,* Vol. 1, No. 1, 1979, pp. 93–106.
[22] Coffin, L. F. in *Fatigue at Elevated Temperatures, ASTM STP 520,* American Society for Testing and Materials, Philadelphia, 1973, pp. 5–34.
[23] Wood, D. S. and Wynn, J. in *Measurement of High Temperature Mechanical Properties of Materials,* Her Majesty's Stationery Office, London, 1982, pp. 113–127.
[24] Konter, A.W.A., Janssen, G.T.M., and Husslage, W., "Effect of Biaxial Loading and Geometry on Prediction of Low-Cycle Fatigue Life," *Transactions,* 5th International Conference on Structural Mechanics in Reactor Technology, Berlin, Aug. 1979, Vol. 1, paper No. L13.
[25] De Los Rios, E. R., Kandil, F. A., Miller, K. J., and Brown, M. W., this publication pp. 669–687.
[26] Kanazawa, K. and Yoshida, S., "Effect of Temperature and Strain Rate on High Temperature Low-Cycle Fatigue Behaviour of Austenititc Stainless Steels," *Proceedings,* International Conference on Creep and Fatigue in Elevated Temperature Applications, Institution of Mechanical Engineers, 1974, paper C226/73.
[27] Abdel-Raouf, H., Plumtree, A., and Topper, T. H., *Metallurgical Transactions,* Vol. 5, Jan. 1974, pp. 267–277.
[28] Abdel-Raouf, H. and Plumtree, A., "Low-Cycle Fatigue of Iron at Elevated Temperatures," in Extension Seminar on High Temperature Strength of Metals of the International Conference on Mechanical Behaviour of Materials, Kyoto, Japan, paper No. 1, Aug. 1971.
[29] Challenger, K. D. and Moteff, J. in *Fatigue at Elevated Temperatures, ASTM STP 520,* American Society for Testing and Materials, Philadelphia, 1973, pp. 68–79.

Edwardo R. de los Rios,[1] *Fathy A. Kandil,*[1] *Keith J. Miller,*[1] *and Michael W. Brown*[1]

A Metallographic Study of Multiaxial Creep-Fatigue Behavior in 316 Stainless Steel

REFERENCE: de los Rios, E. R., Kandil, F. A., Miller, K. J., and Brown, M. W., "**A Metallographic Study of Multiaxial Creep-Fatigue Behavior in 316 Stainless Steel,**" *Multiaxial Fatigue, ASTM STP 853,* K. J. Miller and M. W. Brown, Eds., American Society for Testing and Materials, Philadelphia, 1985, pp. 669–687.

ABSTRACT: A metallographic examination of elevated temperature multiaxial fatigue specimens of 316 stainless steel was conducted to identify the type of damage and other microstructural changes that occurred during testing. The work hardening which takes place at the beginning of the test is associated with the development of either a cell or a maze dislocation structure. Two main factors contribute to the flow stress, that is, dislocation and carbide precipitation hardening. Dislocation hardening prevails, but precipitation hardening, which increases with testing time, becomes significant for long hold-time and low-strain range tests. Fatigue cracks are predominantly transgranular. However, intergranular cracks have been observed in hold-time specimens and are related to grain-boundary sliding and grain-boundary precipitation. The fatigue fracture is a three stage process, the initial stage (Stage I) is crystallographic, extending for one to three grains. The intermediate stage (Stage II) is dominated by striations, with the exception of some featureless facets in biaxial specimens. The final stage (Stage III) is a dimple type fracture (tension fracture), beginning at shorter crack lengths in the hold-time and high-strain range specimens. Striation spacing calculations give approximate life estimates in low-cycle fatigue.

KEY WORDS: austenitic stainless steels, fatigue, metallography, fractography, fracture mechanisms, fatigue striations, strain hardening, dispersion hardening, materials, material science

Many components and structures in today's engineering plant require materials to withstand elevated temperatures and complex load cycles for relatively long periods of time. To increase the efficiency and safety of such plant, much research needs to be undertaken to study the creep and fatigue properties of these materials [*1–4*]. One of the materials most suitable for high-temperature applications is 316 stainless steel, since it is known to have good mechanical and corrosion properties.

[1]Research fellow, post-graduate research student, professor, and research fellow, respectively, Department of Mechanical Engineering, University of Sheffield, Sheffield, U.K.

Copyright© 1985 by ASTM International www.astm.org

In some cases, laboratory simulation of the complex thermomechanical conditions of service requires that multiaxial fatigue experiments need to be designed that permit a creep component to be introduced into the fatigue cycle. The interpretation of the results of such experiments in terms of the fracture behavior is however extremely difficult because the deformation response of the material in the crack-tip region is different to that observed in simple uniaxial tests. In some instances, this is a consequence of some complex metallurgical changes brought about by the multiaxial cyclic loading at temperature.

The understanding of these changes is important if the behavior of the material in service is to be predicted. With this objective in mind a metallographic study of specimens tested under various biaxial conditions was initiated with the specific intention of identifying the type of damage and other microstructural changes that occurred during testing.

Experimental Details

The material used was AISI 316 austenitic stainless steel in a solution annealed condition. The chemical composition in weight percentage was 0.06C, 0.49Si, 1.75Mn, 17.68Cr, 12.30Ni, 2.34Mo, 0.021S, and 0.035P. The grain structure was equiaxed with a mean linear intercept of 19 μm (ASTM grain size of 8).

The fatigue tests were performed at 550°C, on tubular specimens of 25 mm parallel gage length with 22 and 16 mm outside and inside diameter, respectively. The tests were conducted under strain controlled conditions with a triangular waveform for axial, torsion and in-phase combination of both these loading modes. For the latter tests the biaxiality was defined by $\lambda = \Delta\gamma/\Delta\epsilon = 2$, where $\Delta\gamma$ = torsional strain range and $\Delta\epsilon$ = axial strain range.

Constant strain hold periods of 2, 10, and 60 min were introduced to the fatigue cycle of some of the specimens at maximum axial or torsional strain. Full details of the fatigue tests are given elsewhere [*5*].

Specimens for optical and electron microscopy examination were sectioned from the gage length and prepared in the usual way. Optical microscopy specimens were examined to study the location, path, size, and density of cracks and cavities. Transmission electron microscopy (TEM) studies revealed the dislocation and precipitation structures developed during cycling, from which an estimation of cyclic hardening behavior can be derived.

The examination of the fatigue fracture surfaces by scanning electron microscopy (SEM) disclosed the type of fracture mechanism that predominated at each stage of crack growth. It also showed the contribution of creep damage (cavities, grain-boundary cracks) to the fracture process.

Secondary Cracks and Cavities

The examination of secondary cracks gives insight into the crack nucleation sites and crack propagation paths. Zero hold-time specimens showed mainly transgranular cracks, while specimens with hold time showed some degree of intergranular cracking. This is more evident in the axially loaded specimens where a large proportion of the initial microcracks are of an intergranular type, Fig. 1. This figure shows some intergranular damage ahead of the cracks, sited mainly at triple points. This is a type of creep damage associated with grain-boundary sliding [*6*]. When grain-boundary sliding occurs the grain should yield to accommodate the strain. As dislocation and precipitation hardening increase the resistance of the grain to yielding, cracking may occur in those places where concentration of stress is highest, that is, at triple points.

The number and depth of cracks on a polished cross section was recorded and population figures constructed, Fig. 2. This figure shows the size distribution of cracks observed along the external circumference of the tubular cross section in the torsion and biaxial specimens and along an equivalent length (69.1 mm) of a longitudinal section which includes equal lengths of both the internal and external surface in the push-pull specimens. Each box represents the number of cracks in a given 40 μm, that is, 0 to 40 μm, 40 to 80 μm, etc.

For the same maximum plastic shear strain amplitude (for example, $\frac{1}{2}\gamma_{max} = 0.5\%$), the push-pull mode (S33) gave the largest number of secondary cracks, a result which is compatible with a shorter life. On comparing torsion with the biaxial case the opposite effect is observed, the torsion specimens with a higher number of secondary cracks (S20) gave a longer life than the biaxial counterpart (S1). An examination of the geometry of these short cracks may help to explain this discrepancy since in the torsion case each initiation site provides two short cracks at 90° to each other, while the biaxial case shows mainly one, Fig. 3. Therefore, on a polished cross section the number of short cracks in torsion will be approximately twice the number observed in the biaxial case.

Increasing the strain range increases the number of secondary cracks in every multiaxial case. For $\frac{1}{2}\gamma_{max}$ of the order of 0.1% (S34), the number of secondary cracks is very low, and failure always occurs by the propagation of a single crack, while at higher plastic strain amplitudes failure occurs by the combined effort of more than one crack. Figure 2 also shows that specimens sustaining hold times have a greater population of shorter cracks, that is, length of less than three grain diameters. This seems to indicate that the change from Stage I to Stage II is more difficult when a rest period is introduced in the cycle, possibly due to the relaxation of the crack tip stresses.

The direction of microcracks related to the axis of the specimen can be obtained by observing the surface of the specimens with the scanning electron microscope (Fig. 3). The microcracks are formed mainly at 45, 90, and 50 to 70° to the specimen axis for torsion, push-pull, and biaxial specimens, respectively. These are the directions of the principal stress axes, indicating that crack initiation is caused by the maximum tensile stress. For push-pull and biaxial specimens the microcracks propagate to form macrocracks or the main crack along the same direction. For torsion specimens, on the other hand, the microcracks which initially propagated normal to the principal stress directions even-

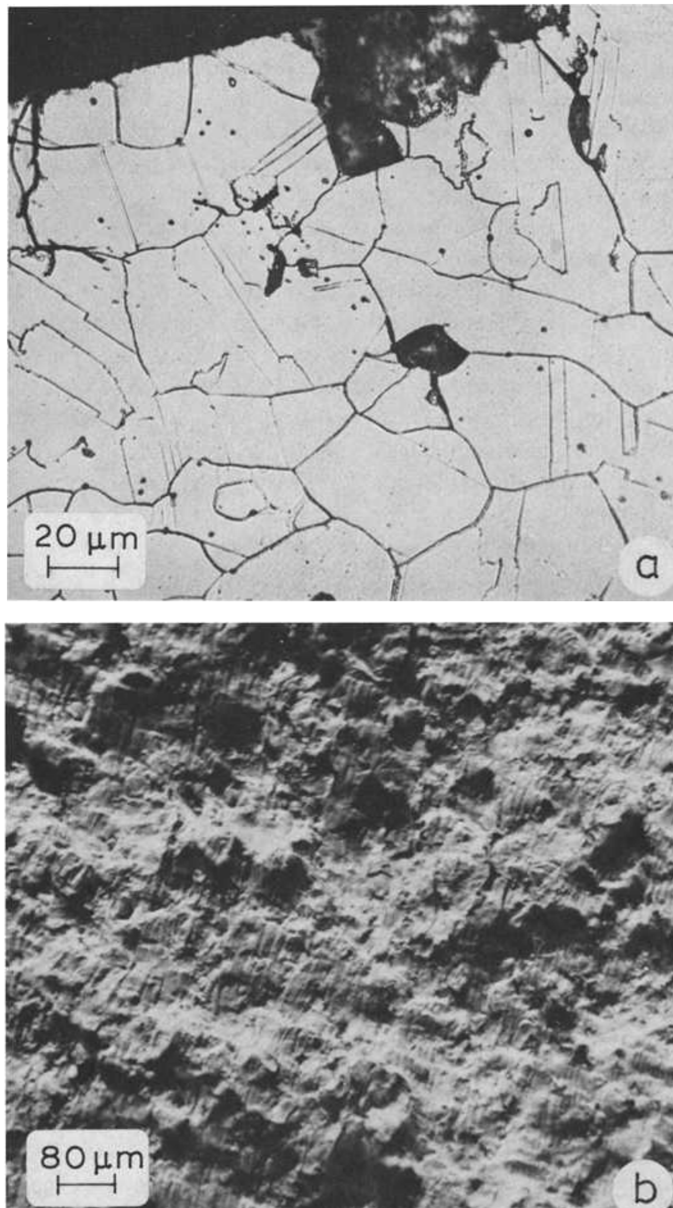

(*a*) On a polished and etched cross section (specimen 29A).
(*b*) On a fatigue fracture surface (specimen 25A).
Crack propagation is from left to right.

FIG. 1—*Intergranular damage in hold-time specimens.*

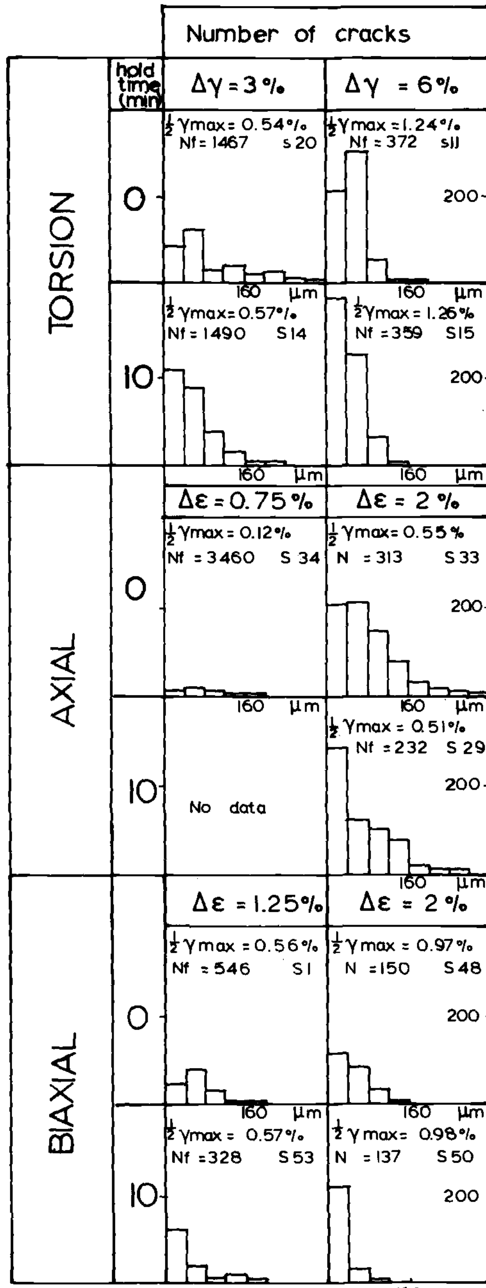

FIG. 2—*Secondary cracks; a size distribution diagram.*

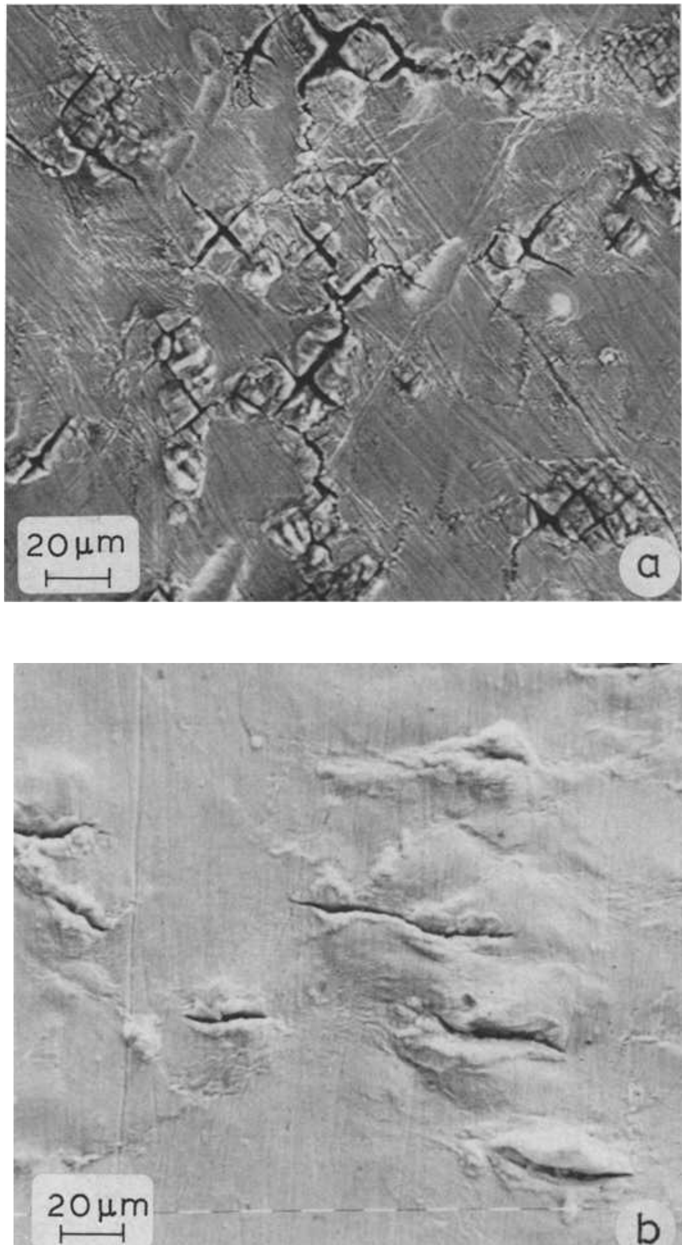

(*a*) Torsion (specimen 11T).
(*b*) Axial (specimen 29A).
(*c*) Biaxial (specimen 48B).

FIG. 3—*Specimen surface microcracks.*

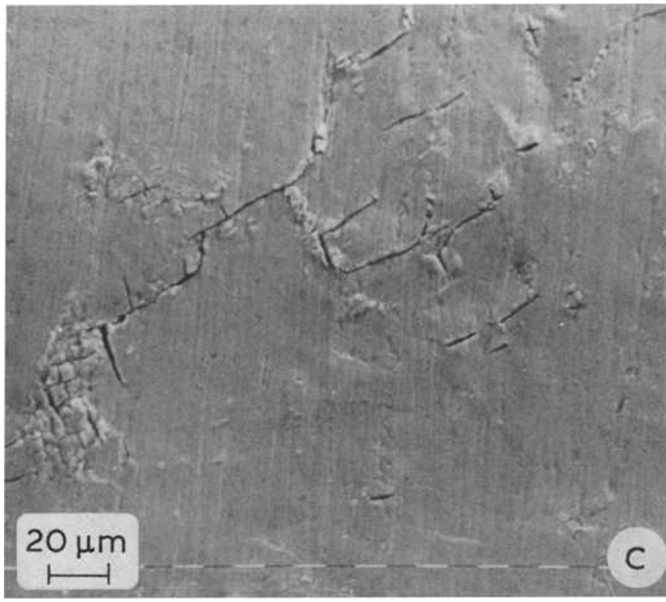

FIG. 3—*Continued.*

tually link to form macrocracks oriented parallel or perpendicular to the specimen axis.

Hold time and strain range are shown to have no effect on the volume fraction and size distribution of cavities in torsion specimens, which suggests that the creep component during hold time is not acting in a manner which would increase the average volume fraction of cavities under torsional loading. Axial specimens, on the other hand, showed an increase in the number of grain boundary wedge cracks in relation to hold time and strain range.

Factors Affecting the Strength of the Fracture Process Zone

In high-strain fatigue the crack tip is enclosed in a fracture process zone which sustains large cyclic plastic deformation. Because the strength of this region enters into most analyses of crack growth, it is therefore most important to examine the factors which control the flow stress. Furthermore, in multiaxial fatigue the choice of a parameter which would best characterize the stress and strain in each cycle becomes increasingly important, and consequently, flow stress calculations based on electron microscopy data could help in selecting this choice.

In an earlier paper [7] two torsion specimens (11 and 12 in Table 1) were studied by electron microscopy to ascertain the microstructural changes which occur during a test, for example, the development of a cellular dislocation

TABLE 1—*Dislocation densities and calculated flow stresses.*

Specimen						
No.	$\Delta\epsilon$ or $\Delta\gamma$, %	ρ, mm^{-2}	ρ_f, mm^{-2}, Eq 1	τ_f, N/mm^2, Tresca	τ_{max}, N/mm^2	Hold Time, min
11T	5.89	4.8×10^8	1.6×10^9	287	266	0
15T	5.94	3.5×10^8	1.05×10^9	236	262	10
12T	2.96	3.0×10^8	1.0×10^9	231	234	0
20T	2.96	2.8×10^8	9.5×10^8	225	232	0
14T	3.04	2.6×10^8	8.0×10^8	206	215	10
33A	2.052	3.6×10^8	1.1×10^9	231	229	0
29A	1.937	3.1×10^8	9.5×10^8	224	219	10
6A	0.978	1.95×10^8	4.8×10^8	160	158	0
28A	0.978	1.70×10^8	4.7×10^8	158	167	10
34A	0.712	1.80×10^8	3.9×10^8	144	146	0
25A	0.733	1.84×10^8	4.0×10^8	145	154	2
48B	1.950	2.85×10^8	1.02×10^9	233	268	0
50B	1.962	2.87×10^8	1.01×10^9	232	265	10
1B	1.235	2.78×10^8	9.1×10^8	220	239	0
53B	1.230	2.3×10^8	7.82×10^8	204	227	10
54B	1.234	2.23×10^8	7.24×10^8	196	210	60
38B	0.594	1.18×10^8	3.95×10^8	145	186	2

NOTE—
A = axial.
T = torsion.
B = biaxial.
ρ = average dislocation density.
$\Delta\epsilon$ = axial strain range (push-pull and biaxial specimens).
$\Delta\gamma$ = shear strain range (torsion specimens).

structure and the precipitation of carbides. Flow stress calculations were based on a model leading to the expression

$$\tau_f = \tfrac{1}{2}\mu b \rho_f^{1/2} \tag{1}$$

where

τ_f = dislocation hardening,
μ = shear modulus = 5.83×10^4 N/mm^2,
b = Burgers vector = 2.5×10^{-7} mm, and
ρ_f = wall dislocation density (Table 1).

In the present work 15 additional specimens were studied, including axial and biaxial specimens as well as torsion specimens with and without hold time. The experimental details of specimen preparation and dislocation density determinations were given in the earlier paper [*7*].

Figure 4 shows the most common type of dislocation structures observed which are equivalent to the structures developed in persistent slip bands in single crystals [*8,9*] when the prevailing mode of deformation is multiple slip.

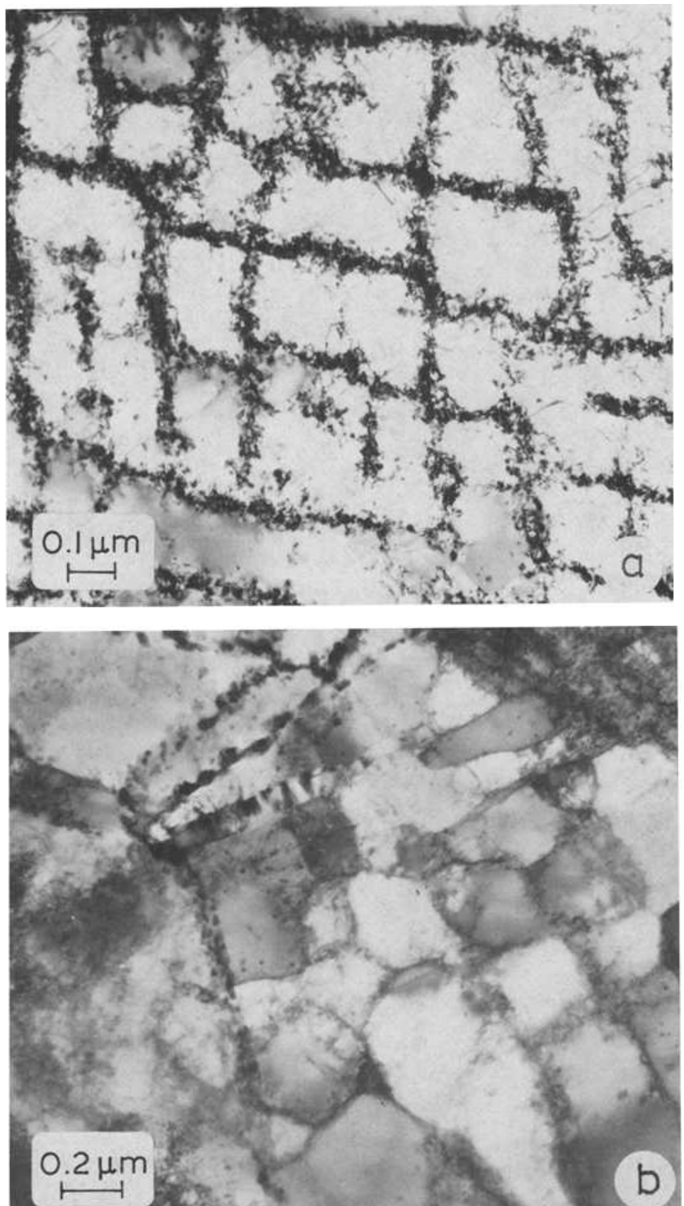

(*a*) Maze structure (specimen 20T).
(*b*) Cell structure (specimen 15T).

FIG. 4—*Typical dislocation structures.*

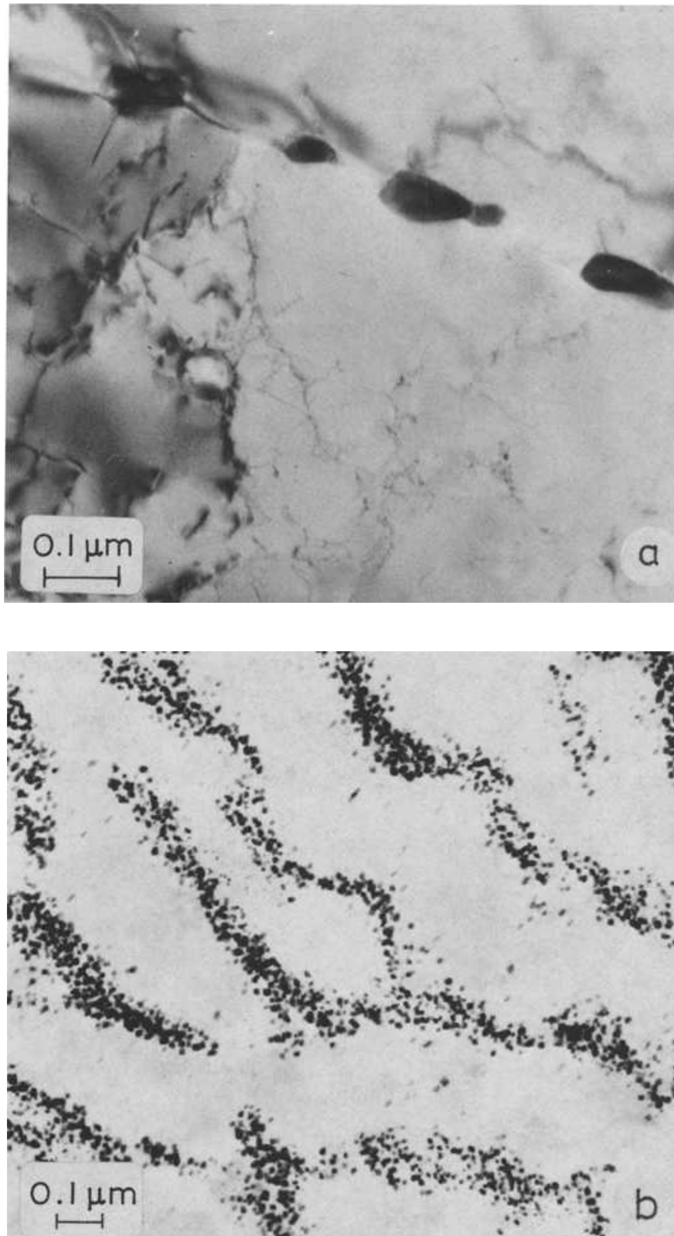

(*a*) At grain boundaries (specimen 29A).
(*b*) At dislocation cell walls (specimen 38B).
(*c*) Dark field electron micrograph (specimen 53B).

FIG. 5—*Carbide precipitation.*

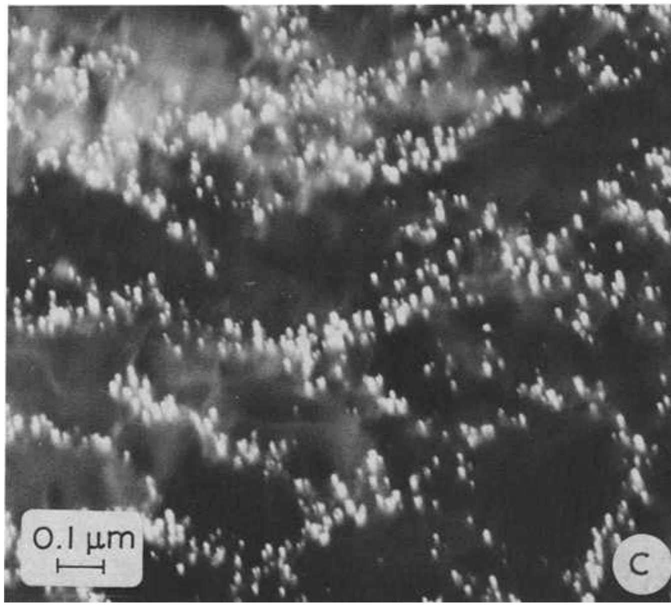

FIG. 5—*Continued.*

Table 1 gives the calculated dislocation hardening obtained from Eq 1. For comparison the flow stress measured in the fatigue tests and then calculated using the Tresca criterion is also included. Two points stand out from this comparison, (*a*) that dislocation hardening is sufficiently close to the actual flow stress as to be singled out as the predominant hardening mechanism, (*b*) as postulated previously from two torsion tests, the applicability of the Tresca criterion for correlation of cyclic stress-strain data in 316 stainless steel at elevated temperature is confirmed, since a sufficient number of specimens covering three different multiaxial states has been tested.

Austenitic 316 stainless steel is known to precipitate carbides when heated at elevated temperatures, during either creep or fatigue experiments [*10–12*], or during heat treatment [*13–15*]. The precipitation of carbides in this investigation follows the same form for all three multiaxial cases studied, that is, coarse intergranular 0.05 to 0.1-µm-diameter carbides and a transgranular fine carbide of 0.01 to 0.02 µm diameter at dislocation cell walls, Fig. 5.

The degree of precipitation hardening was calculated using the same method as before [*7*], given by [*16*]

$$\tau = 2C\mu(f/r \times b \times \gamma)^{1/2} \qquad (2)$$

where

C = a constant of about 0.3,
γ = shear strain,
f = volume fraction of particles, and
r = particle radius.

Table 2 shows some estimated stress values which are lower than those calculated for the dislocation hardening, suggesting that the latter predominates.

The reason why dislocation hardening alone seems to control the flow stress, with very little contribution from the precipitates, can be explained by looking at the type and location of the transgranular precipitation. By precipitating at the cell walls, the carbides are in direct competition with the dislocation substructure; therefore, any nascent dislocation loop would be affected only by the particles when the dimension of the carbide dispersion is of the same order as the dislocation links.

Fracture Mechanisms

The study of the fracture surfaces reveals the type of fracture mechanism operating at different stages of the specimen's life. Torsion specimens had fracture surface features totally obliterated by the rubbing of the two surfaces of the cracks. This present study, therefore, concentrates on the other two stress states, namely, push-pull and biaxial. Both conditions show the three main stages of crack propagation, that is, Stages I, II, and III.

Stage I growth is believed to be fairly fast and short in terms of length. It extends over approximately 100 μm (1 to 3 grain diameters) and is crystallographic in nature, changing direction as it propagates from grain to grain. It is mainly transgranular in specimens without hold time, but specimens with hold time showed some proportion of intergranular initiation. Figure 6*a* shows the Stage I crack initiation for a push-pull specimen and also the beginning of Stage II cracking.

Stage II propagation is characterized by the striation marks, Figs. 6*b* and *c*. The extent of this second stage and the crack propagation rate can be assessed by striation counting. Figure 7 shows some results of these measurements, with

TABLE 2—*Carbide precipitation: size, volume, fraction, and strengthening.*

Specimen	r, mm	f	f/r, mm^{-1}	γ	τ, N/mm^2
54B	1.0×10^{-5}	0.035	3500	0.01568	129
53B	1.0×10^{-5}	0.020	2000	0.01566	98
28A	1.0×10^{-5}	0.030	3000	0.00734	82
6A	0.5×10^{-5}	0.010	2000	0.00734	67
38B	1.0×10^{-5}	0.023	2300	0.007428	72

striation spacing (crack growth rate) plotted against distance from the origin (crack length). The minimum striation spacing measured was limited by the characteristic of the SEM which was of the order of 1 μm. The extent of Stage II is, therefore, from the end of Stage I to the end of linearity of the curves of Fig. 7.

The linear part of the curve could be described by an expression of the form

$$s = \frac{da}{dN} = C(a)^n \tag{3}$$

where

s = striation spacing, μm;
a = crack length, μm;
N = number of cycles; and
C and n = constants.

The measurements of striation spacing were made at well defined locations where the fatigue crack was already in a well established Stage II region; therefore, Eq 3 represents a law governing the latter stages of crack growth, that is, $da/dN > 1$ μm/cycle.

Although Eq 3 adequately describes mathematically the crack growth rate for the present experiments, crack growth data are more commonly presented in the empirical form [17]

$$\frac{da}{dN} = B\ a\ (\Delta\epsilon_p)^\alpha \tag{4}$$

where

$\Delta\epsilon_p$ = plastic strain range, and
B and α = constants.

This is observed both for torsional [18,19] and uniaxial [20] loading.

In a theory developed to assess quantitatively the mechanism of fatigue crack propagation in metals Tomkins [17] proposed that

$$\frac{da}{dN} = \frac{\pi^2}{8}\left(\frac{k}{2T}\right)^2 a\ \Delta\epsilon_p{}^{(2\beta+1)} \tag{5}$$

which is of the same form as Eq 4

where

β = cyclic stress-strain exponent,
k = stress-strain coefficient, and
T = tensile stress within the plastic zone.

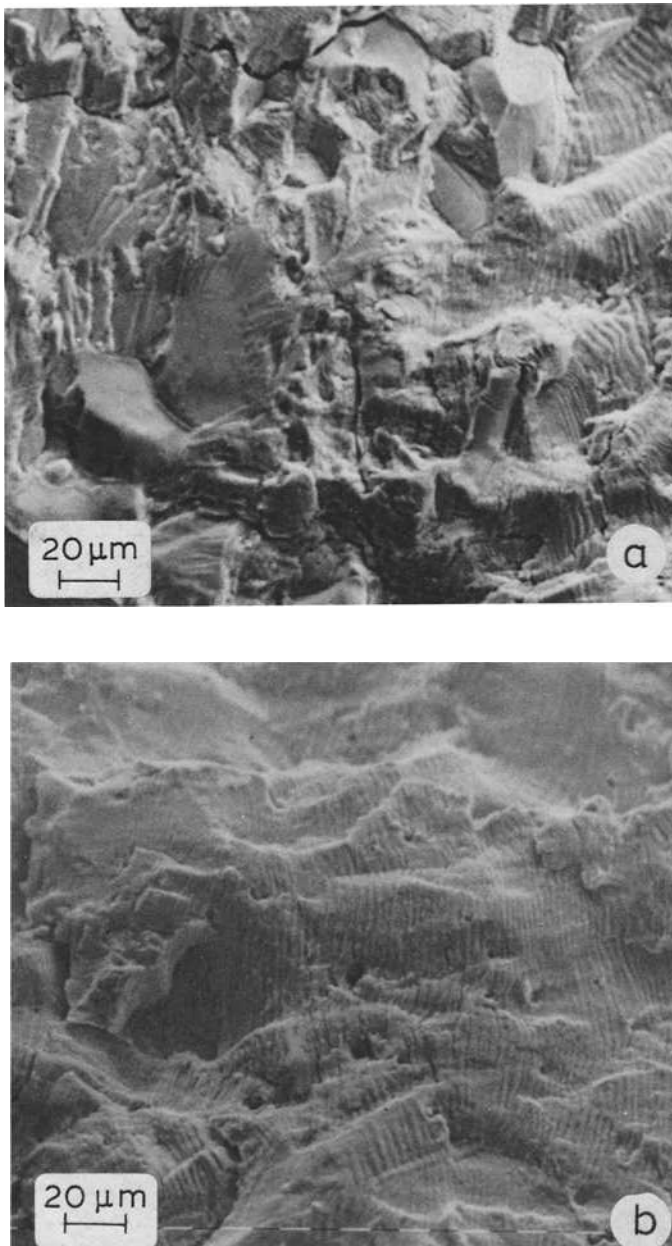

(*a*) Stage I and II of crack propagation (specimen 33A).
(*b*) Stage II crack propagation for axial specimens (specimen 34A).
(*c*) Stage II crack propagation for biaxial specimens (specimen 38B).
Crack propagation is from left to right.

FIG. 6—*SEM fractographs of the fatigue fracture surfaces.*

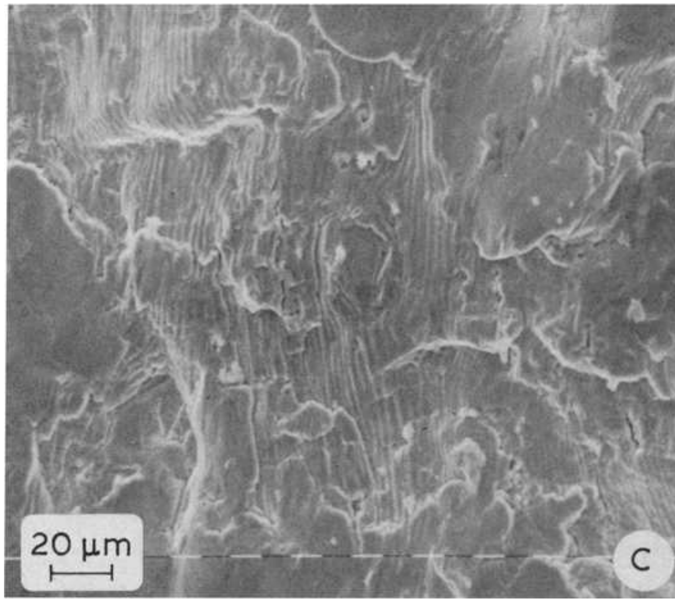

FIG. 6—*Continued.*

Zero hold-time data, presented in Fig. 7, can be replotted in the form of Eq 4, Fig. 8. This figure includes data of Wareing [*20*] for 316 stainless steel at 625°C, 20/25 stainless steel at 750°C, and the theoretical curve derived from Eq 5 in which T = 465 MPa [the ultimate tensile strength (UTS) of 316 stainless steel at 550°C], β = 0.24, and k = 2600 MPa, all these data from Ref 5.

Figure 8 shows that for a given $\Delta\epsilon_p$ and crack length 316 stainless steel tested at 550°C has a lower crack growth rate than at 625°C partly because of the lower flow stress at the higher temperature.

Figure 8 also shows that for the range of crack growth rates experienced in the present work, Eq 5 gives a reasonably good approximation to the experimental results when the value of UTS is adopted for T. The slight difference in the slope may result from the choice of β-value. In the present case the value of β = 0.24 corresponds to bulk cyclic behavior of 316 stainless steel at 550°C. This may be different to the strain hardening exponent of the material within the plastic zone ahead of the crack tip, due to a different dislocation substructure developed in this region.

The end of Stage II fracture and the start of Stage III (end of linearity in Fig. 6) is a function of strain range and hold time. Specimens with hold time reach Stage III earlier. It seems that creep damage, in the form of voids and grain-boundary cracks is significant only in the highly strained regions ahead of the propagating crack. Raj [*21*] has shown that cavities are preferentially formed at particles in the grain boundaries by a combination of energetic and diffusional

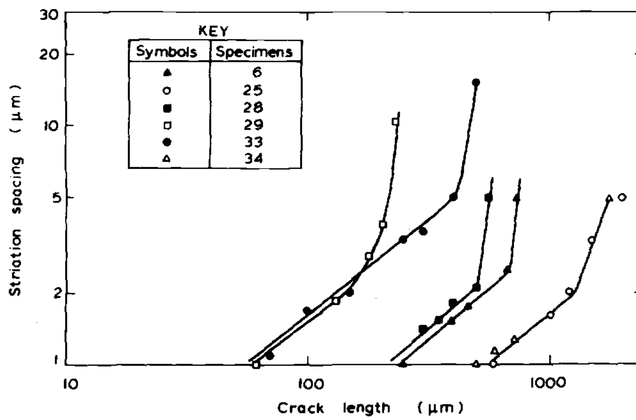

FIG. 7—*Striation spacing curves.*

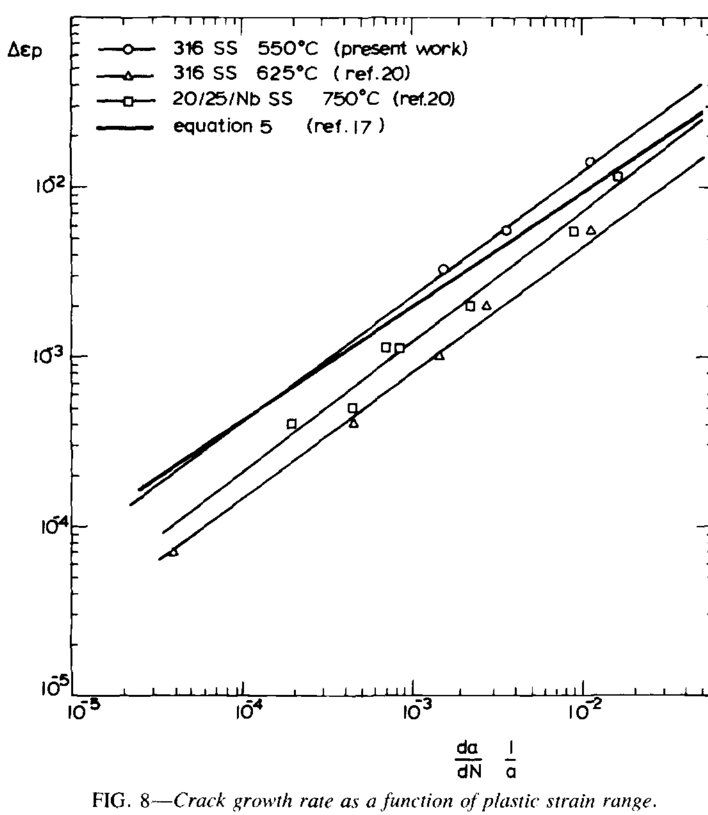

FIG. 8—*Crack growth rate as a function of plastic strain range.*

considerations. Min and Raj [22] studied the effect of cavities in low-cycle fatigue. They showed that for cavities to grow and coalesce with their neighbors a large scale displacement normal to the plane of the grain boundary is needed. Such displacements can be accommodated in the strain field of a crack tip. Voids and intergranular facets were also seen in the Stage II crack growth regime, but, in the present case, they do not seem to accelerate the crack propagation rate (see Fig. 1*b*). The density and size of these voids increases as the crack approaches the end of Stage II, the crack accelerating dramatically on reaching this point, the final fracture appearing to be of the overload type (ductile fracture).

Estimation of Endurance

Since low-cycle fatigue lifetime is dominated by crack growth, the endurance may be estimated from Eq 3 by making certain suppositions. The first assumption to consider is the extent of Stage I. Figure 2, for example, shows that most of the secondary crack lengths are within the range of 0 to 80 μm, while Fig. 6*a* shows that for specimen 33A, Stage I, extends for approximately 100 μm. A figure of 80 μm seems, therefore, a reasonable average value to use in the calculations which follow. Next is the assumption of a law describing Stage I crack growth, and here two separate criteria will be examined. In the first one, Stage I is considered to follow the same law of crack growth as Stage II [17]. Consequently, the integration of Eq 3 between the limits of zero and a_o equal to 80 μm gives the period of Stage I propagation, and between a_o and a_f gives Stage II propagation

$$\left. \frac{a^{(1-n)}}{(1-n)} \right|_{o}^{a_o} = C\,N_{\mathrm{I}} \qquad (6a)$$

and

$$\left. \frac{a^{(1-n)}}{(1-n)} \right|_{a_o}^{a_f} = C\,N_{\mathrm{II}} \qquad (6b)$$

Table 3 gives the results of these calculations, showing reasonable agreement for the uniaxial tests.

Recent work seems to indicate that initiation is negligible in high-plastic strain fatigue [18]. Even in high-cycle fatigue at stresses near the fatigue limit, cracks are seen to initiate readily and grow at a relative high rate until they meet a barrier like a grain boundary or a phase boundary [19]. The present data also suggest that Stage I must be relatively fast in view of the abundance of microcracks observed within the range 0 to 80 μm. The second criterion is based, therefore, on the assumption that the Stage I growth period can be neglected for life time calculations; thus, the endurance is given by N_{II}. This appears to give a lower bound to the experimental fatigue lives, as one might expect. (Note that a further possibility is to equate a_o with a grain size [19], 32 μm, if the grain boundary is the first barrier to fatigue crack growth.)

TABLE 3—*Calculated and experimental cycles to failure.*

Specimen	C	n	a_o, μm	a_f, μm	N_{II}, calculated	N_I, calculated	$N_t = N_{II} + N_I$, calculated	N, experimental
33	0.0345	0.82	80	400	119	354	473	313
29	0.0445	0.76	80	150	44	268	312	232
6	0.008	0.86	80	680	576	1649	2225	2155
28	0.012	0.83	80	500	377	1033	1410	1328
34	0.0055	0.82	80	1250	1423	2223	3646	3460
25	0.0055	0.82	80	1250	1423	2223	3646	3665
1	0.03	0.70	80	1250	530	414	944	546
53	0.03	0.70	80	630	354	414	768	328
54	0.03	0.70	80	550	324	414	738	362
38	0.004	0.90	80	1400	1284	3875	5159	2880

The propagation lives in a real situation should lie between the two options discussed above, which represent an upper and a lower bound. The diversity in the two approaches underlies the difficulty in trying to predict life time with only long crack propagation data which, in view of these calculations, is insufficient.

For biaxial specimens the agreement is close to N_{II}, the calculated values N_t being about double the actual number of cycles. Examination of the fracture surfaces, see Figs. 6*b* and *c*, shows that while for axially loaded specimens striations cover the whole of Stage II fracture surface, with only the occasional occurrence of some intergranular facets (particularly in the hold-time specimens), for the biaxial specimens some large featureless areas are common and they intermingle with the striation zones. These large featureless areas might correspond to faster crack growth, possibly by a shear crack mode of growth rather than the opening mode that produces striations. This would increase the overall crack growth rate relative to the opening mode propagation rate, and, consequently, the specimen life would be less.

Summary

Two main hardening mechanisms operate during testing, (*a*) dislocation hardening and (*b*) precipitation hardening. Although dislocation hardening prevails at all testing conditions, precipitation hardening becomes significant at low strain ranges and long lifetime.

Precipitation along grain boundaries reduces the possibility of grain-boundary sliding but introduces centers of stress concentration conducive to grain-boundary cracking.

Fracture surfaces show characteristic features of the three stages of crack propagation. Crystallographic Stage I is transgranular in the no hold-time specimens.

Stage II is dominated by striation fracture, with the exception of some featureless facets in biaxial specimens. Stage III is predominantly a ductile feature, beginning at shorter crack lengths in the hold-time and the high-strain range specimens.

Striation spacing calculations give approximate life estimates. The push-pull specimens show that crack growth is consistent with previous models.

Acknowledgments

The authors gratefully acknowledge the support and assistance of the Science and Engineering Research Council. They are also indebted to the United Kingdom Atomic Energy Authority for supplying the specimens and to D. J. Marsh from the United Kingdom Atomic Energy Administration for the helpful suggestions and discussion sessions.

References

[1] Ellison, E. G., *Journal of Mechanical Engineering Science*, Vol. 11, No. 3, 1969, p. 318.
[2] Coffin, L. F. in *Fatigue at Elevated Temperatures, ASTM STP 520*, American Society for Testing and Materials, Philadelphia, 1973, pp. 5–34.
[3] Tomkins, B. and Wareing, J., *Metallurgical Science*, Vol. 11, 1977, p. 414.
[4] Plumtree, A., *Metallurgical Science*, Vol. 11, 1977, p. 425.
[5] Kandil, F. A., Miller, K. J., and Brown, M. W., this publication, pp. 651–668.
[6] Morris, D. G. and Harries, D. R., *Journal of Material Science*, Vol. 12, 1977, p. 1587.
[7] de los Rios, E. R. and Brown, M. W., *Fatigue Engineering Materials and Structure*, Vol. 4, 1981, p. 377.
[8] Winter, A. T., *Philosophical Magazine*, Vol. 37, 1978, p. 457.
[9] Woods, P. J., *Philosophical Magazine*, Vol. 28, 1973, p. 155.
[10] Abdel-Raouf, H., Plumtree, A., and Topper, T. H., *Metallurgical Transactions*, Vol. 5, 1974, p. 267.
[11] Challenger, K. D. and Moteff, J. in *Fatigue of Elevated Temperatures, ASTM STP 520*, American Society for Testing and Materials, pp. 68–79.
[12] Challenger, K. D. and Moteff, J., *Metallurgical Transactions*, Vol. 4, 1973, p. 749.
[13] Lewis, M. H. and Hattersley, B., *Acta Metallurgica*, Vol. 13, 1965, p. 1159.
[14] Spruiell, J. E., Scott, J. A., Ary, C. S., and Hardin, R. L., *Metallurgical Transactions*, Vol. 4, 1973, p. 1533.
[15] Weiss, B. and Stickler, R., *Metallurgical Transactions*, Vol. 3, 1972, p. 851.
[16] Ashby, M. F., *Philosophical Magazine*, Vol. 21, 1970, p. 399.
[17] Tomkins, B., *Philosophical Magazine*, Vol. 18, 1968, p. 1041.
[18] Miller, K. J. and Ibrahim, M. F. E., *Fatigue of Engineering Materials and Structures*, Vol. 4, 1981, p. 263.
[19] de los Rios, E. R., Tang, Z., and Miller, K. J., *Fatigue Engineering Materials and Structures*, Vol. 7, 1984, p. 97.
[20] Wareing, J., *Metallurgical Transactions*, Vol. 6A, 1975, p. 1367.
[21] Raj, R., *Acta Metallurgica*, Vol. 26, 1978, p. 995.
[22] Min, B. K. and Raj, R., *Acta Metallurgica*, Vol. 26, 1978, p. 1007.

David R. Hayhurst,[1] *Frederick A. Leckie,*[2] *and David L. McDowell*[3]

Damage Growth Under Nonproportional Loading

REFERENCE: Hayhurst, D. R., Leckie, F. A., and McDowell, D. L., **"Damage Growth Under Nonproportional Loading,"** *Multiaxial Fatigue, ASTM STP 853*, K. J. Miller and M. W. Brown, Eds., American Society for Testing and Materials. Philadelphia, 1985, pp. 688–699.

ABSTRACT: The objective of the study is to quantify the growth rate of damage which occur when materials are subjected to variable nonproportional loading at elevated temperatures. Fast and slow nonproportional cyclic tests are performed on circular tubes and observations made on the deformation history, life, and nature of damage accumulation. The results are then related to a general theory of creep-fatigue damage description which has recently been formulated.

KEY WORDS: creep rupture. fatigue, creep-fatigue damahe, aluminum. copper, 304 stainless steel, multiaxial loading, nonproportional loading

It is well known that when metals operating at elevated temperatures are subjected to cyclic loading, failure is dependent on both the fatigue and creep rupture properties of the metal. In fact, it has been demonstrated in a series of fundamental experiments by Chaboche, Lemaitre, and Plumtree [*1,2*] that creep-fatigue damage growth can be represented by a single scalar parameter of damage and that the growth equation has the form

$$\Delta D = \Delta D_f + \Delta D_c \tag{1}$$

where

ΔD_f = fatigue and
ΔD_c = creep damage increments.

The studies have shown that the expressions for ΔD_f and ΔD_c may be obtained independently by performing fatigue and creep rupture tests, according to stan-

[1]Reader, Department of Engineering, University of Leicester, Leicester, U.K.
[2]Professor, Department of Theoretical and Applied Mechanics, University of Illinois at Urbana-Champaign, Urbana, IL 61801.
[3]Assistant professor, Department of Mechanical Engineering, Georgia Institute of Technology, Atlanta, GA 30332.

Copyright© 1985 by ASTM International www.astm.org

dard procedures. It is then established in the studies reported, that Eq 1 can predict with success the life of specimens subjected to complex loading cycles which introduce creep/fatigue coupling. Unfortunately, the tests performed to date have been limited to uniaxial states of stress, and the purpose of this paper is to attempt to extend the knowledge of uniaxial stress states to nonproportional multiaxial stress histories. Without prejudging the outcome of the study it would appear reasonable, at least initially, to take guidance from the results of the uniaxial studies and to assume that the total damage increment may be separated into the creep and fatigue damage increments according to Eq 1. This adds great simplification (which may finally prove to be unjustified), but the remaining problem is still difficult enough since the knowledge of multiaxial creep rupture and multiaxial fatigue is still at an early formative stage. Other papers in this symposium are concerned with the growth of fatigue damage, and this paper is to concentrate more fully on the effects of nonproportional multiaxial loading on creep rupture behavior, although nonproportional fatigue loading will also be considered in less detail. It is the hope that the knowledge gained from this study of the effect of nonproportional loading on creep rupture and fatigue properties separately will provide the essential ingredients for an understanding of coupled creep/fatigue damage growth.

Creep Ruptures for Constant Multiaxial Stress States

When metals are subjected to constant stress at temperatures above $0{\cdot}3T_m$, where T_m is the absolute melting temperature of the base metal, they undergo time-dependent deformation, and rupture takes place in a finite lifetime. Rupture commences with nucleation and growth of grain boundary defects [*3*], and failure occurs when adjacent defects have grown to a size for final linkage of the defects to occur. The effect of the growth of defects is to cause a progressive weakening of the material resulting in an increase in the strain-rate over a significant fraction of the lifetime, usually referred to as tertiary creep.

The nucleation and growth of defects have been shown to be dependent upon the state of the applied multiaxial stress field [*4*]. Two extreme types of multiaxial creep rupture behavior exist for metals; these are the maximum principal tensile stress criterion, σ_1 = constant, and the effective stress criterion

$$\bar{\sigma} \equiv \{[(\sigma_1 - \sigma_2)^2 + (\sigma_2 - \sigma_3)^2 + (\sigma_3 - \sigma_1)^2]/2\}^{1/2} = \text{constant}$$

where σ_1, σ_2, and σ_3 are principal stresses with $\sigma_1 > \sigma_2 > \sigma_3$. Copper satisfies the former criterion and aluminum alloys the latter. The two criteria are shown schematically in Fig. 1 (without the inequality restrictions) as isochronous rupture loci in plane stress space; the stress spaces have been normalized in terms of the uniaxial stress σ_0. Some metals (for example, steels) satisfy mixed criteria [*4*]. The dependence of the rupture lifetime upon the stress state may be seen by comparing the difference in stress level required to maintain a constant lifetime

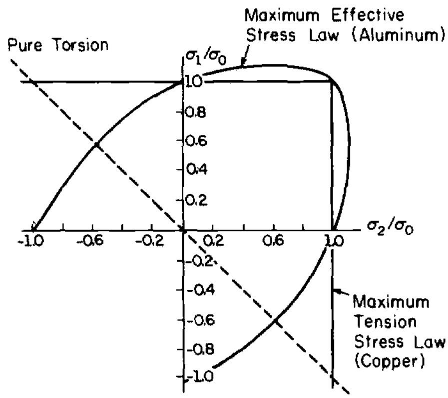

FIG. 1—*Plane stress isochronous rupture loci for copper and aluminum alloys.*

in changing from uniaxial to pure shear or torsion stress; a reduction in the normalized stress (σ_1/σ_0) to almost one half of the value for uniaxial stress is required for the effective stress criterion. Leckie and Hayhurst [*5*] have shown that the multiaxial stress rupture criterion must be taken into account in the estimation of the lifetimes of engineering components which are subjected to multiaxial states of stress. Failure to do so may result in severely nonconservative design.

Based on the results of extensive tension-torsion testing carried out by Johnson et al [*6*], Leckie and Hayhurst [*5*] suggested the following constitutive equations for strain and damage rates

$$\frac{\dot{\epsilon}_{ij}}{\dot{\epsilon}_0} = \frac{1}{(n+1)} \frac{\partial \phi^{(n+1)}(\sigma_{kl}/\sigma_0)}{\partial(\sigma_{ij}/\sigma_0)} \frac{1}{(1-D)^n} \tag{2a}$$

$$\frac{\dot{D}}{\dot{D}_0} = \Delta^{\nu}(\sigma_{ij}/\sigma_0) \frac{1}{(1-D)^{\nu}} \tag{2b}$$

In these equations $\dot{\epsilon}_0$, $\dot{D}_0$, n, and ν are material constants which are readily obtained from uniaxial data. $\phi(\sigma_{kl}/\sigma_0) \equiv \bar{\sigma}/\sigma_0$ and $\Delta(\sigma_{ij}/\sigma_0)$ are homogeneous of degree one in (σ_{ij}/σ_0). The form of Δ is determined by the shape of the isochronous rupture surface. For copper $\Delta = \sigma_1/\sigma_0$ and for aluminum $\Delta = \bar{\sigma}/\sigma_0$. In common with the studies of Chaboche, Lemaitre, and Plumtree [*1,2*], it was found that a scalar damage quantity sufficed to describe damage and strain growth observed by Johnson et al [*6*], under conditions of constant multiaxial stress. However, this scalar description is unlikely to suffice for nonproportional loading especially for materials for which $\Delta = \sigma_1/\sigma_0$. For this class of materials the growth of damage is a consequence of the nucleation and growth of voids by diffusion of vacancies along grain boundaries. It has been proposed by Hull and Rimmer [7] that the principal agency responsible for void growth is the tensile stress acting along the normal to the grain boundary facet. It then seems reasonable to follow the procedure adopted by Hayhurst and Storakers [8] and to assign a damage value to every plane within the material and furthermore to assume that this damage is a functional of the normal tensile stress history for the plane. The damage value which is taken to influence the strain-rate process, described by Eq 2, corresponds to the plane which has been subjected to the most damaging history of tensile stress. When proportional loading occurs, a single plane is subjected to the most severe history of damage; but, when nonproportional loading takes place, the loading history will have to be taken into account and the growth of damage on all possible planes determined in order to identify the most severely damaged plane.

The purpose of the present study is to study the results of nonproportional loading and to determine how the constitutive equations should be modified in order to accommodate the nonproportional loading effects.

Creep Rupture Experiments for Nonproportional Loading

Copper and an aluminum alloy have been selected as materials for study, since they obey the criteria of maximum principal tensile stress and effective stress, respectively. In a nonproportional loading experiment on an aluminum specimen in which $\bar{\sigma}$ remains constant but σ_1 changes direction, one would expect the same lifetime as in a steady-load test, with the same value of $\bar{\sigma}$, since the effective stress is a scalar quantity. But in the same test on a copper specimen one would expect an increase in the lifetime above that measured in a steady-load test provided that during the rupture process there is no interaction between the planes of damage corresponding to the maximum principal stress directions. If Eq 2*a* for deformation rate is appropriate then the creep strain rates before and after the load change should be the same, since the damage term in Eq 2*a* appears as a scalar. This may not prove to be justified for nonscalar damage, but the assumption is the simplest possible and must be verified.

The validity of these suppositions may be checked by carrying out experiments on thin tubes subjected to combined tension and torsion (pure shear) (Fig. 2). The following experiments were selected:

(*a*) steady load; and

(*b*) multiple reversals of the torsion load, the time elapse between reversal being short compared with the lifetime.

In the reverse torsion loading tests the magnitudes of both $\bar{\sigma}$ and σ_1 were maintained constant, but the direction of the maximum principal tension stress was changed. The changes in load are defined in Fig. 2, where the loci of constant values of $\bar{\sigma}$ and σ_1 have been plotted in the $(\sigma_{z\theta}, \sigma_{zz})$ plane. Initial loading took place along the line OA, the point A having been selected so that the magnitudes of $\dot{\gamma}_{z\theta}$ and $\dot{\epsilon}_{zz}$ were equal, or $\alpha = 45°$. This condition was selected

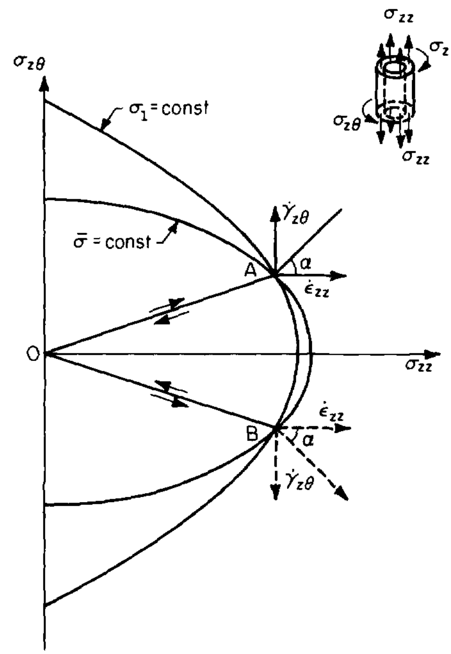

FIG. 2—*Schematic representation of loading conditions.*

to reduce the effect of the rotation of material elements within the stress field. For this loading condition the plane of maximum principal stress makes an angle of 16.9° to the z-direction. In a test during which σ_{zz} remains constant but $\sigma_{z\theta}$ is reversed in direction, the plane of maximum principal stress makes an angle of $-16.9°$ to the z-direction.

For the case of a tube subjected to tension and torsion, the effective stress is given by $\bar{\sigma} = (\sigma_{zz}^2 + 3\sigma_{z\theta}^2)^{1/2}$ and the maximum principal tension stress by $\sigma_1 = \{\sigma_{zz}/2\} + \{(\sigma_{zz}/2)^2 + \sigma_{z\theta}^2\}^{1/2}$. Equation 2 for the strain rates may be written as

$$\frac{\dot{\epsilon}_{ij}}{\dot{\epsilon}_0} = \frac{3}{2}\left\{\frac{\bar{\sigma}}{\sigma_0}\right\}^{(n-1)} \frac{S_{ij}}{\sigma_0} \frac{1}{(1-D)^n} \tag{3}$$

where the stress deviators are given by $S_{ij} = \sigma_{ij} - \frac{1}{3}\delta_{ij}\sigma_{kk}$. Noting that $\dot{\gamma}_{z\theta} = 2\dot{\epsilon}_{z\theta}$, it may be shown from Eq 3 that the condition $\dot{\gamma}_{z\theta}/\dot{\epsilon}_{zz} = 1$ is satisfied when $\sigma_{zz} = 3\sigma_{z\theta}$. This requirement was satisfied in all the tests carried out.

Experimental Results for Aluminum

The responses of a typical steady-load tension torsion test is shown in Fig. 3*a* while that of a constant tension multireverse torsion test is shown in Fig. 3*b*.

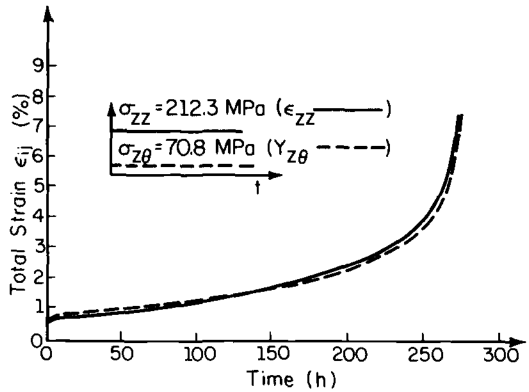

FIG. 3*a*—*Steady tension-torsion tests on aluminum alloy tubes.*

The stress levels selected for the two tests are the same, the cycle time in the multiple-reverse test is 48 h, and the temperature is 250°C. The failure time in the constant stress test is 270 h while that of the multiple-reverse test is 207 h. The shear and axial strains in the constant stress tests are almost identical. If the magnitudes of the shear creep strains recorded in the multiple-reverse test are added together, it is found that they coincide closely with the observed axial creep strain (Fig. 3*a*). Hence, the conclusion drawn from these tests is that the constitutive Eq 2 are appropriate for aluminum even when subjected to nonproportional loading, and that a scalar description of damage is satisfactory.

Experimental Results for Copper

Tests similar to those described in the previous section were also carried out on copper at 250°C. The results are shown in Fig. 4*a* and *b*. The failure time for constant stress tests is 230 h, while that for the multi-reverse torsion is 480

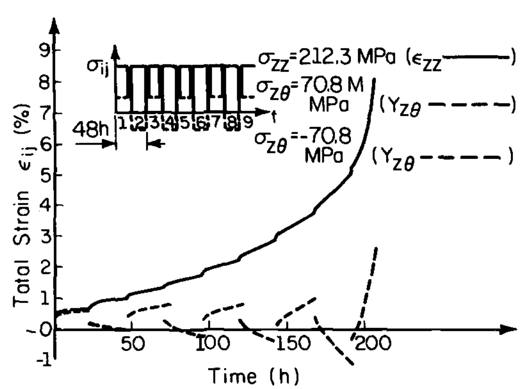

FIG. 3*b*—*Multiple reverse torsion, steady tension load test on an aluminum alloy tube.*

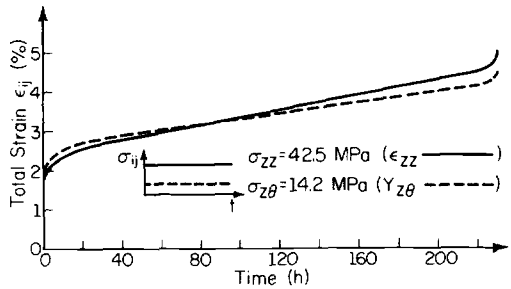

FIG. 4*a*—*Steady-load tension-torsion test on a copper tube.*

h which is almost twice that of the constant stress test. The axial and torsional strains are almost equal in the constant stress test. The most unusual feature of Fig. 4*a* is that it indicates little tertiary creep. This is a point of some concern since a uniaxial test with the same effective stress would show a pronounced tertiary region. The same features were observed by Hayhurst and Storakers [*8*] in tests carried out on Andrade shear disks. The deformation and rupture behavior of the disks was shown to be influenced strongly by the finite rotation strains. The absence of pronounced tertiary creep in the test results reported here, which one would expect to occupy almost one half of the lifetime, may be due to the small but finite rotation strains. The strains recorded in the multireverse loading tests are shown in Fig. 4*b*. If the magnitudes of the creep shear strains are again added, it is found that this total accumulation of creep shear strain closely equals the total axial creep strains, a result which confirms the validity of Eq 3. In the two tests described, the lifetimes may be predicted with good accuracy from the steady-load uniaxial data and the integrated form of Eq 3, when $\Delta(\sigma_{ij}/\sigma_0) = \sigma_1/\sigma_0$. In the reversed torsion steady tension tests the direction of the principal tension stress rotates through an angle of 33.7°. The lifetimes of the reverse load tests are twice those of the steady-load tests, and the inference is that the damage which grows on the two principal planes does not interact. This has been confirmed by metallographic studies which are now described.

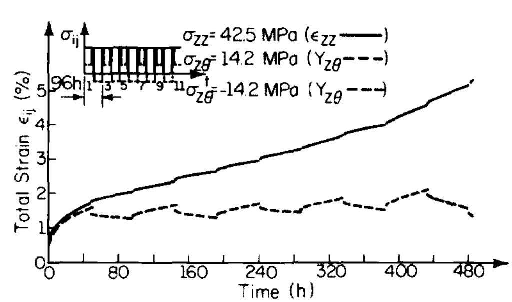

FIG. 4*b*—*Multiple reverse torsion, steady-load tension test on a copper tube.*

Figure 5 shows a midthickness micrograph of a copper tube taken from a region of the specimen gage length which was subjected to the multireverse load test. The grain boundary defects are uniformly distributed over the region of homogeneous stress and are found on planes perpendicular to the maximum principal tension stress σ_1. The two damaged planes correspond to the maximum principal stress planes. Since the load cycle time is short compared with the lifetime the damage on both planes appears equally intense. It appears to be an important characteristic of this material that the damaged planes act independently of one another, and the results for both deformation and damage suggest that Eq 3 may be satisfactorily applied to each of the planes of maximum principal stress when loaded.

Creep Rupture Constitutive Equations and Their Implications

For aluminum, experiments indicate that damage is indeed a scalar quantity and that the following constitutive equations give a good representation of the material behavior when subjected to nonproportional loading

$$\frac{\dot{\epsilon}_{ij}}{\dot{\epsilon}_0} = \frac{1}{(n+1)} \frac{\partial \phi^{(n+1)}(\sigma_{kl}/\sigma_0)}{\partial(\sigma_{ij}/\sigma_0)} \frac{1}{(1-D)^n} \tag{4a}$$

$$\frac{\dot{D}}{\dot{D}} = \phi^{\nu}(\sigma_{kl}/\sigma_0) \frac{1}{(1-D)^{\nu}} \tag{4b}$$

where $\phi(\sigma_{kl}/\sigma_0) \equiv \bar{\sigma}/\sigma_0$.

This material is referred to as a scalar damage material.

For copper the experiments indicate that the material behaves as if the loading acting on each plane of maximum principal stress acts independently. For loading giving maximum principal stress on the i-plane the constitutive equation is

$$\frac{\dot{\epsilon}_{ij}}{\dot{\epsilon}_0} = \frac{1}{(n+1)} \frac{\partial \phi^{(n+1)}(\sigma_{kl}/\sigma_0)}{\partial(\sigma_{ij}/\sigma_0)} \frac{1}{(1-D_i)^n} \tag{5a}$$

$$\frac{\dot{D}_i}{\dot{D}_0} = (\sigma_i/\sigma_0)^{\nu} \frac{1}{(1-D_i)^{\nu}} \tag{5b}$$

where σ_i = the maximum principal stress.

The effect of loading on each maximum plane must be integrated separately. This type of material is referred to as a planar damage material. Conservative results will be obtained, however, if it is assumed that damage is scalar rather than planar, and Eq 5 are integrated with the suffix i dropped. This will have the effect of adding the damage which occurs on the separate planes of maximum principal stress. Provided the number of these planes is small, this procedure

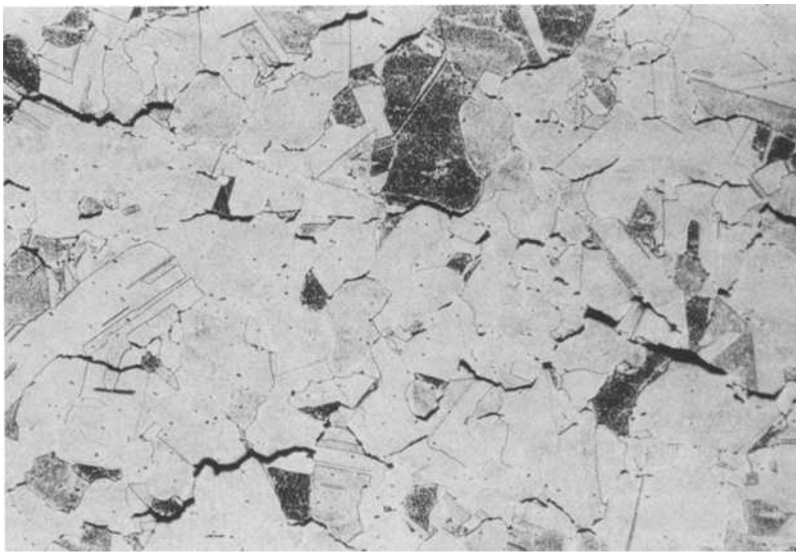

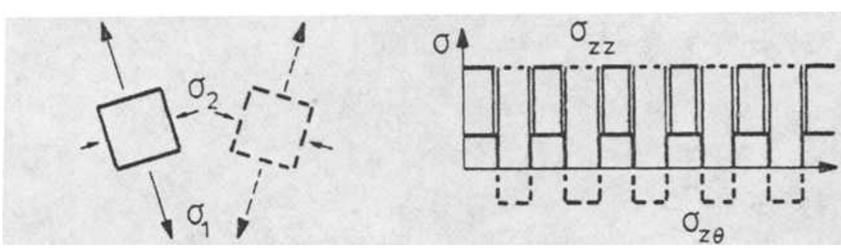

FIG. 5—*Midthickness micrograph of a copper tube tested to failure under multiple reverse torsion steady tension loading. (Magnification ×65).*

should not result in a conservatism any greater than the scatter normally experienced in high-temperature testing.

Nonproportional Low-Cycle Fatigue Experiments

Low-cycle fatigue nonproportional loading experiments have been carried out on Type 304 stainless steel thin-walled tubular specimens. The extensometry permitted axial and shear strains to be independently applied in closed-loop computer control. Details on specimen design and extensometry may be found elsewhere [*9,10*].

Baseline data from completely reversed uniaxial fatigue tests performed in our laboratory on specimens of diameter equal to the thickness of the tubular specimens and from the same batch is correlated by the usual strain-life equation

$$\Delta\epsilon/2 = \sigma'_f/E\ (2N_f)^b + \epsilon'_f(2N_f j)^c \qquad (6)$$

where

$b = -0.13,$
$c = -0.82,$
$\sigma'_f = 1.10$ GPa,
$\epsilon'_f = 1.0$, and
$E = 187.0$ GPa.

Equation 6 can be stated on the basis of effective strain amplitude

$$\Delta\bar{\epsilon}/2 = \sigma'_f/E(2N_f)^b + \epsilon'_f(2N_f)^c \tag{7}$$

where

$\Delta\bar{\epsilon}/2 = (\epsilon_a{}^2 + \gamma_a{}^2/3)^{1/2}$,
ϵ_a = axial strain amplitude, and
γ_a = shear strain amplitude.

Two pure torsion tests were run to verify the applicability of Eq 7 in the life range of interest. Failure in these tests was defined as the presence of a 1 mm surface crack length. Hence, the failure definitions for uniaxial and torsion tests were essentially equivalent based on surface crack length and are oriented toward initiation of cracks. Many previous investigations [*11,12*] which produce lack of correlation between uniaxial and torsion tests based on effective strain suffer from lack of a consistent reported failure criterion. A definition of failure based on specimen separation or global compliance change can lead to rather large discrepancies, since crack growth behavior in torsion tests is completely different from that of uniaxial tests [*10*]. The two torsion tests in this study resulted in lives less than 20% different from those calculated from Eq 7 where $\Delta\bar{\epsilon}/2 = \gamma_a/\sqrt{3}$.

A nonproportional loading test with axial strain amplitude ϵ_a and shear strain amplitude γ_a was subsequently performed. The repeated loading block consisted of the following sequence:

Cycles 1 to 40: $\epsilon_a = 0.0075$, $\gamma_a = 0$
Cycles 41 to 80: $\epsilon_a = 0$, $\gamma_a = 0.01125$

This sequence of loading was repeated until failure occurred. Again failure was defined as a 1 mm surface crack length. During the history, replicas were taken of the surface so that crack initiation and growth could be monitored and measured.

At failure, which occurred when a 1 mm surface cracklength was measured in the specimen longitudinal axis direction, 440 cycle of torsional loading and 460 cycles of axial loading had been applied. For a pure axial test, $\epsilon_a = 0.0075$ would produce a life of 325 cycles according to Eq 7. For a pure shear test, $\gamma_a = 0.01125$ would fail at 415 cycles according to Eq 7. A summary of results is given in the following table.

	Axial	Torsional
Proportional (from Eq 7)	325	415
Nonproportional (actual data)	460	440

These results within the scatter normally associated with fatigue testing indicate that the two forms of loading produces damage planes with negligible interaction and that the life for each loading component (axial or shear) can be determined from Eq 7. The total life in this case can be obtained by summing the lives of each loading component computed from Eq 7 without regard for any type of interaction.

The study of the damage measured from the replicas also indicates that the growth of damage occurs on two distinctly separate planes. When torsion is applied, growth of damage (small cracks) occurs on the set of maximum shear planes stimulated by torsion loading, and no damage growth is observed on the maximum shear planes stimulated by prior axial loading. The reverse occurs during the application of axial loading.

Conclusions

The effects of nonproportional loading have been studied in relation to failure by creep rupture and low-cycle fatigue. Copper in creep rupture and Type 304 stainless steel in low-cycle fatigue demonstrate strong directional properties. The strength is so great that no interaction is observed between the various damage planes, and good estimates of life can be obtained by simply adding the lives of each of the loading directions determined separately.

In the creep rupture of aluminum, no strong damage direction is evident, and the damage appears to grow at a peak independent of the loading direction.

However, in both extremes of behavior, the appropriate extension of life predictions obtained from uniaxial loading is a simple matter, so that the complexities introduced by nonproportional loading may be readily predicted. The experimental results also provide a strong hint that the technique developed by Chaboche, Lemaitre, and Plumtree [*1,2*] for creep/fatigue problems may be readily extended in like manner to nonproportional loading. It is now planned to perform nonproportional creep-fatigue experiments to check the validity of this assertion.

Acknowledgment

The authors acknowledge the support of a grant received from the National Science Foundation, MEA 82-19593.

References

[1] Lemaitre, J. and Chaboche, J. L., *Journal de Mécanique Appliqué*, Vol. 3, 1978.
[2] Lemaitre, J. and Plumtree, A., *Journal Engineering Materials and Technology*, Vol. 101, 1979.
[3] Raj, R. and Ashby, M. J., *Proceedings*, Metal Society Meeting, Cambridge, Jan. 1975.
[4] Hayhurst, D. R., *Journal of the Mechanics and Physics of Solids*, Vol. 20, 1972.
[5] Leckie, F. A. and Hayhurst, D. R., *Proceedings, Royal Society of London*, A340, 1974.
[6] Johnson, A. E., Henderson, J., and Khan, B., "Complex-Stress Creep Relaxation and Fracture of Metallic Alloys," Her Majesty's Stationery Office, Edinburgh, 1962.
[7] Hull, D. and Rimmer, D. E., *Philosophical Magazine*, Vol. 8, No. 8, 1959.
[8] Hayhurst, D. R. and Storakers, B., *Proceedings, Royal Society of London*, A349, 1976.
[9] McDowell, D. L. in *Proceedings*, International Symposium for Constitutive Laws of Engineering Materials, University of Arizona, Tucson, 1983, pp. 125–132.
[10] Waill, L. E., "Crack Observations in Biaxial Fatigue," M.S. thesis, Department of Mechanical and Industrial Engineering, Design and Materials Division, Report No. 108, March 1983.
[11] Garud, Y. S. in *Proceedings*, Winter Annual Meeting of ASME: Methods for Predicting Material Life in Fatigue, New York, Dec. 1979, pp. 247–263.
[12] Krempl, E., *The Influence of State of Stress on Low-Cycle Fatigue of Structural Materials, ASTM STP 549*, American Society for Testing and Materials, Philadelphia, 1974.

David J. Marsh[1] *and Frank D. W. Charlesworth*[1]

The Determination and Interpretation of Thermally Promoted Crack Initiation and Growth Data and Its Correlation with Current Uniaxial Design Data

REFERENCE: Marsh, D. J. and Charlesworth, F. D. W., "**The Determination and Interpretation of Thermally Promoted Crack Initiation and Growth Data and Its Correlation with Current Uniaxial Design Data,**" *Multiaxial Fatigue, ASTM STP 853*, K. J. Miller and M. W. Brown, Eds., American Society for Testing and Materials, Philadelphia, 1985, pp. 700–719.

ABSTRACT: In high-temperature components, secondary stresses are often applied by surface thermal fluctuations that may be sufficient to cause crack initiation and propagation and they may be also accompanied by primary loads. Since the code endurance design lines are based on isothermal uniaxial fatigue data in air, a series of tests have been conducted to study the crack initiation and growth behavior of Type 316 stainless steel under conditions of thermal fatigue in air from a bulk temperature of 650°C.

In general the observed crack initiation correlated with isothermal fatigue data relevant to temperatures towards the lower end of the surface thermal cycle temperature range indicating that the tensile plastic strain was the most important component of the initiation process. For tests without a primary load the crack growth rates in the inner fully elastic regions of the specimens correlated with calculated stress-intensity factors but again relevant to isothermal data for lower temperatures than the specimen bulk temperature. The crack growth rates observed in the plastic surface regions gave a good correlation with total strain range. A test having a surface strain range of half the isothermal fatigue endurance limit showed that limited crack propagation was possible in defected material at such low strain ranges. The addition of primary end loads gave little effect on the crack initiation behavior but did increase the crack growth rates to give an offset in the correlation with total strain range, which increased with increasing primary load.

KEY WORDS: thermal fatigue, secondary thermal stresses, primary loads, strain range, stress profile, stress intensity factors, crack initiation, crack growth

Component designs for high-temperature applications in nuclear power reactors are based on the methodology laid down in the Boiler and Pressure Vessel Code Case N47. The code bases its endurance design curves for fatigue and creep on the relevant properties obtained in uniaxial tests. The structural components of liquid metal cooled fast reactors are generally designed to have low

[1]Springfields Nuclear Power Development Laboratories, United Kingdom Atomic Energy Authority, Preston, U.K.

Copyright© 1985 by ASTM International www.astm.org

steady-state primary stresses principally due to self weight. The major stress systems of concern arise in the form of biaxial cyclic secondary stresses from thermal variations in the coolant and are of broadly two types. The first are long range variations that are the consequence of reactor shut downs or trips in which the power is reduced very rapidly leading to similar rapid changes of the temperature of the liquid metal coolant emerging from the core. These, in turn, lead to a drop of the surface temperature of the structural components of up to 150 or 200°C. Such large changes in surface temperature will be referred to as "thermal shocks." Coupled with the thermal shock situation may be additional follow-up stresses caused by differential contraction or expansion of the whole structure. Short-range thermal variations occur at many points throughout the primary coolant system under steady-state operating conditions due to the mixing of coolant streams of different temperature. Such short-range temperature variations are seen as a randomized spectrum at a single point on a component, but the peak variations may be considered for convenience as having thermal amplitudes (ΔT) in the range 30 to 100°C occurring at a frequency of up to 1 Hz.

The effects of environment are accounted for in the code so that mild environmental effects are allowed for in the design margins. Again, in this respect, the data used for the design curves are those obtained from isothermal cycling tests in air. The work being undertaken at the Springfields Nuclear Power Development Laboratories consists of applying thermal down shocks using an aerosol water spray in order to achieve a comparison of crack initiation and growth behavior under conditions of biaxial thermal shock for comparison with the existing uniaxial isothermal air data. Previous work [*1*] had shown a good comparison with the isothermal data for bulk temperatures of up to 500°C. The present work has concentrated on a bulk temperature of 650°C. In addition crack growth behavior has been studied below the thermal amplitude required for initiation in smooth surfaces and the effect of superimposed end loads of up to ¾ × 0.2% proof stress on the crack initiation and growth occurring in a thermal shock situation has been examined.

Experimental

The test specimens had a gage length of 105 mm with a rectangular section of 10 × 32 mm. Each end had two short lengths of 50 mm diameter for connection to the copper bus-bars of the heating source and also for holding in the water cooled and electrically insulated collet type grips of a servohydraulic machine. The bulk heating was obtained by a-c internal resistance using a thyristor controlled source of up to 2000 A at 3 V. The bulk temperature was controlled from a Chromel-Alumel thermocouple at the specimen center via a closed-loop controller which compared the thermocouple output with a set reference and gave a suitable feedback command voltage into the proportional thyristor controller of the transformer. The bulk temperature was maintained constant at 650°C for all the tests reported.

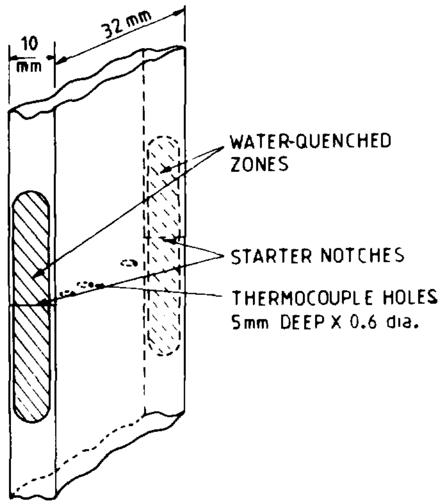

FIG. 1—*Thermal shock specimen.*

A zone 8 × 60 mm on each of the 10 mm wide faces, Fig. 1, was quenched for preset times using precision aerosol sprays supplied by a gravity fed demineralized water supply. Control of the thermal amplitude (ΔT) at the specimen surface was achieved by a balance of quench time, water head height, air pressure, and the nozzle distance from the specimen. It was found that sharper thermal profiles within the specimen were obtained when the resistance bulk heating was switched off during the quench, and hence a relay circuit was designed to control quench time and reheat time in sequence for all the tests.

The estimates of the stress and strain profiles generated in the specimens by the surface quenching were derived from the determination of the thermal profiles existing from quenched face to centerline and thus a high confidence had to be placed on the dynamic temperature measurement. As shown in Fig. 1, a series of 0.6-mm-diameter holes were drilled 5 mm deep parallel to the quenched faces and along the centerline between them at intervals from each quenched face. The thermocouple technique made use of the electromotive force (emf) generated between Chromel and the particular batch of Type 316 stainless steel. The couple was made by inserting a 0.1-mm-diameter Chromel wire in a ceramic insulation tube and welding the Chromel wire to the base of the drilled hole by capacitive discharge, thus giving confidence in the positioning of the hot junctions. The thermocouple outputs were recorded on an instrument of suitable high response and gave the isochronus temperature profiles from the quenched face to the specimen centerline for stages throughout each quench and reheating cycle. A typical set of such profiles are shown in Fig. 2. The remaining item was the estimate of the temperature cycle at the quenched face. If the thermal fluctuations at a surface are known, then the corresponding amplitudes at distances behind the surface can be readily calculated from considerations of wave form, fre-

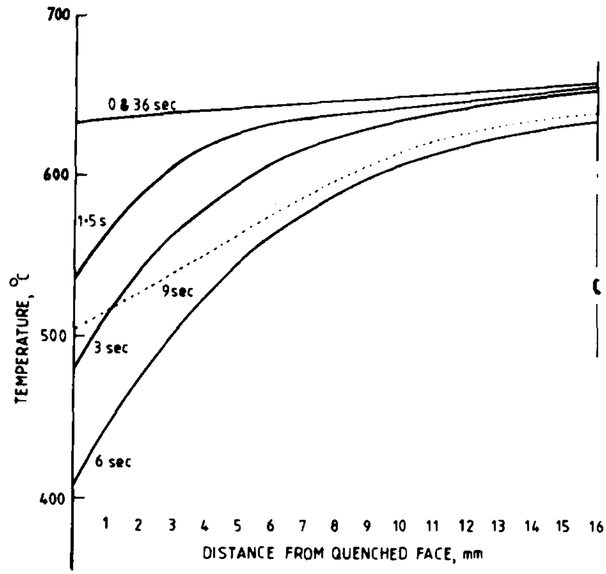

FIG. 2—*Thermal profiles at stages through the quench (effective* ΔT = *150°C).*

quency, and diffusivity [*2*]. Thus, a small computer code was written which used a finite difference method given by Crank [*3*] to solve the thermal diffusivity equation of the form

$$\frac{\partial T}{\partial t} = \alpha \frac{\partial^2 T}{\partial x^2} \tag{1}$$

where

T = temperature,
t = time,
x = distance from the surface, and
α = thermal diffusivity.

The code was used by inserting estimates of the changes in surface temperature with time until the predicted temperature changes at a point 1.0 mm deep matched those actually recorded during a quench. Subsequently, these estimates were found to give good correspondence to measurements of the surface temperature taken with a focusing infrared pyrometer employing a narrow-cut wavelength of 2.15 μm which coincides with a window in the spectra of infrared absorption by water vapor.

The quench conditions were monitored continuously throughout each test. For initial tests this was done using buried 316/Chromel thermocouples with their hot junctions 1 mm from each quenched face. Assuming an error of ±0.05 mm in the siting of the hot junction of these couples, it would result in an error of the top temperature of less than 2°C and of the temperature range of about ±3°C for an actual 200°C amplitude cycle. A comparison was made of couples at 1 mm from the quenched face where one couple was 5 mm deep and the other on the surface of the 32 mm wide face. For a top temperature of 630°C and a thermal amplitude of 190°C at the buried center plane position, the surface couple gave a top temperature of 605°C and a thermal amplitude of 165°C. Early tests had shown that the hole for the buried couple caused early crack initiation due to the high constraint and thermal isolation of the thin remaining ligament at the quenched face. Thus for all the tests noted here the control was accomplished with a surface couple using the empirical relationship mentioned previously for conversion. The control of quench amplitude by varying air pressure could be made quite precise, and the reproducibility of quench amplitude was better than 5%.

Crack growth behavior was determined from two transverse starter notches spark machined 0.18 mm wide × 0.5 mm deep across the center of each quenched face. The crack length measurements were made by an a-c potential drop method by comparing the potential of the large specimen heating current at electrodes placed near the starter notches in reference to the potential existing at the centerline.

For the application of primary axial stresses, a thermal fatigue assembly was placed within a conventional servohydraulic frame. Calibration tests had shown that the specimen temperatures and the shock quench intensities were reasonably constant in an axial direction over a distance of 20 mm either side of the longitudinal center. Strain was measured with a dual beam extensometer so that the measured gage length of 30 mm was equispaced about the longitudinal centerline.

The material tested was taken from a single cast of Type 316 stainless steel that had been categorized for physical, mechanical, creep, and fatigue properties in the solution-treated condition in the laboratories of the U.K. Atomic Energy Authority (UKAEA) Northern Group, Table 1. One further feature was that some of the specimens contained a small zone of weld metal in each of the quenched faces. One face was of a polish finish while the other had been machined to a 1.6 μm centerline average (CLA) surface finish. The steel was in the solution-treated condition except for the weld and heat-affected zones.

Stress-Strain Analysis

Correlation of the results with uniaxial data requires reliable estimates of the effective surface strain range and the range of stress profiles existing from the specimen surface to the centerline at stages throughout the thermal cycle. The latter were used in turn to estimate the crack tip stress intensity factors at stages through the cycle for increasing values of current crack length. Stress-strain analysis was performed by using a modified version of a computer code based on the model outlined in a previous paper [1].

TABLE 1—*Material property and composition.*

CHEMICAL COMPOSITION OF MATERIAL TESTED, WEIGHT %			
Carbon	0.060		
Silicon	0.49		
Manganese	1.75		
Nickel	12.30		
Chromium	17.7		
Molybdenum	2.34		
Sulphur	0.021		
Phosphorous	0.035		
Boron	0.0019		
Nitrogen	0.040		
MECHANICAL PROPERTIES OF MATERIAL TESTED			
	25°C	400°C	625°C
Young's modulus × 10^3 MPa	198	168	149
0.2% proof strength, MPa	230	139	118
Ultimate tensile strength, MPa	570	460	390
Elongation	60%	41%	46%
CYCLIC HARDENING OF MATERIAL TESTED			
Strain range	0.25%	0.5%	1%
Stress range 1st cycle MPa	231	256	287
Stress range continuous cycling MPa	273	442	618

An important feature of the model arises from the symmetrical quenching applied to the specimen which effectively inhibits the introduction of a bending moment. Thus the stresses, that is, elastic strains existing between the surface and the centerline $W/2$ of the specimen must sum up to the value of stress (σ) relevant to the end load applied, this being zero in the case of no end load, namely

$$\int_{o}^{W/2} \sigma \, dx = \sigma_m \tag{2}$$

This boundary condition is satisfied at each stage of the quench in the computer code.

The model commences with the thermal profiles measured from quenched face to specimen centerline (16 mm), taking the temperature at 1 mm intervals for about ten stages through the cyclic sequence. The temperatures are converted into elastic strain using a constant value for thermal expansion coefficient representing a suitable mean of the instantaneous values for the temperature ranges considered (for example, 2×10^{-5} for Type 316 at 500°C). The differences between successive values of strain at a single point were then taken as the changes in incremental strain as the specimen progressed from one stage to the next in the thermal cycle. For the first cycle, the program which treats the material as elastic-perfectly plastic, assigns a value for yield strain appropriate to the monotonic yield stress relevant to the total strain occurring from point to point in the specimen. The strain profile for the first stage of the quench is enumerated and balanced about σ_m or zero, as noted. The appropriate strain increments are added to that profile, the stresses (elastic strains) balanced for the next stage, and so on for successive stages until the cycle is complete. The program continues to iterate successive cycles until a stable set of profiles is attained. This was found to occur in relatively few operations with stability reached in 10 cycles. The result is set of stress (equivalent elastic strain) profiles at stages through the quench as shown in Fig. 3. In addition the printout lists the total elastic plus plastic strain at each time interval, thus enabling the total cyclic strain range at each point to be deduced.

The model is naturally sensitive to the concepts and values taken for yield stress. For these particular tests the durations were small in relation to the total isothermal fatigue lives at the strain ranges employed, especially since the strain ranges experienced within the specimen rapidly reduced away from the surface of the specimen. The proportion of life required for significant cyclic hardening has been demonstrated by Jaske and Frey [4] and at low-strain ranges can be well in excess of 10^5 cycles. The reasoning led to the adoption of the monotonic stress-strain relationship. The relationship was deduced from uniaxial data obtained on the same cast of steel at 620°C. The uniaxial data was converted to equibiaxial conditions using the von Mises yield criterion and for this purpose the elastic and plastic Poisson's ratios were taken to be 0.29 and 0.5, respectively. The result gave the relation

$$\bar{Y} = 1.645 \times 10^{-3} (\epsilon_T)^{0.146} \tag{3}$$

where

$\bar{Y}$ = elastic component of strain and
ϵ_T = total strain.

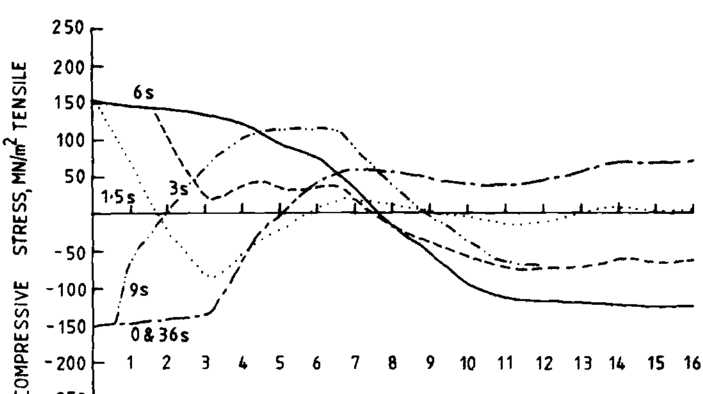

FIG. 3—*Stress distributions at intervals through the thermal cycle (effective* ΔT = *150°C).*

This elastic component of strain at a particular value of total strain was taken to be the yield strain in the elastic-perfectly plastic model used in the analysis.

The stress profiles obtained were used to calculate the stress intensity factors at the crack tip for increasing values of current crack length as follows

$$K = \int_{o}^{a} G\,(a,x)\;\sigma\,(x)\;dx \tag{4}$$

where

K = stress intensity factor,
a = current crack length, and
$G(a,x)$ = Green's function for a crack of length a.

Green's function for a double edged cracked plate of finite width w is as follows [6]

$$G(a,x) = \left\{1 + f\left(\frac{x}{a}\right)\cos^2\frac{\pi a}{2w}\right\}\sqrt{\tan\frac{\pi a}{2w}} \times \frac{1}{\sqrt{1 - \left(\cos\frac{\pi a}{2w}\cos\frac{\pi x}{2w}\right)^2}} \tag{5}$$

where $f(x/a)$ is a function given in graphical form by Tada [5]. The function was approximated by the following polynomial

$$f\left(\frac{x}{a}\right) = 0.29797 - 5.48197 \times 10^{-3}\left(\frac{x}{a}\right) - 0.51369\left(\frac{x}{a}\right)^2 - 0.21659\left(\frac{x}{a}\right)^3 \tag{6}$$

A typical set of stress intensity factor curves are shown in Fig. 4. The picture is one of the stress intensity peak moving into the specimen and decaying as the quench wave moves into the sample.

Results

The details of the test conditions are given in Table 2. The first four tests covered a wide range of effective surface thermal cycling amplitudes (ΔT's). Placing them in perspective, the effective ΔT's of 150 and 106°C are equivalent to points lying on either side of the uniaxial fatigue data curve for Type 316 steel at 625°C at a life of about 10 000 cycles. It is worth noting that such data are from tests on smooth specimens of about 6 mm diameter taken to failure. The small 60°C ΔT of test 4 was selected to explore the possibility of crack

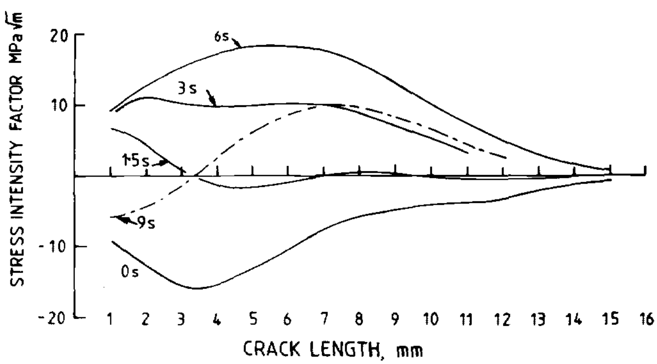

FIG. 4—*Stress-intensity factor distributions at intervals through the thermal cycle (effective* ΔT = *150°C).*

initiation from the ½-mm-deep starter notches and the subsequent crack growth under the conditions of a sharp thermal stress gradient. In this case the surface strain range was equivalent to about half the fatigue limit for the steel. The other two tests explored the effect of the end loads (primary stresses) of 47.5 and 90 MN/m^2 on the behavior of the material when also given thermal cycles of an effective surface ΔT of 150°C. The end loads are equivalent to about 0.4 and 0.75 × 0.2% proof stress for the steel.

Crack Initiation

Longitudinal and transverse sections of the specimens were examined by optical microscopy after test to determine the extent and depth of thermal fatigue crack initiation. In all cases the cracks appeared to be transgranular even for cracks only a few microns long, and all the cracks were filled with oxide. Some evidence of oxide crack blunting was noted but that appeared rare. The following is a summary of the major observations.

TABLE 2—*Specimen test conditions.*

Specimen No.	Total Effective Surface Strain Range, $\Delta\varepsilon_T$, $\times 10^{-3}$	Effective Surface Temperature Range ΔT, °C	No. of Cycles, $\times 10^3$	End Load MN/m^2
1	5.18	270	10	0
2	5.18	270	50	0
3	3.00	150	56	0
4	2.06	106	90	0
5	1.20	60	200	0
6	3.00	150	100	47.5
7	3.00	150	38	90

Sample 1—270°C, 10 000 Cycles

This sample showed very few small cracks of up to 20 μm long occurring within the weld metal and at the vicinity of stress raisers such as thermocouple holes near the quenched surface.

Sample 2—270°C, 50 000 Cycles

There was considerable initiation on both polished and machined faces in both parent metal and weld metal. The majority of cracks had grown up to 0.5 mm long, but a few cracks with a spacing of 2 to 3 mm had propagated to a depth of 2 mm.

Sample 3—150°C, 56 000 Cycles

There was a small amount of cracking on both faces of this specimen. The majority were quite short at about 10 μm, but, as in the previous sample, a few had grown preferentially to 50 μm long. The initiation sites were all remote from the grain boundaries even in the weld metal.

Sample 4—106°C, 90 000 Cycles

Only one crack initiation point was found in the parent metal. It was on the machined face and was 70% of the depth of the disturbed surface layer with a length of 9 μm. A few cracks of up to 27 μm long were present in the weld metal of both smooth and machined faces, illustrating the poorer properties of that material.

Sample 5—60°C, 200 000 Cycles

As expected there were no signs of initiation in either parent or weld metal of the sample.

Sample 6—150°C, 47.5 MN/m² End Load

This sample received 100 000 cycles, but the cracking was very similar to the sample without an end load. The most significant area showing greater growth was the weld zone which contained some cracks that had penetrated completely across the 2.5 mm deep weld zone.

Sample 7—150°C, 90 MN/m² End Load, 38 000 Cycles

Again the extent of crack initiation was no greater than in the sample tested without end load. The main effect of the end load was greater crack penetration during the shorter test to give crack depths of up to 200 μm.

The results have been converted by von Mises criterion [*1*] to equivalent uniaxial surface strain range and plotted as S-N data in Fig. 5. Wareing [*6*] has

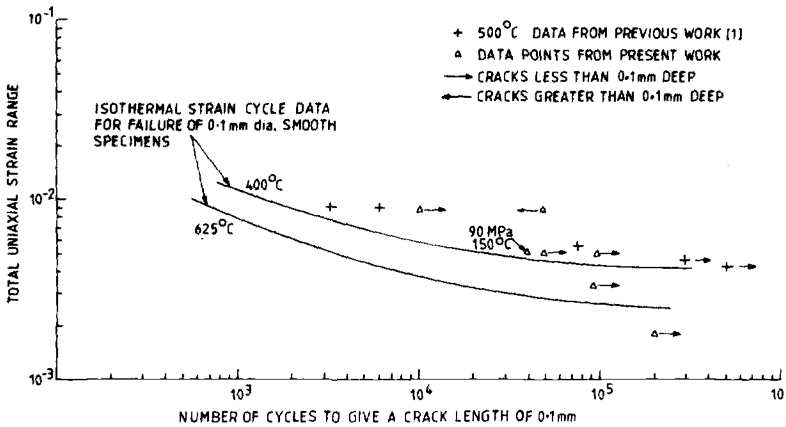

FIG. 5—*Crack initiation results for parent metal (Type 316 stainless steel) compared to uniaxial fatigue data.*

reconstituted his isothermal uniaxial data obtained on 6.35 mm diameter, Type 316 specimens as fatigue life curves for a specimen diameter of 0.1 mm for failure by considering measured crack growth rates using the following relation

$$N_f = N_i + N_p \tag{7}$$

$$\frac{N_p(0.1)}{N_p(6.35)} = \frac{\ln (0.1/a_o)}{\ln (6.35/a_o)} \tag{8}$$

where

N_i and N_f = number of cycles for initiation and failure,
N_p = number of cycles for crack propagation to the relevant depth, and
a_o = initiation crack size, taken as 10 μm.

The calculated 0.1 mm diameter failure curves are indicated in Fig. 5. The thermal fatigue points all indicate longer lives than given by the failure curves for 625 and 400°C, although the specimen tested with an end load of 90 MN/m^2 lay close to the 400°C data line presumably due to the faster growth of the few cracks initiated.

Crack Growth Results

The crack growth results and the analysis data are given in Table 3. Figure 6 shows the effects of varying the surface thermal amplitude and adding primary stress to a constant thermal amplitude on the resulting crack growth obtained from the starter notches. Increasing the surface amplitude (effective $\Delta\epsilon_T$) significantly increased the crack growth rates in the early stages of the tests, but, in all cases, the growth rates had sharply reduced by the time the cracks were

4 to 5 mm deep. In contrast, the effect of adding a primary stress (end load) at a constant thermal amplitude was seen as an increase in the initial crack growth rates, but, in addition, the high growth rates were maintained to much greater depths away from the thermally cycled surface. However, it is worth noting that even under a high end load equivalent to $0.7 \times 0.2\%$ proof stress (PS) the growth rate was decreasing as the crack length increased to 10 mm, even though the greater crack lengths implied greater overall section stress. The effect of the latter was apparent in the extensometer measurements of overall strain. The 47.5 MN/m^2 end load ($0.4 \times 0.2\%$ PS) gave a nett specimen extension of only 0.5% in 10^5 cycles, whereas the 90 MN/m^2 end load gave a 3% extension in 38 000 cycles (400 h). The end of the test gave indications of a rapidly increasing creep or ratchetting deformation.

As noted the analysis provided estimates of the stress intensity factor at the crack tip. Figure 7 shows a plot of the crack growth rate against the stress intensity factors. The results from the previous thermal fatigue work [*1*] are also indicated. They were obtained from more intense thermal shocks having only short range surface plasticity and gave a good K_{max} versus da/dN relationship for crack lengths of 2 to 8 mm. It can be seen that the correlation is poor until the crack lengths of the present tests approached 4 mm long but then the correlation converges on the previous data. The specimens tested with an end load did not conform to this correlation at all, presumably due to the extended plasticity across the specimens.

The specimen given an effective thermal shock range of 60°C did produce limited crack growth in a test duration of 200 000 cycles. At the end of the test, cracks had propagated 0.5 mm from the 0.5 mm deep starter notch. The a-c potential crack growth measurements were not sufficiently sensitive to measure such low growth rates on very short cracks, but it did indicate that growth may have commenced at about half of the test life. Assuming that is the case, an estimate of the probable growth rate is indicated on the stress intensity plot of Fig. 7, and it falls in line with the previous data plot.

Under conditions of high strain in isothermal strain cycling, Wareing et al [*7*] found that crack growth followed the relationship

$$\frac{da}{dN} = Ba \tag{9}$$

and

$$B = \frac{\pi^2}{8}\left(\frac{\sigma}{2Y'}\right)^2 \times \frac{\Delta\epsilon_p}{1 + 2\beta} \tag{10}$$

where

σ = maximum tensile stress in the cycle,
Y' = flow stress, and
β = work hardening exponent.

TABLE 3—*Crack propagation results.*

Specimen No.	Crack Length, a, mm	Crack Growth Rate, da/dN, mm/cycle, $\times 10^4$	$B = \frac{1}{a} \times \frac{da}{dN}$, $\times 10^4$	Total Strain Range (equibiaxial), $\times 10^3$	Stress Intensity, K, MPa m	R Ratio $= \frac{K_{min}}{K_{max}}$
1	1.0	19.0	19.0	3.86	9.75	−1.0
	2.0	12.0	6.0	2.74	13.6	−1.0
	3.0	5.5	1.8	1.80	16.3	−1.0
	4.0	1.5	0.37	1.08	18.1	−0.96
3	1.0	3.6	3.6	2.36	9.13	−1.0
	2.0	3.1	1.6	1.80	12.8	−1.0
	3.0	2.1	0.7	1.30	15.5	−1.0
	4.0	1.4	0.35	0.86	17.4	−0.88
	5.0	0.49	0.08	0.64	18.1	−0.73
4	1.0	2.1	2.1	1.75	8.8	−1.0
	2.0	1.9	0.95	1.41	12.4	−1.0
	3.0	1.6	0.54	1.07	14.9	−0.93
	4.0	0.8	0.20	0.75	16.9	−0.76
5	1.0	0.05	0.05	0.74	7.84	−0.52
	2.0	...	...	0.44	10.8	−0.22
	3.0	...	...	0.20	11.7	−0.05
	4.0	...	...	0.21	10.6	−0.04

6	1.0	5.0	5.0	2.32	10.3	−1.0
	2.0	4.5	2.2	1.76	14.6	−1.0
	3.0	3.9	1.3	1.26	17.9	−0.89
	4.0	2.8	0.7	0.82	20.7	−0.67
	5.0	1.4	0.29	0.60	22.6	−0.45
	6.0	0.75	0.12	0.46	23.7	−0.26
	7.0	0.41	0.06	0.32	24.5	−0.07
	8.0	0.20	0.025	0.38	22.1	+0.11
7	1.0	...	...	2.24	13.9	−1.0
	2.0	11.6	5.8	1.68	20.0	−0.83
	3.0	11.4	3.8	1.18	24.7	−0.59
	4.0	10.4	2.6	0.74	28.7	−0.34
	5.0	8.2	1.6	0.53	31.8	−0.13
	6.0	5.8	0.97	0.39	32.0	+0.05
	7.0	4.3	0.61	0.32	28.0	+0.22
	8.0	3.0	0.38	0.46	23.7	+0.36
	9.0	2.2	0.24	0.60	19.5	+0.48
	10.0	1.1	0.11	0.76	15.4	+0.56
	11.0	0.73	0.066	0.84	11.7	+0.70

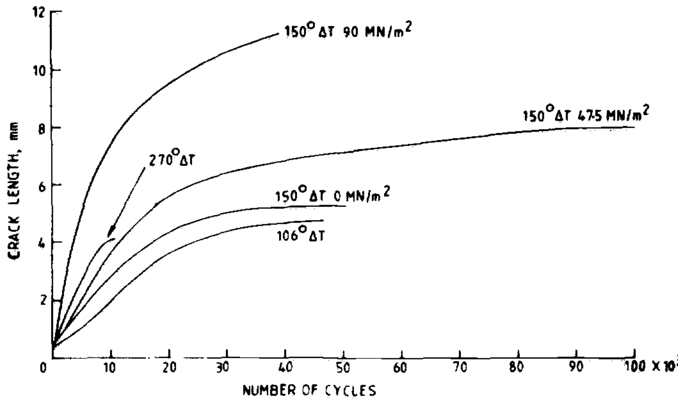

FIG. 6—*Crack length versus duration for cracks grown from starter notches.*

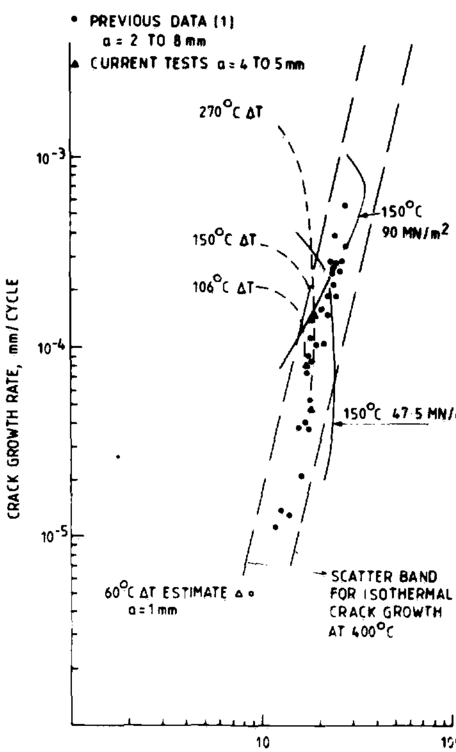

FIG. 7—*Correlation of crack growth rate with stress intensity factor.*

The crack growth results for the subsurface regions which were indicated to be undergoing reversed plasticity in the analysis results are plotted against strain range in Fig. 8. The results for the tests without end load show a good correlation with total strain range, but there is little data at low strain ranges for comparison. The isothermal 625° line shown is for a different batch of material. The data for the end load samples also show some correlation with total strain range but with the effect that increasing end loads raised the growth rates for given strain ranges with all the data lines tending to converge at high strain ranges.

Discussion and Conclusions

The validity of any conclusions in a program of thermal fatigue must rest on the accuracy with which the temperature and thermal cycles actually occurring

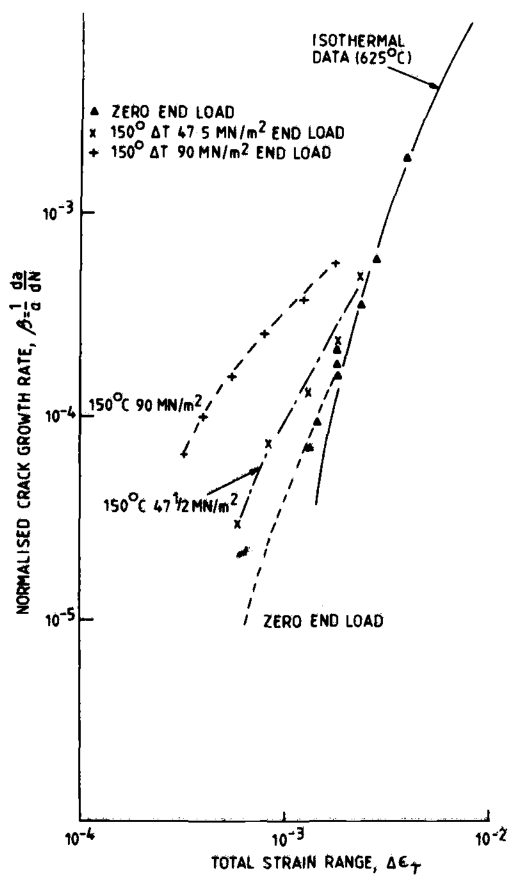

FIG. 8—*Correlation of normalized crack growth rate with total strain for the subsurface regions in fully reversed plasticity.*

within the specimen can be estimated. The fact that in this air/water system, oxidation, etc., will cause emissivity and heat transfer coefficient to change during each test, renders any approach using heat transfer coefficient of extremely doubtful validity. This led to the concept of direct measurement, and the thermocouple system finally used was evolved over a period of initial trials. Those demonstrated that even with high response conventional thermocouples the lack of certainty of the actual position of the hot junction gave unacceptable possible errors in measurement. The use of a 0.1-mm Chromel wire welded to the Type 316 steel specimen removed that doubt. Type 316 steel wire was used for the return leg of couple and tests showed that the emf generated between the Type 316 wire and the specimen, even when the wire was placed at the cold end of the specimen, was insignificant at less than 0.02 mV. The system proved capable of good reproducibility of the quench amplitude, this being most important for the crack initiation work since variations in thermal amplitude would give exactly similar variations in the total strain range at the surface. However these variations in strain range for the elastic/plastically cycling surface would confer only small variations in stress range, so the effect on the crack growth/stress intensity correlations would be very small.

The analysis carried out refers to the conditions that occurred at the axial center plane, that is, that joining the centerlines of the two 10-mm-wide quenched faces. The thickness of 10 mm was a compromise dictated on one hand by the available heating current limiting the specimen thickness and the opposite desire to have a sufficiently thick specimen to afford some biaxiality of stressing conditions near its centerline. The relaxation from these conditions was evidenced by the fact that the crack initiation seen in the specimens was aligned normal to the longitudinal axis. Only 8-mm of the 10-mm-wide face was quenched, and this was reflected in the smaller thermal amplitude measured on the wide face of the specimen near the edge of the quenched face. This reduction in thermal strain range was a surface effect and only of the order of 13%. Although a more exhaustive finite element analysis is planned, it is felt that the approximate analysis outlined in this paper serves usefully to describe the processes occurring during the particular thermal fatigue downshock cycle used in these tests. The approach uses similar concepts to those of Skelton [*8*] for tests on hollow cylindrical specimens.

The thermal fatigue processes in the down shock tests do not result in the much more complicated straining cycle noted for disk shaped specimens by Mowbray and McConnelec [*9*] where there was considerable time for stress relaxation processes to occur particularly in the tensile portion of the cycle where the specimens were at temperatures above the creep range. In the work described here the tensile strain component occurred over a short period of time at temperatures below the creep range (that is, <500°C). Some creep relaxation could occur during the compressive straining, but the dwell times in the creep range for the elastic-plastic surface zones were only of the order of 20 s. These dwell times are too short for significant effect on the material cyclic hardening response of Type 316 material [*10*]. In addition compressive dwells in Type 316 steel do not give the often severe reductions in fatigue life as given by tensile dwells [*11*].

The results have shown a reasonably good correlation with the available isothermal fatigue data with a tendency for both initiation and growth under the thermal fatigue process to be equivalent to the isothermal data relevant to a lower temperature than the bulk temperature of the tests. The pertinent question is whether this correlation is a valid feature of the thermal fatigue process itself or can be explained by the assumptions and simplifications used for the stress and strain analysis. In the course of the work analyses were carried out to compare the effects of using either full cyclic yield or monotonic yield criteria. Although the use of cyclic yield raised the resultant stress profiles and hence stress intensity factor profiles across the specimens, it did not affect the estimations of total strain range at the surface. However, the crack initiation correlation could have been influenced by the stress relaxation given at the surface by the presence of the crack growing from the starter notches. The extent of this relaxation in the thermal fatigue case will be covered in the finite element work just mentioned. However, care was taken to draw conclusions for crack initiation behavior from observations several millimetre away from the starter notches.

Because of the geometry of the test and the moderate rates of quench, a surface thermal cycle of 220°C was needed to give a surface strain range equivalent to an instantaneous ΔT of 150°C. If we consider the progression of strain from the start of a quench during cycling, a large proportion will be taken up as elastic strain in progressing from compressive yield to tensile yield so that the damaging plastic tensile strain occurs at the lower temperatures, that is, below 500°C in this test. The important question here is which component of reversed strain is the more significant in the initiation process, compressive, or tensile. The results of these tests suggest that the tensile one is the most important. Work is underway on tests using mechanical straining with temperatures ramped in phase and out of phase with the mechanical loads, and the results are confirming that in such tests the fatigue life obtained is equivalent to the isothermal fatigue life at the temperature at which the tensile strain occurred in the thermomechanical tests [*10*].

The tests without an end load gave crack growth rates in material below the plastically cycling surface layers that correlated with the relevant stress intensity factors and which were in agreement with the correlation seen in previous work. That relationship lay within the scatterband for da/dN versus K for isothermal crack growth at 400°C [*12*]. This again suggests that the isothermal data for the lower temperatures is the most relevant to the thermal shock situation (since the maximum crack tip opening occurs at the bottom of the cycle). The results for the tests with end load lay within or close to the scatterband. Similarly, the crack growth rate occurring in the cyclically plastic surface zones gave a correlation against total strain range, although the relationship varied with increasing end load. It is felt likely that the use of an elastic-plastic fracture mechanics parameter such as crack-tip opening displacement may be more successful and is being explored.

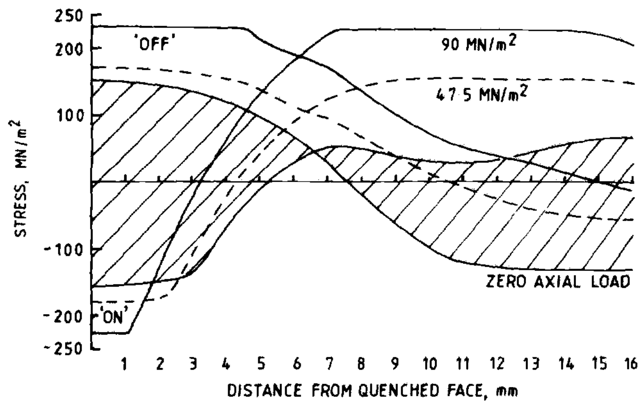

FIG. 9—*Stress profiles for a 150°C Δ effective quench showing the effect of axial loads of 0, 47.5, and 90 MN/m².*

The stress analysis was used to provide balanced stress profiles about the value of end load applied, and Fig. 9 shows the pairs of on and off profiles for 0, 47.5, and 90 MN/m^2 corresponding to the peak quench and reheated steady state. The effect of the end loads was to increase the R ratios for the cyclic stress range occurring within the specimen, and the increase in R ratio may account for the higher observed growth rates. Finally, to summarize, it is concluded the thermal fatigue properties of Type 316 stainless steel can be correlated to isothermal strain cycling data as used in the design codes but that using data relevant to the mean temperature of the surface thermal cycles may still be conservative. Crack initiation was not markedly affected by the 1.6-μm CLA machined surface finish as against a smooth surface and initiation was not increased by the presence of primary end loads up to 90 MN/m^2. A fracture mechanics approach will yield a reasonable estimate of the crack growth rates to be expected in a thermal cycling situation with the rates correlating to strain range in the plastic surface zones and to stress intensity factor within the body of the component. However, the correlations of crack growth rate with strain range for the plastic surface zones showed an increasing divergence towards higher growth rates as increasing primary loads were applied.

Acknowledgments

The authors wish to thank the Managing Director of the United Kingdom Atomic Energy Authority for permission to publish this work and their colleagues Dr. J. Wareing and Mr. A. Clayton for their assistance.

References

[1] Marsh, D. J., *Fatigue of Engineering Materials and Structures*, Vol. 4, 1981, pp. 179–195.
[2] Carslaw, H. S. and Jaeger, J. C., *Conduction of Heat in Solids*, Oxford University Press, Oxford, 1959.

[3] Crank, J., *Mathematics of Diffusion,* Oxford University Press, Oxford, 1957.
[4] Jaske, C. E. and Frey, N. D., *ASME Joint Conference on Pressure Vessels and Piping,* Denver, 21-25 June 1981.
[5] Tada, H., *The Stress Analysis of Cracks Handbook,* Del Research Corporation, Hellertown, PA, 1973.
[6] Wareing, J., private communication.
[7] Wareing J. et al, "Mechanisms of Elevated Temperature Fatigue in Type 316 Stainless Steel, ND-R-477(S), U.K. Atomic Energy Authority.
[8] Skelton, R. P., "Crack Propagation in Simple Metal Components During Thermal Shock, Report No. RD/L/N 54/79, Central Electricity Generating Board, 1979.
[9] Mowbray, D. F. and McConnelee, J. E., in *Thermal Fatigue of Materials and Components, ASTM STP 612,* Philadelphia, pp. 10-29.
[10] Beauchamp, D. J., "Thermal-Mechanical Cycling at Elevated Temperature," Ph.D. thesis, Bristol University, Bristol, U.K., 1982.
[11] Lloyd, G. L. and Wareing, J., *Life Prediction Methods for Combined Creep-Fatigue Endurance, Metals Technology,* August 1981, pp. 297-305.
[12] Lloyd, G. L. and Walls, J. D., "Section Thickness Effects and Temperature Dependence of Fatigue Crack Growth in Type 316 Stainless Steel," ND-R-325(R), U.K. Atomic Energy Authority.

Summary

Summary

This book contains 39 contributions related to the problem of three-dimensional cyclic straining of engineering materials. They show that simple uniaxial laboratory test data either are inapplicable to given practical situations or are, at least, difficult to utilize. Since many practical fatigue problems are concerned with various loading combinations, such as the bending and twisting of shafts or the biaxial tension of plates and shells, or expressed another way, fatigue cracks growing by a mixture of fracture modes, it is required that failure induced by multiaxial cyclic stresses should be better appreciated by all engineering disciplines. It follows that existing design codes of practice should be modified in the light of our new understanding of complex loading systems.

In the following pages it will be seen that traditional and new methods of analysis have been invoked, but it is clear that irrespective of the discipline adopted it is necessary to link the classical deformation approach to fatigue failure, using Basquin/Coffin-Manson type rules, with fracture mechanics analyses that are concerned with crack shapes, sites, and speeds. Considerable advances in our understanding of fatigue failure will only occur when a thorough knowledge of the imposed three-dimensional stress-strain state is associated with given crack orientations and modes of growth. It follows that specimens for use in multiaxial fatigue studies should be carefully designed in order that the complete stress-strain state can be derived. In some cases excellent experimental work has been devalued because insufficient information has been provided concerning either crack formation and propagation or the strain state which produces the fatal crack.

The papers that follow have been divided into eight distinct sections, the contents of which are now summarized.

1. *Multiaxial Fatigue Testing*

The first paper highlights both the advances and the limitations of multiaxial testing techniques. Currently testing machines cover only a limited range of biaxial stress conditions using relatively simple test systems. Indeed all the experimental data provided in this volume have been generated on such facilities. The complex machine described in this introductory paper can achieve any strain state and hence check all multiaxial fatigue theories, although it will be difficult to adapt the machine to high temperature or environmental studies.

The next contribution contrasts with the preceding sophisticated machine by describing an effective yet a simple and cheap machine capable of generating quickly valuable data, and although over only a narrow range it is one of importance to engineering designers. It is apparent from the contents of this book that both types of machine are required and that they complement one another.

Copyright© 1985 by ASTM International www.astm.org

The paper by Lawrence, who has previously designed a number of systems, describes a multiaxial test facility suitable for polymers, and incorporates a number of novel features in the design. It also highlights the problems peculiar to studies of nonmetals susceptible to strain rate effects. There are however other facilities for testing polymer based composites, and readers are directed to section 5 of this volume.

2. *Deformation Behavior and the Stress Analysis of Cracks*

Section two illustrates the complexities of analyzing multiaxial situations. The first paper by Harvey et al reviews the use of plastic deformation theories for cyclic loading and emphasizes the need for kinematic hardening representation. Although cyclically induced anisotropy is discussed, more extensive testing is required to reveal its importance.

McDowell and Socie employ a more complicated loading path with the intention of achieving a simpler representative formula for cyclic hardening behavior. They clearly show that, just as monotonic stress-strain curves are inappropriate in fatigue, uniaxial cyclic stress-strain behavior is insufficient to describe the response of material to multiaxial loading.

The final paper examines a fracture mechanics approach and shows the need to include elastic-plastic deformation effects at crack tips for both Modes I and II extension. Small scale yielding calculations elsewhere in this volume show qualitatively similar results to the finite element analysis employed by Kfouri and Miller, revealing a greater extent of crack-tip plasticity for shear and Mode II conditons. Neither approach is able as yet to demonstrate quantitative agreement with experimental results; nevertheless, this is a promising line of research.

3. *Propagation of Long Fatigue Cracks*

The next papers are divided into two sections concerned with long cracks and short cracks, respectively. Traditionally long crack have been studied by standard linear elastic fracture mechanics (LEFM) type tests, but recent work has shown that short cracks, not covered by LEFM analyses, develop rapidly during the initiation phase of life, thus permitting the endurance of materials to be solely related to crack growth behavior.

The first three papers in section three predominantly concentrate on Mode I cracks, but Smith and Pascoe show that in steels cracks can either initiate and grow in shear (Stage I-Mode II) or change to grow in the opening mode (Stage II-Mode I) under different stress states. The remaining papers in this section examine mixed mode growth, that is, Mode I cracks together with Modes II and III components. The paper by Brown and Miller shows the importance of crack-tip plasticity in controlling crack speed and that crack growth rates are always faster than LEFM predictions suggest. Their rudimentary approach to predicting propagation rates requires further verification. Rhodes and Radon show that even in standard ASTM specimen geometries the crack growth rate is affected by biaxial stress effects. The work of Kitagawa et al confirms that LEFM is only applicable below one third of yield stress and that at higher stress levels there is a need to account for biaxial effects. They also confirm the observation in the following paper by Gao Hua et al that long cracks under mixed mode loading branch to follow the direction where ΔK_{II} is zero. In contrast Gao Hua also observed stable mixed mode growth at stress levels close to threshold in four materials and Smith and Pascoe show that stable Mode II growth is possible for long cracks and high strain amplitudes. This shows that at least one area of conflict yet to be resolved is why shear mode cracks should change to Mode I.

Mode III crack growth studies were attempted by Ritchie et al, Hourlier et al, and Pook. All researchers found it difficult to maintain Mode III growth for long cracks except at the highest stress levels where presumably large crack-tip plastic zones permitted Mode III extension. The characteristic factory roof fracture surface morphology, frequently observed in torsional loading situations, indicates a preference for Mode I cracking. However, the choice of crack path appears to be mean stress and material dependent, and Hourlier et al suggest that cracks will always seek the mode that can generate the greatest propagation rate. Ritchie et al offer an ingenious although contentious model, but observe, in common with many papers in this section, that plastic strain intensity correlates crack growth rates.

4. *Formation and Growth of Short Cracks*

Section four contains five papers which examine short crack behavior. The paper by Hurd and Irving shows the correspondence between initiation and the growth of small cracks generated by the torsion loading of smooth specimens. This work is extended in the succeeding paper which reports on other loading states. Jacquelin et al conclude that mean stress and strain state affect the orientation, shape and growth rate of cracks but that microstructure plays an important role in the crack initiation process. These useful studies need to be extended to more general multiaxial stress-strain states.

Leis et al examine the local multiaxial stress field adjacent to notches in specimens subjected to uniaxial loads and show that the growth rate of short cracks may be rationalized by three dimensional considerations. This approach should be contrasted with the work of Tipton and Nelson reported later.

Another distinctive way of initiating short cracks is by surface frictional stresses generated in fretting experiments. Lindley and Nix show that small cracks can be readily produced early in life. However, in such situations these cracks can be arrested at the threshold value in a similar manner to those observed in the Mode II crack growth tests of Gao Hua et al and also under thermal shock conditions as discussed in the final paper of this volume.

An elegant procedure is introduced by Verpoest et al for testing wires under tension and shear which permits a study of the effects of material anisotropy on fracture. Most importantly cracking directions are identified, although not precisely classified, and the propensity towards longitudinal cracks due to grain shape and other directional properties induced in drawn wires is observed.

5. *Damage Accumulation in Composite Materials*

The first paper on composite materials presents a review of multiaxial effects in fiber reinforced materials and is followed by two more specific studies. It is obvious that a multiplicity of failure mechanisms can be identified, and these dominate the form of the biaxial fracture criteria. Jones et al show that the highly directional nature of woven fiber laminates is sufficient to minimize the effect of stress concentration factors at round notches in biaxially stressed plates. This may be contrasted with the behavior of chopped strand mats studied by Radon and Wachnicki, which is more amenable to adaption of continuum mechanics methods.

Safe life criteria have been derived in some of the cases studied. The form of these failure criteria is invariably based on static tests, but much further detailed work is needed to understand specific cyclic failure mechanisms which could lead to fatigue-based criteria being applicable to lower stress levels and longer endurances.

Specific problems arise in the testing of composite materials, and examples may be seen in the work presented in this section. Various gripping systems may be employed for specimens, with suitable reinforcement to assure a satisfactory transference of stress. However it appears that test procedures still require to be developed in order to generate controlled biaxial stress fields without adversely affecting the mode of failure when examining certain material orientations.

6. *Life Prediction Techniques for Plain and Notched Components*

Section six brings together six papers concerned with deriving, evaluating or implementing design criteria for the complex stress situations faced by designers. The paper by McDairmid is one of the few papers in this volume concerned with designing against high-cycle fatigue, and it shows the influence of material properties on the fatigue limit behavior, emphasizing the need to conduct tests under at least two different biaxial stress states in order to characterize satisfactorily the behavior of any given isotropic material.

The paper by Williams et al presents a modern industrial designer's view of the classical approach to the complex problems of cumulative damage in notched shafts. It is apparent that traditional methods are conservative for crack initiation in torsional loading situations, but the methods have not yet been extended to other stress states which may be more dangerous (for example, see Marloff et al on the use of triaxiality factors).

A thorough study of mean stress effects is presented by Socie et al, who show that these should be incorporated in any failure criterion because uniaxial behavior is not representative of all biaxial stress states. Their paper shows a useful extension of mean stress conditions to the low-cycle fatigue regime, which should be contrasted with established uniaxial loading procedures for evaluating mean stress contributions.

The remaining three papers introduce an extensive series of experiments currently in progress on behalf of the Society of Automotive Engineers, using one type of material, heat treatment, and specimen shape. Leese and Morrow investigated the basic cyclic material properties in tension and torsion, showing that the cyclic stress-strain behavior and the slopes of Coffin-Manson and Basquin plots are independent of the stress state. However these parameters do not take into account the effect of the high degree of material anisotropy which controls both crack growth direction and fatigue endurance, as witnessed by the work of Fash et al in the following paper, and also Verpoest et al discussed previously.

Fash et al extend the previous work to correlate the behavior of plain and notched specimens under combined axial and torsional stress. They demonstrate not only the difficulty of using a number of failure criteria in the presence of fillet radii but also the need to extend multiaxial fatigue studies to notched components. This section is concluded with an extensive review of notched specimen behavior by Tipton and Nelson which is used as a basis for evaluation of the Society of Automotive Engineers generated data. They show that the strain ellipse and the plastic work approaches provide the best life estimates. These two methods are further compared in the next section.

7. *Nonproportional Loading Effects*

The penultimate section is reserved for studies of nonproportional loading and starts with a brief review by Lee on out-of-phase torsion and bending. He presents some critical tests to demonstrate the inappropriateness of Tresca and von Mises criteria and develops a simple rule for predicting long-life fatigue strength. Jordan et al look at complex wave forms to assess critically different design procedures and the dependence of damage accumulation on loading path. They too find that a shear strain based criterion and the hysteresis energy approach are both able to include path dependency although no approach is as yet entirely satisfactory. Conversely, Sonsino and Grubisic extending the classical deformation approach to fracture produce some convincing predictions for both cyclic softening and hardening materials. However, in common with several other papers in this volume, they have difficulty in accommodating torsional fatigue data.

A second paper by McDiarmid, determines the cyclic variation of critical biaxial stress parameters induced in a specimen that is loaded by two modes, each at different frequencies, thereby creating a variable phase pattern. The longest fatigue life reduction occurs when the difference in frequencies is small. He shows that simple design rules can be derived even for these apparently complex problems. This is the only study in this section which does not involve rotating principal stress axes, and therefore the fundamental question arises as to whether conclusions drawn concerning the damaging nature of nonproportional loading in the other four papers can be applied to out-of-phase stressing with fixed principal axes. The group of papers presented here imply that the fixed axis situation produces less severe fatigue life reductions.

Ohnami et al describe a detailed study involving different strain wave forms and compare concurrent with sequential loading modes to produce out-of-phase effects. The occurrence of transgranular fracture at 823 K and intergranular fracture at 923 K complicate the fracture analysis. No single method can predict the behavior of the material under both conditions although in each case greater cyclic work hardening was observed for nonproportional loading.

8. *Elevated Temperature Studies*

The final group of papers continues the theme introduced by Ohnami et al, and is introduced by the work of Marloff et al on cracking at notches caused by stresses in the first quadrant. This is an important area, also addressed by McDiarmid in section six because in this quadrant fatigue life is reduced due to the stress triaxiality factors which forms the basis of Marloff's approach. This is an interesting concept taken from ductile fracture studies, but it also requires further work to evaluate a wider range of biaxial stress states under cyclic conditions.

The following two papers study the mechanical and metallurgical factors, respectively, governing elevated temperature behavior. It is shown that the two parameters governing failure can be combined into a single equivalent shear strain to give a Manson-Coffin type law. However in these tests fatigue micromechanisms predominated, and it is recommended that more tests be done that include longer hold times to derive fatigue-creep design rules.

Failure by cyclic creep processes is addressed by Hayhurst et al. They show that in some materials damage is highly directional whether it is caused by creep or fatigue; in other materials this may not be so. Longer lives are observed under nonproportional loading in the former category. This indicates that current creep fatigue rules need to be reassessed.

The final paper addresses the practical problem of fatigue crack initiation and crack growth due to rapid thermal transients which induce a varying biaxial stress field together with steep temperature gradients. Crack initiation is treated in the traditional manner while crack propagation results indicate that cracks can grow faster than LEFM would predict. The interaction of thermal with mechanical stresses accentuates the biaxial nature of the system and requires a more detailed treatment in this increasingly important class of problems.

Conclusion

From the above brief comments on individual contributions it is concluded that a wide range of topics has been drawn together under the common heading of multiaxial fatigue. It has been demonstrated that the two traditionally distinct disciplines of fatigue, that is the one followed by Committee E-9 in crack initiation and the other of Committee E-24 in crack propagation, in fact examine complementary facets of the single phenomenon of fatigue failure. While studies of deformation behavior play a vital role in our understanding of fatigue, it is clear that the examination of failure modes has given deep insights into the mechanics of fracture, and it is important that our appreciation of the role of different modes of fracture should now be exploited and incorporated in life prediction methodologies.

This volume has concentrated primarily on low-cycle fatigue in combined tension-torsion tests. Undoubtedly this is of great value, but it is clear that long life predictions must be considered by incorporating the effects of thresholds and fatigue limits. Furthermore the need to account for behavior in the neglected first quadrant of stress space, for example, the equibiaxial test, is vitally important. Future work in these fields will inevitably impinge on design procedures, but some of the more complex stress situations, including out-of-phase effects, notches, stress gradients, mean stress, hold periods, etc. will provide other desirable and widely divergent testing modes which, if judiciously selected, can test the veracity of any life prediction technique.

K. J. Miller
M. W. Brown
Department of Mechanical Engineering, University of Sheffield, Sheffield, U.K.; symposium chairmen and editors.

Index

Copyright© 1985 by ASTM International www.astm.org

F

V

W

Y

ISBN 0-8031-0444-8